12th International Conference on Clouds and Precipitation

Proceedings – Volume 2

CANADIAN FREEZING DRIZZLE EXPERIMENT

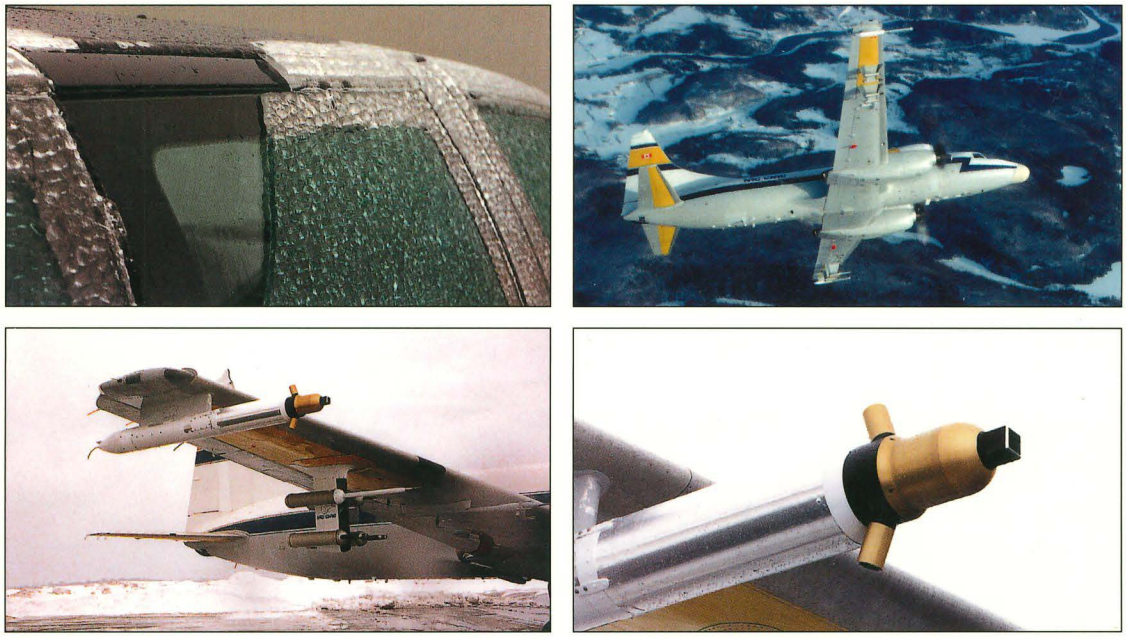

Digital Holographic Camera

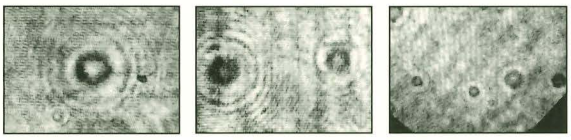

Freezing Drizzle

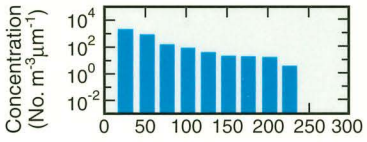

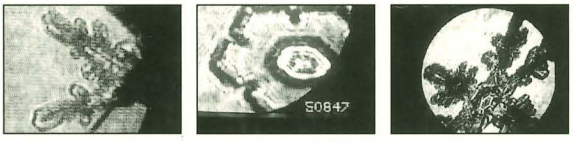

Dendrites/Plates

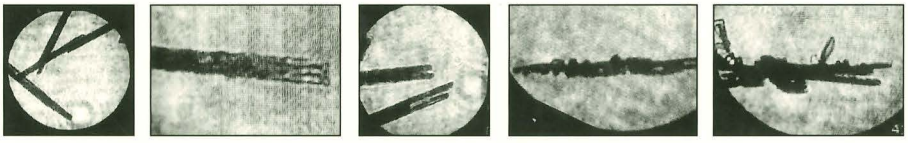

Needles at -6° C

Zurich, Switzerland

19–23 August 1996

Cumulus mediocris

Cumulonimbus mamma

Cirrus spissatus

Stratocumulus stratiformis

Altocumulus lenticularis

Cirrus vertebratus

Cirrus uncinus

Cumulonimbus calvus

Altocumulus undulatus

Altocumulus radiatus

Altocumulus floccus

Cirrus aviaticus

GREG McFARQUHAR

Proceedings Volume 2

12th International Conference on Clouds and Precipitation

Sponsored by

International Commission on Clouds and Precipitation

International Association of
Meteorology and Atmospheric Science

Supported by

Royal Meteorological Society
American Meteorological Society
World Meteorological Organization
Union Bank of Switzerland

FRONT COVER PICTURE

Montage of photographs illustrating the measurement of drop sizes using a new digital holographic camera during the Canadian Freezing Drizzle Experiment. See the paper by Lawson *et al.* on page 365 for fuller details. Many advances in Cloud Physics have come from carefully conducted field experiments making use of state-of-the-art instruments.

Printed and bound by:

Page Bros., Norwich

12th International Conference on Clouds and Precipitation

Zurich, Switzerland

19-23 August 1996

Conference Organization

International Scientific Programme Committee

P R Jonas (UK) (Chairperson)
J-L Brenguier (France)
R T Bruintjes (USA)
P Chylek (Canada)
T L Clark (USA)
A Flossmann (France)
A J Heymsfield (USA)
R A Houze (USA)
J Ogren (USA)
J-L Redelsperger (France)
A Slingo (UK)
H Sundqvist (Sweden)
T Takahashi (Japan)
A-S Wang (P R China)
M K Yau (Canada)

Local Organizing Committee

A Waldvogel (Chairperson)
E Choffat
D Hoegl
J Joss
R Luethi
H-H Schiesser
W Schmid
J Staehelin
M Waldvogel

LIST OF CONTENTS

Sessions 1.1-3.3, pages 1-697, are in Volume 1
Sessions 4.1-7.2, pages 698-1348, are in Volume 2

Session 1.3: OBSERVATIONS OF GLACIATED CLOUD MICROPHYSICS

Session 1.4: BASIC STUDIES OF GLACIATED CLOUD MICROPHYSICS

Session 1.5: AEROSOL MICROPHYSICS

Session 2.1: INSTRUMENTS AND TECHNIQUES FOR IN-SITU MEASUREMENTS

Session 2.2: INSTRUMENTS AND TECHNIQUES FOR REMOTE SENSING

Session 2.3: TECHNIQUES FOR DATA ANALYSIS

Session 3.1: STRUCTURE OF BOUNDARY-LAYER CLOUD FIELDS

Session 3.2: STRUCTURE OF DEEP CONVECTIVE CLOUD SYSTEMS

Session 3.3: STRUCTURE OF FRONTAL AND CIRRUS CLOUD

Session 4.1: MODELLING OF BOUNDARY-LAYER CLOUDS

Session 4.2: MODELLING OF CONVECTIVE CLOUDS

Session 4.3: MODELLING OF FRONTAL AND CIRRUS CLOUDS

Session 4.4: TECHNIQUES FOR CLOUD MODELLING

Session 5.1: AEROSOLS AND RADIATIVE PROPERTIES OF CLOUDS

Session 5.2: LARGE-SCALE PROPERTIES OF CLOUD FIELDS

Session 6.1: IMPACT OF CLOUDS ON AIR CHEMISTRY

Session 6.2: IMPACT OF CLOUDS ON AEROSOL CHEMISTRY

Session 7.1: PARAMETRIZATION OF CLOUD PROPERTIES

Session 7.2: APPLICATIONS OF CLOUD PHYSICS

LATE PAPERS

LIST OF AUTHORS

Volume 2

Sessions 4.1-7.2

EXPLORATORY CLOUD-RESOLVING SIMULATIONS OF COLD-SEASON ARCTIC STRATUS CLOUDS

William R. Cotton[1], Tamir G. Reisin[2], Sonia M. Kreidenweis[1], Graham Feingold[3], Peter Q. Olsson[1], and Jerry Y. Harrington[1]

[1]Colorado State University, Department of Atmospheric Science, Fort Collins, CO, USA
[2]Tel Aviv University, Dept of Geophysics and Planetary Sciences, Ramat Aviv, ISRAEL
[3]CSU/Cooperative Institute for Research in the Atmosphere, Fort Collins, CO, USA

1. INTRODUCTION

Arctic stratus clouds (ASC) are a major challenge to both medium range forecast models and climate models. Being relatively thin vertically and often quite inhomogeneous horizontally, especially over leads, they are difficult to simulate with large scale models having relatively crude horizontal and vertical grid-spacing. Because these clouds play an important role in the global radiation and hydrological budget, it is important to obtain a better quantitative understanding of their behavior.

A natural vehicle for enhancing our understanding of ASC is the application of cloud-resolving models (CRMs) such as large-eddy simulation (LES) models to exploratory simulations of wintertime and springtime ASC. Recently Cotton et al. (1995) discussed some of the challenges of modeling Arctic stratus clouds. This was based on several exploratory CRM simulations of warm-season Arctic stratus clouds using both the bulk microphysics and bin-resolving microphysics versions of RAMS.

The main conclusions in that paper are as follows:

- Systematic meteorological data (soundings) are sparse in polar regions. Initialization and verification often requires using coarse-resolution gridded data from operational forecast models; how real are they?
- Humidity measurements tend to be less reliable because of temperature conditions encountered in the Arctic.
- Good definition of surface characteristics (e.g., snow cover, sea ice, leads, distribution, leads, sea-surface temperatures, vegetation cover) which vary widely in time and space are needed.
- Surface models need to be expanded to include mixed lower boundaries of sea ice, melt pools on ice, and tundra vegetation characteristics.
- Turbulence models, especially sub-grid schemes in LES models, need to be improved to include a better representation of the stable Arctic boundary layer. A suitable scheme should provide a smooth transition between stable to unstable regimes such as might be encountered as low-level flow encounters sea ice and leads.
- Cloud microphysical models need to be refined and calibrated for these low liquid water content clouds. Current bulk autoconversion schemes appear to be inadequate for these layered clouds where CCN concentrations vary widely in time and space. Moreover, winter and spring clouds are mixed-phase in character, which necessitates extending the microphysics models to the ice phase. Measurements of the microstructure of those mixed-phase clouds are sorely needed.
- Most radiation parameterization schemes need to be evaluated to determine their applicability to high latitudes. Owing to high zenith angles and moderate optical depths, simple two-stream models may exhibit large errors in the Arctic. Radiation schemes also need to have cloud-optical properties derived in a consistent way with the existing band structure of the model. Large band-width can lead to overestimation of absorption properties of the hydrometeors in simple parameterizations of cloud-optical properties.

From the microphysical perspective, ASC are sometimes more akin to fogs than to their more dynamically vigorous low- and midlatitude marine stratus cousins. That is, they reside in very stably-stratified air masses with only weak vertical motions to drive those clouds. Subtle changes in cloud radiative properties, such as associated with liquid water path changes due to precipitation, can change a cloud's dynamic structure from one dominated by vertical turbulent mixing to one that is simply radiative cooled, much like a radiation fog. As a result simple parameterizations often used in bulk microphysics models such as autoconversion schemes, accretion, and hydrometeor sedimentation by an "average' terminal velocity are probably not suitable for use in many

ASC. In fact, we find that such schemes tend to make our CRMs quite vulnerable to bifurcation of solutions. We have therefore decided that further exploratory simulations of Arctic stratus should be done with a bin-resolving microphysics model.

2. THE MIXED-PHASE BIN MICROPHYSICS MODEL

The new bin microphysics scheme consists of three (ice crystals, aggregates and graupel) or five (pristine ice, rimed ice, aggregates, graupel and hail) ice species plus liquid cloud droplets and raindrops. The mass distribution functions of the different species are divided into 34 spectral bins spanning the range of masses found in clouds. The method of Multi-Moments (Tzivion et al., 1987) is used in the numerical solution of the different stochastic equations that describe the microphysical processes.

The microphysical processes treated are:

- Nucleation of drops (Stevens et al., 1996)
- Condensation / evaporation (Tzivion et al., 1989 ; Stevens et al., 1996)
- Collision-coalescence of drops (Tzivion et al., 1987)
- Binary breakup of drops (Low and List kernels) (Feingold et al., 1988)
- Nucleation of ice crystals (deposition, condensation-freezing, contact and homogeneous) (Walko et al., 1995)
- Secondary ice production (Hallett-Mossop mechanism) (Mossop, 1985; Ferrier 1994)
- Sublimation / deposition (Reisin et al., 1996)
- Ice-ice and drops-ice interactions (riming, accretion, etc.) (Reisin et al., 1996)
- Melting and shedding (Reisin et al., 1996)
- Sedimentation of drops and ice particles (Smolarkiewicz, 1983 - advection scheme; Beard, 1977 and Bohm, 1989 - terminal velocities)

3. THE CLOUD-RESOLVING MODEL

The mixed-phase bin-resolving microphysics model has been implemented into the large eddy simulation (LES) version of the Regional Atmospheric Modeling System (RAMS) that has been used to simulate marine stratocumulus clouds (Stevens, et al., 1996a,b; Feingold et al., 1996). This model is typically implemented with horizontal grid-spacings of about 50m over a 3000m domain, so that the dominant eddies in Arctic stratus clouds are explicitly represented. To better model the important cloud-radiative processes in Arctic stratus, a new two-stream radiation scheme has been implemented in RAMS. It is based on the work of Ritter and Geleyn (1992) which is essentially Zdunkowski's (1982) model with improvements. The performance of the model in highly anisotropic scattering conditions is similar to that of the delta-Eddington model in which the scattering properties and the distribution of the radiance field are linear in μ_0. This approximation seems to work well for large μ_0, however, it breaks down at the smaller μ_0 where there is strong nonlinearity in the scattering properties (see King and Harshvardhan, 1986). As the scattering properties of the layer become non-conservative ($\omega_0 < 1$) the reflection and transmission become more non-linear over larger ranges of μ_0. Therefore we have implemented appropriate scattering coefficients in the two-stream model that can reduce the errors associated with large zenith angles and non-conservative atmospheres.

To evaluate our cloud-optical properties we compare model derived heating rates with those predicted by more accurate models. Preliminary results seem to show good agreement in the infrared but somewhat worse agreement in the solar bands. For thick clouds our heating rates tend to be overestimated by around 1 K/hour. Cooling rates, however, seem to agree within 0.2 K/hour.

4. TEST CASES

Currently we are seeking case studies of mixed-phase Arctic stratus clouds that provide documentation of both the microphysical, radiative, and dynamical structure of the clouds along with adequate data for initializing the model. We are finding a paucity of suitable cases, but hope that cases observed during BASE (Beaufort and Arctic Storms Experiment) such as the Oct 4-5 flight may suit our needs.

5. ACKNOWLEDGMENTS

Thanks are due to Brenda Thompson for her assistance in processing the manuscript. This research was supported by the Environmental Sciences Division of the U.S. Department of Energy under contract number DE-FG03-95ER61958 as part of the Atmospheric Radiation Measurement Program.

6. REFERENCES

Beard, K.V., 1977: Terminal velocity adjustment for cloud and precipitation. *J. Atmos. Sci.*, **33**, 851-864.

Bohm, H.P., 1989: A general equation for the terminal fall speed of solid hydrometeors. *J. Atmos. Sci.*, **46**, 2419-2427.

Cotton, W.R., S. Kreidenweis, P.A. Olsson, J.Y. Harrington, M.J. Weissbluth, G. Feingold, 1995: Challenges to modeling Arctic stratus clouds. ETL report, National Oceanic and Atmospheric Administration, Boulder, CO, in preparation.

Feingold, G., S. Tzivion, and Z. Levin, 1988: The evolution of raindrop spectra. Part I: Stochastic collection and breakup. *J. Atmos. Sci.*, **45**, 3387-3399.

Feingold, Graham, Bjorn Stevens, W.R. Cotton, and A.S. Frisch, 1995: On the relationship between turbulent kinetic energy and drizzle production in numerically simulated stratocumulus clouds. Submitted to *The Journal of the Atmospheric Sciences*

Ferrier, B.S., 1994: A double-moment multiple-phase four-class bulk ice scheme. Part I: Description. *J. Atmos. Sci.*, **51**, 249-280.

King, Michael D. and Harshvardhan, 1986: Comparative Accuracy of Selected Multiple Scattering Approximations. *J. Atmos. Sci*, **43**, 784-801.

Mossop, S.C., 1985: Secondary ice particle production during rime growth: the effect of drop size distribution and rime velocity. Quart. *J.Roy. Meteor. Soc.*, **111**, 1113-1124.

Reisin, T., Z. Levin, and S. Tzivion, 1996: Rain production in convective clouds as simulated in an axisymmetric mod el with detailed microphysics. Part I: Description of the model. *J . Atmos. Sci.*, **53**, 497-519.

Ritter, Bodo and Jean-Francois Geleyn, 1992: A Comprehensive Radiation Scheme for Numerical Weather Prediction Models with Potential Applications in Climate Situations. *Mon. Wea. Rev.*, **120**, 303-325.

Slingo, A., and H. M. Schrecker, 1982: On the Shortwave Radiative Properties of Stratiform Water Clouds. *Quart. J. R. Met. Soc.*, **108**, 407-426.

Smolarkiewicz, P.K., 1983: A simple positive definite advection scheme with small implicit diffusion. *Mon. Wea. Rev.*, **111**, 479-486.

Stevens, Bjorn, Robert L. Walko, Graham Feingold, and William R. Cotton, 1996: A note: On the spurious production of cloud edge supersaturations by Eulerian models. Accepted to *Monthly Weather Review*

Stevens, Bjorn, Graham Feingold, William R. Cotton, and Robert L. Walko, 1996: On elements of the microphysical structure of numerically simulated stratocumulus. Accepted to *The Journal of the Atmospheric Sciences*

Tzivion, S., G. Feingold, and Z. Levin, 1987: An efficient numerical solution to the stochastic collection equation. *J. Atmos. Sci.*, **44**, 3139-3149.

Tzivion, S., G. Feingold, and Z. Levin, 1989: The evolution of raindrop spectra. Part II: Collisional collection/breakup and evaporation in a rainshaft. *J. Atmos. Sci.*, **46**, 3312-3327.

Walko, R.L., W.R. Cotton, M.P. Meyers, and J.L. Harrington, 1995: New RAMS cloud microphysics parameterization. Part I: the single-moment scheme. *Atmos. Res.*, **38**, 29-62.

Zdunkowski, Wilford G., Ronald M. Welch and Gunther Korb, 1980: An Investigation of the Structure of Typical Two-stream methods for the Calculations of Solar Fluxes and Heating Rates in Clouds. *Contrib. Atmos. Phys.*, **53**, 147-166.

MULTILEVEL SIMULATION OF RADIATIVELY DRIVEN STRATOCUMULUS ENTRAINMENT

David E. Stevens
Courant Institute of Mathematical Sciences, New York University

Cristopher S. Bretherton
Department of Atmospheric Sciences, University of Washington

1 Introduction

Marine stratus clouds are an important component of the earth's climate. These clouds cover a significant fraction of the earth's surface and have a large effect on its radiation budget due to their strong radiative cooling. It is believed that radiative cooling from a 4% increase in global stratocumulus amount would counteract warming from doubling in CO_2. The top of these clouds is a stably stratified region a few tens of meters thick which is being gradually entrained by eddies driven by strong radiative cooling ~ 7 K/day. An important unresolved problem for marine stratus clouds is determining how entrainment at the inversion scales with respect to the strength of underlying convective motions. Diagnosing entrainment is of fundamental importance in predicting the evolution of these boundary layers.

Numerical simulations of these clouds which resolve at least the large eddy motions involved in a stratus boundary layer are increasing in importance. These simulations make possible the analysis of many regimes where observations are unavailable or are difficult to obtain. A GCSS (GEWEX Cloud System Studies) model intercomparison workshop in August 1995 found that currently used resolutions and methods in numerical simulations do not adequately simulate entrainment (MacVean 1996; Bretherton 1996). The goal of the intercomparison was to determine the effect of different numerics and resolution on a standardized test problem. This test problem was first considered by Nicholls and Turton (1986) who compared entrainment calculated from aircraft measurements with a laboratory experiment by McEwan and Paltridge (1976). It is an analogy of a stratocumulus cloud which uses a radiatively active "smoke" tracer to mimic the longwave cooling properties of cloud water droplets without evaporative cooling and virtual effects. This simulation was chosen to isolate the effect on entrainment by radiation and to simplify model comparison.

Simulating entrainment into the tops of stratus clouds is a challenging problem. It involves properly resolving the complicated interactions between radiation, turbulent entrainment and moist thermodynamics that occur there. An important verification of a simulation's accuracy is the extent by which it changes as the resolution and size of the domain are increased. Another verification is to investigate the effect of different numerics. Our research shows entrainment processes can be simulated more accurately using third-order forward-in-time upwinding and a sophisticated scheme for locally refining the entrainment region. Improving the advection method improves results without appreciably increasing the computational expense. local refinement increases the resolution at the inversion without the expense of high resolution everywhere in the domain.

Our research investigated the dependence of entrainment rate on Richardson number and a convective velocity scale for the GCSS test problem. We investigated the effect of varying the resolution used at the inversion by both refining the mesh in each direction and by changing the aspect ratio. We then investigated the effect of using local refinement and varying the advection scheme. The relevance of these tests to simulations presented at the GCSS intercomparison is discussed.

2 Model Description

The model integrates the anelastic equations of Ogura and Phillips (1962) for a dry environment using the numerical flow solver described in Stevens et. al. (1996). It is a forward-in-time solver that uses either second or third-order upwinding and is able to decompose the computational domain into clusters of locally refined grids. The model breaks thermodynamic variables down into an isentropic base state, environmental perturbation in hydrostatic balance and dynamic deviation from the environmental

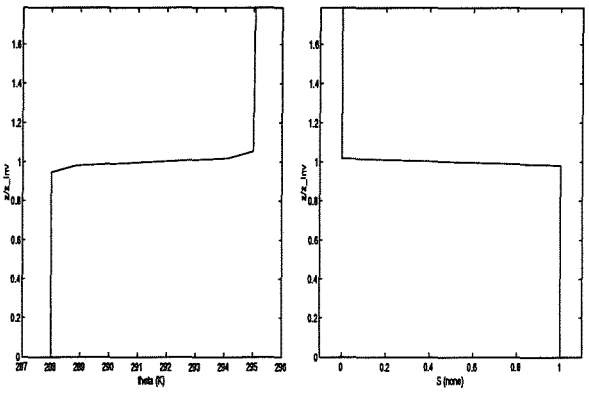

Figure 1: Sounding used in the GCSS intercomparison

state

$$\theta(\vec{x},t) = \theta_0 + \theta_1(z) + \theta_2(\vec{x},t) = \theta_{env}(z) + \theta_2(\vec{x},t).$$

The anelastic equations for the GCSS experiment are:

$$\begin{aligned} \frac{du_i}{dt} &= -\frac{\partial \phi}{\partial x_i} + \delta_{i3} g \theta^*, \qquad (1) \\ \frac{d\theta^*}{dt} &= \frac{-1}{\rho_0 C_{pd}} \frac{\partial F_r}{\partial z}, \\ \frac{dS}{dt} &= 0, \\ \frac{\partial \rho_0 u_j}{\partial x_j} &= 0 \end{aligned}$$

where the scaled pressure perturbation $\phi = C_{pd}\theta_0\pi_2$ is often referred to as the Exner function, ρ_0 is the density associated with the base state, and $\theta^* = (\theta - \theta_{env})/\theta_0$ is a scaled potential temperature perturbation from the environment. Radiation is parameterized with a radiatively active tracer S as a net upward long-wave radiative flux

$$F_r(z) = F_r(H)e^{-K_a S_p(z)}$$

where $F_r(H)$ is the radiative flux at the top of the domain H and S_p is the tracer optical depth

$$S_p(z) = K_a \int_z^H \rho S dz.$$

A scaling relationship for entrainment was proposed by McEwan and Paltridge (1976) and supported by Saylor and Briedenthal (1996) with laboratory experiments. This relationship is useful for measuring the accuracy of numerical simulations and is given by

$$\frac{w_e}{w_*} = \frac{A}{Ri}. \qquad (2)$$

Here Ri is the Richardson number, w_e the entrainment velocity and w_* the convective velocity scale

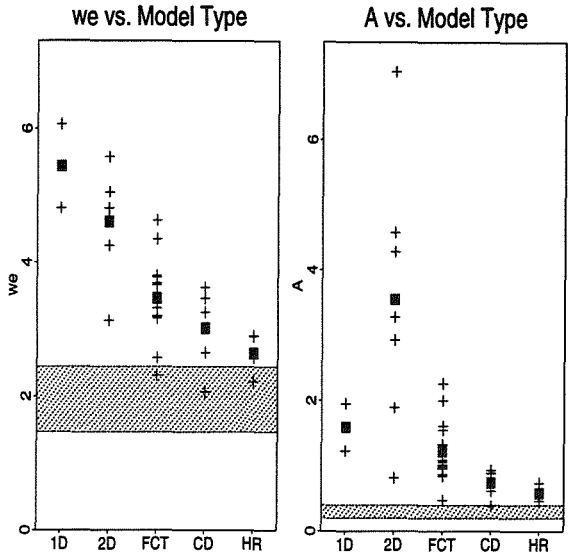

Figure 2: w_e (mm/s) and A for the GCSS intercomparison. The acronyms are: (1D) 1D models, (2D) 2D models, (FCT) flux-corrected models, (CD) centered-difference models, and (HR) simulations with increased vertical resolution (Bretherton 1996).

given by

$$\begin{aligned} Ri &= \frac{g z_{inv} \Delta\theta_{inv}/\theta_0}{w_*^2} \\ w_e &= \frac{\partial z_{inv}}{\partial t} \\ w_*^3 &= 2.5 \int_0^H g \frac{\overline{w'\theta'}}{\theta_0} dz \end{aligned}$$

where g is gravity, z_{inv} is the inversion height, and $\Delta\theta_{inv}$ is the potential temperature jump across the inversion. $\overline{w'\theta'}$ is specified as the horizontal average of the vertical flux of θ.

The GCSS intercomparison simulation was used as reference configuration for each of our tests. This simulation used a domain 3200 meters wide in each horizontal direction and 1250 meters in the vertical. The vertical and horizontal resolutions were 25 m and 50 m, for an aspect ratio of $\Delta z/\Delta x$ of 0.5. The initial soundings of θ and S are presented in Figure 1 and the inversion is located at $z_{inv} = 700$ m. A net vertical radiative flux of $F_r(H) = 60\text{W/m}^2$ with absorption coefficient $K_a = .02\text{m}^2/\text{kg}$ was imposed. This yielded an optical depth of 50 m. Motion was created in an initially calm domain by a random temperature perturbation of 0.1 K at all gridpoints below 700 m. After two hours of simulation, the entrainment rate and other turbulent statistics equilibrated and the next hour was used to calculate average values of these statistics centered at 2.5 hours.

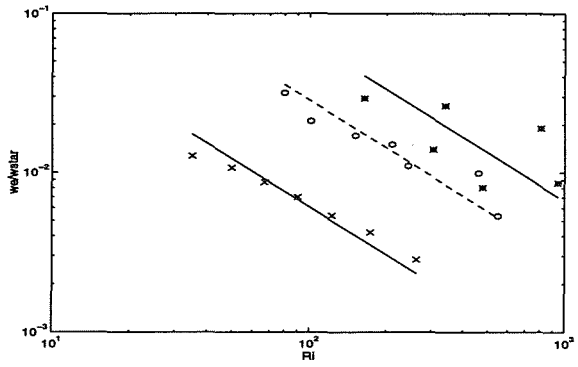

Figure 3: Comparison of 2D second-order upwinding (*), 2D third-order upwinding (o), and 3D third-order upwinding (x). on log-log plot

3 Entrainment Scaling

Our analysis consisted of determining how the scaling law constant A varies over a range of w_* and Ri. A varied considerably from model to model in the GCSS intercomparison (Figure 2) and simulation to simulation (Figure 3). General fits of the form $w_e/w_* = \alpha Ri^{\beta}$ were found to be unreliable, due to shifts in the diagnosed power being compensated by shifts in the constant multiplier. By computing A over sufficiently many simulations, it was possible to verify that (2) is a valid scaling law and that one can observe trends in A due to changes in the simulation. We observed effects on A by computing for each computational configuration the following simulations:

Simulation	1	2	3	4	5	6	7
$\Delta\theta_{inv}$	3	4	5	6	7	8	9
$F_r(H)$	120	105	90	75	60	45	30

By varying $F_r(H)$ and $\Delta\theta_{inv}$ simultaneously, we were able to evaluate the scaling law over a wide range of Ri.

The reference configuration in two-dimensions had quantitatively different behavior than in three. The three-dimensional set of simulations had an A of 0.61 as compared to the two-dimensional 2.85. These values are low in comparison to the other flux-corrected and two-dimensional models. This behavior was consistent with the third-order upwinding models by MacVean (1996) and the high resolution simulations submitted to the GCSS intercomparison. Both sets of simulations exhibited Ri^{-1} entrainment scaling. Simulation 5 corresponds to the GCSS intercomparison simulation. For this particular simulation, our model had a higher entrainment rate, 8 mm/s in two and 5 mm/s in three dimensions than the other flux-corrected and two-dimensional models

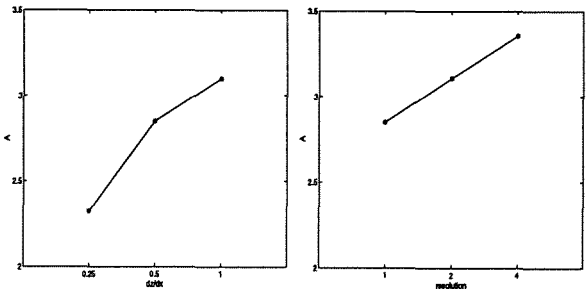

Figure 4: Scaling values A for varying varying mesh aspect ratio $\Delta z/\Delta x$ (left) and resolution (right).

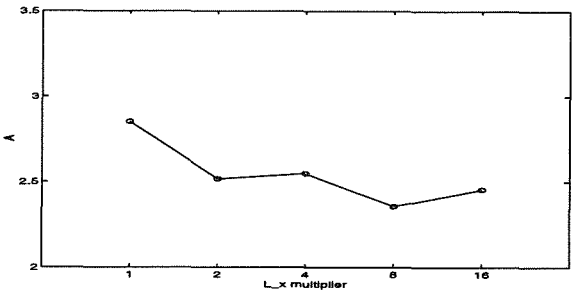

Figure 5: Scaling value A for varying domain size.

in Figure 2. This was offset by higher w_* in each case.

Two-dimensional simulations were used to test variations of domain size and resolution that are currently beyond our computational capacity in three-dimensions. Although results are quantitatively different, these simulations should have similar qualitative behavior to changes in resolution. It was found that doubling the resolution produced a 10% increase in A which was 2.8 for the GCSS reference configuration. This occurred whether the increased resolution was refined in all directions simultaneously or was due to an increase in the horizontal resolution. Increasing only the vertical resolution, actually decreased A running counter to the trend of increasing resolution (Figure 4). The domain width was found to have a small effect on A. By varying the domain width from 1-16 times the width of the reference configuration, it was found that A decreased by 15%, until the domain width was doubled at which point A stabilized around 2.5 (Figure 5). This indicates that doubling the reference domain width is optimal for meaningful results.

The choice of advection scheme had an important effect on the entrainment scaling (Figure 3). Many of the advection schemes used in the intercomparison have second-order dispersive errors. It was found that switching from third-order upwinding to second-order upwinding in two dimensions created noisier results with a higher degree of uncertainty. The second-order upwinding had an A of 6.6.

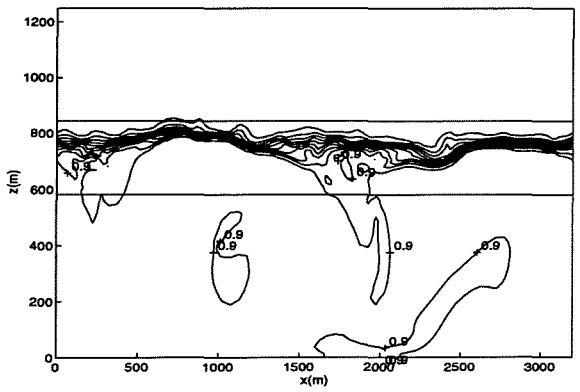

Figure 6: Contour plot of S at 2.5 hours. The contour intervals is 0.1 .

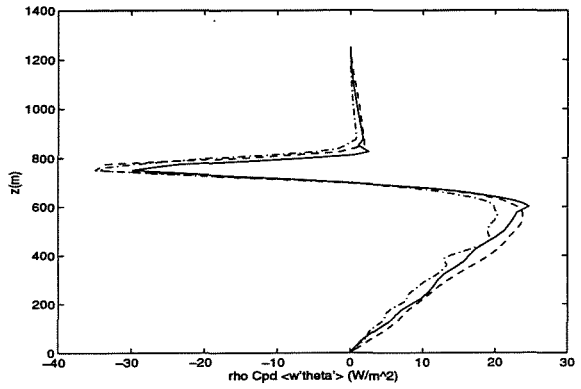

Figure 7: $\rho C_{pd}\overline{w'\theta'}$ for reference simulation (dash-dot), double the reference resolution (dash), and locally refined simulation (solid).

Figure 4b indicates that A converges slowly with increased resolution. More than 4 times the reference resolution is required for A to fully converge. This is a severe limitation on accurately predicting this quantity, due to the 8 and 16 increase in computations required to double the resolution in two and three-dimensions. Local refinement has the promise of avoiding this problem by resolving the sharp gradients and shears at the inversion, where the flow is most weakly resolved. Our locally refined model is based on a conservative formulation of the anelastic equations (1) and is often able to emulate a uniform simulation at the resolution of the most refined mesh (Stevens 1996). Figure 6 shows the reference simulation where the layer between 600 and 800 meters has been refined by a factor of two. This refined simulation when compared to a uniform simulation with only the base domain and a uniform simulation with double the resolution had vertical fluxes that tended towards those of the higher resolution uniform simulation throughout most of the lower mixed layer (Figure 7). The refined simulation was computationally less expensive requiring only half of the work of the high resolution uniform simulation.

4 Conclusions

These simulations indicate that it is possible to numerically compute well-behaved scaling laws for entrainment, although these simulations are still far from resolving entrainment at the inversion. It appears that numerical diffusion, rather than resolved overturning is responsible for most of the entrainment in the more stratified simulations 4-7. Scaling arguments indicate that the Richardson number of the reference configuration requires at least 3 m grid resolution at the inversion to resolve overturning at the inversion. Promising technologies for overcoming this limitation are improved advection methods and adaptive refinement. We are continuing our research by investigating adaptive refinement in two and three dimensions. Future work will compare adaptive simulations with high resolution uniform calculations and investigating the effects of evaporative cooling on entrainment dynamics.

Acknowledgements

This research was supported by NSF grants ATM-8858846 and ATM-9216645.

References

Bretherton, C. S., 1996: GCSS Boundary Layer Cloud Working Group Home Page. *http://amath.washington.edu/breth/.*

MacVean, M. et. al., 1996: *Quart. J. R. Meteor. Soc.*, In preparation.

McEwan, and Paltridge, 1976: Radiatively driven thermal convection bounded by an inversion - a laboratory simulation of stratus clouds. *J. Geophys. Res.*, **81**, 1095-1102.

Nicholls, and Turton, 1986: An observational study of the structure of stratiform cloud sheets: Part II. Entrainment. *Quart. J. R. Meteor. Soc.* **112** 461-480.

Ogura, Y., and N. Phillips, 1962: Scale Analysis of Deep and Shallow Convection in the Atmosphere. *J. Atmos. Sci.*, **19**, 173-179.

Sayler, B., and R. Breidenthal, 1996: in preparation.

Stevens, D. E. and C. S. Bretherton, 1995: A forward-in-time advection scheme and adaptive multilevel flow solver for nearly incompressible atmospheric flow. *J. Comput. Phys.*, Submitted.

DECOUPLING, CUMULIFORM PENETRATIVE ENTRAINMENT, AND THE SIMULATED BREAKUP OF MARINE STRATOCUMULUS CLOUDS

Matthew C. Wyant[1], Christopher S. Bretherton[1], Hugh A. Rand[2], and David Stevens[3]

[1]Atmospheric Sciences and [2]Applied Mathematics, University of Washington, Seattle, WA 98195, USA
[3]Courant Institute of Mathematical Sciences, New York, NY , USA

1. INTRODUCTION

A two-dimensional eddy-resolving model is used to study the transition from the stratocumulus topped boundary layer to the trade cumulus boundary layer in 10-day Lagrangian simulations. We interpret the dynamics of the transition by dividing it into two conceptual stages. The first stage is the decoupling of the initially well-mixed shallow stratocumulus-capped boundary layer, induced by rapid increase in the surface latent heat fluxes. After decoupling, cloud cover remains high, but the cloudiness regime changes to sporadic cumulus that detrain into stratocumulus clouds. In the second transition stage, further SST increase causes the cumuli to become deeper and more vigorous, penetrating further into the inversion and entraining more dry above- inversion air. We show that the increasing entrainment causes significant drying of the cumulus updrafts before detrainment, strongly reducing the lifetime of the detrained stratocumulus clouds. We also have tested the influence of subsidence, surface windspeed, SST, lower-tropospheric stability, and microphysical parameters on the cloudiness transition in several experiments.

2. MODEL PHYSICS

For our simulations we use the two-dimensional HUSCI eddy-resolving model. Only a brief outline of the model physics is presented here; detailed documentation of the model can be found in Wyant et al. (1996). The model uses anelastic momentum equations, leapfrog-trapezoidal time differencing, a momentum flux-corrector (Zalesak 1978) and a positive definite scalar-advection scheme (Smolarkiewicz and Grabowski (1990)). The Smagorinsky-type subgrid-scale turbulence scheme is modified for moisture effects (Mason 1985). A simple two-category microphysics scheme is used. The model uses two-stream radiation schemes; a longwave emissivity scheme and a 3-band shortwave scheme. The surface fluxes are determined from a simple bulk formulation.

3. SIMULATION SETUP

The 10-day simulation presented here is described in detail in Wyant et al. (1996). The simulated domain is 3 km high and 4 km wide, with a grid resolution of 25 m in the vertical and 50 m in the horizontal. The upper and lower boundary conditions are varied with time to follow an idealized trajectory in the summertime subtropical northeast Pacific.

The initial SST is 285 K and increases at a rate of 1.5 K day^{-1} eventually reaching 300 K. The other boundary conditions are kept fixed to simplify the analysis. The effects of the upper-air stability and varying subsidence are explored in sensitivity simulations not presented here. The marine boundary layer (MBL) is initially 600 m deep and well-mixed, with a solid capping stratocumulus deck. The liquid water potential temperature, θ_l , is 283.7 K and the initial total water mixing ratio is 7 g kg^{-1}. The upper air temperature sounding is similar to Weathership N climatology (Klein et al. 1995), with a θ_l above the inversion equal to $(296.3 + 3.36Z)$ K, where Z is the height in km. The vapor mixing ratio above the inversion is set to 3.5 g kg^{-1}. The large-scale divergence, D, is held constant at 3.0×10^{-6} s^{-1} . The large-scale subsidence velocity, W, used in the simulation is given by $W = -Dz$ where z is the height.

The downward shortwave radiation is based on July 30°N conditions. We use a constant down-

ward shortwave radiative flux equal to the mean downward flux averaged over an entire diurnal cycle. An otherwise identical simulation with the full diurnal cycle of radiation is presented in Wyant et al. (1996).

4. RESULTS AND ANALYSIS

The simulation can be divided into three stages: a shallow well mixed stratocumulus-topped boundary layer (days 0-3), a deeper decoupled boundary layer with cumulus rising into stratocumulus (days 3-8), and an even deeper trade-cumulus boundary layer without much overlying stratocumulus (days 8-10). These three stages were analyzed in Krueger et al. (1995) using a two-dimensional cumulus ensemble model in a simulation with similar surface conditions to the simulation presented here.

The evolution of the horizontal-mean soundings of θ_l and q_t is plotted in Figure 1 in two-day intervals. As the SST rises, the boundary layer deepens, and the θ_l inversion shrinks from 15 K to 4 K.

The stratocumulus topped boundary layer in days 0-3 is topped by a horizontally homogeneous cloud deck, about 200 m thick and nearly adiabatic in liquid water content (the mean cloud top liquid water content is 0.3 g kg^{-1}). As the MBL deepens, it decouples into a moist surface layer overlain by a dryer cloud layer. This decoupling is not caused by drizzle effects or shortwave heating, but instead because of the increasing latent heat fluxes due to the rising SST. Increasing latent heat fluxes cause an increasing disparity in buoyancy between updrafts and downdrafts within, but not below, the cloud. This disparity drives more turbulence and cloudtop entrainment, which causes the downdrafts below cloudbase to become warmer than the updrafts. This situation is unsustainable energetically. The resulting 'deepening-induced' decoupling changes the nature of convection in the boundary layer. The process is described in more detail in Bretherton and Wyant (1996).

After decoupling, the updraft cloud base lowers significantly below the mean stratocumulus cloud base, resulting in a MBL with cumulus rising into a solid stratus deck. The extent of decoupling, as measured by the difference in q_t between the lower MBL and upper MBL, grows rapidly, as

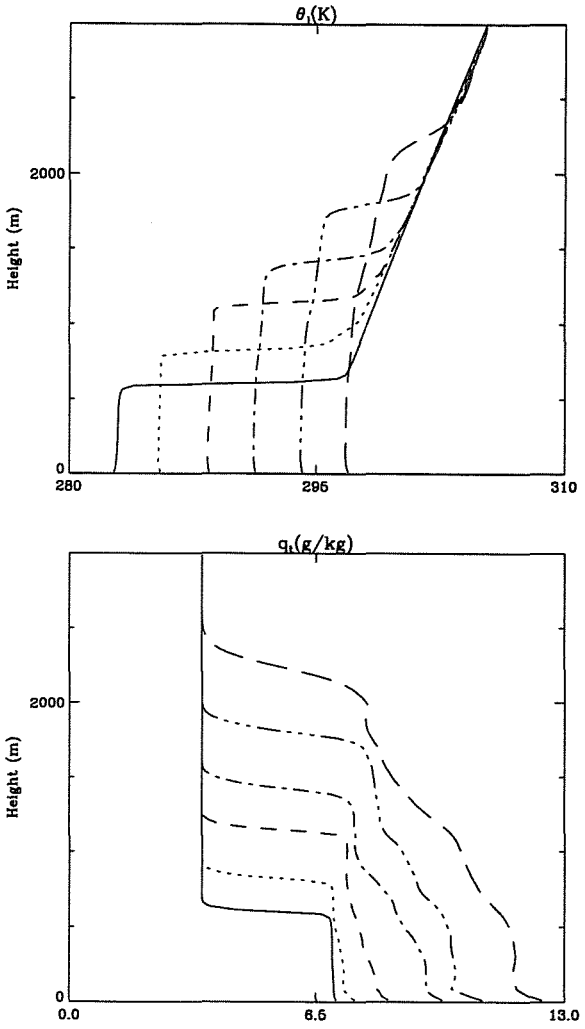

Figure 1: Horizontal mean soundings of θ_l and q_t at day 0 (solid), day 2 (short dashed), day 4 (long dashed), day 6 (long/short dashed), day 8 (long/3-short dashed), and day 10 (very long dashed).

does the degree of convective instability.

At this intermediate stage in the simulation, with shallow cumulus rising into stratocumulus clouds, the cloud fraction remains high. But as the MBL deepens and the cumulus layer deepens, the areal coverage of the stratus becomes smaller, eventually resulting in just a trade-cumulus type MBL. We believe the breakup of the stratocumulus is due to the drying caused by penetrative entrainment generated by cumulus clouds striking the inversion.

The evolution of MBL depth, MBL-top entrainment, cumulus mass flux, and 'satellite' fractional cloudiness during days 5-10 of the simulation are shown in Figure 2. The boundary layer depth is determined as the horizontal- mean level at which the total water mixing ratio drops below 5.0

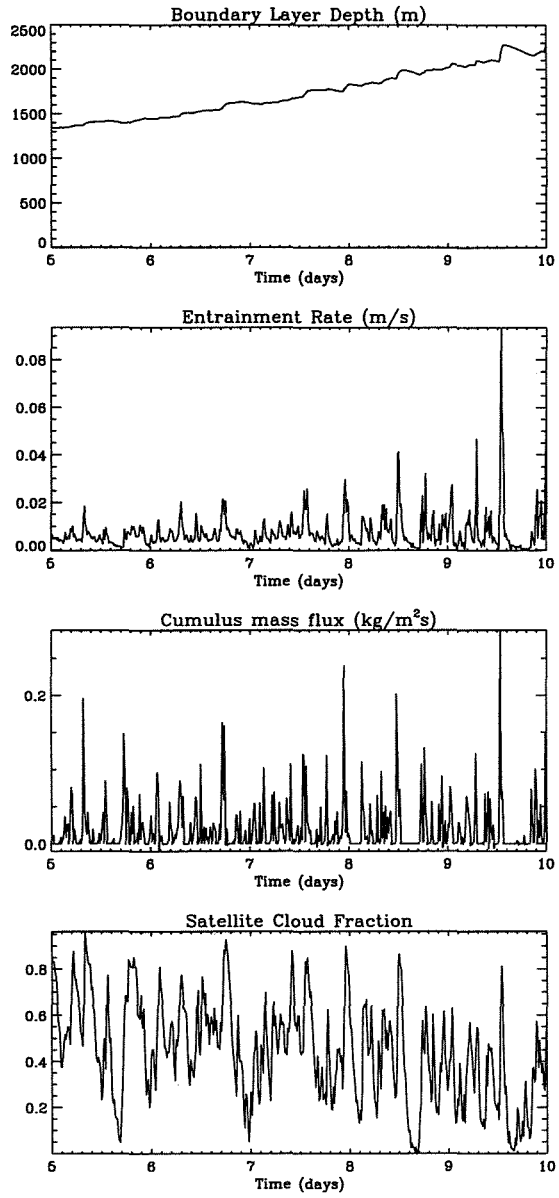

Figure 2: Boundary layer depth (z_i), MBL-top entrainment rate, cumulus mass flux at $0.75z_i$, and cloud fraction for the last 5 days of the simulation.

g kg $^{-1}$. Over this period, the MBL deepens from 1480 m to 2300 m, though the deepening is not as gradual as during the early stages of the simulation. The entrainment rate, also plotted in Figure 2, is highly variable, and is strongly related to cumulus convection. As a measure of the activity of the cumulus, we also plot the cumulus mass flux at 0.75 z_i, where z_i is the instantaneous MBL depth. The largest peaks of cumulus mass flux correspond to maxima in entrainment rate, indicating that the cumulus updrafts are causing significant entrainment as they collide with and penetrate the inversion. The stratocumulus clouds formed by outflow near the top of the MBL take 2 or 3 hours to decay following detrainment, and cause further entrainment due to enhanced longwave cooling and turbulence.

The overall impact on cloudiness is shown on the last plot in Figure 2, the fractional cloudiness during days 5-10. This is computed as the fraction of model-domain columns which have a shortwave cloud optical depth greater than 1.8 . The cloud fraction is highly variable, though the time-averaged cloudiness is gradually decreasing. Local maxima in cloud fraction are nearly coincident with large cumulus clouds, but following the largest cumulus clouds there is frequently a very large drop in cloud fraction. The cumulus convection is the only source of moist surface air sustaining stratocumulus clouds near the MBL-top against entrainment drying. However, the largest cumulus clouds entrain enough dry above-inversion air to dry out the upper-MBL and bring about the dissipation of the stratocumulus.

The large cumulus-induced spikes in entrainment grow larger with time even though the cumulus mass flux spikes are not growing significantly in height. Evidently cumulus clouds are causing more entrainment per unit of updraft mass as the simulation proceeds. Evidence for this is shown in Figure 3, a scatter plot of MBL-top entrainment mass flux versus cumulus mass flux, segregated by day. Also plotted are best fit lines for each 24-hour period. The slopes of the lines are a measure of the efficiency of the cumulus clouds in generating MBL-top entrainment. They increase monotonically with time, indicating that the later cumulus clouds are causing more entrainment.

The cause of this greater entrainment efficiency is the increasing depth of the cumulus layer with time, and the increase in CAPE that accompanies this deepening. The CAPE of the horizontal-mean soundings increases rapidly from 22.0 m^2 s^{-2} during day 5-6 to 86.9 m^2 s^{-2} during day 9-10. This increase results in more vigorous cumulus clouds which entrain more dry air relative to the amount of moisture they transport up to the stratocumulus clouds. The result is the drying out of the upper MBL and the dissipation of the stratocumulus.

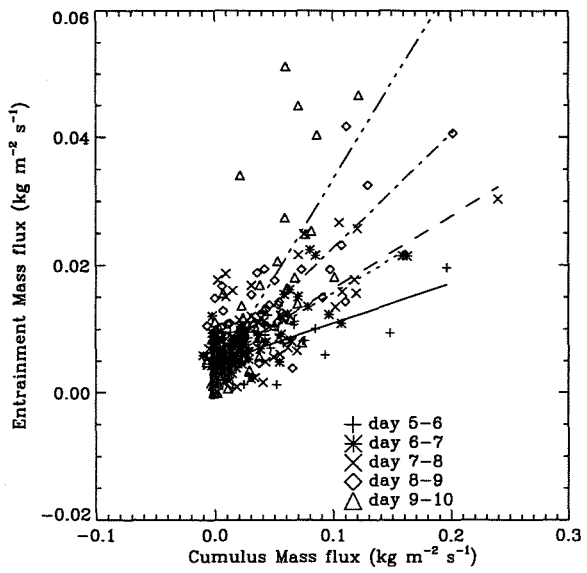

Figure 3: Scatter plot of entrainment mass flux vs. cumulus mass flux for simulation days 5-10. Best fit lines are plotted for day 5-6 (solid), day 6-7 (dotted), day 7-8 (dashed), day 8-9 (dashed/dotted), and day 9-10 (dashed/3-dotted).

5. CONCLUSIONS

The simulation presented here shows two important phases in the stratocumulus to trade cumulus transition. The first phase is decoupling of the boundary layer leading to the formation of cumulus clouds under the stratocumulus deck. The second phase is the dissipation of the overlying stratocumulus clouds due to the increasing penetrative entrainment of the cumulus clouds.

As discussed in Wyant et al. (1996), the role of the cumulus convection in driving MBL-top entrainment appears to be more important in determining the breakup of the stratocumulus clouds than the effects of cloud-top entrainment instability.

6. ACKNOWLEDGEMENTS

This work supported by ONR grant N00014-90-J-1136, NASA grant NAG-1-1711 and a NSF Graduate Fellowship awarded to M. C. Wyant.

7. REFERENCES

Bretherton, C. S., and M. C. Wyant, 1996: Moisture transport, lower tropospheric stability, and decoupling of cloud-topped boundary layers. *J. Atmos. Sci.*, accepted for publication.

Klein, S. A., D. L. Hartmann, and J. R. Norris, 1995: On the relationships among low cloud structure, sea surface temperature, and atmospheric circulation in the summertime northeast Pacific. *J. Climate*, **8**, 1140-1155.

Krueger, S. K., G. T. McLean, and Q. Fu, 1995: Numerical simulation of the stratus-to-cumulus transition in the subtropical marine boundary layer. Part I: Boundary-layer structure. *J. Atmos. Sci.*, **52**, 2839-2850.

Mason, P. J., 1985: A numerical study of cloud streets in the planetary boundary layer. *Bound.-Layer Meteor.*, **32**, 281-304.

Smolarkiewicz, P. K., and W. W. Grabowski, 1990: The multidimensional positive definite advection transport algorithm: Nonoscillatory option. *J. Comput. Phys.*, **86**, 355-375.

Wyant, M. C., C. S. Bretherton, H. A. Rand, and D. Stevens, 1996: Numerical simulations and a conceptual model of the stratocumulus to trade cumulus transition. *J. Atmos. Sci.*, accepted for publication.

Zalesak, S. T., 1979: Fully multidimensional flux corrected transport algorithm for fluids. *J. Comput. Phys.*, **31**, 335-363.

Simulations of the ASTEX Lagrangian Experiments with 1D and 2D Boundary Layer Models

Steven K. Krueger[1], Ching-Hsuan Chen[1], Matthew C. Wyant[2], and Christopher S. Bretherton[2]

[1]Dept. of Meteorology, University of Utah, Salt Lake City, UT, USA

[2]Dept. of Atmospheric Sciences, University of Washington, Seattle, WA, USA

1. Introduction

The representation of stratocumulus and trade cumulus boundary layer clouds in large-scale and mesoscale predictive models continues to be an unsolved problem. The development of boundary layer cloud parameterizations requires an understanding of the processes that are responsible for the generation, maintenance, and dissipation of boundary layer clouds. The Atlantic Stratocumulus Transition Experiment (ASTEX) was designed to address the following questions: (1) What are the physical proceses responsible for the transition from stratocumulus to trade cumulus clouds? (2) What are the physical processes that select cloud type and amount?

The transition from stratocumulus to trade cumulus clouds occurs primarily over the eastern subtropical oceans where the low-level flow is equatorward over increasing SSTs. ASTEX took place in such a transition region over the Atlantic Ocean about 1500 km southwest of Portugal during June 1992. ASTEX used satellites, aircraft, and surface sites (islands and ships) for instrument platforms. ASTEX rawinsonde soundings were incorporated into ECMWF analyses. See Albrecht et al. (1995) for a more complete description of ASTEX.

The primary observational strategy used during ASTEX was an Eulerian approach that examined the temporal variations within a fixed region. The secondary strategy was a Lagrangian approach that follows the evolution of a column of boundary layer air. One of the chief advantages of the Lagrangian approach is that the column's evolution does not depend on horizontal advective tendencies, which are difficult to measure. Two Lagrangian experiments were performed during ASTEX during which the evolution of cloud-topped boundary layers were documented using almost continuous aircraft measurements: Lagrangian 1 (42 hours starting on June 12 at 1600 UTC) and Lagrangian 2 (40 hours starting on June 18 at 2230 UTC). See Bretherton and Pincus (1995) and Bretherton et al. (1995) for a more complete description of the ASTEX Lagrangian experiments.

2. ASTEX Lagrangian Simulations

Krueger et al. (1995a,b) and Wyant et al. (1996) used 2D eddy-resolving models (ERMs) in a Lagrangian framework to study the transition from stratocumulus to trade cumulus clouds over the Eastern Pacific Ocean under idealized conditions. The ASTEX Lagrangian experiments offer an opportunity to perform similar simulations but with comprehensive observational verification.

The GEWEX Cloud System Study (GCSS) Boundary Layer Cloud working group held its second model intercomparison workshop 30 August–1 September 1995 at KNMI, De Bilt, The Netherlands. As part of the workshop, we set up simulations based on the two ASTEX Lagrangian experiments that are appropriate for 1D boundary-layer models and 2D ERMs. (3D large eddy simulations are not currently feasible for these cases.) In the Lagrangian experiments, the diurnal cycle of radiation, drizzle, advection of different airmasses above a given boundary layer air column, and surface fluxes all played important roles, providing a difficult test of the overall ability of a model to predict boundary layer structure and cloud properties.

The ASTEX Lagrangian simulations require initial conditions (profiles of temperature, water vapor, liquid water, and horizontal wind components), time-dependent boundary conditions (SST, above-boundary-layer temperature and water vapor, and downward solar and infrared radiative fluxes at the top of the model domain) and large-scale forcing (divergence) based on observations. In the models, the mean horizontal wind components were nudged toward the observed components.

For all models, the domain height was 3000 m with a 50-m vertical grid interval. For the 2D models, the domain length was 6400 m with a 100-m horizontal grid interval. The 2D models explicitly represent the large convective eddies. Turbulence other than the large eddies is parameterized. In the 1D models, the large convective eddies are also parameterized. All the models contain parameterizations of microphysical processes (including drizzle formation) and of solar and infrared radiative transfer.

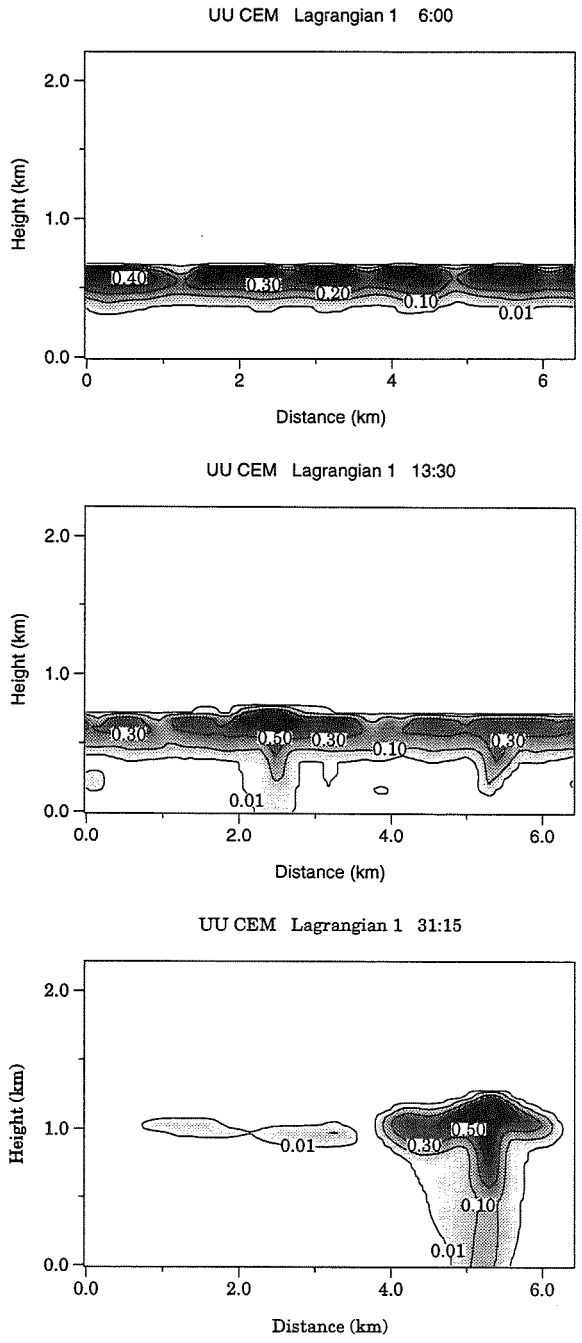

Figure 1. Snapshots of the liquid water mixing ratio from the UU ERM at three times during Lagrangian 1. Top: Overcast stratocumulus with drizzle. Middle: Cumulus rising into broken stratocumulus. Bottom: Cumulus spreading out into stratocumulus ("microcell").

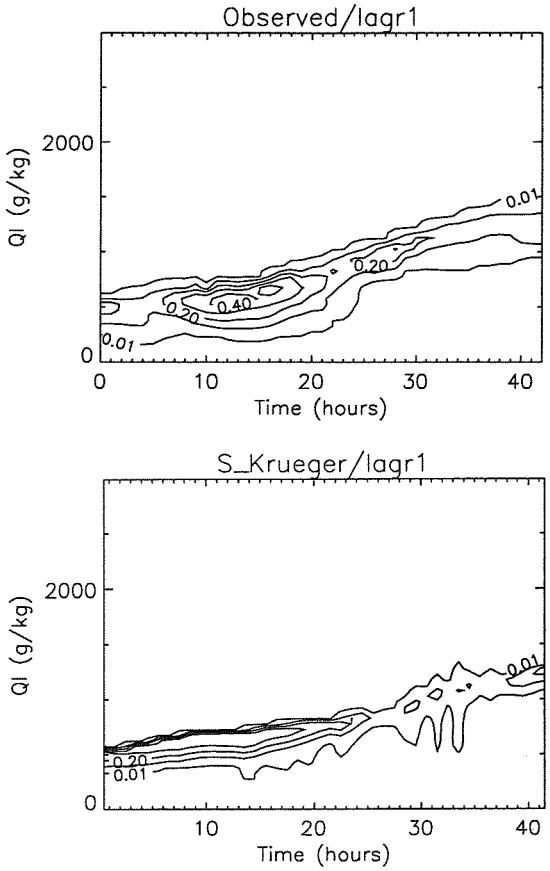

Figure 2. Evolution of the liquid water mixing ratio during Lagrangian 1: observed (top) and from the UU ERM (bottom).

The following modelers participated in the intercomparisons: Peter Bechtold (AERO), Eric van Meijgaard (KNMI), Joao Teixeira (ECMWF), Matthew Wyant and Christopher Bretherton (UW), Steven Krueger and Ching-Hsuan Chen (UU), and Bjorn Stevens (CSU). The first three used 1D boundary-layer models, while the remainder used 2D ERMs.

3. Results

We have compared the model results to observations whenever possible. Here we will focus on the cloud properties simulated for Lagrangian 1.

3.1 Lagrangian 1

The 2D ERMs did a fairly good job at reproducing the overall boundary layer evolution, which included drizzle, rapid deepening, and a transition to a cumulus under stratocumulus regime (an intermediate stage in the transition to trade cumulus) as the boundary layer moved over increasing SSTs. The snapshots in Fig. 1 illustrate the cloud regime evolution simulated by the University of Utah (UU) ERM.

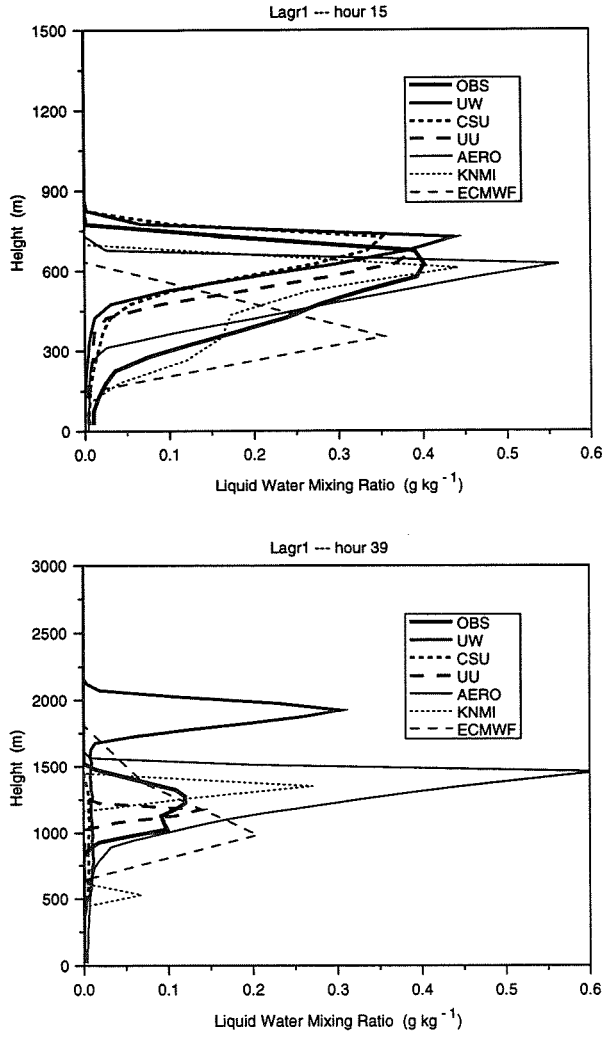

Figure 3. Liquid water mixing ratio profiles from observations and all models for hour 15 (top) and hour 39 (bottom) of Lagrangian 1.

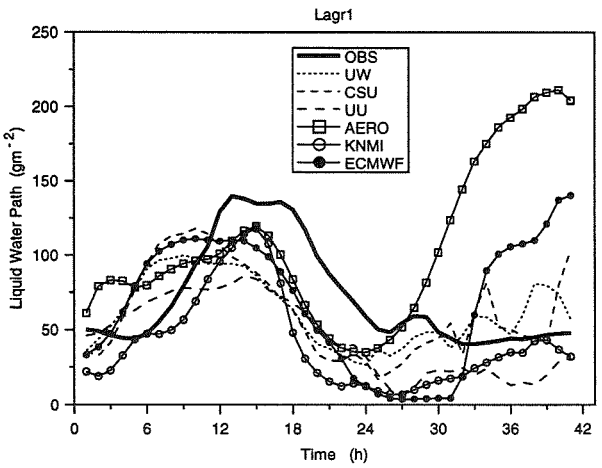

Figure 4. Time series of the liquid water path from observations and all models during Lagrangian 1.

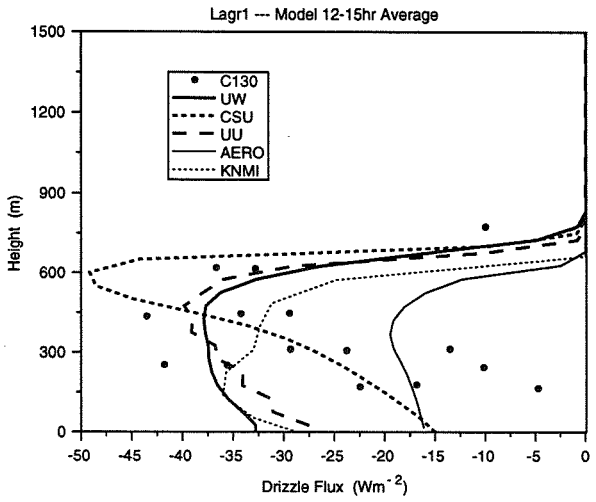

Figure 5. Drizzle flux profiles from observations and all models for hour 15 of Lagrangian 1.

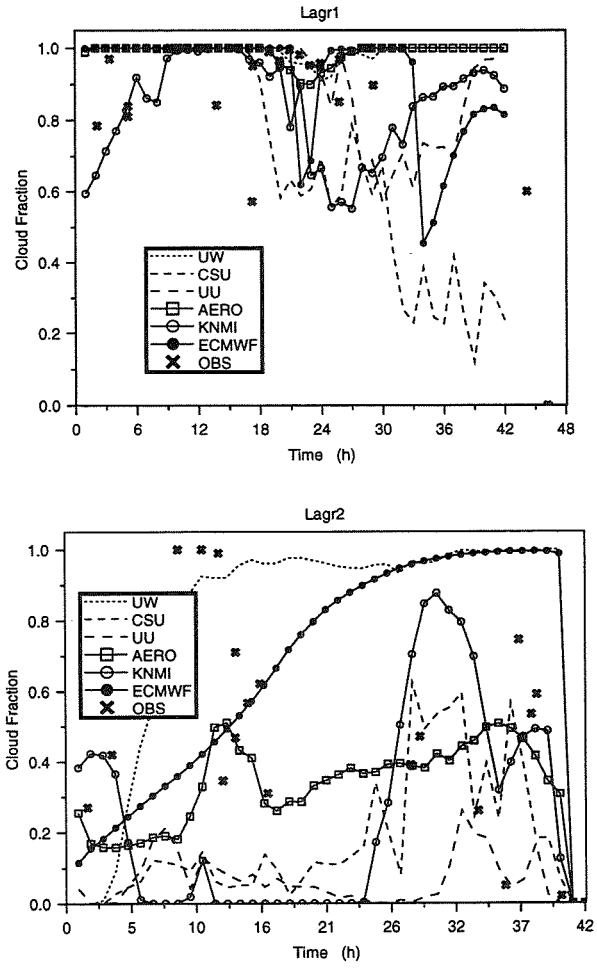

Figure 6. Time series of the cloud amount from observations and all models during Lagrangian 1 (top) and Lagrangian 2 (bottom).

Fig. 2 shows the observed evolution of the liquid water mixing ratio versus height and that simulated by the UU ERM, while Fig. 3 shows profiles of the liquid water mixing ratio from observations and all models for hours 15 and 39 of Lagrangian 1. The agreement between models and observations is greater for hour 15 than for hour 39. Fig. 4 shows the evolution of the liquid water path (LWP, vertically-integrated liquid water) from observtions and all models. There is general agreement during the first 24 hours, and less agreement afterward.

Fig. 5 shows the simulated and observed drizzle flux profiles for hour 15. The models did surprisingly well at predicting drizzle rates at this time. One explanation for this result is that entrainment drying was weak due to the small jump in total water across the inversion. As a result, a balance was achieved in the total water budget primarily between drizzle and surface evaporation. Because the latter agreed well with observational estimates, the drizzle rates did also. This explanation is supported by the results of a simulation with the UU ERM in which drizzle was not allowed.

The models predicted mostly overcast conditions during the first 20 hours, which agrees fairly well with the observations (see Fig. 6). The cloud amount in three models rapidly decreased to about 0.5 after 20 hours, whereas the observations indicate that nearly overcast conditions continued until 30 hours. After 30 hours, the cloud amount in most models either remained overcast or increased to nearly overcast conditions by 40 hours. The limited observations during this time suggest that the cloud amount decreased to scattered by 45 hours.

3.2 Lagrangian 2

The observations showed broken cumulus under stratocumulus during the first half and only scattered stratocumulus during the second half of the period. However, most models predicted just the reverse (see Fig. 6). The reason may be that the weakly stable transition layer was smoothed out in the initial profiles, thus slowing down the process of developing a conditionally unstable subcloud layer.

4. Conclusions

The ASTEX Lagrangian simulations successfully predicted the evolution of cloud type, LWP, and drizzle rates during Lagrangian 1, and the cloud type during Lagrangian 2. The simulations were less successful at predicting the evolution of cloud amount during both Lagrangians.

The ASTEX Lagrangian simulations demonstrate the usefulness of 2D ERMs for studying boundary-layer cloud systems. This should encourage wider usage of such models for basic understanding of cloud systems and for developing and testing 1D boundary layer models.

5. Acknowledgments

This research was supported by the Environmental Science Division, DOE, under Grant DE-FG03-94ER61769, by ONR Grant N00014-91-J-1175, and by NASA Grant NAG1-1711. Computing assistance was provided by NCAR SCD.

6. References

Albrecht, B. A., C. S. Bretherton, and D. Johnson, 1995: The Atlantic Stratocumulus Transition Experiment (ASTEX). *Bull. Amer. Meteor. Soc.*, **76**, 889–904.

Bretherton, C. S., and R. Pincus, 1995: Cloudiness and marine boundary layer dynamics in the ASTEX Lagrangian experiments. Part I: Synoptic setting and vertical structure. *J. Atmos. Sci.*, **52**, 2707–2723.

Bretherton, C. S., P. A. Austin, and S. T. Siems, 1995: Cloudiness and marine boundary layer dynamics in the ASTEX Lagrangian experiments. Part II: Cloudiness, drizzle, surface fluxes and entrainment. *J. Atmos. Sci.*, **52**, 2724–2735.

Krueger, S. K., G. T. McLean, and Q. Fu, 1995a: Numerical simulation of the stratus-to-cumulus transition in the subtropical marine boundary layer. Part I: Boundary-layer structure. *J. Atmos. Sci.*, **52**, 2839–2850.

Krueger, S. K., G. T. McLean, and Q. Fu, 1995b: Numerical simulation of the stratus-to-cumulus transition in the subtropical marine boundary layer. Part II: Boundary-layer circulation. *J. Atmos. Sci.*, **52**, 2851–2868.

Wyant, M. C., C. S. Bretherton, H. A. Rand, and D. E. Stevens, 1996: Numerical simulations and a conceptual model of the stratocumulus to trade cumulus transition. Accepted by *J. Atmos. Sci.*

THE INCEPTION OF DRIZZLE IN MARINE STRATOCUMULUS: A MONTE-CARLO SIMULATION OF CONVECTIVE CORES

Jørgen B. Jensen[1], Sunhee Lee[1], Reinout Boers[1], Paul B. Krummel[1], Dan Gogoasa[1], Jim Hudson[2], Mike Harvey[3], Ingrid Kristament[3]

[1]CSIRO Division of Atmospheric Research, Aspendale, Victoria, Australia
[2]Desert Research Institute, Reno, Nevada, USA
[3]National Institute of Water and Atmosphere, Wellington, New Zealand

1. INTRODUCTION

A long-standing problem in cloud physics is the perceived inability of simple models to predict the onset of coalescence processes, and accordingly, the formation of drizzle drops. Baker and Latham (1979) suggested that "inhomogeneous mixing" might lead to accelerated condensational growth of some drops. Telford and Chai (1980) suggested that "entity entrainment" with repeated vertical cycling could lead to enhanced condensational growth of some drops, whereas Johnson (1982) suggested that giant nuclei ($r > 1$ μm) or ultragiant nuclei ($r > 10$ μm) were responsible for forming the drops which initiate coalescence.

The development of drizzle drops from marine stratocumulus clouds may significantly alter the vertical profiles of heat and moisture in the boundary layer. Clouds observed during the Southern Ocean Cloud Experiment (SOCEX-1 and 2) frequently were cumulus cores which penetrated up into a higher level stratocumulus deck. Drizzle developed and fell from both the stratiform shields and the younger cumulus cores.

Drizzle falling from the upper stratiform cloud would generally evaporate before reaching the altitude of the cumulus cloud base. The effect of this evaporation is to de-couple the stratiform deck and to make the environment of the cumulus cores more unstable. Precipitation may thus be a critical factor in the life cycle of these clouds. Accordingly, it is of great interest to be able to predict whether marine clouds will precipitate or not.

In this study we calculate the early development of drizzle drops in an observed cumulus core. The approach is to use a combination of a Monte-Carlo model of the stochastic coalescence of cloud drops and an adiabatic parcel model for the condensational growth. The aim of the study is to determine if such a simple model can explain the observed concentrations of drizzle drops.

2. OBSERVATIONS

The Southern Ocean Cloud Experiment, SOCEX 1 and 2, took place over the ocean west of Tasmania in the winter of 1993 and the summer of 1995. The principal platform was the F27 research aircraft instrumented with a complete suite of thermodynamic, wind, radiation, CCN and other particle probes. Of particular interest here are the DRI CCN-counter (Hudson, 1989), a PMS ASASP for measurement of aerosol particles, a PMS FSSP for cloud drops, and a PMS 260-x probe for measurement of drizzle drops.

On 1 February 1995 extensive stratiform shields were observed over the ocean west of Tasmania. Low level cumulus clouds would penetrate up into the stratiform cloud. The cloud cover was not 100 %; rather the stratiform decks were of mesoscale dimensions (many tens of kilometers) with clear breaks separating the stratiform decks. The highly localised convective cores were, at least in some instances, organized in long lines roughly perpendicular to the mean wind direction in the boundary layer. Boers *et al.* (1996) has given a more detailed description of this cloud situation; here we focus on the particular aspects which are important for the subsequent modeling.

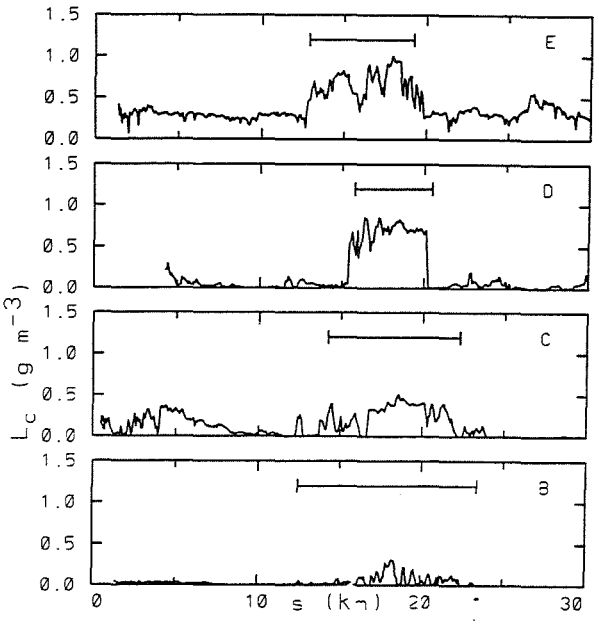

Fig. 1. Profiles of cloud liquid water content, L_c, from the CSIRO-King probe as a function of distance along the flight track, s. Leg B is at an altitude of 830 m (180 m above cloud base), leg C at 970 m (320 m above cloud base), leg D at 1190 m (540 m above the cumulus cloud base), and leg E was at 1400 m (740 m above the cloud base and 100 m below the cloud top). The convective cores are outlined by the horizontal bars.

Fig. 1 shows a set of time series of cloud liquid water content for four horizontal flight legs above cloud base. Fig. 2 shows the corresponding drizzle water content using the 260-x probe for all drops bigger than 20 μm radius; this figure also shows the surface flight leg.

Leg A was made 60 meters above sea surface, and it is used for describing the sub-cloud CCN distribution. It can be seen that there are minute traces of precipitation in the left part of the Fig. 2 A; otherwise the surface leg is free from drizzle. The precipitation free segment of leg A has lifting condensation level (LCL) parameters of p=935 mb and T=8.4 °C; we will assume that these are the cloud base parameters for the convective core.

The next four flight legs (Fig. 1 B-E) clearly show the convective core. In the uppermost flight level the convective core is surrounded by the stratiform cloud deck. The maximum cloud liquid water content in the convective core was approaching the predicted adiabatic values.

Fig. 2 shows that the drizzle drops are most common outside the convective core. Average concentrations of drizzle drops with radius bigger than 20 μm (largest FSSP drops and all of the 260-x drops) in the convective cores are 9, 29, 33 and 61 per litre for legs B-E, respectively. The monotonic increase is consistent with the expectation that cloud parcels highest up have, in general, the largest cloud drops and the

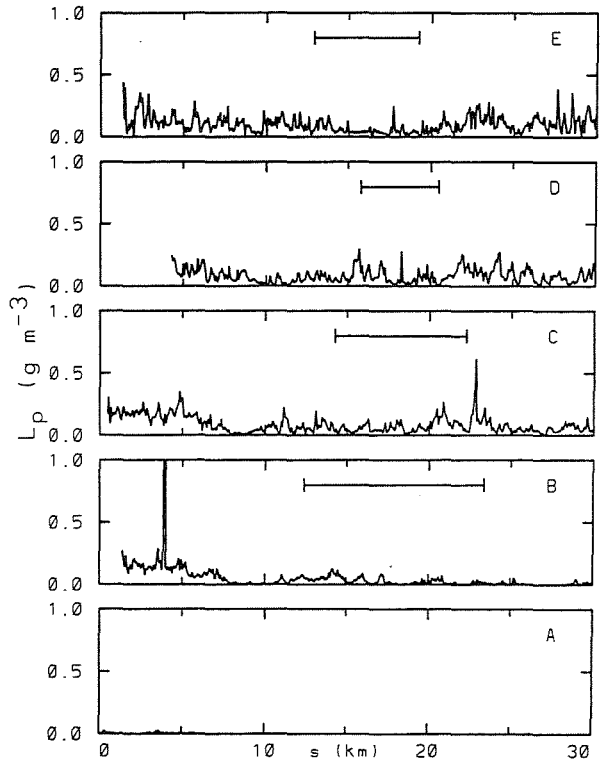

Fig. 2. Same as Fig. 1, but for the drizzle water content, L_p, from the PMS 260-x drops with radii above 20 μm. This figure also shows observations from the surface leg (A) which was 60 m above sea surface.

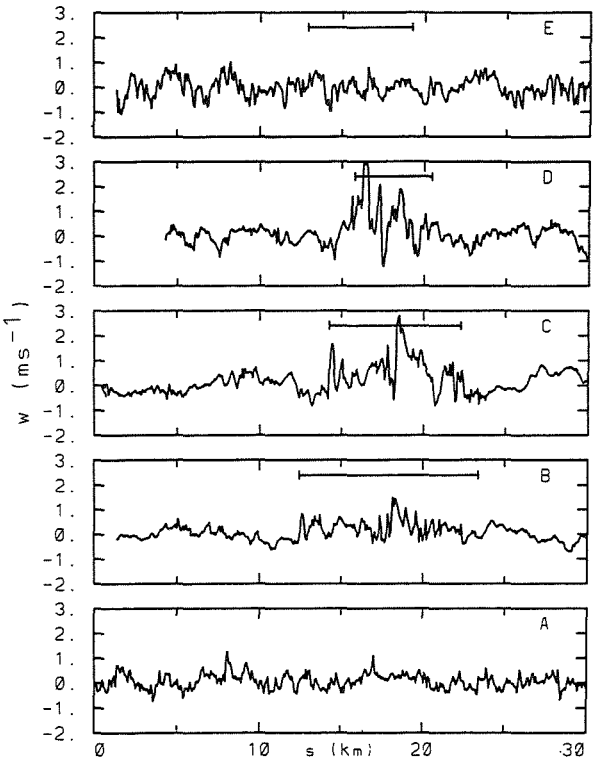

Fig. 3. Same as Fig. 2, but for the vertical wind velocity, w.

greatest age, thus allowing the most time and opportunity for development of drizzle.

The vertical wind velocities for the five legs are shown in Fig. 3. Average velocities in the convective core are 0.3, 0.7, 0.7 and 0.02 m s^{-1} for legs B-E, respectively.

Dry aerosol particle masses have been derived using the DRI CCN spectrometer, the ASASP and the FSSP for the drizzle-free portion of the surface flight leg. The resultant CCN spectrum is shown in Fig. 4.

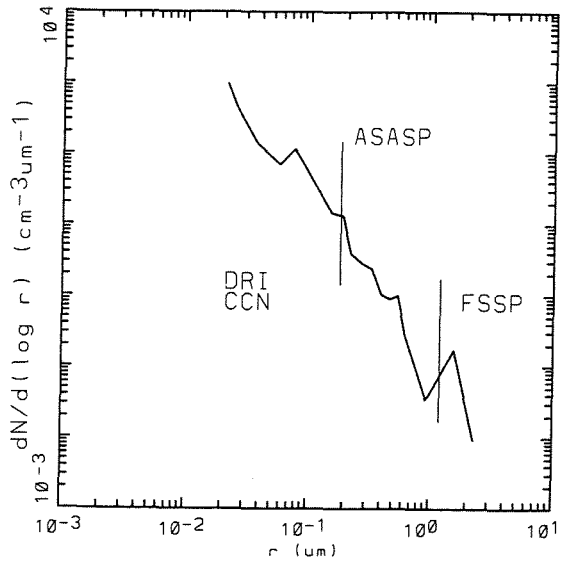

Fig. 4. CCN size distribution expressed as $dN/d(logr)$, where r is the dry aerosol particle radius. The observations were derived from one of three probes depending on particle size.

We have assumed that all particles with dry radii below 0.2 μm consist of ammonium bisulphate, whereas larger particles are composed of sodium chloride.

3. MODEL EQUATIONS

The basis for the present study is a coupling of an adiabatic parcel model with Gillespie's (1975) stochastic Monte-Carlo model.

3.1 Stochastic Monte – Carlo equations.

Consider a cloud volume with N drops. Rank the drops by size such that the following relationship holds for two drops (i and j) which may coalesce: $0 < i < j \leq N$.

The coalescence kernel, C_{ij}, is defined as:

$C_{ij}dt \equiv$ probability that a given pair of cloud droplets with radii r_i and r_j will coalesce in the next infinitesimal time interval dt.

The value of C_{ij} is calculated as [the average "coalescence volume" which an r_j droplet sweeps out relative to an r_i drop per second] divided by [the total cloud volume]; i.e.:

$$C_{ij} \equiv \pi(r_i + r_j)^2 E_{ij}(v_j - v_i)\frac{1}{V} \tag{1}$$

where E_{ij} is the collection efficiency, v_i and v_j are the terminal velocities of drops i and j, respectively, and V is cloud volume containing N drops.

The sum of all possible collection kernels is defined as:

$$C_0 \equiv \sum_{i=1}^{N-1} \sum_{j=i+1}^{N} C_{ij}. \tag{2}$$

The three-variable probability density function, $P(\tau, i, j)$, represents the probability that the next coalescence event happens in τ seconds and that it involves drop i and j. This can be developed as:

$$P(\tau, i, j) = P_1(\tau)\ P_2(i \mid \tau)\ P_3(j \mid \tau, i). \tag{3}$$

The first of the three RHS probability functions describes the probability that the next coalescence event will happen in τ seconds, the second that it given the value of τ will involve small drop number i, and the third probability function describes the probability that the large drop number is j given the previously found values of τ and i.

The Monte-Carlo simulation is initiated by picking a random number f_1 from the unit interval and calculating the corresponding value of τ from

$$\tau = C_0^{-1} \ln(1/f_1). \tag{4}$$

The procedure for choosing the small and large drop indices, i and j, is given in Gillespie (1975). By repeating the procedure for picking three random numbers, the coalescence model is advanced for as long a time as is desired.

We note that the median time, τ_m, until the next coalescence event is defined by setting the random number f_1=0.5 in eq. (4); i.e.:

$$\tau_m = C_0^{-1} \ln(2). \tag{5}$$

This parameter is a good measure of the rate of droplet coalescence.

3.2 Condensation model

The simplest model calculation of droplet growth is the adiabatic Lagrangian parcel model. The adiabatic assumption is only approximately fulfilled for our case study.

The equations for droplet growth (r_i), water vapor mixing ratio (q_v), temperature (T), air density (ρ_a) and altitude (z) are given by:

$$\frac{dr_i}{dt} = \frac{1}{r_i} \frac{S - \exp\left[\frac{2\sigma}{R_v T \rho_w r_i} - \frac{\nu \Phi m_{si} M_w}{M_s\left[\frac{4\pi}{3}\rho_w r^3 - \frac{m_{si}\rho_w}{\rho_s}\right]}\right]}{\frac{L_v^2 \rho_w}{K R_v T^2} + \frac{R_v T \rho_w (r_i + \beta)}{D_v e_s r_i}} \tag{6}$$

$$\frac{dq_v}{dt} = -\sum_{i=1}^{N} \frac{4\pi\rho_w}{V\rho_a} r_i^2 \frac{dr_i}{dt} \tag{7}$$

$$\frac{dT}{dt} = -\frac{L_v}{c_p}\frac{dq_v}{dt} - \frac{g}{c_p}\frac{dz}{dt} \tag{8}$$

$$\frac{d\rho_a}{dt} = -\frac{\rho_a g w}{R_d T} - \frac{\rho_a}{T}\frac{dT}{dt} \tag{9}$$

$$\frac{dz}{dt} = w. \tag{10}$$

The specification of w is given in Section 4.

The five differential equations (6-10) are integrated using a fourth-order Runge-Kutta routine. We note that eq. (6) is expanded into thousands of similar equations, one for each droplet in the relatively large cloud volume used in this study.

4. MODEL CONSIDERATIONS

We intend to model the development of an air parcel ascending from below cloud base, accelerating upwards, and finally coming to rest beneath the inversion.

Vertical air velocity at cloud base was not experimentally determined. Instead we specify w by examination of the observed five profiles, see Fig. 3, and from a comparison of the CCN distributions and the maximum observed cloud drop concentrations. In the 100 m immediately below cloud base an updraft of 0.5 m s^{-1} is assumed. Above cloud base the velocity is assumed to increase linearly to 1.5 m s^{-1} at the highest flight level 740 m above cloud base. The value of 0.5 m s^{-1}at cloud base also results in the activation of about 150 drops per cm^3, which is in agreement with the observed drop concentration higher in the cloud. After passing the uppermost flight level (740 m above cloud base) the air parcel rises a further 100 m to the inversion, falls back down 100 m and resides for five minutes at the uppermost flight level. Implicitly we have assumed that the airmass observed at level D was the same airmass observed nine minutes later at level E.

The condensation model is initiated below cloud base at a relative humidity of 95 % in order to ensure that the solution drop size is in equilibrium with the changing saturation field in the updraft. Droplet terminal velocities are calculated based on the procedures given in Beard (1976). Droplet collision efficiencies are taken from Klett and Davis' (1973) study for large drops. For droplet pairs in which the large drop radius is less than 10 μm, the values from Rogers and Davis (1990) are used.

The combined model is advanced in time by the following procedure. Based on the droplet spectrum all the collection kernels are calculated, and the time period until the next coalescence event, τ, is calculated along with the indices for small and large drops (i and j) to be coalesced. The condensation model is then run for τ seconds, at which time the coalescence takes place. The procedure is then repeated by calculating new collection kernels etc.

The computational requirements of the combined condensation-coalescence model are considerable, hence we have only simulated a cloud air volume of 50 cm^3 with about 8000 drops. The stochastic model involves the calculation of triangular matrices of 8000×8000 elements which must be updated every few seconds of model time. Later we plan to increase both the sample volume and number of runs to increase the statistical significance of the results.

5. RESULTS

The combined condensation-coalescence model was integrated for 21 minutes, at which time the parcel's trajectory was terminated at the uppermost flight level.

Fig. 5 shows the medium time, τ_m, between each coalescence event as a function of altitude. The median time between coalescence events is very large below cloud base. It decreases to 300 s at the level of the maximum supersaturation peak 15 m above cloud base. Further up in the cloud it decreases to 5 s when the parcel first passes level E.

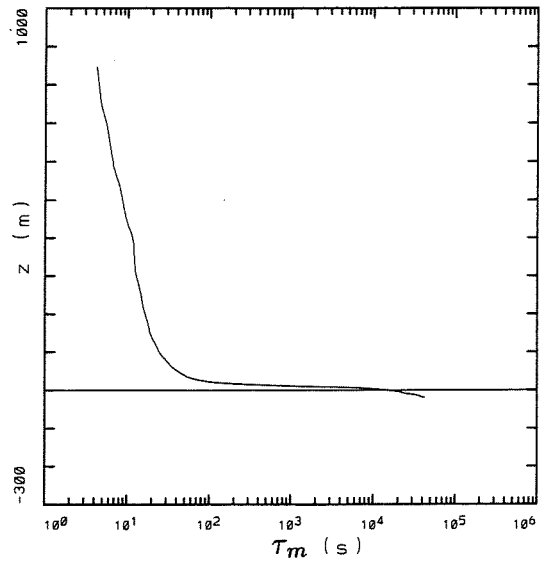

Fig. 5. Median time, τ_m, between coalescence events as a function of altitude up to level E. The time is based on a cloud volume of 50 cm^3.

A total of 4 drops grew sufficiently to have radii above 20 μm in this model run. This is the critical result of the present study: 4 drops in a cloud volume of about 50 cm^3 (or equivalently, 80 drops per litre) is comparable to the 61 drops per litre observed by the aircraft in the highest penetration of the convective core.

Furthermore, the largest drizzle drop formed on an aerosol particle with a radius below 2 μm; this is in the low range of "giant nuclei".

More runs are clearly needed to establish the statistical significance of these results. Yet, for the present cloud case the preliminary results appear to show that the onset of coalescence as calculated with a simple adiabatic condensation-coalescence model can match the observed onset of drizzle formation. On this basis it appears that there is no need to invoke "inhomogeneous mixing", "entity entrainment" or ultra-giant aerosol particles to explain the onset of drizzle formation. Hence, from cloud parameters (e.g., depth, base temperature, life time) and from a complete CCN spectrum it should be possible to predict if a given cloud will produce drizzle sized drops.

ACKNOWLEDGEMENTS

SOCEX was partly funded by CSIRO/INRE, CSIRO/COSSA and the Cooperative Research Centre for Southern Hemisphere Meteorology. Many thanks are due to the staff of the Electronics and Mechanics Laboratories at CSIRO Division of Atmospheric Research.

REFERENCES

Baker, M. B. and J. Latham, 1979: The evolution of droplet spectra and the rate of production of embryonic raindrops in small cumulus clouds. *J. Atmos. Sci.*, **36**, 1612-1615.

Beard, K. V., 1976: Terminal velocity and shape of cloud and precipitation drops aloft. *J. Atmos. Sci.*, **33**, 851-864.

Boers, R., J. B. Jensen and P. B. Krummel, 1996: A line of convection embedded in a stratocumulus layer. Submitted to *Q. J. Roy. Met. Soc.*

Gillespie, D. T., 1975: An exact method for numerically simulating the stochastic coalescence process in a cloud. *J. Atmos. Sci.*, **32**, 1977-1989.

Hudson, J. G., 1989: An instantaneous CCN spectrometer. *J. Atmos. and Ocean. Tech*, **6**, 1055-1065.

Johnson, D. B., 1982: The role of giant and ultragiant aerosol particles in warm rain formation. *J. Atmos. Sci.*, **39**, 448-460.

Klett, J. D. and M. H. Davis, 1973: Theoretical collision efficiencies of cloud droplets at small Reynolds numbers. *J. Atmos. Sci.*, **30**, 107-117.

Rogers, J. R. and R. H. Davis, 1990: The effect of van der Waals attractions on cloud droplet growth by coalescence. *J. Atmos. Sci.*, **47**, 1075-1080.

Telford, J. and S.K. Chai, 1980: A new aspect of condensation theory. *Pure and Appl. Geophys*, **118**, 720-742.

A CASE STUDY OF WINTERTIME OROGRAPHIC PRECIPITATION IN THE NORTHERN MOUNTAINS OF ARIZONA

W D Hall, R T Bruintjes, J Coen and T L Clark

MMM Division, NCAR*
P.O. Box 3000, Boulder, CO 80307

1. INTRODUCTION

The 1995 Arizona Program was a multi-investigator field experiment aimed at advancing the understanding of winter storm development, morphology and precipitation in a mountainous region of central Arizona. From 15 January through 15 March, 1995, a wide variety of instrumentation was operated in and around the Verde Valley southwest of Flagstaff, AZ. These instruments included two Doppler radars, an instrumented aircraft, a lidar, microwave and infrared radiometers, and other surface based instrumentation focused on the analysis of wintertime storms in this geographically diverse area.

Of special interest to the Arizona Program was the interaction of topographically induced gravity waves with the ambient upslope flow. It is hypothesized that these waves may serve to augment the upslope-forced precipitation that falls onto the Mogollon Rim (Bruintjes et al., 1994). A major thrust of the program was to compare the observations of these, and other aspects of the winter storms with those predicted with the Clark-NCAR 3-D, meso/cloud scale numerical model.

The AP95 study area extended from Flagstaff, south to near Pine, east to Prescott, and north to near Ash Fork (all location in AZ, see Figure 1). This region encompasses both high terrain (> 2500m MSL) where significant snow typically falls from November through April, and arid, low valleys (< 800m) where there is much less, usually liquid, precipitation. The large scale topography around the study area is characterized by series of three NW-SE oriented mountain ranges between which are two broad valleys. Typical winter storms approach the region from the west or northwest, with upper air winds from the southwest ahead of the approaching synoptic-scale disturbance. The mountains in the Program area are generally oriented orthogonal to this flow. This often results in producing gravity waves during stable precipitating storm episodes. Previous studies indicated a persistent strong gravity wave over the Verde Valley downwind (northeast) of the Black Hills (Bruintjes et al., 1994).

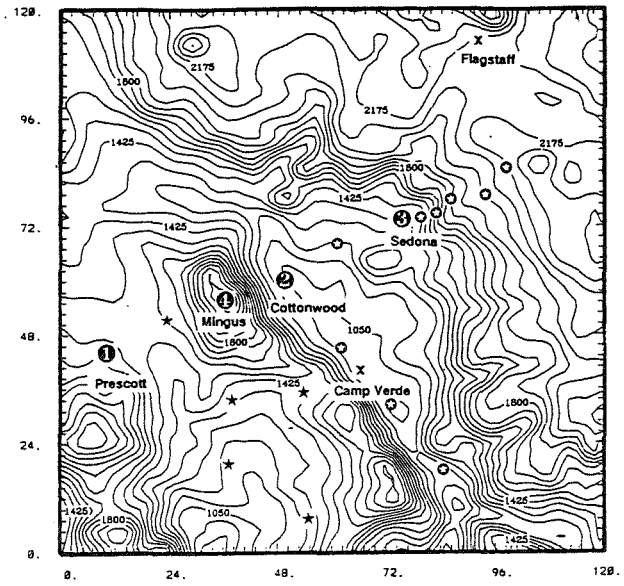

Figure 2. Overview of the Arizona Program Field area and facility locations. The Operations Center, aircraft, modelling activities, and snow sampling will be based out of Embry-Riddle Aeronautical University in Prescott ("❶"). The NOAA K_a- and X-band radars and radiometers, the Univ of Wisconsin Lidar, NASA Ames IR radiometers, and an ALERT surface weather station will all be located at the Cottonwood Airport site ("❷"). The Bureau of Reclamation microwave radiometer and an ALERT surface weather station will be located at the Sedona Airport ("❸"). Mingus Mountain ("❹") will be the location for several chaff and seeding releases, an ALERT surface weather station, and snow, ice crystal, and water vapor measurements and analysis. The other ALERT surface weather stations installed for the Program are located on both private and NFS land, and are shown in Figure 3 with "○" symbols. Other ALERT tipping bucket rain gages not erected specifically for this project are shown by "★" symbols. Axes are in km; all locations are approximate.

This paper presents comparisons between observations and numerical model simulations of a similar event (13/14 February 1995) that occurred during the AP95 field program. During this event resulted in locally heavy precipitation associated with flash flooding in the region.

2. OBSERVATIONS AND NUMERICAL MODEL

The weather over the study area was influenced by abundant moisture in a strong, warm west-southwesterly flow being advected into the area ahead of a slowly approaching cold front in southern California. The first major cloud band moved over the region overnight and into the early morning,

* NCAR is sponsored by the National Science Foundation

Corresponding author address: W D Hall, NCAR, P.O. Box 3000, Boulder, CO 80307

resulting in moderate rain in the valley and heavier amounts on the Mogollon Rim. Scattered light to moderate rain was encountered through the day with the snow level between 2 and 2.4 km MSL. The strong southwesterly flow inducing a strong gravity wave and strong upslope flow increased significantly during the early afternoon with the second major cloud band. Wind gusts associated with downslope flow in excess of 20 m s^{-1} were encountered in the Verde Valley. Excellent wave structures were clearly visible from the surface, aircraft, and were also registered by the radars at Cottonwwod.

The nonhydrostatic meso/cloud-scale interactive grid nesting model of Clark and Hall (1990) with terrain following coordinates was used to simulate this case. Two recent new developments to the model included the incorporation of synoptic scale weather data into the model to be applied in real time and an improved version of the warm rain and ice phase microphysical physics. The synoptic scale data were collected from the large scale analysis and forecast data sets from the Rapid Update Cycle (RUC) at the National center for Environmental Prediction (NCEP). The RUC is a version of the NOAA Forecast Systems Laboratory's Mesoscale and Analysis Prediction System (MAPS, Benjamin et al., 1991). This data was used to initialize and update boundary conditions during the simulation of a coarse resolution (24.3 km horizontal) 1166 by 1166 km grid. The outer domain contained most of the western United States and Northern Mexico. Grid nesting procedures were then employed to improve the spatial and temporal resolutions over smaller areas of interest. The second domain of resolution (8.1 km horizontal) 388 by 388 km grid covers the State of Arizona while a third nested domain (2.7 km horizontal resolution), 194 by 194 km covered the project area. A fourth domain (.9 km horizontal resolution), 97 by 97 km covered the Verde Valley and parts of the Mogollon Rim.

The MAPS data sets were available at 3 hour intervals. The first data set was an analysis data set and subsequent data sets were results of the forecast model that was run for 12 hours. The initial data were projected onto the model surfaces and modified using a potential flow adjustment procedure to satisfy mass continuity to the accuracy of the pressure solver. The model was then integrated forward in time updating the outer boundary conditions by linear interpolation from the MAPS forecast data.

The improved versions of the microphysical parameterization included the incorporation of the Berry (1969) warm rain parameterization scheme, an improved quasi-analytical treatment of the supersaturation field, and the addition of homogeneous nucleation. This warm rain parameterization is a significant improvement to Kessler (1969) since information about the droplet number concentration and spectral dispersion characteristics are included to calculate the autoconversion rate of cloud water being converted to rain water. The improved treatment of the supersaturation uses the quasi-analytical method of Clark (1973). This procedure yields a consistent treatment of the condensational growth and evaporation processes for all the hydrometeor (water and ice) fields. For temperatures below -40°C homogeneous freezing of cloud water is assumed to occur.

3. RESULTS

3.1 *Observations*

This event was marked by a strong gravity wave over the Verde Valley developing of the Black Hills and specifically Mingus Mountain. Deep clouds between 2 and 8 km MSL were persistent throughout the morning of 14 February 1995. The gravity wave did not persist throughout this event but showed oscillations in its strength closely related to wind speed on top of Mingus Mountain and wind data from the Acoustic sounder located near Cottonwood. It was evident that as soon as the mean wind speeds on top of Mingus Mountain dropped below about 8 m s^{-1} (15 kts) and the peak wind gusts below 12 m s^{-1} (25 kts) the gravity wave seemed to be less strong and even sometimes disappeared altogether. A time history of the mean and peak winds on top of Mingus Mountain and at Cottonwood in the Valley are shown in Fig. 2. The winds on top of Mingus Mountain were highly correlated with the winds at Cottonwood with the strongest winds at Cottonwood occurring when the gravity wave was strong and light winds when the gravity wave disappeared or weakened substantially. While the wind direction on top of Mingus Mountain was consistently from the South-southwest during this event the wind direction at Cottonwood in the Valley was from the southeast along the Valley when no wave or a weak wave existed and turned more southerly (indicating a downslope wind) when the wave was strong.

This sequence of events is more clearly illustrated by the winds measured by the acoustic sounder at Cottonwood shown in Fig. 3. It shows the winds in the boundary layer from from 0000 to 1200 MST (Mountain Standard Time, UTC=MST+7 hours). The changes in wind direction between south-southeasterly to southeasterly and back to southerly are clearly evident in the observations. The more southerly winds corresponded with the times when a strong gravity wave was evident while during the southeasterly winds the gravity wave weakened substantially or disappeared. This was substantiated by the radar data collected at Cottonwood (not shown here) which clearly indicated the changes in the strength of the gravity wave.

The precipitation rates at the surface downwind of the gravity wave in the Verde Valley and on the upwind side of the Mogollon Rim were also closely correlated with the strength of the gravity

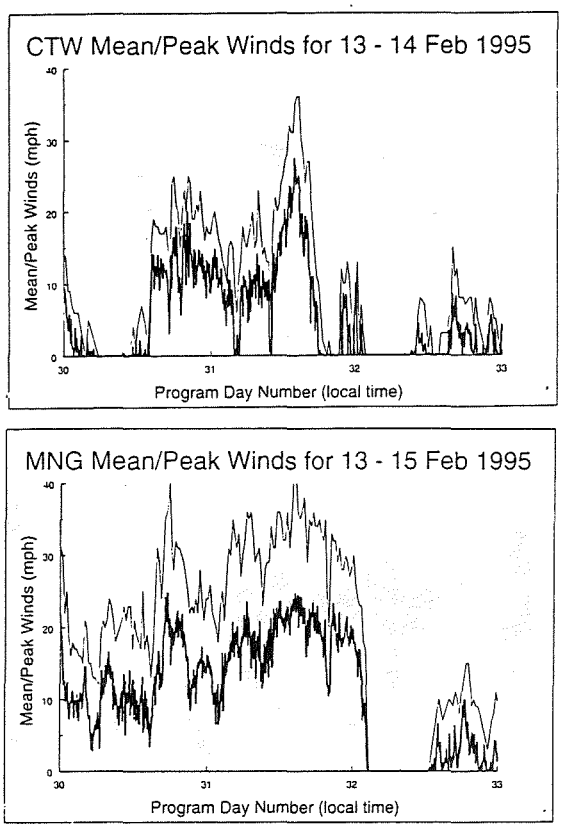

Figure 2. Time history of mean and Peak wind speeds in knots on top of Mingus Mountain (a), and at Cottonwood in the Valley (b) for the period 13-14 February 1995.

wave. Within the Valley at Whiteflat which is located in the middle of the Valley between Cottonwood and Sedona precipitation rates were highest immediately after the weakening or collapse of the gravity wave. The reasoning for this may be that during the strong gravity wave event updrafts of more than 5 m s^{-1} were measured in the wave by an instrumented aircraft producing substantial water loading in the atmosphere. When the gravity wave weakens or collapses this water loading is deposited to the surface. This is clearly evident in the time histories of precipitation for Whiteflat (WHT) and Sedona (SRC) shown in Fig.4. On top of Mogollon Rim (T6) continuous precipitation was experienced as shown in Fig. 4c. It is also important to note that total precipitation amounts increased along the wind through the Valley onto the Mogollon Rim from 27.2 mm at Whiteflat to 54.6 mm at Sedona to 137.9 mm on top of the Mogollon Rim.

3.2 *Modelling results*

The model simulations confirmed the observational results discussed above. The model also indicated varying strength in gravity wave with time. Figure 5 shows the vertical cross-sections through Mingus Mountain and the Mogollon Rim of cloud

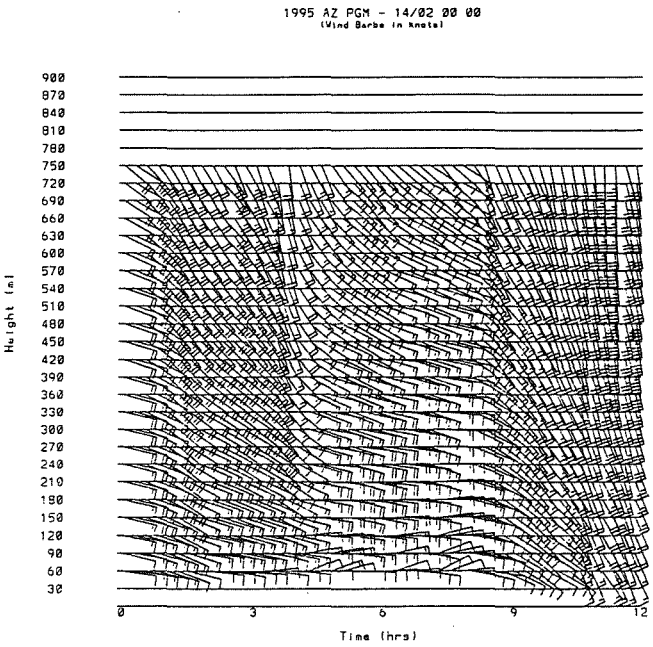

Figure 3. Time history of wind direction and speeds in knots as measured by the acoustic sounder located near Cottonwood.

liquid water (solid contours) and ice/snow (shaded areas) mixing ratios in g kg^{-1} for 1400 UTC (a) when the gravity wave was weak and 1600 UTC when the wave was well developed. At 1400 UTC (0700 MST) the winds in the Valley were southeasterly (Fig. 3) while at 1600 (0900 MST) the winds started to turn more southerly in the valley and also increased in speed (Fig. 3). This is also in agreement with the observations described in the previous paragraph. When the wave is developing (Fig. 5b) cloud liquid water (CLW) contents in the wave increase substantially. When the CLW increases the ice/snow mixing ratios also increases immediately downwind of the CLW region. This enhanced region of ice/snow then subsequently descends into the CLW region associated with the low-level upslope cloud over the Mogollon Rim. This provided for enhanced precipitation at the top of the Mogollon Rim (Fig. 4c) while less precipitation was observed in the Valley during this period. However, when the gravity wave is absent more precipitation falls in the Valley. The timing of the simulated events showed good agreement with the observations.

4. CONCLUSIONS

Good agreement was found between the observations and the modelling results. This case showed that numerical models with detailed microphysics could be used in complex terrain to provide short term predictions (1 to 12 hours) of potential heavy precipitation events with possible local floods.

5. ACKNOWLEDGEMENTS

This work was funded by the NOAA/Arizona

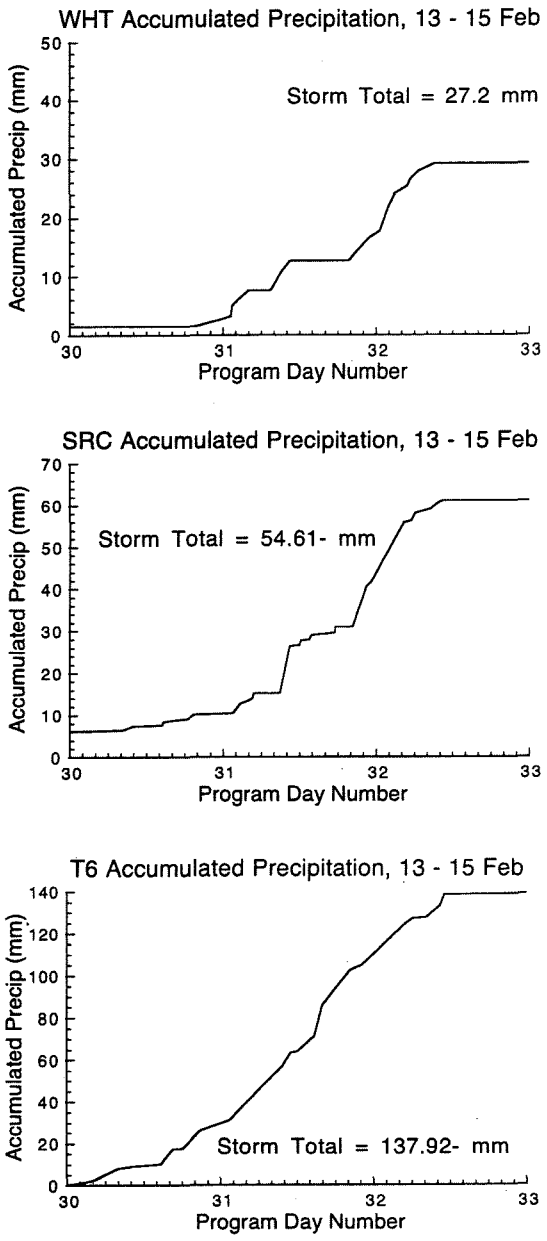

Figure 4. Time histories of precipitation for WHT (a), SRC (b), and T6 (c) for the period 13-15 February 1995.

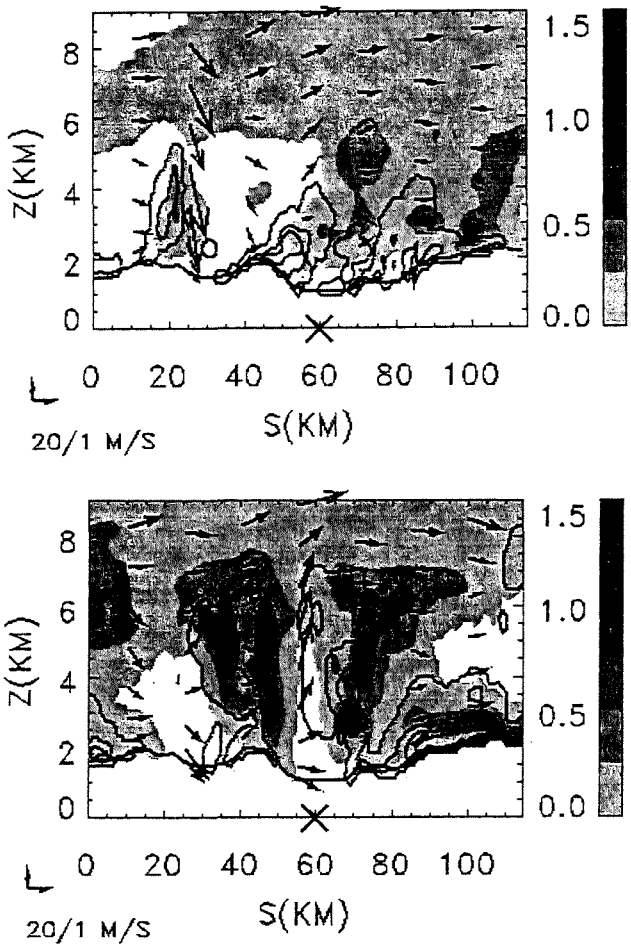

Figure 5. vertical cross-sections through Mingus Mountain and the Mogollon Rim of cloud liquid water (solid contours) and ice/snow (shaded areas) mixing ratios in g kg^{-1} for 1400 UTC (a) when the gravity wave was weak and 1600 UTC when the wave was well developed.

Atmospheric Modification Program, NOAA Cooperative Agreement Number IGA-91-611-189- 1085. Special thanks should go to Dennis Sundie the program manager for the Arizona Program for his support during the field program.

6. REFERENCES

Benjamin, S. G., K.A. Brewster, R. Brummer, B.F. Jewett, T.W. Schlatter, 1991: An isentropic three-hourly data assimilation system using ACARS aircraft observations. *Mon. Wea. Rev.*, , 119, 888-906.

Berry, E.X., 1969: Modification of the warm rain process. Proc. First Int. Conf. on Weather Modification, ..., 81-85.

Bruintjes, R. T., T. L. Clark, and W. D. Hall, 1994: Interactions between topographic airflow and cloud/precipitation development during the passage of a winter storm in Arizona. *J. Atmos. Sci.*, , 51, 48-67.

Clark, T.L., 1973: Numerical modelling of the dynamics and microphysics of warm cumulus convection. *J. Atmos. Sci.*, , 30, 857-878.

Clark, T.L., and W.D. Hall, 1990: Multi-domain simulations of the time dependent Navier Stokes equation: Benchmark error analyses of nesting procedures. *J. Comp. Phys.*, 92 No. 2, 456-481.

CASE STUDY OF STRATOCUMULUS-TOPPED BOUNDARY LAYER USING A LARGE EDDY SIMULATION MODEL WITH EXPLICIT MICROPHYSICS

Y. L. Kogan and M. P. Khairoutdinov

Cooperative Institute for Mesoscale Meteorological Studies
University of Oklahoma, Norman, OK

1. Introduction

Marine stratocumulus cloud layers because of their large cover, persistence, and high reflectivity exert a significant climatic effect. The large eddy simulation (LES) models, although computationally demanding, have the potential of simulating the turbulence effects in the cloud-topped boundary layer most accurately. For climate studies, the parameterization of microphysical effects and the microphysics-radiation interaction is especially important, as demonstrated by the ship condensation trails phenomenon (Radke et al, 1988). The latter is a vivid example of the effect of microphysics on cloud radiative properties.

The need to accurately account for microphysical effects in radiative parameterizations have resulted in the development of LES models with explicit microphysics (Kogan *et al* 1995, Stevens *et al* 1996). The advancement in the microphysical formulation by predicting drop-size distribution functions introduces, however, a new level of complexity and necessitates a vigorous program to verify the model and its overall performance. Kogan *et al* (1995) (K95) described first evaluations of the CIMMS LES explicit microphysics cloud model based on comparisons with observations by Nicholls (1984) (N84). In the present paper the case study is expanded by inclusion of the solar radiation effects that were not considered in K95. In addition, we also discuss the problems related to verification of the model with observations in a highly turbulent boundary layer.

2. CIMMS LES cloud model

In the previous version of the model (K95) the dynamical tendencies for all thermodynamical variables were calculated based on the spectral code of Moeng (1984). The spectral method allows the most accurate calculation of the momentum equations, however, the lack of positive definiteness makes it unfit for advection of microphysical scalars. Therefore, in the previous version of the model the spectral method for the momentum equations was combined with the Smolarkiewicz positive definite finite-difference scheme for calculation of the dynamical tendencies of microphysical variables. As constraints imposed by the continuity equation were satisfied using the spectral formulation, the velocity field remained divergent in the finite-difference representation, resulting in rather large errors in advection of the microphysical fields. In the new version of the model we solved the problem by employing the same finite-difference representation for all model variables, including microphysical.

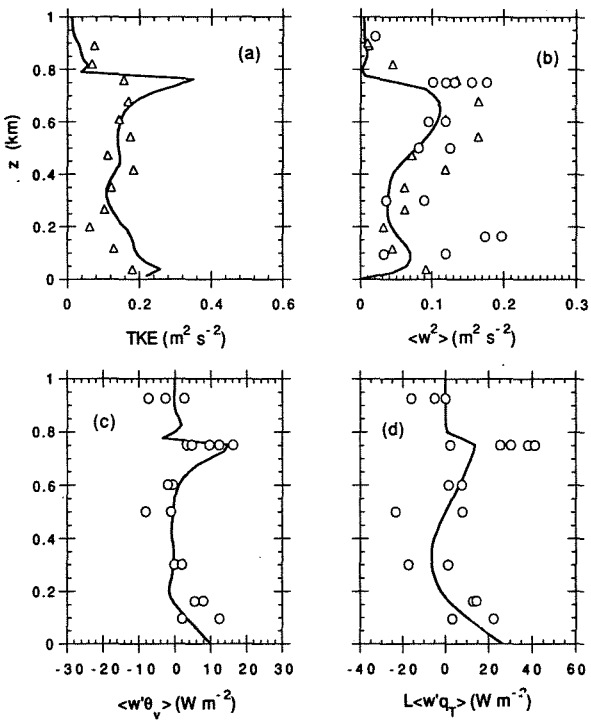

Fig. 1 The simulated vertical profiles of TKE (a), vertical velocity variance (b), buayancy flux (c) and total water flux (d). Nicholls (1984) measurements are shown for horizontal flight legs (circles) and for sounding taken during slow descent at 1100 GMT (triangles).

The finite-difference discretization is based on the staggered Arakawa C-grid. The advective transport of momentum is computed using a flux-conserving advection scheme analogous to Tremback *et al* (1987) with an option to select the order of spatial accuracy from the second to the fifth. The

Corresponding author address: Dr. Yefim L. Kogan, Cooperative Institute for Mesoscale Meteorological Studies, University of Oklahoma, 100 E. Boyd, Norman, OK 73019. Email: ykogan@uoknor.edu

time integration is performed using the third-order Adams-Bashforth (AB) scheme. The numerical scheme is described in detail in Khairoutdinov and Kogan (1996).

The explicit formulation of microphysics is described in Kogan (1991) and K95. The recent improvement is the implementation of the new variational minimization method for remapping the drop spectra during condensation/evaporation calculations. The method (Liu *et al* 1994; Liu *et al* 1996) conserves four moments of the drop size distribution function and significantly minimizes the numerical diffusion of the drop spectra without sacrificing the computational efficiency of the code.

3. Case study

We present results of the CTBL simulation based on the data set collected by Nicholls over the North Sea during the flight 526 from 1100 to 1445 LST on 22 July 1982. Extensive airborne measurements performed on this day include turbulence characteristics, temperature, total water including vapor and liquid, turbulent fluxes, as well as cloud microphysical and radiative measurements (N84). The simulation was made using a rectangular domain with 40x40x50 grid points and 75 m grid size in the horizontal and 25 m grid size in the vertical.

Fig. 1 shows comparison results for the vertical profiles of TKE, vertical velocity variance, and fluxes of the virtual potential temperature and total water. The simulated parameters in general agree well with measurements, except for the top of the cloud, where the simulated TKE has a sharp maximum while the fluxes are underpredicted by the model. The horizontally averaged drop size spectra are shown in Fig. 2 for the 730 and 480 m levels that correspond to the cloud top and cloud base, respectively. The spectra are averaged over all points at the corresponding level where the liquid water content is larger then 0.05 g m^{-3}.

In general, one can see that the model reproduces reasonably well both the position and the magnitude of the maximum of the droplet distribution. The agreement is especially good at the cloud base (480 m). At cloud top, the most apparent discrepancy is the underprediction of the number of drops smaller then about 6 μm. The number of drops with radii between 20 and 50 μm is higher in the model, which, however, may be the result of the instrument error, as the Optical Array Probe (OAP) systematically undercounts drops in this size range (N84).

The integral parameters of the spectra, such as liquid water content, concentration and mean radius (Fig. 2c), are predicted very well. Of special importance is the ability of the explicit microphysical model to predict the large droplet tail of the spectra which determines the drizzle rates and the rain amount.

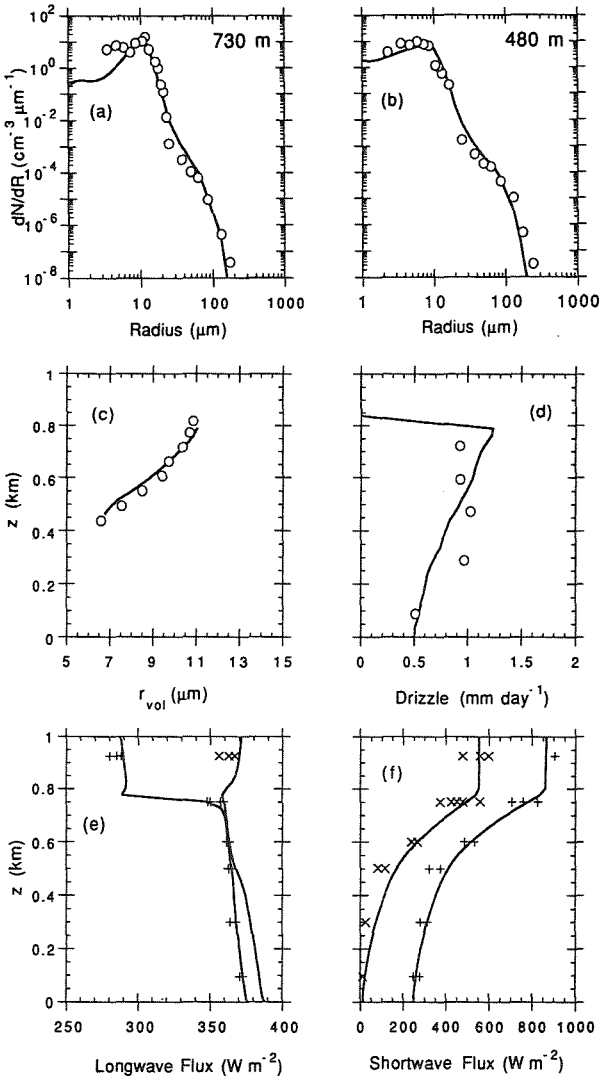

Fig. 2 The horizontally averaged drop size spectra at the cloud top (a) and base (b) together with the vertical profiles of mean volume radius (c), drizzle flux (d) and the upward and downward longwave (e) and shortwave (f) radiation fluxes. Symbols represent the data from Nicholls (1984).

The drizzle part of the spectra is rather well reproduced in the cloud itself (Fig. 2a,b), as well as in the subcloud region and near the surface (not shown). The drizzle rate (Fig. 2d) is slightly overpredicted in the upper part of the cloud and underpredicted in the subcloud region, but agrees well near the surface. However, the difference is not that significant given the fact that, according to Turton and Nicholls (1987), the uncertainty in the drizzle flux measurements may be as large as 40%.

Finally, we show (Fig. 2e,f) the comparison between the simulated and observed longwave (LW) and shortwave (SW) radiation fluxes. One can see that both the LW and SW fluxes are also in good agreement with the measurements.

4. Discussion

We have presented results from a case study based on the LES model that explicitly formulates cloud microphysical and interactive radiation processes. The results showed that the model is capable of predicting reasonably well the observed BL characteristics, including average profiles of the thermodynamical variables, turbulent kinetic energy, velocity variance, heat and moisture fluxes, drop size spectra, drizzle rates and radiative fluxes.

The case study illuminated several problems related to the model verification task. First, in order to make definite conclusions about the quality of the model predictions and to clearly understand its shortcomings, the observational data must have small scatter and fall into a narrow range. However, as distinct from many other branches of experimental science, the impossibility of environmental control and the large variability of meteorological parameters in nature makes the quantitative assessment of model predictions very difficult. This is clear from Fig. 1 where the turbulence parameters evaluated using data from different flight legs show considerable scatter. It is also worth noting that Nicholls data (N84) was collected during the flight lasting nearly 4 hours and covering a spatial domain of several hundred kilometers. The parameters of the boundary layer can change quite significantly over this distance. As an example we show in Fig. 3 the sounding profiles measured in one sortie during the ASTEX flight on June 12 1992. The three profiles were obtained within the 100 km distance and represented different boundary layer structures, as evidenced by a sharp inversion in P1, eroded inversion base and larger moisture of the air above the inversion in P2, and higher inversion height and cloud layer depth in P3. Obviously, the data set should be carefully selected for each specific boundary layer phenomenon. It is not clear if such analysis has been conducted during the 1982 experiment described in Nicholls (1984).

The effect of the inversion erosion on the drop number concentration is illustrated by Fig. 3a, b. In the P2 case, the wind profile (not shown) has a significant wind shear immediately below the cloud top. This leads to the increased entrainment of the above inversion air and partial evaporation of cloud drops. Similar conditions may have existed during the Nicholls flight 562 resulting in the spectrum broadening near the cloud top (Fig. 2a).

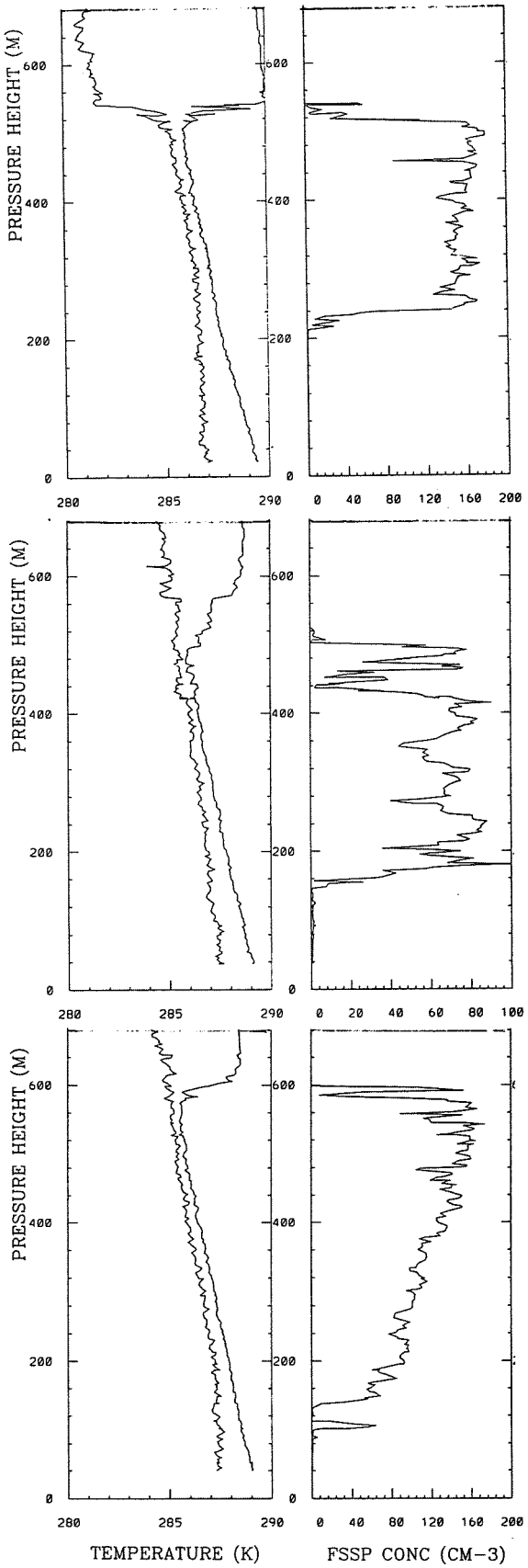

Fig. 3 Profiles of the absolute and dew point temperatures (left) and drop concentration (right) for the soundings P1 (top), P2 (middle) and P3 (bottom) taken during the ASTEX flight 209 on June 12, 1992.

The detailed analysis of ASTEX data made by Hudson and Yum (1996) showed that the standard deviation of the drop spectra decreases with height for stratocumulus clouds with LWC monotonically increasing with height. The latter feature is considered an indicator of cloud adiabaticity. The clouds that do not show such monotonic LWC increase are obviously less adiabatic and, as Hudson and Yum demonstrated, display more or less constant with height standard deviation of the drop spectra. While our simulation was made for a case with LWC monotonically increasing with height, the Nicholls data most likely represented a mix of adiabatic and non-adiabatic situations. The latter will result in broadening of the spectra near the cloud top.

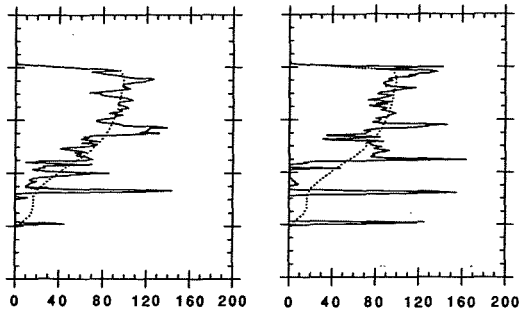

Fig. 4. Two soundings of droplet concentration as simulated by an "airplane flying" in the model domain (solid lines). The dotted lines show the concentration obtained by averaging over each horizontal plane.

We would like to point out another uncertainty which is related to the sampling procedure, namely, the interpretation of spatial observations made in one dimension along the airplane path. The effect is illustrated by Fig. 4 showing the vertical soundings of drop concentration taken along two different paths of a virtual aircraft "flying" in the numerical model domain. One can see that the drop concentration profiles exhibit quite different tendencies depending on the flight path. The more stable signatures are given by the drop concentration profile averaged over the whole horizontal cross-section (the dotted line in Fig.4).

In spite of the aforementioned measurement uncertainties, the case study based on Nicholls (1984) data set showed that the model overall predictions of turbulence, microphysical, and radiative parameters, in general, agree well with observations. A more accurate and judiciously selected data set is needed to make more certain quantitative conclusions about the accuracy of the model's physics and numerics. Such data sets are now available from ASTEX, MAST, and other field programs and will be used for verification of the model's ability to predict cloud drop spectra and drizzle rates in various boundary layer environments.

Acknowledgments. David Lam assisted with the figure preparation. Support for this research was provided by NOAA's Climate and Global Change Program under the Grants NA36GP0334, NA37RJ0203 and by the Environmental Sciences Division of the U.S. Department of Energy (through Battelle PNL Contract 144880-A-Q1 to the Cooperative Institute for Mesoscale Meteorological Studies) as part of the Atmospheric Radiation Measurement Program.

References

Hudson, J. G., and S. S. Yum, 1996: Droplet spectral broadening in marine stratus. Submitted to *J. Atmos. Sci.*

Khairoutdinov, M. F. and Y. L. Kogan, 1996: Case study of radiation and drizzle effects in a LES model with explicit microphysics. To be sumitted to *J. Atmos. Sci.*

Kogan Y.L., 1991: The Simulation of a Convective Cloud in a 3-D Model with Explicit microphysics. Part I: Model description and sensitivity experiments. *J. Atmos. Sci.*, **48**, 1160-1189.

Kogan, Y. L., M. P. Khairoutdinov, D. K. Lilly, Z. N. Kogan, and Q. Liu, 1995: Modeling of stratocumulus cloud layers in a large eddy simulation model with explicit microphysics. *J. Atmos. Sci*, **52**, 2923-2940.

Liu, Q.-F., Y. L. Kogan, D. K. Lilly, and M. P. Khairoutdinov, 1996: Variational optimization method for calculation of cloud drop growth in an Eulerian drop-size framework. Sumitted to JAS.

Liu, Q.-F., Y. L. Kogan, and D. K. Lilly, 1995: Reducing the numerical dispersion of the cloud droplet spectrum in condensation calculations. Preprints of the Conference on Cloud Physics, 15-20 January 1995, Dallas, TX.

Moeng, C.-H., 1984: A large-eddy simulation model for the study of planetary boundary layer turbulence., *J. Atmos. Sci.* , **41**, 2052-2062.

Nicholls, S., 1984: The dynamics of stratocumulus: Aircraft observations and comparisons with a mixed-layer model. *Q. J. R. Meteor. Soc.*, **110**, 783-820

Radke, L. F., J. H. Lyons, P. V. Hobbs, and J. E. Coakley, 1988: In situ measurements of "ship tracks" . *Preprints for 10-th Intern. Cloud Physics Conf.*, Bad Homburg, FRG, August 15-20, 1988. pp. 121-123, (vol. 1).

Tremback, C. J., J. Powell, W. R. Cotton, and R. A. Pielke, 1987: The forward-in-time upstream advection scheme: Extension to heigher orders. *Mon. Wea. Rev.*, **115**, 540-555.

Stevens, B., G. Feingold, W. R. Cotton, and R. L. Walko, 1996: Elements of microphysical structure of numerically simulated nonprecipitating stratocumulus, *J. Atmos. Sci.*, **53**, 980-1006.

Turton, J. and Nicholls, S., 1987: A Study of the diurnal variation of stratocumulus using a multiple mixed-layer model. *Q. J. Roy. Meteor. Soc.*, **113**, 969-1011.

A Microphysical Model of the Cloud Topped Marine Boundary Layer

Andreas Bott

Institut für Physik der Atmosphäre Johannes Gutenberg–Universität, D–55099 Mainz, Germany

1. INTRODUCTION

Stratiform clouds play a dominant role for the global energy budget. Due to their high albedo these clouds reflect very efficiently the incoming solar radiation. On the other hand they emit thermal radiation to space at a different temperature than the Earth's surface. The total radiative forcing of stratiform clouds is negative. To obtain a correct atmospheric energy budget, the accurate parameterization of stratus clouds is an essential task in general circulation models. The quality of a cloud parameterization scheme depends to a large extent on the proper simulation of the physical processes occurring within the clouds. In order to improve our understanding of these processes the one–dimensional **mi**crophysical **stra**tus model MISTRA has been developed. In MISTRA special emphasis is layed on a detailed treatment of cloud microphysical processes.

2. MODEL DESCRIPTION

The thermodynamic part of MISTRA consists of a set of prognostic equations for the components of the horizontal wind (u, v), the specific humidity q and the potential temperature θ

$$\frac{\partial u}{\partial t} = -w\frac{\partial u}{\partial z} - \frac{\partial}{\partial z}\overline{u'w'} + f(v - v_g) \qquad (1)$$

$$\frac{\partial v}{\partial t} = -w\frac{\partial v}{\partial z} - \frac{\partial}{\partial z}\overline{v'w'} - f(u - u_g) \qquad (2)$$

$$\frac{\partial q}{\partial t} = -w\frac{\partial q}{\partial z} - \frac{\partial}{\partial z}\overline{q'w'} + \frac{C}{\rho} \qquad (3)$$

$$\frac{\partial \theta}{\partial t} = -w\frac{\partial \theta}{\partial z} - \frac{\partial}{\partial z}\overline{\theta'w'} - \left(\frac{p_0}{p}\right)^{0.286}\frac{1}{c_p\rho}\left(LC + \frac{\partial E_n}{\partial z}\right) \qquad (4)$$

Here L is the latent heat of condensation and C the condensation rate. The vertical component w of the wind field describing the large scale subsidence must be prescribed in model. The net radiative flux density E_n is calculated from a modified version of the δ– two stream radiation code of Zdunkowski et al. (1982). The turbulent fluxes $\overline{\psi'w'}$, $\psi = u, v, q, \theta$ are determined by means of the level 2.5 model of Mellor and Yamada (1982). In the microphysical part of the model aerosol particles and cloud droplets are treated in a joint two–dimensional size distribution $f(a, r)$ with the radius a of the dry aerosol nucleus and the total particle radius r as independent variables. The size distribution of the dry aerosol particles is subdivided into 40 classes with logarithmically equidistant spacing between $0.025 \leq a \leq 0.5\mu m$. Each of the 40 aerosol classes is associated with 50 water classes where r is also logarithmically equidistant spaced in the range $a \leq r \leq 50\mu m$. The (a, r)– limits may be changed if necessary.

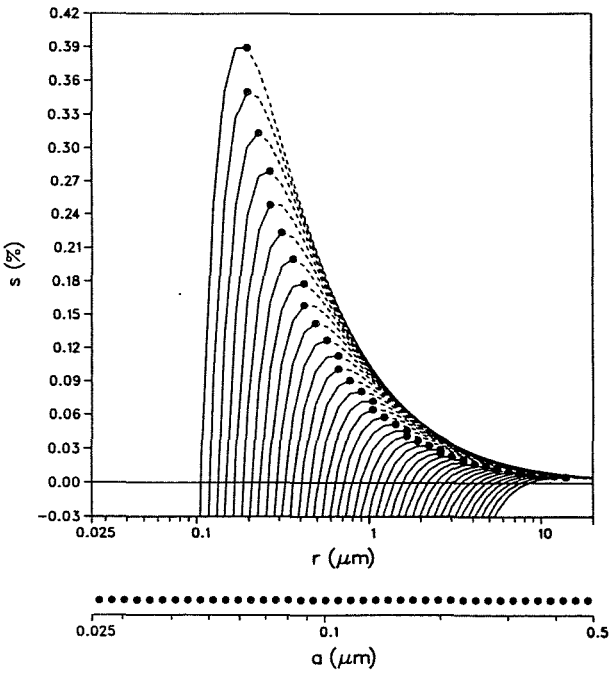

Figure 1. Critical supersaturation spectrum CSS. Lower panel: Size of dry aerosol particles. Upper panel: Stable parts (full curves), unstable parts (dashed curves) and critical supersaturations (big dots) of the 40 Köhler curves.

The activation of aerosols to form cloud droplets strongly depends on their chemical composition as well as on their radius as expressed by the Köhler equation. The smaller the radius of an aerosol particle the higher is its critical supersaturation $s(a, r)$. Due to the subdivision of the aerosol spectrum into 40 different classes, one obtains a critical supersaturation spectrum (CSS) consisting of 40 different values. Figure 1 shows the 40 Köhler curves and the resulting CSS as obtained with the present subdivision of the aerosol spectrum which is indicated in the lower part of the figure. The critical supersaturations are found at the maximum of each curve (big dots). Here the Köhler curves are split into their stable (full lines) and unstable parts (dashed lines).

The set of prognostic model equations is completed by an equation for the time rate of change of the two–dimensional particle size distribution $f(a,r)$

$$\frac{\partial f(a,r)}{\partial t} = -\frac{\partial}{\partial z}\Big((w + w_t(r))\, f(a,r)\Big) - \frac{\partial}{\partial z}\Big(\overline{f'(a,r)w'}\Big) - \frac{\partial}{\partial r}\Big(\dot{r} f(a,r)\Big) \tag{5}$$

In this expression the gravitational settling of aerosols/droplets is considered by adding to the large scale subsidence the terminal settling velocity w_t. The last term in (5) describes the modification of the particle spectrum due to condensation and evaporation processes whereby the droplet growth velocity $\dot{r}$ is calculated by including radiative effects. Finally, the condensation rate C occurring in (3) and (4) is obtained from the integral relation:

$$C = \int_0^\infty \int_0^\infty \frac{\partial}{\partial r}\Big(\dot{r} f(a,r)\Big) m_w(a,r)\, da\, dr \tag{6}$$

For the numerical solution of the model equations the atmosphere is separated into three different regions. In the lowest part ($0 - z_1 = 1000\,\mathrm{m}$) a constant grid distance of $\Delta z = 10\,\mathrm{m}$ is chosen. Between z_1 and $z_2 = 2000\,\mathrm{m}$ the atmosphere is subdivided into 50 logarithmically equidistant layers. In this region the prognostic equations are also solved, however cloud microphysical processes are not considered. The values of z_1, z_2 may be changed in the model if in a particular situation the top of the cloud exceeds z_1. Between z_2 and $z_3 = 50\,000\,\mathrm{m}$ a constant model atmosphere is applied for radiation calculations. The numerical timestep is 10 s, radiation calculations are done once per minute. The set of 40 droplet growth equations is iteratively solved by utilizing a semi–Lagrangian advection algorithm which is based on the positive definite advection scheme of Bott (1989a, b). A detailed description of this treatment may be found in Bott et al. (1990).

3. MODEL RESULTS

The numerical studies of the present paper are based on measurements of a stratocumulus field over the North Sea which was observed on 22 July 1982, (Nicholls 1984). The aerosol particles are assumed to be of the maritime type and the corresponding spectra are taken from measurements by Hoppel and Frick (1990). The model run starts at midnight (–24.00h). During the first 24 hours (between –24.00h and 0.00h) the cloud forms and achieves its quasi–steady state. Model results will now be presented for the period between 0.00–48.00h. Figure 2 depicts a contour plot of the total cloud water content m_w as function of height and time. Here and in the following the cloudy region is defined by the layers in which the liquid water content exceeds 0.01 g m^{-3}. During the day a distinct thinning of the stratus is observed resulting in a strong variation of the cloud water content with maximum values of 0.7 $g\,m^{-3}$ and 0.5 $g\,m^{-3}$ during the night and in the afternoon, respectively. The cloud base varies between 330 m in the early morning hours and 470 m in the late afternoon. At noon the cloud ranges from 400–790 m with a maximum liquid water content of more than 0.5 $g\,m^{-3}$. These model results agree quite well with the corresponding measurements by Nicholls (1984). Furthermore, in accordance with the observations m_w is almost linearly increasing with height as expressed by the equidistant spacing of the contour lines.

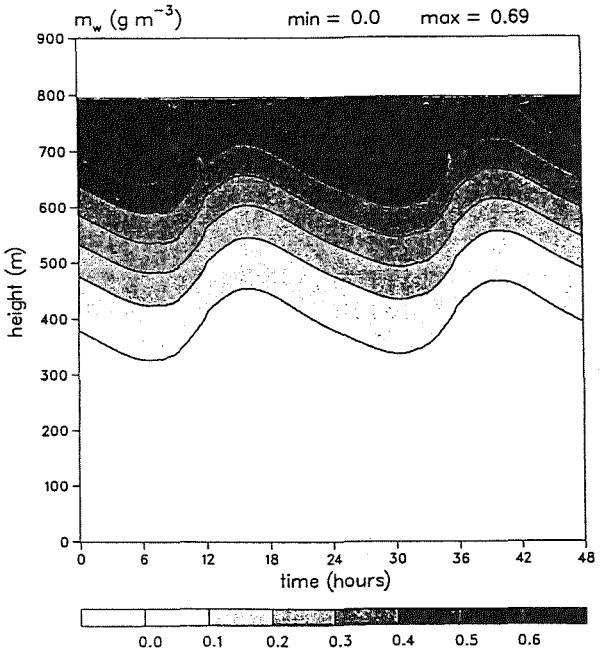

Figure 2. Contour plot of the cloud water content as function of height and time.

Figure 3 shows the contour plot of the turbulent kinetic energy e as function of height and time. The dotted area indicates the cloudy region. As can be seen from this figure, the highest values of the kinetic energy are found during the night and in the central part of the cloud. The model also tends to decouple the cloudy layer from the subcloud layer as expressed by the local e– minimum which occurs around noon (12.00h and 36.00h) immediately below cloud base. Another striking feature of this figure is the strong decrease of turbulence which is observed in the morning hours at cloud top. This is one of the most interesting features of the cloud topped marine boundary layer. During several field measurements it could be shown that within the PBL turbulence is much stronger at night than in the afternoon.

In addition to this, a dynamic decoupling of the cloud and the subcloud layer was observed during the day, (Nicholls 1984; Betts 1990; Hignett 1991). Measurements as well as model studies attribute this decoupling to the solar irradiance yielding during the day an increased radiative warming of lower cloud layers and thus a stabilization of the atmosphere.

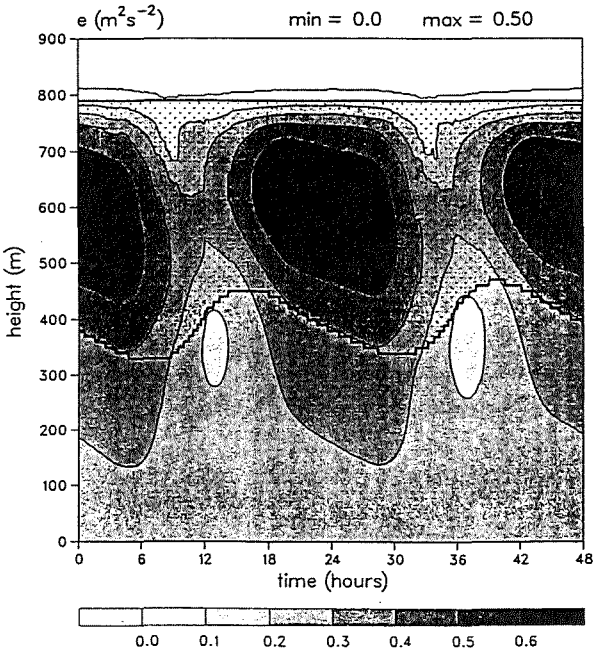

Figure 3. Contour lines of the turbulent kinetic energy as function of height and time.

Atmospheric radiation plays a dominant role in the cloud topped marine boundary layer because of the strong radiative cooling at cloud top and the influence of the solar irradiance on the decoupling of the cloud from the subcloud layer. Figure 4 displays vertical profiles of the radiatively induced temperature changes. The small figure shows a part of the same curves enlarged with different scales of the axes. The most remarkable feature of the profiles is the strong radiative cooling at cloud top which is restricted to a small layer of approximately 50 m. During the day these cooling rates are partially compensated by the solar warming, see the 15.00h and 39.00h curves. At all times the air is radiatively warmed in the lower half of the cloud.

Figures 5 depicts the two–dimensional particle distribution as obtained at 3.00h model time in the layer 780–790 m. The distribution is to be interpreted in the following way: Due to the diffusional growth and the corresponding uptake of water vapor, in each of the 40 aerosol classes with constant radius a_i, $i = 1, \cdots, 40$ the particles can move only along the $r-$ coordinate axis. Particles with the same dry aerosol radius a_i have in general not the same total size r, instead they form a particle subdistribution $f(a_i, r)$. Thus each particle spectrum consists of 40 subdistributions $f(a_i, r), i = 1, \cdots, 40$. The maximum of each subdistribution is given by the full circle, values between 50–99.9 % of the maximum are indicated by open circles while the crosses denote locations of particles with values of the curves between 1–50 % of the maximum. As can be seen from the figure, the smallest aerosol particles are never activated, they are always located in a single water class so that the corresponding subdistributions consists only of one point (the full circle). Nevertheless these aerosols are also humidified since their total radius exceeds the pure aerosol radius, i.e. $r > a$. Although within the two–dimensional aerosol–water grid the position of all particles is determined by solving the droplet growth equation, for the smallest unactivated aerosols this position would also be identically given by the Köhler equation because on the stable part of the Köhler curve the small aerosols achieve their equilibrium size very fast.

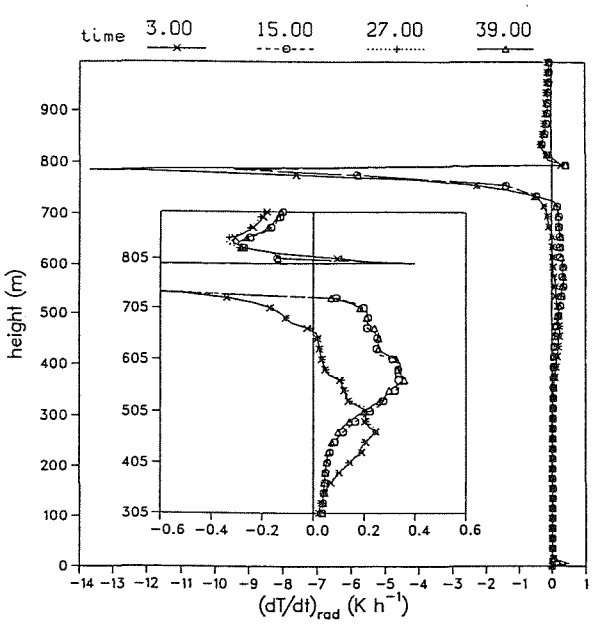

Figure 4. Radiative heating rates at the times indicated at the top of the figure.

Figure 5 contains two more curves. The full line shows the critical radii as function of the aerosol radius. Particles below this curve have not yet been activated while above the curve all particles are already activated. The dashed line splits the particle spectrum into two groups: On the right side of this line at the given supersaturation all

particles should be activated according to the CSS of Figure 1. On the left side of this line the critical supersaturation of the particles is higher than the actual supersaturation so that on this side no particle should be activated. Both curves together divide the aerosol/droplet spectrum into four distinct groups as indicated by the numbers in the corner of each figure.

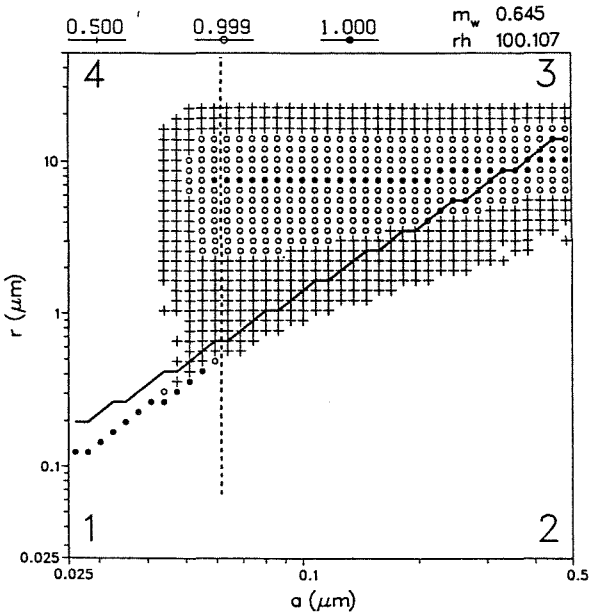

Figure 5. Two–dimensional particle distribution at 3.00 h model time in the layer 780–790 m. For more details see text.

By considering group 1 and 3 it is obvious that the particles of these groups are in accordance with the Köhler equation since they are either not activated (group 1) or activated (group 3). In contrast to this the particles of the other two groups do not behave as expected from the Köhler equation. Particles of group 2 should be activated but they are not while particles of group 4 should not be activated but they are. The latter droplets have been activated in other layers with higher supersaturation and have then been transported by turbulent mixing and eventually by sedimentation into the layer with lower supersaturation. The most interesting feature of Figure 5 is the occurrence of particles in group 2, i.e. nonactivated aerosols which should be activated at the given relative humidity. The discrepancy between the actual size of these particles and the Köhler equation becomes more pronounced with increasing dry aerosol radius a. The larger the aerosols the more of them are unactivated even though the critical supersaturation is decreasing with increasing aerosol size. This behavior is explained by the fact that the time scale of turbulent mixing processes is much shorter than the timescale of the diffusional growth of the large unactivated aerosol particles. These findings are of particular interest for cloud models dealing with one–dimensional aerosol and droplet distributions because in these models the activation process is usually parameterized in contrast to the detailed treatment of the present study. From our results it is seen that a diagnostic determination of the fraction of activated aerosols and the corresponding initial size of the cloud droplets solely as function of the actual supersaturation leads to errors particularly for the large aerosol particles.

4. ACKNOWLEDGEMENTS

This research is funded by the Deutsche Forschungsgemeinschaft, SFB 233, Chemie und Dynamik der Hydrometeore.

5. REFERENCES

Betts, A.K., 1990: Diurnal variation of California coastal stratocumulus from two days of boundary layer soundings. *Tellus,* **42A**, 302–304.

Bott, A., 1989a: A positive definite advection scheme obtained by nonlinear renormalization of the advective fluxes. *Mon. Wea. Rev.,* **117**, 1006–1015.

Bott, A., 1989b: Reply. *Mon. Wea. Rev.,* **117**, 2633–2636.

Bott, A., 1995: The impact of the physico–chemical microstructure of atmospheric aerosols on the formation of stratiform clouds. *J. Aerosol. Sci.,* **26**, S889–S890.

Hignett, P., 1991: Observations of diurnal variation in a cloud–capped marine boundary layer. *J. Atmos. Sci.,* **48**, 1474–1482.

Hoppel, W.A., and G.M. Frick, 1990: Submicron aerosol size distributions measured over the tropical and south pacific. *Atmos. Environ.,* **24A**, 645–659.

Mellor, G.L., and T. Yamada, 1982: Development of a turbulence closure model for geophysical fluid problems. *Rev. of Geoph. and Space Phys.,* **20**, 851–875.

Nicholls, S., 1984: The dynamics of stratocumulus: aircraft observations and comparisons with a mixed layer model. *Quart. J. Roy. Meteor. Soc.,* **110**, 783–820.

Turton, J.D., and S. Nicholls, 1987: A study of the diurnal variation of stratocumulus using a mixed layer model. *Quart. J. Roy. Meteor. Soc.,* **113**, 969–1009.

Zdunkowski, W.G., W.–G. Panhans, R.M. Welch and G.J.Korb, 1982: A radiation scheme for circulation and climate models. *Beitr. Phys. Atmosph.,* **55**, 215–238.

EQUILIBRIUM STATES IN DRIZZLING VERSUS NON-DRIZZLING STRATOCUMULUS

Bjorn Stevens[1], William R. Cotton[1] and Graham Feingold[2]

[1]Colorado State University, Department of Atmospheric Science, Fort Collins, CO, USA
[2]CSU/Cooperative Institute for Research in the Atmosphere, Fort Collins, CO, USA

1. INTRODUCTION

The potential impact of climatological changes in stratocumulus optical properties is by now well appreciated. Unfortunately, our understanding of this particular cloud type is still insufficient to state with any certainty what the nature of its response will be to environmental perturbations, anthropogenically induced or otherwise. Over the years a number of simple theoretical frameworks have been developed to advance our understanding. These frameworks, or models, have been used (as they well should be) to form a variety of hypotheses regarding the behavior of stratocumulus and their sensitivity to external perturbations. A number of these hypotheses appear to be well suited to tests by more sophisticated models—if not observations.

Two such hypotheses motivate our current study. The first states that cloud fractional coverage is a decreasing function of precipitation efficiency (Albrecht 1989; hereafter A89). The second (Pincus and Baker 1994; hereafter PB94) states that vertically-integrated cloud water (i.e., liquid water path LWP) decreases as drizzle production increases; largely because the equilibrium boundary layer is found to be deeper without commensurate changes in the lifting condensation level. Both hypotheses are based on an analysis of steady states produced by simple bulk models which include some measure of precipitation efficiency. For instance A89 uses a two layer model developed for the trade-wind boundary layer with a simple cloud parameterization which is a function of a precipitation efficiency parameter. PB94 modify a mixed layer model to account for precipitation and use cloud condensation nuclei (CCN) as a surrogate for drizzle efficiency.

Both studies raise interesting questions. For instance, do steady-states exist in observed boundary when drizzle is introduced? Additional questions raised by PB94 include the following: Does drizzle really mitigate entrainment and if so why? Is it realistic to expect a boundary layer that achieves a steady state over a deeper layer to necessarily produce a deeper cloud, or is this a result sensitively dependent on ones initial sounding? Lastly, it has been observed that clouds have a limiting depth beyond which their albedo changes little (e.g., Neiburger 1949). Thus raising the question as to whether drizzle production is common in clouds thin enough for their albedos to have an optical depth dependence.

Herein we begin to address the questions raised above. Our approach is to integrate a sophisticated model of the cloud-topped boundary layer and analyze our results. The nature of our model is summarized in §2. In §3 we twice use the model to simulate the observed structure of the ASTEX Lagrangian I boundary layer, once with drizzle and once without. In §4 we use the model to look for steady states for both drizzling and non-drizzling boundary layers, and investigate the simulated turbulent structures. Results presented here are based on a sounding taken from a single case study, integrations over a wider range of parameter space will ultimately be more revealing and will be presented at the meeting.

2. METHOD

In an attempt to avoid some of the assumptions that limit the simple models we directly simulate the radiative-turbulent-microphysical interactions of the energy containing scales of motion in stratocumulus topped boundary layers. To do so we use the Large Eddy Simulation (LES) technique (in which the energy containing scales of motion are explicitly represented) coupled to a detailed representation of the droplet spectrum. This approach, which for the case of stratocumulus clouds has been developed by our group (Stevens et al. 1996, Feingold et al. 1996) and the University of Oklahoma group (Kogan et al., 1995), has the advantage of allowing the eddy motions responsible for processes like supersaturation production, droplet activation, suspension of precipitation sized particles, and in-cloud mixing to be explicitly coupled to the microphysics. One limitation of our current approach is that we assume (as was done by Stevens et al., 1996) that CCN concentrations are fixed in time. This is not justified on physical grounds; CCN are continuously subjected to a variety of sources and sinks. Nonetheless, it does allow us to dispense with a considerable amount of complexity yet still isolate the questions in which we are interested. The reader is referred to the previously cited studies for more details and for a demonstration of the ability of such models to realistically reproduce important features of the desired interactions.

It has been demonstrated that two-dimensional integrations of buoyancy driven boundary layers are able to capture many of the elements of the three dimensional simulations (Moeng et al., 1996), although from a microphysical point of view the different nature of the mixing does constitute a limitation (e.g., Stevens et al, 1996). Nevertheless, the computational expediency of integrating a two dimensional (2D) analog of the LES model

favors its use in many situations. Extensive use of 2D integrations will be made of in this study, but recognizing their limitations we attempt to corroborate our results using LES.

The use of a variety of models requires some clarifying terminology. We use LES to designate three-dimensional simulations. The two dimensional analog to the LES is called an eddy resolving model (ERM). Traditionally boundary layer models are integrated using a saturation adjustment scheme which diagnoses liquid water and doesn't allow precipitation; when using such a scheme we indicate so through the use of the NM (no microphysics acronym). When the full binned microphysics is used we append BM to the acronym designating the dynamical framework. Hereafter we will often refer to integrations of the LES-BM or LES-NM or ERM-BM or ERM-NM models, whose meanings should be clear from the above discussion.

3. ASTEX LAGRANGIAN I: ERM SIMULATIONS

The methodology and results from the ASTEX Lagrangian experiments are well described in the literature (e.g., Bretherton and Pincus, 1995; Bretherton et al., 1995). The model is initialized with the initial sounding from the first Lagrangian and integrated over the full 42 hour duration of the experiment. Results are compared to observations and sensitivity runs. Fields beyond the local control of the boundary layer (i.e., sea surface temperatures, large-scale divergence, free-atmosphere thermodynamic properties and mean winds) are either set to, or nudged toward, their observed values on a three hour time-scale.

Selective model statistics are collected every minute and either written directly to a file or accumulated into hourly averages; a subset of the statistics are plotted as a time sequence in Fig. 1. The most striking feature of the data is the qualitative change in the characteristics of the time-sequence at about hour 18. In the first period the boundary layer grows modestly, produces significant drizzle, maintains solid cloud coverage and is characterized by less variability in w_{max} and q_{max}. As is the case for the observed boundary layer a number of things are happening around the time of the break. Solar insolation and SST is increasing, and drizzle is decreasing. In the second period the stratocumulus begins breaking up, the boundary layer grows more rapidly and by the 27th hour cumulus convection becomes prominent. The change in the convective circulation from stratus-like (with little skewness) to cumulus (with large skewness) results in the large time variability in quantities like LWP, w_{max}, and $q_{l,max}$. The more spike-like features of these fields over the latter period is the signature of cumulus in a domain too small to instantaneously represent an ensemble of cloud activity. During the period of diminishing cloud fraction, cloud base also rises and what drizzle that is produced generally evaporates before reaching the ground. Although not illustrated here, these results agree reasonably well with the observations. The biggest area of discrepancy lies in the fact that the simulated boundary layer grows more rapidly during the night, and less rapidly during the day than what was observed.

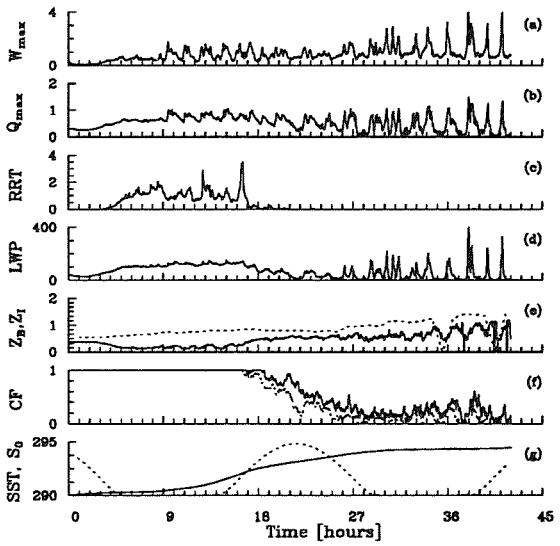

Figure 1: Time sequence of ERM-BM statistics. (a) Maximum vertical velocity [m/s]; (b) Maximum liquid water [g/kg]; (c) Rain rate [mm/day]; (d) LWP [g/m^2]; (e) Cloud base (solid) and Cloud top (dashed) heights [km]; (f) Two measures of cloud fraction (solid line uses presence of liquid water to indicated cloud in a column, dashed line requires column integrated liquid water to be greater than 13 g/m^2); (g) SSTs [K] (solid) and relative solar insolation (dashed).

In order to understand how drizzle affects boundary layer evolution we repeated the integration using the ERM-NM. Nothing else was changed; the model initialization procedure, forcing and configuration were identical to that in the previous integration. In Fig. 2 the time-sequence data from the non-drizzling integration is plotted. In many ways the simulations look similar as the marked transition in the quality of the time-sequence around the 18th hour is evident in both Figs. 1 and 2. There are, however, important differences. For instance, during the first period entrainment rates and LWP differ significantly between the simulations; after 15 hours the ERM-NM integration yields a boundary layer 200 m deeper than that produced by the ERM-BM, with LWPs about twice as large. We expect that such a response, which is similar to what is hypothesized by PB94, to be dependent on the moisture jump across the inversion. This issue will be addressed further at the meeting. Cloud fraction decreases more strongly in the absence of drizzle during the second (or more trade-wind like) period of the simulation. This result does not agree with the hypothesis that suppressing drizzle will lead to larger cloud fractions—although one should keep in mind that the NM model limits drizzle by the extreme assumption of zero phase relaxation time, for which clouds in a subsaturated environment evaporate immediately.

4. ERM STEADY STATES AND LES FIELDS

By fixing the SSTs and divergence at their initial values, and nudging the free-atmosphere temperature and water mixing ratio toward their observed initial values

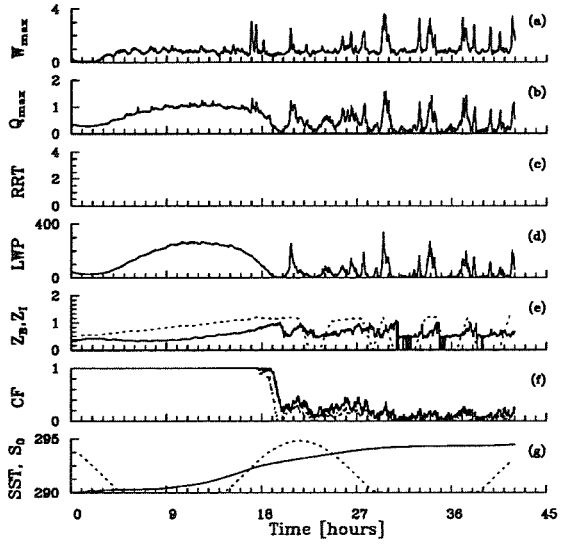

Figure 2: As in Fig. 1 but for the integration of the ERM-NM (i.e., no drizzle is allowed).

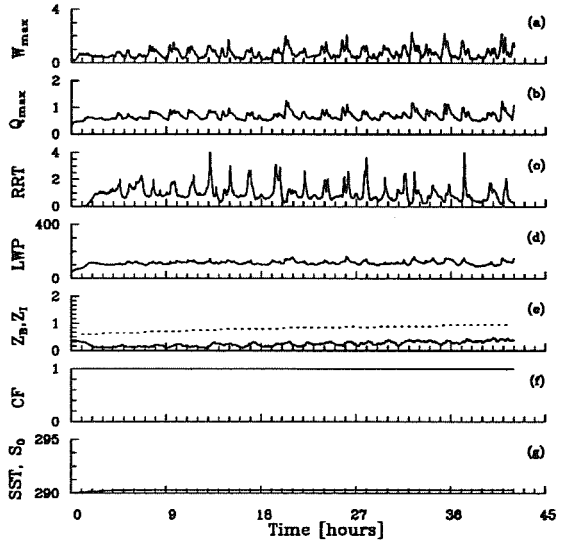

Figure 3: As in Fig. 1 but for the integration with no time-dependent forcing.

we produce a slowly evolving simulation with significant drizzle (see Fig. 3). The simulated state is quite similar to that observed during the first night of the experiment, thereby suggesting that near-equilibrium solutions are relevant to the observed boundary layer and that such solutions can exist in the presence of drizzle. Whether or not the simulation would evolve to a true steady-state is as yet unknown, although the rate of change of state variables is decreasing with time. An interesting aspect of this simulation is that there is nearly 1 K of stabilization in the sub-cloud layer. It is our impression that decoupled drizzling boundary layers are usually thought of as transient states in which drizzle induces decoupling which in turn leads to the breakup of the stratus deck. These results suggest that decoupled drizzling boundary layers can, under favorable conditions, exist in equilibrium with the large-scale forcing. Moreover, they strongly suggest that drizzle is not a necessary condition for stratocumulus breakup.

Although not shown, we have repeated the above simulation without drizzle. In this case the stratus layer grows much more rapidly and deepens considerably, clearly indicating that a non-precipitating boundary layer is far from equilibrium under the forcing characteristic of the ASTEX boundary layer observed during the first Lagrangian.

To better understand the thermodynamic structure of the precipitating boundary layer, and why it entrains less we integrated the LES-BM and LES-NMs model for 12600 s using initial conditions taken from the 12th hour of the first Lagrangian. We used a refined mesh: $\Delta x = \Delta y = 55$ m, $\Delta z = 25$ m and $\Delta t = 2$ s. Because the total length of the integration was only 3.5 hours it was possible to allow many external parameters to evolve freely; however, SSTs were increased with time in accord with the observations. Increasing SSTs subjected the simulation to a persistent surface buoyancy flux which complicates our analysis. Nonetheless a consideration of the mean profiles from the last 40 minutes of the simulation (Fig. 4) and the associated turbulent kinetic energy (TKE) budgets (Fig. 5) is illuminating.

For instance, the profiles indicate that the general behavior noted in the ERM integrations is reproduced by the LES. The LES-BM produces significant drizzle; a drizzle tail is evident in the profile of $\overline{q_l}$ and precipitation rates at the ground (not shown) average about 1 mm day^{-1}. Such a strongly drizzling solution is characterized by substantially reduced values of $\overline{w'w'}$, less entrainment, and a more pronounced stable sub-cloud layer. Note that the warm underlying surface contributes significantly to dry convective circulations in the lower mixed layer (below 300m) resulting in a low level maximum in $\overline{w'w'}$ and less stabilization across cloud base (near 400 m).

Fig 4 shows that the LES-BM entrains less than the LES-NM. Why is that? An answer is suggested by an analysis of the TKE budgets in Fig 5. The most dramatic difference between the simulations is in the buoyancy production and transport terms. The LES-NM has a much larger buoyant production of TKE. This allows significant amounts of TKE to be transported into the inter-facial zone to do the work against buoyancy necessary for entrainment to proceed at the observed rate. Although there is considerable time variability in $\overline{w'\theta_v'}$ (the buoyancy flux, which is a production term in the TKE budget) values produced by the LES-BM are consistently less than what is seen in the LES-NM; the greatest differences are between 300 and 500 m, in the vicinity of cloud base.

What is the relationship between drizzle and buoyancy production near cloud base? It appears clear that the tendency of drizzle to stabilize the cloud base region leads to a diminishment of the buoyant production of TKE which in turn results in smaller values of $\overline{w'w'}$ and less entrainment. Nonetheless, whether there exists a functional relationship between drizzle-flux and buoyancy-flux diminishment has yet to be determined.

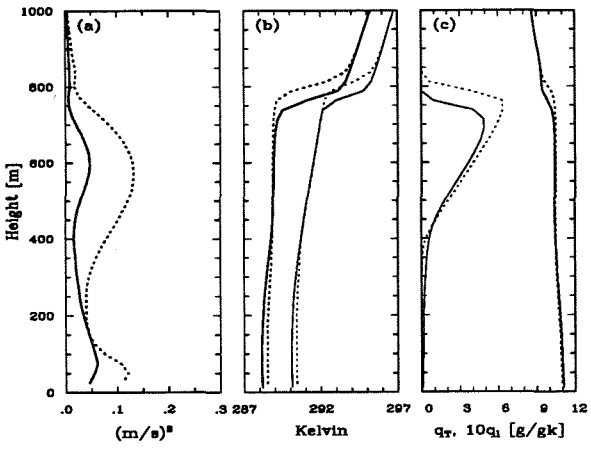

Figure 4: Profiles of various space and time averaged quantities from the LES-BM (solid lines) and LES-NM (dashed) integrations: (a) vertical velocity variance; (b) θ_l (thick lines) and θ_v (thin lines); (c) q_T (thick lines), $10 \times q_l$ (thin lines).

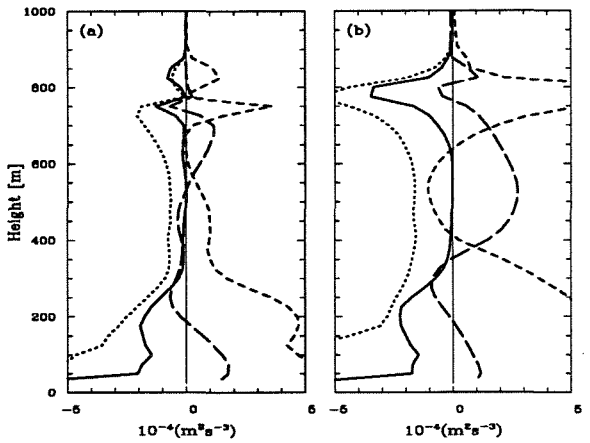

Figure 5: Profiles of various terms in TKE budget. Shear production (solid), dissipation (dotted), buoyancy production (long dash), transport (short dash). (a) LES-BM, (b) LES-NM

Results from a further exploration of this issue will be discussed at the meeting.

5. SUMMARY

Integrations of two and three dimensional models coupled to a detailed representation of warm-phase microphysical processes suggest that drizzle generates significant stabilization across cloud base which in turn leads to reduced buoyancy fluxes and less turbulence. Consequently drizzling boundary layers appear to entrain less than their non-drizzling counterparts. For this particular boundary layer increased entrainment leads to a deeper cloud so that the impact of drizzle on the boundary layer was as suggested by PB94, whether this response holds more generally has yet to be determined.

Equilibrium precipitating boundary layers appear to exist and are characterized by significant stabilization below cloud base. The character of the equilibrium boundary layer (for a given forcing) appears to strongly depend on drizzle production rates for at least one type of sounding. The idea that decoupled precipitating boundary layers can exist in equilibrium with the large scale forcing is contrary to the conventional view that looks on such states as transients living in the transition from a stratocumulus to a trade-cumulus boundary layer.

6. ACKNOWLEDGMENTS

BS is funded courtesy of a NASA Earth System Science Fellowship, WRC and GF receive support under a grant from the National Science Foundation. H. Jiang is thanked for her heroic efforts in resuscitating our computer after it died the week prior to the due date for this abstract. J. Harrington is thanked for providing us with a well behaved radiation model. C. Bretherton and S. Krueger are thanked for their help in setting up the ASTEX case study.

REFERENCES

Albrecht, B. A., 1989: Aerosols, Cloud Microphysics, and fractional cloudiness. *Science,* **245,** 1227–1230.

Bretherton, C. S. and R. Pincus, 1995: Cloudiness and marine boundary layer dynamics in the ASTEX Lagrangian experiments. Part I: Synoptic setting and vertical structure. *J. Atmos. Sci.,* **52,** 2707–2723.

Bretherton, C. S., P. Austin, and S. T. Siems, 1995: Cloudiness and marine boundary layer dynamics in the ASTEX Lagrangian experiments. Part II: Cloudiness drizzle, surface fluxes and entrainment. *J. Atmos. Sci.,* **52,** 2724–2735.

Feingold, G., B. Stevens, W.R. Cotton, and A.S. Frisch, 1996: On the relationship between drop in-cloud ersidence time and drizzle production in stratocumulus clouds. *J. Atmos. Sci.,* **53,** 1108-1122.

Kogan, Y. L., M. P. Khairoutdinov, D. K. Lilly, Z. N. Kogan, and Q. Liu, 1995: Modeling of stratocumulus cloud layers in a large eddy simulation model with explicit microphysics. *J. Atmos. Sci.,* **52,** 52 2293–2940.

Moeng, C-H., and co-authors, 1996: Simulation of a stratocumulus-topped PBL: Intercomparison among different numerical codes. Bull. Amer. Meteo. Soc., **77,** 261–278.

Neiburger, M., 1949: Reflection, absorption, and transmission of insolation by stratus cloud. *J. Meteo.,* **6,** 98-104.

Pincus, R. and M. B. Baker, 1994: Effect of precipitation on the albedo susceptibility of marine boundary layer clouds. *Nature,* **372,** 250–252.

Stevens, B., G. Feingold, W. R. Cotton, and R. L. Walko, 1996: Elements of the microphysical structure of non-precipitating numerically simulated stratocumulus. *J. Atmos. Sci.,* **53,** 980–1006.

ROLE OF RADIATIVE AND EVAPORATIVE COOLING IN THE ENTRAINMENT LAYER OF STRATOCUMULUS

Margreet C. van Zanten and Peter G. Duynkerke

IMAU, Utrecht University, Princetonplein 5, 3584 CC Utrecht, The Netherlands

1. INTRODUCTION

Cloud-top radiative and evaporative cooling are among the driving forces for turbulence in a stratocumulus-topped boundary layer. Radiative cooling occurs at cloud top because the upward long wave radiation from cloudy air exceeds the downward long wave radiation from the clear air above. Evaporative cooling occurs due to entrainment and mixing of cloudy air and clear air near cloud top. Both contribute to the negative buoyancy near cloud top and hence drive turbulence in the stratocumulus-topped boundary layer.

To predict the potential break up of stratocumulus through cloud top entrainment instability (CTEI) one has to understand the entrainment process at cloud top. In the past mainly the effect of evaporative cooling on the entrainment process has been studied (MacVean and Mason, 1990; Nicholls and Turton, 1986; Randall, 1980; Siems et al., 1990). In these studies the radiative cooling was only considered to be indirectly important for the entrainment; radiative cooling destabilizes the boundary layer and thus drives the turbulence that finally controls the entrainment rate. Recently (Shao et al., 1996) it has become clear that there is also a direct effect of radiative cooling on entrainment. From observations it was found that the effect of radiative cooling is of the same order as that of evaporative cooling whereas from Large Eddy Simulations (LES) they found a much smaller role for the radiative cooling.

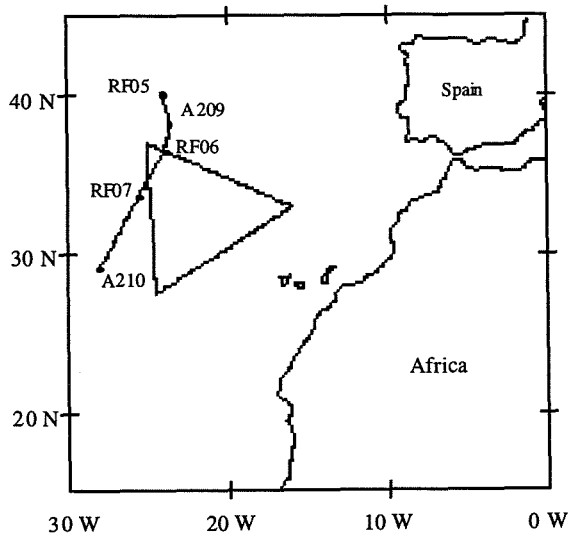

Figure 1: The trajectory of the first Lagrangian (from north to south) from 1600 UTC 12 June until 1600 UTC 14 June. Indicated are the ASTEX triangle and the flights of the NCAR Electra (RF05, RF06 and RF07) and the MRF C-130 (A209 and A210).

In this study we present observations of entrainment properties during the first "Lagrangian" observation period of the Atlantic Stratocumulus Transition Experiment (ASTEX), June 1992. In this experiment a column of air was tracked for 48 hours as it moved south-westward over water with increasing sea surface temperatures. We used the NCAR Electra (flight RF05, RF06 and RF07) and MRF C-130 (flight A209 and A210) aircraft data to study the cloud evolution during this Lagrangian (Fig. 1). During the first Lagrangian the boundary layer deepened with moderate to high wind speeds and substantial drizzle. The cloud developed from a solid well-mixed stratocumulus layer (RF05, A209, RF06 and RF07) to a layer filled with cumulus clouds penetrating thin and broken stratocumulus (A210). The sea surface temperature (Table 1) increased from 16.8 to 21.2 °C along the trajectory. In Table 1 the average height of cloud base and cloud top is given for the five flights.

	RF05	A209	RF06	RF07	A210
day	12	13	13	13	14
depart	17.19	00.32	04.51	16.27	11.11
land	21.33	04.26	10.13	21.09	13.02
T_s °C	16.8	17.2	18.3	20.1	21.1
z_{top}	740	755	770	1070	1600
z_{base}	250	240	280	610	500

Table 1. The observed sea surface temperature (T_s), cloud top (z_{top}) and cloud base (z_{base}) height along the trajectory of the first Lagrangian. Also given are for the time of departure and landing in UTC and the day (June 1992).

It shows that the inversion height and cloud thickness during the first three flights are quite stationary, with values of 750 and 500m, respectively. The cumulus clouds observed on flight A210 have a base at 500m and a cloud top at 1600m. From the aircraft observations we calculated the mixing ratios and the radiative and evaporative cooling. Moreover we performed a LES run based on the observations to investigate the entrainment properties in this model simulation.

2. INVERSION PROPERTIES

In Table 2 the observed mean liquid water content (q_{l2}) and the inversion jumps for the equivalent potential temperature (θ_e) and the total water (q_t) are shown for the five flights.

	RF05	A209	RF06	RF07	A210
$\Delta\theta_e$ [K]	-3.0	2.3	-0.6	-6.2	-6.6
Δq_t [g/kg]	-2.9	-1.2	-2.3	-4.4	-4.5
q_{l2} [g/kg]	0.37	0.60	0.55	0.51	0.12

Table 2. The observed mean liquid water content (q_{l2}) and mean jumps in equivalent potential temperature ($\Delta\theta_e$) and total water content (Δq_t) for the five flights of the first Lagrangian of ASTEX.

In Figure 2 the jumps for q_t are plotted as function of the jumps in θ_e, together with the CTEI criteria of Randall (1980), MacVean and Mason (1990), and Duynkerke (1993). The stability criteria divide the ($\Delta\theta_e$, Δq_t) plane as shown. If the criteria are sharp, we might expect that all jumps taken in persistent stratocumulus conditions have jump values which lie to the right of the critical line. We might expect that soundings taken near the boundary between the stratocumulus and cumulus regime are characterised by points near or to the left of the criteria. The jumps for the first Lagrangian are all made in solid stratocumulus, except for flight A210, and show that the criteria of Randall is often violated. The aim of this paper is to study the entrainment processes in more detail, both from observational and modelling perspective.

3. AN EXAMPLE OF OBSERVED MIXING PROPERTIES IN THE ENTRAINMENT LAYER

In order to study the entrainment properties we used data from porpoising runs through tops of stratocumulus. Here we used data from RF07. Figure 3 shows data (q_l, θ and q_v) from a slow ascent out of a stratocumulus deck. From all the porpoising runs it is clear that the inversion is very sharp and takes place over a vertical distance of several meters. We denote the height of the inversion with h_i. Below the inversion we typically observe a layer in which clear sig-

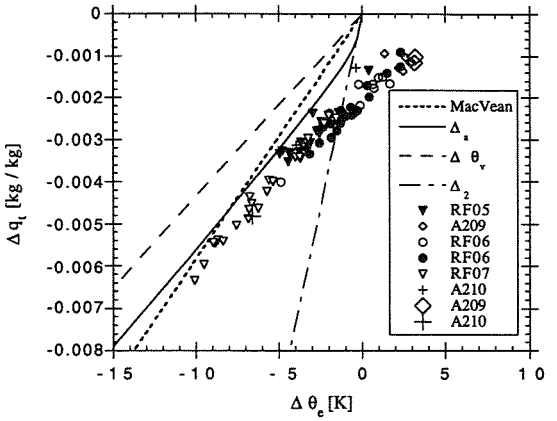

Figure 2: The jumps in total water content (Δq_t) as function of the jump in equivalent potential temperature ($\Delta\theta_e$) as observed during the first Lagrangian of ASTEX. The lines represent the different stability criteria: dash-dot Randall, short-dash MacVean and Mason, full line Duynkerke for q_l = 0.5 g/kg and long-dash $\Delta\theta_v = 0$..

natures of entrainment can be recognised; the so-called entrainment interface layer (EIL). The height of the EIL base is denoted by h_e. Below the EIL we have a well mixed convective layer with small(er) fluctuations in θ and q_t. The jumps in θ_e and q_t are derived from their mean values above h_{i+10m} and below h_e, respectively. The liquid water content in the cloud layer (q_{l2}) is set to the maximum observed.

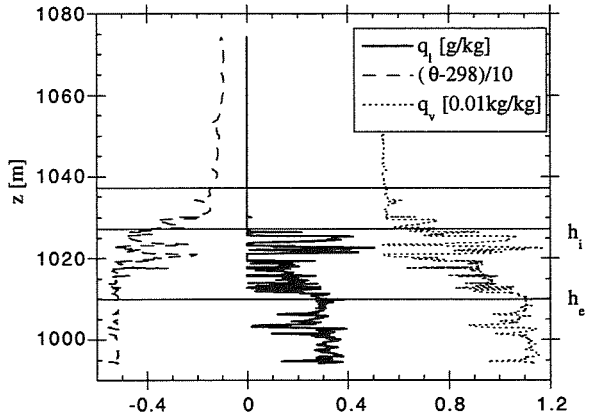

Figure 3: The liquid water content (q_l), potential temperature (θ) and water vapour content (q_v) as a function of height for part of a porpoising run during flight RF07. The height of the inversion h_i = 1027 m and the base of the EIL h_e = 1010 m.

For the calculation of the mixing ratio and the radiative and evaporative cooling terms we make use of the fact that both q_t and θ_e are conserved quantities for adiabatic processes. When precipitation is absent the mixing ratio χ can be calculated from (1), after which the radiative cooling term ($\delta\theta_r$) can easily be determined from (2), where subscript m denotes the mixed parcel value and subscript 2 denotes the cloud layer values. Finally for the calculation of the evapo-

$$q_{tm} - q_{t2} = \chi \, \Delta q_t \qquad (1)$$

$$\theta_{em} - \theta_{e2} = \chi \, \Delta\theta_e + \delta\theta_r \qquad (2)$$

rative cooling term we will use (3). The derivation of this formula can be found in Appendix A, Duynkerke (1993) whereby a radiative cooling term is added.

$$\theta_{vm} - \theta_{v2} = \chi\Delta\theta_e - \chi\Delta q_T \, (l_v/c_p - \psi\theta_{e2}) + \{l_v/c_p - (1 + \psi)\, \theta_{e2}\}(q_{lm} - q_{l2}) + \delta\theta_r \; . \qquad (3)$$

The quantitative effect of evaporative cooling becomes more explicit by writing the equation above into a pure mixing term ($\chi\theta_v$) and an evaporative cooling term ($\delta\theta_{ve}$):

$$\theta_{vm} - \theta_{v2} = \chi\Delta\theta_v + \delta\theta_{ve} + \delta\theta_r \, , \quad \text{with} \quad \delta\theta_{ve} = \{l_v/c_p - (1 + \psi)\, \theta_{e2}\} \left(q_{lm} - (1 - \chi)\, q_{l2}\right) \; . \qquad (4)$$

In figure 4 the results are shown of the calculations of the mixing fraction and different cooling terms. The data for these calculations are taken between h_i and h_e. From figure 4a can be seen that the whole range of mixing fractions is present, with a maximum for χ between 0.2 and 0.4. The q_{lm} for mixing fractions greater than this maximum is for almost all realisations equal to zero (fig. 4b). In figure 4c the evaporative and radiative cooling terms are presented. Clearly can be seen that the effect of radiative cooling is as large as the effect of evaporative cooling.

4. LARGE EDDY SIMULATION RESULTS

In order to compare these results with model simulations, a large eddy simulation is made based on flight A209. The used model is described in Cuijpers and Duynkerke (1993). The domain size of this simulation is 3200m by 3200m with a height of 1500m. The resolution is 50m in the horizontal and 25m in the vertical, with a time step of one second. The calculations are based on instantaneous values of temperature, total water and liquid water after three hours of simulation. The data of three different heights are used: the inversion layer and the layers just above and beneath the inversion layer (respectively, 812.5m, 837.5m and 787.5m). The inversion jumps in θ_e and q_t are derived from the averaged value beneath the inversion and a representative value at 862.5m above the inversion. The value of q_{l2} is taken at the representative height of 762.5m

In figure 5 the entrainment properties of the model simulation are presented. Figure 5a shows the mixing fractions for the three different layers. The complete range of mixing fractions exists; although large values of χ (> 0.8) are present in the heighest layer

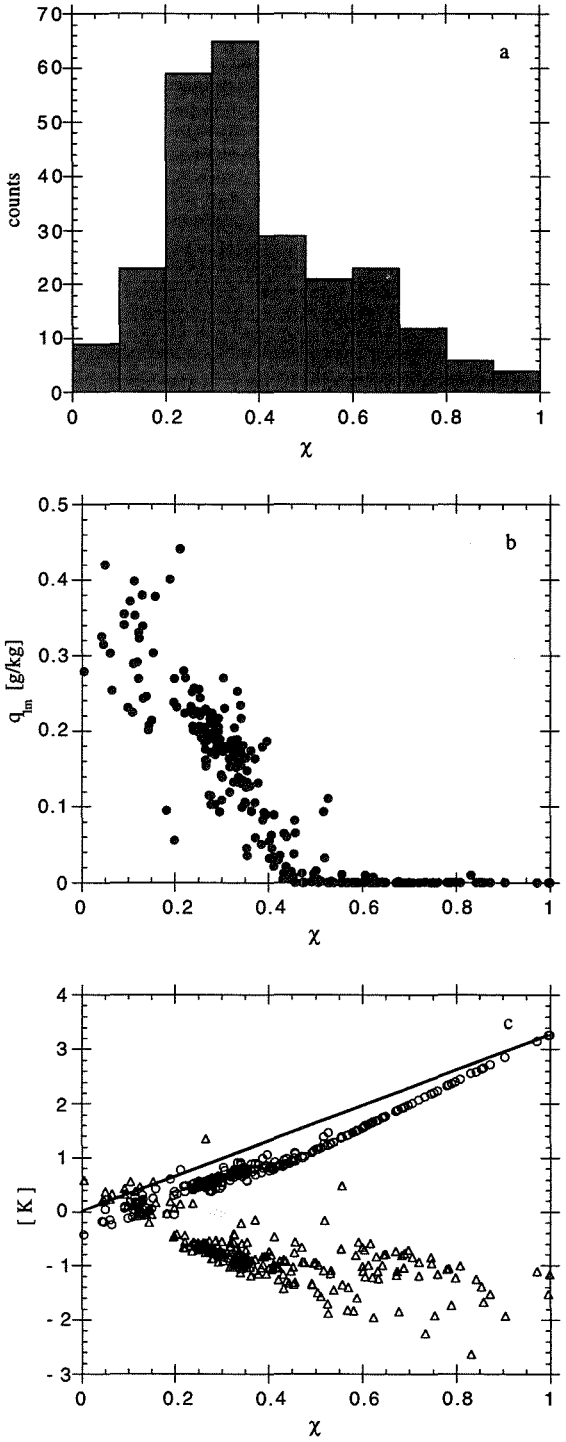

Figure 4: As a function of the mixing fraction (χ): a) the number of realisations, b) the liquid water content of the mixture (q_{lm}) and c) temperature change due to mixing $\chi\Delta\theta_v$ (line), mixing and evaporative cooling $\chi\Delta\theta_v + \delta\,\theta_{ve}$ (circles) and radiative cooling $\delta\theta_r$ (triangles). For a porpoising run during flight RF07.

only. In the lowest layer only values smaller than 0.4 exist. In the inversion layer a wider range of mixing fractions is available with a mean around 0.6. The radiative cooling term is in the model simulation of comparable order to the evaporative cooling term.

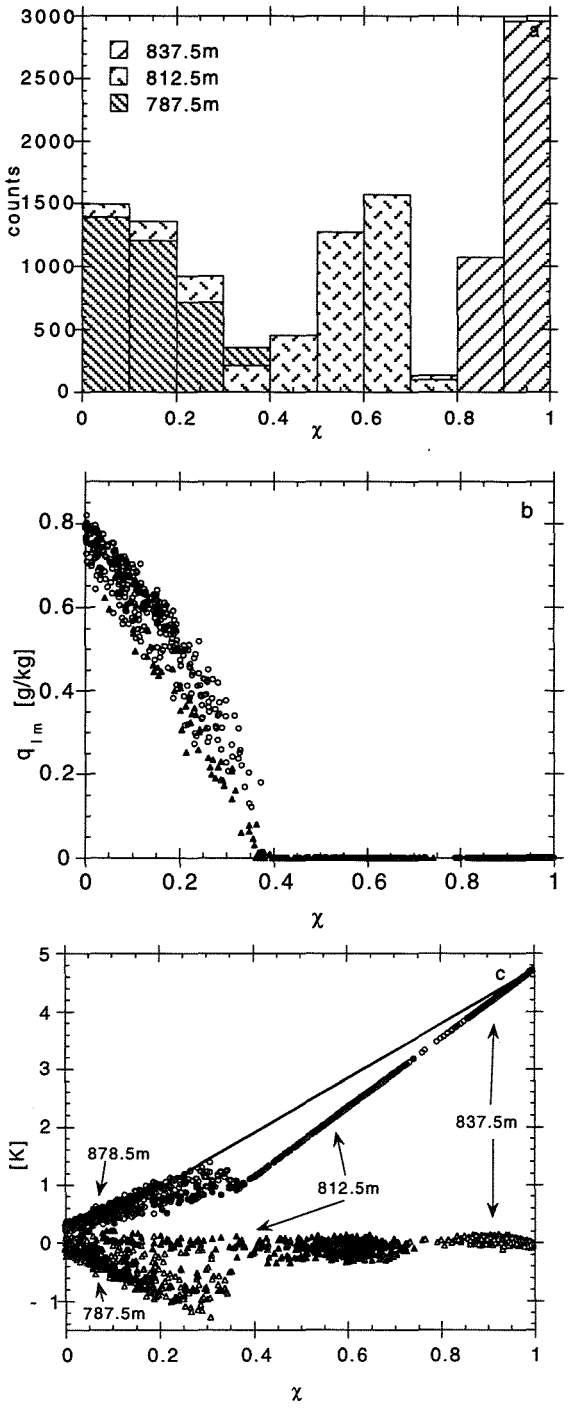

Figure 5: As a function of the mixing fraction (χ): a) the number of realisations, b) the liquid water content of the mixture (q_{lm}) and c) temperature change due to mixing $\chi\Delta\theta_v$ (line), mixing and evaporative cooling $\chi\Delta\theta_v+\delta\theta_{ve}$ (circles) and radiative cooling $\delta\theta_r$ (triangles). For a simulation with a LES model, the data are taken from a height of 787.5, 812.5 and 837.5m. In b and c only every tenth data point is plotted.

This in contrary with the findings of Shao et al. (1995). Largest radiative cooling rates are found in the layer beneath the inversion. While the radiative term above the inversion is zero or slightly positive. Largest evaporative cooling terms are found for χ around 0.4, independent of the height of the layer.

5. CONCLUDING REMARKS

Both from observations and Large Eddy Simulation it is shown that the radiative cooling is as important as the evaporative cooling in the entrainment process. Therefore, in order to develop a conceptual model for entrainment it is necessary to include this radiative cooling term. Future research will address the parametrization of the radiative cooling term and its importance in the entrainment process for stratocumulus.

6. ACKNOWLEDGMENTS

The investigations were supported by the Netherlands Geosciences Foundation (GOA) with financial aid (grant 750.295.03B) from the Netherlands Organisation for Scientific Research (NWO).

7. REFERENCES

Cuijpers, J.W.M. and P.G. Duynkerke, 1993: Large Eddy Simulation of trade wind cumulus clouds. *J. Atmos. Sci.*, **50**, 3894-3908.

Duynkerke, P.G., 1993: The stability of cloud top with regard to entrainment: amendment of the theory of cloud top entrainment instability. *J. Atmos. Sci.*, **50**, 495-502.

Duynkerke, P.G., H. Zhang and P.J. Jonker, 1995: Micro physical and turbulent structure of nocturnal stratocumulus as observed during ASTEX. *J. Atmos. Sci.*, **52**, 2763- 2777.

MacVean, M.K. and P.J. Mason, 1990: Cloud-top entrainment instability through small-scale mixing and its parametrization in numerical models. *J. Atmos. Sci.*, **47**, 1012-1030.

Nicholls, S. and J.D. Turton, 1986: An observational study of the structure of stratiform cloud sheets: Part II. Entrainment. *Quart. J. Roy. Met. Soc.*, **112**, 461-480.

Randall, D.A., 1980: Conditional instability of the first kind upside-down. *J. Atmos. Sci.*, **37**, 125-130.

Shao, Q., D.A. Randall and C-H Moeng, 1996: A new approach to determine the radiative and evaporative cooling rates in the entrainment layer of a stratocumulus-topped boundary layer, (submitted to J. Atmos. Sci.)

Siems, S.T., C.S. Bretherton, M.B. Baker, S. Shy and R.E. Breidenthal, 1990: Buoyancy reversal and loud top entrainment instability. *Quart. J. Roy. Met. Soc.*, **116**, 705- 739.

STUDY OF AEROSOL PROCESSING IN STRATOCUMULUS CLOUDS USING LES EXPLICIT MICROPHYSICAL MODEL WITH THE AEROSOL TRACKING OPTION

Qingfu Liu and Yefim Kogan

Cooperative Institute for Mesoscale Meteorological Studies
University of Oklahoma, Norman, OK

1. Introduction

The interaction between stratocumulus clouds and aerosols involves a variety of mechanisms, among them activation of aerosols by growing cloud drops, their recycling after evaporation, and scavenging of aerosols by falling precipitation. However, before aerosols are removed by precipitation, their parameters are substantially modified due to cloud processing. According to Pruppacher and Klett (1978), the cloud material, on a global scale, goes through about ten condensation-evaporation cycles before cloud eventually precipitates. The effect of the repeated cycling of cloudy air is the decrease of small aerosol particles and the increase of aerosol mass at sizes larger than 0.1 micron. The cloud recycling also produces a minimum at a size determined by maximum supersaturation in cloud. The increased mass of larger particles is the result not only of coalescence of cloud drops, but also Brownian scavenging of interstitial aerosol, as well as gas-to-particle conversion inside cloud drops.

Cloud processing of aerosols has been studied by Hudson and Frisbie (1991) and Hudson (1993) using extensive airborne measurements of CCN spectra and concentrations of total particles during FIRE and Hawaiian Rainband Project (HaRP) experiments. The FIRE observations carried out over the 4-day period showed the decrease in the boundary layer aerosol concentration consistent with the in-cloud scavenging process. Hudson and Frisbie (1991) emphasize the importance of the "coalescence scavenging". It reduces the CCN concentration according to the number of cloud droplet captures, as well as transforms the CCN size distribution. The more active nuclei (corresponding to lower critical supersaturations) are not only preferentially used to form cloud droplets, but also increase in size due to the recycling following coalescence and evaporation of cloud droplets. The efficiency of the in-cloud scavenging processes can be estimated from the measured reduction of CCN concentration in the boundary layer below the inversion, and by comparing the CCN activation spectra in a cloud-free air with those in the air within and around the clouds. Observations by Hudson (1993) confirm that concentrations of CCN are often lower within the boundary layer and they are also composed of larger particles with lower median critical supersaturation. Under conditions with few, or without clouds, the spectra below and above the temperature inversion are similar.

In the present paper we study the processing of aerosol particles due to nucleation scavenging and "coalescence scavenging" using a new version of the CIMMS LES model that allows to track CCN particles inside the cloud.

2. CIMMS LES cloud model

The physical formulation of the CIMMS LES cloud model is described in Kogan et al. (1995). The current version of the model employs a new dynamical framework based on the finite difference discretization. The advective transport of momentum is computed using a flux-conserving advection scheme analogous to Tremback's (1983) with an option to select the order of spatial accuracy from the second to the fifth. The time integration is performed using the third-order Adams-Bashforth (AB) scheme. The numerical scheme is described in detail in Khairoutdinov and Kogan (1996).

The numerical and physical formulation of microphysics is described in Kogan et al (1995). The recent improvement in numerical formulation is the implementation of the new variational minimization method for remapping drop spectra during condensation/evaporation calculations. The method (Liu *et al* 1994; Liu *et al* 1996) conserves four moments of the drop size distribution function and significantly minimizes the numerical diffusion of the drop spectra without sacrificing the computational efficiency of the code.

For the aerosol processing study, the microphysical formulation has been significantly modified by introducing a two-dimensional Drop and Salt Size Distribution (DSSD) function, $N(m,n)$, which allows to follow the salt (CCN) particles transformations as they are processed by cloud drops. The function $N(m,n)$ represents drop mass distribution such that $N(m,n)dmdn$ is the number of particles per unit volume of air in the drop mass range from m to $m+dm$ and the salt mass range from n to $n+dn$. Let N_{ij} denote the DSSD function in the discrete form with the indices i and j referring to the drop and the

* Corresponding author address: Qingfu Liu, Cooperative Institute for Mesoscale Meteorological Studies, University of Oklahoma, 100 E. Boyd, Norman, OK 73019. Email: qliu@tornado.gcn.uoknor.edu

CCN mass categories, respectively. The governing equation for the 2D drop spectrum is (Houze, 1993):

$$\frac{\partial N_{ij}}{\partial t}+\frac{\partial}{\partial x_k}(u_k N_{ij}) = R_{ij}+D_{ij}+C_{ij} + S_{ij}+\frac{\partial}{\partial x_k}(K_m \frac{\partial N_{ij}}{\partial x_k})$$

The changes in the concentration N_{ij} are the result of nucleation (R_{ij}), vapor diffusion (D_{ij}), collection (C_{ij}), sedimentation (S_{ij}) and turbulent diffusion.

For the collection term (C_{ij}), we assume that the collection kernel depends only on the cloud drop mass, and the nuclei are coalesced whenever two parent drops coalesce. The cloud droplet mass m and the nuclear mass n of the newly formed drop are determined by adding the m's and n's of the coalescing drops, respectively. Therefore, the stochastic collection equation can be written as,

$$C_{ij}=\frac{1}{2}\int_0^{m_i}\int_0^{n_j} W(m_i-m',m')N(m_i-m',n_j-n') N(m',n')dn'dm' -\int_0^{\infty}\int_0^{\infty} W(m_i,m')N(m_i,n_j)N(m',n')dn'dm'$$

where W(m,m') is the collection kernel defined in Kogan (1991).

In addition to drop particles, we also account for CCN particles which do not form cloud drops. We specify the mass distribution function $f(n)$ such that $f(n)dn$ is the number of CCN particles per unit volume of air in the mass range between n and $n+dn$. The governing equation for $f(n)$ (f_j in the discrete form) is:

$$\frac{\partial f_j}{\partial t}+\frac{\partial}{\partial x_k}(u_k f_j) = -\sum_i R_{ij}+\sum_i E_{ij} + \frac{\partial}{\partial x_k}(K_m \frac{\partial f_j}{\partial x_k})$$

The RHS of the equation represents changes in the CCN concentration f_j as the result of nucleation (R_{ij}), evaporation of cloud drops (E_{ij}) and turbulent diffusion.

3. Simulation results

We show the simulation results based on the sounding taken during the flight A334 in the Monterey Area Ship Track (MAST) field experiment. In order to save computer time and to accelerate the coagulation process, the sounding was slightly modified to make the cloud layer thicker. We use 25 bins for cloud drops in the size range from 1 to 256 micron, and 11 bins for CCN in the size range from 0.0076 to 18 micron. The total number of prognostic equations in the model is 292, which includes 5 equations for the thermodynamical variables, one for the TKE, 11 for CCN, 275=25x11 for cloud drops. The simulation was made in a domain using 40^3 grid points with grid sizes $\Delta x=\Delta y=100$ m and $\Delta z=20$ m. The simulation was first run in the bulk mode for 1.5 hours until the turbulence was fully developed. Then the model was run for half hour in the detailed microphysics mode without coagulation, afterwards the coagulation was started and the model was run for another 30 minutes

Fig. 1a, b show the horizontally averaged vertical profiles of cloud drop (CD) and total particle concentration (CD+CCN). The removal of particles due to drop coalescence is evident in Fig. 1b by the decrease in the particle concentration compared to the background concentration which was set equal to 161.7 cm^{-3}. Even though the coalescence process is confined to the cloud layer, the particle concentration decreases throughout the mixed layer due to the turbulent mixing. The particle loss is a non-linear process. Its rate increases with the decrease in the drop

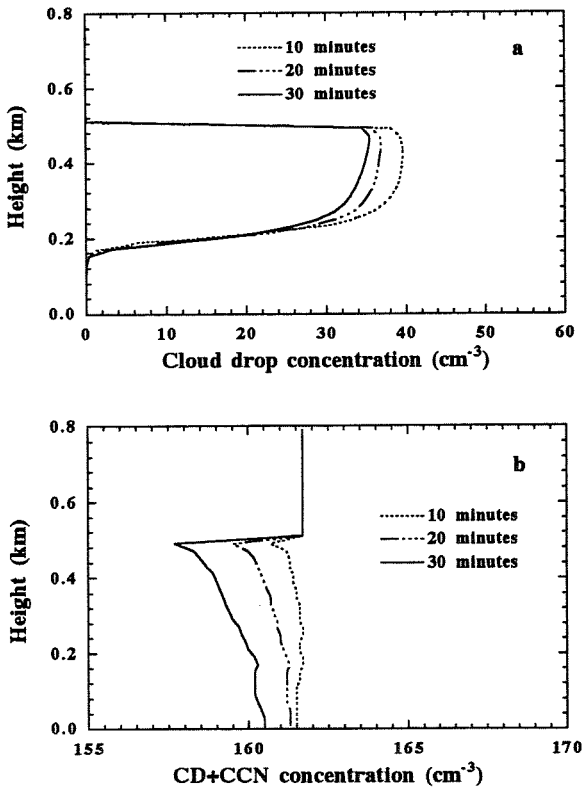

Fig. 1. Horizontally averaged vertical profiles of (a) cloud drop concentration and (b) total particle concentration (CD+CCN) at 10, 20 and 30 minutes after the coagulation started.

number which , in turn, results in acceleration of the coagulation process. During the half hour simulation with the coagulation turned on, the total number of particles in the boundary layer decreased by 0.52%, 1.75%, and 3.50% at 10, 20 and 30 minutes, respectively.

Fig. 2a shows the 2D bar-diagram of the DSSD averaged over the horizontal plane at z=0.47 km level. A quantitative idea about the DSSD at various cloud levels is given by Fig. 2b, c which show the cross-sections of the 2-D DSSD along the CCN size and drop size axis, respectively. More precisely, Fig. 2b shows the liquid water distribution integrated over all drop bins as a function of CCN size, while Fig. 2c shows the same distribution (horizontally averaged and integrated over all CCN bins) as a function of drop size. Near cloud base (z=0.23 km), the liquid water is more or less evenly distributed over all activated CCN categories. However, at higher levels the maximum of the LWC falls into the CCN category which has the maximum number of activated CCN particles (line with crosses in Fig. 3). The mean drop radius at a given cloud level (Fig. 2d) does not significantly depend on the CCN category. This means that cloud drops become diluted rather quickly and the effect of salt on the drop growth is insignificant, except of very small drops.

The average cloud drop spectra shown in Fig. 2c for different levels are mostly unimodal, although the large droplet tail is already evident. We note that coagulation was run in the experiment only for 30 minutes. At longer simulation times the second (drizzle) mode will eventually develop and result in a more significant transformation of the CCN spectra.

The effects of coagulation on the CCN spectra after 30 minutes are summarized in Fig. 3. The initial CCN spectrum in the ambient atmosphere is shown by the solid line, the CCN spectrum at 30 minutes (averaged over the entire domain) that would result if all cloud drops evaporate, is shown by the dashed line with triangles. Part of CCN particles are activated by nucleation (dotted line with crosses) and part of CCNs remain as interstitial aerosol (line with diamonds). We can see that the percentage of activated CCN particles varies from 0 to 100% depending on the CCN category. For example, at bin 5 (CCN size equal to 0.055 μm corresponding to critical supersaturation 0.3%) only about 50% of CCNs are activated. The partial activation is due to the large scatter in vertical velocities and, hence, the large scatter in supersaturations at the cloud base. As a result, some number of large CCN particles will remain unactivated at certain locations and exist as interstitial aerosols. For example, particles in bin 7 (CCN size equal to 0.31 μm which corresponds to critical supersaturation 0.1%) have not been activated and most likely have been brought into the cloud layer by relatively weak updrafts or by entrainment from the cloud top.

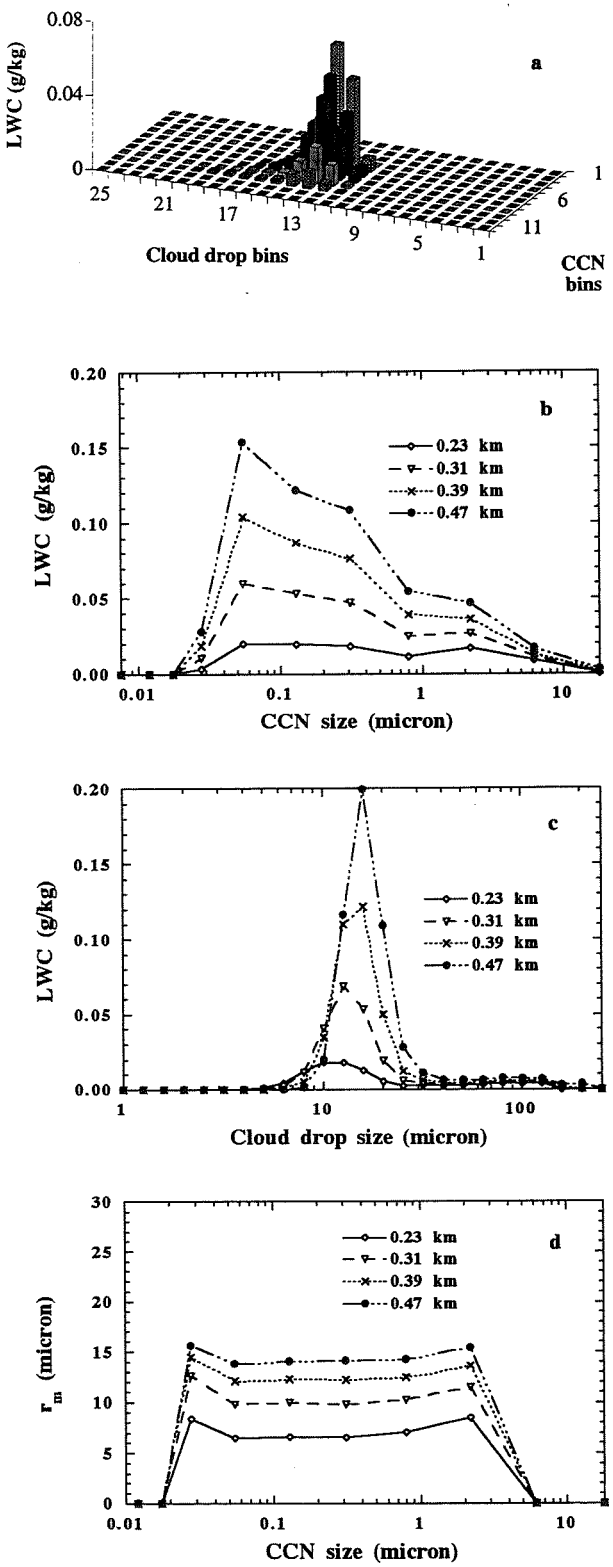

Fig. 2. (a) The horizontally averaged DSSP spectrum at z=0.47 km. (b) and (c) show the horizontally averaged LWC distribution as functions of the CCN size (integrated over all cloud drop bins) and cloud drop size (integrated over all CCN bins), respectively. (d) shows the horizontally averaged mean drop radius as a function of the CCN size.

The dashed line with open circles shows the particle loss due to coalescence process. The loss in terms of particle number is most significant for the smallest activated CCNs. For the largest CCN categories there is a very small gain in concentration, as formulation of one large CCN particle may require hundreds or even thousands of small CCN particles to combine.

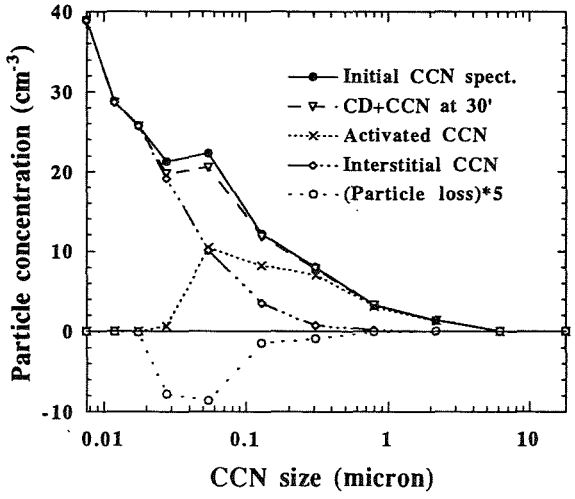

Fig. 3. Summary of the effects of coagulation process on the CCN and cloud drop spectra: solid line shows the initial ambient CCN spectrum; long-dashed line with triangles shows the CCN spectrum if the cloud would completely evaporate at 30 minutes; dotted line with crosses shows the activated CCN distribution; dashed-dotted line with diamond shows the interstitial aerosol distribution; dashed line with circles shows particle loss distribution due to coalescence process (multiplied by 5). All spectra are averaged over the whole cloud domain where LWC is greater that 0.05 g/kg.

4. Conclusions

We presented preliminary results from a new version of the CIMMS LES model that is capable to track the CCN particle transformations as a result of drop coagulation. The cloud microphysical processes are formulated based on a two-dimensional distribution function that depends on the cloud drop size and the aerosol soluble mass inside each drop. This new feature significantly enhances our previous approach based on two separate one-dimensional functions for CCN and cloud drop spectra and allows us to study the aerosol history and transformation of the aerosol spectra as a result of cloud drop collisions and scavenging effects.

The 3-D simulation of the coagulation effects in a stratocumulus cloud-topped boundary layer have demonstrated the effect of coagulation on the salt distribution inside cloud drops and on the transformation of the interstitial aerosol. The quantitative results, so far, are limited only to 30 minutes of coagulation time. Longer time simulations are now underway to evaluate the aerosol transformation effects in more detail. These results will be presented at the conference.

ACKNOWLEDGMENTS: The authors would like to thank Prof. D. K. Lilly for helpful discussions and comments. Support for this research was provided by NOAA's Climate and Global Change Program under the Grants NA36GP0334, NA37RJ0203 and by the Environmental Sciences Division of the U.S. Department of Energy (through Battelle PNL Contract 144880-A-Q1 to the Cooperative Institute for Mesoscale Meteorological Studies) as part of the Atmospheric Radiation Measurement Program.

REFERENCES

Khairoutdinov, M. F. and Y. L. Kogan, 1996: Case study of radiation and drizzle effects in a LES model with explicit microphysics. To be sumitted to JAS.

Kogan Y.L., 1991: The Simulation of a Convective Cloud in a 3-D Model with Explicit microphysics. Part I: Model description and sensitivity experiments. *J. Atmos. Sci.*, 48, 1160-1189.

Kogan, Y. L., M. P. Khairoutdinov, D. K. Lilly, Z. N. Kogan, and Q. Liu, 1995: Modeling of stratocumulus cloud layers in a large eddy simulation model with explicit microphysics. *J. Atmos. Sci*, 52, 2923-2940.

Liu, Q.-F., Y. L. Kogan, and D. K. Lilly, 1995: Reducing the numerical dispersion of the cloud droplet spectrum in condensation calculations. Preprints of the Conference on Cloud Physics, 15-20 January 1995, Dallas, TX.

Liu, Q.-F., Y. L. Kogan, D. K. Lilly, and M. P. Khairoutdinov, 1996: Variational optimization method for calculation of cloud drop growth in an Eulerian drop-size framework. Sumitted to JAS.

Houze, R. A, Jr., 1993: Cloud dynamics. Academic Press, New York, 573 pp.

Hudson, J.G. and P.R. Frisbie, 1991: Cloud condensation nuclei near marine stratus. J. G. R., 96, No. D11, 20795-20808.

Hudson, J.G., 1993: Cloud condensation nuclei near marine cumulus. *J. Geophys. Res.*, 98, 2693-2702.

-------, and P.R. Frisbie, 1991: Cloud Condensation Nuclei Near Marine Stratus, *J. Geophys. Res.*, 96, 20795-20808

Pruppacher, H. R., and J. D. Klett, 1978: *Microphysics of clouds and precipitation.* D.Reidel, 714pp.

Tremback, C. J., J. Powell, W. R. Cotton, and R. A. Pielke, 1987: The forward-in-time upstream advection scheme: Extension to heigher orders. *Mon. Wea. Rev.*, **115**, 540-555.

HAWAIIAN RAINBANDS: EFFECTS OF THERMAL FORCING ON THE RAINBAND DYNAMICS

Vanda Grubišić, Piotr K. Smolarkiewicz, Roy M. Rasmussen, and Richard E. Carbone

NCAR, Boulder, CO 80307, USA

The existence of the upstream, arc-shaped rainbands is one of the striking characteristic of the flow past Hawaii. This approximately 4 km high island represents a large obstacle embedded in a typically easterly tradewind flow, and to the first approximation, many of the mesoscale flow features upstream and downstream of the island can be described with a model of strongly-stratified flow past an isolated three-dimensional obstacle. In the previous modeling studies of Hawaiian rainbands (Smolarkiewicz et al. 1988, Rasmussen et al. 1989), the origin of the band clouds has been linked to the uplifting at the convergence zone associated with the upstream separation line. Both the convergence zone and the separation line were recognized as salient features of the strongly-stratified flow past a 3-D obstacle.

Recent analyses of observations from the Hawaiian Rainband Project (HaRP) offer a new, detailed look at the forcing mechanisms of cloud bands in Hawaii. While the island-scale flow seems to be well described by the idealized conceptual model (Rasmussen and Smolarkiewicz 1996), the local circulation on the windward island slope is often thermally driven as was already emphasized in the early studies by Leopold (1949) and Lavoie (1967). In particular, it is found that the shallow westerly jet below a nocturnal inversion on the upwind island slope behaves like a density current. The negative buoyancy of this current is primarily produced by diabatic cooling from the evaporation of orographic precipitation that is further enhanced by radiational cooling (Carbone et al. 1995, Chen and Wang 1995, Wang and Chen 1995).

The goal of this study is to quantify the ability of thermal forcing to modify simple low-Froude-number predictions for the strength and the location of rainbands. We recognize the orographic forcing as a primary mesoscale forcing mechanism of the band clouds but focus on sensible and latent thermal effects (such as surface boundary-layer forcing, evaporation of precipitation, radiative cooling etc.), which control the morphology of the local flow and thus can influence the development of rainbands. Numerical simulations are performed with a small-scale anelastic non-hydrostatic model (Smolarkiewicz and Margolin 1995, cf. Smolarkiewicz et al. 1996) in a numerical domain that covers 559×508 km^2 in the horizontal and extends 12.5 km in vertical. Horizontal and vertical resolution is 5.08 km and 0.25 km, respectively. Representation of the surface sensible and latent heat fluxes and the bulk warm rain parametrization are the same as in the original study by Smolarkiewicz et al. (1988). We examine a number of cases from HaRP that are representative of a range of different upstream conditions encontoured during the field experiment. Model simulations are initialized with the aircraft sounding taken approximately 100 km upstream of the island.

To illustrate the dynamics of rainband formation in Figures 1–3 we present the case of 8 Aug 1990. This case is characterized by one of the largest rainfall accumulation on the windward island slope for the early morning hours and the largest value of Froude number ($Fr = U/NH = 0.42$) of all HaRP cases. In the definition of Froude number, U, N and H are the far upstream wind speed, the Brunt-Väisälä frequency and a characteristic height of the mountain. This particular simulation was started at 04 UTC (18 HST), i.e. at the time of the local sunset. Nevertheless, during the first two hours of the run, an extensive and strong orographic cloud was present over the windward slope that produced significant precipitation. The convergence zone at this time is located nearly over Hilo, which is at $(x, y) = (72, 22)$ km. By the end of the third hour (Fig. 2a), over the windward slope we find both a precipitating but weak orographic cloud and a weak cloud band. The band is starting to form over a leading edge of the westerly downslope flow that extends all the way up to the orographic cloud on the mountain slope. During next several hours (Fig. 3a), the cloud band intensifies and becomes a rainband but

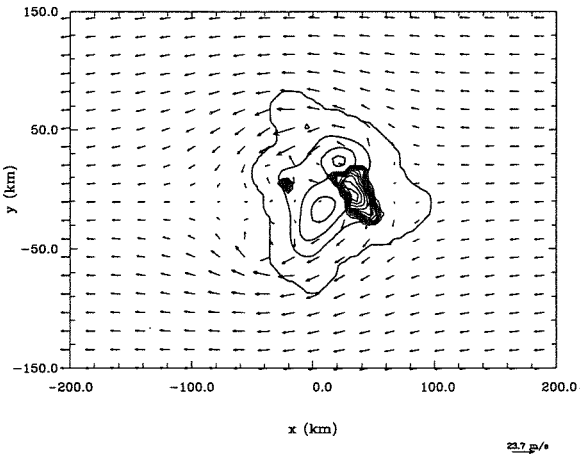

Figure 1: Model results for 8 Aug 1990. Orographic clouds and surface winds at 06 UTC (20 HST on 7 Aug)¿ Maximum value of the cloud water is 0.69 g/kg; contouring interval is 0.0625. Both clouds are precipitating at this time. Topographic contours are shown at 0.5 m and every 1000 m thereafter.

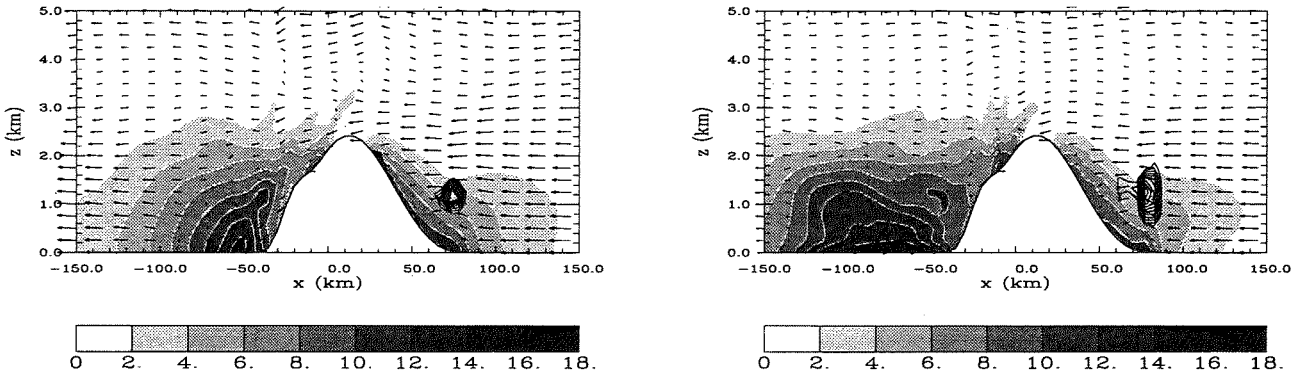

Figure 2: Cloud water field (dark contours) and u-velocity perturbation (gray shadded with white contours) in the xz-cross section at y=0 at a) 07 UTC (21 HST) (left panel), b) 10 UTC (24 HST) (right panel) on 8 Aug (7 Aug) 1990. Mean flow is easterly at $U = -10$ m s^{-1}. Maximum value and the contouring interval for cloud water is a) 0.0625 and 0.0039 g/kg, and b) 0.625 and 0.0625 g/kg.

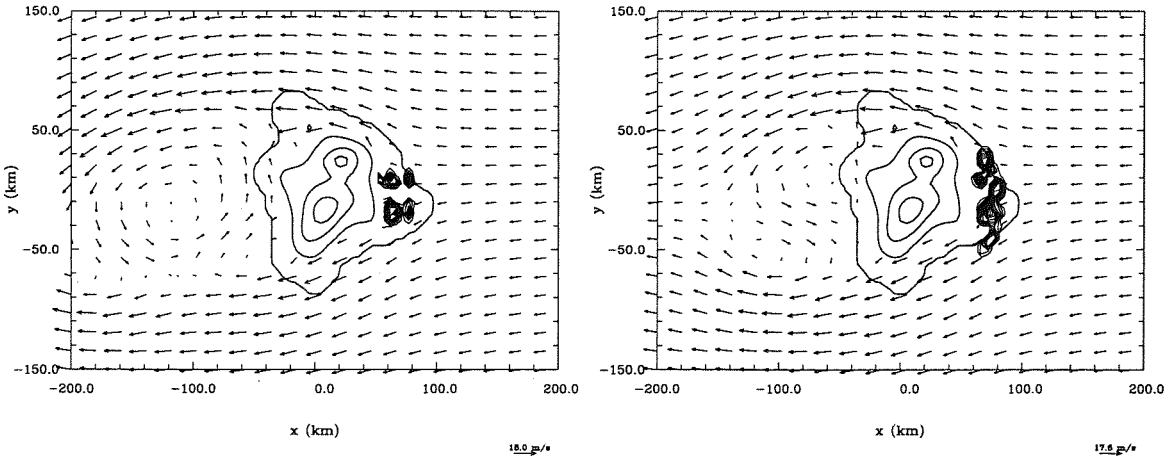

Figure 3: Orographically forced Hawaiian rainbands on 8 Aug 1990. Liquid water content and velocity vectors at 750 m above sea level. a) 10 UTC (00 HST) (right panel), and b) 12:30 UTC (02:30 HST). Maximum value of the cloud water is a) 0.375 and b) 0.469 shown at a contouring interval of 0.0313 g/kg.

remains essentially at the same location. From the local midnight to 06 HST, when our simulation was terminated, the rainband further intensified but also started to slowly move westward, away from the convergence zone. The formation of the second band over the convergence zone and behind the westward moving main band is illustrated in Fig. 3b. These results agree with the observational data analysis by Carbone et al. (1996), which indicates that on elevated Froude number days the envelope of the precipitation maximum stays confined within 10 km of shore, never going through the transition from orographic precipitation to the offshore rainbands characteristic of lower Froude number cases.

Preliminary results of the sensitivity analysis indicate that the variations of the upstream moisture profile strongly effect the rainband formation. The detailed results of the analysis of thermal forcing effects, for this and other HaRP cases, will be given in the presentation.

Acknowledgments: The National Center for Atmospheric Research is sponsored by the National Science Foundation.

REFERENCES

Carbone, R. E., W. A. Cooper, and W.-C. Lee, 1995: On the forcing of flow reversal along the windward slopes of Hawaii. *Mon. Wea. Rev.*, **123**, 3466–3480.

———, J. Tuttle, W.-C. Lee, W. A. Cooper, V. Grubišić, 1996: On the forcing of windward island rainbands in Hawaii. *Preprints. 12th International Conference of Clouds and Precipitation.* 19–23 August 1996. Zürich, Switzerland. (This volume.)

Lavoie, R., 1967: Air motions over the windward coast of the island of Hawaii. *Tellus.* **19**, 354–358.

Leopold, L. B., 1949: The interaction of trade wind and sea breeze, Hawaii. *J. Meteor. Sci.*, **6**, 312–320.

Rasmussen R. M., P. K. Smolarkiewicz, and J. Warner, 1989: On the dynamics of Hawaiian cloud bands: Comparison of model results with observations and island climatology. *J. Atmos. Sci.*, **46**, 1589–1608.

———, and P. K. Smolarkiewicz, 1996: Evaluation of the low Froude number conceptual model for flow past Hawaii. To be submitted to *J. Atmos. Sci.*

Smolarkiewicz, P. K., R. M. Rasmussen, and T. L. Clark, 1989: On the dynamics of Hawaiian cloud bands: Island forcing. *J. Atmos. Sci.*, **45**, 1872–1905.

———, and L. G. Margolin, 1995: On forward-in-time differencing for fluids: An Eulerian/semi-Lagrangian nonhydrostatic model for stratified flows. *Atmos.-Ocean*, (In press).

———, W. W. Grabowski, and V. Grubišić, 1996: Semi-Lagrangian/Eulerian cloud model. *Preprints. 12th International Conference of Clouds and Precipitation.* 19–23 August 1996. Zürich, Switzerland. (This volume.)

LARGE-EDDY SIMULATION OF DEUTERIUM IN THE STRATOCUMULUS-TOPPED BOUNDARY LAYER

Hui He, David E. Stevens, and Ronald B. Smith

Department of Geology and Geophysics, Yale University,
New Haven, Connecticut 06520-8109, U.S.A.

1. INTRODUCTION

The turbulent cloud-topped atmospheric boundary layer plays a key role by controlling the fluxes of heat and moisture between the ocean surface and the free atmosphere. In this paper, we utilize a large-eddy simulation (LES) model to examine the small scale structure and characteristics of deuterium in a non-precipitating maritime stratocumulus-topped boundary layer, by incorporating the basic isotope physics into the LES model. The deuterium assists in the understanding of such processes as phase change of water, cloud top entrainment, and turbulent mixing in the atmospheric boundary layer.

Normal water (H_2O) has two important stable isotopes, deuterium and oxygen 18, in the forms of HDO and $H_2{}^{18}O$. In the atmospheric sciences, they have been used to the modeling of cloud and precipitation processes (Federer *et al.* (1982); Gedzelman *et al.* 1994), the analysis of the history of convective processes associated with phase change of water above the boundary layer (Gedzelman 1988), and the observation of ice in the upper troposphere over the ocean (Smith 1992).

In a shallow and turbulent region like the stratocumulus boundary layer, both local and horizontally averaged variations of isotope concentration can not be fully resolved from simple models. LES offers the advantage of being able to simulate explicitly the detailed circulations and properties of the cloud and subcloud layer. It also exhibits far less sensitivity to the details of turbulent closure parameterization. In the non-precipitating boundary layer that we simulated, LES can reconstruct a mixing line in an isotope-moisture diagram, although it has included more complicated advection, mixing, and radiation schemes.

2. ISOTOPE BASICS

The isotope ratios of hydrogen D/H, and oxygen $^{18}O/^{16}O$, are commonly expressed in terms of delta values, δD and δ^{18}O, which are the relative deviation of isotope ratio from the known standard, SMOW (standard mean ocean water), as

$$\delta = \left(\frac{R - R_{\mathrm{SMOW}}}{R_{\mathrm{SMOW}}}\right) \times 1000 \qquad (1)$$

where R represents the isotope ratio, and R_{SMOW} is the isotope ratio of SMOW. δD and δ^{18}O are linearly correlated in natural water. We concern only on the distribution of deuterium under equilibrium conditions, thus δ^{18}O results are not presented.

In this model, water exists in the forms of water vapor and cloud water. Each of them is divided into two categories, normal water H_2O and its isotope HDO. Their mixing ratios are denoted by Q and Q^{I} (both with subscript v for vapor and c for cloud water), respectively. They are related by

$$Q^{\mathrm{I}} = jR_{\mathrm{SMOW}}Q(\delta\mathrm{D} + 1) \qquad (2)$$

where $j = 19/18$ is the ratio of molecular weight of $\mathrm{HDO}/\mathrm{H_2O}$ and $R_{\mathrm{SMOW}} = 155.76 \times 10^{-6}$.

Due to their lower saturation vapor pressure, the heavy isotopes of water condense more readily than normal water and hence the liquid phase acquire a greater concentration of heavy isotopes than the vapor phase. Under equilibrium conditions, this is

$$(\delta\mathrm{D}_c + 1) = \alpha(T) \cdot (\delta\mathrm{D}_v + 1) \qquad (3)$$

where α is the equilibrium fractionation factor and depends on temperature. We have defined another delta value $\delta\mathrm{D}_t$, which is the delta value of the total moisture if both vapor and liquid are converted into one phase. From (2),

$$(\delta\mathrm{D}_t + 1) = \frac{Q_t^{\mathrm{I}}}{jR_{\mathrm{SMOW}}Q_t} \qquad (4)$$

where $Q_t = Q_v + Q_c$ and $Q_t^{\mathrm{I}} = Q_v^{\mathrm{I}} + Q_c^{\mathrm{I}}$ are the total mixing ratios of H_2O and HDO, respectively.

3. MODEL DESCRIPTION

The LES model uses an Eulerian forward-in-time advection algorithm to solve the transport equation

of a scalar Ψ

$$\frac{\partial}{\partial t}\rho\Psi + \nabla \cdot \rho\Psi\vec{U} = \rho S_\Psi \qquad (5)$$

with source term S_Ψ, and the velocity field $\vec{U}$ in a quasi-incompressible fluid with the continuity equation

$$\nabla \cdot \rho\vec{U} = 0$$

where ρ is the density. The scalars we calculate from (5) are the three variables that are conserved under moist and dry adiabatic processes: the liquid water potential temperature θ_l, the total mixing ratios Q_t and Q_t^{I}. The velocity field $\vec{U}$ has only two components, u and w, in the x-z domain. Detailed descriptions of the LES model are given by Stevens (1994).

The model calculates the δD values of vapor and cloud water according to the following procedures. First, θ_l, Q_t, and Q_t^{I} at each grid point are calculated from their values at the previous time step according to (5), by taking into account the turbulent mixing with the environment air. Then it calculates $\delta\mathrm{D}_t$ from (4). Temperature T is solved implicitly from θ_l and Q_t, by determining the mixing ratios of vapor Q_v and liquid water Q_c from the diagnostic relation

$$Q_v = \min(Q_t, Q_v^{\mathrm{sat}}) \text{ and } Q_c = Q_t - Q_v \qquad (6)$$

where Q_v^{sat} is the local saturation mixing ratio. Finally, the value of $\delta\mathrm{D}_v$ is determined from the resolved variables by

$$(\delta\mathrm{D}_v + 1) = \frac{Q_t}{Q_v + \alpha(T)Q_c} \cdot (\delta\mathrm{D}_t + 1) \qquad (7)$$

which has implied that cloud water is in isotopic equilibrium with vapor. This is because the relaxation time for the exchange of isotopes is less than 1 s and therefore less than the time step used in the model. $\delta\mathrm{D}_c$ exists only in the cloud layer where $Q_c > 0$ and is given by equilibrium relation (3).

4. SIMULATIONS

The initial profiles of the mixing ratio and isotope ratio are set in such a way that Q_t and $\delta\mathrm{D}_t$ have a stratified structure. The lower layer consists of the subcloud layer and the cloud layer. It extends from the ocean surface up to the inversion, which is initially located at the level between 660 m and 670 m. This layer has the total mixing ratio $Q_t = 9.5$ g kg^{-1}, and "total" delta value $\delta\mathrm{D}_t = -80$. The cloud water is initially present only in the cloud layer that extends from 300 m to 650 m altitude, where the air is saturated. In this cloud layer, the deuterium is partitioned between water vapor and cloud water by the equilibrium relation (3). The initial $\delta\mathrm{D}_v$ value resolved from $\delta\mathrm{D}_t$ in the subcloud layer is close to the equilibrium value with SMOW, so that the simulation can reach a steady state much faster.

Above the inversion, the atmosphere contains no liquid water and becomes isotopically lighter, it has the vapor mixing ratio of $Q_v = Q_t = 4.0$ g kg^{-1} and delta value of $\delta\mathrm{D}_v = \delta\mathrm{D}_t = -200$. These values characterize the descending air that has been depleted of most of its moisture and deuterium through precipitation in the deep convective tropical regions. In the subcloud layer, the temperature drops from the surface upward following the dry adiabats in the subcloud layer, and it continues to drops following the moist adiabats in the cloud layer. The strength of the inversion is 7.29°C and the free atmosphere above is isothermal with temperature of 292°K.

In the model, the surface flux of moisture is parameterized as subgrid-scale flux in terms of resolved-scale field by the bulk transfer method. The vertical fluxes of H_2O and HDO from the ocean surface into the boundary layer are proportional to the product of the wind speed at first grid point above the surface, and the difference between their mixing ratios at the saturated air-water interface and at the first grid point above the surface. We have used the same bulk aerodynamic coefficient value for both H_2O and HDO.

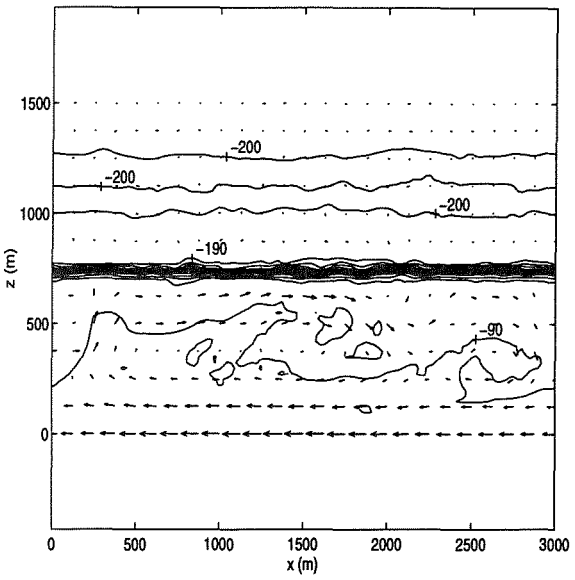

Figure 1: The computed $\delta\mathrm{D}_v$ (closed contours) and wind field (arrows) in the x-z domain at $t = 5$ h. Contour interval is 10. The maximum value for $\delta\mathrm{D}_v$ is -84.79 and the minimum value is -200.72.

The flow variables carried throughout the simulation are the two velocity components u and w, the liquid water potential temperature θ_l, and the total moisture mixing ratios Q_t and Q_t^{I}. The time interval used in the simulations was 5 s and the simulations were carried out in the two-dimensional x-z domain of 3 km × 1.5 km with a mesh of 120 × 60. The domain remains stationary with respect to the horizontal synoptic wind field, which is 5 m s^{-1}. The

periodic boundary condition was used in the x direction and the rigid boundary condition was used at the upper and lower boundaries. The sea surface temperature was fixed at 290°K.

5. RESULTS

5.1 Simulated δD_v and δD_c

The model run for 6 hours. Figures 1 and 2 illustrates the result of the model output of the two-dimensional distribution of δD_v and δD_c with wind field at $t = 5$ h. δD_v still experiences a strong gradient across the inversion, although the boundary layer is constantly becoming isotopically lighter. Also, very light δD_c values can be found near the cloud top, while it is relatively uniform below it. This indicates the effect of both mixing and fractionation. Although the minimum value of the horizontally averaged δD_c never drops below -5, it can reach as low as -35.34 in several regions with high liquid water concentration at the cloud top.

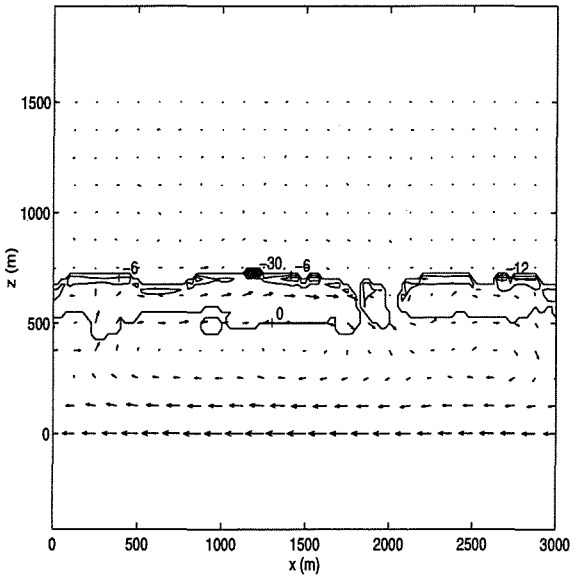

Figure 2: The computed δD_c (closed contours) and wind field (arrows) in the x-z domain at $t = 5$ h. Contour interval is 6. The maximum value for δD_c is 0 and the minimum value is -35.34.

5.2 Averaged Vertical Profiles

In figures 3 and 4, we have plotted the horizontally averaged vertical sounding of Q_v, Q_c, δD_v and δD_c at different time steps. These plots show that the depth of the cloud layer, and Q_c and δD_c have changed constantly over the six-hour period, while Q_v and δD_v are relatively stable throughout the simulation. This suggests that the drying by cloud top entrainment has overruled the moistening of the boundary layer by surface flux in our model setting. In other cases, there is the possibility that the cloud water distribution can approach a steady state. These figures also indicate that the δD_v-Q_v relationship is much more stable in time than δD_c-Q_c relationship.

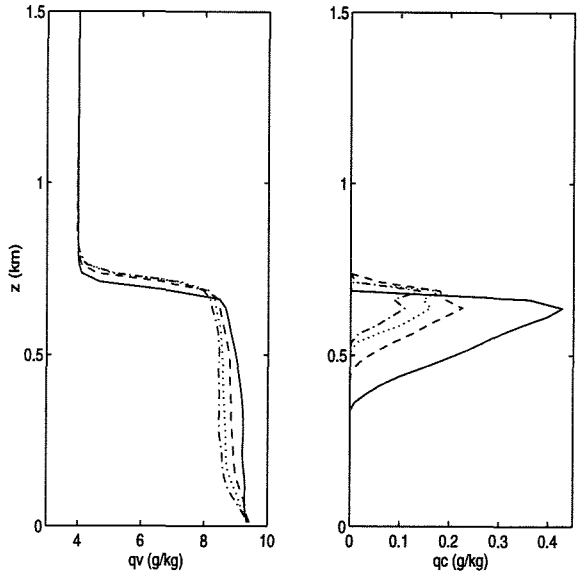

Figure 3: The averaged vertical profiles of Q_v and Q_c at $t = 1.5$ h (solid line), 3.0 h (dashed line), 4.5 h (dotted line), and 6.0 h (dashdot line).

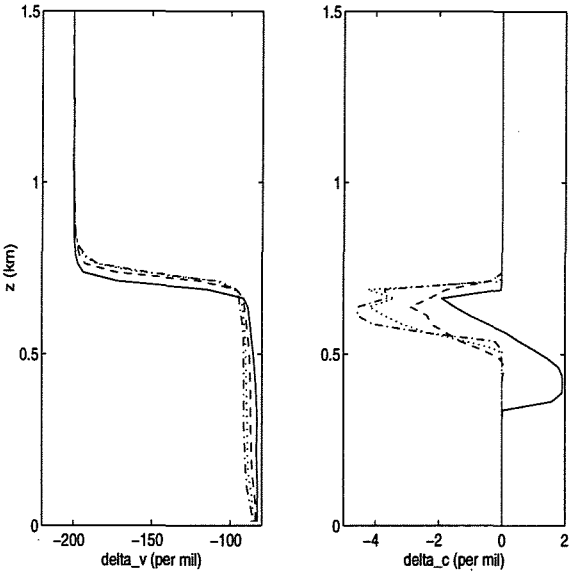

Figure 4: The averaged vertical profiles of δD_v and δD_c at $t = 1.5$ h (solid line), 3.0 h (dashed line), 4.5 h (dotted line), and 6.0 h (dashdot line).

5.3 δD-Q Plot of the Simulation

The mixing line formed by plotting the thermodynamic parameters against each other characterizes the typical boundary layer (Betts and Albrecht, 1987). One of our goals is to reconstruct the theo-

retical mixing line for deuterium. We expect that after a sufficient time period, the thermodynamic variables have been well mixed and the δD_v-Q_v plot from model output will converge to the theoretical mixing line over the depth of the boundary layer.

In figure 5, we have plotted δD_v against Q_v throughout the boundary layer at time $t = 0$ h, 3 h, and 6 h. We can see that at $t = 6$ h, the data points have fallen onto the theoretical mixing line. The five sparsely spaced points in the middle of the curve lie within the inversion, while the points on the upper-right corner represent levels below the inversion, and the clustered points on the far lower-left side represent the strongly stratified free atmosphere that is nearly unperturbed. We have seen that there is a sharp vertical gradient of Q_v and δD_v across the capping inversion, nevertheless, the inversion is also well mixed in terms of deuterium and moisture.

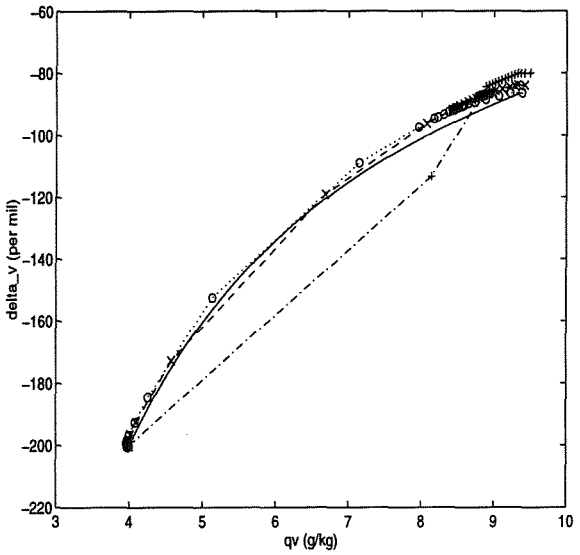

Figure 5: The δD_v-Q_v curves at $t = 0$ h (dashdot line), 3.0 h (dashed line), and 6.0 h (dotted line). The vertical distance between two adjacent marks on each curve is 25 m. The solid line is the theoretical mixing line linking the two end points at the bottom and the top of the domain.

6. CONCLUSIONS

In this research, we incorporated the physics of deuterium into a LES model for incompressible flows and use the model to simulate the detailed structure of δD_v and δD_c in the non-precipitating stratocumulus-topped boundary layer. The model is run for specific initial isotope profiles and boundary layer temperature and moisture soundings. We also introduced the δD-Q phase diagrams that are of special interest for possible field experiments.

The approach of calculating the δD values of vapor and liquid is different from that used by Federer *et al.* (1982) and Gedzelman *et al.* (1994). Instead of applying the governing equations for δD's directly, we calculate Q's and Q^{I}'s following the conservation of mass of H_2O and HDO and derive the corresponding δD values from them afterward. The reason for this is that in our model, the mixing ratios are strictly conserved variables, while calculating δD directly will introduce truncation errors that will not conserve Q^{I}.

Our model shows that the the stable water isotopes may help to study the dynamics of the atmospheric boundary layer. The model also justifies that a theoretical mixing line should be obtained under the ideal situations, hence any deviation from the mixing line will provide such information as non-equilibrium fractionation, horizontal advection, and precipitation fallout.

Acknowledgements. This research was supported in part by the NSF Grant ATM-9121390.

REFERENCES

Betts, A. K., and B. A. Albrecht, 1987: Conserved variable analysis of the convective boundary layer thermodynamic structure over the tropical oceans. *J. Atmos. Sci.*, 44, 83-99.

Craig, H., and L. I. Gordon, 1965: Isotopic oceanography: deuterium and oxygen 18 variations in the ocean and the marine atmosphere. Symposium on marine geochemistry, University of Rhode Island, 277-374.

Federer, B., N. Brichet, and J. Jouzel, 1982: Stable isotopes in hailstones. Part I: The isotopic cloud model. *J. Atmos. Sci.*, 39, 1323-1335.

Gedzelman, S. D., 1988: Deuterium in water vapor above the atmospheric boundary layer. *Tellus*, 40B, 134-147.

Gedzelman, S. D., and R. Arnold, 1994: Modeling the isotopic composition of precipitation. *J. Geophys. Res.*, 99, D5, 10455-10471.

Merlivat, L., and M. Coantic, 1975: Study of mass transfer at the air-water interface by an isotopic method. *J. Geophys. Res.*, 80, 3455-3464.

Moeng, C.-H., 1984: A large-eddy-simulation model for the study of planetary boundary-layer turbulence. *J. Atmos. Sci.*, 41, 2052-2062.

Smith, R. B., 1992: Deuterium in north Atlantic storm tops. *J. Atmos. Sci.*, 49, 2041-2057.

Stevens, D. E., 1994: An adaptive multilevel method for boundary layer meteorology. Ph.D. dissertation, University of Washington, 121 pp.

A RADIATION CLOUD MODEL WITH A DETAILED TREATMENT OF THE MICROPHYSICS
12th INTERNATIONAL CONFERENCE ON CLOUDS AND PRECIPITATION

Christian Issig[1], Uwe Ritzmann[2] and H.D. Schilling[1]

[1]Met. Institute, University Bonn, Germany
[2] Geography Institute, University Bonn, Germany

Introduction

This paper presents a one-dimensional radiation cloud model with a detailed treatment of the drop spectrum evolution.
It has been developed for the study of the interaction between the atmospharic radiative transfer and cloud processes, especially with emphasis to the initial forcing mechanism.
Characteristics features of the parameterized microphysics after Kessler (1969) are compared with the model's detailed microphysics.
The hailstorm on the fourth of July 1994 in Cologne serves as an example for demonstrating the effects of the radiative transfer and the detailed microphysics to the evolution of this storm. However, the following demonstrations were computed without ice-phase.

The Model

It is a spectral version of the 1 1/2 - D model developed by Ogura and Takahashi (1971) and further refined by K.v.D. Emde and P. Kahlig (1989). Whereas the cloud properties are averaged over a cylinder with a fixed radius, the radial wind component's variation with radius r is assumed nonzero and linear. The time evolution of:

water vapor (q_V),
40 size categories of the warm water phase (q_W),
vertical velocity (w),
and the temperature (T)

is computed by the following set of equations:

$$\frac{\partial q}{\partial t} = - w \frac{\partial q}{\partial z} + \frac{2}{a} \alpha^2 |w_e - w| (q_e - q) + \frac{2}{a} (q - \tilde{q}) \tilde{u} + \frac{d q}{d t}$$

$$\frac{\partial T}{\partial t} = - w \frac{\partial T}{\partial z} + \frac{2}{a} \alpha^2 |w_e - w| (Te - T) + \frac{2}{a} (T - \tilde{T}) \tilde{u} - \Gamma dw + S S_T + R_T$$

$$\frac{\partial w}{\partial t} = - w \frac{\partial w}{\partial z} + \frac{2}{a} \alpha^2 |w_e - w| (we - w) + \frac{2}{a} (w - \tilde{w}) \tilde{u} + \left(\frac{Tv - T_{v_e}}{T_{v_e}} \right) g - q g$$

The subscript $_e$ indicates environmental values. The tilded quantities are calculated from the horizontal velocity, which is determined by the anelastic dry continuity equation and represent quantities at the edge of the column. R is the radius of the cylinder and α^2 is a constant using for the parameterization of the horizontal turbulent entrainment.
The microphysical processes are given by the equation of the diffusional growth of the cloud particles and the solution of the coagulation equation:

$$\frac{\partial f(x)}{\partial t} = \frac{\partial f(x) \dot{a}}{\partial x}$$

$$\frac{\partial f(x)}{\partial t} = \int_0^{\frac{x}{2}} f(x') f(x-x') K(x', x-x') dx' - \int_0^{\infty} f(x') f(x) K(x', x) dx'$$

Both equations are solved numerically for 40 drop size categories.

The shortwave radiation flux in the cloud free atmosphere for 40 wave length bands is calculated by using the Bouguer-Lambert law, with absorption by O_3, H_2O, CO_2 and Rayleigh scattering by gas species as well as aerosols (climatological ditribution). The long wave range radiative transfer equation is resolved by 80 wave length bands and is based on H_2O, CO_2 absorption and emission. The parameterization of the radiative characteristics of clouds is based on a scheme by Stephens (1984).

Results

Figures 1 and 2 illustrate the impact of different initial conditions on the evolution. The initial disturbance of the run, depicted by Fig. 1a,b, is an artificial w-distriburion with a maximum vertical velocity of w_0=1m/s at a height of z_0=2000 m, as being expressed by:

$$w(z)=w_0*\sin(\pi*z/z_0).$$

No radiation is taking into account in this run.
In contrast, Fig. 2a,b give the results of a circulation, which is imitated by radiatively heated warm air from near the ground.

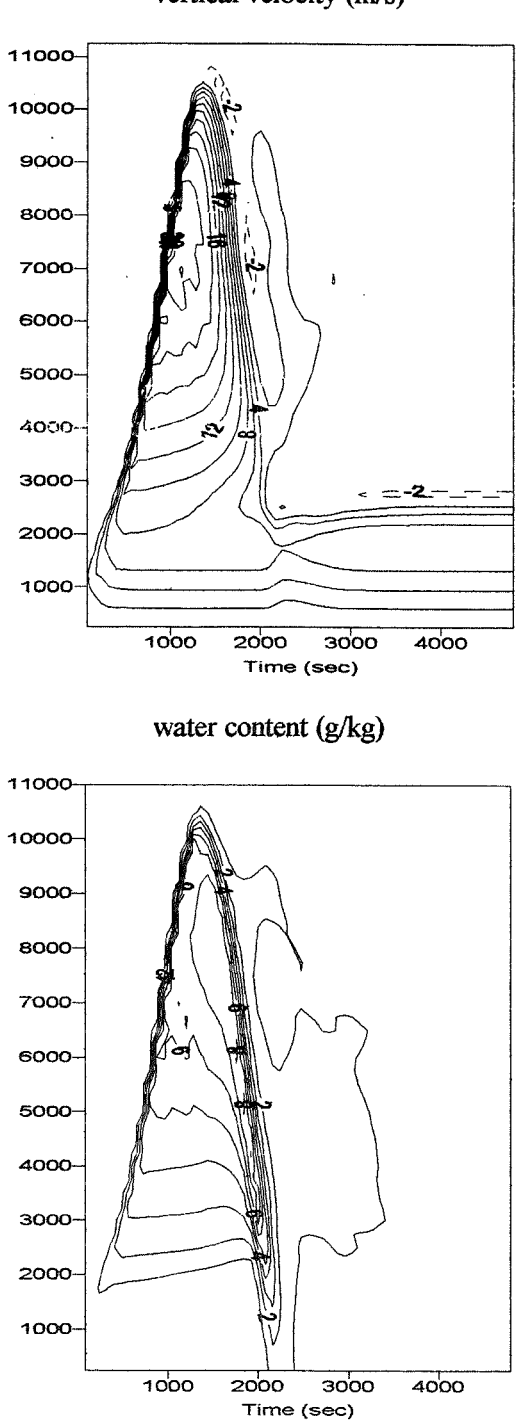

Figure 1a, b: cloud characteristics due to an artificial initial vertical velocity disturbance

vertical velocity (m/s)

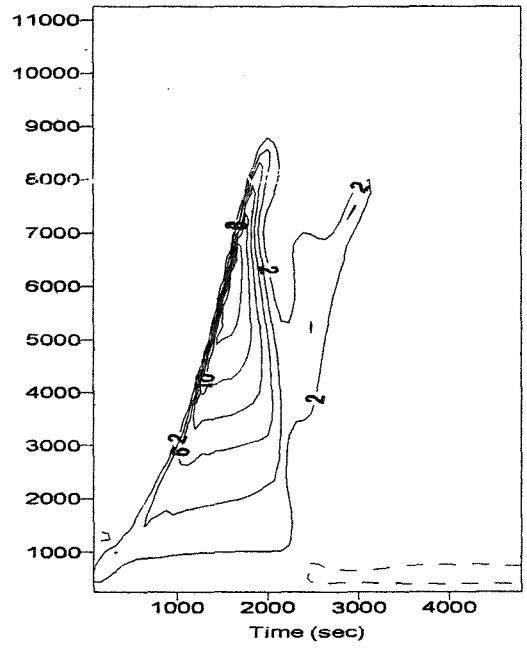

water content (g/kg)

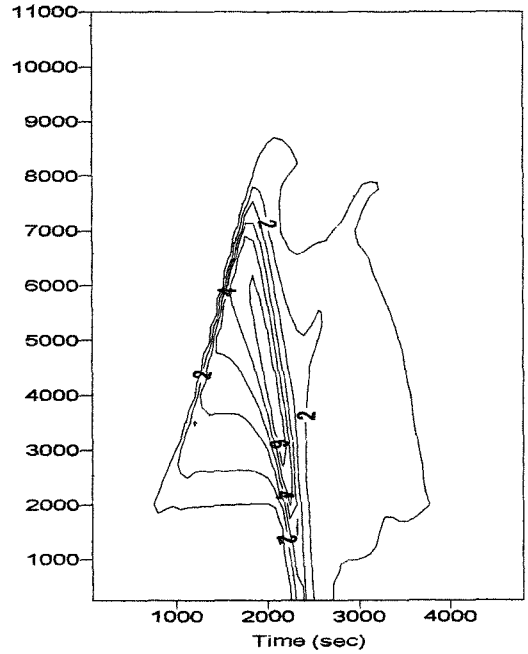

Figure 2a, b: cloud characteristics with the inclusion of the radiative transfer

By comparison it becomes clear, that the details of the forcing mechanism profoundly affect the evolution of the model cloud. The radiative cooling at the top of the cloud supresses buoyancy and the cloud is limited beneath to 9000 m. The precipitation rate in the run with radiative transfer is 14,5 mm, compared to 16,9 mm for the run without radiation.

The second aim was to investigate the effect of the radiation transfer in the later stages of the development. To this end, the results of the run with radiation are compared with these for which the radiation scheme is cut off after the initial 80 sec. Concerning all cloud elements (water content, vertical velocity, drop size spectrum) the radiation processes did not affected the later stages of the development.

By comparing the Kessler parametrization scheme with the detailed microphysics, it can be shown that parametrizations may distort the evolution (Fig. 3a,b). It is well known, that the Kessler scheme gives a conversion from cloud to the rain water too fast. Therefore, the onset of precipitation is earlier as in the basic model run.

vertical velocity (m/s)

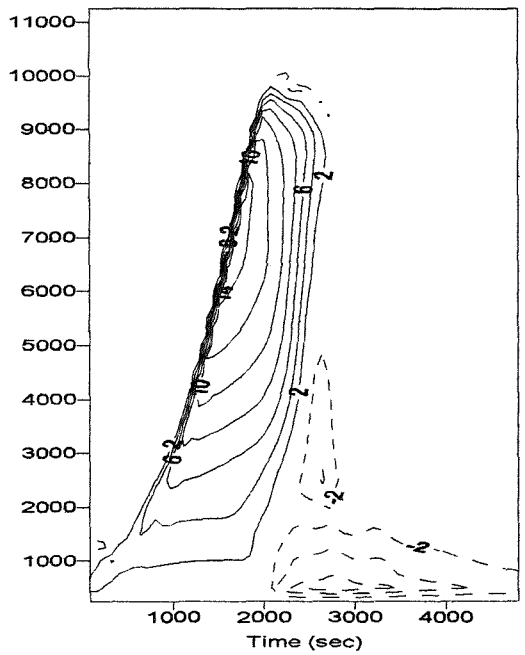

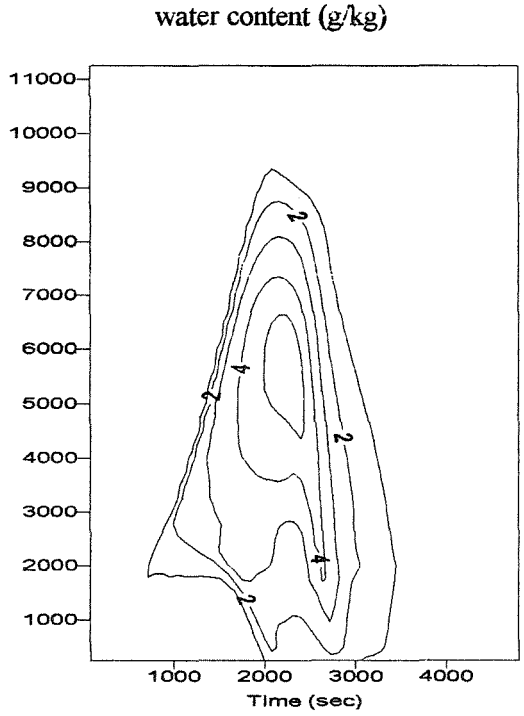

Fig. 3a, b: cloud characteristics with the Kessler scheme

Conclusions

Numerical model investigations of the evolution of cloud parameters and precipitation are undertaken by considering the interaction of cloud and radiation processes and detailed as well as parameterized microphysics.
The simulations show significant dependence on the initial pulse setting and the treatment of the microphysics.
The incorporation of an ice parameter scheme into the cloud model will be done next. Under further investigation is the effect of environmental cooling in the late afternoon, too.

Literature

Emde, K.v.d. and P.Kahlig: Comparison of the observed 19th. July 1981, Montana thunderstorm with results of a one-dimensional cloud model using Kessler parameterized microphysics. Annales Geophysicae 7, p.405-414, 1989.

Kessler, E.: Meteor. Monograph 10, No. 32, Am. Meteor. Soc., Boston, Mass., 1969.

Ogura, Y. and T. Takahashi: Numerical simulation of the life cycle of a thunderstorm cell. Mon. Wea. Rev., 93, p.895-911, 1971.

Stephens, G.L.: The parametrization of radiation for numerical weather prediction and climate models. Mon. Wea. Rev, 112, p.826-867, 1984.

CLOUD-RESOLVING SIMULATIONS OF WARM-SEASON ARCTIC STRATUS CLOUDS

Peter Q. Olsson[a], Graham Feingold[b], Jerry Y. Harrington[a], William R. Cotton[a] and Sonia Kreidenweis[a]

[a]*Department of Atmospheric Science, Colorado State University, Fort Collins, CO, USA.*
[b]*Cooperative Institute for Research in the Atmosphere, Colorado State University, Fort Collins, CO, USA.*

1. INTRODUCTION

The role that high-latitude cloudiness plays in the global climate system remains one of the big uncertainties in studies of climate dynamics. At least part of this uncertainty is due to the inability of global climate models (GCMs) to adequately represent Arctic stratus clouds (ASC). The poor performance of GCMs has been attributed to a number of factors— inadequate vertical and/or horizontal resolution, incorrect latitudinal moisture transport, neglect of aerosols, and incomplete cloud microphysical and radiative transfer schemes, among others. Furthermore, recent studies suggest that high-latitude regions are particularly sensitive to climate perturbations. Thus, to achieve more credible climate simulations, it is vitally important to improve the treatment of ASC in numerical models.

Several issues complicate ASC modeling. These clouds often coexist in multiple layers, and are found in a variety of synoptic conditions. The supporting boundary-layer environment frequently has a complex temperature and shear structure, rendering typical stratus-cloud models inadequate in describing the complex interactions among radiation, cloud microphysical properties, and boundary-layer dynamics in ASC.

2. MODEL DESCRIPTION

To address the role of these interactions in maintaining ASC we are performing cloud-resolving simulations of the summertime cloudy Arctic boundary layer. The model used for this work is essentially the Regional Atmospheric Modeling System (RAMS), which has been described elsewhere (e.g., Pielke et al. 1992). The pertinent modifications will be discussed here.

2.1 Microphysics

Drizzle production and sedimentation can be important factors in the evolution of stratus clouds. Our preliminary modeling work indicated that with the small mean radius ($\bar{r}$) commonly observed in ASC, autoconversion schemes typically used in bulk microphysical models fail to initiate the drizzle process. To address this deficiency, it is possible to use an explicit *B*in-resolving *M*icrophysics (BM) model, one of two approaches we have used here. BM, however, is very expensive in both memory and computational time. As a compromise between cost and accuracy, we are developing a hybrid scheme, which comprises a combination of the bin-resolving and bulk microphysical approaches. Following are brief summaries of the two schemes.

2.1.1 Bin-resolving Microphysics (BM)

In BM, as implemented in RAMS (Feingold et al. 1996; Stevens et al. 1996), 25 drop bins are defined using mass doubling formula $x_{k+1} = 2x_k$, covering a radius range of 1.5 $\rightarrow$ 500 microns. Equations for both mass and number in each bin require a total of 50 prognostic variables for cloud-related scalars. (Herein lies the computational cost in both memory storage and time as these scalars are advected). Moment conserving techniques (mass and number in each bin) which prevent anomalous drop growth are used to solve equations for warm microphysical processes: condensation/evaporation, stochastic collection (Tzivion et al. 1987) and sedimentation. Droplet activation is based on supersaturation, and assumes constant background cloud concentration nuclei (CCN) with a fixed lognormal distribution. The total number of cloud droplets cannot exceed the CCN concentration.

2.1.2 Hybrid Bin/Bulk Microphysics (HM)

In our attempts to simulate precipitating ASC using a more traditional bulk scheme (Walko et al. 1995) several processes, in particular sedimentation and autoconversion, were found inadequate. To address these issues, a *H*ybrid bin/bulk *M*icrophysics (HM) scheme is being developed. In HM, cloud droplet and raindrop distributions are each described by lognormal basis functions. Each distribution is defined in terms of number concentration and mass, with spectral breadth a fixed constant. Supersaturation is calculated and CCN activated using the same scheme as BM.

Several advantages accrue from the hybrid approach. In predicting mass transfer between cloud and rain, use is made of detailed transfer rates at high resolution rather than average rates for the entire distribution. The collection process uses information on kernel function for interacting drops with the same resolution as that in BM and sedimentation is treated by dividing the basis function into bins and allowing each bin to fall at the appropriate fall velocity. At the same time, memory requirements are much less severe than BM, with a total of 4 predictive cloud-related scalars (vs. 50 for BM).

Therefore, HM executes in about one third the time of BM, yet captures some of the essential features of drizzle formation.

2.2 Two-stream radiative transfer model

A new two-stream radiative transfer model has been implemented in RAMS. Gases considered in the model include $H_2O_{(v)}$, CO_2, O_3, O_2, CH_4 and N_2O. The model, which has three solar and five infrared bands, uses exponential sum fits based on correlated-*k* data, with climatological CH_4 and N_2O and O_2 values added to the CO_2 fits. Fluxes are then computed as in Ritter and Geleyn (1992). The cloud properties ω_0 (cloud single-scatter albedo), β_{ext}(extinction coefficient) and the asymmetry parameter are computed through fits to the cloud drop spectrum. Both ω_0 and β_{ext} are computed using anomalous diffraction theory (ADT) and the asymmetry parameter is computed using Mie theory. Raleigh scattering and continuum absorption are included as a simple parameterization.

2.3 Experiment configuration

These two-dimensional eddy-resolving experiments were done in a domain with 50 points in the vertical and 61 in the horizontal (E-W) direction giving a domain width of 3600 m and a domain top near 2800 m. The horizontal grid-spacing was constant at Δx = 60 m while the vertical grid spacing varied between 30 m and 45 m in the lowest 1500 m of the domain (the region of interest) and stretched to 400 m near at the model top. For the radiative calculations only, the domain was extended to 80 mb to improve accuracy in computing radiative fluxes. The Smagorinsky scheme was used to simulate subgrid-scale turbulent fluxes.

3. INITIAL CONDITIONS AND MODEL SPIN-UP

The input sounding, at a latitude of 77.7° N in the Beaufort Sea region of the Arctic, was taken during the Arctic Stratus Experiment (flight 5) on June 28, 1980. This case, which has been studied by several researchers (e.g., Curry 1986; Curry et al. 1988), is characterized by a multi-layered cloud deck with a surface fog extending upward to about 250 m. The upper cloud, with a nominal cloud base at 700 m and cloud top near 1100 m, was well-mixed and capped by a much warmer and drier air mass. Several layers of considerable directional and speed wind shear were present in the lowest 1500 m.

The model was initialized at 8:00 AM local time and run for four hours in a spin-up mode. During this period, cloud water was present but no microphysical scheme was activated. Radiative cooling at cloud-top destabilized the upper cloud layer, with eddies forming as the upper cloud became convectively unstable. Figure 1 contains a vertical cross section of *w* in the boundary layer and the solid line in Fig. 2a shows the mean vertical velocity variance $\overline{w'w'}(z)$ [1]. The general pattern of eddies in Fig. 1 suggests that the dynamics in the

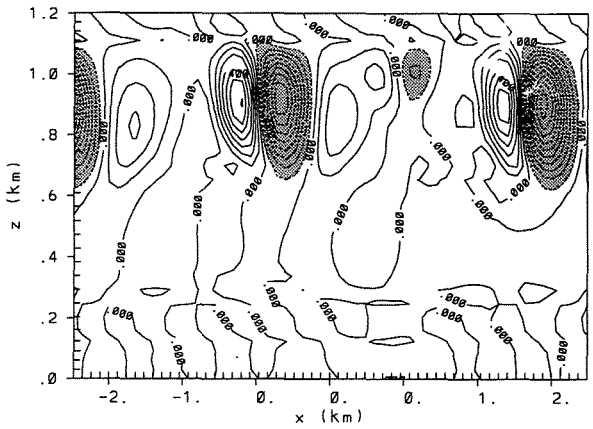

Fig. 1 Vertical velocity in the cloudy boundary layer after four h of spin-up. Contours range from -1.0 m s^{-1} to 0.7 m s^{-1} with an interval of 0.1 m s^{-1}. Regions with w < 0.1 m s^{-1} are shaded.

upper cloud layer are largely decoupled from the fog layer near the surface in agreement with Curry (1986) and Curry et al. (1988). Another consequence of the cloud-top cooling is the enhancement of the liquid-water content (LWC) locally. The LWC in the fog layer between the surface and 275 m decreased during this time as mechanically generated turbulence mixed this layer. The solid line in Fig. 2d shows $\overline{LWC}(z)$ at 4 h.

Using the four-hour results as a common starting point, sensitivity simulations were then performed with varying CCN number concentrations (100, 300 and 500 cm^{-3}) for BM, and 300 cm^{-3} for HM. For convenience we will refer to these runs has BM1, BM3, BM5 and HM3 respectively. Each sensitivity experiment was integrated for 2 hours. A brief summary of results is presented in the following section.

4. RESULTS

The BM studies can be divided into 2 categories: weakly drizzling (BM1) and nonprecipitating (BM3 and BM5). Since in most aspects BM3 and BM5 were similar in nature, we will focus mainly on BM3 here with reference to BM5 where appropriate. Further we will focus attention on the upper cloud as the subgrid closure used here is not appropriate in the very stable surface fog region.

Figure 2a shows plots of $\overline{w'w'}$, a bulk measure of turbulent eddy strength, at the end of the 2 h sensitivity runs. In both the BM3 and the HM3 runs, the eddy strength has decreased somewhat within the cloud, while the in-cloud $\overline{w'w'}$ has increased somewhat for BM1. All the 6-h profiles show an increase in $\overline{w'w'}$ in the subcloud region with a decay of energy in the stable fog.

As expected, the higher initial CCN concentrations produced higher drop concentrations (Fig. 2e). The mean radiative heating tendencies (Fig. 2b) at 6 h show

1. The bar operator is used here to denote a horizontal average unless otherwise noted.

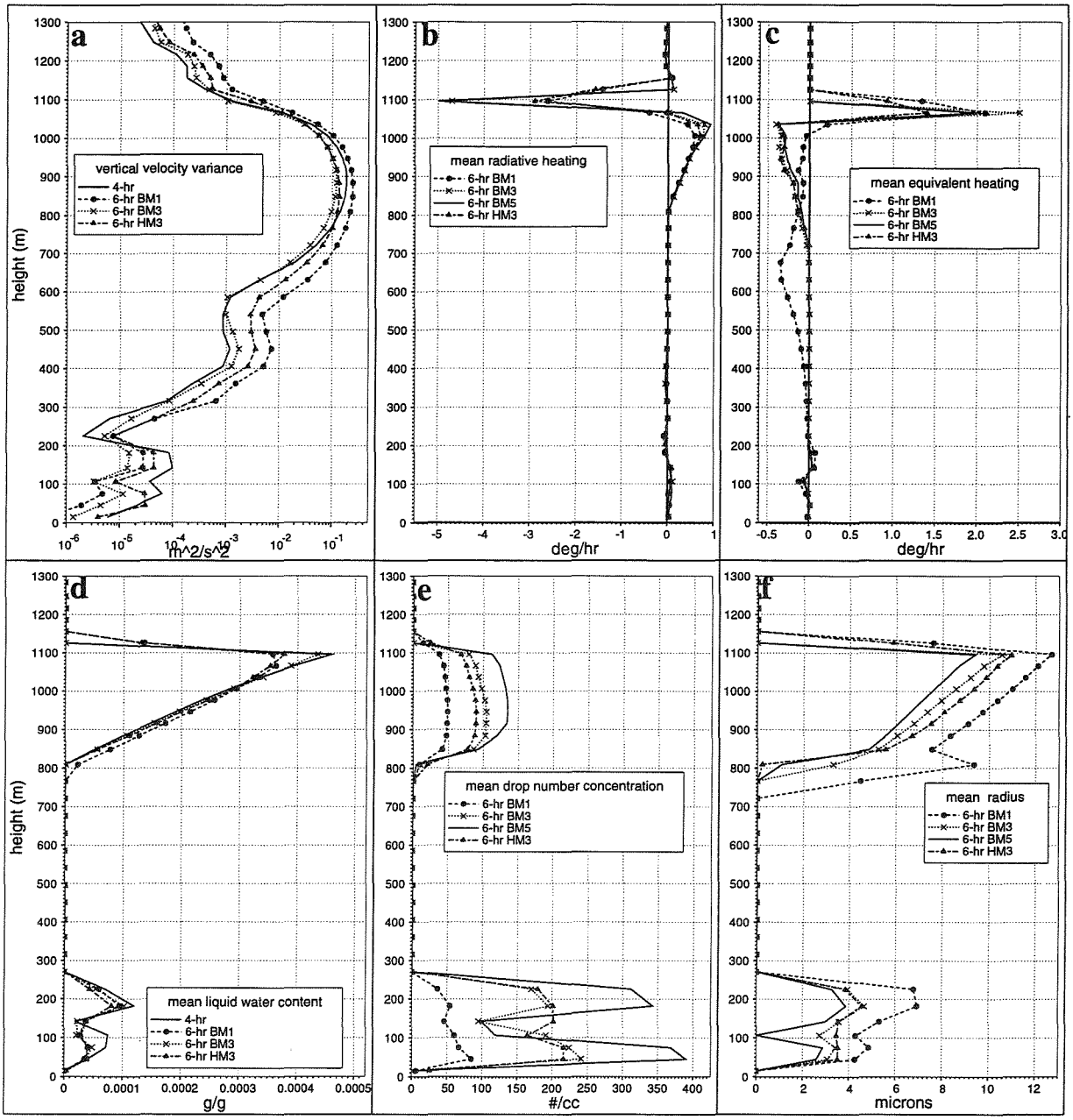

Fig 2. (a) Vertical velocity variance, at four h (solid line) and at six h for BM1, BM3, and HM3. (b) Mean radiative heating tendency at 6 hr for the sensitivity runs (negative values imply cooling). (c) Same as (b) but for equivalent heating. (d) As in (a) except mean liquid water mixing ratio, LWC (g/g). (e) Six-hour mean cloud drop number concentration (# cm^{-3}). (f) Mean radius (μm).

significant variation only near cloud top, with a trend toward more cooling with increasing mean drop number, $\bar{N}$ (Fig. 2e) and concomitantly smaller mean drop radius, $\bar{r}$ (Fig. 2f).

The equivalent heating rates in Fig. 2c are horizontally averaged profiles of heating associated with the drizzle flux divergence. In the sub-cloud layer the negative values represent cooling associated with evaporation. Note that the equivalent heating tends to somewhat compensate the radiative heating. The precipitating nature of BM1 is quite apparent, with a minimum lower in height relative to the nonprecipitating cases, producing a sub-cloud cooling of about 0.3° hr^{-1}. This may be partially responsible for the more vigorous eddies in this simulation.

Microphysical parameters plotted in Fig. 2 can be compared with the FSSP aircraft measurements reported in Herman and Curry (1984). Observed number concentrations were ~300 cm^{-3}, and significantly higher than those modeled here (Fig. 2e). To achieve the observed $\bar{N}$ and $\bar{r}$, it would have been necessary to increase the ambient CCN concentrations in our simulations. We have not done so because BM3 (and HM3) and BM5 produce similar boundary

layers and further increase in drop number is not expected to change this. (Radiative forcing in BM3 and BM5 is very similar.) Moreover, both BM3 and BM5 exhibit minimal collision-coalescence. An increase in N would act to suppress collection even more and decrease the likelihood of a dynamic feedback due to drizzle. Herman and Curry (1984) measured drop dispersions for this case of about 0.5-0.6. These values are much higher than those typical in for non-precipitating California marine stratocumulus (about 0.2; Noonkester 1984). With the high measured N, it seems unlikely that collision-coalescence was the mechanism responsible for spectral broadening in the observed ASC.

5. CONCLUDING REMARKS

Although the results presented here differ quantitatively from those in Herman and Curry (1984), the microphysical fields *do* exhibit the same qualitative features:

(*i*) LWC increases linearly with height with a maximum near cloud top;

(*ii*) $\bar{N}$ profiles are approximately constant with height in the upper cloud layer;

(*iii*) $\bar{r}$ increases with height, with an approximate $z^{1/3}$ dependence as expected from monomodal spectra exhibiting (*i*) and (*ii*).

Comparison of the BM3 and HM3 runs shows that the new hybrid microphysical scheme produces relatively lower N than BM. Since the LWC profiles are similar, this translates to an over prediction of $\bar{r}$. This trend can be mitigated somewhat by adjusting the breadth parameters of the assumed lognormal basis functions. HM was also run for the 100 cm^{-3} case (not shown) and produced results in close agreement with BM. More rigid tests of HM for cases exhibiting stronger collision-coalescence are underway and will be reported at the meeting.

It is clear from the sensitivity studies reported here that the interplay of radiation and cloud microphysical properties plays a significant role in the dynamic structure of ASC. Further, the microphysical properties are strongly affected by the abundance and characteristics of aerosols active as CCN. Unfortunately, accompanying measurements of CCN spectra are generally not as abundant as total aerosol information. As a result, the modeling of specific ASC cases is hampered by lack of information on the horizontal and vertical distributions of CCN present during the event. It is hoped that future field programs will work to address this deficiency.

ACKNOWLEDGEMENTS

This work was supported by the Environmental Sciences Division of the U. S. Department of Energy under contract number DE-FG03-95ER61958 as part of the Atmospheric Radiation Measurement Program (ARM).

REFERENCES

Curry, J. A., 1986: Interactions among turbulence, radiation and microphysics in Arctic stratus clouds. *J. Atmos. Sci.*, **43**, 90-106.

Curry, J. A., E. E. Ebert and G. F. Herman, 1988: Mean and turbulence structure of the summertime Arctic cloudy boundary layer. *Quart. J. Roy. Meteorol. Soc.* **114**, 715-746.

Feingold, G., B. S. Stevens, W .R. Cotton and A. S. Frisch, 1996: The relationship between drop in-cloud residence time and drizzle production in a simulated stratocumulus cloud. *J. Atmos. Sci.*, **53**, 980-1006.

Herman, G. F. and J. A. Curry, 1984: Observational and theoretical studies of solar radiation in Arctic stratus clouds. *J. Climatol. Appl. Meteorol.*, **23**, 5-24.

Noonkester, V. R. 1984: Droplet spectra observed in marine stratus cloud layers. *J. Atmos. Sci.*, **41**, 829-844.

Pielke, R. A., W. R. Cotton, R.L. Walko, C. J. Tremback, W. A. Lyons, L. D. Grasso, M. E. Nicholls, M. D. Moran, D. A. Wesley, T. J. Lee, and J. H. Copeland, 1992: A comprehensive meteorological modeling system-RAMS. *Meteor. Atmos. Phys.*, **49**, 69-91.

Ritter, B. and J.-F. Geleyn, 1992: A comprehensive radiation scheme for numerical weather prediction models with potential application in climate simulations. *Mon. Wea. Rev.*, **120**, 303-325.

Stevens, B., G. Feingold, R. L. Walko and W. R. Cotton, 1996: On elements of the microphysical structure of numerically simulated non-precipitating stratocumulus. *J. Atmos. Sci.* , **53**, 980-1006.

Tzivion, S., G. Feingold, and Z. Levin, 1987: An efficient numerical solution to the stochastic collection equation. *J. Atmos. Sci.*, **44**, 3139-3149.

Walko, R. L., W. R. Cotton, M. P. Meyers, and J. Y. Harrington, 1995: New RAMS cloud microphysics parameterization. Part I: the single moment scheme. *Atmos. Res.*, **38**, 29-62.

A STATISTICAL STUDY OF WARM RAIN FORMATION IN SHALLOW, TROPICAL CONVECTION

Marcin J. Szumowski[1,2], Wojciech W. Grabowski[3], Robert M. Rauber1, and Harry T. Ochs III[1,2]

[1] Department of Atmospheric Sciences, University of Illinois, Urbana, IL, USA
[2] Illinois State Water Survey, Champaign, IL, USA
[3] National Center for Atmospheric Research, Boulder, CO, USA

1. INTRODUCTION

Recent observations of warm rain evolution in shallow, convective tropical clouds suggest that they are very efficient in producing rain on short time scales. Raindrop spectra which develop in these clouds are characterized by presence of giant raindrops with diameters of 3 to 8 mm. The evolution of several shallow convective cells with cloud and rain fields similar to those observed off the windward shore of the Big Island of Hawaii during the Hawaiian Rainband Project (HaRP, 1990) was successfully simulated with the Clark (1977, 1979) anelastic, nonhydrostatic cloud model. Figure 1 shows a comparison of a vertical cross-section of the radar reflectivity field through one of the intense rainshafts embedded in an off-shore rainband on 22 August 1990 and a two dimensional rainwater field generated by the Clark model. Despite the limitation of the two-dimensional approach the model appears to successfuly reproduce the spatial and temporal scales of the convective updrafts and associated rainshafts. In the model individual convective updraft cores are embedded in a region of light precipitation, similar structure of the off-shore rainbands depicted in the radar data. The locally intense model rainshafts have lifetimes on the order of 10-20 minutes, in agreement with the data.

2. THE MODEL

Evolving kinematic and thermodynamic fields, generated by the cloud model and recorded every 8 seconds, are used in a Lagrangian trajectory model to simultaneously calculate trajectories of thousands of growing drops originating near cloud base over time periods of approximately 30-60 minutes. The trajectory model is described in greater detail in another paper in this volume (Szumowski *et al.* 1996). Based on analyses of observational data accretion of cloud water is hypothesized to be the dominant drop growth mechanism. Breakup probability is addressed by using the bulk rainwater fields generated by the cloud model. The multiple trajectory calculations are used to determine the statistical significance of eddy circulations on drop-growth trajectories, in the shallow convective clouds. The main focus of our investigation is the effect of eddies on scales on the order of 100 meters on raindrop growth rates. A direct assesment of the eddy-modified trajectories and the resulting drop growth rates is straight forward with a simple formulation of the drop growth rate (continuous collection) equation. The ensemble of sizes of all individual drops after they complete their trajectories through the cloud will be compared qualitatively with raindrop spectra observed by the aircraft in the Hawaiian rainband clouds. Trajectories of all raindrops which may grow to giant sizes (d > 4mm) will be examined to determine if the hypothesized recirculation mechanism plays a significant role in their formation.

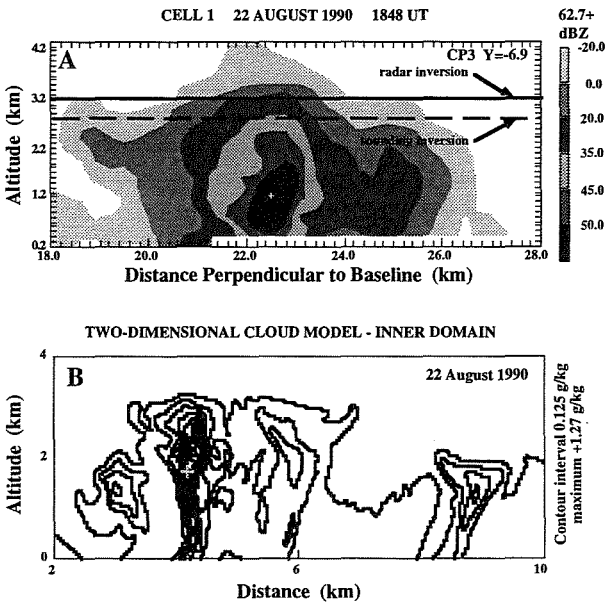

Figure 1. A) Vertical cross-section of the radar reflectivity field through an intense rainshaft embedded in an off-shore rainband on 22 August 1990 at 1848 UT. B) A sample of the rainwater field (g/kg) generated in the inner domain of a nested grid two-dimensional simulation of the Clark cloud model initialized with thermodynamic data collected on 22 August.

3. FUTURE RESEARCH

The role of the hypothesized recirculation mechanism on precipitation formation in warm, shallow convective clouds as well as the hypothesis that accretion is the dominant growth mechanism leading to the formation of giant raindrops will be evaluated in this modeling study. We intend to test the sensitivity to the initial collector drop sizes, their location in the cloud and the formulation of the bulk microphysical parametrization. We consider expanding this experiment to three dimensions and/or including more complex microphysics if necessary.

4. ACKNOWLEDGEMENTS

We thank everyone at the National Center for Atmospheric Research who contributed to the Hawaiian Rainband Project data acquisition and processing. We also wish to thank L. Jay Miller and Bill Anderson for their assistance with radar data analyses software and Terry Clark and William Hall for the assistance with the cloud model. Computing time was provided by the National Center for Atmospheric Research, which is sponsored by the National Science Foundation. This research was sponsored by the National Science Foundation under grants NSF ATM 9020245 and NSF ATM 9223165.

5. REFERENCES

Clark T. L., 1977: A small-scale dynamic model using a terrain-following coordinate transformation. *J. Comp. Phys.*, **24**, 186-215.

Clark T. L., 1979: Numerical simulations with a three-dimensional cloud model: Lateral boundary condition experiments and multicellular severe storm simulations. *J. Atmos. Sci.*, **36**, 2192-2215.

Szumowski, M. J., H. T. Ochs, R. M. Rauber, and W. W. Grabowski, 1996: Lagrangian calculations of raindrop growth in shallow convective clouds based on kinematic fields obtained from both dual-Doppler data syntheses and a cloud model. Preprints, 12th International Conference on Clouds and Precipitation, Zurich, Switzerland.

NUMERICAL SIMULATIONS OF DEEP TROPICAL CONVECTION USING A CLOUD ENSEMBLE MODEL WITH AN IMPROVED EXPLICIT MICROPHYSICS

Tamir G. Reisin[1], Leo J. Donner[2], Richard S. Hemler[2] and Charles J. Seman[2]

[1]Program in Atmospheric and Oceanic Sciences, Princeton University, Princeton, New Jersey, USA.
[2]Geophysical Fluid Dynamics Laboratory/NOAA, Princeton University, Princeton, New Jersey, USA.

1. INTRODUCTION

The development of deep moist convection associated with large–scale tropical disturbances has been recognized to play a significant role in the global radiation and hydrological budget. Convective systems consist of a complex mixture of dynamic and microphysical structures of various scales making their parameterizations a difficult task. One method for evaluating and developing these parameterizations is to use high-resolution, limited-area nonhydrostatic models. These models represent explicitly the physical processes which are parameterized in GCMs. The high-resolution models can be examined against field data for robustness.

In general, these models parameterize microphysical processes in clouds by making some simple assumptions with respect to the size distribution function of the clouds' particles and the microphysical processes they are involved in (Kessler type parameterizations). These models usually cannot predict the particles' sizes as a function of time or differentiate between clouds that develop under different CCN populations.

A three-dimensional, limited-area nonhydrostatic (LAN) model, developed at GFDL (Lipps and Hemler, 1986), has been used to examine tropical convection associated with large-scale moisture convergence. A new explicit microphysics scheme was introduced to the LAN model. This new scheme includes both the warm and ice phases and describes in a more realistic way the formation and development of hydrometeors providing information on the particles' size as a function of time.

2. MODEL DESCRIPTION

The three dimensional cloud ensemble model is described in detail in Lipps and Hemler (1986). The elastic version of the model is used in the present simulations (Held et al., 1993). The microphysical parameterization follows the idea of Clark (1974, 1976) and represents an extension and improvement of the scheme presented by Yair et al. (1995).

Five types of cloud particles are considered: cloud drops, raindrops, ice crystals, aggregates and graupel. The mass distribution function of each of the species is assumed to be represented by a modified gamma function:

$$n_i(m,t) = B_i(t) m^{\alpha_i(t)} \exp^{-\mu_i(t) m^{1/\gamma_i}} \qquad (1)$$

where i represents one the species, $B_i(t)$, $\alpha_i(t)$ and $\mu_i(t)$ are time dependent variables and γ_i is a predetermined parameter. The prognostic variables of the model are the first three moments of the distribution function as defined by:

$$\begin{aligned} M_i^J(t) &= \int_0^\infty m^J n_i(m,t) dm \\ &= \gamma_i B_i(t) \frac{\Gamma\{\gamma_i[\alpha_i(t)+J+1]\}}{\mu_i(t)^{\gamma_i[\alpha_i(t)+J+1]}} \\ & \quad J = 0,1,2 \end{aligned} \qquad (2)$$

where $J = 0$ is for the number concentration (N_i), $J = 1$ for the mass concentration (M_i) and $J = 2$ for the radar reflectivity concentration (Z_i). At each time step the three time–dependent parameters of the distribution function can be calculated as a function of these three moments of the distribution function.

As a contrast to other parameterizations, since the parameters of the distribution function change in time, the distribution itself and other derived parameters, such as the average mass of the distribution also change. Other moments of the distribution function can be calculated as a function of of N_i, M_i and Z_i and the time dependent parameters. For example, the effective radius of the raindrops, needed in radiative transfer calculations, is given by:

$$r_{eff,r} = \left(\frac{3}{4\pi\rho_w}\right)^{1/3} \bar{m}_r(t)^{1/3} \times \qquad (3)$$

$$\times \frac{\{\gamma_r[\alpha_r(t)+5/3]\}^{2/3}}{\{\gamma_r[\alpha_r(t)+4/3]\}\{\gamma_r[\alpha_r(t)+1]\}^{1/3}}$$

where $\bar{m}_r = M_r/N_r$ is the average mass (of the raindrops in this case) and ρ_w is the water density.

The microphysical processes included are: nucleation of CCN, condensation/evaporation of cloud drops and raindrops, collision-coalescence of cloud drops and raindrops (autoconversion and accretion), binary breakup of raindrops (Low & List kernels), nucleation of IN (deposition, condensation–freezing and contact mechanisms), freezing of cloud and raindrops (homogeneous and non–homogeneous), ice multiplication (Hallett–Mossop mechanism), sublimation/deposition of ice particles, drop-ice and ice-ice interactions, melting, shedding and sedimentation.

Cloud drops are created by nucleation of CCN; drops greater than 50 μm in radius are considered raindrops. Ice crystals are formed by nucleation of IN, by freezing of cloud drops or as a result of splinters produced by the Hallett–Mossop mechanism. Graupels are created by freezing of raindrops and by riming. Coagulation of ice crystals produce aggregates. The ice crystals are assumed to be oblate spheroids.

The formulation of the different microphysical processes follows the work by Reisin et al. (1996a,b) in which the calculations were conducted for spectral bins of the distribution functions of the different species. Here, the equations are solved analytically for the whole distribution function and average values are used when necesary. Collision–coalescence is probably the most important process involved in the formation of precipitation size particles and also the most difficult to treat correctly in numerical models, especially within a parameterization framework. In the present parameterization, we adopt the method shown by Yair et al. (1995) for the solution of the stochastic collection equation (SCE). The gamma function representing the distribution function of the particles is split into discrete bins and the interactions between the different bins are calculated. The reclassification of the hydrometeors that result from the interactions between the different ice species and the cloud and rain drops follow the approach presented in Reisin et al. (1996).

3. RESULTS AND COMMENTS

Using the model described above some preliminary results of a simulation of deep convection over the Atlantic Ocean are presented. The initial conditions used in the simulations are characteristic of deep moist convection in the tropics and are based on data from Phase III of the GARP Atlantic Tropical Experiment as reported by Thompson et al. (1979). The initial vertical profile of the temperature and dew point can be seen

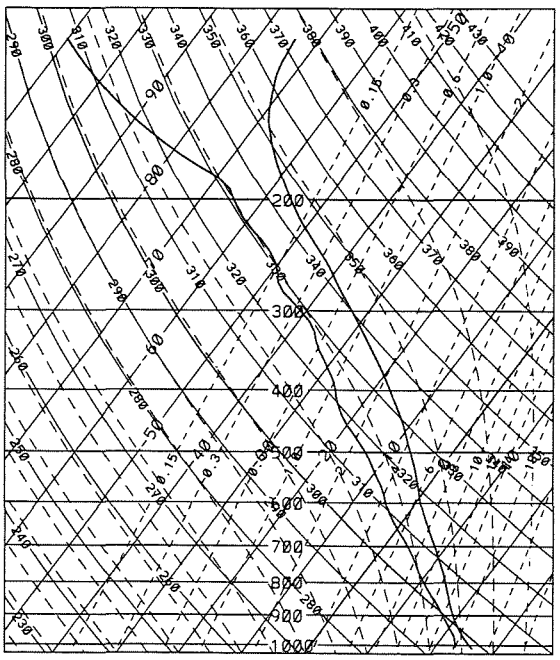

Figure 1: Vertical profiles of temperature and dew point.

in Fig. 1. A large–scale, time–invariant convergence associated with the synoptic flow is assumed to exist. The profile of the vertical velocity associated with this large–scale convergence is shown in Fig.2. As can be seen, this convergent flow is too weak to influence the development of isolated clouds and its dynamical effects are significant over longer time scales. The vertical velocities shown in Fig. 2 are used to calculate the moisture and heat fluxes associated with the large–scale convergence.

The model domain was 50 km in the x and y directions and 16 km in height. The horizontal grid space was 1 km and 250 m in the vertical. In addition to the large scale converegence, a random perturbation of up to 2 g Kg^{-1} was applied to the vapor mixing ratio at the first time step of the simulation at the lowest kilometer of the domain.

The development of deep convection was very slow. Because of the high relative humidity at the higher levels of the atmosphere (see Fig. 1), supersaturation with respect to ice developed relatively fast. After 217 min of simulation an ice cloud developed at 10 km, just above the level of maximum vertical velocity of the large scale converegence. These clouds persisted during all the simulation, reaching a mass content of 0.05 g Kg^{-1} with a number concentration of less than 1 L^{-1}.

Fifty–four min later, a shallow cloud begins develop at 1 km height but another 109 min will pass until a significant vertical velocity develops (>1 m sec^{-1}) and

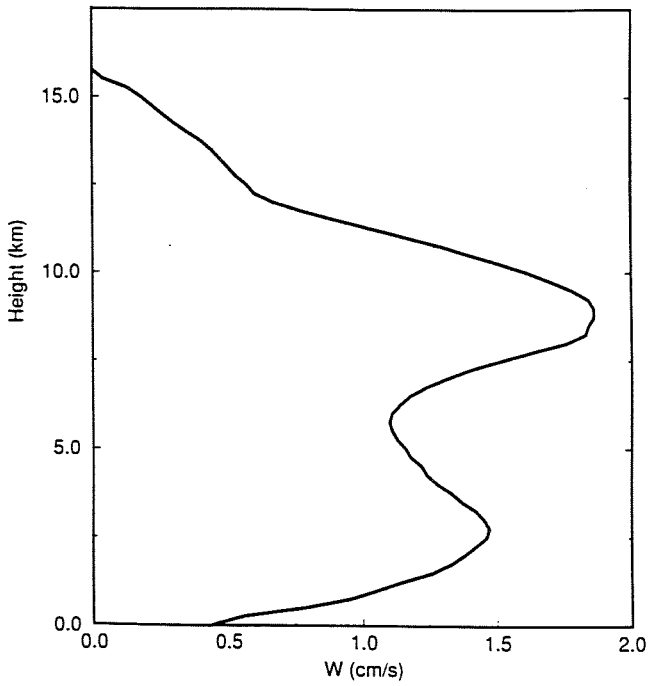

Figure 2: Profile of vertical velocity W associated with the large scale convergence.

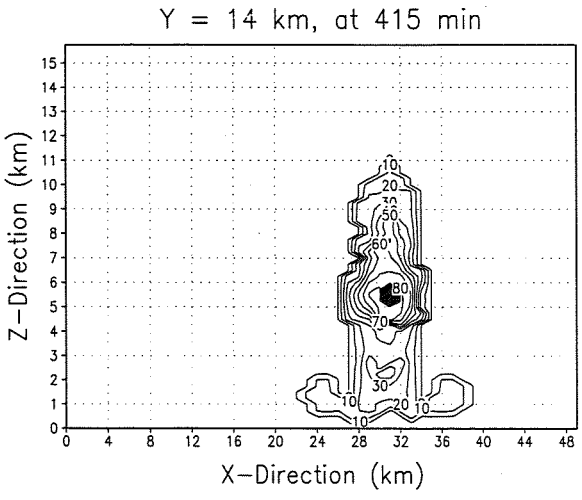

Figure 3: Vertical distribution of average diameter of cloud drops (in μm), 415 min from model initiation.

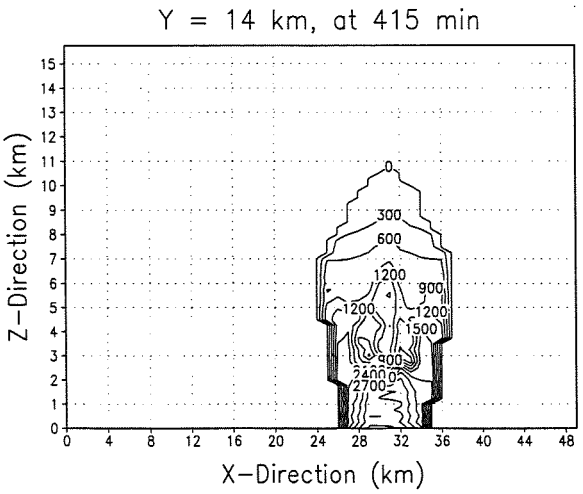

Figure 4: Vertical distribution of average diameter of raindrops (in μm), 415 min from model initiation.

triggers a fast development of deep convection (380 min from model initiation). At 400 min from model initiation vertical velocity reached 12 m sec−1, the maximum cloud drops water content was 4 g Kg^{-1} and rain formation processes were already active with a maximum of 5 g Kg−1 already produced. Ice in the convective areas was just beginning to form, without significant mass contents yet. At this stage, the maximum average diameter of the cloud drops reached 35 μm and of the raindrops 1500 μm. The ice crystals in the high level ice cloud had an average diameter that reached 300 μm.

Fifteen min later (415 min from model initiation) the vertical velocity reached 16 m sec−1 and the ice phase was rapidly developing. In Fig. 3 the vertical distribution of the average diameter of cloud drops is shown. Cloud drops reached the 10 km height level and a maximum average diameter of about 80 μm was achieved at 5.5 km height. Raindrops already reached the surface with an average diameter of almost 3000 μm (Fig. 4). At this stage another cloud began developing at a distance of about 25 km from the main core.

Graupel (Fig. 5) also formed, as a result of heavily rimed ice or of frozen raindrops. They further grew by accretion of cloud and rain drops. They reached a maximum average diameter of about 8000 μm just above the melting level. Ice crystals that began developing within the convective core at altitudes of about 3.5 km penetrated also the layer of high ice clouds already present (Fig. 6). In the convective part the ice crytals reached a maximum average diameter of 350 μm. Probably, bigger ice crystals were efficient rimers and rapidly converted into graupels.

These few examples demonstrate the model ability to properly describe both the dynamics and the micro-

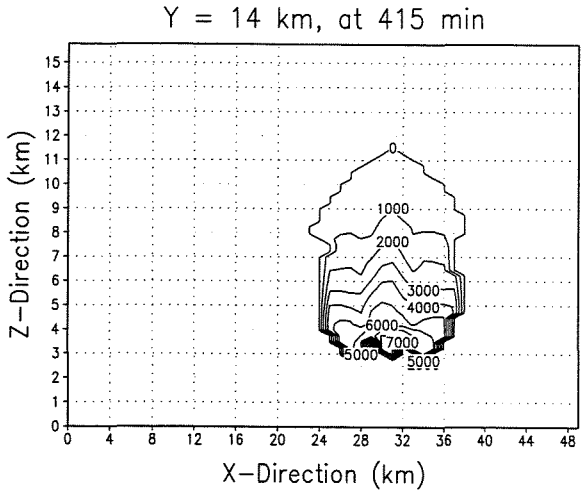

Figure 5: Vertical distribution of average diameter of graupel (in μm), 415 min from model initiation.

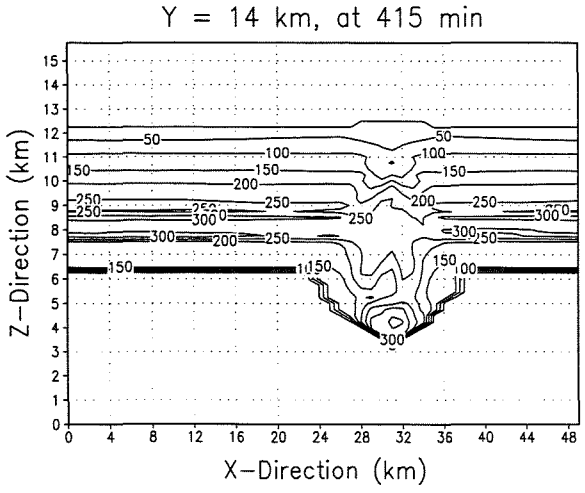

Figure 6: Vertical distribution of average diameter of ice crystals (in μm), 415 min from model initiation.

physical processes present in deep convection systems. Comparisons with results obtained using the Kessler-type parameterization will be presented at the Conference.

4. REFERENCES

Clark, T.L., 1974: A study in cloud phase parameterization using the gamma distribution. *J. Atmos. Sci.*, **31**, 142-155.

Clark, T.L., 1976: Use of log-normal distribution for numerical calculations of condensation and collection. *J. Atmos. Sci.*, **33**, 810-821.

Held, I.M., R.S. Hemler, and V. Ramaswamy, 1993: Radiative-convective equilibrium with explicit two-dimensional moist convection. *J. Atmos. Sci.*, **50**, 3909-3927.

Lipps, F.B., and R.S. Hemler, 1986: Numerical simulation of deep tropical convection associated with large-scale convergence. *J. Atmos. Sci.*, **43**, 1796-1816.

Reisin, T., Z. Levin, and S. Tzivion, 1996a: Rain production in convective clouds as simulated in an axisymmetric model with detailed microphyscs. Part I: Description of the model. *J. Atmos. Sci.*, **53**, 497-519.

Reisin, T., Z. Levin, and S. Tzivion, 1996b: Rain production in convective clouds as simulated in an axisymmetric model with detailed microphyscs. Part II: Effects of varying drops and ice inititation. *J. Atmos. Sci.*, In Press.

Thompson, R.M., S.W. Payne, E.E. Recker, and R.J. Redd, 1979: Structure and properties of synoptic-scale wave disturbances in the Intertropical Convergence Zone of the Eastern Atlantic. *J. Atmos. Sci.*, **36**, 53-72.

Yair, Y., Z. Levin, and S. Tzivion, 1995: Microphysical processes and dynamics of a Jovian thundercloud. *Icarus*, **114**, 278-299.

THERMODYNAMICAL BUDGETS OF AN EXPLICITELY SIMULATED DEEP CONVECTIVE CLOUD SYSTEM

Françoise GUICHARD[1], Jean-Philippe LAFORE[1] and Jean-Luc REDELSPERGER[1]

Centre National de Recherches Météorologiques (Météo-France and CNRS), Toulouse, FRANCE

1. INTRODUCTION

Representation of cumulus convection constitutes a critical point for large scale modelling. Numerous studies have stressed the sensitivity of large scale dynamics to the convection scheme that is used (Lindzen, 1990, Slingo *et al.*1994).

The present study aims to investigate the thermodynamical impact of an oceanic tropical cloud sytem simulated with a Cloud Resolving Model (CRM). Thermodynamical budgets are analysed, and some statistic properties are retrieved and discussed.

2. THE CONVECTIVE CLOUD SYSTEM

We focus on a cloud system observed on 17 February 1993 in the TOGA-COARE region (Fig. 1), formed of two convective lines, oriented approximatively parallel to the low level shear, with a life cycle of a few hours.

The simulation is performed in three-dimensions, with the CRM of Redelsperger and Sommeria (1986), over a spatial domain of 90(x).90(y).20(z) km^2. Ice phase processes (Caniaux *et al.*, 1994) as well as radiative effects (Morcrette 1991 - see Guichard *et al.*1996 for their implementation) are treated. The model starts with homogeneous conditions corresponding to the meteorological sounding, and cyclic

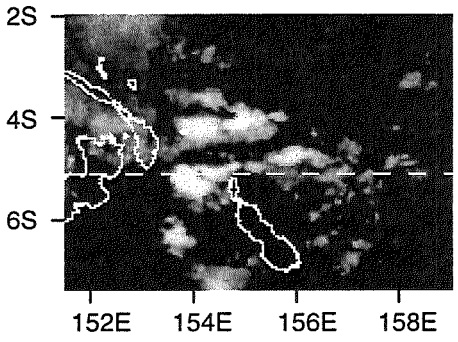

Figure 1: *IR satellite picture derived from the satellite GMS-4, at 21h45 UTC.*

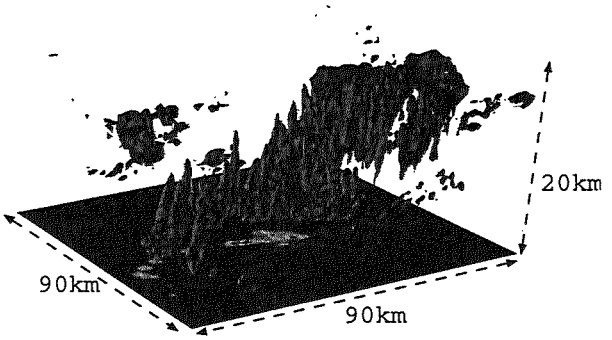

Figure 2: *Instantaneous field of simulated clouds and surface precipitation - isosurfaces (0.32g.kg^{-1}) of the sum of hydrometeors (cloud and precipitating liquid water, ice crystals, aggregates and graupel)*

lateral boundary conditions are used. No large scale ascent is prescribed in the simulation, as there is no evidence of such forcings from observations.

Additional information on this case (observations and conditions of simulation) can be found in Jabouille *et al.*(1996) and Redelsperger *et al.*(1995). As observed by Doppler radars, a convective line develops parallel to the low level shear after a few hours. An instantaneous 3D view (Fig. 2) illustrates the simulated convective system, formed of an ensemble of different cloud types, at different stage of their life cycle. Shallow clouds, deep growing cells as well as ice anvils are simultaneously present.

3. HEAT AND MOISTURE BUDGETS

Fig. 3 shows thermodynamical budgets derived from equations of the model for potential temperature θ and water vapour q_v, horizontally and temporally averaged over the whole domain and the 2 hours of deep convection (multiplied by the Exner function π and $-L/c_p$ respectively, with L the latent heat of vaporisation).

In the present case, without large scale convergence, eulerian evolutions of θ and q_v are due to the

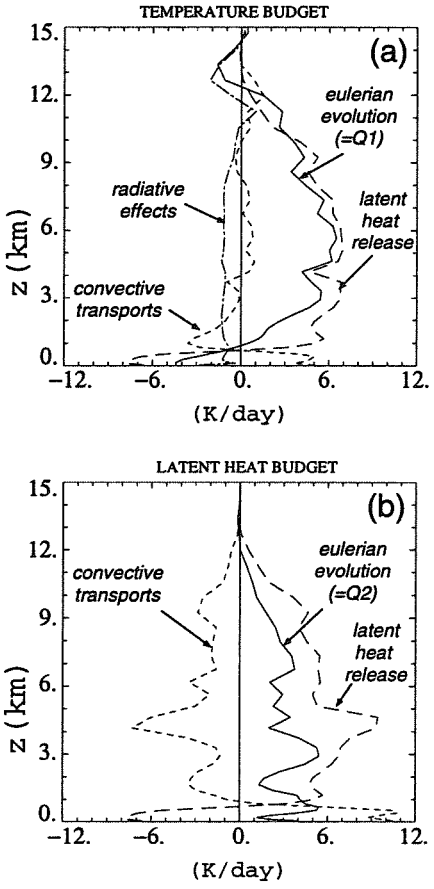

Figure 3: *Budgets of temperature (a) and latent heat (b) horizontally averaged over the whole domain and temporally over the 2 hours of deep convection*

sum of latent heat release, divergence of vertical convective fluxes (subgrid and resolved), and radiative effects (for θ only). Thus, eulerian evolution profiles correspond directly to apparent heat source Q_1 and apparent moisture sink Q_2 as defined at the large scale.

In Fig. 3a, the latent heat release appears to be the dominant process, explaining the average heating of the domain, whereas terms related to radiation and convective transport remain smaller, except below 2 km (where there is large convective transport) and at the cloud top (where large radiative effects occur). Finally, the maximum of Q_1, located around 6 km, is in agreement with observational results obtained during the COARE experiment (Lin and Johnson, 1996).

For water vapour (Fig. 3b), both latent heat release and convective eddy transports are important and in opposing. Latent heat release dries the atmosphere above 1 km and moistens it below through raindrops evaporation, whereas convective transports bring water vapour upwards.

The resulting Q_2 corresponds to a drying over the whole column, with a complex vertical structure. This particular shape differs somehow from the clas-

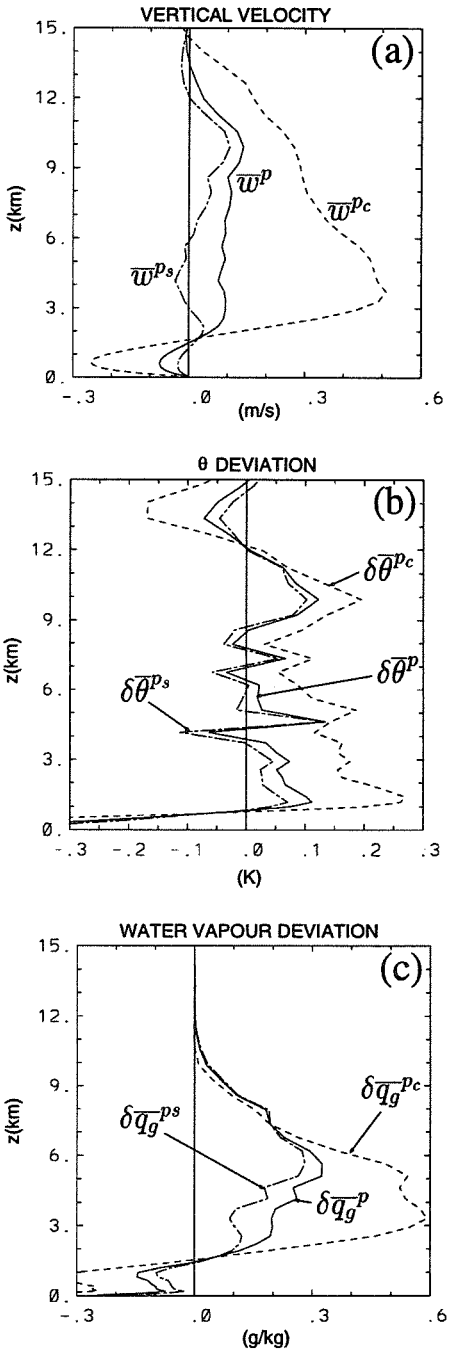

Figure 4: *For the precipitating system P, its convective and stratiform parts P_C and P_S: vertical profiles of (a) vertical velocities and deviations from the average over the whole domain of (b) potential temperature θ - $\overline{\delta\alpha}^k = \overline{\alpha}^k - \overline{\alpha}^T$*

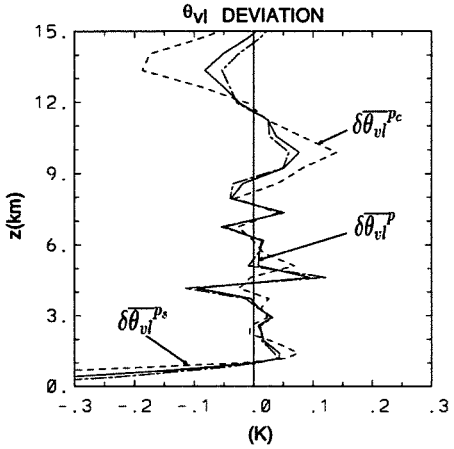

Figure 5: *Same as Fig.4b for deviations of liquid and solid virtual potential temperature θ_{vl}.*

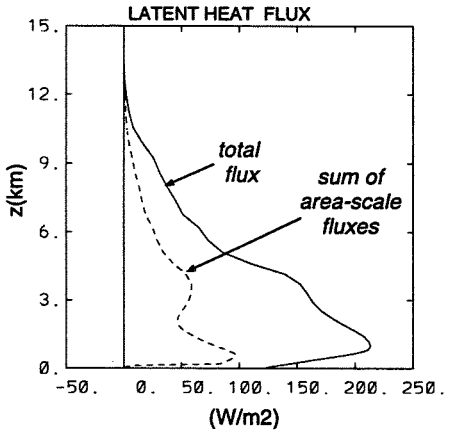

Figure 6: *Vertical fluxes of latent heat: total convective flux (solid line) and the sum of 'area-scale' fluxes (dashed line) - the sum of 'area-scale' fluxes is the sum of mean fluxes in updrafts and downdrafts for each of the 6 defined internal areas (see text).*

sical double peak structure, observed for large convective systems such as squall lines (e.g. Johnson 1984, Lafore *et al.*1988, Caniaux *et al.*1994). In particular, the second high peak is not strongly marked, and a third peak is observed at low level, in addition to the 3 km peak. Differences in the structure of the convective line could explain these differences. In particular, the stratiform part of the system, which is not very developped, can explain differences in high levels, and the presence of shallow convection those noted at low levels.

4. STATISTICAL PROPERTIES OF THE CLOUD SYSTEM

The precipitating system P is defined as the ensemble of columns where the integrated precipitating cloud water content is greater than 1 kg m^{-2}, over the 2 hours of deep convection. P is further split into convective and stratiform parts P_C and P_S, using criteria similar to Tao *et al.*(1989) for the convective area.

The area of convective precipitation is responsible for about 80% of the total latent heat release, although it covers only 4% of the total domain. The precipitating system P extends more widely (20%), whereas the remaining non-precipitating 80% consists of columns of clear sky, with embedded non precipitating shallow and convectively generated anvil clouds. Above the lower layers, air parcels ascend in P with a maximum of velocity located arround 10 km (Fig. 4a). It is higher than the one in P_C, due to stratiform clouds activity. The vertical velocity profile in the convective part of the system shows a typical structure, with strong convective downdrafts below 2 km and a maximum of 0.5m.s^{-1} at 3 km.

Above 1 km, the precipitating system is actually warmer than the environment, except locally, arround the isothermal 0°C in particular (Fig. 4b). However, the temperature excess does not even reach 0.3 K in the convective precipitation area.

These features agree with aircraft data analyses which stress surprisingly weak vertical velocities and temperature excesses in oceanic tropical convective cells (Lucas *et al.*1994).

Water vapour deviations in the precipitating system tend to increase the small buoyancy excess given by potential temperature deviations (Fig. 4c). They are correlated to vertical velocity, moister air is found is ascending layers and dryer air in subsidence layers.

In considering θ_{vl}, the liquid and solid virtual potential temperature, which takes into account water loading, in-cloud θ_{vl} deviations are still weaker (compare Fig. 4b with Fig. 5). The system shows an equilibrium of mass, due firstly to very small temperature deviations, and further reinforced by water in all its phases. The impact of water loading in reducing buoyancy, and thus vertical velocity, is stressed once again in the present simulation. The main point is that this result gives a relation between thermodynamics and microphysics in and outside clouds, this could be interesting for a convection scheme.

5. CONVECTIVE TRANSPORTS SCALE

Moisture budget (Fig. 3b) shows that convective vertical transport has a strong impact on water vapour distribution, so that a parameterization should be able to estimate it correctly.

Several internal areas i are defined, and we analyse whether the total convective transport could be explained as the sum of the different 'area-scale' transports. The total convective flux is decomposed as follow:

$$\rho\,\overline{q_v w}^T = \sum_i \rho\,\sigma_i\,\overline{w}^i\overline{q_v}^i + \sum_i \rho\,\sigma_i\,\overline{w''_i q''_{v\,i}}^i$$

$\overline{\alpha}^T$ and $\overline{\alpha}^i$ are the averages of α over the total domain and the area i respectively, $\alpha''_i = \alpha - \overline{\alpha}^i$, σ_i is the occupation rate of area i and ρ the air density. With this decomposition, it is possible to determine whether fluxes occur at the areas scale (first term of the right hand side), or at an even smaller scale (second term of the right hand side).

In each internal area i, the vertical flux of water vapour is well estimated by the average vertical flux deduced from average water vapour and vertical velocity fields in these areas ($\overline{wq_v}^i \approx \overline{w}^i \overline{q_v}^i$). However, strong compensations occur between vertical transports in the different areas of the domain, so that the total transport is a residual of them.

Six basic internal areas are retained here: the areas of surface convective and stratiform precipitation, the part of the cloud system where precipitation does not reach the ground, the areas of shallow and anvil clouds and clear sky columns (criteria are defined in Guichard 1995). Then, we further distinguish the updraft and downdraft parts of each area. The contribution of each of the twelve areas to the total flux is computed and separated into an average area-scale and a sub-area scale contribution. Results are presented for a 2 hour temporal average, but the conclusion is the same for shorter periods (Fig. 6).

In considering the contributions of both average updrafts and downdrafts in each internal area, it is possible to retrieve only between 1/3 and 1/2 of the total flux (the retrieval is even worse for sensible heat flux). Thus, knowledge of mean vertical properties of internal areas is not reliable, it leads to a large underestimation of the convective flux. Sub-areas draft fluxes are necessary in order to get a good estimation of the total flux. This raises a delicate problem in terms of parameterization.

6. SUMMARY

A convective line has been explicitely simulated. It develops along the shear direction in low levels, as observed during the COARE experiment. Its thermodynamical budgets and statistical properties have been analysed and discussed. In particular, this study brings out the fact that the simulated atmospheric column exhibits an equilibrium of mass, and that convective transports occur on a very fine scale. Additional work is necessary to validate the simulation results with COARE observations (Doppler radar data), and other convective systems have to be similarly analysed for evaluating the sensitivity of cloud statistic properties.

REFERENCES

Caniaux, G., J.-L Redelsperger and J.-P. Lafore, 1994: A numerical study of the stratiform region of a fast-moving squall line. Part I: general description and water and heat budgets. *J. Atmos. Sci.*, **51**, 2046-2074.

Guichard, F., J.-L Redelsperger and J.-P. Lafore, 1994: The behaviour of a cloud ensemble in response to external forcings, *Quart. J. Roy. Meteor. Soc.*, accepted.

Guichard, F, 1995: Impact d'un ensemble de nuages sur l'environnement de plus grande échelle, vu par un modèle de convection nugeuse explicite (cas GATE et TOGA-COARE). cloud ensemble in response to external forcings, PhD thesis, Institut National Polytechnique de Toulouse, 197 pp.

Jabouille, P., J.-L. Redelsperger and J.-P. Lafore, 1996: Modification of surface fluxes by atmospheric convection as viewed from numerical simulation. *Mon. Wea. Rev.*, **124**, 816-837.

Johnson, R.H., 1984: Partitioning tropical heat and moisture budgets into cumulus and mesoscale components: implications for cumulus parameterization, *Mon. Wea. Rev.*, **112**, 1590-1602.

Lafore, J.-P., J.-L.Redelsperger and G. Jaubert, 1988: Comparison between a three-dimensional simulation and doppler radar data of a tropical squall line: transport of mass, momentum, heat and moisture. *J. Atmos. Sci.*, **45**, 3483-3500.

Lin, X. and R.H. Johnson, 1996: heating, moistening and rainfall over the Western Pacific Warm Pool during TOGA COARE, *submitted to J. Atmos. Sci.*.

Lindzen, R. S., 1990: Some coolness concerning global warming. *Bull. Amer. Meteor. Soc.*, **71**, 288-299.

Lucas, C. and E.J. Zipser and M.A. LeMone, 1994: Vertical velocity in oceanic convection off tropical Australia. *J. Atmos. Sci.*, **51**, 3183-3193.

Morcrette, J.-J, 1991: Radiation and cloud radiative properties in the european centre for medium range weather forecasts forecasting system. *J. Geophys. Res.*, **96**, 9121-9132.

Redelsperger, J.-L., and G. Sommeria, 1986: Three-dimensional simulation of a convective storm: sensitivity studies on subgrid parametrisation and spatial resolution. *J. Atmos. Sci.*, **43**, 2619-2635.

Redelsperger, J.-L., P. Jabouille and J.-P. Lafore, 1995: Numerical studies of convective organization observed during TOGA-COARE, Proceedings of the 21st Conference on Hurricanes and Tropical Meteorology, paper 14B.6.

Slingo, J. M., M. Blackburn, A. K. Betts, R. Brugge, K. Hodges, B. J. Hoskins, M. J. Miller, L. Steenman-Clark and J. Thuburn, 1994: Mean climate and transience in the tropics of the UGAMP GCM: Sensitivity to convective parametrization. *Quart. J. R. Met. Soc.*, **120**, 881-922.

Tao, W.-K and J. Simpson, 1989: Modeling study of a tropical squall-type convective line. *J. Atmos. Sci.*, **46**, 177-202.

RADAR OBSERVATIONS AND NUMERICAL SIMULATIONS OF A TOGA COARE SQUALL SYSTEM

Brad S. Ferrier[1,2], Jeffrey B. Halverson[1,3], Robert Pasken[4], Wei-Kuo Tao[1], and Joanne Simpson[5]

[1]Mesoscale Atmospheric Processes Branch (Code 912), NASA/GSFC, Greenbelt, MD 20771 USA
[2]Science Systems and Applications, Inc (SSAI), Lanham, MD 20706 USA
[3]Universities Space Research Association (USRA), Lanham, MD 20706 USA
[4]Dept. of Science and Mathematics, Parks College of Saint Louis University, Cahokia, IL 62206 USA
[5]Chief Scientist for Meteorology (Code 900), NASA/GSFC, Greenbelt, MD 20771 USA

1. INTRODUCTION

Mesoscale convective systems (MCSs) account for a large portion of rainfall in the tropics, as well as the diabatic heating which drives large-scale tropical and extratropical circulations (Simpson et al., 1988). Numerical models are being used to develop algorithms for retrieving profiles of hydrometeors and diabatic heating from space in preparation for the Tropical Rainfall Measuring Mission (Tao et al., 1993; and others). It is therefore important that uncertainties or shortcomings in the parameterized physics be identified by comparing numerical simulations with observations.

On 11 February 1993 several large mesoscale convective systems moved eastward across the Intensive Flux Array (IFA) during the Tropical Oceanic Global Atmosphere Coupled Ocean-Atmosphere Response Experiment (TOGA COARE). One particularly organized storm that formed within range of two Doppler ship radars reached a maximum area of surface rainfall in excess of 10,000 km^2. Reflectivity and Doppler-velocity data of this system were obtained from initiation through early-dissipating stages of development. Preliminary results described herein will compare observed and simulated reflectivities near the time of maximum storm intensity. Dynamical and microphysical characteristics in the convective and stratiform components of the system will be summarized, and some key parameters in the microphysical schemes will be investigated.

2. RADAR OBSERVATIONS

A small, disorganized band of shallow cells was observed 100 km southwest of the TOGA radar at 0701 UTC. Several more bands oriented NNW-SSE developed as they moved to the ENE, such that a series of five parallel bands formed in the vicinity of the ship radars by 1200 UTC. Second-order merging of these bands commenced shortly thereafter (Simpson et al., 1980), and by 1340 UTC the MCS was near maximum intensity with a large area of trailing stratiform rainfall (Fig. 1). The system continued moving to the ENE by cell translation and by the formation of new convective elements to the east and southeast. The southern end of the line moved eastward more rapidly than the northern portion, resulting in a gradual rotation to a NW-SE orientation by 1400 UTC. The leading convection moved beyond the maximum range of the MIT radar after 1600 UTC, leaving behind a large area of stratiform rainfall that was observed until it also moved out of range by 1900 UTC.

The vertical cross section in Fig. 2 shows peak reflectivities of 52 dBZ near the MIT radar. Maximum echo tops defined by the 0 dBZ contour reach 15 km, and are located approximately 20 km to the rear of the leading edge of surface rainfall. Although the upper-level reflectivities are truncated in this plot, cross sections in this portion of the storm and at earlier times suggest that the 10-dBZ echo tops reached a typical maximum height of 10 to 11 km. Farther north in an area of intense surface rainfall (near the tail of the storm motion arrow in Fig. 1), 10-dBZ echoes extended above 14 km. The convective cores in the east-west plane of Fig. 2 appear to be erect or tilted slightly downshear with respect to the low-level wind (Fig. 3b). An area of

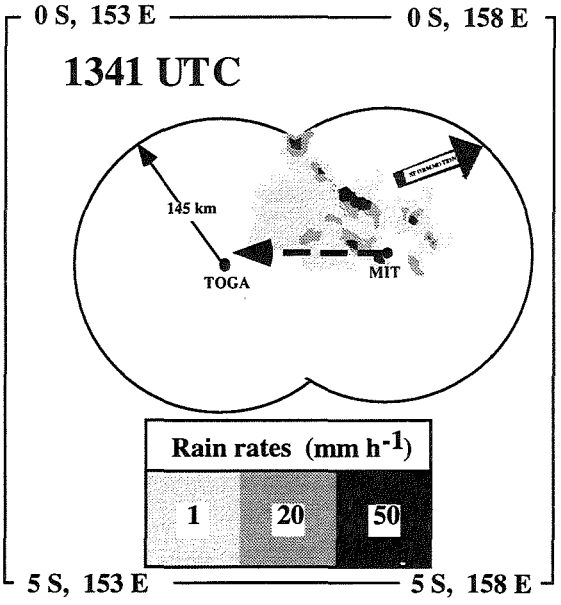

Fig. 1. Surface rain map from the ship radars over the COARE IFA at 1341 UTC. Maximum range in which rainfall estimates were obtained is 145 km. Broken arrow shows the location of the cross section in Fig. 2.

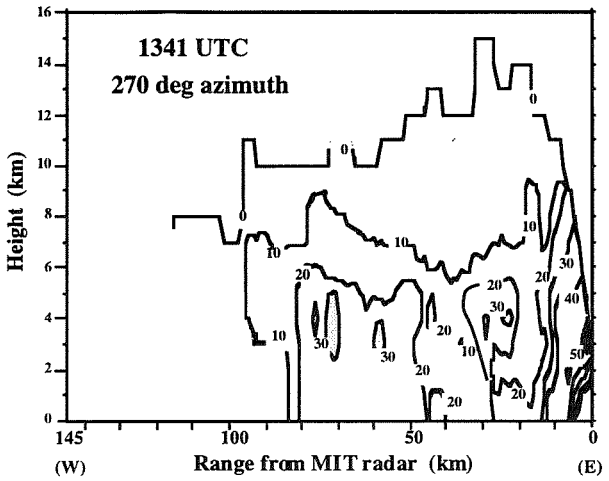

Fig. 2 Vertical cross section of reflectivity at 270 degrees azimuth reconstructed from a MIT radar volume scan at 1341 UTC. Reflectivities beyond 100 km were removed in order to focus on the particular storm of interest.

enhanced reflectivity located below the area of maximum echo top is likely a dissipating convective cell. Further rearward is a 35-km wide area of stratiform precipitation. The reflectivities above 6 km height are below 20 dBZ throughout the system, except in the narrow, leading convective line..

3. MODEL SIMULATIONS

Eight-hour simulations were performed using the two-dimensional (2D), anelastic version of the Goddard Cumulus Ensemble (GCE) model with open lateral boundary conditions (Tao and Simpson, 1993). The domain consists of 912 horizontal and 31 vertical grid points. A constant horizontal grid spacing of 500 m in the innermost 804 grid points is nested within a coarser, horizontally-stretched region (ratio between adjacent grid points is 1.05 to 1), resulting in a domain that is 674 km wide. The vertical coordinate is stretched with the grid spacing varying from 305 m near the surface to 1202 m at the top of the 23.7-km deep domain. A Rayleigh absorption layer is applied above 18 km to damp vertically propagating gravity waves reflected off of the upper boundary.

Dependent variables include horizontal and vertical velocities, potential temperature, perturbation pressure, and the mixing ratios of water vapor, small, non-precipitating cloud droplets (cloud water, q_w) and cloud ice (q_i), and precipitation in the form of rain (q_r), low-density snow (q_s, 0.1 g cm^{-3}), and moderate-density graupel (q_g, 0.4 g cm^{-3}). The microphysical schemes of Rutledge and Hobbs (1984, hereafter RH) and Lin et al. (1983, hereafter LFO) were both used in combination with the saturation adjustment scheme of Tao et al. (1989). A modified version of LFO is used, in which the parameterized density, size distribution, and fall speed of graupel in RH are substituted for the original parameters that more resemble hail in LFO.

The input sounding used to initialize the model is shown in Fig. 3. Thermodynamic conditions at 1100 UTC were obtained from the Shiyan ship #3 at the eastern edge of the IFA, whereas the 1100 UTC winds from Kavieng at the western end of the IFA were used. This is because the large-scale lifting and ambient instability was greater to the east, which is also the environment in which the system moved into as it matured (Fig. 1), whereas the shear in the lowest 1 km was much stronger in the Kavieng sounding. Storm-relative winds for the February 11 environment in Fig. 3b were obtained by subtracting a storm propagation speed of 12.5 m s^{-1} moving to the ENE at 75 degrees. The very strong rearward flow above 9 km distinguishes this case from other tropical systems simulated in the GCE model, including squall lines on 22 February 1993 in COARE (Wang et al., 1996), GATE (Ferrier et al., 1995; note that the actual winds are reversed from those displayed in the figure), and EMEX (Tao et al., 1993). Although the easterlies in the Shiyan sounding are 5-10 m s^{-1} weaker between 13 and 15 km altitude (not shown), the ambient front-to-rear relative flow is still quite considerable at upper levels no matter what sounding in the IFA was selected.

Given the complex development and evolution of the system, a series of model runs were made in which the vertical plane of the 2D model was varied from an E-W orientation (towards 90 degrees) to a SW-NE (towards 37.5 degrees). Model-initialized winds were calculated based on a projection of the environmental three-dimensional shear upon each of the rotated planes (e.g., the winds in Fig. 3b are for the model plane oriented towards 75 degrees). Differences in simulated storm structure were dramatic, supporting the inherently three-dimensional character of the observed storm. Updrafts were strongly tilted against the low-level shear (upshear, or towards the west with height) and developed a broad area of trailing stratiform precipitation when the model plane was aligned in an east-west direction. In contrast, the updrafts were erect and the formation of trailing stratiform rainfall was delayed as the plane of the model rotated towards the northeast. The simulated convection eventually tilted downshear (in the same direction as the low-level shear, or towards the east with height) and weakened considerably at larger rotation angles. The results of these model experiments are described in more detail in Halverson et al. (1996).

The simulated reflectivities at 4 h into the model run using the RH microphysics (Fig. 4a) shows a leading line of intense convection trailed by a broad area of stratiform rainfall, in qualitative agreement with the observations. In the leading convective line, maximum reflectivities exceed 50 dBZ below 4 km and 40 dBZ echoes reach 6 km, which is also consistent with the observations. These echoes are associated with large mixing ratios of rain below 5 km and graupel at higher levels (Fig. 4b). Echo-top heights in the convective region, however, are much lower than observed (0 dBZ was not plotted in Fig. 4a because it was close to the 10 dBZ contour). Deep penetration of radar echoes in the model run occurred 50 and 100 km rearward of the leading line. Simulated reflectivities between 6 and 8

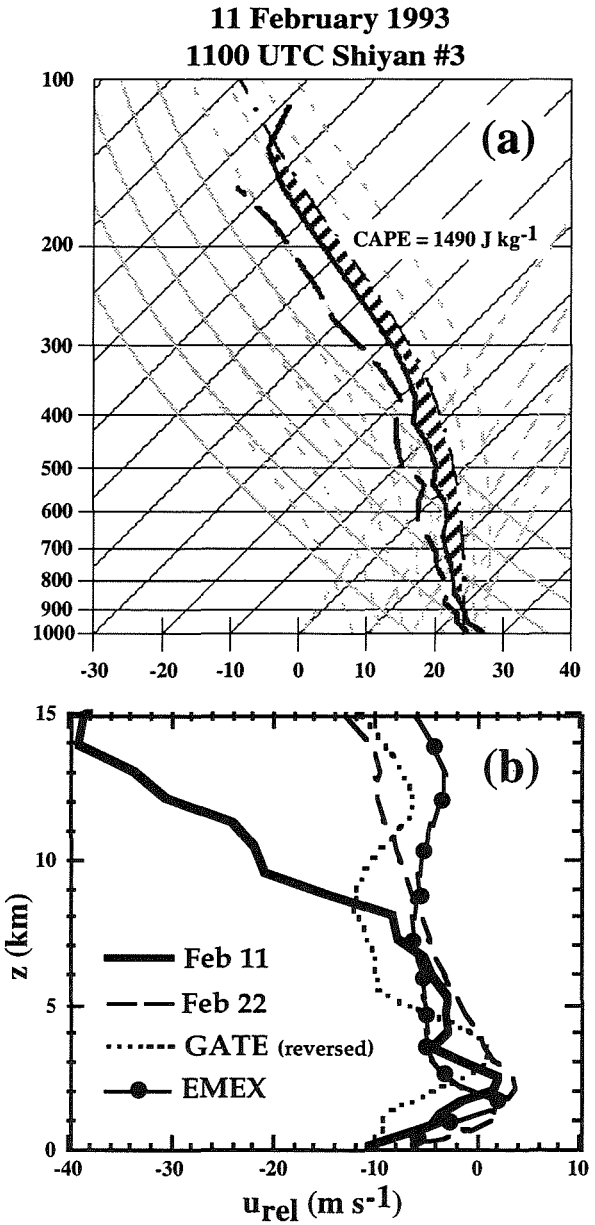

Fig. 3. Input (a) thermodynamic and (b) storm-relative winds (Feb 11 curve) used to initialize the model. The Convective Available Potential Energy (CAPE), which is denoted by the hatched area in (a), was calculated for an assumed mixed-layer depth of 500 m and was closely approximated by the θ_e=354 K isentrope.

km in the stratiform region are higher than observed by as much as 10 dBZ. This is also supported by cross sections from the TOGA radar viewing the stratiform region from the rear, suggesting that attenuation by hydrometeors did not substantially lower the MIT reflectivities. Graupel is prevalent below 7 km, even in the rearward portion of the stratiform rain area far removed from the deep convective cells, where isolated pockets of higher graupel contents melt to produce small shafts of heavier rainfall (Fig. 4b). Riming was the dominant source of graupel growth, as small amounts of cloud water spanned the entire system below 8 km and extended over a deeper layer in the stratiform region (Fig. 4c). Collection of snow was also an important source of graupel, especially above 8 km.

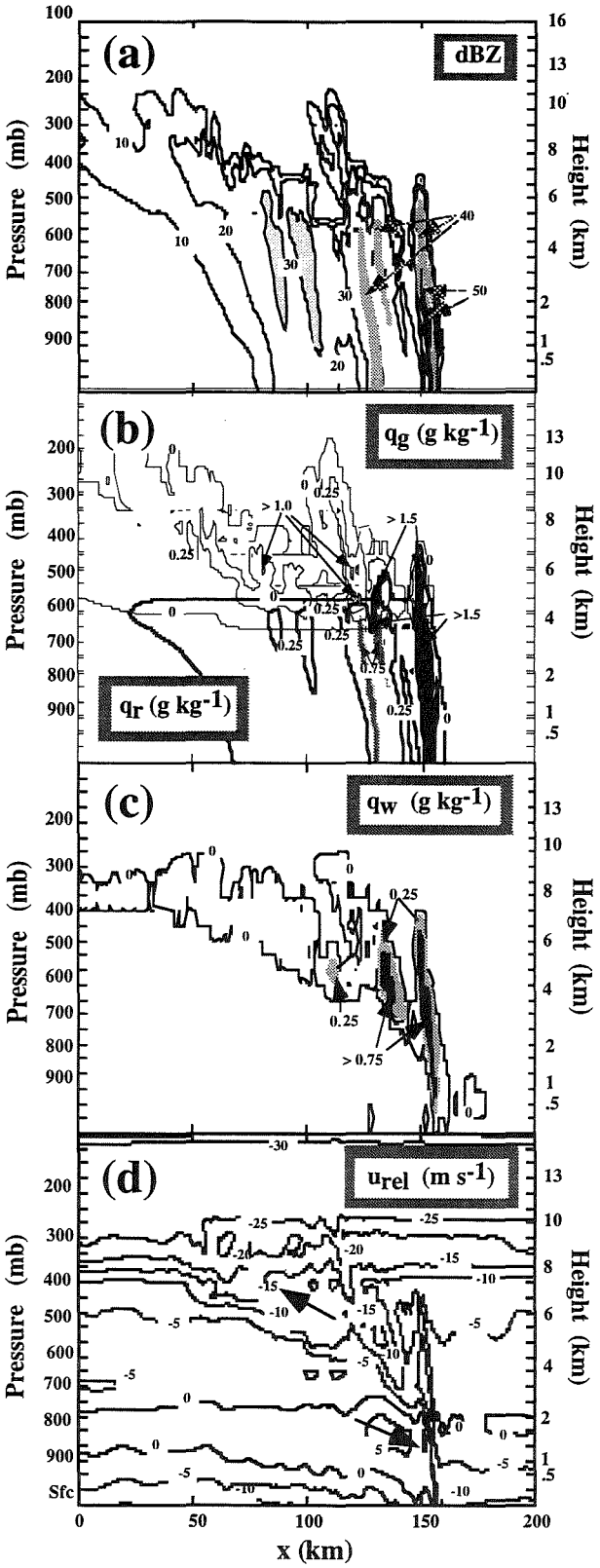

Fig. 4. (a) Reflectivity (dBZ), (b) mixing ratios of graupel (q_g, g kg^{-1}; light contours) and rain (q_r, g kg^{-1}; dark contours), (c) cloud water mixing ratios (q_w, g kg^{-1}), and (d) storm-relative winds (u_{rel}, m s^{-1}) at 4 h in the simulation. A 200-km wide portion of the domain is shown. Light and dark shading highlight areas of high reflectivities in (a) and large hydrometeor mixing ratios in (b) and (c).

System-relative winds in Fig. 4d show substantial front-to-rear flow originating from the leading convective region and ascending rearward throughout the stratiform region. Most of the cloud condensation and subsequent riming onto graupel occurred within this this highly sloped flow. However, Doppler velocities from the MIT radar for the cross section in Fig. 2 suggest that the convection may be more erect than simulated here. System relative winds of -10 to -15 m s^{-1} behind the leading convection between 6 and 8 km altitude in Fig. 4d are stronger than observed by 5-10 m s^{-1}. Although better agreement with the observed Doppler winds is expected in the runs where the model plane is oriented more towards the northeast (Halverson et al., 1996), more work is needed to address this issue. The authors also acknowledge that 2D simulations will not adequately capture all of the salient dynamical processes associated with the three-dimensional structure of this complex convective system.

A series of sensitivity experiments were conducted using the RH and modified LFO schemes, in which ice collection efficiencies were reduced by an order of magnitude, and the parameterized fall speeds and number concentrations of graupel were modified to resemble small hail. The authors realized while formulating these experiments that *sublimation of graupel is not considered in LFO, while sublimation of snow and graupel is also not accounted for in RH.* Additional runs were made that included these processes in the respective ice schemes. Total amounts of ice crystals, snow, and graupel varied between runs, resulting in some differences between stratiform radar structures. Reflectivity profiles in the convective regions, however, were quite similar. Microphysical and diabatic heating budgets revealed the following.

(i) Ice-phase processes were insignificant compared to condensation and coalescence processes in the convective region, in which nearly all of the heating was concentrated below 6 km. By 4h in the run, only the leading 10 km of the surface rain area was classified as convective by the partitioning method (Tao et al., 1993).

(ii) Condensation and evaporation of cloud water remained the dominant processes in the stratiform region. The transition with temperature from condensation and evaporation of cloud water being dominant to deposition and sublimation of cloud ice always occurred between -17 and -20°C (8-9 km height) in the convective, stratiform, *and* non-raining anvil regions. This suggests that the saturation adjustment scheme of Tao et al. (1989) is playing a dominant role in the simulated microphysics of this storm. Deposition and sublimation of snow and graupel were of second-order importance.

(iii) Graupel was dominant in the lower portion of the stratiform region, even in the modified LFO scheme where the autoconversion of snow to graupel is not allowed (see Ferrier et al., 1995). The only way that graupel is *initiated* in this scheme is by the freezing of rain drops. Small amounts of graupel were advected rearward by the strong winds aloft, and grew by collection of cloud ice, snow, and cloud water as it descended through the main portion of the stratiform region.

Simulations using the 4ICE scheme (Ferrier, 1994) will also be presented at the Conference. Future studies will compare two- and three-dimensional model simulations of this system with estimates of convective and stratiform rainfall from surface maps, profiles of heating (Q_1) and drying (Q_2) from the sounding array, and temporal and spatial evolution of storm reflectivity structure.

4. ACKNOWLEDGMENTS

The authors are grateful to Dr. Ramesh Kakar (NASA Headquarters) for providing financial support of this research, Mr. Paul Kucera (ARC) for providing the surface rain fields, and Mr. David Marks (St. Louis University) for assisting with processing the radar cross sections.

5. REFERENCES

Ferrier, B. S., 1994: A double-moment multiple-phase four-class bulk ice scheme. Part I: Description. *J. Atmos. Sci.*, **51**, 249-280.

-----, W.-K. Tao, and J. Simpson, 1995: A double-moment multiple-phase four-class bulk ice scheme. Part II: Simulations of convective storms in different large-scale environments and comparisons with other bulk parameterizations. *J. Atmos. Sci.*, **52**, 1001-1033.

Halverson, J., B. Ferrier, J. Simpson, and W.-K. Tao, 1996: Two-dimensional numerical modeling investigations of the February 11, 1993 TOGA COARE mesoscale convective system. 7th Conf. on Mesoscale Processes, Amer. Meteor. Soc., Reading, United Kingdom.

Lin, Y.-L., R. D. Farley, and H. D. Orville, 1983: Bulk parameterization of the snow field in a cloud model. *J. Climate Appl. Meteor.*, **22**, 1065-1092.

Rutledge, S. A., and P. V. Hobbs, 1984: The mesoscale and microscale structure and organization of clouds and precipitation in midlatitude cyclones. Part XII: A diagnostic modeling study of precipitation development in narrow cold-frontal rainbands. *J. Atmos. Sci.*, **41**, 2949-2971.

Simpson, J., N. E. Westcott, R. J. Clerman, and R. A. Pielke, 1980: On cumulus mergers. *Arch. Met. Geoph. Biocl. Ser. A.*, **29**, 1-40.

Simpson, J., R. F. Adler, and G. B. North, 1988: A proposed tropical rainfall measuring mission (TRMM) satellite. *Bull. Amer. Meteor. Soc.*, **69**, 278-295.

Tao, W-K., and J. Simpson, 1993: The Goddard Cumulus Ensemble model. Part I: Model description. *Terrestrial, Atmospheric and Oceanic Sciences*, **4**, 35-72.

-----, -----, and M. McCumber, 1989: An ice-water saturation adjustment. *Mon. Wea. Rev.*, **117**, 231-235.

-----, -----, C.-H. Sui, B. Ferrier, S. Lang, J. Scala, M-D. Chou, and K. Pickering, 1993: Heating, moisture, and water budgets of tropical and midlatitude squall lines: Comparisons and sensitivity to longwave radiation. *J. Atmos. Sci.*, **50**, 673-690.

Wang, Y., W.-K. Tao, and J. Simpson, 1996: The impact of ocean surface fluxes on a TOGA COARE convective system. *Mon Wea. Rev.* (in revision).

CLOUD–RESOLVING MODELING OF TROPICAL CLOUD SYSTEMS AND ITS APPLICATION TO THE CLOUD–CLIMATE INTERACTIONS

Wojciech W. Grabowski, Xiaoqing Wu and Mitchell W. Moncrieff

NCAR, Boulder, CO 80307, USA

1. INTRODUCTION

Representation of deep convection in large–scale models is one of the most challenging problems of weather forecasting and climate research. The concept of *a cloud system* captures the essence of this problem. In this concept, the collective effects of populations of cloud elements, their interaction with the surface fluxes, boundary layer, radiation, microphysics and turbulence, and their effects on the large–scale flow are all considered. Unfortunately, physical processes within cloud systems are usually associated with spatial scales too small to be resolved in numerical weather prediction (NWP) models and general circulation models (GCMs). It follows that the effects of these subgrid–scale processes on the large–scale circulations have to be parameterized.

Cloud models have been long recognized as a valuable aid in developing and testing cumulus parameterization schemes, especially in the context of the so called cloud–resolving modeling (or cumulus ensemble modeling, see brief discussion in Grabowski et al. 1996). In the cloud resolving modeling (CRM) approach, the emphasis is on the collective effects of clouds and cloud systems in response to the large–scale (i.e., at least several hundred kilometers) conditions. In addition, the CRM approach stresses the long–term effects of clouds in the large–scale dynamics, i.e., on time scales of weeks rather than hours. The effect of large scales in the CRM is usually represented in a very simplified way, namely by imposing these effects homogeneously in the horizontal direction across the domain. The conceptual picture behind this approach is that the large–scale dynamics provides thermodynamic destabilization needed for development and maintenance of convection (mostly through the large–scale ascent), and it also controls the large–scale wind shear essential for convection organization. The destabilization effect is commonly referred to as the large–scale forcing; it is associated with the temperature sink and moisture source that provide energy to the convection (e.g., due to a few cm/sec large–scale ascent). The horizontal winds are taken to represent the large–scale flow over the same area. The horizontal domain is assumed periodic in the horizontal direction and it has to be large enough to accommodate many clouds and descending motions between them (i.e., the horizontal extent should be comparable to the Rossby radius of deformation, $\sim$ 1000 km). The CRM approach is consistent with the assumption that model produced cloud fields represent effects of clouds as seen from the area comparable with a single box of a GCM.

2. SIMULATED CLOUD SYSTEMS

The novel feature of our approach is that *evolving* large–scale forcing terms and *evolving* horizontal wind field are used to drive the cloud model (cf. Grabowski et al. 1996). These fields are derived from datasets obtained in extensive observational campaigns in the tropics, namely the GARP (Global Atmospheric Research Programme) Atlantic Tropical Experiment (GATE) and the Tropical Ocean Global Atmosphere Coupled Ocean Atmosphere Response Experiment (TOGA COARE). Observed sea surface temperature (SST) is used to calculate surface fluxes. We present selected results from numerical simulations of tropical cloud systems in a 7–day period during Phase III of GATE (1–7 September 1974), and in a 39–day period (December 5, 1992 through January 12, 1993) during TOGA COARE. These two periods provide a variety of environmental conditions that lead to the development of cloud systems which include scattered convection and nonsquall clusters, as well as shear–parallel and shear–perpendicular squall clusters. Both 2D and 3D frameworks have been applied to the GATE case, whereas only 2D framework have been applied so far in the TOGA case.

The dynamical model is the Clark's anelastic cloud model (Clark 1977, 1979, Clark and Hall 1991, Bru-

intjes et al. 1994) which applies bulk thermodynamic approximations with 2 classes of ice, bulk aerodynamic formulation for the surface fluxes, and the Smagorinsky–type parameterization of the subgrid–scale turbulent transport. Stretched vertical coordinates (100 m vertical resolution near the surface increasing to $\sim$ 1000 m in the upper troposphere and in the stratosphere) is applied. The large–scale forcing terms are added to the temperature and moisture conservation equations, whereas evolving large–scale horizontal winds are matched through the relaxation procedure (see Grabowski et al. 1996 for details). The cloud model is combined with the Community Climate Model 2 (CCM2) radiation scheme (Kiehl et al., 1994).

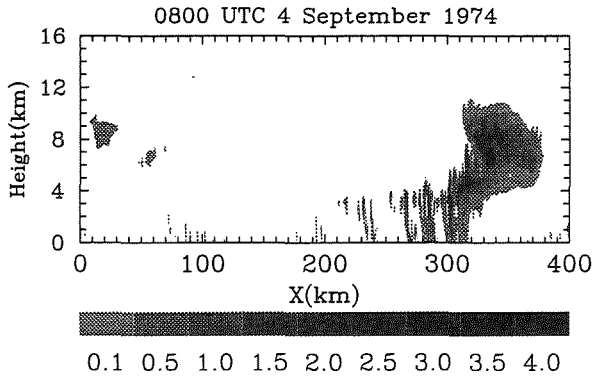

Figure 1: Total condensate field (g/kg) for the high resolution 2D simulation at 0800 UTC on September 4th, 1974.

The 7–day period of the GATE case is characterized by the distinct evolution of cloud systems in response to changing large–scale advective tendencies and low–level wind shear associated with easterly wave activity. Nonsquall cloud clusters, a squall line (or squall cluster) and scattered convection were all observed during this period. Both 2D and 3D simulations were performed for this case (Grabowski et al. 1996, Wu et al. 1996a). Several 2D experiments were performed in which x–axis was aligned with the west–east line in the two–dimensional $x - z$ frame. They applied different resolutions, both in the vertical and in the horizontal directions. The horizontal resolution varied from 200 m to 3 km, and number of levels in the vertical varied from 42 to 102. Horizontal domain size varied from 400 km to 1000 km. The 3D experiment applied horizontal domain of 400 km $\times$ 400 km with 2 km resolution and used 42 levels in the vertical. The objectively–analyzed GATE Phase III dataset (9 $\times$ 9 horizontal array with 1° resolution, 20 vertical levels and 3–hr temporal resolution) was used to calculate large–scale environmental fields (horizontal winds and large–scale advective tendencies of temperature and moisture).

Only 2D simulations have so far been performed for the 39–day period (from December 5, 1992 to

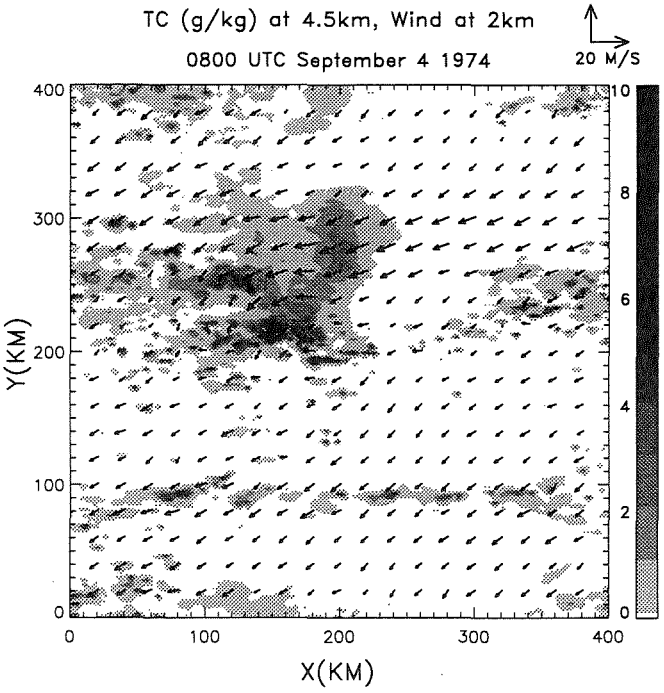

Figure 2: Horizontal cross section of the total condensate field (g/kg) at 4.5 km superimposed on the 2–km wind vectors at 0800 UTC on September 4th, 1974 as predicted by the 3D cloud model

January 12, 1993) during the TOGA COARE (Wu et al. 1996b). The period includes a major westerly wind burst episode during which the warm–pool SST (as measured over the Intensive Flux Array) decreased by almost 2°C. The emphasis of this study is on the interactions between cloud dynamics and microphysics with radiative and surface processes. Horizontal resolution of 3 km was applied in this study and the computational domain was 900 km. Data to drive the cloud model was provided by the CSU group (cf. Lin and Johnson 1996).

3. EXAMPLES OF RESULTS

Figures 1 and 2 show examples of model results from 2D and 3D experiments, respectively, using the GATE setup. The figures show snapshots of the total condensate field (a sum of cloud water, rainwater and ice mixing ratios) for the same time of 0800 UTC on September 4th, 1974, i.e., at the time when low–level shear of the large–scale flow allows development of squall–type convection. Radar composites (Arkell and Hudlow, 1977) show several east–west oriented convection lines and a squall line present in the area on that day. The snapshot from the 2D experiment (Fig. 1) shows a characteristic structure of a squall line in the east (i.e., right–hand–side) part of the domain, and several shallower isolated convective clouds. The snapshot from the 3D experiment (Fig. 2) shows very realistic organization of

the cloudiness, with the squall line in the west part of the domain, and several less organized convective clouds. In both figures, the convective and stratiform part of model–produced squall lines can easily be identified.

Detailed analysis of the 7–day GATE 2D simulation (Grabowski et al. 1996) shows the ability of a cloud model forced by the simple technique to include evolving large–scale conditions to simulate transitions from one regime of convection to another as the environmental conditions evolve. To the authors' knowledge, this is the first time such transitions have been simulated using realistic large–scale conditions and compared with observations. In this comparison, the traditional Q_1 and Q_2 budget terms (apparent heat source and apparent moisture sink) and the tropospheric relative humidity profiles were used (see Grabowski et al. 1996 for details). As at the time of writing, the 3D simulation still awaits detailed analysis.

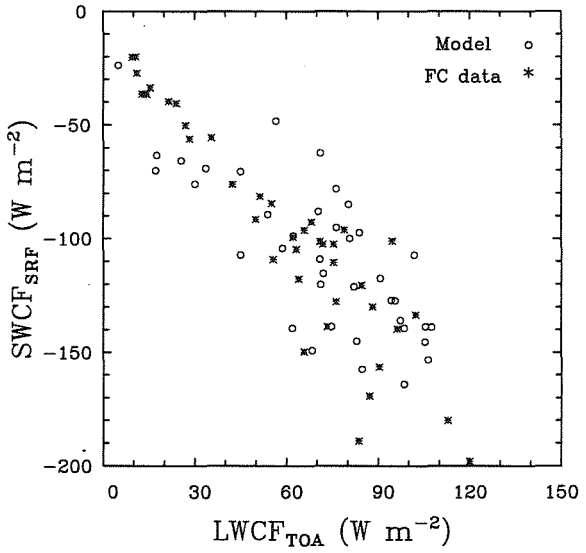

Figure 3: Shortwave cloud forcing at the ocean surface $SWCF_{SRF}$ versus top–of–the–atmosphere longwave cloud forcing $LWCF_{TOA}$ for the 39–day simulation of the TOGA COARE cloud systems (circles) as compared with observations (stars).

Unfortunately, GATE results offer a rather limited amount of data which model results can be compared with. A recent TOGA COARE experiment (November 92–March 93) offers much more comprehensive dataset. Results from the 39–day TOGA COARE simulations were compared with the surface, satellite and shipborne radar data. Surface sensible and latent heat fluxes, surface precipitation, cloud cover, cloud organization, radiative fluxes at the top of the atmosphere and at the surface were all considered in the comparison. In general, very encouraging agreement was found.

From the cloud–climate interaction point of view, the effects of clouds on the atmosphere and on the surface are usually consider in the context of the shortwave and longwave cloud forcings. These forcings describe effects of clouds on the shortwave and longwave radiative fluxes. They are calculated by comparing shortwave and longwave radiative fluxes for cloudy and cloud–free atmospheric columns. The shortwave and longwave cloud forcings at the top of the atmosphere can be derived from satellite measurements. Surface forcings are derived by combining satellite and surface observations. Figure 3 shows a scatterplot of the shortwave cloud forcing at the surface versus longwave cloud forcing at the top of the atmosphere derived from the model–generated data. Data derived from the satellite observations for the same period using the technique described in Rossow and Zhang (1995) and Zhang et al. (1995) are also shown. Every data point in the figure represents the daily averaged forcings. Both model results and observations show surface cooling associated with the increased albedo due to the presence of clouds and corresponding atmospheric warming due to the absorption of the longwave radiation in the cloudy atmosphere (the greenhouse effect). General agreement between the model–produced data and the data derived from satellite observations is apparent.

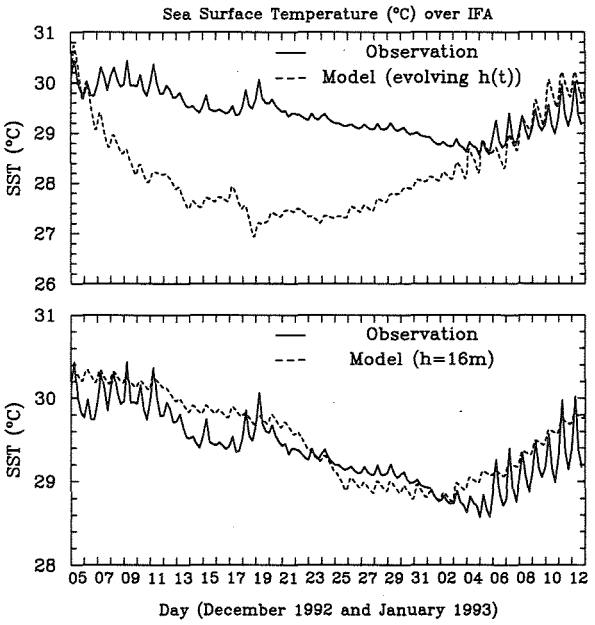

Figure 4: Observed SST applied to drive the cloud model (solid line) and the evolution of the SST based on the surface energy budget (dashed line) using either the observed depth of the oceanic mixed layer (upper panel) or constant depth of 16 m (lower panel). In both cases the initial SST is as at the beginning of model run on December 5th, 1993.

The role of cloud systems associated with the tropical convection on surface energy balance of the

pool region has recently gained attention because of the so–called "thermostat hypothesis" (Ramanathan and Collins 1991). The variations of the assumed SST (used in the cloud model) can be compared with the SST predicted using a simple oceanic mixed layer model which considers only surface heat and radiative fluxes. Figure 4 shows both the observed SST used as input to the model and the SST predicted by the surface heat and radiative fluxes assuming either *observed* mixed layer depth (upper panel) or *constant* oceanic mixed layer depth of 16 m (lower panel). The constant depth is an estimate based on large–scale upper–ocean heat budget (G. Lagerloef, private communication). It is apparent that the observed depth of the mixed layer results in a fairly accurate prediction of the amplitude of the diurnal SST cycle, but the long–term trend is predicted very poorly. Application of the constant depth of the oceanic mixed layer, on the other hand, results in a fairly accurate prediction of the long–term behavior, but the amplitude of the diurnal cycle is strongly underestimated. The inability to predict the long–term behavior of the STT and, concurrently, the amplitude of the diurnal cycle suggests that the simple model for the SST evolution is not sufficient because it does not include key components of the upper ocean heat budget. Both horizontal transport of heat by ocean currents and entrainment of the oceanic deep water are likely significant in the warm pool SST budget. This conclusion also suggests that the "thermostat hypothesis" should be considered in much broader context than the one suggested by Ramanathan and Collins (1991).

Acknowledgments: The data used in this study was provided to us by Richard Johnson and Xin Lin (TOGA COARE IFA soundings and budgets), William Rossow and Yuanchong Zhang (FC data), and Gary Lagerloef (oceanic mixed layer depth data). WWG acknowledges support from NCAR's Clouds and Climate Program. XW acknowledges support from the interagency TOGA grant ATM 9205896. The National Center for Atmospheric Research is sponsored by the National Science Foundation.

REFERENCES

Arkell, R., and M. Hudlow, 1977: *GATE International Meteorological Radar Atlas.* Environmental Data Service, NOAA, 222 pp.

Bruintjes, R. T., T. L. Clark, and W. D. Hall, 1994: Interactions between topographic airflow and cloud/precipitation development during the passage of a winter storm in Arizona. *J. Atmos. Sci.*, **51**, 48–67.

Clark T. L., 1977: A small–scale dynamic model using a terrain following coordinate transformation. *J. Comput. Phys.*, **24**, 186–215.

———, 1979: Numerical simulations with a three–dimensional cloud model: Lateral boundary condition experiments and multicellular severe storm simulations. *J. Atmos. Sci.*, **36**, 2191–2215.

———, and W. D. Hall, 1991: Multi–domain simulations of the time dependent Navier–Stokes equations: Benchmark error analysis of some nesting procedures. *J. Comput. Phys.*, **92**, 456–481.

Grabowski, W. W., X. Wu, and M. W. Moncrieff, 1996: Cloud resolving modeling of tropical cloud systems during Phase III of GATE. Part I: Two–dimensional experiment. *J. Atmos. Sci.* (in press).

Kiehl, J. T., J. J. Hack, and B. P. Briegleb, 1994: The simulated Earth radiation budget of the National Center for Atmospheric Research community climate model CCM2 and comparisons with the Earth Radiation Budget Experiment (ERBE). *J. Geophys. Res.*, , **99**, 20,815–20,827.

Lin X., and R. H. Johnson, 1996: Kinematic and thermodynamic characteristics of the flow over the western pacific warm pool during TOGA COARE. *J. Atmos. Sci.*, (in press).

Ramanathan, V., and W. Collins, 1991: Thermodynamic regulation of ocean warming by cirrus clouds deduced from observations of the 1987 El Nino. *Nature*, **351**, 27–32.

Rossow, W. B., and Y.–C. Zhang, 1995: Calculation of surface and top of atmosphere radiative fluxes from physical quantities based on ISCCP datasets, 2. Validation and first results. *J. Geophys. Res.*, **100**, 1167–1197.

Wu X., W. W. Grabowski, and M. W. Moncrieff, 1996a: Cloud resolving modeling of tropical cloud systems during Phase III of GATE. Part II: Three–dimensional experiment. *J. Atmos. Sci.* (in preparation)

Wu X., W. W. Grabowski, and M. W. Moncrieff, 1996b: Interaction of cloud systems with radiative and surface processes during TOGA COARE. Part I: Two-dimensional cloud resolving modeling. *J. Atmos. Sci.* (in preparation)

Zhang, Y.–C., W. B. Rossow, and A. A. Lacis, 1995: Calculation of surface and top of atmosphere radiative fluxes from physical quantities based on ISCCP datasets, 1. Method and sensitivity to input data uncertainties. *J. Geophys. Res.*, **100**, 1149–1165.

ICE DEVELOPMENT IN CUMULUS CLOUDS: A CASE STUDY USING A 3-D MODEL WITH EXPLICIT ICE AND WARM RAIN MICROPHYSICS

Mikhail Ovtchinnikov[1,2], Yefim L. Kogan[2], and Alan M. Blyth[3]

[1]School of Meteorology and [2]Cooperative Institute for Mesoscale Meteorological Studies, University of Oklahoma
[3]Dept. of Physics and Geophysical Research Center, New Mexico Institute of Mining and Technology

1. INTRODUCTION

The development of ice in cumulus clouds is one of the major outstanding problems in modern cloud physics. There is a great deal of uncertainty in ice nucleus (IN) concentrations as well as in nucleation mechanisms. The determination of a precise nucleation mechanism in each individual case represents a great challenge. The earliest stages of ice formation are not observed with radar. *In-situ* measurements provide more detailed information, but present measuring techniques experience difficulties in resolving small ice crystals. In addition these data are usually incomplete, both spatially and temporally.

The observed concentrations of ice particles (IP), particularly in relatively warm clouds, often exceed even highest values that could possibly be attributed to primary nucleation. This phenomenon is commonly referred to as 'ice multiplication'. Since its first quantitative description by Hallett and Mossop (1974), ice splinter production during riming of ice particles has been considered as a probable explanation for ice multiplication in many cases. The confirmation of this hypothesis, however, is not easy.

Modeling studies represent a useful supplement to observations. Multidimensional models often use bulk formulation of microphysics and highly simplified ice nucleation parameterizations. Lagrangian models with a refined treatment of microphysical processes are unable to reflect the interactions among cloud elements. The goal of this paper it to address the development of ice and precipitation in warm-based cumulus clouds by using a new model which combines three dimensional dynamics, explicit ice and liquid phase microphysics, and a thorough treatment of ice origination processes. The model allows us to investigate the ice nucleation and multiplication processes at a much higher level of sophistication than has been done before. We evaluate the model's performance and investigate ice development based on observations of the evolution of mixed-phase cumulus clouds in New Mexico.

* *Corresponding author address*: Mikhail Ovtchinnikov, CIMMS, University of Oklahoma, 100 E. Boyd, SEC, Rm.1110, Norman, OK 73019, USA
e-mail: movchinn@aardvark.ucs.uoknor.edu

2. NUMERICAL MODEL

The results presented in this paper are obtained using a recently developed three-dimensional cloud scale numerical model (Ovtchinnikov et al., 1995). The model combines non-hydrostatic dynamical framework of Kogan (1991) with explicit formulation of ice and liquid phase microphysics. Two mass distribution functions, containing 28 categories each, are used to describe cloud drops and ice particles. A separate distribution function for cloud condensation nuclei contains 19 size categories. Processes of nucleation, diffusional growth/evaporation, freezing/melting and coalescence are formulated based on the prediction equations for spectra for cloud condensation nuclei, cloud and raindrops, and ice particles. All basic mechanisms of ice nucleation are considered in the model including activation of immersion-freezing, deposition or condensation-freezing, and contact-freezing ice nuclei (IN). Due to computer resource limitations at this point we consider one type of ice particles and assume that the nucleated ice crystals are of plate-like shape. The most important initial diffusional growth occurs in the temperature range -8° to -15°C.

Two major modifications have been introduced to the model for the purpose of this study. The process of secondary ice crystal production during riming of ice particles, known as Hallett-Mossop riming-splintering mechanism (hereafter H-M mechanism) was added to the microphysical part of the model. This mechanism is assumed to be, at least partially, responsible for the production of high concentration of ice in New Mexican clouds (Blyth and Latham, 1993). In addition, special attention was given to the initialization procedure to ensure that the model generates a cloud with realistic geometry and dynamical parameters. Initial perturbations in temperature and moisture fields contained both deterministic and random parts with the scale and intensity of the thermal specified based on boundary layer similarity.

A uniform grid spacing of 100 m was used throughout the domain 7.5 km × 7.5 km × 7.5 km. Coarser resolution of 250 m was implemented in some of the sensitivity tests. A time step of 5 s was used in dynamical calculations while a smaller step of 0.2 s was used in microphysical calculations.

3. CASE STUDY

During August 1987, an extensive experiment involving the NCAR King Air airplane was conducted to investigate the development of cloud particles in New Mexican summertime cumulus clouds. The airplane was fully equipped with cloud physics and standard meteorological equipment, thus providing measurements that allow for a comprehensive comparison between simulated and observed clouds. The detailed information about the field project was reported by Blyth and Latham (1993). We confine our study to simulation of the cloud developed over the Magdalena Mountains on 9 August 1987.

In the present study, one second averages are used for all measured variables. Given the aircraft speed of nearly 100 m s^{-1}, such filtering justifies the comparison with the model data averaged over 100 m grid-point interval. Because measured winds were light and vertical shear was negligible, no-shear and motionless initial state was specified for the simulation. The initial environmental conditions are set by the sounding constructed primarily from aircraft observations in the vicinity of the cloud. A well mixed boundary layer is specified in the lower 1.8 km to account for convective activity that occurred earlier that day (Carpenter et al. 1996).

The general view of the cloud at 20 min is shown in Figure 1. While we cannot expect the simulated and observed clouds to be identical, it is important that the model reproduces closely the observed bulk properties. The comparison of the characteristic features of the simulated and observed clouds is presented in Table 1.

Table 1. Simulated vs. observed cloud properties

	Observed	Simulated
Cloud base alt. (km)	1.7	1.8
Cloud base temp. (°C)	7.4	7.3
Max. cloud-top alt. (km)	5.7*	5.6
Min. cloud-top temp. (°C)	-15*	-13.8
Max. cloud width (km)	4.5	4.1
Max. vert. vel. (m s^{-1})	11.5	13.0
Min. vert. vel. (m s^{-1})	-6.0	-5.5
Max. LWC (g m^{-3})	2.5	4.2
Max. cloud drop concentration (cm^{-3})	597	709
Max. ice particle concentration (L^{-1})	38	136

*estimate

The simulated cloud-top and cloud base heights and the maximum cloud width closely match the observations. The somewhat large difference in maximum values of LWC might be expected taking into account the incomplete sampling of the cloud by the aircraft. The aircraft was likely to miss regions of least diluted cloud-base air. In addition, there was no sampling of the upper portion of the cloud with the highest penetration at the level of about 4.3 km, or more than 1 km below cloud top. For the same reason of scarcity of observations it should be expected for the model data to have greater values of the vertical velocity, concentrations of cloud drops and ice particles, etc.

4. ICE INITIATION

The time evolution of maximum ice crystal concentration reveals two distinct stages of ice production, each dominated by a different process. First increase in the number of IPs is due to the activation of ice nucleus, while the second much stronger peak is a result of the H-M mechanism (Fig. 2).

4.1 Primary ice particle nucleation

Among the three ice nucleation mechanisms, considered in the model in the present simulation, the deposition or condensation-freezing mode is the most efficient. Following Meyers et al. (1992), the number of active deposition nuclei, N_{dn} (L^{-1}), is parameterized as:

$$N_{dn} = \exp(-0.639 + 0.1296\, S_i) \quad (1)$$

where S_i (%) is the ice supersaturation. This formulation predicts about four pristine ice crystals per liter due to deposition-condensation freezing at -15°C and water saturation condition. Nucleation is prevented for temperatures warmer than -5°C.

At 15 min. into the simulation, as the cloud top ascends to its highest level, the maximum IP concentration reaches the value of about 4 L^{-1} (Fig. 2, solid curve). After that the nucleation of new ice crystals weakens due to the decreasing updraft and subsequent decrease in supersaturation. The next stage of cloud evolution is very important in ice development, even though the maximum IP concentration remains nearly constant, or even slightly decreases during this period. After the small pristine ice crystals are formed they begin to grow, mostly through deposition of water vapor. Because of the small sedimentation velocity, these particles are carried along with the flow from the region of their formation in the upper portion of the cloud towards the cloud edges. Downdrafts therefore play a crucial role in transporting IPs to the regions where they will grow by riming and may ignite H-M process.

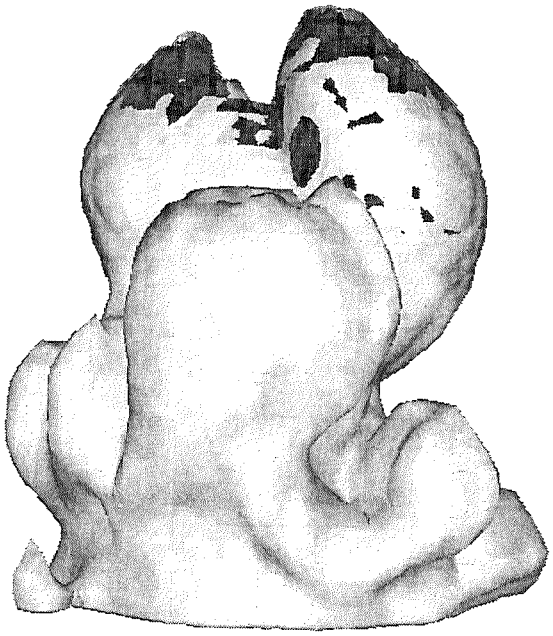

Figure 1. Isosurfaces of liquid water content (0.1 g m^{-3}) and ice crystal concentration (1 L^{-1}) at 20 min. Cloud base is at 1.8 km and cloud top is at 5.4 km

In assessing the results of the simulation, it is essential to evaluate the model's sensitivity to various parameters and parameterizations used. This becomes increasingly important when the model includes a parameterization with a large degree of uncertainty, as the one for primary-ice nucleation. To test the model sensitivity to the nucleation mechanism we rerun the model without the deposition nucleation. The concentration of contact nuclei is kept the same in both cases and given by (Meyers et al., 1992):

$$Ncn = \exp\{ -2.80 + 0.26296 (273.15 - T)\}, \quad (2)$$

Figure 2 indicates that the concentration of primary ice crystals is reduced by a factor of 10^3. Due to the H-M process there is a sharp increase in the IP production rate at about 25 min. As a result the difference in the IP concentrations at the end of the runs is small.

4.2 Secondary ice particle production

Secondary ice splinters are produced when IPs grow by riming. Hallett and Mossop (1974) found that this phenomenon occurs under a narrow range of conditions. Despite the fact that the H-M mechanism has been known for more than twenty years, only rather crude estimates of its efficiency have been made to date. This process strongly depends upon the spectra of ice and liquid cloud particles that are highly variable in space and time. The unique feature of the presented model is that the rime rate is directly calculated by solving the stochastic collection equation for drops and ice particles with size distributions that are explicitly predicted in the model.

In the model the conditions for secondary IP production are set as follows. In the temperature range -3° to -8°C, 500 splinters are produced per milligram of rime counting only accreted drops with diameter greater than 24 μm. Once the conditions are met, the H-M mechanism begins leading to an exponential growth in crystal concentration. Within 15 min after the start of primary nucleation, the right conditions are developed outside the main updraft core. One notable model result is that H-M mechanism operates very locally. Initially the size of the regions with largely enhanced IP concentrations does not exceed 300 to 500 m (Fig.3).

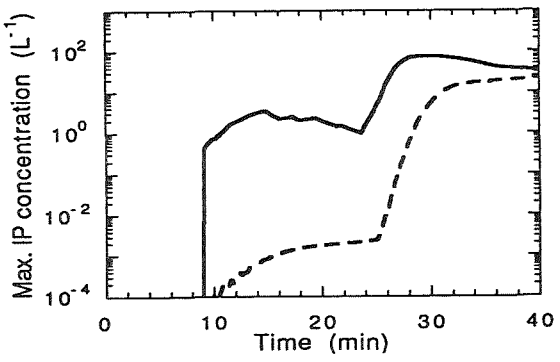

Figure 2. Time series of predicted maximum (over the entire domain) of IP concentration for the basic experiment (solid) and for the experiment without the deposition nucleation (dashed).

The process can be triggered at several locations simultaneously or within a small time difference, however, all these regions still occupy only few percent of the total cloud volume. In each of these places, the H-M mechanism operates for a few minutes. The entire multiplication process in the cloud takes no more than 10 to 15 minutes. This represents another interesting feature of the simulation, namely, that the predicted ice splinter production rate can be very high. At certain locations, the ice particle concentration may increase by an order of magnitude in less than three minutes (Fig.2). This rate, however, may be overestimated in the model because of the use of a constant maximum splinter production rate in the entire temperature range -3° to -8°C when, in fact, it is valid only at around -5°C and decreases toward the ends of the temperature interval. In the described simulation we also neglected the effect of the impact velocity on the splinter production rate.

Figure 2 shows that, when contact nucleation is the only significant source of primary ice (the effect of immersion freezing nucleation is negligible in both cases), much lower initial concentrations of IPs are still able to start the H-M process and produce significant IP concentrations after 40min. It seems, therefore, that particles originated via contact nucleation are more likely to become centers for rime-splintering production. This may be related to the difference in locations in the cloud where these mechanisms operate, as well as to the fact that contact nucleation may freeze drops already grown to larger sizes.

4.3 Comparison with observations

When comparing observations with the model one should keep in mind that the observed cloud system went through several cycles of growth and decay. There were times when more than one turret was rising from the same cloud, as well as when new turrets ascended through the remains of their predecessors. Altogether, the cloud system persisted for several hours. The active

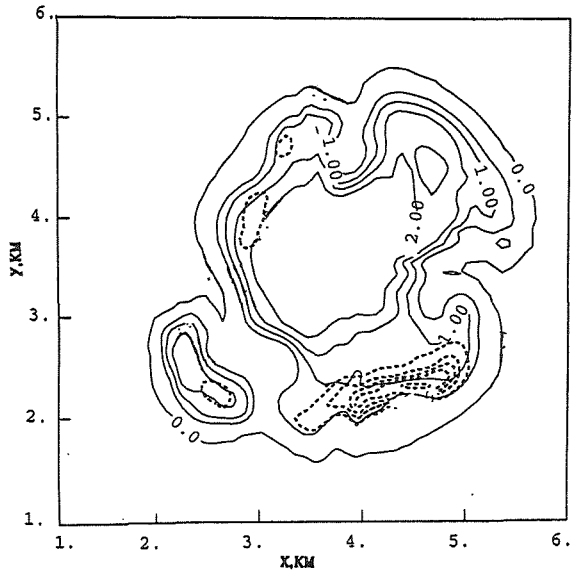

Figure 3. Horizontal cross section of LWC at 0.5 gm^{-3} interval (solid) and IP concentration at 5 L^{-1} interval (dashed) at 25 min. The level is 4 km and the temperature is around -5 °C.

stage of the simulated cloud, on the other hand, lasted only for about 40 min. This agrees well with the lifetime of each individual turret. Furthermore, most observed turrets had only one well defined updraft region with downdrafts at cloud sides, thus supporting the hypothesis of a thermal like circulation. The present study, therefore, can be viewed as a simulation of the most vigorous turret that leads to intense ice production. The effect of the debris of earlier clouds on microphysics of their successors may also be quite important and needs further investigation in a separate study.

One of the repeatedly observed features in New Mexican cumulus clouds was the detection of first IPs in downdrafts while nucleation did not appear to occur preferentially in these regions. In the simulation described here, the nucleation rate is greater when the supersaturation over the ice is large. Since the predicted water vapor pressure within the cloud deviates very little from its saturated value over the liquid water, this means that the nucleation rate increases with decreasing temperature or increasing height. However, the temperature dependence in Eq.1 (through S_i) is rather weak. This results in fairly uniform distribution of newly nucleated IPs throughout the upper portion of the cloud. Still, the initial size of nucleated ice crystals is only 8 μm in the model and probably even smaller in reality. This together with relatively low concentrations (1 L^{-1} or less) suggests that these particles most likely would not be detected with existing instrumentation.

As the ice crystals continue to grow, at this stage mostly by diffusion, they are redistributed within the cloud volume. Figure 4 clearly shows that, although maximum values of the total concentration of ice crystals are very similar for grid points with positive and negative vertical velocities, there are many more larger and, therefore, more easily detectable IPs in downdrafts than in updrafts.

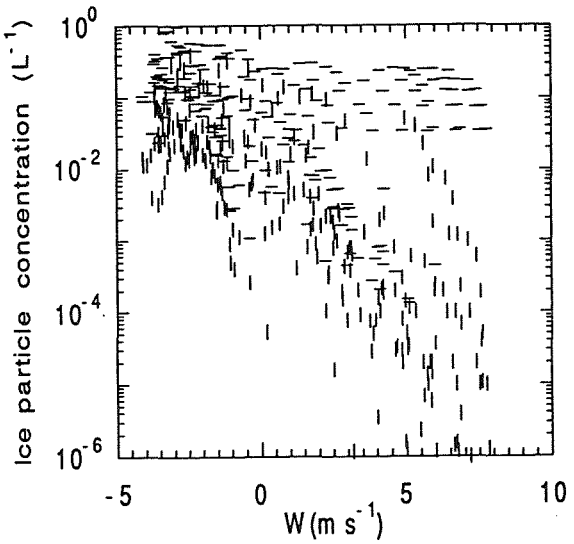

Figure 4. Predicted concentration of ice particles with the equivalent drop diameter smaller (--) and larger (l) than 100 μm versus vertical velocity, W, at a time prior to the start of secondary IP production. Gridpoints are selected in the temperature range -2 ° to -8 °C from a vertical cross section through the center of the domain.

5. CONCLUSIONS

The model reproduces well the observed cloud in terms of cloud geometry, liquid water content, and concentrations of cloud drops and ice particles. Under simulated conditions, the H-M process is shown to be able to produce ice crystals in concentrations of order 100 L^{-1} in about 10 minutes. Comparison with the observations suggests that the secondary ice crystal production is indeed the most likely explanation for the large ice particle concentrations found in small New Mexican summertime cumulus. The revealed extreme inhomogeneity in concentration of secondary ice crystals within the simulated cloud suggests that the current sampling techniques may not be adequate to determine the production rate of this mechanism.

Model sensitivity study is now underway. Preliminary results show that the efficiency of the H-M mechanism depends strongly on the liquid phase microphysics. Several sensitivity tests are also made in order to evaluate the relative importance of various primary-ice nucleation mechanisms. It appears that the H-M mechanism is more susceptible to changes in contact-freezing than deposition/condensation-freezing ice nucleation. These results will be presented at the conference.

6. ACKNOWLEDGEMENTS

This research was supported by NOAA's Climate and Global Change Program under the Grant NA37RJ0203, by the NASA Earth Science and Applications Division, Radiation Dynamics and Hydrology Branch, through Task 460-23-54-20, by the Environmental Sciences Division of the U.S. Department of Energy (through Battelle PNL Contract 144880-A-Q1 to the CIMMS) as part of the Atmospheric Radiation Measurement Program, and by the NSF under the grants ATM-8914116 and ATM-9115694.

7. REFERENCES

Blyth, A. M. and J. Latham, 1993: Development of ice and precipitation in New Mexican summertime cumulus clouds. *Quart. J. Roy. Meteor. Soc.*, **119**, 91-120.

Carpenter, R.L., K.K. Droegemeier, and A.M. Blyth, 1996: Entrainment and detrainment in numerically simulated cumulus congestus clouds. Part I: Model initialization, general results, and comparison with observations. Submitted to *JAS*.

Cotton, W. R., G. J. Tripoli, R. M. Rauber and E. A. Mulvihill, 1986: Numerical simulation of the effect of varying ice crystal nucleation rates and aggregation processes on orographic snow-fall, *J. Climate Appl. Meteor.*, **11**, 1658-1680.

Hallett, J., and S. C. Mossop, 1974: Production of secondary ice crystals during the riming process. *Nature*, **249**, 26-28.

Kogan, Y. L., 1991: The simulation of a convective cloud in a 3-D model with explicit microphysics. Part I: Model description and sensitivity experiments. *J. Atmos. Sci.*, **48**, 1160-1189.

Meyers, M.P., P.J. DeMott, and W.R. Cotton 1992: New primary ice-nucleation parameterizations in an explicit cloud model. *J. Appl. Meteor.*, **31**, 708-721.

Ovtchinnikov, M.V., Y.L. Kogan, and B.N. Sergueev, 1995: Study of the ice nucleation mechanisms in a 3D cloud model with explicit formulation of ice-phase and warm rain microphysics. Proceedings of AMS Conference on Cloud Physics. Dallas, USA, 199-202.

NUMERICAL SIMULATION OF WINTERTIME PRECIPITATION DEVELOPMENT IN GRAVITY WAVE AND UPSLOPE FLOW IN ARIZONA'S VERDE VALLEY

J. L. Coen, R. T. Bruintjes, W. D. Hall, T. L. Clark

National Center for Atmospheric Research*
Boulder, Colorado, USA

R. R. Reinking

NOAA / Environmental Technology Laboratory
Boulder, Colorado, USA

1. INTRODUCTION

This study focuses on meteorological events of March 5-6, 1995, examining a sequence of microphysical processes that occurred before and during a cold frontal passage through the Arizona Field Program (AP95) observing network in the mountains and valleys of north-central Arizona. During this period, a low pressure system passed to the north and a cold front approached from the northwest, producing low level southwesterly and upper level westerly airflow. This flow was perpendicular to a series of NW-SE oriented mountain ranges and, in the presence of storm-modified air, led to strong orographic gravity waves. Some of these waves, such as one associated with Mingus Mountain in the Black Hills, persisted for many hours, producing well-recognized features such as the orographic wave cloud and foehn gap and exerting a strong influence on the airflow and precipitation patterns in the valley downstream. Downstream, upslope clouds produced heavy precipitation (5-7 cm) on the snowpack on the Mogollon Rim, the runoff of which led to flash flooding in the Verde Valley, demonstrating the importance of the partition of precipitation between rain and graupel or snow. This case is the subject of a number of other studies, focused on other aspects. Bruintjes et al. (1996) describes the aircraft seeding and chaff tracking operations on 6 March from 0545 UTC to 0845 UTC. The evolution of the cloud liquid water (CLW) in the gravity wave updraft near Mingus Mountain as observed by Ka-band radar and microwave radiometer is described in these proceedings (Reinking et al., 1996). This case is also being studied in detail at the Fourth International Cloud Modeling Workshop (12-16 August, 1996).

In this work, we examine a numerical model simulation of this sequence of events and compare it with sensor measurements collected during AP95. This work extends previous work of Bruintjes et al. (1994), which initialized the model with a single sounding, by initializing it with large-scale fields provided by RUC data and updating the model boundary conditions with later RUC analyses. This extension was necessary to incorporate large-scale tendencies in the simulation, in this case to recognize the large-scale baroclinicity and the rapid movement of the cold front through the domain.

Our study support the results of Bruintjes et al. (1994), in that the distribution of precipitation is tied closely to topography. Liquid water contents in the gravity wave are substantial and can be as large as those in the upslope cloud. An active seeder-feeder process is at work, transporting ice crystals from gravity wave cloud to upslope cloud and enhancing their precipitation. Also, we show the large-scale influence on the location and timing of the orographically-linked precipitation.

2. OBSERVATIONS AND OBSERVING FACILITIES

The large scale topography around the study area is characterized by a series of three NW-SE oriented mountain ranges between which are two broad valleys. From the southwest to the northeast, these include the Bradshaw Mountains, the Prescott Valley, the Black Hills, the Verde Valley, and the Mogollon Rim. (Fig. 1).

The AP95 observational network was poised to record the passage of this and other winter storms, equipped with instruments to record dynamic and microphysical data. These instruments included the

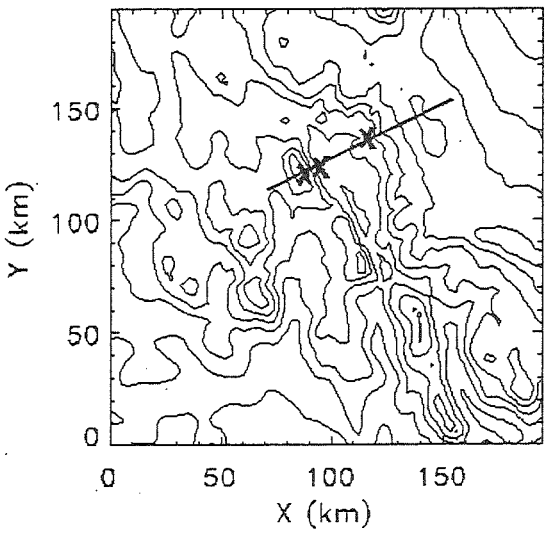

Figure 1. Topography in region covered by finest (third) model domain. Contours each 250 m.

* NCAR is sponsored by the National Science Foundation

Corresponding author address: Dr. Janice L. Coen, NCAR, P.O. Box 3000, Boulder, CO 80307. phone: (303)497-8986, email: janicec@ncar.ucar.edu

NOAA/ETL K- and X-band multiparameter radars deployed at Cottonwood in the Verde Valley and a research aircraft. Other instruments included a mobile CLASS system, the Univ. of Wisconsin HSRL lidar, and a network of 14 Mesonet stations that recorded winds, temperature, humidity, and precipitation rates and amount in the Verde Valley and along the Mogollon Rim. Very moist moderate to strong westerly flow ahead of a shortwave was evident over the Project area from about 0000 UTC on 5 March. Prior to frontal passage, strong gravity waves initiated by the Black Hills (of which Mingus Mountain is the highest point) persisted over the Verde Valley, together with a well-established upslope cloud over the Mogollon Rim. Observing the wave cloud forming in a wave updraft near Mingus Mountain, microwave radiometer and K-a band Doppler radar showed the cloud to contain both cloud liquid water (CLW) and ice crystals. Reinking et al. (1996) comment on the persistence of wave-generated CLW, noting that radiometer measurements indicate its presence for 16 of 21.5 hours of radiometer measurements from 4 March to 6 March. The gravity wave updrafts and upslope flow resulted in enhanced regions of CLW over the Valley and on the upwind side of the Mogollon Rim. Between 00 and 12 UTC, the K-band radar was performing over-the-top RHIs (Range-Height Indicators), and detected both low level liquid upslope clouds and upper level liquid and ice clouds, associated with the gravity wave. The equivalent reflectivity factor at 0827 UTC (fig. 2a) shows a wave cloud lying over the valley, with precipitation increasing across the valley in the upslope clouds towards ENE. A bright band at 2 km suggests particles of precipitation size have fallen from the wave cloud to the melting level, while the differential reflectivity factor (fig. 2b) below reaffirms these are (distorted) precipitation size drops. An increase in differential reflectivity factor

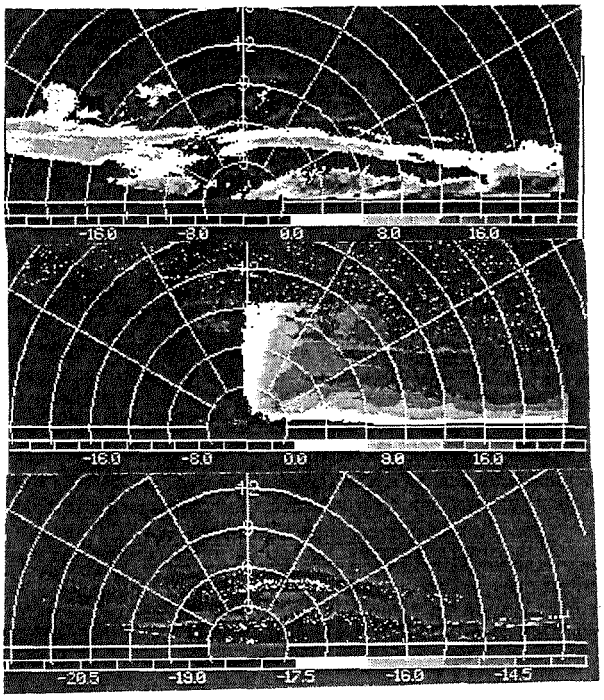

Figure 2. K-a band radar images from an RHI at 81 degrees from 6 March 0827 UTC, including (a) equivalent radar reflectivity factor (DZ), (b) radial velocity (VE), and (c) differential reflectivity factor (DR).

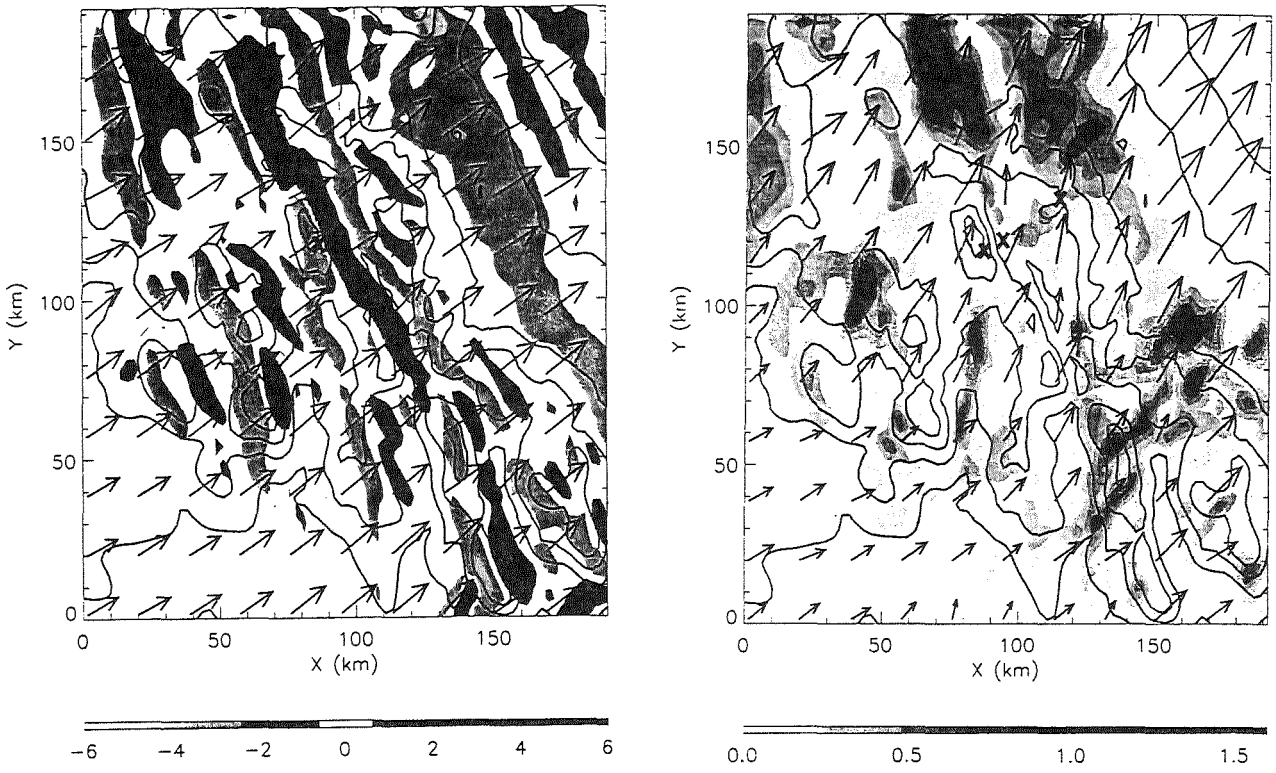

Figure 3. Fields at 0600 UTC of a) vertical velocity at 3134 m AGL, and b) cloudwater mixing ratios at 744 m AGL. X's mark Mingus Mountain, Cottonwood, and Sedona, from left to right. Longest vector is 20 m/s.

near the wave cloud crest suggests that nonspherical (ice) particles are created here as air passes through the wave. At this time, radial velocity (fig. 2c) shows an updraft of 2-3 m/s overhead.

Precipitation increased with the approach of the cold front. Showers began near 1200 UTC and increased during the next 11 hours, peaking just prior to the frontal passage. Winds also increased during this time with peak winds of 20 m/s on Mingus Mountain and 15 m/s in the Verde Valley with the approach of the front. The frontal passage was recorded by the acoustic sounder at 1130 UTC on 6 March 1995, with surface sensors recording a 4 deg C temperature drop.

3. THE NUMERICAL MODEL

This study uses the three-dimensional, nonhydrostatic anelastic meteorological model described by Clark (1977) and Clark and Hall (1991), exploiting features such as two-way interactive grid nesting and vertically-stretched terrain-following coordinates, which allow solutions in regions with complex topography. The model treats both warm rain and ice microphysical processes and uses the quasi-analytical method of treating supersaturation, as described in Clark (1973). The model was initialized and the boundary conditions updated with three-hourly Rapid Update Cycle (RUC) large-scale analysis and forecast data. RUC is a version of the NOAA Forecast Systems Laboratory's Mesoscale and Analysis Prediction System (MAPS, Benjamin et al., 1991). The initialization procedure was performed as described by Hall et al. (1996).

Three nested domains are used to telescope from large-scale to cloud-scale resolution. The large scale flow in the region was simulated with a domain 1157 x 1157 km with 24.3 km horizontal grid spacing, while the innermost domain nested down to 2.7 km horizontal grid spacing focused on the Black Hills, Verde Valley, and Mogollon Rim. Two nested large-scale domains were initialized at 0300 UTC on March 6. At this time, the front was located at a position corresponding to the northwest corner of the largest model domain. The fine-scale (3rd) domain began at 0330 UTC on March 6, and the simulation continued 12.5 hours until 1600 UTC. This contrasts with the simulation of this case presented by Reinking et al. (1996), which was initialized 27 hours earlier.

4. RESULTS

This extends previous work (Bruintjes et al., 1994) with addition of large-scale RUC data. By including large-scale environmental changes in the simulation, we captured the effect of wind speed and direction on gravity wave location, trajectories of hydrometeors produced in the gravity wave, and the location and timing of precipitation.

4.1 *Gravity wave and upslope flow*

The simulation shows that the flow turned from southerly to southwesterly in the lowest few kilometers with the approach of the front. At 3134 m AGL in southwesterly flow, a wave cloud associated with the ridge containing Mingus Mountain contains updrafts of 5-6 m/s at 0600 UTC, (Fig. 3a) with the strongest updrafts at 3-6 km MSL. Beneath it in east-southeasterly flow, an upslope cloud that is 1-2 km deep contains cloudwater mixing ratios up to 2.25 g/kg (Fig. 3b).

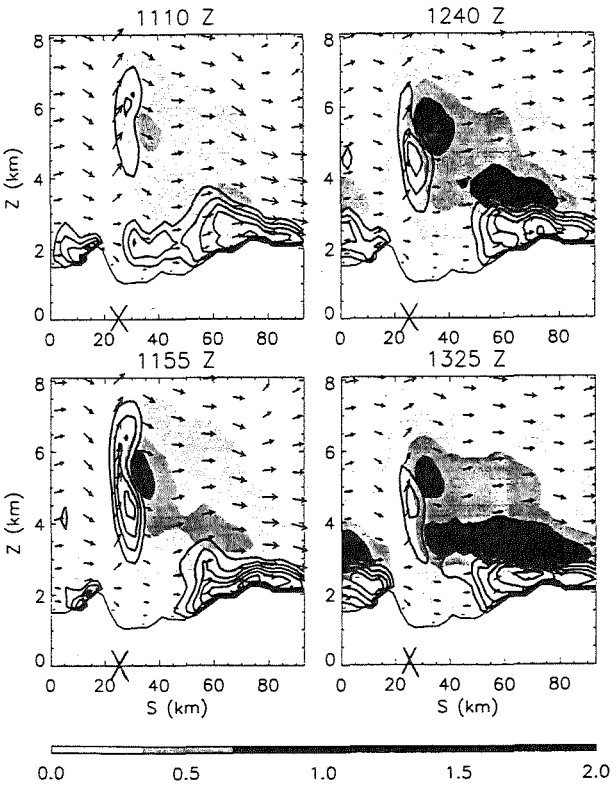

Figure 4. Model vertical cross section (location shown in Fig. 1) of snow mixing ratio (filled contours - see color bar for scale) and cloudwater mixing ratio (line contours at 0.2 g/kg intervals) at 4 times. X marks Cottonwood.

We examine a vertical cross section along the flow that passes through Cottonwood and intersects a gravity wave associated with the ridge containing Mingus Mountain. Figure 4 shows that large values of cloud liquid water (over 0.8 g/kg) sometimes developed in the gravity wave (primarily from 4-6 km MSL), comparable to that in the upslope cloud (over 1.2 g/kg). The peak cloud water mixing ratios in the wave cloud vary with time, accompanying surges in the wave updraft, followed shortly thereafter by an increase in the cloud ice crystal concentration and mixing ratio. Ice crystals were nucleated near the crest of the wave, at concentrations up to 30 l^{-1} but this concentration was not enough to consume all the available liquid water. The crystals grew as they passed through the wave downdraft and deep, moist layer below, and fell into the (liquid) upslope cloud on the slopes of the Mogollon Rim.

4.2 *Frontal passage*

In agreement with observations, the model the gravity waves ceased and precipitation rates increased rapidly in the upslope clouds just as the front passed. The simulation reproduces that the upslope clouds are below the melting level

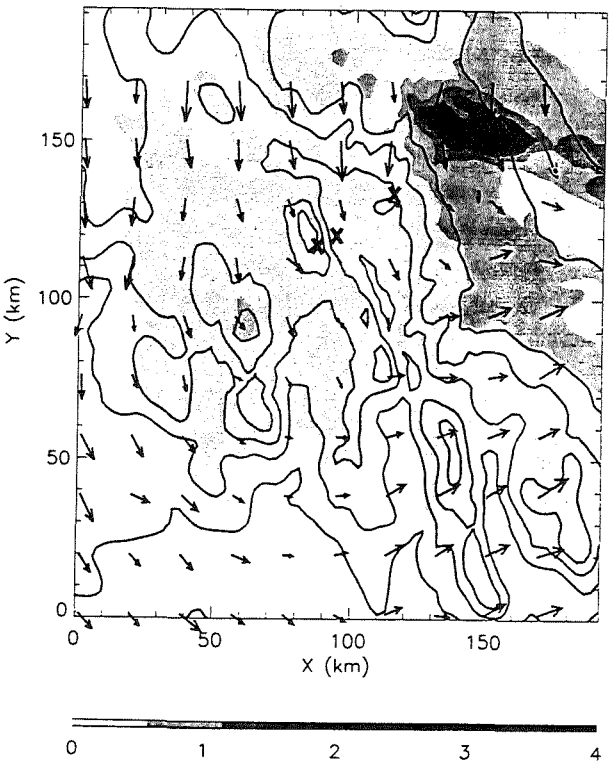

Figure 5. Snow mixing ratio at 1600 Z at 744 m AGL. Longest vector is 19 m/s.

(about 2500 m MSL) and are primarily liquid, with cloud water mixing ratios up to 2.5 g/kg, and producing light rain until the frontal passage, at which time the elevation of the melting level dropped about 1000 m, bringing widespread snow to lower elevations (fig. 5). The frontal passage caused northwesterly winds to overrun the moist, prefrontal southwesterlies, causing convergence in the canyon northeast of Sedona and a sudden increase in graupel and snow precipitation rates near the top of the Rim.

5. CONCLUSIONS

In this work, we have simulated the conditions before the passage of a cold front. We have shown that the radar and model agree on the location, height, and depth of the wave cloud, its persistence for several hours, and the rain-out of the clouds late on March 6.

We have demonstrated the presence of liquid water in the wave updraft, in the presence of an ice crystals nucleation region near the wave crest, in agreement with radar and radiometer measurements. We have linked ice generated in the gravity wave cloud to downstream precipitation, showing how particles are formed in the wave updraft, and follow the wave downdraft into the upslope clouds on the Rim downstream. This is an example of the seeder-feeder process, discussed by Bruintjes et al. (1994) wherein ice particles from upper-level clouds fall into and seed lower level clouds. In this case also, cloud water mixing ratios in the gravity wave are comparable with mixing ratios in large areas of the upslope cloud.

It is apparent that the location of precipitation is tied to small-scale motions and topographic features, but also requires accurate representation of the evolution of large-scale dynamic features. This range of scales makes it difficult to compare model output with rain gauge measurements. In further work, we will apply a fourth domain with horizontal resolution of 900 m and examine how increased resolution affects the calculations.

The large-scale initialization was extremely beneficial, showing how evolution in large-scale dynamics is important in this location to predicting small-scale precipitation, suggesting our single-sounding initialization days are over. It helped us capture the location and characteristics of orographic gravity waves, and without it, the large precipitation rates associated with the passage of a cold front could not have been simulated.

6. ACKNOWLEDGMENTS

This work was funded by the NOAA/Arizona Atmospheric Modification Program, NOAA Cooperative Agreement Number IGA-91-611-189-1085. Special thanks go to Dennis Sundie, program manager for the Arizona Program, for his support during the field program.

7. REFERENCES

Benjamin, S. G., K. A. Brewster, R. Brummer, B.F. Jewett, T.W. Schlatter, 1991: An isentropic three-hourly data assimilation system using ACARS aircraft observations. *Mon. Wea. Rev.*, , 119, 888–906.

Bruintjes, R. T., T. L. Clark, and W. D. Hall, 1994: Interactions between topographic airflow and cloud/precipitation development during the passage of a winter storm in Arizona. *J. Atmos. Sci.*, , 51, 48–67.

Bruintjes, R. T., R. F. Reinking, B. W. Orr, B. A. Klimowski, and E. A. Betterton, 1996: Observational study of silver iodide seeding in a gravity wave cloud in Arizona. 13th Conf. Planned & Inadvertent Wea. Modif., 28 Jan.-2 Feb. Atlanta, Amer. Meteor. Soc. 1–8.

Clark, T.L., 1973: Numerical modelling of the dynamics and microphysics of warm cumulus convection. *J. Atmos. Sci.*, , 30, 857-878.

Clark, T.L., 1977: A small scale numerical model using a terrain following coordinate transformation. *J. Comput. Phys.*, **24**, 186–215.

Clark, T. L. and W. D. Hall, 1991: Multi-domain simulations of the time dependent Navier Stokes equation: Benchmark Error analyses of nesting procedures. *J. Comp. Phys.*, **92**, 456–481.

Hall, W.D., R.T. Bruintjes, J. Coen and T. L. Clark, 1996: A case study of wintertime orographic precipitation in the northern mountains of Arizona. Preprints, 12th Intl. Conf. on Clouds and Precip.

Reinking, R.R., J. B. Snider, R. T. Bruintjes, J. Coen, T. Clark, and W. Hall, 1996: Liquid water in storm-embedded orographic gravity waves. Preprints, 12th Intl. Conf. on Clouds and Precip.

A TWO-DIMENSIONAL CLOUD MODEL: DESCRIPTION AND NUMERICAL EXPERIMENTS

Alexandre A. Costa[1] and Antônio José C. Sampaio[2]

[1]Meteorology Dept., Fundação Cearense de Meteorologia e Recursos Hídricos (FUNCEME)
[2]Physics Dept., Universidade Federal do Ceará (UFC)

1. INTRODUCTION

A two-dimensional warm cloud model is presented. Prognostic equations for the vorticity on the r-z plane, the potential temperature and the water vapor, cloud water and rain water mixing ratios constitute the dynamics of the model. Simple parameterizations are adopted to represent the turbulent and microphysical processes.

Some simulations were performed, under real environmental conditions, corresponding to a sounding made in Fortaleza, Ceará state, Brazil, in April 01, 1995. The results describe the evolution of simulated clouds from their formation to the precipitation development and show the importance of turbulence and microphysics parameterizations.

2. MODEL DESCRIPTION

The present model simulate moist deep convection processes and represents a improvement of the version proposed by Costa (1995). It is similar to the model proposed by Soong and Ogura (1973), but with more accurate numerical schemes.

Cylindrical coordinates are adopted. Mass conservation is represented by the continuity equation for deep convection. The set of prognostic equations represent the time dependence of vorticity, potential temperature and water vapor, cloud water and rain water mixing ratios. The components of the velocity are recovered from a streamfunction, which is connected to the vorticity through a diagnostic equation.

Advection is evaluated using Bott's advective scheme (Bott, 1989a, 1989b, 1992) in its monotone version for vorticity, potential temperature and water vapor mixing ratio and in its positive definite version for cloud water and rain water mixing ratios. Orders from 2 to 6 are available, according to the extension of Bott's scheme performed by Costa and Sampaio (1996), but only 2nd order advection algorithm is adopted in this work. A iterative scheme is used to solve the diagnostic equation for the streamfunction (Stone, 1968; Jacobs, 1972). Turbulent diffusion is parameterized according to a first order closure theory and its discussion is made later. Microphysical processes are represented by simple parameterizations: Kessler (1969) or Berry (1968).

3. THE ENVIRONMENTAL CONDITIONS

The environmental conditions correspond to a sounding carried out in Fortaleza, Ceará State, Brazil, in April 01, 1995, at 09LST (12UTC). The vertical profiles of pressure, temperature and relative humidity are represented in Figures 01-03.

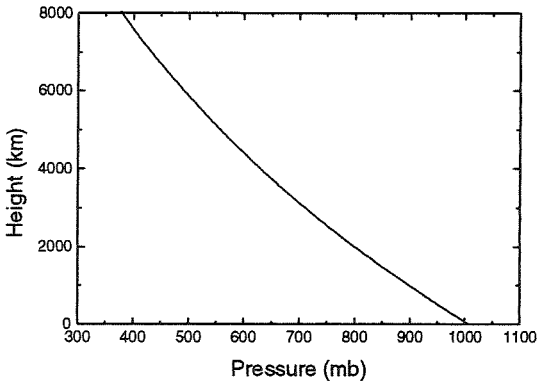

Fig. 01 - Pressure vertical profile

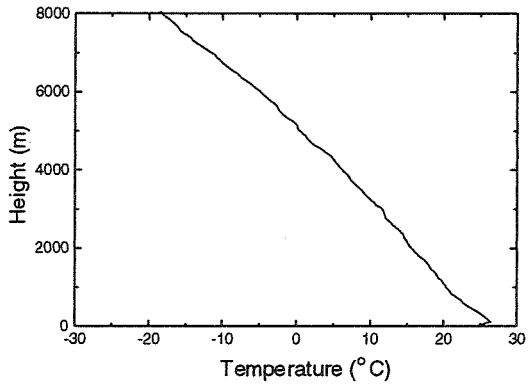

Fig. 02 - Temperature vertical profile

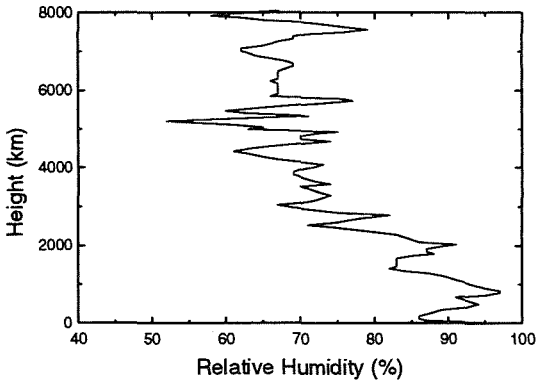

Fig. 03 - Relative humidity vertical profile

The Figures show that temperature decreases at a rate close to the dry adiabatic lapse rate near the surface and that a significant amount of humidity is present in low levels. Those conditions clearly concur to the formation of clouds.

4. THE BASIC SIMULATION

A domain with 40 points in both radial and vertical directions with a spatial resolution of 200m was defined. Rigid boundaries were assumed and radiative effects were considered as negligible.

The initialization of the simulated cloud in the basic numerical experiment was made introducing a parcel with exceeding potential temperature and humidity in the lower, central portion of the domain. The perturbation of potential temperature (maximum value of 0.5K) occurs in a cylindrical region (radius of 1.5 km) from near the ground to an altitude of 3.1 km. A relative humidity of 99%, which allows the rapid incoming of condensation, is introduced in this region, from an altitude of 0.9 km to 3.1 km.

Figs. 04 to 06 depicts the time evolution of vertical velocity, cloud water content and rain water content in the central axis of the cloud.

The vertical velocity increases rapidly when condensation begins. A maximum value of 1.39 m/s is reached after 2.5 min of simulation. At mature stage, a shallow cloud (1.4 km) is formed. A maximum cloud water content of 0.77 g/m^3 occurs before 7 min, when conversion processes become important. The maximum rain water content (0.03 g/m^3) takes place at 10 min of simulation, and two minutes later precipitation reaches the surface. During this time, precipitation causes descending motions. Vertical oscillations occur in the dissipation stage of the simulated cloud.

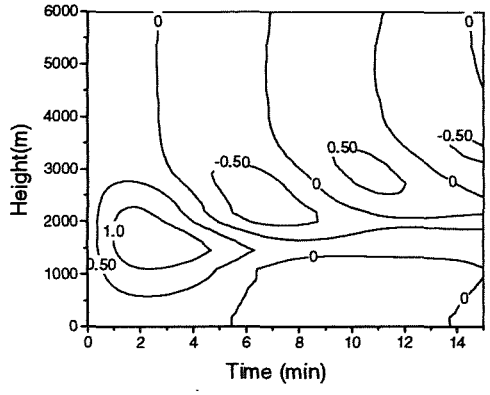

Fig. 04 - Time evolution of the vertical velocity in the central axis of the cloud

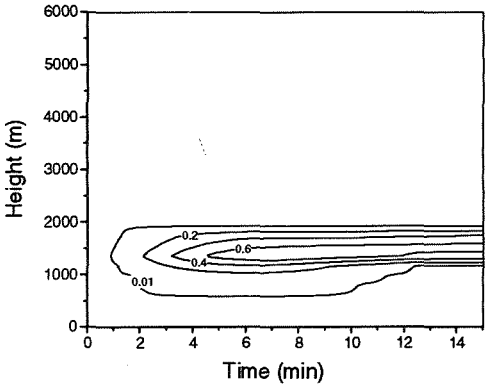

Fig. 05 - Time evolution of the cloud water content in the central axis of the cloud

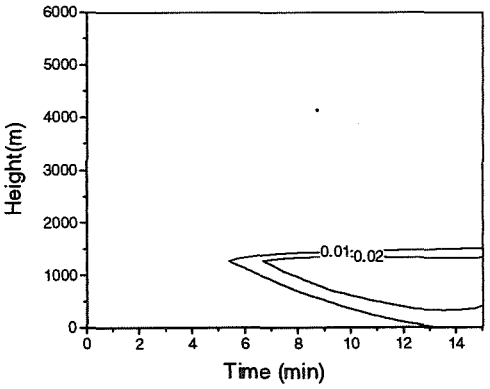

Fig. 06 - Time evolution of the rain water content in the central axis of the cloud

In fig. 07 we show the distribution of the cloud water, after 10 min of simulation.

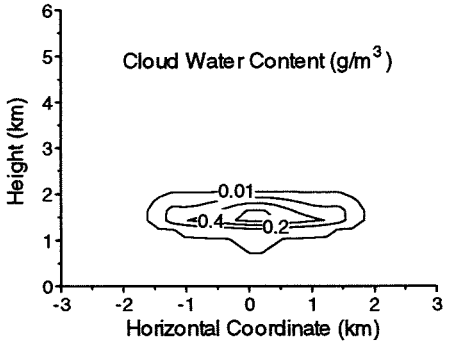

Fig. 07 - Cloud water content after 10 min of simulation

5. THE IMPORTANCE OF THE MAGNITUDE OF THE TURBULENT DIFFUSION COEFFICIENT

In the present model, the turbulence is parameterized according the hypothesis that the diffusion coefficient is proportional to the deformation tensor (Smagorinsky, 1963):

$$K = (c\Delta)^2 D$$

where K is the diffusion coefficient, Δ is the grid spacing, c is an arbitrary parameter and D is the deformation tensor.

Some simulations, carried out with this model, show that turbulent mixing effects are strongly affected by the magnitude of this adjustable, non-dimensional parameter. Its influence acts directly over the dynamical fields. When c varies from 0.15 to 0.30, the maximum updraft goes from 1.55 m/s to 1.17 m/s. This relatively small reduction in the vertical velocity (25%) causes a big reduction is the precipitation field. Table 1 shows the results of four simulations, in which c goes from 0.15 to 0.30, modifying the fields of vertical velocity and liquid water content.

c	maximum cloud water content (g/m^3)	maximum rain water content (g/m^3)	maximum rain water content, ground level (g/m^3)	maximum vertical velocity (m/s)
0.15	0.83	0.039	0.0170	1.55
0.20	0.77	0.030	0.0120	1.39
0.25	0.71	0.022	0.0077	1.26
0.30	0.66	0.016	0.0035	1.17

Table 1 - Results of simulations with variable turbulent diffusion

6. DIFFERENCES BETWEEN MARITIME AND CONTINENTAL CLOUD LIFE CYCLES

It is well known that there are significant differences among clouds formed in air masses of distinct origins. Maritime clouds generally exhibit broad spectra, with small droplet concentration and relatively large values of mean diameter of droplets, while in continental clouds narrow spectra are more commonly present, with large concentration and small mean diameter.

Berry's parameterization (Berry, 1968) is a simple way to represent these differences, considering that autoconversion rate depends on the concentration of droplets (N) and the spectrum relative dispersion (d).

Two simulations were performed, changing these parameters according to the characteristics of typical maritime clouds (N = 100 cm^{-3}; d = 0.35) and continental clouds (N = 1000 cm^{-3}; d = 0.20). With a fixed value of c = 0.20, both of the simulated clouds exhibit very small differences in their macrosctructures and in the dynamical fields. However, it can be seen that a very significant difference in their microphysical evolution occurs, particularly in the liquid water distribution. These results are showed in table 2:

cloud pattern	maximum cloud water content (g/m^3)	maximum rain water content (g/m^3)	maximum rain water content, ground level (g/m^3)
maritime	0.72	0.0530	0.0260
continental	0.82	0.0097	0.0019

Table 2 - Results of simulations with variable microphysical parameters

At least in these simulations, corresponding to an isolated and not deep convective cloud producing a very small amount of precipitation, the reduction of the autoconversion rate in the continental cloud leads to a precipitation several times smaller than in the maritime case. It is important to verify if it also occurs in the case of deep convective cells.

7. GENERAL DISCUSSION

A two-dimensional, axisymmetric model for warm convective clouds is presented. This version of

the model introduces a very accurate numerical advection scheme. The results of the basic simulation show that the model is capable of representing the life cycle of an isolated convective cell, including precipitation development.

Simulations in which the magnitude of the turbulent diffusion coefficient had been modified suggest that the model presents a strong sensibility to this parameter.

Other simulations, using Berry's parameterization, make clear that big differences between simulated maritime and continental clouds appear, particularly in the distribution of the liquid water.

ACKNOWLEDGMENTS

The authors wish to thank Dr. Murilo Pereira de Almeida for his help in the English language.

REFERENCES

Berry, E. X., 1968: Modification of the warm rain process, Proceedings of the First National Conference on Weather, Albany, 81-88.

Bott, A., 1989a: A positive definite advection scheme obtained by non-linear renormalization of the advective fluxes. *Mon. Wea. Rev.*, **117**, 1006-1015.

——, 1989b: Reply. *Mon. Wea. Rev.*, **117**, 2633-2636.

——, 1992: Monotone flux limitation in the area-preserving flux-form advection algorithm. *Mon. Wea. Rev.*, **120**, 2592-2602

Costa, A. A., 1995: Desenvolvimento de um modelo bidimensional axi-simétrico de nuvem quente com microfísica parametrizada. Master's dissertation, Physics Department, UFC, 139 pp.

—— and A. J. C. Sampaio, 1996: The Bott's area-preserving flux-form advection algorithm: extension to higher orders and additional test, submitted to *Mon. Wea. Rev.*

Jacobs, D. A. H., 1972: The strongly implicit procedure for numerical solution of parabolic and elliptic partial differential equations. *Central Electricity Research Laboratory* - Note RD/L/N66/72.

Kessler, E., 1969: On the distribution and continuity of water substance in atmospheric circulation, *Meteor. Mon.*, **10**.

Smagorinsky, J., 1963: General circulation experiments with the primitive equations. I: The basic experiment. *Mon. Wea. Rev.*, **91**, 99-164.

Soong, S. T. and Y. Ogura, 1973: A comparison between axisymmetric and slab-symmetric cumulus cloud models. *J. Atmos. Sci.*, **30**, 879-893.

Stone, H. L., 1968: Iterative solution of implicit approximation of multidimensional partial differential equations. *S. I. A. M. J. Numer. Anal.*, **5**, 530-558.

HAIL SIZE SPECTRUM DOMAIN INFLUENCE ON THE SIMULATED CLOUD LIFE

Mladjen Ćurić, Dejan Janc and Vladan Vučković

Institute of meteorology, University of Belgrade, Yugoslavia

1. INTRODUCTION

Ice accretion is investigated for a number of specific purposes, including the prediction of hail formation. Laboratory investigations on artificially grown hail were supposed to provide clues for the interpretation of the hailstone characteristics in terms of the icing conditions in hail clouds which lead to their growth (Macklin, 1977; Prodi et al., 1991). Despite their number and creative diversity, almost all of these had to be explored under conditions which do not effectively simulate natural conditions.

The modelling and understanding of the hail formation has been considerably advanced by Wisner et al. (1972), Farley et al.(1994), etc. However, the models on hail growth have to evolve in several aspects. So, most working models which operates with the bulk-water parameterization scheme treat the hail accretion rates by help of the Wisner et al. (1972.) approximation of the continuous growth equation with a "sweep-out" concept (Orville and Koop, 1977; Lin et al., 1983; Ćurić and Janc, 1989;1993; Farley et al.,1994). All beforementioned papers treat the hail spectrum contrary to the numerous observations, integrating the corresponding equations over hail sizes from 0 to $+\infty$ (hereafter called the idealized spectrum) without any evaluation of the consequences. According to empirical evidence, a hailstone is a particle with an equivalent sphere diametar, D_H , equal or greater than $0.5\,cm$ (Bohm, 1989). The inclusion of the such spectrum (hereafter called the real hail spectrum) in corresponding accretion rates for hail may considerably changed their values with respect to those with the idealized spectrum.

In this paper we have carried out studies to investigate wheather there could be significant differences in the values of some of the characteristics of the simulated cloud depending only on the hail spectrum domain that was used. The idealized and real spectrum are considered only in the hail accretion rate. All other equations of the 1-D model used are the same. Comparisons were made for 45 environmental soundings taken in midday (12 00 UTC).

2. MODEL CHARACTERISTICS

The model applied is a 1-D time-dependent model proposed by Ćurić and Janc (1988). It was further modified, including the new ways of representing entrainment, forced lifting and presure perturbation (Ćurić and Janc 1993). It combines dynamical equation with water continuity equations that include ice phase microphysical processes. Basically, the model is based on the concept of an entraining jet which radius is allowed to vary with height as required by mass continuity. It is nonhydrostatic convective cloud model, with an entrainment formulation that includes the combined effects of turbulent and organized dynamic processes.

The vertical velocity was calculated by an integration with height of the acceleration due to the modified thermal buoyancy reduced

by the weight of the contained liquid and solid water and adjusted for the entrainment. On this vertical velocity is added the forced component due to the forced lifting of warm air on the gust front head. Our model produces significantly unsteadier clouds whose evolution reproduces some observations more closely than previous ones.

3. THE CALCULATED CLOUD VARIABLES

The variables considered in the comparisons were: maxima in vertical velocity (MW), height of MW (HMW), time at which MW were attained (TMW); maxima in rain water content (MR), height of MR (HMR), time at which MR were attained (TMR); maxima of cloud ice content (MI), height of MI (HMI), time at which MI were attained (TMI); maxima of hail content (MH), height of MH (HMH), time at which MH were attained (TMH); maxima in the temperature difference between cloud and environment (MTD), height of MTD (HMTD), time at which MTD were attained (TMTD).

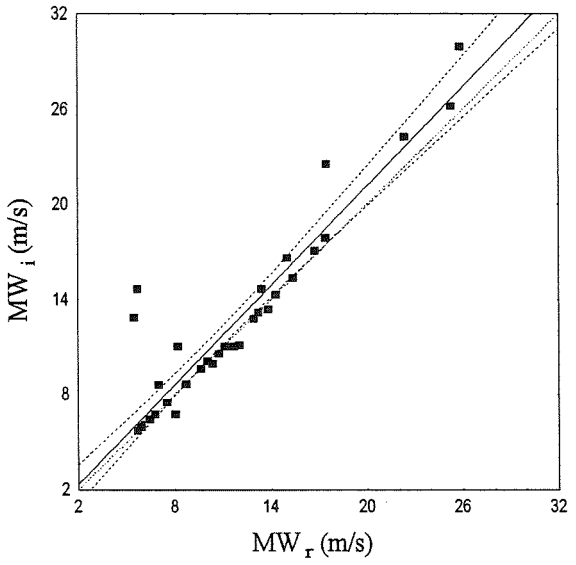

Fig.1 Scatter diagram of maxima in vertical velocity for idealized case MW_i (m/s) versus its real values MW_r (m/s). The doted line is 1:1 correspodence between them, while full line is the regressione curve. The dashed lines indicate 95 % confident interval.

Any one variable ( ) were calculated for real hail spectrum, hereafter designated as $()_r$ and for idealized hail spectrum, designated as $()_i$.

The model simulations were carried out for 45 radiosonde meassurements made at the weather service station at Belgrade for the routine midday (12 00 UTC) soundings during sommer mounths. The simulations were made under the same all others conditions.

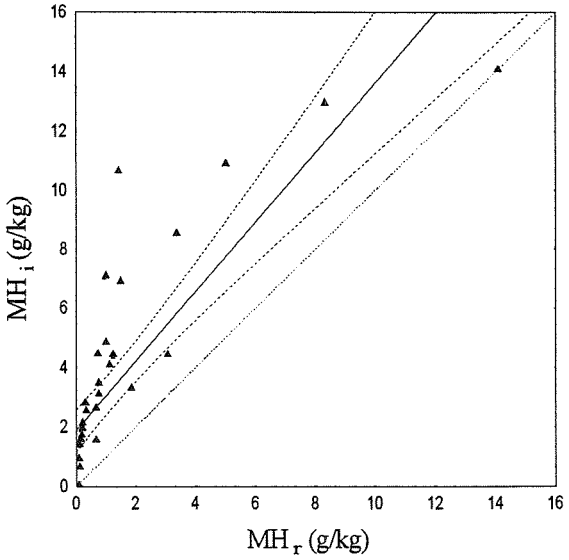

Fig. 2 Same as Fig.1 but for hail content (g/kg).

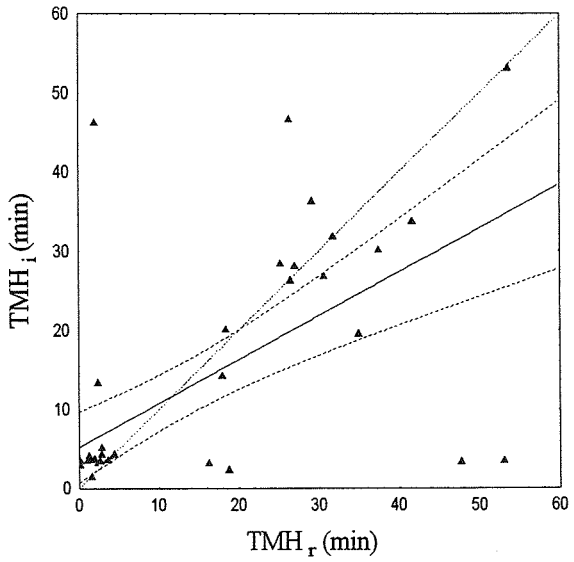

Fig. 3 Same as Fig.1 but for time of maxima appearance of hail (min).

4. COMPARISON OF REAL AND IDEALIZED VARIABLES

The microphysical and dynamical characteristics of a cloud depend critically on the accretion. So, it is instructive to see how these variables are induced by hail size spectrum domain.

The idealized variables of cloud were compared to the real ones to obtain same idea as to the magnitude of the differences between them. In Figs. 1-8 the idealized variables are plotted against the real ones for all simulations.

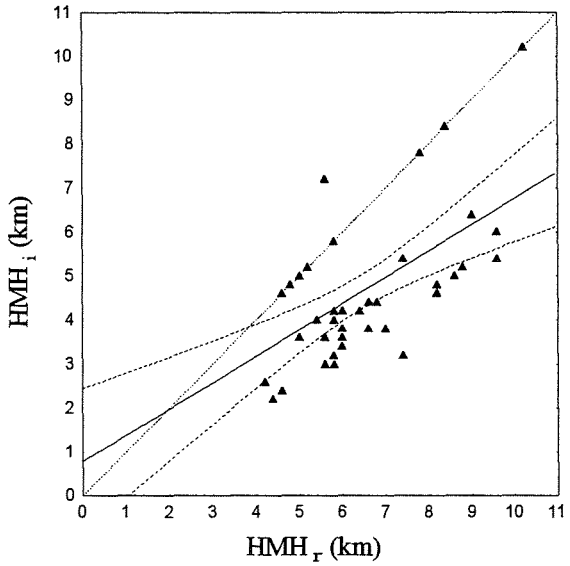

Fig. 4 Same as Fig.1 but for height with maxima of hail (km).

Fig. 2 shows that the idealized values of maxima in hail content overestimate the real ones in all range of contents. It can be seen that maxima of hailstones are produced earlier in idealized case than in real case (Fig. 3), and they appear at the lower part of a cloud in idealized than in real case, as clearly shown in Fig.4.

The rearrangements of maxima in rain water are depicted in Figs. 5 and 6. It can be seen that raindrops are produced with higher values in real than in the idealized case in the most number of experiments. Also, the maxima reached at the higher levels in real case than in idealized one.

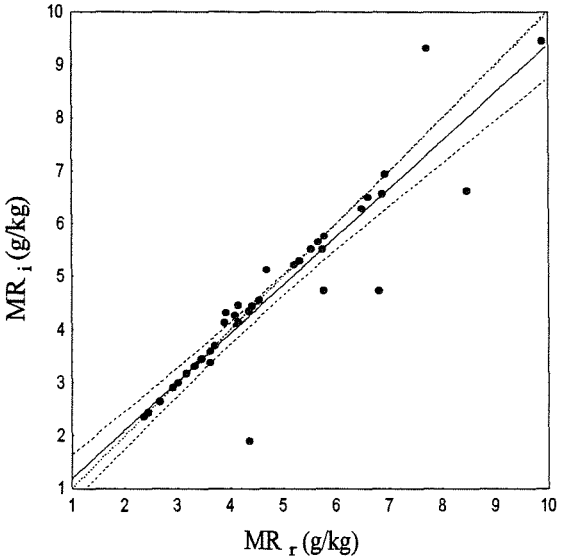

Fig. 5 Same as Fig.1 but for rain water content (g/kg).

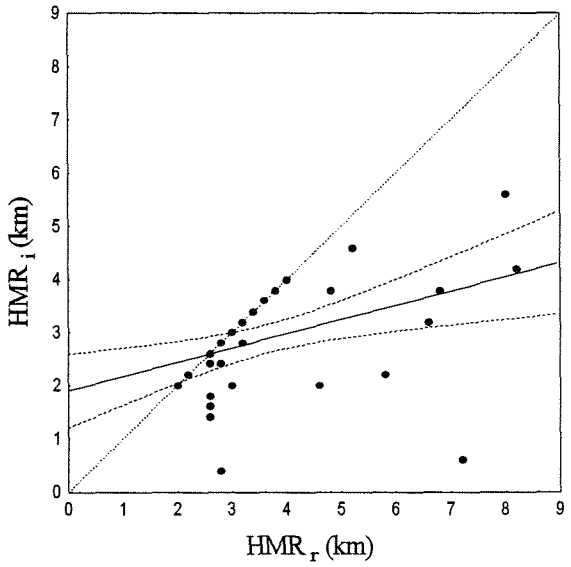

Fig. 6 Same as Fig.1 but for height with maxima of rain (km).

The maxima in vertical velocity (Fig. 1) for this 45 cases covered a similer range of velocities. The idealized values generally overestimate the real ones for the smallest and the highest values, while they underestimate them rather badly when velocities are in the middle range. The dotted line is the 1:1 correspodence between them.

The rearrangements with time is also remarkable. The maxima of raindrops are produced earlier in real than in the idealized

case. This result is in fair agreement with observation.

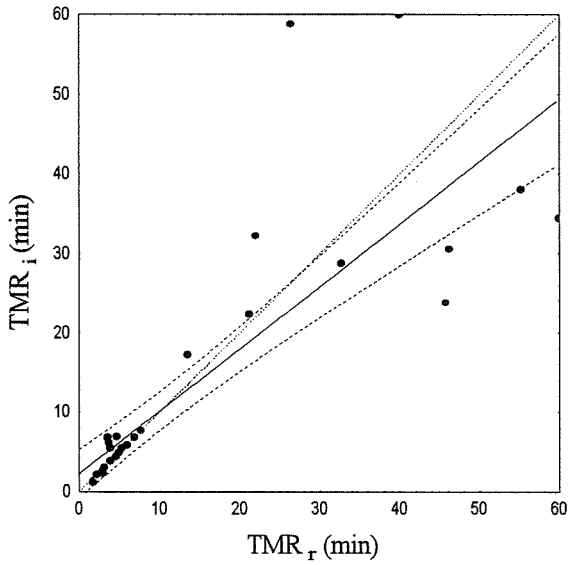

Fig. 7 Same as Fig.1 but for time of maxima appearance of rain (min).

Correlation coefficients for idealized cloud variables versus real ones are shown in Table 1. One can see that the correlation coefficient for cloud characteristics are higher than that for their heights or time of maximum appearance.

Table 1. Correlation coefficients for idealized cloud variables versus real ones.

Cloud characte-ristics	Maxi-mum value	Height with maximum	Time of maximum appearance
Vertical velocity	0.94	0.86	0.74
Hail content	0.81	0.59	0.62
Rainwater content	0.93	0.43	0.83
Cloud ice content	0.80	0.95	0.84
Cloud/ environment temperature difference	0.97	0.95	0.79

5. CONCLUSIONS

This is confirmation of the results of the study Ćurić and Janc (1996), which also indicated that the trancating hail spectrum is sufficient to affect seriously the model predictions. The modeled cloud with the new formula for hail acretion rates is more effective to produce the amount of rainfall and hail in reasonably shorter time than in idealized case.

References

Bohm, H.P.,1989: A general equation for the terminal fall speed of solid hydrometeors. *J. Atmos. Sci.*,46, 2419-2427.

Ćurić, M., and D. Janc, 1989: Dynamic entrainment rate influence on products of a one-dimensional cumulonimbus model. *Atmos. Res.*, 24, 305-323.

Ćurić,M., and D. Janc,1991: Graupel growth and trajectories in shallov Cb cloud determined by a forced 1-D model. *Atmosphere - Ocean* 29, 462-478.

Ćurić,M., and D. Janc,1993: Predictive capabi-lities of a one-dimensional convective cloud model with forced lifting and a new entrainment formulation. *J. Appl. Meteor.*,32,1733-1740.

Ćurić, M., and D. Janc,1996: Sensitivity of modeled hail accretion rates on lower boundary of hail spectrum. *Meteorol. Z.* (in press).

Farley, R.D., Nguyen,P., i H.D. Orville, 1994: Numerical simulation of cloud seeding using a three-dimensional cloud model. *J. Wea. Mod.*, 26, 113-124.

Lin, Y.-L., R.D. Farley i H.D. Orville, 1983: Bulk parameterization of the snow field in a cloud model. *J. Climate Appl. Meteor.*, 22, 1065-1092.

Macklin, W.C.,1977: The characteristics of natural hailstones and their interpretation. *Meteor. Mong.*, 38, 65-88.

Orville, H. D., and F.J. Kopp , 1977. Numerical simulation of the life history of a hailstorm. *J. Atmos. Sci.*,34,1596-1618.

Prodi, E.L.Levi, O.B.Nasello, L.Lubart, 1991; Morphology and density of ice accreted on cylindrical collectors at low values of impaction parameter. II: Rotating deposits. *Quart. J. R. Met. Soc.* 117, 783-801.

Wisner, C., Orville,H.D., i C. Myers , 1972. A numerical model of a hail-bearing cloud. *J. Atmos. Sci.*,29,1160-1181.

EXTENDED COMPARISON BETWEEN AIRBORNE DOPPLER RADAR DATA AND THREE-DIMENSIONAL SIMULATIONS OF A TROPICAL SQUALL LINE OBSERVED DURING TOGA-COARE

Thibaut Montmerle[1,2], J.L. Redelsperger[1],
J.P Lafore[1], Y.Lemaître[2] and G.Sommeria[2]

[1] Centre National de Recherches Météorologiques, 31057 Toulouse cedex, France
[2] Centre d'étude des Environnements Terrestres et Planétaires, 78140 Vélizy, France

1. Introduction

The case of the 22th february 1993 tropical squall line observed during the international experiment TOGA-COARE (Webster & Lukas (1992)) is simulated and compared to observations made by two airborne Doppler radars.

For the simulations, a new non-hydrostatic meso-scale model is used. This model, called Meso-NH, is under progress at CNRM[1] and Laboratoire d'Aérologie in Toulouse.

The comparisons are based on the description of the vertical and horizontal transport of mass, heat and water, and the characteristic of the reflectivity field. Furthermore, we use CFADs (Contoured Frequency by Altitudes Diagrams ,Yuter and Houze, 1995) and other statistical tools to complete this descriptive part.

2. Modeling techniques

a. the model

The numerical model used in this study is a three dimensional non hydrostatic model based on the Lipps & Helmer (1982) modified anelastic system. The three-dimensional turbulent scheme is based on the turbulent kinetic energy equation as in Redelsperger and Sommeria (1986). At the present stage, the model doesn't contain any ice parametrisation scheme, and uses the Kessler (1969) bulk parametrisation. The ice parametrisation should be available soon, and the simulation will hopefully include it at the time of the conference.

b. The mesh definition

The horizontal simulation domain extends 150 km along the squall line (y axis) and 120km across (x axis) with open lateral boundary conditions, because the perturbation generated by convection extends to distances larger than the simulation domain. A gravity wave absorbing layer is situated between 17 and 23 km altitude, below a rigid upper boundary, exerting a free slip condition on the atmosphere. A mesh size of 1250 m is chosen in each horizontal direction. Vertically, a streched grid is used, varying from 70 m at ground level to 700 m at the top of the domain, in order to get a sufficient resolution in the lowest layers and to cover the whole depth of the system. The total simulation time is 6 hours, with a time step of 10 s.

c Initialisation

The initial conditions were specified, as proposed by Trier et al (1996), using a composite sounding composed by P3 flight data and rawinsonde data, and were horizontally homogeneous. The squall line is initiated in the middle of the domain by simulating a density current. Therefore, four mid-ovale shape perturbations were put parallel to the y axis during the first 20 mn. This perturbations were 2.5 km high with a maximum cooling-rate of $6.6.10^{-3}$°C/s along the line, associated with a maximum drying-rate of 2.5 10^{-6} g/kg/s. Both cooling and drying were inversely proportional to their distance to the convective region.

3. Observation techniques

The 22th february case displayed a fastmoving squall line oriented perpendicular to a moderately strong low level jet. This convective system was sampled by two airborne Doppler radars on the two NOAA P-3 aircraft, designated N42 and N43.

The three dimensional wind field is retrieved with the analytical technique MANDOP (for Multiple ANalytical DOPpler), developped by G.Scialom and Y.Lemaître (1990). This technique consists in expressing each of the three wind components as a product of three expansions in terms of orthonormal function series. In order to retrieve the coefficients of the developpement, the analytical form is variationally adjusted to the observations under physical constraints.

A mesh size of 1500 m horizontaly and 500 m verticaly is chosen. The results are represented with the model vertical stretched grid, in order to have a better description of the boundary layer. This computation is possible thanks to the analytical form of the retrieved wind.

4. Simulation Results and comparison with observations

Different problems occur with model-observation comparisons. First, we don't have a proper initialization scheme using a three-dimensional field of real data. Second, the natural variability of the atmosphere and of the model output make it difficult to analyse and to compare them completely. Actually, the convection displays large time and scale fluctuations.

To avoid these difficulties and to synthesize the results, the comparison is based on general features and the statistical properties of the squall line.

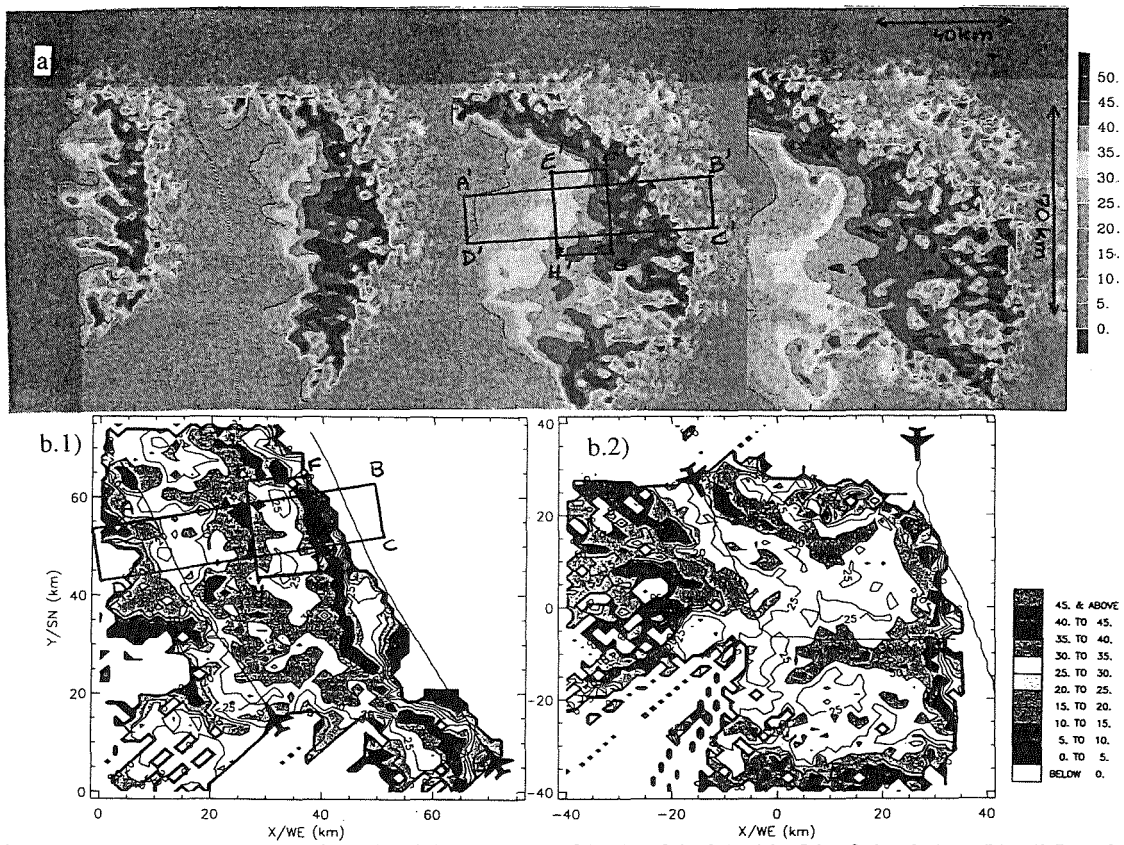

fig 1. (a) Evolution of simulated radar reflectivity at 1 km AGL after 2 h, 3 h, 4 h, 5 h of simulation, (b) tail Doppler radar reflectivity observed between (1) 2109 and 2121 UTC, (2) 2158 and 2207 UTC by the N42 and the N43.

a. The line evolution

The radar reflectivity was derived from the mixing ratio of liquid rain. We used an empirical formulation deduced from the ASTRAIA microphysical data of the 17th february:

$$q_r = \frac{1}{\rho} 1.049.10^{-3} Z^{0.722} \qquad (4.a)$$

where q_r is the simulated rain mixing ratio (g/kg), and ρ the air density.

The evolution of the reflectivity field at 1 km above ground level (AGL thereafter) for the simulation (fig 1) shows good agreements with the observed evolution of the squall line. Between 2 and 4 hours of simulation, the line evolves from a quasi linear structure with a leading edge of high reflectivity (up to 40 dBz) to a bow shaped pattern near the center of the rainband. In the simulation, newborn convective cells appear ahead of the line. These cells are not observed on real data because the N43's Doppler radar did not sample the eastern part of the domain. After 5 hours, the line begins to decay.

The horizontal relative wind at 1.5 km AGL showed in figure 2 for the two approaches presents the same global features. At once, the 2D aspect of the squall line is well represented, as well as the 3D structure in the northern part of the line, where northward fluxes are

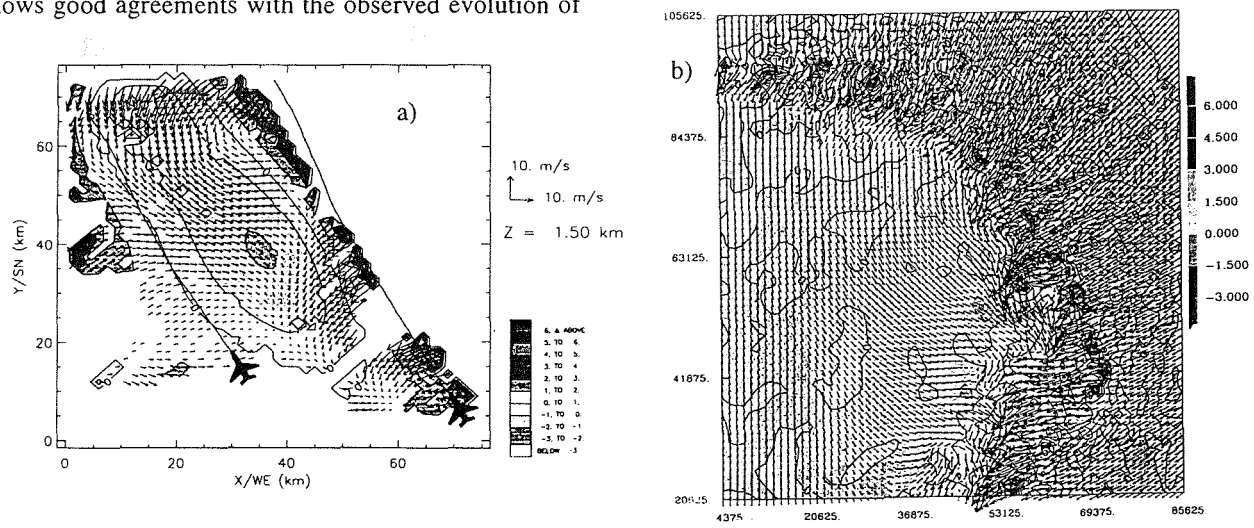

fig 2. Horizontal cross sections at 1.5 km AGL of relative horizontal wind (arrows) and vertical velocity (contours) for (a) observations between 2109 and 2121 UTC and for (b) simulations after 4 hours.

important. 45 mn later, the observed wind field displays a vortex in this part of the domain (not shown here).

b. The two dimensional analysis

Different parts of the domain were chosen, in which each three dimentional field is considered as a superposition of a two-dimensional field and a perturbation (see Redelsperger and Lafore (1988)). The first part of this decomposition represents an average along the line. It corresponds to the mean vertical circulation and structure of the squall line in the new chosen domain. The second part is the residual three-dimensional field and represents the lateral fluctuations along the line direction, representative of the three-dimensional nature of the squall line. This field is analysed in term of standard deviation.

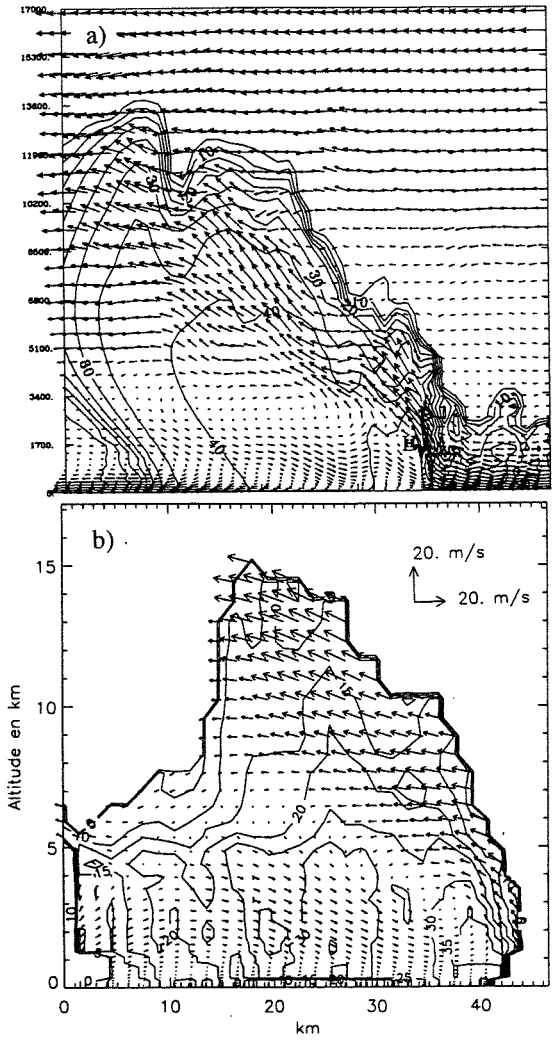

fig 3. 2D average of reflectivity and relative wind cross section for (a) the simulation, with contours every 5 dBz and a maximum arrow of 20 ms^{-1}, (b) the observation with contours every 5 dBz and a maximum arrow of 17 m^{-1}. These 2D cross sections are defined considering the boxes A'B'C'D' of the fig 1.a for the simulation, and ABCD of the fig 1.b.1 for the observation.

The two figures 3.a and 3.b feature the same dynamical properties, including an ascending front-to-rear flow and a rear inflow in the region of heavy stratiform rain. Furthermore, a rotor circulation develops in both cases at 3 km AGL in front of the convective line. On the other hand, the simulation is less extended vertically, probably because of the absence of ice parametrisation scheme. The computed reflectivity field is approximatively 7 dBz greater than the observed one. The principal reason of this deviation is that the simulated rain particles are falling instantaneously as soon as they are formed, since they are produced in liquid phase rather than in ice phase. In the observations, some particles are carried by the ascending front-to-rear flow and become ice particles with low fall velocity at the rear of the system.

The leading edge of the squall line appears in both data sets as a region of heavy convective showers with strong updrafts reaching 6 ms^{-1} vertical velocities (fig 4.a and 4.b). However, the simulation does not reproduce the second core of maximum vertical velocities observed above 10 km. The vertical wind simulated in this part of the domain has a maximum of 2.5 ms^{-1} instead of the 5 ms^{-1} observed. The downdrafts at low levels are weaker too (-0.5 ms^{-1} instead of -2 ms^{-1}).

Two dimensional analysis of the relative cross-line velocity (fig 4.c and 4.d) and potential temperature (not shown) displays the mean structure of the gravity current. The inner circulation of this current is characterized by a subsident jet that is faster than the system propagation (>3 ms^{-1} in both case). Its front is 2 km deep for the simulation and 2.5 km for the observations and extends 40 km rearward of the cold front. The mean standard deviation of the relative cross-line velocity (fig 4.e) shows a strong shear in front of this rear inflow.

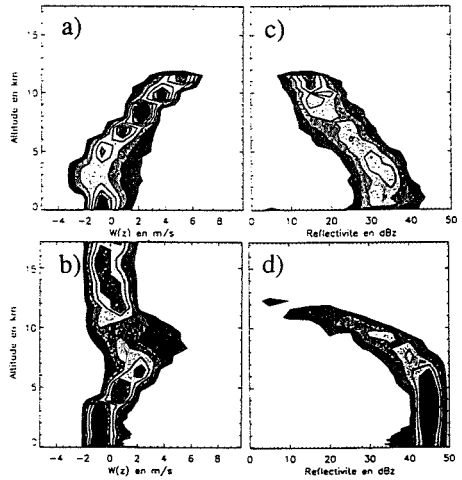

fig 5. CFADs of vertical velocity for (a) the observations and for (b) the simulations, isocontours every 10% of data per ms^{-1}per km. CFADs of reflectivity for (c) the observations and for (d) the simulations, isocontours every 10% dBz^{-1} km^{-1}. These CFADs are defined considering the boxes EFGH for the observation, and E'F'G'H' for the simulation

c. Cfad

In order to get more detailed information about the spatial and temporal distribution of a three dimensional field, we used Contoured Frequency by Altitude Diagrams (Yuter and Houze (1995)) in a selected part of the simulation and observation domain (fig 5). Two boxes were chosen on the convective region, extending 15 km backward, one for the observation, and one for the simulation.

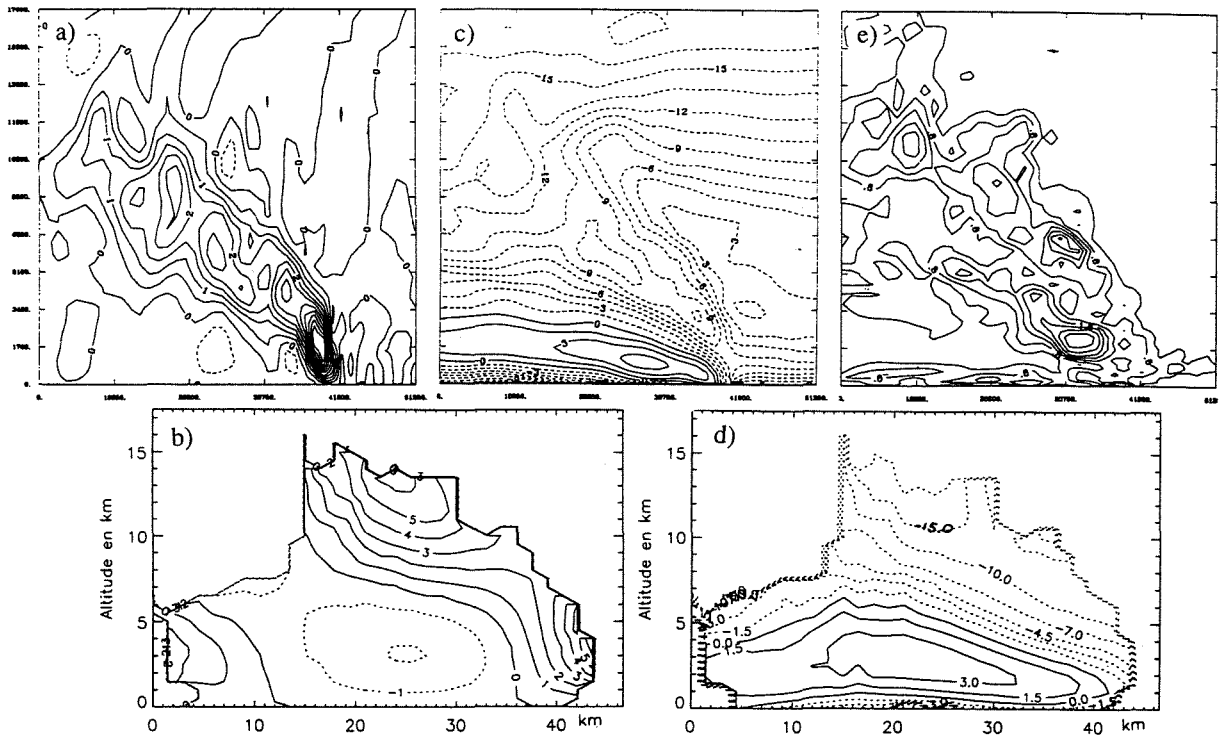

fig 4. 2D average of relative vertical velocity for (a) the simulation with contours intervals of 0.5 ms^{-1}, (b) the observation with contours intervals of 1. ms^{-1}. 2D average of relative cross-line velocity for (c) the simulation with contours intervals of 1.5 ms^{-1}, (d) the observation with contours intervals of 1.5 ms^{-1} at low levels and >3 ms^{-1} above. (e) Mean standard deviation of simulated cross-line relative velocity, contours intervals of 0.2 ms^{-1}. These 2D cross sections are defined considering the box A'B'C'D' of the fig 1.a for the simulation, and ABCD of the fig 1.b.1 for the observation.

Both CFADs show a high distribution of heavier precipitations at low level associated with downdrafts. We find again the same differences as before (cf 4.b). The reflectivity values are weaker for the observations, the simulated downdrafts are less pronounced and the vertical extension of the system is greater for the observations. The reflectivity decrease with increasing height and with increasing vertical velocity in both cases. For the observation, the iso-0° is characterized by a rupture of the reflectivity's slope at 4.3 km.

5. Conclusions

In order to validate the Meso-NH model, we compare a simulated tropical squall line with the observations made during the TOGA-COARE experiment for the case of the 22th february. The simulation shows good agreement with the observed line, except that the convective system simulated is less developed vertically than in the observations and that the stratiform region is less extended at the rear of the line. This fact can be understood in term of ice processes. Indeed, the present version of the model does not contain any ice parametrisation scheme, whereas ice microphysics significantly influences the strength of the convectively-induced cold pool leading to a more consistent updraft. It also prevents the rain particles from falling right away, extending the size of the stratiform region.

However, these results are encouraging, and they display the complementarity between observations and simulations for the description of dynamics, thermodynamics and microphysics of convective systems.

These comparisons represent the first part of a more general study which goal is to initialize the model with a three dimensional mesoscale wind field retrieved from multiple Doppler radar.

6. Acknowledgments

The authors express their appreciation to F.Marks, P.Willis and R.Black of NOAA/AOMI, Miami, for providing the experimental DSD used for the retrieval of the equation 4.a.

7. References

Lipps, F.B., and R.S. Helmer, 1982: A scale analysis of deep moist convection and some related numerical calculations, *J. Atmos. Sci.*, 39, 2192-2210.

Redelperger, J.L., and G. Sommeria, 1986: Three-dimensional simulation of a convective storm: sensitivity studies on subgrid parametrization and spatial resolution, *J. Atmos. Sci.*, 43, 2619-2635.

Redelsperger, J.L., and J.P. Lafore: A three-dimensional simulation of a tropical squall line: Convective organization and thermodynamics vertical transport, *J. Atmos. Sci.*, 45, 1334-1356.

Scialom, G., and Y. Lemaître, 1990: A new analysis for the retrieval of a three-dimensional mesoscale wind fields from multiple Doppler radar, *J. Atmos. and Ocean. Tec.*, vol 7, 640-665.

Trier, S.B., W.C. Skamarock, M.A. LeMone and D.B. Parsons, 1996: Structure and evolution of the 22th february 1993 TOGA-COARE squall line: Numerical simulations, *submitted to Mont Wea. Rev.*

Webster, P.J., and R. Lukas, 1992: TOGA-COARE: The Coupled Ocean-Atmosphere Response Experiment, *Bull. Amer. Soc.*, 1377-1416.

Yuter, S.E. and R. Houze, 1995: Three-dimensional kinematic and microphysical evolution of Florida cumulonimbus, *Amer. Meteor. Soc.*, 1941-1963.

ON THE NUMERICAL SIMULATION OF THE 10 MAY 1993 HAIL STORM USING THE UNIVERSITY OF BUENOS AIRES TWO DIMENSIONAL CONVECTIVE MODEL.

Marcela Torres Brizuela - Matilde Nicolini
-Depto de Ciencias de la Atmósfera. Universidad de Buenos Aires (UBA)-
-Centro de Investigaciones del Mar y la Atmósfera- UBA/CONICET
-Buenos Aires, Argentina-

1. INTRODUCTION

Several studies have been primarily directed toward improving the forecasting of hail storms and icing conditions such as: Farley, 1985. Such storms are very dangerous for its consequences.

The objective of this research is to improve the prognostic of this situations with a numerical model, with simple computational requirements, such as a PC-486.

A bidimensional deep convective model developed at the University of Buenos Aires (UBACM) (Nicolini and Paegle, 1979) has been applied to a severe hail storm occurred on 10 May 1993 in the suburban area of General Rodriguez, Buenos Aires (Argentina).

2. OBSERVATIONS

This event was studied using the synoptic analyses, soundings and satellite images provided by the National Weather Service. Damages on roof buildings and crops were reported by the local newspapers.

The thunderstorm developed during the morning hours and had a duration of near half of an hour. The strong damages in the area were caused by the impact of graupel/hail as big as tennis balls and also by the force of the wind. At the surface, environmental winds were weak.

The closest soundings available for this study were from Ezeiza, Buenos Aires at 00 and 12 UTC 10 May 1993, but the 12 UTC has been used for considering it more representative of the prestorm environment.

3. MODEL DESCRIPTION AND SETUP

The UBACM is a two dimensional deep convective model which uses the anelastic approximation according to Lipps and Hemler (1982). The motion is supposed to be confined into a vertical plane and Coriolis is not included. The model uses a first order turbulence closure. Expressions for the time and spatial dependent eddy diffusion coefficients are derived and included in the system of equations governing moist deep convection.

Cloud microphysical parameterization follows Lin et al (1983) criterium, in which specific humidities for five different condensed water categories are included. These categories are: cloud droplets (q_c), rain water (q_r), cloud ice (q_i), snow (q_s), and graupel/hail (q_g).

The integration domain is 39 km in the horizontal direction and 15 km in the vertical. The grid intervals at both horizontal and vertical direction are uniform and equal to 600 m whereas the time grid interval is of 10 s.

The model was initiated with a thermal bubble centered at the numerical domain.

4. MODEL RESULTS

Temporal evolution of maximum vertical velocity is presented in Figure 1. The simulated storm updraft evolves very quickly and approaches its maximum intensity of 20 m/s within the first 15 min. Maximum downdrafts attains -10 m/s within the rain core. The maximum cloud and rain water evolution are displayed in Figure 2. The maximum for the cloud water occurs at the same time of the maximum updraft (see Fig.1 and 2). The second peak in the curve of maximum rain water is achieved at the time it is reaching the ground.

Figure 3 displays the maximum contents of graupel/hail, snow and cloud ice. The intense growth of the graupel/hail category prevails over the others. This result is consistent with the observed storm characteristics. The maximum of q_g (3.7 g/kg) is located at 3.9 km of

height. The graupel/hail reaches the levels near the ground at about 20 min. of integration (see Figure 4). It remains at those levels for over 10 min, but decreasing fastly its intensity. The field of graupel/hail at 23 min. of integration is shown in Figure 5. At this time corresponds the maximum of rain at surface (see Figure 6).

We notice that after 20 min of simulation the maximum graupel/hail content diminishes quickly, the values reaching the surface are small while the rain water at the surface becomes excessive. In order to explain this result, we examine the microphysical contributions to the net rate production of precipitation at the levels where q_{gmax} is verified. We find out that the main contributor term is the rate of graupel/hail melting whereas the rate evaporation is negligible. Other contribution terms in this equation are quite smaller compared to the graupel/hail melting.

An explanation for it is that the sounding taken (not shown) for the run was close to saturation from the surface to above 700 HPa. This atmospheric conditions give a simulated base cloud too low which inhibits the rain evaporation leading to the high rain water values obtained. The reduction in graupel/hail near the surface may be adressed to an unrealistic feature of the model affecting the graupel/hail melting, because of the fact that a constant N_{og} parameter is used in the formulation of the **N(r)** Marshall-Palmer distribution. Keeping N_{og} constant while the graupel/hail content decreases due to melting means essentially that the large stones are melting more rapidly than the small ones (Orville et al, 1979).

Other reasons could be the current model limitations: not inclusion of the initial wind field and the bidimensionality.

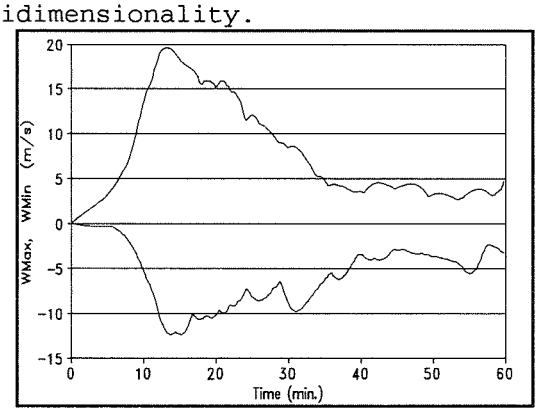

Figure 1: Temporal Evolution of Maximum Vertical Velocity

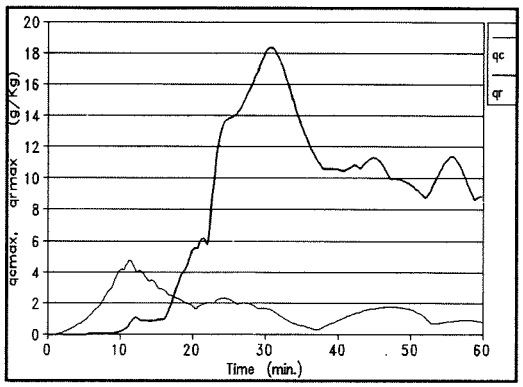

Figure 2: Temporal Evolution of Maximum Cloud Water and Rain Water

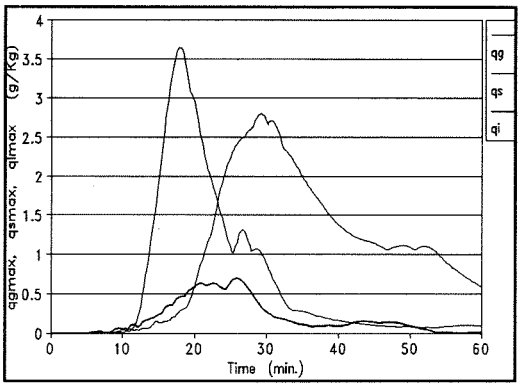

Figure 3: Temporal Evolution of Maximum Graupel/hail, snow and ice cloud Water

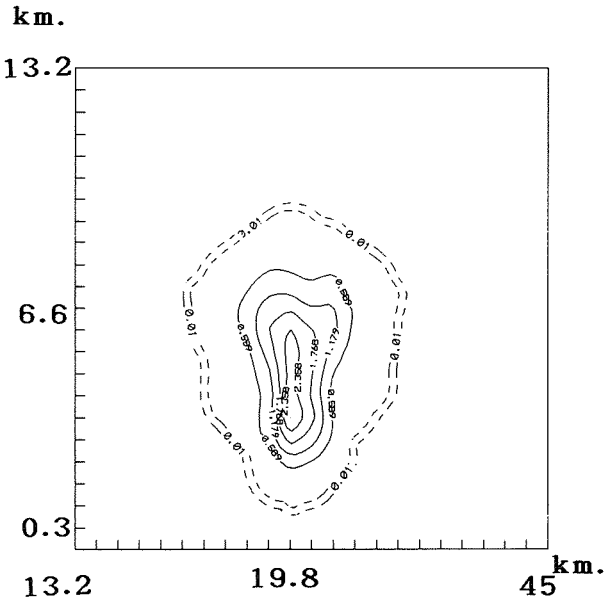

Figure 4: Graupel/Hail Field at 20 min. Bold and dashed lines represent 0.01 g/Kg. Contours lines are of 0.58 g/Kg.

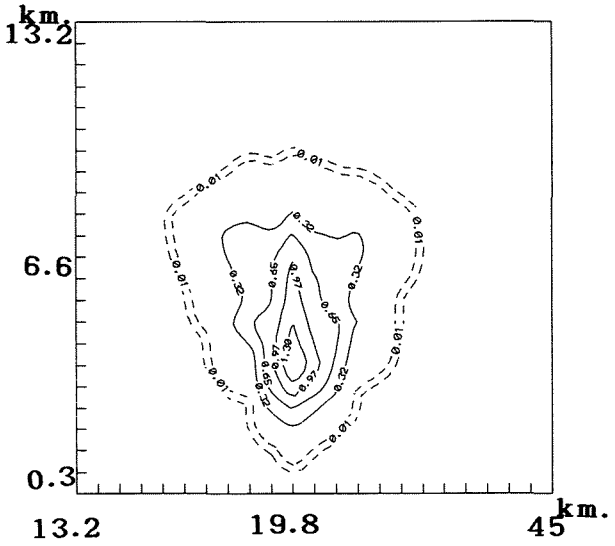

Figure 5: Graupel/Hail Field at 23 min. Bold and dashed lines represent 0.01 g/Kg. Contours lines are of 0.23 g/Kg.

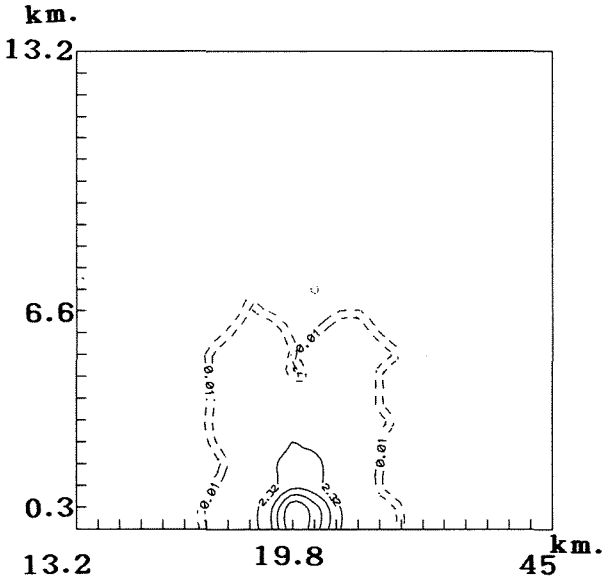

Figure 6: Rain Water Field at 23 min. Bold and dashed lines represent 0.01 g/Kg. Contours lines are of 2.32 g/Kg.

5. CONCLUDING REMARKS

Though MCUBA was able to simulate the main features of the cloud development (intense hail growing up), it underestimated the graupel/hail at the surface.

Further research is in progress to assess the capability of the UBACM with inclusion of environmental winds and/or initialization with regional modelling sounding outputs to reproduce severe convective events and eventually be used as a prediction tool in areas where radar systems are not available.

6. REFERENCES

- Farley R.D., 1985: Bulk parameterization of the snow field in a cloud model. Report of the International Cloud Modelling Workshop/Conference, Irsee Federal Republic of Germany (15-19 July 1985). WMO/TD- No. 139. 85-98

-Lipps F.B., and R.S. Hemler, 1982: A scale analysis of deep moist convection and some related numerical calculations. Journal of Atmospheric Sciences., 39, 2192-2210.

-Nicolini, M. and J. Paegle,1989: Real data deterministic forecasts of the impact of ambient vertical motion fields upon convective precipitation. Report of the Second International Cloud Modelling Workshop/Conference, Toulosse, France. WMO/TD-No 268, 207-220.

- Orville, H.D., R. D Farley, F. J Kopp, J. H. Hirsch, E. Hsieh, C. Chang and P. C. S Chen, 1979: Application of a two-dimensional cloud model to cloud seeding experiments. Report 79-4. Institute of Atmospheric Sciences South Dakota School of Mines and Technology. Rapid City, South Dakota. B1-B26.

A Sensitivity Study of the Mesoscale Characteristics of Squall-Line Systems to Environmental Conditions: Implication of Anvil Cirrus Parameterization

Hung-Neng S. Chin

Atmospheric Sciences Division
Lawrence Livermore National Laboratory

1. INTRODUCTION

Cloud-radiation feedback has been identified as the single most important effect limiting general circulation models (GCMs) to further progress in climate change research, and regarded as major uncertainties in estimating the impact of increasing concentrations of greenhouse gases on climate simulations. Therefore, it is crucially important to further understand the physical processes involved in order to improve the representation of cloud processes in GCMs. To this end, a cloud resolving model with enhanced model physics (Chin 1994; Chin *et al.* 1995) was used to study the impact of microphysics, long- and shortwave radiation on midlatitude and tropical mesoscale convective systems (MCSs).

These earlier studies indicated that a strong coupling exists in the MCSs between deep convection and its related anvil cloud through the interaction among dynamical, thermodynamical and radiative processes. They also showed that the tilting structure of MCSs (sub-GCM-grid feature) has an important contribution to the water budget of anvil clouds, particularly the tropical anvil due to the jetlike wind profile. However, most earlier GCMs did not include a direct and physically consistent representation of this coupling. To this end, Randall et al. (1989) suggested a more realistic anvil parameterization by adding prognostic cloud water (or ice) variables to account for the formation of anvil clouds from cumulus detrainment. In addition to this effort, our recent studies further suggest the need to parameterize the tilting structure of MCSs in GCMs.

The objective of this work is to parameterize the large-scale effects of an important sub-GCM-grid-scale process associated with the tilting structure of MCSs. To this end, our primary interest focuses on MCSs in an environment with substantial wind shear, such as squall-line systems, since they have longer lifetimes and wider coverage to affect the earth-atmosphere radiation budget and climate. Using varied convective available potential energy (CAPE), wind shear intensity, shear depth, and shear profile pattern (i.e., jetlike or non-jetlike wind profile) over a wide range of bulk Richardson number (Ri; Weisman and Klemp 1984) suitable for multicellular convection, a sensitivity study is performed in a cloud resolving model to link its resulting mesoscale ascent / descent with GCM-resolvable variables. The ultimate goal of this research is to develop an anvil cirrus parameterization (ACP), that will couple with cumulus parameterizations in GCMs to improve the cloud-radiation feedback on large-scale climate.

Corresponding author address: Dr. H.-N. S. Chin, P. O. Box 808 (L-103), Livermore, CA 94551.

2. MODEL AND INITIALIZATION

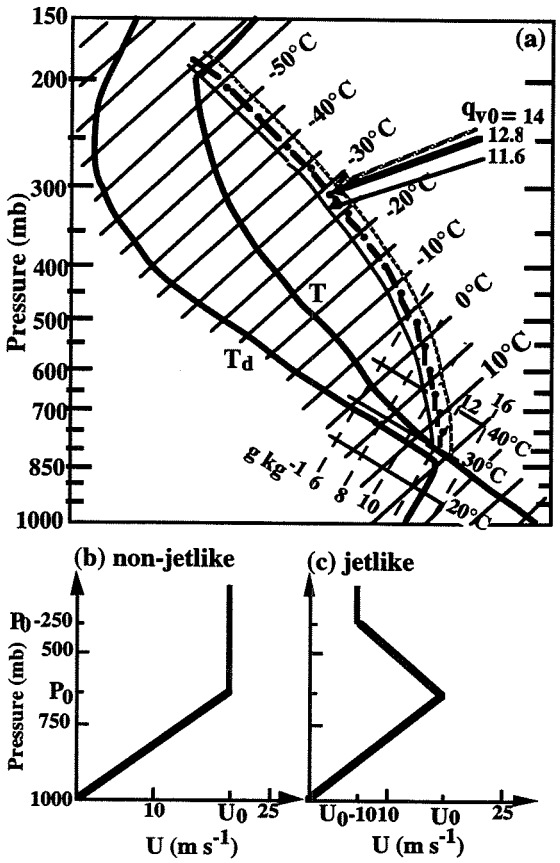

Fig. 1. The modified atmospheric composite sounding for the midlatitude broken-line squall systems. (a) temperature (T) and dewpoint temperature (T_d) profiles. moist adiabats with increasing surface mixing ratio (g kg^{-1}) of moisture represent low, medium, and high CAPE, respectively. (b) - (c) the non-jetlike and jetlike wind profiles. P_0 is set at 750 (500) mb for shallow (deep) shear layer. U_0 ranges from 10 to 25 m s^{-1}.

The model used is an extension of Chin and Ogura's (1989) two-dimensional (2-D) cloud model, which is non-hydrostatic and fully compressible. The major improvements include ice microphysics and radiation transfer schemes for long- (LW) and short-wave (SW). The modified parameterizations of ice microphysics and radiation can simulate midlatitude and tropical squall-line systems with prominent anvils and realistic mesoscale structures. The radiation schemes used can also distinguish the impacts of hydrometeor phase, size, and shape on cloud optical properties. Refer to Chin (1994) and Chin et al. (1995) for the details of model physics.

Due to the computational constraint for a large number of simulations, radiation is not considered in this sensitivity study. The prestorm conditions of this study are shown in Fig. 1, where the bulk Richardson number is chosen between 35 and 240 for multicellular convection (Weisman and Klemp 84; Fovell and Ogura 1989). The detail of these 2-D experiments is listed in Table 1, that contains a total of 36 experiments. The model is initialized by a warm, moist bubble and a horizontally homogeneous sounding.

Table 1. Design of 2-D simulations. L, M, and H stand for low (2058), medium (2704), and high (3403) CAPE (J kg^{-1}), respectively. S and D represent shallow and deep shear layer. The depth and vertical distribution of wind shear is shown in Fig. 1.

(a) Non-Jetlike Wind Profile

Experiment	1	2	3	4	5	6	7	8	9	10	11	12	13	14	15	16	17	18
CAPE	L	L	L	L	L	L	M	M	M	M	M	M	H	H	H	H	H	H
Shear Depth (R_D)	S	S	S	D	D	D	S	S	S	D	D	D	S	S	S	D	D	D
Shear Intensity (U_0)	17.5	15.0	10.0	20.0	15.0	12.5	20.0	15.0	10.0	25.0	20.0	15.0	20.0	15.0	10.0	25.0	20.0	15.0
Bulk Ri	36.9	50.2	113.	72.7	129.	186.	37.1	65.8	148.	61.0	95.0	170.	46.7	83.0	187.	76.9	120.	214.

(b) Jetlike Wind Profile

Experiment	19	20	21	22	23	24	25	26	27	28	29	30	31	32	33	34	35	36
CAPE	L	L	L	L	L	L	M	M	M	M	M	M	H	H	H	H	H	H
Shear Depth (R_D)	S	S	S	D	D	D	S	S	S	D	D	D	S	S	S	D	D	D
Shear Intensity (U_0)	17.5	15.0	12.5	20.0	15.0	12.5	20.0	15.0	12.5	25.0	20.0	15.0	20.0	15.0	12.5	25.0	20.0	15.0
Bulk Ri	50.0	71.9	112.	72.9	129.	186.	48.3	94.5	147.	61.0	95.0	170.	60.7	119.	185.	76.9	120.	214.

In addition, a 3-D simulation of the GATE 4 September 1974 squall line was performed in this research (Chin and Wilhelmson 1996). The comparison of this simulation with its 2-D counterpart is used to assess the representative of 2D-based ACP into 3-D applications to GCMs.

3. RESULTS

a. 2-D sensitivity experiments

These sensitivity experiments are used to study the dependence of mesoscale characteristics of squall-line systems on the convective instability, wind shear intensity, shear layer depth, and the pattern of shear profile. our results indicate that under constant (medium) CAPE and constant (shallow) shear layer depth of a non-jetlike wind profile, the convective strength of the simulated storm is in positive correlation with the shear intensity, while an opposite relation is found in the stratiform region (see exp7, 8, and 9 in Fig 2). With given (medium) CAPE and shear intensity, the deeper shear layer of the non-jetlike wind profile results in stronger convective activity, while it weakens the stratiform region (see exp9 and 11 in Fig. 2). Further, under constant (medium) CAPE and constant velocity difference (U_0) of the shear layer for the non-jetlike wind profile, the deeper shear layer (i.e., weaker shear) leads to stronger convective updraft, stratiform descent, and weaker stratiform ascent (see exp7 and 11 in Fig. 2). Similar findings are also seen in each comparison for low and high CAPE, deep shear depth, and the jetlike wind profile, respectively.

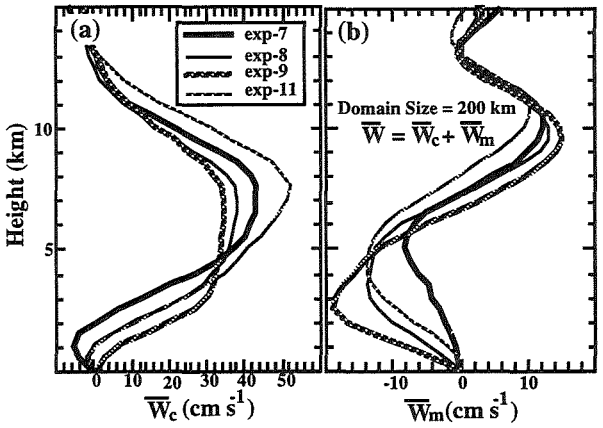

Fig. 2. Vertical profiles of horizontally-averaged vertical velocity for experiment 7, 8 , 9, and 11. The averaging domain is selected from the leading edge to the upshear side for 200 km wide. (a) in the convective region. (b) in the stratiform region.

The scatter diagram of horizontally-averaged maximum stratiform ascent and Ri (Fig. 3) clearly exhibits a close correlation between maximum stratiform ascent and Ri for any given CAPE, shear depth, and shear profile. Another interesting feature of this scatter diagram is attributed to the prominent separation of two different regimes, which are related to the low and deep shear depth cases. In addition, the stratiform ascent is intensified by the jetlike shear profile and the increasing CAPE; however, these two impacts seems to be weaker than the one caused by the shear depth. All of the features aforementioned related

to the stratiform ascent are also seen in its descent counterpart (not shown).

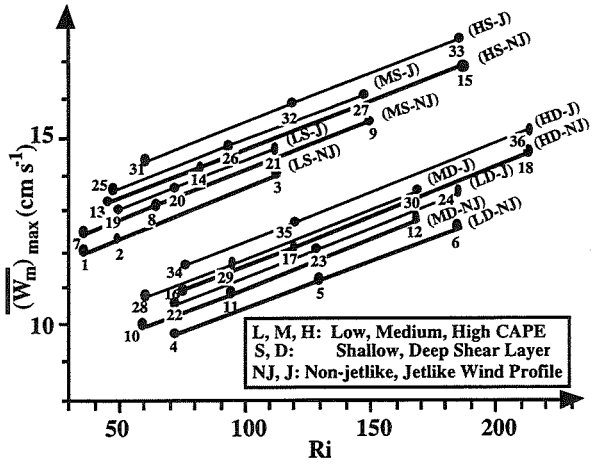

Fig. 3. Horizontally-averaged maximum stratiform ascent strength ($(\overline{W_m})_{max}$) versus the bulk Richardson number (Ri) for varied convective available potential energy (CAPE), wind shear intensity, shear depth, and shear profile pattern for multicellular storms. The numbers beside the dots represent the experiments, listed in Table 1.

In general, our results indicate that the stratiform (convective) ascent / descent is strengthened (weakened) with the increasing bulk Richardson number, except the cases involved in varied shear depths. This suggests that the shallow shear depth case should be treated differently in the ACP from its deep depth counterpart. As compared to the tropical MCS environment, the deep shear depth is a typical representative of most midlatitude cases. As a result of the secondary impact of CAPE and shear profile pattern on the stratiform ascent / descent, the upper regime of Fig. 3 may represent the general mesoscale characteristics of tropical MCSs, and the lower one fits the midlatitude cases. However, this suggestion needs more validations for the tropical case before we can generalize the large-scale effects of the sub-GCM-grid process of concern.

b. 3-D simulation and its comparison with 2-D results

To calibrate our 2D-based ACP into 3-D applications, we performed a 3-D simulation of the GATE 4 September 1974 squall line (Chin and Wilhelmson 1996). This 3-D simulation replicates many observed features (Houze 1977), such as the arc-shaped rainband structure and its orientation normal to the principal wind shear (Fig. 4). The comparison of 3-D and 2-D simulations in the multicellular portion of the modeled GATE storm exhibits strong similarity at the dynamical structure, except the difference at the magnitude (Fig. 5). More case studies of 3-D simulations for midlatitude MCSs are also being undertaken to establish the relationship between 3-D and 2-D simulation as the physical basis for the 3-D applications of the ACP.

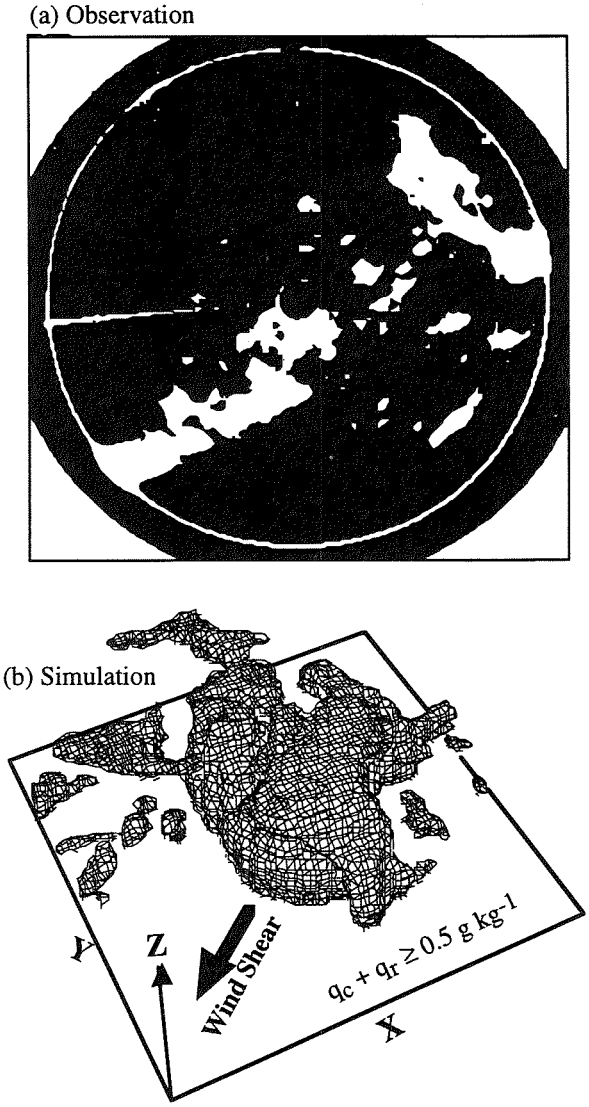

Fig. 4. (a) Radar image taken from the ship Oceanographer at 1015 UTC September 4 1974. The radius of the radar scope is 200 km. (b) 3-D depiction of the isosurface at 0.5 g kg^{-1} for the total water mixing ratio of the control run at 4 hour of simulation time. The arrow denotes the principal wind shear of environmental winds below 4 km.

4. SUMMARY AND DISCUSSION

Our results suggest that the bulk Richardson number is a valuable index to categorize the mesoscale characteristics of MCSs. Therefore, it might be feasible to parameterize the sub-GCM-grid process associated with the tilting structure of MCS.

Due to the computational constraint, we are developing our ACP, based on 2-D simulations. Nonetheless, the strong similarity of resolved mesoscale structure of MCSs between 3-D and 2-D

models suggests a promising clue to calibrate the 2D-based ACP into 3-D applications to GCM.

ACKNOWLEDGMENTS. This work was supported by the Department of Energy (DOE) ARM (Atmospheric Radiation Measurement) program and conducted under the auspices of the U. S. DOE by the Lawrence Livermore National Laboratory under contract No. W-7405-ENG-48.

REFERENCES:

Chin, H.-N. S., and Y. Ogura, 1989: Supplementary modeling study of a tropical convective band. *J. Atmos. Sci.*, **46**, 1440-1447.

Chin, H.-N. S., 1994: The impact of the ice phase and radiation on a mid-latitude squall line. *J. Atmos. Sci.*, **51**, 3320-3343.

Chin, H.-N. S., Q. Fu, M. M. Bradley, and C. R. Molenkamp, 1995: Modeling of a tropical squall line in two dimensions: Sensitivity to radiation and comparison with a midlatitude case. *J. Atmos. Sci.*, **52**, 3172-3193.

Chin, H.-N. S., and R. B. Wilhelmson, 1996: Modeling of a tropical squall line in three dimensions: The arc-shaped rainband structure sustained by a supercell-like storm. *J. Atmos. Sci.*, (to be submitted).

Fovell, R. G., and Y. Ogura, 1989: Numerical simulation of a midlatitude squall line in two dimensions. *J. Atmos. Sci.*, **46**, 3144-3176.

Houze, R. A., Jr., 1977: Structure and dynamics of a tropical squall-line system. *Mon. Wea. Rev.*, **105**, 1540-1567.

Randall, O. A., Harshvardhan, D. A. Dazlich, and T. G. Corsetti, 1989: Interactions among radiation, convection, and large-scale dynamics in a general circulation model. *J. Atmos. Sci.*, **46**, 1943-1970.

Weisman, M. L., and J. B. Klemp, 1984: The dependence of numerically simulated convective storms on vertical wind shear and buoyancy. *Mon. Wea. Rev.*, **110**, 504-520.

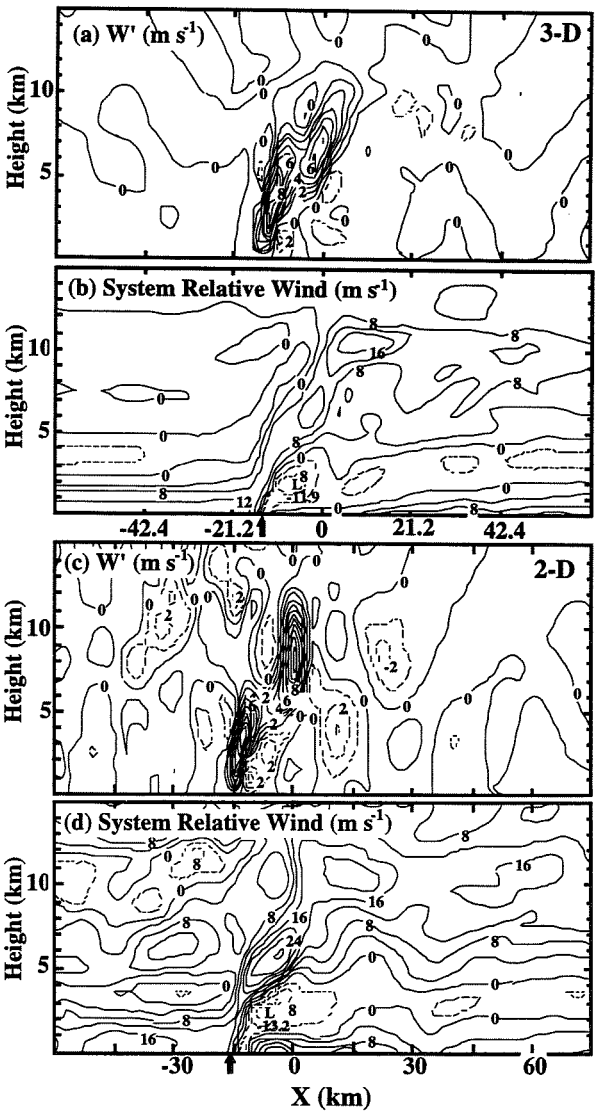

Fig. 5. Crosssections in the vertical-horizontal plane of induced vertical velocity and system-relative horizontal velocity in intervals of 1 and 4 m s^{-1}, respectively, at 4 hour of simulation time. (a) and (b) 3-D simulation. (c), (d) 2-D simulation.

NUMERICAL SIMULATIONS OF TROPICAL CONVECTIVE CLOUDS OVER CUBA USING A ONE-DIMENSIONAL AND TIME-DEPENDENT CLOUD MODEL.

Lester Alfonso, Daniel Martinez and Carlos A. Pérez.

Cloud Physics Dept, Institute of Meteorology, C.P. 11700, Cuba

1.INTRODUCTION.

The goal of our research is to increase our understanding of the dependence of the tropical convective cloud properties upon the environmental conditions.

In particular, we would like to determine the influence of the humidity interchange in the convective develoopment over Cuba.

With this aim, we used a one-dimensional and time-dependent cloud model with parameterized microphysics.

2.THE NUMERICAL MODEL

The model is based upon the one developed by Shiino (1978). The cloud is modelled as a radially symmetric cylindrical air column with the environment at rest.

All equations are formulated in one dimensional space in a manner similar to that of Asai and Kasahara (1967) and Ogura and Takahashi (1971) with respect to the modelling of dynamical terms.

The model consists of the vertical equation of motion, the mass continuity equation, the thermodynamis equation and the continuity equations for water vapor, cloud water, rain water and precipitation ice.

2.1 EQUATIONS OF THE MODEL

Vertical velocity equation:

$$\frac{\partial w}{\partial t} = -w\frac{\partial w}{\partial z} - \frac{2\alpha^2}{a}|w|w + \frac{2}{a}u_a(w-w_a)$$

$$+\frac{1}{\rho_{a0}}\frac{\partial}{\partial z}(k_v\frac{\partial w}{\partial z}) + g\frac{T_v-T_{v0}}{T_{v0}}$$

$$-g(Q_c+Q_r+Q_i) \qquad (1)$$

The continuity equation:

$$\frac{2}{a}u_a + \frac{1}{\rho_{a0}}\frac{\partial}{\partial z}(\rho_{a0}w) = 0 \qquad (2)$$

The thermodynamic equation:

$$\frac{\partial T}{\partial t} = -w(\frac{\partial T}{\partial z}-\Gamma_d) - 2\frac{\alpha^2}{a}|w|(T-T_0)$$

$$+\frac{2}{a}u_a(T-T_a)$$

$$+\frac{1}{\rho_{a0}}\frac{\partial}{\partial z}(K_v\frac{\partial T}{\partial z}) + F_t \qquad (3)$$

The continuity equations for water vapor and precipitation water are:

$$\frac{\partial Q_v}{\partial t} = -w\frac{\partial Q_v}{\partial z} - 2\frac{\alpha^2}{a}|w|(Q_v-Q_0)$$

$$+\frac{2}{a}u_a(Q_v-Q_{va})$$

$$+\frac{1}{\rho_{a0}}\frac{\partial}{\partial z}(K_v\frac{\partial Q_v}{\partial z}) + F_t$$

$$\frac{\partial Q_r}{\partial t} = -(w-V_r)\frac{\partial Q_r}{\partial z} - \frac{2\alpha^2}{a}|w|(Q_r-Q_{r0})$$

$$+\frac{2}{a}u_a(Q_r-Q_{a0})$$

$$+\frac{Q_r}{\rho_{a0}}\frac{\partial}{\partial z}(\rho_{a0}V_r)+F_r \qquad (5)$$

The continuity equation for cloud ice is similar to the vapor one, and the equation for the precipitation ice is similar to the precipitation water. Ft, Fv y Fr are the microphysical processes. Vr y Vi are the terminal velocities of rain droos and precipitation ice. In all the equations **a** is the radius of the updraft, the magnitudes with subscripts **a** denote values at the radial distance **a**, and the ones with 'zero', environmental ones.We assume that the size distribution of raindrops is represented by the Marshall-Palmer distribution:

$$n_D=n_0e^{-\lambda D} \qquad (6)$$

2.2 MICROPHYSICAL PROCESSES.

Ten microphysical processes are treated: condensation, autoconversion and collection, glaciation (heterogeneous freezing), sublimation, melting, evaporation of cloud droplets, evaporation of rain drops, evaporation of ice crystal, evaporation of melting ice crystal, evaporation of melting ice crystal and riming. The autoconversion coefficient we used in the Kessler's autoconversion equation is 10-3sec-1 (Shiino (1978) used an autoconversion coefficient of 10-3sec-1). We used a larger than Shiino (1978) autoconversion coefficient in the autoconversion equation in order to reduce the lifetime of the simulated clouds (Ogura and Takahashi, 1971). We can also regulate the lifetime by varying the treshold cloud water content wherein the autoconversion begins (Orville, Kopp and Myers, 1975).

3.NUMERICAL EXPERIMENTS.

For modelling convective clouds over Cuba we used soundings made in Camagüey Meteorological Site in 1987. When the model was applied to actual meteorological situations consistently underpredicted cloud top heights and lifetime.We carefully tested the influence of each term of the equation of motion and the conservation equations and we found that the dynamical entrainment term in the continuity equation for water vapor (third in the right hand side of the equation), has a great responsibility in this underprediction.Asai and Kasahara (1967), Ogura and Takahashi (1971) and Shiino (1978) assumed that the cloud properties at the radial distance are assumed to be

$$A_a=A_0$$

if

$$u_a<0$$

and

$$u_a>0$$

if

$$A_a=A$$

Cotton (1975) slightly modified this assumption. He diagnosed the cloud properties at the radial distance by a vector flux weighted mean. As we pointed out, we found that the dynamical entrainment term of the water vapor equation is the most important in underoprediction of the cloud top height. The strong intrusion of dry air in the zone with negative radial velocity is not realistic, as a matter of fact, the importance of lateral entrainment in classical models was overevaluated (Paluch, 1979; Perez et. al. 1992). That's why we diagnose the water vapor properties at the cloud edge by using the relationship:

$$Q_{va}=\beta Q_{v0}+(1-\beta)Q_v \qquad (7)$$

Similar to Cotton's (1975) relation. For calculating the weighting parameter β, Cotton used the horizontal and vertical flux contributions. Our approach is not so complex. In our calculations β is a constant with values between 0 and 1.

With β=1 we obtain the expression for calculating the water vapor at the radial distance used by Shiino (1978), and a maximun interchange of humidity with the environment, for β=0, the cloud is protected from the intrusion of dry air from the environment. For calculating the other cloud properties the relation was not modified.

In the present work we present the result of numerical simulations with three soundings made over

the Camagüey Meteorological Site the days 1-07-87, 3-07-87 and 31-07-87 at 1600GMT.

The soundings we selected correspond to different thermodynamical conditions over the sounding area (see Fig 1 A and B). We used three values of β in our simulations (0.1, 0.5, 1.0). A strong decrease of top height in simulated clouds with the increase of β was observed, it reflects the importance of the dynamical entrainment term in the vertical development of the cloud.

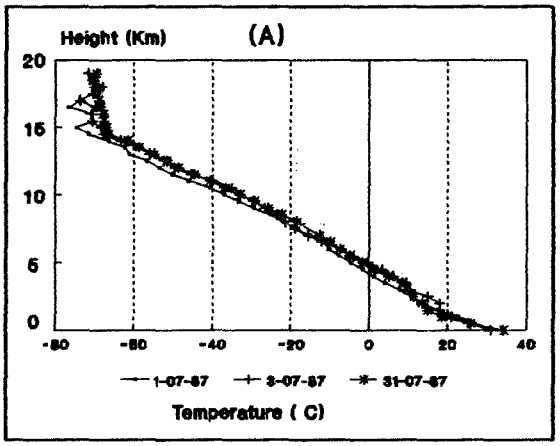

Fig. 1A. Soundings. Vertical profiles of temperature for each day.

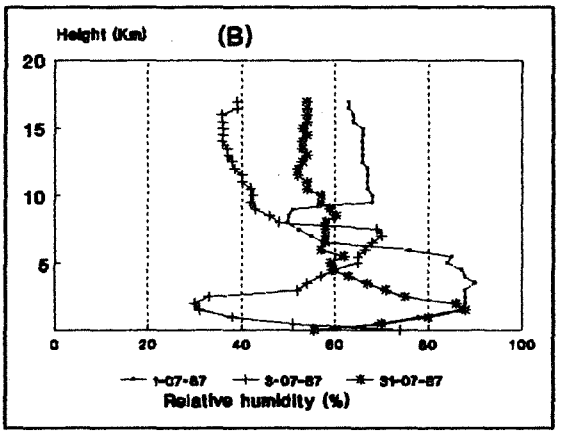

Fig. 1B. Soundings. Relative humidity vertical profiles for each day.

The Table 1 reflects the decrease of the maximun values of cloud and precipitation water while increasing β. This is because of the intensification of the evaporation process as a result of the intrusion of dry air from the environment.

Table 1. Dependence of some characteristics of simulated clouds for different days , on the coeficiente β, for a radius of 1.5 km.

Date	β	HTmax km	Wmax m/s	Qmax g/kg	QRmax g/kg
1-07-87	0.1	14.00	28.1	4.36	4.74
	0.5	8.50	18.9	3.45	4.86
	1.0	6.25	12.9	2.80	3.64
3-07-87	0.1	2.50	12.7	2.32	2.80
	0.5	2.25	10.6	1.53	0.26
	1.0	2.25	9.3	1.50	0.05
31-07-87	0.1	10.00	20.3	4.28	7.22
	0.5	4.00	15.2	3.29	12.56
	1.0	3.00	12.4	2.62	8.21

Comparison of top height of simulated clouds for different values of β, with real radar data showed a correspondence between the model's predictions and the meteorological situation for each day (See Fig.2, the most active day (1-07-87) has the larger values of covered area). However, by analysing the results of the numerical simulations for 1-07-87, which was a very active day, we observed an overoprediction of the lifetime for β=0.1, even for a so active autoconversion process. We can infer the lifetime values, by analysing the time when the top height was reached (See table.3 for 1-07-87 day), for β=0.1 and radius 3.0 Km it was about 90 min. We don't present a similar table for 3-07-87 and 31-07-87, but the lifetime was overpredicted too for β=0.1, for β=0.5 the situation was normal. For β=1.0 the lifetime values obtained were acceptable, but at the same time there is an underprediction of the top height.

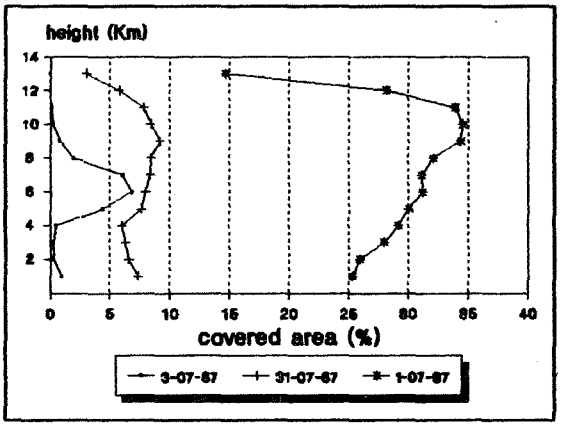

Fig. 2. Convective clouds covered area vertical profiles for each day.

The values of vertical velocity, cloud and precipitation water for β=0.5 during days with deep convection activity, have a good correspondence with measured values in Cg and Cb during field experiments in the Camagüey Meteorological Site, (Martinez et. al., 1992). However, for weak convection situations, there is an overprediction of these values. Tables 2 and 3 reflect the dependence of model predictions with cloud radius. We made numerical simulations with two values: 1.5 Km and 3.0 Km. By increasing the cloud radius we observed an increase of top height, and maximun values of vertical velocity, cloud and precipitation water for a fixed β.

Table 2. Dependence of some characteristics of simulated clouds on radius, for β = 0.5

Day	Radius km	HTmax km	Wmax m/s	Qcmax g/kg	QRmax g/kg
1-07-87	1.5	8.50	18.9	3.45	4.86
	3.0	15.75	23.8	3.68	7.60
3-07-87	1.5	2.25	10.6	1.53	0.26
	3.0	2.50	11.3	1.91	0.49
31-07-87	1.5	4.00	15.2	3.29	12.56
	3.0	7.50	17.1	3.60	2.08

Table 3. Maximun values of some characteristics of the simulated clouds and the height and time they were obtained for different β and radius of the updraft, for the day 1-07-87.

Radius km	β	HTmax km	height km	time min.	Wmax m/s	height km	time min.
1.5	0.1	15.75		79.91	28.2	6.0	9.25
	0.5	9.00		22.91	18.9	5.5	9.67
	1.0	6.50		19.91	12.9	2.25	3.91
3.0	0.1	15.75		90.00	42.17	11.5	13.0
	0.5	14.75		31.91	23.69	6.0	9.68
	1.0	7.00		19.91	13.99	4.0	7.41

Radius km	β	Qcmax g/kg	height km	time min.	Qrmax g/kg	height km	time min.
1.5	0.1	2.29	4.75	7.41	6.03	6.5	10.75
	0.5	1.88	3.75	6.5	6.99	5.0	40.50
	1.0	1.57	3.00	5.33	4.01	4.25	40.50
3.0	0.1	2.54	5.25	7.5	5.86	8.5	69.58
	0.5	2.00	4.00	6.58	6.88	4.25	49.3
	1.0	1.64	3.50	6.16	5.00	4.25	19.5

4.CONCLUSIONS

In general, the model was found to be sensitive to different tropical atmospheric conditions. To determine the dependence of cloud parameters upon different dynamical entrainment regimes an expression for calculating the water vapor at the radial distance was proposed.

For each sounding a strong influence of the humidity transport in the development of this clouds was found.

ACKNOWLEDGMENTS

We would like to thank Mrs Graciela Angulo and Miss Consuelo Fernández for analysing the radar data we used in this work.

REFERENCES

Asai, T. and Kasahara, 1967: A theoretical study of the compensating downward motions associated with cumulus clouds. J. Atmos. Sci., 24, 187-196.

Cotton, W.R., 1975: On parameterization of turbulent transport in cumulus clouds. J. Atmos. Sci.,32, 548-564.

Martinez D., C.A. Pérez, R. Aroche, V.P. Beliaev y V.V. Volkov 1995: Espectros de potencia de la velocidad del viento en las nubes convectivas tropicales sobre Cuba. Atmósfera, 8, pp. 65-80.

Ogura, Y. and T. Takahashi. 1971: Numerical simulation of the life cycle of a thunderstorm cell. Mon. Wea. Rev., 99, 895-911.

Orville H.D., Kopp F.J., Myers C.G., 1975: The dynamics and thermodynamics of precipitating loading. Pageoph., Vol. 113., 983-1004.

Paluch I. R. 1979: The entrainment mechanisms in Colorado cumuli. Jour. Atmos. Sci., 36:2467-2478.

Pérez C.A., Martinez D. and Petrov V.V. 1992: Microstructure, mixing and turbulence in cumulus clouds over Cuba and the caribbean Sea. Proceedings WMO Workshop on Cloud Micriphysics and Applications to global Change. WMO/TD No. 537, pp. 245-256.

Shiino J, 1978: A numerical study of precipitation development in cumulus clouds. Papers in Meteorology and Geophysics, 29, 4, pp. 157-194.

THE ROLE OF ICE GENERATION IN PRECIPITATION FORMATION AS SEEN FROM THE RESULTS OBTAINED USING A MIXED-PHASE CLOUD MODEL WITH SPECTRAL MICROPHYSICS

I. L. Sednev, M.B. Pinsky, A. P. Khain and D. Rosenfeld

The Hebrew University of Jerusalem, Jerusalem 91904, Israel

1. INTRODUCTION

Due to mathematical difficulties and many uncertainties of cloud microphysics there are only a few mixed phase cloud models based on solving stochastic equations for size distribution functions of water (cloud and rain) drops, and ice particles (see, Khain et al., 1993; Khain and Sednev,1995 and corresponding references).

Here a brief description of a mixed phase two-dimensional cloud model, based on the spectral microphysics scheme is presented.

2. CLOUD MODEL

The model is based on a non-hydrostatic equation system of deep convection, the vertical size of the computational domain is of 16 km with resolution 300 m. The horizontal size of the model grid and the horizontal resolution depend on the phenomena to be simulated. The variables of the model are: wind velocity (u,v,w), virtual potential temperature θ_v , mixing ratio q, the number density distribution function for cloud condensation nuclei (CCN) and seven number density distribution functions for water drops, ice crystals of three types (columnar, plate-like and dendrites), snowflakes, graupel and frozen drops/hail. Expressions for bulk densities, the diameter-length and thickness-diameter relations for ice crystals and expressions for the fall velocity of hydrometeors are taken mainly from Pruppacher and Klett. Model microphysics is based on solving kinetic equations for size (mass) distribution functions describing seven types of hydrometeors f_i (i=1,...7):

$$\frac{\partial f_i}{\partial t} + u\frac{\partial f_i}{\partial z} + (w - V_i)\frac{\partial f_i}{\partial z} = [\frac{\partial f_i}{\partial t}]_{\substack{cond\\evap}} + [\frac{\partial f_i}{\partial t}]_{coal} +$$

$$+ [\frac{\partial f_i}{\partial t}]_{nucl} + [\frac{\partial f_i}{\partial t}]_{freez} + [\frac{\partial f_i}{\partial t}]_{melt} + [\frac{\partial f_i}{\partial t}]_{break} + Turb,$$

where $[\frac{\partial f_i}{\partial t}]_{nucl}$, $[\frac{\partial f_i}{\partial t}]_{\substack{cond\\evap}}$, $[\frac{\partial f_i}{\partial t}]_{coal}$ are the rates of change of f_i due to nucleation, condensational growth or evaporation of drops (for i=1) or the condensational freezing and sublimation of ice particles (for i>1). and due to coalescence processes, $[\frac{\partial f_i}{\partial t}]_{freez}$, $[\frac{\partial f_i}{\partial t}]_{melt}$ and $[\frac{\partial f_i}{\partial t}]_{break}$ are the rates of change of f_i due to the freezing of droplets and melting of ice particles and breakup processes. Vi are fall velocities of hydrometeors.

Activation of cloud condensational nuclei (CCN) is carried out in a way similar to that in the work by Flossmann et al.(1985): using the value of supersaturation the size of activated drops is calculated by the size of corresponding CCN. CCN population is described using the size distribution function f_{CCN} containing 43 size (mass) categories with the maximum CCN mass equal to the minimum mass of a drop in the drop spectrum (the minimum radius is 2 μm). A modified gamma distribution was used to describe the size distribution of the aerosol (CCN) particles subjected to nucleation.

Formation of ice crystals is proceed in three ways. 1) The primary nucleation, the rate of which is chosen according to Scott and Hobbs (1977). The nucleation is assumed to take place only for those types of ice crystals, which have a dominant growth rate at corresponding temperatures (Takahashi et al., 1991). A special distribution function for ice nuclei is used which contains several bins of ice nuclei according to the temperature of nucleation. 2) Ice nucleation via drop freezing is determined by the formulae of probability freezing used at temperatures below -10 ^oC . 3) Ice multiplication is assumed to take place during interactions of supercooled drops with graupel and drop and frozen drops. A small part of the collisions is assumed lead to no coalescence, but to the formation of ice crystals with mass of corresponding supercooled drops. The part is determined using observed data (Mossop, 1976) and provides concentrations consisting with the observed data in clouds (Hobbs, 1990). Temperature range of this process is determined according to Hallett-Mossop's observed data.

During *melting* ice particles of all types, except hailstones, are assumed to be transformed into water drops of the same mass inside the first model layer below the level of 0 ^oC. Transformation of hailstones into water drops is assumed to take place at the end of the 'melting

length'. The melting length is the distance between the T=273 K level and the level where hailstones of a particular category are considered to melt.

The rate of change of the mixing ratio and potential temperature due to the condensational growth/evaporation of drops and to the deposition /sublimation of ice particles is described similar to that in Rogers and Yau (1989), Van der Veen (1990) and Kogan (1991). The equations for the growth of single drops or ice particles are solved, along with the system of equations for supersaturation with respect to water and ice.

The term $[\frac{\partial f_i}{\partial t}]_{coal}$ is calculated solving a *system of stochastic coagulation equations* for 7 size (mass) distribution functions for hydrometeors of 7 types. The following interactions between water drops and ice particles are assumed: 1. Water drops - water drops: new particles are water drops. 2. Water drops - crystals: if the mass of drops is less than that of crystals new crystals are formed, otherwise, either graupel or hail are formed depending on air temperature. 3. Water drops - snowflakes collisions: if the mass of drops is less than that of snowflakes new snowflakes are formed, otherwise graupel or hail are formed depending on temperature. 4. Water drops - graupel: either graupel or hail are formed depending on air temperature. 5. Water drops - hail collision: the result is hailstone formation.

The following interactions between ice particles are assumed: 1. Ice crystal - ice crystal: snowflakes are formed. 2. Ice crystal - snowflake: snowflakes are formed. 3. Ice crystal - graupel collision leads to graupel formation if the mass of graupel is greater than that of crystals, otherwise crystals are formed. 4. Ice crystal - hail collision: graupel or hail particles are formed depending on air temperature if the mass of hails is greater than that of crystals, otherwise, crystals are formed.5. Snowflake - snowflake collision results in snowflake formation.6. Snowflake - graupel collision will lead either to snowflake (if its mass is greater than that of graupel) or to graupel formation. 7. Snowflake - hail collision will lead to snowflake if its mass is greater than that of the hail particle. Otherwise, this collision leads either to graupel or hail formation depending on temperature. 8. Graupel-graupel collision leads to graupel formation. There was assumed that there is no graupel- hail and hail-hail collisions.

Transformation of snow to graupel for each mass category is determined by the rate of riming. If riming is so fast that during a certain (5 min) time period the mass of particular snow category would be increased more than twice, some part of the snow of this mass category is transferred to graupel. The same algorithm was used for transformation of frozen drops to graupel.

Calculations of stochastic coalescence are carried out using the Berry and Reinhard (1974) method. We use 43 mass categories for the description of the mass spectra of hydrometeors of all types.

The maximum mass in the spectra grid corresponds to a water drop with the radius of 3.25 cm. The computation of hydrometeors' spectra evolution is carried out for the mass density function $G(\ln r)=3m^2 f(m)$. In case of ice particles r is their melted radius. For the simulation of *water drops' collision* the values of collision efficiencies were taken similar to those employed by Hall (1980). Collection efficiencies for water drops has been used according to Beard and Ochs (1984). Coalescence efficiencies for *columnar crystals- water drop collisions* are introduced using the theoretical data obtained by Schlamp (1975). For ice plate-drop collisions these efficiencies are based on the computations carried out by Pitter (1977)(Pruppacher and Klett, 1978). The results of theoretical studies by Lew and Pruppacher (1983) and Lew et al.(1985) were used for the determination of the capture efficiency of small columnar and small planar ice crystals by large water drops (with the radii greater than 100 μm). Collision efficiencies of *water drops and other types of ice (dendrites, snowflakes, graupel and hail)* are set equal to those used for ice-plate collisions. The collection efficiency *of crystal-ice crystal interactions* are described as in Khain and Sednev (1995).

Turbulence effects. As it was shown by Khain and Pinsky (1995), Pinsky and Khain (1995a,b), Khain and Pinsky (1996) (in the present issue) that in spite of the fact that the inertia of drops is small, it causes a significant relative velocity between drops and the surrounding air within a turbulent atmosphere which, for small drops, can be of the same order of magnitude as their terminal fall velocities. As a result, the significant turbulence-induced relative velocity between drops occurs due to differences in their inertia. The increase in the relative velocity causes the increase in a number of collisions per unit of time (or an increase in the swept volume). It was demonstrated that inertia of droplets can cause substantial droplet spectrum broadening in a turbulent atmosphere. It was also stressed that the corresponding turbulent effects in case of both drop-ice interaction and collisions of crystals and snowflakes will be substantially stronger than in case of water drops because of the greater inertia of the ice particles accompanied by a comparatively smaller still air fall velocity.

As an example, in Figure 1 the ratios of the root mean square values of relative velocity $(\Delta V'^2_{turb})^{1/2}$ induced by the particle inertia to the relative velocity ΔV_t induced by the gravity are presented for case of (a) drop-drop collisions and (b) graupel-drop collisions. Calculations were carried out using a method described in Pinsky and Khain (1996) in detail. The dissipation rate of kinetic energy of turbulence ε was set equal to 400 $cm^2 s^{-3}$ typical of cumulus clouds. One can see that these ratios are significant showing the substantial turbulent effect on swept volumes and the collision kernels. For small particles the ratios of relative velocities are the same for drop-drop and graupel-drop collisions. For larger sizes of hydrometeors, the ratios are greater for case of graupel-drop collisions,

indicating more pronounced turbulent effect in case of collisions with ice particles.

When solving the stochastic kinetic equations swept volumes were corrected by the factor $\sqrt{1+\frac{\Delta V'^2_{turb}}{\Delta V_t^2}}$. Collision efficiencies were taken as in laminar conditions.

At present, the spontaneous breakup of rain drops and snowflakes is included into the model.

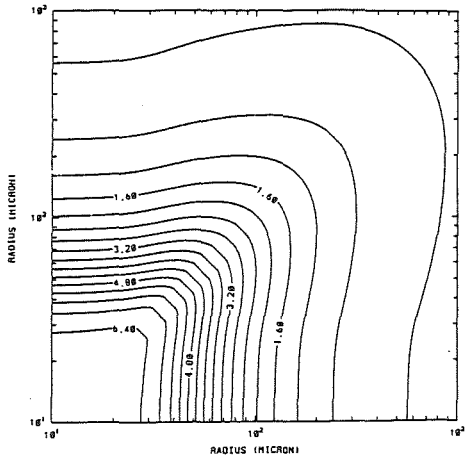

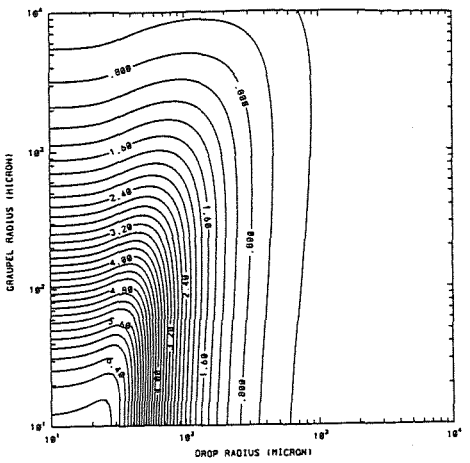

Figure 1. Ratios of the root mean square values of relative velocity $(\Delta V'^2_{turb})^{1/2}$ induced by the particle inertia to the relative velocity ΔV_t induced by the gravity as a function of hydrometeors size for case of (a) drop-drop collisions and (b) graupel-drop collisions.

3. RESULTS

The model was used for simulation of cloud evolution and precipitation formation in a single cumulus cloud typical for the Texas region in summer. The results of four numerical experiments which differs by the model microphysics will be discussed: 1-2) the rain rain microphysics (no ice, with and without the turbulent effects, discussed above, 2) mixed-phase microphysics with and without turbulence effects.

The computational area was 60 km in the horizontal direction and 16 km in the vertical direction. The resolution of the model mesh was 400 m and 200 m, in the horizontal and the vertical, respectively. Evolution of one single cloud results in subsequent formation of new clouds in the vicinity of the dissipating one. The process of cloud ensemble evolution was simulated during two or three hours. in different runs. Preliminary results show that turbulent effects increase the contribution of ice processes to precipitation, so that the cloud with the mixed-phase microphysics provides the accumulated rain 1.3-to 1.5 times greater than the corresponding cloud with warm rain microphysics only.

4. CONCLUSIONS

A spectral microphysics mixed phase cloud ensemble model is designed. The model includes the generation, growth and interactions of hydrometeors of seven types. The model has been used for simulation of evolution of a cloud ensemble (or long-lasting cloud)

5. ACKNOWLEDGEMENTS

This study was partially supported by The Israel Science Foundation administered by The Israel "Academy of Sciences and Humanities", by the Levy Eshkol Foundation of the Israel Ministry of Sciences and by Lady Davis Foundation of the Herbew University of Jerusalem.

REFERENCES

Beard, K.V., and H.T. Ochs III, 1984: Collection and coalescence efficiencies for accretion. J. Geophys. Res, 89, 7165-7169.

Berry, E.X and R.L. Reinhard, 1974: An analysis of cloud drop growth by collection: part 1. Double distributions. *J. Atmos. Sci.*, **31**, 1814-1824.

Flossmann, A.I., W.D. Hall and H.R. Pruppacher, 1985: A theoretical study of the wet removal of atmospheric pollutants. Part 1: The redistribution of aerosol particles captured through nucleation and impaction scavenging by growing cloud drops. *J. Atmos. Sci.*, **42**,583-606.

Hall, W. D., 1980: A detailed microphysical model within a two-dimensional dynamical framework: model description and preliminary results. *J. Atmos. Sci.* **37**, 2486-2507.

Hobbs, P. V., 1990: Ice in clouds. Conference on Cloud Physics, San Francisco, Calif. 600-606.

Khain, A. P., D. Rosenfeld and I. L. Sednev, 1993: Coastal effects in the Eastern Mediterranean as seen from experiments using a cloud ensemble

model with a detailed description of warm and ice microphysical processes. *Atmospheric Research*, **30**, 295-319.

Khain A. P. and I. L Sednev, 1995: Simulation of hydrometeor size spectra evolution by water-water, ice-water and ice-ice interactions. *Atmosph. Research.*, 36, 107-138.

Khain A. P. and M. B. Pinsky, 1995: Drops' inertia and its contribution to turbulent coalescence in convective clouds: Part 1: drops' fall in the flow with random horizontal velocity, *J. Atmos. Sci.* , **52**, 196-206.

Khain A. P. and M. B. Pinsky, 1996: Influence of turbulence on the drop coalescence in clouds and on rain formation. (in this book).

Kogan, E. L. ,1991: The simulation of a convective cloud in a 3-D model with explicit microphysics. Part 1: Model description and sensitivity experiments. *J. Atmos. Sci.* 48, 1160-1189.

Lew, J.K. , and H. R. Pruppacher, 1983: A theoretical determination of the capture efficiency of small columnar ice crystals by large cloud drops. *J. Atmos. Sci.*, **40**, 139-145.

Lew, J.K., D.E. Kingsmill and D.C. Montague, 1985: A theoretical study of the collision efficiency of small planar ice crystals colliding with large supercooled water drops. *J. Atmos. Sci.* 42, 857-862.

Mossop, S.C., 1976: Production of secondary ice particles during the growth of graupel by riming. *Q.J.R.M.S*, 102, 46-57.

Pinsky M. B. and A. P. Khain, 1995a: A model of homogeneous isotropic turbulence flow and its application for simlation of cloud drop tracks *Geophys. and Astr. Fluid Dynamics , 81, 33-55.*

Pinsky M. B. and A. P. Khain, 1995: Simulations of drops' fall in a homogeneous isotropic turbulence flow *Atmosph. Research.* (in press).

Pinsky M. B. and A. P. Khain, 1996: Turbulence effects on the collision kernel Part 1: Formation of velocity deviations of drops falling within a turbulent three-dimensional flow. *QJRMS* (submitted).

Pitter, R. L., 1977: A reexamination of riming on thin ice plates. *J. Atmos. Sci.*, 34, 684-685.

Pruppacher, H. R., and J. D. Klett, 1978: *Microphysics of clouds and precipitation.* Reidel Publishing Company, 714p.

Rogers R.R and M.K. Yau, 1989: *A short course in cloud physics.* Pergamon press, 293 p.

Schlamp R.J., H. R. Pruppacher and A. E. Hamielec, 1975 A numerical investigation of the efficiency with which columnar ice crystals collide with supercooled water drops. *J. Atmos. Sci.*, **32**, 2330-2337.

Scott B.C. and P.V. Hobbs, 1977: A theoretical study of the evolution of mixed-phase cumulus clouds. J. Atmos. Sci., 34, 812-826.

Takahashi, T, T. Endoh, and G. Wakahama, 1991: Vapor diffusional growth of free-falling snow crystals between -3 and -23 ^{o}C. *J. Meteor. Soc. Japan*, **69**, 15-30.

Veen S. H, 1990: A deep convective cloud model with explicit microphysics including the ice phase. *Proceed. of Conference on Cloud Physics*, July, 23-27, San Francisco, 633-637.

ON THE TEMPERATURE OF EVAPORATING PRECIPITATION

Gerd Ragette and Gerhard Wotawa

Zentralanstalt für Meteorologie und Geodynamik

1190 Vienna, Austria

1. INTRODUCTION

The evaporation of precipitation falling through layers of dry air is an important process which needs to be simulated realistically. The temperature T_p and the mass loss dm/dt of single precipitation particles due to evaporation may be computed by an iterative process from the heat balance equation together with the diffusion equation.

For sake of simplicity we assume a constant relative humidity and a constant lapse rate in the subcloud layer. At cloud base the temperature T_p of a precipitation particle is assumed to equal the ambient temperature. The calculations are performed for various initial particle sizes at cloud base and for different environmental conditions in the subcloud layer.

2. EVAPORATION OF A PRECIPITATION PARTICLE

We write the diffusion equation in the usual form

$$dm/dt = 4\pi\, C.D.f.(\varrho - \varrho_s) \qquad (1),$$

where m denotes the mass of the particle, D the diffusivity of water vapor, C the shape factor, f the ventilation coefficient, ϱ the ambient water vapor density and ϱ_s the water vapor density at the particle's surface.

For a rain drop C may be identified with the radius r, for a snow crystal with d/π where d denotes the diameter of the crystal (see for example Pruppacher and Klett, 1978). Thus the evaporation depends on the particle size. The bigger the particle, the more can evaporate. Since the diameter of a snow crystal is much larger than its equivalent radius we may expect that snow flakes evaporate more readily than rain drops of the same mass.

3. HEAT BALANCE OF A PRECIPITATION PARTICLE

Following Rogers and Yau (1989) we write the heat balance equation in the form

$$m.c_w dT_p/dt = Ldm/dt + 4\pi\, C.f.k.(T-T_p) \quad (2),$$

where c_w denotes the heat capacity of water or ice, L the latent heat and k the heat conductivity of air.

At cloud base we assume $T_p = T$. Therefore the temperature change experienced by a particle just falling out of a cloud into a dry layer amounts to

$$dT_p/dt = (L/c_w)((dm/dt)/m).$$

Whereas the mass change dm/dt increases with increasing size, the relative mass change (dm/dt)/m, which for a rain drop is proportional to r^{-2}, decreases with increasing size. Thus the smaller a drop, the faster the temperatur change of the particle due to the onset of evaporation will be.

Due to the evaporative cooling which the particle experiences after leaving the cloud, the heat flux towards the particle increases until the two terms on the right side of (2)

balance each other. Unless there are significant environmental changes - like the assumed sudden change from inside the cloud to the subcloud layer - the time change dT_p/dt of the particle temperature may therefore be neglected. Thus the difference between ambient and equilibrium particle temperatur is obtained from (2) as

$$T - T_p = -L(dm/dt)/(4\pi C.f.k).$$

It is easily shown that the difference $T - T_p$ is independent of the particle size. It depends on the ambient temperature such that for warm air the difference $T - T_p$ is larger than for cold air. This is demonstrated by table 1 where in order to maximize the effect of evaporation a perfectly dry air has been assumed in the subcloud layer.

Table 1: Equilibrium temperature T_p which a rain drop of initial size of 1 mm will reach at the indicated time and height after having dropped out of a cloud at 1500 m into a perfectly dry isothermal layer of temperature T.

T	0 C	20C	30C
T_p	-7,4 C	3,2 C	7,2 C
$T - T_p$	7,4 C	16,8 C	22,8 C
height	1380 m	1400 m	1400m
time	18 s	14 s	14 s

The size of the particle regulates the response to the sudden humidity change from cloud to subcloud layer as is shown in table 2.

Table 2: Elapsed time and distance fallen from cloud base at 1500 m for rain drops of intial size of 1 and 2 mm in order to reach the equilibrium temperature T_p in perfectly dry air of an ambient temperature T of 20 C.

	1 mm	2 mm
Elapsed time	14 s	31 s
height	1400 m	1210 m
T_p	3,2 C	3,4 C
$T - T_p$	16,8 C	16,6 C

In section 3 the response of a rain drop to a change in the ambient relative humidity has been shown to be proportional to r^{-2}. In order to estimate the response of a precipitation particle to a sudden change in the environmental temperature we consider a particle which at the ambient temperature T1 is in thermal equilibrium and find from (2) that

$$Ldm/dt = -4\pi C.f.k.(T1 - T_p).$$

When the particle enters a layer with the temperature T2 it follows from (2) that

$$m.c_w dT_p/dt = 4\pi C.f.k.(T2 - T1).$$

Thus the temperature change dT_p/dt of a rain drop due to a change in environmental temperature is also proportional to r^{-2} and we conclude that small particles respond faster to environmental changes in temperature and humidity than big particles.

4. EVAPORATION OF RAIN AND SNOW DEPENDING ON TEMPERATURE, HUMIDITY AND PARTICLE SIZE.

The obvious dependence of the evaporation of hydrometeors on the ambient humidity is shown in table 3.

Table 3: Size and temperatur T_p of a rain drop at 1400 m, which has fallen with initial size of 1 mm from cloud base at 1500 m through an isothermal layer of 20 C with a relative humidity of 0 % and 50 %.

	0 %	50 %
r	0,97 mm	0,99 mm
m	3,9 mg	4,0 mg
dm/dt	-0,018 mg/s	-0,0076 mg/s
T_p	3,2 C	12,9 C
$T - T_p$	16,8 C	7,1 C
dT_p/dt	-0,037 C/s	-0,0042 C/s

It will be expected that in warm air more can evaporate than in cold air. This is confirmed in table 4.

Table 4: Masse and temperature change of a rain drop of 1 mm leaving cloud base at 1500 m and just falling into a perfectly dry isothermal layer of 20 C and 30 C, respectively.

	20 C	30 C
dm/dt	-0,054 mg/s	-0,098 mg/s
dT_p/dt	-6,1 C/s	-9,7 C/s

Comparing rain and snow we find from table 5 that a snow crystal will evaporate faster than a rain drop. In terms of distance fallen from cloud base this effect is even more pronounced as snow flakes fall slower than rain drops.

Table 5: Mass change dm/dt for a rain drop and a snow crystal of the same equivalent radius of 1 mm leaving cloud base at 1500 m and just falling into a perfectly dry isothermal layer of 0 C.

	rain drop	snow crystal
dm/dt	-0,014 mg/s	-0,055 mg/s

The different evaporation of rain and snow suggests that in cold climates, where a large portion of the precipitation falls as snow, a larger percentage of the precipitation which is generated aloft will evaporate before reaching the ground than in warm climates.

The effect of the humidity in the subcloud layer on the evaporation of precipitation is particularly important in arid regions. Afforestation may mitigate this effect by raising the environmental humidity.

5. REFERENCES

Pruppacher, H. R. and J. D. Klett, 1978: Microphysics of Clouds and Precipitation. D. Reidel Publishing Company, 714 pp.

Rogers, R. R. and M. K. Yau, 1989: A Short Course in Cloud Physics. Pergamon Press, 293 pp.

KINEMATICS OF CLOUD-SCALE LOCAL ATMOSPHERIC PROCESSES

L.G. Kaplan
Scientific and Production Geophysical Center, Stavropol, Russia

1. Introduction

The conditions of the localization and stationarity of the dynamic processes are often arised and kept in the continuous liquid medium as result of the diverse factofs. Hurricanes, tornadoes and thunder-hail processes are the local processes in atmosphere. The main efforts of the book by Kaplan (1993) are directed to search of the dependences on the integral characteristics of the local processes (briefly locals). The main assumptions are made.

Homogeneity of the liquid. At the absence of the disturbances the liquid density and the pressure are same thorough the whole space.

The little value of the variations of the pressure and the density. The pressure p and the density ρ of the liquid depend on the point coordinates in the localization local such LPR can be identifical on process region (LPR) and, generally speaking, differ from the values p_0 and ρ_0 in the stationary continuous medium out of LPR are very small in comparison with their initial values.

Barotropy of the liquid. The variations of the pressure and the density of the liquid are related lineary:

$$p_\Delta = \rho_\Delta c^2, \qquad (1.1)$$

where c is the sound velocity

Stationarity of the process. In the transferal coordinate sistem, related to the region, covered by process, all the physical characteristics at the arbitrary point are constant at time.

Locality of the process. For the locals there is such LPR, in which the medium characteristics at its boundary do not differ from the ones at the far distance from some center. In particular, the density of the side forse becomes equal to zero. At the gradual decrease of the process intensity with the increase of the distance from the center the boundary of LPR is conditional. The decrease of the local intensity of the process up to zero with the increase of the distance from the center does not indicate about the possibility of the identification of the such large LPR that the integral characteristics of the process at its boundary do not differ from the same ones at the free space. The processes, the integral characteristics of which sufficiently differ from zero ones, we shall call weakly localized.

Not only local but the integral characteristics of many processes at the LPR boundary very little differ from the characteristics of the same region of the free space. Such processes occur at every moment of time solely in the LPR, corresponding to this moment actually not affecting the medium as a whole. If for the local such LPR can be identifical on the boundary of which and in the medium as a whole out of LPR not only local but the integral characteristics of the intensity are zero, such processes we·ll call the largely localized.

The core and the zone of flow-around. The process core, if it exists, is the part of LPR for which the interchange of the substance with the rest of medium is absent. If this assumption is fulfilled the orthogonal component of the transferal substance velocity over the whole surface of the core S_c must be zero. In the vector form this condition is equivalent to the requirement that the scalar product of the transferal substance velocity v_D and the element of the surface S_c must be zero over the whole S_c:

$$(v_D * dS_c) = 0. \qquad (1.2)$$

The rest of the part of LPR, excluding the core, is the zone of the flow-around.

2. Integral characteristics of local processes

From the barotropy condition (1.1) the integral difference mass and the integral difference pressure are connected linearly:

$$P_\Delta = m_\Delta c^2. \qquad (2.1)$$

The scalar moment (is introduced by the author for the first time) of the distributed over the space force with the volume density f is equal to:

$$\bar{M} = \int_V (\bar{f} * \bar{r})\, dV, \qquad (2.2)$$

where $\bar{r}$ is the radius-vector of a point of the application of the force, (*) indicate the scalar product. In the opposite to the vector moment of the force the scalar product of the values of the force density and the radius-vector are included into (2.2). The value M characterizes the balance of the forces of the tension and the compression. At $M > 0$ the substance as a whole is stretched and at $M < 0$ is compressed.

The potential energy of the pressure force of the substance of the local relatively to the rest of medium has the second-order of the little in relation to p according to Kaplan (1993) and in many cases it is negligebly small in comparison to the kinetic energy.

Look for other integral characteristics in appendix.

3. Kinematics

The movement and the force equilibrium of the zone covered by the local process are studied. To deduce the equations of the kinematics the following approach was

used.The region in the form of the parallelepiped is considered. This region D is the LPR spread. The parallelepiped shifts in the absolute space together with the process and LPR and is oriented to the direction of the absolute process velocity. In the transferal coordinate sistem the LPR and the region D are immovable. Besides the region D its arbitrary part having the parallelepiped form as well is considered. In the capacity of this part the parallelepiped restricted by the bases S and S_2, is initially specified, and S_1, S_2. The base S is placed between the bases S_1 and S_2 has the arbitrary coordinate x ($x_1 < x < x_2$). As the region D, as a whole, its selected part is immovable in the transferal coordinate system. The base S_2 and the sides S_3, S_4, S_5, S_6 of the selected parallelepiped are out of LPR and substance parametrs on them are the same as in the continuous medium as a whole. As a function the coordinate x the base S can cross the LPR and in this case the substance parameters on the given base can differ from the medium ones at the large distance from the LPR. Further the conditions of the mass invariability of the substance in the selected volume and its force equilibrium are used. In both cases actually we get some equation for the plane S with arbitrary coordinate. Then this equation is integrated in the infinite limits. The analog procedure is for two other axes of the coordinates.

3.1. The equation of movement. This equation connects the linear momentum, the difference mass and velocity of the local in the medium

$$\bar{K} = m_\Delta \bar{v}(D) \qquad (3.1)$$

This formula is analogical to the formula for solid but the velocity of the local and linear momentum are antiparallel if $m_\Delta < 0$. The eq. of the process movement (3.1) is obtained from the very general considerations. Only the continuity equation and the assumption of the process stationarity are used. So (3.1) is often fulfilled yet for the weakly localized processes. It is enough that the difference mass of the process has the limit at the LPR spread. It is important that at the deduction (3.1) the assumptions on the distribution character of the forces effecting on the local volume do not used. This allows us at the concret using of (3.1) for the processes not to take into account the forces or, vice versa, to specify their distributions.

3.2. The integral force equilibrium of the local process. The conditions of the force equilibrium on axes x, y, z are

$$P_\Delta + M_{Sx} + 2E_{kx} - 2E_b = 0, \qquad (3.2)$$

$$P_\Delta + M_{Sy} + 2E_{ky} = 0, \qquad (3.3)$$

$$P_\Delta + M_{Sz} + 2E_{kz} = 0. \qquad (3.4)$$

Here E_{kx}, E_{ky}, E_{kz} are the integral kinetic energies of medium in the process zone in directions x, y, z accordingly; E_b is equivalent energy of solid body; M_{Sx}, M_{Sy}, M_{Sz} are the components of the scalar momentum of

side force; P_Δ is integral pressure deficit.

The global condition of force equilibrium is obtained by summing of the conditions on axes:

$$3P_\Delta + M_S + 2E_k - 2E_b = 0. \quad (3.5)$$

The global condition of force equilibrium is the most common formula included in it the integral forced, dynamic and energitic parameteres of the local. The global condition of force equilibrium is followed of the necessity from the force equilibrium and stationarity of the local. The global condition of force equilibrium and conditions of force equilibrium on axes do not replace, of course, the conditions of force equilibrium in a point or the conditions of force equilibrium of the arbitrary volume.

Example 1. The immovable two dimensional flat circular local. This local is characterized by the velocity depended only of the distance r from the central point $v = v(r)$. If $r > R$ (R is of the process zone radius) $v(r) = 0$. From the local immobility $E_b = 0$. From the side force absence $M_g = 0$. Using (2.1, 3.5a), the global condition of equilibrium for this local transtorm to formula:

$$E_k = - m_\Delta c^2. \quad (3.6)$$

This formula is analogical to know Einstain formula.

Example 2. Immovable three dimensional ring. Those rings are observed at air (the rings of a smoker, the smoke rings of the plant chimney). It is proposed that air moves only inside the ring and does not move outside the ring. One component of speed v_R in the every point inside the ring is directed on the big circle (along ring) and other v_r is directed on the little circle (across ring, on section).

From (3.1) equation of the force equilibrium along ring is

$$P_\Delta + 2E_{kR} = 0, \quad (3.7)$$

where E_{kR} is the energy of the along velocity component.

Equation of the force equilibrium across ring is obtained by summing two other conditions of equilibrium (3.2, 3.3):

$$P_\Delta + E_{kR} = 0, \quad (3.8)$$

where E_{kR} is the sum energy of two cross velocity components.

Correlation between the root-mean-square values of longitudional v_R and transverse v_r speeds is obtained from (3.7, 3.8):

$$v_R = v_r / \sqrt{2}. \quad (3.9)$$

The speed of wind along the ring is in $\sqrt{2}$ less than the transverse speed.

References

Kaplan L.G., 1993: **The local processes in the continuous liquid medium and atmosphere**, ACOK-press, Russia, 244.

DYNAMICS OF A CLOUD-SCALE VORTICAL ATMOSPHERIC PROCESS

L. G. Kaplan

Scientific and Production Geophysical Center,
Stavropol, Russia

A cloud-scale vortical local atmospheric process in the external velocities field is considered. In the localisation process region two zones: core and flow-around zone are differed. Core does not almost change with substance with surrounding flow-around zone and atmosphere. Movement of air inside core poorly connects with atmosphere movement outside core. In flow-around zone the air movement has components connected as atmosphere movement as core being essentially distorting the air velocities pictire in undisturbing atmosphere. Unbreakness of velocities on border core and flow-around zone follows principe of physical realisation.

It is proposed that scale of air movement in free atmosphere is more large than process core size.

From Gromeck-Lamb equation after a lot of transformations we show that sum force acting on process in whole is

$$\bar{F}_c(D) = m_c \bar{v}(D) \hat{} \overline{\mathrm{cirl}\ v_o} - \bar{v}(D) \hat{} \bar{R}_c + q(\bar{v}(D) - \bar{v}_q). \quad (1)$$

Next integral characteristics of process and atmosphere are in this equation :

$\bar{v}(D)$ - core velocity relatively atmosphere in whole; $\bar{v}_q$ - withdrawal velocity of the substance from the core; $\overline{\mathrm{cirl}\ v_o}$ - the vorticity of unperturbed wind atmosphere velocity in the process volume m_c - the substance mass in core volume, q - (dm_c/dt) - specific inflow into the core over its border, $\bar{R}_c$ - angle moment on the side core surface, $(\hat{})$ - sign of vector product. The first summand determines force, depending on movement speed of process relatively atmosphere and its vortex without process. This vortex connects with Earth rotation as well as power and location in macro scale process of described process.

Second summand on the core process vortex itself as well as its movement velocity relatively atmosphere. Third summand depend on the difference of velocity core movement and withdrawal velocity from core.

For atmospheric processes this velocities are near on direction. Therefore first and second summands

determin lateral force, and third one is longitudinal force.

Within the framework of the created theory (Kaplan L.G., 1993) researches of thunderstorm cloud upward jet were carried out. It proposed that movement of jet is determined with its parameters and first summand (1) is not taken into account.

In accordance to adopted jet model we consider that inflow take place in low part of jet and rotation do in middle one. Direction of leading flow is taken same on any height.

Evaluation is obtained for the longitudinal v_{cx} and lateral v_{cy} velocities with respect to the laeding flow:

$$v_{cx} = (q^2 v_{aq} + R^2 v_{aR})/(q^2 + R^2) \quad (2)$$

$$v_{cy} = qR(v_{aq} - v_{aR})/(q^2 + R^2) \quad (3)$$

Here v_{aq}, v_{aR} - the leading flow velocities at the characteristic heights of the inflow zone and of the upward flow jet rotation zone accordingly.

In accordance with (2, 3) and the experimental data the travel velocity of a thunderstorm cloud along the leading flow is less than the flow characterics velocity. The lateral travel velocity depends on the difference $v_{aq} - v_{aR}$. This difference is more suitable for a powerful thunderstorm process, because the zone of air inflow into the upward flow jet and the zone of this process rotation are seperated spatially, and the thermodynamic conditions of its growth suggest the presence of great wind shifting in height. In consequence of this the highest velocities of lateral travel with respect to the leading flow are registered with powerful hailing processes. In some cases lateral velocity may exceed the longitudinal one ($v_{cx} > v_{cy}$). The angle between the direction of a lightning-and-hailing cell travel and that of the leading flow may be approaching to 90° in this case. Large angles sometimes observed in practice are evidently predetermined by the wind turn with height.

References

Kaplan L.G., 1993: **The local processes in the continuous liquid medium and atmosphere**, ACOK-press, Russia, 243.

DYNAMICS OF A STRONG UPWARD FLOW JET IN ATMOSPHERE

L. G. Kaplan

Scientific and Production Geophysical Center,
Stavropol, Russia

1. Introduction

The upward jet of the thunder-hail process is considered as the three-dimensional local process in atmosphere (Kaplan, 1993). We assume that the initial assumptions on the stationarity and the low influence of friction are satisfied. The effects of the geometric limitations (the surfaces of the Earth and upper atmosphere), gravity and variation of the air parameters with altitude and initial rotation of the air mass are taken into account.

The jet is devided into three parts along the vertical conventionally. In the lower part there are an inflow (convergency) of the ambient air and the growth of the vertical and horizontal components of the wind speed. In the middle part the air inflow is very small due to balance of the pressure deficit in jet and the dynamical pressure of the horizontal wind. In the upper zone the air jet spread (divergency) occurs, followed by the gradual decrease of the speeds of the horizontal and vertical components of the air flow.

In the random horizontal section the central zone can be identified where the air motion is vertical predominantly. This central zone is surrounded by the zone of the predominantly horizontal wind. The horizontal wind includes three components. The tangential component is responsible for the circular motion of the air mass around the center, often in cyclonic direction.

Due to the centrifugal force, resulting from the presence of the tangential component of the wind speed, compensation of the pressure difference between the free atmosphere and the center takes place. The air inflow into the central zone occurs at the undercompensation and at the overcompensation we say about the outflow. The rotation and inflow (outflow) of the air are followed by the movement of central part and the whole jet in free atmosphere.

2. Conditions of force equilibrium

According to Kaplan (1993), the conditions of the force equlibrium of the stationary process moving at medium with velocity $\bar{v}(D) = -\bar{v}_\rho$ are:

$$P_\Delta (I - v_\rho{}^2/c^2) + M_{Sx} + 2E_{kx} = 0, \quad (1)$$

$$P_\Delta + M_{Sy} + 2E_{ky} = 0, \qquad (2)$$

$$P_\Delta + M_{Sz} + 2E_{kz} = 0 \qquad (3)$$

and besides P_Δ is the integral difference pressure of process; E_{kx}, E_{ky}, E_{kz} are the integral kinetic energies of medium in the process zone in directions x, y, z; M_{Sx}, M_{Sy}, M_{Sz} are the components of the scalar moment of the side force; $\bar{v}_p$ is the medium speed relatively of local process; c is sound speed.

From (1, 2, 3) the force equilibrium conditions of the stationary atmosphere process moving at the horizontal direction with velocity $\bar{v}(D) = -\bar{v}_p$ are:

$$P_\Delta (I - v_p{}^2/c^2) + 2E_{kx} = 0, \qquad (4)$$

$$P_\Delta + 2E_{ky} = 0, \qquad (5)$$

$$P_\Delta + M_{Sz} + 2E_{kz} = 0 \qquad (6)$$

and besides P_Δ is the integral difference pressure of process; E_{kx}, E_{ky} are the integral energies of horizontal wind in direction of the process movement x and perpendicular to it y; E_{kz} is the integral energy of the vertical wind; M_{Sz} is the scalar moment of the gravity force; $\bar{v}_p$ - the atmosphere speed relatively of the local process; c = 330 m/s is the adiabatic sound speed.

Equations (4, 5, 6) differ from ones (1, 2, 3) by absence of summands M , M . It is determined by mutual compensation of the active-passive forces at horizontal plate. At the last equation the scalar moment M_{Sz} depends on the gravity force.

The speed of the atmosphere process movement v(D) does not usually exceed 20 m/s. So the speed process quantity $v(D) = -v_p$ is least with comparision of the sound one:

$$(1 - v_p^2/c^2) > 0.99 \cong 1 \qquad (7)$$

With calculation of this fact equation (4) allows approximation:

$$P_\Delta + 2E_{kx} \cong 0. \qquad (8)$$

Therefore:

$$E_{kx} = E_{ky}. \qquad (9)$$

There is convenient to consider the process kinetic energy on horizontal in whole:

$$E_{kh} = E_{kx} + E_{ky}. \qquad (10)$$

The condition of the horizontal force equilibrium is obtained by summing of equations (4, 5) and taking into account (7, 10):

$$P_\Delta + E_{kh} = 0. \qquad (11)$$

The horizontal equilibrium of the jet is characterized by the balance of the integral difference of pressure and integral energy of the horizontal wind velocity in the random section of jet.

For the barotropic model of the upward jet they may write next equation:

$$E_{kh} = -m_\Delta \cdot c^2. \qquad (12)$$

Here m_Δ is the integral deficit of air mass at the process relatively on free atmosphere; E_{kh} - the sum energy of the horizontal wind.

According to (12) the section-averaged difference pressure is directly connected to the mean-root-square velocity of the horizontal wind

$$\overline{-p_\Delta(H)} = \overline{\rho v_h^2/2}. \qquad (13)$$

3. Vertical equilibrium

The pressure difference $p_\Delta(H)$ at the random altitude H depends on the variation of the calculated temperatire difference ΔT_p vers its altitude. If the jet altitude is no larger of the vertical scale of atmosphere (8 km), the satisfactory accuracy for the horizontal wind component at the altitude formation of the upward jet can be estimated by:

$$\frac{v_h^2(H)}{2} = -g\int_{H_0}^{H}\frac{\Delta T_p}{T}\,dz. \qquad (14)$$

We'll notice that at the height shaping the under jet pressure is equal to the ambient atmosphere pressure on the same altitude and the jet in whole likely floats in it.

The expression (14) resembles the known Exler formula (Sulakvelidze, 1980), but here we use the horizontal wind velocity instead of the vertical one and minus in the second equality.

From the expression (14) of the necessity follows that in the upward jet must be the zones of the warmer and colder air than the air of ambient atmosphere at same altitude. The natural distribution of zones is the air in the middle part of the jet is warmer than the ambient one and in the upper and lower parts it is colder.

The convection level is the level at which the surface air, rising upward, balances on the temperature with the ambient air. Usually the altitude of the thunder-hail cloud sufficiently exceeds this level. The simple explanation of this fact is a consequence of (14), i.e. in the upper part of thunder-hail cloud the air is colder than the ambient one.

Considering the vertical equilibrium of volume between levels of $H_o = 0$ and H_{max}, containing the whole jet, we can say that in the lower part of jet the mean-root-square horizontal and vertical components of the wind velocities are connected by:

$$v_h > \sqrt{2}\, v_z. \qquad (15)$$

For the air in the upper part of jet the vertical velocity is connected by reverse expression:

$$v_h < \sqrt{2}\, v_z. \qquad (16)$$

The estimation of relationship of horizontal and vertical components of wind in jet on the whole is:

$$v_h = \sqrt{2}\, v_z. \qquad (17)$$

The last equation is directly followed from (6, 11, 15).

The available experimental data (Flemming storm and so on) showed that the severe supercell thunder-hail processes are characterized by the large difference of pressures outside and inside the upward air jet, which is balanced by the strong horizontal flow, the rotation in which occurs in cyclonic direction. The horizontal component of the wind speed in the most severe processes exceeds the vertical one ($v_h \approx 1.4\ v_z$) and the net velocity can be sufficiently larger than the calculated by the Exler formula.

References

Kaplan L.G., 1993: **The local processes in the continuous liquid medium and atmosphere,** ACOK-press, Russia, 243.

Sulakvelidze G., Sulakvelidze Ya., 1980, **Termodynamics of troposphere.** Part 1. - Press of Tbil. University, USSR, 295.

OBSERVATIONAL AND CLOUD-SCALE NUMERICAL MODEL STUDIES OF ANVIL CIRRUS CLOUD.

Philip R.A. Brown and Hugh Swann

Joint Centre for Mesoscale Meteorology, Univ. of Reading, UK

1. INTRODUCTION

The stratiform anvil regions associated with convective cloud systems play an important role in several aspects of the energy and water budget of the atmosphere. The large spatial extent of the anvil by comparison with the convective region increases the impact of the cloud system on the fluxes of longwave and shortwave radiation. The anvils may also contribute a significant fraction of the total precipitation produced by the cloud system and act as a significant source of water vapour for the upper troposphere. There is, therefore, a need for improved parametrizations of anvil cloud for use in global- and regional-scale models. Cloud-Resolving numerical Models (CRMs) are increasingly being used in the development of such parametrizations. The CRMs themselves contain parametrized representations of microphysical processes. Their validation by means of observational case studies is, therefore, a key activity for programmes such as the GEWEX Cloud System Study (GCSS).

This paper presents observations and numerical model results from the case of an anvil formed by an isolated cumulonimbus cloud in a returning polar maritime airstream to the southwest of the UK. In-situ microphysical measurements obtained from the UK meteorological Office C-130 research aircraft at a number of positions relative to the convective core are compared with the evolving fields of microphysical variables generated by the model. The main emphasis is on the validation of the ice water content (IWC) within the model anvil together with its horizontal extent. In an ensemble of such clouds, both of these would have significant effects on the radiative impact of the ensemble. The roles of some key microphysical processes in the convective core and their relationship to the moisture flux into the anvil will also be discussed together with some aspects of the sensitivity to details of the model microphysics scheme.

2. MEASUREMENTS

The measurements described here were obtained on 27 October 1994. A weak polar maritime airstream with convective showers covered the sea area to the south-west of the UK.

The target cloud had already generated a widespread anvil when it was selected for study. Following a descent to measure temperature, humidity and wind profiles, 8 runs were made through the anvil at an altitude of 5.4 km. This was estimated to be approximately 200m below the general top of the anvil. The runs were orientated perpendicular to the mean wind direction at the anvil level. On each run, the minimum separation from the region of intense precipitation was estimated from the aircraft weather radar display. After the flight, the aircraft flight tracks were plotted in cloud-relative coordinates, using a cloud motion velocity derived from the numerical model runs. The estimates of position relative to the precipitation region from a number of runs were found to be mutually consistent.

Measurements from one of these runs are shown in Figure 1. The 2D-C probe showed predominantly irregular particle shapes although with a more rounded appearance than the mixture of bullets, bullet-rosettes, and side-planes commonly found in cirrus. When processing these data, IWC was calculated in two ways. Firstly, particle mass was derived using

$$M(D) = 7.38 \times 10^{11} D^{1.9} \qquad (1)$$

where M is in g and D is the particle diameter in μm. Brown and Francis (1995) found that (1) gave good estimates of IWC in cirrus by comparison with bulk measurements using an evaporative total water content (TWC) probe. Secondly, all particles were assumed to have a constant bulk density, $\rho_i = 0.8g\ cm^{-3}$. In the present case, no rapid-response humidity sensor was available and it was not, therefore, possible to use the TWC measure-

ments directly to estimate the bulk IWC.

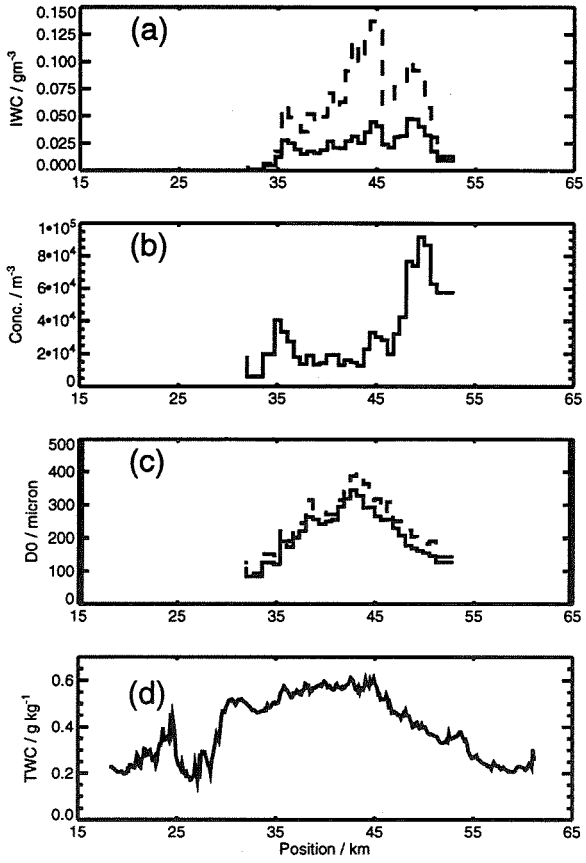

Figure 1: Aircraft measurements from a cloud penetration at an estimated position of 15km downwind from the convective core. The figures show (a) IWC from the 2D-C probe, the solid line obtained using (1) whilst the dashed line assumes ice particles with constant density, $\rho_i = 0.8g\ cm^{-3}$, (b) the 2D-C particle concentration, (c) the 2D-C median-mass particle diameter, $D0$, and (d) the TWC measured by the evaporator.

In the majority of runs, the location of the maximum in IWC corresponds to that of TWC. However, Figure 1(d) shows a region at approximately 47 km where this is not the case. IWC values calculated with $\rho_i = 0.8g\ cm^{-3}$ typically exceed those obtained from (1) by a factor of 2 or 3. The lower values from (1) are, however, considered to be be the better estimate. The typical width of the anvil was 20 km.

3. MODEL

3.1 Description

The numerical model used for these studies is the 3-d Large Eddy model described by Shutts and Gray (1994). A three-phase, bulk-water microphysics scheme is employed. Terms which describe the conversion rates of mixing ratios of microphysical species are generally similar to those described by Lin et al. (1983) with some differences described by Brown and Swann (1996). In addition, the scheme allows the option to operate in "double-moment" mode, to predict both number concentrations and mass contents of the three ice-phase species, cloud ice, snow, and graupel (Swann and Brown, 1996).

In the studies described here, the model was run with 60 × 90 gridpoints in the horizontal at a resolution of 1000m, and 40 levels in the vertical, with a resolution near the surface of 250m. An initial vertical profile of temperature, humidity, and horizontal wind was derived from a combination of aircraft descent measurements in the vicinity of the target cloud together with a nearby radiosonde (launched approximately one hour before and 100km to the north-east of the aircraft measurement region). This is shown in Figure 2. Convection was initiated with a combination of a single warm bubble (approx. 1K temperature elevation) together with random temperature fluctuations of $\pm 0.2K$ throughout the lowest model level.

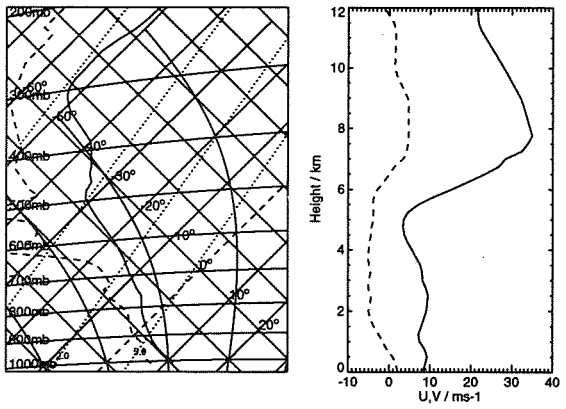

Figure 2: Tephigram (left) showing the initial temperature and humidity profiles used for model runs described in the text. Mixing ratio lines (dotted) are at values of 0.1, 0.6, 2.0, and $5.0gkg^{-1}$. The initial wind profiles are shown at the right of the figure, u (solid) and v (dashed).

3.2 Results

Figure 3 shows a horizontal section through the model domain at an altitude of 5.8km after 230 minutes of integration. This model level was a similar distance below the model anvil cloud top as was the aircraft penetration altitude relative to the observed cloud top. The figure shows that the model anvil is formed chiefly by the non-precipitating cloud ice category. The maximum cloud ice contents lie between 0.1 and $0.2g\ m^{-3}$. These exceed the typical observed

maxima, assuming that the particle masses are described by (1). At its maximum extent, the anvil from cell **A** reaches approximately 40 km downwind. By comparison, the greatest extent of the observed cloud was estimated to be 25-30 km downwind.

The ice crystal concentration at the model 5.8 km level is in the range 1.0 to 1.5 $\times$ $10^5 m^{-3}$. Values observed with the 2DC probe are commonly in the range 2.0 to 4.0 $\times$ $10^4 m^{-3}$, although with maxima of up to 1.0 $\times$ $10^5 m^{-3}$. The 2DC probe is known to undercount crystals below a diameter of about $100\mu m$ (Baumgardner 1987). It is, therefore, expected that the model ice concentrations should generally be larger than observed. Analysis of the ice crystal production rates during the earlier growth of the convective cell suggests that the largest source of ice crystals in this cloud is due to secondary ice formed via the Hallett-Mossop process during the growth of graupel in the -3 to -8C temperature range.

4. DISCUSSION

A characteristic feature of model simulations of this case is a rapid increase in updraught strength as the cloud-top reaches a level of approximately 5.5km. This coincides with the appearance of the first graupel and a decline in the maximum LWC in the growing cell. This is illustrated in Figure 4. Due to the very low windshear across this region, the initial graupel particles are allowed to remain in a high-LWC environment and hence to grow rapidly. The latent heat release from this rapid glaciation of the updraught is responsible for the updraught acceleration. This leads, in turn, to cloud-top heights in the convective core which overshoot the eventual anvil level by around 1.5km. Whilst overshooting tops were observed, it was estimated that these extended only a few hundred metres above the anvil top. When the "double-moment" microphysics scheme was used, it was found that the initial rate of increase of graupel was slightly reduced, thereby reducing the acceleration of the updraught. However, this had no significant impact on the cloud-top altitudes. The excessive overshoot of the convective core may be due an initial temperature profile which is unrepresentatively cold between 4.0 and 5.5 km altitude. This will be considered in subsequent model runs.

Whilst we are unable to use the aircraft TWC measurement to derive a bulk IWC measurement, we may, however, combine the model microphysical fields to simulate the quantity which would be observed by the TWC probe, ie. the sum of vapour plus condensate. From model data at the 5.8 km level, we determine the maximum TWC as a function of distance downwind from the convective core. These values are shown in Figure 5(b) together with the aircraft data. The two model-derived curves are from model fields separated in time by 20 minutes. They suggest that the model flow into the anvil contains the correct total water content. The difference between the model and observed maximum IWC shown in Figure 5(a) may be accounted for by the difference in temperature of approx 4K between the aircraft flight level and the selected 5.8 km model level. The lower saturation mixing ratio near the model cloud top allows more of the anvil TWC to be held as cloud ice.

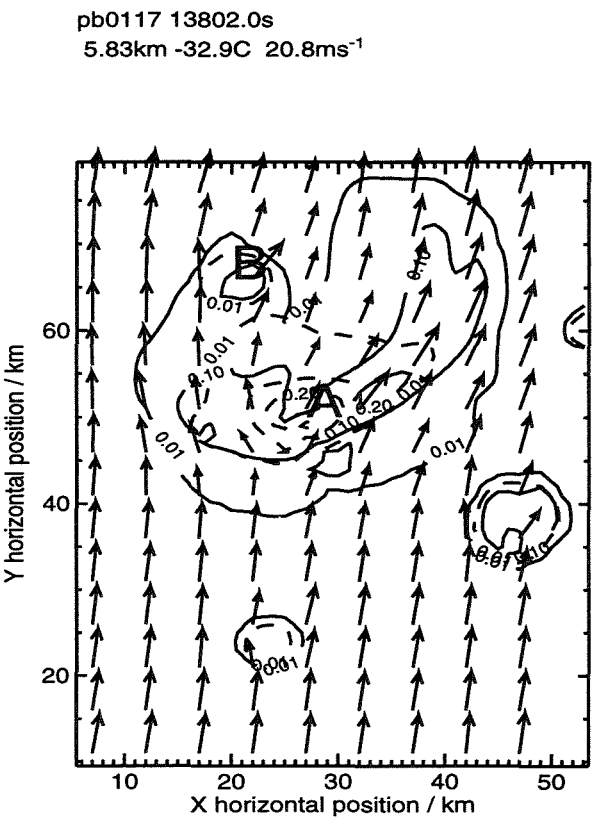

Figure 3: Horizontal section through domain of model run 117 at time T=230 minutes, at an altitude of 5.8km (temperature = $-32.9C$). Solid contours show cloud ice whilst dashed contours indicate snow. Contour intervals are at 0.01, 0.1, and $0.2gm^{-3}$ for both. Arrows indicate wind vectors, with a maximum speed of $20.8ms^{-1}$. Wind vectors are rotated 90 degrees anti-clockwise from the profile shown in Figure 2. **A** indicates the approximation location of the updraught core at lower levels. **B** indicates a secondary convective cell formed at gust-front of the cold outflow generated by precipitation from **A**.

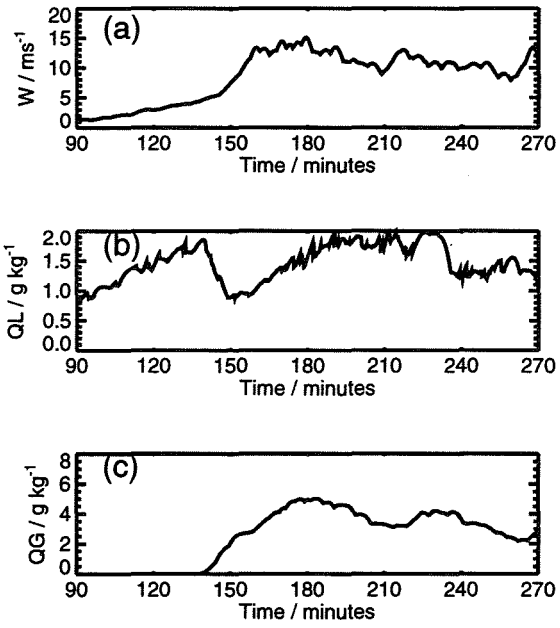

Figure 4: Time-series showing the maximum values occurring within the model domain of (a) updraft velocity, w, (b) LWC, and (c) graupel water content.

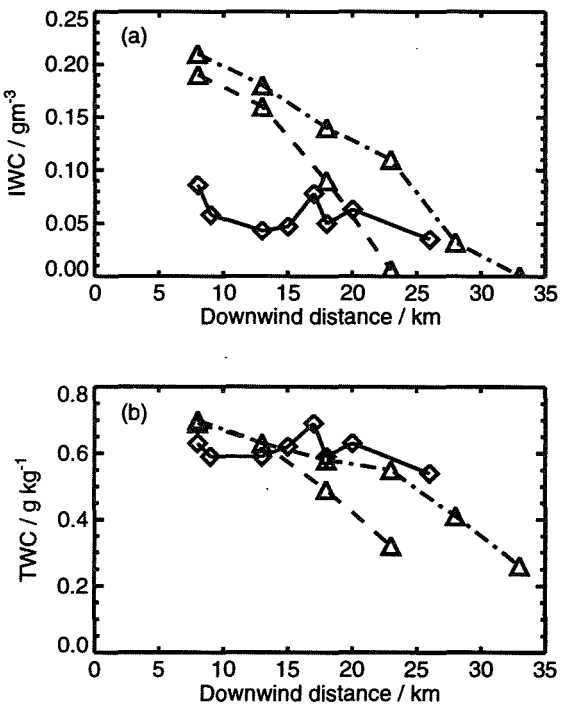

Figure 5: (a) Solid lines show maximum values of IWC as a function of downwind distance from the convective core, as described in the text. Lines with triangular symbols are model results at T=210 minutes (dash) and 230 minutes (dot-dash), respectively. (b) as for (a), but for TWC ie. sum of vapour, ice, and snow.

5. CONCLUSIONS

The model has been able successfully to reproduce some features of the observed case. In particular, it produces an anvil of reasonable lateral dimensions and with a TWC which compares favourably with observations. The tendency to form the anvil at too high an altitude leads to excessive IWC values. The agreement in anvil TWC suggests that the processes which deplete the TWC in the updraught region, principally the production and fallout of graupel, may be well-represented in the current model simulations. The excessive anvil top altitude combined with the strong windshear leads to an excessive downwind extension of the model anvil.

ACKNOWLEDGEMENTS

The Joint Centre for Mesoscale Meteorology is supported by the UK Meteorological Office and the Department of Meteorology, University of Reading.

REFERENCES

Baumgardner D, 1987: Corrections for the response times of particle measuring probes. Amer.Met.Soc., 6th Symp.Met.Obs.Instrum., Jan.12-16 1987, New Orleans.

Brown, P.R.A. and P.N.Francis, 1995: Improved measurement of the ice water content in cirrus using a total water evaporator. J.Atmos.Oceanic Technol. **12**, pp410-414.

Brown, P.R.A. and H.Swann, 1996: The observational validation of a 3-d numerical cloud model used for the development of convective cloud parametrization schemes. (submitted to Q.J.R.Meteorol.Soc.).

Lin, Y-L., R.D.Farley, and H.Orville 1983: Bulk parameterization of the snow field in a cloud model. J.Clim.Appl.Met., **22**, pp1065-1092.

Shutts, G.J. and M.Gray 1994: A numerical modelling study of the geostrophic adjustment process following deep convection. Q.J.R.Meteorol.Soc., **120**, pp1145-1178.

Swann, H. and P.R.A.Brown 1996: Development and validation of a double-moment microphysics scheme for simulating cumulus clouds. *This conference.*

NUMERICAL MODELLING OF CONTRAIL FORMATION AND CONCOMITANT RADIATION FIELD USING A MESOSCALE MODEL WITH EXPLICIT MICROPHYSICS

Vitaly Khvorostyanov[1], Stephan Bakan[2] and Hartmut Grassl[3]

[1] Central Aerological Observatory, Dogoprudny, Moscow Region, 141700, Russia
[2] Max Planck Institut für Meteorologie, Hamburg, 20146 Germany
[3] World Climate Research Programme, Geneva, CH-1211, Switzerland

1. INTRODUCTION

An important atmospheric phenomenon, which is being intensively studied during the last years, are aircraft condensation trails (contrails) in the upper troposphere and pollution of the atmosphere from high-flying aircraft. Contrails are similar to thin cirrus clouds and may change the radiation fields and thus climate.

A first contrail climatology for the eastern North Atlantic and Western Europe derived from satellite images showed a significant cover and clear seasonal variations (Bakan et al., 1995). Statistical analysis of satellite images has shown, that at present time the additional cloud cover attributable to long-lived contrails is very small on a global average, but may reach more than 2% in the transatlantic flight corridor (Bakan et al., 1994). This figure represents a 10-20% increase of the natural cirrus cover in that region as derived by the ISCCP. As this increase is located to the south of the polar front, it may influence the meridional gradients which drive the synoptic instabilities that govern the European weather and climate.

The optical properties of contrails are important to estimate their impact on the radiation balance. There are several hints, that particles in contrails are smaller than in natural cirrus, but details are unknown due to the difficulties with observations near the tropopause. Remote sensing information from surface based or airborne spectrometers are used at Hamburg University/MPI to infer particle size information (Bakan et al., 1994, Betancor and Grassl, 1993).

There are indications of positive cirrus cloud cover and surface temperature trends since the beginning of the 1960's in the areas of intensive air traffic (Seaver and Lee, 1987; Sassen, 1995). Therefore, the impact of contrails on the Earth climatic system may increase and needs further studies. This is especially important due to envisaged increase in air traffic, by 50-100% until 2005, and due to the possible use of new kinds of fuel, which can especially increase aircraft water vapour emissions (Schumann, 1993).

At present, the physics of contrail formation, maintenance, lifecycle, and interaction with radiation are not clear. Particularly, seasonal and interannual variations of contrails, showed by satellite images, need explanation.

Presented in this report are results of numerical simulation of contrails that continue a study performed by Khvorostyanov, Bakan and Grassl (1995), with a 2D/3D cloud-resolving model with explicit water and ice microphysics and radiation (Khvorostyanov, 1994, 1995) jointly improved by all authors for application for cirrus and contrails. The model is based on: 1) two kinetic equations for the droplet and crystal size distribution functions for 30 size classes for both droplets and crystals in the range of 1 micrometer to 3.5 millimeters; 2) equations for the supersaturation with respect to water and ice; 3) equations for the terrestial and solar radiation transfer with account for the evolution of the optical properties of contrails and cirrus

2. SIMULATION OF A CONTRAIL

Simulation results of contrail formation, development, transformation into cirrus and their impact on longwave and solar radiation are presented below with an example, for which initial profiles of temperature, pressure and wind were taken according to the ICE-EUCREX field campaign on 15 October 1989 (kindly provided by Dr. M. Quante). As this model predicts supersaturation, we found that with use of uncorrected humidity profile, supersaturation with respect to ice exists only in a thin layer about 6.5-7.1 km, thus, no crystalline clouds should be observed above. However, thick Ci clouds were observed at this day in the layer nearly 6.5-9.5 km. This is a well-known problem of the humidity measurements, which strongly underestimate humidity below -35...-40 °C. Therefore, we increased relative humidity to provide positive supersaturation with respect to ice, δ_I, in the layer with observed Ci. Such a situation with increased humidity often exists in the regions of the frontal jet streams, wave disturbances and similar areas, where long-lasting contrails (up to 1-2 days) are being observed (Bakan et al., 1994; Betancor and Grassl, 1993); these areas can be called "moisture lens".

The scenario of exhaust was chosen similar to Appleman (1953), but modified for a modern or future planned stratospheric heavy aircraft (Schumann, 1993). A real contrail consists of three main regimes: 1) jet; 2) vortices; 3) diffusion. After the second, "vortex", regime contrail can be distributed in several hundred meters in vertical and horizontal due to the strong downdraft in the aircraft wake and may have a diameter of 300-400 m. (Schumann, 1993). In order to estimate a

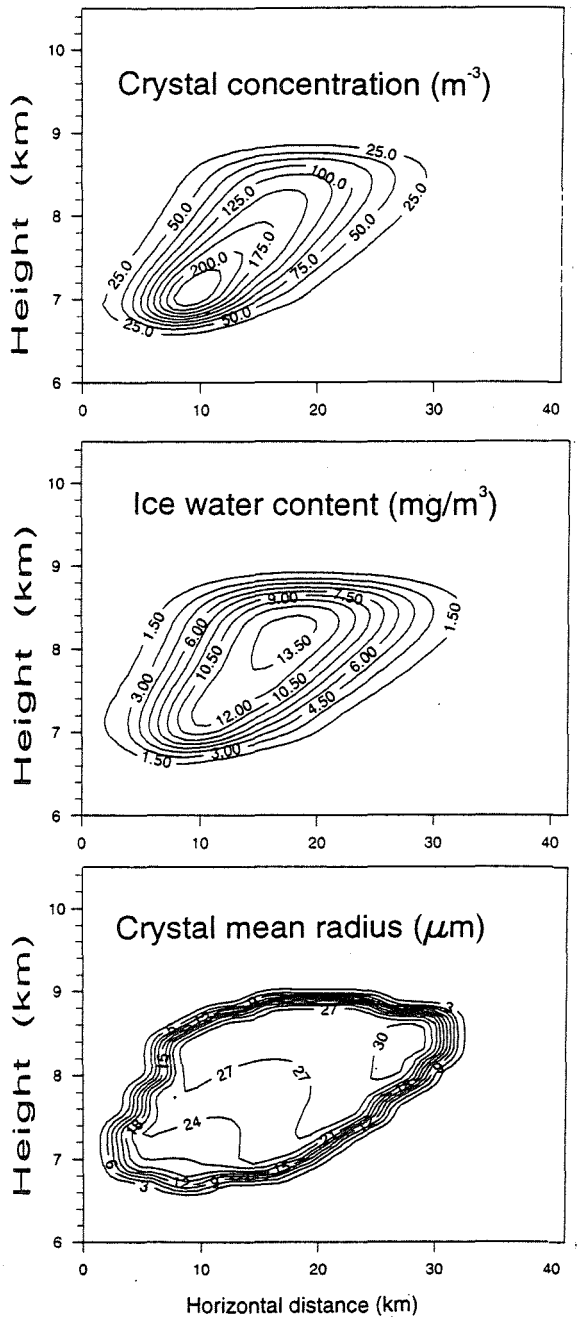

Fig. 1. Contrail microphysics after 40 min

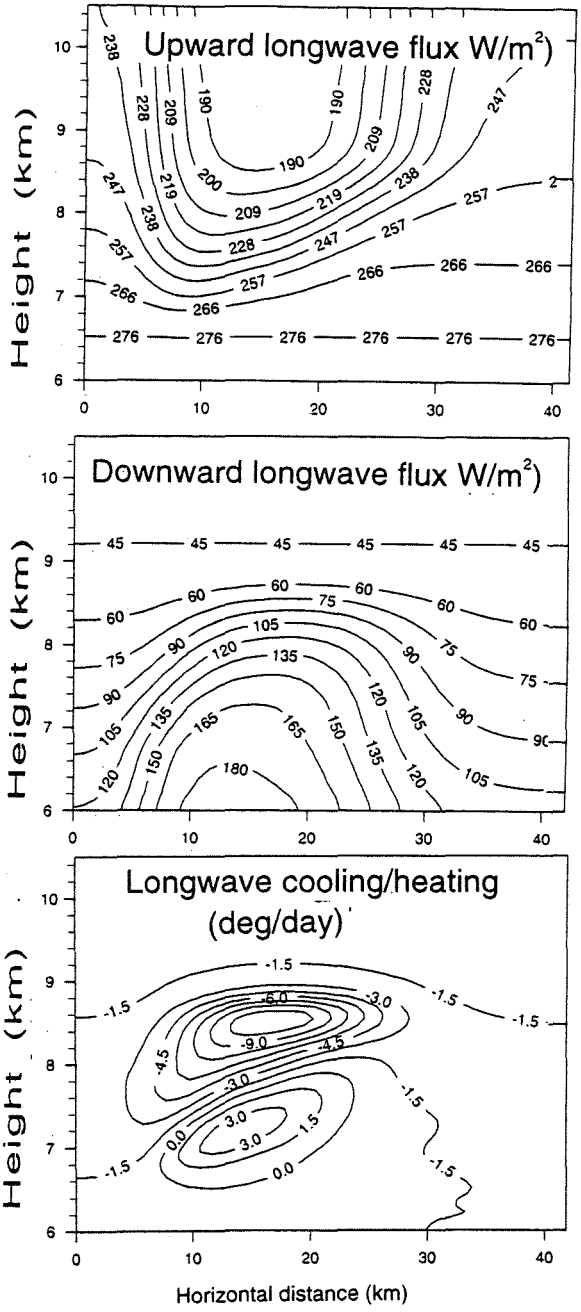

Fig. 2. Longwave radiation field after 40 min

possible effect of a future heavy (e.g., supersonic) aircraft, we increased this value about twice. In the first example, we use a 2D version of the model and consider a vertical plane across contrail. We start our simulation after relaxation of vortices with initial contrail formed after first two regimes (usually, several minutes) and homogeneously distributed in vertical.

Fig. 1(a,b,c) shows a vertical cross-section of the contrail microphysics (crystal concentration, IWC, mean crystal radius) after 40 min of its development. Due to the combined effects of the turbulence and wind shear in the layer of contrail location, where wind speed grows by about 10 m/s, it has a shape of a typical anvil and its upper part is moving and spreading much faster than the lower part. Thus, crystal number density is several times lower in the upper part. Here, "competition" crystals for the moisture is much less, they grow faster and maximum of the mean radius is reached in the upper downwind part of the contrail (Fig. 1c). Maximum of IWC, 12 mg/m^3 appears in the upper part .Release of the latent heat increases buoyancy and causes formation of two large vortices with central updraft region around 12-16 km which follows the shape of the contrail and is declined downwind. But the value of the vertical velocity does not exceed 2 cm/s. Supersaturation with respect to water is negative everywhere, thus droplets cannot exist and supersaturation with respect to ice δ_I is positive, thus crystals are growing, and both these fields show decrease in the region of contrail by 3-4 %, caused by

deposition of the vapour on crystals. Thus, due to contrail development, a small "gap" in water vapour field appears, i.e., not only microstructure of a contrail depends on supersaturation, but the spatial distribution of supersaturation, in turn, is essentially influenced by contrail. Note that in spite of the long enough time of this contrail induced cirrus existence, supersaturation δ_I is large enough, 8-12%, that means that deposition of the vapour on the crystals is not instantaneous, but can take several hours. Thus, long-lasting contrails may evolve and change their radiative properties during several hours.

Calculated crystal size spectra at various horizontal and vertical locations are strongly variable in space, but exhibit two common features: 1) monomodality with slight tendency to the bymodality in the rear left part due to the presence of the large number of small crystals here and in the right lower part due to the effect of accretional growth; 2) the slope of the spectra is essentially steeper in the region of small sizes than that in the region of the large sizes. The second feature can be explained by the stronger influence of turbulence on the larger sizes, where turbulent mixing is responsible for the broadening of the spectra.

Comparison of the calculated contrail microphysical properties are in a good qualitative agreement with aircraft measurements of the aged contrails, performed during ICE-EUCREX for similar conditions (Gayet et al., 1993).

By that time, contrail is already thick and wide enough and can be identified during aircraft or remote measurements as a natural cirrus cloud. Although IWC is rather small, it essentially influences radiative fields (Figs. 2, 3). The longwave cooling rate reaches -10 K/day in the upper part and longwave heating reaches 3 K/day in the lower one (Fig. 2c), that increases instability of the atmosphere. Fig. 3 shows, that Solar heating reaches 3 K/day in the upper part and maximum albedo is 25% above the contrail against 10% in the environment above the sea, thus, the contrail increases albedo by 15%.

After 1h 10 min of development, the horizontal extent of contrail is about 40 km and it is declined downwind due to the windshear. Maximum of crystal number density, 150 l^{-1}, is located in the lower back part, IWC reaches 15-20 mg/m^3 in the central region, but the field of mean radius essentially changed compared to the previous time. If 30 min ago the maximum of mean radius was in the upper part (Fig. 1c), now it is located in the front lower part because the largest crystals precipitate faster in the front part.

A comparison of the contrail effects on the radiative fluxes and total balance at various times is given in the Table.

After 40 min, the upward longwave flux above the contrail is by 60 W/m^2 less than in clear sky environment and downward flux is by 75 W/m^2 more below the contrail; Thus, the strong greenhouse effect

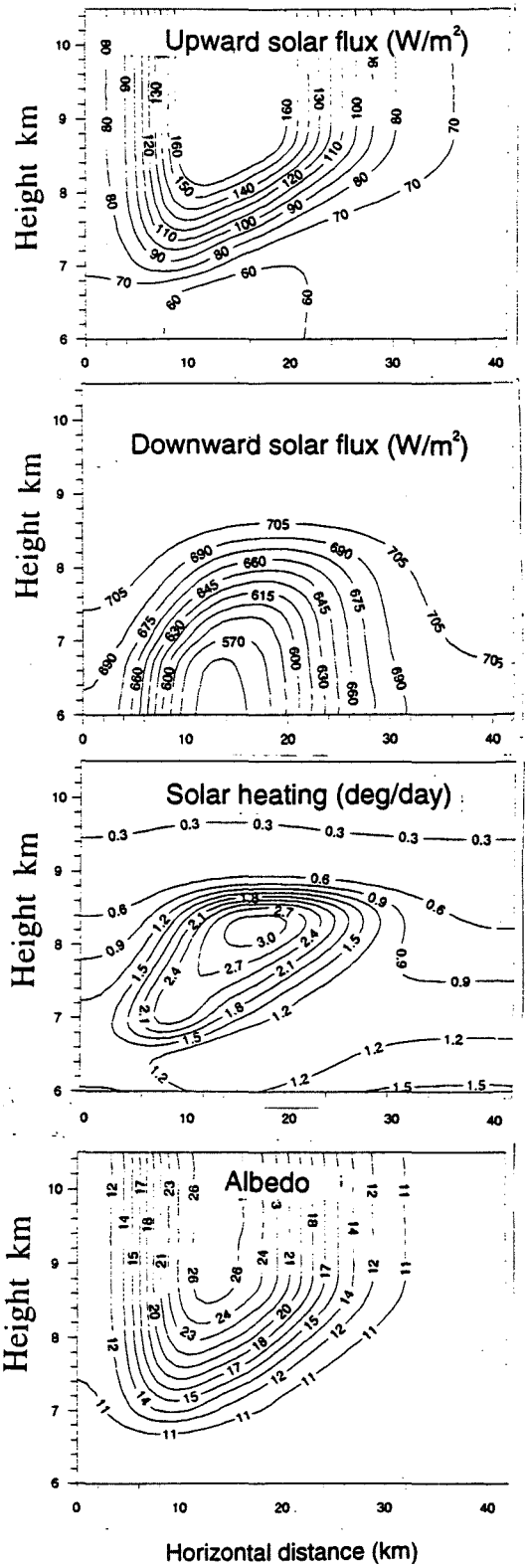

Fig. 3. Solar radiation field after 40 min

with respect to longwave radiation is created by this contrail induced cirrus. The reflected solar flux above contrail is by 80 W/m^2 more and downwelling flux is by 150 W/m^2 less below contrail, i.e., albedo effect is also large enough due to the rather small size of crystals.

By the time 1h 10min, both the greenhouse and albedo effects of contrail have grown.. The decrease in outgoing longwave radiative flux reaches 70 W/m^2 above contrail, increase in downwelling flux is 90 W/m^2 and longwave cooling (heating) reaches -12 (+4) °C/day. The increase in upward and decrease in downward solar fluxes are now 90 W/m^2 and 120 W/m^2.

Table: contrail induced cloud forcing

Variations in upward (index "up") and downward (index "down") radiative fluxes F_{long} (longwave), F_{short} (shortwave) and total balance R_{tot}; units are W/m^2

above contrail	δF^{up}_{long}	δF^{up}_{short}	δR^{up}_{tor}
time=40min	-60	80	-20
time=70min	-70	90	-20
below contrail	δF^{down}_{long}	δF^{down}_{short}	δR^{down}_{tor}
time=40min	75	-150	-75
time=70min	90	-120	-30

The most important quantity, the perturbations of the total radiative balance, at t=40 min are -20 W/m^2 above contrail and -75 W/m^2 below. So, the total albedo effect dominates., and it is greater below the contrail than above. At time 1h 10min, the perturbations of radiative balance are -20 W/m^2 above contrail and -30 W/m^2 below, i.e., after half an hour, the albedo effect still dominates; the cooling effect of contrail almost did not changed above contrail but decreased 2.5 times below contrail.

So, these contrail and contrail induced cirrus exhibit pure negative cloud forcing, that causes negative surface temperature trends. However, this negative forcing is weakening with time and probably may become positive after a while along with the growth of crystals and decrease in albedo. Account for the absorbing properties of aerosols injected from aircraft and imbedded in crystals may influence these effects (Grassl, 1977).

3. SEEDING FROM A CONTRAIL INTO UNDERLYING LIQUID AS CLOUD

A 3D version of the model was used for this simulation. Computational domain was 8 km in x-direction, 50 km in y-direction and 6.5-8.5 km in vertical. The mean wind is directed along the x-axes at the top of the domain and rotates anticlockwise downward according to the Ekman spiral. Initial state was slightly subsaturated and a cloud was absent. A weak upward velocity of 1 cm/s was superimposed in the layer 7.1-7.5 km, and after an hour a liquid As cloud began to form. After 2 hours, its boundaries were 7.1 km and 7.4 km, the mean droplet radius was 6-8 μm and LWC reached 0.08 g/kg, cloud temperature was warmer than -40 °C and the processes of natural crystallization were suppressed. At this time, contrail formation was modelled. It is assumed that an aircraft has passed computational domain along the y-axes) above the cloud at temperature below -40 °C and created a seeding line of small crystals 10 km long (y=20-30km. We assume crystals concentration after jet and vortices regimes is 10^2 L^{-1} in YOZ plane. This is a simplified treatment but it can serve for the qualitative estimation of the effect.

After seeding, the process of vapour distillation from the droplets to crystals starts due to the difference in saturation pressure over water and ice. The droplets evaporate, the crystals grow and precipitate and an artificial crystallization zone (ACZ) is formed. Turbulent mixing and wind transport lead to the spreading and deformation of ACZ (Fig. 4). After 40 min, liquid water near the cloud top disappears in a band 1.8 km wide, this band is broadening downward more than twice and is tilting downwind. This is explained in Fig. 4b. The contrail and crystallization zone are strongly broadening and tilting downward due to the increase in windshear and decrease in wind speed to the cloud bottom. Note that the windshear is different here from the example considered before, this causes the different shapes of these contrails.

In this example, the contrail has the shape of an anvil but turned upside down. It extends to the lee side below the cloud and is much broader here than above the cloud as can be seen from a satellite. So, As cloud has a "masking" effect for viewing from above, but the correct measurements of contrail width can be done with use of lidar polarization technique from the ground (Sassen, 1995).

Somewhat unexpected result is that the properties of the contrail and crystallization zone after 40 min are inhomogeneous even along the originally homogeneous contrail (Fig.4, plane YOZ). This is because the v-component of the wind speed in the layer around 7.1 km is maximum while windshear is minimum. Horizontal extension of the contrail is slowest here and some sort of accumulation zone of crystals occur. Maxima of the crystal number density and IWC are displaced to the lee side of the contrail, they are 1.5-3 times more near the start of the contrail (x=20km) than near the end (x=30km) and are located in the layer with maximum wind speed. This can be also verified by means of remote sensing. The particles in the crystallization zone are an order of magnitude more than in a liquid As cloud, thus these contrail seeding effects can be identified as the local sharp minima in the optical thickness field of the liquid middle-level clouds.

4. CONCLUSION

Results of the simulation, described above, show that it is possible with a numerical model to reproduce the evolution of contrail/cirrus microstructure and its impact on the optical properties and radiative characteristics of these clouds. Our results show that the albedo effect can prevail in young contrails and contrail induced cirrus (negative cloud forcing), while it is decreasing and

Seeding from crystalline contrail into the underlying liquid mid-level cloud As, after 40 min of simulation

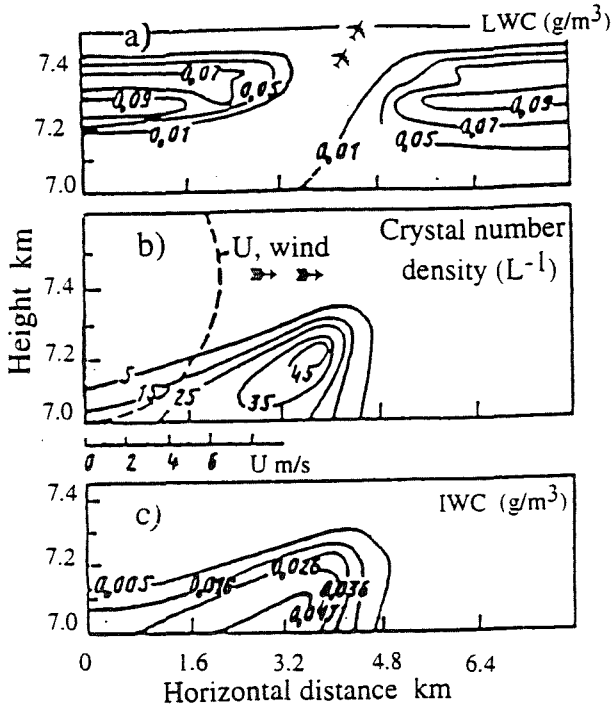

Fig. 4. Vertical cross-section across contrail and crystallization zone (X-Z plane)

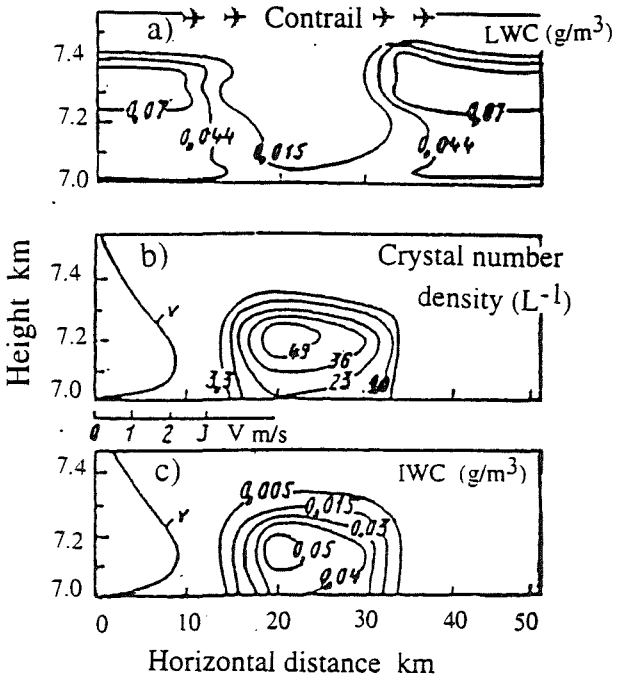

Fig. 5. Vertical cross-section along contrail and crystallization zone (Y-Z plane)

perhaps may be changed by the greenhouse effect for the aged contrails due to the changes in microstructure.

These effects strongly depend on the environmental conditions (humidity, first of all) and on scenario of aircraft exhaust (type of an aircraft). A series of numerical experiments with varying environmental conditions will allow:1) to explain observational, particularly, to clarify their climatology as viewing from satellites (Bakan et al., 1994); 2) to estimate possible effect of developing air traffic on the atmosphere, in particular, to clarify, if it causes global warming or cooling. Precise measurements of humidity are urgently needed.

5. REFERENCES

Bakan S., Betancor M., Gayler V., Grassl H., 1994. Contrail frequency over Europe from NOAA-satellite images. Ann. Geophysicae, v. 12, No 10/11, pp.962-968.

Betancor M., Grassl H., 1993. Satellite remote sensing of the optical depth and mean crystal size of thin cirrus and contrails. Theor. Appl. Climatol., 48, 101-113.

Gayet, J.-F., Febvre G., Brogniez G. and Wendling P., 1993. Microphysical and optical properties of cirrus and contrails: cloud field study on 13 October 1989. 6th ICE/EUCREX Workshop, Stockholm, Sweden, 24-26 June 1993, 30-39.

Grassl, H., 1977. Radiative effects of absorbing aerosol particles inside clouds. In "Radiation in the Atmosphere" (H. J. Bolle, ed.), 180-182. Science Press, Princeton, New Jersey.

Khvorostyanov, V.I., 1995. Mesoscale processes of cloud formation, cloud-radiation interaction and their modelling with explicit cloud microphysics. Atmos. Res., v. 39, No 1-3, pp. 1-67.

Khvorostyanov V., Bakan S., Grassl H., 1995. Simulation of contrails/cirrus formation and their interaction with radiation by a mesoscale cloud model with explicit water and ice microphysics. Proc.. 7th ICE/EUCREX Workshop , Lille, France, September 1994, 210-227.

Liou, K.N., Ou S-C. and Koenig G., 1991 An investigation of the climatic effect of contrail cirrus. In: Air Traffic and the environment. Lect. Notes in Engrg, Ed. U. Schumann, 60, Springer-Verlag, Berlin, p. 154-169.

Sassen K., 1995. The Properties of contrails: Toward an assessment of climatic change potential. Proc. AMS Conf. Cloud Phys., Dallas, January 1995, 407-412.

Schumann U., 1993. On the effects of emissions from aircraft engines on the state of the atmosphere. Report No 1, Institute für Physik der Atmosphäre, DLR, 45 p.

LARGE-EDDY SIMULATION OF CONTRAILS

Andreas Chlond

Max-Planck-Institut für Meteorologie, D-20146 Hamburg, Germany

1. INTRODUCTION

Engine water vapor emissions by aircraft are expected to be of significant importance because they may lead to an increase in high altitude ice clouds (Graßl, 1990; Liou et al. 1990; Schumann, 1994). In terms of atmospheric impact of aviation, there are two key areas of concern. The first deals with the perturbations of radiative properties of the atmosphere through contrail formation. Ice clouds enhance reflection of sunlight as well as thermal emission. The net effect is uncertain because the competition of solar albedo and IR greenhouse effects involving ice clouds is dependent on such factors as cloud position, cloud thickness and microphysical properties. Contrails are expected to enhance the greenhouse effect, owing to their small thickness (Stephens and Webster, 1981; Stephens et al., 1990). The second issue focuses on the chemical effects and mainly on how heterogeneous reactions which might occur on the surface of ice particles within contrails affect the NO_x budget (Schumann, 1995).

2. OBJECTIVES

The objectives of our study have been firstly to investigate the secondary flow structure within clouds to understand the processes that cause contrails to spread out to form cirrus clouds. Secondly, to examine the respective roles of external conditions, such as temperature, humidity, static stability and baroclinicity of the ambient atmosphere in the evolution of contrails and to determine the importance of the initial ice particle size and of physical processes such as radiation on the development of contrails.

3. APPROACH

The approach undertaken is to use a state of the art LES-model (Chlond, 1992, 1994, 1996) that incorporates a detailed description of all relevant physical processes. Unlike earlier contrail models, which were subject to limitations in the ability to resolve the actual eddy structure, our primary interest is in simulating the temporal development of three-dimensional secondary flows within contrails under conditions where latent heat release and radiative fluxes should have a strong effect. Hence, our study confines to the simulation of contrails in the so called dispersion regime, which begins at a time of the order of 100 s after exhaust, because only in this phase large, persistent contrails can evolve which in turn may have impact on climate. During this phase the evolution of the contrail is controlled by the interaction of the ice cloud with the background turbulence field and self-induced dynamics due to differential radiative heating and due to latent heat release. The general idea underlying the model is that of a large-eddy model. The model explicitly represents large-scale three-dimensional motions, while small-scale turbulence is parameterized. The model includes most of the physical processes occurring in ice clouds in the absence of solar radiation. It contains a treatment of the sub-grid scale turbulence which incorporates the effects of stratification, it takes into account infrared

radiative cooling in cloudy conditions (using an effective emissivity model) and the influence of vertical shear of the ambient flow. Moreover, we explicitly resolve the size distribution of ice particles and calculate the evolution of the size distributions, including processes such as deposition growth, sublimation and transport.

The numerical integration scheme is based on an equidistant staggered grid and finite difference approximations. The spatial domain is specified as an elevated box which extends over a finite domain of size 640*640*640 m^3. The domain is divided in 64^3 grid boxes (i.e. $\Delta x=\Delta y=\Delta z=10$ m). For numerical purposes the ice particle distribution is subdivided into 12 classes with equidistant grid spacing in logarithmic scales, resulting in a radius grid that spans from $r_{min}=1$ µm to $r_{max}=64$ µm. A time step of 1.5 s was used for all runs.

4. DESIGN OF NUMERICAL EXPERIMENTS

To set up the control run which serves as a reference case, the model is applied to conditions that are typical for those under which contrails could be observed in the atmosphere; i. e. we anticipate an air volume at a height of 10550 m ($p_{00}=250$ hPa) which is slightly supersaturated with respect to ice ($r_i=129\%$) and at a reference temperature of $T_{00}=220$ K. The initial potential temperature field was assumed to be horizontal homogenous and initially slightly stable throughout ($d\theta/dz=2.5$ K/km). Based on this temperature field, we choose to initialize the moisture field with a relative humidity of $r_i^{env}=129\%$ in the environment of the contrail. Within the contrail we assume that phase relaxation has already occurred, i.e. $r_i^{cont}=100\%$. The contrail is specified as two parallel cloud bands in the middle of the model domain elongated in the y-direction. The lateral distance between the two cloud cores forming the contrail is 50 meters. The initial diameter of each of the two cores of the contrail is 30 meters. The initial ice water content of the contrail is determined by the amount of water which is emitted by the aircraft due to the combustion of fuel (15 g m^{-1} for a B747 aircraft at cruising level) and by the substance of water vapour of environmental air which has been entrained into the contrail and subsequently converted into ice during the jet- and the vortex-phase, resulting in $(\bar{q}_i)_{cont}=4.26\cdot10^{-5}$ kg/kg. Within the contrail the ice particle spectra are initialized as mono-disperse distributions, i.e. the initial ice mass is concentrated in one bin and the mean effective radius was specified as $r_e=2.4$ µm, giving a total number of ice particles of $N_{TOT}=7.87\cdot10^8$ kg^{-1}. The model was run assuming no mean vertical wind shear with the initial condition taken as an atmosphere at rest except for a constant background wind along the contrail, i.e. $u_g=0$ and $v_g=20$ m s^{-1}. The impinging longwave radiative fluxes at the bottom and the top of the model are specified as $F^u(z_B)=250$ W m^{-2} and $F^d(z_T)=30$ W m^{-2}, respectively. To initiate convective motions random temperature perturbations of small amplitude are imposed at the first time step.

Among the reference case 12 sensitivity runs have been performed to clarify the influence of external conditions, initial conditions and physical processes in the evolution of contrails (Table 1). The sensitivity runs (1) to (2) and (4) to (9) (run (3) refers to the control run) were different in that one of the external parameters of the control run is varied while the others are fixed. In this way, we investigate the influence of the ambient temperature T_{00} (run (2) and (4)), static stability $d\theta/dz$ (run (1) and (5)), relative humidity r_w (r_i) (run (8) and (9)), and mean vertical wind shear du_g/dz, dv_g/dz (run (6) and (7)). Run (10) and (11) use the same external parameters as the control run but eludicate the importance of the radiation term. In simulation (10), the radiation term is neglected in the droplet growth equation while in run (11) radiative heating is not included as well in the droplet growth equation as in the thermodynamic equation. Finally, the sensitivity of the numerical results on different choices of the initial ice particle size is investigated. In run (12) and (13) we set $r_e=4.8$ µm and $r_e=1.7$ µm, respectively.

The integrations run over 1200 time steps and each 30 minute simulation required

about 12 hours of CPU time on one processor of a CRAY C916 computer.

Table1: Summary of numerical simulations

Run	T_{00}/K	$\frac{\partial\theta}{\partial z}$ $\left(\frac{K}{km}\right)$	$\frac{\partial u_g}{\partial z}$ $\left(s^{-1}\right)$	$\frac{\partial v_g}{\partial z}$ $\left(s^{-1}\right)$	$r_w(r_l)$/ (%)	remarks
1	220	0	0	0	65(129)	-
2	210	2.5	0	0	65(153)	-
3	220	2.5	0	0	65(129)	control
4	230	2.5	0	0	65(111)	-
5	220	5	0	0	65(129)	-
6	220	2.5	0	510^{-3}	65(129)	-
7	220	2.5	110^{-3}	0	65(129)	-
8	220	2.5	0	0	55(109)	-
9	220	2.5	0	0	75(149)	-
10	220	2.5	0	0	65(129)	no radiation term in droplet growth eq.
11	220	2.5	0	0	65(129)	without radiation
12	220	2.5	0	0	65(129)	r_e=4.8 µm
13	220	2.5	0	0	65(129)	r_e= 1.7 µm

5. RESULTS

In order to asses the influence of external parameters, initial conditions, and of radiation on the development of contrails, we have plotted integral quantities, such as turbulent kinetic energy (TKE), total ice water content (IWC), and the horizontal and the vertical spreading of the contrail (σ_x^2 and σ_z^2) as function of time for the various model experiments (Figure 1). Based on the results of these experiments the following conclusions could be drawn:

1. Persistent contrails can only form in an atmosphere that is supersaturated with respect to ice.

2. The turbulent eddies forming within the contrail are driven by buoyancy. In particular, latent heating due to condensation provides the significant energy source while destabilization due to differential radiative heating plays no role owing to the small optical depth of the contrail.

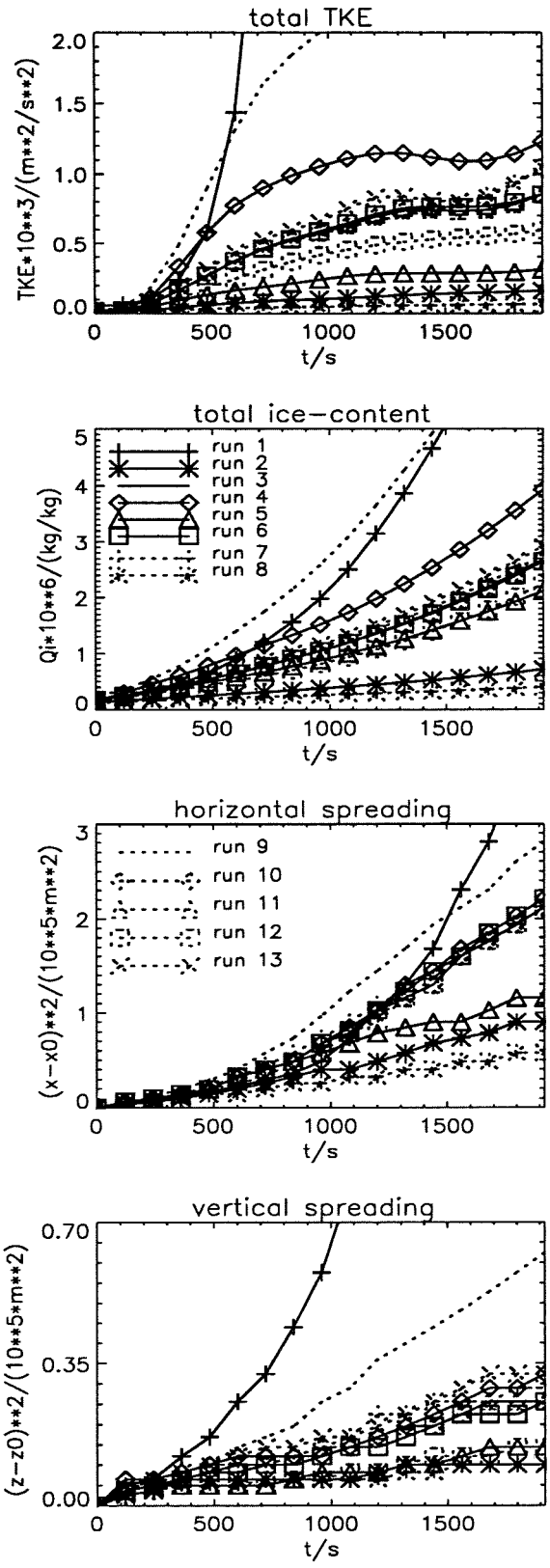

Figure 1: Turbulent kinetic energy, total ice water content, and horizontal and vertical spreading of contrails as function of time for the various model experiments

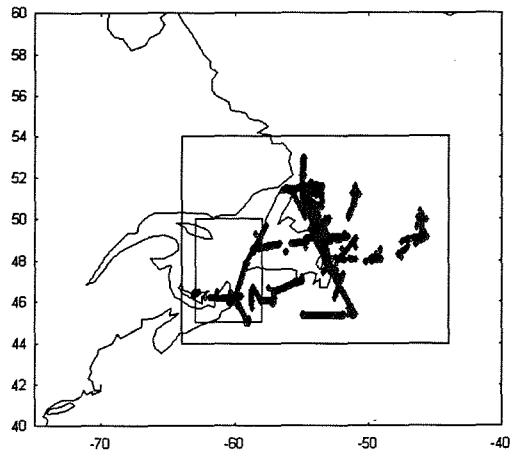

Fig.1: Geographical distribution of data points. The boxes show an example of a MC2 nested grids configuration.

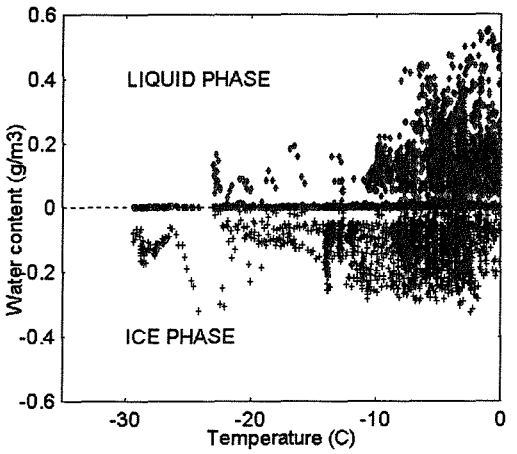

Fig. 2: Distribution of cloud phase with temperature.

3. A MIXED-PHASE CLOUD SCHEME

Considering simplifications from cloud microphysics parameterizations currently used in cloud models, Tremblay *et al.*, 1996 proposed a mixed-phase cloud scheme. The scheme considers only one prognostic variable (the total water content) partitioned diagnostically into solid and liquid phases at subfreezing temperatures. The proposed approach can be used in mesoscale or large-scale atmospheric models since it is computationally fast and easy to implement. Within this framework, the fractional ice content f is obtained from the following relationship:

$$c_R(T,p)M^{\beta_2} f^{\beta_2}(1-f)+c_D(T)M^{\beta_1-1} f^{\beta_1} - \frac{wG(T,p)}{M} f\left[1+(1-f)\xi\right]=0 \quad (1)$$

In the above the thermodynamics functions c_R and c_D follow from formulation of the rate of deposition of water vapor on ice crystals, and from the interaction between solid and liquid phases respectively. The term wG represents the generation of water vapor excess over saturation by moist adiabatic cooling, and the parameter ξ is the mixed-phase sedimentation parameter. The physical constants β_1 and β_2 are related to the moments of solid particles size distribution. Details are in Tremblay *et al.*, 1996.

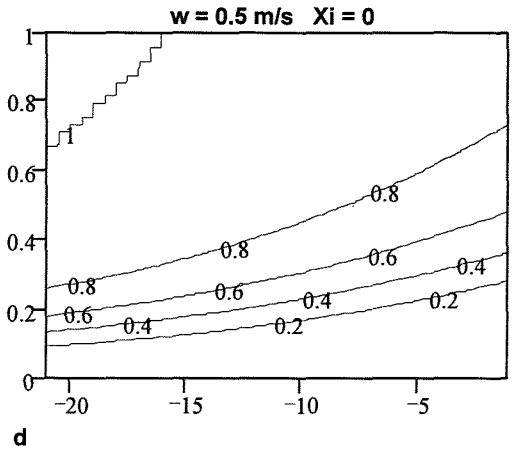

F

Fig. 3: Fractional ice content contoured as a function of temperature T (°C) [abscissa], total water content M (g/m3) [ordinate], and for p = 800 mb

Figure 3 was generated by solving (1) numerically for f and depicts the fractional ice content expressed as a function of temperature and total water content for a value of vertical velocity w = 0.5 m s^{-1}, $\xi = 0$ and for a pressure p = 800 mb. For a given point (M, T), the fractional ice content corresponds to this specific values of w , ξ and p. For example, for M = 0.4 g m^{-3} at a temperature of -5 °C the condensate would consist of 0.24 g m^{-3} (60%) of ice phase and 0.16 g m^{-3} of SLW. The isoline f = 1 in this diagram defines the boundary between glaciated and mixed-phase clouds. In Fig. 4, keeping M constant results in decreasing SLW amount with decreasing temperature as indicated by observations of clouds. It is also apparent that the dependence of f on M is stronger than its dependence on T, as indicated by the shape of the f-isolines. According to proposed approach f = $f(M, T, w, \xi, p)$, and trying to parameterize f in term of T only may be questionable.

4. DATA CLASSIFICATION.

Within the present observational framework, only four independent parameters are measured (q_L, M, T and p). Thus, it is not possible to use these observations to directly validate the relationship $f(M, T, w, \xi, p)$ since the quantities w and ξ are not observed. In other words, it is not possible to dissociate the cloud scheme from an atmospheric model for validation, and it is only possible to evaluate the entire forecast system.

This alternative is explored in the present investigation. For each CFDE flight a high resolution (Δx = 5km) nested simulation was performed with the MC2 model (see Fig. 1). For each of these simulations the model fine grid was positioned over the flight track center and a statistical comparison was performed at flight mid time.

Since the aircraft data set is nonsystematic and biased - the result of not random flight trajectories - , a direct statistical comparison with model-generated data is not possible. To circumvent this problem, it is necessary to stratify the data. The observations were classified within small volumes [δM, δT, δp] in the (M, T, p) space. A coarse stratification (large values of δ's) reflects the biased nature of the data set, but provides a better estimate of statistical parameters (larger population). On the other hand, a fine stratification minimizes the bias effect but reduces the population. In the present context, values of δM = 0.04 g m^{-3}, δT = 2 °C and δp = 5 mb were selected. These values are close to instruments accuracy and define the finest possible classification.

The data set was scanned sequentially, and each observation was classified within its corresponding volume. Classes with $N < 20$ were not considered statistically significant and were rejected from the analysis. This procedure has generated 50 independent classes (Fig. 4) with population ranging from 20 up to 130 items (average, 45 items). Each of these classes is centered on a specific (M, T, p) value and can be considered as an unbiased data subset. Therefore a meaningful statistical description of f, q_L or q_S is possible within each of these category.

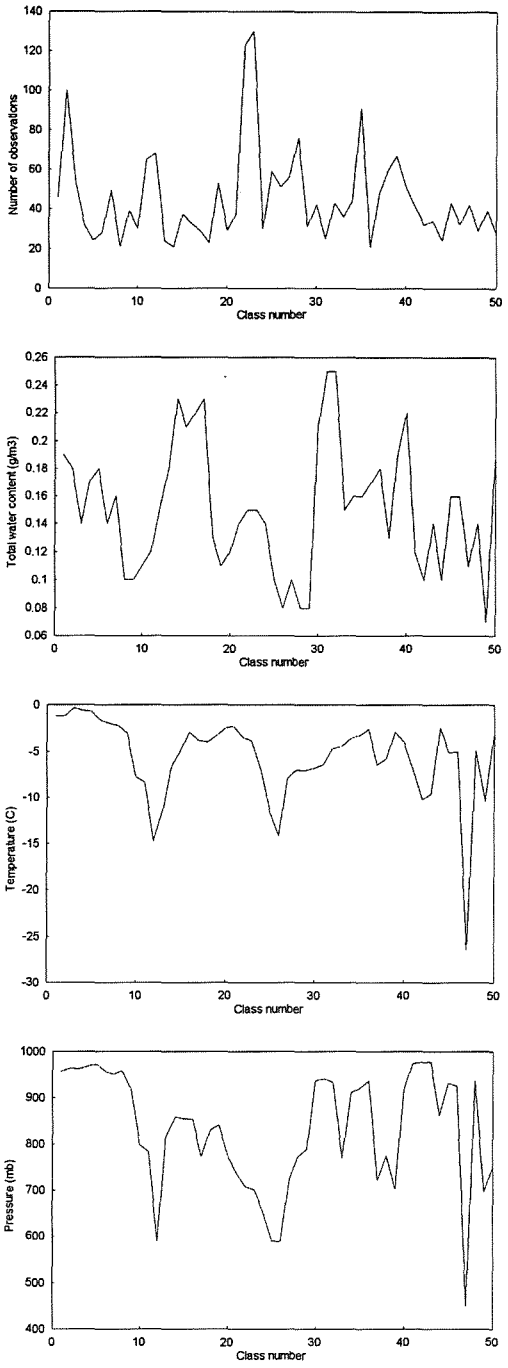

Fig. 4:Aircraft data classification showing the number of points, M, T and p.

5. COMPARISON OF MODEL WITH OBSERVATIONS

In order to evaluate the accuracy of the modeling system in reproducing the statistical behavior (i.e., the climatology), of mixed-phase clouds during the CFDE, the same classification technique was applied to model-generated data. The model outputs were scanned to match all the points within

each class and the statistics of q_L, q_S and f were calculated.

Fig. 5 shows N as a function of the class number for both observations and model. It demonstrates that it was not possible to model all classes, suggesting that the phase-relationship between M, T and p in the model was not accurate enough to retrieve the selected fine classification. Selecting a coarser classification criteria would likely improve this aspect. It is also possible that the initial data were not accurate enough to reproduce the fine scale structure of the cloud field. Obviously, one should also envisage a deficiency in the parameterization itself or in the physical constants used to calculate the microphysical processes involved.

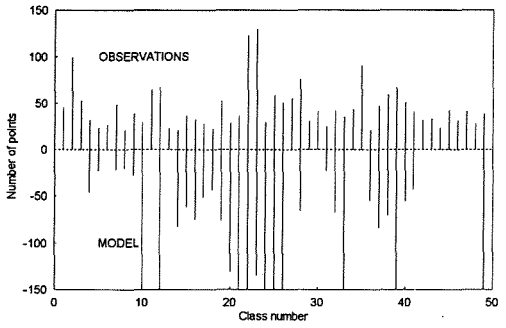

Fig. 5: Number of observed and modeled points for each class.

A comparison of the average supercooled liquid water within each class for both observations and model, is depicted in Fig. 6. It is clear that the model has a tendency to systematically underforecast the amount of SLW. There is a number of possibilities to explain such a behavior, including a too coarse resolution. Additional tests and runs have to be performed to address the present problems.

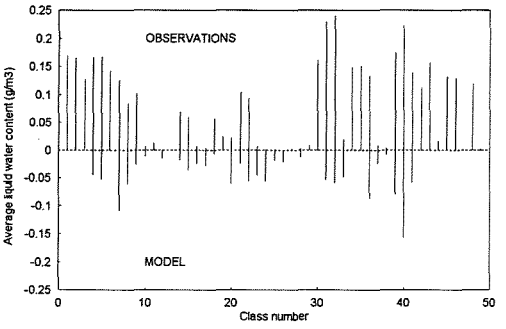

Fig. 6: Average supercooled liquid water content as a function of class number for observations and model.

6. SUMMARY

Based on aircraft data, a methodology allowing a statistic evaluation of cloud schemes used in atmospheric model has been suggested. An example was given with the scheme of Tremblay *et al.* (1996) currently implemented in the MC2 model. It was found that the scheme has a tendency to underforecast the amount of supercooled liquid water. This research is however at a very preliminary stage and more work is still required before a definitive assessment can be done regarding the properties of the scheme. Comparisons with other schemes (e.g., Smith, 1990) still need to be performed.

7. ACKNOWLEDGMENTS

This was funded by the Canadian National Search and Rescue Secretariat, Transport Canada, the Atmospheric Environment Service and the Institute for Aerospace Research of the National Research Council.

8. REFERENCES

Cober, S.G., G.A. Isaac and J.W. Strapp, 1996: Aircraft icing from supercooled drizzle. Proceedings of the 12th Intl. Conf. Clouds and Precipitation.

Isaac, G.A., A. Korolev, J.W. Strapp, S.G. Cober, A. Tremblay and R.A. Stuart, 1996: Freezing drizzle formation mechanisms. Proceedings of the 12th Intl. Conf. Clouds and Precipitation.

Smith R.N.B., 1990: A scheme for predicting layer clouds and their water content in a general circulation model. Quart. J. Roy. Met. Soc., 116, 435-460.

Tremblay, A., A. Glazer, W. Yu and R. Benoit, 1996: A mixed-phase cloud scheme based on a single prognostic equation. Tellus, in press.

A MEASUREMENT AND MODELING STUDY OF YOUNG CIRRUS CLOUDS: PART 2, MODEL PREDICTIONS

Hong Lin[1], Kevin J. Noone[1], Johan Ström[1], Andrew J. Heymsfield[2] and Larry Miloshevich[2]

[1]Department of Meteorology, Stockholm University, S-106 91 Stockholm Sweden
[2]National Center for Atmospheric Research, P.O. Box 3000, Boulder, CO, 80303, USA

1. INTRODUCTION

Cirrus clouds have long been recognized as a sensitive element in the earth's radiative balance. While low clouds tend to have a cooling effect on the Earth, cirrus clouds may have either a cooling or warming effect, depending on their location, thickness and microphysical characteristics.

One of the main properties necessary to assess the radiative effect of cirrus clouds is knowledge of the crystal size distribution. Examinations of the radiative properties of cirrus clouds have led to deductions that cirrus clouds are often composed of small ice crystals [*Ackerman et al.*, 1990; *Prabhakara et al.*, 1988]. In a review of the available measurements, King [*King*, 1993] concluded that the effective radius of ice crystals in the earth's atmosphere is much smaller than our current ability to measure it.

The Counterflow Virtual Impactor (CVI: [*Noone et al.*, 1988; *Ogren et al.*, 1985]) has been used on several occasions to investigate the properties of cirrus clouds [*Noone et al.*, 1993; *Ström and Heintzenberg*, 1994; *Ström et al.*, 1994]. The CVI aerodynamically separates cloud elements larger than 2-3μm radius from interstitial aerosol and ambient gases. Once sampled, the cloud elements (crystals or droplets) are evaporated. The condensed water and volatile material in the crystals/droplets is driven into the gas phase. The non-volatile material remains as *residual* aerosol particles. The condensed water content and number concentration of crystals larger than 2-3μm can be measured with the CVI. In addition, the size distribution of the residual particles from the evaporated crystals can also be measured.

Here we present results from a comparison between model calculations and measurements of ice crystal size distribution, concentration, and residual particle microphysics for the case of a newly-formed cirrus cloud. We wish to see whether the model can predict the presence of small ice crystals and also whether the model can successfully describe the residual particle size distributions.

2. MODEL DESCRIPTION

We have modified an existing cirrus parcel model to accept measured aerosol size distributions as inputs. The previous incarnation of the model [*Heymsfield and Sabin*, 1989] assumed a CCN distribution, then calculated an input aerosol distribution from the assumed CCN distribution. Here we will used measured aerosol size distributions as inputs for the model calculations. In addition to the aerosol information, input values for pressure, temperature, relative humidity and updraft velocity are taken from measured values.

3. MEASUREMENTS

The data we use to both initialize the model and to compare our model results come from a series of flights over southern Germany done during March, 1994 [*Ström et al.*, 1996]. Aircraft instrumentation included a CVI and interstitial aerosol inlet (from which condensed water content, crystal number concentration, residual and interstitial particle size distributions were derived), an ice replicator (from which crystal size distributions were derived) and various sensors for meteorological measurements.

4. RESULTS

Figure 1 shows the input aerosol size distribution used in the model calculations. It is a composite of measurements from the CVI and interstitial inlet taken during the flight on March 18, 1994. The distribution is bimodal. The smaller mode has a geometric mean diameter of 0.1μm, a geometric standard deviation of 1.65, and has a particle concentration of 350cm^{-3}. The larger mode has a geometric mean diameter of 0.725μm, a geometric standard deviation of 1.4, and a concentration of 1cm^{-3}.

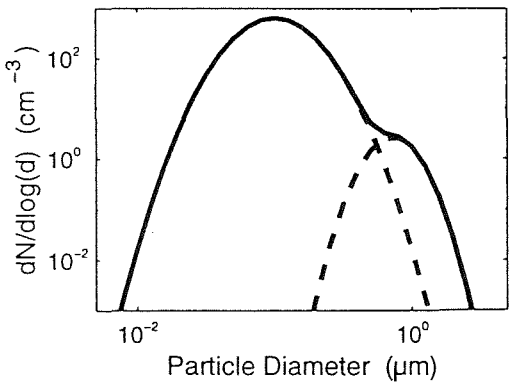

Figure 1. Input interstitial size distribution. The distribution is a composite of measurements taken on 18 March 1994.

We defined a "base case" for the input parameters from the entire set of measurements from the four flights of the experiment. The initial parameters were: Pressure - 330hPa; altitude - 8500m; temperature - -51°C; relative humidity - 85%; updraft velocity - 25cm s^{-1}. We allowed the air parcel to rise 30m in the simulation. The measurements on March 18th indicated a wave motion for the air with an amplitude of approximately 60m. We chose half the amplitude as a representative value for the uplift height.

Crystal Size Distributions and Concentrations

Figure 2 illustrates the predicted and observed crystal size distributions for the base case run.

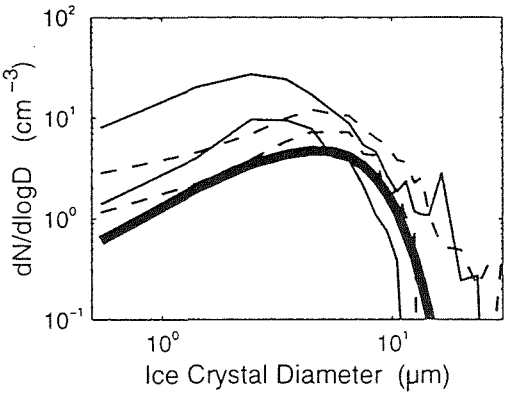

Figure 2. Predicted and observed crystal size distributions.

The thick solid line is the crystal size distribution predicted by the model for the base case. The observed crystal size distributions appeared to fall into two different regimes [*Ström et al.*, 1996]. The thin solid and dashed lines show the envelope of crystal size distributions when classified into two concentration categories. Crystal size distributions were derived from replicator measurements.

Both the model and measurements show a substantial number of ice crystals smaller than 10μm diameter. The model underpredicts the number of crystals below roughly 5μm. Despite this underprediction, the shape of the predicted crystal size distribution closely resembles the measured distributions. The average crystal concentration measured with the CVI (crystals with aerodynamic diameters larger than 5μm) was ca. 2.5cm^{-3} (STP). The concentration of crystals larger than 5μm diameter predicted by the model in the base case was 2.4cm^{-3} (STP).

Residual Particle Size Distributions

Figure 3 illustrates the predicted interstitial and residual particle size distributions for the base case run.

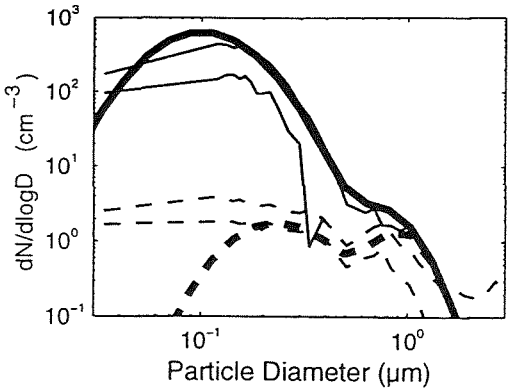

Figure 3. Interstitial and residual aerosol size distributions.

The thick solid curve in Fig. 3 is the model-predicted interstitial aerosol size distribution. The thick dashed curve is the residual aerosol particle size distribution for the base case run for crystals larger than 5μm diameter - the CVI cut size. The area between the thin solid lines represents the envelope of observed interstitial aerosol size distributions, while the area between the thin dashed curves denotes the envelope of observed residual particle size distributions.

The predicted and observed distributions are quite close for particles larger than 0.1μm. Both model results and observations indicate that the residual particles (the particles upon which the crystals formed) had a bimodal distribution, and that particles smaller than 1μm accounted for most of the particle number. This implies that submicrometer particles determined the number concentration of ice crystals in these clouds. The modeled and observed residual particle size distributions diverge at diameters below 0.2μm. It should be noted that the observed size distributions have a single "channel" below 0.1μm. This "channel" was determined as the difference between two different instruments with different lower cut sizes.

Figure 4 illustrates three size distributions. The thick solid line depicts the input aerosol size distribution (the same as in Fig. 1.) The thick dashed line shows the predicted residual particle size distribution for crystals larger than 5μm. The thinner dashed/dotted line is the predicted residual particle size distribution for crystals between 9 and 10μm diameter.

In the base case run, particles as small as 0.05μm were activated to form ice crystals. The similarity in shape between the residual size distributions for all crystals larger then 5μm with the distribution for crystals between 9-10μm indicates that there is no direct relationship between crystal size and residual particle size. In the model, this is a result of the stochastic nature of the freezing parameterization used. While there are no corresponding measurements for crystals between 9-10μm with which to compare, the fact that the model so successfully predicts both the crystal, residual and

interstitial size distributions leads us to believe that the parameterization cannot be too far of for these clouds.

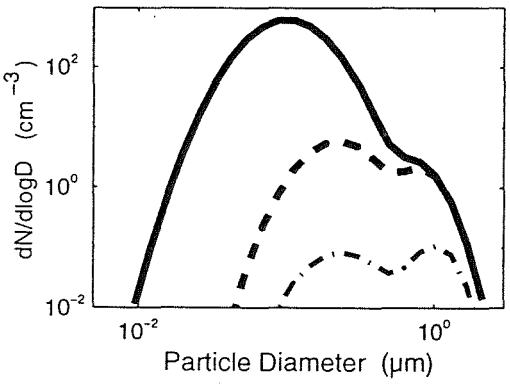

Figure 4. Input aerosol distribution, residual aerosol distribution for crystals larger than 5μm, and residual aerosol distribution for crystals between 9 and 10μm.

Sensitivity Study

A sensitivity analysis of the model with respect to each of the input parameters was carried out. Each input parameter was varied within the range of observed values. We found that we could obtain excellent agreement between observed and modeled crystal size distributions over the entire range of crystal sizes while using input values well within the range of the observations. Crystal size distribution was most sensitive to temperature, relative humidity, updraft velocity and aerosol size distribution.

Condensed water content was always underpredicted by the model when compared to measurements. This is not surprising, since the model only treats a single, 30m adiabatic uplift.

5. DISCUSSION AND CONCLUSIONS

Both model predictions and measurements indicate that there can be substantial concentrations of crystals smaller than 10μm in newly-forming cold cirrus clouds. Additionally, both model predictions and measurements indicate that a substantial fraction of these crystals formed on aerosol particles smaller than 1μm. No strong relationship was predicted between crystal and residual particle size, indicating that crystals of any given size could have formed on particles of widely differing sizes.

The fact that submicrometer aerosol particles are seen to be active in forming cirrus ice crystals leads to the following speculation: It is known that anthropogenic activities (e.g., commercial air traffic, combustion processes) are a substantial source of submicrometer particles. Since particles of this size are active in forming cirrus clouds, it is quite possible that anthropogenic activity has had an influence on cirrus cloud properties.

6. ACKNOWLEDGMENTS

H. Lin was supported by a grant from Stockholm University during the time this research was done. We are grateful to the Office of Naval Research for additional support.

7. REFERENCES

Ackerman, S.A., W.L. Smith, J.D. Spinhirne, and H.E. Revercomb, The 27-28 October 1986 FIRE IFO Cirrus Case Study: Spectral Properties of Cirrus Clouds in the 8-12μm Window, *Mon. Wea. Rev.*, *118* (11), 2377-2388, 1990.

Heymsfield, A.J., and R.M. Sabin, Cirrus crystal nucleation by homogeneous nucleation of solution droplets, *J. Atmos. Sci.*, *46*, 2252-2264, 1989.

King, M.D., Radiative Properties of Clouds, in *Aerosol-Cloud-Climate Interactions*, edited by P.V. Hobbs, pp. 123-149, Academic Press, Inc., San Diego, 1993.

Noone, K.B., K.J. Noone, J. Heintzenberg, J. Ström, and J.A. Ogren, In-situ observations of cirrus cloud microphysical properties using the counterflow virtual impactor, *J. Atmos. Ocean. Tech.*, *10*, 294-303, 1993.

Noone, K.J., J.A. Ogren, J. Heintzenberg, R.J. Charlson, and D.S. Covert, Design and calibration of a counterflow virtual impactor for sampling of atmospheric fog and cloud droplets, *Aerosol Sci. Tech.*, *8*, 235-244, 1988.

Ogren, J.A., J. Heintzenberg, and R.J. Charlson, In-situ sampling of clouds with a droplet to aerosol converter, *Geophys. Res. Lett.*, *12* (3), 121-124, 1985.

Prabhakara, C., R.S. Fraser, G. Dalu, M.L.C. Wu, and R.J. Curran, Thin Cirrus Clouds: Seasonal Distribution over Oceans Deduced from Nimbus-4 IRIS, *J. Appl. Met.*, *27* (11), 379-399, 1988.

Ström, J., and J. Heintzenberg, Water Vapor, Condensed Water, and Crystal Concentration in Orographically Influenced Cirrus Clouds, *J. Atmos. Sci.*, *51* (16), 2368-2383, 1994.

Ström, J., J. Heintzenberg, K.J. Noone, K.B. Noone, J.A. Ogren, F. Albers, and M. Quante, Small crystals in cirriform clouds: A case study of residue size distribution, cloud water content and related cloud properties, *J. Atmos. Res.*, *32* (1-4), 125-141, 1994.

Ström, J., B. Strauss, F. Schröder, T. Anderson, J. Heintzenberg, and P. Wendling, In-situ observations of the microphysical properties of young cirrus clouds, *J. Atmos. Sci.*, submitted, 1996.

EFFECTS OF VOLCANIC AEROSOLS ON CIRRO-FORM CLOUDS

Naihui Song, USRA/GSFC/NASA, Greenbelt, MD
David O'C. Starr, GSFC/NASA, Greenbelt, MD

1. INTRODUCTION

Cirrus clouds are important to the Earth's climate due to their extensive areal coverage and strong effects on the radiation budget (Manabe and Wetherald, 1967; Stephens and Webster, 1981). Aerosols can affect these clouds since they can serve as cloud condensation nuclei (CCN) or, potentially, ice initiation nuclei (IN). This aerosol-cloud-climate interaction is an area critically important to our understanding of the climate system, thereby complicating our assessment of the global warming induced from man-made greenhouse gases.

Our recent analysis shows that volcanic aerosols can cause persistent and widespread increases (approximately 10% or more above base values) in high level cloudiness on a global scale (Song et al., 1996). Sassen et al.(1995) reported that the volcanic aerosols from the June 1991 Pinatubo eruption might have significantly influenced the formation and maintenance of observed cirrus clouds. Thus, volcanic aerosols may have a significant impact on the Earth's climate indirectly through modification of cloud microphysics in addition to the direct effect on the Earth's radiation budget.

Mechanistic understanding and quantification of the aerosol and cloud processes significant to the climate are necessary before correct incorporation of their radiation effects in climate models can become possible. Jensen and Toon (1992) and Jensen et al. (1994) reported a study of the effects of sulfate haze particles of volcanic origin on ice formation in cirrus clouds. They found that volcanic aerosols can increase ice crystal concentration as much as four times under some conditions due to more haze particles being available for freezing even though aerosol effects might not be always significant to the ice initiation of cirrus clouds. However, this aerosol-cloud interaction needs to be examined in the context of complicated cloud environmental conditions. In this study, we examine the aerosol-cloud interaction in a typical cirrus uncinus cloud.

This study is on the basis of 2-D cloud simulation using a detailed cloud model. In Section 2, we present the evidence of aerosol effects on global high level clouds. In section 3, we present the approach of numerical experiments. Results of numerical experiments are given in Section 4, and discussions and future work are given in Section 5.

Corresponding Author Address:
Naihui Song, Code 913, GSFC/NASA, Greenbelt, MD 20771
E_mail: song@climate.gsfc.nasa.gov

2. TIME SERIES OF HCI ANOMALY

We here define a high cloud index (HCI) as the percent of monthly mean OLR values on a 2.5° latitude-longitude grid that are less than 220 W m^{-2}. This corresponds to a blackbody source (that also blocks the infrared radiation upwelling from the surface and lower troposphere) located at a height of about 8 km in the tropics and between about 3 and 8 km in middle latitudes depending on season.

The latitudinal distribution of HCI anomaly time series is shown in Figure 1 for the period of January 1979 to May 1994. Wide-spread increases in HCI anomaly are found after the eruptions of both El Chichon and Pinatubo. These increases are concentrated in the tropics and middle latitudes of both hemispheres, where the major cloud systems occur, and persist for about 2.5 years after the eruptions. Also, there are strong reductions (up to 16%) in HCI in the year before Pinatubo eruption apparently due to lack of volcanic aerosols. Song et al. (1996) examined the causes of HCI variations and suggested that modification of cloud microphysics by the aerosols is likely to be the main reason. Numerical simulations are necessary to identify the responsible microphysical processes.

3. DESCRIPTION OF THE 2-D CIOUD MODEL

The model is a modified version of a one-dimensional lagrangian model described by Song and Marwitz (1989). The improvement in ice microphysics is reported by Song (1994).

3.1 Treatment of cloud microphysical processes

One hundred and sixty discrete bins of particle radius is used to characterize the CCN and drop spectrum. The treatment of coalescence process is similar to that of Berry and Reinhart (1974), while the condensation growth and sedimentation are treated by a moment conservation scheme similar to Egan and Mohoney (1972). Since the model simulations indicate that large drops in stratiform clouds fall out of clouds and do not develop to a size that will induce collision-breakup. The breakup of large drops is ignored in the model for the simulations of strartiform clouds.

In current model, vertical dimension is also treated semi-lagrangianally similarly to Song and Marwitz (1989). A cluster of Air parcels in the vertical direction is followed lagrangianlly. For each time step, falling of large particles between vertical grids is computed. A new air parcel is incorporated in the cluster once the last one is above the

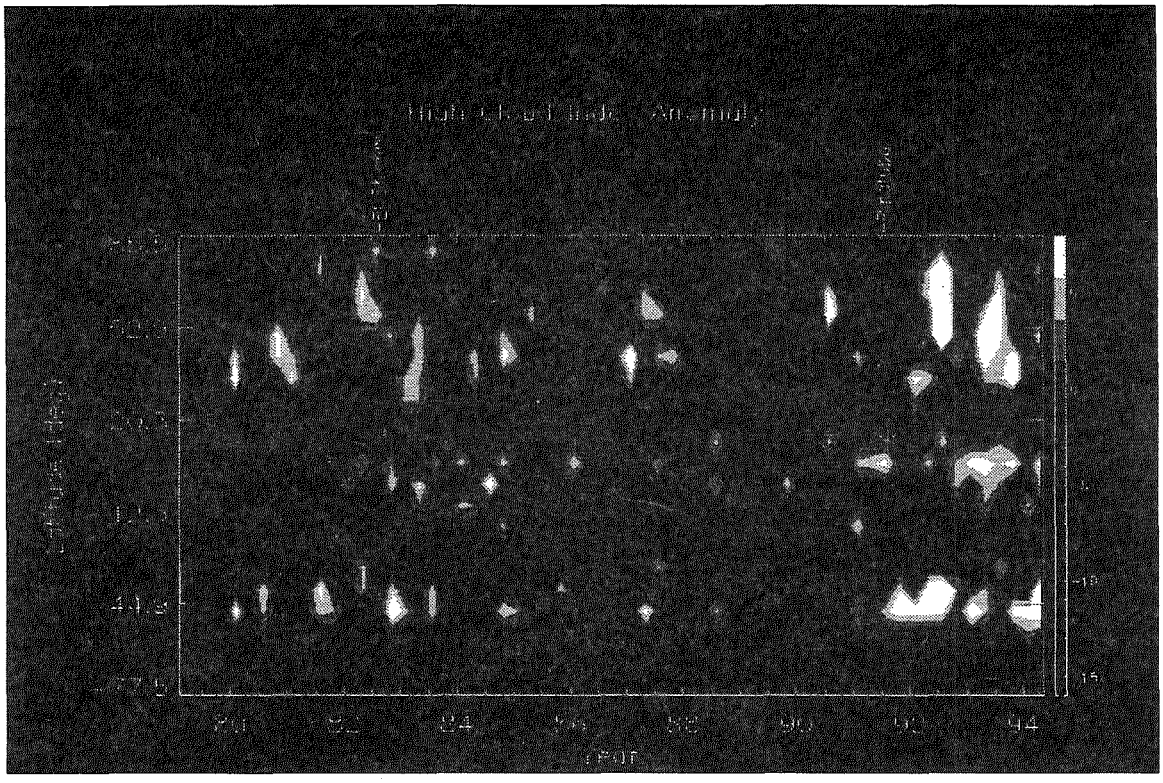

Fig 1. High cloud index anomaly. High cloud index is defined as the percentage of OLR observations less than 220 w/m^2 in a latitudinal circle. * indicates the time and location of the volcanic eruptions.

cloud base. After the cluster becomes twice as big, number of parcels is adjusted by discharging every other parcel.

For cloud drop nucleation, the Twomey's formula for CCN

$$N=C\,S^K \qquad (1)$$

is used. Here S is in the unit of percentage. C is typically around 500 cm^{-3}; and K is typically around 0.4. However, this formula produces unacceptable amount of large drops initially that becomes a significant fraction of total cloud water mass. Thus, CCN particles above 2 μm are reduced without having a significant effect on total CCN counts.

For mixed-phase clouds, one hundred sixty bins are used to account for different sizes of ice nuclei/initiation particles and ice crystals. Ice nucleation summarized by Heymsfield and Sabin (1989) is used. The effects of chemical species in water drops on freezing process is not considered in this preliminary study. However, this issue will be examined in the future. For ice phase, the model simulates vapor deposition growth and sedimentation of ice crystals only. The crystal fallspeed is formulated based on the data summarized by Miller and Wang (1989). Riming and crystal aggregations are ignored due to lacking of data.

3.2 Treatment of cloud dynamics

Air parcel is allowed to advect lagrangianally along stream lines. Air parcels are added to the beginning of the stream lines constantly while parcels are released if they advect out of the domain.

In all simulated cases, vertical velocity in simulated clouds assumed to be a constant (8 cm/s). Horizontal velocity in simulated clouds assumed a linear profile: zero at cloud top and increase by 1 m/s for every 100 meters. An air bubble (800 m in length and 400 m in height) was assumed at 100% water saturation while surrounding air is 95% water saturation. The temperature at the cloud top is -36.5°C. Initially, vertical temperature profile of a cloud assumed a typical stable lapse rate, and is allowed to be modified by latent heat during a cloud process.

4. NUMERICAL RESULTS

Cirrus uncinus is simulated numerically for twelve minutes of cloud evolution. Input aerosols are determined by Equation (1) choosing C and K as 50 and 0.5 for typical upper tropospheric aerosols. Figure 2(a) shows the field of the logarithm of liquid water content. Similarly, Fig. 2(b) and (c) are for ice water and ice concentration (both in logarithm). One can see in Fig. 2(a) that liquid water is concentrated in the cloud top, a short trail extends towards downward and in the down wind direction. Ice water forms a much longer trail as in Fig. 2(b) due to ice crystals being much larger than drops and able to fall farther. High ice concentration at the cloud top is due to continuous homogeneous freezing of cloud drops. The total water field (water and ice combined) gives a typical cirrus uncinus structure (comma) observed in the upper atmosphere.

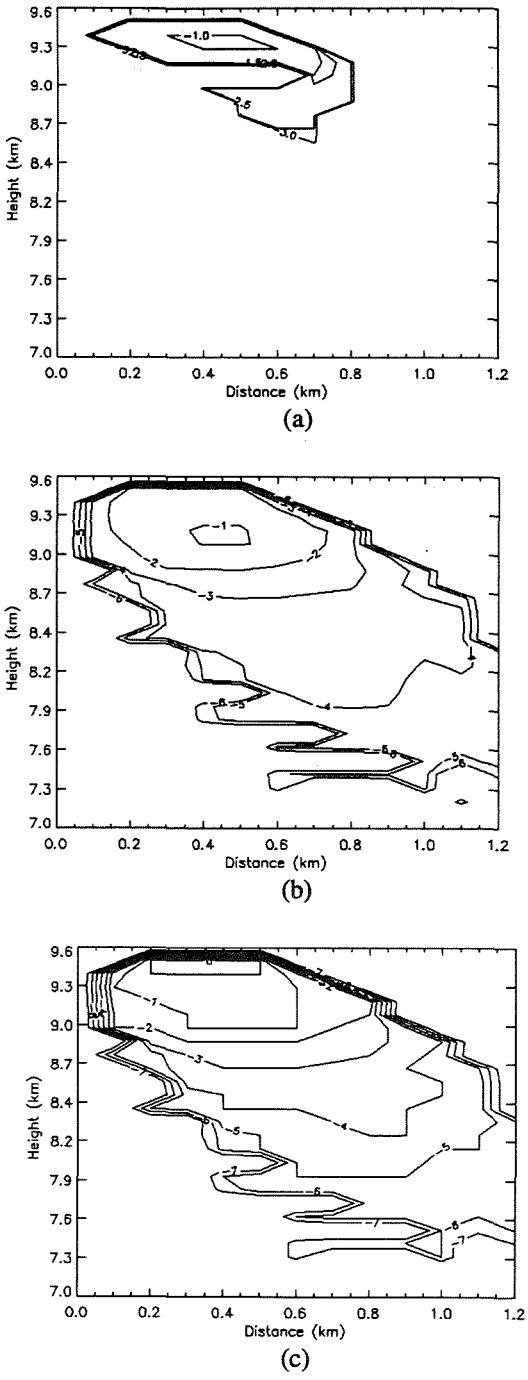

Fig. 2 Cloud property field. Simulation duration is 12 min. Aerosol conditions are given by Equation (1) with C=50 and K=0.5. (a) logarithm of liquid water content (g/m^3), (b) logarithm of ice water content and (g/m^3), (c) logarithm of ice crystal concentration l^{-1}).

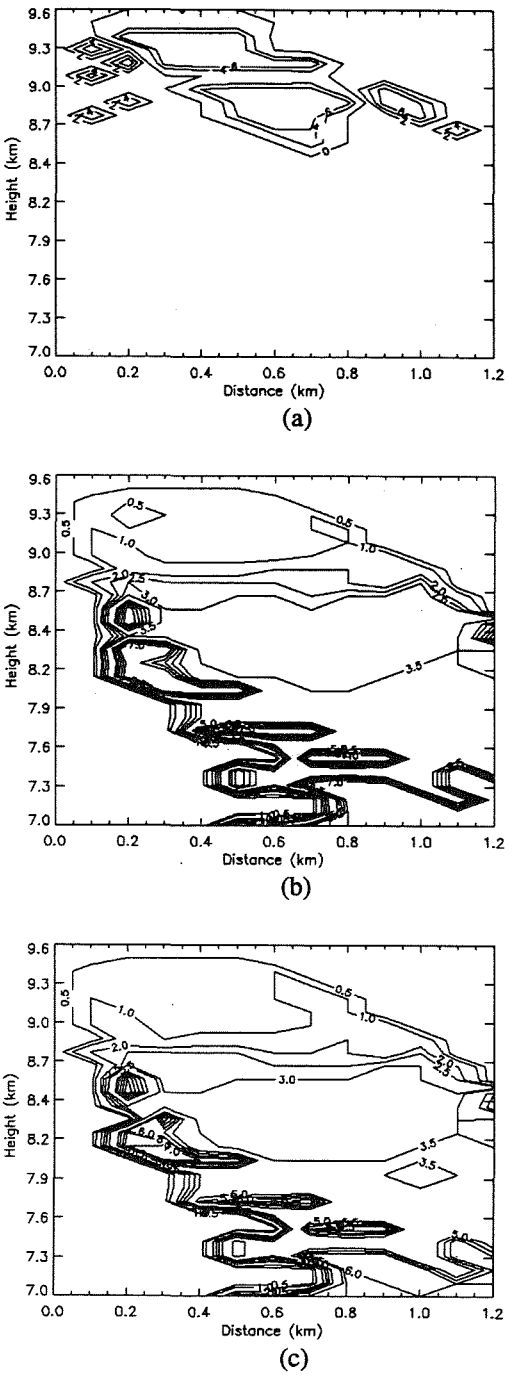

Fig. 3 Logarithm of ratio of cloud property between two sets of aerosol conditions: i) C=500 and K=0.5; ii) C=50 and K=0.5. Simulation duration 12 min. (a) for liquid water content, (b) for ice water content and (c) for ice crystal concentration.

In order to see the effects of aerosols on the cloud properties of cirrus uncinus, cloud evolution under high aerosol concentration (representing an increase in aerosol concentration due to a volcanic eruption) is also simulated for twelve minutes. The high aerosol concentration is determined by choosing C as 500 and K as 0.5 in Equation (1). Results are compared with those from the low aerosol concentration presented in Fig. 2. The logarithm of the ratio of cloud properties from the two sets of simulation is plotted in Fig. 3. One can see significant increases in ice concentration due to the increase in aerosol concentration (Fig. 3c). A corresponding increase in ice water field can be found in Fig. 3(b) and a decrease in liquid water field can be seen most of cloud field except in the upwind tip (Fig. 3a).

5. DISCUSSION AND FUTURE WORK

Our analysis of decadal cloud variation suggests that the stratospheric aerosol loading may play a role in regulating the interannual variability of high level clouds, and consequently, the global climate. Modification of cloud microphysics by the volcanic aerosols appears to be the cause appears to agree with our cloud simulation results.

The model simulations suggest that property fields of a cirrus uncinus is the result of the complicated interplay of environmental wind and microphysical processes. The upper wind tip of uncinus can have a high liquid water content (Fig. 2a) due to sedimentation of ice crystals and vertical shear of horizontal wind. As demonstrated in Fig. 2(a), newly formed crystals in the high liquid water region in the upper left corner drift towards bottom right under the combined effects of crystal sedimentation and an increasing horizontal wind below. Thus, high supersaturation can maintain and new water drops can continuously form due to being free from the water vapor depletion by ice crystals, which leads to continuous production of ice crystals. Thus, the region works as an ice generation cell.

This process is important to how aerosols can affect cloud ice properties, which is found to be a two step process: increasing cloud liquid water content, and a higher ice crystal concentration due to a higher cloud liquid water content. Unlike conventional believing, liquid water content is less than the adiabatic value and quite sensitive to aerosol concentration when aerosol is low. Our previous studies (Song, 1994) show that aerosol can increase liquid water content significantly due to greater condensation rate when supersaturation is high enough as in the ice generation cell. Fig. 3(a) shows that the generation cell has a greater liquid water content. A higher liquid water content produces a greater number of ice crystals since the rate formation of ice embryos is about proportional to the liquid water content (Pruppacher and Klett, 1978).

As shown by Fig. 3(b), the increase in ice production has a great impact on the overall cloud field, especially in the region of cloud trail. The increase in ice water content is as much as two to six orders of magnitude. This should cause a great change in radiation processes of the cloud even though aerosols do not have siginficant direct effcts there.

For the future studies, model simulations will be performed to examine aerosol effects on cirrus clouds in varieties of cirrus cloud conditions with detailed treatments of different aerosol chemistry and physical properties, including those of volcanic aerosols. Proper treatments of aerosol effects on high level clouds for global models will be explored.

6. ACKNOWLEDGMENTS

We thank Climate Analysis Center of NOAA NMC/NWS for providing grid data sets of OLR and Meteorological parameters. The work is partially supported by NASA under contract No. NASA NAS1-19957.

7. REFERENCE

Berry, E., and R. Reinhart, 1974: An analysis of cloud drop growth by collection. Part I: double distributions. *J. Atmos. Sci.*, **31**, 1814-1824.

Egan, B., and Mahoney, J., 1972: Numerical Modeling of Advection and Diffusion of Urban Area Source Pollutants. *J. Appl. Meteor.*, **11**, 312-322.

Heymsfield, A.J., and R.M. Sabin, 1989: Cirrus crystal nucleation by homogeneous freezing of solution droplets. *J. Atmos. Sci.*, **46**, 2252-2264.

Jensen, E. J., and O. B. Toon, 1992: The Potential Effects of Volcanic Aerosols on Cirrus Cloud Microphysics. *G.R.L.*, 19(17), 1759-1762.

Jensen, E. J., O. B. Toon, D. L. Westphal, S. Kinne, and A. J. Heysmfield, 1994: Microphysical Modeling Of Cirrus .1. Comparison With 1986 FIRE IFO Measurements. *J. Geophy. Res.*, **99**, 10421-10442.

Manabe, S., and R. T. Wetherald, 1967: Thermal equilibrium of the atmosphere with a given distribution of relative humidity. *J. Atmos. Sci.*, **24**, 241-259.

Miller, N.L., and P.K. Wang, 1989: Theoretical Determination of the Efficiency of Aerosol Particles Collection by Falling Columnar Ice Crystals. *J. Atmos. Sci.*, **46**, 1662-1663.

Sassen, K., D. O. Starr, G. G. Mace, M. R. Poellot, S. H. Melfi, W. L. Eberhard, J. D. Spinhirne, E. W. Eloranta, D. E. Hagen, and J. Hallett, 1995: The 5-6 December 1991 FIRE II Jet Stream Cirrus Case Study: Possible Influences of Volcanic Aerosols. *J. Atmos. Sci.*, **52**, 97-123.

Song. N., 1994: Parameterizations of Cloud Microphysical Processes for GCM Models. Conference on Atmospheric Chemistry. 1994 AMS Annual Meeting. 23-28 January, 1994, Nashville, Tennessee.

Song, N., and Marwitz, J., 1989: A numerical Study of the Warm Rain Process in Orographic Clouds. *J. Atmos. Sci.*, **46**, 3479-3486.

Song, N., D. O'C Starr, D. J. Wuebbles, Allen Williams and S. Larson, 1996: Factors in Controlling Decadal Variation of High Level Clouds. Submitted to *Geophy. Res. Lett.*

Stephens, G.L., and P.J. Webster, 1981: Clouds and Climate: Sensitivity of Simple Systems. *J. Atmos. Sci.*, **38**, 235-247.

PRECIPITATION FORMATION IN FRONTAL STRATIFORM CLOUDS WITH SEVERAL CRYSTAL FORMS

Vladimir P.Bakhanov, and Boris A.Dorman

Ukrainian Hydrometeorological Researh Inst., Kiev-252028, Ukraine

1. INTRODUCTION

In our previous works (Buikov and Dorman, 1987; Bakhanov and Dorman, 1991) we have constructed a 1D time-dependent microphysical model of stratiform frontal mixed clouds with several crystal forms (needles, columns, plates). In this paper we use this model to investigate the microstructure of frontal clouds and precipitation. The main aim of this paper is to study the phase structure, the crystal form spectrum, the precipitation formation efficiency in precipitating clouds as functions of some dynamic and microphysical parameters (thickness of updraft parcels, updraft velocities, and ice nucleation rates).

2. SHORT DESCRIPTION OF MODEL

Four kinetic equations for dimension spectra $f_i(r_i, t, z)$ of drops and crystals of several forms were considered (i=1 - for drops; i=2 - for needles; i=3 - for columns, i=4 - for plates; t - time, z - height, r_i - the characteristic dimension of particles).

The cloud dynamics is parameterised: z_1 u z_2 denote the lower and upper updraft region boundaries; z_1 = 0.6 km; z_2 was varied. The updraft velocity $w=w(z)$, depends on z parabolically, with the maximum velocity w_m reached at the height $z_3=(z_1+z_2)/2$; w_m was varied.

Sublimation ice nuclei (IN) were considered. They are activatued if the supersaturaton over ice reached, $\Delta_2>0$. Distribution of the ice nuclei by the overcooling has the form

$$F_i=\mu_i A_s \exp[B_s(273,15-T)] \quad (1)$$

where $B_s=0,2(^0K)^{-1}$, A_s was varied in the rage $(0,02....0,5)\ 10^{-1}(g^0K)^{-1}$. Temperature ranges for nucleation of different crystal forms are different - for needles, $\mu_2=1$ in the range $-10<T<-5^0C$; for columns $\mu_3=1$ at $T<-25^0C$; for plates $\mu_4=1$ at $-25<T<-10^0C$; beyond these ranges $\mu_i=0$. Since the share of needles in the total concentration of crystals is below 0,1% we will not discuss here the characteristics of the needles.

Needles and columns were approximated by rotation ellipsoids with the major and minor axes equal to 2r and 2b respectively. The growth process preserves the crystal chape:

$$b_2/r_2=1/16,\ b_3/r_3=1/2. \quad (2)$$

Plates were approximated by cylinders:

$$h_4/r_4=0,1, \quad (3)$$

where r_4 is the plate radius, h_4 - plate thickness.

Our model took into account process of columns transformation into plates (see Buikov and Dorman, 1987). This transformation takes place for small columns when they fall in the region with

heights $z<z_a$, where z_a corresponds to the transformation temperature t_a=-22°C.

3. EVOLUTION OF CLOUD AND PRECIPITATION MICROSTRUCTURE

Table 1 presents the results of calculations with varied parameters z_2, A_s, w_m.. The temperature for $z=z_2$, the total liquid water content (TLWC) Q_{L1}, the maximum concentration of columns (n_{3m}) and plates (n_{4m}), the total precipitation rate $j=j_3+j_4$, the integrated (over height) condensation rate E are listed in Table 1 for the time t=10h. The table shows also the sums of precipitation fallen in 4h after the moment t=10h: $S_0^{(4)}$- the total sum, $S_{03}^{(4)}$- the sum of columns, $S_{04}^{(4)}$- the sum of plates.

Let us consider versions 1-5 of z_2 variation. It can be seen that the dependence of the plate share in precipitation on z_2 (or z_2- z_1) is practically linear. In the case of z_2=3,9 km the precipitation consists virtually plate forms alone. This result is in a good agreement with experimental data. There is a strong dependence of the phase composition and the precipitation formation efficiency on the upper boundary height z_2. If z_2<3,9 km ($T_0(z_2)$>-25°C) the ice nucleation rate is unsufficient and great TLWC $Q_{L1}\geq$1 mm is accumulated. If z_2>5 km ($T_0(z_2)$<-34°C), the cloud becomes crystal till t=10h, the efficiency of the precipitation formation is very high (j≈E), and the share of plates in the precipitation decreases down to 20-30%.

Let us consider another set of options: 12,2, 13,9 (w_m equals 2,5; 5; 7; 7,5; 10 cm/s) for fixed z_2=4,8 km, A_s=0,15 10^{-1}(g°K)$^{-1}$. The specific features of this case are the mixed phase for all clouds, the time-lag for the precipitation formation process and accumulation of Q_{L1} in the initial stage of evolution (Fig.1). Furthermore, Q_{L1} passes the maximum and begins to decrease in connection with the increase j. An interesting result of this calculation is the

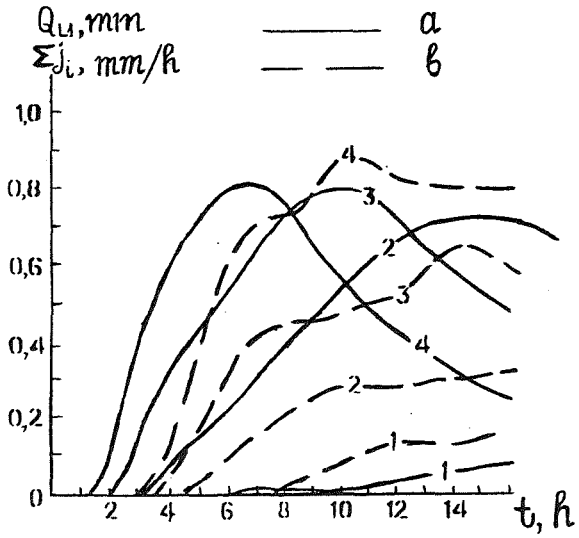

Fig.1. Total liquid water content (a) and precipitation rate (b) as functions of evolution time (z_2=4,8 km). 1 - for option #12 (w_m=2,5 cm/s); 2 - for option #3 (w_m=5 cm/s); for option #13 (w_m=7,5 cm/s); 4 - for option #9 (w_m=10 cm/s).

following : the clouds with greater TLWC give the greater precipitation. This result differs from that for the preceding selection.

We hawe also simulated of dry ice mass seeding for artificial precipitation enhancement (APE) purposes. Sceding was modeled by the "injection" of an additional ice nuclei concentration 300-400 g^{-1} into a 1 km thick seeded layer. It has been shown that changes of the crystal form spectrum provide information about the seeding height z_s. For z_s=2,6-2,8 km, the plate share sharply increases whill for z_s>4,2 km this share drops down to 20-30%.

For the above mentioned seeding rates the so called particular overseeding was demonstrated (the "shade"for one crystal form along with the general increases of precipitation). Fig.2 illustrates this situation: three clouds (options 1, 2 and 5) were seeded at t_s=10r,

Table 1

Characteristics of clouds

Variant number	w_m cm/s	z_2 km	$T_0(z_2)$ °C	A_s $0.1(g^0C)^{-1}$	Q_{L1} mm	n_{3m} g^{-1}	n_{4m} g^{-1}	i mm/h	E mm/h	S_0^4 mm	S_{03}^4 mm	S_{04}^4 mm
1	5.0	3.9	-24.6	0.15	1.21	0.06	1.37	0.02	0.40	0.15	0	0.15
2	5.0	4.8	-29.8	0.15	0.52	2.70	4.27	0.28	0.41	1.13	0.34	0.79
3	5.0	5.1	-31.5	0.15	0.09	5.21	6.94	0.40	0.40	1.56	0.77	0.79
4	5.0	5.4	-33.3	0.15	0.04	7.98	8.30	0.42	0.41	1.69	1.03	0.66
5	5.0	5.7	-35.0	0.15	0	13.2	5.89	0.47	0.43	1.81	1.39	0.42
6	5.0	4.8	-29.8	0.50	0	11.5	18.2	0.43	0.40	1.73	0.75	0.98
7	5.0	4.8	-29.8	0.02	1.75	0.37	0.61	0.01	0.43	0.07	0.03	0.04
8	5.0	7.0	-42.5	0.02	0.29	6.53	2.43	0.41	0.47	1.75	1.51	0.34
9	10.0	4.8	-31.0	0.15	0.58	9.32	13.8	0.86	0.91	3.35	1.41	1.94
10	10.0	5.7	-36.1	0.15	0	41.1	13.7	0.97	0.89	3.81	2.84	0.97
11	10.0	5.4	-34.4	0.15	0.01	28.0	13.6	0.95	0.88	3.72	2.53	1.19
12	2.5	4.8	-29.3	0.15	0.01	1.22	3.95	0.07	0.15	0.47	0.11	0.36
13	7.5	4.8	-30.4	0.15	0.80	5.35	7.90	0.47	0.67	2.13	0.74	1.39

z_s=2,7 km (all "seeded" crystals are plates). It can be seen that $\Delta j_3<0$, along with $\Delta j>0$ i.e. the plates overseeding causes the "shade" for columns.

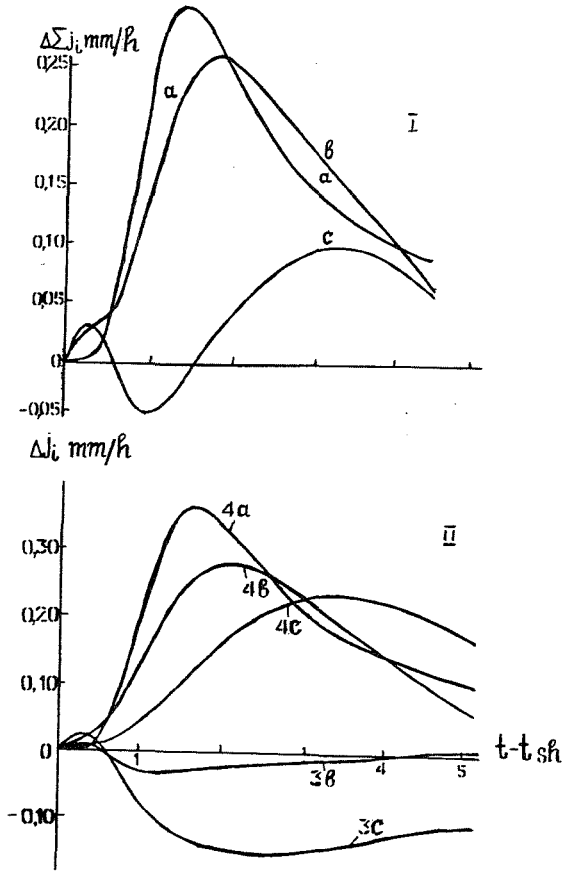

Fig.2. Total rate of seeded precipitation (I) and seeded precipitation rates (II) for columns (i=3) and plates (i=4) as function of time after seeding.

a - for option #1, b - for variant #2, c - for variant #5.

The scale for a in Fig.2.I is 3 mm/h, the scale for 4a in Fig.2.II is 2,5 mm/h.

4. CONCLUSIONS

1. The dynamic structure of the front was found to determine the phase structure, the form spectrum of precipitation crystals, and the efficiency of precipitation formation in frontal clouds.

2. The form spectrum of precipitation particles can be used as predictor of the dynamic structure and the seedability of the frontal cloudiness.

3. It has been shown the possibility of the so called "particular" overseeding effect: the "shade" for one crystal form along with the total increasing of precipitation rate (in the modification zone).

5. REFERENCES

1. Buikov, M.V., and Dorman, B.A., 1987. Influence of the crystal form transformation on the form spectrum of precipitation particles. Trudy UHRI, № 221, pp 24-29 (in Russian).

2. Bakhanov, V.P., Dorman, B.A., 1991. Natural and seeded precipitation formation in frontal stratiform clouds with several crystal forms. Trudy UHRI, № 243, pp 8-23 (in Russian).

THE NUMERICAL MODEL of CONVECTIVE—STRATIFORM MIXED CLOUD AND PARAMETERIZATION OF MICROPHYSICAL PROCESSES

Hong Yanchao

(Institute of Atmospheric Physics, Academia Sinica, Beijing, 100029)

1. INTRODUCTION

The observations indicate that heavy rain in Chain, especially such as the most heavy rain over a large areas occured in Jiang-Huai area in 1991 was mainly caused by mixed cloud consisting of stratiform cloud and convective cloud (MSC). So a numerical of MSC is established, in which the stratiform cloud is caused by low level convergence field and the calculation of convective cloud is mode by a deep convective, anelastic and conservation dynamical model, and we use a new method to calculte accurately streamfunction and dynamical feield. Then, superposition of the cloud—scale field and the convergence field may form the MSC, the two kinds of clouds can interaction and form a organic integer.

In addition, microphysical processes in the cloud are parameterized by more reasonable spectrum with two variable parameters. For purpose of making a comparison between radar echo structure of the model cloud and observation cloud, in calculation of radar echo intensity, the particle shape and ice particle melting are considered, then the mixed cloud can show radar bright band.

2. MODEL DESCRIPTION

The model of MSC ia a two dimensional, time dependent, slab-symmetric, deep convective, anelastic and conservative model. The predicted model variables are the vorticity (Ω), the velocity components (u, w), the potential temperature departure (θ'), mixing ratios (Q_x) and the number concentration (N_x) of various water substance. There by the subscript x stands for rain water (r), ice crystal (i), snow (s) and graupel (g), and in the case of mixing ratios also for vapour (v) and cloud water (c).

The dynamical equations and mass continuity equation are

$$\frac{\partial u}{\partial t} + u\frac{\partial u}{\partial x} + w\frac{\partial u}{\partial z} + c_p\bar{\theta}\frac{\partial \pi'}{\partial x} = F_u \tag{1}$$

$$\frac{\partial w}{\partial t} + u\frac{\partial w}{\partial x} + w\frac{\partial w}{\partial z} + c_p\bar{\theta}\frac{\partial \pi'}{\partial z} = g\left(\frac{\theta'}{\bar{\theta}} + 0.61Q_v' - Q_t\right) + F_w \tag{2}$$

$$\frac{\partial(\overline{\rho\theta}u)}{\partial x} + \frac{\partial(\overline{\rho\theta}w)}{\partial z} = 0 \tag{3}$$

Now, we give definitions of the streamfunction ψ and the vorticity η.

$$\overline{\rho\theta}u = \frac{\partial \psi}{\partial z} \tag{4}$$

$$\overline{\rho\theta}w = -\frac{\partial \psi}{\partial x} \tag{5}$$

$$\eta = \frac{\partial(\overline{\rho\theta}u)}{\partial z} - \frac{\partial(\overline{\rho\theta}w)}{\partial x} = \frac{\partial^2\psi}{\partial x^2} + \frac{\partial^2\psi}{\partial z^2} \tag{6}$$

Thus, a vorticity equation is derived from (1), (2), (3) and (6), but it contains π' term, so that we give other definition of vorticity,

$$\Omega = \frac{\partial}{\partial z}\left(\frac{u}{\bar{\theta}}\right) - \frac{\partial}{\partial x}\left(\frac{w}{\bar{\theta}}\right) \tag{7}$$

and derive a new vorticity equation without π' term

$$\frac{\partial \Omega}{\partial t} + u\frac{\partial \Omega}{\partial x} + w\frac{\partial \Omega}{\partial z} = \frac{w}{\bar{\rho}}\Omega\frac{\partial \bar{\rho}}{\partial z} - \frac{uw}{\bar{\theta}^2}\left[\frac{\partial^2\bar{\theta}}{\partial z^2} - \frac{1}{\bar{\rho}}\frac{\partial \bar{\rho}}{\partial z}\frac{\partial \bar{\theta}}{\partial z} - \frac{2}{\bar{\theta}}\left(\frac{\partial \bar{\theta}}{\partial z}\right)^2\right] - \frac{g}{\bar{\theta}}\frac{\partial}{\partial x}\left(\frac{\theta'}{\bar{\theta}} + 0.61Q_v' - L\right) + D_\Omega \tag{8}$$

where $D_\Omega = \frac{1}{\bar{\theta}}\left(\frac{\partial F_u}{\partial z} - \frac{\partial F_w}{\partial X}\right)$

$$F_u = \frac{\partial}{\partial X}\left(K_{mx}\frac{\partial u}{\partial X}\right) + \frac{1}{\bar{\rho}}\frac{\partial}{\partial z}\left(K_{mz}\bar{\rho}\frac{\partial u}{\partial z}\right)$$

$$F_w = \frac{\partial}{\partial X}\left(K_{mx}\frac{\partial w}{\partial X}\right) + \frac{1}{\bar{\rho}}\frac{\partial}{\partial Z}\left(K_{mz}\bar{\rho}\frac{\partial w}{\partial Z}\right)$$

From (6) and (7), we have

$$\eta = u\frac{\partial \overline{\rho\theta}}{\partial z} + \bar{\rho}u\frac{\partial \bar{\theta}}{\partial z} + \overline{\rho\theta^2}\Omega \tag{9}$$

$$\frac{\partial^2\psi}{\partial x^2} + \frac{\partial^2\psi}{\partial z^2} - \left(\frac{2}{\bar{\theta}}\frac{\partial \bar{\theta}}{\partial z} + \frac{1}{\bar{\rho}}\frac{\partial \bar{\rho}}{\partial z}\right)\frac{\partial \psi}{\partial z} = \overline{\rho\theta^2}\Omega \tag{10}$$

The equation of θ' and the continuity equations for water substance are:

$$\frac{\partial \theta'}{\partial t} + u\frac{\partial \theta'}{\partial x} + w\frac{\partial \theta'}{\partial z} + w\frac{\partial \bar{\theta}}{\partial z} = D_{\theta'} \quad (11)$$

$$\frac{\partial Q_x}{\partial t} + u\frac{\partial Q_x}{\partial x} + w\frac{\partial Q_x}{\partial z} = \frac{1}{\bar{\rho}}\frac{\partial}{\partial z}(\overline{\rho V}_x Q_x) + D_{Qx} + S_{Qx} \quad (12)$$

$$\frac{\partial N_x}{\partial t} + u\frac{\partial N_x}{\partial x} + w\frac{\partial N_x}{\partial z} = \frac{1}{\bar{\rho}}\frac{\partial}{\partial z}(\overline{\rho V}_x N_x) + D_{Nx} + S_{Nx} \quad (13)$$

in which,

$$D_\varphi = \frac{\partial}{\partial x}(K_{hx}\frac{\partial \varphi}{\partial x}) + \frac{1}{\bar{\rho}}\frac{\partial}{\partial z}(K_{hz}\bar{\rho}\frac{\partial \varphi}{\partial z})$$

$$\varphi \in (\theta', \theta_x, N_x)$$

$\overline{V}_x$ is the mass-averaged fall volocity and $V_c = V_v = 0$,S is the sources and sinks due to microphysical processes. Where D stands for the changes due to diffusion. The eddy diffusion terms are calculated by a first order closure. The equation (8),(11), (12),(13)and (4),(5),(6),(9)[equation (10) may stand for (6) and (9)] compose a closure equation set.

The boundary layer convergence value

$$\text{conv} = -\frac{\partial \bar{u}}{\partial x} \quad (14)$$

The convergence velocity $\bar{u}, \bar{w}$ are derived from (3) and (14). In (8),(11), (12) and (13),

$$\begin{cases} u = \bar{u} + u', \\ w = \bar{w} + w', \\ \Omega = \bar{\Omega} + \Omega' \end{cases} \quad (15)$$

where u', w' *and* Ω' are cloud-scale values. Here the teachnique for superimposing a convergence field(Chaing et al. ,1980)] are used.

First, we can calculate the vorticity Ω from (8), then the streamfunction ψ is solved from (10) [or (9) and (6)] by overrelax — iteration method, with the cloud-scale volocities (u' *and* w') computed from (4) and (5). Thus, u *and* w can be found from (15).

At initial time, $\bar{\rho}, \bar{\theta}, \bar{P}, \bar{\pi}$ *and* $\bar{Q}_v$ are determined from the atmospheric sounding, $u = \bar{u}, w = \bar{w}, Q_v = \bar{Q}_v(z)$, other predictive variables are set to zero; when the stratiform cloud form, potential temperature and vapor perturbations are applied, at this time, initial values of all predicted variables equal to those in the stratiform cloud and $\bar{\rho}, \bar{\theta}, \bar{P}, \bar{\pi}$ *and* $\bar{Q}_v$ are calculated from stratification in the stratiform cloud.

At the lateral boundary the *K-W* open boundary conditions are used for dynamical field.

Q_v' *and* π' are calculated from θ' at the initial time, and π' is derived from (1) after that time.

3. PARAMETERIZATION OF MICROPHYSICAL PROCESSES

In consideration of less hailfall from MSC, water is categorized in up to six forms: vapour, cloud droplet, raindrop, ice crystal, snow and graupel. Cloud droplets are assumed small enough to not fall, while all other categories do fall. Ice crystals grow mainly by vapor deposition. The snow category is defined here as consisting of snow crystals and aggregation of ice crystals, and the former are relatively large ice crystals which have grown by vapour deposition and riming. Graupel is an ice particle to be approximately spherical in shape and formed by nucleation and freezing from rain drop and autoconversion of ice crystals and snow which have grow by high riming rate.

Every category of particle is assumed to has a size distrbution in the form $N(D) = N_0 D^\alpha e^{-\lambda D}$, in which, $\alpha_c = 5$, $\alpha_r = 2$, $\alpha_s = 0$ *and* $\alpha_g = 0$, spectrun parameters of cloud droplet and rain drop are taken from a new result of observation and anlyses (Yan et al. ,1990).

8 kinds of microprocesses are considered in this mode: condensation (deposition or evaporation) (VD), collection (CL), aggregation (AG) multiplication (P), nucleation (NU), melting (ML) , melting-evaporation(MVD) and autoconversion (CN) processes. Detail parameterization equations of various microphysical processes can be seen in Hong(1996(a)).

4. CALCULATION OF RADAR ECHO INTENSITY

In general, radar reflectivity factor Z calcutated in cloud numerical model is only relative to size and number concensation of rainfall particles. So that it is not comparable with Z_R from radar observation, because Z_R contains contributions of meting and shape of ice particles. Thus, we consider these factors in calculating the radar refectivity factor Z_R . Rain drops are spherical,

$$Z_r = \int_0^\infty N_r(D_r) D_r^6 \mathrm{d}D_r = \Gamma(9) 10^{18} N_{or} \lambda_r^{-9}$$

For ice particles such as ice crystal, snow and graupel, their Z values without melting equal to that of their equivalent shperes, i. e. ,

$$Z_i = \sum n_i \tilde{D}_i^6 = \sum n_i (\frac{6A_{mi}}{\pi \rho_{io}})^2 D_i^4$$

$$Z_i = (\frac{6A_{mi}}{\pi \rho_{io}}) \int_0^\infty N_i(D_i) \cdot D_i^4 \mathrm{d}D_i$$

$$= \Gamma(6) \cdot 10^{18}(\frac{6A_{mi}}{\pi\rho_{io}})^2 N_{oi}\lambda_i^{-6}$$

in the same way,

$$Z_s = \Gamma(5) \cdot 10^{18}(\frac{6A_{ms}}{\pi\rho_{so}})^2 N_{os}\lambda_s^{-5}$$

$$Z_g = \Gamma(7) \cdot 10^{18}(\frac{\rho_g}{\rho_{go}})^2 N_{og}\lambda_g^{-7}$$

in which, ρ_{io}, ρ_{so} and ρ_{go} are all density of pure ice and are taken as $0.98 \times 10^6 g/m^3$. When ice particles are meting their scattering power nearly equals to waterdrops with same valume if leaving shape effect out of consideration. So that when $T \geqslant T_0, \rho_{io} = \rho_i, \rho_{so} = \rho_s, \rho_{go} = \rho_g$

$$Z = Z_i + Z_S + Z_g + Z_r \qquad (mm^6/m^3)$$

or $Z = 10log(Z_i + Z_S + Z_g + Z_r)$ (dbz)

Form radar eqation and considering melting and shape of ice particles, echo power from population of particle is

$$\overline{P} = c'(|K_x|^2 F_x Z_x + |K_r|^2 Z_r)/R$$
$$x \in (i,s,g)$$

where c' is radar constant, $|K|$ mode of complex refractive index, R slant range of target away from radar, F is shape factor of ice particle. If echo intensity is expreessed in db,

$$Z_g = 10log[\frac{c'}{R^2 P_{min}}(|K_x|^2 F_x Z_x + |K_r|^2 Z_r)],$$

When $T < T_0, |K_x|^2 = 0.197$. The shape factor almost has no dffect on the scatter, i. e., $F_x = 1.0$; when $T \geqslant T_0$, $|K_x|^2 = |K_r|^2 = 0.93$, the shape factor make the scatter enhancement, according to culcalating, $F_i = F_s \approx 3.5$, but graupel pareicle is sphere, $F_g = 1.0$.

In this model, assuming the model cloud is observed by 711-type radar made in China, the radar echo intensity

$$Z_{711} = \begin{cases} 10log\{[5.192 \cdot 10^7(Z_i + Z_s + Z_g) \\ + 2.451 \cdot 10^8 Z_r]/R^2\} & (T < T_0) \\ 10log\{[8.577 \cdot 10^8(Z_i + Z_s) \\ + 2.451 \cdot 10^8(Z_r + Z_g)]/R^2\} & (T \geqslant T_0) \end{cases}$$

5. MODEL TEST

Because heavy rain in China is mainly caused by MSC, we simulated and studied some remarkable features of MSC using averaged atmospheric stratification of 26 heavy rain processes, the results of this work may be seen in the other paper (Hong, 1996(b)). The model results are as follows: (1) The covective cloud developing in stratiform cloud has longer life cycle, and it can not dissipate and occurs cyclic processes of developing and enhancement—splitting—merging—splitting. The splitting appears generally after high rate rainfall and the merging may be caused by the convergence. This process can be seen clearly from the evolution of the water content field. (2) The radar echo zone with high reflectivity is always located in the mid—low part in the convective cloud. There is a radar bright band with high reflectivity zone and precipitation echo in the stratiform cloud surrounding convective cloud (Fige. 1). (3) In MSC, the convective cloud produces lasting precipitation with high intensity (> 50mm/h) and intermittent precipitation with ultra — high intensity (150 — 250mm/h). So that there is continually high rate rainfall in the convective zone in MSC, and precipiltation rate of the stratiform cloud varys 1.0 to 3.0mm/h. The numerical experiments show that rainfall amount from the convective cloud in MSC is tens times larger than isolated cumulus cloud, i. e., under the influence of the stratiform cloud, the rainfall amount of the convective cloud increases greatly. Saturated environment provided by the stratiform cloud, dynamic action of the convergence and ice phase microphysical processes are main factors to cause heavy rain. MSC is a very effective precipitation system with precipitation efficiency of 85—90%. (4) In MSC, interaction of stratiform and convective cloud is remarkable, when cloud splits and weakens, the stratiform cloud enhances and hrizontal scale extends to 75km, its water content increases from place near by the convective cloud to lateral boundary (Fig. 2a), but when splitted convective cloud merges again and strengthens, it first dissipate from near the convective cloud and horizoutal size decreases to 45km (Fig. 2b).

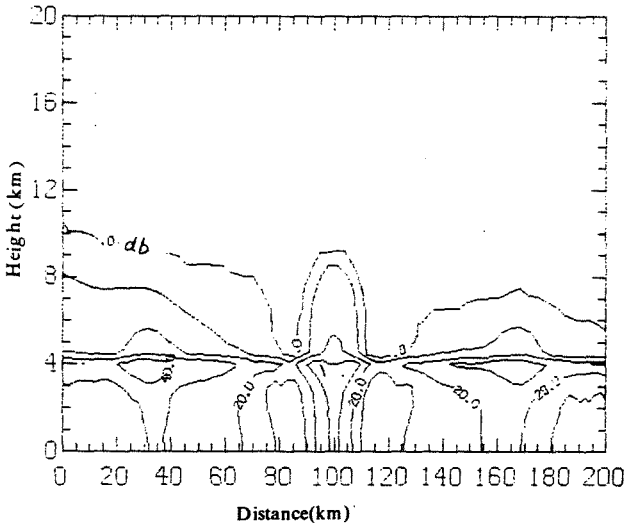

Fig 1. Radar echo struture of MSC.

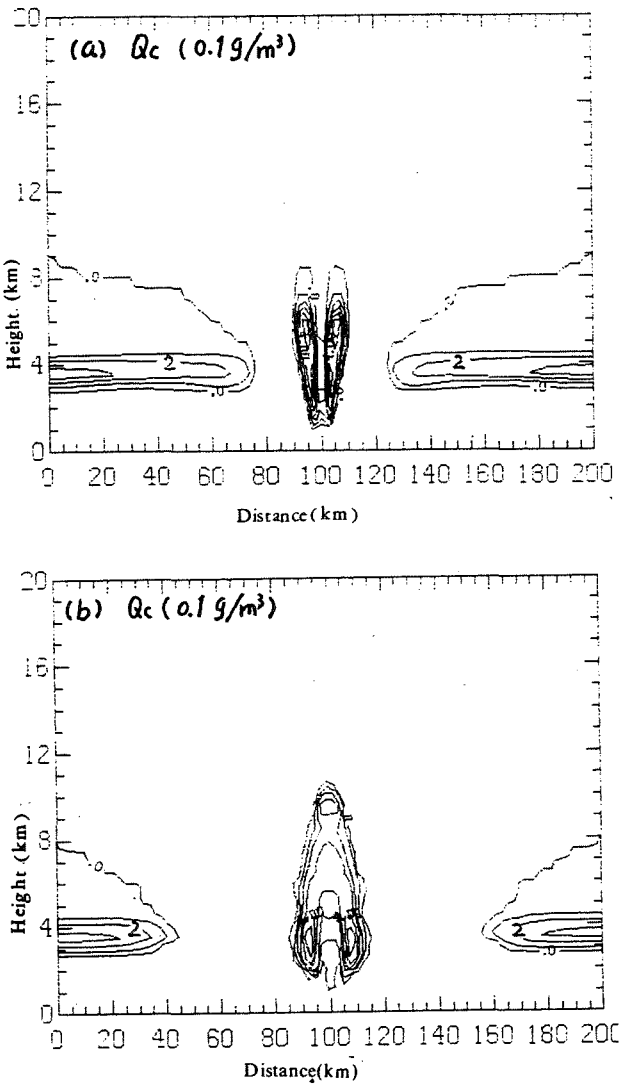

Fig. 2. Interaction of stratiform and convective cloud in MSC.

Above the echo struture, precipitation features, life cycle, radar bright band and interaction of the two kinds of cloud in MSC are all consistent with general observation results. Calculated water content and its distribution with height, averaged size and number concentration of particle are also reasonable.

References

Chaing H. C. and H. D. Orville, 1980: Effects of mesoscal convergence on cloud convection, *J. Appl. Meteor.* 256—274.

Yan Caifan and Chen Wankui, 1990: The stratus cloud droplet number/size distributions and spectral parameters calculation, *Quarterly Journal of Applied Meteorology*, 1, 352—359.

Yan Caifan and Chen Wankui, 1990: Raindrop parcicle size distribution in the lower troposphere, *same as above*, 191—198.

Hong Yanchao, 1996 (a): Numerical simulation study on covective—stratiform mixed cloud, part I: The model and parameterizations of microphysical processes, *Acta Meteorologica Sinica* (to be published).

Hong Yanchao, 1996 (b): Numerical simulation study on covective—stratiform mixed cloud, part II: Cloud interaction and formation mechanism of heavy rain, same as above.

MESO- AND MICROSTRUCTURE OF STRATIFORM FRONTAL CLOUDS AND MECHANISMS OF PRECIPITATION FORMATION IN FRONTAL SYSTEMS OVER UKRAINE

Vladimir P. Bakhanov, Alexandra A. Manzhara, and Valentina T. Kolezhuk

Ukrainian Hydrometeorological Research Inst., Kiev-252028, Ukraine

1. INTRODUCTION

The present study continues our previous works on the subject (Bakhanov et al., 1989-1994). This paper presents results of numerical simulations of the meso- and microstructure of winter frontal clouds and precipitation systems over Ukraine, including mechanisms and efficiency of natural precipitation formation in these systems.

Two-dimensional (2D) time-dependent numerical models with detailed microphysics were constructed. The initial cross-sections of frontal systems were based on rawinsondes and aircraft data.

The following microphysical processes were taken into account: drop and ice crystal nucleation, particle growth through condensation and sublimation, sedimentation of crystals, drop freezing, and riming. Only one type of ice nuclei (condensation-freezing) was considered. The values of parameters were the same as in our earlier paper (Bakhanov et al., 1992).

2. MESOSTRUCTURE OF FRONTAL CLOUD AND PRECIPITATION SYSTEMS

Let us consider some examples of frontal systems over Ukraine. Fig.1 depicts the warm front of February 9, 1970. Fig.1a shows the stream function field $\psi(x,z)$ constructed from rawinsonde data as of 14 h 30 min of LST.

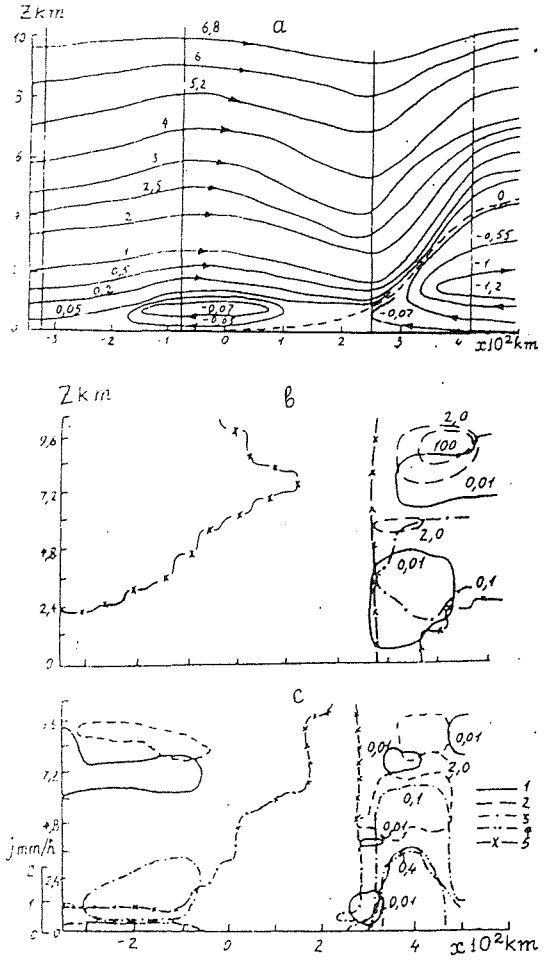

Fig.1. Vertical cross-sections of the warm front system of February 9, 1970: (a) stream function field in 10^5 g/cm·s units; (b,c) cross-sections of cloudiness at t=2h (b) and t=6h (c); 1 - q_{L1} in g/kg, 3 - q_{L2} in g/kg, 2 - n_2 in g^{-1}, 4 - j in mm/h, 5 - supersaturation over ice Δ_2=-1%.

(The coordinate system is moving together with the front, and x denotes the horizontal coordinate perpendicular to the front line).

There is a whirl in the prefrontal region, while the front has a vast area of downdrafts (x=-50...+250 km), with the downdraft velocity reaching w=-15 cm/s. The presence of the downdraft area results in formation of two separate cloud systems. The prefrontal region has two areas of intensive updrafts (x=340 km, z=5 km, w_m=+24 cm/s) and (x=300 km, z=2.1 km, w_m=+15 cm/s). The second area is located at low heights (T=-7.6...-13.6°C), so that the ice nucleation rate is insufficient, and this region permanently contains a considerable amount of water.

Fig.1b depicts the vertical cross-section of the system after 2 hours of evolution. Two liquid drop clouds have arisen in the prefrontal zone. The liquid water content (LWC, q_{L1}) in the lower cloud has reached 0.47 g/kg. In the upper layer (x=320...470 km, z=7.2 km), the crystal concentration n_2 has increased up to 160 g^{-1}, and the "seeder-feeder" mechanism in this area is of principal importance for precipitation formation. Though the mean thermodynamical condensation rate E in the prefrontal zone equals 1.93 mm/h, the precipitation intensity is as low as j=0.02 mm/h. This relation (E>>j) shows that precipitation formation is still insufficient. At t=2h, there are no clouds in the x<0 zone.

Fig.1c depicts the state of the same system at t=6h. An area with a high ice content (IC, q_{L2}>0.4 g/kg) has formed and descended to the ground, and a shower rainband emerged. The mean values of j and E are equal to 1.3...1.4 mm/h.

Let us consider another example of the warm front of January 3, 1985 (Fig.2). In this case, the frontal zone has no vast regions of downdrafts, so that a continuous cloudiness arises. On the other hand, there are high parcels of updrafts (x=-350...-50 km, z=6...9 km), (x=250...300 km, z=6.9...7.2 km) with large velocities (w=+15...+24 cm/s). This results in very intensive ice nucleation (n_2=1500 g^{-1} at z=8 km) and "seeder-feeder" processes. The clouds become completely crystal at t=6 h and have a very weak potential for artificial precipitation enhancement (APE). At t=2h (a "young" system, see Fig.2b), high values of q_{L1} (above 0.4 g/kg) are observed, with a seedable area x=0...150 km.

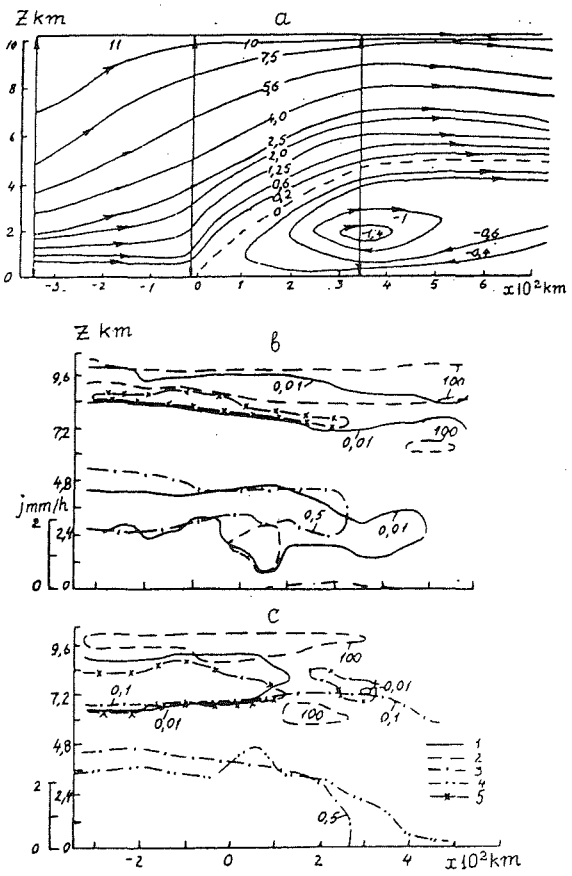

Fig.2. Vertical cross-sections of the warm front of January 3, 1985: (a) stream function field, (b) cloudiness at t=2h, (c) cloudiness at t=6h. Designations same as in Fig.1, except for curve 5 now displaying supersaturation over water Δ_1=0).

Finally, consider the last example of the occluded front of February 17, 1981. There are three large-scale whirls in the lower troposphere layers (Fig. 3a). In the x<0 zone, there is a vast downdraft region and a region with undersaturation over ice (Δ_2<0, Fig. 3b). The warm front region (x>0) has a complex

structure of updraft parcels with small velocities (w=+4...+5 cm/s).

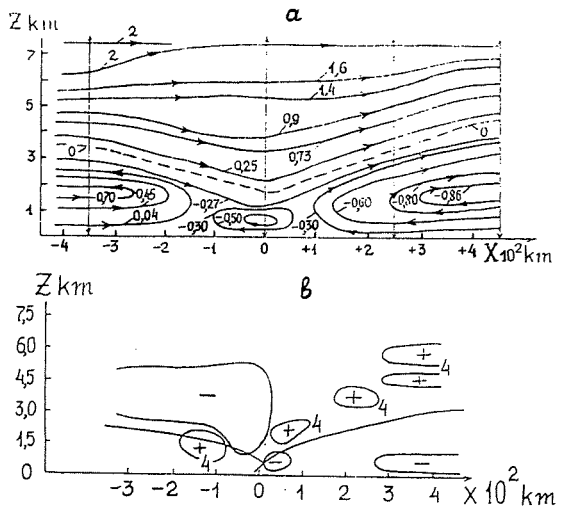

Fig.3. Cross-sections of the dynamic structure of the occluded front of February 17, 1981: (a) stream function field in 10^5 g/cm·s units; (b) updraft (+) and downdraft (-) parcels.

In this case, the tropopause is located very low, and the temperatures are high (T>-25°C). For this reason, the ice nuclei (IN) of the first type (Mason, 1957) are not active, and the precipitation rate is moderate (n_2=5...8 g^{-1} at z=5...6 km, j=0.4...0.6 mm/h). **Fig.4a** and Fig.4 depict the state of the system at t=6h and t=9h, respectively. These figures demonstrate that large LWC values (q_{L1}>0.3 g/kg, in good agreement with the observation data) exist constantly. This frontal system has a great potential for APE.

3. IFLUENCE OF RIMING ON PRECIPITATION FORMATION

The riming is taken into consideration in the continuous growth approach, with the coagulation coefficient E_c=0 for ice crystal radii r<40 μm and E_c=0.2 for r>40 μm. The riming not only washes out LWC, but rimy ice crystals change their shape (become less flat) and therefore grow slower. The calculations show that initially (t=3...4 h) the riming leads to an

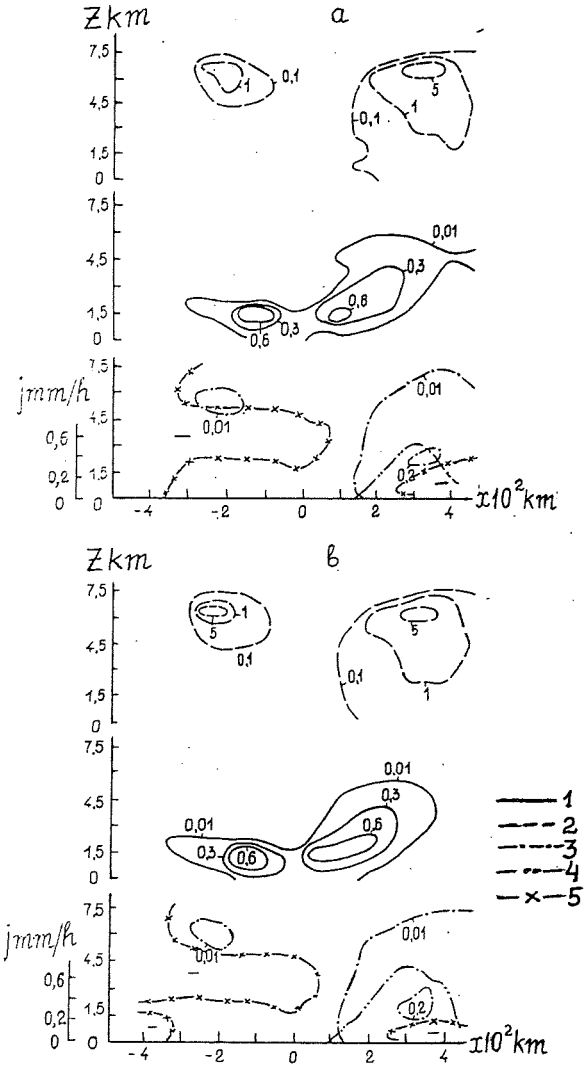

Fig.4. Cross-section of cloudiness of the front of February 17, 1981: (a) t=6h, (b) t=9 h. Designations same as in Fig.1, except for curve 5 now referring to Δ_2=0.

essential decrease of LWC, increase of IC, and nearly twofold rise in the precipitation rate. For t>5...6 h, a "self-balancing" state is achieved, and the values of j are nearly same for E_c=0 and E_c=0.2.

4. MICROPHYSICAL MECHANISMS OF FRONTAL CLOUD STRATIFICATION

Using a 1D microphysical model, we have studied the possibility of optical stratification of growing and steady-state clouds. It was

found that microphysical mechanisms can stratify frontal clouds, due to the presence of three sources of ice crystals in the atmosphere at different heights (Mason, 1957): IN of the second type (which become especially active for T=-18...-22°C), IN of the first type (T=-35...-37°C), and freezing of small drops.

5. CONCLUSIONS

1. The fronts studied exhibit a complex system of large-scale whirls (up to 5) occupying the lower layers of the atmosphere (up to 2...4 km).

2. The efficiency of precipitation formation is to a large extent controlled by the dynamic structure of the front (tropopause height, presence of the above-mentioned whirls, and, as a consequence, thickness and height of the updraft parcels).

3. When the updraft parcels are located at small heights (z<3...4 km, T>-20...-25°C), the ice nucleation and precipitation formation have insufficient efficiency. In this case, the condition $j \approx E$ is not reached in 6h of the evolution period, the total LWC can reach 1 mm, and the clouds have a considerable potential for APE.

4. In case of high updraft parcels (z>6 km, T<-35°C), ice nucleation and precipitation formation processes are very intensive. There are "splashes" of ice nucleation when $n_2=10^3$ g^{-1} in Ci, and very intensive "seeder-feeder" processes. The condition $j=E$ is reached in 3h of evolution, after which the complete crystallization takes place.

5. Model Ci always have mixed phase composition resulting from the IN nature.

6. The riming leads to an essential increase in the precipitation rate during the first 2...3 hours of cloud evolution. Afterwards, the effect of riming on the precipitation is weaker.

7. Optical stratification of frontal clouds is partially explained by the existence of three sources of ice nuclei at different heights.

6. REFERENCES

Bakhanov, V.P., Dorman, B.A., Kolezhuk, V.T., and Manzhara, A.A., 1989. Numerical simulation of frontal mixed stratiform cloud seeding for precipitation enhancement. *In: Proc. 5th WMO Sci. Conf. Weather Modif. (Beijing)*, pp. 251-254.

Bakhanov, V.P., Manzhara, A.A., Kolezhuk, V.T., and Zabolotskaya, T.N., 1992. Numerical simulation of natural and seeded precipitation in frontal cloud systems. *Trudy UHRI*, 2433: pp.39-59 (in Russian).

Bakhanov, V.P., Dorman, B.A, Kolezhuk, V.T., Manzhara, A.A., and Zabolotskaya, T.N., 1994. Natural and seeded precipitation formation in frontal cloud systems over Ukraine. *In: Proc. 6th WMO Sci. Conf. Weather Modif. (Paestum)*, pp. 459-462.

Mason, B.J., 1957. The Physics of Clouds. Oxford at the Clarendon Press. 542 pp.

A NEW APPROACH TO PARAMETERIZATION OF CLOUD DROPLET FREEZING PROCESSES IN NUMERICAL CLOUD MODELS

Ilia P.Mazin[1] and Mark V. Gurovich[2]

[1] Cloud Phys. Lab., Central Aerological Observatory, Dolgoprudny, Moscow Region, 141700, Russia
[2] Dept. of Exper. Atm. Phys., Russian State Hydromet. Inst., St.Petersburg,195196, Russia.

1. INTRODUCTION

The adequate parameterization of ice particles origination (IPO) is one of the most important and less grounded elements of known numerical cloud models at negative temperatures. At temperatures higher -35°C, droplet freezing is the main process of IPO in clouds. To our opinion, the development of semi-empirical approach to parameterization of supercooled droplet freezing processes is a step in a required direction.

2. PARAMETERIZATION OF CLOUD DROPLET FREEZING

In a general way we may write that the density of unfreezing droplet size distribution n(r,t) decreases with time t according to eq.(2):

$$dn\ (r,t) / n\ (r,t) = -\theta(\vartheta)\dot{\omega}\ (r,\vartheta,t)\ dt\ , \quad (1)$$

$$n\ (r,t) = n\ (r,0)\exp[-\omega\ (r,\vartheta,t)\ \theta(\vartheta)]. \quad (2)$$

Here ϑ=-T°C is an absolute value of temperature. The step function $\theta(\vartheta)$= 0, if $\vartheta \leq$ 0 and $\theta(\vartheta)$=1, if $\vartheta >$ 0. The $\omega(r,\vartheta,t)$ is a function to be defined. There are several mechanisms for droplet freezing, the main of these are heterogeneous freezing due to immersion (1) or contact (2) nucleation for T > -35°C and homogeneous freezing (3) for T<-35...40°C. If we assume that the cloud water has the same properties independently of droplet size, then it may be written:

$$\dot{\omega}_i(r,\vartheta,t) = r^{\alpha_i}\dot{\Omega}_i(\vartheta,t). \quad (3)$$

Index, i indicates the ith mechanism of droplet freezing. There is no freezing, if ω_i = 0 for each i. For the first mechanism α_1= 3, for the second (according to Brownian collision) α_2= 1 and we may write for immersion freezing nuclei (FN)

$$\omega_1(r,\vartheta,t) = \theta(\dot{\vartheta})r^3\dot{\Omega}_1(\vartheta), \quad (4)$$

for contact FN

$$\omega_2(r,\vartheta,t) = r\dot{\Omega}_2(\vartheta)\xi(\vartheta,t)\ . \quad (5)$$

If all cloud droplets have the same "age", and IN concentration in the cloud air is constant, then ξ= t. The functions $\dot{\Omega}_1$ and $\dot{\Omega}_2$ depend on FN temperature efficiency which is usually taken as exponential as it was found by Fletcher in the sixties. But this dependence does not satisfy the evident condition that $\dot{\Omega}\to 0$, and $\Omega\to 0$ if $\vartheta\to 0$. To satisfy these conditions, I.Mazin in 1974 suggested to assume for Ω the product of polynom $P(\vartheta)$ and a power function, namely

$\Omega_1(\vartheta)=\beta_1\vartheta^k P_1(\vartheta)$ and $\Omega_2(\vartheta)=\beta_2\vartheta^l P_2(\vartheta)$.

Following his arguments (see Mazin and Shmeter, 1983,) and also restricting our

consideration to $P_1(\vartheta)=P_2(\vartheta)=1$, we finally obtain

$$\frac{dn(t,t)}{n(r,t)} = -\theta(\vartheta)[\theta(r-\varepsilon)\theta(\dot{\vartheta})\beta_1 k\dot{\vartheta}\, r^3\vartheta^{k-1}\delta_1 + \beta_2 r\vartheta^{l-1}(\vartheta + l\, t\, \dot{\vartheta})\, \delta_2]\, dt. \quad (6)$$

Here the parameter ε allows to assume that there are no immersion ice nuclei in small droplets ($r \le \varepsilon$). Factors δ_1 and δ_2 are equal to 0 or 1 and introduced in (6) to allow to include or exclude the first (immersion) or the second (contact) mechanism or both of them.

$\beta_1(r_0,\vartheta_m)=\ln 2 r_0^{-3}\vartheta_m^{-k}$, and

$\beta_2(r_0, \vartheta_m, t_m)=\ln 2 r_0^{-1}\vartheta_m^{-l}t_m^{-1}$.

$T_m=-\vartheta_m$ is the temperature at which 50% of droplets of the size $r=r_0$ freeze due to immersion FN, and t_m is the time for freezing due to contact nucleation of 50% of droplets with $r=r_0$ at the temperature T_m, k and l are free parameters to be defined.

3. NUMERICAL EXPERIMENTS

To analyse a relative role of each parameter in parameterization (6), two sets of numerical experiments were performed based on the convective cloud model developed by Gurovich and Bekryaev, 1991. The qualitative results are presented in Table 1 where set A relates to strong and set B to weak atmospheric instability. There is no place to show the results of numerical experiments in detail, so we restrict ourselves to Table 1, Figs 2 and 3 and to some conclusions.

Table 1. Qualitative description of the differences between the given numerical experiments and base Exp.1

Numb of exper.	The values of the parameters in the eq.(6)								The difference in					
	δ_1	δ_2	ε (μm)	κ	r_0 (μm)	l	ϑ_m (°C)	τ_m (min)	level of liq. water penetrat.		liquid precip. amount.		solid precip. amount.	
									A	B	A	B	A	B
0	-	-	-	-	-	-	-	-	++	00	++	00	–	00
1	1	1	0	10	30	10	40	20	Base Experiment					
2	*	0	*	*	*	-	*	-	00	00	00	00	00	00
3	*	0	*	*	*	-	20	-	–	–	–	0	–	+
4	*	0	*	27	*	-	*	-	++	00	-	00	++	00
5	*	0	*	4	*	-	*	_	–	–	–	00	–	+
6	*	0	*	*	90	-	*	-	+	00	+	00	+	00
7	*	0	*	*	10	-	*	-	+	00		00	-	00
8	0	*	*	-	*	*	*	*	++	00	-	00	++	00
9	0	*	*	-	*	20	*	*	++	00	-	00	++	00
10	0	*	*	-	*	5	*	*	-	-	-	0	-	+
11	0	*	*	-	*	2	*	8	–	–	–	00	–	–
12	*	*	*	*	*	*	*	10	00	00	00	00	00	00
13	*	*	30	*	*	*	*	*	0	00	0	00	0	00

The asterisks in Table 1 indicate that the value of these parameters were not changed in comparison with Exp.1. The Exp.0 was carried out for liquid clouds ($\delta_1 = \delta_2 = 0$). The hyphen in the left part of the table 1 indicates that the results do not depend on these parameters.

The results of each experiment were compared to the base one (Exp.1) and the comments are presented in the right part of Table 1. Marks 00 indicate that the results are in close agreement with Exp.1. Marks 0 indicate slight difference. Plus (+) indicates somewhat higher and two pluses (++) noticeably higher penetration of liquid water in cloud or increasing the amount of liquid or solid precipitation. On the contrary sign (-) indicates somewhat lower and (--) noticeably lower penetration of liquid water in cloud or decreasing the liquid or solid precipitation amount.

4. CONCLUSIONS

The numerical experiments with suggested semi-empirical parameterization of cloud droplet freezing permits to separate the main parameters which determine the freezing processes and lead to the conclusions:

1. The ice particle origination strongly effects the cloud phase structure and precipitation formation. The stronger the atmospheric instability (larger cloud thickness), the more significant the influence of the rate of freezing.

2. The rate of ice particle origination and cloud phase transformation to a marked degree depends on CCN constitution. If it is mainly mixed then $\varepsilon \approx 0$, the immersion FN play a main role and it may be taken that $\delta_2 = 0$. If on the contrary, ε is large enough, the contact nucleation is important and $\delta_1 = \delta_2 = 1$. To make final conclusions, more experiments are needed.

3. The most important parameters in.(3) are κ and ϑ_m at given r_0 . For $r_0 = 20\mu m$ ϑ_m is between 15 and 40°C. Apparently $k \subset (5, 15)$ (Vali, 1994).

4. Before the new data on cloud phase structure are obtained, simpler parameterization may be recommended to be used for T > -35°C with two free parameters k and ϑ_m.

$$dn(r,t)/dt = -\theta(\vartheta)\ \theta(\dot{\vartheta})\ \theta(r-\varepsilon) B\ n(r,\vartheta,t)\ , \qquad (7)$$

where

$$B = \frac{k}{\vartheta_m}(r/20)^3(\vartheta/\vartheta_m)^{k-1}\dot{\vartheta}\ .$$

Two possibilities for ε should be tested: $\varepsilon = 0$ and $\varepsilon = 10$ μm.

5. For T <-35°C,other mechanisms of ice particle origination and, first of all, the homogeneous droplet freezing must be taken into consideration.

5 REFERENCES

Gurovich, V.V., and V.I. Bekryaev, 1994: Numerical model of convective cloud: some results and conclusions for naturally evolving and suppressed cases. *VI WMO Sci. Conf. on Weather Modific.* Geneva, 22 0, 471-478.

Mazin, I.P., and S.M.Shmeter, 1983: Clouds, their structure and formation. *Gidrometeoizdat,* Leningrad, 299 pp.(Ch.8, 8.3.2. Freezing as a source of ice particle origination in clouds, 187-190,) (in Russian).

Vali, G., 1994: Freezing rate due to heterogeneous nucleation. *Journ. Atm. Sci.* 251 ,1843-1856.

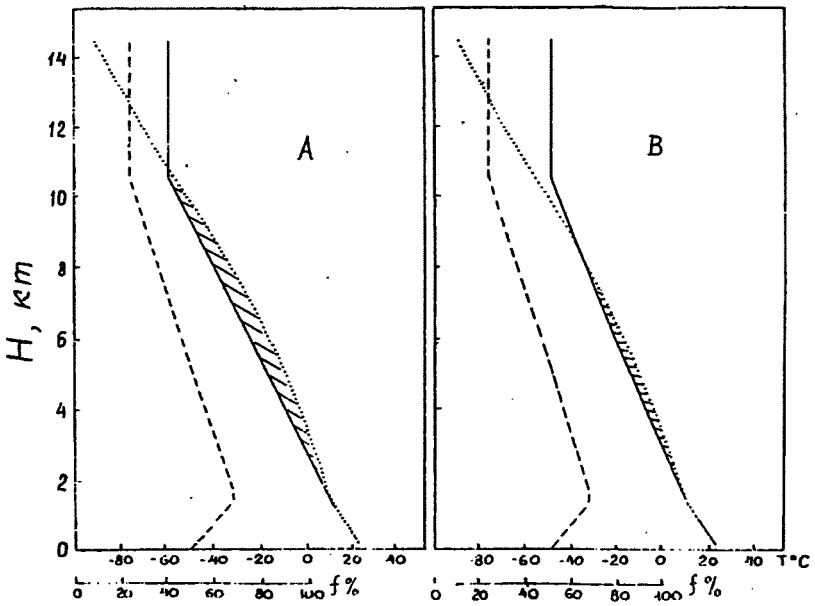

Fig. 1. The initial stratification of temperature (solid curves) and humidity (dashed curves) in experiments A and B. Dotted lines are moist adiabate. Shaded area characterizes the energy of moist instability.

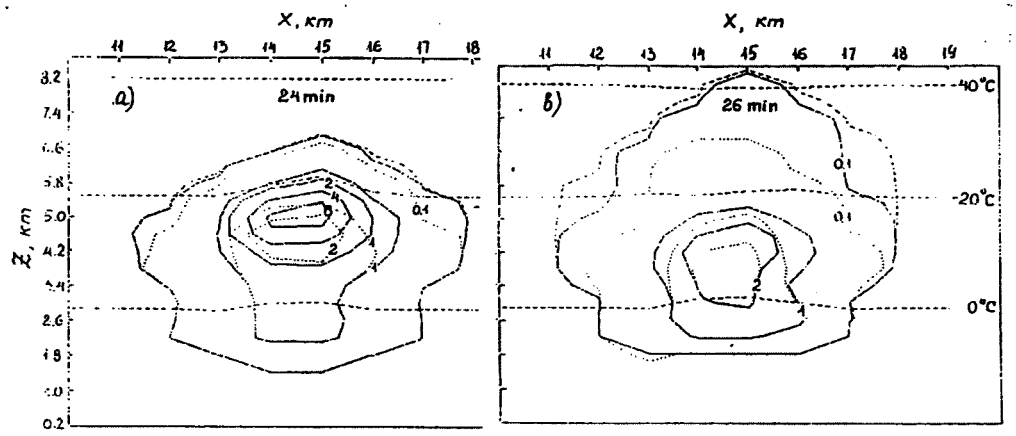

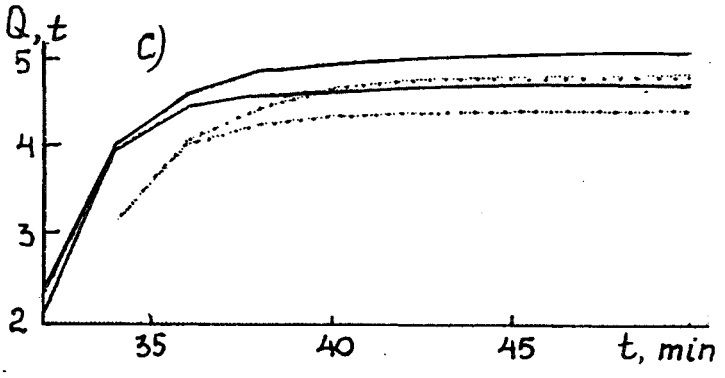

Fig.2. Liquid water isolines in the section y=15.5 km at 24 (a) and 26(b) minutes of cloud development.

Solid lines are Exp.2A, dotted lines are Exp.3A. Cloud boundary lines correspond to LWC = 0.01 gm^{-3} .Numbers on curves, are LWC in gm^{-3}.(c) Total amount of precipitation (upper curves) and solid precipitation amount (lower lines) in tons.

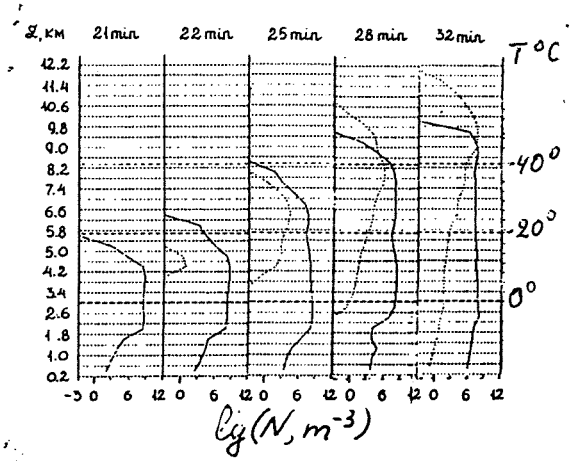

Fig.3. Changing in droplet (solid lines) and ice particles (dotted lines) concentration with time on the cloud axis in Exp.1.

EXPLICIT CLOUD MICROPHYSICS AND CODE PARALLELIZATION: POSSIBLE STRATEGIES AND FIRST EXPERIENCES ON A MASSIVELY PARALLEL SUPERCOMPUTER

Thomas Trautmann[1] and Erich Strohmaier[2]

[1]Inst. für Physik der Atmosphäre, Johannes Gutenberg-Universität, 55099 Mainz, Germany
[2]Department of Computer Science, Knoxville TN 37996, USA

1. INTRODUCTION

The simulation package MISTRA (Bott *et al.* , 1996) is a one-dimensional code for simulating stratiform clouds in the atmospheric boundary layer. In each computational layer the model explicitly accounts for the microphysics of aerosol and droplet growth. Simulation times for a cloud evolution of two days require approximately 12-24 hours of CPU time, even on the most powerful workstations. Thus there is a big need for speeding up the code by parallelization.

We parallelized MISTRA using compiler directives on a HP-Convex Exemplar SPP1200 distributed shared memory supercomputer. In its current hardware implementation at the University of Mainz Computer Center the SPP1200 supports up to 48 processors each being able of a peak performance of 240 MFLOPS. In this paper we present our experiences during the task of parallelization and discuss the various methods employed for achieving a considerable speed-up of the code. Besides the description of the computational results we will also discuss various performance results. Further extensions of the microphysical part and possible generalizations of the dynamics to two or three dimensions will be discussed at the end of this paper.

2. HARDWARE ARCHITECTURE

Any efforts which are to be put into parallelization require a certain knowledge of the properties of the underlying hardware. In this section these aspects will be shortly discussed. The HP-Convex Exemplar SPP1200 is a virtual shared memory system. This means that for a large number of processors the memory is distributed physically in the system, while the operating system still gives the programmer the view of a single shared memory. This has certain advantages for the user, since he can easily access all parts of the memory. On the other hand, it does not imply that a parallelized programme will run with satisfying efficiency, because efficient programms for virtual shared memory systems must take account of the complex memory hierarchy.

The overall architecture of the SPP1200 is hierarchical. Eight HP PA-RISC 7200 processors (120 MHz CPU clock) share a physical memory using a very efficient crossbar for accessing memory addresses. Such a complex of eight processors is called a hypernode. The entire system is built up of several such hypernodes with additional hardware realizing the shared memory view for the user. The Exemplar SPP1200 may consist of up to 16 hypernodes.

On HP-Convex SPP systems the memory hierarchy includes a processor cache of 256 kB size and a hypernode memory of up to 2 GB. The global shared memory containing the memories of all hypernodes is linked via the virtual shared memory hardware. A variety of compiler directives and library calls are available for optimizing the data layout and the access to the memory (Convex, 1995). This gives many possibilities for performance tuning on such systems. It is emphasized that the efficiency of the memory access is considered to be the major determining factor for the overall efficiency of codes utilizing the virtual shared memory. Parallelization based on message passing is also available on the SPP1200 via HP-ConvexPVM functions (PVM=Parallel Virtual Machine), but is not considered in this paper.

3. MODEL DESCRIPTION

The microphysical cloud model consist of the following equations for the horizontal wind velocities, u, v, the potential temperature θ, the turbulent kinetic energy e, the specific humudity q, the upward and downward radiative fluxes $E_i^{\pm}$ for a wavelength

interval i, and the particle size distribution function

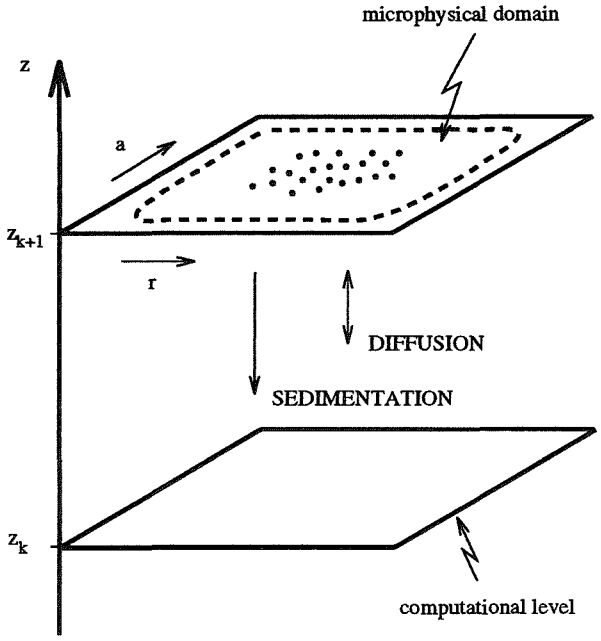

Figure 1: Computational domain showing the independent radii a, r of the cloud microphysical model.

$f(a,r)$, where a, r denote the dry nucleus radius and the total radius of an atmospheric particle (aerosol or droplet), respectively:

$$\frac{\partial u}{\partial t} = \frac{\partial}{\partial z}\left(K_m \frac{\partial u}{\partial z}\right) + f(v - v_g) - w\frac{\partial u}{\partial z}\,,$$

$$\frac{\partial v}{\partial t} = \frac{\partial}{\partial z}\left(K_m \frac{\partial v}{\partial z}\right) - f(u - u_g) - w\frac{\partial v}{\partial z}\,,$$

$$\frac{\partial \theta}{\partial t} = \frac{\partial}{\partial z}\left(K_h \frac{\partial \theta}{\partial z}\right) - w\frac{\partial \theta}{\partial z} - \left(\frac{p_0}{p}\right)^{0.286} \frac{1}{\rho c_p}\left[L_v C + \frac{\partial (E_i^+ - E_i^-)}{\partial z}\right]\,,$$

$$\frac{\partial q}{\partial t} = \frac{\partial}{\partial z}\left(K_h \frac{\partial q}{\partial z}\right) - w\frac{\partial q}{\partial z} + \frac{1}{\rho} C\,.$$

$$\frac{\partial e}{\partial t} = \frac{\partial}{\partial z}\left(K_m \frac{\partial e}{\partial z}\right) + \sigma(e) - w\frac{\partial e}{\partial z}\,,$$

$$\frac{\partial E_i^{\pm}}{\partial z} = \pm[\alpha_{1,i}^{\pm} E_i^{+} - \alpha_{2,i}^{\pm} E_i^{+}] \pm \alpha_{3,i}^{\pm} J_i^{\pm}$$

$$\frac{\partial f}{\partial t} = \frac{\partial}{\partial z}\left(K_h \frac{\partial f}{\partial z}\right) - \frac{\partial}{\partial z}\left([w + w_\infty] f\right) - \frac{\partial}{\partial r}\left(\dot{r} f\right)\,.$$

Here σ of the production of e, and $J_i^{\pm}$ is the source term for radiation, see Zdunkowski *et al.* (1982). C is the condensation rate which is obtained from

$$C = \int_0^\infty \int_0^\infty \frac{\partial}{\partial r}\left(\dot{r} f(a,r)\right) m_w(a,r)\, da\, dr\,.$$

where $m_w(a,r)$ is the water mass of the particle. The meaning of all other quantities can be found in Bott *et al.* (1996).

The dynamics of the model runs with a time step of 10 s. Condensation/evaporation is calculated iteratively using the same time step. The particle spectrum is resolved with 40 size bins for the dry aerosol mass and 50 size bins for the water mass. Note that an atmospheric particle is assumed to consist of an aerosol core (partially dissolved) surrounded by a water shell. Therefore, the microphysical model has to solve a total of 2000 scalar differential equations for discretizing the (a,r) domain at each computational level, see Fig. 1. The radiative fluxes are calculated every 60 s of model time. The spectral integration requires 52 quasi-spectral calculations. The turbulent diffusion terms a solved fully implicitly employing a tridiagonal solver. The vertical variable z is discretized in $K = 100$ different levels.

A major issue is the time dependent determination of the optical properties of aerosols and droplets. A large set of precomputed Mie data is used to derive the wavelength dependent absorption and scattering coefficients from the particle distribution at time t and level z. An inspection of the set of prognostic equations reveals that the lion's share of computational work is spent for solving the evolution equation for f. The numerical treatment of the condensation term requires an accurate treatment of the advection-type equation. The positive definite scheme of Bott (1989) has been used for this purpose.

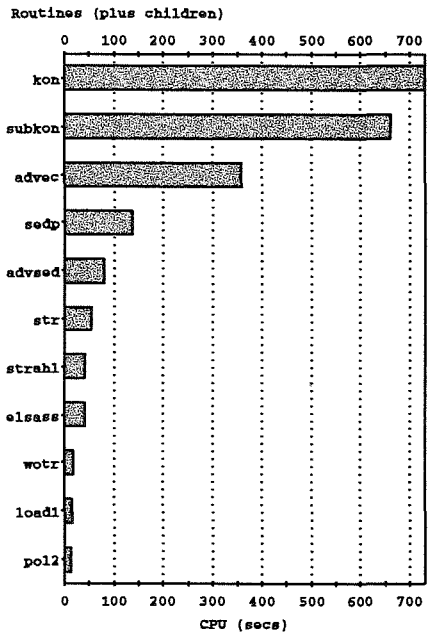

Figure 2: Results of the serial performance analysis.

A performance analysis of the sequential code has been carried out by using the HP-Convex CXPA performance analyzer tool. For this purpose the model has been run for one hour. Fig. 2 summarizes

the results of the performance measurements. The CPU times quoted refer to the cumulative time the code has spent in a particular programme module. The top three routines belong to the condensational growth, 'sedp' and 'advsed' symbolize the routines for the vertical advective transport. The remaining six routines from 'str' to 'pol2' refer to the radiative transfer computations. It is interesting to note that i) nearly 78 % of the CPU time is spent for the condensation calculation, ii) about 12 % is needed to advect the particles downward, iii) 4 % is spent for each radiative transfer and particle diffusion, and that iv) all other model equations require together only about 1-2 % of the total computation time.

4. PARALLELIZATION

Due to the complexity of the data structure in MISTRA, the parallelization strategy was based on virtual shared memory from the very beginning. Using automatic parallelization failed totally since typically loops have to be parallelized which contain complicated call structures. The passing of data by common blocks had first to be removed. This is necessary for generating reentrant code from modules to be called in parallel. Furthermore, in parallel segments the appropriate variables and arrays had to be declared private. The data structure of the model can be deduced from Fig. 1. The microphysical processes can be treated vertically independently. Thus loop-level parallelism over the z domain proves to be efficient.

A further necessary step is load balancing, which means each of N processors should be given approximately the same amount of work to do. We employed a dynamic load balancing mechanism in the following way. Execution times a recorded for the condensational growth process for a suitable number of adjacent z_k levels. Then an algorithm is used which rearranges the K vertical levels into N adjacent pieces (N is the number of concurrent processors) so that each piece roughly needs the same amount of work.

In contrast to the condensational treatment, the mechanisms of particle diffusion and particle advection have been parallelized over the (a, r) domain, since these transport processes have to be solved with the vertical index k being the running index. This implies that for each time step all data from the major working arrays have to be exchanged between processors. The virtual shared memory of the HP-Convex SPP simplifies the programming of this exchange quite a lot, but it was not clear from the beginning that this would be efficient. Finally, radiative transfer uses the spectral index i as independent loop index over which parallelism can easily be achieved.

5. RESULTS

In Fig. 3 we present the CPU/wall clock ratio as analyzed by the HP-Convex CXPA performance tool. The wall clock time records the time elapsed for a program, including disk accesses, memory accesses, input/output, and operating system overhead. For parallel regions, this ratio corresponds to the concurrency factor, which is an indicator of the speed-up achieved through parallelization. Values that approach N, where N is the number of processors, indicate good parallel concurrency.

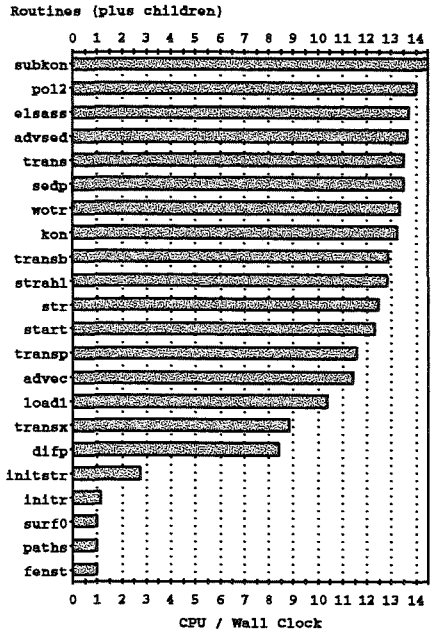

Figure 3: Results of the parallel performance analysis using $N = 16$ processors.

A comprehensive run time statistics has been performed in order to determine average numbers for the parallel efficiency, $E_{p,N}$, and the speed-up, S_N, as a function of N. Figures 4 and 5 are the result of a total of 120 identical cloud simulations, each predicting 24 hours of cloud evolution. Following Amdahl's laws (Wang, 1993) the parallel efficiency of the code is defined as

$$E_{p,N} \stackrel{def}{=} \frac{t_1}{N t_N} \approx \frac{1}{N - \alpha(N-1)},$$

where t_1 is the CPU time the sequential code requires, t_N is the time used for the parallel code on N processors, α is an estimate of the overall degree of parallelization, and the definition of the speed-up

is

$$S_N \stackrel{def}{=} \frac{t_1}{t_N} \approx \frac{1}{N - \alpha(N-1)/N} ,$$

The dotted lines in Fig. 5 depict the value of $E_{p,N}$ for the α value specified. It can be concluded that we were able to achieve a 96 % degree of parallelization for the entire code. It should be noted that both the dynamics of the model as well as the I/O still run serially. Therefore, using 20 processors and more one steadily approaches saturation, which is fully in accordance with Amdahl's law.

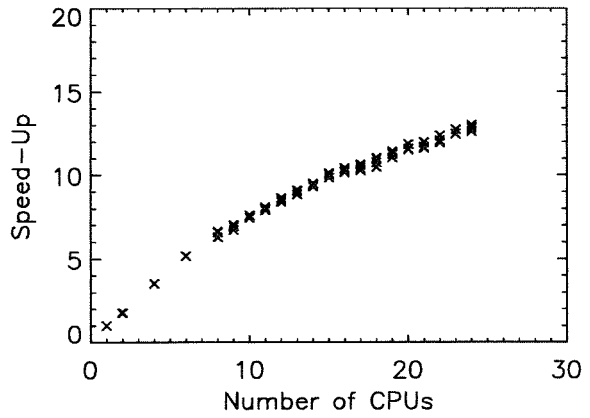

Figure 4: Speed-up of the code versus the number of processors.

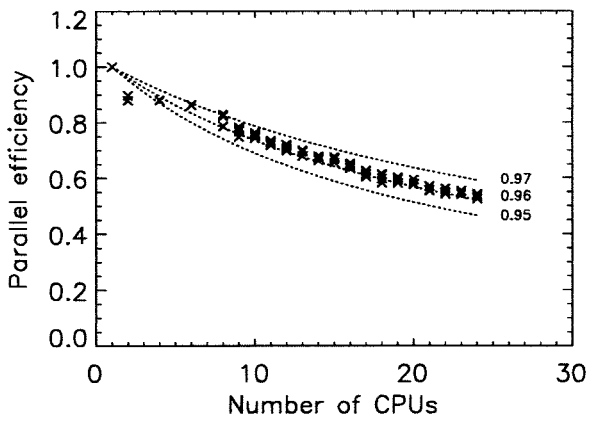

Figure 5: Measurements of the parallel efficiency versus the number of processors.

6. CONCLUSION

Taking into account the complicated data structure, we obtained a rather good parallelization ratio without having to port the code to a message passing interface like PVM or MPI. Fig. 4 clearly demonstrates that the HP-Convex SPP1200 is able to achieve a rather homogeneous data access, even over as much as four hypernodes. The gradual decline of the speed-up for a large number of processors indicates that the load balancing could be optimized even a bit further. In summary, as much as $N = 15$ processors yield a speed-up by a factor of 10. However, getting to much higher efficiencies on this architecture for $N = 50 - 100$ would require much more work, because then a combination of shared memory programming and message passing would have to be used.

Presently work is in progress to incorporate the much more CPU demanding coalescence process as well (c. f. Seeßelberg *et al.* , 1996; Trautmann, 1996) which can run in parallel in analogy to the condensation process and which is able to increase $E_{p,N}$ further. Finally, we wish to add, that the considerable speed-up, as achieved with the above described strategies, will put us in a position to tackle the even more challenging problem of cloud microphysical modeling in two and three spatial dimensions. Considering our present experiences, the HP-Convex SPP1200 should offer a good prospect for achieving this goal.

7. REFERENCES

Bott, A., 1989: A positive definite advection scheme obtained by nonlinear renormalization of the advective fluxes. *Mon. Wea. Rev.*, **117**, 1006–1015.

Bott, A., T. Trautmann, and W. Zdunkowski, 1996: A numerical model of the cloud topped planetary boundary layer: Radiation, turbulence and spectral microphysics in a marine stratus. *Quart. J. of the Royal Meteor. Soc.* (in print).

Convex, 1995: *The Convex Exemplar Programming Guide*, 2nd. Ed., Order No. DSW-067. Convex Press, Richardson (Texas), USA.

Seeßelberg, M., T. Trautmann, and M. Thorn, 1996: Stochastic simulations as a benchmark for mathematical methods solving the coalescence equation. *Atmosph. Research* (in print).

Trautmann, T., 1996: Reformulation of a fast discrete bin method for solving the droplet coalescence equation. Submitted to *Atmosph. Research.*

Hwang, Kai, 1993: *Advanced Computers Architectures*, McGraw-Hill, New York.

Zdunkowski, W. G., W.-G. Panhans, R. M. Welch, and G. J. Korb, 1982: A radiation scheme for circulation and climate models. *Beitr. Phys. Atmosph.*, **55**, 215–238.

APPLICATION OF THE VOLUME OF FLUID METHOD TO THE ADVECTION-CONDENSATION PROBLEM

Jon Reisner[1], Len Margolin[1], and Piotr Smolarkiewicz[2]

Los Alamos National Laboratory[1]
Los Alamos, NM 87544

National Center For Atmospheric Research[2]
Boulder, CO 80307

1. INTRODUCTION

In an Eulerian framework, the difficulties encountered while advecting fields with sharp gradients or discontinuities (i.e., sharp gradients not resolved on the computational mesh) using finite-differencing techniques are well-recognized. Low-order linear methods smear the regions of rapid change, while higher-order techniques introduce spurious oscillations. Nonlinear (nonoscillatory) techniques, such as flux-corrected transport (FCT), and TVD schemes can maintain steep gradients without introducing oscillations in simple advective problems. But in problems where the advected field also appears in forcing terms on the right-hand-side of the equation, the feedback between advection and forcing can lead to oscillations in the vicinity of steep gradients, even when nonoscillatory advective techniques are employed. As noted in previous studies (Klaassen and Clark 1985, Mac Vean and Nicholls 1988, Grabowski 1989), the coupled processes of advection and condensation occuring in clouds are a particular example of such a problem.

Grabowski and Smolarkiewicz (1990, hereafter GS) constructed FCT algorithms that directly incorporate information regarding the phase changes, and were able to eliminate most of the spurious oscillations at the cloud boundary. However, the FCT approach itself leads to additional smearing of steep gradients. Also, the resultant algorithms are relatively complex. Furthermore, FCT algorithms are designed to identify spurious oscillations by comparing a high-order and a low-order solution. No oscillations found in the low-order approximation can be corrected by an FCT scheme.

An alternative suggested by GS is to track the actual position of the cloud boundary within a grid box. In principle, any Lagrangian method (such as, e.g., Interface-Tracking, MAC, PIC, etc.) could be used for this purpose. However, strong convolution of the cloud boundaries makes such techniques computationally inefficient due to the associated distortions of the Lagrangian mesh. An alternative approach is interface reconstruction (Hirt and Nichols 1981), where partial volumes of two materials separated by an interface become the grid-cell variables advected with the fluid. Local differentials of such volume-of-fluid variables are then used to reconstruct the interface. The VOF approach is easier to implement, more accurate, and less computationally intensive than particle methods (Ashgriz and Poo 1991). The efficacy of VOF is due to its local nature—VOF needs to be applied only in grid cells in vicinity of a cloud boundary.

Although the notion of VOF is fairly simple (see the following section), VOF computer programs can be tedious (especially in 3D). The latter is related to a substantial logic component associated with the geometry of the problem. In essence, VOF reduces to: a) locating the position and orientation of the interface within the cell, and b) evaluating volumes (areas in 2D) of material advected through cell boundaries. The overall accuracy and technical complexity of the approach strongly depend on an analytic equation assumed for approximating the locus of interfacial points within a cell. Early VOF algorithms (Hirt and Nichols 1981) assumed interfaces parallel to the cell walls; more recent schemes such as PLIC (Kothe and Rider 1995) and FLAIR (Ashgriz and Poo 1991) assume piecewise-linear interfaces . Consequently, the latter schemes are more complex but preserve shapes of advected fields more accurately than the early algorithms. Although in theory FLAIR seems to be more accurate than PLIC, the differences between FLAIR and PLIC solutions have been shown to be small for 2D advection (Parker and Young 1992; to our knowledge a 3D version of FLAIR does not yet exist). In our work we have chosen to follow PLIC approach, primarily for its relative simplicity. Since the VOF method is relatively unknown to atmospheric science, below we will present the method itself with results being presented at the conference.

* The National Center for Atmospheric Research is sponsored by the National Science Foundation

Corresponding author address: Jon Reisner, reisner kokopelli.lanl.gov

2. VOF METHOD

Eulerian techniques have well-recognized difficulties simulating flows with two or more material regions. Even when the material interface lies initially along a cell boundary, its Lagrangian motion cannot be resolved on a stationary mesh. When the interface moves into a computational cell, the two materials are immediately mixed uniformly, effectively creating a new material. This new material has interfaces with its neighbors along the cell boundaries, and so on the next cycle the process will be repeated, creating a wider region of mixed materials. Inevitably, the initially sharp material interface will be spread over many cells.

It is the advection operator, representing the movement of the fluid through the fixed mesh, that is the source of this fundamental difficulty. The main purpose of VOF techniques is to provide subgrid scale information about the position of a material interface within a cell, thus allowing a more accurate treatment of the advection. Instead of mixing different materials within a cell, VOF keeps the materials separate and allows the advection process to move the proper amount of each material into or out of a cell.

In order to summarize the VOF approach, let us consider first an elementary problem of a scalar advection in an incompressible Boussinesq fluid

$$\frac{\partial \phi}{\partial t} + \nabla \cdot v\phi = 0 \, . \tag{1}$$

Here, $\phi = \phi(t,x)$ is a nondiffusive scalar variable, $v = v(t,x)$ is a prescribed solonoidal velocity field, and t, and x have usual meanings of temporal and spatial independent variables. Given some Lagrangian interface that marks the boundary between two immiscible materials, (1) can be reformulated as two auxiliary, conjugate equations

$$\frac{\partial \Lambda\psi}{\partial t} + \nabla \cdot \tilde{v}\psi = 0 \, , \tag{2a}$$

$$\frac{\partial \Lambda'\psi'}{\partial t} + \nabla \cdot \tilde{v}'\psi' = 0 \, , \tag{2b}$$

where $\psi \equiv \Lambda\phi$, $\psi' \equiv \Lambda'\phi$, $\tilde{v} \equiv \Lambda v$, $\tilde{v}' \equiv \Lambda' v$, $\Lambda' \equiv (1 - \Lambda)$, and $\Lambda(t,x)$ is the characteristic function of one of the materials equal either 1 or 0 depending on whether x belongs in the material or not; by design,

$$\frac{D\Lambda}{Dt} = 0 \, . \tag{3}$$

Such a reformulation is possible because the definition of Λ implies the identities $\Lambda \cdot \Lambda = \Lambda$, $\Lambda' \cdot \Lambda' = \Lambda'$, $\Lambda \cdot \Lambda' = 0$, and

$$\phi \equiv \psi + \psi' \equiv \Lambda\psi + \Lambda'\psi' \tag{4}$$

which together with (3) lead from (1) to (2).

Any flux-form finite difference scheme for, say, (2a) can be always interpreted as some particular approximation to the formal integral of (2a) over time step Δt and a volume element ΔV of a discrete grid:

$$\frac{1}{\Delta V}\int\limits_{\Delta V} (\Lambda\psi)^{n+1} d^3x = \frac{1}{\Delta V}\int\limits_{\Delta V} (\Lambda\psi)^{n} d^3x - \frac{1}{\Delta V}\oint\limits_{\Sigma(\Delta V)}\int\limits_{\Delta t} n \cdot \tilde{v}\psi dt d\sigma \, , \tag{5}$$

where all undefined symbols have their usual meaning. Finite difference approximations to (5) can be symbolically written as

$$\vartheta_i^{n+1}\psi_i^{n+1} = \vartheta_i^n\psi_i^n - \sum_{I=1}^{3}(\tilde{\alpha}^I_{i+1/2e_I}\psi^*_{i+1/2e_I} - \tilde{\alpha}^I_{i-1/2e_I}\psi^*_{i-1/2e_I}) \, , \tag{6}$$

where I labels the spatial directions, i denotes position on the grid, e^I is the unit vector in the Ith direction, and products of the effective local Courant numbers $\tilde{\alpha}^I$ and the effective transported field ψ^* are the effective fluxes of ψ through the cell walls. The auxiliary dependent variable ϑ appearing in (6), has the sense of a grid-volume average of the characteristic function

$$\vartheta_i^n \in [0,1] \; = \; \frac{1}{\Delta V}\int\limits_{x_i-\Delta X/2}^{x_i+\Delta X/2} \Lambda(t^n, x') d^3x' \, , \tag{7}$$

and is usually referred to as the 'partial volume fraction' (hereafter, PVF) of one of the materials within a cell ΔV. Note that for a single material problem in (1), $(\Lambda \equiv 1) \Longrightarrow (\vartheta \equiv 1, \; \psi \equiv \phi, \; \psi^* \equiv \phi^*)$. Then (6) is merely a symbolic form for a standard flux-form Eulerian transport scheme, where (in general) both $\tilde{\boldsymbol{\alpha}}$ and ψ^* may be complicated functions of velocity components and transported field defined at temporal and spatial locations surrounding (n,i). Particular choices for these functions define a particular transport scheme. It is apparent, therefore, that generalized form of the algorithm in (6) needs to be only considered in a vicinity of 'mixed' cells where $0 < \vartheta < 1$. From here on, we reserve the term "mixed" for the cells containing two materials and, when necessary, will explicitly identify viscous mixing.

The algorithm in (6) provides a general framework for incorporating subgrid-scale information (on material interfaces) into the Eulerian transport problem, but offers no specific recipes for approximating ϑ or $\tilde{\boldsymbol{\alpha}}$ in mixed cells. The uniqueness of

VOF is in such approximations. What essentially distinquishes VOF from either particle or interface-tracking methods is that VOF never makes explicit use of Λ (or any other Lagrangian marker) and (7), but rather relies on the auxiliary dependent variable ϑ to reconstruct an approximate material interface within mixed cells at each time step of computations. After assigning an initial condition ϑ_i^0, the evolution of PVF is approximated (as is any other transported variable) by Eq. $(6)|_{\psi\equiv\psi^*\equiv\phi\equiv 1}$

$$\vartheta_i^{n+1} = \vartheta_i^n - \sum_{I=1}^{3}(\widetilde{\alpha}^I_{i+1/2e_I} - \widetilde{\alpha}^I_{i-1/2e_I}) \ , \qquad (8)$$

whereupon the provision of proper $\widetilde{\boldsymbol{\alpha}}$ becomes the central issue of the VOF approach. Here, we emphasize that to arrive at (6) and/or (8) from (1) through (5) necessarily requires the assumption of flow incompressibility.

Choosing $\psi \equiv 1$ in (5) and (6) implies

$$\widetilde{\alpha}^I_{i+1/2e_I} = (\Delta V)^{-1} \int_{\Sigma_W}\int_{\Delta t} \widetilde{v}^I dt d\sigma = (\Delta V)^{-1} \int_{\Sigma_W}\int_{x_W-\overline{v}^I\Delta t}^{x_W} \Lambda dl^I d\sigma \ , \qquad (9)$$

where subscript W refers to the $i+1/2e_I$ location, surface integration is over a cell wall normal to v^I, dl^I is a length element parallel to v^I, and $\overline{v}^I \equiv (\Delta t)^{-1}\int_{\Delta t}\widetilde{v}^I_W dt$. In 'full' cells where $\vartheta = \Lambda = 1$, (9) recovers the standard meaning of a local Courant number. In mixed cells, however, $\widetilde{\alpha}$ acquires a sense of the normal flux of PVF through a cell wall. Having an approximation to Λ within a cell (and an approximation to $\overline{v}^I$, discussed later in this section) the evaluation of α in (9) is straightforward but tedious (especially in 3D).

In order to evaluate (9) and close the entire algorithm, one must provide a recipe for reconstructing the interface (and therefore Λ) within mixed cells. By definition, Λ is constant along an interface, so

$$\mathcal{D}\Lambda|_{\mathcal{F}} = 0 \ , \qquad (10)$$

where $\mathcal{F}$ symbolizes the locus of interfacial points and $\mathcal{D}$ is a total spatial derivative on $\mathcal{F}$. Thus, when $\mathcal{F}$ can be described as $z = z(t,x,y)$, the local interfacial slopes $\partial z/\partial x$ and $\partial z/\partial y$ are given by

$$\frac{\partial\Lambda}{\partial x} + \frac{\partial\Lambda}{\partial z}\frac{\partial z}{\partial x} = 0 \ , \qquad (11a)$$

$$\frac{\partial\Lambda}{\partial y} + \frac{\partial\Lambda}{\partial z}\frac{\partial z}{\partial y} = 0 \ . \qquad (11b)$$

Since Λ is unknown in detail, the VOF method approximates Λ in (10) and/or (11) with its grid-scale representation ϑ defined in (7). Then standard finite differences can be employed to estimate the local interfacial slopes. For example, in 2D applications, the mean slope is evaluated using the PLIC algorithm of Parker and Young (1992):

$$\frac{dz}{dx}|_{i,j} = -\frac{\vartheta_e - \vartheta_w}{\vartheta_n - \vartheta_s}\frac{\Delta Z}{\Delta X} \ , \qquad (12)$$

where,

$$\vartheta_s = (\vartheta_{i-1,j-1} + 2\vartheta_{i,j-1} + \vartheta_{i+1,j-1})/4 \ ,$$

$$\vartheta_n = (\vartheta_{i-1,j+1} + 2\vartheta_{i,j+1} + \vartheta_{i+1,j+1})/4 \ ,$$

$$\vartheta_e = (\vartheta_{i+1,j+1} + 2\vartheta_{i+1,j} + \vartheta_{i+1,j-1})/4 \ ,$$

$$\vartheta_w = (\vartheta_{i-1,j+1} + 2\vartheta_{i-1,j} + \vartheta_{i-1,j-1})/4 \ .$$

Having some finite-difference analogs to (10) and/or (11), the intercept of the linear equation for the interface can be found by requiring that the two partial volumes (areas in 2D) reproduce the known values of ϑ and ϑ'; see (7). In our work, we use an iterative process—e.g., take an initial guess for the location of the interface within a cell and compute the area underneath the interface; if the area is larger/smaller then the actual value of ϑ, move the interface down/up by half of the initial distance from the bottom of a cell, etc.

In summary, given the initial condition of the auxiliary fields ϑ, ϑ', ψ and ψ', in each time step of integration, a VOF algorithm consists of four distinct steps (note the reversed order compared to that in the presentation above): a) reconstruction of the interface based upon knowledge of ϑ; b) evaluation of PVF fluxes from (9); c) updating ϑ from (8); and d) updating transported fields according to (6). The total field ϕ in (1) need not be updated nor stored, but may be reconstructed from (4) whenever required (e.g., for display).

The last d) step of VOF procedure admits an arbitrary transport algorithm in (6). Here, we use a second-order, sign-preserving, conservative MPDATA scheme (broadly documented in Smolarkiewicz 1984, Smolarkiewicz and Clark 1986, and Smolarkiewicz and Grabowski 1990). MPDATA consists of a few iterations of the donor-cell (upwind) flux-form advection scheme. The first iteration is a first-order-accurate advection of a scalar field in a given flow. Subsequent iterations reduce the truncation error of the first iteration. As in traditional VOF schemes, we do not correct for truncation errors at the walls of the mixed cells; i.e., (6) assumes the classical donor-cell scheme wherever $0 < \vartheta < 1$ in either cell adjacent to that wall, whereas we use a fully second-order-accurate MPDATA wherever $\vartheta = 0$ or 1. This is in the spirit

of the FCT methods that reduce the local accuracy of approximation to first order in vicinity of steep gradients.

Before we close this note, we draw the reader's attention to an important physical assumption underlying the VOF approach. The theory of VOF relies on the flux-form approximation (8) to (3). Formally, this is only valid for incompressible flows. In general, the incompressibility assumption will lead to $\mathcal{O}(\Delta t)$ and $\mathcal{O}(\Delta t^2)$, errors in (8) and (6), respectively, proportional to $\vartheta \nabla \cdot v \sim \vartheta D \ln \rho / Dt$. In principle, one might correct for such zeroth- and first-order errors in the spirit of the thermodynamic adjustments discussed in section 3. This is, however, a moot issue since we address shallow convection and, consequently, use a Boussinesq approximation. Thus the standard incompressible PLIC approach is appropriate. The extension of VOF schemes for the anelastic equations of motion appears straightforward, and will be addressed in future studies.

3. ACKNOWLEDGMENTS

The authors acknowledge helpful discussions with Wojciech Grabowski, Douglas Kothe, Billy D. Nichols, and David Youngs. Special thanks go to Wojciech Grabowski who designed and performed the smooth advection-condensation test mentioned in section 4.1, and who provided an in-depth personal review of the manuscript. This work has been supported in part by the Department of Energy "Computer Hardware, Advanced Mathematics, Model Physics" (CHAMMP) research program.

4. REFERENCES

Ashgriz, N., and J.Y. Poo, 1991, Flair: Flux line-segment model for advection and interface reconstruction. *J. Comput. Phys.*, **93**, 449-468.

Hirt, C.W., and B.D. Nichols, 1981: Volume of Fluid (VOF) Method for the Dnamics of Free Boundaries. *J. Comput. Phys.*, **39**, 201-225.

Grabowski, W.W., 1989: Numerical experiments on the dynamics of the cloud-environment interface: small cumulus in a shear-free environment. *J. Atmos. Sci.*, **46**, 3513–3541.

———, and P.K. Smolarkiewicz, 1990: Monotone finite-difference approximations to the advection-condensation problem. *Mon. Wea. Rev.*, **118**, 2082-2097.

Klaassen, G.P., and T.L. Clark, 1985: Dynamics of the cloud-environment interface and entrainment in small cumuli: Two-dimensional simulations in the absence of ambient shear. *J. Atmos. Sci.*, **42**, 2621-2642.

Kothe, D.B., and W.J. Rider, 1995: Comments on modeling interfacial flows with volume-of-fluid methods. submitted to *J. Comput. Phys.*

MacVean, M.K., and S. Nicholls, 1988: A fine resolution two-dimensional numerical study of a cloud-capped boundary layer. Preprints, *Tenth Int. Cloud Physics Conf.*, Bad Homburg (FRG), 425-427.

Parker, B.J., and D.L. Youngs, 1992: Two and three dimensional eulerian simulation of fluid flow with material interfaces. AWE Preprint No. 01/92.

Smolarkiewicz, P. K., 1984: A fully multidimensional positive definite advection transport algorithm with small implicit diffusion. *J. Comput. Phys.*, **54**, 325–362.

———, and T. L. Clark, 1986: The multidimensional positive definite advection transport algorithm: Further development and applications. *J. Comput. Phys.*, **67**, 396–438.

———, and W. W. Grabowski, 1990: The multidimensional positive definite advection transport algorithm: Nonoscillatory option. *J. Comput. Phys.*, **86**, 355–375.

THE APPLICABILITY STUDY OF THE Γ DISTRIBUTION OF RAINDROP SIZE

Liu Jicheng [1] Gong Fujiu [2] Chen Weidong [1] Li Zihua [1]

[1]Nanjing Institute of Meteorology, Nanjing ,P.R.C
[2]Liaoning Weather Bureau, Shenyang, P.R.C.

1. INTRODUCTION

Raindrops are the final products of micro-physical process of clouds. By observing the raindrop spectrum, we can study the coalesence and evaporation of raindrop,water content in clouds, rainfall intensity and the structure of clouds, then we can know more about the micro-physical process of natural precipitation. By observing the raindrop spectrum, we can also calculate the radar reflectivity factor,attenuation and absorption coefficient, and provid the basical data to atmospheric remote sensing , microwave engineering and quantitative observing of precipitation by radar. Because all of these studies must be base on a universally applicabal distribution function for various type of precipitation, the study of raindrop size distribution (DSD) is very important.

The well-known and commonly used function is M-P distribution originally given by Marshall and Palmer in 1948

$$N(D) = N_0 e^{(-\lambda D)}, \quad D_{min} \le D \le D_{max} \qquad (1)$$

where N_0 ($m^{-3}mm^{-1}$) and λ (mm^{-1}) are parameters of the distribution and D_{max} is the maximum drop diameter. There exist many experimental results which suggest that Eq.(1) is a very good approximation to the raindrop size distrition in conditions similar to those which apply to the Marshall and Palmer, where sufficient areraging in space and/or time is performed. However, some other results have shown that large and sudden changes in N_0 can occar from moment to moment within a given rainfall type or rainfall intensity. Later, Cartton and others developed a gamma(Γ) distribution, which is

$$N(D) = N_0 D^{\mu} e^{(-\lambda D)}, \quad D_{min} \le D \le D_{max} \qquad (2)$$

where the exponent can have any positive or negative value and the coefficient N_0 now is in $m^{-3}mm^{-1}$. Though Eq.(2) involves three DSD parameters and is more complex than M-P distribution,the problem caused by N_0 in M-P distribution is settled.

In this paper, the DSD data ovserved in Shenyang from July to August in 1994 with GBPP-100 made by PMS company in the United States of America are analysed and a comparison between the Γ distribution and the M-P distribution is made.

2. INTRODUCTION FOR INSTRUMENT

GBPP-100 is a spectrometer designed for static operation at ground level to measure raindrop spectrum. Principlly, when raindrops pass through the probe's field-of-view, they are measured by a linear array of photodiodes because the particles are illuminated by a He-Ne lasar and shadowgraphs are projected onto the photodiode array. If the shadowing of each photodiode elements is of sufficient magnitude (dark enough), a flip-flop memory element is set. The particle size results from a determination of the number of elements shadowed by a particle's passage, the spacing of the array elements, and the magnification of the optical system. The system is constructed contains 64 active photodiode elements and is capable of sizing into 62 size channels. The

between the other two,approaching the case of the stratiformis at the end of small drops and approaching the case of the cumulus on the side of large drops, that is, its mean raindrop spectrum has both the feature of the stratiformis raindrop spectrum (may small drops) and the feature of the cumulus raindrop spectrum (wide size). The three types of clouds have one thing in common, that is, there occurs a peak at the drops 0.8-1.0mm in diameter. This is quite in agreement with the observations by Doulos and Jones[1]. It is important to notice that there is another peak, about 2mm in diameter of the third peak from the result of the model calculation by Steiner And Walavogel[2]. The third peak in the Cu-St merging cloud raindrop spectrum may be associated with the collection and breaking up of the raindrops in the convective bubbles when they are falling into the dense stratiformis cloud.

3.2 Microphysical characteristic parameters

Table 1. Means of the Characteristic Parameters in Three Types of Cloud Rainfall

Cloud form	N (m^{-3})	I (mm/h)	D_{max} (mm)	D_1 (mm)	D_3 (mm)	D_0 (mm)
Cu.	851.6	16.7	5.8	1.46	1.58	1.9
St.	1702.6	2.5	2.6	0.75	1.03	1.2
Cu-St	1811.7	13.5	5.4	0.83	1.28	1.7

The means of the microphysical characteristic parameters of the three types of precipitation is shown in Table 1. It is seen that the number density of the Cu-St merging cloud raindrops is the largest, roughly twice as large as that of the cumulus raindrops. The raindrops are the largest in diameter in the cumulus rainfall, next in the merging cloud rainfall and the smallest in the stratiformis rainfall. The cumulus rainfall has the largest mean rain intensity, the merging cloud rainfall next and the stratiformis rainfall the smallest. The former two types of rainfall have large rain intensity due to their wide spectra and the large number density of their big raindrops. The number density of the stratiformis rainfall is lager but its raindrop spectrum is narrow and the big drops have small number density, thus resulting in small rain intensity. Fig.2 gives the contribution rates of different grades of raindrop scales to rain intensity, I_i being the rain intensity of the ith-grade raindrops and I the total rain intensity. It is seen that the rate curves of the contribution that raindrops of different scales of the three cloud types makes assume in the main the normal distribution. Raindrops which make the greatest contribution to rain intensity are 1.0mm in diameter in the stratiformis, 1.3mm in the Cu-St merging cloud and 1.4mm in the cumulus,contribution rates being 14%, 11% and 9%, respectively. Calculation indicates that the accumulated rain intensity of the raindrops smaller than 1.0mm in diameter accounts for 36% of the total intensity in the stratiformis.19% in the Cu-St merging cloud and only 1.1% in the cumulus. The physical meaning of the volume medium diameter D_0 is the diameter of the raindrops,from smaller raindrops, where the accumulated rain intensity reached 50%. The value of D_0 in Table 1 is 1.2mm in the stratiformis, 1.7mm in the Cu-St merging cloud and 1.9mm in

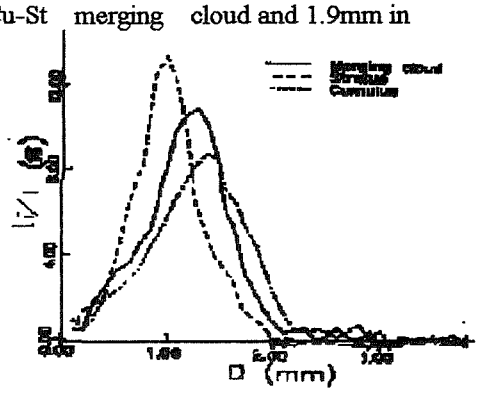

Fig.2 Contribution of raindrops on differnet scales to rain intensity

the cumulus. All these show that small raindrops make remarkable contributions to the stratiformis rain intensity, cumulus rain intensity is great mainly owing to large raindrops, and the Cu-St merging cloud rain intensity owes much to both the large raindrops and the small raindrops with very large number density.

3.3 Evolution of raindrop spectrum

Fig.3 shows the evolution of rain intensity I, raindrop number density N and mean diameter of

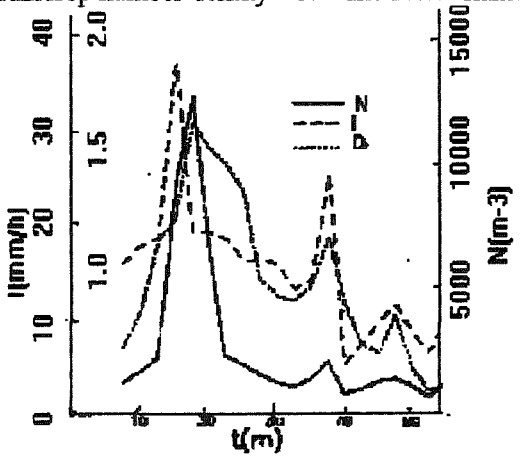

Fig.3 Evolution of I, D_1 and N of the Cu-St merging cloud rainfall with time

the Cu-St merging cloud rainfall. The time interval is 5 min. It is clear that the evolution trend of rain intensity and number density in the three types of cloud shows no difference. The three types of clouds,however, have different features of their changes in rainfall.The raindrop number density and rain intensity of the stratiformis rainfall assume smooth and rain intensity of the stratiformis rainfall assume smooth and relatively steady evolution. The cumulus rainfall varies remarkably and shows great fluctulation. The Cu-St merging cloud rainfall develops sometimes enormously (resembling the cumulus) and sometimes slightly (resembling the stratiformis) as shown in Fig.3. The rain intensity peak region of the Cu-St merging cloud rainfall corresponds to its convective bubble rainfall, the range of the peak being about 10-20 min, while the strong rainfall of the cumulus lasts between 20 and 40 min, suggesting that convective bubbles are usually small in the Cu-St merging cloud than in the cumulus. The relatively steady stage of the Cu-St merging cloud corresponds to that of the dense stratiformis. In this stage the rain intensity is about 10mm/h, much greater than in pure stratiformis rainfall (5mm/h), suggesting that the convective bubbles in the Cu-St merging cloud play an important role in the dense stratiformis rainfall. The mean diameter of the raindrops changes very slightly in the three types of cloud rainfall,mostly 1.4mm in the cumulus,0.7mm in the stratiformis, 1.2-1.5mm in the bubbles of the Cu-St merging cloud,and about 0.7mm in the dense stratiformis.

4. RAINDROP SPECTRUM DISTRIBUTION FUNCTION

We fit the M-P distribution form the actual spectrum and make correlation significance tests with it so as to study the applicability of the M-P distribution to the summer rainfall in Shengyang. The result shows that the M-P distribution does not apply to rainfall with great intensity or wide spectrum. It is also noted that when I<1mm/h, P is slightly smaller and thus for rainfall with too small rain intensity and very narrow spectrum, the M-P distribution is not a good expression either. This agrees with the conclusion drawn by Willis[3]. In the single log coordinate, the M-P distribution is a straight line. If there are many actual lager or small rainfall particles, great deviation will occur from the M-P distribution.

Compared with the result of the M-P distribution, N_0 and λ have the same trend of change rain intensity.In the stratiformis,P is small only when raining intensity<5mm/h and Γ distribution is not so good as the M-P distribution.In the cumulus and Cu-St merging cloud,the Γ distribution fitting is much better than the M-P distribution and the rate of the correlation significance lever smaller than 0.001 is always 100% and only when I<1mm/h it is 86% or 93%.

It is obvious that the Γ distribution is a good expression for the two types of cloud raindrops spectrum.

Comparision of the M-P distribution and the Γ distribution with the actual mean spectrum indicates that the M-P distribution has the best effect for the stratiformis rainfall fitting,the correlation coefficient being 0.96, very close to the actual spectrum. The Cu-St merging cloud has poorer fitting effect with the correlation coefficient being 0.86, mainly because most of the particles are large and deviate from M-P distribution. The cumulus has the poorest fitting effect, with deviation occurring at either end of both large and small particles and the correlation coefficient being only 78%. It is clear that the M-P distribution applies to steady stratiformis rainfall but not for the cumulus and Cu-St merging cloud rainfall. The Γ distribution curve is not only very close to the actual raindrop spectrum of the cumulus and Cu-St merging cloud rainfall as shown in Fig.4, but also reflects the actual distribution of the stratiformis rainfall spectrum.Thus,the Γ distribution has universal applicability.

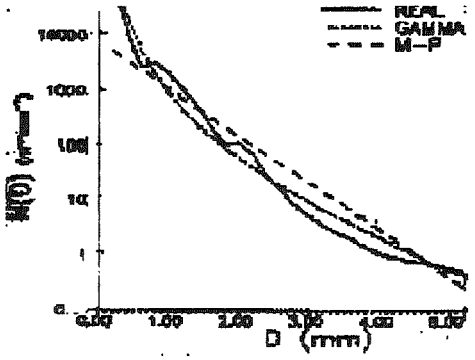

Fig.4 Comparison of the actual raindrop spectrum in the Cu-St merging cloud rainfall with the fitted M-P and Γ distributions

The Γ distribution formula (Eq.2) has one more D factor than the M-P distribution formula (Eq.1). This factor plays a role in the correction of the sections of small and large particles in the M-P distribution. As a

result, in the single log coordinate, the Γ distribution is not a straight line but approaches the actual curve. In fact, the M-P distribution is the special case of the Γ distribution when μ =0.

5. CONCLUSION

Based on the above analyses we come to the conclusions as follows:

(1) The Cu-St merging cloud raindrop spectrum has both the feature of the stratiformis raindrop spectrum (many small raindrops) and the feature of the cumulus raindrop spectrum (wide spectrum), and its third peak occurs at the raindrops about 2mm in diameter.

(2) The Cu-St merging cloud rainfall has great rain intensity and makes the same contribution as both the large raindrops (resembling the cumulus rainfall) and the small raindrops with very great number density (resembling the stratiformis rainfall). Owing to the long duration of this kind of cloud rainfall,heavy rain or rainstorm often occurs.

(3) The M-P distribution applies to the steady stratiformis rainfall. The Γ distribution has universal applicability. It is not only an ideal expression of the cumulus and Cu-St merging cloud raindrop spectra, but also a good reflection of the actual distribution of the stractiformis raindrop spectrum.

(4) Changes in number density and rain intensity are steady in the stratiformis raindrops, fluctuate greatly in the cumulus raindrops, and are moderate in the Cu-St merging cloud raindrop sometimes resembling the stratiformis and sometimes resembling the cumulus.

REFERENCES

1.Doulus M.A. Jones, Raindrop spectra at ground, J. Appl. Mete., 31,1219-1225,1992;

2.Steiner M. and A.Walavogel, Peaks in raindrop size distribution, J. Atmos. Sci.,44,3127-3133,1987;

3.Willis, P.T., Function fits to some observed drop size distribution and parameterization of rain, J. Atmos. Sci.,41,1048-1161,1984

CONSTRUCTION OF THE VARIOUS NUMERICAL MODELS FOR RESEARCH OF DYNAMICS AND MICROPHYSICS OF CLOUDS AND PRECIPITATION IN WINTER FRONTAL CLOUD SYSTEMS

Anne M. Pirnach, UHRI, Kiev, Ukraine

1. INTRODUCTION

During a number of years combined theoretical and field studies of winter frontal clouds have been made at the Ukrainian Hydrometeorological Research Institute. As result, the fundamental theory of stratiform frontal cloud and precipitation formation have been developed.

At present, for to study the processes of cloud and presipitaton formation, one-, two- and three- dimensional steady-state and time-dependent models have been developed and are used for theoretical interpretation of the field experiments and fundamental investigation.

At first, the microphysical processes were basic objects of this investigation (see Buikov and Dehtyar, 1968, Buikov and Pirnach, 1975, 1978, Buikov, 1978, etc.). In recent years the principal intention were replaced to the cloud dynamics problems. The paket of models that imitated natural frontal cloud systems that were conducted to field experiments were developed (Pirnach, 1987, Pirnach and Krakovskaya, 1994, etc.).

2. GOVERNING EQUATIONS

The formation and development in space and time of clouds and rainbands in the frontal zones are simulated by integration of the following set of the primitive equations.

$$\frac{dS_i}{dt} = F_i + \Delta S_i \qquad (1)$$

$$\frac{\partial ru}{\partial x} + \frac{\partial rv}{\partial y} + \frac{\partial \rho\omega}{\partial z} = 0 \qquad (2)$$

$$\rho = P/RT \qquad (3)$$

$$S_i = (u, v, w, T, q, f_k)$$

$$i = 1, 2, \ldots, 9; \; k = 1, 2, 3, 4$$

$$\frac{d}{dt} = \frac{\partial}{\partial t} + u\frac{\partial}{\partial x} + v\frac{\partial}{\partial y} + w\frac{\partial}{\partial z}$$

$$\Delta S_i = k_x (S_{xx} + S_{yy}) + k_z S_{zz}$$

$$F_1 = lv - P_x/\rho + \Delta u$$

$$F_2 = -l(u+u_f) - P_y/\rho + \Delta v$$

$$F_3 = -g - P_z/\rho + \Delta w$$

$$F_4 = \sum_{k=1}^{4} \alpha_k \varepsilon_k + \alpha_p \frac{dp}{dt} + \Delta T$$

$$F_5 = -\sum_{k=1}^{4} \varepsilon_k + \Delta q$$

$$F_6 = -\frac{\partial}{\partial r}(r_1 f_1) - v_1 \frac{\partial f_1}{\partial z} + I_a - I_{f1} - (c_{21}+c_{31}+c_{41}) f_1 + \Delta f_1$$

$$F_7 = -\frac{\partial}{\partial r}(r_2 f_2) - v_2 \frac{\partial f_2}{\partial z} - I_{f2} -$$

(Buikov, 1978, Pirnach, 1987, 1989, Pirnach and Krakovskaya, 1994).

SOLUTION SCHEMES

The solution of Eqs.1 is based on the splitting method (Marchuk, 1974). A general system of equations was split on several approximation to the equations which presented several physical processes.

$$\frac{\partial S_i}{\partial t} = F_{i1}+F_{i2}+F_{i3}+F_{i4}+F_{i5} \qquad (4)$$

$$S_{i1}^{j+1/5} = S_{i1}^{j} + F_{i1} t_s \qquad (5)$$

$$S_{i2}^{j+2/5} = S_{i2}^{j+1/5} + F_{i2} t_s \qquad (6)$$

$$S_{i3}^{j+3/5} = S_{i3}^{j+2/5} + F_{i3} t_s \qquad (7)$$

$$S_{i4}^{j+4/5} = S_{i4}^{j+3/5} + F_{i4} t_s \qquad (8)$$

$$S_{i4}^{j+1} = S_{i5}^{j+4/5} + F_{i5} t_s \qquad (9)$$

Eq.5 included the equation of continuity, the heat, humidity, air and particles transfer and the fall, freesing and forminc processes of the cloud particles (Marchuk, 1974, Buikov and Pirnach, 1975).

Eq.6 included processes wich were defined by pressure gradients (Pirnach, 1987).

Eq.7 shows the influence of Coriolis acceleration on air motion (Pirnach, 1987).

Eq.8 expresses condensation and particle growth processes (Pirnach, 1974, 1980, Ibragimov and Pirnach, 1988).

Eq.9 shows coagulation growth processes of droplets, crystals and agregates (Buikov and Pirnach, 1976, Pirnach, 1979).

Each equation needs special consideration. The theoretical design of solution schems for each one are given in Buikov and Pirnach, 1975, 1976, Pirnach, 1973, 1979, 1980, 1987, 1989, etc.

As example, the solution schemes for Eq.6 and 8 will be considered in recent work more detail. Eq.6 are as follows:

$$u^{j+2/5} = u^{j+1/5} - t_s (P_x/\rho)^{j+2/5}$$

$$v^{j+2/5} = v^{j+1/5} - t_s (P_y/\rho)^{j+2/5}$$

$$P_z^{j+2/5} = g\rho^{j+1/5} \qquad (10)$$

$$P_x^{j+2/5} = - g\int_0^{Zm} \rho_x^{j+1/5} Z_s$$

$$Py^{j+2/5} = - g\int_0^{Zm} \rho_y^{j+1/5} Z_s$$

$\rho = P/RT$

t_s and z_s are t- and z-interval of integration, respectively. Zm is the highest z.

Investigation of solution stability of Eq.(10) is given in Pirnach, 1987.

Original solution shemes was developed for Eq.8 (Buikov and Pirnach, 1975, Pirnach, 1974, 1980, Ibragimov and Pirnach, 1988). Eq.8 was presented as follows:

$$T^{j+4} = T^{j+3} \sum_{k=1}^{4} \alpha_k \varepsilon_k^{j+4} - \gamma_a w$$

$$q^{j+4} = q^{j+3} - \sum_{k=1}^{4} \varepsilon_k^{j+4} \qquad (11)$$

$$f_K^{j+4} = f_K^{j+3} - \frac{\partial}{\partial r}(r_K f_K)$$

$K = 1, 2, 3, 4$

In Eq.8 indexes j+k were substituted for j+k/5 (k=3,4). The relationships

$$Y_i = a_i (q - q_i) = a_i D_i, \quad i=1,2 \qquad (12)$$

$a_i = 2D_i \rho / \rho_i \Gamma_i$

were used for reformation of Eqs.11.

The difference solution sheme is as follows:

$$T^{j+4} = T^{j+3} + b_1 Y_1^{j+4} + b_2 Y_2^{j+4} \gamma_a w$$

$$Y_1^{j+4} = (Y_1^{j+3} b_3 \; Y_2^{j+3} b_4)/c_1 \qquad (13)$$

$$Y_2^{j+4} = (Y_2^{j+3} - b_5 Y_1^{j+4} + b_6)/c_2$$

$$- \frac{\partial}{\partial r}(r_{c21} f_2) - c_{42} f_2 + \Delta f_2$$

$$F_8 = - \frac{\partial}{\partial r}(r3f3) - v3\frac{\partial f_3}{\partial r} + \frac{\partial}{\partial r}(r_{c31} f_3) - c_{43} f_3 + I_s + I_{f1} + I_{f2} + \Delta f_3$$

$$F_9 = - \frac{\partial}{\partial r}(r_4 f_4) - \frac{\partial f_4}{\partial r} - \frac{\partial}{\partial r}(r_{c41} f_4) - \frac{\partial}{\partial r}(r_{c42} f_4) - \frac{\partial}{\partial r}(r_{c43} f_4) + I_{f1} + I_{f2}$$

where t is the time; u, v, w are the components of wind velocity along x, y, z axes.

Axes x, y, z have been directed across and along the front and perpendicular to the Earth respectively. There is assumption that the coordinat systems is moving and its velocity is the same as a front velocity u_f. k_x, k_z are the coefficients of horisontal and vertical diffusion; γ_a is dry-adiabatic gradient; ρ is the density of air; l, g are the Coriolis parameter and free fall acceleration; S_{xx}, S_{yy}, S_{zz} are the second order derivatives of the functions wich respect to x, y, z respectively; P_x P_y P_z are the pressure gradients in x, y, z directions. P, T are the pressure and temperature of air. R is the gas constant of dry air. q is the the specific humidity of air. f_k are cloud particle size distribution functions (small droptet, rain drop, crystals, agregates, etc.).

The rate of individual particles growth by condensation (sublimation) is (Mason, 1971, Buikov, 1978, Pirnach, 1979)

$$r_k = \frac{K_{2k} D\rho\Delta_k}{\Gamma_k \rho_k r_k K_{1k}}, \quad \Delta_k = q - q_k .$$

There are water vapor molecular diffusion coefficient, D; water (k=1,2), crystals (k=3) and agregateice (i=4) density, ρ and ρ_k, respectively; specific saturated humidity in respect to both the water and ice, q_k; water and ice supersaturation, Δ_k. Γ_{ik} is a factor which correct the differences between particles and air temperature (see Buikov, 1978), K_{1k}, K_{2k} are the corrected coefficients of cloud particles form and capacity.

The rate of continuous growth of large particles by collection of small parficles is (Buikov and Dehtyar, 1968, Buikov and Pirnach, 1976)

$$r_{cnk} = \frac{\rho_k \rho\pi}{3\rho_n r_n^2 K_{1n}} \int_0^R E(r_n + r_k)(v_n - v_k)^2 * * r_k f_k dr, \quad n = 2,3,4; \quad k = 1,2,3$$

n, k are numbers of larger (rain drop, crystal, agregate) and smaller particles (small droplet rain drop, crystal), respectively

$$c_{nk} = \pi\rho \int_0^R E(r_n + r_k)(v_n - v_k) f_n dr$$

There are: the gravitation coagulation coefficient, E; highest value of the particle radius, R; the fall velocity, v_k; I_a, I_s and I_{fk} are values which described cloud particles generation on the cloud condensation nuclei and ice nuclei and the processes of droplet freezing; ε_k are the condensation (sublimation) rate. In more detail about these and rest parameters see in

The equations for f_k are:

$$\frac{f_l^{j+4}-f_l^{j+3}}{t_s} + r_l \frac{f_l^{j+4}-f_{l-1}^{j+4}}{r_{sl}} + f_l \frac{f_{l+1}^{j+4} - f_l^{j+4}}{r_{sl+1}} = 0, \text{ if } r_l > 0 \quad (14)$$

The description of the Eqs. 13 coefficients, investigation of the solution stability are given in Pirnach, 1973, 1980, Ibrahimov and Pirnach, 1988. Mainly the Fourier analisis and the experimental testing was used to investigate. Finally, schemes found to be stability are combined into scheme for general systems and its stability is tested by numerical experiments.

4. CONCLUSION

The solution schemes of non-steady partial differential equations based on the splitting method were developed. The stability of these equations is examined by theoretical investigation and numerical experiment testing.

Numerical models with detailed description of cloud particles evolution (nuclei, drops, crystals, agregates, snowflakes, etc.) including condensation (sublimation) and coagulation processes were constructed to study the inner structure of frontal mixed stratiform clouds and precipitation development.

REFERENCES

Buikov, M. V. 1978. Numerical simulation of stratiform clouds. Obninsk. 68pp (in Russian).

Buikov, M. V. and Dehtyar, M. I. 1968 Stratiform clouds theory. Tr. UHRI. 70: 21-49 (in Russian).

Buikov, M. V. and Pirnach, A. M., 1975. A numerical simulation of precipitation in mixed stratiform clouds taken into account its microstructure. Isv. AS USSR, A0, 2, No. 5: 469-480 (in Russian)

Buikov, M. V., Pirnach, A. M., 1976. Ifluence on precipitation formation into mixing stratiform clouds of coagulation processes. Tr. UHRI. 144; 3-13 (in Russian)

Ibrahimov, K. U. and Pirnach, A. M. 1988. Microphysical features of two-component cloudiness into atmospheres of planet-gigants. Kinematic and physics of sky bodies. V. 4. No2: 22-28 (in Russian).

Marchuk, G. I., 1974. Numerical simulation for the Weather Prediction. Hydrometeoisdat, Leningrad, 303pp (in Russian).

Mason, B. J., 1971: The Physics of Cloud. Oxford Univ. Press, London, 540 p.

Pirnach, A. M., 1973. Construction of stable solution algorithm for the system of equation describing evolution of a mixing stratiform clouds taken into account its microstructure. Tr. UHRI. 130: 61-68 (in Russian).

Pirnach, A. M., 1979. Study of agregation in stratiform mixing clouds (numerical experiment). Tr. UHRI. 170: 32-43 (in Russian)

Pirnach, A. M. 1980. About several features of a numerical solution of equations describing a particles condensation growth in mixing cloud. Tr. UHRI. 178: 15-26 (in Russian)

Pirnach, A. M., 1987. Numerical simulation of frontal cloud system taken into account dynamics and microphysics processes (3-D models). Tr. UHRI. 221: 81-83 (in Russian)

Pirnach, A. M., Krakovskaya S. V., 1994. Numerical studies of dynamics and cloud microphysics of the frontal rainbands. J. Atmos. Res., 33; 333-365.

3-D SIMULATION OF CLOUDS ACCOUNTING FOR SUBGRID FLUCTUATIONS OF TEMPERATURE AND HUMIDITY

L. Levkov, B. Rockel, H. Schiller and L. Kornblueh
GKSS–Forschungszentrum Geesthacht GmbH,
Max Planck–Straße, D–21502 Geesthacht, Germany

1 Introduction

There is no doubt that fluctuations of specific humidity and temperature are very important for processes connected with cloud formation. Different distributions are used to account for the joint fluctuations of specific humidity and temperature. A review of ensemble averaging used in cloud parametrizations is given in Cotton and Anthes, 1989.

This study uses the mesoscale model GESIMA (Geesthacht Simulation Model of the Atmosphere) (Kapitza and Eppel, 1992) with a cloud scheme (Levkov et al., 1992) for numerical studies of cirrus and stratus clouds. A shortcoming of the former cloud model is the assumption that a computational grid volume is either entirely saturated or entirely unsaturated.

In this paper we propose a new scheme which does not require the choice of the joint distribution of specific humidity and potential temperature for the whole simulation volume. Rather we estimate local values for the first and second moments of this joint distribution from the model itself. These estimates of the moments are used to generate pairs of values for specific humidity and potential temperature , respectively, to obtain a Monte–Carlo–integration about the cloud formation processes. Numerical simulations have been done with the new predictive cloud scheme and compared to the old schemes' results without subgrid-scale condensation. The old scheme will be furthermore abbreviated as OS, the cloud scheme using a Monte-Carlo-integration as NS.

2 Accounting for subgrid fluctuations of specific humidity and potential temperature

Due to the structure of cloud scheme to account for the fluctuations we can not perform the integration analytically as in Sommeria and Deardorff, 1977. So for each grid cell we proceed as follows:

- get an estimate of the first and second moments of the joint specific humidity (q_v)–potential temperature (Θ)–distribution
- generate n_{MC} pairs of specific humidity –potential temperature –values from a Gaussian distribution with such moments. For each pair
  - apply the cloud scheme (Levkov et al., 1992) to derive values of mixing ratios of water species, concentration of aerosol particles and temperature corrections due to phase changes of water.
- average the n_{MC} results.

Doing the ensemble averaging this way has the following advantages:

- any form of cloud formation could be integrated this way
- using different Gaussians for each cell has the potential for the whole volume to interpolate between overall Gaussian (Sommeria and Deardorff, 1977), any skewed distribution like Binormal and even the limiting two delta function distribution.

To obtain estimates of the first and second moments of the joint specific humidity –potential temperature –distribution for a given grid cell we use the values of these variables q, Θ in the cell as well as from the eight neighbouring cells in the same grid layer (diagnostic estimate).

$$\begin{aligned} \bar{q} &= \frac{1}{9}\sum_{i}^{region} q_i \\ \bar{\Theta} &= \frac{1}{9}\sum_{i}^{region} \Theta_i \\ \sigma_q^2 &= \frac{1}{9}\sum_{i}^{region} (q_i - \bar{q})^2 \\ \sigma_\Theta^2 &= \frac{1}{9}\sum_{i}^{region} (\Theta_i - \bar{\Theta})^2 \\ cov_{q\Theta} &= \frac{1}{9}\sum_{i}^{region} (q_i - \bar{q})(\Theta_i - \bar{\Theta}) \end{aligned} \quad (1)$$

The moments (1) are used to generate n_{MC} pairs of random numbers for specific humidity and potential temperature with a Gaussian distribution

$$f(\vec{x}) = \frac{1}{2\pi\sqrt{detC}} \exp\{-\frac{1}{2}(\vec{x}-\vec{\mu})C^{-1}(\vec{x}-\vec{\mu})^T\} \quad (2)$$

where

$$\vec{x} = \begin{pmatrix} \bar{q} \\ \bar{\Theta} \end{pmatrix} \text{ and } C = \begin{pmatrix} \sigma_q^2 & cov_{q\Theta} \\ cov_{q\Theta} & \sigma_\Theta^2 \end{pmatrix}.$$

Then the cloud formation scheme is applied to these n_{MC} pairs and average values of conversion rates for one integration time interval in every grid point are used by calculating of the tendencies of water species, humidity and temperature.

3 Initialisation of the model and results

The model used in this study is three-dimensional, time-dependent, non-hydrostatic mesoscale model. Predicted variables are the three velocity components u, v and w, the potential temperature θ, the mixing ratio for water vapour q_V and the mixing ratios q and number concentrations N for the cloud species. The mesoscale model used 27 x 27 points horizontally to provide a 3 km horizontal resolution over the 81 x 81 km^2 region of the EUCREX. The vertical grid interval ranges from 100 to 250 m in the cloud levels to 1 km near the top of the model domain. Total number of vertical levels is 40.

The focus of numerical simulation is one research day during EUCREX, 18 September 1993 (Greensmith, 1993). The model was run for 4 hours physical time starting at 12:30 UTC. The model initial fields were created using the radiosonde sounding and aircraft data during mission EUCREX102. Three cloud levels by a moderately occluded frontal system, associated with a low pressure centre were observed between 12:30 and 16:30 UTC on this day: low level broken cumulus with top at 1000 m; cirrus and cirrus patches between 6500 and 9000 m with altostratus below at level between 3500 and 5500 m.

To investigate the role of statistical variations of humidity and temperature in the subgrid scale by cloud modeling two types of simulations are performed and the cloud activity is compared. First the mesoscale model is run (Run 1) with a microphysical modul which produces clouds when $\bar{q}_v > \bar{q}_{sw}(\bar{q}_{si})$ or $\bar{q}_v > \bar{q}_{sw}$ and $\bar{q}_v > \bar{q}_{si}$, i. e. the computational grid volume is entirely supersaturated. Here $\bar{q}_v$ is the grid volume average mixing ratio of specific humidity and $\bar{q}_{sw}$ and $\bar{q}_{si}$ is the saturation mixing ratio with respect to water and ice respectively. A second simulation using identical conditions was undertaken (Run 2) calculating q_{sw} and q_{si} for each generated n_{MC} pairs of q_v and Θ switching on the cloud scheme and average the results i. e. cloud water and cloud ice is allowed to form even though the average state has been below saturation.

Three cloud layers have formed after 1 hour and 45 min simulation time applying the NS (Run 2): a cirrus layers between 6 and 9 km height, altostratus mixed clouds at level between 4.5 and 6.0 km and low broken cumulus below 1400 m (Fig. 1). The maximum value of ice mixing ratio in cirrus clouds is found to be 0.05 gkg^{-1} and a maximum

ice crystal concentration of 0.5 cm^{-3}. Simulated maximum values of cloud ice and cloud water in altostratus clouds are found to be 0.2 gkg^{-1} and 0.1 gkg^{-1} respectively. The highest droplet concentration in these clouds is 200 cm^{-3} and the maximum ice concentration - 2 cm^{-3}. The maximum droplet concentration in broken cumulus is 250 cm^{-3}. Applying the OS, condensation doesn't occure in the first 2 hours of simulation time. The middle levels clouds and the cirrus clouds are thinner and denser and disappear quickly. The low cloudiness is not present in the model domain after 1 hour and 45 min simulation time (Fig. 2).

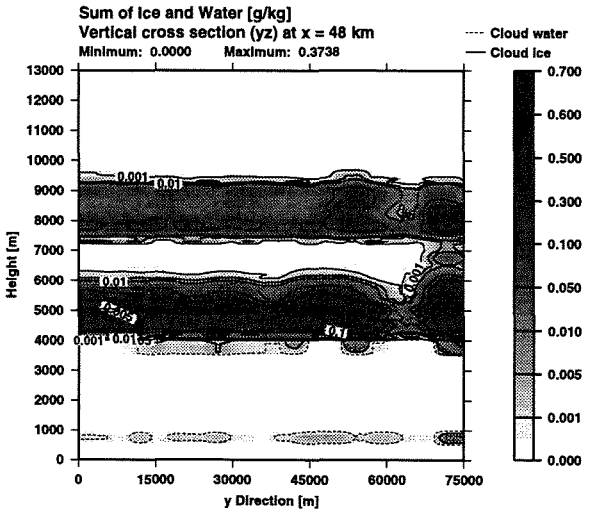

Figure 1: Density and isolines of cloud ice and water (Monte-Carlo simulation)

The prognosticated part of a grid volume with clouds after 6 min simulation time shows the role of subgrid fluctuations of temperature and humidity by the evolution of cloud system. Applying the NS. a part of the given grid volume can be supersaturated and condensation or ice formation (Figs. 3 and 5) occures without a supersaturation of the entire volume to be realized (Figs. 4 and 6).

4 Conclusion

The vertical structure of the observed clouds of 18 September between 12:30 and 16:30 UTC was well represented when the modell worked with the NS. Cloud tops, bases, and layered

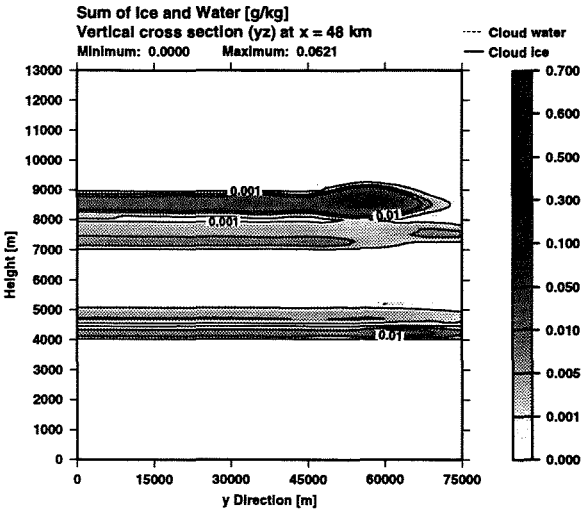

Figure 2: Density and isolines of cloud ice and water (entirely saturated volume)

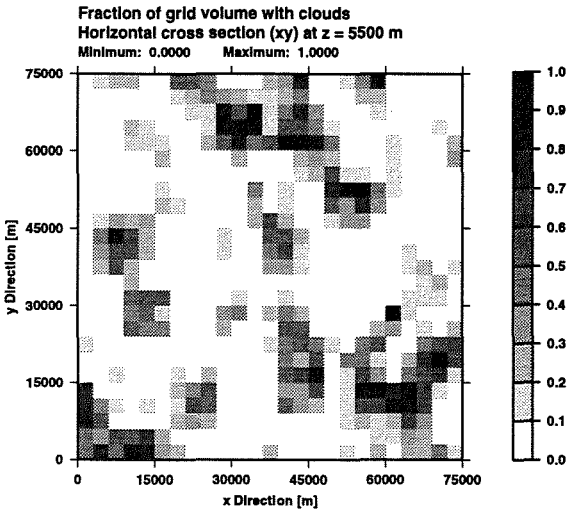

Figure 3: Fraction of grid volume with ice and water [%] in 5500 m (Monte-Carlo simulation)

structure as well as the typical values of mixing radio and number concentration of cloud water and cloud ice all given by the model simulations matched aircraft to a good degree. The allowance of a subgrid distribution for the liquid water and ice results in an increase in the time-average cloud activity, smooth the moisture field and thus reducing the temporal and spacial variations of cloud species. The simulations without subgrid distribution for the specific humidity and temperature were not capable of producing observed cloud system.

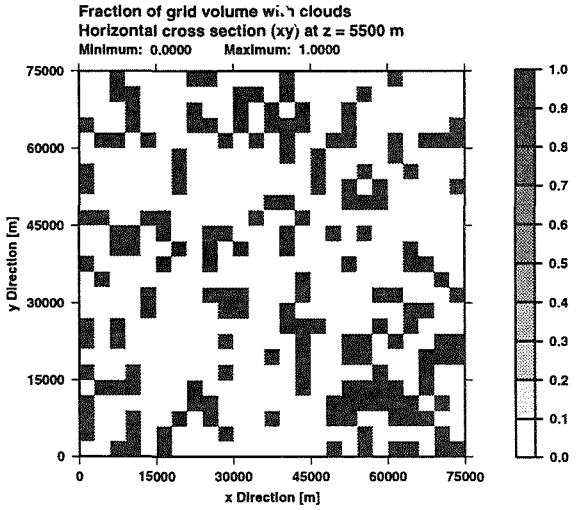

Figure 4: Fraction of grid volume with ice and water [%] in 5500 m (entirely saturated volume)

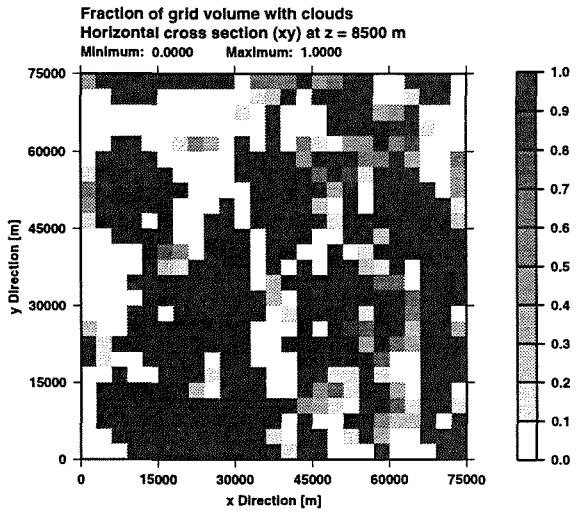

Figure 5: Fraction of grid volume with ice and water [%] in 8500 m (Monte-Carlo simulation)

The assumption that a local condensation can occure in the presence of turbulent fluctuations, even though the average state is below saturation is a part of a general effort to improve the sub-scale cloud modeling and would appear to be necessary for a model using a larger mesh and therefore needing more accurate hypotheses for the subgrid turbulence.

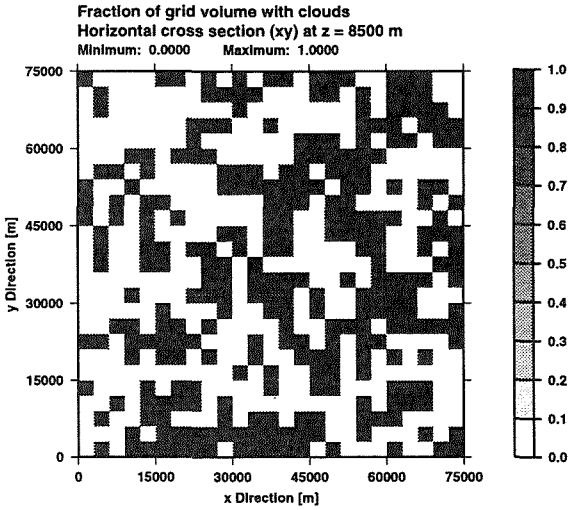

Figure 6: Fraction of grid volume with ice and water [%] in 8500 m (entirely saturated volume)

References

Cotton, W. R. and R. A. Anthes, 1989: Storm and Cloud Dynamics. *Academic Press*, 872 pp.

Kapitza, H. and D. Eppel, 1992: The Non-Hydrostatic Mesoscale Model GESIMA. Part I: Dynamical Equations and Tests. *Beitr. Phys. Atmosph.***65**, pp. 129-145.

Levkov, L., B. Rockel, H. Kapitza and E. Raschke, 1992: 3D Mesoscale Numerical Studies of Cirrus and Stratus Clouds by Their Time and Space Evolution. *Beitr. Phys. Atmosph.* **65**, pp. 35-57.

Greensmith, Helen, 1993: EUCREX FLIGHT SUMMARY for U.K.MRF Hercules, *14th September - 13th October 1993*, 91 pp.

Sommeria, G., and J. W. Deardorff, 1977: Subgrid-scale condensation in models of non-precipitating clouds. *J. Atmos. Sci.***34**, pp. 344-355.

SEMI-LAGRANGIAN/EULERIAN CLOUD MODEL

Piotr K. Smolarkiewicz, Wojciech W. Grabowski and Vanda Grubišić

NCAR, Boulder, CO 80307, USA

A new numerical model for simulating flows of moist, precipitating, rotating, stratified anelastic fluids past a specified time-dependent irregular lower boundary has been developed. The model assumes the two-time-level temporal discretization consistently for all dependent variables. This enhances the accuracy of computations while leading to a simple yet robust solver. The model contains both semi-Lagrangian (Smolarkiewicz and Pudykiewicz 1992, Grabowski and Smolarkiewicz 1996) and Eulerian (Smolarkiewicz and Margolin 1996) "nonoscillatory" approximations, selectable by the user. The model has been used for a variety of problems including various cases of hydrodynamic (shear/density) instabilities, small- and large-amplitude internal gravity wave problems; nonhydrostatic shearing stratified flows over an obstacle; as well as low Froude number flows past three-dimensional obstacles. Comparisons with results obtained with a traditional cloud model show excellent performance of the new code both in terms of accuracy and computational efficiency.

Effective semi-Lagrangian approximations are not necessarily straightforward because departure points of precipitation trajectories differ from those of flow trajectories, and the terminal velocity of the precipitation depends on the concentration of the precipitation itself (Grabowski and Smolarkiewicz (1996). Some simplifying assumptions are adopted which compromise formal accuracy and computational efficiency of the method. Comparisons with corresponding results obtained using a more traditional, flux-form Eulerian cloud model (Clark 1977, 1979) document highly competitive performance of the semi-Lagrangian approach. As an example, Figure 1 shows results of simulations in which moist thermals, initially at rest, rise in a stably-stratified environment due to the initial buoyancy perturbation. Rising motion and accompanying adiabatic cooling lead to condensation and, eventually, to rain development. Details of the experimental setup are similar to Grabowski and Clark (1991), see Grabowski and Smolarkiewicz (1996). The figure shows cloud water and rainwater mixing ratio as predicted by the semi-Lagrangian version of the semi-Lagrangian/Eulerian cloud model, and the same fields predicted using the Clark's Eulerian cloud model. Both models apply high spatial resolution of 5 m. The solutions shown are at $t = 7$ min, when the evolution of the thermal is governed predominantly by the vorticity dynamics of the unstable, thermal/environment interface (Grabowski and Clark 1991). Both the cloud water and rainwater fields show very similar structures, and the timing of the rain reaching the ground is almost identical in both models. Although the predictions of both models agree for the high spatial resolution, the solutions quickly diverge as the spatial resolution decreases (Grabowski and Smolarkiewicz 1996).

An application of the Eulerian version of the new semi-Lagrangian/Eulerian model to a problem of the rainband formation in a low-Froude-number-flow past the Island of Hawaii is illustrated in Figure 2 (see Grubišić et al. 1996 and Carbone et al. 1996 for further references on the Hawaiian problem). The figure shows the numerically simulated rainband for the case of 1 August 1985, which was examined in detail in the original numerical study of Smolarkiewicz et al. (1989). The model used in the latter study was the Clark's Eulerian small-scale dynamical model (Clark 1977, 1979) with the fully interactive nesting scheme of Clark and Farley (1984) that allowed simultaneous simulations in two or three domains with different resolutions: a) the outer domain with the resolution of 10.16 and 0.5 km in the horizontal and vertical, and the two nested domains, b) domain 2 with the resolution of 5.08 and 0.25 km, and c) domain 3 with 1.016 and 0.0625 km. The current simulation uses the same environmental profiles and the representation of surface sensible- and latent-heat fluxes. The numerical domain corresponds to that of the outer model but at the uniform resolution of the domain 2 in the original study. The individual convective cells in Figure 2 are stronger than those shown in Figure 8b of Smolarkiewicz et al. (1989), but in addition they form a continuous arc-shaped band.

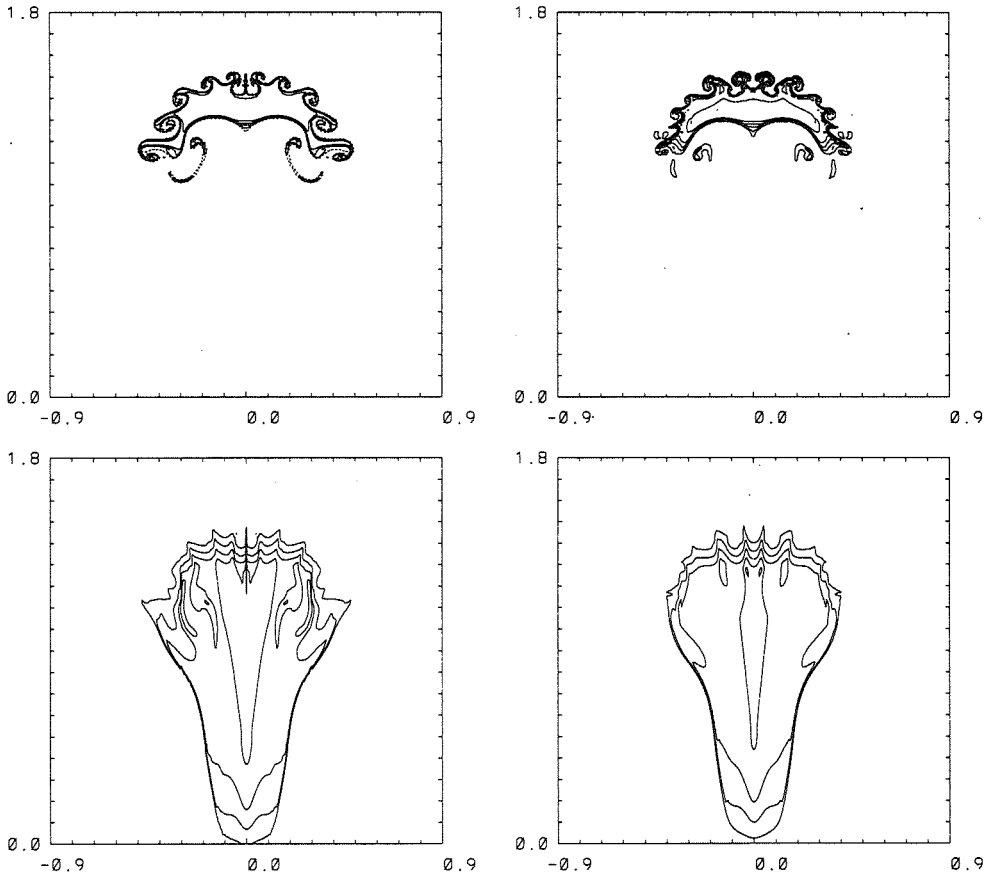

Figure 1: Results of simulations of the precipitating thermal using the semi-Lagrangian version of the semi-Lagrangian/Eulerian model (left panels) and the Eulerian model of Clark (1977, 1979) at $t = 7$ min. Upper and lower panels show isolines of the cloud water and rainwater mixing ratios with contour intervals 0.2 g kg^{-1} and 0.01 g kg^{-1}, respectively.

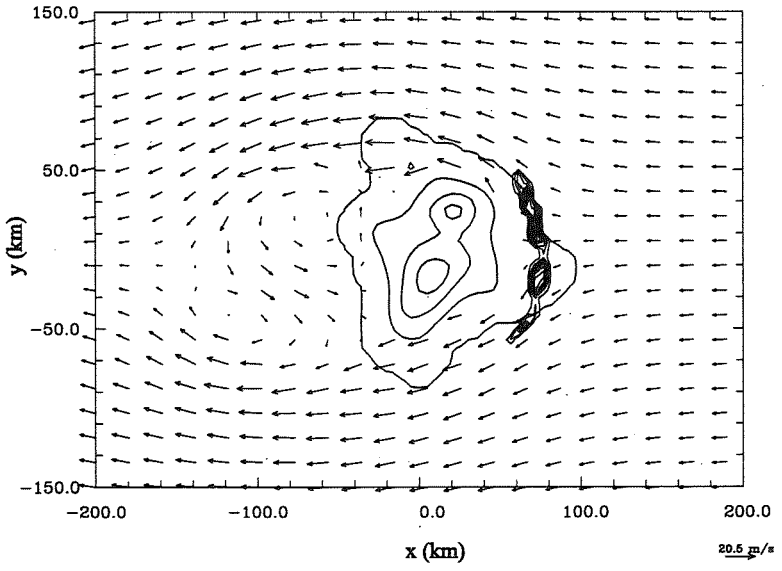

Figure 2: Cloud water content of an orographically forced Hawaiian rainband and velocity vectors at 750 m above sea surface. Maximum value in the cloud water is 0.56 g kg^{-1} with a contour interval of 0.0625 g kg^{-1}.

Acknowledgments: The National Center for Atmospheric Research is sponsored by the National Science Foundation.

REFERENCES

Carbone, R. E., J. Tuttle, W.-C. Lee, W. A. Cooper, V. Grubišić, 1996: On the forcing of windward island rainbands in Hawaii. *Preprints. 12th International Conference of Clouds and Precipitation.* 19–23 August 1996. Zürich, Switzerland. (This volume.)

Clark, T. L., 1977: A small–scale dynamic model using a terrain–following coordinate transformation. *J. Comp. Phys.*, **24**, 186–215.

———, 1979: Numerical simulations with a three–dimensional cloud model: Lateral boundary condition experiments and multicellular severe storm simulations. *J. Atmos. Sci.*, **36**, 2192–2215.

———, and R. Farley, 1984: Severe downslope windstorm calculations in two and three spatial dimensions using anelastic interactive grid nesting: A possible mechanism for gustiness. *J. Atmos. Sci.*, **41**, 329–350.

Grabowski, W. W., and T. L. Clark, 1991: Cloud-environment interface instability: Rising thermal calculations in two spatial dimensions. *J. Atmos. Sci.*, **48**, 527–546.

———, and P. K. Smolarkiewicz, 1996: On two-time-level semi-Lagrangian modeling of precipitating clouds. *Mon. Wea. Rev.* **124**, 487-497.

Grubišić, V., R. M. Rasmussen, P. K. Smolarkiewicz, and R. E. Carbone, 1996: Hawaiian rainbands: Effects of thermal forcing on the rainband dynamics. *Preprints. 12th International Conference of Clouds and Precipitation.* 19–23 August 1996. Zürich, Switzerland. (This volume.)

Smolarkiewicz, P. K., R. M. Rasmussen, and T. L. Clark, 1989: On the dynamics of Hawaiian cloud bands: Island forcing. *J. Atmos. Sci.*, **45**, 1872–1905.

———, and J. A. Pudykiewicz, 1992: A class of semi-Lagrangian approximations for fluids. *J. Atmos. Sci.*, **49**, 2082–2096.

———, and L. G. Margolin, 1995: On forward-in-time differencing for fluids: An Eulerian/semi-Lagrangian nonhydrostatic model for stratified flows. *Atmos.-Ocean*, (In press).

A Cloud-Resolving Model with the Radiation Scheme Based on the Monte Carlo Method

Darko Koračin and Vlad Isakov, *Desert Research Institute, Reno, NV, US*
Luis Mendez-Nuñez, *University of California, Davis, CA, US*

1 Introduction

One of the challenges in simulating atmospheric boundary layer (hereafter ABL) is an appropriate treatment of cloud and radiation processes. Calculation of radiative heat transfer in mesoscale and regional scale models ranges from bulk schemes (e.g., Rogers and Koračin 1992) to Monte Carlo methods (e.g., Chylek and Dobbie 1995). A critical element in all cloud processes is sufficient horizontal and vertical resolution, treatment of aerosols, local vertical motions, and cloud particle interactions. Frequently clouds are not continuous entities, and in that case broken cloud elements govern dynamics and radiative effects. More atmospheric measurements of broken clouds are needed, and consequently simulations of inhomogeneous cloud fields are in the preliminary stages. A cloud-resolving model was developed that simulates broken cloud fields and provides horizontal inhomogeneity of input parameters determining radiative properties. This is a report on the preliminary results of applying the Monte Carlo method to a shortwave radiation scheme for the mesoscale simulation of lower clouds.

2 The Model

2.1 Basic Equations

The model is fully compressible and based on the set of 2D equations describing conservation of mass (the continuity equation), conservation of water (the continuity equation for total water), equations of motion, and the first law of thermodynamics:

$$\frac{\partial \rho}{\partial t} + \frac{\partial \rho u}{\partial x} + \frac{\partial \rho w}{\partial z} = 0$$

$$\frac{\partial \rho_w}{\partial t} + \frac{\partial \rho_w u}{\partial x} + \frac{\partial \rho_w w}{\partial z} = 0$$

$$\frac{\partial \rho u}{\partial t} + \frac{\partial u \rho u}{\partial x} + \frac{\partial w \rho u}{\partial z} = -\frac{\partial P}{\partial x}$$

$$\frac{\partial \rho w}{\partial t} + \frac{\partial u \rho w}{\partial x} + \frac{\partial w \rho w}{\partial z} = -\frac{\partial P}{\partial z} - \rho g$$

$$\frac{\partial \rho \Theta}{\partial t} + \frac{\partial u \rho \Theta}{\partial x} + \frac{\partial w \rho \Theta}{\partial z} = \frac{\Theta Q}{C_p T}$$

where u and w are wind components in X and Z directions, respectively; ρ is air density, ρ_w is water density; g is the acceleration of gravity; Θ is the potential temperature; T is the temperature; C_p is the specific heat at constant pressure; Q is the source/sink term of heat; P is the atmospheric pressure.

The condensation process is introduced in the model according to relative humidity and temperature.

2.2 Numerical Solution

The solution for air density, wind velocity components, potential temperature, and density of total water is obtained by using a MacCormack type finite difference scheme (MacCormack 1969) modified by Mendez-Nuñez and Carroll (1994) for the non-linear system of equations described in the foregoing text. Each step consists of predictor and corrector steps. According to Mendez-Nuñez and Carroll (1993, 1994), this scheme compares well with a semi-implicit Smolarkiewicz' and leap-frog schemes. The MacCormack scheme is of a second-order accuracy and does not require filtering and grid staggering. Boundary conditions are opened and the selected grid resolution determines the time step that is necessary for convergence of solution according to the Courant number. The nonlinear system of equations (1–5) can be written in a general form:

$$\frac{\partial \mathbf{V}}{\partial t} + \frac{\partial \mathbf{E}}{\partial x} + \frac{\partial \mathbf{F}}{\partial z} = \mathbf{H}$$

where

$$\begin{aligned} \mathbf{V} &= (\rho, \rho_w, \rho u, \rho w, \rho\theta) \\ \mathbf{E} &= (u\rho, u\rho_w, u\rho u + P, u\rho w, u\rho\theta) \\ \mathbf{F} &= (w\rho, w\rho_w, w\rho u, w\rho w + P, w\rho\theta) \\ \mathbf{H} &= (0, 0, S_u, -\rho g + S_w, S_\theta) \end{aligned}$$

where S_u, S_w, and S_θ are sub-grid contributions to the grid-resolving solution with respect to equations of motion in X and Z direction and the thermodynamic equation, respectively. For this study

we focused on the resolved fields, with a model grid resolution of 100 m in both horizontal and vertical directions. Therefore, sub-grid contributions are not considered in this study.

The predictor step is:

$$V^*_{i,k} = V^n_{i,k} - \frac{\Delta t}{\Delta x}(E^n_{i+1,k} - E^n_{i,k}) - \frac{\Delta t}{\Delta z}(F^n_{i,k} - F^n_{i,k-1}) + \frac{\Delta t}{2}(H^n_{i,k} + H^n_{i,k-1}).$$

The corrector step is:

$$V^{n+1}_{i,k} = \frac{1}{2}\{V^n_{i,k} + V^*_{i,k} - \frac{\Delta t}{\Delta x}(E^*_{i,k} - E^*_{i-1,k}) - \frac{\Delta t}{\Delta z}(F^*_{i,k+1} - F^*_{i,k}) + \frac{\Delta t}{2}(H^*_{i,k+1} + H^*_{i,k})\}.$$

where i and k are indices in the X and Z directions, respectively.

We tested a wide range of resolution, from 10 meters to several kilometers in both the horizontal and vertical dimensions. The model is being run on both a PC and a workstation.

2.3 Radiation Scheme

Use of Monte Carlo method offers an appropriate treatment of radiative transfer in a horizontally inhomogeneous atmosphere or broken-cloud sky. In this case five coordinates characterize the photon, three physical coordinates and two angular coordinates (photon zenith angle and azimuthal angle). Several possible processes are considered for a photon passing through the atmosphere: it can travel along the free path length, it can be scattered, absorbed in the atmosphere or reflected from the surface. The present computational scheme utilizes a statistical weight of the photon. The weight indicates a limit of the photon path. When the statistical weight is negligible, the trajectory is completed and photon is not considered anymore. The number of photons counted in each grid point of the model domain provides information for upward and downward radiative fluxes. Then, net flux divergence and heating rate are calculated and used in the model as inputs.

3 Numerical Experiment

We compared the model results with other compressible models using an idealized experiment of buoyancy due to a "hot" bubble. The results agree well for both stable (Droegemeier 1985) and neutral (Mendez-Nuñez 1990) environments and were reported elsewhere.

The model grid consisted of 60 vertical and 60 horizontal points with both horizontal and vertical resolution of 100 meters.

The initial conditions were designed to generate homogeneous cloud fields within a well-mixed atmospheric boundary layer. Potential temperature was set to 297.5 K within the first 3 km above the surface and then increased linearly to 310 K at 6 km AGL. Specific humidity was constant within the first 3 km (5 $g \cdot kg^{-1}$) and decreased linearly to 1 $g \cdot kg^{-1}$at 6 km. Discontinuities of +2 K in temperature and -3 $g \cdot kg^{-1}$in specific humidity were introduced at the top of the boundary layer (3 km AGL). Simulated cloud formation is then a consequence of thermodynamic processes. The threshold for cloud formation was simply taken as 85% relative humidity, which indirectly implies that there are aerosols present (that are not considered explicitly). The homogeneous cloud layer was simulated in the upper 600 meters of the ABL (Fig. 1). In order to generate inhomogeneities in the cloud layer, a sinusoidal heat perturbation was imposed at the lower boundary. The amplitude of the perturbation was 5% of the initial temperature (i.e., excess of 15 K) in the ABL:

$$\Theta = \Theta_0 \left(1 + 0.05 \sin\left(2\Pi \frac{i-1}{i_{\max}-1}\right)\right)$$

where i is a actual horizontal grid point, and $i_{\max}$ is the number of grid points in the X direction.

Fig.1a shows the initial horizontally homogeneous cloud fraction ratio plotted in terms of fractional relative humidity.

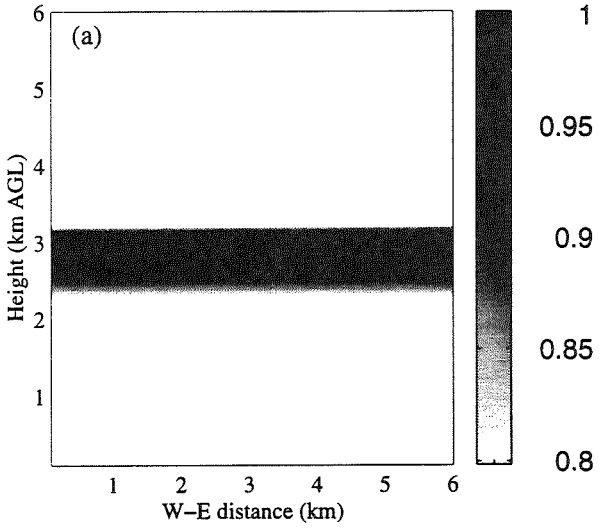

Fig. 1 Gray-shade plot of simulated cloud ratio for an initially homogeneous layer (a) and an inhomogeneous layer, generated by the large perturbation in surface temperature, after 40 min (b).

The surface temperature perturbation generates strong heat flux above the largest temperature perturbations and can eventually penetrate the cloud layer and/or inversions. The time scale of the process depends on the amplitude of the perturbation. The effect of penetrating an inversion is dependent on the amplitude of perturbation and the strength of the inversion. After 30 minutes the cloud started breaking up and the inhomogeneous cloud field was present in the western side of the domain (Fig. 1b).

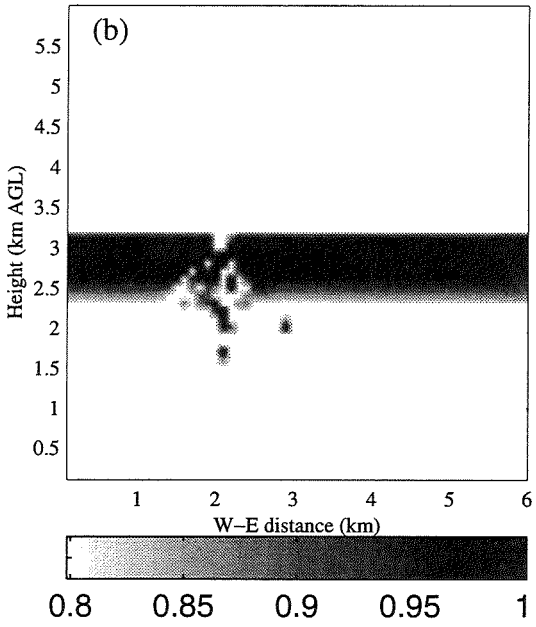

The dynamics associated with this case can be characterized by the large standard deviation of the vertical velocity within the plume which penetrates the inversion (Fig. 2).

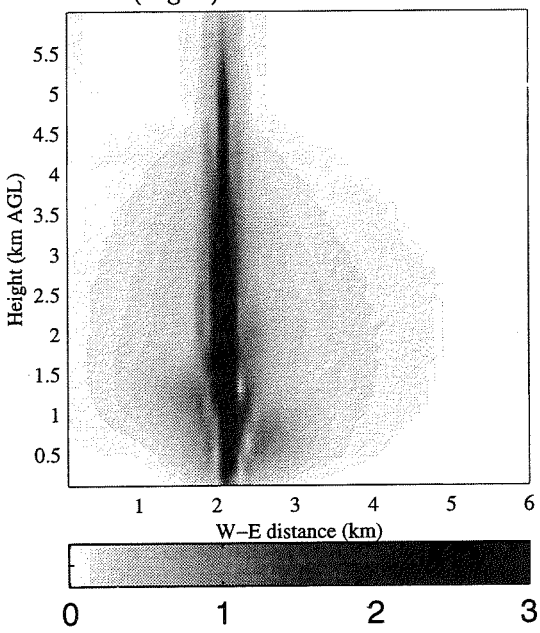

Fig. 2 Gray-shade plot of 10-minute standard deviation of vertical velocity associated with a large localized perturbation in surface temperature.

In order to investigate the effect of broken clouds on the modification of radiative flux field we considered a simple case with incoming solar radiation at a nadir angle at the top of the atmosphere. The net radiative flux was calculated by using the Monte Carlo method for homogeneous and broken-cloud cases.

We related cloud optical depth to the total water mixing ratio. Other cloud optical properties are taken as standard values for stratus clouds. Background values for aerosol optical properties are also considered in the model (optical depth, single-scattering albedo and phase function).

Figure 3a shows net shortwave radiative flux for the initial case of a solid cloud. The effect of a decrease in net flux due to diffuse radiation is present in the subcloud layer. The change of net shortwave radiation in the broken-cloud region is shown in Figure 3b.

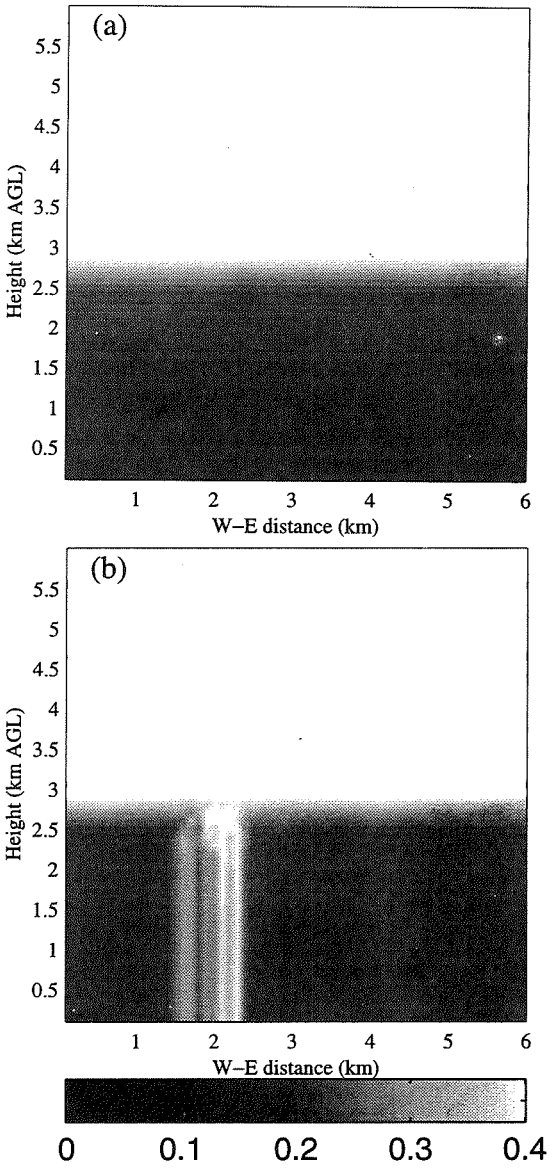

Fig. 3 Gray-shade plot of net shortwave radiative flux normalized by the solar constant for homogeneous (a) and inhomogeneous (b) cloud layers.

Since the elements of a broken cloud are scattered, the net flux becomes asymmetric with respect to the vertical axis. The effect of asymmetry is further evidenced in Figure 4, where the difference in net flux between solid and broken cloud cases is related to the change in optical depth for the same cases.

Even for small changes in the optical depth (i.e., 0.2), the net flux changed up to 30%. The large changes in optical depth initiated a large spectrum of changes in the net flux. In some cases the elements of broken clouds imposed even larger flux for the broken cloud case than for the solid cloud case.

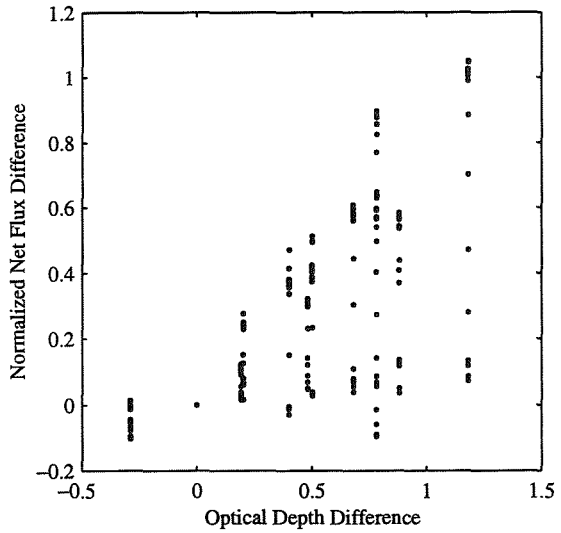

Fig. 4 Scatter plot of difference in the optical path between the solid and broken cloud layers versus difference in the net shortwave flux between solid and broken cloud layers.

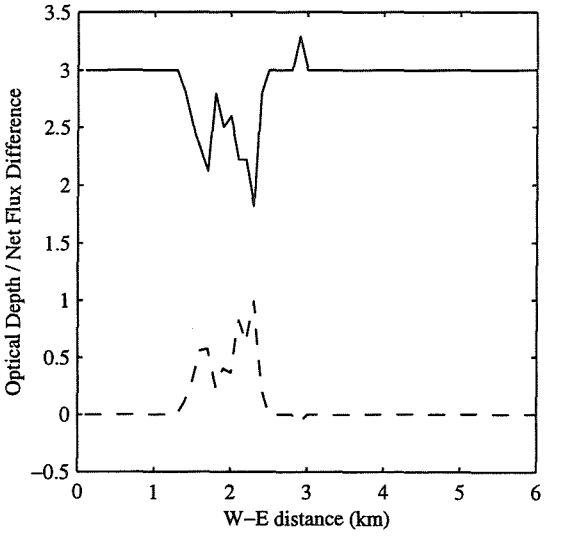

Fig. 5 Total atmospheric optical depth (solid line) and difference in shortwave net radiative flux of the surface between solid and broken cloud cases (dashed line)

The total atmospheric optical depth is shown in Figure 5, together with the corresponding net flux difference at the surface. The decrease in optical depth due to cloud dissipation corresponds to the increase in the difference between the solid and broken cloud elements. The results indicate that a horizontal change of optical depth within a few kilometers in the inhomogeneous cloud layer can cause large changes in the net flux with respect to the solid-cloud case.

References

[1] Chylek, P., and Dobbie, J. S., 1995: Radiative Properties of Finite Inhomogeneous Cirrus Clouds: Monte Carlo Simulations. *J. Atmos. Sci.*, **52**, 3512–3522

[2] Droegemeier, K. K., 1985: The numerical simulation of thunderstorm outflow dynamics. Ph.D. dissertation, University of Illinois at Urbana-Champaign, 695 pp.

[3] Mendez-Nuñez, L. R., 1990: Application of the MacCormack Scheme to atmospheric nonhydrostatic models. Ph.D. dissertation, University of California at Davis, 254 pp.

[4] Mendez-Nuñez, L. R., and Carroll, J. J., 1993: "Comparison of Leapfrog, Smolarkiewicz, and MacCormack Schemes Applied to Nonlinear Equations." *Mon. Wea. Rev.*, **121**(2): 565–578

[5] Mendez-Nuñez, L. R., and Carroll, J. J., 1994: "Application of the MacCormack Scheme to Atmospheric Nonhydrostatic Models." *Mon. Wea. Rev.*, **122**(5): 984–1000

[6] Rogers, D. P., and Koračin, D., 1992: Radiative transfer and turbulence in the cloud-topped marine atmospheric boundary layer. *J. Atmos. Sci.*, **49**, 1473–1486

AEROSOL AND TURBULENCE IN CLOUD-SCALE PROCESSES

Guerman M. Teptin, Lubov V. Morozova, Paul N. Douriaguine

Physics Dept., University of Kazan, 18 Lenin St., Kazan, 420008, Russia

1. INTRODUCTION

In general, in real atmosphere cloud-scale processes are influenced by many different factors. But the most significant of them are local air humidity, parameters of atmospheric turbulence and, of course, existence of condensation centers. There are great amount of works devoted to consideration of only one of these main factors, [see for example in Feigelson (1964) and Chen (1975)]. The presented work is devoted to attempt of complex consideration of cloud-scale processes as the factor of atmospheric turbulence and as the factor of distribution of possible condensation centers, a role of which aerosol particles play in real atmosphere in most cases.

Our work is devoted to developing of the model, which can find its applications in researches in the problem of cloud-scale processes. This is the model of spatial distribution of aerosol particles in turbulent temperature stratified atmosphere. This model permits to receive concentration of aerosol particles, which can be keeping in turbulent atmosphere, in particular, the maximal possible concentration. Using these data in the different concrete models of cloud-scale processes it would permits to take into account not only direct influence of atmosphere turbulence on these processes, but the indirect turbulence influence too.

2. DESCRIPTION OF THE MODEL

The model of spatial distribution of aerosol particles in turbulent atmosphere is based on the theory of suspended particles sedimentation in temperature stratified turbulent atmosphere developed by Teptin and Morozova (1982). The base equation of this theory is the equation of balance of turbulent energy in standard form for free turbulent atmosphere.

$$\frac{d\rho_{air}}{dt} = -\overline{\rho'\omega' g} - \frac{\partial \overline{p'u_\alpha}}{\partial x_\alpha} + \frac{\partial q_\alpha}{\partial x_\alpha} - \rho\cdot\varepsilon - \frac{\partial}{\partial x_\alpha}\left[\frac{1}{2}\cdot\rho\sum_{i=1}^{3}\overline{\left(u_i'\right)^2 u_\alpha'}\right] - \frac{1}{2}\cdot\overline{\rho\cdot u_\alpha' u_\gamma'}\cdot\frac{du_\gamma}{dx_\alpha} - \beta\overline{T_v'\cdot\omega'} \qquad (1)$$

where :

$\rho = \rho_{\alpha i\rho} + (\rho_r - \rho_{air})S$, ($\rho_r$ is a density of particles, ρ_{air} is a density of air) ;
S is a specific volume of particles;
b is a cinematic energy of turbulent whirlwinds;
g is an acceleration of gravity;
ω' is a component of speed pulsation;
p' is a pressure pulsation;
T_n' is a potential temperature;

This equation was found in assumption that horizontal components of speed of particles and horizontal components of air flux speed is equal due to suspended particles is extremely small but vertical components of their speed is different on speed of sedimentation of single particle in non-limit media.

The left member of equation shows variance of cinematic energy of turbulent movement in time. The first member in the right part describes work of turbulence against gravity sedimentation of aerosol particles. The second member in the right part describes the work of pressure pulsation. It was shown that this member gives redistribution of energy in direction, so final work of it is equal zero. The third member corresponds to flux of pulsation energy due to molecular transferring of turbulence. As it was shown in Teptin at al. (1982) this member and following ones is small in free atmosphere, except the sixth member that describes pulsation energy of averaged movement. The seventh member is significant too. In our model it was rewritten according to general accepted form :

$$\overline{\rho\omega' T_n'} = \alpha_T\cdot\overline{\rho}\cdot K\cdot\frac{dT_n}{dz} \qquad (2)$$

Where dT_n/dz is altitude gradient of potential temperature.

In mentioned work it is shown that in stationary case this equation can be retyped for free turbulent atmosphere in following form :

$$\overline{\rho'\cdot\omega'\cdot g} = \left[K\cdot\left(\frac{d\bar{u}}{dz}\right)^2 - \alpha_T\cdot\beta\cdot K\frac{d\bar{T}_n}{dz} - \varepsilon\right]\cdot\rho \quad (3)$$

where :

$\omega = u_z$
K is a turbulent exchanging coefficient;
α_T is a constant (close to 1);

The equation for averaged movement of the system is following :

$$\frac{\partial\overline{\rho\omega}}{\partial z} = 0 \quad => \quad \overline{\rho\omega} = \text{const} \quad (4)$$

Averaging this equation and using S (specific volume of particles) it is possible to show that

$$\bar{\omega} = -\left(\frac{\rho_r}{\rho}\right)\cdot a\cdot S \quad (5)$$

where
a is a speed of impurity sedimentation;

Using equation (1) with (4) we find that

$$S = \frac{\rho}{\rho_r\cdot g\cdot a}\left[K\cdot\left(\frac{d\bar{u}}{dz}\right)^2 - \alpha_T\cdot\beta\cdot K\frac{d\bar{T}_n}{dz} - \varepsilon\right] \quad (6)$$

The numeric concentration of particles is connecting with specific volume by

$$N = \frac{S}{\frac{4}{3}\cdot\pi\cdot r^3} \quad (7)$$

On the base of mentioned theory it is possible to construct the stationary theory of aerosol particles distribution. The condition of stationary

$$\overline{\rho\cdot\omega} = \bar{\rho}\cdot\bar{\omega} + \overline{\rho'\cdot\omega'} = 0 \quad (8)$$

means that gravity sedimentation of particles is compensated by vertical movement of particles due to turbulence.

In this case $\overline{\rho'\cdot\omega'\cdot g}$ must be above zero. Then

$$\left[K\left(\frac{d\bar{u}}{dz}\right)^2 - \alpha_T\cdot\beta\cdot K\frac{d\bar{T}_n}{dz} - \varepsilon\right] > 0 \quad (9)$$

It is the main equation used in our model for forecasting behavior of the particles.

For applying this equation for modeling the following parameters have to be known : size-distribution function of aerosol particles (in real atmosphere aerosol particles are polydispersion ones practically always), minimal and maximal particles size, density of aerosol particles, speed of sedimentation and parameters of turbulent atmosphere.

As a size-distribution function of aerosol particles the most generally accepted distribution - log-normal distribution was used.

$$f(r) = \frac{1}{\sqrt{2\pi}\sigma r}\exp\left(-\frac{\ln\left(\frac{r}{r_0}\right)^2}{2\sigma^2}\right) \quad (10)$$

Where :
r is a particles radius;
r_o is a median particles radius;
σ is a variance of logarithm of particles radius;

The speed of aerosol particles sedimentation in free atmosphere was used in standard form :

$$a = \frac{2\cdot r^2\cdot\rho_r\cdot g}{9\cdot\mu} \quad (11)$$

where :

ρ_ρ is a density of particles;
g is an acceleration of gravity;
r is a particles radius;
μ is a dynamic viscosity;

Using these data it is possible to find concentration of aerosol particles N_o at certain

height. As it is shown by Teptin and Morozova (1989) N_0 can be found as follow :

$$N_0 = Q\cdot\left[4.19\cdot K\cdot\exp\left[\frac{5}{2}\cdot\left(2\cdot\lg(r_0) + \sigma^2\right)\right]\right. \quad (12)$$
$$\left.\times\ \left[\Phi(U_2) - \Phi(U_1)\right]\right]^{-1}$$

where :

$$Q = -\frac{\rho_{air}\cdot\varpi}{\rho_r}$$

$$U = \frac{\lg(r) - (\ln(r_0) + 4\sigma^2)}{\sigma}$$

$\Phi(U)$ is Laplas-Gauss integral

Concentration of particles with $r \in [r_1 , r_2]$ can be found by

$$N[r_1 , r_2] = N_0\cdot\int_r^{r_2}\rho(r)\,dr \quad (13)$$

3. CONCLUSION

The scale of atmospheric turbulence is correlating as with aerosol particles distribution as with scale of cloud processes. So using the data about aerosol particles distribution it is possible to judge about the scales of cloud processes.

Described model permits to receive the data of spatial distribution of aerosol particles of different type on the base of data about parameters of aerosol particles and parameters of turbulent atmosphere. These data can be useful in different concrete model of cloud-scale processes because they permit to account as direct influence of turbulence by mean aerosol particles distribution on cloud-scale processes as indirect influence of atmosphere turbulence.

The presented model based on the stationary theory of aerosol particles distribution. But there is non-stationary theory (Teptin and Morozova, 1988), which would permits to investigate cloud-scale processes in dynamics.

It is also possible to take into account non-linear effects connecting with atmospheric turbulence as shown in Fachrtdinov, et al. (1993).

So presented model would be developed and would play an important role in the problem of cloud-scale processes investigation.

4. REFERENCES

Chen C.C. (1975) Attenuation electromagnetic radiation by haze, fog, cloud and rain. Santa Monica.

Fachrtdinov R.H, Morozova L.V., Teptin G.M. (1993). Non linear effects of spaced distribution of aerosols in turbulent atmosphere. J. Aerosol Sci. **24**, S397-S398.

Feigelson E.M. (1964) Radiation processes in stratified clouds. Mir., Moscow.

Teptin G.M., Morozova L.V. (1982) On distribution of suspended particles in higher atmosphere. Izv. AN SSSR, FAO **18**, 697-704.

Teptin G.M., Morozova L.V. (1988) Non stationary model of aerosol particles distribution in higher atmosphere. Izv. AN SSSR,FAO **24**,92-95.

Teptin G.M., Morozova L.V. (1989) Stationary model of aerosol particles distribution in higher atmosphere. Izv. AN SSSR, FAO **25**, 439-441.

COMPARISON OF NUMERICAL MODEL SIMULATIONS AND SATELLITE OBSERVATIONS OF AN UPSLOPE CLOUD SYSTEM

Gregory Thompson[1], Roelof Bruintjes[1], and James F. Bresch[2]

[1]National Center for Atmospheric Research, Boulder, CO, USA
[2]Dept. of Atmos. Sci., Univ. of Washington, Seattle, WA, USA

1. INTRODUCTION

The Colorado State University Regional Atmospheric Modeling System (RAMS) and the Pennsylvania State University/National Center for Atmospheric Research mesoscale model (MM5) were used to simulate a complex wintertime event on 7 March 1994. This event occurred during the Winter Icing and Storms Project (WISP, Rasmussen et al., 1992) field program and included a variety of precipitation and cloud physics. At the surface, freezing drizzle, snow, and some graupel were reported. Aloft, there existed a mixture of stratus, stratocumulus, and isolated cumulus clouds. Aircraft penetrations of the stratus cloud revealed a region of supercooled liquid water including drizzle-size droplets.

The main focus of this study is the intercomparison of the two numerical model simulations with each other and the observations. Observational data for this event include: sounding data, aircraft measurements of droplet spectra (as well as thermodynamic measurements), satellite data and reports of precipitation at the surface. Of particular importance to this study is the prediction of supercooled liquid water and its application to aircraft icing forecasts.

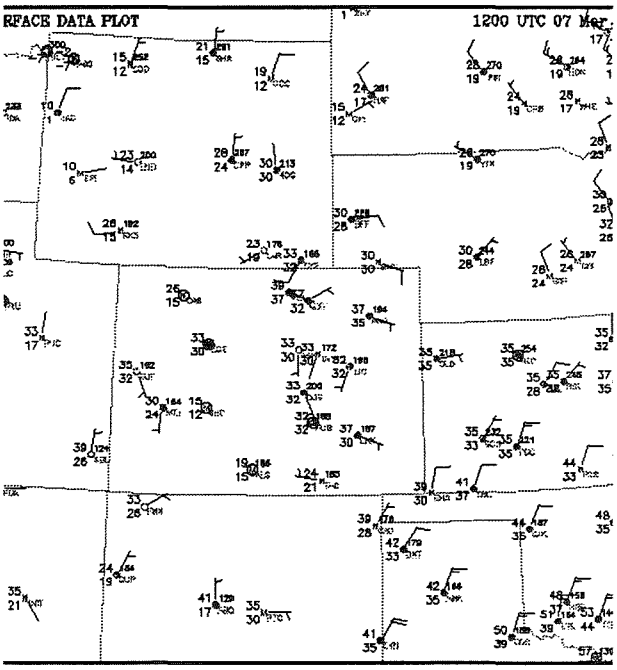

Figure 1: Surface observations at 1200 UTC 7 March 1994. Temperature (°F) (above-left), dewpoint (°F) (below-left), mean sea level pressure and wind barbs (full barb=10 knots) are plotted.

2. 7 MARCH 1994 CASE STUDY

At 1200 UTC 7 March 1994, a cool, Canadian airmass was situated across the northern High Plains and Rocky Mountains of the United States. The surface high pressure associated with this cooler air was located in Alberta and was elongated into central Nebraska. This created light easterly surface wind flow in the lee of the Rocky Mountains, particularly in eastern Colorado/Wyoming and western Nebraska (see Figure 1). This upslope flow contained sufficient moisture to produce a cloud (predominantly stratus) throughout much of the region.

Satellite imagery reveal that extensive cloud cover existed in eastern Colorado/Wyoming and western Nebraska with relatively warm cloud tops (-5° to -16°C) (see Figure 2). Figure 3 shows the AVHRR shortwave infrared (channel 3 = 3.9 m) reflectance image at 1524 UTC 7 March 1994. Because of the different reflectance properties of ice and water particles to shortwave IR radiation, water clouds appear reflective (bright) while ice particles appear non-reflective (dark) in imagery such as Figure 3. Therefore, one can see that the large cloud region east and west of Scottsbluff, NE is likely a water cloud while the darker area to the south of Scottsbluff and also in South Dakota likely contains ice.. This is also in agreement with Figure 2 which shows the ice cloud regions to have cloud top temperatures of -16° to -20°C. This goal of this study is to simulate this cloud system using two mesoscale numerical models. To accomplish this goal, comparisons of precipitation type at the ground as well as microphysical species within the cloud will be

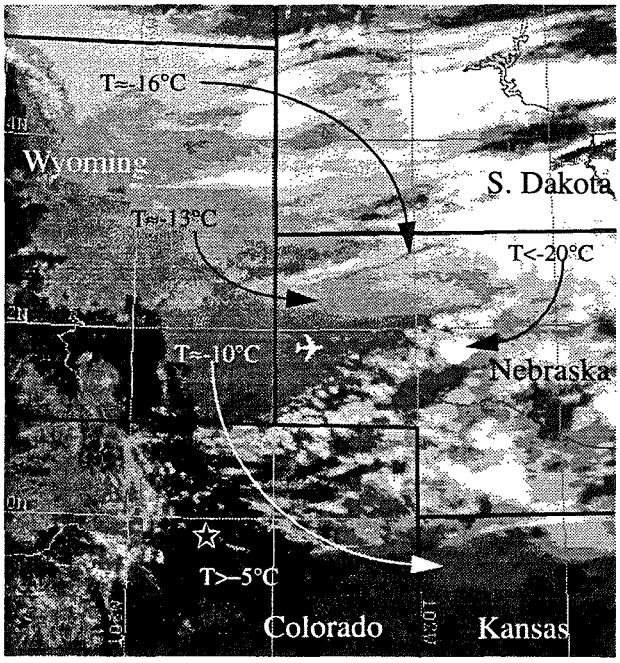

Figure 2: Longwave infrared (10.8 μm) satellite image valid 1524 UTC 7 March 1994. Approximate cloud top temperatures indicated on image. Scottsbluff, NE (✈) and Denver, CO (☆) are marked.

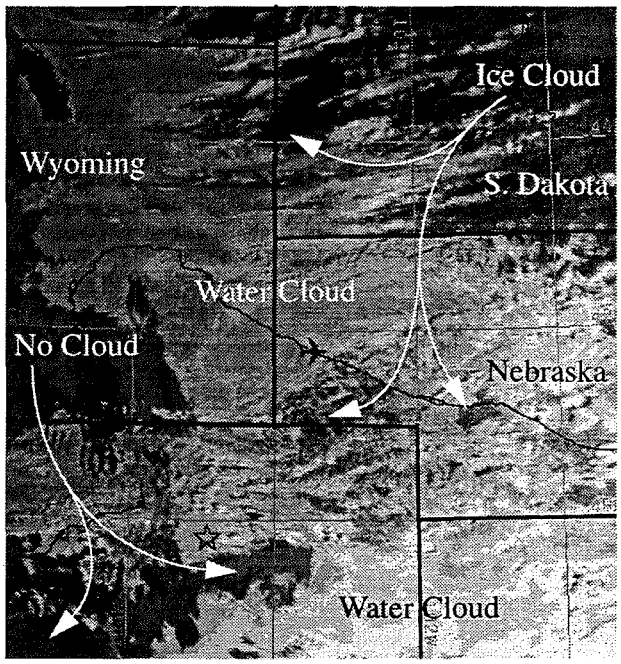

Figure 3: Shortwave infrared (3.9 μm) satellite image valid 1524 UTC 7 March 1994. Clouds which are likely composed of water droplets versus ice particles are shown.

performed. Furthermore, satellite observations of cloud top temperature and hydrometeor phase will be compared against those predicted by each numerical model.

3. MODEL DESCRIPTION

The two research numerical models, RAMS and MM5, were configured as similarly as possible. Each model used three interactive nested grids (see Figure 4). The coarse grid had a 60 km grid increment covering the western 3/4 of the continental United States. The first nested grid had a 20 km grid increment covering all of Colorado and Wyoming and the western portions of Nebraska and Kansas. The finest grid had 6.7 km spacing encompassing the WISP domain of northeast Colorado and southeast Wyoming. Vertically, each model used 37 levels with 75 m spacing at the bottom and was stretched to larger increments at the upper levels but maximized to a 800 m increment (from about 6 to 20 km). The models were initialized with 0000 UTC 7 March 1994 data using gridded pressure level data, surface airway observations, and rawinsonde data from the NCAR data archives. In addition, because of the WISP field program, two special soundings were launched in western Nebraska and were included with the archived rawinsonde data. It is felt that the two additional soundings greatly improve the model initialization since a pre-existing cloud was present in the region but not of significant scale for the National Weather Service's rawinsondes to capture adequately. Both numerical models include detailed bulk microphysical schemes which contain both warm rain and ice parameterizations.. These schemes allow for the prediction of: cloud water, rain, snow, pristine ice, and graupel (and aggregates in the RAMS model). [Details of the RAMS microphysical scheme can be found in Walko et al., 1995 while MM5's scheme is found in Reisner et al., 1993.].

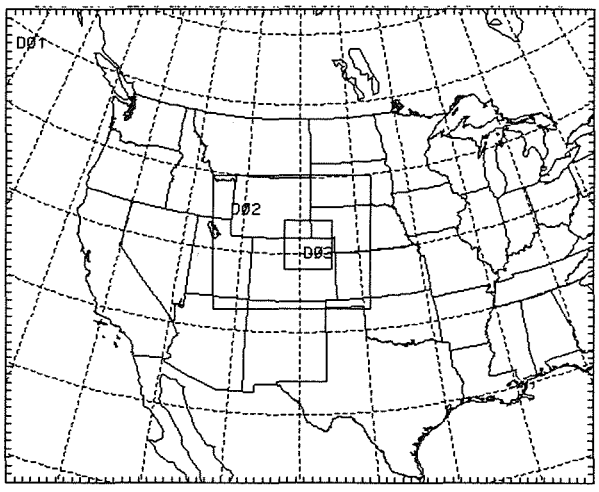

Figure 4: Grids used by the numerical models. The coarsest grid had a 60 km grid increment while the second and third had 20 and 6.7 km, respectively.

4. RESULTS

Results from each numerical model experiments will be presented at the conference.

ACKNOWLEDGEMENTS

Thanks to Tom Lee for the AVHRR satellite imagery and Bob Walko, Craig Tremback, Jason Nachamkin and Michael Meyers for their suggestions for the RAMS model.

This research is sponsored by the National Science Foundation through an Interagency Agreement in response to requirements and funding by the Federal Aviation Administration's Aviation Weather Development Program. The views expressed are those of the authors and do not necessarily represent the official policy or position of the U.S. Government.

REFERENCES

Rasmussen, R., M. Politovich, J. Marwitz, W. Sand, J. McGinley, J. Smart, R. Pielke, S. Rutledge, D. Wesley, G. Stossmeister, B. Bernstein, K. Elmore, N. Powell, E. Westwater, B. Stankov and D. Burrows, 1992: Winter Icing and Storms Project (WISP). *Bull. Amer. Meteor. Soc.*, **73**, 951-974.

Reisner, J., R.T. Bruintjes and R.M. Rasmussen, 1993: Preliminary comparisons between MM5 NCAR/Penn State model generated icing forecasts and observations. Fifth Int'l Conf. on Aviation Weather Systems, Vienna, VA, 2-6 August. Amer. Meteor. Soc., Boston 65-69.

Walko, R.L., W.R. Cotton, M.P. Meyers, J.Y. Harrington, 1995: New RAMS cloud microphysics parameterization. Part I: the single-moment scheme. *Atmos. Res.*, **38**, 29-62.

NUMERICAL SIMULATIONS OF ALTOCUMULUS USING AN EDDY RESOLVING MODEL AND A MIXED LAYER MODEL

Shuairen Liu and Steven K. Krueger

Dept. of Meteorology, Univ. of Utah, Salt Lake City, Utah, USA

1. INTRODUCTION

Altocumulus (Ac) clouds cover large portions of the earth and play an important role in the earth's energy budget through their effects on solar and infrared radiation. However, Ac clouds have been little investigated by either modelers or observational programs. Ac layers are usually vertically sub-grid scale in global climate models (GCMs) and have either been neglected or implicitly represented through a "fractional cloudiness" scheme. Since such schemes are empirically rather than physically based, they are not suitable for climate change prediction.

Our numerical simulations of Ac clouds with a 2D eddy-resolving model (ERM) suggest that Ac layers are well-mixed. This has motivated our development of two simpler model for Ac layers: a 1D turbulence closure model and a mixed layer model (MLM). The results of the 1D turbulence closure model closely match those of the 2D ERM (Liu and Krueger, 1995). In this paper, we compare the MLM results to those from the ERM. This is a step toward incorporating a physically based Ac mixed layer model into a GCM. We briefly describe the ERM and Ac MLM first. Then, we discuss the results of the ERM and Ac MLM simulations.

2. DESCRIPTION OF MODELS

The ERM is based on the anelastic set of equations. It includes third-moment turbulence closure, bulk microphysics parameterization, and an advanced radiation code. The model is more fully described in Krueger (1988) and Xu and Krueger (1991). The radiative transfer parameterization used in the ERM is described in Fu (1991), Fu and Liou (1992) and Krueger et al. (1995). Neither ice-phase nor precipitation is considered in our simulations.

The mixed layer prognostic equations (Lilly, 1968, Schubert et. al., 1979) for moist static energy, h_M, total water mixing ratio, q_{wM}, Ac mixed-layer top height, z_T, and Ac mixed-layer base height, z_B, are

$$\rho_{\text{ref}} \frac{dh_M}{dt} = -\frac{(F_h)_{T-} - (F_h)_B - \Delta F_{RM}}{z_T - z_B}$$

$$\rho_{\text{ref}} \frac{dq_{wM}}{dt} = -\frac{(F_q)_{T-} - (F_q)_B}{z_T - z_B}$$

$$\frac{dz_T}{dt} = w_{LT} + w_{eT}$$

$$\frac{dz_B}{dt} = w_{LB} + w_{eB}$$

where $(F)_T$ and $(F)_B$ represent turbulent fluxes at the mixed-layer top and at the mixed-layer base, ΔF_{RM} is the radiative flux change over the mixed layer, w_L is the large scale vertical velocity, and w_e is the entrainment velocity.

In 13 out of 14 Ac soundings examined from Salt Lake City, Utah, there were no jumps in h and q_w at the mixed-layer base. We therefore assume that $(F)_h$ and $(F)_{qw}$ are zero at the lower boundary of the mixed-layer. The turbulent fluxes of h and q_w just below the upper boundary of the mixed layer, as derived from heat and moisture budget equations in the inversion layer, are

$$(F_h)_{T-} = \rho_T(\overline{w'h'})_{T-} = -\rho_T w_{eT} \Delta h_T - \Delta F_{RT}$$

$$(F_{qw})_{T-} = \rho_T(\overline{w'q'_w})_{T-} = -\rho_T w_{eT} \Delta q_{wT}$$

in which $\Delta h_T = h_{T+} - h_M$ and $\Delta q_{wT} = q_{wT+} - q_{wM}$ are the jumps in h and q_w across the upper boundary, and ΔF_{RT} is the radiative flux jump in the inversion. To close the MLM, w_e must be parameterized based on assumptions about the turbulent structure of the mixed layer. We use the closure of Wyant and Bretherton(WB, 1992) which is based on the entrainment parameterization of Turton and Nicholls (1987). The entrainment velocity at the mixed layer top is then:

$$w_{eT} = \frac{A}{(z_T - z_B)\Delta s_{vT}} \int_{zB}^{zT} \overline{w's'_v} dz$$

where s_v is the virtual dry static energy and Δs_{vT} is the jump in s_v across the upper boundary of the mixed layer. We set the constant $A = 2.5$ following WB. Presently, we set $w_{eB} = 0$. We will relax this assumption in the future. We also need to determine the height of the condensation level, z_C. That can be easily obtained as the temperature lapse rate is dry adiabatic below z_C within the mixed-layer.

3. SIMULATIONS AND RESULTS

The profiles of temperature (T) and water vapor mixing ratio (q_v) we used for the ERM simulation are similar to those used by Starr and Cox (SC, 1985). The model domain is 6.4 km long and 8.9 km high. The horizontal grid interval is 100 m, while the vertical grid interval is 1 km from surface to 5 km, 500 m to 5.5 km, and 50 m from 5.5 km to 8.9 km. The time step is 5 seconds. The reference state is the U.S. Standard Atmosphere (USSA). The temperature and water vapor mixing ratio from 5.5 km to 8.9 km is initialized the same as in SC. At the levels outside this range, T and q_v are the same as in the USSA, but q_v below 5.5 km is linearly adjusted so that the relative humidity is the USSA value at the surface and 0.6 at the level just below 5.5 km. Random perturbations in potential temperature between heights 6.95 and 7.15 km are used to initiate motions. The maximum initial magnitude of the perturbations is 0.1 K. The ground temperature is fixed at the USSA surface air temperature. The large-scale vertical velocity is zero, so $w_{LT} = w_{LB} = 0$. The resulting surface turbulent flux is near zero. The solar radiation for this case is zero, corresponding to nocturnal conditions. The total simulation time is 6 hours.

In Fig. 1, the simulated field of liquid water mixing ratio (q_c) for the ERM simulation at t=1 hour is displayed. This is a typical q_c snapshot for the simulations. There are several cellular patterns. The heights of cloud top and base are nearly constant except in the cellular regions. In these regions, the cloud top is higher and cloud base is lower so that the depth of the cloud is greater.

The profiles of h and q_w for the ERM simulation are displayed in Figs. 2 and 3, respectively. The profiles in the figures represent the averages in the last 5 minutes of each hour. There is a quite uniform layer evident at each hour in the h and q_w profiles. This shows that the Ac layer can be approximately thought of as a well-mixed layer. There

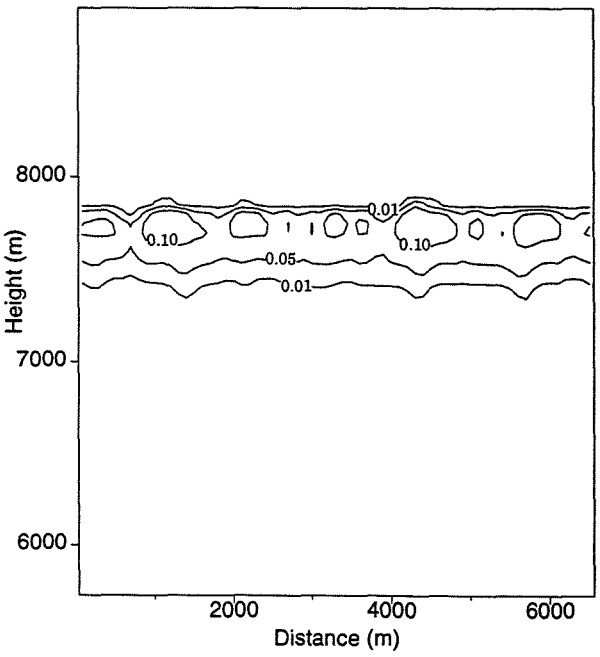

Figure 1. Contour plot of the cloud water mixing ratio(g/kg) at time t=1 hour for the ERM simulation.

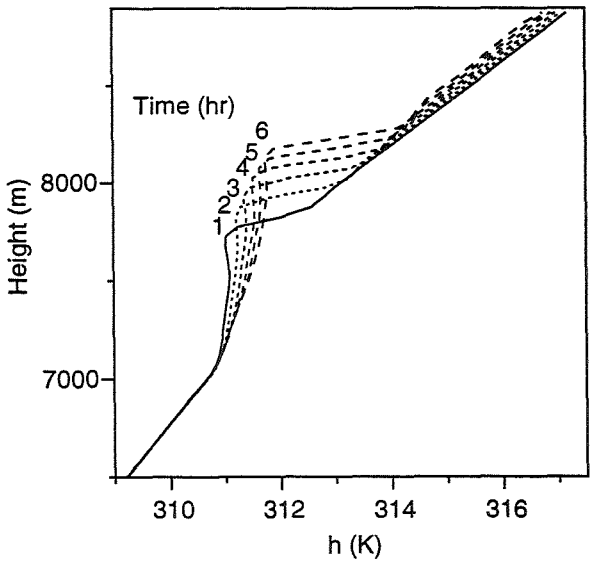

Figure 2. Vertical profiles of moist static energy at various times for the ERM simulation.

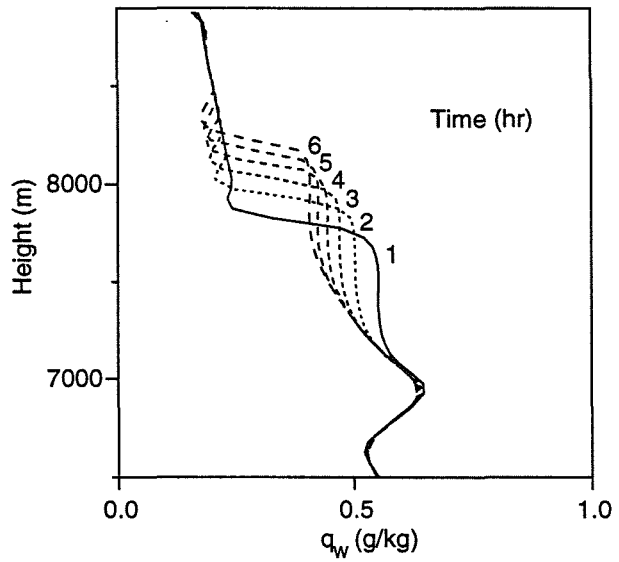

Figure 3. Vertical profile of total water mixing ratio at various times for the ERM simulation.

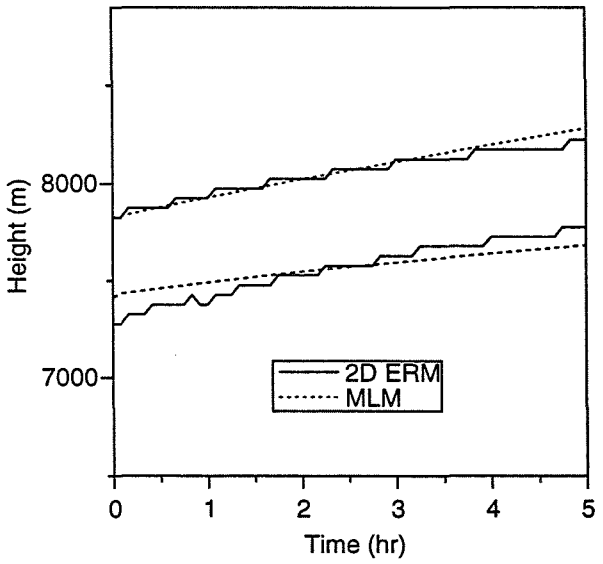

Figure 4. Evolution of of cloud base and top heights for the ERM and MLM simulations.

are jumps above the cloud layer in the h and q_w profiles. There is also a jump above the cloud in the temperature profile. Since cloud-top jumps and a well-mixed layer are often the characteristics of a stratocumulus cloud, Ac may be investigated with similar methods. Stratocumulus has been studied with a mixed layer model, so it is reasonable to simulate Ac formation and structure with an elevated mixed-layer model.

As there is not a mixed layer in the initial profiles for the ERM simulation, we cannot use these profiles to initialize a MLM simulation. The liquid water content for the ERM simulation increases rapidly during the first hour, and decreases slowly after the first hour. The mixed layer characteristics are not evident until one hour of simulation. Therefore, we use the profiles from the last 5 minutes of the first hour of the ERM simulation as the initial conditions for the MLM simulation. The lower boundary of the mixed layer obtained from the ERM simulation is 7150 m. The upper boundary is at the cloud top. The values of h_M and q_{wM} are obtained approximately from the ERM simulation, too. We also need to know h and q_w just above the jump. We use simple relations derived from the ERM simulation:

$$h_{T+}(\mathrm{J/kg}) = 3.84131t + 284574,$$

$$q_{wT+}(\mathrm{g/kg}) = -1.12565 \times 10^{-4}t + 1.11125,$$

where t is the time in seconds.

The radiation code used for the MLM is the same as that for the ERM. The temperature and water vapor profiles outside the cloud region are obtained from the initial profile for the MLM simulation. In order to calculate the radiative fluxes, we divide the cloud layer into ten equal layers. To consider the radiative effect of liquid water, we define ΔF_{RT} between z_{T+} and the second level from the top in the cloud layer, and ΔF_{RM} between the second level from the top in the cloud layer and z_{C+}.

The entrainment velocity at the cloud top (w_{eT}) in the MLM simulation decreases slowly with time. The entrainment velocity is between 2 and 3 cm/s, which is in good agreement with the measurements for stratocumulus. In Fig. 4, the evolution of cloud top and base heights for the ERM and MLM simulations is shown for the entire 5 hours. For both cases, the cloud top and base heights increase with time. The cloud top heights are in good agreement. The cloud base for the MLM simulation is higher than for the ERM simulation at the beginning. This is because the Ac layer in the ERM is not completely mixed. The cloud thickness for the MLM simulation increases slowly with time. The reason is that we do not consider detrainment at the mixed layer base in the MLM simulation. We are working on this problem.

In Fig. 5, the evolution of the liquid water mix-

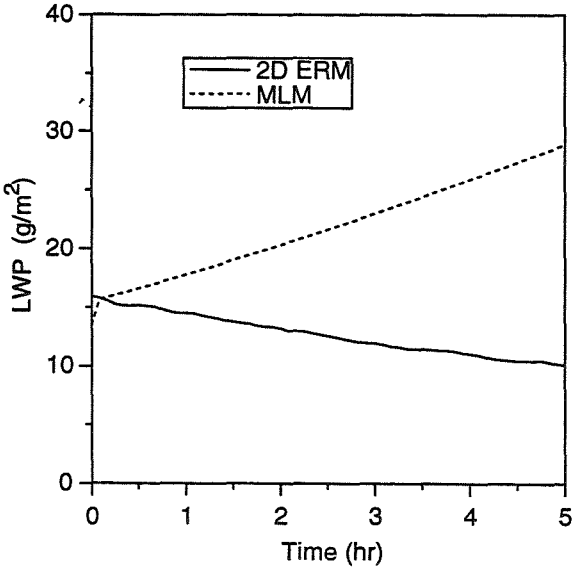

Figure 5. Evolution of the vertically integrated liquid water mixing ratio (LWP) for the ERM and MLM simulations.

ing ratio integrated over the cloud (LWP) is compared for the ERM and MLM simulations. The LWP decreases slowly with time in the ERM simulation but increases with time in the MLM simulation due to the increase in cloud thickness.

4. ACKNOWLEDGMENTS

This research was supported by the Environmental Science Division, DOE, under Grant DE-FG03-94ER61769 and by NSF under Grant ATM 89-14348. Computing assistance was provided by NCAR SCD.

5. REFERENCES

Fu, Q., 1991: Parameterization of radiative processes in vertically nonhomogeneous multiple scattering atmospheres. Ph.D. dissertation, University of Utah, 259 pp.

Fu, Q. and K.N. Liou, 1992: On the correlated k-distribution method for radiative transfer in nonhomogeneous atmospheres. *J. Atmos. Sci.*, **49**, 2139–2156.

Krueger, S.K., 1988: Numerical simulation of tropical cumulus clouds and their interaction with the subcloud layer. *J. Atmos. Sci.*, **45**, 2221–2250.

Krueger, S.K., G.T. McLean, and Q. Fu, 1995: Numerical simulation of the stratus to cumulus transition in the subtropical marine boundary layer. Part I: Boundary layer structure. *J. Atmos. Sci.*, **52**, 2839-2850.

Lilly, D. K., 1968: Models of cloud-topped mixed layers under a strong inversion. *Quart. J. R. Met. Soc.*, **94**, 292-309.

Liu, S. and S.K. Krueger, 1995: Numerical simulations of altocumulus with a cloud resolving model. *Proceedings of the Fifth Atmospheric Radiation Measurement (ARM) Meeting,* U.S. Department of Energy, Washington, D.C.

Schubert, W.H., J.S. Wakefield, E.J. Steiner, and S.K. Cox, 1979: Marine stratocumulus convection. Part I: Governing equations and horizontally homogeneous solutions. *J. Atmos. Sci.*, **36**, 1286-1307.

Starr, D.O'C. and S.K. Cox, 1985: Cirrus clouds. Part II: Numerical experiments on the formation and maintenance of cirrus. *J. Atmos. Sci.*, **42**, 2682– 2694.

Turton, J.D. and S. Nicholls, 1987: A study of the diurnal variation of stratocumulus using a multiple mixed layer model. *Quart. J. R. Met. Soc.*, **113**, 969-1009.

Xu, K.-M., and S.K. Krueger, 1991: Evaluation of cloudiness parameterizations using a cumulus ensemble model. *Mon. Wea. Rev.*, **119**, 342–367.

Wyant, M.C., and C.S. Bretherton, 1992: The dynamics of decoupling in a cloud-topped boundary layer. *Proc. 11th Int. Conf. on Clouds and Precipitation,* Vol. 1, Montreal, Quebec, Canada, International Commission on Clouds and Precipitation and International Association of Meteorology and Atmospheric Physics, 417-420.

NON-STATIONARY MODEL OF ADMIXTURE DISTRIBUTION IN THE CLOUDY ATMOSPHERE

L.G. Kaplan,

Ya.A. Ekba, M.R. Vatiashvili

Scientific and Production Geophysical Center, Ctavropol, Russia

I.E. Naats, E.A. Semenchin

Stavropol Politechnic University, Russia

Suppose we have a reagent introduced into a cloud at the time moment t_0. Let us denote $q_1 = q_1(t,x,y,z)$ for the reagent concentrations field in the cloud, $q_2 = q_2(t,x,y,z)$ - for the concentrations field of the environment natural component (water drops), $q_3 = q_3(t,x,y,z)$ - for the concentrations field of the resultant component (ice crystals), $t \in [t_0, T]$.

To describe the changes q_i = 1, 2, 3 (in the space and in time the following mathematical model is suggested:

$$\frac{\partial q_i}{\partial t} + \alpha_i q_i + \beta_i^{(1)} V_x \frac{\partial q_i}{\partial x} + \beta_i^{(2)} V_y \frac{\partial q_i}{\partial y} + \beta_i^{(3)} V_z \frac{\partial q_i}{\partial z} = \gamma_i D\, q_i + S_i(x,y,z)\,\delta(t - t_0); \quad (1)$$

$$i = 1, 2, 3; \qquad t \in [t_0, T],$$

$$S_1(x,y,z) = S(x,y,z),$$

$$S_2(x,y,z) = 0, \qquad S_3(x,y,z) = 0;$$

$$D = \frac{\partial}{\partial x} K_x \frac{\partial}{\partial x} + \frac{\partial}{\partial y} K_y \frac{\partial}{\partial y} + \frac{\partial}{\partial z} K_z \frac{\partial}{\partial z}; \quad (2)$$

$$\frac{\partial V_x}{\partial x} + \frac{\partial V_y}{\partial y} + \frac{\partial V_z}{\partial z} = 0, \quad (3)$$

$$q_i(t_0,x,y,z) = \varphi_i(x,y,z); \quad (4)$$

$$q(t, x, y, z) \to 0,$$

$$x^2 + y^2 + z^2 \to \infty; \quad (5)$$

$$i = 1, 2, 3,$$

which represents a system of three differential equations with partial derivatives (1), the solutions of which q_i, $i = 1, 2, 3$ should fulfil the initial (4) and boundary (5) conditions.

Here $\vec{V} = \vec{V}(t,x,y,z) = (V_x(t,x,y,z), V_y(t,x,y,z), V_z(t,x,y,z))$ - a speed vector of the air masses (wind), $K_x = K_x(t,x,y,z)$, $K_y = K_y(t,x,y,z)$ $K_z = K_z(t,x,y,z)$ - the coefficients of the substance turbulent diffusion along axes O_x, O_y, O_z accordingly; α_1, α_2, α_3 - the quantities, characterizing concentrations q_1, q_2, q_3 changes accordingly due to the conversion (changes) of the substances determining them; $S(x,y,z)$ - the power of the reagent source; $\delta(t-t_0)$ - δ - Dirac function; $\beta_i^{(1)}$, $\beta_i^{(2)}$, $\beta_i^{(3)}$, γ_i, $i = 1, 2, 3$ - the parameters providing for a good fit of the model to the experimental data.

Model (1) - (5) is studied by an analytical (at the definite restrictions on the coefficients in (1)) and a numerical methods. With the help of the splitting theory methods the boundary-value problems (1) - (5) a brought (at rather small intervals $[z_j, z_{j+1}]$ or $[t_j, t_{j+1}]$, $j = 0, 1, 2...$) to the sequence of more simple boundary-value problems for which they manage to find solutions in an explicit form.

When studying (1) - (5) by numerical methods it is suggested, as a preliminary step, to expand the solutions q_i, $i = 1, 2, 3$, by a certain given beforehand system of basis set functions, and then to pass over to the finite difference Crank-Nicolson scheme.

The aforestated methods for problem of (1) - (5) type solution are expounded in detail in the the works listed hereunder.

References

Naats I,E., Semenchin E.A., 1995: **Mathematical modelling of atmosphere boundary layer dynamics solving the problems of environment monitoring.** Stavropol: SGPU Publishing House, 196.

Semenchin E.A., 1993: **Analytical solutions of boundary-value problems in a mathematical model of atmospheric diffusion.** Stavropol: SKIUU Publishing House, 142.

DEVELOPMENT AND VALIDATION OF A DOUBLE–MOMENT MICROPHYSICS SCHEME FOR SIMULATING CUMULUS CLOUDS.

Hugh Swann and Philip R.A.Brown

Joint Centre for Mesoscale Meteorology, Univ. of Reading, UK

1. INTRODUCTION

The Science Plan of the GEWEX Cloud System Study (GCSS) emphasises that cloud resolving models (CRMs) are a useful tool for providing a proxy data set against which parametrizations of convection in global and regional models can be compared. Domains of the size of the grid boxes of large-scale models (greater than 100km squared) can be modelled with a resolution of the order of 100m in the horizontal and the vertical. The subgrid processes in the CRMs themselves (ie. turbulence, radiation and microphysics) need to be accurately parametrized for simulating a variety of different conditions around the globe. The parametrization of microphysics in particular has shown to be crucial for the simulation of the evolution of heat and moisture profiles during deep convection. This paper compares the behaviour of different versions of a CRM microphysics scheme for two convection cases with different precipitation production mechanisms.

2. BRIEF DESCRIPTION OF THE MICROPHYSICS SCHEME

A microphysics scheme has been developed and incorporated into a non-hydrostatic cloud resolving model (the UK Met. Office Large Eddy Model) for the development of parametrizations of convection in GCMs. The scheme is a three-phase bulk water scheme where 30 distinct processes are modelled, which predict the mass-mixing ratios of snow, graupel, rain, ice cloud and liquid cloud. The scheme also has the capability of 'double-moment' representation of hydrometeors so the number concentration is predicted as well as the mass-mixing ratios. This removes the need to prescribe the number concentration as a function of mass-mixing ratio, which is the method more commonly used in single-moment bulk-water schemes. The double-moment scheme, therefore, is more physics based than conventional schemes and requires fewer adjustable coefficients. One aim behind the development of this scheme is to enable the model to describe the evolution of convective clouds and their impact on the large-scale environment for a wide range of conditions, without the need for extensive adjustments to the microphysics parameters.

The microphysics scheme is based on that described by Lin *et al.* (1983). An additional variable to predict ice crystal number concentration was included and the processes that initiate ice crystals (contact freezing of cloud water droplets with aerosols, deposition onto natural ice nuclei and ice splinter production during riming) were parametrized following Flatau *et al.* (1989). The inclusion of two further variables to represent snow and graupel number concentrations and the use of a generalised gamma function to describe the size spectra of precipitating particles, rather that the inverse–exponential used by Lin *et al.* (1983), is based on Ferrier (1993).

The concentration of precipitating particles with diameter in the range from D to $D + dD$ is assumed to be,

$$n_x(D)dD = n_{0x} D^{\alpha_x} e^{-\lambda_x D} dD$$

where x stands for g, s or r for graupel, snow and rain respectively. λ_x is the slope parameter, n_{0x} is the intercept parameter and α_x is the shape parameter and is equal to zero for an inverse–exponential distribution. For single–moment representation of a particle type the intercept parameter is assumed to be constant or a simple function of λ_x. When double–moment representation is implemented and the number concentration n_x is predicted so the intercept parameter is defined as;

$$n_{0x} = \frac{\rho n_x \lambda_x^{(1+\alpha_x)}}{\Gamma(1+\alpha_x)}.$$

In models using single-moment representation of precipitating particles much attention is given to the

value of intercept parameters which determines the mean particle size. When using the double-moment scheme, however, it is the parametrization of the processes that initialise particles of a given type that is crucial to predicting the correct particle number concentrations and hence the mean particle size.

3. TWO CASE STUDIES OF CONVECTION OVER SOUTHERN ENGLAND

In order to test and validate the new microphysics scheme two case studies are modelled. The cases occurred over Southern England and have been identified from radar observations to have different dominant precipitation mechanisms. In CASE1 the rain was formed by the melting of snow and in CASE2 rain was formed by the melting of graupel near to the cell cores, and by melting of snow away from the cell cores.

It is hoped that the model will produce satisfactory simulations using the same microphysics scheme for the different case studies. The simulations are validated by comparing the radar reflectivity derived from the modelled precipitation fields with the actual radar reflectivity. The dominance of snow or graupel in the model can be validated qualitatively using radar observations of L_{DR} (linear depolarization ratio) which has high values in a shallow layer below the freezing level where melting snow is present, and a lower value over a larger depth where melting graupel is present.

In all the case studies the most active convection took place in the early afternoon so the model was initialised using the temperature, humidity and wind profiles from the midday radiosonde ascent at Crawley, situated 100km east of the radar site, as shown in Figures 1 and 2. Random temperature perturbations was added to the lower levels of the model to trigger the convection, the magnitude of the temperature perturbations being chosen so that cloud top height in the model matched that observed by radar. A constant surface heat flux of $100\mathrm{Wm}^{-1}$ was applied to the model which maintained convection for the 220 minutes of the simulation. In each simulation the peak convective activity was reached at 150–160 minutes, after which the rate of precipitation decreased. In each case the model domain was 30km × 30km × 12km with a resolution of 500m in the horizontal and 300m in the vertical.

3.1 Simulations of CASE1

Three simulations of CASE1, the snow dominated case, were carried out, differing only in their microphysics parametrizations, as described below;

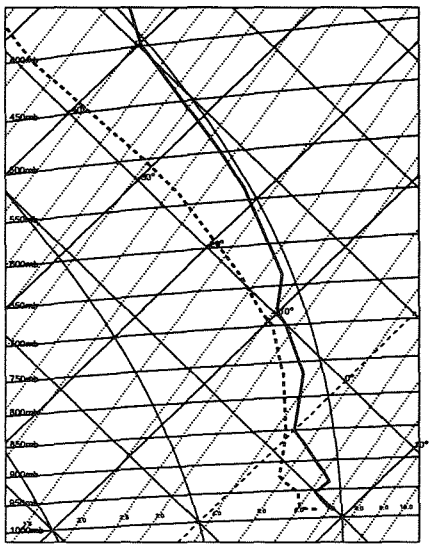

Figure 1: Tephigram for CASE1. Recorded at Crawley, midday 17^{th} March, 1991. The cloud top was observed by radar to be at height of 3.8km (620mb).

Run 1.1– Double-moment representation of ice cloud but only single–moment representation of snow and graupel. The intercept parameters are assumed to be n_{0g}=$4\times10^6\mathrm{m}^{-4}$ and n_{0s}=$3\times10^6\mathrm{m}^{-4}$ (Brown and Swann 1996). The parametrization of the conversion of snow to graupel is the same as that used in Run 1.3.

Run 1.2– Double-moment representation of ice cloud, snow and graupel. The parametrization of the conversion from snow to graupel follows that used by Flatau *et al.* (1989).

Run 1.3– Double-moment representation of ice cloud, snow and graupel. A new parametrization is used for the conversion from snow to graupel due to growth of snowflakes by riming liquid cloud. This is similar to that in Run 1.2, but with a threshold value of snow mixing-ratio of q_s = 0.3g/kg required before the process is active. This value was determined by analysis of L_{DR} at the melting layer and maximum radar reflectivity above the melting layer for a large number of convective showers (A.J. Illingworth personal communication).

In Table 1, a number of important points in the radar observations are highlighted and compared to the simulations. The most intense convection (*ie.* producing the highest radar reflectivity) occurring in the simulations is compared to that observed. As an

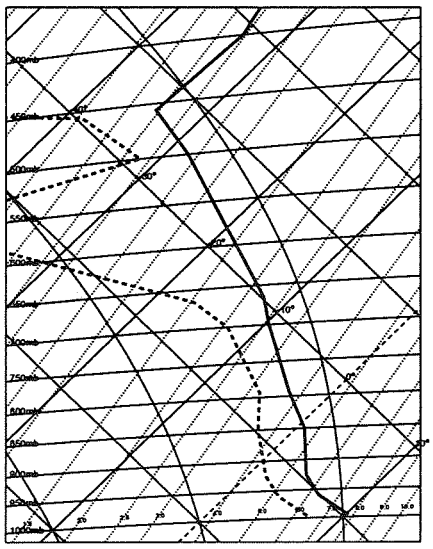

Figure 2: Tephigram for CASE2. Recorded at Crawley, midday 10^{th} May, 1990. The cloud top was observed by radar to be at height of 6.0km (440mb).

indicator of the effect of the microphysics on the large scale transports of water, the total rain accumulation at the ground and the amount of ice cloud at the end of the simulations are also given in the tables.

It can be seen that Run 1.1, with single–moment representation of snow and graupel, over predicts the amount of graupel. The under estimate of the radar reflectivity field above the melting layer in Run 1.1 suggests that the single-moment scheme over estimates the graupel particle concentration when a small amount of graupel mass is present, hence the graupel grows too quickly by riming and deposition. The effect of the over estimate of graupel on the large scale water transports is to increase the precipitation efficiency and reduce the amount of ice cloud left in the anvil at the end of the simulation. Run 1.2 also produces graupel where none was observed in analysis of the L_{DR} radar observations. Imposing a threshold value of snow mass–concentration before snow is converted to graupel in Run 1.3 reduces the amount of graupel to almost zero.

Plots of the model fields from Run 1.3 after 160 minutes of simulated time in the vertical slice through the most active region in the domain are shown in Figure 3. It can be seen that the dominant rain production mechanism is the melting of snow. The snow is initiated by the autoconversion of cloud ice then the grows by riming and deposition.

		Run number		
	Obs.	1.1	1.2	1.3
$Z_{max}(h$=0.2km)	26dbZ	36dbZ	33dbZ	31dbZ
$Z_{max}(h$=1.2km)	38dbZ	32dbZ	36dbZ	38dbZ
$Z_{max}(h$=2.7km)	24dbZ	22dbZ	25dbZ	28dbZ
Snow proportion	100%	12%	82%	99%
Rain on ground	—	290Gg	220Gg	180Gg
Total ice cloud	—	20Gg	50Gg	60Gg

Table 1: Summary of results from Runs 1.1, 1.2 and 1.3. Z_{max} is calculated 160 minutes into the simulation at a level below the melting layer, at the m.l. (1.2km) and above the m.l. 'Snow proportion' is the proportion of frozen water that is snow at the melting layer 160 minutes into the simulation. Rain on the ground and total ice cloud are calculated at the end of the integration.

3.2 Simulations of CASE2

Three simulations of CASE2 (the snow/graupel mixed case) were carried out, referred to as Runs 2.1, 2.2 and 2.3 using the same microphysics as in Runs 1.1, 1.2 and 1.3 respectively. Table 2 shows a summary of the results of simulations of CASE2.

		Run number		
	Obs.	2.1	2.2	2.3
$Z_{max}(h$=0.7km)	44dbZ	41dbZ	47dbZ	49dbZ
$Z_{max}(h$=1.2km)	52dbZ	46dbZ	51dbZ	53dbZ
$Z_{max}(h$=3.5km)	42dbZ	41dbZ	43dbZ	43dbZ
Snow proportion	≈50%	19%	46%	55%
Rain on ground	—	520Gg	400Gg	390Gg
Total ice cloud	—	65Gg	50Gg	55Gg

Table 2: Summary of results from Runs 2.1, 2.2 and 2.3. The line headings are the same as in Table 1.

Table 2 shows that the run with single–moment representation of snow and graupel over predicts the amount of graupel at the melting layer, as it did when modelling CASE1, causing an increased precipitation efficiency. Runs 2.2 and 2.3 are very similar, the inclusion of a threshold value of snow before conversion of snow to graupel is active clearly has little effect. Figure 4 shows the model fields from Run 2.3, it can be seen that the that threshold value of snow mass–concentration (0.3 g/kg) is exceeded over a large volume of the domain. The vertical sections of model fields show that the melting of graupel to rain is the dominant mechanism by which rain is produced in the cell core, and that away from the cell core and in smaller cells the melting of snow is the dominant mechanism.

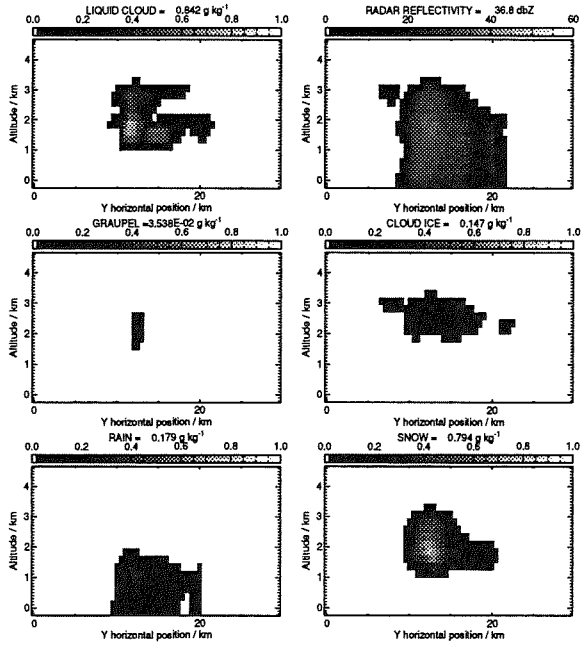

Figure 3: Vertical cross sections of model fields from Run 1.3. The maximum values are printed above each plot.

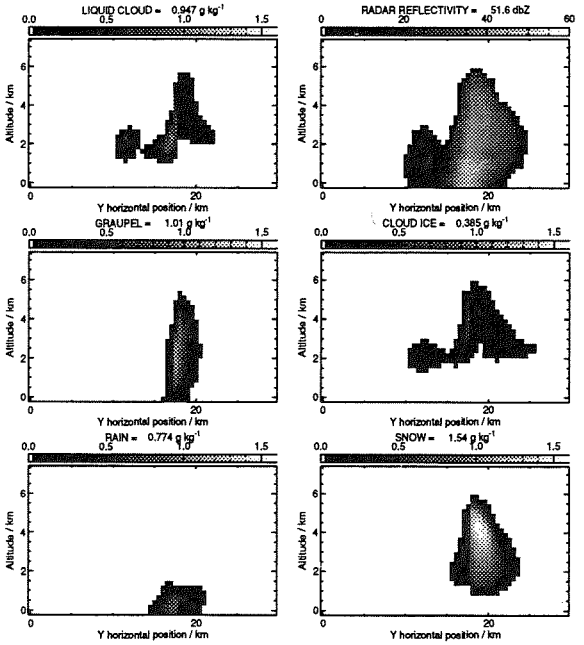

Figure 4: Vertical cross sections of model fields from Run 2.3. The maximum values are printed above each plot.

4. CONCLUSIONS

These results suggest that the double-moment scheme generates a clearer distinction between the different precipitation processes. The prognosed number concentration of snow and graupel leads to more realistic mass conversion rates than those calculated by the single–moment scheme with fixed intercept parameters. A new parameterization of the process of snow converting to graupel due to growth by riming has improved simulations of a snow–dominated convective case.

The sensitivity of the vertical transports of heat and moisture to the type of microphysics parametrization is examined by the comparison of the total precipitation reaching the ground and the total amount of ice cloud formed by the end of active convection. It has been found that the modelled precipitation efficiency can change by a factor of 1.5 depending on the type of microphysics scheme employed.

Radar polarization data in the melting layer allow the characteristics of the dominant precipitation particles to be determined. They are, therefore, an important tool for the validation of the microphysics component of CRMs. In the future, we hope to compare 'double–moment' simulations with multi-wavelength radar observations using combinations of 10cm/8mm and 10cm/3mm wavelengths. These will enable the estimation of both concentration and mass content for particles in the millimeter and sub–millimeter size ranges respectively, thereby extending the ability to validate the 'double–moment' scheme in regions above the melting layer.

5. ACKNOWLEDGEMENTS

The Joint Centre for Mesoscale Meteorology is supported by the UK Meteorological Office and the Department of Meteorology, University of Reading.

6. REFERENCES

Brown, P. R. A. and H. Swann, 1996: The observational validation of a 3-d numerical cloud model used for the development of convective cloud parametrization schemes. (submitted to Q. J. R. Meteorol. Soc.).

Lin, Y-L., R. D. Farley, and H. Orville, 1983: Bulk parametrization of the snow field in a cloud model. *J. Climate. Appl. Met.*, **22**, 1065-1092.

Ferrier, B. S., 1993: A Double-Moment Multiple-Phase Four-Class Bulk Ice Scheme. Part1: Description. *J. Atmos. Sci.* **51**, 249-280.

Flatau, P. J., G. J. Tripoli , J. Verlinde and W. R. Cotton, 1989: The SCU-RAMS Cloud microphysics module general theory and code documentation. *Colorado State University, Paper No.* **451**.

Initialization of a non-hydrostatic cloud model with airborne Doppler radar data

Soline Bielli and Frank Roux

(Laboratoire d'Aérologie, Toulouse, France)

1. Introduction

Doppler radar and numerical cloud models can provide detailed information on atmospheric circulations associated with mesoscale precipitating systems. Both approaches have their own advantages and limitations. Radar data give direct measurements of precipitation and dynamics, but are restricted to the part of the atmosphere where there are enough hydrometeors to return a detectable signal. Outputs from numerical models are more complete, but artificially specified thermal perturbations are needed at the initial stage. Although these techniques have been widely used for 20 years, they still appear as separate ways to analyze similar meteorological situations.

Lin *et al.* (1993) were the first to develop a method to initialize convective storm simulations with Doppler radar-derived fields. They established the feasibility of the method and obtained encouraging results when they applied their technique to the case of the 20 May 1977 Del City tornadic supercell storm, though some discrepancies appeared in the evolution of the observed and simulated storms. They concluded that further experiments on different meteorological situations are needed to more generally assess the applicability of such an approach.

Preliminary results from a similar study are presented here. The Doppler radar data are from airborne observations of a mesoscale convective system on 9 February 1993 during TOGA-COARE (Webster and Lukas, 1992). The numerical cloud model is MESO-NH, currently developed by CNRM (Météo-France, Toulouse) and Laboratoire d'Aérologie. After a survey of the structure and evolution of the 9 February 1993 MCS and a brief presentation of MESO-NH, we analyze the results obtained for different initializations of the cloud model. Further studies and applications are finally discussed.

2. Airborne Doppler radar observations

The MCS observed with the airborne Doppler radars on 9 February 1993 from 1630 till 2030 (all times UTC) during TOGA-COARE is a west-east oriented Class-3 system (area of IR cloud-top temperature smaller than 208 K between 6000 and 60 000 km^2). At 1830, it is approximately centered at 4°S, 159°E. The MCS is composed of a line of cumulonimbus at northeast and more stratiform precipitation at southwest (Fig. 1). It propagates northwards at 5 ms^{-1}.

The kinematic and thermodynamic characteristics of the MCS environment are deduced from radiosoundings launched from ships n°1 and 3 in the IFA, dropsonde data from NASA DC-8, and flight-level measurements from the turboprops (Zipser and Caesar, personnal communication). The atmosphere is very moist ($T-T_d$ was less than 5°C) up to 10 km altitude. The lifting condensation level is below 1 km, the level of free convection (LFC) at about 2.5 km and the equilibrium temperature level above 14 km. The CAPE value is about 1400 m^2s^{-2}. This MCS is aligned parallel to the shear (LeMone *et al.*, 1994). The low-level (1000-700 hPa) wind is about 10 ms^{-1} eastward and the upper-level wind is characterized by a westerly shear of $2.7x10^{-3}$ s^{-1} between 700 and 100 hPa.

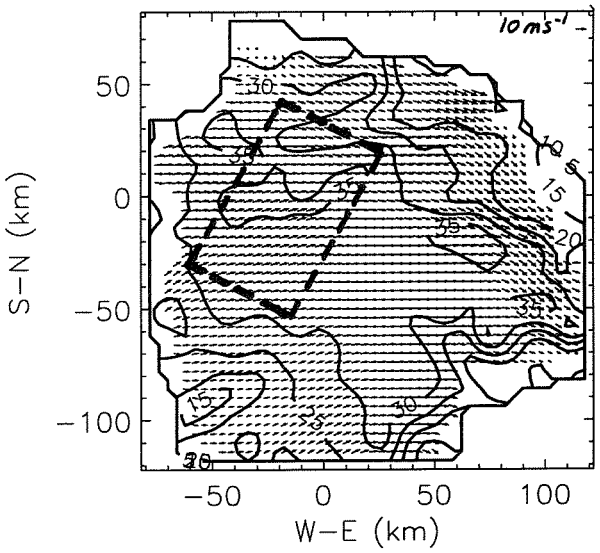

Figure 1: Radar reflectivity (in dBZ) and relative horizontal wind at 0.75 km altitude in a domain of 200 km x 200 km, centered on 3.9°S, 159.25°E, deduced from airborne Doppler radar data between 1630 and 2000 UTC on 9 February 1993. The box indicates the region where the averaged winds and precipitation contents are deduced.

The system-relative horizontal airflow shows a confluence zone along the system's northeastern edge and a predominantly along-line flow (Fig. 1). The vertical circulation in the cross-line direction (not shown) is evolving. At the earlier times, the upward motions are intense (up to 10 ms^{-1} at 10-12 km altitude) and relatively high reflectivity values are observed in the northeastern part. Then, upward motions and reflectivity progressively decrease. A secondary reflectivity maximum appears below the level of the 0°C isotherm (at about 5 km) in the southwestern part of the domain. This "bright band" signature is due to melting hydrometeors and is characteristic of stratiform regions of MCS.

Three-dimensional fields of reflectivity and cartesian wind components deduced from the airborne Doppler data collected during the period 1715-1915, and retrieved pressure and temperature perturbation fields (Roux and Bousquet, 1995) are used to determine the initial conditions from which the non-hydrostatic cloud model is started. For this purpose, the data void regions are first filled with the environmental winds. The rainwater mixing ratio is derived from the reflectivity values. The water vapor mixing ratio is assumed to be at saturation and the cloud water mixing ratio is taken as 0.5 g/kg below 5 km altitude and as a decreasing function of height above, in regions with rain and where the production rate of precipitation (Roux *et al.* 1993) is positive, everywhere else the environmental humidity is used and the cloud water content is assumed to be zero. Then, an average is made over 50 km in the along-line direction (see Fig. 1), and a two-dimensional streamfunction is calculated to insure balanced circulation.

The results (valid for 1745) are shown in Fig. 2. Two main horizontal flows are observed: a mid- to upper level front-to-rear (FTR) flow, a weaker low-level rear-to-front (RTF) flow. The updraft in the FTR flow reaches 3 ms^{-1} at 9 km altitude, it is followed by a 1 ms^{-1} downdraft feeding the FTR flow. The largest precipitation content is found below the updraft, while unsaturated air is found in the low-level RTF flow.

3. The MESO-NH non-hydrostatic cloud model

The MESO-NH model is the result of joint efforts of Centre National de Recherches Météorologiques (Météo-France, Toulouse) and Laboratoire d'Aérologie. It is non-hydrostatic, based on the Lipps and Helmer (1982) modified anelastic system, and utilizes a subgrid turbulence parameterization and liquid-phase microphysics according to Kessler (1969). It can be initialized with idealized or analyzed meteorological fields.

In the present study, open and cyclic lateral boundary conditions are used in the directions perpendicular and parallel to the convective line axis, respectively. The horizontal dimensions of the considered domain are 80 km x 80 km with a grid size of 3 km. The domain height is 18 km with a grid size of 600 m. A constant value of 5 ms^{-1} northwards (equal to the MCS propagation) is substracted to the initial wind profile in order to keep the simulated cloud within the domain throughout the considered period. A set of 10 numerical simulations has been performed in order to test different initializations and environmental conditions (Table 1).

SIMU-LATION	INITIAL WIND FIELD	INITIAL THERMO-DYNAMIC FIELD	INITIAL PERTUR-BATION	MODEL
1	(U,V)env	(T,QV)env	WARM BUBBLE	3D
2	(U,V)env	(T,QV)env	COLD BUBBLE	3D
3	(U,V)env	(T,QV)sat	WARM BUBBLE	3D
4	(U,V)env	(T,QV)sat	COLD BUBBLE	3D
5	(U,W)radar	(T,QV)env	NO	2D
6	(U,V,W)radar	(T,QV)env	NO	3D
7	(U,W)radar	(T,QV)sat	NO	2D
8	(U,V,W)radar	(T,QV)sat	NO	3D
9	(U,W)radar	(T,QV,QC,QR) radar	NO	2D
10	(U,V,W)radar	(T,QV,QC,QR) radar	NO	3D

***Table 1:** Characteristics of the different simulations.*

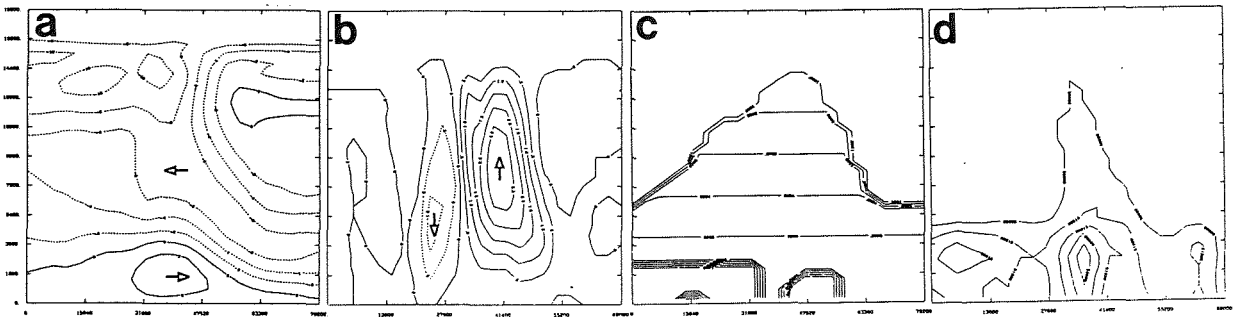

***Figure 2:** Initial fields of (a) horizontal wind component normal to the line (contours every 2 ms^{-1}), (b) vertical velocity component (0.5 ms^{-1}), (c) cloud water content (0.1 g/kg), (d) precipitation water content (0.05 g/kg). The size of the domain is 80 km x 18 km.*

3. Results

Two control runs are conducted, using the environmental values for the horizontal wind components, temperature and humidity. These simulations are initiated with the "traditional" method: a 5°C warmer (run 1) or colder (run 2) bubble of 40 km diameter and 2 km depth is inserted at the center of the domain into a horizontally homogeneous environment to trigger convection. The center of the warm and cold bubbles are at 1 and 6 km altitudes, respectively. The results are rather disappointing: the development of vertical motions and the formation of cloud accompany the vertical displacement of the bubble, but everything stops as soon as the bubbles reach their equilibrium levels. This is probably related to the rather high LFC (2.5 km) which implies that a substantial and continuous lifting is needed for convection to develop.

The same procedure with the warm and cold bubbles is then applied to a modified environment where the water vapor mixing ratio is changed everywhere to its saturation value (runs 3 and 4). Then, convective motions develop, but the structure and evolution of the simulated fields differ strongly from those observed with radar. In this case, the convective instability of the environment has considerably increased.

Simulations in two (slab-symmetric) and three dimensions are conducted using the Doppler-derived wind field and the environmental thermodynamic characteristics (runs 5 and 6). As it happens for runs 1 and 2, vertical motions, cloud and rain are only transient and the wind components evolve rapidly toward a stable state. We do not observe significant structural difference between the 2D and 3D simulations. When saturated humidity values are used (runs 7 and 8), convection develops, but it becomes much stronger than observed. Moreover, in this case, both FTR and RTF flows feed the updraft, while sporadic and intense downdrafts originate from the upper troposphere. This type of structure and evolution is very different from the radar observations.

More satisfying results are obtained with the complete initialization for runs 9 and 10. This clearly shows that a proper description of water vapor, cloud water and rain is required for the model to correctly handle the radar-derived kinematics. It is also to be outlined that the simulated structure and evolution becomes realistic less than 2 hours after the initial time, a shorter interval than models initialized with the "traditional" method usually need. Only the results obtained from the 2D version of MESO-NH (run 9) are presented and discussed here. Those from the 3D version (run 10) are very similar, except for slightly smaller amplitudes of the maximum horizontal and vertical wind components.

The results obtained for simulation 9 at 120, 140, 160 and 180 min after the initialization are shown in Figs. 3 to 6. The evolution of the wind component normal to the line (Fig. 3) reveals the presence of moving maxima (up to -21 ms^{-1}) in the FTR and RTF flows. These features have been suspected, but can hardly be unambiguously identified with the airborne Doppler data, owing to the time (10 to 20 min) necessary for the aircraft to achieve a survey of the considered zone.

The vertical velocity contours (Fig. 4) show that the maxima of the FTR flow are related to updraft zones, probably through the horizontal pressure perturbation force. The main updraft (up to 8 ms^{-1})

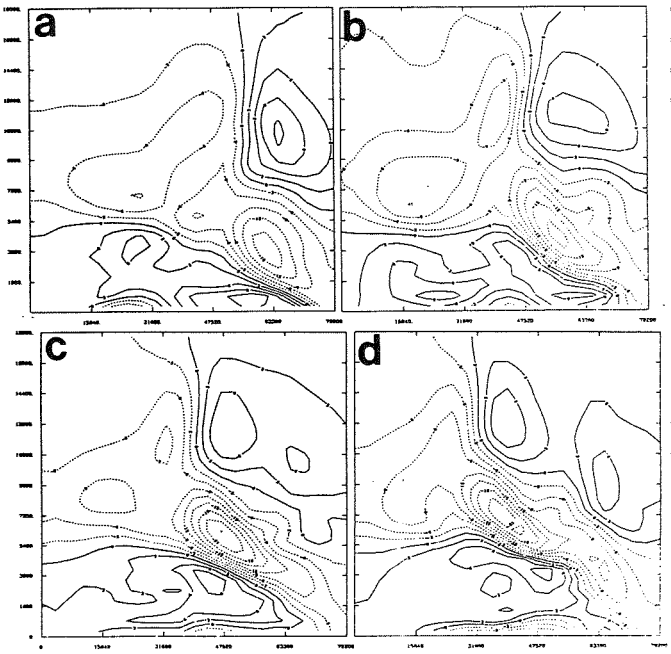

Figure 3: Simulated fields of horizontal wind component normal to the line at (a) 120 min, (b) 140 min, (c) 160 min, (a) 180 min (contours every 3 ms^{-1}).

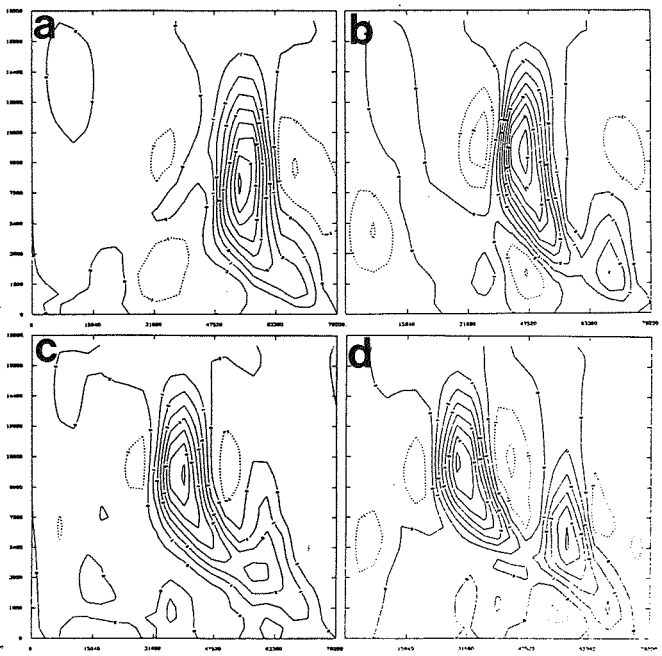

Figure 4: As in Fig. 3, except for the vertical velocity (1 ms^{-1}).

moves rearwards and upwards. Once it reaches the upper troposphere, a new updraft forms at the leading part of the domain (Fig. 4d). This evolution repeats throughout the simulation time (10 h). Below the main updraft, a weaker downdraft ($\geq$-2 ms^{-1}) is observed. It plays an important role in the dynamics as it feeds the low-level RTF flow of colder air which facilitates the initial lifting of the potentially unstable air. This feature is not reproduced in the other simulations.

The cloud water content (Fig. 5) is correlated with the updraft zones, with maximum values of 1 to 1.5 g/kg. No cloud is found in the unsaturated low-level RTF flow and in the rear part of the domain. The rain water content (Fig. 6) is linked to the updrafts. As the primary maximum (up to 7.5 g/kg) is advected rearwards, a secondary one (up to 3.5 g/kg) forms with the new updraft. Such a sequence repeats throughout the simulation time.

4. Discussion

From the above results, we can conclude that the initialization of a non-hydrostatic cloud model with Doppler radar-derived fields is feasible, provided that great care is taken to the water-related variables. In the absence of microphysical retrieval, this is however a rather subjective task, although the calculated production rate of precipitation provides some indication on the saturated and unsaturated regions. The proper identification of the unsaturated RTF low-level flow is very important for realistic simulation.

Major differences between the simulated and observed fields concern the much larger precipitation contents and the fact that no stratiform region develops in the simulation. Both aspects are related to the limited microphysical scheme in the present version of MESO-NH. It is well known that ice physics must be taken into account to accurately simulate the dynamics and microphysics of tropical convective systems. Inclusion of a microphysical scheme for ice in MESO-NH is currently under progress, and we will use it in our simulations as soon as possible.

Finally, we would like to outline that this study is a first step in a program aimed at developping analyses coupling observational and numerical approaches to study mesoscale precipitating systems. As a matter of fact, the precipitating part of atmospheric perturbations (the only one that can be investigated with Doppler radar) represents a limited part of the considered atmospheric perturbation. The next step in this program concerns the combined use of Doppler radar, radiosounding and/or dropsonde data, and model analyses to deduce mesoscale fields suitable for MESO-NH initialization.

Acknowledgments

We are indebted to Evelyne Richard and Jacqueline Duron for their help in operating the MESO-NH model.

References

Kessler, E., III, 1969: *Meteorol. Monogr.*, **10**.

LeMone, M.A., D.P. Jorgensen and B.F. Smull, 1995: *Preprints 6th Conf. on Mesoscale Processes*, Amer. Meteor. Soc., 40-44.

Lin, Y., P.S. Ray, K.W. Johnson, 1993: *Mon. Wea. Rev.*, **121**, 2757-2775.

Lipps and Helmer, 1982: *J. Atmos. Sci.*, **39**, 2192-2210.

Roux and Bousquet, 1995: *Preprints 27th Conf. on Radar Meteorology*, Amer. Meteor. Soc., 740-742.

Roux, F., V. Marécal and D. Hauser, 1993: *J. Atmos. Sci.*, **50**, 951-974.

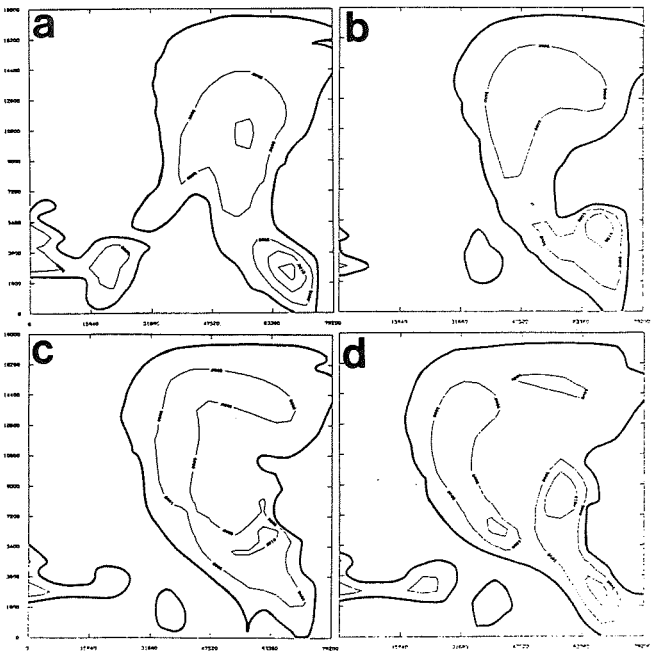

Figure 5: *As in Fig. 3, except for the cloud water content (0.5 g/kg).*

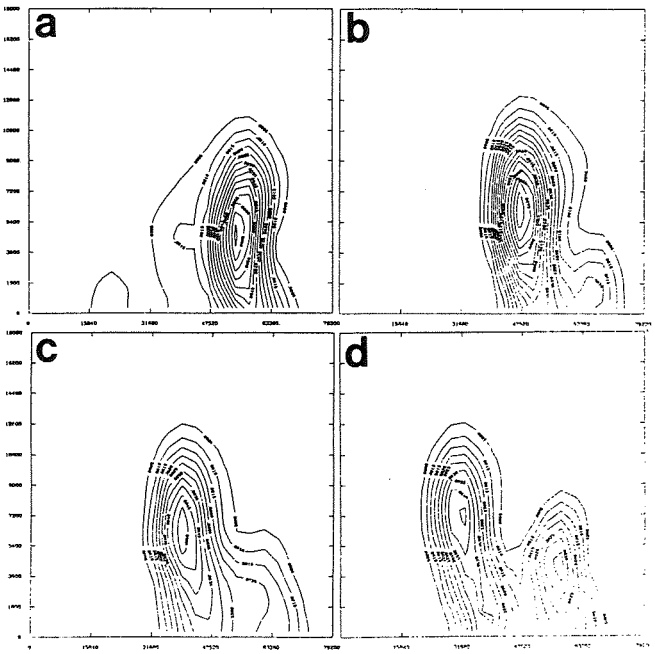

Figure 6: *As in Fig. 3, except for the rain water content (0.5 g/kg).*

MASS CONSERVING FRAGMENT DISTRIBUTION FUNCTIONS

Philip S. Brown, Jr. and Jason A. Walde

Trinity College, Hartford, CT 06106, USA

1. INTRODUCTION

Model formulation of raindrop breakup requires an analytic expression to describe the size distribution of water fragments created by the collision of two drops of arbitrary diameter. The fragment distribution functions derived by Low and List (1982a,b) [henceforth, LLa and LLb] have provided the foundation for most of the recent modeling studies of raindrop collision. The fragment distribution functions of LLb were obtained by representing frequency distributions of laboratory data in histogram form and then deriving analytic formulas to fit the histograms. The formulas provide reasonably accurate approximations to the histograms but produce a distribution of drop fragments whose masses do not sum to the masses of the colliding drops. To eliminate the inconsistency, new analytic formulas are derived using least squares fits of the histograms of LLa,b in conjunction with an explicit constraint on the total water mass content of the fragments. For certain cases, the resulting fragment distribution functions differ significantly from those derived by LLb.

2. THE FRAGMENT DISTRIBUTION

The raindrop size distribution is obtained by solution of the coalescence/breakup equation [e.g., Gillespie and List (1978/9)] in which the fragment distribution function is a key constituent. The fragment distribution function P is defined so that $P(D; D_L, D_S)\Delta D$ represents the average number of fragments of diameter D to $D+\Delta D$ produced by collision and subsequent breakup of two drops, the larger of diameter D_L and the smaller of diameter D_S. The function is formulated according to LLb as a weighted sum of three separate distribution functions, each corresponding to one of the three distinct types of breakup (filament, sheet and disk) that were observed in the experiments. Accordingly, P is written as

$$P(D) = R_f P_f(D) + R_s P_s(D) + R_d P_d(D) \qquad (1)$$

where the subscripts f, s, and d refer to filament, sheet and disk types of breakup, R with subscript represents the proportion of fragmentation found to occur and P with subscript the distribution function for the corresponding type of breakup. (For brevity, the dependence of the distribution functions on the colliding drop diameters D_L and D_S has been suppressed.) The fragment distribution function for each type of breakup is, in turn, broken down into a sum of normal- or lognormal-type distributions. For filament breakup, which will be the focus of this investigation,

$$P_f(D) = P_{f,1}(D) + P_{f,2}(D) + P_{f,3}(D) \qquad (2)$$

where

$$P_{f,i}(D) = H_{f,i}\exp[-(\frac{D - \mu_{f,i}}{\sqrt{2}\,\sigma_{f,i}})^2],\ i = 1,2 \qquad (3)$$

and

$$P_{f,3}(D) = \frac{H_{f,3}}{D}\exp[-(\frac{\ln D - \mu_{f,3}}{\sqrt{2}\,\sigma_{f,3}})^2]. \qquad (4)$$

The domain of each $P_{f,i}$ is restricted to the interval, $D_0 \le D \le D_C$, where D_0 is the smallest drop diameter resolved in the experiments and where D_C is the diameter of the largest drop that can be created; i.e.,

$$D_C = (D_L^3 + D_S^3)^{\frac{1}{3}}, \qquad (5)$$

so that the mass of a resulting fragment cannot exceed the sum of the masses of the colliding drops.

Some basic properties of filament breakup allow formulation of relations that can be used in determining the parameters that appear in the normal and lognormal

distributions. It is found that in a filament-producing collision, there always remains a single remnant of each colliding drop. Thus, if the subscripts 1 and 2 refer to remnants of the larger and smaller of the colliding drops, respectively,

$$\int_{D_0}^{D_C} P_{f,1}(D)\,dD = 1 \qquad (6)$$

and

$$\int_{D_0}^{D_C} P_{f,2}(D)\,dD = 1. \qquad (7)$$

Furthermore, the peak of each remnant distribution occurs at the diameter of the drop before fragmentation. Thus,

$$\mu_{f,1} = D_L \qquad (8)$$

and

$$\mu_{f,2} = D_S. \qquad (9)$$

A further property of the breakup process is based not on the observations but on the physical principle that the total mass of the drop fragments resulting from the collision must be equal to the sum of the masses of the two colliding drops. This mass-conservation requirement can be written as

$$\int_{D_0}^{D_C} D^3 P_f(D)dD = D_L^3 + D_S^3 \qquad (10)$$

Relations (6) - (10) are taken to be fundamental properties of filament breakup that hold regardless of the sizes of the colliding drops even though the first four relations are based on a limited number of observations rather than on physical principles.

3. THE DATA FITTING PROCEDURE

For the case of filament breakup, the nine parameters $H_{f,i}$, $\mu_{f,i}$, and $\sigma_{f,i}$, i=1, 2, 3, are determined first for each of the 10 drop-size pairs (D_L, D_S) used in the experiments. Then by the construction of formulas to interpolate the parameters over the two-dimensional region,

$$D_0 \le D_L \le D_C,\ D_0 \le D_S \le D_L, \qquad (11)$$

P_f can be calculated for arbitrary values of D_L and D_S as required for numerical solution of the coalescence/breakup equation.

For each experimental drop-size pair (D_L, D_S) where filament breakup occurs, nine relations are required to determine the nine parameters that describe the normal and lognormal distributions. Since the basic properties of filament breakup provide only five applicable relations (6) - (10), the remaining relations must be supplied by requirements that arise from procedures to fit function $P_f(D)$ to the data for the given drop-size pair. LLa,b present their data in histogram form but do not describe the fitting procedure used to arrive at the analytic representations of the data. Fig. 1 is a reconstruction of one of the histograms (LLa, Fig 11i) for the case in which D_L = .40 mm and D_S = .0395 mm.

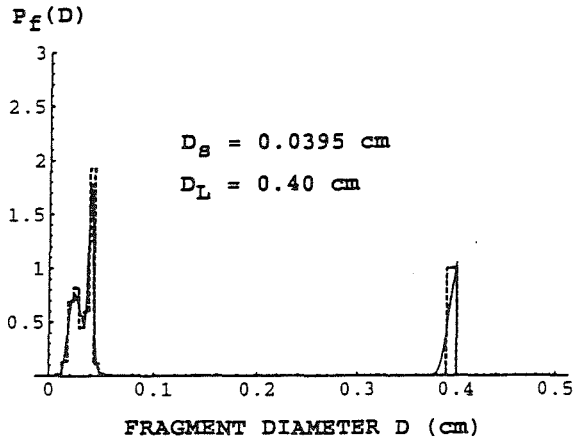

Fig. 1. Fragment distribution histogram recreated from histogram presented by LLa for colliding drops of diameters D_L = .40 cm and D_S = 0.0395 cm. Smooth curve represents approximating function obtained by least squares fit of histogram values without mass conservation constraint. Values for $P_f(D)$ are in numbers of fragments per 0.01 cm drop size interval.

In this work, least squares fits with integral constraints are used to fit data values read from the LLa histograms. An integral constraint, in addition to those of (6), (7) and (10), can be obtained through use of the average total fragment number F_f given by LLb for filament-producing collisions. Since each colliding drop produces a single, identifiable remnant accounted for in $P_{f,1}$ or $P_{f,2}$, it follows that the distribution of satellite drops $P_{f,3}$ satisfies the relation

$$\int_{D_0}^{D_C} P_{f,3}(D)dD = F_f - 2. \qquad (12)$$

To perform the least squares fit, values for the fragment distribution have been extracted from the LLa diagrams for drop diameters D_j, j=1, ..., n (n a value between 17 and 33, depending on the particular drop size pair), where the D_j include both the boundary points and midpoints of the histogram bins. If D_j represents a midpoint, the corresponding function value y_j is assigned the histogram value for the bin; if D_j represents a boundary point, y_j is taken to be the average of the histogram values for the two bins adjacent to the boundary point. The effect of the averaging procedure is to replace step functions values with values representative of a continuous, piecewise-linear function that can be better approximated by the normal and lognormal distributions. Least squares relations then can be written to minimize the sum of the squared errors at the data points with respect to any of the nine parameters. In this work, best results have been obtained by selecting minimization relations from the following set:

$$\frac{\partial}{\partial H_{f,1}} \sum_{j=1}^{n} [P_f(D_j) - y_j]^2 = 0, \qquad (13)$$

$$\frac{\partial}{\partial H_{f,2}} \sum_{j=1}^{n} [P_f(D_j) - y_j]^2 = 0, \qquad (14)$$

$$\frac{\partial}{\partial H_{f,3}} \sum_{j=1}^{n} [P_f(D_j) - y_j]^2 = 0, \qquad (15)$$

and

$$\frac{\partial}{\partial \mu_{f,3}} \sum_{j=1}^{n} [P_f(D_j) - y_j]^2 = 0. \qquad (16)$$

Since $\mu_{f,1} = D_L$ and $\mu_{f,2} = D_S$ by virtue of (8) and (9), there remain seven parameters to be determined. A nested iterative procedure has been devised to solve the seven equations needed to determine those parameters. In the outer iteration, approximating equations derived from (6) and (7) are used to write $\sigma_{f,1}$ in terms of $H_{f,1}$ and $\sigma_{f,2}$ in terms of $H_{f,2}$ The remaining parameters $H_{f,1}$, $H_{f,2}$, $H_{f,3}$, $\mu_{f,3}$ and $\sigma_{f,3}$ are determined through solution of five equations that may include the mass conservation equation (10), the specification of the total number of satellite drops (12), or the least squares relations (13) - (16). Since the number of available equations exceeds the number of unknown parameters, there is some flexibility in the choice of fit. In this work the five equations have been solved by an extension of Newton's method for systems of equations. The solution values for $H_{f,1}$ and $H_{f,2}$ are used to begin the next step of the outer iteration. The procedure is repeated until convergence is achieved.

4. RESULTS OF THE FIT

The case in which the large-drop diameter greatly exceeds the small-drop diameter turns out to be of considerable interest. Accordingly, the data for colliding drop pairs with D_L = .40 cm and D_S = .0395 cm is examined in detail. The histogram for this case (Fig. 1) given by LLa has drop-size categories, or bins, of about .005 cm in width in the small-drop range and .01 cm in the large-drop range. The distributions occurring near drop diameters D_L and D_S represent the large and small drop remnants, respectively, while the distribution with peak near drop diameter .025 cm represents the satellite drops. The bin widths were selected by LLa,b in such a way that in the neighborhood of a peak each bin would contain a significant number of fragments. Such a criterion places a lower limit but not an upper limit on the width of the bins. It will be shown that the upper limit placed on the bin width can be of considerable importance.

Application of the data fitting procedure described in the preceding section has been carried out using fragment number constraints (6), (7) and (12), peak-location designations (8) and (9), and the least squares relations (13) - (16). The resulting fit, shown by the solid curve in Fig. 1, is nearly identical to the fit of LLa (their Fig. 11i). While mass conservation was not imposed in the derivation of the fit shown in Fig. 1, the water mass content of the fragment distribution, which is computed to be 0.0321 g, differs only by 4.2% from the value 0.0335 g that represents the combined mass of the colliding drops. Modest scaling of the fitted distribution then would yield the correct water mass content at the sacrifice of a small error in the fragment number. The failure to incorporate the mass conservation constraint in the fitting procedure, however, masks an inherent problem in the construction of the histogram that leads to a large error in the fragment distribution function. Fig. 2 shows the fit obtained by replacing (13), the least squares requirement for $H_{f,1}$, with mass conservation requirement (10). The truncated normal distribution that desribes the large-drop remnant is seen to have an extremely small standard deviation and commensurately high peak $H_{f,1}$

that is, in fact, cut off in the figure as the distribution $P_{f,1}$ extends far beyond the bounds of the graph.

For such collisions in which $D_L > D_S$ and in which the satellite drops have diameters less than D_S, the distribution representing the large-drop remnant is necessarily a narrow spike of the type shown in Fig. 2 and not the broader type of distribution shown in Fig. 1. When $D_L = 0.40$ cm and $D_S = 0.0395$ cm, the maximum size of a drop resulting from collision would be $D_C = 0.4001$ cm.

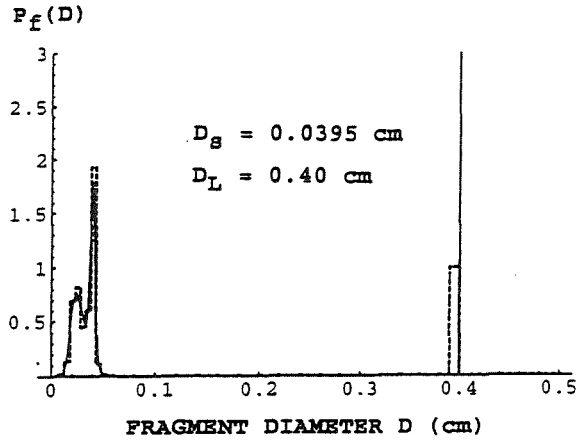

Fig. 2. As for Fig. 1 but with approximating function obtained by least squares fit with mass conservation constraint.

Furthermore, if all the satellites (whose combined mass is about 2×10^{-5} g) were created from mass supplied by the large drop while the small drop remnant has no more than double the original small-drop mass, the large-drop remnant would have diameter at least 0.3996 cm. Accordingly, the normal distribution representing the large-drop remnant should be expected to have a standard deviation of order .0001 cm. This estimate is consistent with the fit shown in Fig. 2 in which $\sigma_{f,1}$ is calculated to be 0.00018 cm.

5. SUMMARY AND CONCLUSIONS

In this work, new fitting procedures have been developed to arrive at fragment distribution functions that approximate data provided by LLa in histogram form. Two procedures are compared, one that employs a least squares fit with constraints on the fragment number and another that employs a least squares fit with constraints on both fragment number and water mass content of the fragments. Comparison of the fits shows that for the case of filament breakup in which the mass of the larger colliding drop far exceeds that of the smaller colliding drop, extremely large differences occur in the shape of the distribution of the large-drop remnant. Fitting the peak of the histogram by least squares gives a relatively low, broad distribution (in accordance with the histogram); fitting by the imposition of mass conservation results in an extremely high, narrow distribution. The disparity of the fits brings to light the need for extreme care in the choice of bin widths in construction of the histograms. For collisions between very large and very small drops, an appropriate histogram bin size for the large drop remnant can be found in the manner described in Section 4. In such cases the diameter range of the large drop remnant can be estimated by finding a bound on the mass contained in the small drop remnant and in the satellite drops created by collision.

Preliminary tests show that when the modified fragment distribution is incorporated in the coalescence/breakup equation, numerical solutions produce raindrop size distributions that contain a greater number of large drops and less prominent peaks than have been found in previous studies.

6. ACKNOWLEDGMENTS

This work was supported by the Division of Atmospheric Science of the National Science Foundation under Grant ATM-9424423. Computer support was provided by the Trinity College Computing Center and by the National Center for Atmospheric Research, which is sponsored by the National Science Foundation.

7. REFERENCES

Gillespie, J. R., and R. List, 1978/9: Effects of collision-induced breakup on drop size distributions in steady-state rainshafts. *Pure Appl. Geophys.*, **117**, 599-626.

Low, T. B., and R. List, 1982a: Collision, coalescence, and breakup of raindrops. Part I: Experimentally established coalescence efficiencies and fragment size distributions in breakup. *J. Atmos. Sci.*, **39**, 1591-1606.

___, and___, 1982b: Collision, coalescence, and breakup of raindrops. Part II: Parameterization of fragment size distributions. *J. Atmos. Sci.*, **39**, 1607-1618.

A NEW NUMERICAL TREATMENT FOR THE DRAG COEFFICIENT LAW USED IN HAIL TRAJECTORY SIMULATIONS

Olga B. Nasello and Nesvit E. Castellano

Facultad de Matemática Astronomía y Física
Universidad Nacional de Córdoba
Ciudad Universitaria - Córdoba - Argentina

1. INTRODUCTION

In the past years many studies have been focused on the nature of hail embryos and mechanisms by which they develop into hail. Conventionally, these investigations were carried out simulating the development of ice particles within the different fields which represent a cloud. A careful analysis of the reported hail trajectory simulation models (HTSM) shows that they generally used the same basic equation to describe the trajectories of the growing hailstones, but different parameterizations for the microphysical variables. Within these variables there is a strong evidence that the drag coefficient C_D is one of the most important in the determination of the hail simulated trajectories (HT), (Foote, 1984, Levi and Lubart, 1991; Castellano *et al*, 1994). Consequently, many works have been reported in order to improve the C_D treatment in the HTSM. Generally, these works have been pointed out to give the best parameterization for the C_D values (Böhm, 1990, Heymsfield, 1982).

Looking at the reported C_D experimental values, it may be noted that the scattering of the data is very high. In Fig. 1 we show the C_D vs. Re values obtained by different authors for lump graupel and hail. As explained by Castellano and Nasello (1995), in order to perform this plot the C_D experimental values reported by the different authors were digitized. In most cases the corresponding Re values were those given by the author, but in others they were inferred. In Fig. 1, it can be seen the wide scattering previously mentioned. Moreover, it is noted that the Zikmunda and Vali (1972) and Heymsfield's (1978) parameterizations represent the high values of the C_D vs. Re data, the Abraham's (1970) curve describes the low values, and the Heymsfield and Kajikawa (1987) and Heymsfield and Knight' (1983) fitting curves, run over the mean values (hereafter, we call these the high, low and mean C_D law, ${}_HC_D$, ${}_LC_D$, and ${}_MC_D$ respectively). It is interesting to note that if the C_D vs. Re values corresponding to conical graupel are included in Fig. 1, the general characteristic of this figure remains undisturbed.

The C_D vs. Re values plotted in Fig. 1. correspond to particles with a different shape factor and fall attitude so, it might be inferred that this is the cause of the observed scattering. However, if we look at the Heymsfield and Kajikawa's values, which according to the authors correspond to spherical grauple, it can be seen that the scattering of these experimental data is the same as the whole. These results show that even when two hailstones exhibit similar features their motion might be different, so it seems impossible that an experimental determination of C_D in order to reduce the scattering of the experimental points can be planned. Consequently, taking into account the striking dependence of the HT on the C_D parameterization and even though we confine our analysis to one type of particle (for instance that reported by Heymsfield and Kajikawa) the following question arises: Will the HT obtained from one C_D parameterization be representative of all the possible HT that the corresponding described particles may follow? To answer this question HT are evaluated assigning to the simulated hails a C_D value, chosen in a probabilistic way among all the experimentally determined C_D values, corresponding to a given Re Then, the results are compared with those obtained following the standard procedure using the deterministic high, low and mean C_D laws.

2. HAIL TRAJECTORY CALCULATION

The new method to evaluate the HST was implemented in the HSTM described by Castellano *et al* (1994) using their stationary cloud fields. The trajectories were calculated applying the complete motion equations, (Castellano *et al*, 1994, Eq.2). These equations were solved numerically using a time interval Δt=0.1 sec. The parameterizations used for the microphysical variables were those described by Castellano *et al.*, except for the C_D coefficient. In order to assign a C_D to a growing hailstone the following procedure was followed:

- The initial Re_o number corresponding to an initial embryo of r_o diameter located at an x_o position was evaluated using the terminal velocity expression obtained from Abraham (1970), and a particle density ρ= 0.917 g/cm^3. The corresponding $C_D(Re_o)$ was chosen in the $[{}_HC_D(Re_o), {}_LC_D(Re_o)]$ interval.

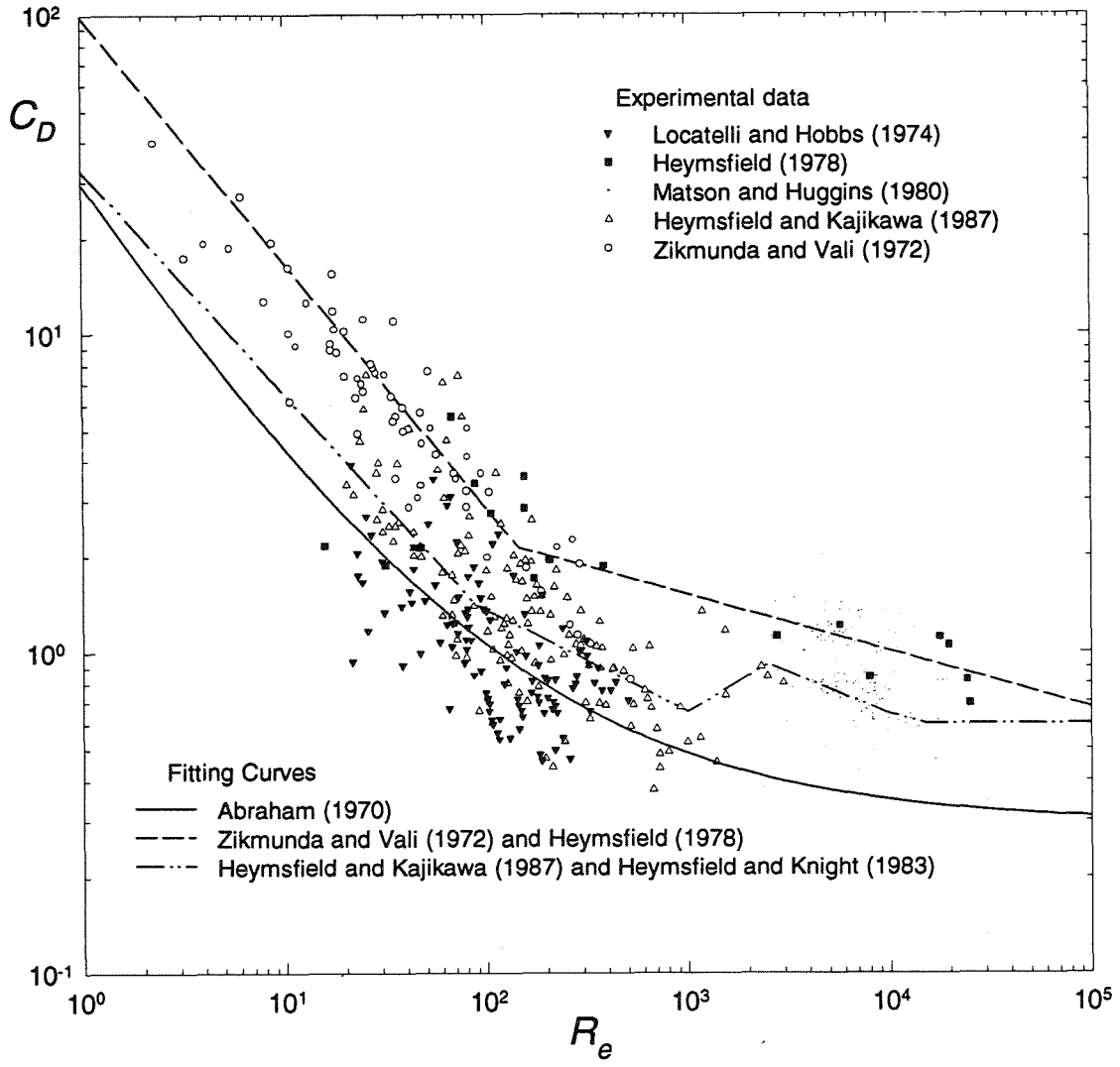

Figure 1: Values of the drag coefficients corresponding to lump graupels and hails, obtained by different authors, as a function of the Reynolds number.

- The motion equation was solved using $C_D = C_D(Re_o)$ and the particle velocity and Re number at the time $t+\Delta t$ were evaluated
- The drag coefficient at the time $t+\Delta t$ was obtained calculating, first, the variation that C_D would have if the drag coefficient were described by a drag law ${}_BC_D(Re)$ such as the previously cited high, low or mean drag laws, namely

$$\Delta C_D(t+\Delta t) = {}_BC_D(Re(t+\Delta t)) - {}_BC_D(Re(t))$$

Then $C_D(Re(t+\Delta t))$ was calculated using the following equation:

$$C_D(Re(t+\Delta t)) = (C_D(Re(t)) + \Delta C_D(t+\Delta t))(1 \pm 0.01n)$$

where n is a random number in the [0,1] interval. If $C_D(Re(t+\Delta t))$ occurred within the $[{}_HC_D(Re(t+\Delta t)), {}_LC_D(Re(t+\Delta t))]$ interval the new position of the particle was evaluated, other wise, a new value of $C_D(Re(t+\Delta t))$ was found.

The procedure previously described was applied to embryo hailstones of r_o=0.25 mm initially located in the zone cloud defined by the intersection of a vertical plane which goes through the center of the cloud and that horizontal one coinciding with the region of high convergence. In the used cloud the updraft-downdraft distance is ~6 Km being the updraft located at the

coordinate x=8 Km. The embryos were seeded at x positions in the [5 Km, 8 Km] interval and at a distance of 500m. For each initial embryo position 300 trajectories were calculated and the C_D vs. Re values that the particles had during their growth were recorded. The size R_f and the position x_f of each particle at the 0°C isotherm and the growing time t_f were also stored.

3. RESULTS AND DISCUSSION.

Fig. 2 shows some of the C_D vs. Re values obtained for embryos initialized at x_o=5.5 Km and with $C_D(Re_o) = {}_L C_D(Re_o)$. For each C_D vs. Re curve the final radius attained by the particle is indicated. In this figure again it is possible to observe the high dependence of the final radius on the C_D drag law.

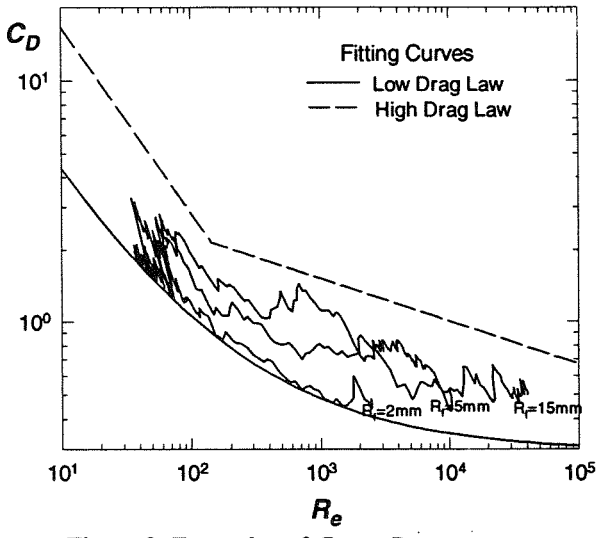

Figure 2: Examples of C_D vs. Re curves.

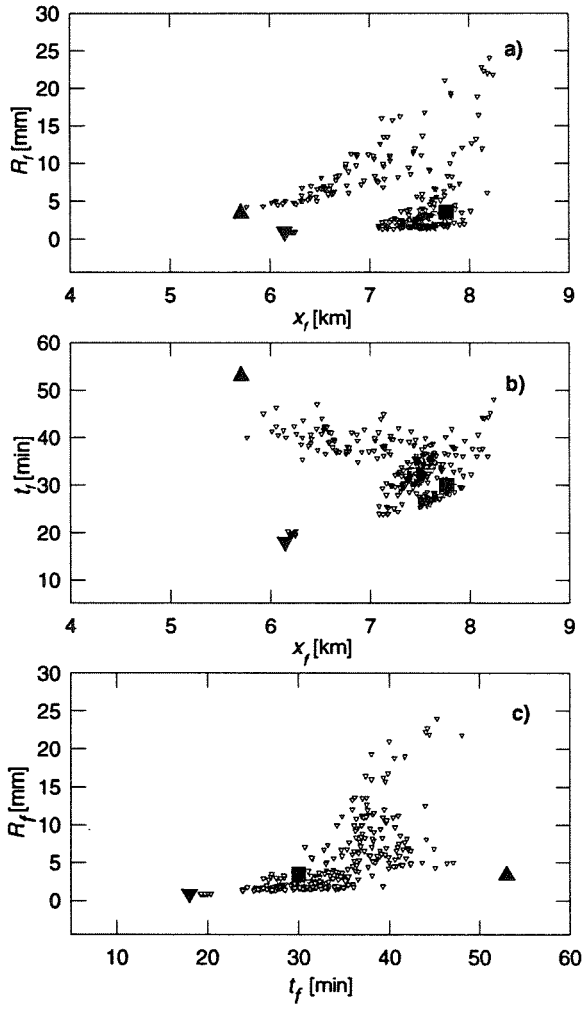

Figure 3: Effect of the C_D parameterization on x_f, R_f and t_f for groups of hailstones injected at x_o=5.5 Km

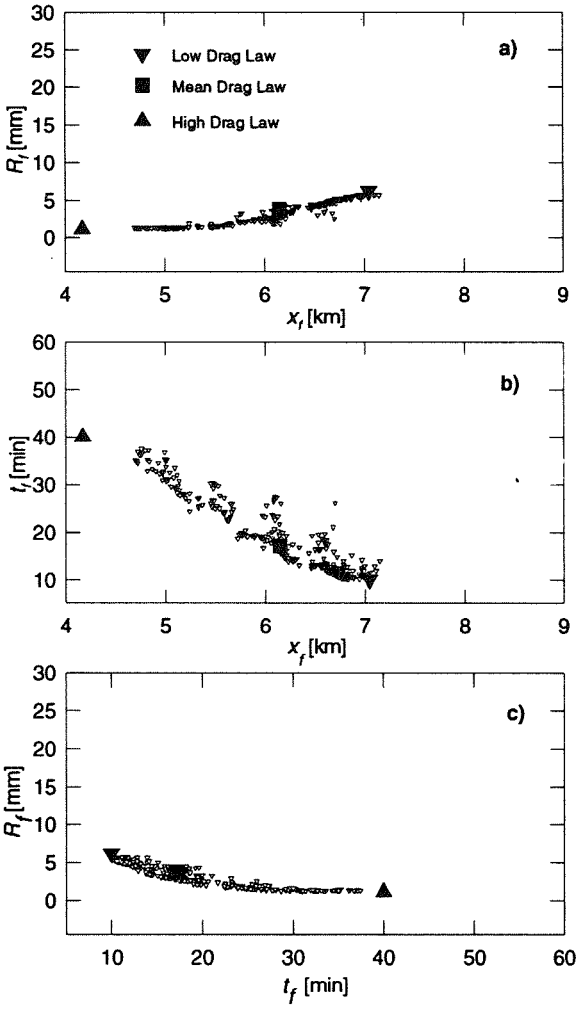

Figure 4: Effect of the C_D parameterization on x_f, R_f and t_f for groups of hailstones injected at x_o=8 Km

Fig. 3 and 4 display the R_f, x_f and t_f values obtained, following the new procedure, for embryos initialized at x_o=8 Km and x_o=5.5 Km respectively. In these figures the values R_f, x_f and t_f calculated with the deterministic high, low and mean drag laws are also shown.

In Fig. 3 it is noted that all the values obtained for R_f, x_f and t_f following the new procedure are limited by those obtained with the ${}_HC_D$, ${}_LC_D$, and ${}_MC_D$ drag laws. The maximun values of R_f, and t_f are 6mm and 40 min respectively. It is also noted that according to Xu (1983)] the larger stone grows in the shorter time. This general behavior it is not observed in Fig. 4. In fact, in Fig. 4c it can be noted that there is a high probability of finding simulated hailstones with final size greater than those obtained from the deterministic drag laws. Fig. 4 shows that embryos located initially at x_o=5.5 km may grow to hailstones of up to 5 cm in diameter. This R_f value is five times greater than the maximum R_f corresponding to embryos initialized at x_o=8 Km, i.e. at the updraft zone (see Fig. 3). The growing times of these higher embryos are among the highest, but they are lower than 50 min., so they occur within the real time values that a particle can travel inside a cloud. Finally, Fig. 3 and 4 show that all the higher hailstones fall to ground near the updraft zone. This behavior applies to all the initial positions of the analyzed embryos thus the results are in agreement with the radar observations which show that the maximum reflectivity regions are those near the updraft.

5. CONCLUSIONS

The results presented in this study once again evidence the striking dependence of the simulated hailstone final size on the drag coefficient. The new implemented procedure, also shows that the results obtained in a HSM with the fitting curve of the experimental C_D data do not represent properly the general behavior of all the particles. When the initial embryos are released in cloud zones near the updraft, it is observed that final values of the hailstone radii that result from the non deterministic C_D laws are limited by those obtained from the ${}_HC_D$, and ${}_LC_D$, drag law. i.e. the C_D laws that limit the experimental C_D data. However, with embryos released in cloud zones far from the updraft, it is observed that a non negligible number of particles can attain values of R_f much higher than those obtained using the high, low or mean drag laws. It must be noted that, the last zones, following an standard treatment would not be considered as embryo sources, because all the deterministic drag laws predict R_f values lower than those of the considered hailstones (R_f <5 mm). Therefore, the new method allows to find possible cloud zone of embryo source that traditionally were disregarded. Finally, it is shown that the higher simulated hailstones always fall to ground near the updraft zone, independently of the cloud zones where the embryos were initialized. Consequently, these facts show that even though the results of one HSM may agree with the radar high echo regions, this finding may not definitely prove the accuracy of the predicted zone of initialized embryos.

6. REFERENCES

-Abraham F. F., 1970: "Functional dependence of drag coefficient of a sphere on Reynolds number". *J. Geophys. Res,* **79**, 3098-3100.

-Bohm J. P., 1990: "On the Hydrodynamics of cloud and precipitation particles". *PD*

-Castellano N, Scavuzzo C, Nasello O, Caranti G and Levi L., 1994: "A comparative study on hailstone trajectories using different motion equations, drag coefficients and wind fields". *Atmos. Res.*, **33**, 309-331.

-Foote G. B., 1984: "A study of hail growth utilizing observed storm conditions". *J. Climate Appl. Meteor,* **23**, 84-101

-Heymsfield A. J., 1978: "The characteristics of graupel particles in northeast Colorado cumulus congestus clouds". *J. Atmos. Sci.*, **35**, 284-295

-Heymsfield A. J., 1982: "A comparative study of the rates of development of potencial graupel and hail embryos in high plains storms". *J. Atmos. Sci.*, **39**, 2867-2897

-Heymsfield, A. J. and Kajikawa, M., 1987: "An Improved Approach to Calculating Terminal Velocities of Plate-Like Crystals and Graupel" *J. Atmos. Sci.*, **44**, 1088-1099.

-Knight N. C. and Heymsfield A. J., 1983: "Measurement and interpretation of hailstone density and terminal velocity". *J.Atmos. Sci.*, **40**, 1510-1516

-Levi L. and Lubart L., 1991: "Analysis of hailstones from a severe storm and their simulated evolution" *Atmos. Res.*, **26**, 191-211

- Locatelli J. P. and Hobbs, 1974: "Fall speeds and masses of solid precipitation particle" *J. Geopys. Res.*, **79**, 2185-2197

- Matson R. J. and Huggins A. W., 1980: "The direct measurement of the sizes, shapes and kinematics of fallings hailstone" *J. Atmos. Sci.*, **37**, 1107-1125

-Xu Jiau-Liu, 1983: "Hail growth in a three-dimensional cloud model". *J. Atmos. Sci.*, **40**, 185-203

-Zikmunda J. and Vali G., 1972: "Fall patterns and fall velocities of rimed ice crystals". *J. Atmos. Sci.*, **29**, 197-208

AN APPROXIMATION FORMULA FOR DROP/DROP-COLLISION EFFICIENCIES

K.D.Beheng

Institut für Meteorologie und Klimaforschung
Forschungszentrum Karlsruhe / Universität Karlsruhe, D-76021 Karlsruhe, Germany

1. INTRODUCTION

The collection kernel describing the collisional interaction of drops with radii a and A is defined by

$$K(a, A) = \pi (a + A)^2 E(a,A) \, | v(a) - v(A) | \qquad (1)$$

where E(a, A) is the collection efficiency and v(a), v(A) are the fall velocities of the drops. Whereas the terminal fall velocity can be expressed by proper mathematical relations (see e.g. Pruppacher and Klett, 1978) the collection efficiency, or strictly speaking, the collision efficiency is usually evaluated from tabulated values as compiled e.g. by Hall (1980).
In this study a parametric form of the collision efficiency is presented. Moreover, it will be shown that specific features appearing in the numerical solution of the stochastic collection equation (SCE) can be explained by a particular property of the parametric formulation of the collision efficiency.

2. PARAMETERIZATION OF THE COLLISION EFFICIENCY

The ***collision*** efficiency $E_1(a, A)$ is one factor of the collection efficiency E(a, A) generally defined by $E(a, A) = E_1(a, A) \times E_2(a, A)$ with $E_2(a, A)$ = coalescence efficiency.
Led by the tabulated values of E_1 it is found that E_1 can be parameterized by a separation ansatz of the form

$$E_1(a, A) = E_a(a) \times E_A(A) \qquad (2)$$

$$= \left[1 - \exp\left(-\mu\, a^2\right)\right] \times \left[1 - \exp\left(-\lambda\, A^4\right)\right]$$

where a, A are the radii of the smaller and the larger drop, respectively. The parameters are $\mu = 5 \times 10^5\ cm^{-2}$ and $\lambda = 10^{10}\ cm^{-4}$.
In Fig.1 a comparison of collision efficiency values calculated by Eq.(2) as well as by use of the tabulated values similar to Hall (loc.cit.) is presented. It can be seen that for the radii of the larger drops $A \geq 20\mu m$ and for $0.3 \lesssim q \lesssim 0.8$ with $q = a/A$ the agreement is sufficient. For $A \lesssim 20\mu m$ there are large differences as well as for $A \gtrsim 40\mu m$ and $q \lesssim 0.15$. Clearly the parametric equation (2) cannot show any decrease or increase of E_1 for q tending to 1.
The quality of the parameterization of E_1 presented should now be tested by its use in numerically solving SCE. This well - known equation has recently been investigated by Seeßelberg et al. (1996) who find that the numerical solution method proposed by Berry and Reinhardt (1974) is - amongst others - the best one so that it is adopted here. Briefly, this method consists of (i) a logarithmic transformation of the mass (or radius) range into integer space as well as (ii) of a transformation of the number density function into a corresponding mass density function g(J), J = 1,2,3 ... , given also in integer space. For details we refer to the two papers mentioned.

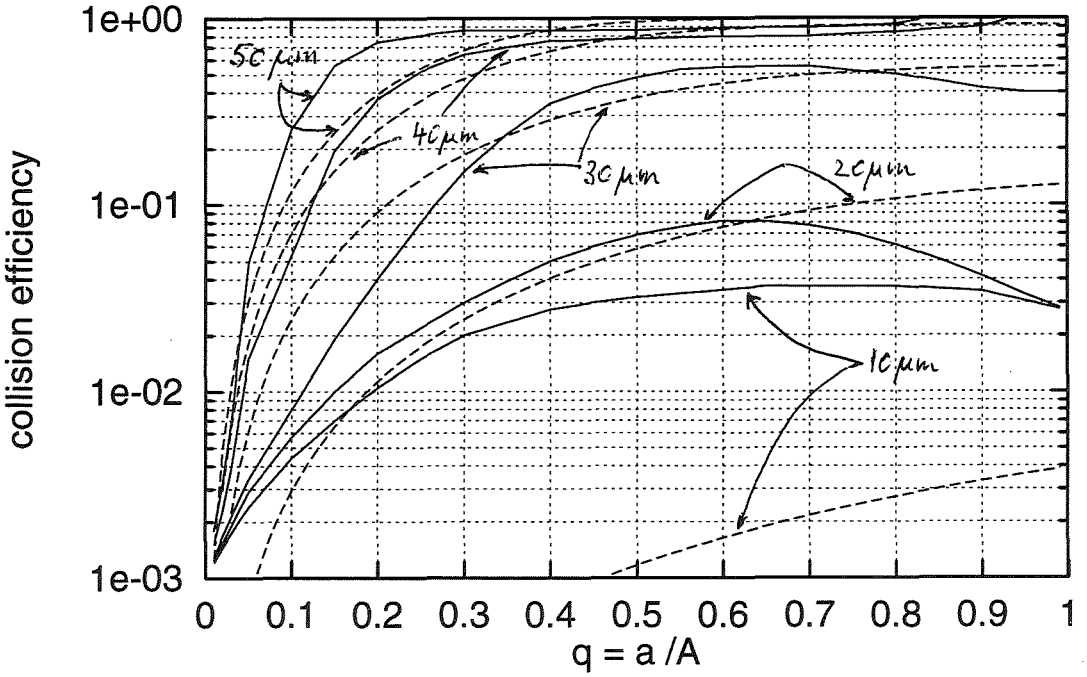

Fig. 1: Collision efficiency as function of q = a/A with a,A = radii of the smaller, larger drop: solid lines refer to calculations with tabulated values, dashed lines to those using Eq.(2). The radius of the larger drop A is indicated.

As initial drop spectrum we apply that originally used by Berry and Reinhardt (loc.cit.) with the parameter set: width parameter $\nu_o = 0$ (broad spectrum, Fig.2a) and $\nu_o = 3$ (narrow spectrum, Fig.2b), number density $N_o = 100\,cm^{-3}$ and mean radius $r_o = 14\,\mu m$. In both cases the liquid water content amounts to $L = 1.15 \times 10^{-6}\,g\,cm^{-3}$. The simulations are performed by assuming the coalescence efficiency to unity. The time step chosen is 1 s and the maximum simulation time amounts to 1800 s. Note that for longer simulation times the break-up process becomes more and more important. In order to clearly separate the effect of coagulation and break-up we have neglected the break-up terms here.

The results of the numerical simulations are shown in Fig.2. One can see that for the broad spectrum ($\nu_o = 0$) the overall agreement between both simulations is good. Note in particular that the evolving minimum is well met.

The comparison becomes worse if a narrow initial distribution is chosen (Fig.2b with $\nu_o = 3$). In that case the secondary maximum value is too low and the corresponding radius value is too small; in contrast, the value at the minimum of the function is too large. The radius position of the minimum value, however, is nearly the same.

As an extreme case we present a simulation where a constant g(J)-distribution is initially prescribed (Fig.3). Its integrals are : $N_o = 3.1 \times 10^3\,cm^{-3}$, liquid water content $L = 1.6 \times 10^{-6}\,g\,cm^{-3}$ and mean radius $r_o = 5\,\mu m$. After 1800 s simulation time the curve, calculated by use of tabulated collision efficiencies, shows a minimum at 56 μm whereas in case of using the parameterized collision efficiencies the minimum is found at 31 μm. This case study makes the deficiencies of the current parametric Eq.(2) obvious: Since for large drops and a small ratio q = a/A the parameterization Eq.(2) fails to well represent the tabulated efficiencies the time evolution of both cases differ considerably.

Nevertheless, if one orientates at the more realistic conditions exhibited in Fig.2 the parameterization works sufficiently.

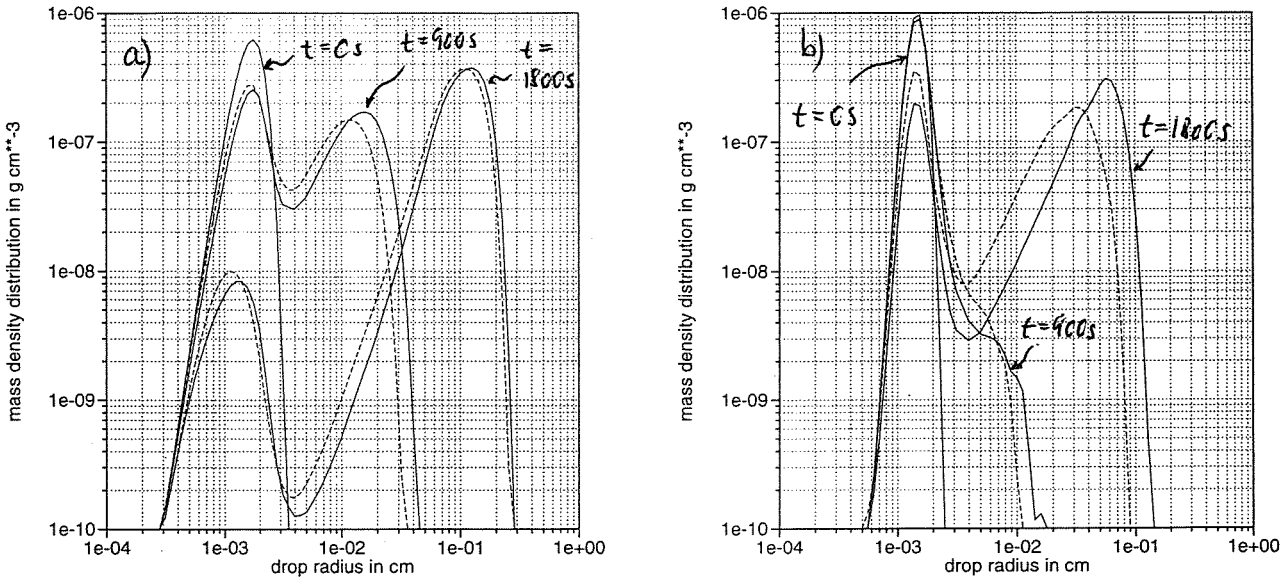

Fig. 2: Mass density distribution function (in its transformed version) in g cm^{-3} as function of drop radius in cm for simulation times as indicated. Solid lines refer to simulations with tabulated collision efficiencies, dashed lines to those using the collision efficiency parameterization Eq.(2). (a): width parameter $\nu_o = 0$, (b) $\nu_o = 3$.

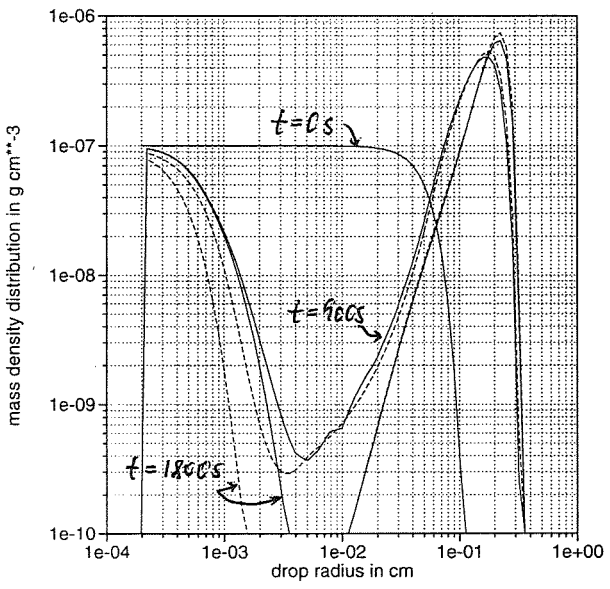

Fig. 3: Same as Fig.2, but for an initial almost constant mass density distribution function. For details see text. Line indication as in Fig.2.

It should be noted that the minimum of the g(J)-function which is, as mentioned, the transformed version of the genuine number number density function for which SCE is originally formulated, corresponds to a gentle convex curvature of the number density function at the same radius position where also the g(J)-minimum occurs.

3. THE MINIMUM CONDITION

After the determination of an analytical form of the collision efficiency (see Eq.(2)) and by inspecting numerous numerical solutions of SCE considering very different initial spectra it has been recognized that there seems an only small influence of the size distribution function on the shape of the spectrum attained after longer simulation times. This presumption is supported by solving SCE using collision efficiencies of unity. In that case (not shown here) the g(J)-spectrum develops no minimum.

Consequently it has been speculated that some property of the collision efficiency function is responsible for the typical minimum appearing at about 35 - 40 μm (cf. Fig.2).

In looking for a condition determining the minimum radius value it turned out that this radius appears there where the curvature of E_A is at maximum, i.e. $d^3E_A/dA^3 = 0$. The corresponding radius A_c follows then with

$$A_c = y_1^{1/4} \qquad (3a)$$

where

$$y_1 = 9/(8\lambda) + \left\{[9/(8\lambda)]^2 - 3/\left(8\lambda^2\right)\right\}^{1/2} \qquad (3b)$$

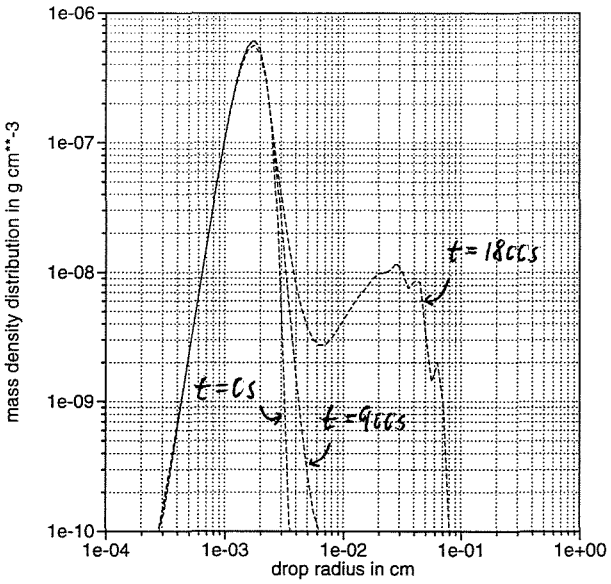

Fig. 4: Same as Fig.2a, but for $\lambda = 10^9\,cm^{-4}$ in Eq.(2). Simulation with parameterized collision efficiencies only.

Applying $\lambda = 10^{10}\,cm^{-4}$ yields $A_c = 38\mu m$. Inspecting Fig.2 confirms the correctness of the fact that at A_c the minimum is attained. In order to test this condition λ has arbitrarily given a value of $\lambda = 10^9\,cm^{-4}$ yielding then $A_c = 67\mu m$. A corresponding simulation is shown in Fig.4 where in fact this minimum shows up at this particular radius.
The rationale behind the development of the g(J)-minimum at the radius A_c given by Eqs.(3a,b) is that the strong slope of the collision efficiency function, especially that of E_A, causes, on the one hand, the development of the secondary maximum at early simulation times and, on the other hand, the steady deepening of the minimum for longer simulation times.

4. ATTEMPT OF A PARAMETERIZATION OF THE COLLECTION KERNEL

Encouraged by the results concerning the collision efficiency parameterization we finally report on an attempt to parameterize the collection kernel function. This, however, has found to be very difficult since, as is shown by Eq.(1), strong nonlinear terms comprise the whole collection kernel formula.

The best parameterization found was $K(a, A) = 4.3 \times 10^4\, A^{3.2}\, E_1(a, A)$ (cgs units) with E_1 from Eq.(2). In applying this relation the major deficiency is that too many drops with too large a radius are created. An improvement seems possible if a reliable and relative simple formula for the terminal fall velocity v(A) can be found which covers the whole radius range, say between 5 and 5000 μm.

5. REFERENCES

Berry, E.X., R.L. Reinhardt, 1974: An analysis of cloud drop growth by collection: Part I: Double distributions. J. Atmos. Sci., **31**, 1814-1824

Hall, W.D., 1980: A detailed microphysical model within a two-dimensional dynamical framework: Model description and preliminary results. J. Atmos. Sci., **37**, 2486-2507

Pruppacher, H.R., J.D. Klett, 1978: Microphysics of clouds and precipitation. D. Reidel Publ.Co., Dordrecht, 714 pp.

Seeßelberg, M., T. Trautmann, M. Thorn, 1996: Stochastic simulations as a benchmark for mathematical methods solving the coalescence equation. Atmos. Res., **40**, 33-48

THE MODIFIED KOVETZ AND OLUND METHOD FOR THE NUMERICAL SOLUTION OF STOCHASTIC COALESCENCE EQUATION

Elena N. Stankova , Mikhail A. Zatevakhin

International Institute for Interphase Interactions, St.Petersburg, Russia.

1. INTRODUCTION

Numerical simulation of convective cloud life cycle and its precipitation history depend essentially upon the manner in which microphysical processes are treated. Nowadays stochastic collection equation is used for the description of the time evolution of the droplet spectrum in the most of convective cloud models. Integration scheme for numerical solution of the stochastic coalescence equation must satisfy various requirements, the most important of which is the requirement of precise fulfilment of the mass conservation law. In fact, since the supersaturations in convective clouds do not usually exceed 1%, the amount of the water obtained by the condensation process can be comparable with the water content obtained at the expense of the error produced while calculating collection process . Also, it would be highly desirable if the droplet size range of interest could be represented by fewer size classes to reduce computer memory and processing time requirements. Reduction of the droplet size intervals number becomes particularly essential when one attempts to solve stochastic coalescence equation for droplet density function dependent on several parameters, on drop size and chemical content for example. In such situation the amount of the required computer resources increased greatly.

The present paper deals with the modification of the well - known Kovetz and Olund method, which allow to obtain good solution of stochastic collection equation at relatively low number of drop size intervals.

2. DESCRIPTION OF THE METHOD

The development of cloud droplet spectrum with time due to collection is described by the integral equation, written for the cloud drops density function $f(m)$ (number of drops per volume per mass interval dm at mass m):

$$\frac{\partial f(m)}{\partial t}=\frac{1}{2}\int_0^m K(m-m',m')f(m-m')f(m')dm' - f(m)\int_0^\infty K(m,m')f(m')dm'. \quad (1)$$

Here $K(m,m')$ is the collection kernel. The equation (1) can be rewritten in the following form (Voloshchuk 1984):

$$\frac{\partial f(m)}{\partial t} = \frac{1}{2}\int_0^\infty\int_0^\infty K(m',m'')\delta(m-m'-m'')f(m')f(m'')dm'dm'' - f(m)\int_0^\infty K(m,m')f(m')dm', \quad (2)$$

where $\delta(m-m'-m'')$ is the delta function.

It can be shown that (2) is the continuous analog of the formulas proposed by Kovetz and Olund (1969).

In the original Kovetz and Olund method the mechanism of redistributing the new drops into the nearest size classes was provided in such a manner as to preserve both droplet number and mass. The requirement of droplet number conservation is not, strictly speaking, necessary one, because particles number is not the integral of the stochastic coalescence equation, and its value must be calculated from the equation solution. If one omits this requirement, then the method can be modified by the following way.

Let m_i, $i = 0, 1,\ldots, N$ be the discrete points along the m axis, $m_0 = 0$, then unlike the original method, one can consider instead of droplet number the magnitude of M_i - mass of the droplets in the interval $[m_{i-1/2},m_{i+1/2}]$, where $m_{i\pm1/2}=(m_i+m_{i\pm1})/2$:

$$M_i=\int_{m_{i-1/2}}^{m_{i+1/2}} mf(m)dm \approx m_i f_i \Delta m_i,$$
$$f_i=f(m_i),\ \Delta m_i=m_{i+1/2}-m_{i-1/2}.$$

Then the equation for M_i can been written in the following form:

$$\frac{dM_i}{dt}=S_i^+-S_i^-, \qquad (3)$$

$i = 1, 2,..., N - 1.$

The item S_i^-, which describes the departure of the particles from the given interval, can be obtained by the following transformation of the second term in the right hand side of the equation (2):

$$S_i^-=\int_{m_{i-1/2}}^{m_{i+1/2}} mf(m)\int_0^\infty f(m')K(m,m')dm'dm$$
$$\approx M_i\sum_{j=1}^{N}\int_{m_{j-1}}^{m_j} K(m_i,m')f(m')dm'$$
$$\approx\frac{M_i}{2}\sum_{j=1}^{N}(K(m_i,m_{j-1})f_{j-1}+K(m_i,m_j)f_j)(m_j-m_{j-1})$$
$$=\frac{M_i}{2}[K(m_i,m_0)f_0(m_1-m_0)+2\sum_{j=1}^{N-1}K(m_i,m_j)M_j/m_j$$
$$+K(m_i,m_N)f_N(m_N-m_{N-1})]=\sum_{j=1}^{N-1}S_{ij}^-,$$

where $S_{ij}^-=K(m_i,m_j)M_iM_j\ /\ m_j$.

While obtaining the last relation, the first term in the square brackets is neglected, as it was suggested that $m_0 = 0$ and the mass appeared as a result of the collision of the droplets with masses m_0 and m_i does not contribute to the droplet mass redistribution process. The last term in the square brackets is neglected as it is suggested that at the sufficiently high values of m_N $f(m_N)\to 0$. The last condition will be discussed in detail later.

The term S_i^+ can be derived by applying the same redistribution procedure as proposed by Kovetz and Olund (1969). Let us locate mass interval $m_k<m_i+m_j\le m_{k+1}$ and calculate the following values:

$$S_{ijk}^+=\frac{m_{k+1}-m_i-m_j}{m_{k+1}-m_k}S_{ij}^-,$$
$$S_{ijk+1}^+=\frac{m_i+m_j-m_k}{m_{k+1}-m_k}S_{ij}^-,$$

The values of S_k^+ can be obtained by summing up S_{ijk}^+ over all values of i and j.

3. NUMERICAL RESULTS

The usefulness of the scheme outlined above was tested by comparing numerical results with the analytic solution, proposed by Golovin (1963) and with the results obtained by using the original Kovetz and Olund method.

In the calculations collection kernel was taken proportional to the sum of droplet masses (Golovin's kernel) (Golovin, 1963). The discrete points along the m axis were chosen according to the procedure proposed by Berry (1967):

$$m_i=m_1\exp(3(i-1)/i_0),\ i_0=3(N-1)/(\ln m_N-\ln m_1).$$

The parameters of initial spectrum, collection kernel and droplet size range were the same as used by Berry (1967).

The results of original Kovetz and Olund method calculations were obtained by using scheme fully coinciding with the described above with the exception of using $N_i=f_i\Delta m_i$ instead of M_i, $S_{ij}^-=K(m_i,m_j)N_iN_j$ and this value was multiplied by the coefficient 1/2 while calculating the final magnitude of S_k^+ .

Fig.1 describes the results of numerical experiments, concerning the solution of the equation (3) in comparison with analytical Golovin's solution. The number of drop mass intervals N varies from 101 to 11. Droplet spectrum there is displayed by the droplet mass density function with respect to the natural logarithm of droplet radius $g(\ln r)=3m^2f(m)$. The results correspond to t = 30 min.

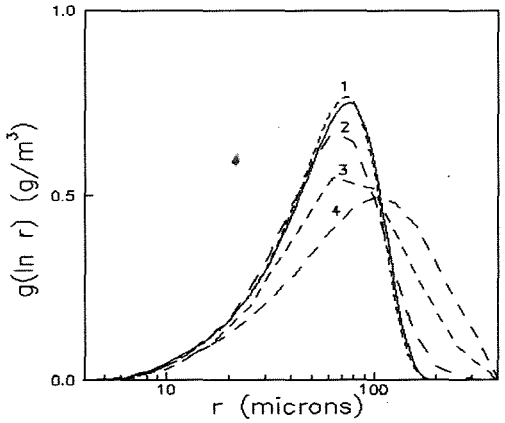

Fig. 1. Droplet mass density function. Solid line - analytic solution, dashed lines - numerical solution. 1 - N=101, 2 - N=21, 3 - N=11, 4 - original method of Kovetz and Olund, N=21.

As it can be seen from the figure, when the number of droplet size intervals N is equal to 101, the modified method reproduces analytic solution with high

accuracy. The original method gives the same result (not shown in the picture). At $N = 21$ modified method gives better approach to the analytic solution than that, obtained by original scheme. And even at $N = 11$ modified method gives rather reasonable solution, when the solution obtained by Kovetz and Olund method completely diverges from the analytic one.

The scheme, presented above, constructed in such a way that at $m_N \to \infty$ it preserves mass precisely. However while numerical simulation, magnitude of m_N always has finite value. At this situation the problem of proper mass redistribution appear, as it is evident that at any grid, effect of collision can result in the appearance of the drop with mass that exceeds m_N.

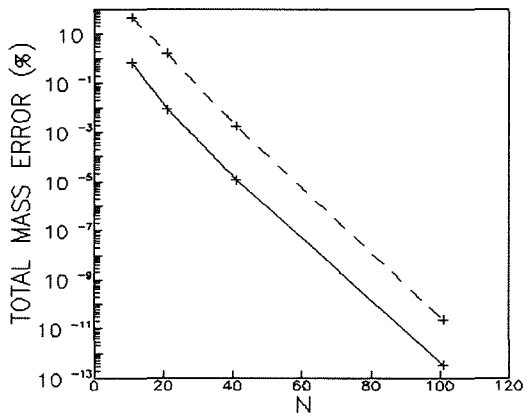

Fig. 2. Total mass errors for different mass interval number. Solid line - modified method. Dashed line - original Kovetz and Olund method.

There are two approaches of this problem solution. The first one is as follows: the point m_N can be included in the calculations with the appropriate mass interval, to which all the particles with masses greater than m_N can be prescribed. This method was realized and it appeared to preserve mass precisely within the limits of the computer. However on coarse grids such approach resulted in the noticeable distortion of the spectrum at the low end of the distribution. That is why the scheme, outlined above, when M_N was set equal to zero and particles were redistributed only under the condition $m_i+m_j<m_N$ was used and it gave much better results. Fig.2 shows the dependency of the total mass error on the number of size interval obtained by modified method in comparison with the original Kovetz and Olund method. It is easy to see that the modified method preserved mass with better accuracy and less suffered from excessive "anomalous spreading" than original method (it can be clearly seen in the Fig.1 also). Besides, the comparison with analytic solution shows that modified method permits to calculate the total droplet number more precisely than Kovetz and Olund method.

4. REFERENCES

Berry, E.X., 1967: Cloud droplet growth by collection. *J. Atmos. Sci.*, **24**, 688-701.

Golovin, A. M., 1963: The solution of the coagulation equation for cloud droplets in a rising air current. *Bull. Acad. Sci. USSR, Geophys. Ser.*, **No. 5**, 482-487.

Kovetz, A., and B. Olund, 1969: The effect of coalescence and condensation on rain formation in a cloud of finite vertical extent. *J. Atmos. Sci.*, **26**, 1060-1065.

Voloshchuk, V.M., 1984: *The Kinetic Theory of Coagulation.* Leningrad, Gidrometeoizdat, 284 pp.

SOUTHERN OCEAN CLOUD EXPERIMENT: OBSERVATIONS OF MARINE STRATOCUMULUS IN AN UNPOLLUTED ENVIRONMENT

R. Boers, J. B. Jensen, J. L. Gras, P. B. Krummel, S.-H. Lee

Division of Atmospheric Research, CSIRO, Aspendale, Victoria 3195, Australia

1. INTRODUCTION

Charlson *et al.* (1987) suggested that cloud albedo is naturally regulated by the emission of dimethyl sulfide (DMS) by oceanic phytoplankton. DMS is regarded as the precursor of Cloud Condensation Nuclei (CCN) which in turn control the concentration of cloud droplets. Since the cloud droplet concentration controls cloud optical depth and hence cloud albedo, the hypothesis suggests a possible climate feedback loop connecting DMS emissions to cloud albedo. One method to test this hypothesis is to study the seasonal variations of all of these quantities in unpolluted air. The concentration of CCN recorded at the Cape Grim Baseline Air Pollution Station (CGBAPS, 40° 41' S, 144° 41' E) over a period of 15 years under conditions where the sampled air was assured to be almost devoid of anthropogenic influences has been observed to go through a distinct seasonal cycle with a peak in early January, and a minimum in early July. The seasonal cycle in CCN is in phase with locally observed seasonal cycles in DMS (Gras, 1990; Ayers and Gras, 1991; Ayers *et al.*, 1991), and with seasonal cycles in satellite derived stratocumulus cloud optical depth (Boers *et al.*, 1994). However, none of these observations has shown any light on the microphysical properties of stratocumulus clouds which are the connecting link between CCN and cloud albedo.

The Southern Ocean Cloud EXperiment (SOCEX) has been designed to overcome this problem by studying the seasonal variation in the microphysical and radiative properties of stratocumulus clouds in an unpolluted environment. Clearly, any evidence of a natural seasonal variability in the microphysical structure of these clouds would underpin the Charlson *et al.* (1987) hypothesis. The venue of the experiment was the Southern Ocean just upwind from CGBAPS. SOCEX consisted of two experimental phases: one in the winter of 1993 (July), when the cycle in DMS and CCN was near its minimum, the other in summer (January / February 1995), when the cycle was near its maximum.

2. INSTRUMENTS AND FLIGHT PLANS

The main instrument platform was the F-27 aircraft formerly owned by CSIRO, which was fitted with a comprehensive set of instruments designed to capture the microphysical structure of water clouds at high resolution. The basic set of cloud probes consisted of a PMS Forward Scattering Spectrometer Probe (FSSP), a PMS 2D-C probe, a CCN counter, broad band pyranometers and pyrgeometers, and a standard set of instruments to record the state variables.

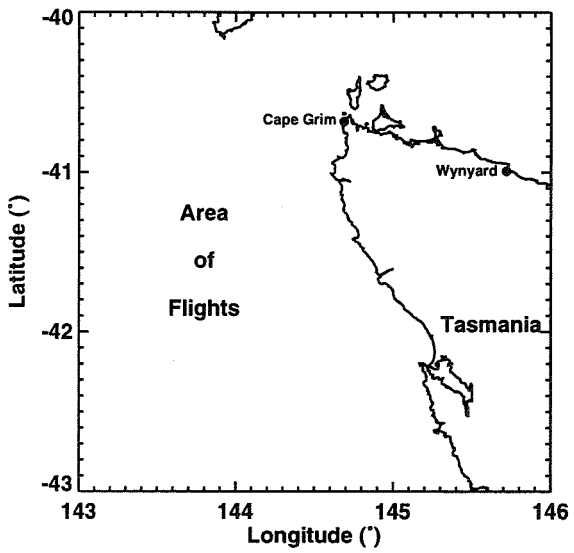

Figure 1. Map of the area where SOCEX was conducted

Figure 1 shows the area where the experiment took place. Cape Grim is located at the northwestern tip of Tasmania about 300 km south of the mainland of Australia.

The prerequisites for aircraft flights were the occurrence of stratocumulus clouds within 150 km from the coast of Tasmania, and the existence of 'baseline' conditions. Baseline conditions occur when the wind direction at CGBAPS is between 190° and 280°. Satellite imagery was used as the primary guidance tool for determining the exact geographic location where the aircraft stacks were to be flown. During the 1.5 to 2 hours on station one to two complete aircraft stacks were flown, consisting of cross-wind flight legs of 40 km length, at levels above the cloud, inside the cloud, near cloud base and near the surface. A total of 80 hours of flying time was available (40 hours per season) spread over 16 flights.

In the end only 12 flights (6 in winter, 6 in summer) were judged to be executed in truly baseline conditions, and analysed in terms of the microphysical and radiative structure. The flights are summarised in Table 1.

Winter 1993	July 16 (morning)
	July 16 (afternoon)
	July 19
	July 20
	July 26 (morning)
	July 26 (afternoon)
Summer 1995	February 1 (morning)
	February 1 (afternoon)
	February 6
	February 8 (morning)
	February 8 (afternoon)
	February 9

Table 1. Summary of aircraft flights during SOCEX

3. ATMOSPHERIC CONDITIONS

Northwest Tasmania is situated in the 'roaring forties'. As a result it usually exposed to a quick succession of high and low pressure systems. Averaged over many years, the classical winter position of the dominant high pressure system is over central Australia, while during summer it is displaced towards the south over the Australian Bight region. The frequent movement of the dominant high pressure systems means that the occurrence of stratocumulus clouds (often behind cold front passages) is not always guaranteed, in particular in winter months, when Cape Grim is located closer to the dominant low pressure cell over the Southern Ocean. The difference in synoptic conditions between summer and winter is reflected in the cloud conditions observed during SOCEX: Three of the winter flights took part in a stratocumulus capped boundary layer (16, 20 July), while the other three were conducted in a convective cumulus capped boundary layer; on the other hand, all summer flights were conducted in stratocumulus-capped layers, although during one flight (6 February), the cloud layer was very deep (1000 m) and convective.

Of all baseline days that were sampled only one day (16 July 1993) can be considered to represent a classical well-mixed stratocumulus capped boundary layer. The clouds observed on the other days were decoupled from the surface boundary layer. However, the degree of decoupling as judged from the thermodynamic profiles and cloud conditions varied markedly. Sometimes the decoupling was weak with no perceptible thermodynamic jumps below cloud base (20 July 1993), sometimes it was very distinct (1 February 1995) with potential temperature jumps of close to 1 K.

4. DRIZZLE

Clouds were observed to precipitate on all days. Frequently, the precipitation droplets contributed 30 to 70 % of the total liquid water present in the clouds. Furthermore, none of the observed cloud liquid water profiles followed the predicted adiabatic profile, implying that a significant portion of the potentially available liquid water was already removed from the clouds, presumably by precipitation processes. The impact of drizzle on the cloud microphysical and radiative structure is profound. The production of drizzle droplets from suspended cloud droplets removes a large portion of the geometric cross-sectional area of the cloud responsible for the scattering of light. The result is a reduction in the optical depth of the cloud. For the winter clouds (SOCEX I) Boers *et al.* (1996) calculated a reduction of up to 18 % in cloud albedo due to this process. For the summer clouds, the overall influence of drizzle on cloud albedo was less than for winter clouds. The largest precipitation flux was recorded on 26 July 1993, a winter case study.

5. SEASONAL DIFFERENCES

The motivation for the experiment was to examine seasonal differences in the microphysical and optical properties of the boundary layer clouds. Therefore, of primary interest are observations of the seasonal differences in droplet number concentration N (drizzle excluded), cloud droplet effective radius r_{eff} (drizzle excluded), and the cloud droplet extinction coefficient σ . The cloud optical depth τ is the height integral of σ and proportional to the one-third power of N. So, seasonal changes in N and σ directly affect τ and the cloud albedo. Both N and r_{eff} were measured with the FSSP.

The analysis procedure consisted of determining average cloud base pressure for each of the six case studies for each of the summer and winter experiments. Next, the values of both N and r_{eff} were averaged in 10 hPa bins. The procedure yields average vertical profiles for N and r_{eff} for both the summer and the winter campaign. The results presented below are based on a preliminary calculation using the averaged for each day. The final results will be published at a later date.

Figure 2 shows the results for N. N is the highest near cloud base, and is steadily decreasing with pressure above cloud base. This characteristic decrease is probably due to drizzle formation which depletes the suspended cloud droplets near the top of the clouds. The winter and summer profiles are well separated. Near cloud base there is more than a factor of three difference between the winter and summer figures (27 and 93 cm^{-3}). These numbers are almost identical to earlier calculations by Boers *et al.* (1994) of 35 and 92

cm^{-3}, that were based on 10 year averaged baseline values of CCN reported at CGBAPS.

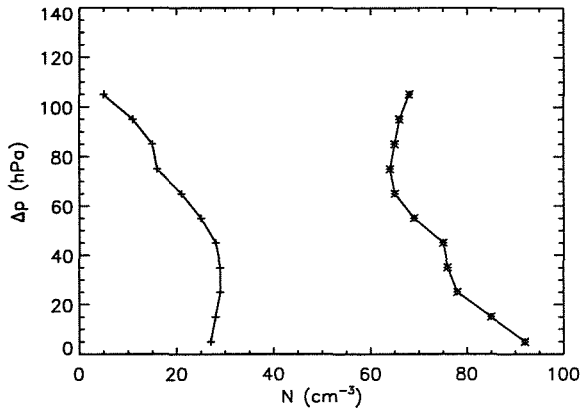

*Figure 2. Droplet number concentration as a function of the pressure above cloud base. The + represents winter values, the * represents summer values.*

Figure 3 shows the results for r_{eff}. r_{eff} is increasing with altitude as would be expected when cloud droplet grow larger above cloud base. Near cloud top, the growth rate tapers off. As was found for N there is a very significant difference between the summer and winter results. On the average the fraction ($r_{eff, winter}$/ $r_{eff, summer}$) = 1.42 which corresponds well with (N_{summer} / N_{winter})$^{1/3}$ = 1.39 .

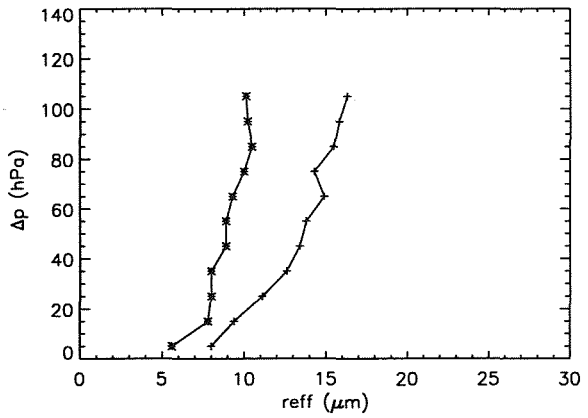

*Figure 3. Effective radius as a function of pressure above cloud base. The + represent winter values, the * represent summer values.*

Since the optical depth is a function of N and the depth of a cloud, and because variations in cloud depth are caused by external factors, a straight comparison of the optical depths of the winter and summer clouds would yield only limited information.

Figure 2 and 3 indicate that for the same cloud depth the optical depth in summer is larger than in winter by a factor of about 1.4, all other factors being equal.

This information can now be used to compute the impact of the seasonal differences in cloud microphysical properties on cloud albedo. The approach taken was to insert a cloud in a mid-latitude atmosphere thermodynamic profile and compute cloud albedo. The microphysical properties of the cloud were determined from Figure 2 and 3.

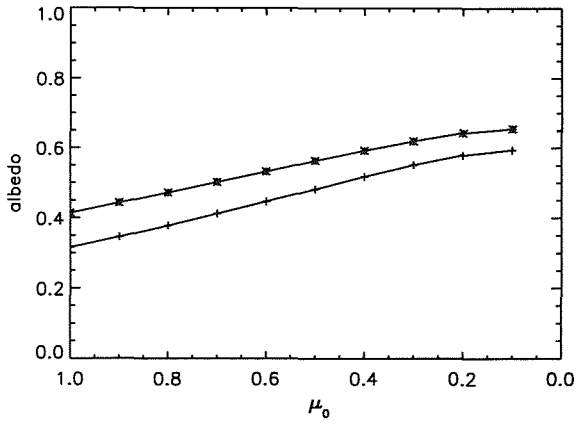

*Figure 4. Albedo as a function of the cosine of solar zenith angle μ_0. The + represent calculations for the winter optical depth, the * represent the calculations for the summer optical depth*

We used a standard 24-band two-stream delta-Eddington model (Boers and Mitchell, 1994) and fixed the cloud depth to roughly 300 m. Given the winter profiles of N and r_{eff} from Figures 2 and 3, this yield an optical depth of 7.3. From the same Figures this implies fixing the summer optical depth to 10.4. For these two optical depths the albedo was calculated for a range of sun angles. The results are plotted in Figure 4.

Figure 4 clearly shows the profound impact on cloud albedo of the seasonal differences in droplet number concentration. The true sensitivity of cloud albedo to the seasonal variation in droplet concentration can be calculated by finding the two albedo values intersecting the two plotted curves in Figure 4 at specific values of the cosine of solar zenith angle. For example, for a typical value of $\mu_0 = 0.5$ in Figure 4, the cloud albedo S_{winter} = 0.482, while the cloud albedo S_{summer} = 0.563. This represents an increase of 17 % from the winter to the summer value. These are very large values. With a low level cloudiness of 50 to 70 % over the Southern Ocean, this result suggests a natural variability of more than 10 % in overall albedo, which is entirely due to natural variability in droplet number concentration in boundary layer clouds. Albedo is a function of μ_0 as

well, but that simply reflects the seasonal changes in sun angle.

The values, that were chosen for the summer and winter optical depths, are representative for typical stratocumulus clouds (Boers *et al.*, 1994). Since cloud albedo increases non-linearly with cloud optical depth, and will eventually become asymptotically constant for very large values of the optical depth, this implies that the percentage change in cloud albedo will decrease with increasing optical depths.

6. CONCLUSIONS

The twelve flights from which we show the results in this paper were conducted under baseline conditions. Baseline conditions exist when the wind direction at Cape Grim is from an angle section where it can be reasonably assured that the sampled air has traversed long distances over the ocean. Therefore, it can be assured that it is mostly devoid of anthropogenic injection of aerosol and CCN from the surface. Despite this lack of anthropogenic influence the results from our case studies clearly indicate a substantial variation of microphysical and optical properties of boundary layer clouds between summer and winter months. The difference is almost exactly what was predicted based on the seasonal changes in CCN that have been observed at Cape Grim, and which have been demonstrated to be in coherence with seasonal changes in the injection of DMS into the atmosphere. Therefore, the preliminary conclusion of the experiment is that a biogenic influence on the microphysical and radiative properties of the boundary layer clouds is highly likely. This result would therefore seem to indicate that the hypothesis of Charlson *et al.* (1987) of a natural climate feedback loop connecting DMS to cloud albedo is correct.

7. ACKNOWLEDGMENTS

The staff at CGBAPS is gratefully acknowledged for their work in developing and maintaining instruments at Cape Grim for close to two decades. SOCEX would not have been possible without the dedication of many staff at the Division of Atmospheric Research. The experiment was partly funded from contributions from CSIRO's Institute of Natural Resources and Environment, CSIRO's Office of Space Science and Applications, the Cooperative Research Center for Southern Hemisphere Meteorology at Monash University and Colorado State University.

8. REFERENCES

Ayers, G. P, and J. L. Gras, 1991: Seasonal relationships between cloud condensation nuclei and aerosol methanesulphonate in marine air. *Nature*, **353**, 834 - 835

Ayers, G. P., J. P. Ivey, and R. W. Gillett, 1991: Coherence between seasonal cycles of dimethyl sulphide, methanesulphonate and sulphate in marine air. *Nature*, **349**, 404 - 406

Boers, R., and R. M. Mitchell, 1994: Absorption feedback in stratocumulus clouds: Influence on cloud top albedo. *Tellus*, **46A**, 229 - 241

Boers, R., G. P. Ayers, and J. L. Gras, 1994: Coherence between seasonal cycles in satellite observed cloud optical depth and boundary layer CCN concentrations at a mid-latitude Southern Hemisphere site. *Tellus*, **46B**, 123 - 131

Boers, R., J. B. Jensen, P. B. Krummel, and H. Gerber, 1996: Microphysical and radiative structure of wintertime marine stratocumulus clouds over the Southern Ocean. *Quart. J. Royal Meteor. Soc.*, in press

Charlson, R. J., J. E. Lovelock, M. O. Andreae, and S. G. Warren, 1987: Oceanic phytoplankton, atmospheric sulphur, cloud albedo, and climate. *Nature*, **326**, 655 - 661

Gras, J. L., 1990: Cloud condensation nuclei over the Southern Ocean. *Geophys. Res. Letters*, 1565 - 1567

STUDY OF THE ANTHROPOGENIC SULFATE AEROSOLS INDIRECT EFFECT IN MARINE STRATOCUMULUS CLOUDS

Zena N. Kogan, Yefim L. Kogan and Douglas K. Lilly

Cooperative Institute for Mesoscale Meteorological Studies
University of Oklahoma, Norman OK

1. INTRODUCTION

The three-fold anthropogenic increase of sulfur emissions into the atmosphere results in increased sulfate aerosol concentrations, mainly in the Northern Hemisphere (NH). These aerosols scatter and absorb solar radiation directly and increase reflection indirectly by changing cloud microstructure (Charlson et al. 1992, Penner et al. 1994, Schwartz and Slingo, 1995). We evaluate the "indirect", i.e. cloud-induced, shortwave effect of anthropogenic sulfate aerosols in marine stratocumulus clouds. The latter have a pronounced climatic effect due to their high reflectivity compared to the sea surface, their large global coverage, and near-absence of greenhouse effects. The indirect effect is thought to be less pronounced in continental clouds, in part because these clouds evolve in more abundant CCN environments and, therefore, are less susceptible to the aerosol augmentation, and in part because the reflectivity of deep convective clouds and storms which prevail over land is less affected by the anthropogenic aerosol changes confined mostly to the boundary layer.

In this paper we evaluate the indirect forcing of aerosols, as well as its seasonal cycle, using observation-derived cloud climatology. We also evaluate contributions to the indirect effect due to insolation, sulfate burden, cloud amounts and types, as well as estimate the role of uncertainties in determination of the cloud albedo susceptibility.

2. METHOD

Previous estimates of the indirect effect (Charlson et al. 1992, Boucher and Rodhe 1994, Jones et al. 1994) rely either on simplified assumptions about cloud layer microphysics and their global distribution or on global climate model (GCM) simulations. Given the inherent difficulties of GCMs in predicting cloud properties and, consequently, the resulting uncertainties in the estimate of the indirect forcing, we rely in this study on the empirical data on cloud cover and frequency taken from the 30 year data on global stratocumulus cloud climatology (Warren et al. 1988, Hahn et al. 1990). Other input parameters include the data on sulfate aerosol pollution taken from a 3-D chemical transport model (Langner and Rodhe 1991) and an evaluation of stratocumulus cloud albedo susceptibility based on a large eddy simulation cloud model (Kogan et al. 1995).

This model combines the 3-D LES dynamics with explicit formulation of the processes of nucleation, condensation, evaporation, and coalescence. The LES model is run with a range of input CCN values similar to those found in marine environments and a cloud depth of about 300-500 m. Two numerical simulations were made with the initial CCN count of 25cm^{-3} and 75 cm^{-3} (Woodcock, 1957). A more polluted marine atmosphere was simulated in the third case based on the CCN spectrum with a total count of 328 cm^{-3} (Warner, 1969). The cloud droplet number varies with the input CCN content, but also locally within the modeled domain due to buoyant updrafts and downdrafts and their effects on cloud microphysics. The high resolution simulations, using grid spacings of 30-50 m, provide about 5000 vertical profiles of cloud drop spectra and corresponding radiative parameters, comprising a wide range of dynamical and microphysical conditions.

For each of these combinations of input parameters, we concurrently calculate the column averaged drop number concentration and cloud albedo. Based on regression analysis of the constructed data set, we then determine the cloud albedo susceptibility dA/dN. This quantity, first introduced by Twomey (1991), determines the indirect radiative forcing. Fig. 1a shows the susceptibility dA/dN derived from the LES model data together with the susceptibility estimated from aircraft observations (Taylor and McHaffe 1994). The modeled and observed values agree rather well and demonstrate that low droplet count clouds are much more susceptible to changes in drop concentration than are those with high droplet counts. The range of susceptibilities derived from the model coincides with that obtained by Platnick and Twomey (1994) from satellite observations. They found that susceptibilities retrieved with the 3.7 mm channel on the AVHRR in California stratus vary from $0.5*10^{-3}$ to $10*10^{-3}$ cm^3. In addition to drop number, the susceptibility is also a function of liquid water path. The scatter in Fig. 1a essentially represents susceptibility dependence on liquid water path in the investigated 30-180 gm^{-2} range.

The data points on the plot can be reasonably approximated by the best fit curve:

$$dA / dN = C N^k \qquad (1)$$

where C = 0.044 and k = -0.86. This relation is in good agreement with the one derived by Twomey (1991) based on a radiative model that predicts

susceptibility to be an inverse function of drop concentration. The C and k coefficients are somewhat different for different cloud layer depths, but except for cloud layers of order 1 km and deeper, where the albedo becomes insensitive to drop number, the qualitative effects are similar. Fig. 1a also depicts two curves with C and k coefficients equal to (0.069, -0.92) and (0.015, -0.65) respectively. The curves give the upper and lower bound for the susceptibility function and are used to estimate the sensitivity of the indirect forcing to uncertainties in this parameter.

To compute distribution of cloud drop concentration over the globe we use the sulfate aerosol distributions obtained from the Langner and Rhode (1991) "slow oxidation" chemical model. This is a global transport model of the tropospheric sulfur cycle, with a 10 degree resolution in longitude and latitude and ten vertical layers. All pollution sources in the model are divided into anthropogenic and natural emissions. The anthropogenic sources arise from fossil fuel combustion emissions and various industrial processes. In addition, 90% of biomass burning is considered as anthropogenic. Four types of natural emissions are considered: DMS in oceans, emissions from plants and soils, volcanoes, and 10% of natural biomass burning.

Following Kiehl and Briegleb (1993) and Jones et al (1991), we assume a log-normal size distribution of sulfate aerosol number concentration with a median radius of 0.05 micron and a standard deviation of 2. Consistent with Jones et al (1991), we also assume that half of the column integrated aerosol mass is located in the stratocumulus-topped boundary layer and, thus, translates to sulfate CCN changes. To calculate the number of cloud drops, N, formed on the sulfate CCN with concentration N_{ccn}, we use the analytical fit of Jones et al (1991) to the empirical data obtained by Martin et al (1994) in various regions of the globe:

$$N = 375\,(1 - \exp[\,-2.5 \times 10^{-3} N_{ccn}\,]) \qquad (2)$$

Finally, the indirect shortwave radiative effect is calculated following the approach of Charlson et al (1992). The power function (1) that defines cloud albedo susceptibility allows exact integration over N and, thus, determination of cloud albedo augmentation due to changes in drop concentration between the pre-industrial and modern environments. The cloud albedo augmentation is further multiplied by factors that account for cloud cover and frequency. The planetary albedo augmentation at the top of the atmosphere (TOA) and, hence, the net TOA radiation flux change also account for the attenuation of the downward and reflected solar flux, as well as absorption and reflection by high and mid altitude clouds when they overlap the low layer stratocumulus.

3. RESULTS

As Fig. 1b shows, the strongest pollution is in the NH within the 30^{o} - 70^{o} N zone, produced by major industrial sources in Europe, north-eastern North America, and China. The anthropogenic augmentation to natural sources is about 5 times less in the SH, but the susceptibility of the SH clouds (Fig. 1b) is more than double that in the NH. The quite large forcing in the SH mid latitudes (Fig. 1c) is evidently due to the cleaner clouds and greater cloud susceptibility there. Although industrial sulfate in the NH is about 3 times larger than in the SH, the hemispheric forcings differ only by 40% (NH=-1.3 Wm^{-2} and SH=-0.9 Wm^{-2}). It is interesting that the extreme values of the zonal forcing

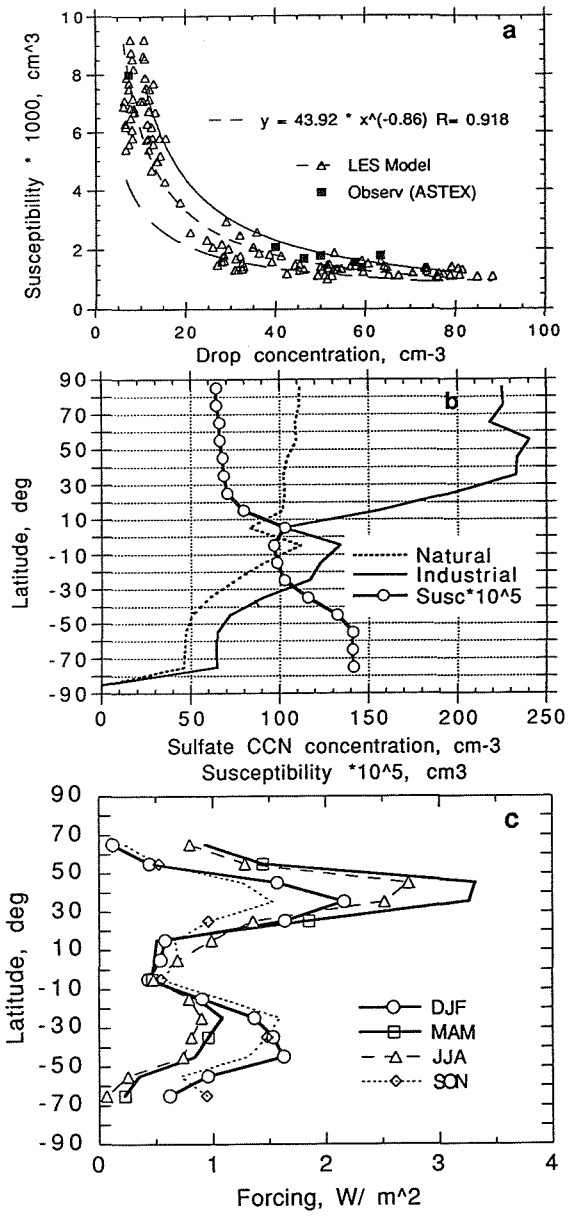

Fig. 1. (a) Cloud albedo susceptibility as a function of drop concentration. Triangles show the data obtained from the LES cloud model, squares represent estimates derived from the ASTEX field observations (Taylor and McHaffe, 1994). (b) The zonally averaged profiles of the sulfate aerosol concentration and cloud albedo susceptibility. The dashed line shows contribution from natural sources only, while the solid line from all sources (natural plus anthropogenic). The solid line with circles depicts the zonal cloud susceptibility (multiplied by a factor of 10^5). (c) The seasonal variations of the zonally averaged profiles of the shortwave forcing (Wm^{-2}) due to the indirect effects of anthropogenic sulfate aerosols.

are much greater in the NH (-3.3 W m^{-2} and -1.5 W m^{-2}) than in the SH (-1.7 W m^{-2} and -0.9 W m^{-2}) (Fig. 1c). Regionally, the forcing varies over two orders of magnitude, from -0.08 W m^{-2} near the equator to about -8 W m^{-2} near the major pollution sources in Europe and North America. The maximum radiative forcing lies within the 30°-50° N zone (see Fig. 1c), consistent with the high anthropogenic pollution in these areas.

The global forcing has rather weak seasonal variations with a maximum of -1.2 W m^{-2} in the spring and minimum of -1.0 W m^{-2} in the fall (Fig. 2a). It, however, represents a balance between hemispheric forcings that exhibit significant seasonal changes (Fig 1c and 2a,b). The contribution of the NH forcing to the global forcing is about 70% during the NH spring and summer, but only 40%-50% during the NH fall and winter. The hemispheric forcing seasonal cycle is largely determined by the changes of insolation and major sources of sulfate emissions.

Fig 2a and b show contributions to the indirect forcing from insolation, sulfate burden, and cloud amount and frequency. The different curves illustrate the role of different factors in the forcing seasonal cycle. The solid lines without marked points (NH and SH) are the benchmark cases with all factors included and represent hemispheric averages. The solid line with black squares (GL) represents the global forcing. Line with diamonds (INS) represents the case when only the insolation varies with season (sulfate and cloud amounts are kept fixed at the NH winter level); the line with open squares (INS+Cl) represents the case when insolation and cloud amounts follow their seasonal cycle (sulfate amounts are kept fixed at the winter level); the line with open circles (Su+Cl) represents the case when sulfate and cloud amounts vary with season (insolation is kept fixed at the winter level). The effect of insolation in the NH is offset by the seasonal variations in the sulfate amounts as demonstrated by the difference between the cases "INS" (variation in insolation only) and "Su+Cl" (variation in sulfate and cloud amounts). The cloud seasonal changes (illustrated by the difference between the cases "INS" and "INS+Cl") have a rather minor impact in the NH due to relatively small seasonal variations in cloud amounts (Warren et al. 1988, Hahn et al. 1990). Thus, the seasonal variations of the NH forcing are mainly determined by insolation and the level of anthropogenic pollution, which is much greater in the NH winter. The decrease in anthropogenic sulfate burden in the NH from winter to summer offsets the increase in insolation and results in the maximum forcing shift to spring.

In the SH the major sulfate source is marine phytoplankton emission (Charlson et al. 1987). As it decreases from the SH summer to winter, it makes the clouds cleaner and, consequently, more susceptible. As our calculations show, the decrease in sulfate burden nearly cancels the increase in cloud albedo susceptibility, resulting in a negligible seasonal sulfate effect (in Fig. 2b the line with squares coincides with the solid line). The effect of cloud amounts is demonstrated by the difference between the cases "INS" and "INS+Cl". The seasonal variations in cloud amounts result in up to

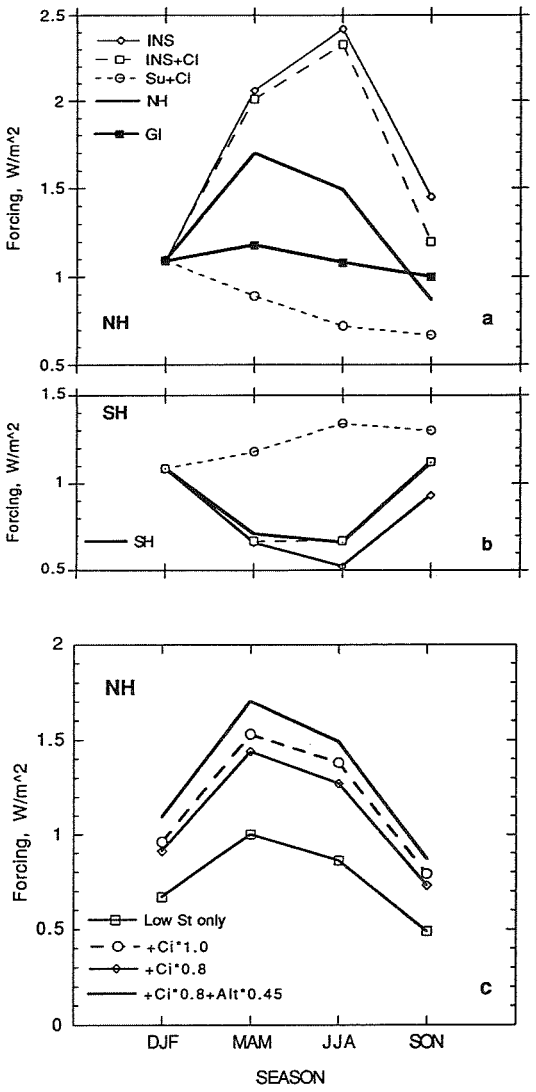

Fig. 2. The seasonal variations of the forcing in the Northern (a) and the Southern (b) Hemispheres. See text for details. (c) The contribution to the forcing in the NH from different cloud types. See text for details.

30% variation in the indirect forcing. This is significantly larger than in the NH, again due to larger susceptibilities of the SH clouds. Another test revealed that the major contribution to the forcing comes from clouds in mid latitudes. Thus, a reduction in cloud amounts by 20% in latitudes higher than 55° in each hemisphere resulted only in a 5% reduction in forcing.

Hahn et al (1990) climatological data estimates that single layer St/Sc account for about 30% of all cases when St/Sc are present. In 70% of other cases, they are overlapped with either upper level Cs/Cc or mid level Ac/As clouds (we do not consider Ns or convective clouds because they have much higher albedos). Using Hahn et al (1990) data for the global distribution of these types of clouds, we have calculated the contribution to the forcing from each of these multilayer cloud types (Fig. 2c). The solid line with squares shows contribution from single layer St/Sc not overlapped with other clouds; the two other cases represent situations when low St/Sc clouds are overlapped by

Ci/Cc/Cs. In one case we consider thin cirrus with transmittance of 1.0 (line with open circles) and in another case we take the cirrus transmittance to be 0.85. The upper solid line represent the benchmark case when we consider contributions from single layer St/Sc clouds, as well as from low layer St/Sc overlapped by mid level and upper level clouds. We take transmittance for mid level Ac/As to be 0.45 and transmittance for upper level cirrus 0.85 We can see that due to the attenuation caused by the overlapping cloud layers, the single layer Sc contribute most to the indirect forcing (about 60%), with another 25% from St/Sc overlapped by Ci/Cs and 15% from St/Sc overlapped with mid level As/Ac. The results, however, will depend on the optical thickness of the overlying cloud layers that determines the amount of transmitted solar radiation, both from space and reflected back from the low layer cloud tops.

Finally, we also made tests using the upper and lower curves that form the envelope of the cloud susceptibility data (Fig. 1a). The use of the upper curve increases the forcing by 19%, while the lower curve decreases the forcing by 7%. Thus, the uncertainty in the estimate of susceptibility is less important that the uncertainties related to sulfate amounts.

4. CONCLUSIONS

We have evaluated the indirect shortwave effect of anthropogenic sulfate aerosol augmentation in marine stratocumulus clouds using global cloud climatology, sulfate aerosol data from the three-dimensional chemical model, and cloud albedo augmentation obtained from the LES cloud model with explicit microphysics. The hemispheric forcing has a strong seasonal cycle with the NH forcing exceeding the Southern Hemisphere (SH) forcing during the NH spring and summer and the SH forcing prevailing during the SH spring and summer. The hemispheric forcing is a strong function of the aerosol burden and of cloud albedo susceptibility which is 2 times larger for cleaner clouds in the SH.

We note that the magnitude of the indirect forcing depends strongly on the assumptions made about the links between sulfate amounts, CCN and drop concentrations. The large uncertainties related to these links is the main problem in evaluation of the indirect forcing. This study employed the approach of Jones et al (1994) in determining the effect of sulfate emissions on cloud microstructure which most likely should be considered as the upper limit for the sulfate emissions-cloud microstructure effect and, consequently, for the estimate of the indirect forcing. As our study showed, the sulfate load has the largest impact on the indirect forcing, therefore, reducing uncertainties related to determination of the sulfate amounts and their effect on cloud microstructure is the major factor in obtaining a more accurate estimate of the indirect effect of anthropogenic aerosols.

ACKNOWLEDGMENTS. We thank Prof. H. Rodhe for providing the data from chemical model simulations. David Lam helped with data preparation. Support for this research was provided by NOAA's Climate and Global Change Program Under the Grants NA36GP0334 and NA37RJ0203. This research was also supported by the Environmental Sciences Division of U.S. Department of Energy (through Batelle PNR Contract 144880-A-Q1 to the Cooperative Institute for Mesoscale Meteorological Studies) as part of the Atmospheric Radiation Measurement Program.

5. REFERENCES

Boucher, O. and U. Lohmann, The sulfate-CCN-cloud albedo effect: a sensitivity study with two general circulation models, *Tellus*, 47B, 281-300, 1995.

Boucher, O. and H. Rodhe, The sulfate-CCN-cloud albedo effect: a sensitivity study, Report CM-83, Dept. of Meteor., Stockholm Univ., 1- 21, 1994.

Charlson, R.J. , J.E. Lovelock, , M.O. Andreae, and S.G. Warren, Oceanic phytoplankton, atmospheric sulphur, cloud albedo and climate, *Nature*, **326**, 655-661, 1987.

-------, Schwartz, S. E., Hales, J. M., Cess, R. D., Coakley, J. A. Jr., Hansen, J. E. and D. J.Hoffman, Climate forcing by anthropogenic aerosols, *Science*, **255**, 423-430, 1992.

Hahn, C.J., Warren, S.G., London, J., Chervin, R.M., and R.Jenne, Simultaneous Occurrence of Different Cloud Types over the Ocean. NCAR/TN-201+STR, NCAR Technical Notes, 1990.

Jones, A., Roberts, D.L. and A.Slingo, A climate model study of indirect radiative forcing by anthropogenic sulphate aerosols, *Nature*, **370**, 450-453,1994.

Kiehl, J.T. and B.P.Briegleb, The relative roles of sulfate aerosols and greenhouse gases in climate forcing, *Science*, **260**, 311-314, 1993.

Kogan, Y. L., M. P. Khairoutdinov, D. K. Lilly, Z. N. Kogan, Q. Liu, Modeling of stratocumulus cloud layers in a large eddy simulation model with explicit microphysics. *J. Atmos. Sci*, **52**, 2923-2940, 1995.

Langner, J., and H.Rodhe, A global three-dimensional model of the tropospheric sulfur cycle, *J. Atmos. Chem.*, **13**, 225-263, 1991.

Martin, G.M., D. W. Johnson, and A. Spice, The measurment and parameterization of effective radius of droplets in warm stratocumulus clouds. *J. Atmos. Sci.*, **51**,1823-1842, 1994.

Penner, J.E., Charlson, R.J., Hales, J.M., Laulainen, N.S., Leifer, R., Novakov, T., Orgen, J., Radke, L.F., Schwartz, S.E. and L.Travis, Quantifying and minimizing uncertainty of climate forcing by anthropogenic aerosols, *BAMS*, **75**, 375-400, 1994.

Platnick, S. and S.Twomey, Determining the susceptibility of cloud albedo to changes in droplet concentration with the advanced very high resolution radiometer, *J. Appl. Meteor.*, **33**, 334-347, 1994.

Schwartz, S. E., & A.Slingo, Clouds, Chemistry and Climate, Proc. of NATO Advanced Research Workshop, Crutzen P. and Ramanathan V., Eds. Springer, Heidelberg, 1995.

Taylor, J.P. and A. McHaffe, Measurements of cloud susceptibility, *J. Atmos. Sci.*, **51**, 1298-1306, 1994.

Twomey, S., Aerosols, clouds and radiation, *Atmos. Environ.*, **254**, 2435-2442, 1991.

Warner, J., The Microstructure of Cumulus Cloud. *J. Atmos. Sci.*, **26**, 1272-1282, 1969.

Warren, S.G., C.J. Hahn, J. London, R.M. Chervin, and R.L. Jenne, Global Distribution of Total Cloud Cover and Cloud Type Amounts over the Ocean. U.S. Department of Energy report DOE/ER-0406, 212pp.,1988.

Woodcock, A. H., Atmospheric sea-salt nuclei data for project shower, *Tellus*, **9**, 521-524, 1957.

ROLE OF ATMOSPHERIC AEROSOL IN THE INDIRECT CLIMATE COOLING MECHANISM

Michael H Smith[1], Andrew Jones[2], Jason A Lowe[1], and Colin D O'Dowd[1]

[1] Physics Dept, UMIST, Manchester M60 1QD, UK
[2] Hadley Centre, Meteorological Office, Bracknell RG12 2SY, UK

1. INTRODUCTION

One of the major issues facing mankind at the present time concerns the impact of anthropogenic activities upon the environment. Unfortunately, the time scales of change and the variability of the global climate are such that it is not possible to wait until such changes are unambiguously apparent before decisions are made and action taken. Accordingly, in addition to careful monitoring of the global climate, computer models capable of simulating climate change are being developed. For these models to possess the requisite degree of accuracy, a comprehensive knowledge of the factors influencing the climate is necessary. Since atmospheric aerosol particles play a key role in moderating the global warming expected to result from anthropogenic releases of 'greenhouse' gases, a clear understanding of their formation, evolution and fate within the atmosphere must be established.

In the atmospheric environment, the 'background' aerosol particles produced by natural processes are supplemented by particles arising from anthropogenic sources, either directly in the form of soot and other components, or indirectly from pollutant gases such as sulphur dioxide or nitrogen oxides. Such particles may affect the climate directly through their ability to scatter and absorb incoming solar radiation, or indirectly via their influence upon cloud microphysical properties, since clouds in turn influence the global albedo, see Charlson *et al* (1987). These indirect feedback processes are not simple because cloud droplet radii (and hence cloud albedo) are governed by complex interactions between cloud dynamics - which determine the rate at which water vapour is released during cloud formation - and the prevailing CCN spectrum. In addition to determining cloud albedo, the droplet size distribution may also influence cloud lifetimes, giving a further impact of indirect forcing upon global albedo.

The susceptibility of clouds to indirect forcing is greatest for clouds in clean maritime air masses whose dynamics are largely invariant and characterised by gentle updraughts with low peak supersaturations, Hobbs (1993). Under these conditions, there is a need to be especially concerned about the size distributions and types of CCN available. Finally, aerosol particles are, in turn, involved in the feedback process as they represent a sink for trace gas species, as recognised by Chameides and Stelson (1992) who showed that the lifetimes of trace gases, such as SO_2 and NH_3, could be strongly influenced by aerosol solution droplets acting as a rapid removal mechanism.

2. MODELLING INDIRECT RADIATIVE FORCING

In a previous attempt to quantify the indirect radiative forcing by anthropogenic sulphate aerosols upon global climate, Jones *et al* (1994) used a model developed by Langner and Rodhe (1991) to obtain two-dimensional global distributions of total sulphur from which aerosol mass distributions were estimated assuming the sulphur was in the form of ammonium sulphate. Particulate number concentrations were then derived by adopting a log-normal size distribution of mode radius 0.05μm and geometric standard deviation of 2. The aerosol particles were considered to be evenly dispersed throughout the lowest 1.5km of the atmosphere. An empirical relationship, based upon aircraft data from a wide range of geographical locations, was used to derive the number of cloud droplets formed on those particles which act as CCN within the total concentration of aerosol.

Since the available liquid water is determined by the cloud dynamics, the effective droplet radius could be directly estimated once the droplet concentration is established. However, there are several limitations in this approach since other aerosol species with activities different from that of ammonium sulphate, such as sea-salt, make significant contributions to the CCN population. In addition, a sizeable fraction of the aerosol sulphate

may be internally mixed with these other types of aerosol particles, thus reducing the number of ammonium sulphate particles. Finally, the parameters describing the aerosol population are uncertain with a wide variation in values reported by different workers.

During a series of field campaigns in maritime air masses, O'Dowd et al (1996a) were able to establish similar relationships between sub-cloud aerosol particle numbers and cloud droplet concentrations to those used by Jones *et al*, but noted that some data points did not conform to the regression relationship, as shown in Figure 1. Using thermal analysis techniques to determine aerosol particle composition (O'Dowd *et al*, 1993), they were able to show that, at moderate and high wind speeds, sea salt particles were present at sizes and in concentrations sufficient to influence cloud microphysics.

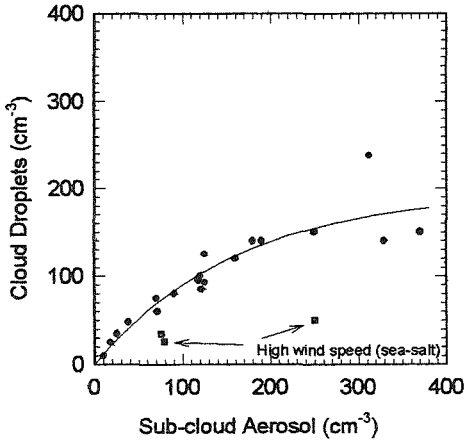

Figure 1: Relationship observed between sub-cloud aerosol and cloud droplet concentration.

3. INFLUENCE OF SEA SALT PARTICLES

3.1 Contribution to the CCN Distribution

In order to examine the interactions between ammonium sulphate and sea salt particles during the early stages of cloud droplet initiation and growth, modelled particle size distributions based upon observations in the marine environment at altitudes of about 10m were employed. It was found that the ammonium sulphate particulate spectrum could be readily approximated by a log-normal distribution (O'Dowd *et al*, 1993 and Lowe *et al*, 1996a) with a fixed mode radius of 0.075μm, standard deviation of 1.4 and an amplitude governed by the concentration of particles. In contrast, the sea salt particles required three log-normal curves to define their concentration, reflecting the contribution of film, jet and spume production processes to the particulate spectrum (O'Dowd *et al*, 1996b). Modelled particle spectra for a specific set of conditions are illustrated in Figure 2 and demonstrate the contrast between the narrow distribution typical of the ammonium sulphate aerosol compared with that for the sea salt particles, which span almost four orders of magnitude in radius. The dry mode radii for the sea-salt film, jet, and spume modes are 0.1μm, 1μm, and 6μm respectively; their geometric standard deviations are 1.9, 2 and 3. The number concentration in each of the sea-salt modes is a strong function of wind speed, at 17m s^{-1} the film, jet, and spume modes contain 70 cm^{-3}, 3 cm^{-3}, and 0.005 cm^{-3} respectively.

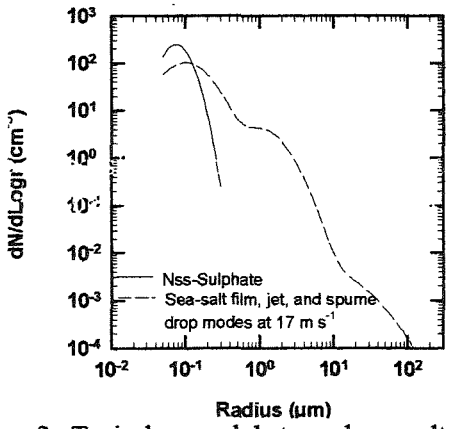

Figure 2: Typical nss-sulphate and sea-salt aerosol distributions. Sea-salt corresponds to 17 m s^{-1} wind speeds.

While the largest sea salt particles (those with r>5 μm) are unlikely to reach cloud base altitudes in sufficient numbers to play a significant role in cloud droplet development, the smaller particles are sufficiently numerous and do possess a lower activity threshold than similar sized sulphate particles. If the earliest stages of cloud formation are considered, it should be noted that cloud droplet formation represents a dynamic relationship between the release of water vapour to the liquid phase, as a consequence of air parcel cooling, and the availability of sufficient activated nuclei to absorb this released water vapour. The larger, and/or more hygroscopic, CCN will be activated at the lowest supersaturations and, only if their concentration and rate of growth is insufficient to absorb the available water vapour, will the supersaturation increase. Only if the supersaturation is able to increase, because of either a more rapid ascent of the air parcel or a shortage of activated nuclei, will smaller or less hygroscopic nuclei be used as sites for cloud droplets.

To indicate the effect of particle composition upon the cloud droplet formation process, the number of CCN activated for ammonium sulphate and sea salt aerosol concentrations typical of the marine environment were plotted against supersaturation, as shown in Figure 3. The number concentration of activated particles was determined by first calculating

the smallest size of dry particle that could be activated for a given peak supersaturation using the Kohler curve equation. Those aerosol particles greater than this critical dry size, obtained by integrating the particle spectra between the critical size and the largest size of particle mixed up to cloud base, were then considered to be activated.

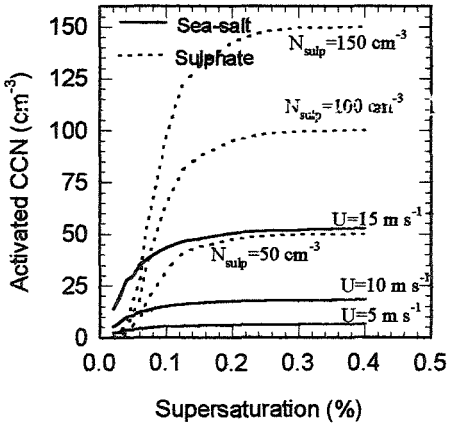

Figure 3: Typical sulphate and sea-salt supersaturation spectra for a range of conditions.

It may be noted from this figure that sea salt particles will be preferentially activated, relative to ammonium sulphate, for supersaturations up to about 0.1%. Furthermore, in clouds with low updraught velocities (and low supersaturations), these salt particles will not only contribute to the CCN distribution but will compete with the sulphate particles for the available water vapour and thereby reduce the peak supersaturations below the levels which would be effective in clouds containing only ammonium sulphate particles. This interaction between the aerosol species is illustrated in Table 1, where the peak supersaturations attained for various realistic combinations of aerosol components have been calculated using a simple Lagrangian cloud model (Lowe *et al*, this issue). Values in this table were derived assuming cloud conditions typical of maritime stratocumulus.

Table 1: Peak Supersaturation versus sea-salt and nss-sulphate CCN input.

Horizontal Wind speed (m s^{-1})	5	10	15
Sulphate (cm^{-3})			
0	0.341	0.201	0.111
50	0.157	0.136	0.097
100	0.133	0.119	0.090
200	0.120	0.108	0.085
200	0.111	0.101	0.081
250	0.104	0.096	0.078

While the specific peak supersaturations derived by this method are a function of the initialisation values, the reduction of peak supersaturation, and hence the inhibition of the activation of ammonium sulphate particles, brought about by the addition of sea salt, pertains for all realistic starting conditions.

The relative contributions of ammonium sulphate and sea salt particles to the activated droplets are presented in Figure 4 as a function of peak supersaturation for the extreme conditions defined in Figure 3. Bearing in mind the peak supersaturations likely to be encountered for these combinations (as indicated in Table 1), the substantial contribution of sea salt aerosol to the effective CCN concentrations for moderate and high wind speeds may be readily discerned.

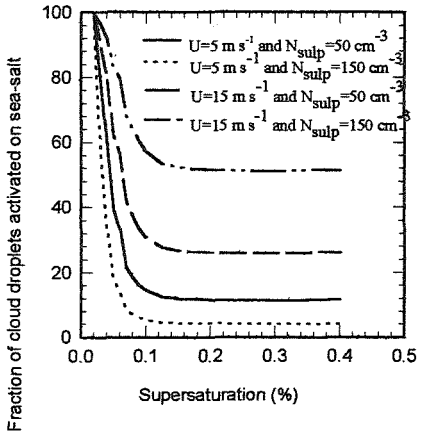

Figure 4: Fractional contribution of sea-salt to cloud droplet formation for a variety of conditions.

3.2 Depletion of Sulphate Particle Precursors

In addition to the role of sea salt aerosol as CCN in marine clouds, there is growing evidence that these particles may scavenge the trace gases which constitute the precursors of non-sea-salt sulphate aerosol (Sievering *et al*, 1992). Furthermore, the large surface area associated with the sea salt aerosol under moderate and high wind conditions makes it an effective sink for low volatility, sulphur-derived aerosol precursors, such as H_2SO_4 and MSA (O'Dowd *et al*, 1996c).

Finally, the presence of sea salt within those cloud droplets formed upon them may strongly affect the heterogeneous production of sulphate and the corresponding exchange of sulphur dioxide between the gaseous and aqueous phases (Lowe *et al*, this issue).

4. ASSESSMENT OF INDIRECT AEROSOL FORCING

In order to make an improved assessment of the indirect aerosol forcing of global climate, incorporating the processes outlined above, the first requirement is to establish more realistic predictions of the aerosol spectrum within the marine environment. The number of cloud droplets formed upon these aerosol particles must then be predicted in a manner similar to that used previously, but which takes account of feedback processes between the different aerosol types and which allows for the role of cloud microphysics within the cloud formation processes.

Sea salt concentrations are readily derived from the wind speed relationships defined in the literature (O'Dowd *et al*, 1996b), as illustrated in Figure 4. The sulphate mass will be obtained from the transport model as for the previous modelling work but with the losses of sulphur species to the sea salt aerosol taken into account before the number of sulphate particles contributing to the CCN distribution is calculated. A simple parcel model, as used in producing Table 1, is being employed to develop relationships between sea salt and sulphate particle concentrations and the relevant droplet concentrations activated upon them (Lowe *et al*, this issue). Results from an improved global climate model, incorporating both sea-salt and sulphate aerosol, will be presented at the conference.

5. REFERENCES

Jones A., Roberts D.L. and Slingo A., 1994: A climate model study of indirect radiative forcing by anthropogenic sulphate aerosols. *Nature*, **370**, 450-453.

Charlson R.J., Lovelock J.E., Andrae M.O. and Warren S.G., 1897: Oceanic phytoplankton, atmospheric sulphur, cloud albedo and climate. *Nature*, **326**.

Chameides W.L. and Stelson A.W., 1992: Aquaeous-phase chemical processes in deliquescent sea-salt aerosols: a mechanism that couples the atmospheric cycles of sulphur and sea-salt. *J. Geophys. Res.*, **97**, 20565-20580.

Hobbs P.V., 1993: Aerosol-cloud-climate interactions. *Academic Press.*

Langner J. and Rodhe H, 1991: Global three-dimensional model of the tropospheric sulphur cycle, *J. Atmos. Chem.*,**13**, 225-263.

Lowe J.A. Smith M.H., Davison B.M., Benson S.E., Hill M.K., O'Dowd C.D., Harrison R.M. and Hewitt C.N., 1996a: Physico-chemical properties of atmospheric aerosol at South Uist. *Atmos. Environ.*, submitted.

Lowe J. A., Smith M.H., O'Dowd C.D. and Clegg S.L., 1996b: The effects of sea-salt aerosol on the production of sulphate in the marine atmospheric boundary layer and its effect on stratiform clouds. *This issue.*

O'Dowd C.D., Smith M.H., and Jennings S.G., 1993: Submicron particle, radon and soot carbon characteristics over the north east Atlantic. *J. Geophys. Res.*, **98**, 1123-1135.

O'Dowd C.D., Smith M.H., Kaye A. and Lowe J.A, 1996a: The relative importance of nss-sulphate and sea-salt aerosol to the marine CCN population. *This issue.*

O'Dowd C.D., Smith M.H., Consterdine I.E. and Lowe J.A., 1996b: Marine aerosol, sea-salt and the marine sulphur cycle. *Atmos. Environ.*, in press.

O'Dowd C.D., Davison B., Lowe J.A., Smith M.H., Hewitt C.N. and Harrison R.M., 1996c: Biogenic sulphur emissions and inferred nss-sulphate CCN in and around Anarctica. *J. Geophys. Res.* submitted.

Sievering H., Boatman J., Galloway J., Keane W., Kim Y., Luria M. and Ray J., 1992: Removal of sulphur from the marine boundary layer by ozone oxidation in sea-salt aerosols. *Nature*, **360**.

PREDICTING CLOUD DROPLET EFFECTIVE RADIUS AND INDIRECT SULPHATE AEROSOL FORCING USING A GENERAL CIRCULATION MODEL

Andy Jones and Anthony Slingo

Hadley Centre, Meteorological Office, Bracknell RG12 2SY, UK

1. INTRODUCTION

Using the Hadley Centre GCM we have carried out simulations of low cloud droplet effective radius (r_e) using a parametrisation of droplet size based on Martin *et al.* (1994) and Bower & Choularton (1992). We have used three different parametrisations of the relation between sulphate aerosol loading and cloud droplet concentration (N_{tot}) (Jones *et al.* 1994, Hegg 1994 and Boucher & Lohmann 1995), and annual-mean distributions of sulphate from two different chemical transport models (Langner & Rodhe 1991 and Penner *et al.* 1994). Using the three different methods for determining N_{tot} and utilising the sulphate data of Langner & Rodhe, we have then made estimates of the indirect radiative forcing by anthropogenic sulphate aerosols since the beginning of the industrial era.

2. RESULTS

Comparing the simulations of r_e with satellite retrievals for liquid water clouds (Han *et al.* 1994) showed a sensitivity to the form of the relation between sulphate and droplet concentration, with the simulations using the relations of Jones *et al.* and Hegg being closest to the satellite data (see Table 1; all values are for the domain of the satellite data, approx. 45°N to 45°S, and the simulations use the sulphate data of Penner *et al.*).

TABLE 1. Annual-mean effective radii (μm) from simulations using the three parametrisations of N_{tot} (J = Jones *et al.*, H = Hegg, BL = Boucher & Lohmann), compared with satellite retrievals (SAT. = Han *et al.*).

	SAT.	J	H	BL
Global	10.74	11.08	10.58	9.49
N.H.	10.11	10.32	10.38	9.27
S.H.	11.32	11.82	10.81	9.73
Ocean	11.54	11.13	10.44	9.33
Land	8.14	10.98	11.08	10.04

However, the comparison with satellite data indicated no strong preference for either of the modelled sulphate distributions.

For the indirect radiative forcing of sulphate aerosol we obtain values in the range −0.5 to -1.5 Wm^{-2} in the global annual mean, depending on the method used for parametrising N_{tot}. In contrast to the results for r_e, in this case it was the simulations using the relations of Hegg and Boucher & Lohmann which were the most similar, with global annual mean forcings of −0.5 and −0.6 Wm^{-2} respectively (see Fig.1). These negative (cooling) forcing estimates are comparable with those of the direct effect of sulphate (−0.25 to −0.9 Wm^{-2}), and are significant when compared with the positive (warming) forcing of +2.5 Wm^{-2} due to the increase in greenhouse gases to date (all estimates from IPCC 1995).

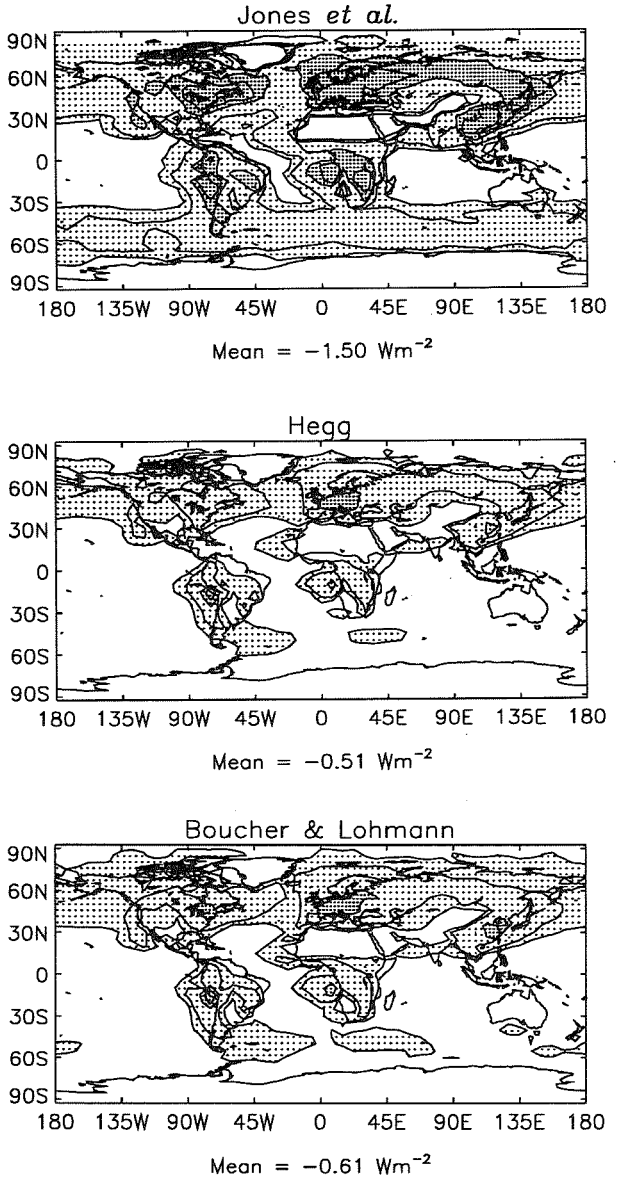

Figure 1. Annual mean indirect radiative forcing (Wm^{-2}) due to anthropogenic sulphate aerosols using the three different relations for N_{tot}. Contours are at −0.5, −1.0, −3.0 and −5.0 Wm^{-2}; regions between −0.5 and −3.0 Wm^{-2} are lightly shaded, those of greater (more negative) forcing are more heavily shaded.

3. DISCUSSION

Examination of observational data on the relation between sulphate aerosol and cloud droplet number concentration suggests that whilst there seems to be a fairly good relation in maritime airmasses, in continental airmasses it is not clear that there is such a relation. This suggests that there may always be sufficient aerosol over land to act as CCN, whatever the sulphate concentration. We therefore conducted a simple sensitivity experiment in which we assumed that the cloud droplet concentration over land was independent of sulphate concentration. The range of forcing estimates was reduced to −0.3 to −0.8 Wm^{-2}. If CCN are indeed always present "in excess" in continental regions, then despite these areas being those of highest pollutant concentration, the magnitude of anthropogenic sulphate indirect forcing will not be as large as the sulphate concentrations in these regions might at first suggest. However, the degree to which the indirect effect of sulphate is reduced in these areas depends in part on how much of the non-sulphate continental CCN are themselves anthropogenic, and how much are natural background aerosols: there might still be considerable anthropogenic forcing, but not necessarily due just to sulphate.

4. ACKNOWLEDGEMENT

This work was supported by the U.K. Department of the Environment under contract PECD 7/12/37.

5. REFERENCES

Boucher, O., and U. Lohmann, 1995: The sulfate-CCN-cloud albedo effect: A sensitivity study with two general circulation models. *Tellus*, **47B**, 281-300.

Bower, K. N. and T. W. Choularton, 1992: A parametrisation of the effective radius of ice free clouds for us in global climate models. *Atmos. Res.*, **27**, 305-339.

Han, Q., W. B. Rossow and A. A. Lacis, 1994: Near-global survey of effective droplet radii in liquid water clouds using ISCCP data. *J. Clim.*, **7**, 475-497.

Hegg, D. A., 1994: Cloud condensation nucleus-sulfate mass relationship and cloud albedo. *J. Geophys. Res.*, **99**, 25903-25907.

IPCC (Intergovernmental Panel on Climate Change), 1995: *Climate Change 1994: Radiative Forcing of Climate Change and An Evaluation of the IPCC IS92 Emission Scenarios* (Eds. Houghton, J. T., L. G. Meira Filho, J. Bruce, Hoesung Lee, B. A. Callander, E. Haites, N. Harris and K. Maskell), Cambridge University Press.

Jones, A., D. L. Roberts and A. Slingo, 1994: A climate model study of indirect radiative forcing by anthropogenic sulphate aerosols. *Nature*, **370**, 450-453.

Langner, J., and H. Rodhe, 1991: A global three-dimensional model of the tropospheric sulfur cycle. *J. Atmos. Chem.*, **13**, 225-263.

Martin, G. M., D. W. Johnson and A. Spice, 1994: The measurement and parametrisation of effective radius of droplets in warm stratocumulus clouds. *J. Atmos. Sci.*, **51**, 1823-1842.

Penner, J. E., C. S. Atherton and T. E. Graedel, 1994:'Global emissions and models of photochemically active compounds.' Pp. 223-248 in *Global Atmospheric-Biospheric Chemistry* (Ed. Prinn, R.), Plenum, New York.

IMPACT OF ANTHROPOGENIC SULFUR EMISSIONS ON CLOUD-CLIMATE INTERACTIONS

Catherine C. Chuang and Joyce E. Penner

Lawrence Livermore National Laboratory
Livermore, CA 94551, U. S. A.

1. INTRODUCTION

It has been estimated that anthropogenic sulfur emissions dominate over natural sulfur emissions by about a factor of 2 on a global average (Spiro et al., 1992) and they have been significantly increased during the past several decades (Charlson et al., 1992). Photochemical reactions of the emitted anthropogenic sulfur compounds lead to a large increase in the number concentration of sulfate-containing aerosols. These soluble aerosols modify the microphysics of clouds by acting as cloud condensation nuclei (CCN) and enhancing the reflectivity of low-level water clouds. They might also alter the development of precipitation by affecting the mean drop size and thereby influencing cloud lifetime. However, the magnitude of cloud optical property change associated with anthropogenic sulfur emissions is quite uncertain because of the large uncertainty in the relationship of aerosol size distribution to sulfate mass concentration. There are further complications as a result of the non-linearity of cloud microphysics where the cloud drop number concentration is a function of updraft velocity and aerosol characteristics. In this paper, we coupled a climate model with a 3-D chemistry model to simulate the global sulfur cycle and estimated radiative forcing by anthropogenic sulfur emissions through cloud processes (i.e., indirect forcing).

2. FORMATION OF PARTICULATE SULFATE

To assess the impact of anthropogenic sulfate on cloud optical properties, two different approaches for the formation of anthropogenic sulfate are applied in this study. The first one is referred to as the internal mixing approach where aerosols with the same size are assumed to have identical chemical composition. The aerosol size distribution is thus determined by the condensation of sulfuric acid vapor (H_2SO_4) on a prescribed pre-existing particle distribution and by aqueous-phase oxidation of SO_2 followed by evaporation of cloud drops. Langner and Rodhe (1991) estimated that the amount of sulfate transformed by OH oxidation is between 19% and 55% of that by in-cloud oxidation. Thus, if sulfate is produced by these two pathways only, 65% - 85% of sulfate would be transformed by in-cloud oxidation of SO_2. These lower and upper values are used in this work to provide an estimate of the sensitivity of the predicted change of cloud drop number concentration to the assumed fraction of different oxidation pathways. We simulate the aerosol size distribution using the process described by Chuang and Penner (1995) with a prescribed pre-existing particle distribution. The continental and marine aerosol size distributions simulated by the internal mixing approach with the fraction of anthropogenic sulfate converted through the aqueous pathway specified as 85%, 75%, and 65%, respectively, are shown in Fig. 1.

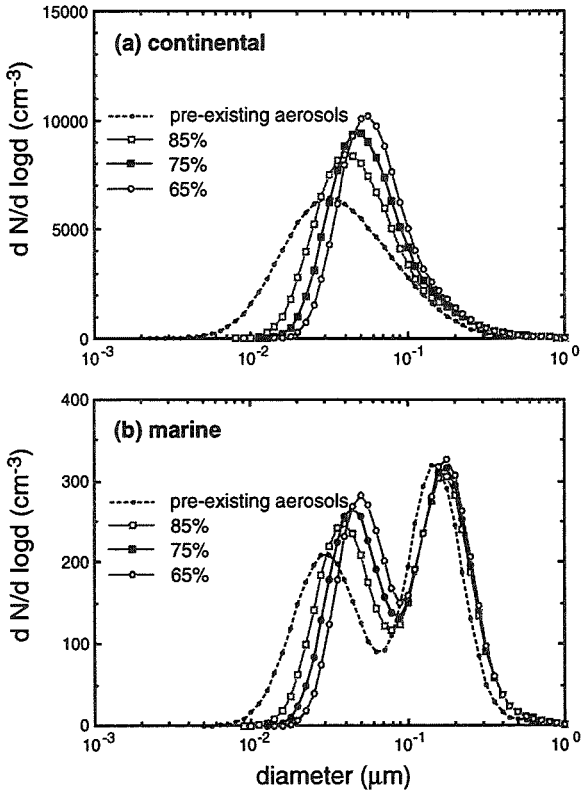

Fig. 1. Simulated aerosol size distributions. Aerosol number and anthropogenic sulfate mass concentrations are 5500 cm^{-3} and 5 μgm^{-3} for continental case; 250 cm^{-3} and 0.5 μgm^{-3} for marine case.

The second approach is referred to as external mixing where the particulate sulfate is formed by homogeneous nucleation or condensation onto pure existing sulfate particles. Pure sulfate might also be formed in a drop which formed on a pure pre-existing sulfate particle. In this approach, aerosols with the same size would have different chemical composition. The anthropogenic sulfate aerosols are assumed to have a size distribution from fitting the average measured sulfate data summarized by Milford and Davidson (1987). The fitted sulfate aerosol mass distributions as well as their corresponding number distributions in the external mixing approach are presented in Figs. 2a and 2b. Since the sulfate data measured in the marine boundary layer contains sea spray aerosols, the coarse-particle sulfate is attributed to sea salt. Therefore, we only fit the measured data with particle size < 1 μm for the marine case.

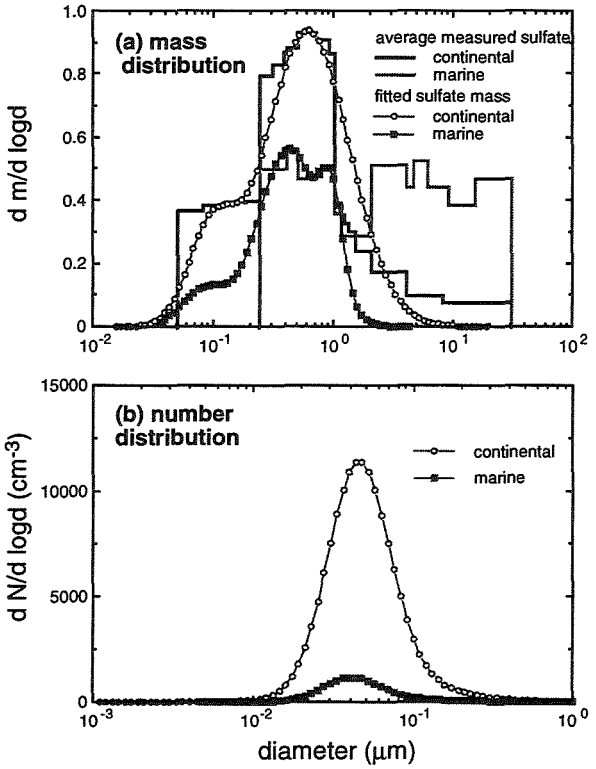

Fig. 2. (a) Dimensionless sulfate mass distributions. (b) Fitted sulfate aerosol number distributions. The number concentration is 5960 cm^{-3} for the continental case and 580 cm^{-3} for the marine case. These values correspond to anthropogenic sulfate concentrations of 5 μgm^{-3} and 0.5 μgm^{-3}, respectively.

Our coupled climate/chemistry model together with detailed emission inventories is used to predict the global aerosol distribution. Figure 3 presents the simulated seasonal variation of aerosol number concentration. Figure 3a shows that the lowest global average aerosol number concentration is in April, a time in between two high seasons of aerosol generation by biomass burning in winter and summer. Figures 3b and 3c reveal that anthropogenic sulfate reaches its peak magnitude during the N. Hemisphere summer time It is also noted that biomass burning is the major aerosol source in the S. Hemisphere.

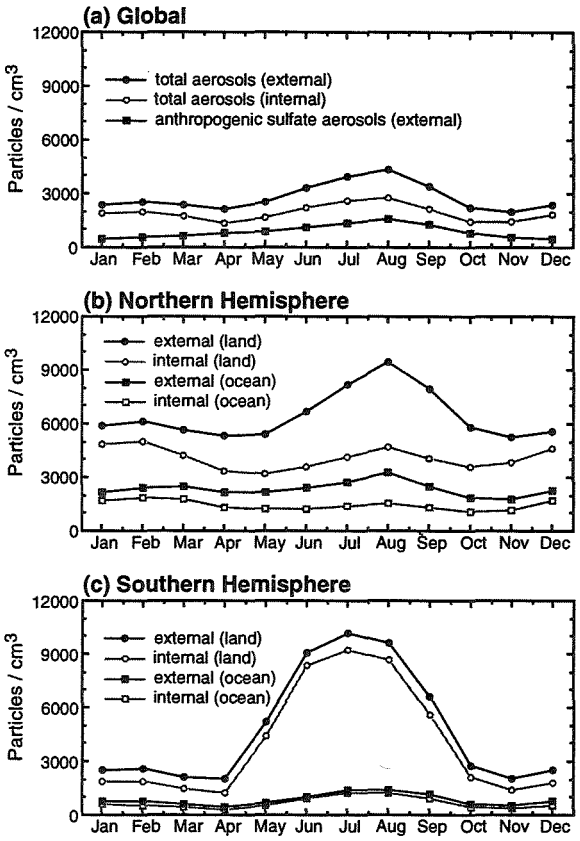

Fig. 3. Simulated seasonal variation of aerosol number concentration.

3. CLOUD DROP PARAMETERIZATION

A series calculations have been performed to investigate the relationship between aerosol size distribution and cloud drop number concentration. We parameterized the number concentration of cloud drops activated through the nucleation process using a detailed microphysical Lagrangian model (Chuang et al., 1992). Following Chuang and Penner (1995), the drop number concentration (in cm^{-3}) is expressed in the form of $N_d = w N_a / (w + c N_a)$, where N_a (cm^{-3}) is the aerosol number concentration, and w (cm s^{-1}) is the updraft velocity. The coefficients c developed from two different approaches are listed as follows

(a) Internal Mixing Approach

over land $c = 0.0410 + 21.59\, X_L$

over ocean $c = 0.0222 - 0.133\, X_O + 3.074\, X_O^2$

where $X_L = \log w\, [1 - \log w\, (.5 + \gamma/\alpha^4) / (\log N_a)^2] / (\log N_a)^{5+\gamma/\alpha^3}$, and $X_O = \log w [1 - \log w\, (.5 + .2\gamma/\alpha^3) / (\log N_a)^2] / (\log N_a)^{2+.1\gamma/\alpha^2}$. γ is defined as the ratio of anthropogenic sulfate loading (in $\mu g\ m^{-3}$) to the total aerosol number (in 1000 cm^{-3}). α is the ratio of the

fraction of anthropogenic sulfate converted by the aqueous pathway to the mean value used here (75%).

(b) External Mixing Approach

over land $c_s = 0.0412 + 3.698\ X_{s,L}$

$c_b = 0.0410 + 21.59\ X_{b,L}$

over ocean $c_s = 0.0117 + 5.015\ X_{s,O}^2$

$c_b = 0.0222 - 0.133\ X_{b,O} + 3.074\ X_{b,O}^2$

where c_s and c_b are coefficients for anthropogenic sulfate aerosols and pre-existing particles with number concentrations N_s and N_b, respectively. $X_{s,L} = \log w\ [1 - .055\ (\log w)^2\ \log N_s] / \log N_s^4$, $X_{b,L} = \log w\ [1 - .5\ \log w / (\log N_b)^2] / (\log N_b)^5$, $X_{s,O} = \log w\ [1 - .525\ \log w / (\log N_s)^{.5}] / (\log N_s)^{3.5}$, and $X_{b,O} = \log w\ [1 - .5\ \log w / (\log N_b)^2]/(\log N_b)^2$. The total aerosol number concentration $N_a = N_s + N_b$, and cloud drop number concentration nucleated is approximated by $N_d = (N_s/N_a) w N_a / (w + c_s N_a) + (N_b/N_a) w N_a / (w + c_b N_a)$.

These parameterizations are introduced into the coupled climate/chemistry model to predict the cloud drop number concentration. Simulated seasonal variation of the percentage change in cloud drop number concentration due to anthropogenic sulfate is shown in Fig. 4. Both approaches indicate that April has the highest percentage increase in cloud drop concentration.

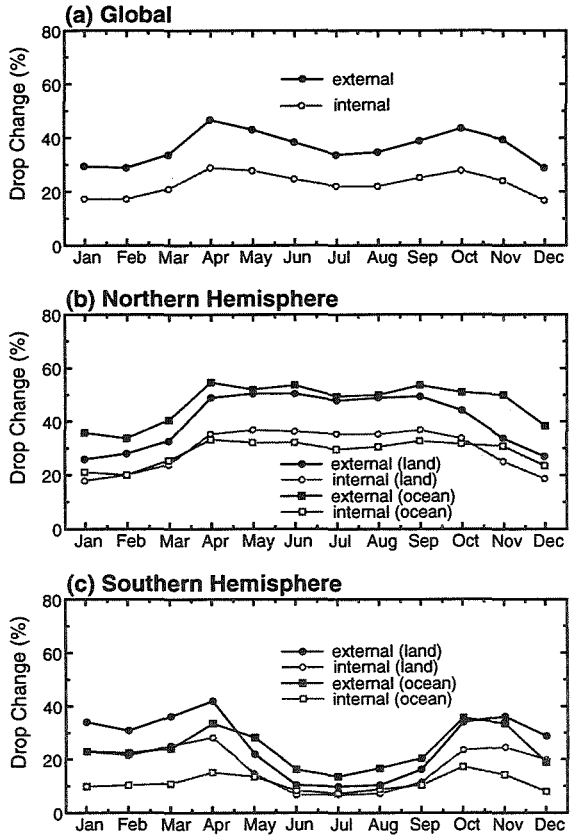

Fig. 4. Simulated seasonal variation of the percentage change in cloud drop number concentration due to anthropogenic sulfate.

4. INDIRECT ANTHROPOGENIC SULFATE RADIATIVE FORCING

We calculate the indirect anthropogenic sulfate radiative forcing as the difference in top of the atmosphere solar radiation with and without anthropogenic sulfate at each time the radiation routine is called. Results are listed in Table 1.

Table 1. Global average annual mean indirect anthropogenic sulfate forcing (Wm^{-2})

	Internal mixing with aqueous conversion fraction			External mixing
	65%	75%	85%	
N. H.	-1.74	-1.25	-0.91	-2.15
Land	-1.37	-0.99	-0.73	-1.55
Ocean	-1.98	-1.41	-1.02	-2.53
S. H.	-0.75	-0.49	-0.34	-1.12
Land	-0.64	-0.44	-0.31	-0.76
Ocean	-0.77	-0.51	-0.35	-1.20
Global	-1.24	-0.87	-0.62	-1.63

The indirect effect is much more pronounced over the ocean where the pre-existing aerosol number concentrations are lower than over continental areas. This low concentration yields a higher fractional increase in cloud drop number for the same amount of anthropogenic sulfate deposited (Chuang and Penner, 1995). Because of the significance of the indirect effect over the ocean, we investigated the sensitivity of the indirect forcing to the number concentration of pre-existing particles with marine origin. A prescribed particle number concentration of 200 cm^{-3} was added to the lowest marine boundary layer, and exponentially decreased with altitude by

$$N\ (cm^{-3}) = 200\ e^{-2\ (1 - \sigma)} \quad \text{for } \sigma \geq 0.15$$

$$= 36.5\ e^{-15\ (.15 - \sigma)} \quad \text{for } \sigma < 0.15$$

where $\sigma = p/p_s$, and p_s is the surface pressure. These particles simulate a possible source of marine background particles such as sea salt. The simulated indirect forcing is then reduced by about 34% globally. These reductions are mainly over the ocean and are as large as 50% locally. This indicates that the global radiation balance is sensitive to the change in cloud drop concentration over the ocean. Therefore, the large extent of marine stratus and stratocumulus clouds may play important role in determining the net change in reflected solar radiation.

5. DROP EFFECTIVE RADIUS COMPARISON

Han et al. (1994) developed a scheme to retrieve cloud particle effective radii (r_e) in liquid water clouds using International Satellite Cloud Climatology Project

(ISCCP) data. Here, we compare their survey with our predictions to validate the accuracy of our cloud drop parameterization and to determine whether our treatment of cloud processes is reasonable (see Fig. 5). The general features of Figs. 5a and 5b are quite similar, although small discrepancies do exist. However, since the uncertainty in the retrieved data reported by Han et al. is about 1 - 2 μm, we conclude that the simulated cloud drop effective radii are in good agreement with those retrieved from satellite data and the effect of anthropogenic sulfate on cloud drop effective radii is more pronounced in the mid-latitude continents of the Northern Hemisphere (Fig. 5c).

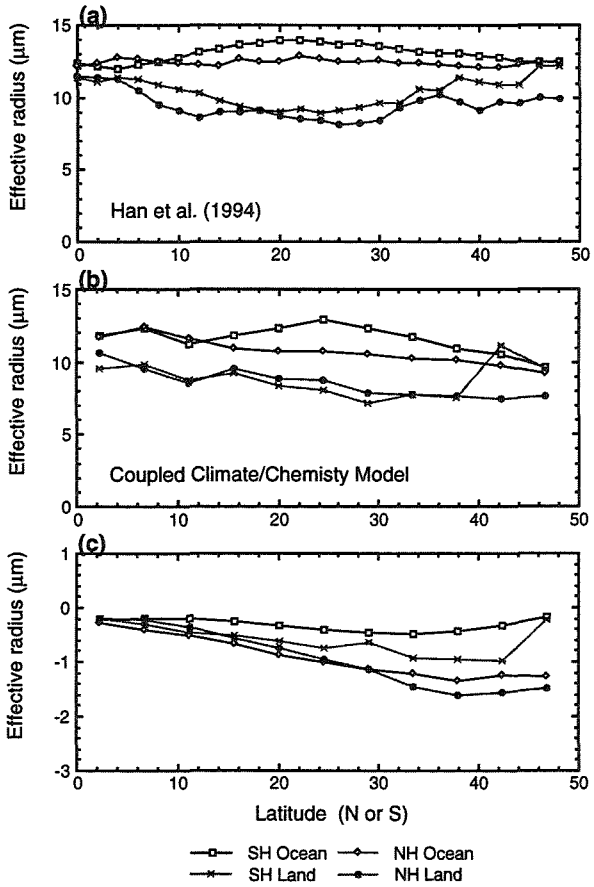

Fig. 5. (a) Annual, zonal mean cloud drop effective radii from NOAA-9 for 1987. (b) Same as (a) but simulated by the coupled climate/chemistry model using the internal mixing approach with an assumed aqueous conversion fraction of 75%. (c) Simulated changes in effective radii due to anthropogenic sulfate.

6. DISCUSSION AND CONCLUSIONS

Our estimate for indirect anthropogenic sulfate radiative forcing ranges from -0.6 to -1.6 Wm^{-2} and it reduces to -0.4 to -1.1 Wm^{-2} if a prescribed marine background particle number concentration is applied over the ocean. Uncertainty in the magnitude of the calculated indirect forcing may arise from the assumed "pre-existing particle size distribution" which must result from a variety of processes and sources involving the entire suite of aerosol types (Penner et al., 1994). The prescribed pre-existing size distribution was chosen to represent an "average" particle distribution where no anthropogenic sulfate was present. Although it may remain questionable whether the pre-existing distribution is independent of anthropogenic sulfate and can be treated separately, we believe that the approaches used in this study provide a reasonable estimate of the possible range of forcing by the indirect effect.

7. ACKNOWLEDGMENTS

This work was performed under the auspices of the U. S. Department of Energy by the Lawrence Livermore National Laboratory under contract No. W-7405-ENG-48. We are grateful for the partial funding of this work by NASA under interagency agreement NAGW-1287 and by DOE under the Quantitative Links Program and Atmospheric Radiation Measurement (ARM) Program.

8. REFERENCES

Charlson, R.J., S.E. Schwartz, J. M. Hales, R.D. Cess, J.A. Coakely Jr., J.E. Hansen, and D.J. Hofmann, Climate forcing by anthropogenic aerosols, *Science*, **255**, 423-430, 1992.

Chuang, C.C., J.E. Penner, and L.L. Edwards, Nucleation scavenging of smoke particles and simulated drop size distributions over large biomass fires, *J. Atmos. Sci.*, **49**, 1264-1275, 1992.

Chuang, C.C., and J.E. Penner, Effects of anthropogenic sulfate on cloud drop nucleation and optical properties, *Tellus*, **47B**, 566-577, 1995.

Han, Q., W.B. Rossow, and A.A. Lacis, Near-global survey of effective droplet radii in liquid water clouds using ISCCP data, *J. Climate*, **7**, 465-497, 1994.

Langner, J., and H. Rodhe, A global three-dimensional model of the tropospheric sulfur cycle, *J. Atmos. Chem.*, **13**, 225-263, 1991.

Milford, J.B., and C.I. Davidson, The sizes of particulate sulfate and nitrate in the atmosphere - A review, *JAPCA*, **37**, 125-134, 1987.

Penner, J.E., C.S. Atherton, and T.E. Graedel, Global emissions and models of photochemically active compounds, *Global Atmospheric-Biospheric Chemistry*, R. G. Prinn (Ed.), Plenum Press, New York, 223-247, 1994.

Spiro, P.A., D.J. Jacob, and J.A. Logan, Global inventory of sulfur emissions with 1°× 1° resolution, *J. Geophys. Res.*, **97**, 6023-6036, 1992.

EFFECT OF REPEATED CLOUD EVENTS ON AEROSOL PARTICLES AND THEIR DIRECT AND INDIRECT RADIATIVE PROPERTIES

Nikos Hatzianastassiou, Andrea I. Flossmann and Wolfram Wobrock

Laboratoire de Météorologie Physique (LaMP), Aubiere Cedex 63177, France

1. INTRODUCTION

The aerosols which are solid and liquid particles suspended in the air are one kind of pollutants, the other one being the gases. The loading of the atmosphere by pollutants is determined on the one hand by the rate of their introduction and on the other hand by the rate of their removal by wet or dry deposition involving clouds and precipitation. Wet deposition of APs operates via nucleation and impaction scavenging. The gaseous pollutants are removed by convective diffusion into the drops where they may be oxidized and transported to the ground by the drops if the cloud precipitates.

The importance of aerosols regarding cloud microphysics and precipitation processes is well known. Moreover, aerosols and clouds are very important affecting atmospheric radiation. Together with molecular scattering from gases they determine what fraction of the solar radiation incident at the top of the atmosphere reaches the earth's surface and what fraction of the longwave earth radiation escapes to space. Therefore, aerosol and clouds play a very important role determining the earth's climate.

Once an aerosol spectrum has entered the cloud and has served as CCN spectrum, it is changed while several microphysical processes occurs during a cloud lifetime cycle. At the end of this cycle and after the cloud has evaporated the AP spectrum is released back into the atmosphere and can be different from the original spectrum as it has been processed by the cloud. Nevertheless, it can eventually form a new cloud. It is possible, thus, to have successive cloud cycles just as e.g. in mountain waves. Such a case has been studied allowing us to determine the repeated effect of cloud events on an atmospheric aerosol population. Climatic impacts were also studied by calculating the evolution of the radiative properties during a cloud cycle.

2. NUMERICAL MODEL - SIMULATIONS

The microphysical spectral model DESCAM(DEtailed SCAvenging Model), developped by Flossman et. al. and containing spectral liquid phase microphysics as well as scavenging was coupled with the simple dynamics of an entraining air parcel. Microphysical processes as condensation, evaporation, nucleation scavenging, impaction scavenging, collision and coalescence of drops, break up of drops, entrainment and gaseous absorption with oxidation were considered. We chose to study the processing of sulfate assuming that aerosols consisted entirely of ammonium sulfate. Sulfate mass was added through the uptake of SO_2 into the drops and subsequent oxidation by H_2O_2 and O_3.

The formulation of the model can be found in Flossmann et. al., 1985. The model was initialized according to sounding of Lee et. al., 1980 for a warm cloud. We chosen two types of aerosol spectra: rural and maritime. These spectra results from a combination of 3 log-type distributions given by Jaenicke, 1988:

$$\frac{dN_{APa}}{dlnr_N} = f_{APa}(lnr_N) = \sum_{i=1}^{3} f_{APa,i}(lnr_N) =$$

$$= \sum_{i=1}^{3} \frac{n_i}{(2\pi)^{1/2}\, log\sigma_i\, ln10} \times exp\left(-\frac{(log(r_N / R_i))^2}{2(log\sigma_i)^2}\right)$$

where: r_N is the dry AP's radius, R_i is the mean geometric radius, n_i is the AP's concentration and s_i is the standard deviation of the i- didtribution. N_{APa} is the total number concentration of APs. The values of n_i, R_i, s_i for both maritime and rural spectra are given by Jaenicke, 1988.

To study the gaseous absorption we simulated two cases for gas concentration which can be seen in the Table 1.

TABLE 1. Cases of gas concentrations (in ppb)

CASE	$[SO_2]$	$[H_2O_2]$	$[O_3]$
CASE1	5	0.5	50
CASE2	0.5	0.5	30

The air parcel starts its ascent having an initial radius of 350m and a vertical velocity of 1m/s from a height of 1Km. The relative humidity was 99%. The time step was 2s and the size range for APs and droplets were between 0.001-10μm and 1-2500μm, respectively. The duration of the simulations was 1600s.

We carried out four simulations whose characteristics are given in the Table 2.

The processing of the APs has been studied in the following way. First we compared the following spectra:

TABLE 2. Cases of the simulations

SIMULATION	TYPE OF SPECTRUM	GAS CONCENTRATION
1	RURAL	CASE 1
2	RURAL	CASE 2
3	MARITIME	CASE 1
4	MARITIME	CASE 2

i) the initial dry AP spectrum, i.e. the input spectrum before the cloud formation (at 0s).
ii) the interstitial dry AP spectrum at the end of the cloud life-time cycle (at 1600s) i.e. the population of APs in the air being not activated.
iii) the dried-off spectrum at 1600s i.e. the population of APs that would result if we instantaneously evaporated the cloud and considered all the soluble material contained in a droplet becoming a single particle.

Then we studied the activation (CCN) spectra that corresponds to the beginning (0s) and the end (1600s) of the simulation for both maritime and rural cases.

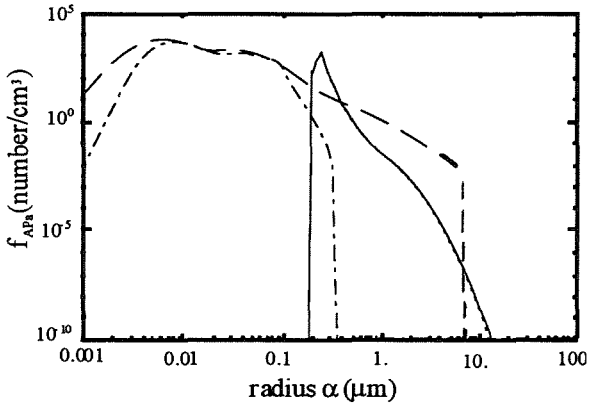

FIG. 1. Processing of a rural aerosol spectrum consisted of $(NH_4)_2SO_4$ for a high gas concentration (case 1). The dashed line represents the initial (0s) dry AP spectrum, the dashed-dotted one the final (1600s) interstitial spectrum, the dotted line corresponds to the dried-off spectrum (0s) without gas scavenging and the solid line to dried-off with gas scavenging (0s).

The figure 1 corresponds to simulation 1 which is for a rural AP spectrum consisted entirely of $(NH_4)_2SO_4$ (i.e. it has a solubility ε equal to 1) and a high gas concentration. The dashed line corresponds to the initial AP spectrum. The final AP spectrum consists of two parts: one from the interstitial AP spectrum (dashed-dotted line) which became depleted at its small end by impaction scavenging. The other part results from the dried-off droplets. We see that the final AP spectrum is weakly broader than the initial one in a way that the number of giant CCN is increased while the number of smaller CCN (of radius around 1μm) has decreased. This weak broadening is due to the weak collision/coalescence processes owing to the high number of the APs that have been activated and the relativelly small supersaturation affecting them. We notice also the overlap occuring between the interstitial and the dried-off spectra which can be explained by the entrainment.

In the figure 2 is shown the result of the second simulation. The only difference in comparison with the figure 1 is the lower gas concentration (case 2). The lower gas concentration seems to lead to a so weak gas scavenging that the difference in the shifts produced in the final AP spectra is nearly invisible in figure 2.

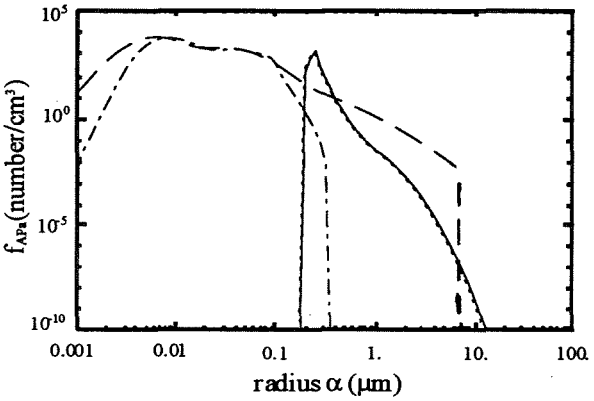

FIG. 2. Processing of a rural aerosol spectrum consisted $(NH_4)_2SO_4$ of for a low gas concentration (case 2). The lines are the same as in figure 1.

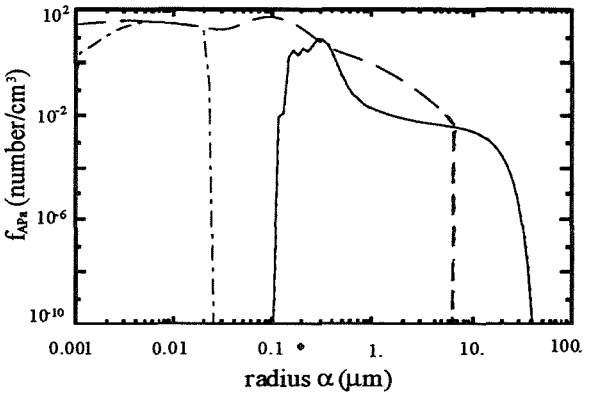

FIG. 3. Processing of a maritime aerosol spectrum consisted of $(NH_4)_2SO_4$ for a high gas concentration (case 1). The lines are the same as in figure 1.

The figure 3 shows the processing of a maritime aerosol spectrum consisted entirely of $(NH_4)_2SO_4$ during a first cloud cycle with a high gas concentration (third simulation). There are the same kind of curves for the dry initial AP spectrum, the final interstitial, the final dried-off without and with gas scavenging. Now a larger broadening of the AP spectrum is well marked which can be explained by the smaller number of activated CCN which produces stronger collision and coalescence effects. These strong processes exceeding the

air-entrainment are the origin of the large gap separating the interstitial and the dried-off AP spectra.

We see a similar effect in figure 4 where the results for the simulation 4 are shown. Simulation 4 differs from the simulation 3 in the gas concentration which is lower (case 2). In both figures 3 and 4 the shift caused by the gas scavenging is more remarkable than in the figures 1 and 2 remaining deeper in figure 3 (high gas concentration), than in figure 4 (lower one).

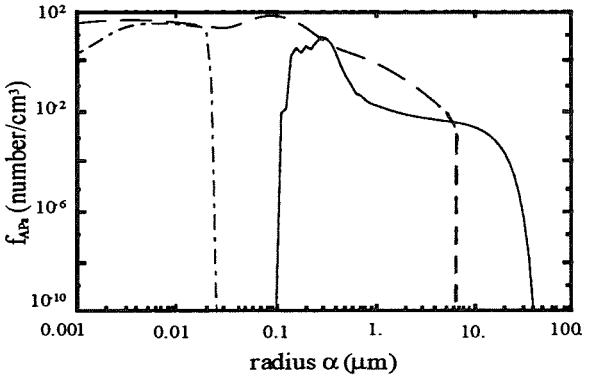

FIG. 4. Processing of a maritime aerosol spectrum consisted of $(NH_4)_2SO_4$ for a low gas concentration (case 2). The lines are the same as in the figure 1.

A comparison between the initial and the final CCN spectra (at the beggining - 0s - and at the end - 1600s - of the simulation) is shown in the figures 5 and 6 for the rural and the maritime cases respectively. In each figure the ordinate corresponds to the number of APs (in number per cm^3) which became activated at a certain supersaturation (in %) corresponding to the x-axis. The solid lines tally with the initial AP spectra at 0s of the simulation while the dashed ones to the final spectra at 1600s simulation. We see that the processing of the AP spectrum by the convective cloud results in a smaller number of CCN in a way that if the processed final AP spectrum had become activated it could lead easier and faster to formation of precipitation (taking into account the higher number of giant CCN as we saw before).

To confirm that indication we used the processed AP spectrum of maritime type (at the end of the 1-st cycle) which consisted of the interstitial and the dried-off spectra as an input for a second air parcel model run during a new (second) cloud lifetime cycle. The figure 6 shows the droplet number distribution spectra at the end (1600s) of the first and the second cloud lifetime cycles.

We notice that a second cloud event results in a higher number of precipitation sized drops.

There is a big need to study the radiative microphysical properties of clouds in view of a better comprehension of the earth's climate and its response to anthropogenic and natural variability (Hobbs, 1993). Clouds are very important because they can modulate the energy balance of the earth and atmosphere through their interaction with shortwave and longwave radiation.

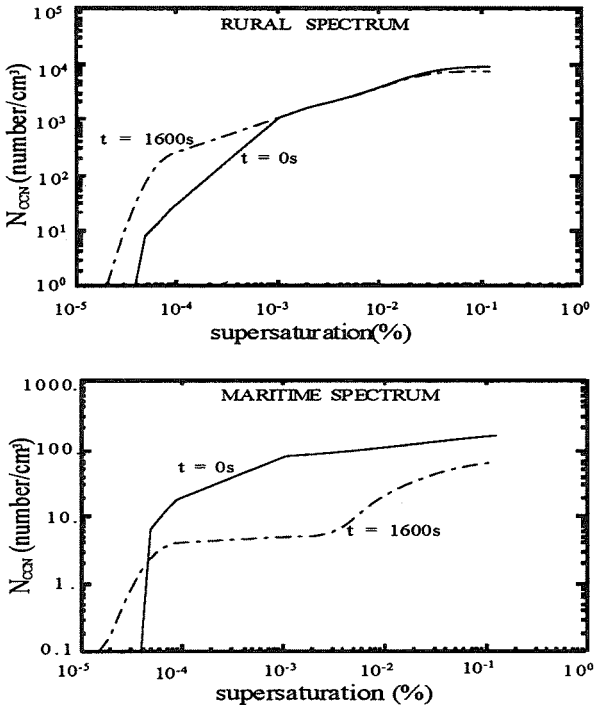

FIG. 5. Comparison of initial and final CCN spectra for a rural and a maritime aerosol spectra consisted by $(NH_4)_2SO_4$.

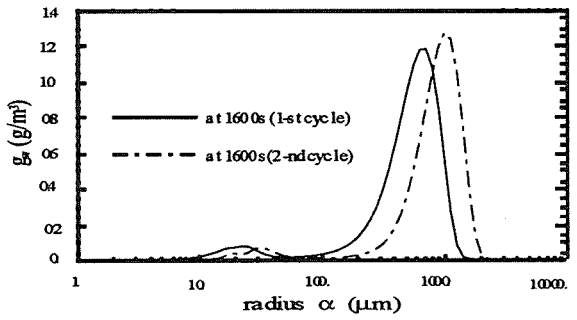

FIG. 6. Comparison between the mass droplet spectra at the end of a first and a second cloud life-time cycle for a maritime cloud.

By changing the droplet size distribution and concentration the optical properties of a cloud may be altered sufficiently to change the global energy budget and thus the climate (Twomey 1977, Charlson et. al. 1987). Two of the most important parameters needed to describe the radiative properties of clouds are the single scattering albedo ω_0 and the asymmetry factor g.

Attempts have been made to study the dependance of cloud radiative properties on the liquid water path (which is the integrated liquid water content) and on the

droplet concentration and number distribution taking into account variation of one of these parameters the others kept fixed (Slingo and Schrecker 1982, Stephens 1978, Martin et. al. 1994, Jonas 1990).

An attempt has now been made to study the evolution of main radiative properties such as the single scattering albedo and the asymmetry factor of a cloud during its lifetime cycle.

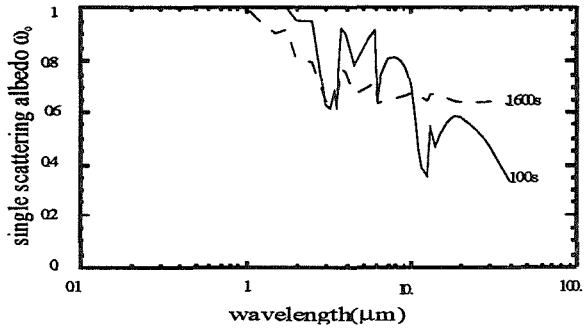

FIG.8. Comparison of single scattering albedo of a maritime cloud at the beggining and the end of its lifetime cycle.

The figure 8 shows the wavelength dependent single scattering albedo for two stages of a maritime cloud evolution: at the beginning (100s) and at its end (1600s). We see that for the shortwave wavelength band the single scattering albedo decreased while for the longwave band (>0.8μm) it increased. This is explained by the fact that at 1600s we have more big and less small droplets than at 100s.

In the figure 9 the evolution of the asymmetry factor g during the cloud lifetime cycle is shown. We see again an increase of the asymmetry factor in the longwave band and a decrease in the shortwave region at the end of the cloud cycle (1600s).

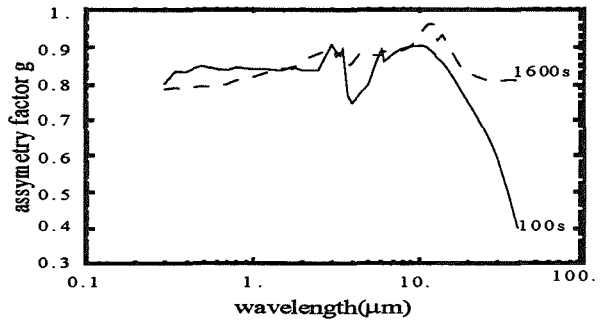

FIG.9. Comparison of assymetry factor of a maritime cloud at the beggining and the end of its lifetime cycle.

3. CONCLUSIONS

An aerosol particle spectrum experiences a processing by a convective cloud during its lifetime cycle, in a way that the processed spectrum becomes broader containing more big aerosol particles. This broadening is stronger in maritime clouds than in the rural ones. The effect of gas scavenging has been assessed and estimated to contribute only little due to its low initial concentration. The broadening results in a production of more precipitation sized drops in a second lifetime cycle (cloud event).

During the first cloud cycle an essential evolution of radiation properties has been estimated leading to a decrease of the single scattering albedo and the asymmetry factor in the shortwave band and an increase in the longwave region.

4. REFERENCES

Charlson, R.J., J.E. Lovelock, M.O. Andreae and S.G. Warren, 1987: Ocean phytoplancton, atmospheric sulfur, cloud albedo and climate. *Nature*, **326**, 655-661.

Flossmann, A.I., 1987: A theoretical investigation of the removal of atmospheric trace constituents by means of a dynamic model. *Ph.D. Thesis*, Mainz.

Flossmann, A.I., W.D. Hall and H.R. Pruppacher, 1985: A theoretical study of te wet removal of atmospheric pollutants. Part I: the redistribution of aerosol particles captured through nucleation and impaction scavenging by growing cloud drops. J. Atm. Sci., 42, 583-606.

Hobbs, P.V., 1993: *Aerosol-Cloud-Climate Interactions*. Academic Press, Inc.,xi.

Jaenicke, R., 1988: *Aerosol physics and chemistry. In Landolt-Boernstein: Zahlenwerte und funktionen aus naturwissenschaften und technik*, V4b, G. Fischer, Editor, Springer, 391-457.

Jonas, P., 1990: On the parameterization of clouds containing water droplets. *Quart. J. Roy. Meteor. Soc.*, **117**, 257-263.

Lee, I.Y., G. Hanel and H.R. Pruppacher, 1980: A numerical determination of the evolution of cloud drop spectra due to condensation on natural aerosol particles. *J. Atm. Sci.*, **37**, 1839-1853.

Slingo, A. and H.M. Schrecker, 1982: On the shortwave radiative properties of stratiform water clouds. *Quart. J. Roy. Meteor. Soc.*, **108**, 407-426.

Stephens, G.L., 1978: Radiation profiles in extended water clouds.II: parameterization schemes. *J. Atm. Sci.*, **35**, 2123-2132.

Twomey, S., 1977: The influence of pollution on the shortwave albedo of clouds. *J. Atm. Sci.*, **34**, 1149-1152.

RETRIEVAL METHODS FOR THE EFFECTIVE RADIUS IN NUMERICAL MODELS

Klaus Wyser

Dept. of Meteorology, Stockholm University, 106 91 Stockholm, SWEDEN

1 INTRODUCTION

Clouds interact with atmospheric radiation and the importance of clouds for the energy budget is well-known. However, clouds have been dealt with in a crude way in GCM and NWP models and radiative transfer calculation with different numerical models scatter in a wide range (Fouquart et al., 1991). The reflection and absorption of both solar (SW) and terrestrial (LW) radiation takes place in the cloud particles and the lack of microphysical information leads to the large uncertainty concerning radiative cloud forcing.

Three parameters are sufficient to describe a cloud in radiation computations:

- the optical thickness τ
- the single scatter albedo ω
- the asymmetry parameter g

Several suggestions have been presented that relate τ, ω and g to the microphysical composition of the cloud (e.g. Slingo and Schrecker, 1982; Ebert and Curry, 1992). The radiative properties may be parameterized in terms of the effective radius r_e which contains information about the size distribution of the cloud particles. How can r_e be obtained from a large scale model that does not contain explicit microphysics? The problem is treated separately for (liquid) water clouds and ice clouds.

The total number of droplets in water clouds is related to aerosol concentrations dependant upon the geographic location. The widely accepted distinction between marine and continental clouds is here further refined for stratiform clouds. Two more types are introduced: Polar clouds and clouds over remote continental areas (deserts). The effect of the different cloud types on the reflection and absorption of radiation is investigated.

The problem of finding r_e for ice clouds is twofold: What do particle spectra in ice clouds look like? How to define r_e for non-spherical particles? A particle spectrum is suggested where special attention is paid to small, often undetected, ice crystals. Based on this spectrum, r_e may be parameterized in terms of temperature and ice water content.

2 WATER CLOUDS

2.1 Stratiform Clouds

Assume a droplet spectrum $n(r)$ with respect to the radius r and the total number of droplets N. The liquid water content LWC can be written as

$$LWC = \frac{4\pi}{3}\rho_\ell N r_3^3 \tag{1}$$

where the mean volume radius is

$$r_3^3 = \frac{\int r^3 n(r)\,dr}{\int n(r)\,dr} \tag{2}$$

The effective radius r_e is defined as the ratio of the 3rd to the 2nd moment of the distribution

$$r_e = \frac{\int r^3 n(r)\,dr}{\int r^2 n(r)\,dr} \tag{3}$$

Martin et al. (1994) relate r_e and r_3:

$$r_3^3 = k r_e^3 \tag{4}$$

Type	N [cm^{-3}]	Height [m]
Polar	16	500
Marine	52	1000
Continental	274	2500
Desert	394	2500
Background	87	

TABLE 1: Droplet concentration for different locations at the surface, background denotes value in the free troposphere.

where k=0.80 for marine and k=0.67 for continental clouds is obtained from observations. Together with (1) follows

$$r_e = \left(\frac{3LWC}{4\pi\rho_\ell k N} \right)^{\frac{1}{3}} \qquad (5)$$

Hence, the problem is to find suitable values for N. Martin et al. (1994) relate N to A, the number concentration of aerosol with radius between 0.05–1.5 μm. Instead of having two relations, one for marine and one for continental clouds, a more general approach would be

$$N = N_0 \left(1 - \exp\left(-A/A_0\right)\right) \qquad (6)$$

where the parameters N_0=400 and A_0=500 are derived from a visual fit through the data in Fig. 8 of the article by Martin et al. (1994). The generalisation takes into account that all aerosol particles are activated as droplets at low aerosol concentration, while at higher aerosol concentrations the droplet number is lower than the aerosol number.

Jaenicke (1993) presents typical aerosol spectra for 7 different locations. The number of aerosol particles in the range between 0.05–1.5 μm is obtained numerically from the distributions, which together with (6) yields the number of droplets shown in Tab. 1. Note that N for urban and N for rural areas derived in that way do not differ very much even though the total aerosol concentration is 15 times higher in urban areas. 'Rural' and 'urban' from Jaenicke are thus combined to one type 'continental' in this study. 'Remote continental' from Jaenicke was measured in Siberia but is used here as type 'desert'. Han et al. (1994) observe the smallest r_e over deserts and conclude that the number of droplets is largest there. The dry Siberian plains with wind produced aerosol serve as generalisation for desert regions. In agreement with Han's finding the number of droplets is highest for the type 'desert'. Aerosol and droplet concentrations are assumed to change linearly with height to reach the background value of the free troposphere at the height given in column 3 of Tab. 1.

The impact of the different cloud types is illustrated with an example. A 1000 m thick stratiform cloud with a LWC of 0.3 gm^{-3} is placed in a U.S. standard atmosphere with cloud base at 340 m. Activation of cloud droplets takes place at cloud base. Thus, N is calculated in the lowest cloud layer and kept constant through the whole cloud. A GCM type 1-dim radiation model with high vertical resolution calculates the radiative fluxes through the cloud. SW reflectivity is defined as the ratio of up- to downwelling radiation at cloud top and SW absorptivity is the ratio of radiation absorbed in the cloud to the downwelling radiation at cloud top. Tab. 2 presents results for SW reflectivity and absorptivity. The largest differences between the cloud types may be found in the reflectivity: Clouds over land consist of smaller particles and reflect more sunlight than clouds over the oceans. The new types 'polar' and 'desert' do not differ very much from the main types 'marine' and 'continental' respectively.

Type	Ref [%]	Abs [%]	r_e [μm]
Polar	77.4	11.6	10.5
Marine	76.8	11.7	11.0
Continental	81.4	10.5	7.5
Desert	82.5	10.1	6.8

TABLE 2: SW cloud reflectivity and absorptivity for stratiform clouds at different locations. Temperature, humidity and cloud water profile is the same for all runs.

2.2 Convective Clouds

Based on observations, Bower et al. (1994) propose a fixed value for r_e if the vertical cloud extension exceeds a certain limit. Here a slightly different approach is suggested: Take N at cloud base and calculate r_e according to (5) in the lowest 500 m in clouds over land or the lowest 1500 m over sea, the value of r_e is thereafter kept constant in the upper part of the cloud.

Tab. 3 presents SW reflection and absorption calculated with the suggested parameterization r_e for a convective cloud located over land or over sea. Cloud base is at 340 m and top at 3400 m in a standard atmosphere. LWCincreases linearly to 0.6 gm^{-3} at 200 m above cloud base and remains constant in the upper part of the cloud. The smaller r_e over land leads to higher reflection and less

Type	Ref [%]	Abs [%]	r_e [μm]
Sea	82.5	15.4	14.7
Land	85.9	12.8	9.5

TABLE 3: As Tab. 2 but for convective clouds. The effective radius is from the upper part of the cloud.

absorption of sunlight than over sea.

3 ICE CLOUDS

In general ice particles are non-spherical and thus r_e must be defined in a different way than in (5). Based on Liou (1992)

$$r_e = 0.5 \frac{\int D^2 Ln(L)\, dL}{\int DLn(L)\, dL} \qquad (7)$$

where $n(L)$ is the particle distribution with respect to the maximum particle dimension L. The width (minimum dimension) D of the particles is parameterized in terms of L under the assumption of the particles being hexagonal columns for L>30 μm and spheres otherwise.

$$D = \begin{cases} L & L \leq 30\,\mu\text{m} \\ L/\left(.0016\,(L-30)+1\right) & L > 30\,\mu\text{m} \end{cases}$$

The spectrum $n(L)$ is parameterized in a way similar to the widely accepted parameterization of Heymsfield and Platt (1984)

$$n(L) \sim L^B \qquad (8)$$

This study suggests a parameterization of B as a function of ice water content IWC and temperature T_C (in °C).

$$B = B_0 + B_1 |T_C|^{1.5} \log_{10}(IWC/IWC_0) \qquad (9)$$

The parameters are B_0=−2, B_1=10^{-3}, and IWC_0=50 gm^{-3}. The last expression is an attempt to fit B for the data from Heymsfield and Platt (1984) and recent data from CEPEX (A. Heymsfield, pers. communication). The form of (9) is chosen in such a way that the spectrum broadens for warmer T and/or larger IWC.

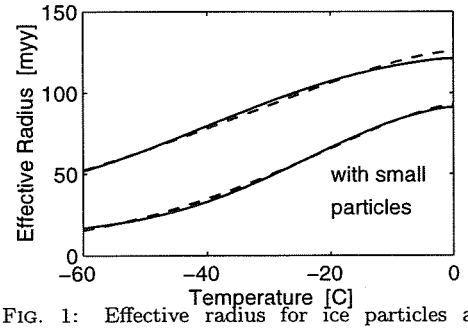

FIG. 1: Effective radius for ice particles as a function of temperature, shown are values with IWC=0.01 gm^{-3}. Solid lines denote results from the 'exact' calculation (7) and dashed lines the fit according to (10). The upper lines are from calculations without small particles.

Limits [μm]	i	a_{i2}	a_{i1}	a_{i0}
40 − 1000	1	-0.09	-0.90	123.5
	2	-0.049	-2.6	7.94
1 − 1000	1	-0.20	-0.70	93.7
	2	-0.22	-5.3	18.9

TABLE 4: Values for a in the parameterization of A_1 and A_2. 'Limits' denotes the integrations limit used in (7). The upper two rows are for a spectrum without small ice particles.

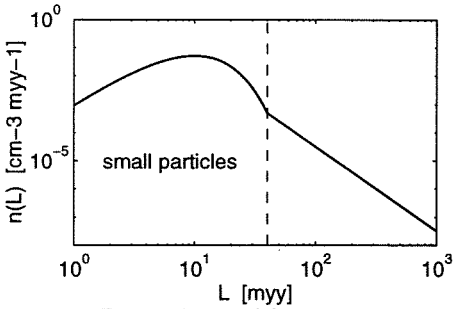

FIG. 2: Ice particle spectrum.

Next, r_e is computed for a wide range of T_C and IWC according to (7). The integration limits in (7) are crucial; see the comments in Sec. 3.2. In a first approximation the lower and upper limit have been chosen as 40 μm and 1000 μm respectively. Fig. 1 shows r_e as a function of T_C for a fixed IWC. Finally, a fit through the calculated r_e yields a simple parameterization, $\hat{r}_e$, in terms of T_C and IWC

$$\hat{r}_e = A_1 \exp\left(-A_2 |T_C|^{1.5}\right) \qquad (10)$$

with

$$\begin{aligned} A_1 &= a_{12}X^2 + a_{11}X + a_{10} \\ A_2 &= \left(a_{22}X^2 + a_{21}X + a_{20}\right) \times 10^{-4} \end{aligned}$$

where $X = \log(IWC)$ means the natural logarithm of the IWC in gm^{-3} and $\hat{r}_e$ is in μm. The values for a are given in the upper two rows of Tab. 4.

3.1 Impact of small ice particles

Ice particles are difficult to measure and small ice particles even more so. In many available datasets, particles with L smaller than a few 10 μm are neglected. This is unimportant for the IWC, but the radiative parameters may be affected seriously. Smaller ice particles reflect more and absorb less radiation than larger ones. In a recent study, Sun and Shine (1995) correct τ, ω and g to include the effects of small ice particles. In this study, the small particles are

included already in the parameterization of r_e by adding a gamma distribution at the lower end of (8).

$$n(L) = \begin{cases} \gamma L^{\alpha} \exp(L/\beta) & L < 40\,\mu\text{m} \\ AL^{B} & L \geq 40\,\mu\text{m} \end{cases}$$

The parameters A, α, β, and γ are chosen so that $n(L)$ resembles typical observed particle spectra in Ci clouds (see Fig. 2). The same procedure as described above is applied to deduce a parameterization for r_e. Expression (10) is still valid but the parameters for A_1 and A_2 change, see the lower two lines in Tab. 4. The given A_1 and A_2 are for a mode radius r_m=$\alpha\beta$=5 μm. A sensitivity study where r_m is varied shows that the exact knowledge of the spectrum for small particles is of minor importance. The ratio of r_e computed with small particles to r_e computed without is 0.35 for r_m=2 μm and 0.5 for r_m=15 μm.

The effect of small particles is demonstrated in an example: An ice cloud is located between 8000 m and 9000 m in a standard atmosphere with an ice water path of 10 gm^{-2}. SW reflectivity and absorptivity is calculated for two cases and presented in Tab. 5. In case 1, r_e is parameterized under the assumption that the cloud contains no small particles while case 2 includes particles below 40 μm. Small ice particles change the radiative properties of a cloud tremendously.

3.2 Integration Limits

In the spectrum ranging from 1 μm to 1000 μm, the particles with L<40 μm stand for 95% of the total number, 70% of the surface and 20% of the volume. On the other hand 10% of the surface and 50% of the volume are in the range with L>200 μm. Broadly speaking, scattering is proportional to the total surface area and absorption to the total volume contained in the particle spectrum. Hence, r_e must contain information about both small and large particles. In the case of the lower integration limit beeing 40 μm, r_e is two times larger compared to the case where the small particles are included. If the upper integration limit is set to 200 μm, r_e is only half the value obtained by a full integration to 1000 μm. These examples elucidate the sensitivity of r_e to the presence of small and large particles. Clearly, more information is needed about the abundance and size of ice particles in the atmosphere.

Case	Ref [%]	Abs [%]	r_e [μm]
1	12.3	2.6	108
2	17.8	3.1	48

TABLE 5: As Tab. 2 but for an ice cloud. Case 1 does not include particles below 40 μm in the parameterization of r_e while case 2 includes small particles. The given r_e is a mean value for the cloud.

4 ACKNOWLEDGEMENTS

This study has been supported by the Swedish National Research Council (NFR) under contract G-AA/GU02923-316.

REFERENCES

Bower, K. N., T. W. Choularton, J. Latham, J. Nelson and M. B. Baker, 1994: A parameterization of warm clouds for use in general circulation models. *J. Atmos. Sci.*, **51**, 2722–2732.

Ebert, E. E. and J. A. Curry, 1992: A parameterization of ice cloud optical properties for climate models. *J. Geophys. Res.*, **97**, 3831–3836.

Fouquart, Y., B. Bonell and V. Ramaswamy, 1991: Intercomparing shortwave radiation codes for climate studies. *J. Geophys. Res.*, **96**, 8955–8968.

Han, Q., W. B. Rossow and A. A. Lacis, 1994: Near-global survey of effective radii in liquid water clouds using ISCCP data. *J. Climate*, **7**, 465–497.

Heymsfield, A. J. and C. M. R. Platt, 1984: A parameterization of the particle size spectrum of ice clouds in terms of the ambient temperature and ice water content. *J. Atmos. Sci.*, **41**, 846–855.

Jaenicke, R., 1993: Tropospheric aerosols. in P. V. Hobbs, editor, *Aerosol-Cloud-Climate Interactions*, pp. 1–31. Academic Press.

Liou, K. N., 1992: *Radiation and cloud processes in the atmosphere.* Vol. 20 of *Oxford monograph on geology and geophysics.* Oxford University Press, 487 pp.

Martin, G. M., D. W. Johnson and A. Spice, 1994: The measurement and parameterization of effective radius of droplets in warm stratocumulus clouds. *J. Atmos. Sci.*, **51**, 1823–1842.

Slingo, A. and H. M. Schrecker, 1982: On the shortwave radiative properties of stratiform water clouds. *Quart. J. Roy. Meteor. Soc.*, **108**, 407–426.

Sun, Z. and K. P. Shine, 1995: Parameterization of ice cloud radiative properties and its application to the potential climatic importance of mixed-phase clouds. *J. Climate*, **8**, 1874–1888.

THE CONDENSATION COEFFICIENT REDUCTION AS A MAJOR FACTOR FOR ALBEDO ENHANCEMENT IN POLLUTED CLOUDS

N. Fukuta and Y.S. Zou

Department of Meteorology, University of Utah, Salt Lake City, UT 84112, USA

1. INTRODUCTION

The microphysical properties of clouds are known to affect the Earth's radiative balance as well as the subsequent precipitation development. The number concentration, N, and size of cloud droplets are largely decided in the initial stage of their formation in which the activity spectrum of Cloud Condensation Nuclei (CCN) and growth of nucleated droplets interact in the updraft of supersaturation generating air. This interaction is a key to understanding the problem but is poorly understood, or else the mistreatment is not uncommon.

In regard to the microphysics-dynamics interaction above the cloud base, analytic solutions exist (Twomey, 1959; Fukuta and Xu, 1996) that employ the Maxwellian droplet growth theory. While the functional relationships among the variables are well exposed, these analytic solutions face two major uncertainties, the haze process before the nucleation and the resistance effects of vapor and heat transportation across the surface of growing droplets, i.e., the condensation coefficient, β, and the thermal accommodation coefficient, α. Numerical modeling approach has been frequently taken to solve these problems. However, there exist different diffusion-kinetic (DK) droplet growth equations dealing with the accommodation coefficient effects, and their choice largely affects the model outcome. Therefore, we shall critically examine different DK equations, select the correct one and incorporate it into the interaction model to evaluate the accommodation coefficient effects on the supersaturation maximum, the droplet number concentration and the resultant cloud albedo change.

2. CRITICAL EVALUATION OF DROPLET GROWTH EQUATIONS

It has been well established that the Maxwellian droplet growth equation is a special case of the DK equation under droplet radius $r \to \infty$ (Fukuta and Walter, 1970). Apart from minor treatment differences, a major discrepancy is observed among the DK equations, i.e., some add the mean free path length, Δ, to r in the solution of continuum flow field. It appears to have originated from Fuchs (1959) as

$$\frac{dm}{dt} = \frac{4\pi r(S-1)}{\dfrac{r}{r+\Delta} + \dfrac{D}{v\beta r}} \cdot \frac{1}{[A+B]}, \qquad (1)$$

v being the average molecular velocity.

Fitzgerald (1978) used;

$$\frac{dm}{dt} = \frac{4\pi r(S-1)}{\left[\dfrac{A}{f'_\alpha} + \dfrac{B}{f'_\beta}\right]}, \qquad (2)$$

$$f'_\alpha = \left[\frac{r}{r+\Delta} + \frac{\ell'_\alpha}{r}\right]^{-1}, \quad \ell'_\alpha = \frac{K(2\pi R_a T_\infty)^{1/2}}{\alpha P C_p},$$

$$f'_\beta = \left[\frac{r}{r+\Delta} + \frac{\ell'_\beta}{r}\right]^{-1}, \quad \ell'_\beta = \frac{D}{\beta}\left(\frac{2\pi}{R_a T_\infty}\right)^{1/2}.$$

Whereas, Fukuta (1992) gives;

$$\frac{dm}{dt} = \frac{4\pi r(S-1)}{\left[\dfrac{A}{f_\alpha} + \dfrac{B}{f_\beta}\right]}, \qquad (3)$$

$$f_\alpha = \frac{r}{r+\ell_\alpha}, \quad \ell_\alpha = \frac{2-\alpha}{2\alpha}\frac{K(2\pi R_a T_\infty)^{1/2}}{P(C_v + \tfrac{1}{2}R_a)},$$

$$f_\beta = \frac{r}{r+\ell_\beta}, \quad \ell_\beta = \frac{2-\beta}{2\beta} D\left(\frac{2\pi}{R_v T_\infty}\right)^{1/2}.$$

$$A = \left(\frac{L_c}{R_v T_\infty} - 1\right)\frac{L_c}{K T_\infty}, \quad B = \frac{1}{\rho_{s\infty} D}.$$

Notations are:

C_v : specific heat of air at constant volume
C_p : specific heat of air at constant pressure
D : diffusivity of water vapor in air
K : thermal conductivity of air
L_c : specific latent heat of water vapor condensation
m : mass of droplet
P : air pressure
R_a : the specific gas constant of air
R_v : the specific gas constant of water vapor
S : saturation ratio

(S − 1): supersaturation
t : time
T_∞ : absolute temperature of environmental air
$\rho_{s\infty}$: saturation vapor density at T_∞

In the treatment, Δ comes in as $\partial\rho/\partial r \propto (r + \Delta)^{-1}$, where ρ is the vapor density. This is to say that water vapor has a uniform density between r and r + Δ under the steady state, which violates the continuity condition of vapor flow under the steady state. There exists no special zone at distance Δ away from the surface where molecules are "prepared" to fly into the droplet surface totally without collision in between. As a matter of fact, a continuum flow is a succession of free molecular flows. It should also be mentioned that in the Fitzgerald equation, C_p is used so that a work energy is exchanged, in this case, by expansion. This happens only when the system is changing towards the steady state or under the non-steady state, but when it achieves the steady state, no more expansion to lose the work energy outside takes place. Accordingly, the system takes up only C_v. The $\frac{1}{2}R_a$ term in Fukuta's equation is a correction due to the extra-contribution by higher velocity fraction of the gas molecules. There also exists a confusion between R_a and R_v in Fitzgerald's equation.

The DK equation given in Fukuta (1992) and Fukuta and Xu (1996) is based on the Knudsen treatment of accommodation phenomena right above the surface of the droplet (Chapman and Cowling, 1970) and is basically the same as that of Fukuta and Walter (1970) except that the representative α and β of the latter are replaced with their true values. Essentially the same equation is also used by Hagen et al. (1989).

Figure 1 compares the supersaturation profiles the numerical model generated during the cloud base nucleation-growth interaction using Eqs. (1), (2) and (3) as well as the Maxwellian equation. It may be seen that use of the Fitzgerald equation leads to an overestimation of supersaturation due to the slowest droplet growth and resultant lowering of supersaturation reduction which arises from $(r + \Delta)^{-1}$ contribution.

While the Fuchs equation has other serious problems such as the unrealistic symmetry between the vapor and temperature fields (cf. Fukuta and Walter, 1970), the Fuchs (r + Δ) treatment in place of r has been exercised by other researchers as discussed above (Fitzgerald, 1978; Young, 1993) without clear reasoning. The difference is indeed insignificant if the Knudsen number Kn = Δ/r « 1 (Pruppacher and Klett, 1978). However, in the microphysics dynamics interaction just above the cloud base, the whole process passes through the zone of Kn ≥ 1, and this problem can no longer be ignored.

A numerical cloud model has been assembled along the line described by Mason (1971) and Fukuta (1993) including the Cloud Condensation Nuclei (CCN) activity spectrum and haze process before nucleation for ammonium sulfate as the CCN compounds (Zou, 1996).

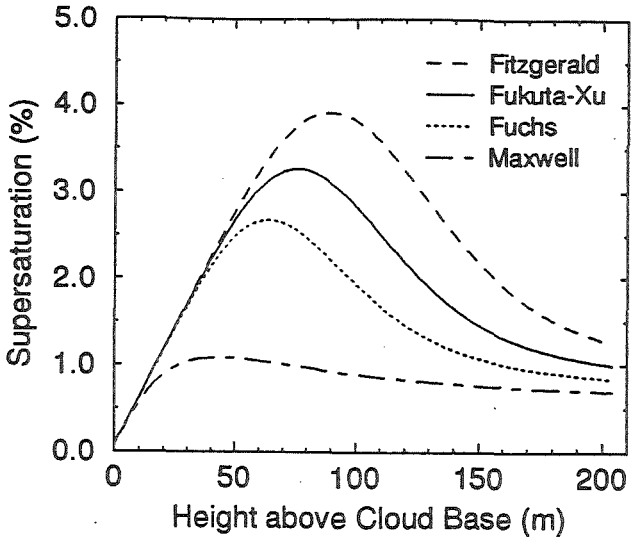

Fig. 1. Comparison of supersaturation maximum in the cloud base interaction predicted by different droplet growth equations. Condition; α = 1, β = 0.03, w_u = 2 m/s, P_b = 889.7 mb and T_b = 9.07 °C.

3. SUPERSATURATION MAXIMUM AND RESULTANT CLOUD ALBEDO CHANGE

The numerical cloud model using Eq. (3) was run for the CCN activity spectrum

$$N = C(S - 1)^k \qquad (4)$$

where N, C and k are the integral number of active nuclei and the CCN activity parameters, respectively. For the maritime cloud, C = 100, k = 0.5 were used and for the continental one, C = 500, k = 0.7 were taken. Ascent of the air parcel initiates at a pressure P_0 = 809.21 mb and a temperature T_0 = 10.93 °C with relative humidity RH = 95%, which gives the cloud base pressure P_b = 800 mb and the temperature T_b = 10 °C.

Figure 2 shows the effect of β with α = 1 on the maximum supersaturation, $(S - 1)_{max}$. For the maritime cloud, with β = 0.03, it may be seen that $(S - 1)_{max, DK} \approx 4(S - 1)_{max, MXW}$, where subscript DK and MXW stand for diffusion kinetic and Maxwellian, respectively.

Figure 3 shows the same effect for the continental cloud. For β = 0.03, $(S - 1)_{max, DK} \approx 6(S - 1)_{max, MXW}$. The β-effect is apparently larger with the continental cloud due to the smaller droplet size.

In view of gentle vapor and heat fluxes of cloud droplet growth under which α and β, β in particular, take small values (Pruppacher and Klett, 1978) which is in support by a laboratory measurement under the atmospheric condition (Hagen et al., 1989), it is clear that use of the Maxwellian droplet growth equation, which is rather common, will induce a large error in $(S - 1)_{max}$

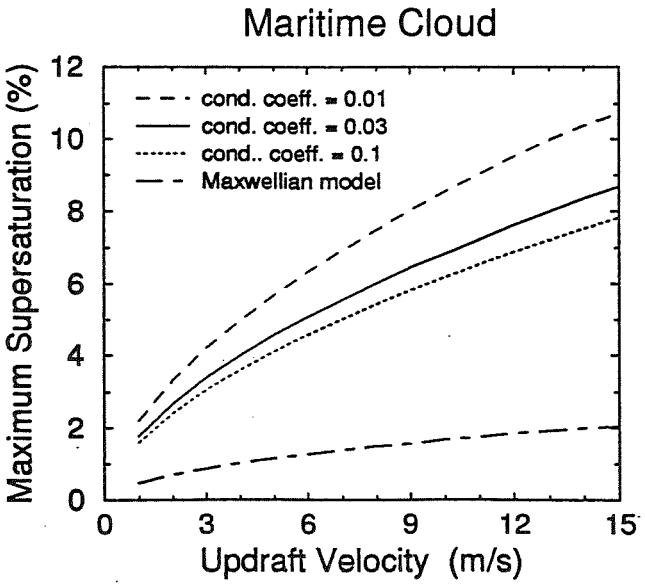

Fig. 2. Computed maximum supersaturation of maritime cloud plotted as a function of updraft velocity for different β with $\alpha = 1$.

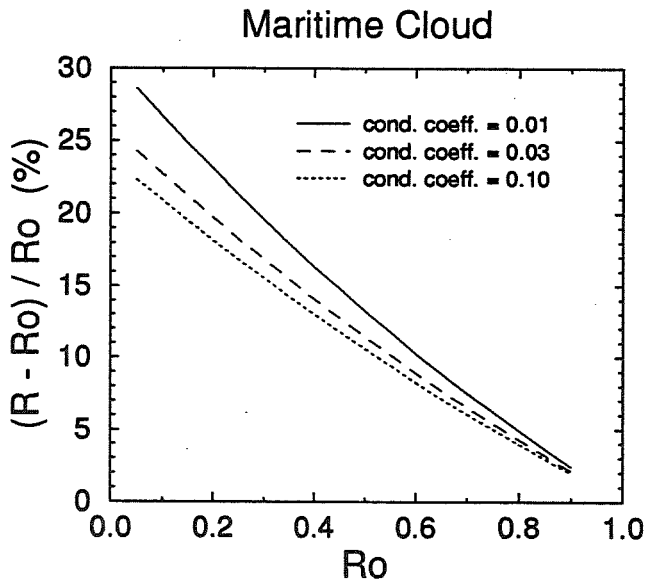

Fig. 4. Variation of computed relative albedo change of a maritime cloud plotted as a function of albedo for different β with $\alpha = 1$.

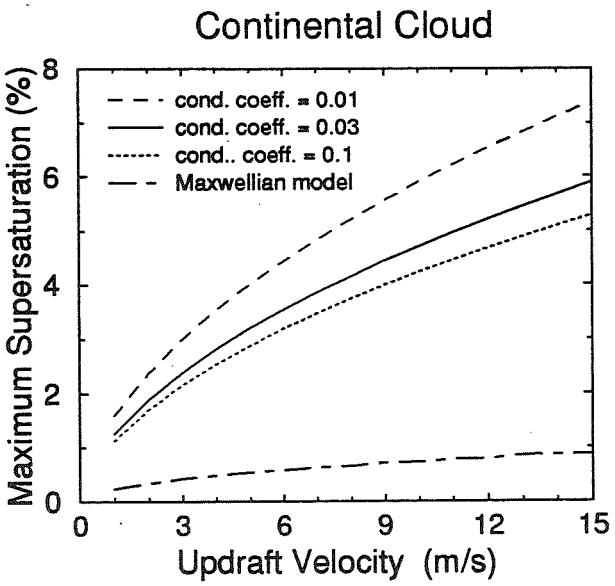

Fig. 3. Same as Fig. 2 except for continental cloud.

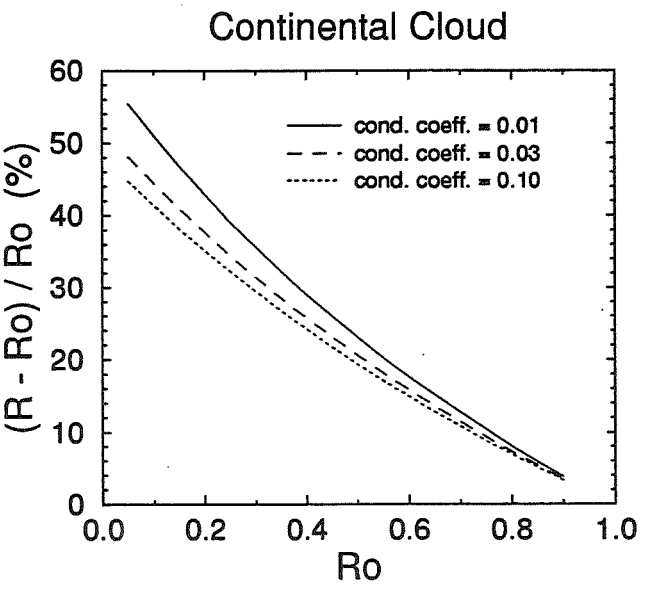

Fig. 5. Same as Fig. 4 except for a continental cloud.

estimation. The corresponding change of cloud albedo may be estimated based on the integral form of the equation given by Twomey (1991), assuming the relative effect remains in the cloud, as

$$R = \left[1 + \frac{1 - R_0}{R_0}\left(\frac{N_0}{N}\right)^{1/3}\right]^{-1}, \qquad (5)$$

where R is the cloud reflectivity with the droplet number concentration N at solar wave length under constant liquid water content and subscript 0 denotes the reference condition which is taken here as the value of Maxwellian case (Fukuta et al., 1995).

Figure 4 describes the relative albedo change $(R - R_0)/R_0$ for the maritime cloud as a function of the initial albedo R_0 for different β in the DK-droplet growth equation used in the model.

Figure 5 gives the relative albedo change for the continental cloud. The values are higher than those of the maritime cloud. This is obviously due to smaller droplet size in the continental cloud, and the DK effect on the droplet growth rate reduction is more enhanced with the smaller droplets (Fukuta and Walter, 1970).

In Fukuta et al. (1995), we showed that CCN doubling at the source does not result in the relative

albedo change equivalent to $N/N_0 = 2$, due to the non-linearity of the activation process and particle coagulation. The values shown in Figs. 4 and 5 are approximately additive to the Maxwellian one, and the use of the DK theory instead of the Maxwellian gives about 4 times more for the maritime cloud and about 8 times more than the relative increase of albedo under doubled CCN concentration under coagulation.

The DK effect on the relative albedo change is large. Nevertheless, variation of β from the background value by the air pollution is difficult to assess at this moment due to the lack of measurement. Considering strong dependence of the relative albedo change on β, such a measurement should be carried out, though not easily, since the data are crucial for this problem.

4. CONCLUSION

For the DK theory of droplet growth, use of $r + \Delta$ in place of r in the gradient was shown to be erroneous. Using a correct DK theory of droplet growth, a numerical cloud model was formulated and the effect of β was evaluated. Both the maximum supersaturation and the relative albedo variations were found to be larger with the continental cloud than with maritime cloud due to the smaller droplet size. In both clouds, β reduction was shown to increase the albedo drastically showing β as the major factor in albedo change evaluation by the anthropogenic activities. It was shown that use of the Maxwellian droplet growth theory induces a large error in the albedo evaluation, and the importance of β measurement in background and polluted air masses was pointed out.

Acknowledgment. This work was supported by the Division of Atmospheric Sciences, National Science Foundation, under Grant ATM-9112888.

5. REFERENCES

Chapman, S., and T.G. Cowling, 1970: *The Mathematical Theory of Non-Uniform Gases.* Cambridge Univ. Press, Cambridge, 422 pp.

Fitzgerald, J.W., 1978: A numerical model of the formation of droplet spectra in advection fogs at sea and its applicability to fogs off Nova Scotia. *J. Atmos. Sci.*, **35**, 1522-1535.

Fuchs, N.A., 1959: *Evaporation and Droplet Growth in Gaseous Media.* Pergamon Press, 72 pp.

Fukuta, N., 1992: Theories of competitive cloud droplet growth and their application to cloud physics studies. *J. Atmos. Sci.*, **49**, 1107-1114.

——, 1993: Water supersaturation in convective clouds. *Atmos. Res.*, **30**, 105-126.

——, N. Xu, and Y.S. Zou, 1995: CCN change, droplet generation and cloud albedo variation. *Preprints Conf. on Cloud Physics*, Amer. Meteor. Soc., Dallas, Texas, 487-492.

——, and N. Xu, 1996: Nucleation-droplet growth interactions and microphysical property development in convective clouds. *Atmos. Res.* (in press).

Hagen, D.E., J. Schmitt, M. Trueblood, J. Carstens, D.R. White, and D.J. Alofs, 1989: Condensation coefficient measurement for water in the UMR cloud simulation chamber. *J. Atmos. Sci.*, **46**, 803-816.

Mason, B.J., 1971: *The Physics of Clouds*, 2nd ed. Oxford Univ. Press, London, 671 pp.

Pruppacher, H.R., and J.D. Klett, 1978: *Microphysics of Clouds and Precipitation.* D. Reidel Publishing Co., Boston, 714 pp.

Twomey, S., 1959: The nuclei of natural cloud formation. II. The supersaturation in natural clouds and the variation of cloud droplet concentrations. *Geofis. Pura. Appl.*, **43**, 243-249.

——, 1991: Aerosols, clouds and radiation. *Atmos. Env.*, **25A**, 2435-2442.

Young, K.C., 1993: *Microphysical Processes in Clouds.* Oxford Univ. Press, N.Y., 427 pp.

Zou, Y.-S., 1996: *Model Simulation of Convective Cloud Formation and Its Influence on Cloud Optical Properties.* Ph.D. Dissertation, Department of Meteorology, Univ. of Utah.

THE EFFECTS OF AEROSOL ON WARM STRATOCUMULUS CLOUD LAYER MICROPHYSICS: AN INVESTIGATION USING SHIP TRACK EMISSIONS.

Doug W. Johnson, Simon R. Osborne and Jonathon P. Taylor

Met. Research Flight, Y46, DERA, Farnborough, Hants GU14 6TD, U.K.

1. INTRODUCTION

The indirect effect of aerosols has been identified as one of the largest uncertainties in the radiative balance of the Earth's atmosphere (IPCC 1996 report) and needs to be determined for climate change prediction. Stratus and stratocumulus clouds have relatively high albedos and reduce the shortwave radiation received at the Earth's surface (Albrecht et al 1988). These boundary layer clouds are therefore important components of the Earth's energy budget. They are observed to occur in very persistent sheets covering large areas of the eastern parts of subtropical ocean basins. The reflectivity of these clouds is very sensitive to their liquid water content and the microphysical processes going on within them. Twomey (1974) has suggested that their albedo is modified by the characteristics of the cloud condensation nuclei (CCN) available to form the cloud drops. One of the more convincing pieces of evidence for this is the appearance in satellite photographs of long lived, bright tracks in stratus and stratocumulus layers (Conover 1966) associated with ships steaming underneath the cloud layers.

Until recently there have been very few in situ measurements of these ship tracks (Radke et al 1989). However, during June 1994 a major international effort called the Monterey Area Ship Track (MAST) experiment was carried out to investigate the important processes involved in the formation of these high reflectivity clouds. Three aircraft were involved - the Meteorological Research Flight's (MRF) C-130, the University of Washington's C-131 and NASA's ER-2; along with the research vessel M/V Glorita which was instrumented by investigators from Penn State University, the N.R.L, Los Alamos National Laboratory, D.R.I. and Johns Hopkins University. The area off the coast of California was chosen as persistent stratocumulus occurs there and several thousand ship tracks are observed there each year during the summer months. Several dedicated ships from the U.S. Navy as well as ships of opportunity were used in attempts to produce ship tracks.

2. MEASUREMENTS

This paper describes the results of some of the measurements from the MRF C-130 aircraft. Its main role during the experiment was to measure the dynamic and thermodynamic background conditions in the marine boundary layer (MBL) through which the ships were steaming, and the microphysical and radiative properties of the cloud layers, both in and outside of the ship tracks. Full details of the instruments mounted on the C-130 are given in Rogers et al (1995). The major instruments used to obtain the microphysical data that was analysed were the Particle Measuring Systems (PMS) passive cavity aerosol spectrometer probe (PCASP) which measures aerosol particles in the size range 0.1 - 3.0μm, the PMS forward scattering spectrometer probe (FSSP) which counts and sizes cloud droplets in the size range 1.0 - 45.0μm, the PMS 2-D cloud probe which measures cloud particles in the size range 25.0 - 800.0μm (Baumgardner 1989), and the Johnson-Williams liquid water probe.

3. EFFECT OF SHIP EMISSIONS ON CLOUD MICROPHYSICS

During sixteen flights by the C-130 the plume from twenty ships were investigated. The propulsion units of the ships varied from diesel powered to gas turbine. In most cases the ships were steaming through relatively well mixed, shallow boundary layers. Therefore, usually, any pollution from the ships was rapidly mixed throughout the depth of the boundary layer and circulated through the cloud. Invariably it was found that only the diesel powered ships were producing large enough changes in the cloud microphysics to significantly alter the radiative transfer characteristics of the clouds and thus enable a ship track to be observed. This was primarily due to the fact that the particulate matter being emitted by the diesel powered ships was much larger than that produced by the stream turbine, gas turbine and nuclear powered ships. Large quantities of accumulation mode aerosol (up to 25,000 particles per cm^{-3}) were found from the

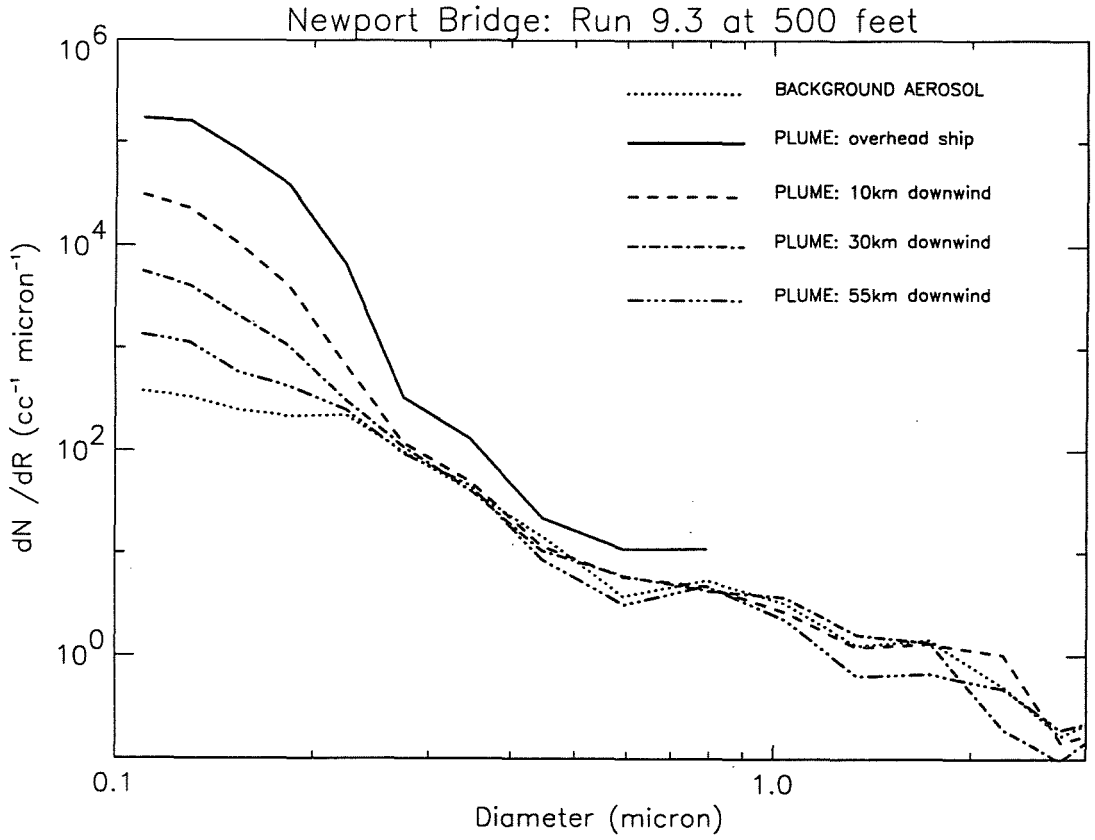

Figure 1 - Aerosol size spectra in a ship plume on 9 June 1994 in cloud free conditions at different distances from the ship compared with the background aerosol size spectra.

diesel ships whereas the plume from the other types of ships was not detectable with the PCASP. Figure 1 presents some typical aerosol size spectra from a diesel powered ship (the Newport Bridge) encountered on the 9 June 1994 in a cloud free MBL. It shows spectra in the plume at different distances away from the ship compared with a representative aerosol size spectra from the background air. It can be seen that the spectra are almost identical with the background air spectra at sizes large than 0.25μm. However, at sizes smaller than this the concentrations are several orders of magnitude larger within the plume and as the plume moves away from the ship it becomes diluted by the background air. Particles of this size, if they are soluble or coated in soluble material (e.g. sulphate coated carbon particles), will be very good CCN as they can be activated into cloud droplets at supersaturations that are typically found in the cloud capped MBL (~0.1%). Therefore it is not surprising that these types of ships were having a dramatic effect on the cloud microphysics.

Figure 2 shows a satellite picture of a ship track that was investigated on the 8 June 1994. The ship involved was the Hyundai Duke and as can be seen in the top half of the picture, it was producing a very marked cloud track. In-situ measurements of the cloud microphysical characteristics 60 and 70km away from the ship during aircraft transects of the track are shown in figure 3. Droplet concentrations within the track were increased by almost an order of magnitude to 500cm^{-3} and the effective radius was reduced from 10μm to nearly 4μm. The track here was nearly 15km in width and was well correlated with the aerosol plume beneath the cloud. Drizzle droplets bigger than 25μm were reduced in number within the cloud track implying drizzle is suppressed by the perturbation in aerosol. However, there was no evidence that the liquid water contents in the track were increased. The Hyundai Duke was steaming through a relatively clean airmass which made the cloud layer in this case particularly susceptible to a local perturbation in aerosol concentrations. Analysis will be presented of other cases where the background boundary layer was much dirtier and the cloud layer less suscepti ble to producing a ship track.

4. PROCESSING OF AEROSOL BY CLOUDS

One of the more surprising results of this investigation was how rapidly the aerosol from the ships was being processed by the clouds which resulted in a significant change in the aerosol size spectrum with time.

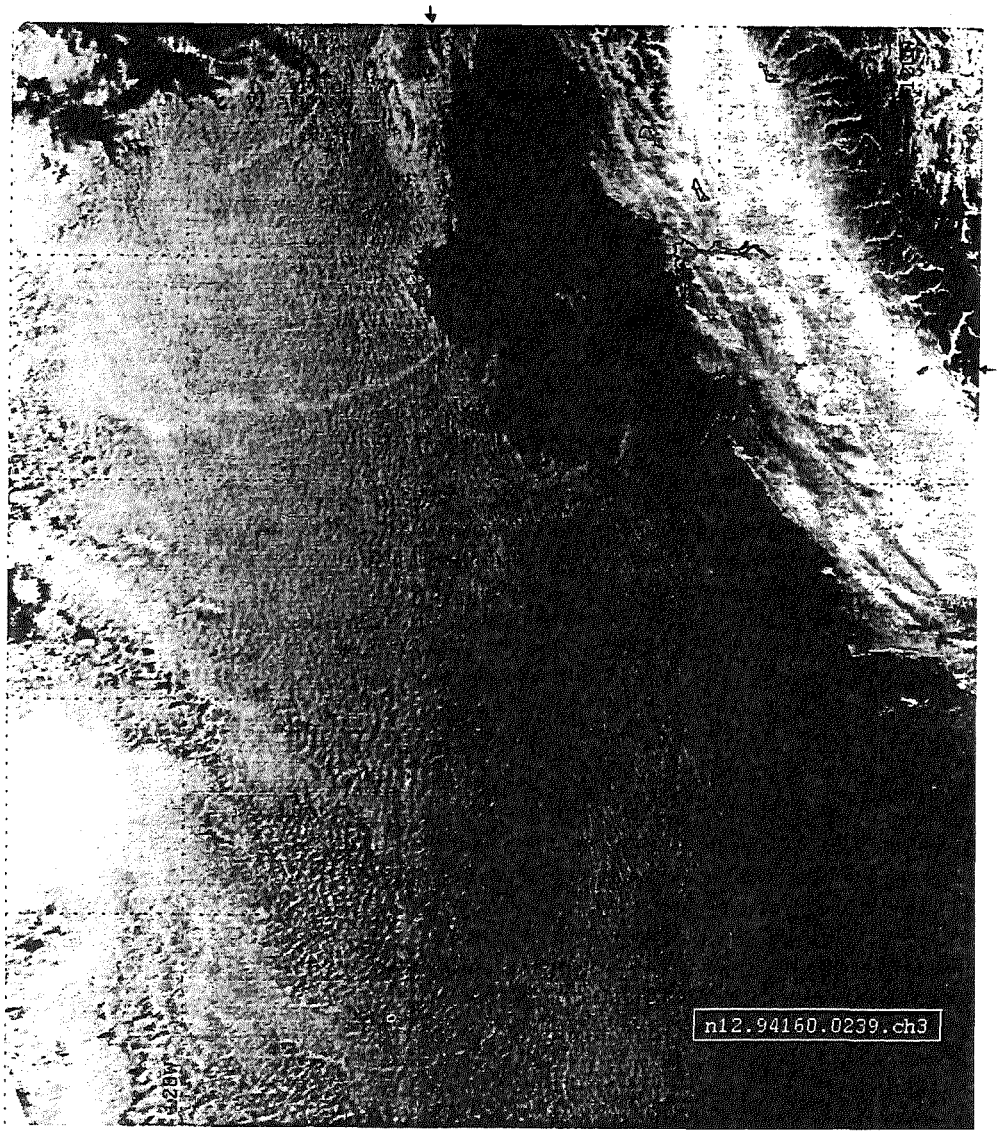

Figure 2 - AVHRR channel 3 satellite picture of a ship track off the California coast on 8 June 1994. The head of the track is indicated by the arrows.

Figure 4 shows a contour map of the time series of the aerosol size spectrum during a flight leg underneath cloud where the aircraft was zig-zagging in and out of a the plume from the Hyundai Duke as it moved away from the ship. The aircraft makes at least five complete transects of the plume during this run. Overhead the ship the particle sizes emitted by the ship are relatively small and are no larger than 0.2μm. However, 70km away from the ship the largest particle sizes in the plume are greater than 0.4μm. Each time it re-enters the plume at a greater distance from the ship particles in the size range 0.2 - 0.4μm have increased in number. The concentrations of these particles sizes are much larger than in the background air. Thus this can not be accounted for by dilution with the background air alone. As can be seen from figure 1 this evolution of the aerosol size spectrum was not being seen when there was no cloud present in the boundary layer which implies that coalescence and aqueous phase reactions in cloud have an important role in modifying the aerosol spectrum. It shows that cloud processing of aerosol can very rapidly produce large enough particles to be important in the direct effect of aerosol if and when the cloud dissipates.

5. SUMMARY AND DISCUSSION

During the course of the MAST experiment the background aerosol conditions varied considerably from day to day. On occasions boundary layer airmass trajectories brought the air from the centre of the Pacific and thus the air was extremely clean and clouds

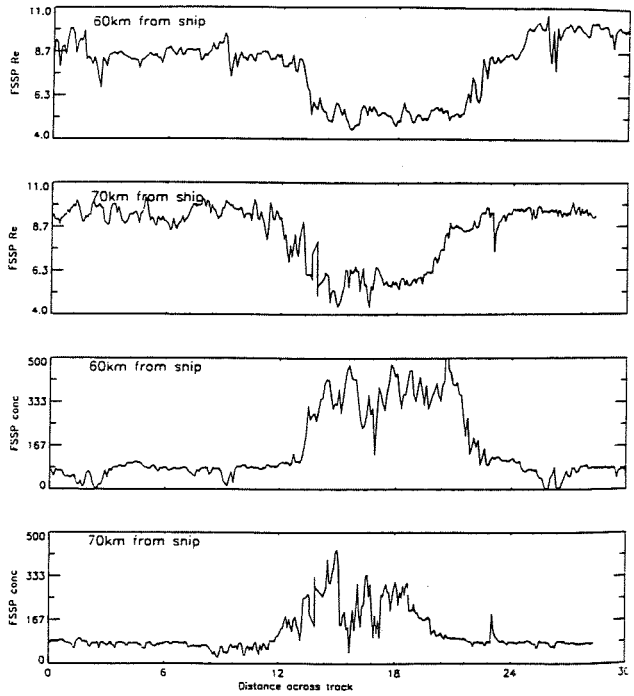

Figure 3 - Time series of 2 transects through a ship track in cloud 60 and 70km from the ship of cloud droplet effective radius (μm) and cloud droplet concentration (cm^{-3}). The centre of the ship track is at ~16km along run.

relatively dark. On other days the airmass came from northern California and was much more polluted so that clouds forming in it were quite bright. These background conditions and the type of propulsion unit used by the ships had a significant influence on whether a ship track was produced. The MAST experiment has enabled us to produce a unique data set for studying the effects of a local aerosol perturbation on the microphysics of MBL clouds. Analysis is being undertaken to test a series of hypotheses that were proposed before the experiment for the formation of ship tracks and their persistence.

6. REFERENCES

Albrecht, B.A., D.A.Randell and S. Nicholls, 1988: Observations of marine stratocumulus during FIRE. Bulletin of Amer. Met. Soc., 69, 618-626

Baumgardner, D. 1989: Airborne measurements for cloud microphysics. NCAR Research Aviation Facility Bulletin No. 24, NCAR.

Conover, J.H. (1966) Anomalous cloud lines. 23, 778-785

Radke, L.F., J.A.Coakley and M.D.King (1989) Direct and remote sensing observations of the effects of ships on clouds. Science, 246, 1146-1149

Rogers, D.P., D.W.Johnson and C.A.Friehe (1995) The stable internal boundary layer over a coastal sea I. Airborne measurements of the mean and turbulence structure. J. Atmos. Sci., 52, 667-683

Twomey, S. (1974) Pollution and the planetary albedo. Atmos. Environ., 8, 1251-1256

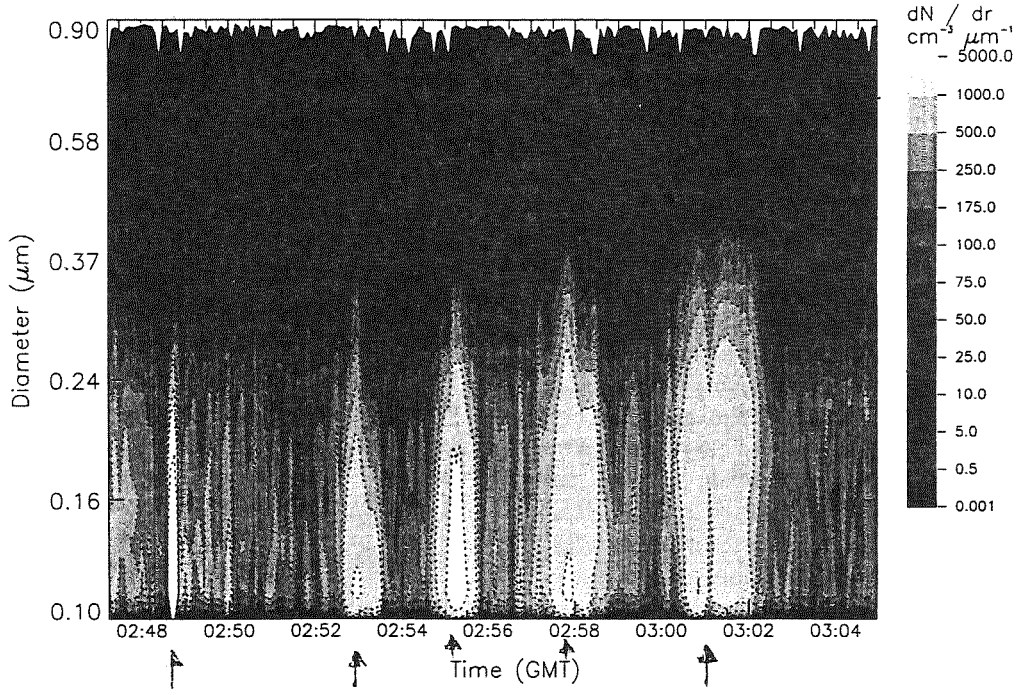

Figure 4 - A contour map of a time series of aerosol size spectrum measured by the C-130 underneath cloud while zig-zagging at a constant height through a ship's plume as it moved away from the ship on 8 June 1994. The arrows indicate the 5 penetrations of the plume.

ARTIFICIAL ENHANCEMENT OF PRECIPITATION AND CHANGE OF THE CLIMATE IN THE REGION

G. Kh Badakhova

Scientific and Production Geophysical Center,
Stavropol, Russia

1. Introduction

The Stavropol area is a region of highly developed agricultural production. Winter wheat is a main plant-growing culture of the region. The radiation and thermal conditions of the region in full measure provide for the plants requirement in heat and solar radiation, and the main limiting factor for agricultural crops, winter wheat in particular, development at the Stavropol territory is humidification of air and soil. So far as the hydrographic network of the Stavropol region is extremely poor, precipitation plays a decisive part in the supply of crops with moisture. The character of the atmosphere circulation and the lay of the ground caused extremely uneven distribution of precipitation over the region territory and that makes it possible to subdivide it into two large taxonomic zones: a droughty one (north-easterly) and a supplied with moisture zone (south-westerly).

To prevent winter wheat crops losses due to drought at the arid zone of the region precipitation artifical enhancement (PAE) operations have been carrying out since 1986 here. The terms for the PAE operations carrying out are determined by the terms of the crucial period for winter wheat vegetation (sprouting - wax stage of ripeness) when there is lack of moisture for it. This is May-June under the Stavropol conditions. The steadily achieved effect makes 14 - 20 % of precipitation enhancement as compared with their natural quantity.

This work is an attempt to study the problem of probable influence of operations on precipitation artificial enhancement upon the region climate.

2. Climatic characteristic of Stavropol region

The air relative humidity has a strongly pronounced annual succession. Its minimum values are noted in July-August. In May f = 52, in June - 50 % . In the northern and eastern areas of the region f often drops to 30 % and less. In separate years such low humidity may be observed for several weeks in succession. Thus, for example, in 1979 the number of days with f < 30 % made on all the flat part of the Stavropol region 17-25 days in May

and 22-29 days in June. The average number of days with f < 30 % made in May-June 18-20 in the east and 5-6 in the western areas.

Unsufficient quantity of precipitation combined with high temperatures at flat areas results in dryness of not the air only, but of the soil as well, and this causes high recurrence of droughts, dry hot winds and dust - storms.

Atmospheric droughts and dry hot winds are a characteristic feature of this region climate, and most frequently they are repeated in the eastern areas where they happen on 100-110 days annually. In the north of the region there are, on the average, 95 days with drought and dry hot winds, of which droughts and dry hot winds of medium intensity make more than 30 days, the intensive ones - more than 10, and highly intensive - 5-6 days. Intensive droughts probability in the eastern areas of the region is 100 %, and that of highly intensive ones - from 80 to 95 %. To the west and south-west the probability of intensive and higly intensive droughts is decreased to 50 and 15 % accordingly.

Arid winds processes are often accompanied dust-storms. They come into existence mainly when winds of the east component blow and dust is detained by the slopes of the Stavropol Hills. In the north and east of the Stavropol region on the average 10-15 days with dust-storms are observed, but in some years they are up to 50 here, and in 1957 86 days with dust-storms were registered. Owing to the protective role of the Stavropol Hills dust-storms are noted considerably less in the west of the region.

3. Procedure of analysis

In order to reveal the probable influence of precipitation artificial enhancement upon the climate of the region a comporative analysis of the two different climatic zones climates is carried out taking the Stavropol region as an example. A number of years under consideration is subdivided into two periods: the one before PAE work was started at the drought-afflicted zone and a period after it. An experimental territory is alloted at the drought-afflicted zone where the work is carried out, and a control territory - at the well-provided with moisture one. Ascertained are correlational dependencies between various weather elements of these zones climate in the years before the work was commenced. Then in accordance with the actual values of weather elements at the control territory in the years of work on PAE, the expected values of these weather elements at the experimented territory are calculated. Comparison of the calculated values with the actual ones shows their change due to the PAE work carried out. At the same time values analysis of these weather elements by historical series taking the trend into account was carried out. At the analysis of the recurrence and intensity such phenomena wich are not practically encountered on the well-provided with

moisture territory (such as dust storms and the like) comparison was made by data historical series only.

4. Primary results

The results of the carried out analysis proved that the done PAE work resulted in a certain change of the climate at the region.

In the years when PAE was effected the air relative humidity over the experimental territory (ET) increased by 14 % as compared with the average value for many years prior to PAE, and it became practically equal to the air humidity at the control territory (CT).

Average saturation deficit of the air humidity in the PAE years at the ET decreased by 25 %, and at the CT - by 16 %. If in the 1980s the difference between the average saturation deficits of the air humidity made 3.0-6.5 hPa, in the PAE years it made 1.0-2.6 hPa.

On all the territory of the region the total number of days with relative humidity f < 30 % decreased. However on the ET this decrease made 58 %, and on the CT - 42 %.

There was a considerable decrease in the average maxima of a saturation deficit. However in the zone supplied with moisture it made 8 hPa, or 22 % of the average value for many years, and in the arid zone - 6 hPa, or 18 %.

Besides, in the arid zone the duration of periods without rain decreased, and those with dust-storms decreased as well. The dry hot winds intensity decreased, the boundary of dust-storms spread got shifted to the east, and this is also indicative of their intensity decrease.

A hydrothermic coefficient (HTC) characterizing the soil humidification proved to be a good index of the humidification conditions change in the region. Thus, in the years prior to PAE the average HTC values were from 0.9 to 1.4 in various points on CT, and on the ET they were from 0.4 in to 0.8. In the years of PAE carrying out the HTC values on ET increased 1.5-2 times and made 0.8-1.3. As for the CT the HTC has not practically changed.

A good index of the regional climate quality class improvement is agricultural crops capacity, in particular that of the regional main culture - winter wheat. During the PAE years the crop capacity has considerably become equal to that in the zone supplied with moisture. Calculating the climate quality class with respect to winter wheat (taking the trend of the crop capasity) by the known formula

$$Q = C / (0{,}01 \sum t),$$

where Q - quality class, C - crop capacity, $\sum t$ - the temperature more than 15°C sum, for experimental territory and for the control territory prior to PAE and in the PAE years, we find out that the climate quality class increased on all the territory region. However on the

experimental territory this increase is twice as many as on the control territory.

The analysed by the authors the 125-years data series on winter wheat crop capacity made it possible to conclude that drougths are not an agriculture scourge any more for the Stavropol region. Thus for example, 115 years prior to PAE droughts took place in 40 % of years; there were 3-5 arid years in each of the 10 years. The crops losses made from 70 to 40 % at that. During the 10 years of PAE operations carried out in the Stavropol region droughts were noted in 1994 and 1995. Though by all the meteorological and economical indices those droughts were rather intensive and caused considerable damage to the agriculture on the territories adjacent to Stavropol from the east and north, droudht was practically staved off on the ET of the Stavropol region at the result of the effected activities influence, and the crops losses made only 13 % in 1994 and 10 % in 1995.

The represented preliminary results reveal that PAE to some extent influences the region climate and improves its quality class.

References

Badakhova G.Kh., Ekba Ya.A., 1993: **Agroclimatic Resourses and Conditions of Precipitation in Stavropol Region.** Trudy SF VGI, No 1, 9-19.

Climatological Handbook of the USSR, 1948. Hydrometeoizdat, 311.

Handbook of the USSR climate, 1968. Hydrometeoizdat, 363.

Meteorological Montlhy, 1951 - 1995.

THE RADIATIVE PROPERTIES OF INHOMOGENEOUS CLOUD FIELDS

Paul F. Coley and Peter R. Jonas

Department of Physics, UMIST, Manchester, M60 1QD, UK.

1. INTRODUCTION

Many studies have shown that cloud fields exhibit both long and short range variability in their microphysical and geometrical properties. As a consequence, the cloud optical properties can vary considerably between one region and another even within the same cloud. Numerous studies have attempted to model the radiative behaviour of inhomogeneous cloud fields. However, many of these previous calculations employed simple cloud geometries which bore little resemblence to real cloud fields, for example Bréon (1992). We have used cloud fields from a Large Eddy Simulation to model the behaviour of highly inhomogeneous cloud fields with regard to the reflection and transmission of shortwave solar radiation. These clouds contain highly irregular distributions of cloud and liquid water. The L.E.S. model was developed by Mason (1989) and is the UK's Meteorological Office 3D L.E.S. model.

2. THE MODEL

A Monte Carlo model was used to model the radiative properties of inhomogeneous cloud fields. The model was similar to that described in Jonas (1994), however the Pontikis and Hicks (1992) effective radius parametrization was used. Unless stated to the contrary the droplet concentration was assumed to be constant throughout the cloud fields with 400 droplets cm^{-3}. A wavelength of $0.4\mu m$ was considered for the radiation.

Two cloud fields were considered. These were originally two dimensional clouds, created with periodic boundary conditions. The clouds covered a horizontal length of 10 km and a vertical height of 3.6 km. The model used 200 and 60 grid points horizontally and vertically. For compatability with the Monte Carlo model the clouds were assumed to be independent of the second horizontal direction, therefore they became cloud bands.

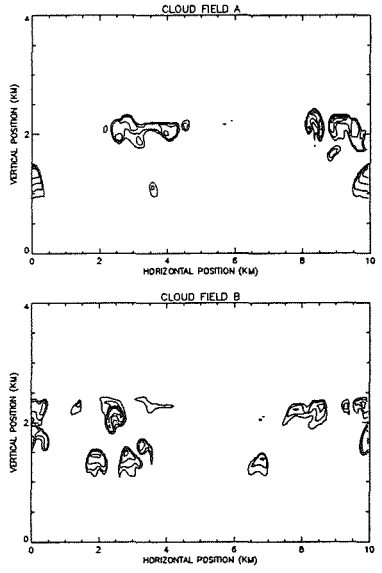

Figure 1: Contours of the liquid water for cloud fields A and B.

Figure 1 shows the contours of liquid water content for two cloud fields known as A and B. The two contour profiles consist of six contour levels where the spacing is determined by the maximum and minimum water content values. The vertical scale indicates the cloud

height. The maximum water content value in cloud field A is 1.09gm^{-3} whilst 1.22gm^{-3} for B. Cloud field B has a 26% greater sky cover than cloud field A and also holds 70% more liquid water.

3. RESULTS

The reflectances of the cloud fields were calculated for solar zenith angles between 0°and 80°. The cloud bands were illuminated in a direction perpendicular to their axes. Figure 2 shows a plot of the total reflectances of the two cloud fields against the incident solar zenith angle. As the solar zenith angle is increased both cloud fields show an increase in the reflectance which is generally consistent with modelled broken cloud fields (Jonas 1994). The reflectance for B is considerably higher than for A due to the greater fractional sky cover and mass of liquid water.

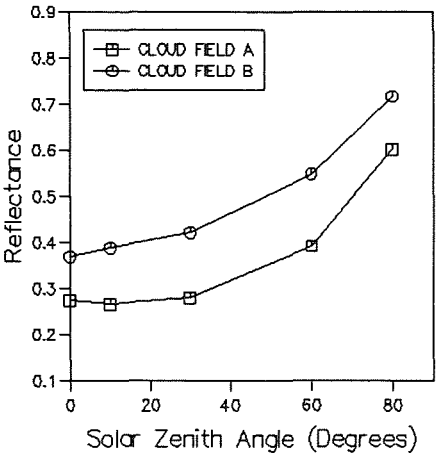

Figure 2: The reflectances of cloud fields A and B.

3.1 Water Distribution

The two L.E.S. cloud fields have both geometric structure and also within that, a distribution of water determined by various physical processes in the L.E.S. model. For both cloud fields the water content at each point was replaced by the in cloud average value, that is, the average value from all the grid points which have a non zero water content. Therefore, the cloud field shape was identical to the original field, but each cloud point had the same water content value. The reflectances were then recalculated with each new cloud field. Figure 3 shows a plot of the new reflectances which are of a similar form to those in Fig. 2. Here each new field is labelled with a subscript R to give the two new cloud fields A_R and B_R. Comparing the two plots of Figs. 2 and 3 it is seen that this redistribution of the water increases the reflectance of each cloud field relative to its original value. This occurs even though the total water content and cloud fraction remain constant. Therefore, the increase in the water content where the cloud was optically thin had a greater impact on the radiation than the reduction in the water content in the optically thicker regions. If the optical depth of the optically thick regions is sufficiently large, then a modest reduction in their optical depth would still result in a large fraction of the photons being reflected.

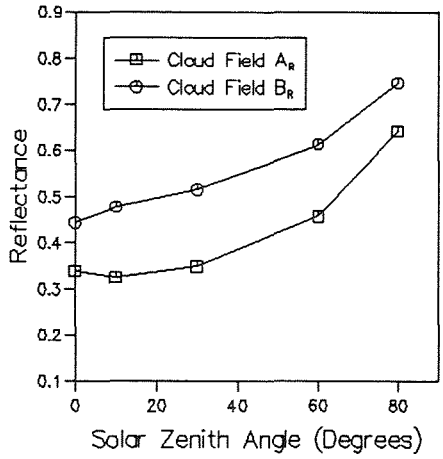

Figure 3: The reflectances of the modified cloud fields A_R and B_R.

3.2 Droplet Concentration

A comparison was made with droplet concentrations of $2000\text{cm}^{-3}$and 50cm^{-3}, typical of heavily polluted and marine clouds (Twomey 1977). Figure 4 shows the reflectances for all three concentrations from the cloud field B. The fractional increases in the reflectance be-

tween solar zenith angles of 0°and 80°increases as the droplet concentration decreases.

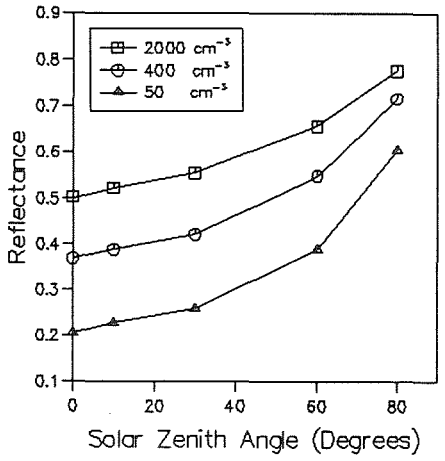

Figure 4: The reflectances of the B cloud field for droplet concentrations of 2000, 400 and 50cm^{-3}.

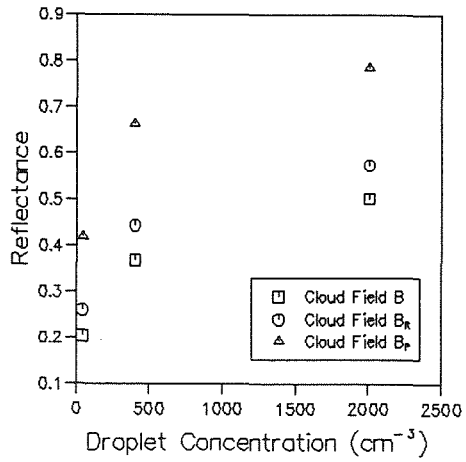

Figure 5: The reflectances of the B, B_R and B_P cloud fields against the droplet concentration.

Figure 5 shows the reflectances of the B and B_R cloud fields plotted against the droplet concentration for a solar zenith angle of 0°. Also plotted are the reflectances for a plane parallel cloud with the same horizontally averaged water content as the cloud field B (labelled as B_P). The plots show that the increase in reflectance with concentration is greatest towards the lower droplet concentrations. However, the fractional increase in the reflectance for each cloud field as the concentration is increased is also found to be dependent upon the degree of inhomogenity in the cloud as well as the solar zenith angle.

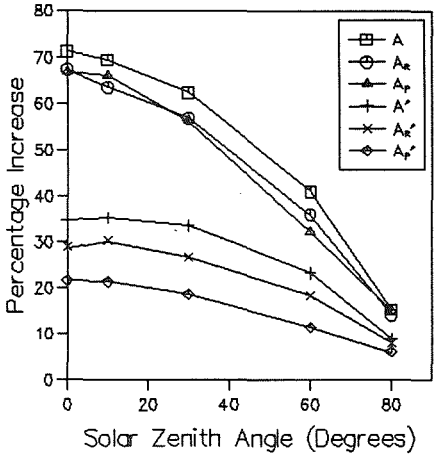

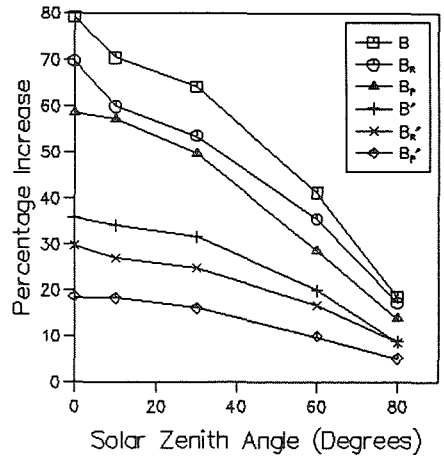

Figure 6: Plots of the percentage increases in the reflectance as the droplet concentrations are increased from 50-400 cm^{-3}and 400-2000 cm^{-3}. The prime indicates the results for the concentration increase of 400-2000 cm^{-3}.

For the changes in the reflectance between concentrations of 50-400 cm^{-3}and 400-2000 cm^{-3}the fractional change was found to be greatest for the original L.E.S. broken clouds and least for the plane parallel clouds. The importance of the type of cloud considered is displayed in Fig. 6. Here, plots show the percentage increases in the reflectances as the droplet concentrations are increased between 50 and 400 cm^{-3}and then between 400 and 2000 cm^{-3}. The first graph shows the re-

flectances for A, A_R and A_P (A_P is the plane parallel cloud based upon cloud field A). The second graph shows B, B_R and B_P. Within each of the graphs there are two groups of plots, the higher value group is for the concentration increase between 50 and 400 cm^{-3}. Within the two groups the original cloud fields (which contain the greatest degree of inhomogenity) are found to be the most sensitive to changes in the droplet concentration. Conversely, the plane parallel clouds are found to be the least sensitive to changes in the droplet concentration. As the solar zenith angle increases the fractional changes all decrease. This is consistant with the plot in Fig. 4 where the reflectances for all three concentrations begin to converge as the solar zenith angle increases.

4. CONCLUSIONS

The calculations have shown a broad agreement between the reflective properties of idealised broken cloud fields and inhomogeneous cloud fields produced from a L.E.S. cloud model. It has also been demonstrated that there is a strong sensitivity in the cloud field reflectance to changes in the droplet concentration combined with the level of cloud inhomogenity. Plane parallel clouds are found to be the least sensitive to changes in the droplet concentration with regard to their reflective properties. Highly irregular broken clouds are found to be the most sensitive to changes in the droplet concentration.

5. ACKNOWLEDGEMENTS

Thanks go to Jacques Pasquier at UMIST for supplying the original L.E.S. cloud fields.

6. REFERENCES

Bréon, F., 1992: Reflectance of broken cloud fields: Simulations and parameterization. *J. Atmos. Sci.*, **49**, 1221-1232.

Jonas, P. R., 1994: On the reflectance of cellular cloud layers. *Quart. J. Roy. Meteor. Soc.*, **120**, 221-229.

Mason, P., 1989: Large eddy simulation of the convective boundary layer. *J. Atmos. Sci.*, **46**, 1492-1516.

Pontikis, C., and E. Hicks, 1992: Contribution to the cloud droplet effective radius parameterization. *Geopys. Res. Lett.*, **19**, 2227-2230.

Twomey, B., 1977: The influence of pollution on the short-wave albedo of clouds. *J. Atmos. Sci.*, **34**, 1149-1152.

A MODELING STUDY OF THE EFFECT OF DRIZZLE PRODUCTION ON CLOUD OPTICAL DEPTH

Graham Feingold[a], Reinout Boers[b], Bjorn Stevens[c], and William R. Cotton[c]

[a] CIRA, Colorado State University
Fort Collins CO

[b] CSIRO, DAR, Australia,

[c] Dept. of Atmospheric Sciences, Colorado State University, Fort Collins CO 80523

1. INTRODUCTION

The radiative forcing of clouds is well recognized as a central component of the climate system (e.g., Twomey, 1974, 1977). In particular, boundary layer clouds such as marine stratocumulus are important, largely because of their high frequency and extensive spatial coverage (annually averaged cloud cover of 34%; Warren et al., 1986). Numerous studies have investigated the relationship between cloud condensation nucleus CCN concentration and drop concentration N, as well as the relationships between cloud optical depth τ and N, and cloud albedo A and N. For non-precipitating clouds with unimodal spectra, the relationship between τ and N at constant liquid water content *lwc* and constant depth is fairly simple:

$$\tau \propto N^{1/3} \qquad (1)$$

(e.g., Platnick and Twomey, 1994). These clouds have spectra with varying breadth, depending on mixing, supersaturation and updraft fluctuations. However, the size of the largest droplets will normally not exceed about 20 μm .

When drops larger than about 20 μm are formed, through a number of possible (although uncertain) mechanisms, drizzle can be initiated through collection (collision-coalescence). In this case, droplets from the uni-modal spectra are removed to form a secondary (or drizzle) mode. The size of the drizzle drops is on the order of 100 μm depending on the depth of the cloud and the size of the largest (non-drizzle) droplets (Nicholls, 1984; Frisch et al., 1995). This transfer of drops from the cloud to the drizzle mode with concomitant reduction in N reduces cloud optical depth (Eq. 1), and hence cloud albedo (Wiscombe et al., 1984). The introduction of drizzle into the discussion raises another important issue; once drizzle-sized drops fall below cloud, there will be a decrease in cloud *lwc* and the relationships derived at constant *lwc* are no longer valid. Thus one must make the distinction between the impact of the collection mechanism on the drop spectrum *at constant lwc*, and cases where drizzle depletes *lwc*.

Corresponding author address: Graham Feingold, CIRA, Colorado State University, Fort Collins, Colorado 80523, USA

In order to address this problem, we have used a theoretical/numerical modeling approach, as very few observations are available to shed light on the process of drizzle formation. The study consists of two parts. In the first part we examine the influence of collection on typical droplet spectra, and compute its influence on cloud optical depth (at constant *lwc*). The results quantify the reduction in cloud optical depth related to the mass transfer to the drizzle mode, and decrease in drop number. The aim here is to build on the results of Wiscombe et al. (1984) by quantifying the magnitude of this effect over the range of parameter space. This reduction depends on the initial droplet number concentration, so that for smaller N, collection rates at a given *lwc* are faster. One can then analyze the relationship between τ and N for situations where N changes due to the rate of the collection process, rather than due to varying CCN concentrations. (Of course the impact of CCN on N and τ is not in dispute.)

To capture the complexity of real clouds, we attempt in the second part to simulate stratocumulus clouds using a large eddy simulation model coupled to a drop-size resolving microphysical model. We consider a case study of a cloudy marine boundary layers capped by an inversion, and vary only the initial CCN concentration (N_{CCN}= 25 cm^{-3}, 50 cm^{-3}, 100 cm^{-3} and 250 cm^{-3}). It is shown that (i) the 4 runs evolve to quite different solutions, and that (ii) the ratio of cloud optical depths (τ/τ_0, where $\tau < \tau_0$) *at constant LWP* is consistently smaller than the ratio of cloud drop number concentration ($[N/N_0]^{1/3}$, where $N < N_0$). Thus the τ dependence on $N^{1/3}$ on which most predictions of the indirect effect of anthropogenic aerosol on climate is based, represents an upper limit of the prediction of τ.

2. BOX-MODEL CALCULATIONS OF COLLECTION

Since drop collection conserves mass, we attempt to examine the effect of drop collection on N and τ in a simple box-model of stochastic collection (Tzivion et al., 1987). The initial conditions for this model are N_0, *lwc* and an assumed drop dispersion. Initial spectra are assumed to be lognormal with a geometric standard deviation σ of 1.4. The *lwc* is varied over

the range (0.15 g m^{-3}; 1.1 g m^{-3}) and N_0 is varied over the range (10 cm^{-3}; 500 cm^{-3}). The model is integrated with time, and at each time, τ and N are calculated and compared to the initial values. Figure 1 shows the results of these simulations in (lwc; N_0) space as contours of the time required for τ to be depleted by 10%. We note that for a given N_0, the time required for 10% depletion in τ decreases with increasing lwc. For a given lwc the time required for 10% depletion in τ increases with increasing N_0. This can largely be explained by the dependence of collection on the size of the largest drops.

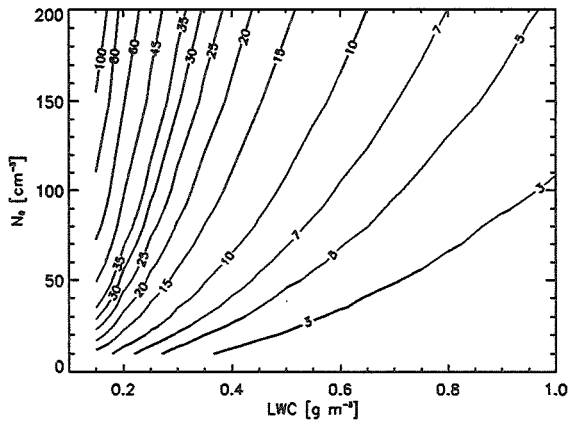

Figure 1: *Time (in minutes) required for 10% depletion in τ for drop spectra initially defined by (N_0; LWC), evolving through collection*

Next, the model is run for 10 min, which is a typical parcel in-cloud residence time (Stevens et al., 1996). Figure 2 displays the depletion in τ as a function of the depletion in number to the power 1/3. By normalizing the optical depth, we avoid assumptions about cloud depth, other than that it is constant. One sees that the depletion in τ simply due to mass-transfer to a drizzle mode is consistently larger than the corresponding depletion in N to the power 1/3. The degree to which this is true depends on the amount of collection; it is a relative maximum when $(N/N_0)^{1/3}$=0.4, and occurs for an N_0 of 70 cm^{-3} and lwc of 1.1 g m^{-3}; it is a relative minimum for negligible depletion (low lwc and large N). This result is important because it seems to indicate that for a fixed cloud depth, the change in albedo (which is proportional to the change in τ) due to drizzle formation is at a maximum for specific values of lwc and N, and not necessarily for the largest lwc; smallest N pair. The results do depend on the initial value of σ, the time available for collection, and the collection kernel used, but all have a consistent qualitative picture.

3. THE LARGE-EDDY SIMULATION MODEL

The LES model is described in detail in Stevens et al. (1996) and Feingold et al. (1996). The strength

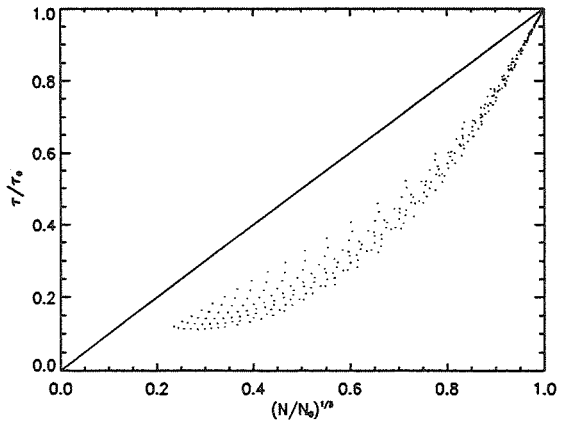

Figure 2: *Depletion in τ as a function of the depletion in number to the power 1/3 after 10 min of collection.*

of this model lies in its emphasis on both dynamics and microphysics through the coupling of an explicit warm microphysical model (Tzivion et al. 1987) with an LES model that resolves the large eddies. Thus cloud and drizzle formation respond to resolved eddy motions: CCN are activated to drops (depending on supersaturation, which is in turn related to updraft w); drop growth through condensation (evaporation) and stochastic collection is explicitly calculated; drizzle in-cloud residence is related to size-dependent fall velocity and local w.

A number of experiments have been performed using a 2-d version of this LES model (3-d runs will be presented at the meeting). The runs are initiated from the Betts and Boers (1990) July 7 stratocumulus sounding. A constant CCN concentration of either 25 cm^{-3} (at S=1%), 50 cm^{-3}, 100 cm^{-3} or 250 cm^{-3} is used throughout the domain. Only longwave radiation (responding to lwc) is simulated. The 50 cm^{-3} case exhibits significant drop number depletion (on the order of 60% over 3 hrs) but with negligible wet deposition (< 0.1 mm $day^{-}1$ at the surface); lwc and LWP achieve a quasi-steady state, assisting in interpretation of the results within the framework of Eq. (1). (For brevity, these have not been shown.) For the 25 cm^{-3}, drizzle does deplete lwc and LWP, but all intercomparisons between model runs are performed for constant LWP, or constant cloud-average lwc, or constant depth.

Figure 3 shows just one representation of the data, namely a τ-LWP plot after Stephens (1978). The slope of this plot is inversely proportional to the drop effective radius r_e; We note that the run with CCN=250 cm^{-3} forms a straight line plot indicative of a constant r_e. The run with CCN=25 cm^{-3}, on the other hand shows a temporal evolution, with r_e initially constant, but followed by increasingly larger r_e. A maximum LWP of close to 100 g $m^{-2}$is reached, after which the points double-back towards lower τ, higher r_e and lower LWP, as wet deposition depletes cloud water.

(For clarity, data for the 100 cm^{-3} and 50 cm^{-3} runs are not shown; the plot for N_{CCN}= 100 cm^{-3} exhibits similar constant r_e ("straight line") behaviour to that of the 250 cm^{-3} run. The plot for 50 cm^{-3} shows points evolving towards larger r_e and smaller τ, but with minimal depletion in LWP.)

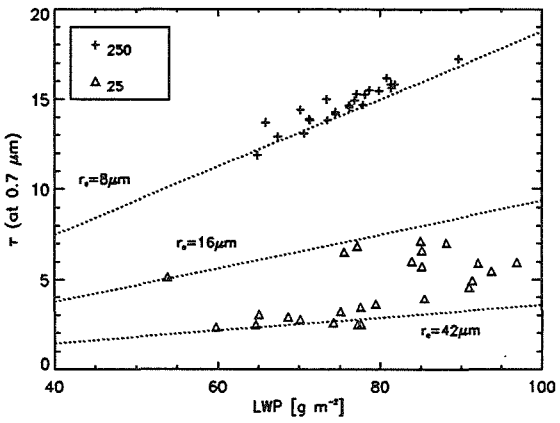

Figure 3: *LWP-τ representation of ERM results for two initial CCN concentrations (25 cm^{-3} and 250 cm^{-3}).*

Figure 4 displays the data from the 2-d model in the same manner as used in Fig. 2 for the box-model collection calculations. All data are displayed for clouds at different stages of their evolution, the only requirement being that they are of equivalent LWP (within 2.5%). Similarly, in Fig. 5, data are for equivalent cloud-average *lwc*, while in Fig. 6 data are displayed for equivalent cloud depth. Thus clouds displaying not only different N, but also different spectral form (resolved into 25 size-bins) are being compared.

Figure 4 shows that the ratio τ/τ_0 (where $\tau < \tau_0$) is consistently smaller than that of the ratio $(N/N_0)^{1/3}$. For larger $(N/N_0)^{1/3}$ (i.e., spectra with similar numbers of drops) the points tend to be closer to the 1:1 line and converge to the behaviour predicted by Eq. (1). Similar results are seen in Figs. 5 and 6; although the scatter in points is somewhat larger, there is an indication that clouds exhibiting strong differences in N - usually manifested by different drop spectral shape - always have τ values somewhat smaller than predicted by $(N/N_0)^{1/3}$.

4. DISCUSSION

The results for both the box-model simulations of the collection process, as well as the 2-d eddy resolving simulations indicate that the creation of bimodal spectra through the collection process tends to deplete the optical depth to a greater extent than that predicted by the depletion in drop number to the power one-third. This suggests that the scaling of τ with $N^{1/3}$ given by Eq. (1) for clouds of similar depth and *lwc* represents an upper limit for the prediction of τ based on N.

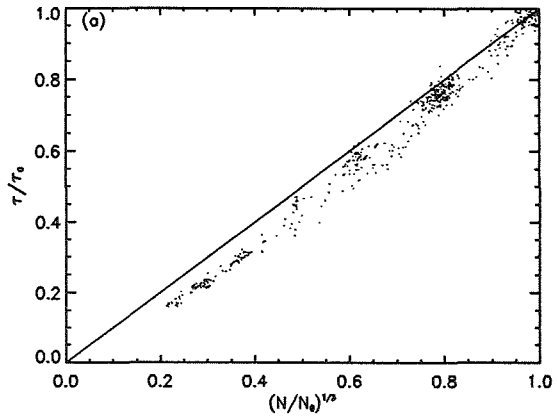

Figure 4: *Depletion in τ as a function of the depletion in number to the power 1/3. Each point represents a comparison of 2 realizations of the ERM where the requirement is that LWP is constant*

Thus, the upper limit is only valid for a non-precipitating cloud. At the onset of the collection process, which induces precipitation, two processes occur: (i) the reduction in total number of particles occurs together with a shift towards larger particles. At constant liquid water content this reduces the geometric cross section of the particles; (ii) the *lwc* is reduced by fall-out, which ultimately produces the same result. The full impact on τ and hence cloud albedo can be gauged by comparing the two model runs of Figure 3. After an adjustment to the initial conditions, the progression of points for the run with 25 cm^{-3} CCN is towards higher values of r_e and lower values of LWP while for the 250 cm^{-3} CCN run the points merely follow a trace towards higher LWP at constant r_e. For the 25 cm^{-3} run, r_e increases about 2.5 fold from 16 to 42 μm , which is entirely due to the collection process. In the 50 cm^{-3} run, r_e increases 1.5 fold from about 14 μm to 20 μm at approximately constant LWP; under the latter constraint, $(\tau_2/\tau_1) \simeq (r_{e1}/r_{e2})$, indicating a decrease in τ of 30 %. With albedo close to linear in τ in this region, a similar reduction in albedo is implied. These are large numbers and strongly indicate the importance of the collection process in reducing cloud albedo, even without wet removal.

Acknowledgments:
This research was partially supported by grants from the Office of Naval Research #N00014-93-F0029 and the DOD/ISSO Lidar Wind Program. Additional support came from the Environmental Sciences Division of the U.S. Department of Energy under contract number DE-FG03-95ER61958 as part of the Atmospheric Radiation Measurement Program.

REFERENCES

Betts, A. K., and R. Boers, 1990: A cloudiness transi-

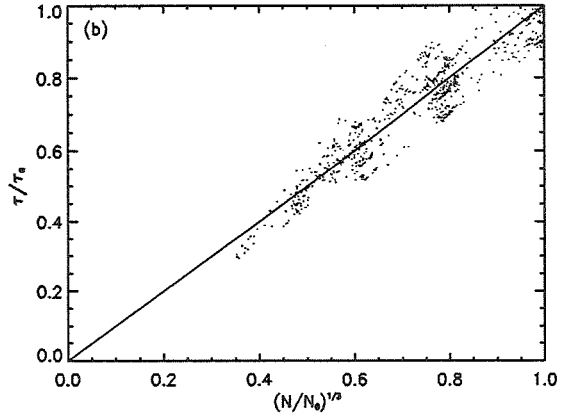

Figure 5: *As in Fig. 4 but for the requirement that cloud-average lwc is constant*

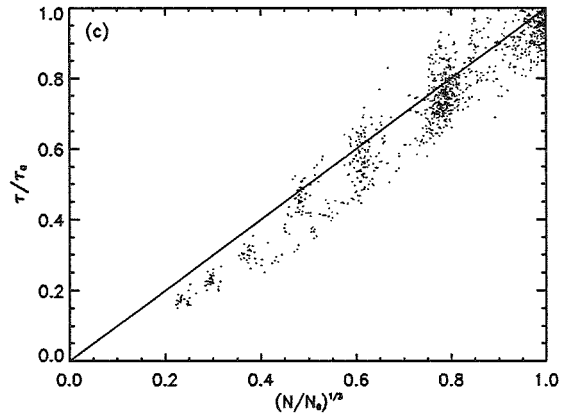

Figure 6: *As in Fig. 4 but for the requirement that cloud depth is constant*

tion in a marine boundary layer. *J. Atmos. Sci.*, **47**, 1480-1497.

Feingold, G., B. Stevens, W. R. Cotton, and A. S. Frisch, 1996: On the relationship between drop in-cloud residence time and drizzle production in stratocumulus clouds. *J. Atmos. Sci.*, **53**,1108-1122.

Frisch, A. S., C. W. Fairall and J. B. Snider, 1995: On the measurement of stratus cloud and drizzle parameters with a K_α- band Doppler radar and a microwave radiometer. *J. Atmos. Sci..*, **52**, 2788–2799.

Nicholls, S., 1984: The dynamics of stratocumulus. *Quart. J. Roy. Meteor. Soc.*, **110**, 821–845.

Platnick, S., and S. Twomey, 1994: Determining the susceptibility of cloud albedo to changes in droplet concentration with the advanced very high resolution radiometer. *J. Appl. Meteor.*, **33**,334–347.

Stephens, G. L., 1978: Radiation profiles in extended water clouds. I: Theory. *J. Atmos. Sci..*, **35**, 2111–2122.

Stevens, B., G. Feingold, R. L. Walko and W. R. Cotton, 1996: On elements of the microphysical structure of numerically simulated non-precipitating stratocumulus. *J. Atmos. Sci.*, **53**,980–1006.

Twomey, S., 1974: Pollution and the planetary albedo. *Atmos. Environ.*, **8**, 1251-1256.

Twomey, S., 1977: The influence of pollution on the short wave albedo of clouds. *J. Atmos. Sci.*, **34**, 1149-1152.

Tzivion, S., G. Feingold and Z. Levin, 1987: An efficient numerical solution to the stochastic collection equation. *J. Atmos. Sci.*, **44**, 3139–3149.

Warren, S.G., C.J. Hahn, J. London, R.M. Chervine and R.L. Jenne, 1986: Global distribution of total cloud cover and cloud type amounts over ocean. *NCAR Technical Note*, NCAR/TN-317+STR, 42pp.

Wiscombe, W. J., R. M. Welch and W. D. Hall, 1984: The effects of very large drops on cloud absorption. Part I: parcel models. *J. Atmos. Sci.*, **41**,1336–1355.

GLOBAL CLOUD MICROPHYSICAL PROPERTIES DERIVED FROM MULTISPECTRAL AVHRR DATA

Patrick W Heck[1], Patrick Minnis[2], David F Young[1], and Shalini Mayor[1]

[1]Analytical Services and Materials, Inc., Hampton, VA 23666, USA
[2]Atmospheric Sciences Division, NASA Langley Research Center, Hampton, VA 23681, USA

1. INTRODUCTION

Knowledge of global distributions of cloud microphysical properties such as phase, effective particle size, and optical depth is essential for accurately balancing the cloud water and radiation budget in climate and mesoscale models. Previous retrievals of these parameters from satellite data (e.g., Han et al., 1994; Ou et al., 1993) have relied on a temperature threshold to select the phase of the clouds so that many clouds having temperatures between -40 and 0° C were not analyzed. Furthermore, the dependencies of these methods on angular and background conditions have not been examined in much detail. Plane-parallel cloud models based on idealized cloud particle size distributions are used to interpret the cloud properties. In this paper, a new model-based objective technique that explicitly determines cloud phase in addition to the other properties is applied to global Advanced Very High Resolution Radiometer (AVHRR) data. The effective cloud particle sizes are examined in terms of background, angles, cloud temperature, and optical depth.

2. DATA AND METHODOLOGY

Daytime, 4-km, Global Area Coverage AVHRR data taken October 2, 1986 from the NOAA-9 are analyzed with the method of Minnis et al. (1995) to derive optical depth, phase, water path, and the effective radii r_e of liquid-water droplets and the effective diameters D_e of cloud ice crystals. This method, which uses the 0.67, 3.7, and 10.8 μm radiances, was first tested and partially validated by Young et al. (1994) with surface-based radar and microwave radiometer data. A pixel is cloudy if its 0.67-μm (VIS) reflectance exceeds a threshold above the clear-sky value or is colder than a threshold below the 10.8-μm (IR) clear-sky temperature T_{cs}. The technique then uses a modification of the Han et al. (1994) iterative method for deriving r_e and determines D_e in a similar manner using the definition of D_e proposed by Ou et al. (1993). In the second guess of this VIS-IR-solar-IR technique (VIST), a pixel is assumed to be liquid, if its corrected cloud temperature $T_c > 273$K, or ice, if $T_c < 233$K. Between these values, the phase determination is based on how closely the observations fit the ice or liquid water model calculations. Generally, there is a distinct separation in the model calculations when all three AVHRR channels are considered. In some cases, such as very thin clouds or overlapping ice and liquid water, the technique fails to find a satisfactory solution and no retrieval is returned. The pixels are processed in 16 x 16 arrays using the mean viewing and illumination conditions at the center of the array.

The clear-sky VIS reflectances and IR temperatures are primarily based on the 250-km resolution, C1 product monthly means from the International Satellite Cloud Climatology Project (ISCCP; see Rossow et al., 1991). Over ocean, an updated version of the Minnis and Harrison (1984a) clear-ocean bidirectional reflectance model is used to estimate the clear-sky reflectance $\rho_s(\theta_o,\theta,\phi)$ based on an overhead-sun albedo of 0.045. The solar and viewing zenith and relative azimuth angles are θ_o, θ, ϕ, respectively. Over land, the ISCCP 3-hourly mean clear-sky albedo is interpolated to match the time of the NOAA-9 overpass. The albedo is then adjusted to the AVHRR view using the clear-land bidirectional reflectance model of Minnis and Harrison (1984b). Over mixed land and water areas, the land reflectance is derived by proportionately subtracting out the ocean value from the ISCCP mean. Values for T_{cs} are interpolated from the ISCCP 3-hourly means and adjusted to the AVHRR view using the limb-darkening model of Minnis and Harrison (1984a). These values are increased on an instantaneous basis if warmer temperatures are observed within the analysis array. If no clear pixels are observed in the array, the 3.7-μm (SI) clear temperature is $T_{SIcs} = T_{cs} + \Delta T(k)$, where k is the background type. When clear pixels are observed, T_{SIcs} is the mean SI temperature of the clear pixels. Optical depth τ and particle size are determined using lookup tables and a parameterization of VIS reflectance at the top of the atmosphere. In this analysis atmospheric corrections for IR and SI water vapor absorption were not included. The 12-hourly National Meteorological Center gridded analyses are interpolated to estimate the temperature and humidity profiles for a given pixel array.

3. RESULTS

The analyses were performed using NOAA-9 data taken Oct. 2 and 29, 1986 and July 2, 1988. The mean cloud effective droplet and ice crystal sizes for the 15° zones between 60°S and 60°N are shown in Figs. 1 and 2, respectively. Over ocean, r_e ranges from 12.5 to 16.5 μm. The

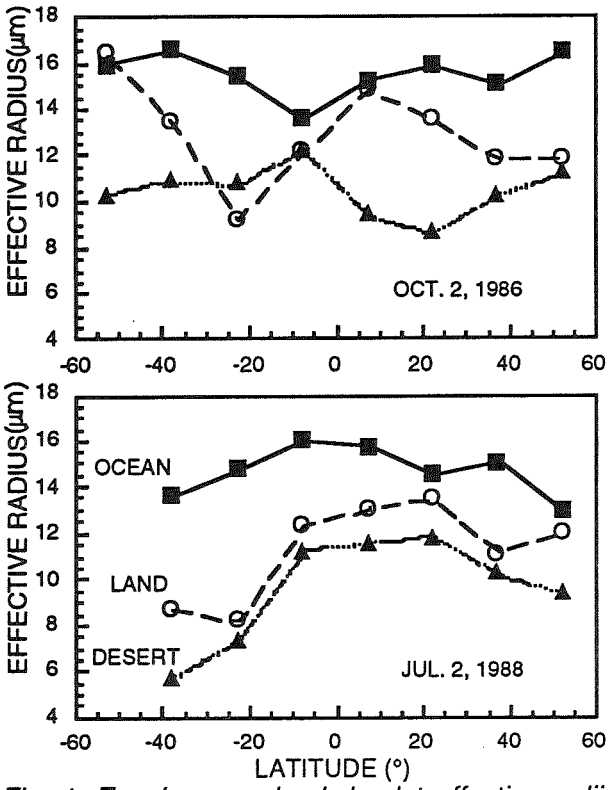

Fig. 1. Zonal mean cloud droplet effective radii from NOAA-9.

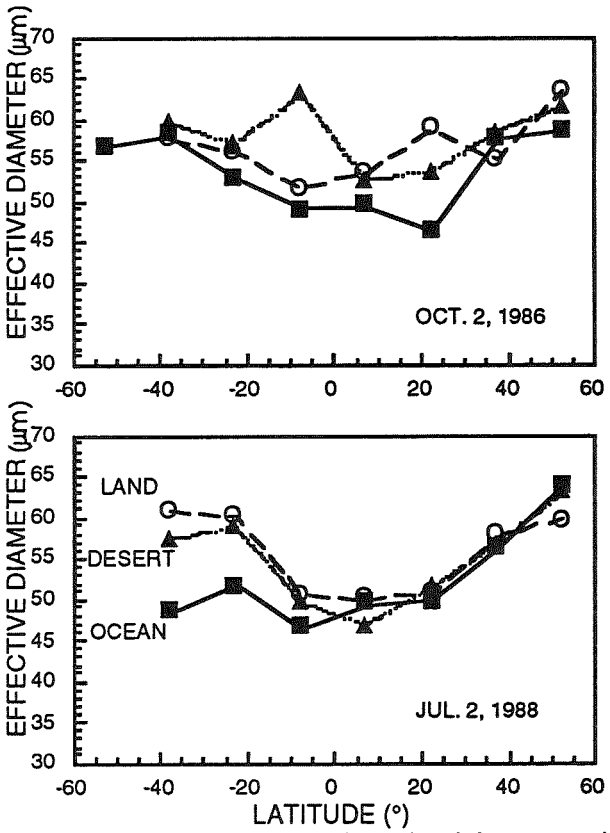

Fig. 2. Zonal mean effective cloud ice crystal diameter from NOAA-9.

land values are generally smaller, ranging between 9 and 16 μm. In desert regions, the clouds tend to have even smaller droplets that vary from 5 to 12 μm. Except for the small amount of land at 50°S, the largest droplets over land occur in the tropics and the smallest in the subtropics. During July, r_e tends to increase toward the tropics over all surfaces. The minimum ocean mean droplet radius occurs near 10°S during Oct. 2. Overall, the respective ocean, land, and desert mean values of r_e are 15.6, 12.0, and 9.9 μm for Oct. 2 and 14.6, 11.8, and 10.5 μm for July 2.

The variation in ice crystal sizes is considerably different. The values of D_e over land tend to be equal to or greater than those over water. During July, there seems to be no dependency on surface type in the northern hemisphere but a significant difference between land and ocean in the southern hemisphere. The largest differences between land and ocean during Oct. 2 are found in the tropics. The respective ocean, land, and desert mean values of D_e are 54, 57, and 58 μm for Oct. 2 and 52, 56, and 59 μm for July 2. Results for both ice and water for Oct. 29 are similar to those for Oct. 2 and will not be discussed here.

Figure 3 shows how often the VIST determined cloud water phase as a function of T_c. The frequencies were computed relative to the total number of pixels of the given phase. Of the 23.5 million pixels analyzed for Oct. 2, 41, 18, and 4% were classified as liquid, ice, or no retrieval possible. The remainder are clear. It appears that most ice clouds have tops near the homogeneous freezing temperature of 233K, although ~50% of them are found at warmer temperatures. Very few ice clouds are at T_c > 265K. The frequency of supercooled liquid water clouds (T_c < 273K) is 68% of the observed liquid-water clouds. Thus, nearly 58% of the observed clouds fall in the supercooled water temperature range.

The optical depth distribution for each phase is shown in Fig. 4. The mode optical depths for both ice and liquid water are near $\tau = 10$. The mean optical depths are 11 and 13 for liquid and ice, respectively. Approximately 45% of both the ice and liquid clouds are optically thin ($\tau < 6$).

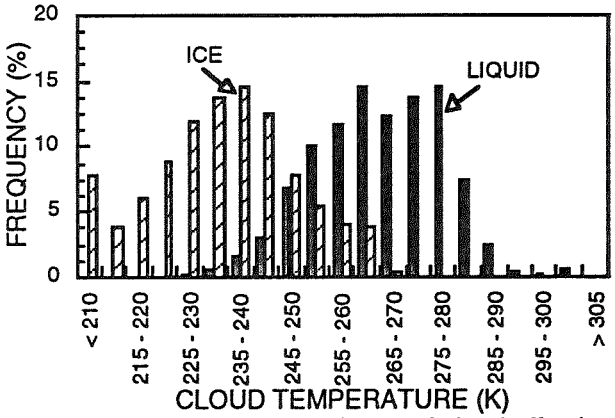

Fig. 3. Temperature dependence of cloud effective particle size from Oct. 2, 1986.

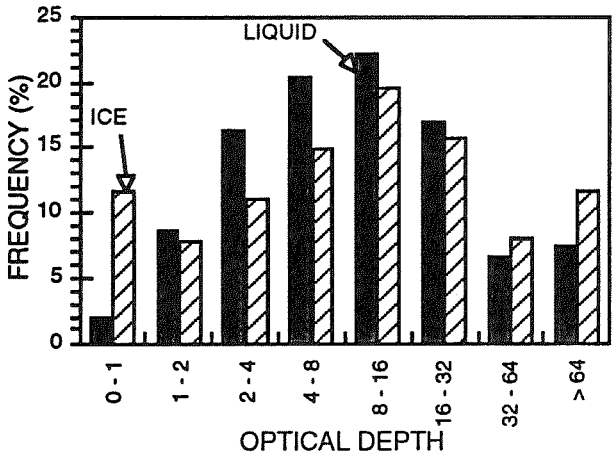

Fig. 4. Frequency of occurrence of cloudy pixels as a function optical depth.

4. DISCUSSION

The droplet sizes in Fig. 1 are significantly larger than those found by Han et al. (1994). Their analysis produced mean values of r_e between 12.5 and 13.5 μm over ocean and 9-10 μm over land from NOAA-9 taken during October and July 1987, respectively. Despite the bias between these two results, the zonal patterns are almost identical in relative terms even though the present dataset uses only 1 day out of each month and the Han et al. (1994) data are restricted to $\cos\theta > 0.9$ and $T_c >$ 273K. To explore these differences, the values of r_e from Oct. 2 are plotted against T_c in Fig. 5.

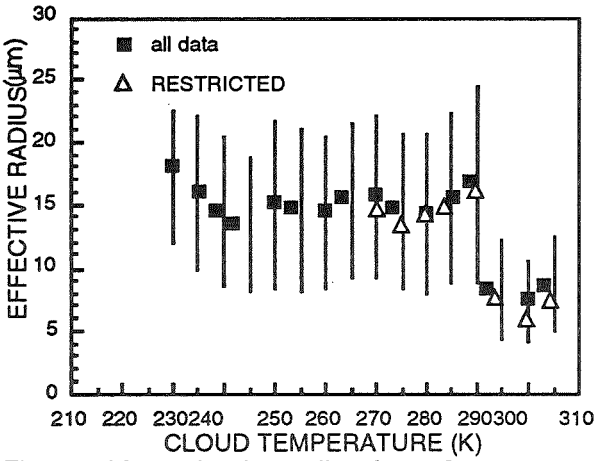

Fig. 5. Mean droplet radius from Oct. 2, 1986. Lines indicate one standard deviation.

The data were also averaged according to the restrictions placed on the Han et al. (1994) dataset. The results suggest that the restrictions may account for almost half of the discrepancy (~0.7 μm) between the two results. The histogram in Fig. 6 shows a distribution similar to those presented by Han et al. (1994) with the peak value near 10 μm. The difference is primarily in the relatively high frequencies for $r_e > 20$ μm which are not seen in the earlier dataset. The inclusion of the supercooled clouds apparently does not affect

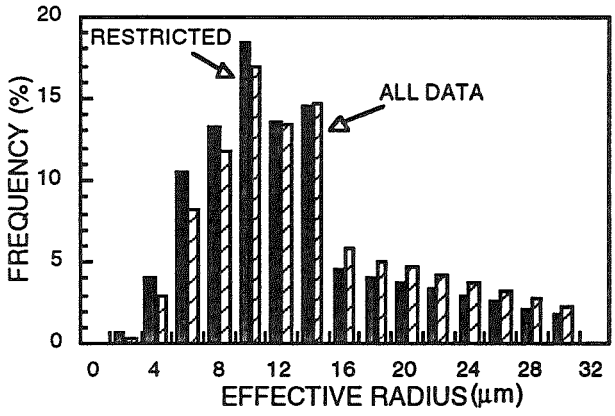

Fig. 6. Histogram of r_e for Oct. 2.

the results because the mean droplet size does not increase with decreasing temperature. Given these results, it is probable that there is a viewing angle bias and, perhaps, some differences in the solar constant used for

the 3.7-μm channel. An examination of this question indicates that r_e increases slightly with θ and is ~1 μm greater in the backscatter direction than in the forward scatter direction.

Figure 7 shows some forward-backscatter differences for the ice crystal retrievals. The peak for the forward direction occurs at the smallest sizes but is peaked at 30 μm when the sun is behind the satellite. In this case, the backscatter effective diameter is ~3 μm greater than the forward counterpart. This result suggests that the models used in the analyses are not a perfect representation of the actual ice crystals. The strong similarities in the distributions indicate that

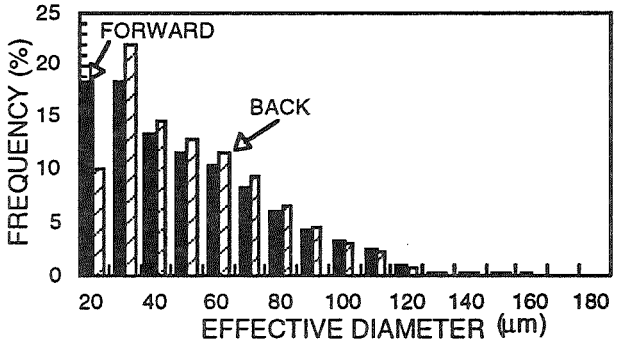

Fig. 7. Histogram of D_e for Oct. 2, 1986.

the crystal shapes are reasonable, however. Figure 8 shows the variation of D_e with cloud temperature. Overall, there is a decrease of particle size with decreasing temperature from 45 μm at 210K to 61 μm at 270K. This variation is not nearly as steep as the model employed by Ou et al. (1993). The relationship has a larger slope for thick clouds than for the thin clouds.

The flat behavior of r_e with cloud temperature and the increase of D_e with T_c indicate that the phase determination is working well. When the models are close together, the water droplets will be large and the ice crystals

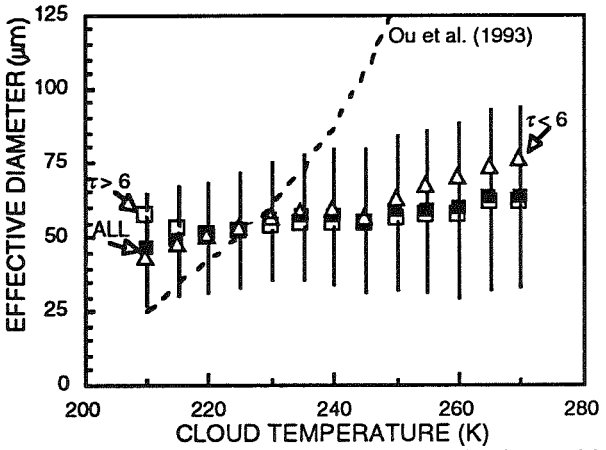

Fig. 8. Dependence of ice crystal size with temperature for Oct. 2, 1986.

small. Thus, if there is a tendency for misclassification of phase, the water droplet sizes should increase with decreasing temperature and the ice crystals should be smaller. Some of the retrievals are likely to be multi-layered clouds that exhibit primarily ice or water behavior. There is also some tendency for water droplet sizes to decrease with increasing solar zenith angle and for ice crystal size to behave in the opposite manner. It is difficult to separate the solar angle dependency from natural latitudinal variations. The inclusion of atmospheric absorption in the analysis may diminish some of the angular dependencies and the bias relative to the Han et al. (1994) results for r_e. Atmospheric absorption will have minimal effect on the ice crystal sizes.

5. CONCLUDING REMARKS

This paper has presented global distributions of cloud phase and particle size for 2 days from different seasons. The analyses reveal extensive coverage by supercooled liquid water clouds in the tropics and midlatitudes. These clouds have been ignored in previous studies of global cloud particle sizes, yet they constitute a majority of the observations. It is also clear that the present results are biased relative to earlier analyses. An examination of the data indicate that there are many factors that can affect the retrievals. Solar constant values, angular dependencies, and background conditions are all important factors. The determination of cloud microphysics from space is a relatively new endeavor that requires considerable study to understand all of the variables that are operative in the determination. Nevertheless, important information can be derived using simple approaches to this complex problem.

6. REFERENCES

Han, Q., W.B. Rossow, and A.A. Lacis, 1994: Nearly global survey of effective droplet radii in liquid water clouds using ISCCP data, J. Climate, 7, 465-497.

Minnis, P. and E. F. Harrison, 1984a: Diurnal variability of regional cloud and clear-sky radiative parameters derived from GOES data, Part I: Analysis method. *J. Climate Appl. Meteorol.*, **23**, 993-1011.

Minnis, P. and E. F. Harrison, 1984b: Diurnal variability of regional cloud and clear-sky radiative parameters derived from GOES data, Part III: November 1978 radiative parameters. *J. Climate Appl. Meteorol.*, Vol. **23**, 1032-1052.

Minnis, P., D. P. Kratz, J. A. Coakley, Jr., M. D. King, R. Arduini, D. P. Garber, P. W. Heck, S. Mayor, W. L. Smith, Jr., and D. F. Young, 1995b: Cloud optical property retrieval (Subsystem 4.3). "Clouds and the Earth's Radiant Energy System (CERES) Algorithm Theoretical Basis Document, Volume III: Cloud Analyses and Radiance Inversions (Subsystem 4)", *NASA RP 1376 Vol. 3*, edited by CERES Science Team, December, pp. 135-176.

Ou, S. C., K. N. Liou, W. M. Gooch, and Y. Takano, 1993: Remote sensing of cirrus cloud parameters using advanced very-high-resolution radiometer 3.7- and 10.9-μm channels. *Appl. Opt.*, **32**, 2171-2180.

Rossow, W.B., L.C. Gardar, P.J. Lu, and A.W. Walker, 1991: International Satellite Cloud Climatology Project (ISCCP) documentation of cloud data, WMD/TD No. 266 (Revised), World Meteorological Organization, Geneva, 77pp.

Young, D. F., S. Mayor, P. Minnis, J. M. Intrieri, S. Matrosov, and J. Snider, 1994: Comparison of satellite and surface-based remote sensing of cloud microphysical properties during FIRE Cirrus Phase II. *Proc. 8th Conf. Atmos. Radiation*, Nashville, TN, Jan. 23-28, 231-233.

CLIMATOLOGY AND MICROPHYSICS CHARACTERISTICS OF CUMULUS CLOUDS OF CEARÁ STATE IN THE NORTHEAST REGION OF BRAZIL

Carlos Jacinto de Oliveira[1], Alexandre Araújo Costa[2], Antônio José da Costa Sampaio[3] and José Carlos Parente de Oliveira[3]

[1] Departamento de Física e Química, Universidade Estadual do Ceará, Brazil
[2] Fundação Cearense de Meteorologia e Recursos Hídricos (FUNCEME), Brazil
[3] Laboratório de Física de Nuvens e Mesoescala (LFNM), Departamento de Física, Universidade Federal do Ceará, Brazil

1. INTRODUCTION

Several tropical regions around the world have extremely variable annual rainfall, both spatially and temporally. Ceará State is situated in the Northeast of Brazil(NEB), a semi-arid region, where the irregularity of rainy seasons causes serious drought problems and generates great scientific interest. We have flown through a set of non-precipitating cumulus clouds with an aim to characterize their microstructures. This is done using microphysics and thermodynamics parameters obtained by direct measurements of an instrumented aircraft (de Almeida et al., 1992), described in section 2. The flights, described in section 3, were realized in the coastal and continental regions of Ceará State. The analysis of the data, in section 4, shows that coastal and continental clouds exhibit differences in their microstructures. In section 5, a coastal and a continental cloud are analyzed, showing the correlation between some microphysical and thermodynamical parameters. Section 6 is dedicated to a general discussion and conclusions.

2. INSTRUMENTATION

The aircraft is an Embraer EMB 110 Bandeirante. This is a twin Pratt & Whitney turboprop, medium class, non-pressurized, with a Global Position System (GPS). Table 1 presents the instrumentation on board the aircraft and their characteristics.

The FSSP is the main instrument for this study, and their data were processed using the correction algorithm of Brenguier and Amodei (1989).

Table 1. Instruments installed in aircraft.

Parameter	Instrument
Cloud droplets	PMS FSSP-100
Cloud drops	PMS OAP 200X
Hidrometeors	PMS OAP 200Y
Cloud Condensation Nuclei	CCNC UW-83
Liquid Water Content	CSIRO KING
Dynamic pressure	Rosemount 122
Static pressure	Rosemount 120
Total temperature	Rosemount 102
Dew point temperature	EG & G 137C3

3. THE FLIGHTS

Table 2 shows a brief description of the flights and their characteristics. The total flight time of 9 hours made it possible to pass about two hundred clouds. Thus, it was possible to obtain a good characterization of the mean behavior of the non-precipitating cumuli in these regions over a period from February to June of 1994.

Table 2 - Description of the flights.

Flight	Date and Hour (LST)	Departure Point	Turning Points
1	Feb. 02, 1994, 0825	1	2, 7
2	Feb. 08, 1994, 1326	1	2
3	May 19, 1994, 1430	5	4
4	May 30, 1994, 0901	1	2, 3
5	Jun. 22, 1994, 1350	1	6, 7

In this work, we present the data of five flights, carried out in Ceará State and its neighborhood. These areas are shown in Figure 1.

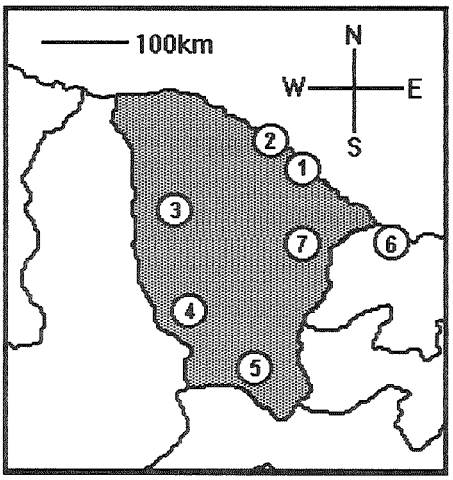

Fig. 1 - North portion of NEB, with Ceará State marked (dark area) and cities of Fortaleza (capital of Ceará State) (1), Paracuru (2), Nova Russas (3), Tauá (4), Juazeiro do Norte (5), Mossoró (6) and Morada Nova (7).

4. DIFFERENCES BETWEEN COASTAL AND CONTINENTAL CLOUDS

A number of 121 non-precipitating cumulus clouds was selected for the present study from the total of about two hundred clouds. Clouds whose pass time was smaller than 4s, or that presented precipitation development, were excluded.

The differences between microphysical characteristics of continental and maritime clouds are well known. In this study, 63 clouds of the coastal region and 58 over the continent were analyzed. Different droplet concentration and mean diameter are expected. It suggests that these two categories should be analyzed separately to identify these differences. There is an expectation that the continental clouds in north portion of NEB respond according to the continental cloud behavior described previously and that the coastal clouds show intermediate characteristics.

It can be seen in Figures 2 and 3 that smaller concentrations occur in coastal clouds in which maximum values between 200 cm^{-3} and 300 cm^{-3} predominate. However, we can observe that some coastal clouds have high droplet concentration. In this cases we believe that those clouds show strong influence from Fortaleza (capital of Ceará State). In the continental clouds, maximum concentrations between 300 cm^{-3} and 400 cm^{-3} are most frequent.

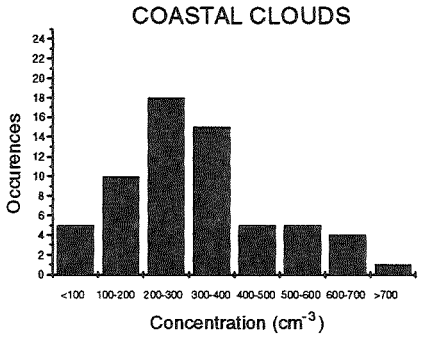

Fig. 2 - Frequency of maximum values of concentrations - coastal clouds

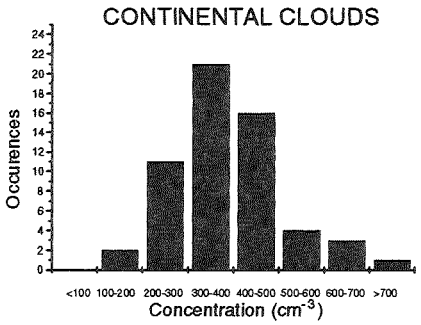

Fig. 3 - Frequency of maximum values of concentration - continental clouds

Figures 4 and 5 show the frequency of maximum values of the droplet mean diameter. As it was expected, bigger values occurred in coastal clouds. The values between 10μm and 12μm are most frequent. In continental clouds maximum mean diameters between 8μm and 10μm are predominating.

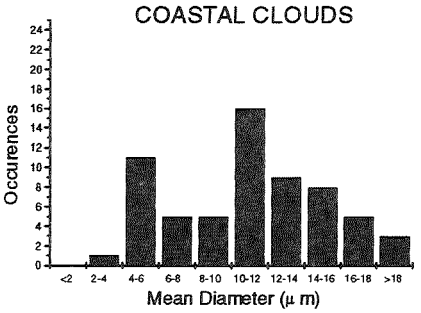

Fig. 4 - Frequency of maximum values of droplet mean diameter - coastal clouds

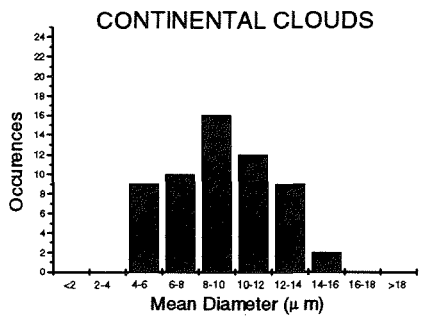

Fig. 5 - Frequency of maximum values of droplet mean diameter - continental clouds

These differences become more evident when an average over the maximum values of concentration (C) and droplet mean diameter (d) is made for both categories of clouds. The Table 3 summarizes the characteristics of clouds. The mean concentration of the continental clouds is about 25% bigger than correspondent for coastal clouds, while the mean diameter of coastal clouds is near 20% bigger.

Table 3 - Average of the maximum values of concentration and droplets mean diameter

Category	$\langle C \rangle$ (cm^{-3})	$\langle d \rangle$ (μm)
Coastal	317	11.1
Continental	388	9.3

5. ANALYSIS OF SOME OBSERVATIONS

A sample data collected for one coastal and one continental cloud are shown in Figures 6 and 7, respectively. For the coastal cloud (flight 2 - Table 2) the time was from 13:56:05 to 13:56:18. The horizontal distance through this cloud was around 1.5 km. The liquid water content obtained with the FSSP (curve a), the mean diameter (curve b), the droplet concentration (curve c) and the equivalent potential temperature (curve d) were analyzed. It can be seen in Figure 6 that there is a good correlation among the liquid water content (a) with all the others parameters. We can observe around 13:56:08 a big droplet concentration (b), small LWC (a) and small mean diameter (c). This behavior probably is due to the entrainment in the boundary of the cloud.

Figure 7 shows the same set of parameters for the continental cloud (flight 4 - Table 2). For this cloud the time was from 10:44:35 to 10:44:55. Here we also observed a good correlation among those parameters. The horizontal distribution of the LWC indicates non-uniform features, as the result of turbulent mixing. The same can be said about the mean diameter.

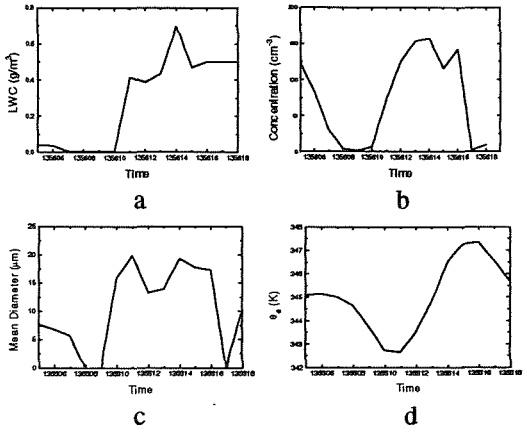

Figure 6. Time series for the coastal cloud (data averaged over 1 s intervals)

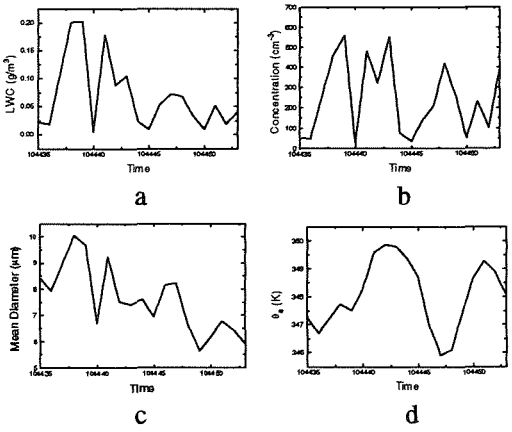

Figure 7. Time series for the continental cloud (data averaged over 1 s intervals)

ACKNOWLEDGMENTS

The authors wish to thank to Dr. Jean Louis Brenguier (CNRM, France) and the Department of Atmospheric Science of the University of Wyoming for the permissions to use processing data software. This work was partially supported by FUNCEME and by the Brazilian agencies CNPq and FUNCAP.

REFERENCES

Brenguier, J.L. and L. Amodei, 1989: Coincidence and dead-time corrections for the particle counters. Part I: A general mathematical formalism. *J. Atmos. Oceanic Technol.*, **6**, 575-584.

de Almeida, F.C., G.W. Munroe, C.A.R. Morales, M.C. Pereira, F.A. Barros, A.J.C. Sampaio and J.C.P. de Oliveira, 1992: An instrumented aircraft for tropical precipitation physics research: description and opportunity. WMP report, **19**, 145-150.

CLOUD-CLIMATE FEEDBACK MECHANISMS: RESULTS FROM A GROUND-BASED CLOSURE EXPERIMENT

V.K. Saxena[1], P.A. Durkee[2], S. Menon[1], John Anderson[1], and K.E. Nielsen[2]

[1] North Carolina State University, Department of Marine, Earth and Atmospheric Sciences, Raleigh, NC, USA
[2] Naval Postgraduate School, Department of Meteorology, Monterey, CA, USA

1. INTRODUCTION

The indirect forcing mechanism by anthropogenic sulfates has been thought to be comparable though of opposite sign to that caused by the doubling of anthropogenic CO_2 (e.g. Charlson et al., 1987; 1992). The effect of anthropogenic influence on cloud albedo is based on the fact that there is an increase in aerosol particle number concentrations with an increase in industrial emissions (Schwartz and Slingo, 1996). This gives rise to an increase in cloud droplet number concentrations (CDNC) which results in enhanced multiple scattering within clouds. This leads to an increase in the cloud optical depth and its reflectivity.

Although the relationship between cloud albedo and cloud condensation nuclei (CCN) has not yet been fully established theoretically, direct impact of CCN on the cloud albedo has been reported by Coakley et al., (1987) when they investigated ship exhausts and reflectance. Radke et al. (1989), have reported that larger concentrations of droplets of smaller radii were associated with higher reflectances of clouds formed over ship tracks. The purpose of this paper is to investigate the relationship between the cloud albedo (obtained both from in situ measurements and from satellite retrievals) and the cloud microphysical properties with particular emphasis on the effect of sulfate-rich aerosols on the cloud albedo.

2. METHODOLOGY

Mountain top locations offer unusual and unique opportunities for investigations of cloud-climate feedback mechanisms because they are often immersed in thin clouds (see for example, Saxena et al., 1989). A field experiment was conducted in Mount Mitchell (2038 m msl; 35°44'05" N, 82°17'15" W) State Park during 1993-1995. The location of our site is unique in that it frequently stays in the free troposphere. The observational platform consists of a 17.1 m walk up tower equipped with instruments which provide continuous meteorological measurements. Cloud water samples were collected on an hourly basis by means of an ASRC passive string collector (Atmospheric Science Research Center, Albany, New York) located 17.6 m above the ground level. A Particle Measuring System (PMS) forward-scattering spectrometer probe (FSSP) situated below the ASRC collector provided cloud-droplet size measurements. The pH of the cloud water was analyzed using ion chromatography. The pollution sources along the path of the cloud forming air mass were inferred from back-trajectory analysis using a Hybrid Single Particle Lagrangian Integrated Trajectory (HY-SPLIT) model (Draxler, 1992).

The optical depth (τ) of the cloud is calculated as shown by Twomey (1977),

$$\tau = H\{(9/2)\pi(LWC)^2 CDNC(\rho^{-2})\}^{\frac{1}{3}} \quad (1)$$

where the density (ρ) of liquid water is 1000 kg m^{-3} and the cloud thickness H is obtained from the HY-SPLIT sounding. LWC, the cloud liquid water content and CDNC are obtained from the FSSP size distributions. The albedo (A) is then evaluated using the relationship (Lacis and Hansen, 1974),

$$A = \frac{\tau}{\tau + 7.7} \quad (2)$$

Equations (1) and (2) were used to calculate the in situ cloud albedo. These were compared to the ones retrieved from the Advanced Very High Resolution Radiometer (AVHRR) aboard NOAA-11 and NOAA-12 polar orbiting satellites which provide the visible (Channel 1, λ = 0.63 μm), infrared (Channel 3, λ = 3.7 μm), and thermal infrared (Channel 4, λ = 11 μm) information.

3. RESULTS AND DISCUSSION

Table 1 contains data from six satellite passes that were coincident with in situ measurements along with the relevant cloud microphysical properties.

Table 1. Relevant cloud characteristics and derived albedo for six cases coincident with AVHRR satellite retrievals.

Event Date	pH	CDNC	Re	LWC	$[SO_4^{=}]$	H	τ	Albedo (%)	
		(cm^{-3})	(mm)	($g\ m^{-3}$)	($meq\ l^{-1}$)	(m)		AVHRR	In situ
14-Jun-93	2.84	823 ± 150	2.88 ± .57	0.18 ± .03	664.17	148 ± 20	10.8 ± 1.5	60.0 ± 10.0	58.1 ± 3.4
19-Jun-93	3.77	218 ± 160	4.51 ± .92	0.19 ± .04	162.08	238 ± 51	11.5 ± 2.4	70.0 ± 5.0	59.3 ± 5.2
19-Aug-93	2.97	613 ± 100	3.36 ± .83	0.15 ± .03	1110.21	105 ± 5	6.1 ± 0.3	35.0 ± 5.0	44.4 ± 1.1
29-May-94	3.42	237 ± 91	2.56 ± .80	0.09 ± .01	742.27	88 ± 3	2.7 ± 1.0	25.0 ± 3.0	26.3 ± 0.6
21-Jul-94	3.47	54 ± 15	5.79 ± .44	0.26 ± .05	420.00	276 ± 23	11.1 ± 0.9	56.5 ± 6.5	59.0 ± 2.1
24-Jul-94	2.92	231 ± 91	3.33 ± .90	0.07 ± .01	105.00	101 ± 10	2.5 ± 0.3	22.0 ± 6.0	24.0 ± 2.0

It can be seen from Table 1 that lower pH values are associated with higher sulfate contents, lower effective radii and higher CDNC, for almost identical LWC. We use the cloud water pH as an operational indicator for the pollution content of the cloud forming air masses. In case of the resulting short-wave albedo, we classified the six cases depending on the cloud thickness. The cloud events for 29 May, 24 July, and 19 Aug had similar cloud thickness. The 19 Aug cloud event was the most reflective of all the three cases and also had the highest sulfate concentration. Our criterion for designating air masses as polluted (P), continental (Co), and marine (M) is based on the emission inventories of the U.S. Environmental Protection Agency. The back-trajectory analysis indicated that the cloud forming air mass for the 19 Aug event was from the polluted sector as compared to the other two events which were continental and had lower sulfate concentrations.

The other three cases; namely; 14 June, 19 June, and 21 July had cloud thickness ranging from 148 m to 276 m. Back-trajectory analysis indicated that the 21 July event was produced by the marine air mass and consequently had a low sulfate content and was less reflective as compared to the 14 June event which was continental and had a higher sulfate content and was also more reflective. The 19 June event although highly reflective, as indicated by satellite estimates, had a very low sulfate content and a high pH. These cases serve to illustrate the fact that the sulfate content of the cloud forming air mass has a definite impact on the reflectivity of the cloud.

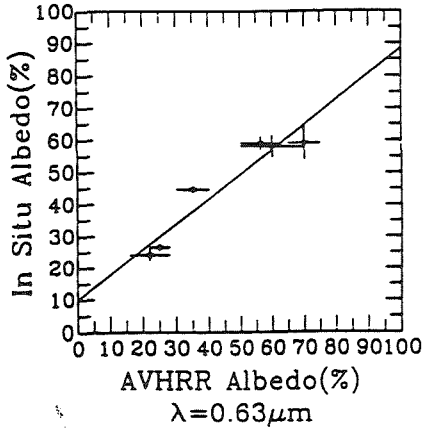

Figure 1 is the short-wave cloud albedo calculated from in situ measurements plotted against those determined from the AVHRR channel one (l = 0.63 mm) measurements. The correlation coefficient between the two is very good inspite of the fact that the cloud thickness above the mountain top varied by a factor of 3 (range: 88-276 m ACL) and the LWC varied by a factor of 3.7 (range: 0.07-0.26 g m^{-3}) for the six cases considered.

In order to investigate the effect of cloud water acidity on the CCN, the relationship between the two was examined. For the 1995 field season, the CCN activation spectra were measured by a Horizontal Thermal Gradient Cloud Condensation Nucleus Spectrometer described by Fukuta and Saxena (1979a, b). Activation spectra obtained an hour prior to the cloud event were assumed to represent the cloud forming air mass. The CCN concentration activation spectrum is represented in terms of a power function as;

$$N = C\ (S)^k \qquad (3)$$

where N is the number of CCN that would be active at or below the supersaturation S (in %), and C and k are concentration and slope parameters which are obtained empirically.

Fig. 1. Albedo (%) determined from *in situ* measurements vs coincident AVHRR albedo (%) (channel 1, $\lambda = 0.63\ \mu m$). The horizontal lines represent the range of the AVHRR albedos whereas the vertical lines represent the estimated uncertainties of the albedos determined from the *in situ* measurements. The solid line represents the direct one-to-one correspondence (correlation coefficient = 0.95) between the two independently derived albedos.

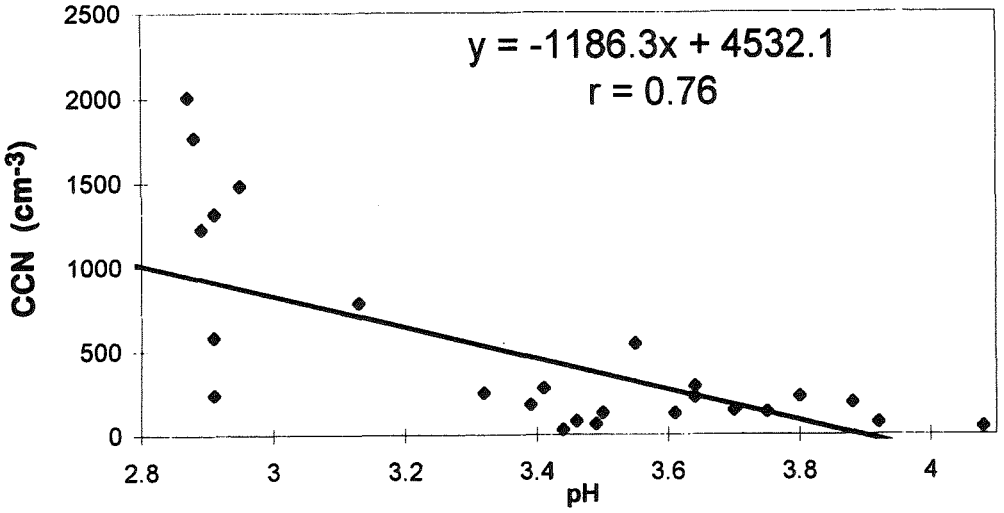

Figure 2: CCN Concentration at 1% supersaturation plotted as a function of cloud water pH.

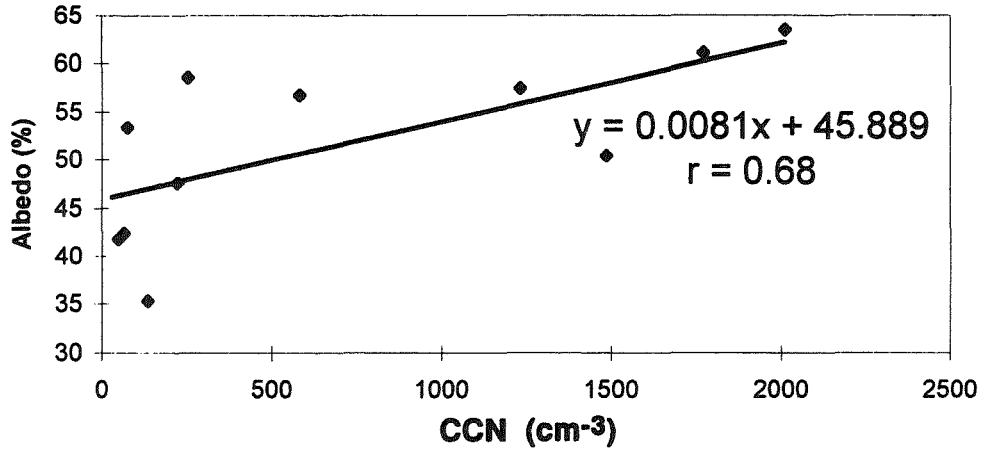

Figure 3: Cloud albedo calculated from in situ measurements plotted as a function of CCN concentration.

From Fig. 2 it can be observed that the air masses containing higher CCN concentrations lead to the formation of more acidic clouds. The back trajectory analysis indicated that the more polluted air masses had higher CCN concentrations as compared to the continental or marine air masses. This is in conformity with the previous findings of the enhancement of CCN concentrations due to anthropogenic emissions (Twomey et al., 1978, Radke and Hobbs, 1976, Hudson, 1991, Frisbie and Hudson, 1993).

Figure 3 depicts the cloud albedo calculated from Eqns. (1) and (2) using in situ measurements plotted as a function of the CCN concentration. With higher CCN concentrations, the cloud albedo increases. This is in agreement with the indirect effect which suggests that with an increase in CCN, the cloud droplet concentrations would also increase. The increase in CDNC leads to a change in the optical properties of clouds which, in turn, leads to a change in the cloud albedo. The relationship is, of course, non-linear, as evident in Eqn. (1) where the optical depth varies as $(CDNC)^{1/3}$. Positive correlations were obtained when the optical depth was plotted as functions of $(CCN)^{1/3}$ and $(CDNC)^{1/3}$, with correlation coefficients being 0.75 and 0.83 respectively. Similar findings were also obtained by Boers et al. (1994) in measurements taken at Cape Grim, Tasmania. The sensitivity of cloud albedo to sulfate aerosol addresses an important issue of determining the magnitude of anthropogenic perturbation in regional climate. This has not yet been conclusively resolved. Ghan et al. (1990) calculated that a factor of four increase in CCN concentrations in marine stratus clouds would lead to an increase in cloud albedo by 2% thereby counteracting the doubling of CO_2. Our observations reported here and elsewhere (Saxena et al., 1996) lend support to their modeling results.

4. CONCLUSIONS

The magnitude of anthropogenic perturbation to the earth's radiation budget is essential for estimating the sensitivity of climate from observed climate change, for future climate predictions, and also in evaluating the performance of climate models (e.g. Charlson et. al., 1992). In this paper we have presented results from a "local closure" field study in which retrieved cloud albedos of thin mountain top clouds were compared to the ones computed from in situ measurements. We investigated clouds formed in marine, continental and polluted air masses. From the field study we can conclude that the effective radii of the cloud droplets get smaller and the CDNC gets larger as the cloud water pH decreases. Cloud water acidity may be considered to be a good indicator of the sulfate content of the cloud forming air mass. As the cloud water acidity increases, the cloud albedo begins to increase. The correlation coefficient for the cloud albedo computed from in situ measurements and cloud water pH is about -0.70. The agreement between satellite retrieved cloud albedo and in situ calculated albedo is very good, with a correlation coefficient of 0.95.

The above findings indicate that on a regional scale, anthropogenic sulfur emissions influence the reflectivities of thin continental clouds which result in important cloud-climate feedback mechanisms. Results from such a "local closure" field study can be used to conduct sensitivity tests which will yield more quantitative information that can assess the role of aerosols in terms of climate forcing. Such long-term ground-based measurements (taken at a site which has been designated as a United Nations Biosphere Reserve), provide information that is not readily obtained from airborne measurements. A necessity for information of this kind has recently been expressed by Schwartz and Slingo (1996). Our field measurements will aid in answering some of the issues raised in terms of climate forcing by aerosols which can be incorporated into climate models.

Acknowledgments – This research was supported through the Southeast Regional Center for the National Institute for Global Environmental Change, in Tuscaloosa, Alabama, by the United States Department of Energy under cooperative agreement number DE-FCO3-90ER61010.

5. REFERENCES

Boers, R., G.P. Ayers, and G.L., Gras, 1994: Coherence between seasonal variation in satellite-derived cloud optical depth and boundary layer CCN concentration at a mid-latitude Southern Hemisphere station, *Tellus*, **46B**, 123-131.

Charlson, R.J., J.E. Lovelock, M.O. Andreae, and S.G. Warren, 1987: Oceanic phytoplankton, atmospheric sulphur, cloud albedo and climate, *Nature*, **326**, 655-661

Charlson, R.J., S.E. Schwartz, J.M. Hales, R.D. Cess, J.A. Coakley Jr., J.E. Hansen, and D.J. Hofmann, 1992 Climate forcing by anthropogenic aerosols. *Science*, **255**, 423-430.

Coakley, J.A. Jr., R.L. Bernstein, and P.A. Durkee, 1987: Effects of ship-stack effluents on cloud reflectivities, *Science*, **237**, 1020-1022.

Draxler, R.R., 1992: Hybrid single-particle Lagrangian integrated trajectories (HY-SPLIT): Version 3.0-- User's guide and model description. *NOAA tech. Memo. ERL ARL*- **195**, 26pp.

Frisbie, P.R., and J.G. Hudson, 1993: Urban cloud condensation nuclei spectral flux, *J. Appl. Meteorol.*, **32**, 666-676.

Fukuta, N., and V.K. Saxena, 1979a: A horizontal thermal gradient cloud condensation nucleus spectrometer. *J. Appl., Meteorol.*, **18**, 1352-1362.

Fukuta, N., and V.K. Saxena, 1979b: The principle of a new horizontal thermal gradient cloud condensation nucleus spectrometer. *Atmos. Res.*, **13**, 169-188.

Ghan, S.J., K.E. Taylor, J.E. Penner, and D.J. Erickson III, 1990: Model test of CCN-cloud albedo climate forcing, *Geophys. Res. Lettrs.*, **17**, 607-610.

Hudson, J.G., 1991: Observations of anthropogenic cloud condensation nuclei, *Atmos Environ*, **25A**, 2449-2455.

Lacis, A.A., and J.E. Hansen, 1974: A parameterization of the absorption of solar radiation in the earth's atmosphere. *J. Atmos. Sci.*, **31**, 118-133.

Radke, L.F., and P.V. Hobbs, 1976: Cloud condensation nuclei on the Atlantic seaboard of the United States, *Science*, **193**, 999-1002.

Radke, L.F., J.A. Coakley, and M.D. King, 1989: Direct and remote sensing observations of the effects of ships on clouds, *Science*, **246**, 1146-1149.

Saxena V.K., R.E. Stogner, A.H. Hendler, T.P. DeFelice, and R.J.-Y. Yeh, 1989: Monitoring the chemical climate of the Mt. Mitchell State Park for evaluation of its impact on forest decline, *Tellus*, **41B**, 92-109.

Saxena, V.K., P.A. Durkee, S. Menon, J. Anderson, K.L. Burns, and K.E. Nielsen, 1996: Physico-Chemical measurements to investigate regional cloud-climate feedback mechanisms, *Atmos. Environ.*, **30**, (in press).

Schwartz, S.E., and A. Slingo, 1996: Enhanced shortwave cloud radiative forcing due to anthropogenic aerosols, in *Clouds, Chemistry and Climate*, ed. P.J. Crutzen and V. Ramanathan, Springer-Verlag Berlin, Heidelberg, 191-236.

Twomey, S., A.K. Davidson, and K.J. Seton, 1978: Results of five years' observations of cloud nucleus concentration at Robertson, New South Wales, *J. Geophys. Res.*, **35**, 650-656.

MEASUREMENTS OF THE MICROPHYSICS OF LOW STRATUS AND THE RADIATION ABOVE, IN AND BELOW CLOUD

Catharine M. Banic, W.R. Leaitch, H.W. Barker, K.B. Strawbridge[1], A.V. Korolev, G.A. Isaac, M.C. Couture, J.I. MacPherson[2], J.W. Strapp and I. Gultepe

Atmospheric Environment Service, 4905 Dufferin St., Downsview, Ontario, Canada, M3H 5T4
[1]Centre for Atmospheric Research Experiments, Atmospheric Environment Service, Egbert, Ontario
[2]Institute for Aerospace Studies, National Research Council, Ottawa, Ontario, Canada

1. INTRODUCTION

Thin low-level clouds that form over the ocean play a significant role in the energy balance of the earth. In order to further our understanding of the radiative effect of these clouds and the impact of aerosol on their properties, marine stratus was studied as part of the Radiation, Aerosol and Cloud Experiment (RACE). Here we give a brief overview of the relationship observed between microphysics and extinction, and illustrate two cloud cases.

2. METHOD

Two aircraft, a DH6 Twin Otter and a Convair 580 operated by the National Research Council of Canada, were used to measure the microphysics and radiative flux above, in and below stratus found over the Bay of Fundy and the Atlantic Ocean near the southern tip of Nova Scotia from August 15 through September 9, 1995. All measurements given here are averages of 1 s data taken with the Twin Otter flying at 60 m s^{-1} and the Convair at 100 m s^{-1}. All data given here, except the lidar results, were collected with the Twin Otter.

Broadband shortwave radiative flux (0.3 to 2.8 μm), both downwelling and upwelling, was measured with Eppley pyranometers mounted almost horizontally, with known orientation, on the top and bottom of the fuselage. Measurements of downwelling radiative flux made under clear skies were corrected for aircraft attitude and heading. Pyranometer data were rejected if the combination of roll, pitch and mounting angles exceeded 6 degrees. Cloud liquid water content (LWC) was measured with a PMS King probe mounted below the wing; zero-removed values are used. Cloud droplet number concentrations (N) for diameters between 2 and 47 μm (Flights 4, 10, 11, 12) or 1.2 and 63.3 μm (Flights 13, 14, 15, 18, 19, 21) were measured with PMS FSSP probes mounted below the wing; deadtime corrected values are used. Extinction of shortwave radiative flux by cloud (E) was measured with a Nevzorov extinction meter (Kosarev et al., 1976) mounted between the upper fuselage and the tip of the tail of the aircraft. The extinction of white light from a halogen lamp over a path of 12 m is determined. The effective radius (r_{eff}) was calculated from the E and the LWC, and also from the FSSP size distributions.

The Convair carried a Nd:YAG lidar system significantly modified from that described in Strawbridge and Hoff (1996). The dual-wavelength system (1064 nm @ 5.0 mrad and 532 nm @ 0.9 mrad) operating in a near-nadir orientation obtained cloud structure and reflectivity with resolution of 100 m in the horizontal and 12 m in the vertical. Cloud top height is calculated by determining the maximum first derivative from the lidar profile. Measurements were made from an altitude of 3 km while the Twin Otter obtained simultaneous in-situ measurements below.

3. RESULTS

3.1 E and N in marine stratus

On each flight during which cloud was encountered, cloud water samples were collected for chemical analysis. These sampling times define a data set for microphysical parameters which can ultimately be related to the cloud water chemistry.

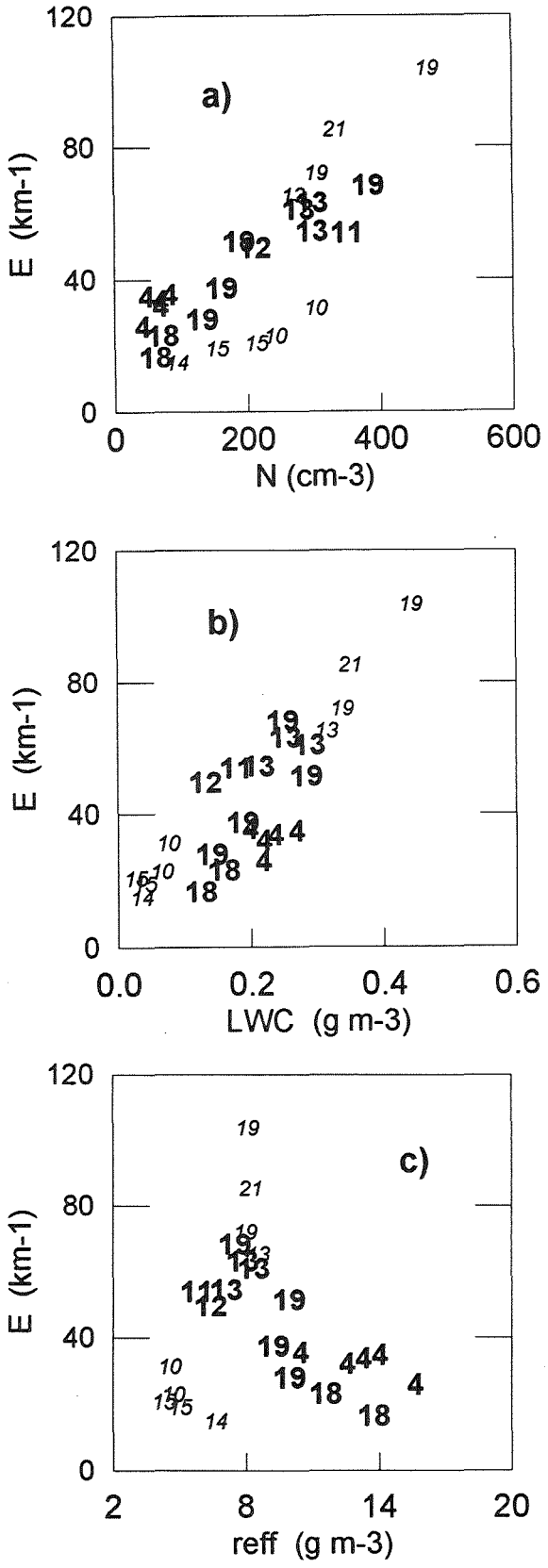

Figure 1: The relationship of E with a) N, b) LWC and c) r_{eff} in marine stratus. The flight numbers are given, with bold indicating LWC between 0.1 and 0.3 g m^{-3}. The r_{eff} is calculated from the FSSP size distribution.

Table 1: Characteristics of the clouds.

Parameter	Flt4	Flt11
cloud base (m)	170	555
cloud top (m)	420	655
average over profile of:		
FSSP (cm-3)	73	271
LWC (g m-3)	.19	.10
r_{eff} (μm)	10.5	3.7
E (km-1)	28.4	32.9
integrated optical depth	7.1	3.3
at bin of maximum extinction in profile:		
altitude (m)	355	630
FSSP (cm-3)	108	356
LWC (g m-3)	0.28	0.18
r_{eff} (μm)	8.8	5.1
E (km-1)	47.3	54.2
in level flight:		
elapsed time (s)	254	213
altitude (m)	294	622
FSSP (cm-3)	46	386
LWC (g m-3)	0.29	.20
r_{eff} (μm)	12.3	5.1
E (km-1)	35.3	60
elapsed time (s)	217	311
altitude (m)	290	635
FSSP (cm-3)	48	338
LWC (g m-3)	0.24	.17
r_{eff} (μm)	12.0	4.9
E (km-1)	29.9	51
elapsed time (s)	336	
altitude (m)	294	
FSSP (cm-3)	72	
LWC (g m-3)	0.26	
r_{eff} (μm)	11.8	
E (km-1)	35.1	
above cloud - altitude (m)	488	710
elapsed time (s)	260	18
solar zenith angle (degrees)	51.4	38.2
shortwave radiative flux (W m^{-2})		
downwelling	593	811
upwelling	254	150
below cloud - altitude (m)	159	372
elapsed time (s)	216	310
solar zenith angle (degrees)	50.2	37.8
shortwave radiative flux (W m^{-2})		
downwelling	337	253
upwelling	26	8.2

The relationship observed between N and E is shown in Figure 1a. The mean and standard deviation of the average LWC for each of these periods are 0.2 ± 0.1 g m^{-3}, and the data are shown stratified by LWC. Linear regression gives R^2 of 0.83 and 0.65 for data with LWC between 0.1 and 0.3 g m^{-3}, and the full data set, respectively, suggesting that for relatively small variations in LWC, N has a strong influence on E. The relationship between E and LWC, shown in Figure 1b, shows a linear correlation with R^2=0.72 for all data points. Consistent with E increasing with N, Figure 1c shows that E increases with decreasing r_{eff} for LWC between 0.1 and 0.3 g m^{-3}.

3.2 Case Studies

Flight 4 (Flt4) sampled stratus over the Atlantic Ocean 65 km to the south of Yarmouth from 19:23 to 20:01 UTC on August 21. Flt11 sampled stratus over the Bay of Fundy from 14:20 to 14:41 UTC on August 30. Skies above were clear on both days. A layer of fog obscured the surface of the water below the cloud on Flt4, but the underlying water was clearly visible from below cloud on Flt11. In each case, all sampling in, above and through cloud was confined to multiple passes up and down a line of approximately 20 km.

The characteristics of the clouds are given in Table 1. The r_{eff} is calculated from E and LWC. All radiative flux below cloud is treated as diffuse. Each individual pass through cloud follows a turn at the end of the line. All the in-cloud data were averaged in 10 m altitude bins, and these values were then averaged to get the profile averages shown. Horizontal variabilty in cloud can be estimated from the standard deviations seen in level flight segments in Table 1 (units as given in the table): $\pm$ 15 for FSSP < 50, $\pm$ 40 for FSSP = 72, $\pm$ 75 for FSSP >300, LWC $\pm$ 0.1 for Flt4 and $\pm$ 0.04 for Flt11, $r_{eff} \pm 2$ for the first two cloud passes of Flt4 and $\pm$ 9 for the final pass, $r_{eff} \pm 0.6$ for Flt11 and E $\pm$ 10 in all cases. The standard deviations for all flux measurements listed are $\pm$ 20 to 30 W m^{-2} except downwelling below cloud on lt11 ($\pm$ 60) and the upwelling below cloud ($\pm$ 30%).

During Flt11 the lidar obtained data from three passes sampling within 0.5 to 1 km of the line. Cloudtop heights calculated from both wavelengths, shown in Figure 2, are in very good agreement but there are differences of up to 200 m between the passes. The backscatter coefficient (β_π), which.

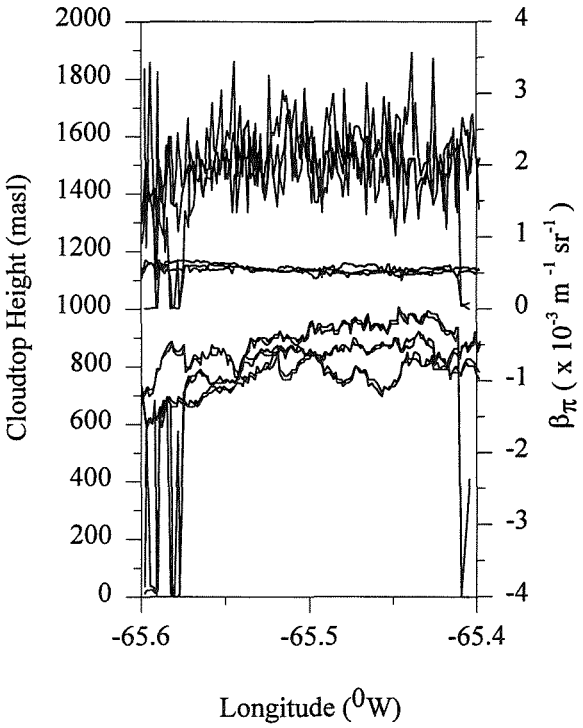

Figure 2: Lidar data for the three passes over the cloud of Flt11. Cloudtop heights in metres above sea level calculated from both wavelengths are shown in the lower curves. Values of 0 indicate little or no cloud within the laser footprint. The middle and top sets of curves give the backscatter coefficient for the 1064 nm and 532 nm channels, respectively.

---

should be proportional to cloud reflectivity, is also shown in Figure 2.

Profiles of solar radiative flux were generated by a version of the code used in the AES-GCM (Barker and Li, 1995), in which the solar spectrum is divided into 15 wavebands. Nineteen vertical layers are used. Cloud optical properties are based on the parameterization of Slingo (1989).

The clouds were considered to be homogeneous in the vertical and the model resolution was chosen so that cloud filled a single layer corresponding to the observed thickness. Aerosol was not included. The observed surface albedo was used for each case. The r_{eff} and the optical depth were 10 μm and 3.75 μm and 7 and 3.9 for Flt4 and Flt11, respectively. Results are given in Table 2. Since the cloud was horizontally extensive and vertically thin the effective thickness approximation of Cahalan et al.

(1994) was used to assess the influence of the observed inhomogeneity in LWC in the horizontal. The effect of inhomogeneity was found to be small; the optical depth was reduced by a factor of 0.94 for Flt4.

Table 2: Model shortwave radiative flux (W m^{-2}) scaled to the observed input flux.

	Flt4	Flt11
above cloud		
downwelling	593	811
upwelling	292	283
below cloud		
downwelling	303	534
upwelling	23	18

4. DISCUSSION

The data of Figure 1 show E to be dependent on N and the LWC. Examination of the data for a range of LWC within one standard deviation of the mean (i.e. 0.1-0.3 g m^{-3}) indicates that E increases with increasing N, and E decreases with increasing r_{eff}. The explanation for this may lie with the relatively larger range of N values compared with r_{eff}.

The radiative balance for Flt4 can be derived from Table 1 by comparing the incoming radiative flux (593 W m^{-2}) with that scattered back above cloud (254 W m^{-2}) added to that absorbed at the surface (337-26=311 W m^{-2}), and from similar data taken earlier between two of the passes through cloud (635 compared with 264+395-58= 601, in W m^{-2}). The differences seen are small, about 5%. The radiative transfer model predicts a higher albedo for the cloud in Flt4 than was observed (.49 vs .43), and similar absorption in cloud (4%).

The measurement uncertainty for the incoming flux and the sum of the measured loss terms estimated from the standard error in the means for the data of Table 1 is less than 3 W m^{-2}. Other errors (e.g. due to correction for attitude) have not been considered. The uncertainty in the true spatial representativeness of the measurement is difficult to quantify, but the two estimates made for absorption in the same cloud at different times agree. The same calculation shows poor agreement for Flt11 (811 W m^{-2} compared with 150+253-8=395 W m^{-2}). Further analysis incorporating a detailed study of the lidar data will be required to understand this discrepancy.

The β_π values calculated from the two lidar wavelengths differ by a factor of 4, which is of the right order based on preliminary Mie calculations using the observed r_{eff}. However, β_π is highly dependent on particle size distribution and this will be considered in further analyses. In addition, β_π can provide a measure of cloud homogeneity. Pronounced differences in the lidar data due multiple scattering effects resulting from the different divergences for the two wavelengths are seen, and will provide a very interesting study.

5. CONCLUSIONS

The microphysical characteristics of the stratus during RACE varied considerably. A direct relationship was seen between extinction and cloud droplet number concentration. As well, extinction increased with increasing liquid water content, but the relationship with effective radius was less clear.

The radiation balance for a cloud formed in a clean marine boundary layer (Flt4) indicated that the radiation backscattered from the cloud/surface system and absorbed by the surface accounted for about 95% of the incoming radiation. The remaining 5% may be absorbed in cloud. The same approach applied to a thin, short-lived cloud of smaller spatial extent (Flt11) led to a 50% discrepancy in the radiative balance.

6. REFERENCES

Barker H.W. and Z. Li, 1995: Improved simulation of clear-sky solar radiative transfer in the CCC-GCM. J. Climate, 8, 2213-2223.

Cahalan R.F., W. Ridgeway, W.J. Wiscombe, T.L. Bell and J.B. Snider, 1994: The albedo of ractal stratocumulus clouds. J. Atmos. Sci., 51, 2434-2455.

Kosarev A.L., I. P. Mazin, A.N. Nevzorov and V.F. Shugaev : Optical density of clouds (experimental data). Moscow, Gidrometeoizdat, 1976.

Slingo A., 1989: A GCM parameterization for the shortwave radiative properties of water clouds. J. Atmos. Sci., 46, 1419-1427.

Strawbridge, K. B. and Hoff, R. M. (1996) LITE Validation Experiment Along California's Coast: Preliminary Results. Geophys. Res. Lett. 23, 73-76.

COMPARISONS OF AIRCRAFT AND LANDSAT OBSERVATIONS FOR CLOUD-CLIMATE INTERACTIONS

I. Gultepe, W. R. Leaitch, G. A. Isaac,
C. M. Banic, J. W. Strapp, and A. Korolev

Cloud Physics Research Division, Atmospheric Environment Service, Ontario, Canada

1. INTRODUCTION

Low level clouds play an important role in the radiation budget of the earth's atmosphere (Albrecht et al., 1988). Their thickness is not more than a few hundred meters for many cases (Gultepe et al, 1996, Isaac et al, 1995) and are difficult to resolve in general circulation models (GCMs). The relationship between cloud droplet number concentration (N_d) and pre-cloud aerosol number concentration (N_a) is critical to the radiative forcing from these clouds (Jones 1994). In GCMs, N_d is taken as separate constant for clouds over land and ocean. These N_d are used in the calculation of optical depth and effective radius (r_{eff}) (Slingo, 1990) which determine the radiative forcing.

In this study, measurements in clouds over the Bay of Fundy (ocean), and Ontario (land) during the Radiation, Aerosol, and Cloud Experiment (RACE), which took place in the late summer of 1996, are used to obtain relationships among N_d, N_a, and r_{eff}, and to compare aircraft and LANDSAT determinations of r_{eff} for clouds formed over ocean or land.

2. OBSERVATIONS

a. By Convair on the 16 August case

Observations in the clouds over the Bay of Fundy were obtained by the National Research Council of Canada (NRCC) Convair-580 on the 16 August 1995. Measurements from the Convair were used to obtain N_d, N_a, and r_{eff} for each second. N_d was obtained from two Particle Measuring Systems (PMS) Forward Scattering Spectrometer Probes (FSSP-100) operated in the 2-47 μm and 5-95 μm diameter range. Interstitial aerosol number concentration (N_i) were obtained with a PMS ASASP-100X probe which measures particles between 0.17 μm and 2 μm diameter.

b. By Twin Otter on the 4 October case

Observations in the clouds over Ontario were made from the NRCC Twin Otter on the 4 October 1995. N_d and r_{eff} were obtained from a FSSP-100 with a measuring interval between 1.2 and 63.3 μm diameter. N_i was measured by a PMS Passive Cavity Aerosol Spectrometer Probe (PCASP-100X) which samples in the 0.13-3 μm range.

The uncertainty in counting is about 12% for both the ASASP and the PCASP (Gultepe and Isaac, 1996). Liquid water content (LWC) was obtained from Nevzorov, FSSP, and King probes. Temperature (T) was measured by a Reverse Flow probe. The uncertainty in LWC and T is about 0.02$\pm$10% g m^{-3} and $\pm$0.5°C, respectively.

c. By LANDSAT

LANDSAT over passes at 1411 GMT for the 16 August and 1452 GMT for the 4 October case were near concurrent with the aircraft flights. The difference between the aircraft flight time and the LANDSAT over pass was about one hour for the 16 August case and 1 minute for the 4 October case. Radiation observations were collected at 6 solar reflectance channels from 0.45 μm up to 2.35 μm of the Thematic Mapper (TM) with 30 m resolution over a 100$\times$100 km^2 area. The infrared channel for 10.4-12.5 μm had a field of view of 114 m. In order to reduce the uncertainty due to cloud system advection, LANDSAT reflectivity (R) values are used from an area approximately covering 600 km^2 around the aircraft flight path. These R values are used for comparisons with calculated R values from Wielicki et al. (1990) for given r_{eff} values.

3. RESULTS

Observations from the aircraft are used to calculate r_{eff} and N_a (N_i+N_d) along the flight paths for each second (Gultepe et al, 1996). r_{eff} is plotted against N_d and LWC after grouping observations at Δr_{eff}=2 μm intervals. Independent variables are averaged and the standard deviation (sd) is calculated at each interval.

a. Clouds Over Ocean on the 16 August case

Clouds over the ocean at about 1 km were generally homogeneous in the horizontal, but some irregularities were seen at the cloud top in the LANDSAT images. Fig. 1a compares observed R values with R values computed by Wielicki et al. (1990) for the indicated r_{eff}. R at 2.21 μm from the LANDSAT along the flight track changed from 0.05 to 0.3 while r_{eff} from the aircraft changed from 3 to 18 μm. High R values may reflect larger N_d values. A comparison of the LANDSAT R with the calculation of Wielicki et al. (1990) suggests that r_{eff} varied from 3 to 30μm. The aircraft r_{eff} versus N_d, and LWC are shown in Fig. 1b and 1c, respectively. Open circles represent 1 s observations and solid circles with bars represent averaged and sd values over Δr_{eff}. r_{eff} decreases with N_d, and increases with LWC. Fig. 1d shows that N_d does not change significantly with N_a.

b. Clouds Over Land on the 4 October case

Dynamical structures within the clouds for the 4 October case were more apparent compared to the 16 August case. LANDSAT images indicate that there were convective cells with sizes about 0.5 to

1 km. Fig. 2a is obtained similar to Fig. 1a. R at 2.21 μm from the LANDSAT along the flight track changed from 0.1 to 0.5, slightly higher than this for the 16 August case. The r_{eff} from the aircraft changed from 3 to 14 μm, whereas the LANDSAT derived r_{eff} varied from 3 to about 30μm. Aircraft measurements of r_{eff} increased with increasing LWC (Fig. 2b), and decreased with increasing N_d (Fig. 2c). N_d increased with increasing N_a (Fig. 2d).

c. Comparisons

General characteristics for both days are summarized in Table 1. In this table, clouds indicated by I and II are shown for both the 16 August and 4 October cases. All values in this table are averaged along the flight path. Convective cells at about 1 km scale were seen within clouds on the 4 October case, but not for the 16 August case. Size spectra over the ocean (Fig. 3a) are bimodal, but over land there is only one peak value at about 10 μm (Fig. 3b). N_d is about two times larger in the clouds over land (see Table 1) compared to these over ocean. LWC in the clouds over land is found much higher than that for over the ocean. r_{eff} of clouds over ocean is approximately 3-4 micron greater than that for over land (see Table 1, Fig. 4a,b). Clouds for both cases showed similar characteristics for extended areas and their dynamical structures in the small and and larger scales for the same day were persistent. Larger r_{eff} values from LANDSAT compared to aircraft values were obtained at lower R values in the 2.21 μm channel for the 4 October case (Fig. 1a). For the 16 August case, larger r_{eff} values were seen at higher R values in the same channel (Fig. 2a). Differences in r_{eff} values from aircraft and LANDSAT observations can be due to cloud development within the time difference between aircraft and satellite observations, in the retrieval of r_{eff} from LANDSAT observations at small R values, or the uncounted droplets at higher sizes of the FSSP probes. Larger r_{eff} values for the 4 October case can also be explained by the presence of embedded cells. Total aerosol concentrations were found similar for these cases.

4. DISCUSSIONS AND CONCLUSIONS

Microphysical characteristics of the clouds depend on cloud micro (e.i. turbulence, particle size) and macro structures (cells), and environmental influences such as antropogenic pollution sources, and synoptic scale circulations. The r_{eff} obtained from cloud particle spectra, in fact, depend on cloud and larger scale processes. The r_{eff} changes from 3-4 μm as a lower limit for liquid clouds up to 50 μm for ice clouds dependent on the cloud type and its microphysical structure. Current GCMs assumed r_{eff} or N_d as constant. They use 5 μm for clouds over land, and 10 μm over ocean (Kiehl et al, 1987). r_{eff} clouds over land and ocean from this study were found larger about 5-10 μm compared to other studies (Ishizaka et al, 1995). If droplet spectra have a bimodal shape, then the mean r_{eff} does not represent the cloud characteristics properly. Therefore, r_{eff} should be analyzed carefully. Droplet spectra in the clouds over the ocean close to land show very different distribution characteristics compared to that only over either ocean or land. LANDSAT observations of cloud microphysical and dynamical characteristics with high resolution (about 30 m) together with aircraft observations can be further used for analyzing cloud-climate interactions.

ACKNOWLEDGEMENTS

The authors would like to thank M. Couture and P. S. K. Liu of Cloud Physics Research Division of the Atmospheric Environment Service (AES) for discussions related to aircraft data analysis. The aircraft data were obtained with the assistance of the National Research Council of Canada.

REFERENCES

Albrecht, B. A., D. A. Randall, and Stephen Nicholls, 1988: Observations of marine stratocumulus clouds during FIRE. *Bull. Amer. Meteor. Soc.*, 69, 618-266.

Gultepe, I, G. Isaac, W. R. Leaitch, and C. Banic, 1996: Parameterizations of marine stratus microphysics based on in-situ observations: Implications for GCMs. *J. Climate*, 9, 345-357.

Gultepe, I, and G. Isaac, 1996: The relationship between cloud droplet and aerosol number concentrations for climate models. *Inter. J. Climate*, July issue.

Isaac, G. A., I. Gultepe, R. A. Stuart, and H. W. Barker, 1995: Using observations to develop and test cloud microphysical and precipitation parameterizations within GCMs. World Climate Research Program Workshop on Cloud Microphysics Parameterizations in Global Atmospheric Circulation Models, Kananaskis, Alberta, Canada, WMO/TD-No. 713, 141-154.

Ishizaka, Y., Y. Kurahashi, and H. Tsuruta, 1995: Microphysical properties of winter stratiform clouds over the Southwest Island are in Japan. *J. Meteor. Soc. Japan*, 73, 1137-1151.

Jones, A., D. L. Roberts, and A. Slingo, 1994: A climate model study of indirect radiative forcing by anthropogenic sulphate aerosols. *Nature*, 370, 450-453.

Kiehl, J. T., R. J. Wolski, B. P. Briegleb, and V. Ramanathan, 1987: Documentation of radiation and cloud routines in the NCAR CCM1. NCAR Tech. Note NCAR/TN-288+IA, Boulder CO. 102 pp.

Slingo, A., 1990: Sensitivity of the earth's radiation budget to changes in low clouds. *Nature*, 343, 49-52.

Wielicki, B. A., J. T. Suttles, A. J. Heymsfield, R. M. Welch, J. D. Spinhirne, M. C. Wu, D. O'C. Starr, L. Parker, 1990: The 27-28 October 1986 FIRE IFO Cirus case study: Comparison of radiative transfer theory with observations by satellite and aircraft. *Mon. Wea. Rev.*, 2356-2376.

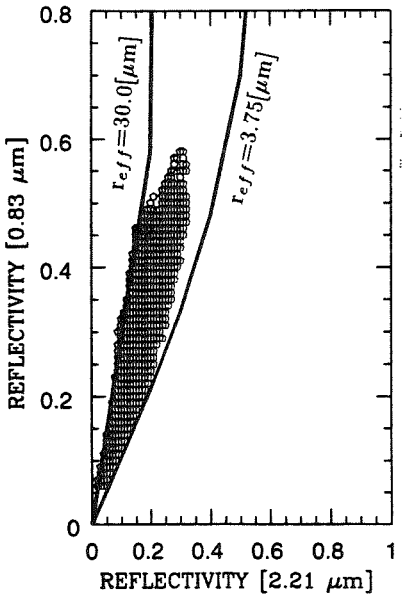

Fig. 1a: Observed cloud nadir reflectance (R) versus calculated R with r_{eff}=3.75 μm and 30 μm values which are taken from Wielicki et al. (1990). R values are approximately obtained along the aircraft flight track for the 16 August case.

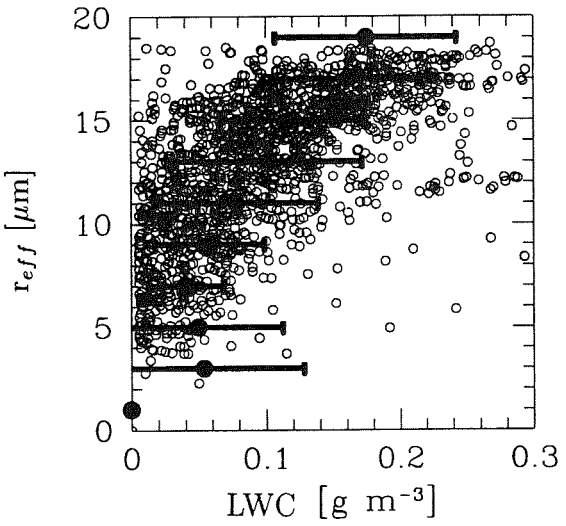

Fig. 1b: r_{eff} versus N_d from aircraft observations for the 16 August case.

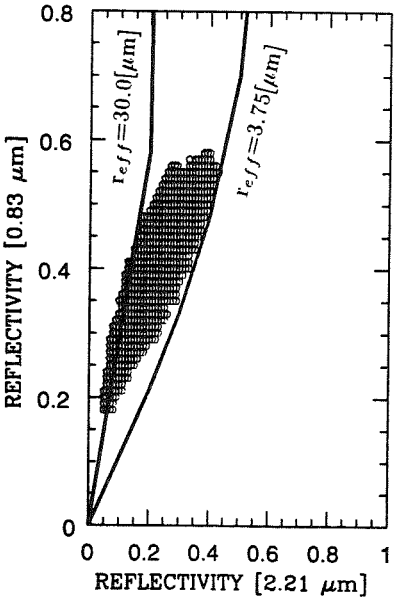

Fig. 2a: Observed cloud nadir reflectance (R) versus calculated R with r_{eff}=3.75 μm and 30 μm values which are taken from Wielicki et al. (1990). R values are approximately obtained along the aircraft flight track for the 4 October case.

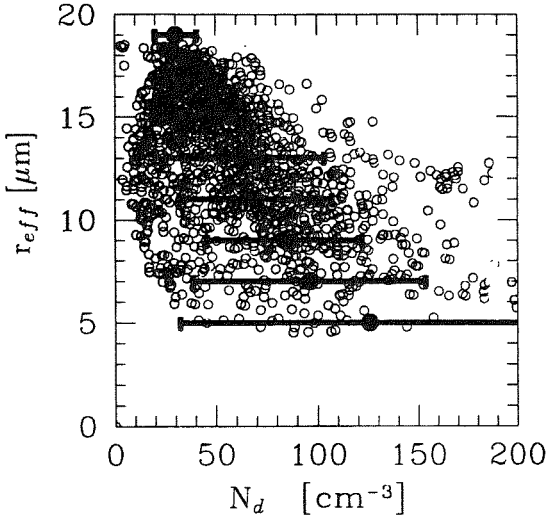

Fig. 1c: r_{eff} versus LWC from aircraft observations for the 16 August 16 case.

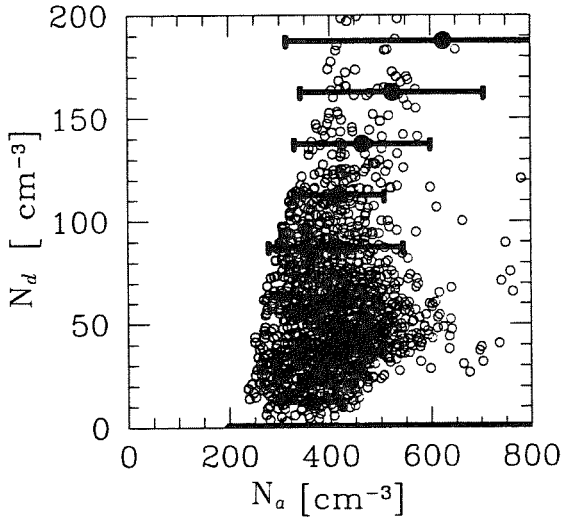

Fig. 1d: N_d versus N_a from aircraft observations for the 16 August case.

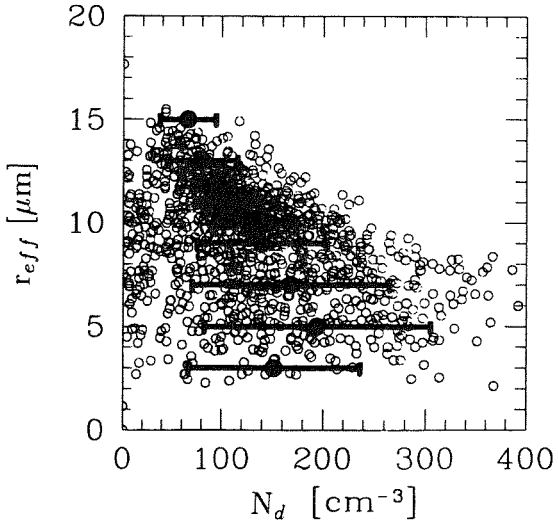

Fig. 2b: r_{eff} versus N_d from aircraft observations for the 4 October case.

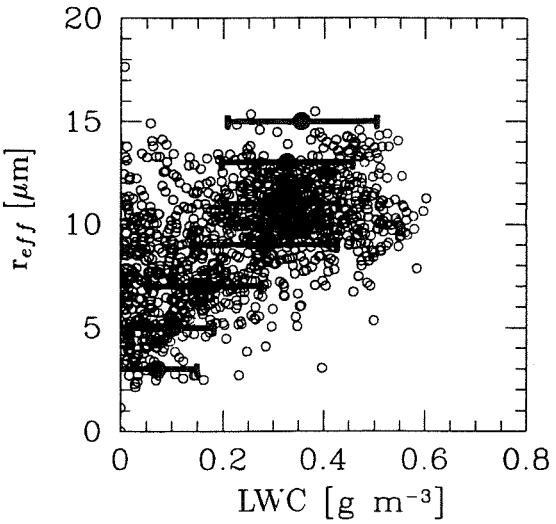

Fig. 2c: r_{eff} versus LWC from aircraft observations for the 4 October case.

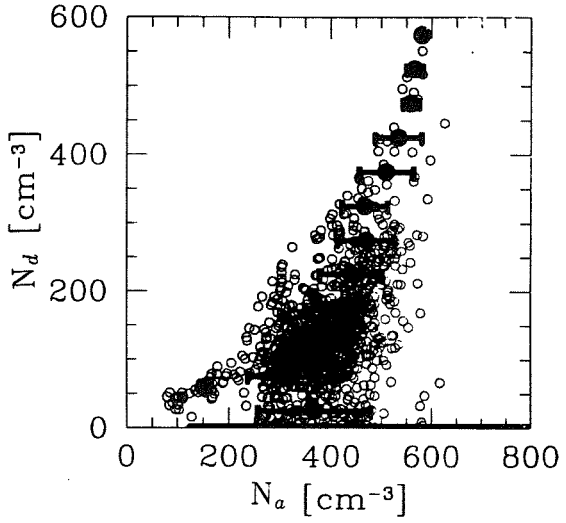

Fig. 2d: N_d versus N_a from aircraft observations for the 4 October case.

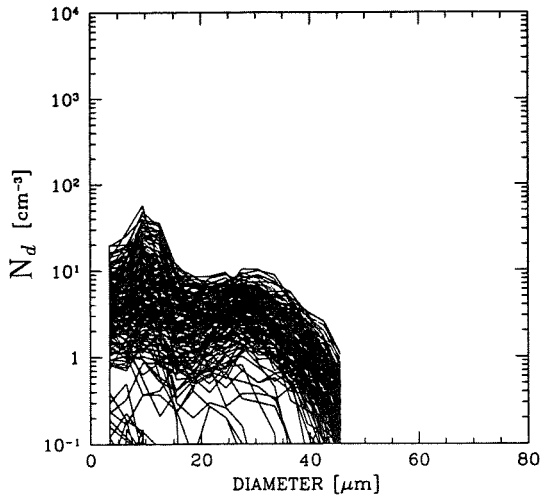

Fig. 3a: Droplet spectra for each second for a cloud for the 16 August case.

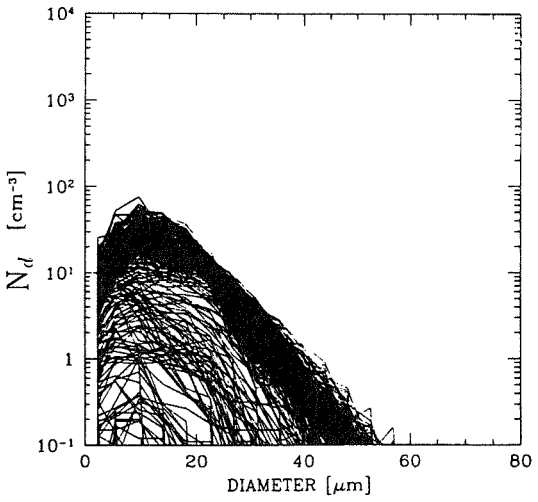

Fig. 3b: Droplet spectra for each second for two clouds for the 4 October case.

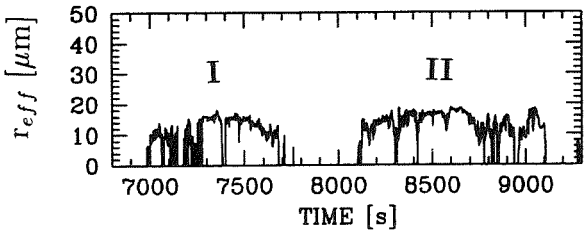

Fig. 4a. Time series of r_{eff} for entire flight for the 16 August case.

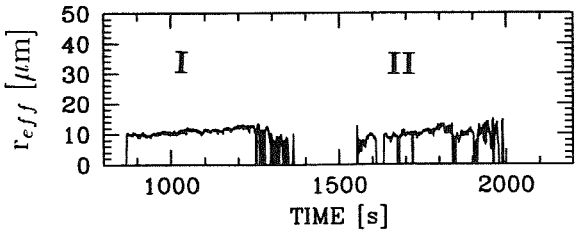

Fig. 4b. Time series of r_{eff} for entire flight for the 4 October case.

Table 1: Statistics of cloud observations.

Statistics	Clouds over ocean (I)	Clouds over ocean (II)	Clouds over land (I)	Clouds over land (II)
Spectral shape	bimodal	bimodal	unimodal	unimodal
Cells	No	No	yes	yes
$\overline{N_d}$/sd	62/37	58/33	101/43	130/73
$\overline{N_a}$/sd	423/65	403/79	339/41	437/37
$\overline{LWC}$/sd	0.09/0.06	0.12/0.07	0.28/0.11	0.29/0.19
$\overline{r}_{eff}$/sd	12.5/3.1	13.7/3.2	10.6/1.5	9.9/1.9

LABORATORY FTIR MEASUREMENTS OF ICE CRYSTAL AND WATER DROPLET CLOUDS: PARTICLE SIZE SPECTRUM INVERSION

W. Patrick Arnott, Carl Schmitt, Yangang Liu, and John Hallett
Atmospheric Sciences Center, Desert Research Institute, PO Box 60220, Reno NV 89506, USA

1. INTRODUCTION

Early measurements (Arnulf and Bricard, 1957) of the infrared optical depth of natural fog and haze were performed at a few wavelengths, and were away from strong water vapor absorption bands. These measurements revealed definite spectral variability, especially a reduction in optical depth at 10 μm compared with the optical depth at 2 μm. Qualitative agreement was achieved among measured and modeled-with-Mie-theory optical depth spectra. Haze and fog were defined in terms of the measured optical depth though haze generally turned out to also have most water droplets in the diameter range 1-16 μm. This diameter range also covers the range of droplet sizes observed in our measurements. One conclusion from the early work was that IR emission from warm bodies could be sensed more readily in haze than fog due to the differences in optical depth at 10 μm. Infrared extinction measurements and calculations for hazes, fogs, and water clouds have been performed by a large number of researchers (Zuev 1970, McCartney 1976, Tomasi et. al. 1976, Clay et. al. 1981) since the early measurements.

These early measurements caught the attention of workers interested in retrieving droplet size spectra from spectral optical depth measurements. While it is now well-known that the integral equation used in the retrieval is ill-posed in the sense that a wide range of aerosol size spectra produce basically the same synthetic extinction spectra, one quickly learns that not just any assumed size spectra produce synthetic extinction spectra in good agreement with measured spectra. Indeed, Eldridge (1957a) was able to retrieve droplet size spectra and synthetic optical depth spectra in reasonable agreement with the measured values. Penndorf (1957) was quick to point out that the retrieval was not unique. Eldridge (1957b) argued that the retrieval was still useful and that better measurements would probably help. This same sense of utitily has motivated much development in retrieving a wide variety of information from spectral measurements (Twomey, 1977).

Infrared extinction optical depth (500-5000 cm^{-1}) has been measured using a Fourier Transform Infrared Spectrometer for artificial fogs made with an ultrasonic nebulizer. Direct measurement of the fog droplet size spectra agree well with size spectra retrieved from inversion of the extinction measurements, and both indicate the range of droplet size is within 1 to 14 μm. The retrieval is accomplished using an itterative algorithm that is demonstrated to be useful for obtaining water vapor concentration at the same time. The basis set of extinction functions are computed once using numerical integration of the Mie theory over narrow size bins, and a measured water vapor extinction curve is used in the inversion. Extinction and size spectra were measured and computed for both steady state and dissipating fogs. Calculations of fog liquid water content from retrieved size distributions agree favorably with a parameterization (Chylek, 1978) based on optical depth measurements at a wavenumber of 906 cm^{-1}.

The approach we took was to measure IR extinction and droplet size spectra for artificial fogs, and to retrieve droplet size spectra using an itterative algorithm. The goals of these measurements are to demonstrate the feasibility of retrieving droplet spectra and water vapor concentration from IR extinction measurements made with a FTIR spectrometer with possible application to natural haze, fog, and water cloud droplet retrieval, and to demonstrate that measurements can help determine the validity of models for extinction. Natural haze can obscure long path FTIR measurements of trace gases. The results described here may assist in accurately assessing obscuration by haze, and perhaps extend the information content retrievable by these measurements. Finally, droplet size spectra measurements by this technique is a non-contact procedure with reasonable time resolution (about 1 sec per FTIR scan), and thus is well suited for laboratory cloud physics experiments where cloud evolution or changes are of interest.

2. MEASURED AND RETRIEVED DROPLET SIZE AND EXTINCTION OPTICAL DEPTH SPECTRA

Much of the experimental arrangement used for IR extinction measurements has been described in a previous publication (Arnott, et. al. 1995), though some changes were made to accommodate measurements of water clouds. Briefly, the FTIR was used as a transmission spectrometer. A broad band IR source already modulated by the Michelson interferometer in the FTIR was reflected by a concave mirror in the 1 m^3 cloud chamber into a nearly co-aligned detector located at twice the focal distance of the mirror. A reference spectrum was taken with no cloud present, and the optical depth for a cloud was determined by taking the logarithm of the transmission measurement (ratio of cloud and no

cloud spectra). It was found that the 32 cm^{-1} resolution setting on the FTIR spectrometer gave sufficient resolution and signal to noise discrimination for the vapor and droplet spectral measurements. Cloud droplets were produced using an ultrasonic nebulizer, more commonly known as ultrasonic humidifiers for routine household use (Sunbeam Model 694), and were delivered to the chamber via a 2.54 cm diameter corrugated hose used to direct the droplet laden air stream issuing from the device.

Radiation is absorbed in some bands by water vapor and carbon dioxide present in the air between the IR source and detector, and by the plastic wrap used both as a window and to confine the cloud in the chamber. The plastic wrap was stretched to thin it and to make it tight over the opening in the chamber. The plastic wrap was heated by a warm air stream from outside the chamber to prevent condensation, while the concave mirror inside the chamber was heated from its back side with an attached film heater for the same purpose. Temperature changes in the chamber or surrounding air occuring between acquistion of the reference and transmission spectrum will also change the concentration of absorbing molecules and hence will potentially alter the optical depth results in selected bands. Even slight changes of droplet temperature in the cloud will result in appreciable water vapor concentration changes.

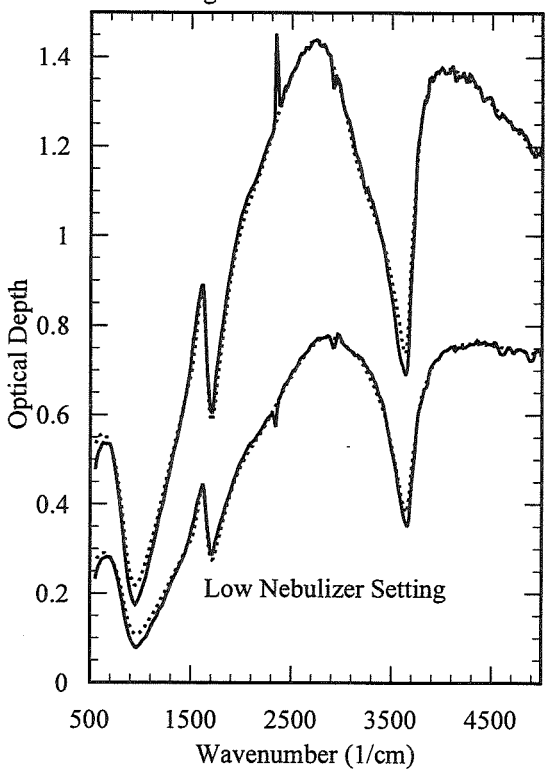

Figure 1. Measured and modeled (broken curves) optical depth for 2 settings of the ultrasonic nebulizer.

While the ice clouds studied previously had water vapor concentration essentially at ice saturation at the chamber temperature during both the reference and cloud spectrum measurements, the vapor concentration for water clouds was variable. In most instances, the vapor concentration was driven very near water saturation at the chamber temperature for the reference measurement by placing shallow pans of water in the bottom of the chamber and evaporating water into the air by turning on the circulation fan in the chamber. This procedure was followed by a series of cycles of cloud injection and dissipation. Vapor concentration was checked by taking a reference spectrum before new cloud was injected, and by taking an optical depth measurement after it had dissipated. Eventually the chamber was very close to water saturation as judged by the lack of optical depth at known water vapor lines. To obtain a water vapor optical depth spectrum for use in the retrieval algorithm, a reference spectrum was taken with significantly undersaturated air having RH $\approx$ 35% at room temperature. The water vapor spectrum was then obtained by changing the vapor concentration to near water saturation at room temperature using the procedure described above, and then taking the transmission measurement.

Figure 1 shows measured and synthetic optical depth spectra of water droplets for two settings of the ultrasonic nebulizer. All synthetic spectra discussed in this section were computed using the retrieval algorithm with smoothing (Arnott, et. al., 1996). The agreement between measured and modeled spectra is worse near the same spectral regions of disagreement for the real part of the refractive index among the various workers (Downing and Williams, 1975, Hale and Querry, 1973, Zolatarev, et. al., 1969). The lack of smoothness in the measured spectra between 4000 cm^{-1} and 5000 cm^{-1} is due to the relatively high optical depth for water droplets and relatively low source spectral energy. Low spectral energy due to carbon dioxide and plastic wrap absorption contributed to the lack of smoothness between 2300 cm^{-1} and 2400 cm^{-1}, and between 2900 cm^{-1} and 3000 cm^{-1}, respectively. The reference and transmission spectra were an average of 10 FTIR scans (approximately 4 seconds total time).

Figure 2 shows the retrieved droplet size distributions that gave the synthetic optical depth spectra in Fig. 1. The higher nebulizer setting apparently corresponds to a broader droplet size spectrum than the lower setting. The liquid water content inferred from these curves was 0.45 g/m^3 and 0.88 g/m^3, mean diameter was 2.85 μm and 5.37 μm, and total concentration was 16.4 mm^{-3} and 8.5 mm^{-3} for the lower and higher nebulizer settting, respectively. The nebulizer was operated continuously at a lower setting so that a steady state droplet cloud was achieved. Optical depth was monitored in the visible with a 685 nm laser diode and indicated fluctuations from the average optical depth of about 5% for the steady state clouds. Steady state equilibrium is achieved when the rate of

droplet addition matches the rate of droplet removal. The nebulizer fan results in a breeze within the chamber of approximately 1-2 cm/s that carries droplets to the chamber walls and floor.

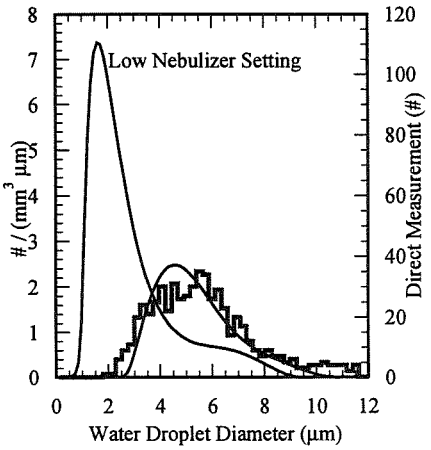

Figure 2. Measured (binned) and retrieved water droplet distributions for 2 settings of the ultrasonic nebulizer. The measured result was for the higher nebulizer setting.

Also shown in Fig. 2 is a direct measurement of the droplet size distribution performed by passing a magnesium coated slide through the droplets very near the nebulizer, and using a microscope equipped with a calibrated grid to count and size droplet images. The collection efficiency was enhanced by rapidly waving the hand-held slide through the droplets, and by turning the slide edge on so that one of the edges along the length of the slide was first to pass through the droplets. Droplet diameters were determined directly from the measured circle diameters seen under the microscope, even though Mason, 1971 recommends scaling from circle diameters to spheres by multiplying measured diameters by 0.86 for droplets larger than 5 μm, and by an unknown factor greater than unity for circles less than 5 μm. Mason, 1971 cautions against using this technique for droplets smaller than 5 μm diameter because of the typical grain size achieved when magnesium is burned to coat the slide, though by trial and error we found that grain size could be reduced enough that smaller circles were reasonably discernable. Details of the inversion algorithm and retrievals obtained for a variety of fogs can be found in Arnott, 1996.

3. ACKNOWLEDGEMENTS

This work was supported by the National Science Foundation.

4. REFERENCES

Arnott, W. P., Y. Y. Dong, and J. Hallett, 1995: Extinction efficiency in the infrared (2-18 μm) of laboratory ice clouds: observations of scattering minima in the Christiansen bands of ice. Appl. Opt. **34**, 541-551.

Arnott, W. P., Carl Schmitt, Y. Liu, and J. Hallett, 1996: Droplet size spectra and water vapor concentration retrieval in artificial fogs by inversion of IR (500-5000 cm^{-1}) optical depth measurements obtained with a FTIR spectrometer. Submitted to Appl. Opt.

Arnulf, A., and J. Bricard, 1957: Transmission by haze and fog in the spectral region 0.35 to 10 microns. J. Opt. Soc. Am. **47**, 491-498.

Chylek, P., 1978: Extinction and liquid water content of fogs and clouds. J. Atmos. Sci. **35**, 296-300.

Clay, M. R., and A. P. Lenham, 1981: Transmission of electromagnetic radiation in fogs in the 0.53-10.1-μm wavelength range. Appl. Opt. **20**, 3831-3832.

Downing, H. D., and D. Williams, 1975: Optical constants of water in the infrared. J. Geophys. Res. **80**, 1656-1661.

Eldridge, R. G., 1957a: Measurements of cloud drop-size distributions. J. Meteor. **14**, 55-59.

Eldridge, R. G., 1957b: Measurements of cloud drop-size distributions: Reply. J. Meteor. **14**, 575-577.

Hale M., and M. R. Querry, 1973: Optical constants of water in the 200-nm to 200-μm wavelength region. Appl. Opt. **12**, 555-563.

Mason, B. J., 1971: *The Physics of Clouds*, (Clarendon Press, Oxford England) 93-94.

McCartney, E. J., 1976: *Optics of the Atmosphere, Scattering by Molecules and Particles,* (John Wiley & Sons, New York) 133-142.

Penndorf, R., 1957: Comments on 'Measurements of cloud drop-size distributions'. J. Meteor. **14**, 573-574.

Tomasi, C., and F. Tampieri, 1976: Infrared radiation extinction sensitivity to the modified gamma distribution parameters for haze and fog droplet polydispersions. Appl. Opt. **15**, 2906-2912.

Twomey, S., 1977: *Introduction to the Mathematics of Inversion in Remote Sensing and Indirect Measurements* (Elsevier, New York).

Zolatarev, V. M.., B. A. Mikhailov, L. I. Aperovich, and S. I. Popov, (1969) Dispersion and absorption of water in the infrared. Opt. Spectrosc. **27**, 430-432.

Zuev, V. E., 1970: *Atmospheric Transparency in the visible and infrared,* (Israel Program for Scientific Translations, Jerusalem).

THE EFFECTS OF LONGWAVE RADIATION IN A SMALL CUMULUS CLOUD

Hong Guan, M.K. Yau and R. Davies

Department of Atmospheric and Oceanic Sciences, McGill University, Montreal H3A 2K6, CANADA

1. INTRODUCTION

In the past, considerable progress has been made on understanding the interaction between horizontally homogeneous clouds and longwave radiation. However, few such studies have dealt with horizontally finite clouds. Guan et al. (1995) showed from calculation of longwave cooling rate in three-dimensions that cloud side cooling is of the same order of magnitude as cloud top cooling for a finite cumuliform cloud. This strong cooling may be important in affecting the microphysics and dynamics of the clouds by favoring local condensation and inducing negative buoyancy. The effect of the latter can be twofold. First, the negative buoyancy from cloud top cooling tends to decrease (increase) local upward (downward) motion. Second, radiatively forced sinking air at the sides of clouds may lead to lower-level convergence and enhancement of the upward motion in the interior of the cloud. We will examine these effects using a fully interactive three-dimensional radiative transfer model and a slab-symmetric cloud model.

2. THE MODEL

The cloud model is essentially the same as the one used by Hedley and Yau (1988) and Reuter and Yau (1987a,b). Condensation produces cloud water but precipitation processes are not included.

Convection is initiated by diffusing heat and moisture from the ground to the lowest grid point. At the ground, the water vapor mixing ratio is kept at a constant value of 16.5 g/kg. Surface heating was applied by prescribing a time-dependent surface temperature with maximum amplitude at the center of the domain. The initial sounding is almost the same as given in Veyre et al. (1980) which is representative of the environment in Puerto Rico when small cumuli (300-500 m in thickness) occur (Pennell and LeMone, 1974). The grid resolution is uniform at 25 m and the domain has a size of 20kmx20kmx3km.

The longwave radiation model is very similar to that given in Guan et al. (1995) except that the horizontal net flux divergence is expressed in x-coordinates. The radiance is calculated in three dimensions. To compute the fluxes, the angular integration is performed using Gaussian quadrature. The cooling rates were calculated every 30 s using the temperature, water vapor and cloud water contents from the cloud model. The moist entropy equation is modified to include the effect of radiation. Following Stephens (1978), we treat absorption and emission within the atmospheric window region (8-13.4 μm) where the main absorbers are water vapor and cloud droplets. The spectral absorption coefficient for cloud water was calculated using a simple expression used extensively by others (Pinnick et al., 1979; Chylek et al., 1982; Stephens et al., 1982; Stephens, 1984; Chylek et al., 1992). The spectral absorption coefficient for a given wavelength is a function only of the cloud liquid water content.

3. RESULTS IN A CALM ENVIRONMENT

3.1 Effect on cloud water content

To examine the total effect of longwave radiation, we display the temporal evolutions of maximum and total cloud water content for the CONTROL (no longwave radiation) and the LW (with longwave radiation) runs in Fig.1. Longwave radiative cooling increases the maximum liquid water content (LWC) for most of the simulation time. Significant differences are detected at the mature stage (maximum enhancement 96% at 47 min). To a lesser degree, the total cloud water content also increases at the growing and mature stages (maximum increase about 20% from 50 min to 55 min). Longwave cooling, however, tends to accelerate the dissipation of the cloud. Fig.2 and Fig. 3 depict the vertical cross section of the cloud water content for the two runs at 40 min and 55 min, respectively. At 40 min, the enhancement of condensation, as indicated by larger LWC, is mainly concentrated near the cloud top and its sides. The height of the cloud top is slightly lower in the LW run for the two times.

3.2 Positive feedback of longwave cooling on condensation

To understand the enhancement of cloud water content mainly near the cloud top and sides at 40 min, we display the distribution of longwave radiative cooling rate in the LW run at 40 min (Fig.4). Significant radiative cooling can be detected near the

cloud top and sides particularly in the regions with high LWC (maximum 6 K/h). Since the variation of saturation vapor pressure with temperature is more pronounced at higher temperatures (see Rogers and Yau,1989), the effect of condensation induced by pure radiative cooling should be more significant for clouds associated with warmer temperatures. The strong radiative cooling can lower saturation water vapor pressure, leading to enhanced condensation. This radiation-condensation interaction is a positive feedback process, as a larger LWC produces a larger radiative cooling rate, which in turn induces more condensation. Thus at the initial stage of our simulated cloud, radiation-condensation feedback serves to increase the maximum cloud water content.

3.3 Secondary circulation induced by longwave radiative cooling

Similar to the situation at 40 min, the strongest cooling rates were found near the cloud top and upper sides of the cloud at 55 min (not shown). As is shown in Fig. 3, for the mature stage, the cloud water content in the LW run exceeds that of the CONTROL run even in the interior of the cloud. Therefore the increase in total cloud water during the mature stage must arise from processes other than the direct effect of radiation-condensation feedback which acts primarily near the cloud top and the upper cloud side region.

Table 1: Comparison between CON and LW runs

	max. downdraft	max. updraft at center of cloud	min. TP at cloud sides
CON	0.89 m/s	0.50 m/s	- 0.50 K
LW	1.28 m/s	0.65 m/s	- 0.64 K

Table 1 lists the temperature perturbation (TP) and vertical velocity for the two runs. The LW cloud is colder than the CONTROL near the cloud edges. The maximum downdraft and the area of downdraft is larger in Expt. LW. The ratio of the areas of the downdraft with magnitude larger than 0.5 m/s is 1.7. Thus longwave radiative cooling near the cloud top and the upper cloud edges also induces a dynamic response. The radiatively cooled air near the upper cloud sides subsides at the cloud edges and is continuously cooled by radiation and evaporation during descent. The enhanced cloud edge downdrafts further induces additional low-level convergence, and consequently, enhanced upward motion near the center of the cloud. Longwave radiative cooling at the cloud edges therefore initiates a secondary circulation which enhances cloud development.

3.4 Rapid decay of cloud induced by longwave radiation

Fig. 1b shows that the LW cloud begins its decay at 56 min, 5 minutes earlier than the CONTROL. To examine the process for the faster decay, we plotted the time series of cloud water content, vertical velocity, and temperature perturbation at a central point 200 m above the cloud base (x=12.5m, z=800m) in Fig.5. Note that at 56 min, the LW cloud has slightly smaller negative temperature perturbation but larger cloud water content. Its vertical updraft is also stronger at 56 min and begins to weaken after 57 min. Since the negative temperature perturbation is slightly less negative at 56 min, the rapid decay of the LW cloud must be initiated by the larger drag force exerted by the greater cloud water content. Once the decay process sets in, further erosion of the cloud takes place as cooling from evaporation and longwave radiation quickly generates negative temperature perturbation and weakens further the updraft.

4. THE EFFECTS OF WIND SHEAR

To examine the effect of wind shear, we repeated the CON and LW experiments using the same atmospheric sounding and initial conditions used in the no wind runs. However, the ambient wind is now of constant direction (parallel to the x-axis) with a shear of 0.5 m/s/km between the height of the cloud base (600m) and the top of the domain (3000m). Below the cloud base, the wind is set to zero to keep the circulation and the simulated cloud within the simulation domain and to prevent fictitious advection over the lower boundary where surface heating is being applied.

The results (not shown) showed that similar to the case of a calm environment, longwave cooling strengthens the secondary circulation and the cloud water content. However, shear does suppress convection and the cloud becomes weaker. Longwave cooling also enhances the asymmetric characteristics of the simulated cloud. In conjunction with horizontal momentum transport, radiative cooling results in a more negative temperature perturbation and a stronger downdraft on the downshear flank relative to the upshear side.

5. CONCLUSIONS

The effects of longwave radiation on the development of a small cumulus cloud was investigated by a combination of three-dimensional radiative transfer model as well as slab-symmetric cloud model. It was found that longwave radiative cooling substantially enhances the maximum cloud water content (maximum 96%). The total cloud water was also increased somewhat (maximum 20%). In the

initial stage of the development, the augmentation of cloud water content near the cloud top and sides is traced mainly to the direct effect of longwave radiative cooling on microphysics. In the mature stage of the cloud, the increase of total cloud water content comes from a combination of the effects of radiation on microphysics and dynamics. The cooling from radiation and evaporation produces additional downward motion at the sides of the cloud. The enhanced low-level convergence invigorates the updraft promoting further cloud development. In the decaying stage , the negative buoyancy produced by cloud top radiative cooling and a higher liquid water load speeds up the decay process in the LW run.

In a sheared environment, longwave coolin g produces a more asymmetric structure. In conjunction with horizontal momentum transfer, radiative cooling results in a more negative temperature perturbation and a stronger downdraft on the downshear flank relative to the upshear side.

REFERENCES

Chylek, P., and V. Ramaswamy, 1982: Simple approximation for infrared emissivity of water clouds, **J. Atmos. Sci., 39**, 171-177.

———, P. Damiano, and E. P. Shettle, 1992: Infraed emittance of water cloud, **J.Atmos. Sci.,49**, 1459-1472

Guan, H., R. Davies, and M. K. Yau, 1995: Longwave radiative cooling rates in axially symmetric clouds, **J. Geophys. Res., 100**, 3213-3220.

Hedley, M., and M. K. Yau, 1988: Radiation boundary conditions in numerical modeling, **Mon. Wea. Rev., 116**, 1721-1736.

Pennell, W. T., and M. A. LeMone, 1974: An experimental study of turbulence structure in the fair-weather trade wind boundary layer, **J. Atmos. Sci., 31**, 1308-1323.

Pinnick, R. G., S. G. Jennings, P. Chylek, and H. J. Auvermann, 1979: Verification of a linear relationship between IR extinction, absorption and liquid water content of fogs. **J. Atmos. Sci., 36**, 1577-1586.

Reuter, G. W., and M. K. Yau, 1987a: Mixing mechanisms in cumulus congestus clouds. Part II: Numerical simulations, **J. Atmos. Sci., 44**, 798-827.

———, and ———, 1987b: Numerical modeling of development in a sheared environment, **Contrib. Atmos. Phys., 60**, 65-80.

Rogers, R. R., and M. K. Yau, 1989: A short course in cloud physics, third edition, Pergamon Press, 293 pp.

Stephens, G. L., 1978: Radiation properties in extended water clouds, I, Theory, **J. Atmos. Sci.,35**, 2111-2122.

———, and P. J. Webster, 1978: Sensitivity of radiative forcing to variable cloud and moisture,**J. Atmos. Sci., 36**, 1542-1556.

Veyre, P., G. Sommeria, and Y. Fouquart, 1980: Modélisation de l'effet des hétérogénéités du champ radiatif infra-rouge sur la dynamique desnuages, **J. Rech. Atmos., 14**, 89-108.

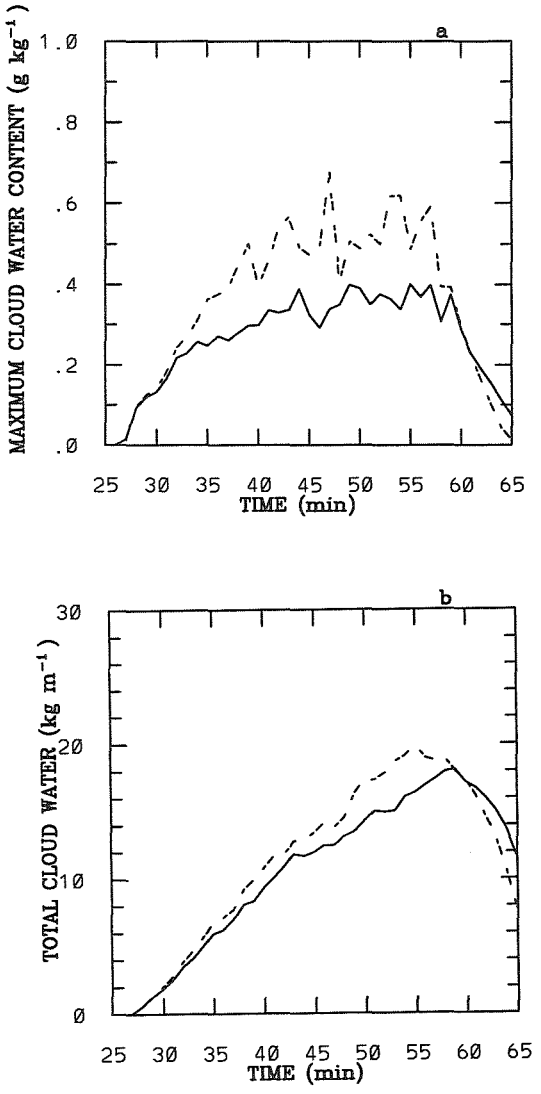

Fig. 1 Evolution of a) maximum cloud water content and b) total cloud water content for the Control (solid) and LW (dashed) runs.

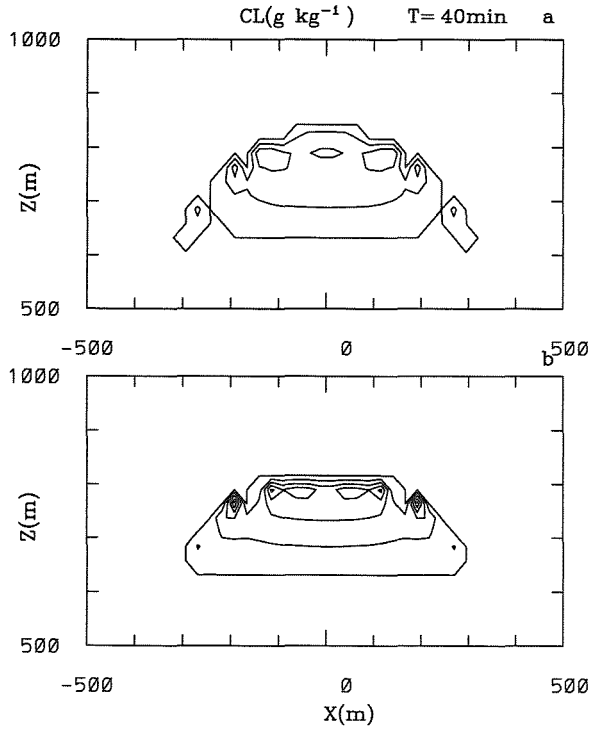

Fig. 2 Vertical cross-section of cloud water content at 40 min for a) Control run and b) LW run. The contour interval is 0.1 g/kg.

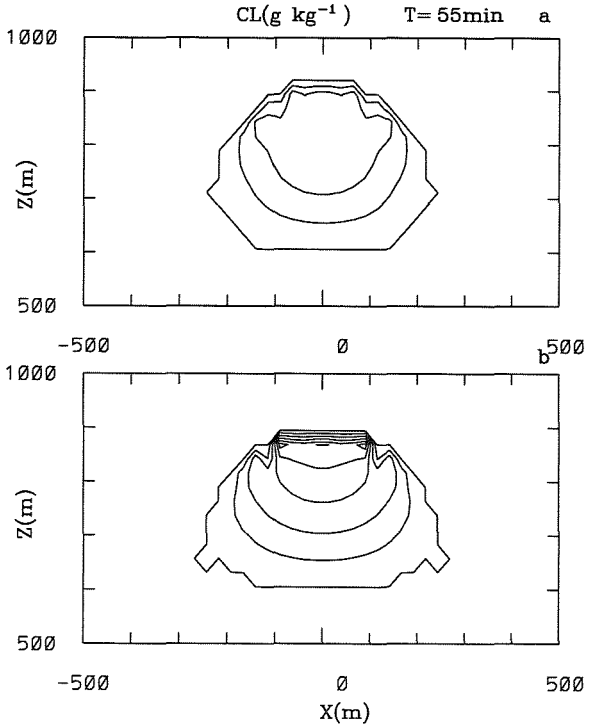

Fig. 3 Same as in Fig. 2 but at 55 min.

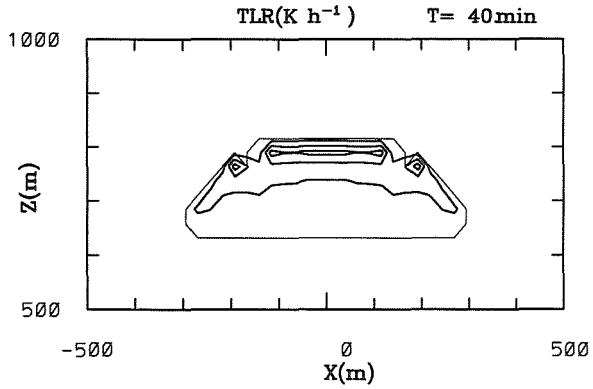

Fig. 4 Vertical cross-section of radiative cooling rates at 40 min. The contour interval is 1 K/h and the cloud boundary is indicated by the thin solid line.

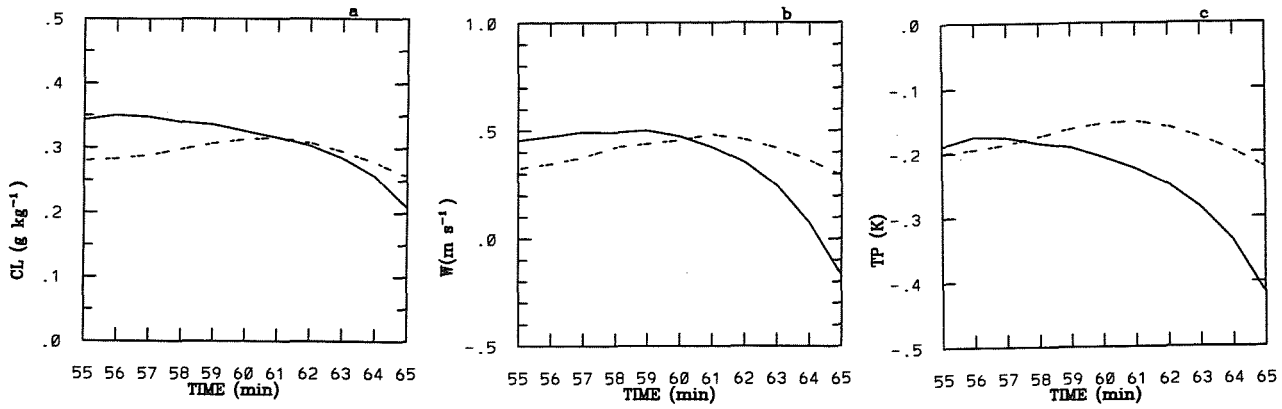

Fig. 5 Evolution of a) cloud water content, b) vertical velocity, and c) temperature perturbation for the Control (solid) and LW (dashed) runs.

THE IMPACT OF CLOUD LAYERS OVERLAPPING ON THE ESTIMATION OF CLOUD AMOUNT IN ANY LAYER BASED ON GROUND AND SATELLITE-BORNE OBSERVATIONS

Kosarev A.L.and I.P.Mazin

Cloud Physics. Lab., Central Aerological Observatory,
Dolgoprudny, Moscow Region, 141700, Russia

1. INTRODUCTION

Cloudiness is one of important climate system elements which substantionally influences the climate sensibility to random fluctuation of other elements. Thus, cloudiness monitoring is timely and important problem in climate and climate change projects. The global monitoring of cloudiness may be achieved only from satellites which may actually ensure continuous observations of the degree of cloudiness (DC) (sky coverage with clouds) all over the globe and of cloud heights.

The question is: "What should we call this or that cloud layer when observing from above?" It is evident that the existing cloud classification adapted for surface observations and based on the evaluation of the height of cloud lower boundary is not valid for satellite observations. For observions from space, the classification should be based on the evaluation of the height of cloud upper boundary. This brings up the question: "To what degree the climatology of clouds of different layers, based on satellite observations, agrees with the climatology of cloudiness, based on many-year observations from surface and ship stations?" The necessity to answer this question is evident. The present work is apparently a first attempt to find an answer.

2. METHODS OF SOLVING THE PROBLEMS

In 1957-63, in the former USSR there was a network of 31 stations for airborne sounding, distributed over the territory of the USSR (see Mazin et al., 1993). During six years of operation, 54595 soundings were made. In each sounding, the cloud amount of each layer was estimated irrespective of cloud height, and the total cloudiness above 6 km. When preparing this paper, we confined ourselves to analyzing the data obtained at 10 arbitrarily selected stations (Table 1).

Table 1. 10 selected aircraft sounding stations of the USSR ASS network operated in 1957-1963.

	Stations	n
1	Arkhangelsk	2036
2	Kasan	1616
3	Minsk	1782
4	Moscow	5482
5	Omsk	1757
6	Riga	2117
7	Ekaterinburg	2634
8	Tashkent	1620
9	Tbilisi	2311
10	Kharkov	1813

The comparison of the frequencies of occurrence of the given DC for different layers during the whole observational period, based on airborne and ground data, confirms the representativeness of the airborne data and their validity for studying the discrepancies in cloud amount estimates for different layers, as obtained from space (from satellite) and from the ground. Thus, a possibility is provided to use the unique data of airborne sounding in order to answer the question set in Item 1. Below it is assumed that when observed from satellite, a cloud layer is determined by the height of the upper boundary, H_{ub}. Low layer clouds are those with $H_{ub} \leq 2$ km, middle layer clouds with $H_{ub} \subset (2;6)$ km,and upper layer ones with $H_{ub} > 6$ km.

3. THE ANALYSIS OF OBSERVATIONAL DATA

In fact, cloudless situations (clear sky) when observed either from below or from above, look just the same, differences in DC estimates may occur only when clouds are present. That is why when defining those differences, clear-sky days were excluded from consideration. Shown in Fig.1 is the frequency of occurrence, $F(N_i)$, for the whole period of observations of cloudiness less than N_i for different cloud layers. F_g refers to ground observations (layers are determined by the height H_{lb}) and F_s refers to satellite observations (layers are determined according by the hight H_{ub}). The analysis of the differences $\Delta F = F_s - F_g$ obtained results in the following conclusions:

- The amount of low layer clouds is underestimated from satellite in comparison with ground observations. $\Delta F(N_l)$ varies from +5, to +15% due to the fact that when observed from space, part of clouds with $H_{ub} > 2$ km does not come within this group. Besides, if one confines himself to situations when middle-plus upper-layer clouds do not cover more than 75% of the sky, the difference $\Delta F(N_l)$ decreases and may be twice as .

- For middle-layer clouds, $\Delta F(N_m)$ values for all the stations, on the average, varies from 0 to 10%. The amount of middle-layer clouds determined from satellite, is somewhat larger than that from ground observations. If we take into account the role of overlapping, this difference decreases and basically does not exceed 5%.

- The values of $|\Delta F(N_u)|$ are also rather small for upper-layer clouds and do not come beyond the limit of 5-10%.

Thus, if we judge by the cloud observational data obtained over the territory of the former USSR, we can fortunately conclude that the climatology of middle and upper cloudiness, based on satellite data, must not differ strongly from that based on ground observations, and only the cloud amount of the lower layer may be underestimated.

REFERENCES

Mazin I.P., Burkovskaya S.N. and Ivanova E.T., 1993. On the climatology of upper layer clouds. *J. Climate*, **6**, 10, pp.1812-1821.

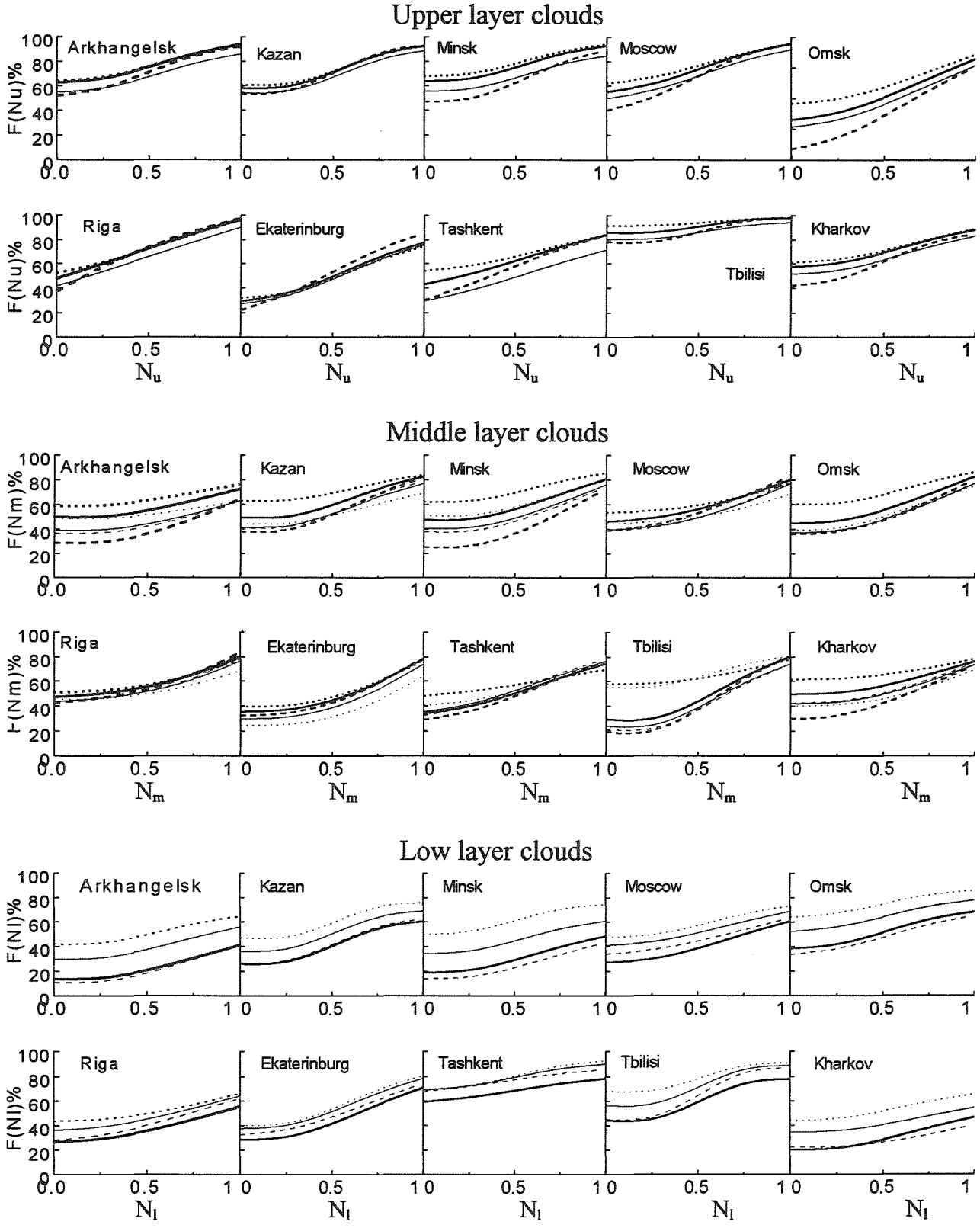

Fig.1.The frequency F(N<N_i%) of low, middle and upper layer clouds occurrence at 10 selected stations, averaged over the whole period of observations (1957-1963). N_i is the cloud amount in %, i=l, i=m, and i=u for low, middle and upper layer clouds, respectively. Bold lines show the ground observations and thin lines show the sattelite (from above) observations. Dotted lines are for overlapping exceeding 75%, dashed lines for overlapping less than 75%, and solid lines for overlapping is not taken into consideration.

ON THE INFLUENCE OF CONVECTIVE CLOUDS ON SOME CLIMATEFORMING FACTORS

V.A. Amiranashvili[1,3], R.I. Doreuli[2], T.V. Kheladze[2], K.A. Tavartkiladze[3]

[1]Main Adm. of Hydrometeorology, 150 D.Agmashenebeli, Tbilisi, Georgia
[2]Geophysics Institute, 1 M.Aleksidze, Tbilisi, Georgia
[3]Geography Institute, 1 M.Aleksidze, Tbilisi, Georgia

In the recent years the problem of forthcoming climate change caused by increasing anthropogenic influence on the environment has been drawing more attention. This problem has a special significance for Georgia. Georgia, being situated on a relatively small area (about 70,000 Km^2), is

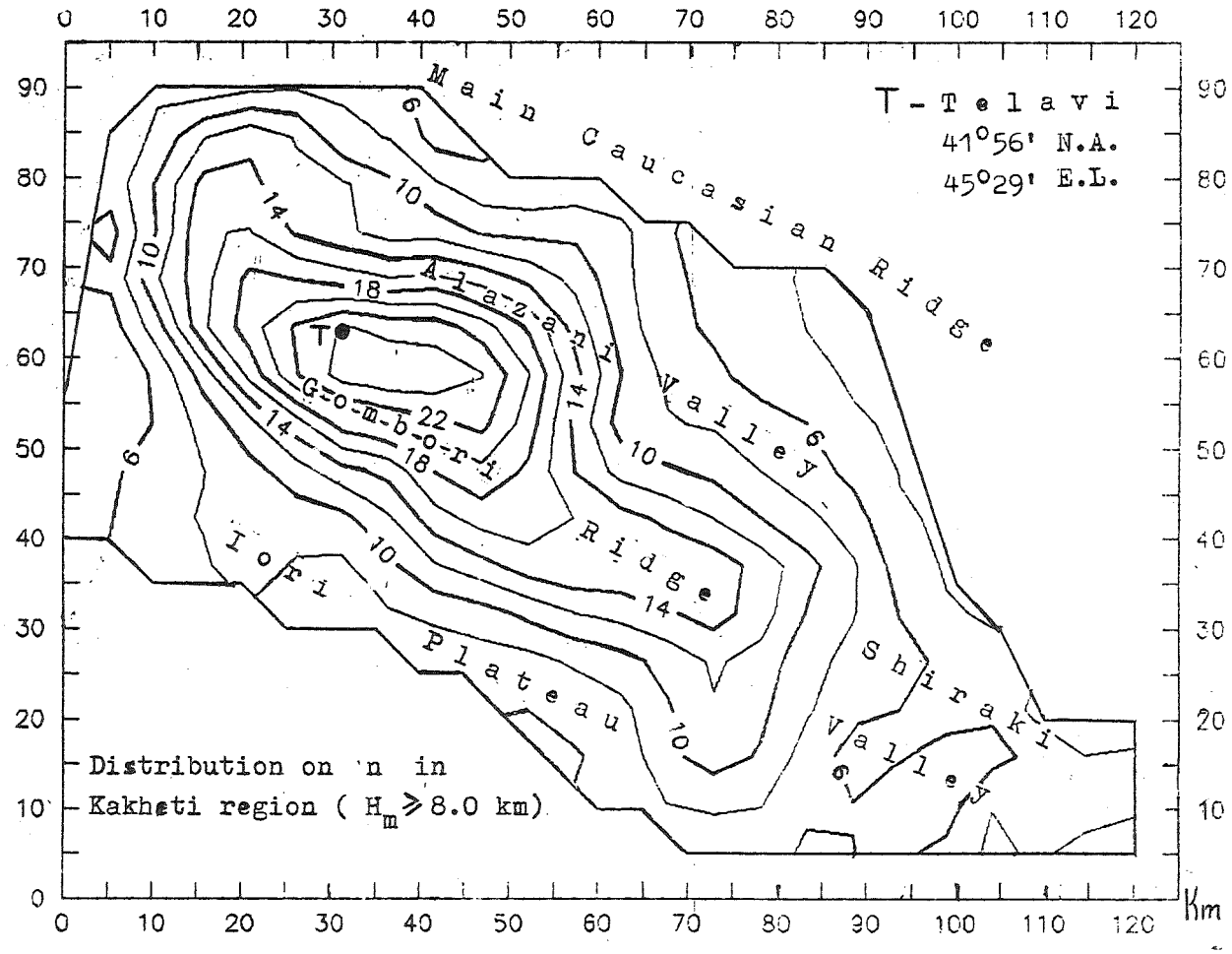

Figure 1

Distribution of convective cloudness in Kakheti region

distinguished by large diversity of climatic conditions.Almost all kinds of climates may be encountered here - from humid subtropics with a high temperature background and surplus humidity to the cold climate of eternal snows and glaciers zone. On the total there may be distinguished as many as 15 climatic zones in Georgia. The mean temperature variation ranges for this region amounts to:in January from - 12 to + 7°C, in July from + 7 to + 24°C, meanannual from - 5 to + 15°C. The maximum and minimum temperature vary from -42 to +42°C,precipitation per year from 400 to 2700 mm etc.[1].

The indicated climatic conditions were created in Georgia as a result of the interaction over its territory,having complex relief and a diversity of physical - geographycal conditions, of global and local atmospheric - circulation processes. Hence it should be expected that even inconsiderable changes in global climate will be quickly responded by changes in the climate of Georgia,not talking about the forecast considerable warming of the earth atmosphere in the nearest decades as a result of a greenhouse effect. From this point of view the territory of Georgia and its separate regions can be considered as a natural laboratory for detection and study of global and local climatic effects, and also separate climateforming factors.

In this work the results of an investigation of the influence of big convective clouds on some climate elements in Kakheti region of Eastern Georgia are presented. The territory of the region with a size about 160 x 55 Km was divided into 350 equal squares with areas 25 Km^2. For each square the meanseason (from May to September) repetitiveness of the number of observed convective clouds with various maximum vertical size H was calculated, which eanabled to build detailed maps of the convective cloudness distribution over the territory of Kakheti.Fig.1 represents such map for clouds with $H_m \geq 8.0$ Km. As it follows from this figure the distribution of the convective cloudness repetitiveness over the investigated territory has a very inhomogeneous character. This enabled to carry out assessments of the cloud influence on various climate elements (surface air temperature T , soil surface temperature t, water vapour partial pressure e, realative air humidity u, wind velocity v in the surface layer of the atmosphere and atmospheric precipitation A). Meanseason values of y_i of the abovementioned elements and also their variations Δy_i in the form $\Delta y_i = (y_i - \bar{y}_i)/\bar{y}_i$, where y_i are multiennial mean values of meteorological elements from May to September, $\bar{y}_i$ - meanannual multiennial values of these elements, were considered. Analysed were the data from 15 meteorological stations located in various places of the region on heights H_R from 0.294 to 1.085 Km above the sea level.

The repetitiveness of the number of convective clouds n over the stations on average per season varies from 5.8 to 24.8 per 25 Km^2 and actually does not depend on the local height (correlation coefficient between n and H_R ammounts to 0.31 while significance level is not less than 0.44 with confidence 0.95). This fact is quite noteworthy and allows to estimate the influence on y_i and Δy_i separately of H_R and n. The results of these estimations are represented in Tab.1.

As it follows from Tab.1 all meteorological except atmospheric precipitation are sufficiently well correlated with the local height, whereas values of n correlate with T, u,A,ΔT,Δt,ΔA.On the variations of the surface air temperature and soil surface temperature the local height and number of convective clouds have contrary influence - for H_R - warming and for n - cooling effects are observed. It is noteworthy also that although values of the correalation coefficient between n and ΔT and n and Δt are sufficiently high, the relation between these parameters has a character near to linear in a range of n variations from 5.8 to 12 clouds per 25 Km^2.With an increase in n the

Table 1

Correalations of meanseason (May - September) characteristics of meteorological elements and their variations with the local height and meanseason number of clouds over the location

Meanseason characteristics of meteorological parameters	Local height H_R	Number of clouds n	Meanseason variations of characteristics of meteorological parameters	Local height H_R	Number of clouds n
Air temperature,T	-0.94	0.40	ΔT	0.72	-0.60
Soil surf.temp.,t	-0.85	0.17	Δt	0.73	-0.66
Water vapor pr.,e	-0.93	0.21	Δe	0.70	-0.32
Rel. air humid.,u	0.45	-0.67	Δu	0.46	-0.01
Wind velocity, v	0.54	0.31	Δv	-0.40	0.21
Atmosph.precpt.,A	0.08	0.66	ΔA	-0.001	0.44

values of ΔT and Δt change little (Fig. 2 and 3). Thus the value n = 12 clouds per 25 Km^2 can be considered for the investigated region critical, above which stable variations of the meanseason surface temperature are observed and below - a warming effect is detected.

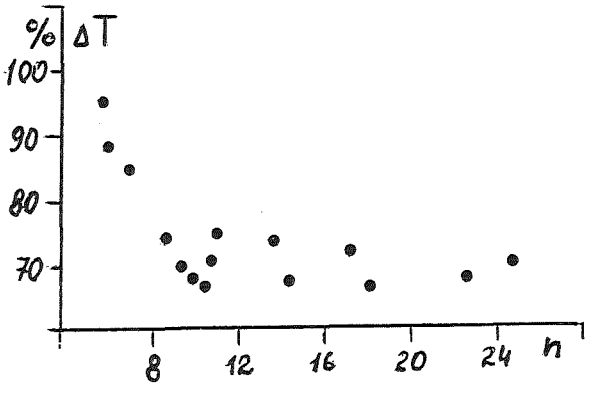

Figure 2
Dependence of meanseason temperature of surface layer of atmosphere on number of convective clouds over observation point

Considerable influence convective clouds have on atmospheric precipitation. Fig. 4 shows the relation between values of n and A.

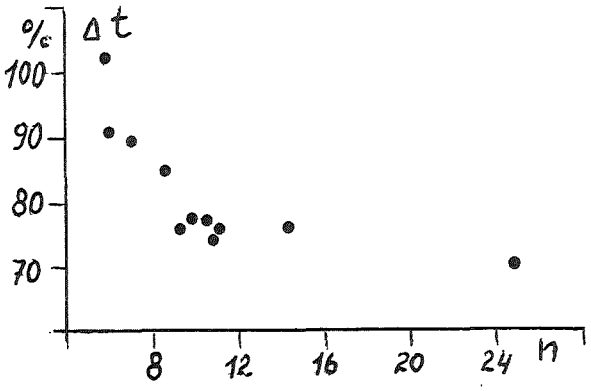

Figure 3
Dependence of meanseason soil surface temperature on number of convective clouds over observation point

It is noteworthy also that the relation between the atmospheric precipitation variations and number of clouds has the following form : $\Delta A = (0.5\ n + 30.6)\%$. The dependence between u and H_R is direct whereas between u and n - inverse (Tab.1). The range of e and u variations for various H_R and n is inconsiderable and does not exceed 6 - 7%.

One of important climateforming factors is atmospheric aerosol. In early investigations it was shown

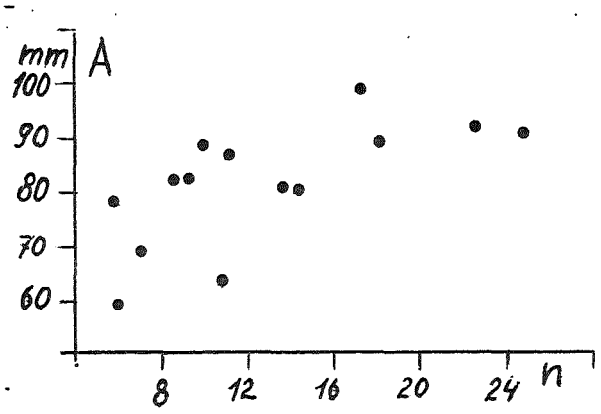

Figure 4
Dependence of meanseason values of atmospheric precipitation on number of convective clouds over observation point. (A = 1.24 n + 65.6) mm.

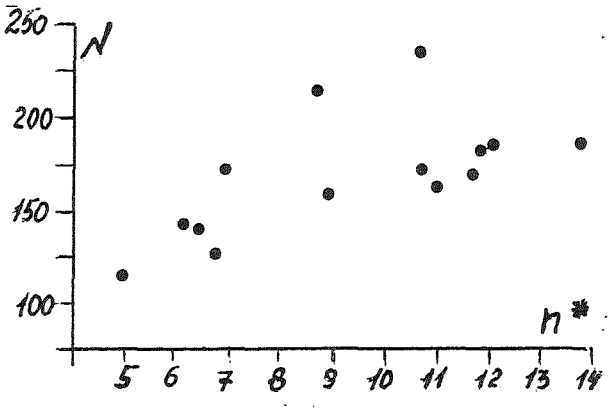

Figure 5
Dependence of meanseason values of aerosols common content in atmosphere (relative units) on number of haildangerous clouds per season, subject to weather modification (normalized on area 100 Km^2).

that convective cloudness conduces gathering of aerosols in the low troposphere [2].With the purpose of confirming the same effect in interesting for climatology time scales,we compared the data (1971 - 1984) of the anti - hail service on the number of haildangerous clouds n^* subject to weather modification on the territory of Kakheti with meanseason values of aerosols common content in the atmosphere N. The correlation coefficient between these parameters amounts to +0.63, regression equation has the form : $N = 7.4\ n^* + 99.4$.

Thus, convective cloudness considerably influences the relative humidity in the surface layer of the atmosphere,atmospheric precipitation, variations of the surface layer air and soil surface temperature,and also the aerosols content in the atmosphere. Main mechanisms of this influence apperently are strengthened convective and turbulent air movements in places of high repetitiveness n,conducing intensive intermixing of the air along the vertical and correspondingly leading to effects of surface layer cooling. Convective processes in addition conduce carrying of aerosols from the earth surface to the troposphere, gathering them in clouds and eventually increasing of the common content of aerosols in atmosphere.

There may be other mechanisms of convective cloudness influence on climateforming factors (e.g.solar radiation inflow change, generation by clouds of new aerosol formations etc.), the role of which will be studied in further investigations.

REFERENCES

1.Klimat i klimaticheskie resursi Gruzii. Trudi Zak. NIGMI,vip. 44(50), Gidrometeoizdat,Leningrad,1971,384 p.

2.A.G. Amiranashvili,T.G. Gziriahvili Aerosoli i ledianie kristali v atmosphere, "Metsniereba", Tbilisi, 1991, 113 p.

3.K.A. Tavartkiladze, Modelirovanie aerosolnogo oslablenia radiatsii i metodi kontrolia zagriaznenia atmospheri, " Metsniereba", Tbilisi, 1989, 203 p.

EVIDENCE FOR CLOUD-CLIMATE INTERACTIONS DUE TO ATMOSPHERIC ELECTRICITY EFFECTS ON ICE NUCLEATION

Brian A. Tinsley

Los Alamos National Lab., Los Alamos, and
University of Texas at Dallas, Richardson, TX 75083-0688

1. INTRODUCTION

The particular cloud-climate interaction discussed here involves changes in the rates of nucleation of initial ice at cloud tops and the effects of the associated changes in the flux of sedimenting ice. There are two consequences of interest for climate change. For light cloud cover, e.g., in relatively thin altostratus clouds, the results of ice sedimentation (as virga) can be to transport cloud particles to lower and warmer levels, where they become water vapor, with a reduction in cloud albedo and opacity. At high latitudes in winter this is likely to result in tropospheric cooling, but for low latitudes the result could be atmospheric heating. For heavy cloud systems that are likely to produce precipitation, e.g., warm core winter cyclones and mesoscale convective systems, the increased ice sedimentation is capable of enhancing the rate of glaciation of mid-level clouds, with an initial release of heat due to latent heat of freezing, followed by reduced evaporation into entrained air as liquid water is removed by precipitation. This effective heating enhances the feedback processes bringing warm moist air up from the surface. The overall result can be an increase in the intensity of the storm, both for tropical mesoscale convective systems of the ICZ and for winter cyclones. Both of these consequences can affect the meridional transport of heat and momentum. For winter cyclones the effects are likely to be strongest at the longitudes for greatest cyclogenesis, with effects on planetary wave amplitude.

There are a large number of analyses that show correlations between changes in solar activity and changes in atmospheric dynamics. The effects are small compared to other sources of atmospheric variability, but consistent with the effects capable of being produced by changes in the rate of ice sedimentation. We have identified changes in the latitude distribution of air-earth current density in the global circuit that are associated with these solar activity changes. The vertically downward air-earth current density (J) is 1-2 pA m^{-2} at low latitudes and 2-4 pA m^{-2} at high geomagnetic latitudes, driven by the 200-300 kV potential difference between the lower ionosphere and the surface. When this downward current is impeded by clouds, for which the conductivity can be an order of magnitude lower than for clear air, a layer of electrostatic charge builds up at the interface. It is this electrostatic charge, becoming attached to what are initially supercooled water droplets formed by condensation and cooling near the tops of clouds, that appears to be responsible for changes in ice nucleation and sedimentation rates, that can explain the correlations reported.

2. SOLAR WIND MODULATION OF THE GLOBAL CIRCUIT

There are three main processes by which changes in the solar wind modulate the latitude distribution of J, at amplitudes of order 10%:
(A) Reductions in the flux of lower energy (<5GeV) galactic cosmic ray particles, which affect tropospheric conductivity and are confined by the geomagnetic field to > 50° geomagnetic latitude, (a) on the quasidecadal solar cycle, and (b) on the day-to-day timescale (Forbush decreases) (Tinsley, 1994; 1996a);
(B) Changes in the Birkeland currents and the high latitude ionospheric potential distribution, on the day to day timescale (Tinsley and Heelis, 1993);
(C) Changes in the flux of precipitating relativistic electrons, which increase stratospheric conductivity on the day to day timescale at middle and high latitudes. Only when stratospheric volcanic aerosols (which decrease stratospheric conductivity on a longer time scale) are also present, are effects on J observed (Kirkland et , al., 1996).

3. SIX MANIFESTATIONS OF CORRELATIONS BETWEEN ATMOSPHERIC DYNAMICS and CHANGES OF J INTO CLOUDS, from Tinsley, (1996b).

(1) NORTHERN WINTERS and SUNSPOT CYCLE: CHANGES in atmospheric dynamics, and INTENSIFICATION of storms at MID-HIGH GEOMAGNETIC LATITUDES for sunspot min. years with INCREASED J, with effects of QBO;
(a) Sea level pressure in eastern N. Atlantic (~ 100 yr.)(Kelly, 1977).
(b) Air temperature for N. Atlantic (~100 yr)(Deser and Blackmon, 1993; Mann and Park, 1994).
(c) Cyclogenesis in western N. Atlantic (~40 yr.)(Labitzke and van Loon, 1989).
(d) Storm tracks in eastern N. Atlantic (~70 yr.)(Brown and John, 1979; updated in Tinsley and Deen, 1991).
(e) Wind direction at 700 hPa in N. Atlantic (~40 yr.)(Venne and Dartt, 1990).

(2) SOUTHERN WINTERS AND SUNSPOT CYCLE: CHANGES in atmospheric dynamics at MID-HIGH GEOMAGNETIC LATITUDES for CHANGES in J, with effects of QBO;

(a) Surface pressure in Southern Ocean (~40 yr)(Labitzke and van Loon, 1989, updated in Tinsley, 1996b).

(3) LOW LATITUDES ALL YEAR and SUNSPOT CYCLE: INTENSIFICATION of storms for sunspot max. years for INCREASED J, independent of QBO;

(a) Increases in upward convection in Intertropical Convergence Zone and subsidence in the sinking branch of Hadley circulation (van Loon and Labitzke, 1994).

(4) NORTHERN WINTERS AND FORBUSH DECREASES: WEAKENING of storms on time scale of DAYS at MID-HIGH GEOMAGNETIC LATITUDES with Forbush decreases of cosmic ray flux for DECREASE of J;

(a) Vorticity area index (VAI, i.e., area of high cyclonic vorticity); implications for decreases in cyclogenesis (Roberts and Olson, 1973; Padgoankar and Arora, 1981; Tinsley and Deen, 1991).

(5) POLAR CAPS and IONOSPHERIC POTENTIAL: CHANGES in tropospheric dynamics on time scale of DAYS with changes in IMF B_y affecting polar cap ionospheric potential for CHANGES in J on time scale of DAYS;

(a) Opposite changes in surface pressure in northern and southern polar caps with opposite changes in J in the two caps (Mansurov et al., 1974, 1975; Page, 1989; Tinsley and Heelis, 1993).

(6) NORTHERN WINTERS and HELIOSPHERIC CURRENT SHEET CROSSINGS: CHANGES in atmospheric dynamics and WEAKENING of storms on time scale of DAYS at MID-HIGH GEOMAGNETIC LATITUDES with heliospheric current sheet crossings associated with decrease in relativistic electron precipitation, for DECREASE in J on time scale of DAYS with effects of stratospheric volcanic aerosols;

(a) VAI decreases, implying decrease in cyclogenesis, (Wilcox et al., 1973; Larsen and Kelley, 1977; Padgoankar and Arora, 1981; Tinsley et al, 1994; Kirkland et al., 1996).

(b) Changes in kinetic energy for planetary wavenumber 5 (Williams and Gerety, 1980).

(c) Temperature decreases at 500 hPa at high latitudes (Misumi, 1983).

(d) Surface pressure changes at high latitudes (Rostoker and Sharma, 1980).

The phase of the QBO is found to affect the manifestations (1) and (2) in the North Atlantic and Southern oceans. The QBO is the quasibiennial oscillation of equatorial stratospheric winds, and its effects are ubiquitous throughout the global atmosphere. It is the solar wind process (Aa) that produces the J variations in the manifestations (1), (2), and (3). The process (Ab) produces the J variations of (4), and the processes (B) and (C) produce the J variations of (5) and (6) respectively.

4. EVIDENCE FROM CLOUD MICROPHYSICS FIELD OBSERVATIONS, LABORATORY STUDIES, AND NUMERICAL SIMULATIONS

Observations show that in many cases there is a discrepancy between the rates of production of initial ice at cloud tops, and the concentrations of ice forming nuclei (IFN) (e.g., Hobbs and Rangno, 1990; Beard, 1992). The ice particle concentrations are up to several orders of magnitude greater than those expected on the basis of the counts of IFN. The IFN measurements are made by counters that neutralise the charge before counting the numbers of effective nuclei. It has been shown by Pruppacher and Jaenicke (1995) and Rosinski (1995) that condensation nuclei participate on average in 3 condensation-evaporation cycles in clouds before being precipitated. In this process condensation nuclei which are effective IFN without charge would nucleate ice particles which would grow large enough by the Wegener-Bergeron-Findeisen mechanism to sediment to lower altitudes and be removed from the cloud forming layer. In later cycles of condensation, ice formation, sedimentation and evaporation there would be a depletion of these effective IFN.

Thus if electrostatic charge on less effective IFN promotes them to become more effective IFN, as has been proposed previously on the basis of laboratory experiments and numerical modeling, (see Tinsley and Deen, 1991; Tinsley, 1996b, c), then the involvement of electrostatic charge could explain the discrepancy described above.

5. SOME QUANTITATIVE ASPECTS

The fluxes of galactic cosmic rays and relativistic electrons into the atmosphere, that are modulated by the solar wind, have an energy flux ~ 10^{-3} erg cm^{-2} s^{-1}. These fluxes change the latitude distribution of conductivity in the global circuit, for which the generator is tropical thunderstorms, and for which the energy flux in the return path through the global troposphere ranges from 2 - 12×10^{-4} erg cm^{-2} s^{-1}. An amplification by ~10^7 - 10^8 is necessary to account for the ~10^{-3} w cm^{-2} of energy flux represented by observed apparent responses in the VAI, or of changes in the general circulation in the manifestations listed above. (These changes consist of a redistribution of energy rather than a change in total energy.) However, it takes only enough energy to rearrange about 200 water molecules into the ice configuration to freeze a 20 micron radius droplet with ~10^{15} molecules (Fletcher, 1970, p 96), for an energy amplification (latent heat release / electrical energy input) of ~10^{12}. Further energy amplification occurs when the resulting ice crystals grow to millimeter size by the Wegener-Bergeron-Findeisen process. For winter cyclones additional energy is extracted from the shear in the zonal circulation as the storm intensifies. The tropospheric energy is measured over larger areas and longer timescales than those for which electrical energy would

be utilized in ice nucleation; and we are tracking a change ~10% in the input, nevertheless even if these account for a factor of 10^3 there is still no energy amplification problem in accounting for the correlations of atmospheric dynamics and J described above.

For light cloud cover, it is the change in cloud albedo and opacity that modulates the tropospheric radiation balance. According to Dickinson, (1975), a change in upper level cloud opacity by 20% would produce heating rates in the column below of the order of 0.1°C /day. Across a zone 15° wide at mid latitudes, a 0.1°C temperature difference between atmospheric columns would lead to changes in zonal winds at tropopause altitudes of order 2 ms^{-1}. Thus the time constant for changes in atmospheric dynamics with changes in tropospheric heat budget in response to changes in sedimentation rate for light clouds is likely to be days, in comparison to a time constant of hours for the storm intensification response.

Another quantitative consideration concerns the amount of ionization available for inducing ice nucleation compared to the rate of production of ice that must be accounted for. Rutledge and Hobbs (1983) used a seeder ice concentration of $7x10^{-3}$ cm^{-3} in their models of the "seeder feeder" process. These concentrations are consistent with measured values in fall streaks. With an estimated fall speed of about 1 m s^{-1} (Wallace and Hobbs, 1977 p. 196-197) the downward flux of ice crystals is 0.7 cm^2 s^{-1}. The air-earth current into clouds is equivalent to $0.6x10^3$ to $2.5x10^3$ elementary charges cm^{-2} s^{-1}, so that about 1000 to 4000 positive elementary charges are available for each ice nucleation event. This is consistent with the scenario of Beard, (1992). The production rate of ions in the upper troposphere is about 10 cm^{-3} s^{-1}, so in addition about 10^3 positive as well as negative ions are produced each second for each 1 m of vertical 1 cm^2 column in which ice nucleation is occurring.

According to Mason, (1971), the generation of precipitation by ice processes in clouds (the Wegener-Bergeron-Findeisen process) is probably responsible for 90% of continental air mass precipitation in mid-latitudes. Rutledge and Hobbs (1983) found that their typical ice crystal flux produced roughly a doubling of the precipitation rates in warm frontal rainbands. This would be associated with a doubling of net latent heat release in rainbands (typical precipitation efficiencies are not more than a few tens of percent, so water that is precipitated does not re-evaporate in the cloud mass, equivalent to a release of the latent heat there). Thus the change in latent heat release in cyclones is a significant fraction of the total latent heat released, without considering the feedback effects on vertical transport. The release of latent or sensible heat at mid levels in a warm core cyclone intensifies its development (Pauley and Smith, 1988; Zimmerman et al., 1989; van Delden, 1989]. An increase in precipitation efficiency from say 10% to 11% in a rainfall rate of say 1 cm hr^{-1} would provide about 10^{-1} w cm^{-2} for atmospheric heating. Averaged over time and space, this is enough to account for the measured tropospheric changes ~10^{-3} w cm^{-2} without considering the additional energy extracted from the shear of the winter circulation.

6. ACKNOWLEDGEMENTS

Support has been provided by NSF grant ATM-9504828 and by the Los Alamos National Laboratory.

7. REFERENCES

Beard, K. V., 1992: Ice initiation in warm base convective clouds: An assessment of microphysical mechanisms, *Atmospheric Research*, **28**, 125-152.

Brown, G. M., and J. I. John, 1979: Solar cycle influences in tropospheric circulation, *J. Atmos. Terr. Phys.*, **41**, 43-52.

Deser, C., and M. L. Blackmon, 1993: Surface climate variations over the north Atlantic ocean during winter: 1900-1989, *J. Climate*, **6**, 1743-1753.

Dickinson, R. E, 1975: Solar variability and the lower atmosphere, *Bull. am. Meteorol. Soc.*, **56**, 1240-1248.

Fletcher, N. H., 1970: *The Chemical Physics of Ice*, Cambridge University Press, New York, 1970.

Hobbs, P. V., and A. L. Rangno, 1990: Rapid development of high ice particle concentrations in small polar maritime cumuliform clouds, *J. Atmos. Sci.*, **47**, 2710-2722.

Kelly, P. M., 1977: Solar influence on north Atlantic mean sea level pressure, *Nature*, **269**, 320-322.

Kirkland, M. W., B. A. Tinsley and J. T. Hoeksema, 1996: Are stratospheric aerosols the missing link between tropospheric vorticity and Earth-transits of the heliospheric current sheet? *J. Geophys. Res.*, **101**, in press.

Labitzke, K. and H. van Loon, 1989: Association between the 11 year solar cycle, the QBO, and the atmosphere, III, Aspects of the association, *J. Climate*, **2**, 554-565.

Larsen, M. F., and M. C. Kelley, 1977: A study of an observed and forecasted meteorological index and its relation to the interplanetary magnetic field, *Geophys. Res. Lett.*, **4**, 337-340.

Mann, M. E., and J. Park, 1994: Global-scale modes of surface temperature variability on interannual to century timescales, *J. Geophys Res.*, **99**, 25,819 - 25,833.

Mansurov, S. M., L. G. Mansurova, G. S. Mansurov, V. V. Mikinevich and A. M. Visotsky, 1974: North-south asymmetry of geomagnetic and tropospheric events, *J. Atmos. Terr. Phys.*, **36**, 1957-1962.

Mansurov, S. M., G. S. Mansurov, and L. G. Mansurova, 1975: Certain regularities of geomagnetic and baric fields at high latitudes, *Possible Relationships Between Solar Activity and Meteorological Phenomena*, Ed. W. R. Bandeen and S. P. Maran, p. 53-58, NASA-SP 366, Washington.

Mason, B. J. 1971: *The Physics of Clouds*, 2nd. ed., Clarendon, Oxford.

Misumi, Y., 1983: The tropospheric response to the passage of solar sector boundaries, *J. Met. Soc. Japan*, **61**, 686-694.

Padgoankar, A. D., and Arora, 1981: Tropospheric vorticity response to the solar magnetic sector structure and geomagnetic disturbances, *Pure. Appl. Geophys.*, **119**, 893-900.

Page, D. E.., 1989: The interplanetary magnetic field and sea level polar pressure, p. 227-234 in *Workshop on Mechanisms for Tropospheric Effects of Solar Variability and the Quasi-bienniel Oscillation*, eds. S. K.. Avery and B.A. Tinsley, Univ. of Colo., Boulder.

Pauley, P. M., and P. J. Smith, 1988: Direct and indirect effects of latent heat release on a synoptic scale wave system, *Mon. Weather Rev.*, **116**, 1209-1235.

Pruppacher, H. R., and R. Jaenicke, 1995: The processing of water vapor and aerosols by atmospheric clouds, a global estimate, *Atmospheric Research*, **38**, 283-295.

Rosinski, J., 1995: Cloud condensation nuclei as a real source of ice forming nuclei in continental and maritime air masses, *Atmospheric Research*, **38**, 351-359.

Rostoker, G., and R. P. Sharma, 1980: Correlation of high latitude tropospheric pressure with the structure of the interplanetary magnetic field, *Canad. J. Phys.*, **58**, 255-269.

Roberts, W. O., and R. H. Olson, 1973: Geomagnetic storms and wintertime 300 mb trough development in the North Pacific-North America area, *J. Atmos. Sci.*, **30**, 135-140.

Rutledge, S. A. and P. V. Hobbs, 1983: The mesoscale and microscale structure and organization of clouds and precipitation in midlatitude cyclones, VIII, a model for the "Seeder Feeder" process in warm frontal rainbands, *J. Atmos. Sci.*, **40**, 1185-1206.

Tinsley, B. A., 1994: Solar wind mechanism suggested for weather and climate change, *Eos, Trans. Am. Geophys. Un.*, **75**, 369-374.

Tinsley, B. A., 1996a: Solar wind modulation of the global electric circuit and apparent effects on cloud microphysics, latent heat release, and tropospheric dynamics, *J. Geomag. Geoelect.*, **48**, in press.

Tinsley, B. A., 1996b: Solar wind induced changes of air-earth current into clouds; correlations with changes in atmospheric dynamics and storm intensity. *J. Geophys. Res.*, **101**, in press.

Tinsley, B. A., 1996c: Does electrostatic charge at cloud tops affect rates of nucleation and sedimentation of ice? *Proceedings of the 14th International Conference on Nucleation and Atmospheric Aerosols*, ed Kulmana and Wagner, Elseiver, in press.

Tinsley, B.A., and G.W. Deen, 1991: Apparent tropospheric response to MeV-GeV particle flux variations, A connection via electrofreezing of supercooled water in high-level clouds?, *J. Geophys. Res.*, **96**, 22,283 - 22,296.

Tinsley, B. A. and R. A. Heelis, 1993: Correlation of atmospheric dynamics with solar activity: Evidence for a connection via the solar wind, atmospheric electricity, and cloud microphysics, *J. Geophys. Res.*, **98**, 10,375 - 10,384.

Tinsley, B. A., J. T. Hoeksema and D. N. Baker, 1994: Stratospheric volcanic aerosols and changes in air-earth current density at solar wind magnetic sector boundaries as conditions for the Wilcox tropospheric vorticity effect, *J. Geophys. Res.*, **99**, 16,805 - 16,813.

van Delden, A., 1989: On the deepening and filling of balanced cyclones by diabatic heating, *Meteorol. Atmos. Phys.*, **41**, 127-145.

van Loon, H., and K. Labitzke, 1994: The 10-12 year atmospheric oscillation, *Meteorol. Zeitschrift*, **3**, 259-266.

Venne, D. E. and D. G. Dartt, 1990: An examination of possible solar cycle-QBO effects in the northern hemisphere troposphere, *J. Climate*, **3**, 272-281.

Wallace, J. M. and P. V. Hobbs, 1977: *Atmospheric Science, An Introductory Survey*, Academic, San Diego.

Wilcox, J. M., P. H. Scherrer, L. Svalgaard, W. O. Roberts and R. H. Olson, 1973: Solar magnetic structure: influence on stratospheric circulation, *Science*, **180**, 185-186.

Williams, R. G., and E. G. Gerety, 1980: A further study of the tropospheric energetics of a particular sun-weather relation, *J. Atmos. Terr. Phys.*, **42**, 27-34.

Zimmerman, J. E., P. J. Smith and D. R. Smith, 1989: The role of latent heat release in the evolution of a weak extratropical cyclone, *Mon. Wea. Rev.*, **117**, 1039-1057.

ON THE CLIMATIC IMPACT OF CONTRAILS

Bernhard Strauss, Ralf Meerkötter, Bruno Wissinger, and Peter Wendling

Deutsche Forschungsanstalt für Luft- und Raumfahrt
Institut für Physik der Atmosphäre
Oberpfaffenhofen, D-82234 Wessling, F.R. Germany

1. INTRODUCTION

Airtraffic influences the atmosphere by emission of various gases and particles. Among these, water vapour and aerosol particles acting as cloud nuclei are of special interest because they support cloud formation thus, modifying an important climate factor. In view of the strongly growing worldwide aircraft traffic the impact of contrail clouds is discussed recently again within the scope of air-traffic and climate in general (Schumann, 1994). The global influence of contrails on climate was studied by Liou et al. (1990) using a two dimensional energy balance model. As result, an increase in surface temperature of 1 K in the case of an increase of cloud cover of 5 % between 20° and 70° N was obtained. Ponater et al. (1995) studied the influence of an increase in water vapour and in cirrus cloud cover induced by airtraffic using a three-dimensional climate model. They show that a significant climate effect is more likely to occur on the basis of an additional contrail cloud cover rather than on the basis of an additional water vapour amount due to air traffic. For a contrail induced cloud cover of 5 % the lower troposphere is warming by about 1 K at 50° N.

However, one may expect that contrails have a stronger impact on a regional scale than on a global. To estimate this, a case study was carried out for an area of increased air traffic in Southern Germany. This was done by use of a one-dimensional radiative convective model (RCM), originally developed by Liou and Ou (1983) and modified within the present study to allow modelling of regional climate by taking into account advection as an additional energy source besides radiation and convection. The effects of an increased cirrus cloud cover on the equilibrium temperature of a July and October atmosphere were calculated and the results are presented in the following.

2. MODIFICATION OF THE RADIATIVE CONVECTIVE MODEL

2.1 Parameterization of advection

Radiative convective models are based on the assumption of a balance between the radiative and turbulent heat exchange in each atmospheric layer of a single column that represents globally averaged atmospheric conditions. They are widely used to determine the vertical temperature profile as a global mean considering various forcing and feedback mechanisms. The model of Liou and Ou (1983) that is used within this study divides the atmosphere into 22 layers containing three cloud layers with a fixed cloud cover. To allow for a calculation of the temperature profile on a regional scale and for limited time periods, advection of energy has to be taken into account. For this purpose an 'atmospheric box' with vertical boundaries surrounding the region of Southern Germany was defined and the net energy flux of heat due to advective processes through the lateral faces of the box was determined by use of radiosonde data from the nearly station of Munich that were averaged for the years 1981 to 1985. The vertical profile of advected heat energy was set proportional to the wind profile. The absolute value of the advected energy was chosen such that the net radiative energy loss or gain at the top of the atmosphere is equal to the value determined by measurements of the ERBE-satellite experiment. These fluxes are - 59 W m^{-2} and 97 W m^{-2} for the months of July and October respectively, the minus sign indicating an energy gain for the box. The satellite data were taken for the area from 47.5° to 50° N and 10° to 12.5° E and cover quite accurately the area of Bavaria in Southern Germany. For July, a five years average of monthly averaged net fluxes is used (years 1985 to 1989). For October, corresponding data were available only for two years, 1985 and 1986 respectively.

2.2 Microphysical and radiative properties of cirrus clouds

Special emphasis is given to the parameterization of the radiative properties of ice clouds. In the original version of the RCM high level ice clouds consist of cylindrically shaped monodisperse ice particles with a mean length of 200 μm, a mean radius of 30 μm and a mean concentration of 0.05 cm $^{-3}$. However, recent research results enforce these assumptions to be modified. Models tend to underestimate the solar albedo of ice clouds when compared to measurements (Stackhouse and Stephens, 1991), whereby measurements indicate (Ström, 1993; Forkert et al., 1994) that a significant amount of ice particles with sizes smaller than 50 μm exists in ice clouds. These particles will have an appreciable influence on the radiative characteristics of ice clouds by enlarging the number of backscattered photons and herewith increasing cloud albedo. Therefore, the original parameterization of ice clouds in the RCM model was modified by assuming ice clouds to consist of a particle size distribution based on measurements of small ice particles down to 2 μm particle size (Forkert et al., 1994) and for particles larger than about 20 μm on the parameterization of Heymsfield and Platt (1984) which is a function of temperature. The measurements of Forkert et al. (1994) were carried out with an airborne Formvar ice particle replicator (Hallett, 1976) in a cirrus layer approximately at an altitude between 9.5 and 11 km in the area north of the Alps.

The shape of the particles was assumed to be that of hexagonal columns, the ratio of length to diameter following the measurements of Ono (1969) and the calculations of Hess and Wiegner (1994). Table 1 shows the discretized ice particle size distribution as derived from the two separate data sources. The given size represents crystal length.

Table 1 Size distribution of ice cloud particles; particles in classes I and II are referred as 'small' particles in the text

size class	size range μm	particle number m^{-3}
I	2 - 6	$1.69 \cdot 10^{5}$
II	6 - 20	$3.87 \cdot 10^{5}$
III	20 - 40	$6.58 \cdot 10^{3}$
IV	40 - 90	$1.44 \cdot 10^{3}$
V	90 - 200	$2.36 \cdot 10^{2}$
VI	200 - 400	$3.70 \cdot 10^{1}$
VII	400 - 900	$8.25 \cdot 10^{0}$
VIII	900 - 2000	$1.32 \cdot 10^{0}$

In order to show the effect of neglecting the small particles with sizes lower than 20 μm calculations of the radiative properties of ice clouds are carried out in the following for two ice particle size distributions, with and without small particles. For the two cases, the total particle concentration is $5.64 \cdot 10^{-1}$ cm^{-3} and $8.33 \cdot 10^{-3}$ cm^{-3} respectively, meaning that 98.5 % of all particles are within the two classes I and II. Additional measurements in contrails near the Alps (Forkert et al., 1994) showed that within the particle size range from 2 to about 100 μm the measured size distribution for aged contrails (age larger than about 0.5 hour) lies within the variability of the one measured in natural cirrus. Therefore, for the following calculations with the RCM the radiative properties of natural and contrail induced high clouds have been assumed to be the same.

The applied radiative convective model (Liou and Ou, 1983) uses a parameterization of broadband infrared and solar radiative transfer and needs for this purpose the flux reflection, absorption/emission and transmission properties of separate distinct scattering layers (clouds) embedded in the atmosphere. These have been calculated by use of a radiative transfer model (RTM) based on the Matrix-Operator-Theory (Plass et al., 1973). This RTM accounts for processes of multiple scattering, absorption and thermal emission. The vertical profiles of temperature, pressure, air density and aerosol and gaseous absorbers were specified according to mean July and October conditions for the considered region of southern Germany.

In the visible part of the spectrum the optical properties of high ice clouds are approximated by the assumption of hexagonal crystal shapes and geometrical optics. The sharp forward peak of the phase function is truncated in the visible by applying the delta function approximation. In the terrestrical spectral range, a Hennyey-Greenstein approximation of the phase function is adapted which depends only on the asymmetry factor. Since the approximation of geometrical optics is no more valid in this spectral range ice particles were assumed as spheres with the same volume as those given in Table 1 and Mie calculations were carried out to determine the optical properties. Tables 2 and 3 list the resulting broadband radiative properties of high level ice clouds finally used interactively in the RCM. The radiative properties of middle and low level clouds were taken as those from the original RCM corresponding to the mid-latitude case of Liou and Ou (1983). According to the results of Table 2 the solar reflection of high ice clouds is strongly dominated by the amount of particles with sizes smaller than 20 μm. Table 3

lists the corresponding properties for the broad-band infrared cloud properties.

Table 2 Solar radiative properties of the cirrus layer as derived from RTM calculations

case	solar zenith angle	transmittance	reflectance
Jw	58.71°	0.961	0.031
JO	58.71°	0.980	0.012
OW	69.78°	0.936	0.054
OO	69.78°	0.970	0.021

JW : July, cloud with small particles
JO : July, cloud without small particles
OW : October, cloud with small particles
OO : October, cloud without small particles

Table 3 Derived ice cloud radiative properties in the terrestrial spectral range

case	emittance	transmittance	reflectance
JW	0.381	0.695	0.024
JO	0.319	0.784	0.011
OW	0.315	0.733	0.024
OO	0.248	0.751	0.010

3. MODEL RESULTS

Figure 1 shows results for the reference case, i.e. the case with climatological values of cloud cover in October. Cloud cover values are taken from Warren et al. (1988) and are based on ground observation averages for the years 1971 to 1981. Two resulting temperature profiles are shown, the one results from including advection as outlined above, whereas the other results from neglecting it. For comparison, the climatological October values of temperature as derived from radiosonde data of the Munich station are shown.

Remarkable is the great influence of advection inducing a temperature difference of up to 25 K throughout the troposphere. It is important to note that the uncertainty of the satellite data is in the order of 10 W/m^2 corresponding to an uncertainty in the temperature profile of about 3 K.

The impact of additional high cloudiness induced by air traffic is estimated by comparing the RCM results for an increased cloud cover with the ones for reference cases in July and October. It is assumed that the additional high cloudiness adds to the natural cloudiness at the expense of the uncovered area. The obtained results are depicted in Fig. 2.

Fig. 1 Modelled temperature profiles for October with (solid) and without (dashed) advection compared to radiosonde measurements (triangles)

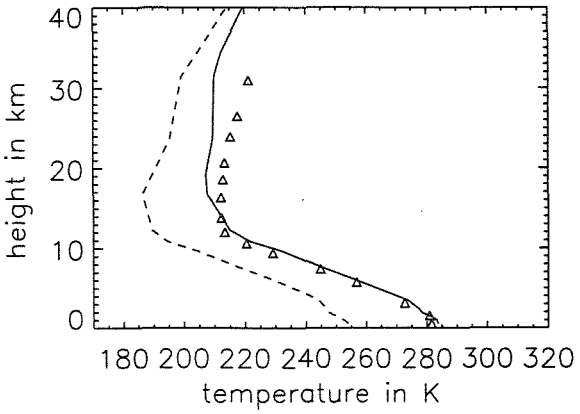

Fig. 2 Increase in surface temperature ΔT_{surf} as function of the additional cirrus cloud cover due to contrails η in the case of July (solid) and October (dashed over Southern Germany

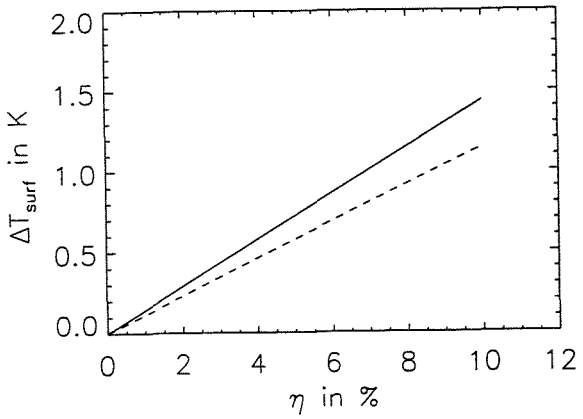

As can be seen, an additional increase in high cloudiness of 10 % causes surface temperature increases of 1.4 K and 1.2 K, respectively. A linear relation between cloud cover and surface temperature is obtained, because the RCM weights fluxes linearly with cloud cover. Assuming the high clouds to be composed only of larger particles leads to corresponding increases in surface temperature of 1.5 K and 1.3 K for July and October conditions, respectively. This indicates that with inclusion of small ice particle the effect of the solar albedo increase exceeds the corresponding effect of the increase in terrestrial emission of radiation. The current cloud cover which is due to aircraft induced contrail cloudiness is estimated to be in the order of 0.5 % over Europe (Bakan et al., 1994). In this

case the increases in surface temperature are 0.07 and 0.06 K in July and October, respectively.

4. REFERENCES

Bakan, S., M. Betancor, V. Gayler, H. Grassl, 1994: Contrail frequence over Europe from NOAA-Satellite images. Ann. Geophysicae., 12, 962-968

Forkert, T., B. Strauss, P. Wendling, 1994: On the climatic impact of contrails. In: U. Schumann and D. Wurzel (Eds.): 'Impacts of Emissions from Aircraft and Spacecraft Upon the Atmosphere', Proceedings of an International Scientific Colloquium Köln, Germany, 18-20 April 1994, DLR-Mitteilung 94-06

Hallett, J., 1976: Measurements of size, concentration and structure of atmospheric particulates by the airborne continuous replicator. Final report: Cloud particle replicator for use on a pressurized aircraft, 92 pp. I, II Supplementary Final Report, 1511 pp. Contract FGL-TR-76-0149, Air Force Geophys. Lab

Hess, M., and M. Wiegner, 1994: COP: Data Library of Optical Properties of Hexagonal Ice Crystals. Appl. Opt., 33, 7740-7746

Heymsfield, A.J., and C.M.R. Platt, 1984: A parameterization of the particle size spectrum of ice clouds in terms of the ambient temperature and the ice water content. J. Atmos. Sci., 41, 846-855

Liou, K.N , and S.C. Ou, 1983: Theory of equilibrium temperatures in radiative-turbulent atmospheres. J. Atmos. Sci., 40, 214-229

Liou, K.N., S.C. Ou, and G. Koenig, 1990: An investigation on the climatic effect of contrail cirrus. In: U. Schumann (Ed.): 'Air Traffic and the Environment - Background, Tendencies and Potential Global Atmospheric Effects'. Proceedings of a DLR International Colloquium, Bonn, Germany, 15-16 November 1990, Springer Verlag

Ono, A., 1969: The shape and riming properties of ice crystals in natural clouds. J. Atmos. Sci., 26, 138-147

Plass, G.N., G.W. Kattawar, and F.E. Catchings, 1973: Matrix operator theory of radiative transfer. I: Rayleigh scattering. Appl. Opt., 12, 314-323

Ponater, M., S. Brinkop, R. Sausen, and U. Schumann, 1995: Simulating the global atmospheric response to aircraft water vapour emsissions and contrails. Submitted to: Ann. Geophysicae

Schumann, U, 1994: On the effect of emissions from aircraft engines on the state of the atmosphere. Ann. Geophysicae., 12, 365-384

Stackhouse, P.W., and G.L. Stephens, 1991: A theoretical and observational study of the radiative properties of cirrus: Results from FIRE 1986, J. Atmos. Sci., 48, 2044-2059

Ström, J., 1993: Numerical and airborne experimental studies of aerosol and cloud properties in the troposphere. Dissertation, Department of Meteorology, Stockholm University, ISBN 91-7173-168-8

Warren, S.G., C.J. Hahn, J. London, R.M. Chervin, R.L. Jenne, 1988: Global distribution of total cloud cover and cloud type amounts over land. NCAR Technical Notes

CONDITIONS OF ATMOSPHERIC CONVECTIVE PRECIPITATION IN STAVROPOL REGION

G.Kh.Badakhova,

Ya.A.Ekba, L.K.Golouz

Scientific and Production Geophysikal Center, Stavropol, Russia

1. Introduction

The Stavropol region is located in the south-east of the European part of Russia and in the central part of the areas adjoining the Caucasus. Here on comparatively small area one may come across all the relief forms - from semiarid plains to alpine grasslands. Besides, this region is a junction place of various systems of atmospheric circulation. With this in view detailed study of convective precipitation conditions in such a compound region seems to be of great scientific interest.

Apart from that the knowlege of precipitation conditions in the Stavropol region is of great practical importance for the Russia's agriculture, as this region being the one with the most highly developed agricultural production and the main wheat grain supplier, is in the same time a zone of risky farming due to recurrent droughts on the plains and hail-damages at the foot-hill areas of the region. The knowledge of precipitation conditions makes it possible to determine the expediency and terms of precipitation artificial enhancement (PAE) or hailing-protection work carrying out correctly on any areas of the region.

2. Distribution of Liquid Precipitation

The territory of the Stavropol region can be divided by the large terrain features into two parts: a flat north-eastern part and an elevated south-western one. The character of the underlying surface caused heterogeneousness of the climate on the territory of this region. The Stavropol highland is a barrier in the way of the humid air masses coming in from the west and for dry winds of the eastern component. Due to this precipitation distribution over the region territory is uneven. In the northern and easttern areas the precipitation fall-out make 300-400 mm per annum including 200-300 mm in the warm period; in the western and south-wester by areas these characteristics make 400-500 and 300-380 mm accordingly. Thus, the Stavropol Hills have divided the territory of the region into two zones: a droughty zone and a

humidificated one.

The total guantity of precipitation falling out in the Stavropol region is not great. An exception to this are only the foothill areas and the central part of the Stavropol plateau where precipitation fall out make up to 500 mm per a warm period and up to 700 mm per annum.

The annual precipitation sums vary within great limits. Thus, for example in Boudyonnovsk at the average precipitation sum of many years 354 mm per annum the fall out in 1947 made 208 mm, and in 1967 - 549 mm. The spread in data is even more characterictic for the monthly precipitation sums. As an example of this may be taken the August of 1967 and 1979 in Roshchino when at the norm of 30 mm the precipitation sum per a month made 196 and 2 mm accordingly. The summer monthly precipitation sums exceed the winter ones 1.6-3.0 times. The precipitation maximum falls on June, and it is bound up with the intensification of the Atlantic cyclones cold fronts. While moving to the north-east precipitation annual sum is decreasing and the monthly maximum is expressed less. The minimum of the montly sums is noted in Januaru-March when the inflow of cold dry continental air from the east is observed most freguently. The total precipitation sum of a warm period more than 2 times exceeds that of a cold period. The number of days with precipitation is more in winter. However the precipitation rate is insignificant, and rarely exceeds 5 mm. Precipitation maxima per day fall on a summer period. In 50 % of years the maximum quantity of precipitation per day make 30-35 mm. The probability of heavy showers diving more than 50 mm of precipitation doesn't exceed 10 %.

3. Hydrotermal Coefficient and Solar Activity

Analysing the agroclimatic conditions of the Stavropol region the authors calculated the value of a hydrothermal coefficient (HTC) and this made it possible to subdivide the territory of the region into areas by the degree of their humidification. It was ascertained that the two lagre zones, in their turn, may be subdivided into 5 sub-zones: very droughty, drouhgty, a zone of unsteady humidification, moderately humidified and humidified zones (Badakhova, Ekba,1993) (Fig.1).

Between the precipitation of droughty territories and those sufficiently provided with moisture there exists a rather close linear regression connection:

$$h_м = a + b\, h_д,$$

where a = 46,8 and b = 0,9; the coefficient of correlation r = 0.84 (Ekba et al., 1992).

For a period of the analysed 115 years preceding to the beginning of the work on PAE in this region in 42% of years noted werw droughts often accompanied by dust-and-sand storms. In the 1940's a tendency to the climat droughtiness increase is noted.

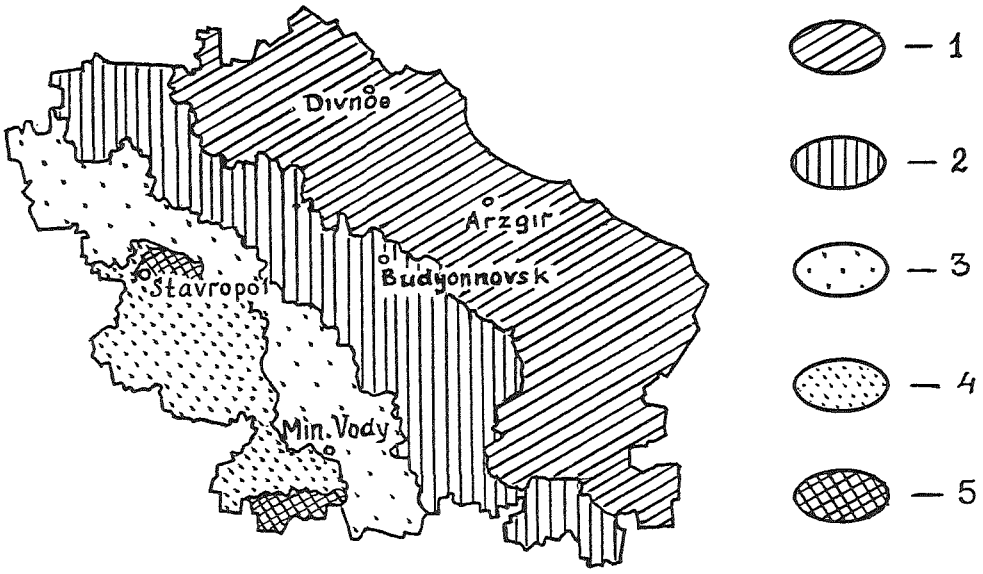

Fig.1. Humidification Distribution in Stavropol Region

In order to ascertain a probable connection of the droughts with the solar activity an analysis of the HTC series and Woolf number W was carried out. It was found out that both W and HTC get changed in antiphase, and especially clear this is observed at the maximum and minimum points of the 11-years cycle of the solar activity; it manifested itself most of all on the ascending branch in the 80-years cycle. In the 11-years cycle HTC gets increased on the branch of solar activity growth.

Correlation in the first three years after the minimum of solar activity is determined by the regression equation:

$$y = 0{,}078 + 0{,}0248\,x;$$

$r = 0{,}801 \pm 0{,}1$. In the subsequent 2 years HTC gets sharply down and the minimum falls on the years of the solar activity maximum. The HTC growth is observed on the branch of the solar activity decay. The connection with the 22-years cycle of solar activity is also ascertained.

4. Hail Precipitation

The data analysis of hail-damages for the last 30 years proved that in the south-westerly part of the Stavropol region territory there happen from 6 to 20 hail-damages annually which cause damage to the agricultural crops over the area from 12 thousand to 50 thousand hectares. The most hail-dangerous during the last 30 years were: 1972 - the area of damaged agriculture crops made 56320 hectares, 1977 - 68313 ha, 1983 - 51992 ha, 1988 - 52080 ha, 1992 - 67768 ha. 1987 was the most hail-dangerous year of the period under consideration; the area of the damaged agriculture crops made 149003 ha and evaluated in 100 % damage - 94571 ha.

Hail-dangerous season covers the period from April to September including though hail-dangerous processes are very seldom in April and September. They are registered most frequently in June. In June, accordingly, the largest areas with damaged cropes are being registered. However, the most intensive hailing processes take place in May and July. The largest areas with damaged agricultural crops due to one hail-damaging (both total and brought to 100 % damage) are registered in May. Thus, one the strength of all the characteristics of hail-danger the most hail-dangerous monthes are May and June. It should be noted, nevertheless, that in certain years it happens so that there is not a single hailing process in these monthes. Thus, for example, in 1968, 1986 and 1995 there were no hailing processes in May, and in 1979 there was not a single hailing process in June. The distribution of hail-danger by monthes is listed in the Table.

Distribution of hail-danger by monthes

Month	Share of the annual quantity of hail processes, %	Average multiyear area of damaged crops, ha	Average area of damaged srops at 1 process, ha	Share of the annual hail hit area, %	Average degree of crop damage, %
April	4	496	539	1,5	52
May	25,5	11186	2860	34	74
June	41	15065	2071	46	64
July	19	4611	1534	14	72
August	9	1240	857	3,5	69
September	1,5	393	1146	1	47

References

Badakhova G.Kh., Ekba Ya.A.,1993: **Agroclimatic Resourses and Conditions of Precipitation in Stavropol Region.** Trudy SF VGJ, No 1, 9-19.

Climatological Handbook of the USSR, 1948. Hydrometeoizdat, 311.

Ekba Ya., Kaplan L., Zakinyan R., 1992: **On Estimation of the Physical Efficiency of the Artificial Enhancement of the Liquid Precipitation in Stavropol Region** Trudy VGI, No 85, 71- 77.

Meteorological Montlhy, 1951-1995.

CLOUDINESS CLIMATOLOGY OF THE CENTRAL PART OF THE NORTH CAUCASUS

G.Kh.Badakhova,

Ya.A.Ekba, Yu.K.Lashmanov

Scientific and Production Geophysical Center,
Stavropol, Russia

The central part of the Northern Caucases under review here is limited by 43°50'N and 46°15' E. The area of this region makes 70 sq km. From the North this region is limited by the soutchern russian steppe from the West it is ajoined to the Prikoubanskaya plain, from the South and South - West - to the Great Caucasus mountains foothills, from the East - to the Caspian lowland. In the centre of this region there is a vast plateau of the Stavropol Hills the altitude of which is up to 827 m. In view of the great variety of the natural landscape the disribution of cloudiness characteristics and atmosphere phenomena on the territory under review also varies greatly.

Average cloudiness conditions of many years are formed under the influence of the circulation processes determining the predominant direction of air masses transfer and moisture content in them, as well as under the influence of an underlying surface effect. The not uniform terrain relief of the Northern Caucasus central part creates a compound air masses circulation promoting the creation of local cloudiness or its destruction. The cloudiness character and the amount of it differ considerably in cold and warm seasons.

In winter due to low moisture content of the air, presence of a snow cover and connected with it ground inversions low stratified clouds prevail. Frontal cloudiness is also represented mainly in the cold half of a year by strati forms. In the warm half of a year when the processes of air masses transfer are developing washing-out of a continuous cloud cover and formation of vertically development clouds take place. Repeatabilty of cloudiness main forms during a year differs considerably in the droughty north - easterly and in the well provided with water south-western parts of the territory under consideration (Table 1).

In the cold period a spur of the Asian anticyclone (along the soutchern periphery of which cold air inflows) settles down on the northern part of the region. This eastern current favours the cloudiness formation over the plains approaching the Eastern Caucasus, Stavropol Hills and in the foothills where

Table 1

The repeatability of the main cloudiness forms by monthes

Cloud form	Month											
	I	II	III	IV	V	VI	VII	VIII	IX	X	XI	XII
	Humidificated zone											
Ac	25,4	29,3	25,4	29,9	31,0	30,2	32,8	33,4	33,6	28,2	22,3	24,0
As	3,8	5,0	3,8	3,7	1,7	1,2	0,9	0,6	1,0	1,2	2,0	2,8
Cu	0,3	0,6	3,7	7,3	14,1	17,7	19,2	20,1	12,0	4,7	1,0	0,1
Cb	6,4	6,3	8,5	16,0	22,5	23,7	19,5	20,4	17,8	11,0	10,6	8,2
St	16,3	16,0	15,2	3,9	0,7	0,1	0,2	0,6	1,0	7,5	18,7	18,6
Sc	32,3	32,0	34,5	33,5	27,2	25,8	26,0	24,0	33,3	38,7	31,2	31,7
Ns	8,0	6,4	4,0	2,6	0,5	0,4	0,4	0,3	0,5	3,7	6,6	7,4
FrNb	7,5	4,4	4,9	3,1	2,3	0,9	1,0	0,6	0,8	5,0	7,6	7,2
	Droughty zone											
Ac	24,9	20,7	24,2	41,8	44,5	42,6	48,1	48,4	46,8	35,8	24,6	21,3
As	9,9	10,6	8,6	8,2	4,7	3,4	3,4	2,1	1,7	3,8	4,2	6,4
Cu	1,0	1,0	4,6	8,7	12,5	15,9	18,2	17,2	12,6	4,4	1,6	0,8
Cb	5,3	6,7	6,8	13,4	17,3	22,7	15,8	15,8	13,5	7,5	5,9	5,9
St	19,8	20,4	17,4	3,5	2,0	0,4	0,1	0,5	0,8	7,7	16,4	21,8
Sc	29,9	29,7	32,2	20,7	16,5	13,3	13,7	14,4	23,4	37,0	37,1	31,4
Ns	6,1	7,4	3,8	2,3	1,3	1,3	0,7	1,4	0,8	2,3	6,6	8,8
FrNb	3,1	3,5	2,4	1,4	1,2	0,4	0	0,2	0,4	1,5	3,6	3,6

orographical lift of air masses favours cloud formation. In winter period heavy cloudiness is noted here. For the regions which are in the orographic shadow of the Stavropol plateau north-easterly winds are foehnic winds, and they favour cloudiness destruction repeatability of the sky cloudiness is much lower (Fig.1a).

In the warm period of a year the solar radiation inflow increase over the steppe and semiarid regions favours the heating of the continental air and its drying, consequently cloudiness here is not great. In the cyclones passing by in summer in the northern part of the territory mainly high and middle clouds are formed, and they don't give precipition. The amount of cloudiness grows at the foothills areas.

The relief and seas proximity greater affect low clouds formation and distribution than the distribution of total cloudiness. The largest quantity of low cloudiness is observed on the plains approaching the Eastern Caucasus and on the north-easterly slopes of the Stavropol Hills where dull sky repeatability exceeds 60% in January. On the flat northern part of the territory due to predominance of anticyclonic weather conditions dull sky repeatability by the low clouds makes 50-60 %. Getting up into

the mountains due to frequent winter inversions low cloudiness, as a rule, gets decreased. However this decrease is unequal at the western and eastern regions of the territory under consideration.

In the warm period of a year low cloudiness distribution little differs from that of the total cloudiness. As it is shown on the July map (Fig.1b) the dull sky repeatability over the most part of the flat territory doesn't exceed 10-15%. At the Caucasian foot-hills and in the south of the Stavropol Hills the observed increase of the dull sky repeatability makes up to 20-30 %.

Both for the total cloudiness and for the low one the greater repeatability of half-clear sky is characteristic in the summer period. Over the flat part of the territory it is greater and at the foot-hill areas - less that the dull sky repeatability at that.

The annual movement of the total and low cloudiness according to the variety of the physico- geographical conditions is also various. The amplitude of the dull sky repeatability annual movement is expressed most clearly on the flat territory and ubsides gradually towards the foot-hills. The annual movement of clear sky repeatability is almost a mirror reflection of the dull sky annual movement of repeatability, but its amplitude is somewhat less.

The low cloudiness annual movement over a flat territory is

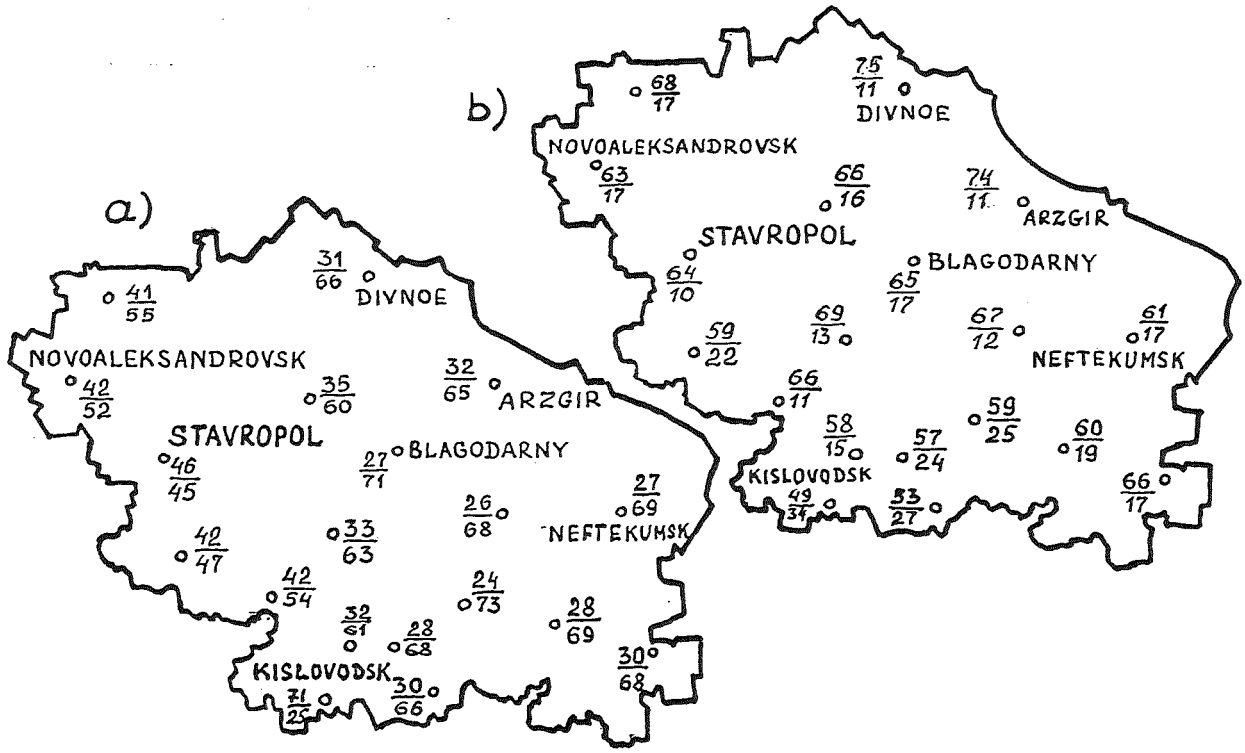

Fig.1. The repeatability of a dull sky by total (numerator) and low cloudiness; a) - January, b) - July

similar to that of total cloudiness, and at the mountain regions it, as distinct from the total cloudiness, has two maxima of the dull sky repeatability: the main maximum is observed in spring, and the secondary - in autumn.

Besides the annual movement cloudiness has also daily fluctuations. In the cold half of a year over the flat territory maximum repeatability of the dull sky is observed in the morning hours, and the minimum one - in the evening. In the warm period of a year maximum cloudiness is observe on the plains in the day-time hours. At the foot-hill regions in the cold period it is cloudy most of all in the morning, and in the warm period - in the day-time.

The number of clear and dull days considerably supplement the repeatability data on clear, half-clear and dull sky, as this makes it possible to judge to a certain extent degree, about the stability of the sky one or another conditions during twenty-four hours. The notion of clear or cloudy weather stability for the total or low cloudiness is given by the stability coefficients of clear or dull weather calculated by the known formulae and inserted in Table 2.

Table 2

Stability coefficients of clear (Cc) and dull (Cd) weather by low cloudiness

Station altitude	Cc Cd	Month											
		I	II	III	IV	V	VI	VII	VIII	IX	X	XI	XII
Neftecumsk (70 m)	Cc	47	47	49	65	77	77	77	73	63	49	41	44
	Cd	76	70	58	46	31	22	25	16	35	51	71	78
Divnoe (77 m)	Cc	35	36	47	68	77	78	83	83	77	57	39	31
	Cd	62	55	48	40	21	10	15	12	33	39	60	67
Novoaleksandrovsk (110 m)	Cc	46	48	53	69	69	69	73	74	76	66	60	53
	Cd	51	55	54	50	36	25	17	25	32	46	59	58
Nevinnomyssk (333 m)	Cc	45	47	51	63	66	68	71	70	72	64	54	46
	Cd	49	50	54	50	37	32	34	32	40	47	60	35
Kislovodsk (887 m)	Cc	68	65	62	66	57	55	59	65	69	70	70	72
	Cd	27	29	39	46	41	34	40	37	50	49	39	35

The summary annual number of dull days are fluctuating by the total cloudiness from 110 to 160, and by the low one - from 57 to 107. In the annual movement of dull days number by the total cloudiness there was noted one maximum and one minimum. The annual movement of the clear days number is opposite to that of dull days. The number of clear and dull days by the low cloudiness is distributed similarly.

The comparison of clear weather stability coefficients for the periods of 1936-1965 and 1966-1995 made their increase at the flat regions.

CLOUD SIMULATIONS WITH THE MAX PLANCK INSTITUTE FOR METEOROLOGY GENERAL CIRCULATION MODEL ECHAM4 AND COMPARISON WITH OBSERVATIONS

C.-T. Chen[1] and Erich Roeckner[2]

[1]Dept. of Earth Sciences, National Taiwan Normal University, Taipei, Taiwan
[2]Max Planck Institute for Meteorology, Hamburg, F. R. Germany

1. INTRODUCTION

This study documents several cloud parameters simulated by the latest version of the atmospheric GCM (ECHAM4) at the Max Planck Institute for Meteorology and evaluates them using a variety of observations. Due to the limitation and considerable uncertainties in the cloud related observations, we consider mainly the following three parameters - total cloud amount, total cloud liquid water path, and the effective droplet radius in water cloud.

2. DATA SETS

2.1 Model

A detailed description of the dynamical and physical structure, and the simulated climatology of the fourth generation model (ECHAM4) is documented by Roeckner et al. (1996). Compared to the previous model version ECHAM3 (Roeckner, 1992). Many physical parameterizations has been changed to eliminate the most apparent systematic model errors and to improve the physical basis. They includes the semi-lagrangian transport, radiation model, vertical diffusion, convection closure and surface data set.

The model simulated results are obtained from a 15 year integration with monthly observed SST and sea ice for the period 1979-1993 extended from the so-called Atmospheric Model Intercomparison Project (AMIP) data set (Gates, 1992). The model data reported are the ensemble annual and monthly means derived from the 15 year integration unless mentioned elsewhere.

2.2 Observations

The products from International Satellite Cloud Climatology Project (ISCCP, Rossow and Schiffer, 1991; Han et al. 1994), Ground-based cloudiness data (Hahn et al., 1994), and Special Sensor Microwave/Imager (SSM/I, Greenwald et al., 1993; Weng and Grody, 1994) are used for the validation of the referred cloud parameters. In the validation work, frequently we show more than one observational data set. The purpose is to provide an estimation of the current range of cloud parameters retrieving techniques besides the uncertainty and error analyses in each data set as described in the respective documentation.

3. TOTAL CLOUD COVER

3.1 Zonal Mean

The ensemble annually averaged zonal mean total cloud amount (hereafter, TCA) in the three data sets is shown in Fig. 1. Qualitatively, the latitudinal structure of TCA in the data sets is similar between 50 °S and 50 °N. Larger TCA is found in the tropical convergence zones and over the mid-latitude storm track regions. The smaller TCA in the subtropics is related to the large scale circulation pattern. While the simulated TCA in the tropics is in good agreement with both observations, there are systematic underestimates for the zonal mean TCA over the subtropics and mid-latitudes in the model. The ground-based cloud climatology is always greater than the satellite-based in the polar region. The TCA simulated by ECHAM4 in the northern hemisphere high-latitudes is comparable to the surface observation. The simulated TCA over Antarctica is larger than the observed one.

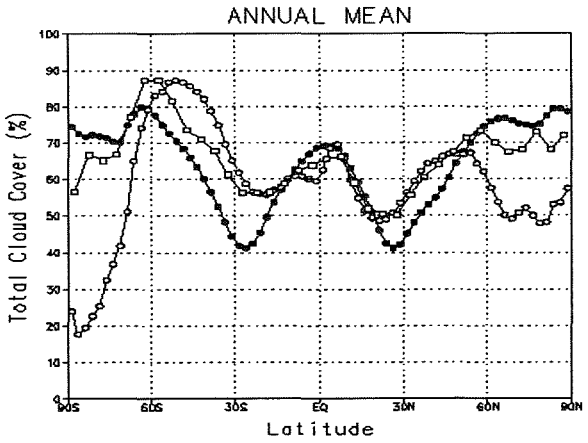

FIGURE 1. Annual and zonally ensemble averaged total cloud amount form ECHAM4 (filled circle), ISCCP (open circle) and SFCC (open square).

3.2 Geographic Distribution

Figures 2a-2c show the geographical distributions of ensemble July mean TCA from ECHAM4, ISCCP, and surface observation, respectively. The TCA pattern of ISCCP and surface observations agree reasonably well except over the Arctic region where larger TCA is found in the ground observations. ECHAM4 underestimates TCA over the mid-latitude oceanic region. The systematic underestimate in TCA also leads to the underestimate of the planetary albedo over these regions (Chen and Roeckner, 1996). TCA over the continents agree well with ISCCP except for the underestimate of cloud amount over the western US. Subtropical cloudiness over the ocean is also generally underestimated. Although a fair amount of marine stratocumulus is simulated off the west coast of continents in the subtropics, it is not extended far enough over the ocean as indicated in the observations. The overestimated TCA in the West Pacific warm pool region is indicative of enhanced water vapor transport in convectively active regions. The excessive large scale subsidence in the equatorial eastern Pacific leads to a slight decrease in the simulated TCA over the ITCZ as compared to the relatively uniform TCA along the ITCZ in ISCCP data.

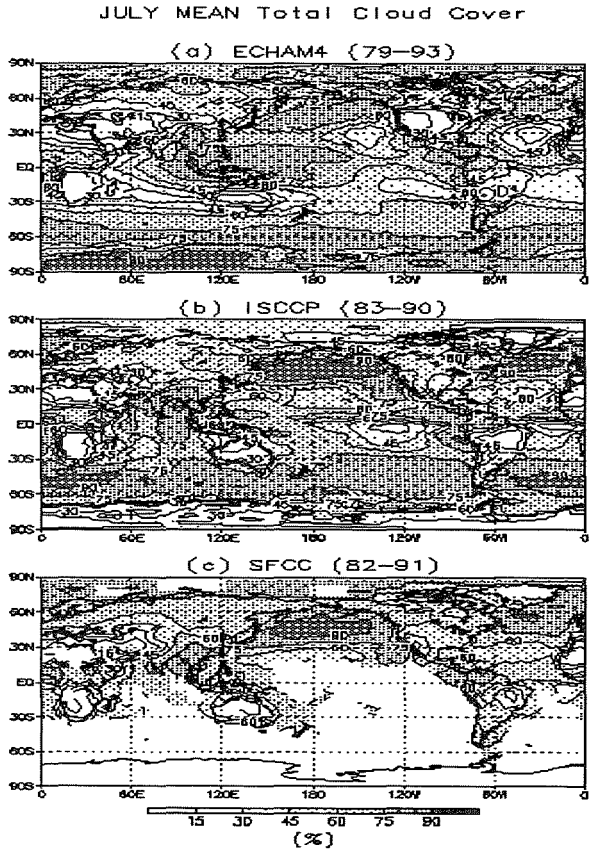

FIGURE 2. Geographic distribution of the ensemble July mean total cloud amount for (a) ECHAM4, (b) ISCCP and (c) surface observations.

The ensemble January mean TCA pattern of ISCCP and SFCC agree reasonably well except over Europe, Russia and Alaska where larger TCA is found in SFCC (not shown). ECHAM4 again reproduced the main pattern of the TCA distribution rather well. Major discrepancies are the underestimate over the midlatitude oceanic regions and overestimate over the northern hemisphere mid-latitude continent. The overestimate is less significant when the model simulation is compared with surface observations. The amount of marine stratocumulus over the subtropical eastern Pacific in ECHAM4 is smaller than the observed. The extent of the simulated maximum TCA (more than 80%) over the Pacific warm pool, ITCZ and SPCZ is broader than in ISCCP. Considerable overestimates are also found over the Arctic and Antarctic regions in ECHAM4. However, the quality of satellite and surface observations is degraded by the problems in the cloud identification over polar regions and limited number of the surface observations, respectively.

4. TOTAL CLOUD LIQUID WATER PATH

ECHAM4 separates the prognostic water cloud into the liquid and ice part according to the ambient temperature. It is a crude empirical method, For a fair comparison, we integrated the liquid part from the prognostic cloud water content to obtain the total cloud liquid water path (hereafter, CLWP).

4.1. Zonal Mean

The latitudinal structure of ensemble annual mean CLWP from the model and SSM/I retrievals is shown in Fig. 3. Both SSM/I retrievals show a narrow local maximum near 5 ^{o}N corresponding to the ITCZ. The higher CLWP found in mid-latitudes in the two observed data coincide with the location of storm tracks and frequent low-cloud occurrence region (Warren et al.1988). Large systematic differences (~30 g/m^2) in the two retrievals are found for almost all latitudes. Near the tropical convergence zone, the model predicts more CLWP than the retrieval from Weng and Grody (1994; hereafter WG94) indicates. However, it is close to the retrievals from Greenwald (1993; hereafter G93). Over the mid-latitudes, the model simulation is closer to WG94. Relatively low contrast in the annual mean CLWP between the subtropics and mid-latitudes is found in the model. The major differences from G93 is the underpredicted CLWP in the summer oceanic mid-latitudes, probably related to the underestimate of cloud amount in the model.

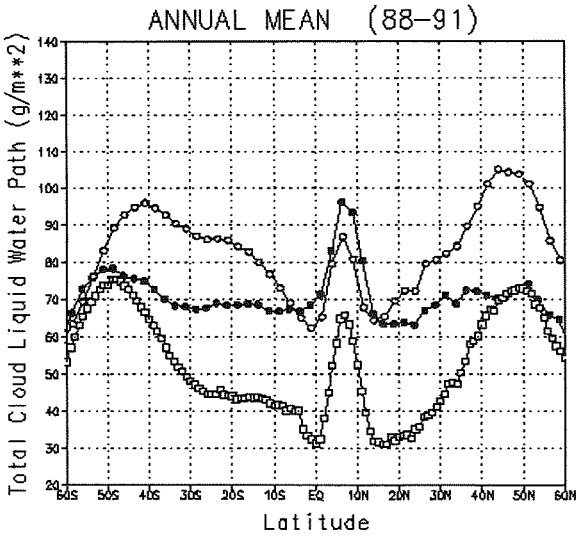

FIGURE 3. Annual and zonally ensemble averaged total cloud liquid water path amount form ECHAM4 (filled circle), SSM/I Greenwald's retrieval (open circle) and SSM/I Weng and Grody's retrieval (open square).

On the other hand, the differences between WG94 and the model data are found mostly in the relatively dry subsidence region.

4.2. Geographic Distribution

Figures 4a-4c show the geographical distribution of ensemble July mean CLWP from ECHAM4, G93, and WG94, respectively. Note that WG94 data has a different horizontal resolution, although this should not affect the comparison of the main features in the CLWP geographical distribution. The main pattern of the observed local maximum CLWP associated with ITCZ and mid-latitude circulation system is predicted by the model. Also differences in CLWP between model and G93 over the mid-latitude and between model and WG94 over the subtropics are similar to those shown in January results. One bias of the pattern in the model is over the subtropical eastern ocean basins. While the minima in CLWP are limited to near the coast in the SSM/I retrievals with a relatively large CLWP further away from the coast corresponding to the prevalence of marine stratocumulus, the model actually has local minima as opposite to the observations in these regions.

The main pattern of observed January CLWP (not shown) is also well captured by the model, especially the location of the ITCZ and the storm tracks. Over the southern ocean, the model simulation is closer to WG94. Considerably larger CLWP in the southern ocean are shown in G93. While similar magnitudes of CLWP from ECHAM4 and G93 are found in the subtropics, lower subtropical CLWP is found in WG94. It should be emphasized that the comparison of the absolute CLWP values from the model and observations does not serve as a strict model validation. Owing to the large uncertainty in the observation and crude separation of liquid and solid phase of cloud water in the model, we limit the scope to whether the reasonable range (from various retrieval algorithms) of cloud liquid water path and the main pattern in geographic distribution can be reasonably captured by the simple parameterization in the model.

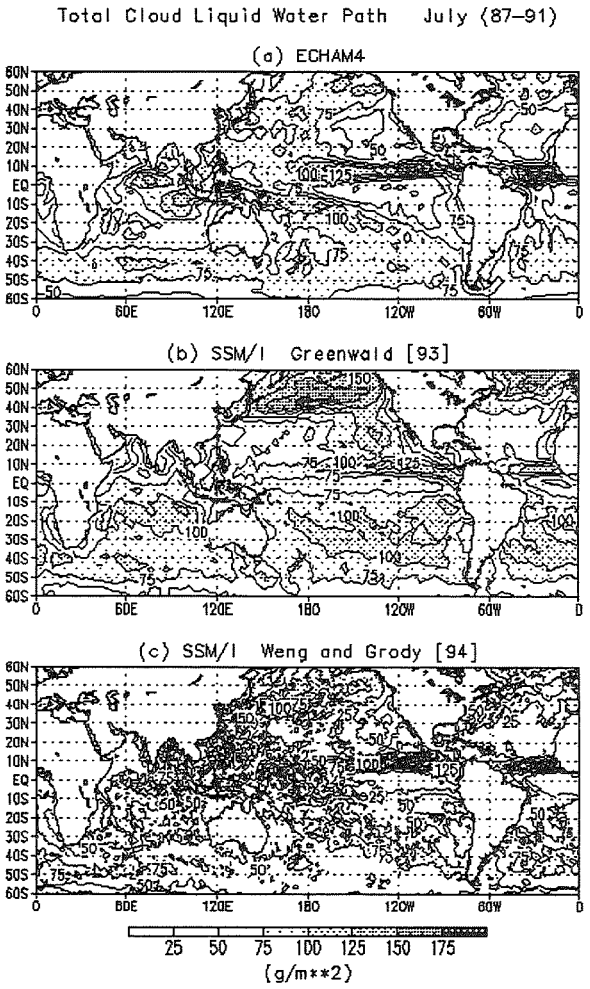

FIGURE 4. Geographic distribution of the ensemble July mean total cloud liquid water path for (a) ECHAM4, (b) SSM/I Greenwald's retrieval, and (c) SSM/I Weng and Grody's retrieval.

5. EFFECTIVE RADII FOR LIQUID WATER CLOUD

A near-global survey of the effective drop radii in water cloud using ISCCP data by Han et al. (1994; hereafter H94) is used to assess the effective drop radius in water cloud predicted in the model, which assumes water droplets are spheres and prescribed the number concentration of cloud droplets separately for cloud formed over the land and ocean.

Figures 5a and 5b show the monthly mean effective cloud radii in July 1988 from ECHAM4 and H94, respectively. Strong land sea contrast is found in most of the observational data except in the active convective centers over land and particularly in regions where monsoonal circulations dominate. (H94). The land-sea contrast in cloud droplet number concentration in the model can not include mechanisms such as the influences from the air mass advection across the coastline or reduced drop number concentration from frequent precipitation area. However, the ECHAM4 model is able to simulate the magnitude of the water cloud effective radii and the land-sea contrast in the tropics reasonably well. The model indeed predicts smaller drop radii off the west coast of the continents, although it is extended further away from coast. The model result is due to the relatively small CLWP as simulated in the model (Fig. 4). The larger effective radii in the convective region over land is absent in the model, because of the limitation of the parameterization as indicated above. Other significant differences are found over the mid-latitude oceans in the northern hemisphere. The comparison reveals the shortcoming of the model parameterization and points to the direction for further improvement. The definition of effective radii for water cloud is not exactly the same in the model and the observations. The methodology for comparison of cloud effective radii inferred from observation and simulated in the model also deserves further investigation.

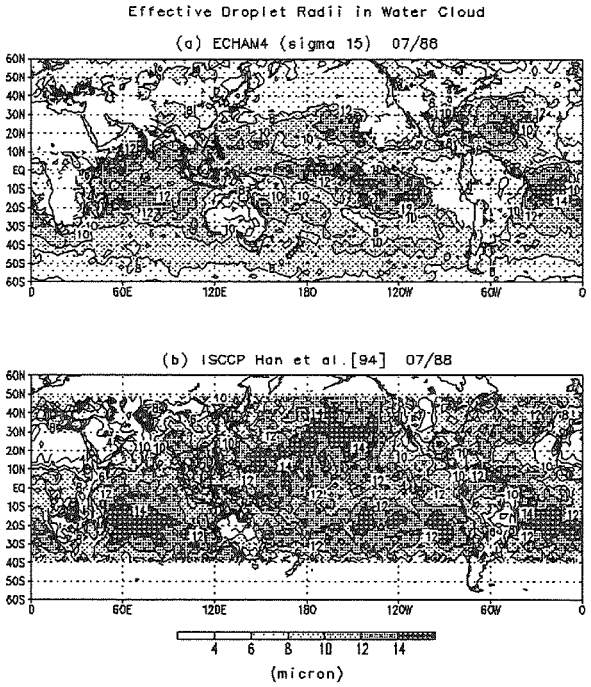

FIGURE 5. Geographic distribution of the 1988 July mean effective droplet radii in water cloud for (a) hybrid vertical level 15 in ECHAM4 and (b) ISCCP [Han et al., 1994].

6. ACKNOWLEDGEMENTS

We thank T. Greenwald, F. Weng and Q. Han for providing the related data sets. We also thank Lennart Bengtsson and U. Lohmann for helpful discussion.

7. REFERENCE

Chen, C.-T., E. Roeckner, 1996: Validation of the Earth radiation budget as simulated by the Max Planck Institute for Meteorology general circulation model ECHAM4 using satellite observations of the Earth Radiation Budget Experiment, In press, *J. Geophys. Res.*.

Gates, W. L., 1992: AMIP: The atmospheric model intercomparison project, *Bull. Amer. Meteor. Soc.*, **73**, 1962-1970.

Greenwald, T. J., G. L. Stephens, and T. H. Von der Haar, 1993; A physical retrieval of cloud liquid water over the global oceans using special sensor microwave/imager (SSM/I) observation, *J. Geophys. Res.*, **98**, 18471-18488.

Hahn, C. J., S. G. Warren, and J. London, 1994: Climatological data for clouds over the globe from surface observations, 1982-1991: The total cloud edition, *ORNL/CDIAC-72, NDP-026A*, Oak Ridge National Laboratory, Oak Ridge, Tennessee, USA.

Han, Q., W. B. Rossow, and A. Lacis, 1994: Near-global survey of effective droplet radii in liquid water clouds using ISCCP data, *J. Climate*, **7**, 465-497.

Roeckner, E., K. Arpe, L. Bengtsson, S. Brinkop, L. Dümenil, M. Esch, E. Kirk, F. Lunkeit, M. Ponater, B. Rockel, R. Sausen, U. Schlese, S. Schubert, M. Windelband, 1992: Simulation of the present-day climate with the ECHAM model: Impact of model physics and resolution. *Max-Planck-Institut für Meteorologie, Report No.* **93**, Hamburg 171pp.

Roeckner, E., K. Arpe, L. Bengtsson, M. Christoph, M. Claussen, L. Dümenil, M. Esch, M. Giorgetta, U. Schlese, U. Schulzweida, 1996: The Max Planck Institute for Meteorology fourth-generation atmospheric general cir-culation model ECHAM4: Model description and climatology, In preparation.

Rossow, W. B. and R. A. Schiffer, 1991, ISCCP cloud data products, *Bull. Amer. Meteor. Soc.*, **72**, 2-20.

Warren, S. G., C. J. Hahn, J. London, R. M. Chervin, and R. L. Jenne, 1988: Global distribution of total cloud cover and cloud type amounts over ocean, *NCAR/TN-317+STR*, 40pp., 170 maps.

Weng, F. and N. C. Grody, 1994: Retrieval of cloud liquid water using the special sensor microwave imager (SSM/I), *J. Geophys. Res.*, **99**, 25535-25551.

SECULAR REGIME OF CLOUDNESS IN GEORGIA

V.G. Khorguani, R.A. Gvazava

Geophysics Institute, Ac. Sci. of Georgia, M. Alexidze 1,
Tbilisi, 380093, GEORGIA

The cloudness is one of the climate formation factors of our Planet. So the evidents about its statistical characteristics are necessary in order to investigate the change and variations of climate. The systematic observations of the total cloudness over Tbilisi – the capital of Georgia – were made since 1894, since 1924 additionally the lower cloudness was identified. If we make the table and according it consider in amount of cloudness the mean–anniversary amount of the total clouds and clouds of low layer from the beginning of observations up to 1994, we'd not find any outstanding phenomena. Also, it is even difficult to judge about cloudness dynamics. So we have to observe the averaging over the random time interval. The known Steklov's integral function (Akhiezer, 1965) was taken as such averaging. It is known that this function is defined by the continuous or, in the last resort, by the integrated function. Usually the observation of cloudness (the amount of clouds) is made in the definite time of a day, then is averaged over the months and then over the years. Thus, according to the observation data the function of the total cloudness L(t) is not continuous, it is a discrete one. Due to this the function of the total cloudness in the form of Lagrange polynomial was constructed on the basis of the pointed discrete function:

$$L_1(t) = \sum_{\tau=1}^{99} \frac{\prod_{\substack{k=0 \\ k\neq i}}^{99} (t - t_k)}{\prod_{\substack{k=0 \\ k\neq i}}^{99} (t_i - t_k)} \qquad (1)$$

After this step the Steklov's integral averaging in time interval (t_1, t_2) is introduced into the consideration:

$$M(t_1, t_2) = \frac{1}{t_2 - t_1} \int_{t_1}^{t_2} L_1(t)\, dt \qquad (2)$$

With integer values of t_1 and t_2 Eq.(2) coincides with the arithmetic mean of the cloudness in the time interval (t_1, t_2). It is worth noting that this approach was used before to study the secular regime of the net precipitation and surface temperature of air (Gvazava, 1988; Gvazava, Khorguani, 1989).

The L(t) function was constructed according to the table data on the total amount of clouds. Then the numerical values of $M(t_1, t_2)$ were estimated. This function describes the distribution of the total amount of clouds in the random time interval from t_1 to t_2 and thereby characterizes its distribution as a whole.

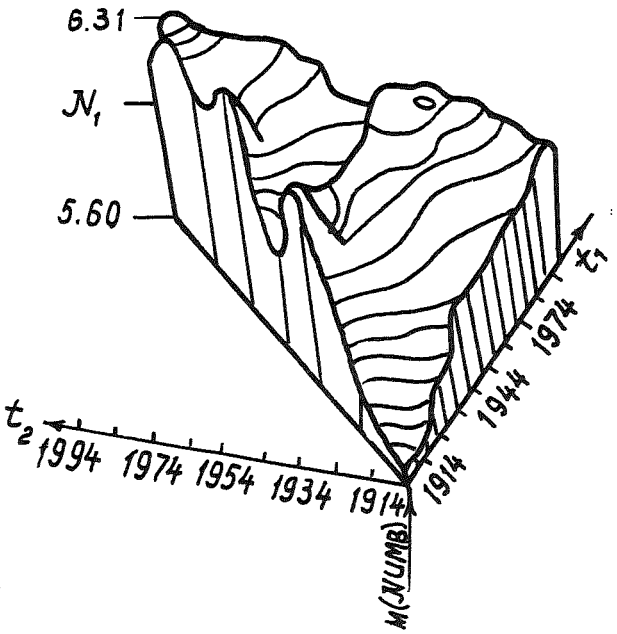

Fig.1. Plot of averaged function of total cloudness M (null level corresponds to total cloudness of 5.6 numbers).

Fig.1 gives a plot of the averaged function of the cloud amount $M(t_1, t_2)$. As one can see that $M(t_1, t_2)$ function is symmetrical about its

arguments, i.e. $L(t_1, t_2) = L(t_2, t_1)$. Taking this into account at the graphical presentation of the function in the three-dimensional space of the variable values t_1, t_2, M we limited our consideration by $t_1 > t_2$ case. It is enough for our aims. Fig.1 shows that the norm of the total cloudness is 6.1 numbers per year. At the same time the increase of the total cloudness with time takes place.

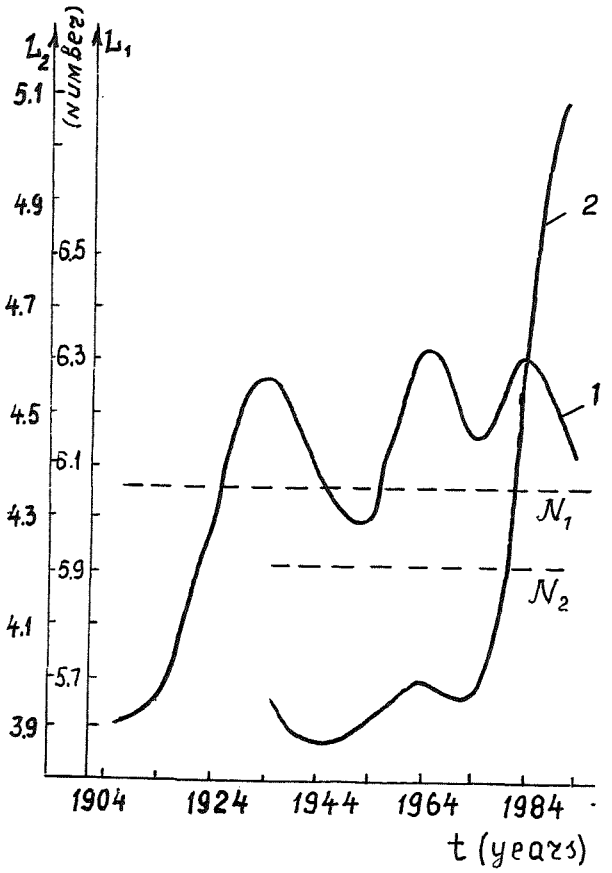

Fig.2. Total cloudness L_1 (curve 1) and lower layer cloudness L_2 (curve 2) in numbers averaged over the decades.

Fig. 2 shows the functions of the total L_1 and lower L_2 cloudness averaged over the decades. The figure shows also the increase of the total cloudness in particular during 3 last decades. The maximum increase in comparison with the norm is 0.3 numbers.

The cloudness of the lower layer is of special interest. For this cloudness the norm of cloud amount is 4.2 numbers and the difference between maximum value of the lower cloudness and the norm is 0.9 numbers. The growth of the cloudness is pronounced during 2 last decades. So large increase of cloudness of lower layer is thought to be induced by the anthropogenic pollution of atmosphere. Furthermore, the anthropogenic aerosols polluting our atmosphere contain in excess the active nuclei of condensation and ice-forming nuclei which at the specific stratification of atmosphere promote the cloud formation in lower layer, in particular.

REFERENCES

Akhiezer N.I., 1965: The lectures on approximation theory, M. Nauka, 477 p. (in Russian).

Gvazava R.A., 1988: Features of atmospheric regime in Tbilisi since middle of last century up to nowdays. Bull. Ac. Sci. Georgia, 130, 2, 323-325 (in Russian).

Gvazava R.A., Khorguani V.G., 1989: On the secular regime of surface air temperature in Tbilisi. M.Meteorology & Hydrology, 11, 111-113 (in Russian).

ICE PARTICLE DENSITY EFFECT ON THE REFLECTANCE AND TRANSMITTANCE OF CIRRUS

Chun-Lei Liu[1], Anthony J. Illingworth[1] and Peter R. Jonas[2]

[1] JCMM, Department of Meteorology, University of Reading, Reading, RG6 2AU, UK
[2] Department of Pure and Applied Physics, UMIST, Manchester, M60 1QD, UK

1. INTRODUCTION

Cirrus clouds play an important role in earth's climate, through the modification of the radiation field of the earth-atmosphere system. Due to the lack of observational data, the ice crystal particle density in cirrus has often been assumed to have the constant value of solid ice in previous studies of cirrus cloud radiative properties, but from recent field observations, the ice particle density in cirrus is found to decrease with the increase of the particle size (Brown and Francis, 1995), due to the air inside the aggregated large ice particles. This density variation will affect the particle bulk optical properties by modifying the refractive index, particularly for cases when the median particle size D_o (defined so that there are equal particle volumes greater than and less than D_o for given particle size spectrum) is large; the large particles with lower density will contribute more to the bulk particle optical properties.

The purpose of this paper is to study the effect of different particle density assumptions on cirrus reflectance and transmittance at visible and infrared wavelengths using a Monte Carlo model (Jonas, 1993). Two density assumptions are used: Firstly, solid ice: ρ_1=0.92g/cm^3, and secondly: ρ_2=0.07D$^{-1.1}$ g/cm^3 (where D is in millimetres) for D>100μm and ρ_2= ρ_1 for D<100μm (Brown and Francis, 1995). It is difficult to describe the shape of these large low density particles precisely, but 2-D probe aircraft data suggest they are quasi-spherical, so, following Intrieri *et al.* (1994), the spherical particle assumption is used here for fast and exact particle optical parameter calculation from Mie theory.

2. MODEL

The Monte Carlo model is based on those of McKee and Cox (1974) and Jonas (1993). By tracing the individual incident photons during their path through the cirrus cloud, the reflectance and transmittance (defined as the fraction of the incident radiation which emerges from the cloud travelling upwards and downwards, respectively) of the cirrus cloud for visible (0.54 μm) and infrared (2.24 μm) wavelengths can be calculated. For the visible wavelength of 0.54 μm, the absorption can be neglected, and the photons are traced until they emerge from the cloud. For the infrared wavelength of 2.24 μm, there is absorption, and the photons are traced until its weight is 10^{-6} of the original weight. The refractive indices of solid ice particles at these two wavelengths are 1.311-*i*2.814x10^{-9} and 1.258-*i*3.664x10^{-4}, respectively (Warren, 1984), and the lower density ice particle refractive index at these two wavelengths can be calculated from the Maxwell-Garnett formula (1904). The photon paths between the scattering events are randomly determined according to the volume extinction coefficient, and the scattering direction is also randomly determined based on the particle bulk scattering phase function cumulative angular distribution. The cirrus cloud studied here is a finite cloud having horizontal dimension of 50 km, and the cloud thickness varies from 1 to 5 km for D_o=120 μm, and from 0.1 to 1 km for D_o= 400 μm. Though the cirrus cloud is very inhomogeneous spatially, it is still treated as homogeneous here, in order to emphasize our aim of investigating the particle density effect on the cloud reflectance and transmittance. Other input parameters to this Monte Carlo model are the incident photon number 2x10^6, and the incident solar angle (assumed to be 0°, 30° and 60°).

For an ice crystal size distribution n(D) represented by the exponential,

$$n(D) = N_o e^{-3.67\frac{D}{D_o}}$$

the phase function for a sample of ice crystal of different sizes may be obtained from

$$P(\theta) = \frac{\int_{D_1}^{D_2} P'(\theta, D) C_s(D) n(D) dD}{\int_{D_1}^{D_2} C_s(D) n(D) dD}$$

where D_o and N_o are constants, related to size spectra shape and total IWC (ice water content), respectively. C_s is the particle scattering cross section, and $P'(\theta, D)$ is the phase function for ice particle of diameter D. D_1 and D_2 are the lower and upper limits of ice particle size, they are assumed to be 2μm and 4000μm, respectively.

3. RESULTS

In order to see the density effect on bulk particle optical properties, for particle density ρ_1 and ρ_2, the corresponding total scattering coefficient (σ_{s1} and σ_{s2}) and backscattering coefficient (σ_{b1} and σ_{b2}) are calculated using same ice particle size distribution, which implies that the number density is constant, but the IWC varies with different particle density assumptions during our calculations. The coefficient ratios r_s ($=\sigma_{s1}/\sigma_{s2}$) and r_b ($=\sigma_{b1}/\sigma_{b2}$) at visible and infrared wavelengths are plotted in Figure 1. It can

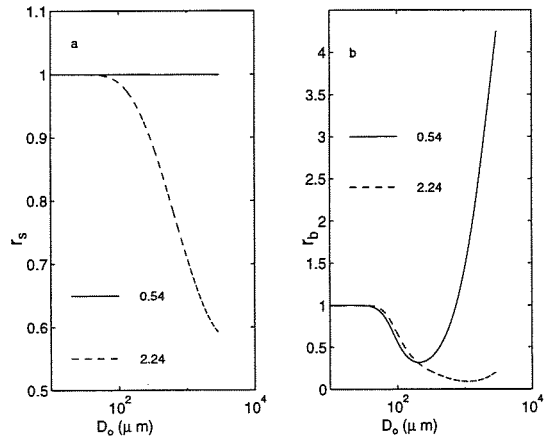

Figure 1. Total scattering and backscattering coefficient ratio variations with D_o. The wavelengths are 0.54μm and 2.24μm, respectively.

be seen that when D_o <70μm, the ratios are equal to 1. This is due to the small particles which have the density of solid ice dominating the size spectra. When D_o increases, for visible wavelength, because the particle size parameter is large, the scattering efficiency is always close to 2, regardless of the particle density, so the ratio is 1; for infrared wavelength, large particles have a relatively weak absorption due to a decrease in the imaginary part derived from the lower particle density, so there is stronger scattering than for the solid ice density assumption, and so the ratio is less than 1.

The backscattering coefficient ratio for large D_o is very different from one, particularly at visible wavelengths. The reason for this is still under investigation. These differences due to different particle density assumptions will result in different cirrus cloud reflectance and transmittance at visible and infrared wavelengths.

3.1 Visible wavelength

The phase function and its cumulative angular distributions are plotted in Figure 2, for D_o=120 and 400 μm, respectively. There are only slight differences between the phase functions of different particle density assumptions. From Takano and Liou (1989), the ice crystal number density in different cirrus clouds are about 0.2 cm^{-3}, and for D_o=120 and 400 μm, the corresponding extinction coefficients are of the order of 10^{-4} m^{-1} and 10^{-3} m^{-1}, respectively.

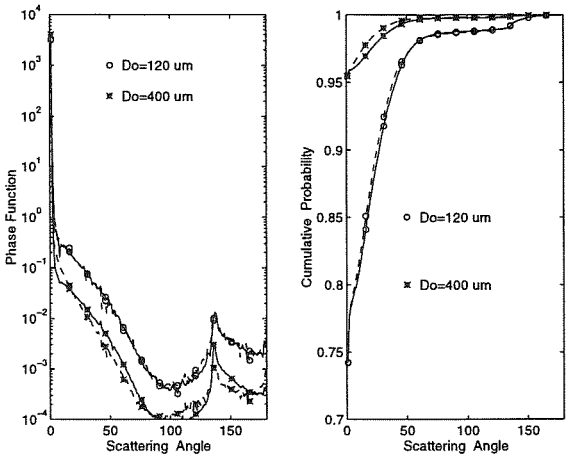

Figure 2. Phase function and its cumulative probability angular distributions. Particle densities are assumed to be ρ_1 (solid line) and ρ_2 (broken line), respectively.

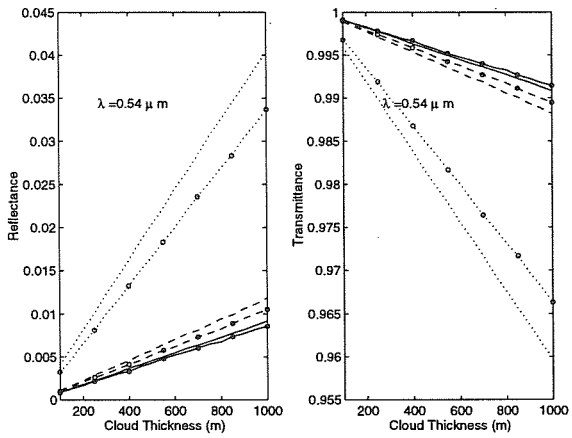

Figure 3. The reflectance and transmittance variations with cloud thickness, for incident solar angle of 0° (solid line and solid line with circle), 30° (broken line and broken line with circle), and 60° (dotted line and dotted line with circle).

The reflectance and transmittance variations with cloud thickness is plotted in Figure 3 for D_o=400μm, and for incident solar angles of 0°, 30° and 60°, respectively. The lines with and without circles are for ρ_2 and ρ_1, respectively. There are differences between these results for different particle density assumptions. As expected, the reflectance increases with the increase of incident solar angle. The reflectance is much smaller than transmittance due to the small volume extinction coefficients considered here.

If X and Y are reflectances (or transmittances) of cirrus cloud consisting of ice particles of density ρ_1 and ρ_2, respectively, then the fractional error defined as |X-Y|/|X| (plotted in Figure 4) is a measure of the percentage differences due to the density difference. For the reflectance error (Figure 4a) with D_o=120 μm, the smaller incident solar angle gives a larger error, this is partly due to the small reflectance value. It is also noted that the reflectance error is nearly constant with the increase of the cloud thickness due to thin cloud optical depth. The transmittance error increases with the increase of the cloud thickness, and also with the large incident solar angle, but the overall transmittance error is very small because most of the incident photons are transmitted through the cirrus cloud having small volume extinction coefficient. Considering results of Figures 3 and 4, it is expected that the error of solar fluxes at the top or bottom of the cirrus cloud is very small using different particle densities, for the case considered here.

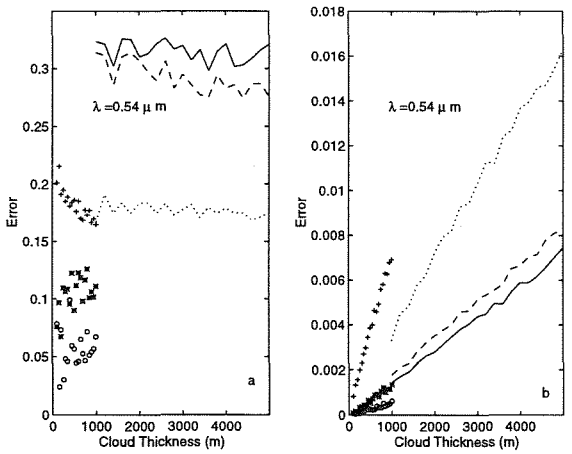

*Figure 4. Reflectance and transmittance fractional error variations with cloud thickness for various incident solar angles θ, and for D_o=120μm (— : θ=0°, ---- : θ=30°, ... : θ=60°) and 400 μm (o : θ=0°, * : θ=30°, + : θ=60°), respectively.*

3.2 Infrared wavelength

Some of the incident photons will be absorbed by the cloud at the wavelength of 2.24μm, but because of the small cloud extinction coefficient considered here, the absorption will not have too much effect on the reflectance and transmittance. In order to investigate the difference of these values at different incident wavelengths, the above procedures for visible wavelength are repeated here for wavelength λ=2.24μm. The phase function and its cumulative angular distributions are plotted in Figure 5 for D_o=120 and 400 μm, respectively. There are only slight differences between the phase functions with

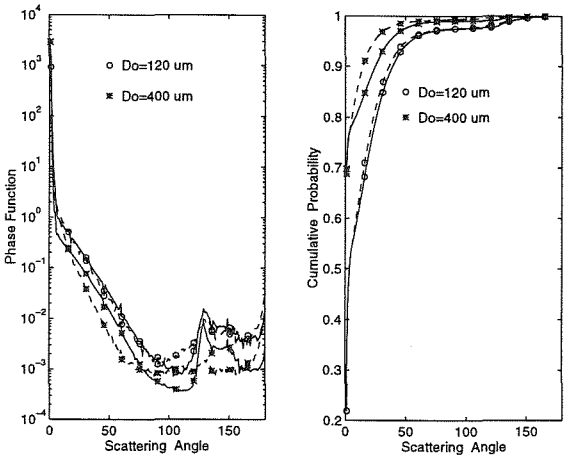

Figure 5. Phase function and its cumulative probability angular distributions at λ=2.24μm. Particle densities are assumed to be ρ_1 (solid line) and ρ_2 (broken line), respectively.

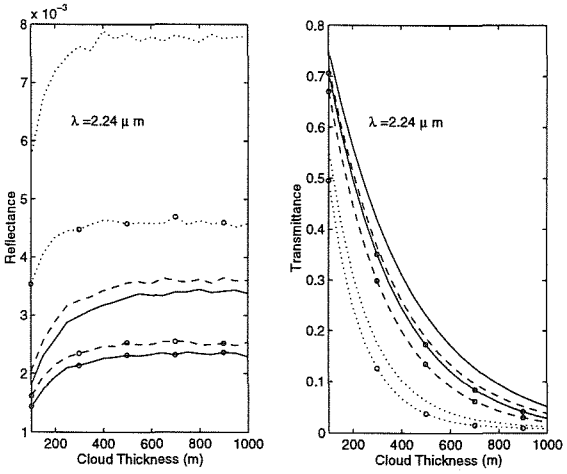

Figure 6. The reflectance and transmittance variations with cloud thickness, for incident solar angle of 0° (solid line and solid line with circle), 30° (broken line and broken line with circle), and 60° (dotted line and dotted line with circle).

different particle density assumptions. The cumulative probabilities for different D_o are smaller than those at visible wavelength.

The reflectance and transmittance variations with cloud thickness at this wavelength is plotted in Figure 6 for D_o=400 μm, and for incident solar angles of 0°, 30° and 60°, respectively. The lines with and without circles are for ρ_2 and ρ_1, respectively. The trend of the results are very similar to those at λ=0.54μm. Because some photons are absorbed, the transmittance decreases rapidly with the increase of the cloud thickness. The reflectance value is also very low. Figure 7 is the plot of the fractional errors. The results show that for reflectance (Figure 7a), the error decreases with the increase of the cloud thickness for D_o=120 μm, but it increases with the increase of the cloud thickness for D_o=400 μm. The transmittance (figure 7b) increases as the increase of cloud thickness, and this transmittance error is big relative to the transmittance value, so it will result in large energy flux error. It is also noted that the reflectance and transmittance error are of the same magnitude.

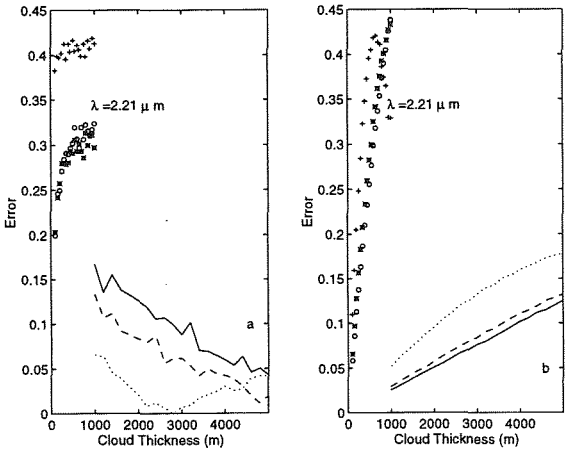

*Figure 7. Reflectance and transmittance fractional error variations with cloud thickness for various incident solar angles θ, and for D_o=120μm (— : θ=0°, ---- : θ=30°, ... : θ=60°) and 400 μm (o : θ=0°, * : θ=30°, + : θ=60°), respectively.*

4. CONCLUSIONS

Two wavelengths considered in this paper are representative of visible and infrared solar radiation wavelength ranges, respectively. For the visible wavelength case considered here, the different particle density causes only a small error in the solar energy fluxes at the top and bottom of the cirrus cloud. For the infrared wavelength case, this error is small for the reflectance, but is large for the tramsmittance (see Figure 7b).

It may be concluded that the infrared transmittance through cirrus cloud will be affected by using different ice particle densities, which will result in large uncertainty of the input optical parameters in a climatic model. It is expected that this uncertainty will be worse for a large median particle diameter D_o. This effect will result in errors in solar energy flux calculations at the top and bottom of cirrus clouds, and affect the calculation of the energy balance of the earth-atmospheric system, therefore it could affect models used for predicting climate change.

ACKNOWLEDGEMENTS

This work has been supported by NERC grant GR3/8765, ESTEC 10568/93 and CEC EV5V CT94-0463.

REFERENCES

Brown, P. R. A., and P. N. Francis, 1995: Improved Improved measurement of the ice water content in cirrus using a total water evaporator. *J. Atmos. Oceanic technol.*, **12**, 410-414.

Intrieri, J. M., G. L. Stephens, W. L. Eberhard, and T. Uttal, 1993: A method for determining cirrus cloud particle sizes using lidar and radar backscatter techniques.*J. Appl. Met.*, **32**, 1074-1082.

Jonas, P. R., 1992: Some effects of spatial variations of water content on the reflectance of clouds. *Ann. Geophys.*, **10**, 260-266.

Maxwell-Garnett, J. C., 1904: Colours in metal glasses and in metallic films. *Philos. Trans. R. Soc.*, **A203**, 385-420.

McKee, T. B., and S. K. Cox , 1974: Scattering of visible radiation by finite clouds. *J. Atmos. Sci.*, **31**, 1885-1892.

Takano, Y., and K. N. Liou, 1989: Solar radiation transfer in cirrus clouds. Part I: Single-scattering and optical properties of hexagonal ice crystals. *J. Atmos. Sci.*, **46**, 3-19.

Warren, S. G., 1984: Optical constants of ice from the ultraviolet to the microwave. *Appl. Optics*, **23**, 1206-1225.

THE INFLUENCE OF IN-CLOUD CHEMICAL REACTIONS ON OZONE FORMATION IN CLOUDY ATMOSPHERES

Chris J. Walcek and Hong-H. Yuan

State University of New York, Albany, New York, U. S. A.

1. INTRODUCTION

Ozone (O_3) is a harmful secondary air pollutant produced during the photochemical oxidation of organic hydrocarbons in the presence of nitrogen oxides ($NO+NO_2=NO_x$). Previous studies of O_3 pollution consider only gas-phase reactions among pollutants. However, several recent cloud chemistry studies (Jacob, 1986; Lelieveld & Crutzen, 1990) show that chemical processes occurring in clouds significantly influence O_3 formation. Unfortunately, existing studies on the influence of heterogeneous-phase chemistry on O_3 formation have examined only a limited set of chemical conditions, and have not considered the effects of clouds under polluted conditions.

In this study, we apply a comprehensive photochemical reaction model that includes several important aqueous-phase reactions to a wide range of pollutant concentration conditions. Ozone chemistry is examined under conditions when the concentrations of primary pollutants NO_x and NonMethane HydroCarbons (NMHC) range from heavily polluted to cleaner, more remote conditions.

2. HETEROGENEOUS CHEMISTRY MODEL

Aqueous-phase equilibria and reactions identified by Jacob et al., (1989) are coupled with the gas-phase reaction mechanism of Stockwell et al., (1990) to define a comprehensive *heterogeneous* reaction mechanism capable of simulating O_3 formation in clouds. The model is initialized with a mix of primary pollutants representative of air in a midlatitude summertime boundary layer (40°N, 20 June, 15°C, 100% Rh). Noon-time, clear-sky photolysis rates are used.

The box model used for subsequent calculations simulates chemical processes only (no removal or additional emissions) for a parcel of air that has been given an initial emission dose of NO_x and NMHC pollutants. The model is first used for a series of short-term (30 min.) simulations, designed to understand how cloud chemical processes affect chemistry at individual points in the polluted atmosphere. Following this, longer simulations are performed investigate the possible longer-term and larger-scale impacts of heterogeneous chemistry on the ozone budget in the lower troposphere.

3. SHORT-TERM, LOCAL IMPACTS

In order to understand the influence of aqueous-phase chemistry at a wide range of NO_x and NMHC concentrations, the model is integrated forward in time for 30 minutes, during which highly reactive, short-lived chemicals reach a photo-chemical steady-state, while longer-lived primary pollutants remain close to specified

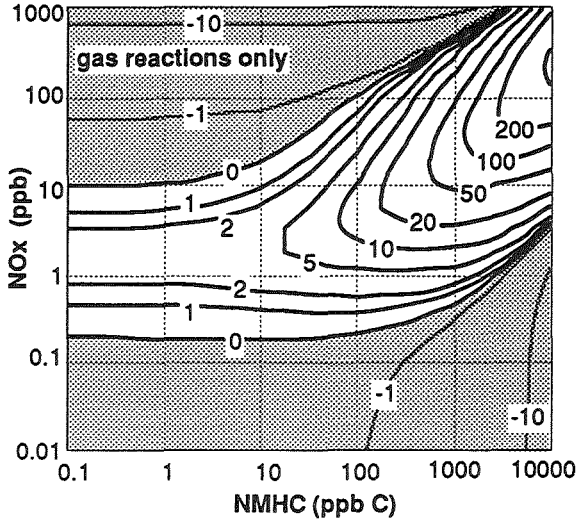

Figure 1. Ozone formation rate (ppb h^{-1}) as a function of the concentration of NO_x and NMHC. Gray areas denote regimes of net ozone destruction.

initial values. O_3 formation rates are averaged during the last 10 minutes of the integration period. Thus the model calculates local chemical tendencies for atmospheric constituents at individual "points" in a polluted boundary layer. Fig. 1 shows O_3 formation rates as a function of the concentration of NO_x and NMHC considering only gas-phase chemical reactions. O_3 forms most efficiently when [NMHC] = 10-100 x [NO_x], and its formation rate increases with increasing concentrations of both precursors. When NO_x concentrations fall below about 0.2 ppb, O_3 is slowly destroyed by its photolysis and reaction with HO_2. Gray areas on Figs. 1&2 denote areas where ozone formation via NO_x-catalyzed reactions is insufficient to balance its slow photochemical destruction. At NO_x concentrations greater than 10 - 100 ppb, there is insufficient HO_x to catalyze ozone formation, since the radical sink reaction $HO + NO_2 \rightarrow HNO_3$ efficiently removes HO_x from the atmosphere. In the atmosphere over the eastern U. S., NO_x concentrations range from a few tenths of a part per billion in areas remote from major cities, to 10-100 ppb in urban areas. Hydrocarbon concentrations are typically 10-100 times greater than NO_x, but rarely fall below about 10 ppb carbon.

Fig. 2 shows O_3 formation rates within a cloud (liquid water content=0.5 g m^{-3}, pH=4) where additional aqueous-phase reactions occur. All other factors are the same as the conditions considered in Fig. 1. There is a dramatic shift in the shape of the O_3 formation contours, and overall, O_3 formation rates are considerably reduced by the additional heterogeneous reactions.

Fig. 3 shows the relative difference between O_3 formation rates with and without in-cloud heterogeneous

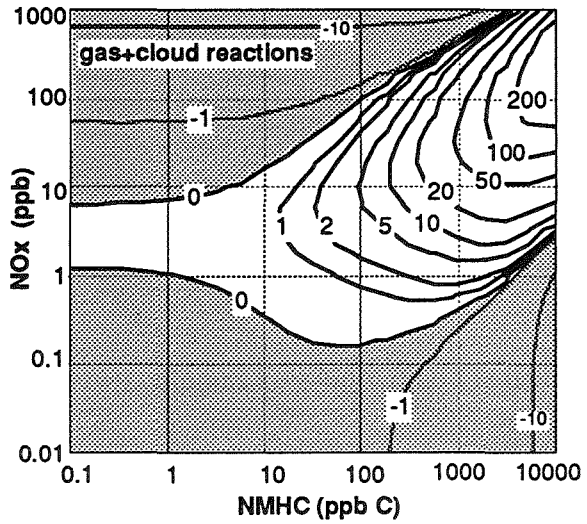

Figure 2. Same as Fig. 1 except both gas and aqueous-phase chemical reactions considered.

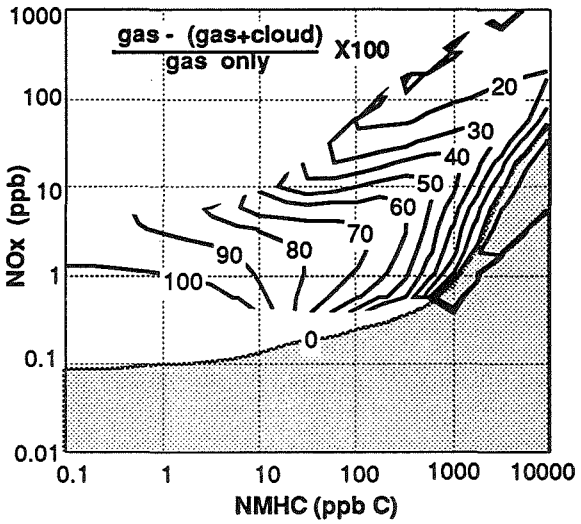

Figure 3. Percent difference between Figs. 1&2. Percent differences only shown when gas-phase $\partial O_3/\partial t > 1$ ppb h^{-1}. Gray area shows regime where O_3 derivatives are enhanced by aqueous reactions.

reactions considered. Heterogeneous reactions suppress O_3 formation rates by 20-100% under a wide range of NO_x and NMHC concentrations, consistent with earlier studies in remote areas. However, there are regimes where in-cloud reactions enhance O_3 formation in the atmosphere, denoted as shaded areas of Fig. 3.

O_3 formation in polluted areas is largely governed by the following catalytic NO_x reaction cycle:

$$NO_2 + \text{sunlight} \xrightarrow{O_2} NO + O_3 \quad (1)$$

$$NO + HO_2 \rightarrow NO_2 + HO \quad (2)$$

with reaction (2) being the rate-limiting step in this sequence. NO concentrations are determined by local photostationary equilibria, and therefore the overall O_3 formation rate is controlled by the concentration of hydroperoxy radical (HO_2). Analysis of our reaction mechanism shows that the dominant influence of in-cloud chemical reactions is to dramatically reduce HO_2 concentrations by 20 - 90% via the following reactions of dissolved HO_2 (O_2^- is an ionized form of HO_2):

$$O_2^-(aq) + Cu^{2+} \rightarrow Cu^+ + O_2 \quad (3)$$

$$O_2^-(aq) + Cu^+ \xrightarrow{H_2O} Cu^{2+} + H_2O_2 + 2OH^- \quad (4)$$

$$O_2^-(aq) + O_3 \rightarrow HO + 2O_2 + HO^- \quad (5)$$

$$HO_2(aq) + O_2^-(aq) \xrightarrow{H_2O} H_2O_2 + O_2 + HO^- \quad (6)$$

Most other aqueous reactions were found to have a relatively minor impact on ozone formation. Even without copper, reactions (5-6) reduce HO_2 and O_3 formation rates by 60-70% over a wide range of pollution conditions. Reactions (5-6) also occur in the gas-phase, and the "effective" rate coefficient is a factor of 10^2-10^3 (depending on temperature and pH) faster under in-cloud conditions. Therefore, there is a much greater potential for HO_2 destruction when clouds are present.

Under some high NMHC, low NO_x conditions, the gray regions on Fig. 3 show that O_3 derivatives are enhanced by aqueous-phase reactions. In these regimes, O_3 is destroyed by its reaction with HO_2:

$$HO_2 + O_3 \rightarrow HO + 2O_2 \quad (7)$$

and aqueous-phase reactions destroying HO_2 significantly reduce the O_3 destruction rate.

4. LONGER-TERM, REGIONAL IMPACTS

Since concentrations of HO_2 are so dramatically reduced by aqueous-phase reactions, there will be corresponding reductions in the concentrations of HO radical and therefore the rate at which longer-lived NO_x, O_3 and NMHC are oxidized in the atmosphere. Therefore, there is a significant feedback between the occurrence of aqueous-phase reactions in the atmosphere and the concentrations of ozone and ozone precursors.

In order to obtain a crude estimate of how in-cloud reactions influence longer-term or larger-scale distributions of O_3 in the atmosphere, we integrate our box chemical model forward in time for a longer period, until all the NO_x and much of the NMHC precursors are oxidized. Non-chemical processes such as deposition or additional emissions are neglected, in order to ascertain only the effects chemical processes on ozone concentrations. Essentially, we "follow" a parcel of air that has been given an initial dose of O_3 precursors for 48 hours, during which most of the O_3 precursors become oxidized, and ozone formation ceases. For this longer-term simplified numerical experiment, photolysis rates and other meteorological factors are held constant. These longer-term simulations are carried out primarily to gain some preliminary insights into how mixtures of emitted pollutants behave over longer time scales in the atmosphere.

Fig. 4 shows how concentrations of NO_x (Fig. 4a) and O_3 (Fig. 4b) change over a two day integration for two pollutant concentration conditions. Fig. 4b shows ozone concentrations under "pristine" conditions (0.01 ppb NO_x, 0.1 ppbC NMHC) and slightly more "polluted" conditions (1 ppb NO_x; 10 ppbC NMHC). The solid curves show the time evolution considering gas-phase reactions only, and the dashed curves show the evolution when aqueous reactions occur. Under very clean conditions, ozone is not even produced, and is slowly destroyed by its photolysis and reaction with HO_2. Under slightly polluted conditions, there is a burst of ozone formation while NO_x concentrations are above about 100-200 ppt, during the first 3-4 hours after emission.

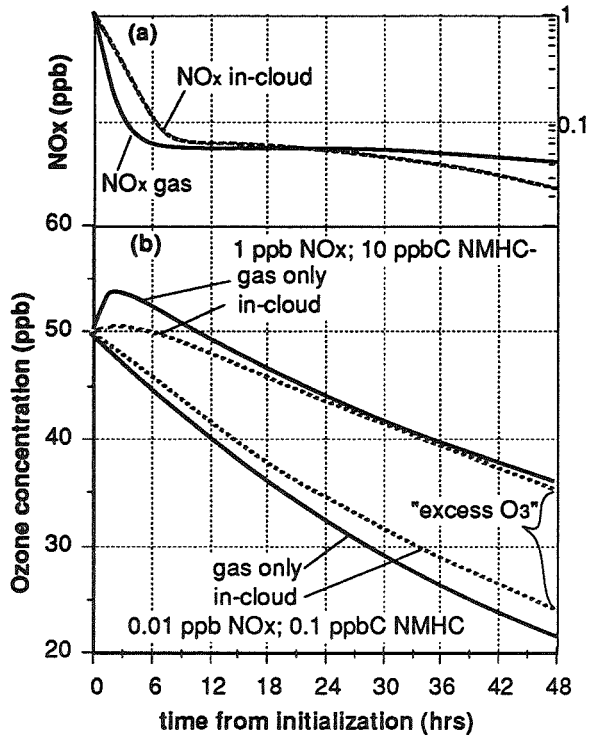

Figure 4. (a) NO_x and (b) O_3 concentrations within an air parcel during 48-hours of continuous noon photolysis conditions for pristine (0.01 ppb NO_x, 0.1 ppbC NMHC) and more polluted (1 ppb NO_x 10 ppbC NMHC) conditions. Excess O_3 is defined as the additional ozone in the polluted case minus the ozone in the pristine case. Model is run with (in-cloud) and without (gas only) heterogeneous reactions.

Once NO_x is depleted, ozone concentrations fall off as in the extremely clean case. Initially, ozone is much more rapidly formed under cloud-free conditions, but NO_x is also oxidized much faster. Fig. 4a shows that NO_x concentrations are depleted after 3-4 hours of continuous noon photolysis conditions with only gas-phase reactions occurring. In contrast, when both gas and aqueous reactions are occurring, it takes 8-9 hours for NO_x to become oxidized. During those additional 3-4 hours, ozone tendencies are elevated when aqueous reactions are occurring relative to the simulation where aqueous reactions are neglected.

On Fig. 4b, we define "excess O_3" as the amount of ozone within an air parcel above "pristine" conditions. This excess O_3 results from the addition of NO_x and NMHC pollutants to the atmosphere. Within a period of less than two days, the excess ozone approaches an approximately constant value, and if this "excess O_3" is divided by the concentration of initial NO_x, one can define the Ozone Production Efficiency (OPE), a measure of ozone precursor reactivity used by previous researchers (Liu et al., 1987). OPE is defined as the number of ozone molecules produced per NO_x molecule emitted.

Over a wide range of initial NO_x and NMHC concentrations, Figs. 5-6 shows the O_3 production efficiency calculated using only gas-phase reactions (Fig. 5) or both gas and aqueous-phase reactions (Fig. 6). In both Figs. 5-6, the lower left corner of the figure is defined to have an OPE of zero. The shapes of the ozone production efficiency are only slightly modified, and therefore the percent difference between Figs. 5&6 is

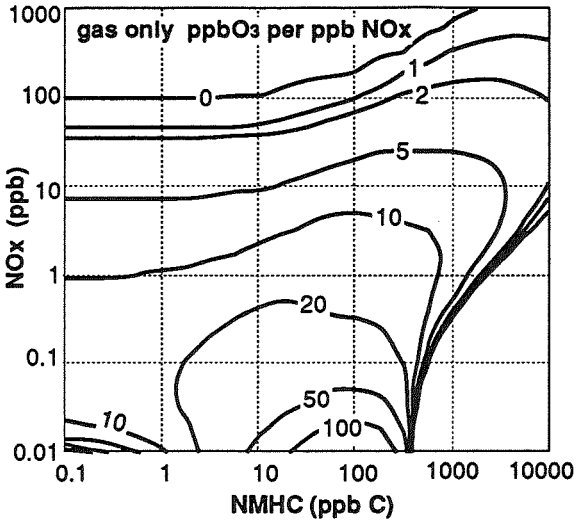

Figure 5. O_3 production efficiency (molecules of O_3 formed per molecule of NO_x emitted) after NO_x oxidized to HNO_3. Only gas-phase reactions considered.

shown in Fig. 7. Gray areas on Fig. 6-7 show regimes where ozone production is enhanced by aqueous-phase reactions. The percentage changes for longer-term ozone formation shown in Fig. 7 are in the range of several tens of percents, and there are regimes where aqueous reaction both enhance and inhibit ozone formation. These longer-term results are a sharp contrast to the local impacts of aqueous processes shown in Fig. 3, where ozone formation rates were generally reduced by 50-80%.

The significantly reduced impact of cloud-phase reactions over longer time scales results from two compensating effects. At high pollutant concentrations, ozone formation rates are significantly reduced by aqueous-phase reactions occurring in clouds. However, as NO_x concentrations fall below a few tenths of a part per billion, ozone is normally slowly destroyed, and additional aqueous-phase reactions reduce the ozone destruction rate. Thus, cloud reactions inhibit both ozone formation and destruction simultaneously, and sometimes

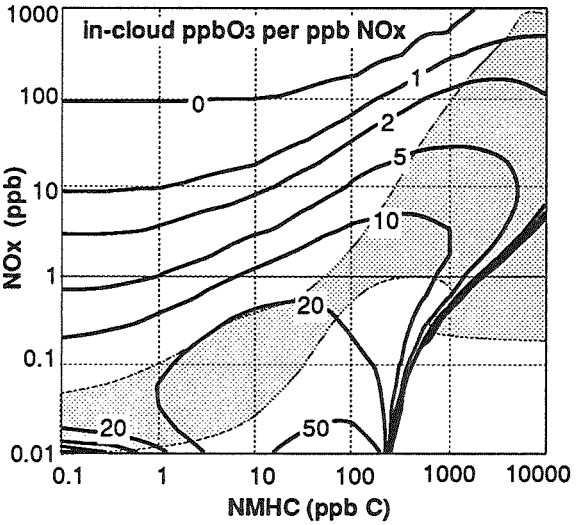

Figure 6. Same as Fig. 5, except aqueous-phase reactions allowed to occur. Gray areas denote regions where OPE is higher when aqueous reactions occur.

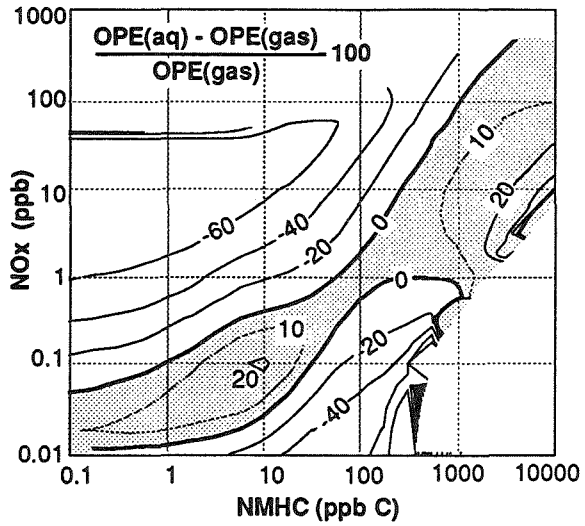

Figure 7. Percent difference in OPE for atmosphere where in-cloud radical reactions are allowed to occur relative to atmosphere where only gas-phase reactions occur. Gray areas denote regimes where aqueous-phase processes enhance OPE.

this results in lower net ozone formation, and under other conditions this results in enhanced ozone formation over longer time scales.

Ozone production efficiencies calculated in this study assume continuous cloudiness during the entire time it takes NO_x and NMHC precursors to become oxidized. In the atmosphere, the average residence time of air parcels in clouds might approximately equal the cloud volume fraction, about 10-30% for the lower troposphere. The changes in ozone formation shown in Fig. 7 therefore represent an upper limit for the influence of in-cloud chemistry on ozone formation in the atmosphere. In-cloud chemical reactions would change overall atmospheric O_3 concentrations by the cloud fraction multiplied by the percentage changes noted in Fig. 7. Therefore, we expect to see changes on the order of 1-10% in global-scale O_3 budgets resulting from the addition of aqueous-phase reactions to global models of ozone formation.

5. CONCLUSIONS

Aqueous-phase reactions have been incorporated into a gas-phase chemical reaction mechanism in order to asses their impacts on the formation of O_3 in polluted areas that are partially covered by clouds. O_3 formation rates are calculated to be significantly reduced under most regimes of NO_x and NMHC when heterogeneous reactions in clouds are occurring. However, under some high-NMHC or NO_x conditions, the reduction is considerably less and highly variable. Changes in the chemical reactivity of a cloudy environment result primarily from the efficient scavenging and aqueous-phase reaction of HO_2 in cloudwater, which enhances the formation rate of H_2O_2, while reducing total concentrations of HO and HO_2.

Aqueous-phase reactions in the atmosphere reduce not only the rate of ozone production from NO_x, but also reduce the rate of ozone destruction from reaction with HO_2. Therefore, over a longer-term, aqueous phase reactions can either enhance or retard net ozone production in the atmosphere, depending on the concentration regimes at which ozone precursors are emitted into the atmosphere.

Reductions in O_3 formation resulting from reductions in NO_x or organic compound concentrations (via emission reductions) are significantly modified when considering the effects of heterogeneous reactions, suggesting that emission control strategies designed to limit the buildup of O_3 that are based on models considering only gas-phase reactions may contain significant uncertainties if heterogeneous reactions are occurring in clouds within polluted areas.

Acknowledgments. The authors are grateful to the United States EPA and the NSF for supporting this research.

REFERENCES

Jacob, D. 1986: Chemistry of OH in remote clouds and its role in the production of formic acid and peroxymonosulfate. *J. Geophys. Res.*, **91**, 9807-9826.

Jacob, D., E. Gottlieb and M. Prather, 1989: Chemistry of a polluted cloudy boundary layer. *J. Geophys. Res.*, **94**, 12975-13002.

Lelieveld, J. and P. Crutzen 1990: Influences of cloud photochemical processes on tropospheric ozone. *Nature*, **343**, 227-233.

Liu S. C., Trainer M., Fehsenfeld F. C., Parrish D. D., Williams E. J., Fahey D. W., Hübler G. and Murphy P. C. 1987: Ozone production in the rural troposphere and the implications for regional and global ozone distributions. *J. Geophys. Res.* **92**, 4191-4207.

Stockwell, W., P. Middleton J. Chang and X. Tang, 1990: The second generation regional acid deposition model chemical mechanism for regional air quality modeling. *J. Geophys. Res.*, **95**, 16343-16367.

THE SIZE-DEPENDENT CHEMISTRY OF FOG DROPLETS

S. Fuzzi[1], P. Laj[1], L. Ricci[1], A. Berner[2], D.Schell[3], M. Wendisch[4], W. Wobrock[5]

[1]Istituto FISBAT-CNR, I-40129 Bologna, Italy
[2]Institut für Experimentalphysik, Universität Wien, A-1090 Wien, Austria
[3]Zentrum für Umweltforschung, Universität Frankfurt, D-60325 Frankfurt, Germany
[4]Institute for Tropospheric Research, D-04303 Leipzig, Germany
[5]Laboratoire de Météorologie Physique, F-63117 Aubière, France

1. INTRODUCTION

The solute composition and concentration of cloud droplets vary with droplet size as a result of both the chemical composition and size distribution of the aerosols on which the cloud nucleates and the dynamical factors controlling the droplet growth inside the cloud. Cloud droplets inhomogeneities are of considerable importance because the efficiency of many processes in cloud, such as the scavenging of gases and kinetics of chemical reactions, are controlled by the composition and concentration of the liquid phase. However, at present, the relative importance of the different processes driving the solute size dependency is still unclear. Analyses of droplet residues from stratus clouds have shown an increase of solute concentration with droplet size [Noone et al., 1988; Noone et al., 1990]. On the contrary, solute concentrations were observed to decrease with droplet size during fog episodes in the Po Valley [Ogren et al., 1992]. Depending on meteorological conditions, both patterns of solute size-dependency were found in orographic clouds [Schell et al., submitted]. Finally, recent water collection from two mountain top clouds revealed ion concentrations in large and small cloud droplets higher than those found in intermediate sized drops [Collett et al., 1995]. The processes driving droplet growth play a major role in determining their composition and concentration. For example, coalescence leads to smaller droplets composed of more concentrated solution [Flossman et al., 1985], while the opposite is true if nucleation scavenging is the controlling factor [Ogren and Charlson, 1992]. In addition, the scavenging of soluble gases in the droplets can significantly modify the solute size dependency [Pandis et al., 1990].

The field project "Chemical composition and processes in clouds and fogs: dependence on the size of particles and droplets (CHEMDROP)" took place in the Po Valley during November 1994. It aimed to investigate the inhomogeneous composition of fog droplets in relation to the size dependent chemical composition of the cloud condensation nucleii (CCN) and its influence on the gas/liquid partitioning of soluble gases. Here we present results of a size segregated sampling of fog droplets performed during four fog events, and we analyse possible causes for the observed solute size distribution and phase partitioning within the fog system.

2. EXPERIMENTAL

The CHEMDROP campaign took place at the FISBAT station of San Pietro Capofiume in the Po Valley during November 1994. The site is characterised by fog containing high concentrations of chemical species, and by a long residence time of air masses during fog periods, extensively studied during previous campaigns [Fuzzi et al., 1992]. A comprehensive set of meteorological, microphysical and chemical measurements was carried out. The fog water was sampled by means of three different impactors allowing for the collection of both bulk and size segregated droplet samples. The bulk collector consisted of a series of sixteen impacting plates sampling at typical time resolution of 20 min. The size segregated sampling was carried out using two different collectors: the first collector samples the droplets into two different diameter ranges (5-10 μm and >10 μm) and the second, a newly developed instrument consisting of a series of four 2-stage droplet impactors, allowing for a size-fractionated sampling in five diameter ranges: 9-16μm; 16-19.6μm, 19.6-23μm, 23-32μm, and 32-47μm. The sampling time resolution of the two collectors was typically 1 to 2 hours depending on the fog event. The determination of fog sample pH and conductivity was performed in the field. The concentrations of major anions (including organic acids) and cations were measured by ion chromatography, several hours after sampling. Concentrations of aldehydes were determined by

HPLC. Analytical procedures for sampling, analysis, and quality control are described by Arends et al. [1994]. Aerosols were collected at ambient conditions both during and outside of fog episodes, using a set of two Berner type impactors: first, a high volume 6-stage impactor used at a 3 hour sampling resolution; second, an 8-stage Berner impactor usually run for 8 hour periods outside of fog events. In both impactor types, aerosols are impacted onto Tedlar foils, and subsequently extracted in 10 ml of deionized water by sonication. Continuous measurements of several gases were performed during CHEMDROP, including NH_3 by a continuous wet denuder [Arends et al., 1994] and HCOH by an enzymatic technique [Lazrus et al., 1988].

3. RESULTS AND DISCUSSION

The CHEMDROP campaign consisted of four different fog events as listed in Table 1. Average LWC content, mode of the droplet volume distribution, average pH and the sum of major ions of the bulk fog samples are also indicated in the Table. Comparisons between the four events show large variations of the fog physical and chemical characteristics. Droplet chemical analysis shows that between 80 and 90 % of the ionic strength is accounted for by NH_4^+, NO_3^- and SO_4^{2-} in concentrations of up to several ppm. The relative proportions of the chemical species are in agreement with previous studies performed in the Po Valley [Fuzzi et al., 1992]. A strong size dependency of fog droplet composition and concentration was found for all fog episodes. Ionic strength of the droplet solutions varied as a function of droplet diameter, showing maximum values in the 9-16 μm diameter range, except during the fourth event for which the distribution is bimodal (see figure 1). Higher concentrations of Na^+, Ca^{2+}, and Mg^{2+} are found in the larger droplets, while concentrations of SO_4^{2-}, NO_3^- and NH_4^+ are higher in the smaller droplets. These patterns are reflected in the size-dependency of droplet pH, showing that intermediate sized droplets are more acidic than both large and small droplets (except for samples corresponding to the onset of fog) (see Figure 2). Also seen in Figure 2 is the temporal evolution of pH size dependency during a fog event. The solute size dependency of HCOH shows an opposite pattern with higher concentrations in the large droplets.

The effects of droplet growth on the resulting solute size-dependency was simulated using the diffusional growth model of Wobrock [1988]. Preliminary results show that the observed droplet

Table 1: Average pH, concentration, LWC, and mode of the volume distribution of droplets for the four fog episodes

Event	Duration	pH	sum ions (μeq l^{-1})	LWC (mg m^{-3})	Mode (μm)
1	13/14 November, 23:00-2:00	6.5	1940	150	26-29
2	14/15 November, 20:00-10:00	3.8	8890	90	26-29
3	28/29 November 23:20-7:00	6.9	1250	220	26-29
4	29/30 November, 20:00-23:35	6.0	2610	330	no data

Figure 1. Sum of the concentrations of SO_4^{2-}, NO_3^- and NH_4^+ in the droplets in six diameter ranges, averaged over the entire event. Missing points are due to the very low LWC in the 19.6-23.5 diameter range.

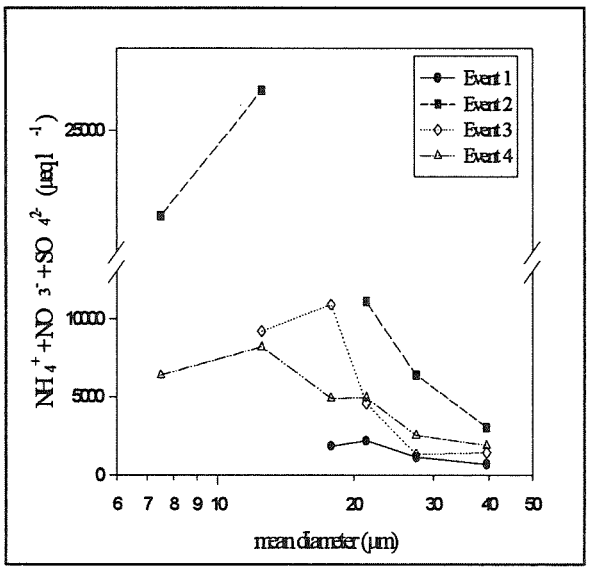

Figure 2. Evolution of droplet pH in five diameter ranges during the November 14th /15th fog episode. Each curve corresponds to a 2 hour sampling of which the starting time is indicated in the legend.

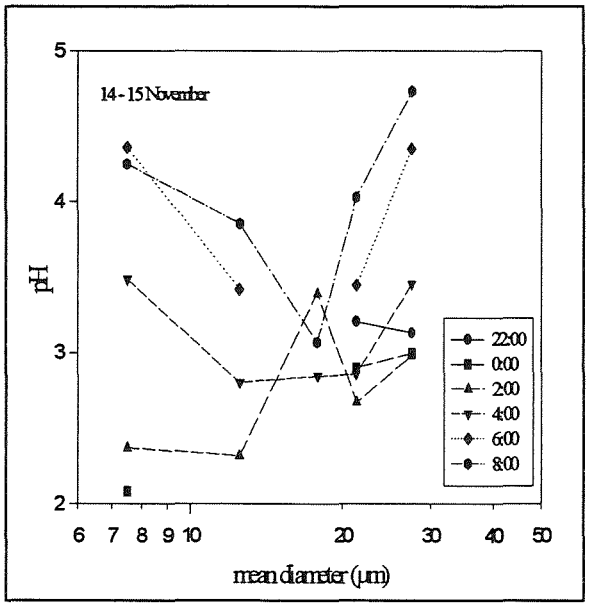

concentration can in principle be simulated under the assumption that just diffusional growth is affecting the size dependence of the droplet solute concentration. Additional work is needed to take into account the size dependency of the soluble fraction in the aerosol and the possible dissolution of gases into the wet aerosol.

Figure 3. Deviations from the Henry's law equilibrium for NH_3. Calculation were performed using bulk and size-resolved collectors (diameter ranges are indicated)

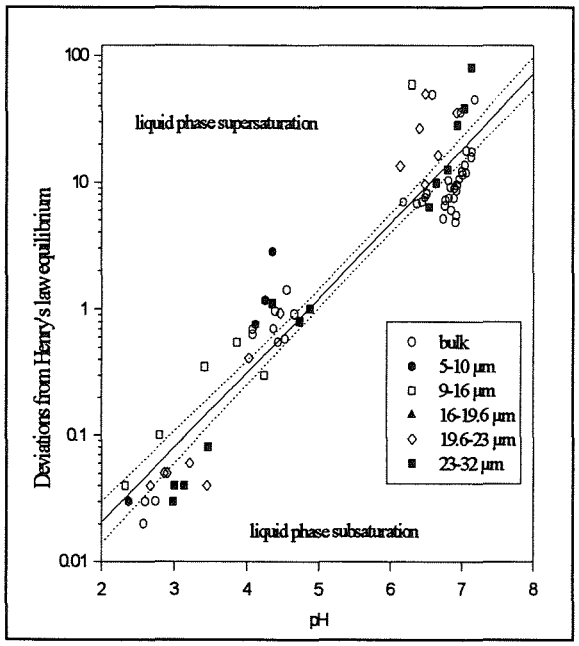

We investigated the effect of sampling time resolution and mixing of droplets of different pH on the resulting deviations from the Henry's law equilibrium. The deviations from the Henry's law equilibrium were calculated for both NH_3 and HCOH. according to Winiwarter et al., [1994] using both bulk and size segregated samples. Droplets are found much closer to equilibrium than during previous campaigns, especially for HCOH for which deviations are in the range of 0.5 to 2.5. Results of the calculations for NH_3 are shown in Figure 3. Contrary to what is found for HCOH, there is a clear pH dependency in the deviations from the equilibrium. However, no differences are found between the different droplet sizes, or when the sampling time resolution is changed: these results indicate that neither mixing of droplets with different pH in equilibrium with the same surrounding gas nor sampling over time periods larger than the typical time variations of the cloud LWC are responsible for the observed deviations from the equilibrium.

4. CONCLUSIONS

The experimental determination of the solute size-dependency in fog showed that the concentration of soluble material decreases with droplet size above 10 µm except for HCOH, for which the largest concentrations are found in the larger droplets. The present findings result from the physical and chemical characteristics of the original CCN distribution, the processes involved in droplet growth and, in the case of the soluble gases, the efficiency of gas scavenging. Investigation on gas/liquid partitioning for NH_3 showed that sampling artefacts from mixing over the whole droplet spectra and from long sampling times do not significantly affect the equilibrium. Additional work is necessary to quantify the role of each mechanism in the resulting solute size dependency of the fog droplets.

6. ACKNOWLEDGEMENTS

This research was supported by the EC Environment and Climate Research Programme (contract EV5V-CT93-0314, Climatology and Natural Hazards). P. Laj acknowledges the EC Human Capital and Mobility programme for individual fellowship (contract ERB4001-GT93-2667).

5. REFERENCES

Arends, B.G., L. Ricci, P. Laj, M. Wendisch, M. Schwanz, D. Schell, J. Wohlgemuth, W. Jaeschke, M. Preiss, A. Guenther, and A. Berner, 1994:Quality control procedures for the CHEMDROP fog experiment 1994. ECN, Petten.

Collett, J., R. Iovinelli, and B. Demoz, 1995: A three-stage cloud impactor for size resolved measurement of cloud drop chemistry. *Atmos. Environ.*, **29**, 1145-1154.

Flossman, A.I., W.D. Hall, and H.R. Pruppacher, 1985: A theoretical study of the wet removal of atmospheric pollutants, I: The redistribution of aerosol particles captured through nucleation and impaction scavenging by growing cloud drops. *J. Atmos. Sci.*, **42**, 583-606.

Fuzzi, S., M.C. Facchini, G. Orsi, J.A. Lind, W. Wobrock, M. Kessel, R. Maser, W. Jaeschke, K.H. Enderle, B.G. Arends, A. Berner, I. Solly, C. Kruisz, G. Reischl, S. Pahl, U. Kaminski, P. Winkler, J.A. Ogren, K.J. Noone, A. Hallberg, J. Grieser, H. Fierlinger-Oberlinninger, H. Puxbaum, A. Marzorati, H.C. Hansson, A. Wiedensohler, I.B. Svenningsson, B.G. Martinsson, D. Schell, and H.W. Georgii, 1992: The Po Valley Fog Experiment 1989, an overview. *Tellus*, **44B**, 448-468.

Lazrus, A.L., K.L. Fong, and J.A. Lind, 1988: Automated fluorometric determination of formaldehyde in air. *Anal.Chem.*, **60**, 1074-1078.

Noone, K.J., R.J. Charlson, D.S. Convert, J.A. Ogren, and J. Heintzenberg, 1988: Cloud droplets: solute concentration is size dependent. *J. Geophys. Res.*, **93D**, 9477-9482.

Noone, K.J., J.A. Ogren, and J. Heintzenberg, 1990: An examination of clouds at a mountain-top site in Central Sweden: the distribution of solute within cloud droplets. *Atmospheric Research*, **25**, 3-15.

Ogren, J.A., and R.J. Charlson, 1992: Implications for models and measurements of chemical inhomogeneities among cloud droplets, *Tellus*, **44B**, 208-225.

Ogren, J.A., K.J. Noone, A. Hallberg, J. Heintzenberg, D. Schell, A. Berner, I. Solly, C. Kruisz, G. Reischl, B.G. Arends, and W. Wobrock, 1992: Measurements of the size dependence of the concentration of non-volatile material in fog droplets. *Tellus*, **44B**, 570-580.

Pandis, S.N., J.H. Seinfeld, and C. Pilinis, 1990: Chemical composition differences in fog and cloud droplets of different sizes, *Atmos. Environ.*, **24A**, 1957-1969.

Schell, D., W. Wobrock, R. Maser, M. Preiss, W. Jaeschke, H.W. Georgii, M.W. Gallagher, K.N. Bower, K.M. Beswick, S. Pahl, M.C. Facchini, S. Fuzzi, A. Wiedensohler, H.C. Hansson, M. Wendisch, The size-dependent chemical composition of cloud droplets, *submitted to Atmos. Envir.*, 1996.

Winiwarter, W., H. Fierlinger, H. Puxbaum, M.C. Facchini, B.G. Arends, S. Fuzzi, D. Schell, U. Kaminski, S. Pahl, T. Schneider, A. Berner, I. Solly, and C. Kruisz, 1994: Henry's law and the behaviour of weak acids and bases in fog and cloud, *J. Atmos. Chem.*, **19**, 173-188.

Wobrock, W., 1988: Numerische modellsimulation von stralhlungsnebelsituation unter Berucksichtinggung spektraler wolkenmikrophysik, Frankfurt.

NUMERICAL SIMULATION ON PHOTOCHEMISTRY OF STRATIFORM CLOUDS

Qin Yu[1] and Zhang Yuanhang[2]

[1]Department of Geophysics, Peking University, Beijing 100871, China
[2]Center of Environmental Sciences, Peking University, Beijing 100871, China

1. INTRODUCTION

Clouds play an important role in the regional and global cycle of air pollutants because they transport and redistribute pollutants, significantly speed up chemical transformation over the rates that occur in dry air and produce precipitation which is a efficient mechanism for removing many pollutants from the atmosphere. In addition, clouds may alter the distribution of actinic radiation, especially, increase and decrease radiation fluxes near their tops and bases relative to cloudless conditions. Thus, they are effective on the photochemistry of the air and must influence the aqueous chemistry in cloudwater and wet deposition conversely.

Madronich (1987) developed a optical radiation transfer model to calculate the actinic flux through a thin layer of cloud with uniform water content, located at 4-5 km. levels. The actinic flux has a factor 1.7 above the cloud top and only 0.4 below the cloud base comparing with that in cloudless condition. To study this effect on the cloud chemistry and wet deposition, we develop a physico-chemical model of stratiform clouds coupled with a radiation transfer module taken from Madronich's model to calculate the distribution of actinic flux and photochemical reaction coefficients with the evolution process of clouds. Some results of numerical experiments are given in this paper.

2. THE MODEL

In our model, there are three modules: micro-physics, chemistry and optical radiation transfer.

2.1 The microphysics of clouds

A time-dependent parameterized module of cloud physics is used like that in the previous paper. (see Qin 1989, 1992) The water substance is classified into water vapor, cloudwater and rainwater. Water transfer processes, such as the condensation of water vapor, the autoconversion from cloudwater to rainwater and the collection of cloudwater by rainwater, are considered. Under a defined meteorological condition with given air temperature, humidity and updraft velocity profiles, the temporal and spatial variation of water contents can be determined by the mass-conservation equations.

$$\frac{\partial Q_i}{\partial t} + (W - V_i)\frac{\partial Q_i}{\partial z} = \frac{\partial}{\partial z}\left(k\frac{\partial Q_i}{\partial z}\right) + \left(\frac{dQ_i}{dt}\right)_{ss}$$

where Qi denotes the mixing ratio of water class i or the concentration of species in gas phase, cloudwater and rainwater; W is the updraft velocity of the air, Vi is the terminate velocity of raindrop, for cloud droplets or aerosol particles,it is zero; (dQi/dt)ss represents the sources and sinks based on microphysics and chemical processes.

2.2 The Chemistry

A condensed gas chemical reaction mechanism ARCMG is used in which 39 species and 87 reactions are contained.(Zhang et. al., 1992) This mechanism has been tested to simulate 17 UNC outdoor smog chamber experiments and the results were in agreement with those from Calchem mechanism (Carter W.P.L. et. al.1986) for the main species founded in photochemical smog and acid rain. The aqueous chemical mechanism ARCML applied in this model contains 33 species and 59 reactions (Zhang et. al. 1992). In addition to that, many mass-transferred and transformation processes are included in the mechanism such as gas dissolution, dissociation, aqueous reaction in cloudwater and rainwater, even nucleation of aerosol as CCN and its collection by rainwater. The mass-transferred processes of species from cloudwater into rainwater are also considered as processes associated with the autoconversion and collection of cloudwater by rainwater.

2.3 The radiation transfer

Photolysis coefficients used in the chemical module are taken from the radiation transfer module. (Madronich 1996) The optical depths of clouds are

reduced directly from the output of the cloudwater content calculated with microphysical module in which the Khrgian-Mazin distribution of cloud droplets are assumed. The actinic flux profile can be obtained with the modified Madronich program.. Then, the photolysis coefficients of various species can be calculated with their scattering sections and quantum yields.

In microphysical and chemical modules of this model, mass-conservation equations are solved with the finite differential method. The vertical extent of the model is 4 km. from the ground and is divided into 20 levels with 200m. spatial resolution. The model generally simulate a evolution process of precipitating cloud for 4 hours with a 10 sec. step. In radiation transfer module, 40 levels are taken from the ground to 4km. i.e. a layer depth is 100m. Above 4km to 50 km, there are 46 levels and the depth is 1 km. same as that in Madronich model. The main program of the model allocates the radiation module once every simulated 10 minutes to calculate the actinic fluxes and the photolysis coefficients at every level with cloud parameters which are taken from the output of the microphysical module. The results are put into the chemical module to calculate the photochemical reactions.

3. RESULTS

Given the meteorological condition which is same as that in papers (Qin 1989, 1992), Simulated results show that at begining, cloudwater forms at the middle level owing to the lift of sutuation air and quickly fills in the whole column from 0.8 to 3.4 km. About 80 minutes. later, a cloudwater maximum arises at upper part of cloud column and the cloudbase drops down to 0.6 km. due to the evaporation-recondensation process of cloudwater at the base. The formation of rainwater starts in middle and upper parts of cloud column at 70 minutes. Then it extends down and arrives at the ground at 90 minutes. The mean rainfall intensity at the ground is about 1 mm/hr during 2.5 hours. This simulated rainfall process is like the real process in south China during spring season.

Table 1. the initial values of the species at the lower bound (G: gas, ppbv; A: aerosol, nmol/m^3)

O_3 G	40	CO G	100	RCHO G	1
H_2O_2 G	1.0	ALK G	14.75	HCOOH	0.5
HNO_3 G	0.1	TOLU G	2	NO_3^- A	30
NH_3 G	5	XYLE G	1	NH_4^+ A	70
NO_2 G	5	ETHE G	7	SO_4^{2-} A	70
NO G	15	OLE G	4	Cl^- A	20
CH_4 G	1400	HCHO G	2	Ca^{2+} A	50

Table 1 gives initial conditions which are concentrations of species at the ground. The concentrations of the most species decrease with the height as exponential function and the scale height is 1.5 km. SO_2 initial ground concentration is 10 ppb with 2km. scale height. As for O_3, H_2O_2 and HNO_3, uniform distributions in the column are assumed.

Under such initial condition, the simulated results are consistent with observational results generally. Some results of numerical experiments are presented here.

3.1 Comparing with old model

In previous papers (Qin 1989,1992), we have not considered effects of gaseous photochemical reactions on composition of cloudwater and rainwater for the shorter duration of precipitation formation. Usually, only aqueous reactions were considered in that model. Thus, some gases could be removed quickly by cloudwater and rainwater, because they had not additional supply. In addition, the free radical reactions had not been included. In Figure 1, the compositions of rainwater at the ground from the new comprehensive model are compared with that from old model. We assume that the simulated cloud evolutes during 7:00 am. to 11:00 am. i.e. in the morning. The solar radiation increase gradually in whole process. The concentrations of SO_4^{2-} and NO_3^- in rainwater obtained from new model are higher than that from old model, especially, the concentration of SO_4^{2-} of the new model increase with time during the later two hours. The pH value of rainwater from the new model is lower than that from the old model and drops to very low value.

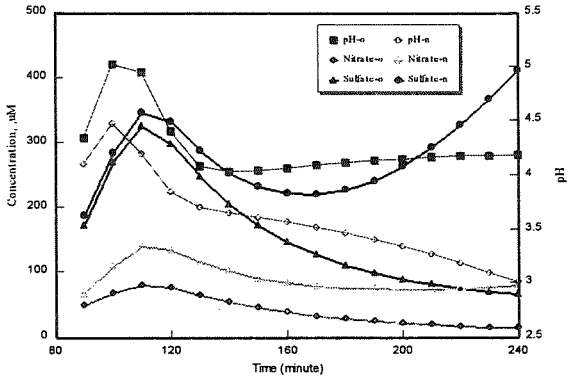

Fig.1 The simulated concentrations of sulfate and nitrate and pH of rainwater at the ground (o: old model, n: new model)

In Figure 2, the oxidizing ways of S(IV) in rain-water are given for both models. The contribution of ozone is not important in both models. Since the H_2O_2 can be produce through the photochemical

reaction in new model, its contribution to the oxidation of S(IV) in rainwater is stationary and increase slightly during later two hours instead of decrease with time in the old model. It is interesting that the contribution of the free radical is not ignorable, although that of H_2O_2 is the first one. The effect of free radical could be greater than that of H_2O_2 in later term of precipitation, if the solar radiation is strong enough.

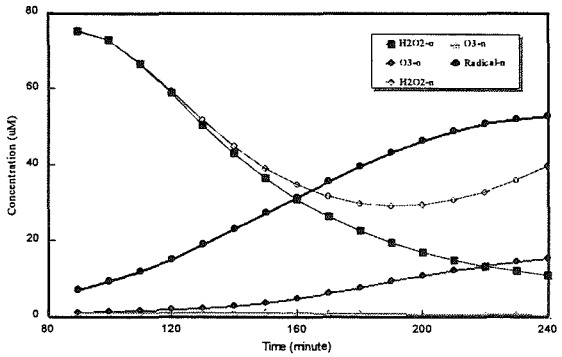

Fig. 2 The contribution of species to S(IV) oxidation in rainwater(o: old model, n:new model)

3.2 The photolysis coefficients

From previous paragraph, we learn that the photochemical reaction process is important to the cloud chemistry. In this paragraph, three numerical experiments are given to study the effects of cloud on the photochemistry. In three scenario, meteorological and chemical conditions are same. The only difference is that the formation time and evolution time of clouds are different. For those three cases: Morning, Noonday and Afternoon, evolution duration of clouds are 7-11am. 10am.-14pm and 13-17pm. respectively.

Considering NO_2 as a representative, we calculate the ratio of photolysis coefficients with the effect of cloud to that in the cloudless case. Those ratio at 3.4 km., 2 km. and 0.6 km. levels are given in Fig.3 a, b and c, which are corresponding to the cloud top, the middle part of cloud and the cloud base. Generally, there is a close relation between the ratio of photolysis coefficients and the zenith angles of the sun. From Fig.3a, we can find the ratio varies 1-3 at cloud top. The ratio in the Morning Case increase and that in Afternoon Case decrease with time, this tendency is consistent with the diurnal variation of the zenith angles of the sun. The ratio in Noon Case is 2-3 and a small peak arises at near 70-80 min.in simulated time which matches to the maximum of the column cloudwater content. For same cause, minimum values of the ratio derive during same time in Fig 3c. These values of the ratio are different with Macronich's, since the optical depth of cloud in this model is larger.

3.3 The effects of cloud formation time on composition

The difference in cloud formation time means the condition of solar radiation is different that must affect photochemical process. Thus, the compositions and pH values of the cloudwater and rainwater should be different. In Figure 4, we compare compositions of rainwater at the ground obtained from numerical experiments in Morning Case and the Noonday Case. Concentrations of SO_4^{2-} and NO_3^- in Noonday Case are about 50% higher than that in Morning Case and its pH is lower due to stronger solar radiation.

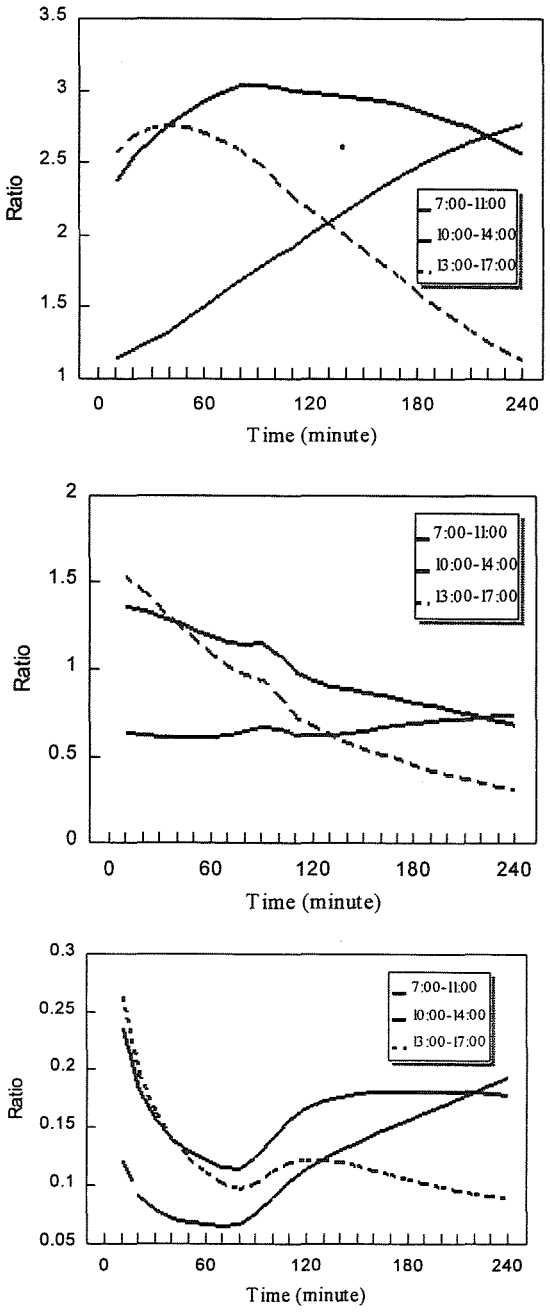

Fig. 3 The ratio of photolysis coefficients between considering cloud effects and cloudless case (3a: at 3.4km.: 3b: at 2 km.: 3c: at 0.6 km.)

It is interesting that the organic acid concentration of HCOOH in rainwater obtained from Noonday Case simulation is lower than that from Morning Case for its lower pH value which reduces the solubility of HCOOH in rainwater, although its gaseous concentration is higher due to the stronger photochemical reaction.

Since Ca^{2+} in rainwater is not a photochemical producer, so the concentrations in both conditions have same values.

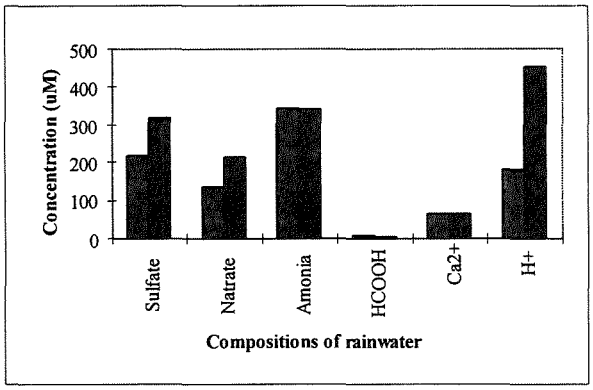

Fig.4 The concentrations of species in rainwater at the ground, in Morning and Noonday Cases.

4. CONCLUSIONS

From above-mentioned results, we can learn that although a precipitation event may maintain only several hours, but the photochemical reactions can still affect the compositions of cloudwater and rainwater. Since the photochemical reactions are dependent on the solar radiation strongly, the concentrations of species and the pH value of rainwater forming in deferent time could be different, even the meteorological and chemical initial values are same. In assessment of the precipitation chemistry, we should consider that.

5. ACKNOWLEDGMENTS

This work is a part of the project supported by National Science Foundation of China. Authors wish to thank Dr. S. Madronich, NCAR for his kind help.

6. REFERENCES

Carter, W.P.L. et al, 1986: Development and testing of a surrogate species chemical reaction mechanism. Vol I, *EPA 69-02- 4140.*

Madronich, S., 1987: Photodissociation in the atmosphere. 1. Actinic flux and the effects of ground reflections and clouds. *J. Geophy. Res.* , **92**, 9740-9752.

Qin, Y., 1989: Numerical simulation n the rainout removal of sulfur dioxide and acidification of precipitation from stratiform clouds, *Adv. in Atmos. Sci.*, **6**,75-87.

Qin, Y., 1992: Numerical Simulation of pollutants removal by precipitation. *J. Atmos. Chem.*, **14**, 143-151.

Zhang, Yuanhang et al, 1992: Evaluation of the effect of Nox and Hcs to cloud acidification, *Paper Am. Chem. Soc. Div Pet .Chem.*, **37**, 1556-1563.

OBSERVATIONS IN AND NEAR ANVILS OF NEW MEXICO THUNDERSTORMS INFLUENCE ON UPPER TROPOSPHERIC COMPOSITION BY TRANSPORT, NOX PRODUCTION BY LIGHTNING AND OTHER MECHANISMS

J.E. Dye, B.A. Ridley, J.G. Walega, J. Zheng, F.E.Grahek

National Center for Atmospheric Research
Boulder, Colorado USA

B. Rison

New Mexico Institute of Mining and Technology
Socorro, New Mexico USA

Thunderstorms play an important role in the chemical composition of the troposphere. They can transport species from the boundary layer to the upper troposphere in a relatively short time, or bring species from the mid-troposphere into the boundary layer. They redistribute water vapor throughout the troposphere both by transport and the formation and fallout of precipitation. Chemical/physical processes within the storms can change the mixing ratios of chemical species. Lightning in thunderstorms is know to be an important source of NOx to the troposphere, but it has been particularly difficult to quantify this source. Estimates vary by over an order of magnitude.

In 1989 the NCAR Sabreliner aircraft was used to probe conduct an exploratory study in and around anvils of convective storms over central New Mexico. In addition to measurements of horizontal and vertical winds, thermodynamic parameters, water vapor, hydrometeors >50 micron diameter, and cloud liquid water content, relatively high temporal resolution measurements of NOy, NO, O3 and NO2 were made. NOy is the sum of reactive nitrogen species, NO, NO2, HNO3, ... While the emphasis of the project was an exploratory study of the production of NOx (NO + NO2) by lightning, the measurements also provided information on the effects of transport of constituents, motion around the storms and removal of soluble species by both electrically active and inactive storms.

As shown by Ridley et al., (1994) outside of the urban Albuquerque region the boundary layer is relatively clean with low mixing ratios of NOx. The observations showed that storm updrafts transported air from the boundary layer with low mixing ratios of NOx and ozone to upper levels where NO, NOy and ozone were usually higher. As a consequence, for non-electrified storms the values of NO and NOy in anvils were less than the extra-cloud air and O3 was less in most cases whether the storm was electrified or not, showing that transport by storms in remote, clean regions can reduce the concentration of species important for O3 production or loss as well as increasing them in polluted regions. (Pickering et al., 1992)

There was no evidence for the production of O3 by lightning. However, enhancements up to 1 ppbv in NO and NOy were found in the anvil of 2 storms with lightning. The largest increases in active nitrogen were observed in the upper levels of the anvil with decreasing amounts in the lower anvil, and no evidence of enhancement just below the anvils of the storms. If air was being detrained from this region of the storm it was not detrained from a region in which lightning had occurred. An example of one pass throught the anvil of the August 12, 1989 storm is shown in Figure 1. This penetration was made at about 11 km and was the 9th of ten made either below or through the anvil. Anvil top was about 12 km. NO levels in the boundary layer were about 100 to 200 pptv. The very large levels of 1500 to 2000 pptv seen in the anvil could only have been produced by lightning. A total of 61 cloud-to- ground lightning flashes had been observed in 50 min. from this storm up to the time of this pass and probably at least as many in-cloud flashes also occurred.

Note in Figure 1 (from Ridley et al., 1996) that ozone mixing ratios mostly decreased throughout the anvil. However, near 13.10 (decimal hours MDT) ozone had elevated values with low values of NO and NOy. This air must have originated at levels above the highest flight level because all ozone measurements at all lower levels were less. THis suggests that air from above the storm was mixing downward into the edge of the anvil, but the mechanism is not clear. In Figure 1 650 pptv has been added to the NO signal in order to compare the enhanced NO with the NOy signal. Note that in the region of enhanced NO/NOy the signals lie almost on top of each other showing that almost all of the enhancement due to lightning was in the form NO and very little NO2. Inside the anvil the

Corresponding author address: J.E. Dye; NCAR; PO Box 3000; Boulder

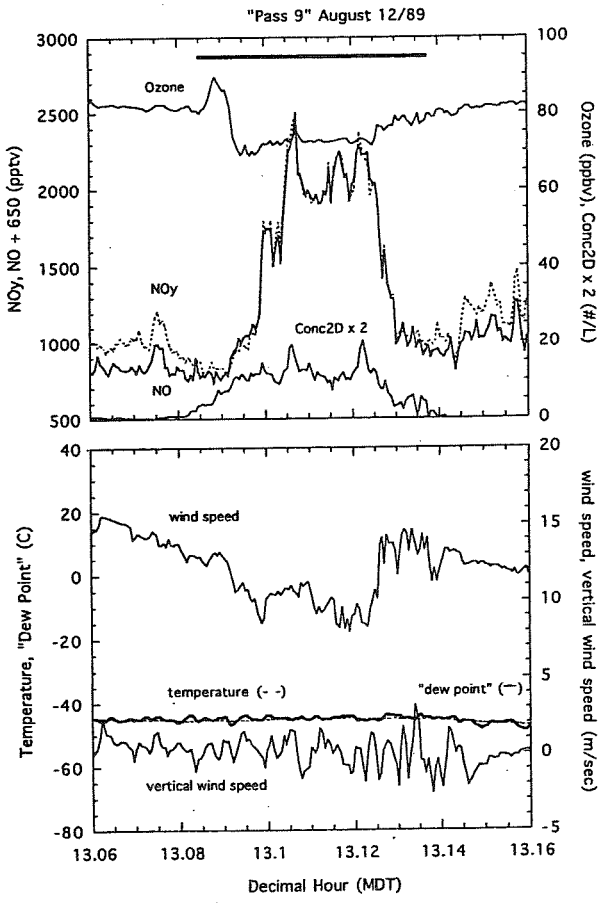

Figure 1. Measurements made at 11 km in a August 12, 1989 New Mexico thunderstorm.

horizontal wind speed decreased, consistent with previous measurements which show that the storm acts as an obstacle to the flow and that air of lower momentum has been transported to the upper levels of the anvil.

An interesting feature in Figure 1 which was seen in a number of other passes as well is the correspondance between the peaks in the NO signal with ice particle concentrations measured by the PMS 2D probe. The highest peaks of NO were often but not always correlated with peaks in particle concentration. A preliminary examination of particle sizes and the concentration of particles in different sizes intervals, for example the concentration of particles larger than 1mm did not reveal any striking relationships. Non-theless this correspondance is interesting and will be pursued further. The correspondance suggests a possible link between where lightning has occurred in the cloud (as evidenced by the enhanced NO values) and regions of the cloud which were sufficiently electrified to have conducted a lightning channel, ie higher particle concentrations.

As noted above this was an exploratory project and as such raised a number of interesting questions. One of them is what is the net effect of the NOx produced by a storm on the upper troposphere, ie. what are the residual effects? The Sabreliner had a flight duration of approximately 2 hours so it was not possible to address this question. However, it was interesting that enhanced values of NOx were seldom observed outside of the anvil. Those that were observed outside were very wispy and of short duration (small dimension). This suggests that most of the altered air remains within the anvil and that there is little air mixed to the outside. Although we were not able to examine the upper part of the downwind anvil because of the limited flight durations, the passes made in the downwind region of the lower anvil did not show enhanced values. It may be that any residual effects are in fact contained within the anvil. We hope to address this important question in the upcoming STERAO-Deep Convection Experiment. (Stratospheric/Tropospheric Experiment: Radiation, Aerosols and Ozone) The major components of this experiment will be the NSF/NCAR WB57F aircraft which will make a number of chemical, electrical and aerosol measurements in the upper tropopshere and lower stratosphere; the NOAA WP3D aircraft with tail Doppler radar which will investigate the chemical composition of the lower and mid-troposphere and air motions within the storms; the Colorado State University-CHILL radar which will provide multiparameter Doppler radar measurements of the microphysical and air motion structure of the storms; the French ONERA 3-D lightning interferometer to map the 3-D lightning channels of the storm: and hopefully the North Dakota Citation Citation for penetrations of the anvil. The overarching goal is to examine the effects of thunderstorms on the chemical composition of the upper troposphere/lower stratosphere, particularly the distribution of water vapor and also the production of NOx by lightning. Some preliminary findings from this project will be reported at the conference.

1. ACKNOWLEDGMENTS

We thank the many people in the NCAR Research Aviation Facility and at New Mexico Institute of Mining and Technology who were involved in this project. NCAR is partially supported by the National Science Foundation.

2. REFERENCES

Pickering, K.E., A.M. Thompson, J.R. Scala, W.-K. Tao, R.R.Dickerson, and J. Simpson, 1992: Free tropospheric ozone production following entrainment of urban plumes into deep convection, *J. Geohys. Res.*, **97**, 17,895-18000.

Ridely, B.A., J.G. Walega, J.E. Dye and F.E. Grahek, 1994: Distributions of NO, NOx, NOy, and O3 to 12 km altitude during the summer monsoon season over New Mexico, *J. Geohys. Res.*, **99**, 25,529-25,534.

Ridley, B.A., J.E. Dye, J.G. Walega, F.E. Grahek, and W. Rison, 1996: On the production of active nitrogen by thunderstorms over New Mexico, *J. Geohys. Res.*, submitted manscript.

EFFECTS OF NITRIC ACID VAPOR ON CLOUD FORMATION

Dennis Lamb and Alfred M. Moyle

Meteorology Dept., Penn State University, University Park, PA 16802, USA

1. INTRODUCTION

Clouds form initially by condensation of water vapor onto aerosol particles that contain soluble, but nonvolatile constituents. These solutes are often the ionic products of dissolved salts (e.g., NaCl, $(NH_4)_2SO_4$), when the relative humidity is above the deliquescence point, or of low-vapor pressure liquids that are hydrophilic, such as sulfuric acid. The relatively strong molecular-scale attractions that arise between the solutes and water allow the liquid state to form well below the pure-water saturation point. In effect, the equilibrium vapor pressure of water over the solution is suppressed relative to what it would otherwise be. The effect of nonvolatile solutes on lowering the activity of water in solutions is particularly strong at low humidities, when the haze particles are smallest and the solutions are most concentrated. Traditional cloud physics relies heavily on this vapor-pressure lowering effect of solutes and its consequent impact on the critical supersaturations of particles (see Pruppacher and Klett, 1978).

When a soluble trace gas, such as nitric acid, is present in an expanding and cooling parcel of moist air, additional interactions must be considered. The traditional assumption that the solute content of the solution droplet is constant during the uptake of water from the environment can no longer be valid. The trace gas tends to be absorbed by the solution to a variable extent depending on its chemical properties, leading to nonlinear interactions. The theory of multicomponent condensation that leads to a generalization of Köhler theory has been developed and used to show that modest mixing ratios of nitric acid lower the critical supersaturations of CCN significantly (Kulmala et al., 1993; Lamb, 1992).

Investigations of the effects that a soluble trace gas like nitric acid have on aerosol particles and their ability to serve as cloud nuclei demand several research approaches. Ultimately, numerical modeling, when based on a comprehensive theory, is required to deal with the diverse chemical and physical phenomena taking place simultaneously during the uplift of an air parcel. Each particle in the aerosol population experiences the co-condensation of water vapor and nitric acid vapor, and unique chemical equilibria occur within the solution that depend on the amount and chemical nature of the nonvolatile solute present. At the same time, the depletion of vapor must be taken into account before an accurate measure of particle growth or other effects can be gained. In order to ensure accuracy, appropriate parts of the theory need to be verified against data from laboratory experiments or atmospheric observations. Laboratory measurements have provided most of the basic physicochemical data upon which chemical thermodynamic models are based, and they have helped identify the nature of surrogate bulk solutions in various liquid and solid states (e.g., Zhang et al., 1993). In the stratosphere, multicomponent condensation has been used to explain the growth of the aerosol in response to airmass cooling (Dye et al., 1992; Carslaw et al., 1994).

The purpose of this paper is to provide further evidence that nitric acid can lead to enhancements of aerosol growth. We utilize data from laboratory experiments involving individual aerosol particles to show how volatile and nonvolatile solutes differ in their effects on aerosol properties. Inferences from these results lead one to consider possible consequences of the phenomenon in the atmosphere.

2. PARTICLE EXPERIMENTATION

The influence that volatile solutes have on the growth of aqueous particles has been studied via laboratory experimentation. The apparatus and procedures have been described recently (Lamb et al., 1996), so only an overview is provided here. It should be appreciated at the outset, however, that special care is needed when dealing with a soluble trace gas like nitric acid vapor. Due to its large solubility in aqueous solutions, nitric acid interacts strongly with most surfaces of an apparatus, especially when water vapor is also present. Some attention is therefore drawn to the specialized flow system used in the experiments.

Individual charged particles were levitated electrodynamically at the geometrical center of a cubic cell

(inside dimension about 2.5 cm). Each face of the cube served both as an electrode and as an interface to the other subsystems that made up the complete experimental system. The four electrodes on the vertical faces of the cell were supplied with two-phase AC voltages between about 300 and 1500 V (peak), as well as modest DC potential differences that were used to locate the particle in a horizontal plane. The top and bottom electrodes carried DC voltages only and served to position the particle vertically. The relative mass of the particle was obtained from measurement of the vertical potential difference needed to maintain the particle in the center of the cell. Additional details about the electronic design and distribution of fields inside the cell are given by Allison and Kendall (1996).

The gaseous environment of the particle was controlled by adjusting the properties of a gentle flow of gas that passed horizontally and continuously through the cell. The flow induced a small drag force on the particle that was compensated for by adjustment of the horizontal potential gradient. The moisture content of the carrier gas (nitrogen) was controlled by adjusting the amount of gas passing through a humidifier (bubbler outfitted with filter) upstream of the cell. The relative humidity was later calculated from the measured dew-point and gas temperatures. Nitric acid vapor was introduced into the main cell flow just upstream of the particle by a special grid injection system that also served as an electrode on one side of the cell. This grid flow originated as very dry nitrogen that was passed slowly over a liquid solution of 50% nitric acid and 50% sulfuric acid in a temperature-controlled trap. Injection of this reagent flow into the cell near the particle ensured that the walls of the cell did not interfere with the concentration of nitric acid experienced by the particle.

The current set of experiments each started with a sulfuric acid droplet that had been exposed to dry nitrogen for at least 12 h. The desired partial pressure of nitric acid vapor was then established in the gas flows and maintained for an entire run. The humidity was incrementally increased, while the response of the particle was noted. The relative mass of the particle was taken as the ratio of the vertical DC voltages needed to center the particle under moist and completely dry conditions, respectively.

3. NITRIC ACID EFFECTS

The data from the experiments with sulfuric acid particles illustrate the different ways that volatile and nonvolatile solutes respond to changes in relative humidity. Figure 1 displays the results in a way that parallels that often used to illustrate Köhler theory. However, all particles in our experiments were larger than a few micrometers in diameter, so no effects of curvature show up. The bold curve in Fig. 1 represents the relative mass growth of sulfuric acid particles that were not exposed to any nitric acid vapor. This curve was derived from the bulk thermodynamic data of Zeleznik (1991) and summarizes the experimental data from a number of separate particles. Particles composed of H_2SO_4 exhibit no deliquescence point in the traditional sense and grow by the uptake of water at all subsaturated humidities. For reference, the dashed curve shows the growth behavior expected from an ideal (Raoult-type) solution. Clearly, the strongly hygroscopic nature of sulfuric acid contributes to the mass growth of the particles.

The data points shown in Fig. 1 resulted from experimental runs during which the sulfuric acid particle was exposed to various fixed concentrations of nitric acid vapor. The curves that pass through the data points were derived from the bulk-thermodynamic model of Jaecker-Voirol et al. (1990). As the relative humidity increased from dry conditions during a given run, little distinction was initially found in the mass growth despite large variations in the concentration of HNO_3 in the vapor phase. However, at higher relative humidities, substantial effects of HNO_3 were apparent. The ternary solution droplets then grew strongly with

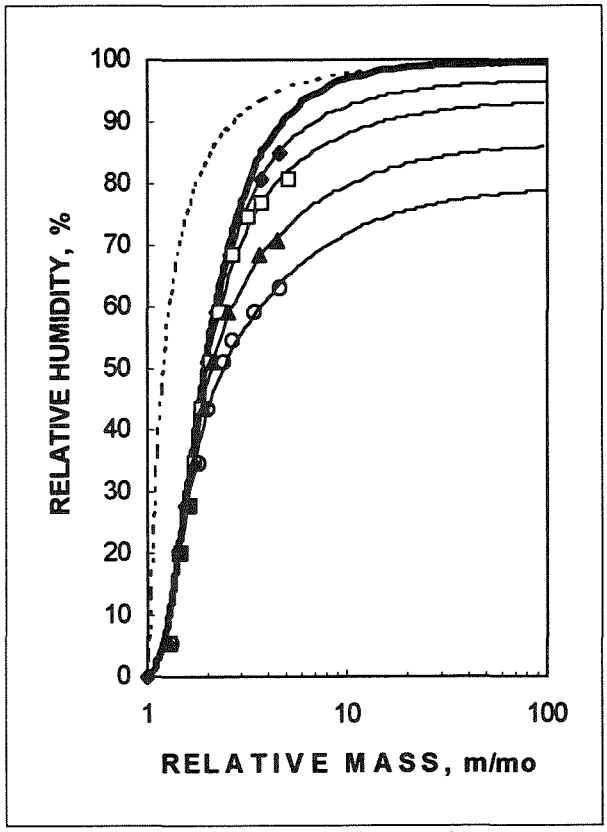

Fig. 1. Experimental data of particle mass gain versus relative humidity under room-temperature conditions. Bold curve: no HNO_3; lighter solid curves (from top): HNO_3 saturation ratios =$4.4x10^{-5}$, $1.2x10^{-4}$, $3.8x10^{-4}$, $8.5x10^{-4}$; dashed curve: Raoult-type particle.

increasing humidity, in part because of the added mass of the nitric acid itself, but also because of its impact on the activity of water in the solution and the consequent increase in the water mass taken up from the environment. This particle mass gain is linked intimately to the nonlinear solubility of HNO_3 in sulfuric acid solutions, which in turn seems to be limited by the ability of the HNO_3 to dissociate in the solution once it is absorbed (Van Doren et al., 1991).

These experimental results with individual particles confirm expectations that the mass growth of aerosol particles can increase dramatically once the saturation ratios of water and nitric acid are sufficiently large. Indeed, if certain critical values of these environmental variables are exceeded, we can expect the particle mass to increase without bound, even under subsaturated conditions. This behavior is evident in Fig. 1 as the flattening of the curves toward the right-hand side. The larger the saturation ratio of HNO_3 in the vapor phase, the smaller the relative humidity needs to be before bulk co-condensation of these vapors takes place. In this asymptotic limit, the concentration of H_2SO_4 is negligible, and each particle behaves as a binary nitric acid - water solution. Unlike the nonvolatile solute (H_2SO_4), the volatile solute (HNO_3) tries to maintain a constant activity in the solution, meaning that additional solute will be taken up from the local environment as water vapor condenses onto the particle. The only check on this co-condensation process is the finite supply of the trace gas in a given air parcel, so vapor depletion must be considered in any quantitative treatment of a population of particles, as in the atmospheric aerosol.

The atmospheric importance of the multicomponent condensation phenomenon described here depends on the availability of nitric acid vapor in the air at any given temperature T. The 'saturation ratio' of HNO_3 vapor, $S_N \equiv P_{HNO_3} / P^0_{HNO_3}$, where $P^0_{HNO_3} = P^0_{HNO_3}(T)$ is the saturation vapor pressure of pure HNO_3, is a natural variable to consider because of its close conceptual link to the activity of the substance in the solution (Atkins, 1986, p. 182). However, atmospheric chemists tend to use the concept of volume (or molar) 'mixing ratio', $y_N \equiv P_{HNO_3} / P$, where P is the total pressure. Nevertheless, once we establish a criterion for assigning a 'significant' effect of HNO_3 on the aerosol particles, then we can calculate the equivalent mixing ratio needed in the atmosphere. For instance, we may require that the equilibrium relative humidity over the limiting binary solution must by lowered by 20%, in which case we find from the experiments that a nitric acid saturation ratio in excess of about 10^{-3} is needed. Because of various temperature dependencies, we expect the lowest threshold values of nitric acid mixing ratios to exist at low temperatures. Preliminary estimates, using this line of reasoning and computational results from a chemical mixing model (Carslaw et al., 1995), suggest that only a few tenths of a ppb of HNO_3 are needed in the upper troposphere. Comparable abundances of HNO_3 have been suggested to exist in the upper troposphere over continental regions by Penner et al. (1991), so there may be enough of this soluble trace gas to bring about substantial changes in the sizes of the aerosol particles and other atmospherically relevant effects. Further study of this phenomenon is underway.

4. ACKNOWLEDGMENTS

This work was supported in parts by NSF Grants ATM-9115590 and -9528255 and by NASA Grant NAG 2-751. We also express appreciation to S. Clegg for sharing the code of a chemical mixing model.

5. REFERENCES

Allison, E., and B. Kendall, 1996: Cubic electrodynamic levitation cell with transparent electrodes. Rev. Sci. Instr., in press.

Atkins, P.W., 1986: Physical Chemistry, Freeman, New York, 857pp.

Carslaw, K., et al., 1994: Stratospheric aerosol growth and HNO_3 gas phase depletion. GRL, **21**, 2479.

Carslaw, K.S., et al., 1995: A thermodynamic model of the system HCl-HNO_3-H_2SO_4-H_2O, J. Phys. Chem., **99**, 11557-11574.

Dye, J.E., et al., 1992: Particle size distributions in Arctic polar stratospheric clouds. JGR, **97**, 8015.

Jaecker-Voirol, A. et al., 1990: Vapor pressures in the ternary system water-nitric acid-sulfuric acid at low temperatures. JGR, **95**, 11857-11863.

Kulmala, M. et al., 1993: The effect of nitric acid on CCN activation. JGR, **98**, 22949-22958.

Lamb, D., 1992: Microphysical and chemical aspects of cloud formation at low temperatures. 11th Inter. Conf. on Clouds and Precipitation, Montreal, 869.

Lamb, D., et al., 1996: The environmental control of aqueous particles in a cubic electrodynamic levitation system. Aerosol Sci. Tech., in press.

Penner, J.E., et al., 1991: Tropospheric nitrogen: A three-dimensional study. JGR, **96**, 959-990.

Pruppacher, H.R., and J.D. Klett, 1978: Microphysics of Clouds and Precipitation. Reidel, Boston, 714pp.

Van Doren, J.M., et al., 1991: Uptake of N_2O_5 and HNO_3 by aqueous sulfuric acid droplets. J. Phys. Chem., **95**, 1684-1689.

Zeleznik, F., 1991: Thermodynamic properties of the aqueous sulfuric acid system to 350 K. J. Phys. Chem. Ref. Data, **20**, 1157-1200.

Zhang, R. et al., 1993: Vapor pressure measurements for the H_2SO_4/HNO_3/H_2O and H_2SO_4/HCl/H_2O systems. J. Phys. Chem, **97**, 8541-8548.

A LABORATORY INVESTIGATION ON UPTAKE OF SO_2, HNO_3 AND HCL BY SINGLE SNOW CRYSTALS

K. Diehl, S.K. Mitra and H.R. Pruppacher

Institut für Physik der Atmosphäre, Johannes Gutenberg–Universität Mainz, Germany

1. INTRODUCTION

It has been well established by field observations that not only cloud and raindrops but also individual unrimed snow crystals and snow flakes contain water soluble compounds. Thus, in the melt water of snow crystals ions such as $SO_4^{2}-$, NO_3^-, Cl^-, Na^+, K^+, NH_4^+ have been identified. Some of these are the result of aerosol particles which have been scavenged by the crystals during their life time. However, some of these ions may also be the result of gases which entered the crystals by adsorption. In the recent past, a number of laboratory experiments have been devoted to this problem (Sommerfield and Lamb, 1986; Johannson and Granat, 1986; Valdez and Dawson, 1989; Mitra et al., 1990; Conklin and Bales, 1993; Diehl et al., 1995; Dominé et al., 1995). Most authors, except Dominé et al. (1995) who studied HCl, Johannson and Granat (1986) and Diehl et al. (1995) concerned themselves with studying SO_2. Unfortunately, also rather high gas concentrations were used which do not allow any conclusion as to the significance of the uptake of gases by snow crystals at atmospheric concentrations. In addition, the following questions remained open:

1. Is the gas uptake gas-type specific? 2. Is the gas uptake affected by the intrinsic quasi–liquid layer on ice? 3. Is the gas uptake affected by the equilibrium melting–point depression? 4. Is the gas uptake affected by the growth of the ice crystal from water vapor? 5. Does the gas taken up by ice crystals remain on its surface or does it enter the body of the ice crystal? 6. Is a gas, once taken up by an ice crystal, able to desorb again? 7. Is a gas taken up by an ice crystal able to affect the rate of evaporation of the crystal? 8. Is the gas uptake by an ice crystal significant in comparison to the gas uptake by a drop?

2. PRESENT EXPERIMENTS

The questions formulated and listed in the previous section were studied by us during the past five years by means of a horizontal wind–tunnel inside a walk–in cold chamber. The ice crystals studied were dendritic, rested on a teflon-net and were exposed to a stream of ice-saturated nitrogen to which SO_2, HCl or HNO_3 were admixed in the desired proportions. The air stream was adjusted to the terminal velocity of ice crystals.

Temperature, humidity and the concentration of the foreign gases were carefully monitored by various gas analyzing instruments. After exposure to the foreign gas the ice crystals were extracted from the tunnel and the amount of gas taken up by the crystals determined by measuring the amount of foreign species present in the melt water described in detail by Mitra et al. (1990) and Diehl et al. (1995).

3. RESULTS

Space limitations do not permit to illustrate all our results with diagrams and tables. We therefore decided to summarize our findings regarding the eight questions listed in section 1 in terms of brief texts using only a few diagrams to highlight two of our results.

1. The gas uptake by an ice surface is gas-type specific. For the three gases SO_2, HCl and HNO_3 the uptake order is $HNO_3 > HCl > SO_2$, at similar gas partial pressures. With increasing partial pressure the gas uptake increases for all gases.

2. The gas uptake is a strong function of temperature. Generally, with increasing temperature the gas uptake increases, with the exception of HNO_3 which exhibits very high gas uptake below -20° C. The increasing gas uptake with increasing temperature is a result of the intrinsic quasi–liquid layer which increases in thickness as the temperature approaches 0° C.

3. As gas becomes dissolved in the intrinsic quasi–liquid layer the equilibrium freezing point

may be depressed, causing surface melting with an associated increasing thickness of the quasi–liquid layer. Whether or not surface melting takes place is determined by the equilibrium phase diagram.

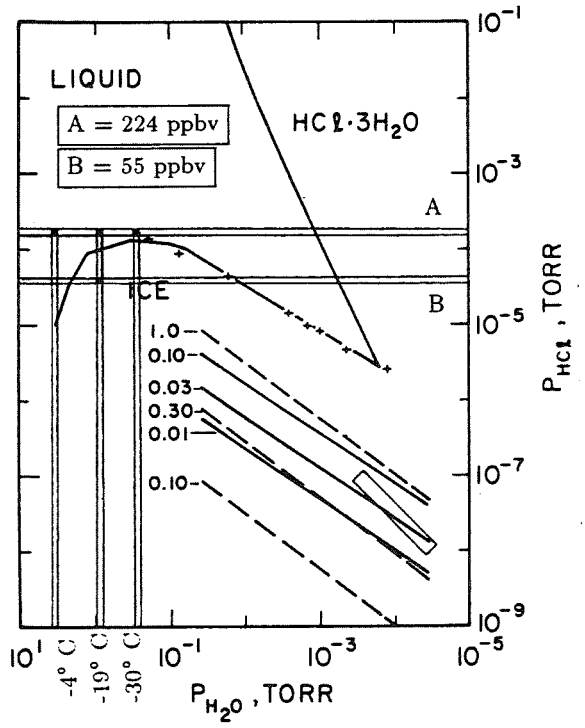

Fig. 1 Equilibrium phase diagram for a HCl/H_2O system (according to Hanson and Mauersberger, 1990. The bands indicate the error margins around the experimental values.).

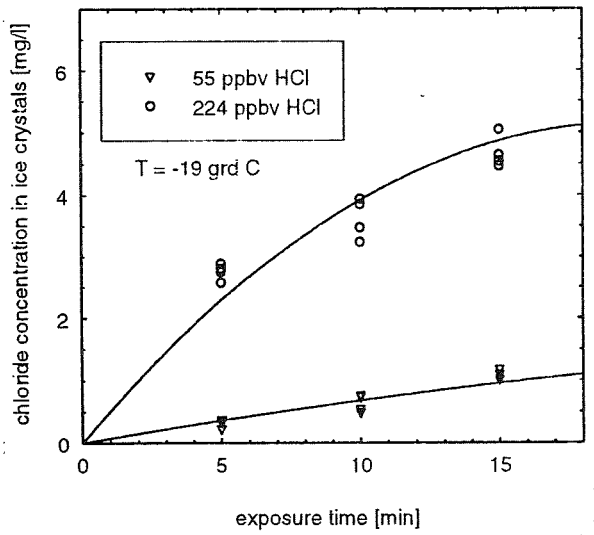

Fig. 2 Variation of the chloride concentration in the melt water of dendritic ice crystals with gas concentration and exposure time at a temperature of -19° C.

This is exemplified in Figure 1 which shows the equilibrium phase diagram of the system HCl/H_2O according to Hanson and Mauersberger (1990). If the partial gas pressure of HCl is above a critical value (about 10^{-4} torr at -19° C) surface melting commences which eventually causes complete melting of the crystal. Below this critical pressure, no surface melting takes place and only the intrinsic quasi–liquid layer is present at the surface.Therefore, it is expected, and demonstrated in Figure 2, that the uptake of HCl is significantly larger above the critical partial pressure than below this pressure.

4. An ice crystal which during the gas uptake grows by diffusion of water vapor incorporates an amount of gas which is proportional to the mass of water vapor converted to ice. Gas uptake by a non–growing crystal involves complicated adsorption isotherms which are affected by the quasi–liquid layer in an unknown manner.

5. The gas adsorbed on a growing or non–growing crystal does not remain only on the ice surface. It is capable of diffusing into the ice along grain boundaries if the ice is polycrystalline and along dislocations if the ice is a single crystal. The diffusivity we found for HCl at -19° C is $D_g = 1.05 \times 10^{-8}$ cm^2sec^{-1} which compared well with values quoted in literature. We note that this value for the gas diffusivity is larger by a factor of about three orders of magnitude than the diffusivity of H_2O in ice.

6. Gases such as HCl and HNO_3, and SO_2 in presence of H_2O_2, which dissociate into ions in the quasi–liquid layer do not desorb anymore unless the crystal evaporates.

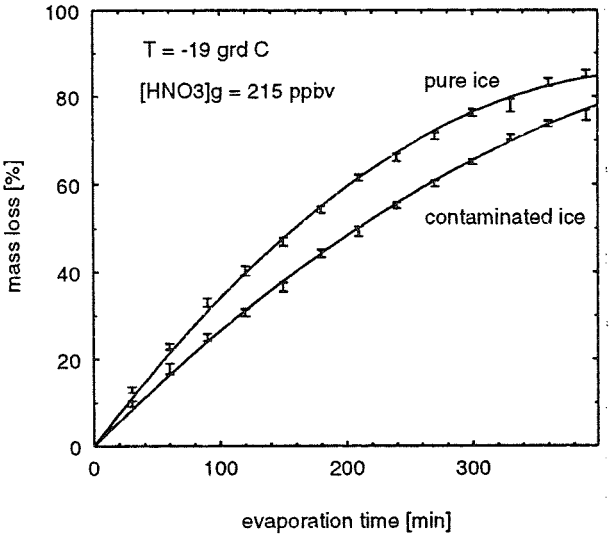

Fig. 3 Evaporation rate of pure ice spheres and ice spheres previously exposed to a HNO_3 gas concentration of 215 ppbv at a temperature of -19° C.

7. Gases taken up by an ice surface affects the flux of water vapor leaving the ice surface and therefore the evaporation rates of the crystal. This is demonstrated in Figure 3 for HNO_3, and in Figure 4 for SO_2 taken up simultaneously with H_2O_2.

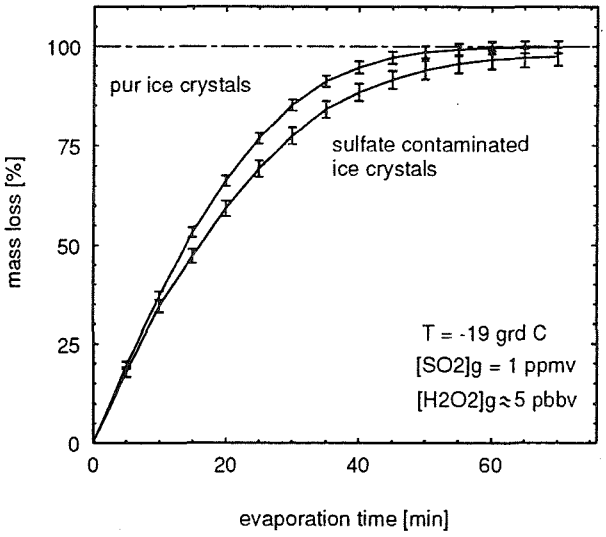

Fig. 4 Evaporation rate of pure ice crystals and ice crystals which grew in an environment with a SO_2 gas concentration of 1 ppmv and H_2O_2 of about 5 ppbv.

8. A comparison of the gas uptake by ice crystals with the gas uptake by cloud and rain drops shows that at similar gas partial pressures drops take up gas much more rapidly and accomodate also more gas mass than an ice particle of the same water mass. In fact, the present studies show that at typical atmospheric gas concentrations the direct uptake of gas by ice crystals may be neglected against the gas uptake by drops. This implies that atmospheric gases enter cloud ice particles mainly by riming.

4. ACKNOWLEDGEMENTS

These studies were supported by the Ministry for Research and Technology of the Federal Republic of Germany under project 0704580B/9. Further fundings were provided by the DFG under SFB 233.

5. REFERENCES

Conklin, M.H., and Bales, R.C., 1993: SO_2 uptake on ice spheres. *J. Geophys. Res.*, **98**, 16, 851–855.

Clappsaddle, C., and Lamb,D., 1989: The sorption behavior of SO_2 on ice at temperatures between -5 and -30° C. *Geophys. Res. Lett.*, **16**, 1173–1176.

Diehl, K., Mitra, S.K., and Pruppacher, H.R., 1995: A laboratory study on the uptake of HNO_3 and HCl vapor by snow crystals and ice spheres at temperatures between 0 and -40° C. *Atmos. Environm.*, **29**, 975–981.

Dominé, F., Thibert, E., Silvente, E., Legrand, M., and Jaffrezo, J.L., 1995: Determining past atmospheric HCl mixing ratios from ice core analyses. *J. Atmos. Chemistry*, **21**, 165–186.

Hanson, D.R., and Mauersberger, K., 1990: HCl/H_2O solid phase vapor pressure and HCl solubility in ice. *J. Phys. Chem.*, **94**, 4700–4705.

Johannson,C., and Granat, L., 1986: An experimental study of the dry deposition of gaseous nitric acid to snow. *Atmos. Environm.*, **20**, 1165–1170.

Mitra, S.K., Barth, S., and Pruppacher, H.R., 1990: A laboratory study on the uptake of SO_2 by snow crystals. *Atmos. Environm.*, **24 A**, 2307–2312.

Sommerfield, R.A., and Lamb, D., 1986: Preliminary mesurements of SO_2 adsorbed on ice. *Geophys. Res. Lett.*, **13**, 349–351.

Valdez, M.P., and Dawson, G.A., 1989: Sulfur dioxide incorporation into ice depositing from the vapor. *J. Geophys. Res.*, **94**, 1095–1103.

A THEORETICAL MODEL FOR SO_2 UPTAKE INTO PACKED ICE BEDS

Thomas Huthwelker[1], Thomas Peter[1], Dennis Lamb[2], Marcia Baker,[3] Brian Swanson[3]

[1] Max-Planck-Institut für Chemie, Mainz, Germany
[2] Atmospheric Sciences Department, Pennsylvania State University (USA)
[3] Geophysics Program, University of Washington (USA)

1. INTRODUCTION

The uptake of sulfur dioxide (SO_2) into ice particles is of great environmental interest: the trace gas is a main precursor of acid rain and its concentration in ice cores reveals information about the history of the Earth's atmosphere. The uptake of SO_2 onto ice was investigated by several researchers [Valdez and Dawson, 1989; Clapsddale and Lamb, 1989; Mitra et al., 1990; Conklin et al., 1993; Sommerfeld and Lamb, 1986; Langenberg and Schurath, 1995] using various experimental techniques and performing the experiments under different physical conditions. For example, uptake was measured onto snowflakes by Mitra et al., into packed poly-crystalline ice beds by Clappesdale and Lamb and by Conklin et al. This renders a direct comparison of the results and an identification of the involved physical elementary processes difficult.

There are a number of conceivable processes responsible for uptake of trace gases onto ice particles: (i) physical adsorption onto the surface; (ii) uptake of the gas into a quasi-liquid layer (QLL); (iii) diffusion into grain boundaries; (iv) diffusion into the bulk of the ice. The temperature dependence of these processes is remarkably different, which should in principle make them experimentally distinguishable. For instance, an increase of the uptake with decreasing temperature is expected when physical adsorption is the dominant process because the sticking of the gas to the surface is the stronger the lower the temperature enabling a larger coverage. This should be the case when there are no QLL and no grain boundaries, or when the transport within them becomes inefficient, as has been indeed observed at very low temperatures by Langenberg and Schurath [1995]. On the other hand, when diffusive processes play the major role, matters are more complicated, because solubility and diffusivity might show an opposing temperature dependence. Since the diffusivity strongly decreases with falling temperature a behaviour opposite to adsorption might be expected, that is the uptake per time unit is the higher the warmer the ice is. Also this has been observed in several experimental studies at high and moderate temperature. However, it should be noted that the diffusivity is a kinetic, not a thermodynamic quantity, hence the speed of uptake is influenced, not necessarily the final amount when equilibrium is established. But in laboratory experiments with a finite measurement time it must in principle be envisaged that equilibrium conditions are not easily reached. Finally, when the QLL is responsible for the uptake the analysis is rendered more difficult. There is at present no self-consistent theory describing the uptake, in particular because the mutual influence of trace gas ions in the QLL and the interfacial forces establishing the QLL is not known. Therefore the saturation concentration of the ionic species and the thickness of the QLL are presently not known.

In this paper we reanalyse some of the packed ice bed experiments of Clapsaddle and Lamb [1989] by applying a flow tube description. In these experiments the uptake was monitored over a period of typically one to two days. The analysis suggests that after the initial 30 minutes to 4 hours the uptake was governed by a diffusive process, while the time dependence is slower than diffusive during the first half hour. We compare this result with other experiments and briefly discuss its consequences.

2. PREVIOUS EXPERIMENTAL FINDINGS

Recently, Langenberg and Schurath [1995] measured the uptake of 1 Pa (10^4 ppb) SO_2 onto ice at temperatures between -68°C and -43° C and found indeed a larger uptake when the temperature is lower. In contrast, at temperatures between –60 and –1°C the opposite temperature dependence, larger uptake at higher temperatures, was found in packed ice bed experiments both by Clapsaddle and Lamb [1989] (hereafter called CL) and Conklin et al. [1993] (called Co). The two experiments are very similar in their setup with the main difference being the length of the packed ice bed, 25 cm in CL's and 12.5 cm in C's experiment. These studies differ by about an fac-

cannot be used to describe this part of the breakthrough curves. Note, that the deviation from equation (1) becomes more significant at lower temperatures which is consistent with an increasing importance of adsorption phenomena at lower temperatures. We used the slope in Fig.2 to determine the quantity $HD^{1/2}$ for the three cases (pb = packed ice bed, w = water, i = ice):

T [°C]	μ [ppb]	$H^*D^{1/2}$ [cm $s^{-1/2}$] SO_2 (pb)	$H^*D^{1/2}$ [cm $s^{-1/2}$] SO_2 (w)	$H^*D^{1/2}$ [cm $s^{-1/2}$] HCl (i)
-5°	90	0.0266	71	0.15
-15°	90	0.0152	86	4.13
-30°	95	0.0057	111	–

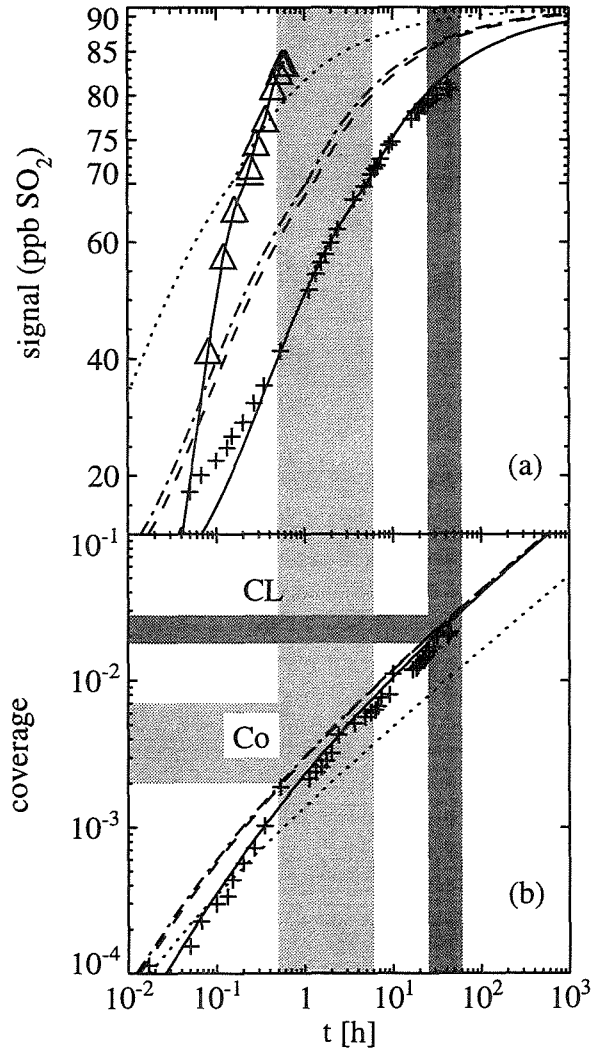

Fig.3 *Breakthrough curves and uptake calculated for $HD^{1/2}$ = 0.0266 cm $s^{-1/2}$ (-5C, 90 ppb) for different reactors. solid line : A_{ice} = 3.17m^2, F=830 cm^3/s, dashed: A_{ice} = 1.58 m^2, F=830 cm^3/s, dash - dot: A_{ice} = 1.04 m^2, F=600 cm^3/s dotted: A_{ice} = 1.04 m^2, F=600 cm^3/s, $HD^{1/2}$ = 0.01cm $s^{-1/2}$ For a description see text.*

From –5°C to –30°C, $H^*D^{1/2}$ decreases by about a factor of 5. In order to interpret this behavior we have calculated $H^*D^{1/2}$ values for the dissolution of SO_2 in supercooled water (with H^* taken from Seinfeld [1986] and D extrapolated from data given by Landolt Boernstein [1969], see fourth row of Table 1. We also compare with measurements of HCl uptake into the bulk of single crystals [Domine et al., 1994], since there are no appropriate SO_2 data. The CL data for $H^*D^{1/2}$ are more than three orders of magnitude smaller than the uptake in supercooled water. However, the temperature behaviour of the CL data is opposite to that of $H^*D^{1/2}$ in water. This contradiction is not eliminated when the data are interpreted in terms of diffusion into single ice crystals instead of diffusion into supercooled water, because also in ice the diffusivity decreases with decreasing temperature. The data for H^* and D in single crystals for HCl from Domine et al [1994] support this conclusion.

Next we use the diffusive flow-tube model to discuss the discrepancies between the measurements of CL and C. Figure 3a shows the breakthrough curve of SO_2 in the the packed ice bed for $HD^{1/2}$ = 0.0266 cm $s^{-1/2}$ (corresponding to –5° C, 90 ppb in CL). Crosses mark data taken by CL, the solid line is calculated from equation (1). The dashed line refers to a tube with half the length (as in Co), while the dash-dotted line is the case with both, A_{ice} and F as used by C. The average surface coverage

$$\theta(t) = \frac{F\sigma_0}{A_{ice}} \int_0^t \frac{p_{in} - p(t')}{kT} dt' \qquad (2)$$

($\sigma_0 = 10^{-15}$ cm^2 molec^{-1}) has been calculated by numerical integration and is shown in Figure 3b. The experimental determination of the end of the breakthrough curve strongly depends on the experimental parameters chosen, as can be seen from comparison of several model lines in Figure 3a. The shaded vertical bars show typical experimental times assumed by CL an C.

But even when the breakthrough curve approaches its final value p_{in} the coverage will still increase due to continuous diffusion. Asymptotically we find for the average surface coverage

$$\theta(t \gg b^2) \rightarrow \frac{\sigma_0 H^*}{2kT} \sqrt{\frac{Dt}{\pi}} \qquad (3)$$

with $b^2 \sim 0.5$ h for CL and 0.1 h for C. Consequently, the average coverage in the experiments mainly depends on the total experimental timescale. Noting the very different timescales in the work of Co (less the 6 h) and CL (25 to 60 h) we find about a factor of 4 difference in the average coverage (shaded horizontal bars in Fig.3b). Note that the breakthrough curves in Co's experiment clearly approached p_{in}, while in CL's experiment the zerosignal was never

tor of 15 in the measured uptake of SO_2. This is illustrated in Figure 1, where we show the uptake per unit area expressed as surface coverage. Coverage 1 corresponds to 10^{15} molecules per cm^2. Coverages for the CL experiment are calculated by using an average ice surface area of 3.17 m^2. In both experiments a gas mixture with a constant partial pressure p_{in} of SO_2 was pumped through a glass column, which was filled with ice spheres of 100 μ m radius. Breakthrough curves, i.e. the temporal development of the SO_2 partial pressure $p(t)$ leaving the packed ice bed, was measured. As soon as the outflowing SO_2 concentration equals the inflowing (i.e $p(t) = p_{in}$) within experimental accuracy, the uptake was considered to be finished and the ice surface to be saturated.

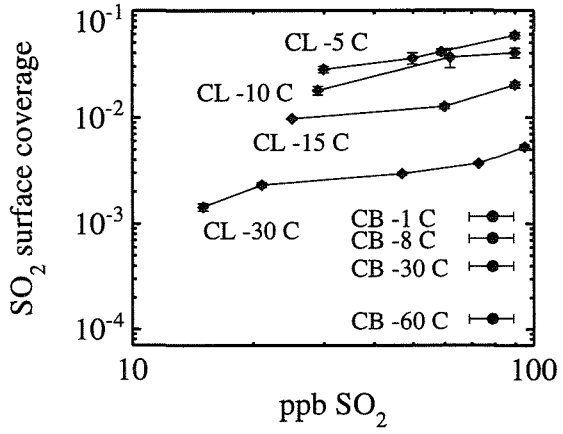

Fig.1 SO_2 *surface coverages derived from the measurements of CL and Co. Surface coverage=1 corresponds to* 10^{15} *molec* cm^{-2}.

Co determined the uptake by analysis of the ice, which was melted after the experiment, while CL integrated the the signal $p(t)$ to determine the loss onto the ice. Furthermore the ice surface area was determined by different methods. It is difficult to assess the systematic error induced by different data evaluation methods.

Remarkable are also the different times needed to reach apparent saturation. In CL's experiments typically measurements times were 1-2 days, while in Co's experiments saturation was reached already after 1-6 hours. We will show that the differences in uptake as well as in saturation times to a large degree can be understood in terms of the lengths of the packed ice beds and the applied flow rates.

CL showed their uptake data as functions of time could be represented by a superposition of two expotential curves which they interpreted as two different physical regimes. Conklin [1993a] used a more sophisticated thermodynamical uptake model and argued that the uptake could possibly be explained by the presence of a QLL, but they did not compare their results with the CL data. In the following we apply a flow tube description to these experiments and compare the CL and Co results in more detail.

3. FLOWTUBE MODELING

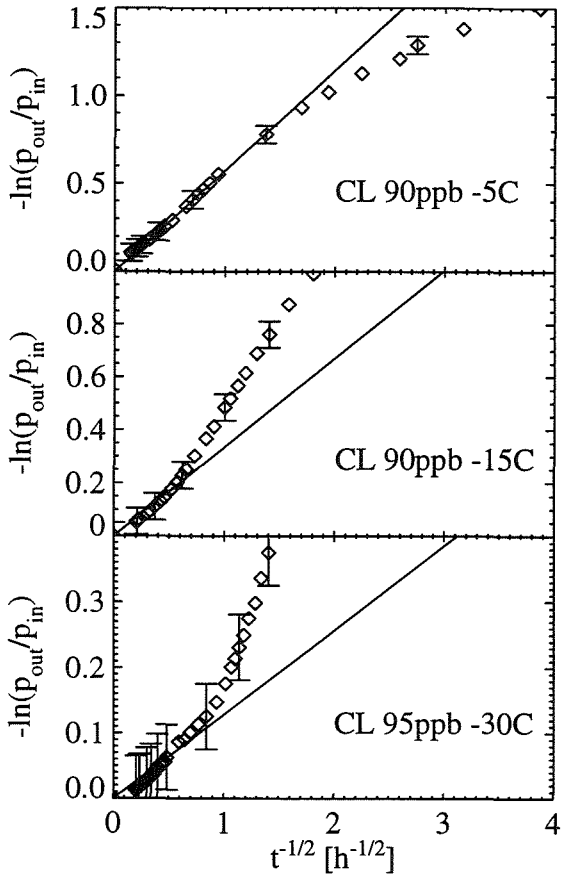

Fig.2 *Determination of* $HD^{1/2}$ *from the CL measurements by comparison with equation (1).*

Since the uptake of trace gases into ice is a composite process consisting of surface processes (e.g. physical adsorption) and of bulk processes like diffusion into grains and the bulk ice, we expect the breakthrough curve to have two regimes: the initial part will be governed by surface processes, but once the ice surface is saturated either the uptake should stop if diffusive processes are absent, or the uptake is governed by diffusion which then determines the form of the breakthrough curve $p(t)$. In the diffusive regimes the uptake process can be described by an analytical expression for the breakthrough curve $p(t)$ (cp. Hanson and Ravishankara [1993])

$$p(t) = p_{in} e^{-b/\sqrt{t}} \qquad (1)$$

where $b = A_{ice} H^{\star} (D/\pi)^{1/2}/F$. Here, A_{ice} is the ice surface area, F the gas flow rate, $H^{\star} = n_l/n_g$ the effective Henry's law constant and D the diffusivity. In Figure 2 we show three cases of the CL data, plotted as $-\ln(p(t)/p_{in})$ vs. $t^{-1/2}$ to test the validity of equation (1). It can clearly be seen, that the diffusive model describes the data for long times quite well. As expected, surface processes dominate the initial phase of the uptake and the diffusive model

reached. The latter used an extrapolation method to determine the end of the uptake, which lead to 53,9 nmol/g (corresponding to $\theta = 0.057$ with $A_{ice} = 3.17m^2$ for the case presented in Fig. 3, while numerical integration of the experimental data yielded $\theta = 0.021$. This gives rise to another factor of 2 difference between the work of CL and Co, thus a diffusive model can account for about a factor of 8 difference between the two studies.

The dotted line in Fig.3 is calculated with equation (1) for a typical case of Co's setup taken and $HD^{1/2} = 0.01$ cm $^{-1/2}$. The triangles in Fig.3a are taken graphically from Fig.2a in Co for the case with -1 ∘C. The diffusion model roughly reproduces the experimental timescale of Co's experiment, but utterly fails to describe the form of the signal. The much steeper increase with time of Co's data possibly suggests that adsorption dominated over diffusive processes. We have no explanation for this different behaviour at present.

There still remains a factor of 2 unexplained, but this may be caused by a systematic difference between the studies: (i) CL determine the loss from the gas phase, while Co analyses the ice phase, consequently the CL data will have wall losses included. Thus the CL data should be higher than the Co data. (ii) The different methods of surface area determination will introduce an unknown sytematic error in the data.

In summary, the presented analysis of the packed ice bed measurements indicates that diffusive uptake of SO_2 may be a major uptake process in such experiments.

It is yet unclear whether the SO_2 diffuses into the bulk ice or into the grain boundaries. Comparision with $H^*D^{1/2}$ values recently measured by Domine et al [1995] on single crystals for HCl show that the uptake into bulk ice can be substantial. In contrast the work of Mulvaney et al. [1988] indicates that the sulphur may accumulate in grain boundaries instead in the bulk ice crystal.

The initial part of the breakthrough curve still remains unexplained and indicates the importance of surface processes, which cannot be described by the present analysis. Our approach could be improved using a more general description of the kinetics including diffusive processes in packed ice columns as presented by Conklin and Bales [1993b], applied to the uptake of H_2O_2 onto ice.

ACKNOWLEDGMENTS

We like to thank Dr. Roger Bales and Dr. Martin Anklin for helpful disscussion. This work was supported by the German Secretary of Education and Research under contract 01 LO 9221/4 and by NSF grant ATM 9223563 and by the University of Washington Graduate School.

REFERENCES

Clapsaddle, C., and D. Lamb, 1989: The Sorption of SO_2 on Ice at Temperatures between -30°C and -60°C; *Geophys. Res. Lett.*, **16**, 1173–1176.

Conklin, M.H. R.A. Sommerfeld, S.K. Laird and J.E.Villinski, 1993: Sulfur Dioxide Reactions on Ice Surfaces: Implications for the dry Deposition to Snow; *Atmospheric Environment*, **27A**, 159–166.

Conklin, M.H. and R.C. Bales,1993a: SO_2 Uptake on Ice Spheres: Liquid Nature of the Ice-Air Interface; *J. Geophys. Res*,**98**,16851–16855 .

Conklin, M.H., A. Sigg, A. Neftel, 1993b: Atmosphere-Snow Transfer Function for H_2O_2: Microphysical Considerations; *J. Geophys. Res.*, **98**, 18367 –18376 .

Domine, F., E. Thibert, F.V. Landeghem, E. Silvente and P. Wagnon, 1994: Diffusion and Solubility of HCl in ice: preliminary results; *Geophys. Res. Lett.*, **21**, 601–604.

Sommerfeld, R.A. and D. Lamb, 1986: Preliminary Measurements of SO_2 adsorbed on ice; *Geophys. Res. Lett.*,**13**, 349–351.

Hanson, D.R. and A.R. Ravishankara , 1993: Uptake of HCl and HOCl onto Sulphuric acid: Solubilities, Diffusivities, and Reaction; *J. Phys. Chem.*, **97**, 12309–12319.

Landold-Börnstein, Zahlenwerte und Funktionen aus Physik, Chemie, Astromomie, Geophysik und Technik; Bd. 5a Transportphänomene I, edited by K. Schäfer, Springer-Verlag 1969.

Langenberg, S. and U. Schurath, 1995: Temperature dependent trace gas – water interactions; in: Tropospheric Oxidation Mechanism, published by the European Commision, Luxemburg, edited by K.H. Becker.

Mitra, S.K., S. Barth and H.R. Pruppacher, 1990: A Laboratory Study on the Scavenging of SO_2 by Snow crystals; *Atmospheric Environment*, **24A**, 2307 – 2312.

Mulvaney, E.W. Wolff and K.Oates, 1988: Sulphuric acid at grain boundaries in Antarctic ice; *Nature*, **331**, 247 – 249.

Seinfeld, J.H.: Atmospheric Chemistry and Physics of Air Pollution (Wiley-Interscience, New York, 1986)

Valdez, M.P. and G.A. Dawson, 1989: Sulfur Dioxide Incororporation into Ice Deposition from the Vapor; *J. Geophys. Res.*,**44**, 1095–1103.

Factors Influencing the Entrapment of Hydrogen Peroxide and Molecular Oxygen in Rime Ice

Jefferson R. Snider and Jun Huang
Department of Atmospheric Science, University of Wyoming, Laramie, WY

1. INTRODUCTION

During the formation of clouds containing liquid droplets those trace gases that have a strong affinity for condensed water are rapidly and efficiently transferred from the gas to the solution phase. This is the case for hydrogen peroxide (H_2O_2), formaldehyde and its hydrate, many inorganic and some organic acid vapors, and ammonia. Growing by vapor diffusion, the droplets seldom reach radii larger than 20 μm and frequently exist at temperatures colder than 0 °C. Supercooling sets the stage for droplet capture and removal via collision with super–millimetric ice particles (i.e., snowflakes or graupel). During capture the droplets impinge against the surface of falling ice particles and are rapidly frozen. This process results in the entrapment of some of the dissolved gas. Precipitation resulting from this growth mechanism, commonly referred to as riming, enhances the vertical transport of trace gases (Cho et al., 1989) and mediates an important removal process.

Current understanding of how entrapment varies with molecular structure of the entrapped gas and with physical properties of the rime substrate, are lacking. As a result, extrapolations of the limited observations to clouds are associated with considerable uncertainty. In this regard it should be pointed out that the field measurements of Snider et al., 1992 (hereafter referred to as SMV) yielded substantially lower H_2O_2 entrapped fractions compared to that indicated by the laboratory studies of Iribarne and Pyshnov (1990). Here we present field measurements of the fractions of both O_2 and H_2O_2 entrapped during riming and compare these results to those previously published by SMV. The discussed retention efficiency values, symbolized by $\Gamma_{H_2O_2}$ and Γ_{O_2}, are expressed as the ratio of the concentration in melted rime ice relative to the liquid–phase concentration predicted by Henry's law.

2. EXPERIMENTAL

The experiments were conducted in supercooled wintertime clouds at Elk Mountain Observatory (EMO, 3.3 km above mean sea level, 41°37' N, 106°32' W), located on an isolated peak in southeastern Wyoming, USA. Rime ice samples were collected on a set of cylinders (3.2 and 9.5 mm diameter) at wind tunnel velocities varied between 4 and 21 m s^{-1}. We refer to this collection device as the cloud water impactor (CWI). At the end of each collection interval the ice samples were removed from the CWI and weighed. The results presented here were analyzed using a mass–medium droplet radius of $\bar{r} = 4.3$ μm (Snider and Huang, 1996).

Measurements of O_2 entrapped in the rime ice were conducted using a vacuum isolation technique. The collected rime ice was put into a thermostated flask (–10 °C), the pressure was lowered to 10 hPa for three min, and then O_2–free water was added. The concentration of O_2 in the melted rime ice/O_2–free water mixture was evaluated using the Winkler method (Carritt and Carpenter, 1966). A mass balance equation was used to calculate the concentration of O_2 entrapped in the rime ice ($C_{O_2,R}$). O_2 losses due to pumping are estimated to be less than 1.8 mg/L (Snider and Huang, 1996). Measurements of dissolved H_2O_2 ($[H_2O_2]$) were conducted using the method of Kok et al. (1986). The concentration measurements discussed above correspond to the total amounts of O_2 and H_2O_2 entrapped in the ice; no attempt was made to distinguish between gases entrapped within the ice lattice or inside bubbles.

A hydroperoxide monitor identical to the instrument described in Snider and Murphy (1995) was used to measure the gas–phase mixing ratio H_2O_2. A device consisting of a small wind tunnel and a reverse–facing air sample inlet was used for sampling air at the EMO. The studies of Snider and Huang (1996) demonstrate that this device samples cloud–interstitial air.

3. CALCULATIONS

Assuming equilibrium, the droplet–dissolved concentrations are given by

$$[H_2O_2]^* = K_{H_2O_2}(T_a) \cdot P_{EMO} \cdot \chi_{H_2O_2} \quad (1)$$

and similarly for O_2

$$C^*_{O_2} = \frac{K_{O_2}(T_a) \cdot P_{EMO} \cdot \chi_{O_2} \cdot M_{O_2}}{V_0} \quad (2)$$

Here T_a is the ambient temperature, $K_{H_2O_2}$ is the Henry's Law constant for H_2O_2 (Lind and Kok, 1994), K_{O_2} is the Bunsen coefficient for O_2 (Weiss, 1970), P_{EMO} (670 hPa) is the pressure at EMO, $\chi_{H_2O_2}$ and χ_{O_2} are the gas mixing ratios, and V_0 (22.41 L/mol) and M_{O_2} (32 gm/mol) are unit conversion factors. The retention coefficients were calculated in the following manner:

$$\Gamma_{O_2} = \frac{C_{O_2,R}}{C^*_{O_2}} \quad (3)$$

$$\Gamma_{H_2O_2} = \frac{[H_2O_2]}{[H_2O_2]^*} \quad (4)$$

Following the work of SMV we have utilized a modified formula for calculating the droplet impaction time

$$\tau_{im} = \frac{4\varrho_w \bar{r}}{3S^2\beta} \quad (5)$$

Here β is the collection–interval–averaged riming rate per unit area of collection surface, ϱ_w is the density of liquid water, and S is the droplet spreading factor. Values of S were interpolated from the experimental data of Macklin and Payne (1969) and depend on both the droplet impaction velocity (V_{im}, m/s) and the ice substrate temperature (T_S). Calculated values of S were used to infer the height of the spread droplet (h). Our assessment of the time constant characterizing droplet freezing (τ_2) is based on the theoretical work of Macklin and Payne (1967) and the experimental studies of Carras and Macklin (1975).

Diffusive transport through the freezing or frozen droplet is characterized by a time constant which is expected to vary with the length of the diffusion path and the diffusivity of the solute. If solute diffusion is via liquid inclusions (Mulvaney et al., 1988), as we have assumed here, then a lower–limit value for the solute diffusion time constant is

$$\tau_D = h^2/D \quad (6)$$

Here D is the diffusivity of either O_2 or H_2O_2 in liquid solution. Considerably larger values of τ_D are expected if there is tortuosity associated with the diffusion path, or if diffusion from the frozen droplet is controlled by the much smaller diffusivities associated with volume diffusion through the crystal lattice.

The characteristic times discussed in the previous paragraphs are ranked in the following manner: τ_{im} (~10^{+0} s) >> τ_D (~10^{-3} s) > τ_2 (~10^{-4} s). The fact that τ_D is larger than the τ_2 and smaller than τ_{im} reinforces our hypothesis that solute volatilization continues subsequent to freezing.

4. RESULTS

Rime ice collections conducted using the CWI correspond to droplet impaction velocities which are considerably smaller than those for the rotating cloud water sampler (CWS) used by SMV. Smaller values of V_{im} result from the fact that both the large and the small cylinders of the CWI are broader than the width of the CWS and because the air velocity in the wind tunnel was lower than the tangential velocity of the CWS. Positive correlations between retention and V_{im} are seen for both O_2 and H_2O_2 in Figure 1. Also plotted is the domain of CWS H_2O_2 retention values, defined by two standard deviations in both $\Gamma_{H_2O_2}$ and V_{im}, and the extreme values. Larger values of V_{im} are associated with larger droplet spreading factors and therefore smaller values of τ_{im}. The results shown in Figure 1 are therefore consistent with our previous assertion (SMV) that volatilization of H_2O_2 occurs subsequent to droplet freezing and prior to burial. Support for this inference is provided by the inverse relationships between τ_{im} and retention shown in Figure 2.

At substrate temperatures warmer than approximately –10 °C the impinged droplets form units composed of several to tens of droplets. Consolidation at T_S > –10 °C is evident both at impact velocities less than 0.1 m/s (Macklin and Payne, 1968) and at values of V_{im} greater than 2 m/s (Macklin, 1962). Parameterizations of droplet spreading are consistent with these observations; both the slope dS/dV_{im} and S increase with increasing T_S. Consolidation may also be influenced by the redistribution of water mass which occurs in response to transient variations in surface temperature and phase description (Baker et al., 1987). Although these inferences are tentative, they point

to the following entrapment scenarios: When droplets impact a rime substrate at temperatures warmer than –10 °C, subsequent impaction events result in consolidation and burial. With continued riming the distance required for solute diffusion increases and solute volatilization is diminished. At temperatures colder than –10 °C the droplets freeze as spheres or truncated spheres. Under these circumstances the extent of entrapment, although it is expected to be less than in the previous scenario, may be controlled by vapor diffusion from droplets which subsequently impinge on the ice substrate. In either case an inverse relationship between retention and τ_{im} is expected and this is what is observed.

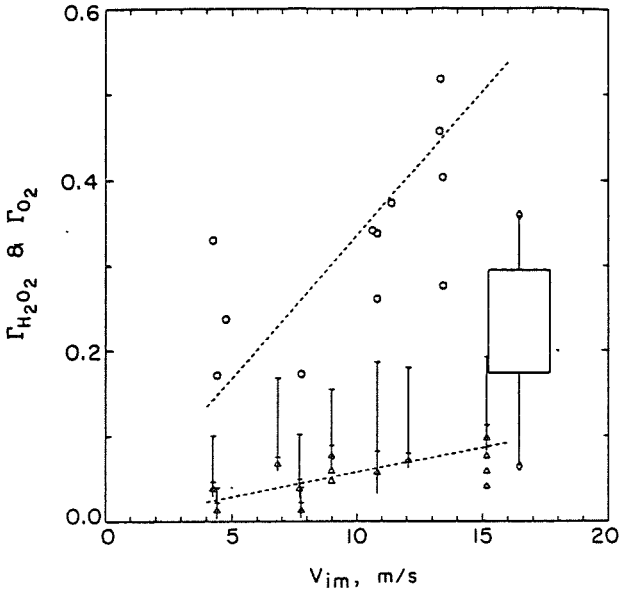

Figure 1 – Values of $\Gamma_{H_2O_2}$ (diamonds and triangles) and Γ_{O_2} (circles) plotted versus droplet impact velocity. Measurements made using the CWS (SMV) are represented by the large rectangle. The width and height of the rectangle are equivalent to two standard deviations of the V_{im} and $\Gamma_{H_2O_2}$ averages. Extreme CWS $\Gamma_{H_2O_2}$ values (diamonds) are also shown. All other samples were collected using the CWI. Statistical uncertainties are indicated by vertical lines. Potential biases in the measurements of $\Gamma_{H_2O_2}$ (Snider and Huang, 1996) are indicated by vertical line segments which extend above the lower horizontal segment and terminate at the upper horizontal segment. The dashed lines are fits of the measurements made using the CWI.

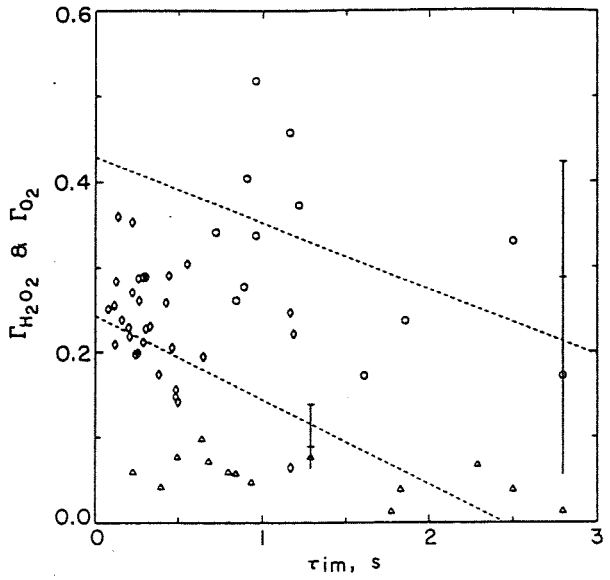

Figure 2 – O_2 (circles) and H_2O_2 (diamonds and triangles) retention coefficients versus droplet impact time. Typical errors are shown as in Figure 1, but for only two data points. Measurements made using the CWS (SMV) are indicated by diamonds. The dashed lines are fits of the form $y = m \cdot x + b$; both the CWI and CWS data were used to infer the $\Gamma_{H_2O_2}$ best–fit line.

The manner in which the properties of the solute influence retention is still a matter of debate. The results presented in Figures 1 and 2 indicate that O_2 is retained with greater efficiency than H_2O_2. This conclusion is reinforced by the studies of Carras and Macklin (1975) which demonstrate that Γ_{O_2} increases with freezing rate (i.e., h/τ_2) and that Γ_{O_2} is equal to ~0.7 at a freezing rate of 1 cm/s. We also found a positive correlation between Γ_{O_2} and h/τ_2, but the range of the latter variable (0.9 to 1.7 cm/s) was small compared to that produced in the laboratory by Carras and Macklin. Values of Γ_{O_2} larger than $\Gamma_{H_2O_2}$ are consistent with the five–fold larger ice/solution distribution coefficients for O_2 relative to H_2O_2 (Körber, 1988; Sigg and Neftel, 1988). As a consequence more H_2O_2 is rejected into the unfrozen liquid where it can readily diffuse to the air/substrate interface.

The retention measurements shown in Figures 1 and 2 also allow us to predict the extent of dissolved gas entrapment during collisional interactions between rimed hydrometeors and supercooled droplets. Based on the data presented in Figure 1 we conclude that O_2 and H_2O_2 retention increase with fall speed and that the $\Gamma_{H_2O_2}$ values published by SMV represent upper–limit estimates for most rimed hydrometeors. Furthermore, the results presented in Figure 2 indicate that the rate of droplet burial significantly influences the scavenging of H_2O_2 from mixed–phase clouds. These observations suggest that in addition to fall velocity there are other important determinants of trace gas retention, i.e., cloud water content, droplet radius, and substrate temperature.

5. CONCLUSIONS

The averaged value of $\Gamma_{H_2O_2}$ is 0.05 when collections are made on a set of cylindrical collection rods, the CWI. The average increases to 0.23 for samples collected using a rotated collector, the CWS (SMV). The CWI cylinders (3.2 and 9.5 mm) are broader than the CWS impaction ribbons (0.5 mm). Also, the CWI was used to sample cloud droplets from a wind tunnel operated at velocities equal to or smaller than the tangential velocity of the CWS. Averages of the retention efficiency for molecular oxygen derived from measurements made using the CWI are 0.32 and varied with many of the same physical properties found to influence $\Gamma_{H_2O_2}$. These field measurements of $\Gamma_{H_2O_2}$ are considerably smaller than the laboratory measurements of Iribarne and Pyshnov (1990). Recent work conducted at the EMO indicates that this disparity is not due to subsaturated H_2O_2 concentrations in the cloud droplets (Snider and Huang, 1996).

Our observation of larger retentions for molecular oxygen relative to hydrogen peroxide is attributed to the fact that the ice/solution partition coefficient for O_2 is larger than that for H_2O_2. Hence, a larger fraction of dissolved H_2O_2 is excluded into the unfrozen solution and lost to the gas phase via diffusive mass transfer. Although the proposed entrapment mechanism is consistent with recent measurements of solute diffusivity in polycrystalline ice (Diehl et al., 1995), more work is needed to characterize the physical and chemical properties of liquid inclusions within rime ice and the manner in which subsequent droplet impaction events affect the rate of solute volatilization.

6. REFERENCES

Baker, B., M. B. Baker, E. R. Jayaratne, J. Latham, and C. P. R. Saunders, The influence of diffusional growth rates on the charge transfer rebounding collisions between ice crystals and soft hailstones, *Quart. J. R. Met. Soc.*, *113*, 1193–1215, 1987.

Carras, J. N. and W. C. Macklin, Air bubbles in accreted ice, *Quart. J. R. Met. Soc.*, *101*, 127–146, 1975.

Carritt, D.E., and J.H. Carpenter, Comparison and evaluation of currently employed modifications of the Winkler method for determining dissolved oxygen in seawater; a NASCO report, *J. Marine Res.*, 24, 286–318, 1966.

Cho, H. R., M. Neiwiadomski, J. V. Iribarne, and O. Melo, A model of the effect of cumulus clouds on the redistribution and transformation of pollutants, *J. Geophys. Res.*, *94*, 12895–12910, 1989.

Diehl, K., S.K. Mitra, and H.R. Pruppacher, A laboratory study of the uptake of HNO_3 and HCl vapor by snow crystals and ice spheres at temperatures between 0 and –40 °C, *Atmos. Environ.*, 29, 975–981, 1995.

Iribarne, J. V., and T. Pyshnov, The effect of freezing on the composition of supercooled droplets–I. Retention of HCl, HNO_3, NH_3 and H_2O_2, *Atmos. Environ., 24A*, 383–387, 1990.

Kok, G. L., K. Thompson, A. L. Lazrus, and S. E. McLaren, Derivatization technique for the determination of peroxides in precipitation, *Anal. Chem.*, *58*, 1192–1194, 1986.

Körber, C., Phenomena at the advancing ice–liquid interface: solutes, particles and biological cells, *Quart. Review of Biophys., 21*, 229–298, 1988.

Lind, J. A., and G. L. Kok, Correction to "Henry's law determination for aqueous solutions of hydrogen peroxide, methylhydroperoxide, and peroxyacetic acid" by John A. Lind and Gregory L. Kok, *J. Geophys. Res.*, *99*, 21119–21119, 1994.

Macklin, W.C., The density and structure of ice formed by accretion, *Q. J. R. Meteorol. Soc.*, 88, 30–50, 1962.

Macklin, W. C. and G. S. Payne, A theoretical study of the ice accretion process, *Quart. J. R. Met. Soc.*, 93, 195–213, 1967.

Macklin, W. C. and G. S. Payne, Some aspects of the accretion process, *Quart. J. R. Met. Soc.*, *96*, 167–175, 1968.

Macklin, W. C. and G. S. Payne, The spreading of accreted droplets, *Quart. J. R. Met. Soc.*, *95*, 724–730, 1969.

Mulvaney, R., Wolff, E.W., and K. Oates, Sulfuric acid at grain boundaries in Antarctic Ice, *Nature*, 331, 247–249, 1988.

Sigg, A., and A. Neftel, Seasonal variations in hydrogen peroxide in polar ice cores, *Ann. Glaciol.*, *10*, 157–162, 1988.

Snider, J. R., and J. Huang, Factors influencing the entrapment of hydrogen peroxide and molecular oxygen in rime ice, manuscript submitted to *J. Geophys. Res.*, 1996.

Snider, J. R., D. C. Montague, and G. Vali, Hydrogen peroxide retention in rime ice, *J. Geophys. Res.*, *97*, 7569–7578, 1992.

Snider, J.R., and T. Murphy, Airborne hydrogen peroxide measurements in supercooled clouds, *J.Geophys.Res.*, 100, 23039–23050, 1995

Weiss, R. F., The solubility of nitrogen, oxygen and argon in water and seawater, *Deep–sea Research*, *17*, 721–735, 1970.

7. ACKNOWLEDGEMENTS

This work was supported by National Science Foundation Grants ATM–9012805 and ATM–9314358.

IN-SITU TRACE GAS OBSERVATIONS IN DISSIPATING THUNDERCLOUDS DURING POLINAT

H. Huntrieser[1], H. Schlager[1], P. van Velthoven[2], P. Schulte[1], H. Ziereis[1], U. Schumann[1], F. Arnold[3], J. Ovarlez[4]

[1] DLR, Institut für Physik der Atmosphäre, Oberpfaffenhofen, Germany
[2] Koninklijk Nederlands Meteorologisch Instituut (KNMI), AE de Bilt, Netherlands
[3] Max-Planck Institut für Kernphysik, Heidelberg, Germany
[4] LMD Ecole Polytechnique, Palaiseau, France

1. INTRODUCTION

This study is a preinvestigation for a field campaign scheduled for summer 1996 in southern Bavaria to study the production of NO_X by lightning discharges and the transport in convective storms. During the POLINAT (*Pollution from Aircraft Emissions in the North Atlantic Flight Corridor*) field experiment performed last summer (1995) near Shannon (Ireland) some of the aircraft-based trace gas measurements turned out to be useful for this prestudy. One of the major objectives of POLINAT is to quantify the contribution of NO_X ($NO+NO_2$) aircraft emissions with regard to other nitrogen oxide sources in the upper troposphere and lower stratosphere. These include: 1) upward transport of polluted air from the planetary boundary layer, 2) downward transport from the stratosphere and 3) production by lightning discharges (e. g., Ehhalt et al., 1992). The vertical redistribution of airmasses can occasionally cause an increase in NO_X, since the vertical NO profile exhibite a C shape (Drummond, 1988). In addition, electrified clouds are an important source of atmospheric NO_X as observed by e.g. Drapcho et al. (1983) and Franzblau and Popp (1989). During and following convective activity photochemical ozone (O_3) production can be enhanced in the upper troposphere (Dickerson et al., 1987; Crutzen, 1988). Deep convection is also capable of transporting and redistributing significant amounts of trace species in the troposphere. In the present study in-situ trace gas measurements in dissipating thunderclouds during POLINAT are presented and discussed.

2. MEASUREMENTS

Most of the flights during the POLINAT field experiment in summer 1995 were carried out to measure signatures of aircraft emissions in the North Atlantic flight corridor. However, one flight (1 July 1995) was performed to search for remnants of a squall line that caused severe thunderstorms the day before over southern Ireland (Fig. 1). The research aircraft Falcon of DLR (Deutsche Forschungsanstalt für Luft- und Raumfahrt) was deployed with chemical instruments for measurements of NO, CO_2, O_3 [DLR], H_2O [LMD], HNO_3 and acetone $(CH_3)_2CO$ [MPI]. Figure 2 shows time series of various measured trace gases from 1 July along a constant-altitude flight track at 31.000 ft (9.5 km) south of Ireland. Indeed, five distinct segments with enhanced NO concentration were observed labeled 1 to 5 in Figure 2. Apart from the variations of the trace gas abundances, we also analysed Meteosat images, and backward and forward trajectories of the probed air parcels to explain the cause for the NO enhancements in the upper troposphere.

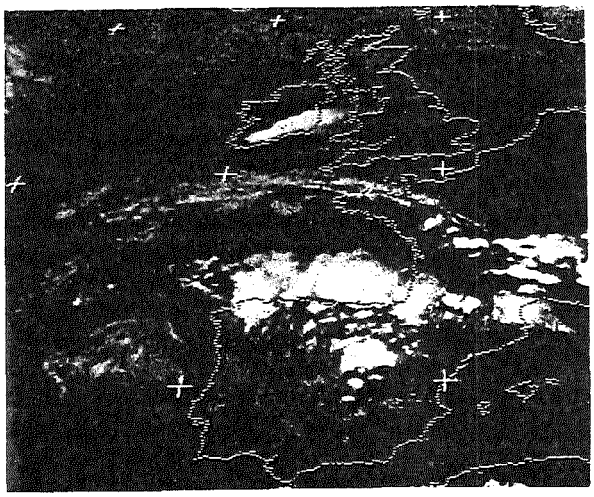

Fig. 1 Meteosat image (IR) from 30 June 1995 at 17 UTC. A distinct squall line is visible over southern Ireland, a thin cloud belt is approaching Ireland from the south and large thunderstorm clusters are visible over northern Spain.

The location of the flight segments with enhanced NO are shown in Figure 3. One segment (number 5) has a horizontal extent of almost 100 km. In comparison the extent of NO-signatures caused by aircraft plumes reaches about 1 km. The horizontal extent of all five flight segments with enhanced NO concentrations is listed in Table 1. The flight track (Fig. 3) was located in a region with a high pressure bridge between two lows, one cut-off-low over the Bay of Biscay and one more extensive low over Scandinavia. Weak winds are blowing from the north in the western part of the flight track and from the south in the eastern part of the flight track.

Segment No.	Length (km)
1	63
2	0.5
3	27
4	20
5	90

Tab. 1 Horizontal extent of flight segments with markedly enhanced NO concentrations.

Segment	1	2	3	4	5
CO_2	-	+	-	-	-
O_3			-		-
H_2O	+		+	-	+
Acetone	-		-	+	-
HNO_3			+		+

Tab.2 Enhancements (+) and reductions (-) of trace gas abundances in the flight segments with enhanced NO concentration. The empty cells indicate that no significant trace gas variations were observed.

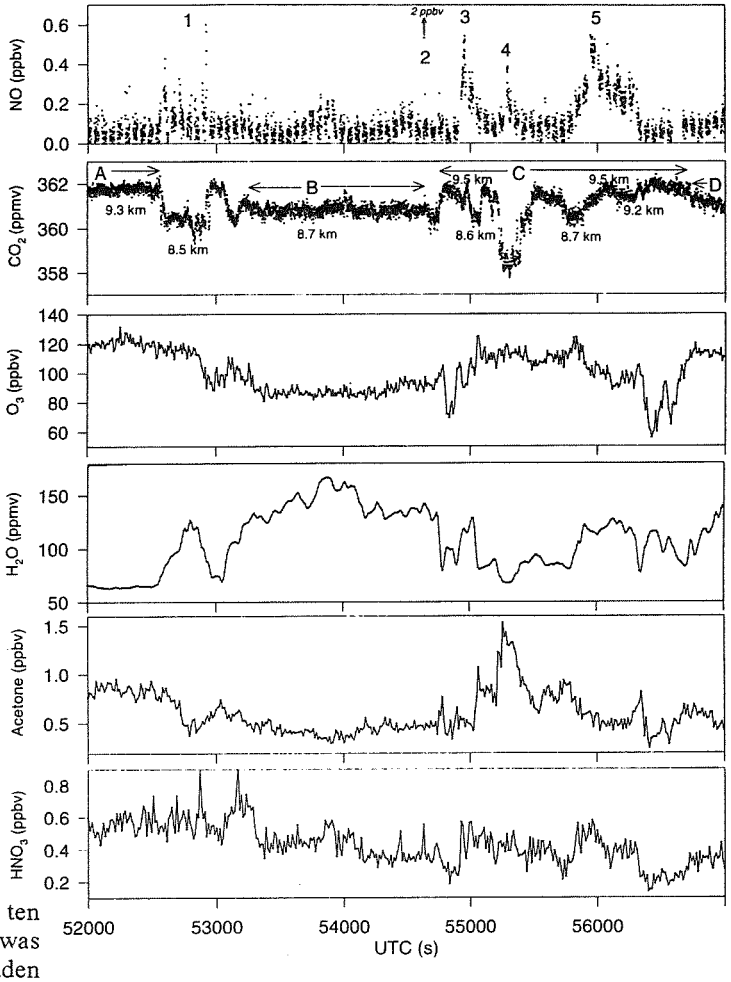

Fig. 2 Time series for NO (resolution 1 s), CO_2 (1 s), O_3 (10 s), HNO_3 (~15 s), H_2O (10 s) and acetone $(CH_3)_2CO$ (~15 s) measured on 1 July 1995 at constant pressure altitude of 31.000 ft (9.5 km). Several flight segments (altogether 5) with markedly enhanced NO concentrations were observed. Airmasses with different trace gas characteristics are labeled with A, B, C and D (the origin height of each airmass is given in km).

During flight segment 3 and 5 a five to ten times higher NO concentration (~0.6 ppbv) was measured in comparison to the background. A sudden increase in O_3 and decrease in CO_2 was also observed at the margins of these two flight segments together with other chemical similarities. It is also striking that both segments 3 and 5 show nearly the same structures (variations of trace gas abundances) but mirrored (e.g., for O_3 in Fig. 4). Overall, flight segment 3 and 5 show a reduced CO_2 and O_3 concentration in comparison to the background (margins of the flight segments excluded).

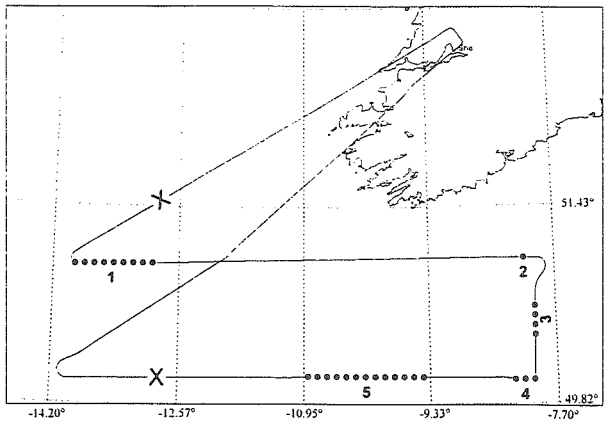

Fig. 3 Detailed presentation of the flight track south of Ireland from 1 July 1995. The horizontal extent of the five flight segments with enhanced NO concentrations are indicated with bold dots. The begin and end of the flight at constant cruise level (31.000 ft = 9.5 km) is indicated with X.

The observed trace gas variations in the segments 1 to 5 are summarized in Table 2. Extremly low CO_2 and high acetone concentrations are measured in flight segment 4. Striking is also that flight segment 2 is the only one with an increase in CO_2.

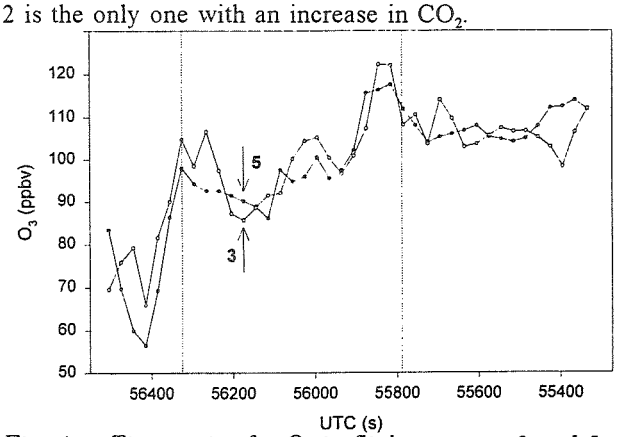

Fig. 4 Time series for O_3 in flight segment 3 and 5 (mirrored)

3. RESULTS

3.1 Possible NO sources for flight segment 1-5

The possible NO sources responsible for the enhanced NO concentration in the five flight segments are discussed in this section. The trace gas variations in flight segment number 2 are quite different than in the rest, since the CO_2 concentration shows a positive correlation with the NO concentration. In addition, this flight segment has a very small horizontal extent (0.5 km) in comparison to the rest (Tab. 1). Flight segment 2 shows the typical pattern of an aircraft plume with a narrow increase in NO (2 ppbv) and CO_2 (Schumann et al., 1995). The horizontal extent of the other flight segments with enhanced NO concentration (number 1, 3, 4 and 5) varies between 20 and 90 km. Therefore, and because of the fact that the CO_2 concentration shows a distinct negative correlation with the NO concentration, emissions from aircraft are unlikely as a possible NO source for these flight segments.

Simultaneous observations of tracer species allow to specify the origin of the airmasses encountered in segment 1, 3, 4 and 5. If the NO increases in these segments would be due to downward transport from the stratosphere, the O_3 and CO_2 concentrations should increase simultaneously and the H_2O concentration should decrease. However, the opposite observations were made in flight segment 1, 3, 4 and 5 as shown in Table 2. It follows, that only two NO sources remain: upward transport of polluted air from the PBL and production by lightning discharges. The CO_2 and acetone signatures (decrease) in flight segment 1, 3 and 5 show that the sampled air originated from the middle or upper troposphere and has not been transported from the PBL, considering the observed vertical distribution of these trace gases in the eastern North Atlantic region during POLINAT. Thus, the only possible source for the large NO increase in these flight segments appears to be NO production by lightning discharges, since transport of air from the middle or upper troposphere can hardly enhance the NO concentration (C-shape). In contrast, very high acetone and low CO_2 concentration were observed in flight segment 4 indicating that the air must have been transported from the PBL.

3.2 Origin of the encountered airmasses

The whole flight can be divided into segments with different CO_2 levels labeled A (~362 ppmv), B (~360.5 ppmv), C (maximum ~362 ppmv) and D (~360.5 ppmv) as shown in Figure 2. A comparison between the average trace gas concentrations in segment A and B shows a distinct lower O_3, CO_2, HNO_3 and acetone concentration and a distinct higher H_2O concentration in segment B (NO concentration is similar). The transition zone between A and B can be regarded as a transition zone between airmasses originating from different heights. Lower CO_2 values (in segment B) indicate that the airmass has been transported from altitudes below the measuring level. O_3, H_2O and acetone are also useful tracers for the determination of the origin height of an airmass for the short transport time scales relevant here. For example, similar trace gas concentrations (CO_2 and acetone) are measured in airmass A and C (maximum concentrations) which indicate that the origin height of these two airmasses must be similar (see also Section 3.3). In addition, airmass B (before flight segment 3) and D (after flight segment 5) must be identical (confirmed by the observed trace gas concentrations), since there exists a connection between flight segment 3 and 5 (Section 2). A correlation plot for NO and CO_2 (Fig. 5) indicates which flight segments contain NO produced by lightning (flight segment 1, 3, and 5) and NO transported from the PBL (flight segment 4). The two accumulations of dots indicate the trace gas conditions existing in airmass A and B. It is obvious that the maximum vertical transport (min. CO_2 level = 360.5 ppmv) in flight segment 3 and 5 is similar to the vertical displacement of airmass B. However, this upward transport cannot be responsible for the increase in the NO concentrations.

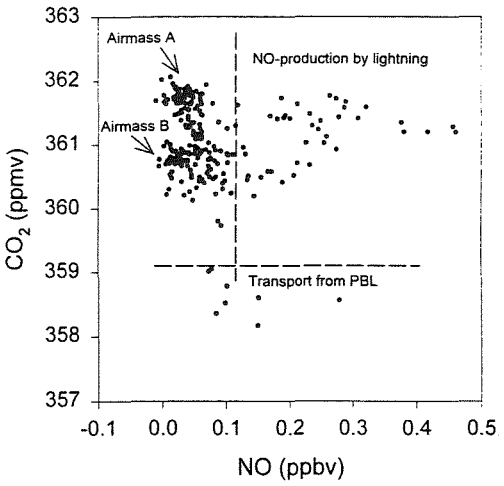

Fig. 5 Correlation plot for NO and CO_2.

3.3 Trajectory calculations

Backward trajectory calculations (by using ECMWF data) have been carried out from positions along the flight track with a time resolution of 5 min. However, in the flight segments with enhanced NO concentration a higher temporal resolution of 1 min was used. The trajectories were followed back 5 days to 26 June 12 UTC (Fig. 6). Again three different airmasses (A, B=D, C) can be distinguished as by the separation using trace gases (CO_2). In the western part of the flight track (airmass A) the trajectories are moving very slow from the north-west (origin height: 9.3 km). In the middle part of the flight track (airmass B and D) the trajectories are also moving rather slow, however, from the south-east (8.7 km). In comparison the trajectories in the eastern part of the flight track (airmass C) are moving very fast from the south (8.6-9.5 km). For example, 24 hours before the flight these trajectories just left Spain. The origin height of each airmass was determined for the moment when the backward trajectories the last time experienced marked upward motions. The backward trajectories of the flight segment 3 and 5 could be clearly followed back to the centre of a large thunderstorm over the northern coast

of Spain (45.0°N, 8.0°W) which has been active the evening before the flight (Fig. 1). At this time flight segment 3 and 5 experienced the largest upward motion (from 8.6 and 8.7 km, see Fig. 2). Corresponding to the statement made in Section 3.1 the trajectories of flight segment 1, 3 and 5 show that no airmass transport has taken place from the PBL or stratosphere. The only explanation left for the enhanced NO concentration measured in these flight segments appears to be NO production by lightning discharges. If the background NO concentration measured in airmass A or B is subtracted from the NO concentration in flight segment 3 and 5 (Fig. 2) the NO concentration left corresponds to the remnant amount of NO produced by lightning discharges about 24 hours earlier (~0.5 ppbv). The variations in the CO_2 concentration in flight segment 3 and 5 ("W-pattern", partly also visible in O_3 except at the margins) can also be explained by the vertical airmass transport from different heights. In flight segment 5 the first minimum value ~360.5 ppmv is transported from 8.6 km, the maximum value ~362 ppmv is in flight level 9.5 km (no vertical transport) and the second minimum value ~361.5 ppmv is transported from 9.2 km (Fig. 3).

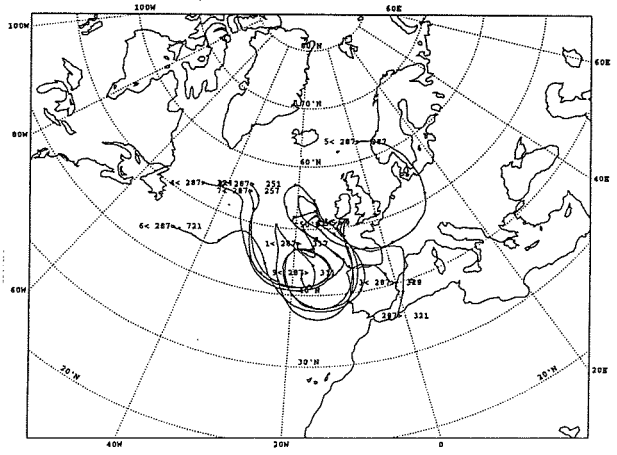

Fig. 6 Backward trajectories (-122 h) for the flight track from 1 July 1995 14-15 UTC.

Finally, as a test forward trajectories were calculated starting 20 hours before the flight from three distinct cloud belts as described in Figure 1 (start: 30 June 18 UTC). The calculations show that the squall line over southern Ireland (the day before the flight) moved to central England and no remnants of that line were penetrated by the measuring aircraft. However, the other two cloud belts from Spain were crossed by the flight track.

4. CONCLUSIONS

The observed variations in trace gas concentrations during the flight from 1st July 1995 south of Ireland can be divided into three different scales as defined by Orlanski (1975). The largest scale variations (meso-α: 200-2000 km) are due to airmass changes A-D (transported from different heights) which are clearly visible in CO_2 and also recognizable in H_2O and acetone. The NO-values at cruise altitude (9.5 km) varies in the different airmasses between ~0.05-0.10 ppbv. The mid scale variations (meso-β: 20-200 km) correspond to the scale of single thunderstorms or thunderstorm lines. Satellite images from the afternoon of the 1 July indicate that the Falcon twice crossed a very thin (less than 50 km) but very long cloud belt during the measurements of enhanced NO (flight segment 3 and 5). The increase in NO (~0.5 ppbv) has probably mainly been produced by lightning discharges during the active phase of a large thunderstorm over northern Spain about 20 hours earlier. The upward transport of the probed air parcels in the thunderstorm line was rather small (origin height 8.7 km). Therefore, it is assumed that the majority NO was produced by lightning. The smallest scale variations (meso-γ: 2-20 km) correspond to the scale of a fresh aircraft plume (visible in NO and CO_2). One distinct plume was measured during the flight with a maximum NO concentration of 2 ppbv. More investigations in this direction will be carried out this summer (1996) including direct observations in thundercloud anvils. It is also planned to make several trace gas measurements during different stages of the thunderstorm development (pre and post convective conditions).

ACKNOWLEDGEMENTS

The authors are grateful to B. Messmer and R. Lühti (Atmosphärenphysik, ETH, Zürich) for providing the Meteosat images and to H. Mannstein (Institut für Physik der Atmosphäre, DLR, Oberpfaffenhofen) for processing the satellite images.

REFERENCES

Crutzen, P. J., 1988: Tropospheric ozone: an overview, in *Tropospheric Ozone, Regional and Global Scale Interactions* edited by I. S. A. Isaksen, D. Reidel, Norwell, Mass., 73-81.

Dickerson, R. R., Huffman, G. J., Luke, W. T., Nunnermacker, L. J., Pickering, K. E., Leslie, A. C. D., Lindsey, C. G., Slinn, W. G. N., Kelly, T. J., Daum, P. H., Delany, A. C., Greenberg, J. P., Zimmermann, P. R., Boatman, J. F., Ray, J. D., and Stedman, D. H., 1987: Thunderstorms: An important mechanism in the transport of air pollutants. *Science*, **235**, 460-465.

Drapcho, D. L., Sisterson, D., and Kumar, R., 1983: Nitrogen fixation by lightning activity in a thunderstorm. *Atmos. Environment*, **17**, 729-734.

Drummond, J. W., Ehhalt, D. H. and Volz, A., 1988: Measurements of nitric oxide between 0-12 km altitude and 67°N to 60°S latitude obtained during STRATOZ III, *J. Geophys. Res.*, **93**, 15831-15849.

Ehhalt, D. H., Rohrer F. and Wahner, A., 1992: Sources and distribution of NO_x in the upper troposphere at northern mid-latitudes. *J. Geophys. Res.*, **97**, 3725-3738.

Franzblau, E. and Popp, C., J., 1989: Nitrogen oxides produced from lightning. *J. Geophys. Res.*, **94**, 11089-11104.

Orlanski, I., 1975: A rational subdivision of scales for atmospheric processes. *Bull. Amer. Meteor. Soc.*, **56**, 527-530.

Schumann, U., Konopka, P., Baumann, R., Busen, R., Gerz, T., Schlager, H., Schulte, P., and Volkert, H., 1995: Estimation of diffusion parameters of aircraft exhaust plumes near the tropopause from nitric oxide and turbulence measurements. *J. Geophys. Res.*, **100**, 14147-14162.

THE ACCURACY OF APPROXIMATE NUMERICAL SOLVER TECHNIQUES IN SOLVING THE GAS-AQUEOUS CHEMICAL SYSTEM

Mary C. Barth, Peter Hess and Sasha Madronich

National Center for Atmospheric Research
Boulder, Colorado

1. INTRODUCTION

Chemistry transport models have proven to be useful tools for predicting air quality regionally and globally. With the exception of models describing acid deposition, during the past two decades chemical transport models have focused primarily on clear air conditions, but recently the importance of clouds to atmospheric chemistry has been addressed (Lelieveld and Crutzen, 1991).

In developing chemistry transport models one of the most difficult problems has been solving a stiff set of chemical equations efficiently and accurately. Several studies have addressed this problem for clear air conditions (Hesstvedt *et al.*, 1978; Gong and Cho, 1993). Subsequent studies (Saylor and Ford, 1995) have attempted to assess the accuracy and efficiency of various approximate solvers for gas-phase chemical mechanisms, but none of these studies has examined the gas-aqueous system of clouds. When clouds are included in chemistry models, they introduce a strong shock to the chemical system that may be difficult for chemical transport models with large timesteps to handle.

Chemistry transport models and cloud models have vastly different temporal and spatial scales. Cloud models usually have integrated with a timestep of 1–10 seconds, regional-scale models have integrated with a timestep of a few (~5) minutes, and global-scale models have integrated with a timestep of about 30 minutes. With large timesteps such as those found in regional and global chemical transport models, using the correct numerical solution technique to solve both gas and aqueous chemistry may be crucial when the solver is shocked by the introduction of liquid water. In this presentation we will discuss how well the Hesstvedt *et al.* (1978) solution method and the Euler Backward Iterative (EBI) solution method predict the chemical concentrations in a gas-aqueous system by comparing the results from the approximate solutions for different timesteps to the results from the Gear (1971) solution.

2. DESCRIPTION OF SOLUTION TECHNIQUES

To solve the chemical concentration of a species in a chemical transport model, the equation

$$\frac{dC}{dt} = P - L\,C \tag{1}$$

is solved, where C is the concentration of the species, P the production rate of the species, and L the first order rate constant depicting the destruction of the species. For the purposes of comparing numerical solver methods, species concentrations are only changed through using Eq. (1). Because chemical species found in the troposphere have vastly different lifetimes and because the chemical species mutually depend upon each other, equation (1) becomes a stiff set of ordinary differential equations. In the following sub-sections, a description is presented of the way the Hesstvedt *et al.* (1978) and the Euler backward iterative methods solve equation (1).

2.1 Hesstvedt Technique

The Hesstvedt solution technique uses three methods of solving the ordinary differential equations depending upon the characteristic time, $\tau = 1/\mathrm{L}$, of a chemical species. The following solutions may be determined when τ is compared with the timestep, Δt, of the integration.

If $\tau \ll \Delta t$, then a steady state solution is assumed, that is,

$$C^{n+1} = \frac{P}{L}. \tag{2}$$

If $\tau \gg \Delta t$, then an Euler forward solution is used,

$$C^{n+1} = C^n + (P - L\,C^n)\,\Delta t. \tag{3}$$

If $\tau \sim \Delta t$, then a semi-analytical solution is used,

$$C^{n+1} = \frac{P}{L} + (C^n - \frac{P}{L})\,exp(-\frac{\Delta t}{\tau}). \tag{4}$$

The semi-analytical solution is termed the quasi-steady-state approximation (QSSA) and the simulations that used the Hesstvedt technique are noted as QSSA in this paper. To give a more accurate solution, the production term, destruction term, and characteristic time are evaluated at t + $\frac{1}{2}$ Δt resulting in the need to iterate the solution. Note that because the semi-analytical method is nonlinear, the Hesstvedt technique, in general, does not conserve mass.

2.2 Euler Backward Iterative Technique

The Euler backward iterative (EBI) technique is an implicit scheme,

$$C^{n+1} = \frac{C^n + P^{n+1}\,\Delta t}{1 + L^{n+1}\,\Delta t} \qquad (5)$$

As indicated in the equation, the production and loss terms are evaluated at time t + Δt. Therefore the solution must be iterated until the concentrations at t + Δt are found. Because Eq. (5) is a linear relation, the EBI technique conserves mass once the solution has converged. A characteristic of this technique especially for long timesteps is that it can develop an oscillatory behavior. To minimize the oscillations, the solution of one of the iterations is averaged with the solution from the previous iteration.

2.3 Gas Chemistry Example

A simple methane reaction scheme excluding night time chemistry (Gregoire *et al.*, 1994) was used for this study. The box model solved for 13 species, O_3, H_2O_2, OH, HO_2, CO, CH_4, CH_3OO, CH_3OOH, CH_2O, HCOOH, NO, NO_2, and HNO_3.

The experiment was integrated for 2 days with diurnally varying light at constant temperature (T=287.7 K) and pressure (p=818 mb). The photolysis rates used in this study are representative of a 5 km altitude at 30°N during equinox conditions. Unless otherwise noted, the number of iterations used to solve the EBI and QSSA techniques was 5. To exemplify the ability of the approximate solution techniques in predicting the concentration of the above species, a gas chemistry only simulation was performed where the initial concentrations of NO and NO_2 were much higher than their equilibrium values (Table 1).

The percent error of the concentration of each species of the EBI and QSSA approximate solvers from the Gear solution at the end of the 2 day simulation was calculated. We found, that without any treatment of the mechanism (e.g. simulating $[O_3]$ – [NO], Hesstvedt *et al.*, 1978), that the percent errors for timesteps of 30 seconds or less were ~1 % or less for both solvers. At larger timesteps, NO and NO_2 showed the greatest sensitivity and incurred nearly a 30% error when the timestep was 2 minutes for both solvers. At timesteps of 4 minutes and greater the QSSA solver was unreliable and the EBI solver incurred significant errors for all constituents.

3. GAS-AQUEOUS SYSTEM

When simulating chemistry in both gas and aqueous phases, mass transfer between phases must be considered. This may be accomplished by either solving for the gas and aqueous concentrations of a species separately,

Table 1. Initial concentrations of the constituents.

	Gas Chemistry	Gas-Aqueous Chemistry
O_3	5.9×10^{11}	5.9×10^{11}
H_2O_2	8.3×10^{10}	8.3×10^{10}
OH	5.2×10^{6}	5.2×10^{6}
HO_2	5.8×10^{8}	5.8×10^{8}
CO	3.3×10^{12}	3.3×10^{12}
CH_3OO	3.9×10^{8}	3.9×10^{8}
CH_3OOH	1.9×10^{10}	1.9×10^{10}
CH_2O	1.3×10^{10}	1.3×10^{10}
HCOOH	1.1×10^{8}	1.1×10^{8}
NO	2.6×10^{9}	2.6×10^{8}
NO_2	6.4×10^{9}	6.4×10^{8}
HNO_3	4.0×10^{9}	4.0×10^{9}

$$\frac{dC_g}{dt} = P_g - L_g\,C_g + \frac{k_t}{H_{eff}}C_a - k_t\,LWC\,C_g \qquad (6)$$

$$\frac{dC_a}{dt} = P_a - L_a\,C_a - \frac{k_t}{H_{eff}}C_a + k_t\,LWC\,C_g \qquad (7)$$

where k_t is the transfer coefficient (s^{-1}), H_{eff} the effective Henry's Law constant (dimensionless), and LWC the liquid water content (cm^3/cm^3), or by solving for the total concentration, $C_{tot} = C_g + C_a$,

$$\frac{dC_{tot}}{dt} = P_g - L_g\,C_g + P_a - L_a\,C_a \qquad (8)$$

followed by partitioning C_{tot} into C_g and C_a following Henry's Law equilibrium or through a diffusion-limited process.

To determine whether a species should be solved separately (Eq. 6 and 7) or as a total concentration (Eq. 8) depends on the characteristic time of a species. Table 2 shows the time constants of each species associated with gas chemistry, aqueous chemistry, the flux going into a 10 μm drop with a 1×10^{-6} liquid water content, the flux going out of the 10 μm drop, and the time constants appropriate for the gas-phase concentration, the aqueous-phase concentration, and the total concentration of the species. For all the species except OH, the flux into the drops is much faster than the gas chemistry. For all the species except OH, HO_2, and CH_3OO, the flux out of the drops is much faster than the aqueous chemistry. Thus, it is more accurate to solve the species (except OH, HO_2, and CH_3OO) using the total concentration and then partition between gas and aqueous phases because of the larger time constants of the chemistry compared to mass transfer.

Table 2. Characteristic times of species for a liquid water content of 1×10^{-6} with cloud drops of 10 μm radius.

	$\frac{1}{k'_g}$	$\frac{1}{k'_a}$	$\frac{1}{k_t LWC}$	$\frac{H_{eff}}{k_t}$	$\frac{1}{k'_g+k_t LWC}$	$\frac{1}{k'_a+\frac{k_t}{H_{eff}}}$	$\frac{1}{k'_g+k'_a}$
O_3	1.82×10^{5}	0.19	3.71	1.27×10^{-6}	3.71	1.27×10^{-6}	1.37×10^{5}
H_2O_2	1.98×10^{5}	3.99×10^{4}	3.65	14.1	3.65	14.1	4.78×10^{4}
OH	0.75	1.07×10^{-4}	3.56	0.76	0.68	1.07×10^{-4}	6.10×10^{-4}
HO_2	290.	1.66	3.64	0.57	3.60	0.43	11.8
CO	1.90×10^{9}	–	3.62	8.54×10^{-8}	3.62	8.54×10^{-8}	1.90×10^{9}
CH_3OO	462.	5.82	3.70	0.39	3.68	0.37	55.0
CH_3OOH	2.52×10^{5}	3.48×10^{4}	3.71	0.04	3.71	0.04	2.37×10^{5}
CH_2O	2.03×10^{4}	775.	3.63	1.17	3.63	1.17	2.83×10^{3}
HCOOH	1.43×10^{9}	880.	3.70	2.03	3.70	2.03	2.53×10^{3}
NO	107.	–	3.63	1.96×10^{-7}	3.52	1.96×10^{-7}	107.
NO_2	138.	–	3.70	7.55×10^{-7}	3.60	7.55×10^{-7}	138.
HNO_3	3.73×10^{6}	–	3.76	1.18×10^{7}	3.76	1.18×10^{7}	3.73×10^{6}

k'_g is the pseudo first order rate constant for the gas phase chemical reactions.
k'_a is the pseudo first order rate constant for the aqueous phase chemical reactions.
– signifies that there are no aqueous reactions for the species.

3.1 Gas-Aqueous Chemistry Example

A two day simulation of gas and aqueous chemistry was performed using initial NO and NO_2 concentrations near photochemical equilibrium (Table 1). During the simulation a cloud of 0.2 g/kg mixing ratio occurred from 4 a.m. to 10 a.m. and a cloud of 1.0 g/kg mixing ratio occurred from 3 p.m. to 6 p.m. on both days of the simulation. The size of the cloud drops was set to 10 μm and the pH of the drops was set to 4.16.

The percent error of the concentration of each species of the EBI and QSSA approximate solvers from the Gear solution at the end of the 2 day simulation was calculated. For timesteps of 60 seconds and less, both solvers agreed with the Gear solver by less than 4% error. At larger timesteps the error from the Gear solution grew substantially. For example, Table 3 (Base Case) shows the percent error of the concentration of each species of the EBI and QSSA approximate solvers from the Gear solution at the end of the 2 day simulation for 2 and 4 minute timesteps. At $\Delta t = 4$ min. NO and NO_2 had errors of about 50% for the EBI solver and 150% for the QSSA technique.

3.2 "Variable" Timestep

Some studies have suggested implementing a variable timestep (Verwer *et al.*, 1996; Chang, 1995 personal communication) to improve the accuracy of the solution. In an attempt to find the benefits of reducing the timestep in places where errors in the solver are occurring, the simulation described in 3.1 was repeated but during 7 timesteps surrounding the beginning and end of cloud the timestep was reduced to 15 seconds.

The benefit of this method is shown in Table 3 where the errors for NO and NO_2 dropped to below 50% for the EBI technique and dropped to about 60% for the QSSA technique for $\Delta t = 4$ min. This improved performance was found for all timesteps.

3.3 Number of Iterations

Another variable that was prescribed was the number of iterations the numerical solver used when solving the concentrations of the species. To find what kind of change occurs when the 4 minute timestep simulation shown in 3.2 uses a higher number of iterations, we repeated the simulation in 3.2 for the 4 minute timestep using 10 iterations instead of 5.

The EBI solution technique greatly benefitted from increasing the number of iterations from 5 to 10. In fact, the 4 minute timestep with 10 iterations produced a more accurate solution than the 2 minute timestep with 5 iterations for the EBI solver. The QSSA solution technique improved marginally with the increased number of iterations. The QSSA technique had a much greater improvement with smaller timesteps.

4. SUMMARY

In this study we compared the accuracy of the approximate solution techniques described by Hesstvedt *et al.* (1978) and the Euler Backward Iterative method to the solution found using the Gear technique (Gear, 1971) for a gas and aqueous chemical system. For a gas and aqueous chemical

Table 3. Percent error of approximate solutions from the Gear solution for the gas-aqueous system.

	Base Case				Variable Δt				Increased Iterations	
	2 m		4 m		2 m		4 m		4 m	
	EBI	QSSA	EBI	QSSA	EBI	QSSA	EBI	QSSA	EBI	QSSA
O_3	0.51	0.55	1.66	4.01	0.50	0.54	1.57	2.10	0.10	1.49
H_2O_2	0.65	4.36	1.51	47.15	0.65	1.56	1.41	3.06	0.27	10.92
OH	2.26	2.72	5.89	86.87	2.18	2.17	5.33	6.57	0.76	4.77
HO_2	0.45	1.02	2.28	12.22	0.41	0.51	2.04	2.90	-0.42	3.08
CO	-0.07	-0.09	-0.14	-0.42	-0.07	-0.06	-0.13	-0.14	-0.04	-0.09
CH_3OO	-1.39	-1.00	-4.48	-8.17	-1.29	-0.70	-3.95	-3.94	0.19	-0.51
CH_3OOH	-2.12	-0.29	-5.36	-0.15	-2.02	0.08	-4.83	-1.70	-0.97	8.61
CH_2O	2.92	4.63	8.07	34.11	2.89	4.63	7.60	14.23	-0.19	21.11
HCOOH	1.55	1.04	6.03	17.82	1.64	1.87	6.23	10.62	-0.96	17.07
NO	18.13	20.75	52.53	154.2	17.26	18.42	46.39	62.10	2.31	49.13
NO_2	18.73	21.73	54.19	167.5	17.85	19.20	47.95	64.65	2.62	52.17
HNO_3	1.67	24.29	4.12	143.6	1.66	4.14	3.93	5.41	0.86	4.67

system it is important to determine the mass transfer of species between air and liquid properly, whether it is limited by diffusion or by Henry's Law equilibrium. We found that the Hesstvedt solution technique can simulate the gas and aqueous chemical system at small timesteps (on the order of seconds). At timesteps on the order of minutes, the Hesstvedt technique could not handle shocks to the system well (the Hesstvedt technique performed better when the timestep was reduced during the transition through the shock). The Hesstvedt solution technique therefore is not recommended to solve the gas-aqueous chemical system with timesteps on the order of minutes.

The Euler Backward Iterative (EBI) technique performed well for timesteps of seconds to minutes using a reasonable number of iterations (10 or less). The EBI technique did not perform well at large timesteps of 20 minutes unless many iterations were used. The EBI solution technique is recommended for the gas-aqueous chemical system for timesteps of the order of a few minutes or less.

A consequence of these results is to approach with caution the conclusions reached in studies of the gas-aqueous chemical system in which the Hesstvedt *et al.* (1978) technique was employed.

5. ACKNOWLEDGMENTS

The National Center for Atmospheric Research is sponsored by the National Science Foundation.

6. REFERENCES

Gear, C. W., 1971: The automatic integration of ordinary differential equations. *Commun. ACM.*, **14**, 176-179.

Gong W. and H-R Cho, 1993: A numerical scheme for the integration of the gas-phase chemical rate equations in three-dimensional atmospheric models. *Atmos. Environ.*, **27A**, 2147-2160.

Gregoire, P. J., N. Chaumerliac and E. C. Nickerson, 1994: Impact of cloud dynamics on tropospheric chemistry: Advances in modeling the interactions between microphysical and chemical processes. *J. Atmos. Chem.*, **18**, 247-266.

Hesstvedt, E., O. Hov, and I. S. A. Isaksen (1978) Quasi-steady-state approximation in air pollution modeling: Comparison of two numerical schemes of oxidant prediction, *Int. J. Chem. Kinet.*, **10**, 971-994.

Lelieveld, J. and P. J. Crutzen, (1991) The role of clouds in tropospheric photochemistry, *J. Atmos. Chem.*, **12**, 229-267.

Saylor R. D. and G. D. Ford, 1995: On the comparison of numerical methods for the integration of kinetic equations in atmospheric chemistry and transport models. *Atmos. Environ.*, **29**, 2585-2593.

Verwer, J. G., J. G. Blom, M. Van Loon and E. J. Spee, 1996: A comparison of stiff ODE solvers for atmospheric chemistry problems. *Atmos. Environ.*, **30**, 49-58.

RESULTS OF RAIN WATER CHEMICAL CONTENT INVESTIGATION IN ALAZANI VALLEY

L.Sh. Abesalashvili[1], A.G. Amiranashvili[1], G.D. Supatashvili[2]

[1] Geophysics Institute, M.Aleksidze 1, Tbilisi, Georgia
[2] Tbilisi State University, I.Chavchavadze 1, Tbilisi, Georgia

In the recent years considerable attention has been drawn to investigations of the interaction between clouds and gas and aerosol admixtures in the atmosphere. On the one hand these small atmospheric components play a significant role in the formation of cloudness, its microstructure, precipitation chemical content etc. On the other hand processes taking place in clouds (the interaction between droplets and aerosols and gases, electric discharges etc.) can lead to generation of gas components (nitrogen oxides, ozone etc.) and eventually to changing of the air and precipitation chemical content.

Investigations of the air and atmospheric precipitation chemical content have been carried out in Georgia since long ago [1,2], however except work [3], these investigations were mainly purposed for enviromental control. In Geophysics Institute of Georgian Acad. of Sci. there are also stored the data of multiennial measurements of rain water chemical content in Alazani valley (Eastern Georgia), where activities on hailstorm prevention were carried out. In the precipitation the content of main ions, biogenic components, concentration of lead and iod contained by the reagent of antihail rockets, copper and other microelements were determined. Chemical analyses of precipitation samples were carried out by the method [4,5] with measurement error not more than ±10%. Sample taking was carried out in 7 points of Alazani valley (most intensively from 1965 to 1978, then episodically). This work presents some results of an investigation of the rain water chemical content in Alazani valley and its variation under the influence of natural and anthropogenic factors.

Tab. 1 and 2 represent compiled

Table 1

Atmospheric precipitation chemical content in Alazani valley
$Mg \cdot L^{-1}$, (500 samples)

	pH	Cl^-	SO_4^{2-}	HCO_3^-	Na^+	Mg^{2+}	Ca^{2+}	$\sum u$	Water index	NH_4^+	NO_2^-	NO_3^-	PO_4^{3-}
Average	6.32	1.1	4.0	5.0	1.3	0.7	2.6	14.7	S^{Ca}_{II}	0.26	0.03	1.58	0.12
min	3.90	0.1	0.0	0.0	0.0	0.0	0.1	1.2		0.0	0.0	0.0	0.00
max	7.85	9.4	20.3	46.2	17.9	3.5	18.9	94.8		4.56	1.53	9.3	1.19

Table 2

Content of microelements in atmospheric precipitation in Alazani valley ($Mcg \cdot L^{-1}$).

elements	B	F	P	As	Br	I	Fe	Ni	Cu	Zn	Pb
number of samples	177	17	165	13	80	107	63	13	197	26	199
average	12	7	32	1.4	6.7	12.1	40	1.3	2.2	5.5	9.0
min	0	0	0	0	0.2	2.1	0	0	0	3.0	0
max	56	22	185	2.5	38.2	30.8	150	2.8	7.8	12.4	37.0

data on the precipitation chemical content in Alazani valley.

As it follows from these tables precipitation in Alazani valley relate to neutral - weakacid waters, the content of main ions, their sums $\sum u$, biogenic componenets, and also microelements varies within considerablr ranges. In comparison to other regions in Georgia in the precipitation of Alazani valley is a higher concentration of sulphates, nitrates and calcium ions. One of the reasons of this, is a high content of plaster and nitrogen containing fertilizers in the regional soils (Alazani valley is an agricultural region) [6].

According to [6] in the years of active influence on hail processes the content of lead and iod in the precipitation of Alazani valley increased on average in comparison to years without the influence 4.3 and 3.3 times respectively. Tab.3 presents the dynamics of the precipitation

Table 3

Dependence of lead content in atmospheric precipitation on quantity of reagent introduced to clouds

Quantity of reagent PbI_2 (Kg)	up to 10	10 - 100	100 - 300	above 300
Content of lead in precipitation, $Mcg \cdot L^{-1}$	3.6	5.3	6.9	13.9

lead content increse versus the quantity of reagent introduced to clouds.

Despite the fact that, at large, from the sanitary point of view the increased lead content in the atmosphere was not of any danger to human health, from 1985 the reagent in antihail rockets was changed to a new one not containing lead. It is noteworthy that for various reasons antihail activities in Georgia at present are stopped.

In precipitation of Alazani valley there is also a high content of copper sulphate solution, used for agricultural purposes. A maximum copper content in the precipitation

is observed in the period of intensive spraying of vineyards with this solution during the warm period of a year (Tab. 4).

Table 4

Monthly variations of copper content in atmospheric precipitation of Alazani valley

Month	I	II	III	IV	V	VI	VII	VIII	IX	X	XI	XII
Precipitation Mcg·L^{-1}	1.8	1.9	2.6	3.7	4.0	3.1	2.0	1.6	2.1	1.9	1.8	2.2

The role of thunderstorm processes in precipitation chemical content variation was estimated (Tab. 5).

Table 5

Chemical content of precipitation from thunderstorm and non - thunderstorm clouds (1967 - 1968) Mg·L^{-1}

Type of precipitation	Number of samples	pH	NO_3^-	NH_4^+	SO_4^{2-}	Ca^{2+}
I) Rain without thunderstorm	57	6.44	0.58	0.41	4.20	1.76
II) Rain with thunderstorm	42	6.15	1.43	0.83	6.39	1.89
Ratio II/I (%)	--	95.5	246.6	202.2	152.1	107.4

As it follows from Tab. 5 in precipitation fallen out from thunderstorm and non - thunderstorm clouds the variation of pH and the calcium content (microelement of terrigenic origin) is insignificant. On the other hand a considerable increase in nitrogen and sulphate compounds in thunderstorm cloud precipitation is detected. Thus, electric processes taking place in clouds in a certain way can influence the precipitation chemical content. In particular it may be a result of acceleration of the SO_2 oxidation by air and nitrogen dioxide, being intensively initiated on carbon particles in cloud droplets during thunderstorm discharges [7]. Verification of this and other mechanisms of gas-particle reactions in cloud media with a presence of electric discharges will be the subject of further investigations.

REFERENCES

1. Supatashvili G.D. Nekotorie zakonomernosti formirovania khimitcheskogo sostava atmosfernikh osadkov v Gruzinskoi SSR, Tr. Instituta okeanologii ANSSSR, N 63, 1973, p.72 - 92

2. Gunia G.S. Voprosi monitoringa zagriaznenia atmosphernogo vozdukha na territorii Gruzinskoi SSR , L. Gidrometeoizdat,1985, p. 1 - 84

3. Kharchilava D.F.,Amiranashvili A.G. Studies of atmospheric ozone variations in Soviet Georgia,Moscow 1988, p. 1 -144 (in Russian).

4. Supatashvili G.D. Karsanidze N.K., Opredelenie microelementov v prirodnikh vodakh.Extraktsionno -

fotometricheski metod opredelenia Pb^{2+},Cu^{2+},Ni^{2+}, i Zn^{2+} v odnoi probe vodi. Trudi Tbilisskogo gosudarstvennogo universiteta, A1 (137),1971, p. 161 - 163.

5. Supatashvili G.D.,Gidrohimicheskaia kharakteristika atmosphernikh osadkov na territorii Gruzinskoi SSR. Trudi Tbilisskogo gosudarstvennogo universiteta,N 126 1968, p.73 - 84.

6. Supatashvili G.D.,Kartsivadze A.I., Abesalashvili L.Sh.,Karsanidze N.K. Microelementi v osadkakh Alazanskoi dolini. Soobsh. AN Gruzinskoi SSR , 66, N1, 1972, p. 121 - 124.

7. Rogovski S.R. i dr. Okislenie SO_2 vozdukhom i dvuokisiu azota na chastitsakh ugleroda, vzveshennikh v zhidkosti.Geterogennaia khimia atmosferi,L.,Gidrometeoizdat,1986, p. 319 - 323.

ACID BUFFERING CAPACITIES OF FOG AND CLOUDWATER

X. Rao, A. Bator, K. Hoag, E. Sherman, and J. Collett, Jr.

Atmospheric Science Dept., Colorado State University, Ft. Collins, CO 80523 USA

1. INTRODUCTION

Clouds and fogs play important roles in atmospheric sulfate production due to the existence of effective aqueous oxidants. In-cloud sulfate production has been considered to occur mainly via S(IV) oxidation by H_2O_2, O_3 and O_2 (catalyzed by trace metals). Kinetic studies of S(IV) oxidation rates reveal that cloud pH is a critical determinant of the importance of the different S(IV) oxidation pathways. While oxidation by H_2O_2 is not a function of pH (in typical cloud and fog drops) and is typically the fastest oxidation pathway at low pH, rates of S(IV) oxidation by O_3 and O_2 (catalyzed by Fe(III) and Mn(II)) increase with cloud pH and can be important at high pH or in the absence of significant H_2O_2.

Model studies of in-cloud S(IV) oxidation typically calculate an initial oxidation rate using information about sulfur dioxide concentrations, oxidant concentrations and cloud drop pH. The initial pH is generally determined from the composition of the cloud condensation nuclei and any soluble gases assumed to establish equilibrium with the cloud drops. As S(IV) is oxidized sulfuric acid is produced leading to acidification of the cloud drops. Seidl (1989) predicted that the time scale for small, basic drops to acidify is of the order of seconds for conditions simulated in their model, without considering neutralization from dissolution of gaseous ammonia. In the presence of significant atmospheric ammonia concentrations the time scale can be longer.

In addition to sulfuric acid neutralization from uptake of atmospheric ammonia, fog or cloudwater itself can contain hydrogen ion absorbing materials which provide an internal capacity to buffer acid addition. If significant internal acid buffering capacity exists in fog or cloudwater, it will permit more sulfuric acid production than is often predicted by models. Internal acid buffering would also influence the fractions of S(IV) oxidized by the different chemical pathways. Because the droplet pH would remain elevated longer, pH sensitive pathways, such as the trace metal catalyzed autooxidation of S(IV) or S(IV) oxidation by ozone, could be more important than predicted in the absence of internal acid neutralization. The purpose of this paper is to determine whether cloud/fogwater possesses any significant buffering capacity toward acid addition and to determine its effects on in-cloud S(IV) oxidation.

2. EXPERIMENTAL

Ground-based sampling of clouds and fogs was conducted at a variety of sites between July 1993 and January 1996. Coastal stratus clouds were sampled in June 1993 and 1994 at La Jolla Peak, California, situated near the southern end of the Santa Barbara Channel, and at Angora Peak, a remote site on the northern Oregon coast. Radiation fogs were sampled at three locations (Bakersfield, Fresno, and at a rural site near the Kern Wildlife Refuge (KWR)) in California's San Joaquin Valley during January 1994 and December 1995-January 1996.

Various combinations of cloudwater samplers were used at different sites. The collectors included a Caltech Active Strand Cloudwater Collector 2 (CASCC2) and a CASCC with a size-fractionating inlet. The CASCC2 (Demoz et al., 1996) is designed to collect droplets larger than 3.5 μm diameter. The size-fractionating CASCC (Munger et al., 1989; Demoz et al., 1996), was used to collect two independent drop size fractions, one containing mainly drops larger

than 23 μm diameter and one with drops mainly between 3.5 and 23 μm.

The pH of all samples was measured shortly after collection. Sample pH was measured using a portable pH meter equipped with a combination microelectrode calibrated with pH 4 and 7 buffers. Acid titration experiments were conducted at the sampling sites in 1995/96. Earlier samples were titrated after refrigerated storage for several months. Titrations were performed by making sequential additions of 10 μl of sulfuric acid (1 or 10 millinormal) to 1.0 ml cloud or fog samples. After each acid addition, the sample was mixed and the pH measured.

3. RESULTS AND DISCUSSION

Results of acid titrations for fog samples from Bakersfield, California are shown in Figure 1. The depicted fog events from January 15, 1994 and December 10, 1995 featured highly polluted and moderately polluted fogwater, respectively. In the highly polluted fogwater, sufficient acid buffering capacity was present to permit several hundred micromolar hydrogen ion to be added before the drop pH decreases to a value of 5. In contrast only 10 micromolar hydrogen ion is needed to decrease the pH of deionized water to a value of 5. Since the sulfate production rate at high pH increases strongly with increasing pH, this suggests that several tens of times more sulfuric acid could be produced in the strongly buffered fog samples than in fogwater with no

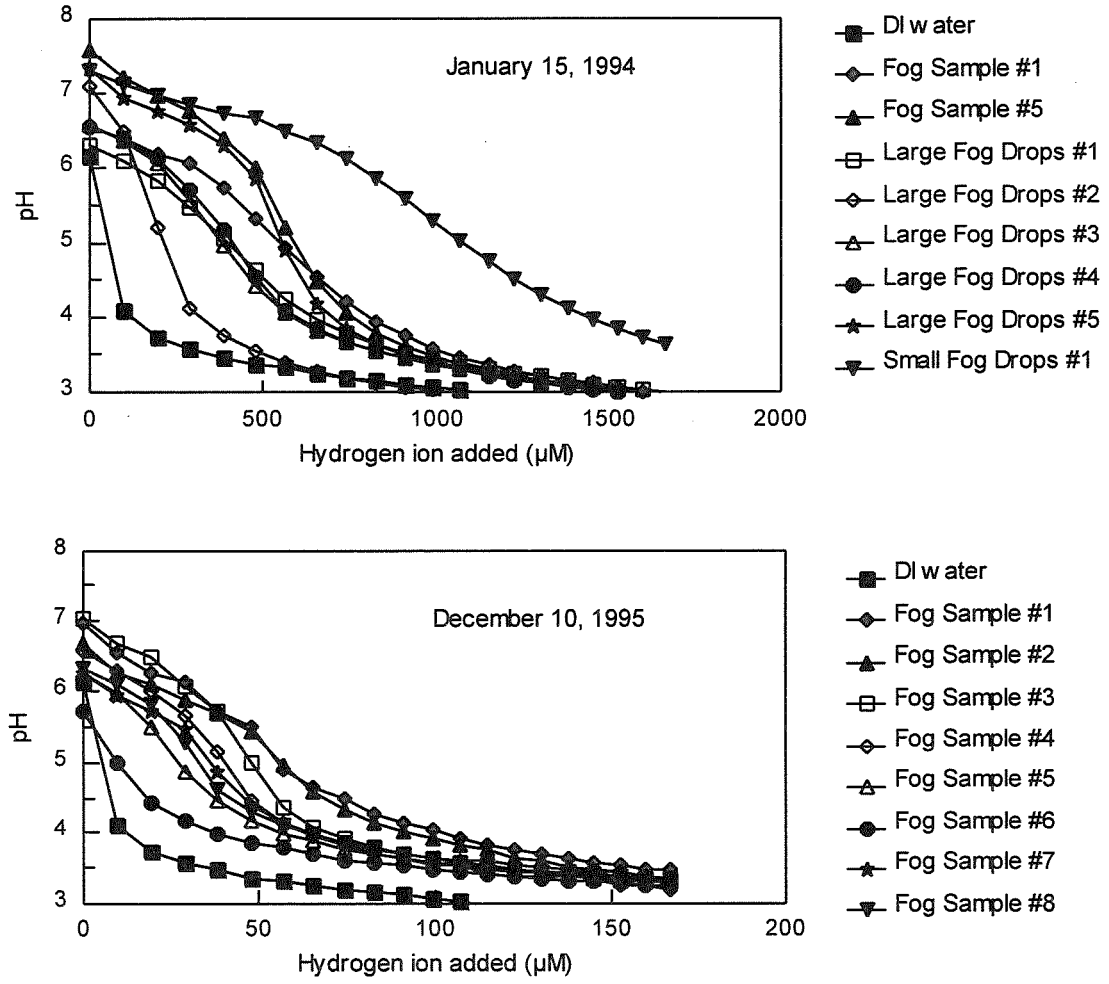

Figure 1. Acid titration curves of fog samples collected at Bakersfield, California. Titrations of highly polluted fog samples from January 15, 1994 are depicted in the top panel. Titrations of moderately polluted samples from December 10, 1995 are included in the lower panel. Note the different scales used in the two panels. Sample numbers refer to different sampling periods during each fog event. Titration curves for deionized water are included in each panel as a reference.

internal acid buffering capacity. For the moderately polluted fogwater collected on December 10, 1995 even the modest amount of acid buffering capacity available can support several times more sulfuric acid production than is possible in an unbuffered situation.

In order to quantitatively compare acid buffering capacities among fog/cloud samples we define the acid buffering capacity (ß) as the unit increase of acid needed per unit of hydrogen ion increase in cloudwater ($dC_a/d[H^+]$). By definition ß's value should be approximately one for water containing no buffer capacity. Clearly the value of ß can change with pH as a sample containing internal acid buffering capacity is titrated. For example, the buffering capacity due to a specific species will rise and then fall as the pH approaches and passes the pK_a of that species. ß values can be calculated at any pH from measured acid titration curves.

In Figure 2 we compare initial ß values for titrated fog and cloudwater samples collected at different sites. ß values for deionized water in the pH range of 3 to 7 are also shown in Figure 2 for comparison. The highest initial acid buffering capacities (the initial ß values) were observed during the highly polluted Bakersfield fog event of January 15, 1994. For this event, we see that the initial acid buffering capacity increases strongly with initial sample pH above 6, suggesting that the compound or compounds responsible for much of the buffering exhibit their greatest effect at a pH value above 6. High acid buffering capacities between pH 6 and 7 rule out most low molecular weight organic acids as

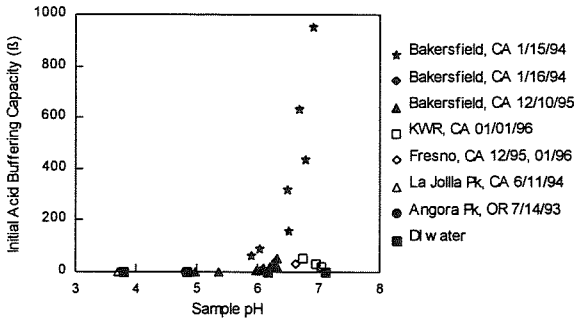

Figure 2. Acid buffering capacities determined at the pH values measured in the field shortly after sample collection.

likely contributors. High total organic carbon contents in the samples, however, suggest that other organic species may be responsible.

It is interesting, too, that the highest initial buffering capacities in our data set occur at high pH. Normally we would expect high pH samples to acidify very rapidly with only minor acid additions. Our findings suggest this may not always be the case.

The presence of significant buffering capacity within fog drops provides an important mechanism for absorbing hydrogen ions released in the drops as a result of sulfuric acid production, meaning fog pH could remain high for a longer time in a well buffered system. Consequently, the S(IV) oxidation rate may be enhanced, especially for those oxidation pathways effective at high pH. If rates of the pH sensitive pathways remain elevated for some time, they may play a greater role in total S(IV) oxidation than is typically expected.

A simple simulation of S(IV) oxidation for the January 15, 1994 fog event at Bakersfield was made to investigate likely effects of the acid buffering capacity on S(IV) oxidation. Three S(IV) oxidation pathways were considered: oxidation by H_2O_2, by O_3, and autooxidation catalyzed by both Fe(III) and Mn(II). Fog chemical compositions are taken from our measurements with an assumption of constant oxidant and catalyst concentrations during the process of S(IV) oxidation. Although this assumption does not strictly hold, the results obtained are adequate for purpose of discussion. Surface ozone levels are typically quite low in

Table 1. S(IV) oxidation rates (at 25°C)

H_2O_2 (Seinfeld, 1986)

$$-d[S(IV)]/dt = 7.45\times10^{7}\,[H^+][H_2O_2][HSO_3^-]/(1+13[H^+])$$

O_3 (Hoffmann, 1986)

$$-d[S(IV)]/dt = (\,2.4\times10^{4}[SO_2H_2O] + 3.7\times10^{5}[HSO_3^-] + 1.5\times10^{9}[SO_3^{2-}])[O_3]$$

O_2/Fe-Mn (Ibusuki and Takeuchi, 1987)

$$-d[S(IV)]/dt = 2.51\times10^{13}[H^+]^{0.67}[Fe(III)][Mn(II)][S(IV)]$$

this region during winter stagnation episodes while sulfur dioxide concentrations can be rather high. Atmospheric partial pressures of 10 ppbv were selected for both species and were held constant during the simulation. Rate expressions used for S(IV) oxidation are listed in Table 1.

Changes in S(IV) oxidation rates with the progress of sulfuric acid production are shown in Figure 3. In the simulation the initial fog pH is 6.4. Without any acid buffering capacity the pH decreases sharply during the first ten minutes of S(IV) oxidation. As a result, S(IV) oxidation by O_3 becomes unimportant after ten minutes and trace metal catalyzed autooxidation dominates the S(IV) oxidation. Without buffering, the fog pH decreases one and one-half units in 5 hours. In contrast if the acid buffering capacity measured in the fog is taken into account only a one-half unit pH decrease is predicted after 5

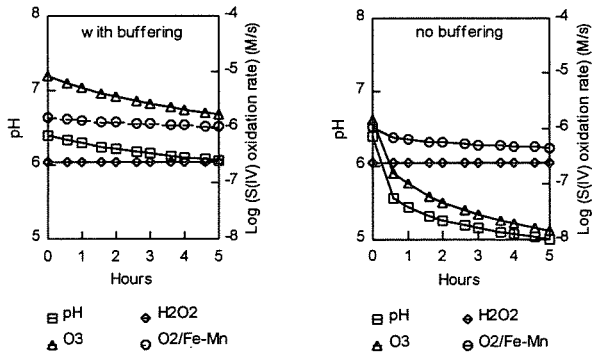

Figure 3. Simulated S(IV) oxidation rates and pH in Bakersfield fog on December 15, 1994. The initial fog composition and the acid buffering capacity are taken from observations. The left panel shows changes in S(IV) oxidation rates and pH expected in the presence of the observed acid buffering capacity. The right panel shows the results obtained if the acid buffering capacity is ignored.

hours of S(IV) oxidation, much closer to the pH change observed in the fog. Consequently, S(IV) oxidation by O_3 remains important throughout the entire period. Total sulfate production for the 5 hour simulation is increased 50 times as a result of the acid buffering capacity.

4. CONCLUSIONS

Significant acid buffering capacities were observed in some fog samples collected in California's San Joaquin Valley. Other samples from this region and elsewhere contained lesser amounts. The presence of acid buffering capacity can change the relative importance of individual S(IV) oxidation pathways and enhance overall sulfate production. It also suggests that large, alkaline cloud drops (Collett et al., 1994) may be able to sustain rapid sulfur oxidation. Preliminary evidence suggests that organic species may be responsible for some of the buffering observed, but further work is required to examine this hypothesis.

5. ACKNOWLEDGEMENTS

This work was supported in part by the Department of the Navy, Office of the Chief of Naval Research, the Midwestern Regional Center of the National Institute for Global Environmental Change, the San Joaquin Valleywide Air Pollution Study Agency, and the National Science Foundation (ATM-9509596). We are grateful to several individuals and organizations who provided access to fog and cloud sampling sites and to B. Demoz, O. Graf, A. Sautman, P. Van Rens, and E. Walke who assisted with some of the sampling.

6. REFERENCES

Collett, Jr., J. L., A. Bator, X. Rao, and B. Demoz, 1994: Acidity variations across the cloud drop size spectrum and their influence on rates of atmospheric sulfate production. *Geophys. Res. Lett.*, **21**, 2393-2396.

Demoz, B., J. L. Collett, Jr., and B. C. Daube, Jr., 1996: On the Caltech Active Strand Cloudwater Collectors. *Atmos. Res.*, in press.

Hoffmann, M. R., 1986: On the kinetics and mechanism of oxidation of aquated sulfur dioxide by ozone. *Atmos. Environ.*, **20**, 1145-1154.

Ibusuki, T. and K. Takeuchi, 1987: Sulfur dioxide oxidation by oxygen catalyzed by mixtures of manganese (II) and iron (III) in aqueous solutions at environmental reaction conditions. *Atmos. Environ.*, **21**, 1555-1560.

Munger, J. W., J. L. Collett, Jr., B. Daube, Jr.,and M. R. Hoffmann, 1989: Chemical composition of coastal stratus clouds: Dependence on droplet size and distance from the coast. *Atmos. Environ.*, **23**, 2305-2320.

Seidl, W., 1989: Ionic concentrations and initial S(IV)-oxidation rates in droplets during the condensational stage of cloud. *Tellus*, **41B**, 32-50.

Seinfeld, J. H., 1986: *Atmospheric chemistry and physics of air pollution*; Wiley Intersience, New York.

THE INTERACTION OF AMMONIA WITH CLOUD

M.Wells[1], J.N.Cape[2], T.W.Choularton[1], K.N.Bower[1]

1: Physics Dept, UMIST, Po Box 88,Manchester,M60 1QD,UK
2: Institute of Terrestrial Ecology, Edinburgh Research Station,
Bush Estate, Penicuik EH26 0QB, UK

1. INTRODUCTION

Reduced nitrogen exists as either gaseous ammonia ($NH_{3(g)}$) or particulate ammonium (NH_4^+). It is now well recognised that reduced nitrogen has many roles in the atmosphere, influencing aerosol formation, cloud droplet acidity, cloud chemistry , and the global radiation budget amongst others. Its deposition, through either dry or wet mechanisms affects soil acidity, and leads to a decrease in species bio-diversity. Gaseous ammonia is much more rapidly deposited through dry deposition than ammonium aerosol, and so the phase of reduced nitrogen will dictate its residence time in the atmosphere, and hence its long range transport. Cloud chemistry is of great importance in the atmosphere as it offers a mechanism to modify aerosol particles, and can change the phase of reduced nitrogen.

2. THE GCE 93 EXPERIMENT

The Ground Based Cloud Experiment group held its third and final field project at Great Dun Fell (GDF) , Cumbria, England in the spring of 1993. The initial experiments had investigated a polluted radiation fog in the Po Valley, Italy (Fuzzi 1992), and strato and strato-cumulus clouds impinging upon Kleiner Feldburg, Germany (Wobrock 1990). The experiment at GDF was to investigate an orographic cloud in non-polluted conditions. By compiling a reduced nitrogen budget over GDF evidence of the phase changes that occur in cloud become clear.

GDF situated on the ridge of the Pennines is used as a field laboratory to investigate orographic clouds acting as a flow-though reactor . Sites placed upwind, at the summit, and in cloud sample the air before during and after cloud processing. Cloud chemistry will increase the mass of aerosol particles, through sulphate production and addition of other gases. This modifies the optical properties of the accumulation mode, increasing the cooling effect the aerosol have on the global radiation budget.

3.THE FIELD OBSERVATIONS

Four field cases are presented from the GDF 1993 field project. Table 1 lists the observed and modelled change to the aerosol sulphate and ammonium loadings respectively. Reduced nitrogen is detected before and after the cloud by the bulk Rotheroe-Mitchell filter (ammonium) and the rotating annular denuder (gaseous ammonia). The total reduced nitrogen measured before and after the cloud

	Run	Sulphate	Ammonium
Observed	1	+ 25%±25%	+ 13±13%
	2	+ 25%±10%	- 9%±4%
	3	+ 0.25±0.5 μg m^{-3}	- 0.6±0.1 μg m^{-3}
	4	+ 0.4±0.1 μg m^{-3}	+ 0.7±0.4 μg m^{-3}
Modelled	1	+ 19%	- 5% → +14%
	2	+ 60%	- 3% → + 20%
	3	+ 0.29 μg m^{-3}	+ 0.09 → + 0.15 μg m^{-3}
	4	+ 1.2 μg m^{-3}	+ 0.08 → 0.61 μg m^{-3}

Table 1: Comparison of model and observed change in sulphate and ammonium.

agrees well with equivalent loadings calculated from cloud samples (not presented). Cloud chemistry fixed gaseous ammonia as ammonium (Run 1 and 4) to neutralise sulphate production and acidic aerosol as expected. However, field data also shows a net loss in particulate ammonium between the pre- and post-cloud sites (Run 2 and 3). This has been attributed to ammonia outgassing from evaporating cloud droplets.

4. COMPUTER MODELLING

The GDF orographic cloud model (Bower *et al.* 1991) is used in tandem with field observations to verify our understanding of the chemical and microphysical processes that dominate in orographic clouds. Evidence from field observations indicated that ammonia was observed downwind of the cloud. However, the ideal cloud chemistry model consistently underestimated the post cloud ammonia concentration. Since large cloud droplets scavenge gases, it was hypothesised that outgassing occurred during the evaporation of cloud droplets to aerosol particles.

The model was adapted to examine the evaporation of cloud droplets. Once the cloud liquid water content had dropped below 1 mg m^{-3} the droplets were evaporated to 90% relative humidity (r.h), here the wet aerosol droplets are very concentrated (1-6 molal) and we must take into account the electrostatic and short range intermolecular forces. The Pitzer Parameterisation determines the effective fraction of molecules that are active. The active fraction of a species is described by Equation 1.

$$X' = f_x[X] \qquad 1$$

where [x] is the molal concentration of an electrolyte, f_x is the activity coefficient of species x, and X' is the active fraction of X. For neutral species the activity coefficient is evaluated by equation 2

$$\gamma_N = 10^{\beta I} \qquad 2$$

where β is the salting coefficient, taken as 0.1.

To model the evaporation of cloud droplets the aerosol is held at 90% relative humidity for 55 seconds. Approximately the time it takes for the aerosol to reach the downwind sampling site, where it is considered to have dropped below its deliquescence point.

Therefore two values are presented in Table 1 for the post cloud ammonium from the model. The first is the output from the ideal chemistry model. The second is from the non-ideal chemistry model which has attempted to simulate the evaporation of cloud droplets to solid aerosol particles.

5 DISCUSSION

The investigation of non-ideal chemistry and microphysics of evaporating cloud droplets has shed light onto a previously un-recognised but possibly important phenomena; that aerosol may provide a means of transporting reduced nitrogen large distances and then, through the action of cloud (or high relative humidity) provide a source of gaseous ammonia.

For example, ammonium laden aerosol may first be generated in areas rich in ammonia emissions. At a humid site near this source the aerosol will form an equilibrium (determined by Henry's Law) with the gas phase ammonia.

As the air-parcel moves from the ammonia source region, it is likely that the aerosol particles will drop below their deliquescence point, which is about 73% relative humidity for pure ammonium sulphate. Once this occurs the aerosol can be considered to be a locked system, only interacting with its external environment through surface chemistry. We can assume that this is a slow process, if indeed any chemistry takes place.

Ammonia in this air-parcel will be rapidly deposited to non-agricultural land, and the sea. The aerosol particles will cease to be in equilibrium with the gas phase ammonia, yet will be unable to 'outgas' ammonia to return to an equilibrium state due to their solid nature.

Once the air-parcel becomes humid, through the addition of water vapour, or reduction in the temperature of the air-parcel through advection or radiation cooling, the aerosol particles may take up water, and deliquesce. At this point nuclei will begin to dissociate and species will attempt to re-attain equilibrium with their environment.

In summary, for elevated ammonia levels, cloud processing will convert ammonia to ammonium, reducing local reduced nitrogen deposition, and leading to long range transport of reduced nitrogen.

At low ambient ammonia levels, aerosol containing an excess of reduced nitrogen can act as a source of gaseous ammonia through cloud processing. This ammonia can either be re-deposited near the site of the cloud, or be involved in the creation of new aerosol particles by reacting with acidic gases which may also have been 'ejected' from the aerosol during the evaporation of the cloud.

References

Fuzzi, S., The Po Valley Fog Experiment. An overview. *Tellus* **44B**, 448-468. (1992)

Wobrock W., The Kleiner Feldberg cloud experiment 1990. An Overview. *J.Atmos.Chem.* **19** 3-35 (1994)

Bower,K.N, Hill,T.A., Coe,H. and Choularton, T.W. Sulphur Dioxide Oxidation in an Entraining Cloud Model with Explicit Microphysics. *Atmospheric Environment.* Vol 25A, No 10. pp 2401-2418. (1991)

THE ORGANIC COMPONENT OF FOG DROPLETS

Sandro Fuzzi[1] and Sergio Zappoli[2]

[1]Istituto FISBAT-CNR, I-40129 Bologna, Italy
[2]Dipartimento di Chimica Fisica e Inorganica, Università di Bologna, I-40136 Bologna, Italy

1. INTRODUCTION

The knowledge of organic cloud and fog chemistry is much less advanced compared to that of inorganic chemistry [Graedel and Goldberg, 1983; Warneck, 1988]. Moreover, observations of organic compounds in clouds and fogs are scarce, non-systematic and mainly oriented toward the identification of priority pollutants [Glotfelty et al., 1987; 1990; Czucwa et al.,1989; Capel et al.,1990; 1991].

On the other hand, the importance of organic compounds for cloud formation and chemistry has recently been stressed by a number of authors [Novakov and Penner, 1993; Saxena et al., 1995, Shulman et al., 1996].

As a first step of a larger experimental investigation, we performed a systematic study to characterise and quantify the main categories of organic compounds present in fog droplets. Our measurements show that the organic component of fog water is an important fraction of the dissolved material: from one fourth to one half. We also classified the solvent extractable organic component of fog in different categories, according to their polarity, and discovered that three quarters of the mass of the organic compounds extracted from fog water samples are high-polarity species. However, a considerable amount of organic compounds, up to 80 %, appear not to be extractable with solvents. This missing amount of organic compounds appears to be accounted for by macromolecular species, perhaps of natural origin.

2. EXPERIMENTAL

Fog samples were collected in the Po Valley, Northern Italy, an area were fog occurrence can be as high as 30 % of the time during the fall-winter months. Fog chemistry in this area has been extensively studied over the last fifteen years. [Fuzzi et al., 1983; 1988; 1992a;b; 1996a].

Fog water was collected, on an event basis, using an automated high-volume string collector with a 50 % collection efficiency for droplets of 6 μm diameter [Fuzzi et al.,1996b]. The samples (500 mL at least) were filtered through a 0.22 μm quartz fibre filter immediately after sampling, and 50 mL of the filtrate was used to determine the amount of dissolved organic carbon (DOC) by means of an Organic Carbon Analyser. The remaining part of the sample was then extracted with a separatory funnel with CH_2Cl_2 at pH 10 (base-neutral fraction, BNF) and then at pH 2 (acid fraction, AF). BNF and AF extracts were both reduced to a volume of 1 mL. A portion of 200 μL of both extracts was used to determine, by weight, the extractable organic matter (EOM). The remaining part of BNF was fractionated on a silica column into two further fractions of increasing polarity. In the first fraction the compounds of low and medium polarity (LPC) were eluted with n-hexane and a mixture of CH_2Cl_2:n-hexane (1:1); the higher polarity compounds (HPC) were eluted using CH_2Cl_2 and methanol. Four sub-samples were therefore obtained from each fog sample: three from BNF and one from AF.

The fog samples were also analyzed for pH, conductivity and major inorganic ions.

The samples were further analysed using size exclusion chromatography. This technique allows for the separation of organic compounds according to their molecular size: the molecules of greater size are eluted faster than the smaller ones.

3. RESULTS AND DISCUSSION

The concentration of dissolved organic carbon (DOC) in fog samples ranged from 30 to 100 mg/L, with an average value of 50 mg/L. Figure 1 shows that organic matter represent an important part of total dissolved species in fog water. In fact, organic species represent from 25 to 50 % of the total dissolved compounds. Such concentrations do not

Figure 1. Amount of total dissolved organic and inorganic compounds in fog water

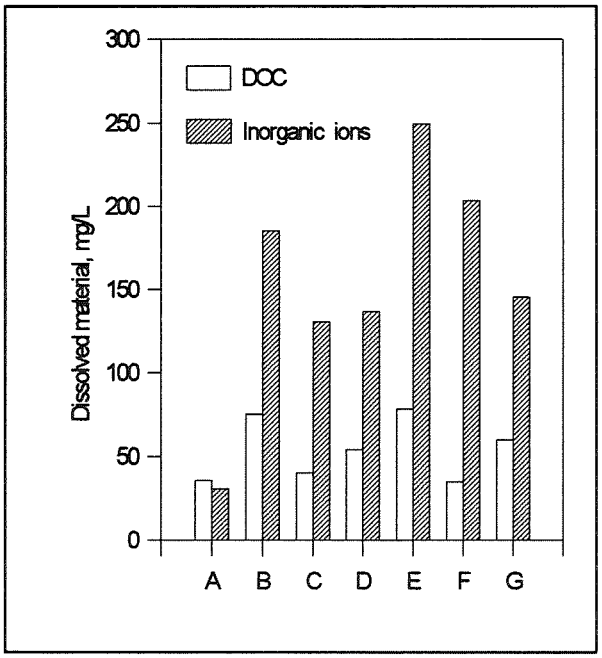

Figure 2. Distribution of extractable organic compounds according to their polarity in fog water

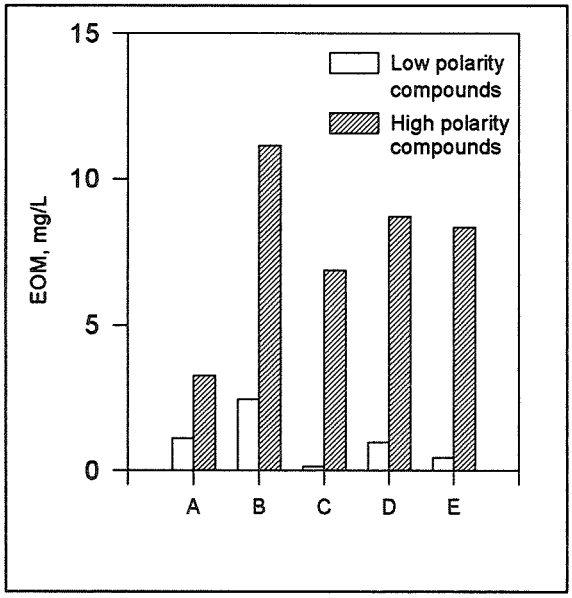

seem to be affected by the sampling location and/or sampling season.

When the total amount of DOC in fog-water is compared with the amount of organic carbon recovered from the liquid-liquid extraction steps

Figure 3. Size–exclusion chromatogram of a fog sample

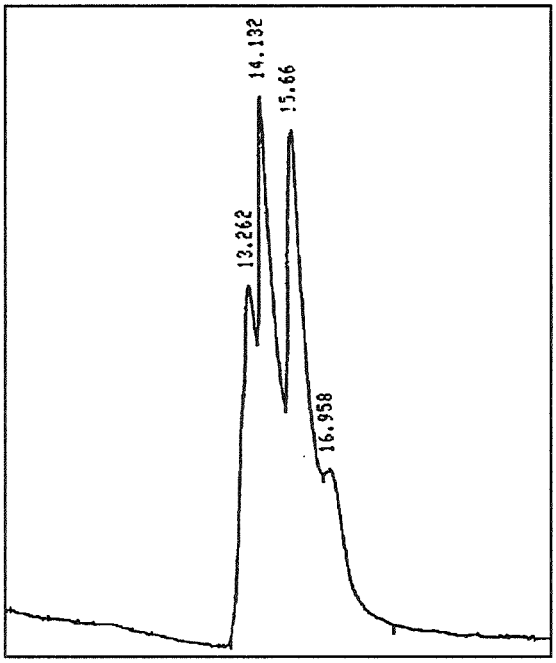

(BNF + AF), it is possible to notice that a large fraction of organic matter is missing. In fact, solvent extraction allowed for an organic carbon recovery ranging from 10 to 20 % of the total DOC. This poor recovery was similar for all samples and could be explained by the fact that the missing organic components are stronghly hydrophilic or amphiphilic and therefore scarcely extractable using conventional liquid-liquid extraction methods with non polar solvents. The polar characteristics of the organic compounds in fog is further confirmed when the extracts are fractionated in classes of compounds according to polarity. In Figure 2 it is evident that the polar species represent around 70 % of the total mass of the extractable organic compounds.

To investigate the nature of the non-extractable compounds in fog samples, we used size-exclusion chromatography. This technique would evidence the presence of macromolecular compounds. In fact, all samples exhibit a similar chromatographic profile (Figure 3) highlighting the existence of three (or four) main distributions of molecular weight, ranging from approximately 8000 to 10000 AMU. An estimate of the total concentration of these macromolecular compounds adds up to values in the same order of magnitude of the organic carbon amount missing from the extraction procedure. A chemical identification of these substances has, as yet, not been performed and will be the subject of future work.

As a first approach, it is possible to hypothesize that the large amount of macromolecular compounds detected in the fog water samples is of natural origin (natural surfactants, compounds from the degradation of biota, proteins etc.).

4. CONCLUSION

The organic chemistry in the atmospheric dispersed liquid phase (cloud and fog droplets) is a relatively new research area; the preliminary experiment described in this paper aimed at characterizing the different categories of organic compounds in fog water and is, we believe, a first step toward a more extensive study on the occurrence of organic substances in clouds and their effects on the physical and chemical properties of clouds themselves.

5. ACKNOWLEDGEMENTS

This work was partly financed within the NEVALPA project, sponsored by ENEL S.p.A.– Centro Ricerche Ambiente e Materiali, Milano.

6. REFERENCES

Czucwa, J., V. Katona, G. Pitts, M. Zimmerman, F.DeRoos, F., P. Capel, and W. Giger, 1989: Analysis of fog samples for PCDD and PCDF. *Chemosphere*, **18**, 847-850.

Capel, P.D., R. Gunde, F. Zurcher, and W. Giger, 1990: Carbon speciation and surface tension of fog. *Environ.Sci.Technol.*, **24**, 722-727.

Capel, P.D., C. Leuenberger, and W. Giger, 1991: Hydrophobic organic chemicals in urban fog. *Atmos. Environ.*, **25A**, 1335-1346.

Fuzzi, S., G. Orsi, and M. Mariotti, 1983: Radiation fog liquid water acidity at a field station in the Po Valley. *J. Aerosol Sci.*, **3**, 135-138.

Fuzzi, S., G. Orsi, G. Nardini, M.C. Facchini, S. McLaren, E. McLaren, and M. Mariotti, 1988: Heterogeneous processes in the Po Valley radiation fog. *J. Geophys. Res.*, **93D**, 11141-11151.

Fuzzi, S., M.C. Facchini, G. Orsi, and D. Ferri, 1992a: Seasonal trend of fog water chemical composition in the Po Valley. *Environ. Pollut.*,**75**, 75-80.

Fuzzi, S., M.C. Facchini, G. Orsi, W. Wobrock, M. Kessel, R. Maser, W. Jaeschke, K.H. Enderle, B.G. Arends, A. Berner, I. Solly, C. Kruisz, G. Reischl, S. Pahl, U. Kaminski, P. Winkler, J.A. Ogren, K.J. Noone, A. Hallberg, H. Fierlinger-Oberlinninger, H. Puxbaum, A. Marzorati, H.-C. Hansson, A. Wiedensohler, I.B. Svenningsson, B.G. Martinsson, D. Schell, and H.W. Georgii, 1992b: The Po Valley Fog Experiment 1989. An overview. *Tellus*, **44B**, 448-468.

Fuzzi, S., M.C. Facchini, G. Orsi, G. Bonforte, W. Martinotti, G. Ziliani, P. Mazzali, P. Rossi, P. Natale, M.M. Grosa, E. Rampado, P. Vitali, R. Raffaelli, G. Azzini, and S. Grotti, 1996: The NEVALPA project: a regional network for fog chemical climatology over the Po Valley basin. *Atmos. Environ.*, **30A**, 201-213.

Fuzzi, S, G. Orsi, G. Bonforte, B. Zardini, and P.L. Franchini, 1996: An automated fog water collector suitable for deposition networks: design, operation and field tests. *Water Air Soil Pollut.* (in press).

Glotfelty, D.E., J.N. Seiber, and L.A. Liljedahl, 1987: Pesticides in fog. *Nature*, **325**, 602-605.

Glotfelty, D.E., M.S. Majewski, and J.N. Seiber, 1990: Distribution of several organophosporous insecticides and their oxigen analogues in a foggy atmosphere. *Environ.Sci.Technol.*, **24**, 353-357.

Graedel, T.E., and K.I. Goldberg, 1983: Kinetic studies of raindrop chemistry. Inorganic and organic processes. *J. Geophys. Res.*, **88**, 10865-10882.

Novakov, T., and J.E. Penner, 1993: Large contribution of organic aerosols to cloud condensation nuclei concentrations. *Nature*, **365**, 823-826.

Saxena, P., L.M. Hildemann, P.H. McMurry, and J.H. Seinfeld, 1995: Organics alter hygroscopic behavior of atmospheric particles. *J. Geophys. Res.*, **100D**, 18755-18770.

Shulman, M.L., M.C. Jacobson, R.J. Charlson, R.E. Synovec, and T.E. Young, 1996: Dissolution behavior and surface tension effects of organic compounds in nucleating cloud droplets. *Geophys. Res. Lett.*, **23**, 277-280.

Warneck, P., 1988: *Chemistry of the Natural Atmosphere.* Academic Press, London.

A SIMULTANEOUS STUDY OF ACID PRECIPITATION IN THE RAPIDLY DEVELOPING AREAS OF XIAMEN, QUANZHOU, ZHANGZHOU AND TONGAN IN THE SOUTHEAST COAST OF CHINA

Shaocai Yu[1], Xiaojian Cheng[2], Zhemian Cheng[3], Shuentian Cheng[4], Jian Xiao[5] and Wenxian Ye[6]

1.Department of Marine, Earth and Atmospheric Sciences, North Carolina State University, Raleigh, NC 27695-8208, U.S.A
2. Xiamen Environmental Research Institute, Xiamen 361006, P.R.China
3. Xiamen Meteorological Observatory, Xiamen 361004, P.R. China
4. Quanzhou Environmental Monitoring Station, Fujian, P.R.China
5.Zhangzhou Environmental Monitoring Station, Fujian, P. R. China
6. Tongan Environmental Monitoring Station, Fujian, P. R. China

1. INTRODUCTION

In the past decade, many researchers have widely debated the problems of acid precipitation in Europe, in the northeast United States and in Southern China (Galloway et al., 1982; Saxena and Yeh, 1988; Zhao et al., 1988; Yu et al., 1991). The SO2 and NOx gases that are mostly emitted by industries and anthropogenic activities, are the major sources of the acid rain via long-range transport even over non-industrialized areas (Galloway et al., 1982; Saxena and Yeh, 1988). In this paper, We show the results of simultaneous investigation of acid precipitation over the areas of Xiamen, Quanzhou, Zhangzhou, and Tongan in southeast of China where the economics is developing very rapidly.

2. Experimental

2.1. Outline of research areas

The region of Xiamen, Quanzhou, Zhangzhou, and Tongan is called "Minnan Golden Triangle" which lies at the southeast of Fujian province in the southeast China coast, to the west of Taiwan Straight (see Fig. 1). Xiamen is one of four special economic zones in China. The region has a subtropical oceanic climate, and lies in the typhoon track. Four or five typhoons may pass the areas annually.

2.2. Sampling and analytical methods

Sampling: To investigate the situation and distribution of acid rain in Minnan Golden Triangle, four monitoring stations were established in Xiamen, Quanzhou, Zhangzhou, and Tongan to simultaneously monitoring the same rain event The rain sample pH was measured at sites and rain samples were treated at sites and stored in refrigerator before analysis.
Analytical Methods: Anion ion concentrations (SO_4^{2-}, NO_3^-, F^-, Cl^-) were determined using IC and cation ions (Na^+, K^+, Ca^{2+}, Mg^{2+}) were determined using atomic absorption spectrophotometer. NH_4^+ was analyzed by classical colorimeteric method. Radar was Radar-731 type (made in China).

Fig 1. Map of "Minnan Golden Triangle"
(* sampling site)

3. Results and discussion

3.1. Spring rain

The spring rain period in these areas is from February to April, and the spring rain is usually very acidic. Thirteen and three spring rain events were simultaneously sampled at four monitoring stations for 1990 and 1991, respectively. In the table 1 is listed the pH values in simultaneous rain samples and the corresponding meteorological parameters such as cloud types, sites of cloud refer to Xiamen prior to and after rain, surface and high-altitude (500mb) synoptic systems. Table 2 presents volume weighted concentrations of ions in spring rain. The sample of radar echo map and the satellite image for the precipitation cloud of April 19, 1990 was showed in Fig 2. Fig 3 illustrated the synoptic scale map at 0800 and 2000 LST on April 19, 1990. The frontal system and accompanying precipitation system moved from west of research areas where is the south China mainland and the heavy acid rain was regularly observed (Zhao et al., 1988; Yu et al., 1991). This suggested that the spring low pH rainfall in research areas was mainly caused by long-transport of pollution from the southern China mainland.

3.2. Mold rain and Typhoon rain

The mold rain period in these areas is from May to middle June. In Table 3 is presented the results of simultaneous mold rain samples at the four sites. The ion concentrations for mold rain were listed in Table 2. The mold rain was less acidic than the spring rain. Most of precipitation cloud of mold rain moves from the southeast, and maybe this made the differences between the spring rain and mold rain.

Table 1. The pH of simultaneous spring rain in "Minnan Golden Triangle" area in 1990 and 1991

No.	Sampling time(1990)	Xiamen	Zhangzhou	Quanzhou	Tongan	Avg.pH	Prec..	site of cloud	surface	high-altitude
1	4.9,1930-4.10,0830	4.62	5.65	6.59	5.34	5.1	Sc,Cb	S/E	rear of high press	SW frontal trough
2	4.10,1930-4.11,0830	4.83	6.07	5.15	4.93	5.06	Sc,Ac	W/NE	reverse trough	SW frontal trough
3	4.11,0945-4.11,1530	4.31	4.53	4.44	4.4	4.41	=,Cb	W/E	reverse trough	SW frontal trough
4	4.11,1930-4.12,0830	4.13	4.53	4.34	4.36	4.32	Sc	W/E	reverse trough	SW frontal trough
5	4.14,1930-4.15,0900	4.5	5.48	4.57	4.57	4.65	Sc	W/E	low pressure	W shear
6	4.15,1900-4.16,0900	4.52	/	4.64	5.1	4.69	Sc,Fn	W/E	low pressure	W shear
7	4.16,1100-4.16,1745	4.44	5.09	4.5	4.6	4.6	Sc,Fn	W/E	stationary front	W shear
8	4.16,1930-4.17,0900	4.74	/	4.64	4.84	4.73	Sc,Cb	W/E	rear of high press	W shear
9	4.17,1900-4.18,0900	4.43	5.31	4.57	4.54	4.61	Sc,Ac	W/SE	rear of high press	W rear of trough
10	4.18,1900-4.19,1000	4.12	/	4.32	4.46	4.28	Sc,Cb	W/E	rear of high press	NW rear of trough
11	4.19,1000-4.19,1445	4.22	4.6	4.37	4.56	4.41	Sc,Fn	W/E	low pressure	SW frontal trough
12	4.19,1700-4.20,0800	4.03	5.01	4.06	/	4.2	Sc,=	W/E	low pressure	SW frontal trough
13	4.40,0800-4.21,0800	4.13	4.6	4.81	4.64	4.46	=	W/SE	rear of front	SW shear
Total average pH		4.32	4.86	4.5	4.62	4.51				
	(1991)									
14	4.30,1900-5.1,1700	4.59	5.21	4.27	4.57	4.55	Sc	W/E	front	W trough
15	5.1,1900-5.2,0900	4.79	/	4.33	/	4.5	Sc,Fn	W/E	cold front	W trough
16	5.2,1900-5.3,1930	6.54	6.57	5.03	5.09	5.35	Sc	W/E	rear of high press	W shear

Table 2.The volume-weighted concentrations of ions in spring rain, mold rain, and typhoon rain in Minnan Golden Triangle (μeq/l)

	F^-	Cl^-	NO_3^-	SO_4^{2-}	Na^+	NH_4^+	K^+	Ca^{2+}	Mg^{2+}
Spring rain									
Xiamen	4.9	12.79	13.71	70.03	5.25	61.76	4.44	30.26	4.07
Zhangzhou	12.95	15.75	17.81	114.7	2.32	57.87	2.5	14.44	1.99
Quanzhou	14.28	7.51	19.07	50.86	3.55	44.55	5.65	19.86	3.31
Tongan	13.22	9.74	19.16	62.16	6.14	59.24	5.95	10.34	3.02
Mold rain									
Xiamen	8.86	11.48	5.16	58.49	8.98	21.84	2.95	15.8	2.45
Zhangzhou	10.18	13.25	9.36	86.5	11.83	53.83	6.34	52.13	6.19
Quanzhou	8.95	98.21	20.52	59	75.19	61.43	43.1	15.05	1.55
Tongan	8.12	32.09	7.67	70.08	23.72	37.73	9.74	32.88	7.69
Typhoon rain									
Xiamen	7.89	44.64	2.98	47.69	29.03	16.25	2.8	22.16	11.15
Zhangzhou	20.66	17.66	12.62	69	24.47	6.56	16.8	15.45	14.8
Quanzhou	10.63	12.11	2.75	31.27	12.34	8.71	3.32	9.22	4.34
Tongan	5.71	13.19	2.41	18.88	9.21	12.11	2.64	1.87	3.52

The mold rain period in these areas is from May to middle June. In Table 3 is presented the results of simultaneous mold rain samples at the four sites. The ion concentrations for mold rain were listed in Table 2. The mold rain was less acidic than the spring rain. Most of precipitation cloud of mold rain moves from the southeast, and maybe this made the differences between the spring rain and mold rain.

The typhoon rain period is from the middle June to September. In Table 4 is listed the results of typhoon rain, and the ion concentrations were listed in Table 2. The typhoon rain was less acidic than the spring rain and mold rain. The differences among the results of our monitoring sites were very large. This was because the wind was very strong, and the concentrations of aerosol particles would be very high. Some aerosol particles could neutralize some acidity in typhoon rain. The local situations of pollution had more effect on the typhoon rain. Most precipitation cloud of typhoon rain moved from the southern directions where is South China Sea.

3.3. Statistical analysis

A multivariate progressive regression model was used to find the relationships between pH and inorganic ion contents in every type of rain. The following regression equation can be gotten for 39 spring rain samples in Xiamen (n=39):

$$[H^+]=5.383+1.378[Cl^-]+1.703[NO_3^-]+0.334[SO_4^{2-}] - 1.235[Na^+]-0.113[NH_4^+]-0.801[K^+]$$

$$R=0.880$$

The regression equation for 13 Quanzhou spring rain samples was as follows (n=13):

$$[H^+]=31.983-0.257[F^-]+0.627[SO_4^{2-}]-0.648 - 3.368[Mg^{2+}] \quad R=0.862$$

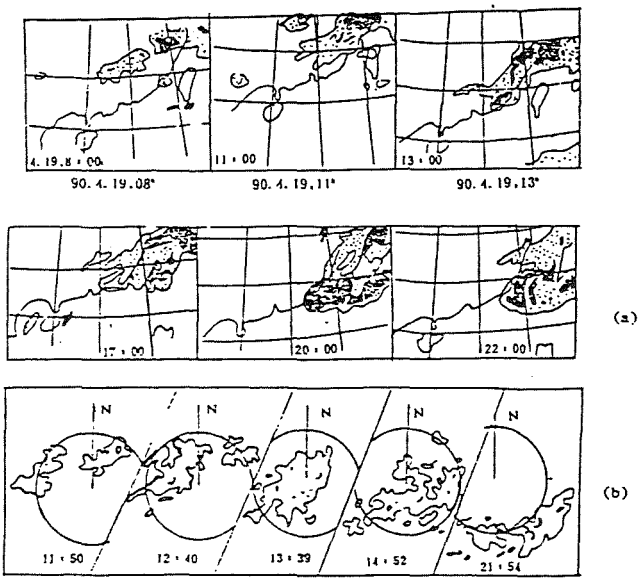

Fig 2. (a) The satellite image
(b) Radar echo maps (each contour represents 100 km) on April 19, 1990

Table 3 . The pH of simultaneous mold rain in "Minnan Golden Triangle" area in 1990 and 1991

No.	Sampling time(1990)	Xiamen	Zhangzhou	Quanzhou	Tongan	Avg.pH	Prec.	site of cloud	surface	high-altitude
1	5.11,1200-5.11,1500	6.12	6.61	6.9	7.26	6.52	Sc,Fn	W/E	high press	SW frontal trough
2	5.12,1530-5.13,0800	4.39	5.39	4.67	5.25	4.77	=	SW/NE	stationary front	SW frontal trough
3	5.17,1400-5.18,0915	4.79	5.59	5.29	5.46	5.16	Cu,Cb	W/E	cold front	W frontal trough
4	5.18,0925-5.19,0845	4.64	4.55	4.64	5.15	4.69	Sc	W/E	rear of front	trough
5	5.19,0845-5.19,1230	4.73	/	4.86	4.78	4.79	Sc	W/E	rear of high press	trough
Average pH		4.7	5.06	4.93	5.18	4.93				
	(1991)									
1	5.15,1800-5.16,0900	5.45	/	6.1	4.89	5.24	Sc,Cu		high press	N high press
2	5.18,0900-5.18,1530	4.26	5.49	6.43	4.79	4.73	Sc,=	SW/E	rear of high press	SW frontal trough
3	5.22,1615-5.22,1700	5.4	/	/	5.39	5.39	Sc,Cu		high press	high press
4	6.8,1200-6.9,1800	4.85	/	4.75	/	4.8	Sc,Cu	SSW/NNE	rear of front	high press
5	6.24,1500-6.25,1630	4.69	/	5.22	6.12	5.04	Sc,Fn	SW/NE	rear of front	SW frontal trough
6	6.25,1700-6.26,1945	4.9	5.3	4.62	/	4.86	Fn, Cb	SW/NE	stationary front	SW frontal trough
7	6.26,2000-6.27,0840	4.63	5.24	4.77	6.16	4.93	Fn, Cb	SW/NE	high press	SW frontal trough
Total average		4.76	5.39	4.71	5					

Table 4 . The pH of simultaneous typhoon rain in "Minnan Golden Triangle" area in 1990 and 1991

No.	Sampling time(1990)	Xiamen	Zhangzhou	Quanzhou	Tongan	Avg.pH	Prec.	site of cloud	surface	NW typhoon
1	6.24,1200-6.25,0900	4.87	5.32	4.88	5.98	5.09	Sc, Cb	S/SE	typhoon	SE typhoon
2	6.29,1155-6.30,0900	6.43	6.09	5.4	5.76	5.76	Sc,Cu	S/W	typhoon	SW typhoon
3	6.30,0900-7.1,1800	5.04	4.83	4.75	/	4.86	Sc, Fn	S/NE	low press	SW trough
4	7.1,1800-7.2,0845	5.17	5.28	4.67	/	4.95	Sc,Nc	SW/NE	stationary front	SW trough
5	7.30,0800-7.31,1600	5.68	5.24	/	5.33	5.37	Sc, Fn	S/N	typhoon	typhoon
Average pH		5.2	5.2	4.85	5.6	5.14				
	(1991)									
6	7.19,1230-7.19,1815	5.64	/	5.63	6.48	5.78	Cu,Fn	ESE/WNW	typhoon	ENE typhoon

In order to study the relationships among samples and ions in every monitoring site, Q-R factor correspondence analysis model was used. Fig 4 showed point accumulation result of analysis for spring rain at four sites. Point No.1 to No.10, No.11 to No.20, No.21 to No.33, No.34 to No.40 represented the spring rain samples in Xiamen, Tongan, Quanzhou and Zhangzhou, respectively. There were three regions in Fig 4. Region I consisted of No.2, 3, 4, 5, 6, 7, 8, 9, 10,12, 19,20,21,23,24,25,26,27,30,34,38,40, and Cl^-, NO_3^-, SO_4^{2-}, Na^+, NH_4^+, Mg^{2+} ions. Region II consisted of No.1, 11, 13, 14, 16, 17, 18, 22, 28, 29, 31, 32, 35, 36, 37, 39, and F^- ion. The region III was composed of No.33 and K^+, H^+ and Ca^{2+}. The results in Fig 4 showed that there were not essential differences among simultaneous spring rain samples at four sites.

4. Conclusions

The following conclusions were drawn from this study:

(1) The precipitation in "Minnan Golden Triangle" region was acidic, and spring rain was the most acidic in the three types of rain. The spring rain, mold rain, and typhoon rain were caused by precipitation cloud from different directions and had different acidity. This suggested that acid rain in these areas may be mainly caused by long-transport of pollutants.

(2) Q-R factor correspondence analysis showed that there were not essential differences among rain samples simultaneously collected at four monitoring sites although there were some distances among them.

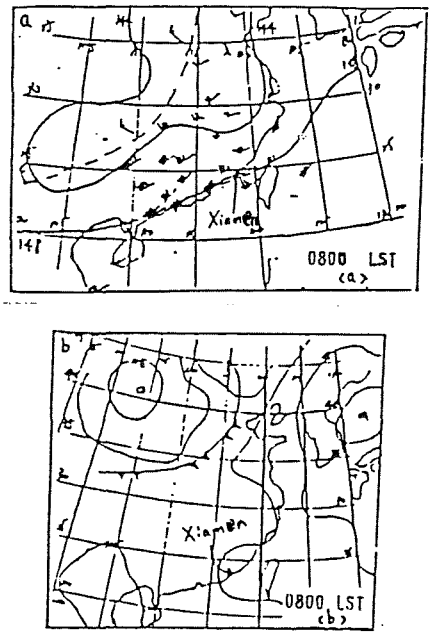

Fig 3. (a) The high altitude synoptic maps
(b) The surface synoptic maps
on April 19, 1990

Acknowledgments: This work was supported by Xiamen Municipal Science Commission. One of author (Shaocai Yu) would like to thank Prof. Tang Xiaoyan, Prof. Bi Mutian of Peking University and Prof. V.K Saxena of NCSU for their helps. We also thank Mr. Wu Zilin, Lin Hanzhon and Cao Chentie of Xiamen EPA.

References

Galloway, J.N., Liken, G.E., Keene, W.C., and J. M. Miller, 1988: The composition of precipitation in remote areas of the world. J Geophys. Res., 87, 8771-8786.

Saxena, V.K., and R.-Y, Yeh, 1988: Temporal variability in cloud water acidity: physicochemical characteristics of atmospheric aerosols and windfield. J. Aerosol. Sci., 19, 1207-1210.

Smith, F. B., and R.D. Hunt, 1978: Meteorological aspects of the transport of pollution over long distances. Atmos. Environ. 12, 461-477.

Yu, Shaocai, Bi Muitan, Lin Xin, Yao Rongkui, and Tang Xiaoyan, 1991: Organic acids in precipitation from Baiyun Mountain, Guangzhou, and cloudwater from Miaoer Mountain, Guangxi, Acta Sci. Circumstantiae, 11(1), 25-30.

Zhao, D., Xiong, J., Xu, Y., and W.H. Chan, 1988. Acid rain in southwestern China. Atmos. Environ., 22, 349-358.

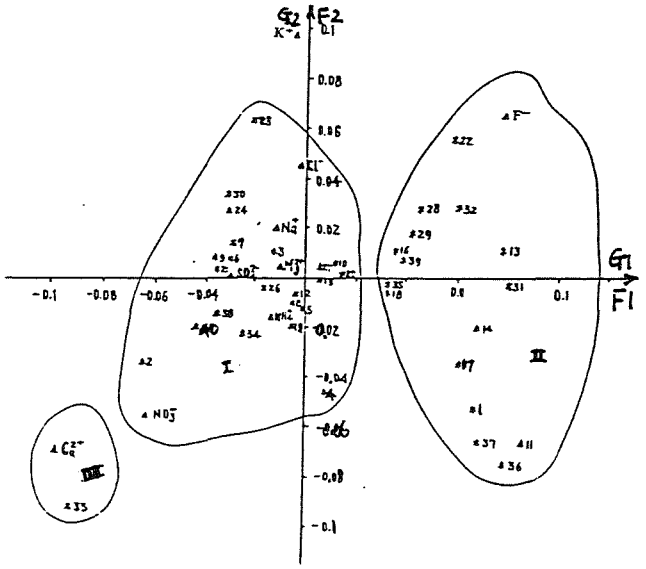

Fig 4. Results of Q-R factor correspondence analysis of samples and variables for spring rain in the areas

A FIELD STUDY OF THE REACTION BETWEEN SULFUR DIOXIDE AND HYDROGEN PEROXIDE IN CLOUDS

Liaquat Husain,[1,2] Vincent A. Dutkiewicz,[1,2] R. Balasubramanian[1] and M.M. Hussain[2]

1)Wadsworth Center, NYS Dept. of Health, Albany, NY, USA 12201-0509
2)Department of Environmental Health and Toxicology, School of Public Health, State University of NY at Albany, Albany, NY, USA 12201-0509

1. INTRODUCTION

Chemical transformations of pollutants such as SO_2 in the atmosphere have received great attention beacuse of a wide range of environmental consequences. However, it is difficult to make a direct observation of a chemical reaction in the atmosphere because of a large number of associated variables. Moreover, it is not generally possible to simulate field conditions accurately in the laboratory or in models. To counter this problem, we have developed a tracer technique to follow the reaction between SO_2 and H_2O_2 in clouds (Husain, 1989; Burkhard et al., 1995; Dutkiewicz et al., 1995). This technique enables a determination of the SO_4 formed from the reaction between SO_2 and H_2O_2 in cloud drops. We present here results from an intensive field study conducted during July 1995 to evaluate the reaction in large stratus cloud systems at Whiteface Mountain, New York.

2. TRACER TECHNIQUE

The SO_4 aerosols formed in gas-phase oxidation primarily reside on accumulation mode aerosols, which later act as cloud condensation nuclei (CCN). Oxidation of SO_2 can take place in these cloud droplets via reactions with H_2O_2. Thus, SO_4 in cloud water (CW) may be derived from both gas- and aqueous-phase oxidation. The only accurate method to determine in-cloud SO_4 production is a tracer technique recently developed in this laboratory. The technique is based on the fact that atmospheric aerosol in addition to SO_4 contain trace elements such as Se, As, and Sb that can also act as CCN. The only source of these trace elements in the cloud droplets is nucleation scavenging. Therefore these trace element(s) can be used to quantitatively trace the uptake of aerosol SO_4 in CW and hence, by difference, the in-cloud SO_4 formed $[(SO_{4in})_{CW}]$, (Husain, 1989),

$$(SO_{4in})_{cw} = [(SO_4/M)_{cw} - (\alpha/\beta)(SO_4/M)_{aa}] (M)_{cw}. \quad (1)$$

where α and ß are the respective fractions of aerosol SO_4 $[(SO_4)_{aa}]$ and tracer $(M)_{aa}$ taken up in clouds or the scavenging efficiencies, L is the liquid water content in g $(H_2O)/m^3$ of air, and aa represents measurements in ambient aerosols. Therefore if α/β is known, by determining the (SO_4/M) ratio in the CW and pre-cloud aerosols, and the concentration of M in CW, the amount of SO_4 formed in the cloud can be determined. Values of $(SO_4/M)_{aa}$ can be determined either in pre-cloud or in-cloud air. We have shown that for Se, As and Sb $\alpha/\beta = 1$, and these elements are reliable tracers for determing in cloud SO_4 production. (Burkhard el al., 1995).

3. EXPERIMENTAL

A detailed discussion of the experimental methods may be found elsewhere (Burkhard et al., 1995; Dutkiewicz et al., 1995).

A field campaign was conducted during July 1995 at Whiteface Mountain. Two sites were used. Cloud water, and suspended aerosol were collected at the summit (1.5 km amsl) along with gas-phase measurements of SO_2 and H_2O_2, while aerosols and SO_2 were collected/measured at a site at 0.6 km amsl. The CW was collected with a passive collector in 15 minute intervals. The aliquot for SO_4 and trace elements were filtered with 0.45 micron Nuclepore filters at the site and stored at 4°C until analysis. Liquid water content was measured with a Gerber forward light scattering device by USEPA (Drs. Ralph Baumgardner and Jim Anderson, personal communication).

Gas-phase H_2O_2 was measured in real time using an automated instrument (Aero Laser model AL-1002) that utilizes a dual-channel fluorometric method, described in detail by Lazrus et al. (1986), with a few modifications in the design. In this instrument, ambient air, drawn at a rate of 2 L/min through a PFA teflon tubing (1/4 inch I.D.), is split into two channels and peroxide is stripped from the air using a collection reagent that flows concurrently with the air through a coil. The first channel allows soluble hyroperoxides to be detected. The second channel receives an enzyme catalase that destroys only H_2O_2; this allows organic peroxide to be detected. Hydrogen peroxide is determined as the difference of the two channels. The minimum detection limit of H_2O_2 is 50 pptv. The analyzer was calibrated at least daily using gas-phase H_2O_2 during measurements in

clear air and more frequently during cloud events. Based on the accuracy of the calibration, the signal to noise ratio, transmission efficiency of the sampling line, and the catalase correction, our experimental error is 15% at ≤ 0.5 ppbv and 10% at ≥ 0.5 - 3.0 ppbv. SO_2 measurements were made with a commercial pulsed fluorescence analyzer, Thermo Environmental Co (TECO) model 43S. The calibration were done at least once a day using a NIST certified SO_2 permeation tube-dilution system over the range of 0 to 20 ppbv. The detection limit of the instrument is 0.1 ppbv. The measurement uncertainty is estimated as ranging from 20% at 0-2 ppbv to 10% at 2-20 ppbv. Data for both instruments were recorded every 3 minutes and averaged hourly.

Cloud water samples were analyzed for pH, conductivity, and the concentrations of SO_4, Se, As, Sb, and H_2O_2. Concentrations of SO_4 and the trace element were also measured in the aerosol samples using well established methods described elsewhere (Burkhard et al., 1995; Dutkiewicz et al., 1995).

4. RESULTS AND DISCUSSIONS

During the 1 month intensive sampling campaign, samples were collected from 23 cloudy periods. The clouds were collected on 14 different days as summarized in Table 1. In all, 86 hours of clouds were studied (395 individual cloud water and 683 aerosol samples). The CW pH varied from 2.4 to 6.0 but usually only several tenths of a pH unit within a specific cloud. The pH at this site is most strongly related to the concentration of SO_4 (Mohnen and Kadlecek, 1989). Aerosol SO_4 concentrations at this site are strongly related to the air mass direction; highest concentrations are related to air masses that arrive from high SO_2 emission region in the Midwestern US (Husain and Dutkiewicz, 1990). The lowest pH clouds (Table 1) are also associated with air masses from this direction. The lowest pH, 2.4, during this study was recorded on July 23. Results from the July 23 cloud will be used to study in-cloud oxidation of SO_2 by H_2O_2.

Table 1. Summary of Cloud Events Sampled at Whiteface Mountain during July 1995

Date	Time Start-End	Samples (No.)	pH	Wind Direction
1	0215-1100	22	3.2-3.9	SW
1	2200-2245	11	3.4-3.9	N
3	0000-0715	28	4.5-6.0	N
5	0615-0815	7	3.3-3.4	N
6	0400-0530	7	3.0-3.2	SW
7	0500-1300	27	3.0-3.6	SW
8	0635-1015	11	3.0-3.5	SW
8	1400-1730	13	4.0	SW
9	2200-0145	14	4.2	SW
10	0630-1030	13	3.6	SW
15	0015-0545	22	3.4-3.7	W
15	1500-1715	8	4.0-4.7	W
17	0700-1200	19	3.9-4.6	SW
17	1515-1800	10	3.4-3.6	SW
18	0900-1030	5	3.0-3.9	SW
18-19	2315-1115	48	3.9-4.4	W
20	0600-1030	18	3.4-3.9	SW
20-21	1530-1100	67	3.5-4.0	SW
23	0600-1800	45	2.4-3.4	SW

Figure 1 shows hourly SO_2, and H_2O_2 concentrations during July 22 - 23 at the 1.5 km site. The cloud was associated with a large frontal system and a heavy stratus deck covered much of the region. During the non-cloudy period on July 22, SO_2 remained around 0.4 ppb. As the cloud reached the site on July 23, SO_2 began to increase. Between 0600 and 0800 hr there was a very sharp rise in SO_2 with a peak concentration of 7 ppb.

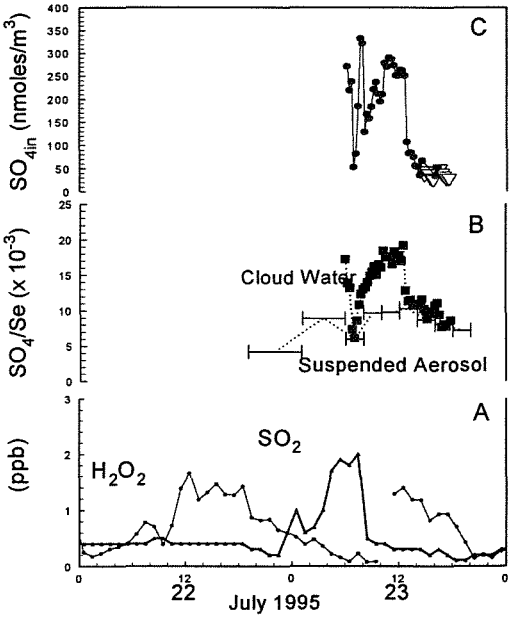

Figure 1. Variations of H_2O_2, SO_2, and the ratios of SO_4/Se in aerosols and in cloud water along with the concentrations of SO_4 formed in clouds based on (1).

During the clear air period on July 22 there is a distinct diurnal variation in H_2O_2. Maximum concentrations occurred at 1300 hr, 1.7 ppb, while SO_2 concentrations were near detection limits during the early morning of July 22. Prior to the cloud commencing at 0200hr on July 23, H_2O_2 concentrations were around

0.5 ppb and steadily decreased as the liquid water content increased (Fig. 1). Apparently, a significant amount of H_2O_2 was transferred from the gas-phase into cloud water and reacted with SO_2. H_2O_2 concentration was at a minimum at ~0700 hr while SO_2 was at a maximum. Subsequently, SO_2 concentration decreased precipituously. Concurrently, H_2O_2 showed a sudden rise, peaking at about ~1200 hr. Thereafter, H_2O_2 concentration in the interstitial air decreased steadily as SO_2 remained between 0.2 to 0.3 ppb. These observations suggest reaction occurring between the two reactants. This could be further confirmed by following the product of the reaction; i.e., SO_4, with the help of the tracer technique. Although As and Sb as well as Se data are available, due to space limitation we present here only Se results. Fig 1B shows the SO_4/Se ratios in aerosols and in cloud water. Initially, the SO_4/Se ratio in the CW was ~18,000 (compared to ~9,000 in the aerosols) and sharply declined to ~6,000. At that time, SO_4/Se ratio in aerosol was also measured to be ~6,000. The 3-min SO_2 data (not shown in Fig. 1) showed that the initial high SO_4/Se ratio in the cloud water coincided with a sharp but brief peak in SO_2 concentration of ~8 ppb. Subsequent rise in SO_4/Se ratios in the cloud water is associated with rise in SO_2 concentrations. Since the difference in SO_4/Se ratios in CW and aerosols is a direct measure of in-cloud SO_4 formation (Equation (1), the data in Fig. 1 are quite consistent. Fig. 1C shows the amounts of SO_4 formed from the reaction between H_2O_2 and SO_2 in the individual samples. Since the L affects the cloud water concentrations (but not the SO_4/Se ratios), the values of SO_{4in} are shown in nano-moles/m^3 (i.e., corrected for the variation in the liquid water content). There is a general similarity in the SO_{4in} and SO_4/Se ratios in CW. The above data can be used to assess the relationship between

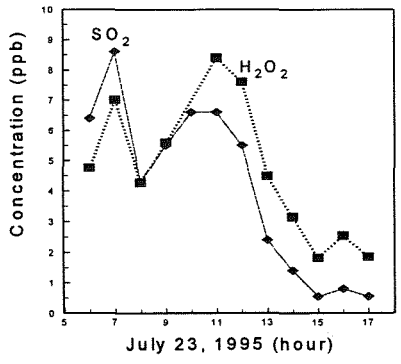

Figure 2. Derived total SO_2 and H_2O_2 including measured gas- and aqueous-phase concentrations and equimolar contributions from SO_{4in}.

SO_2 and H_2O_2 in the atmosphere and to respond to the question whether there is sufficient H_2O_2 in the atmosphere to oxidize SO_2 in clouds in the northeastern US. Fig.2 shows the total SO_2 and H_2O_2 present on 23 July. The results show that initially when SO_2 concentration was ~8.5 ppb, there was a deficiency of H_2O_2 by about 2 ppb. Later on, however, H_2O_2 concentration exceeded throughout the remainder of the cloud event. It should be pointed out that H_2O_2 values in Fig. 2 include H_2O_2 values measured in the cloud interstitial air, in cloud water as well as the amount needed to form the observed value of the in-cloud SO_4 formation. Hence, no H_2O_2 source is left unaccounted. However, from the limited data presented here, a generalized picture on the question of oxidant sufficiency cannot be deduced. That should await the completion of this study.

7. ACKNOWLEDGEMENT

We thank Adil Khan, Steven Chace, David Teiger and Kamal Swami for assistance in chemical analysis. This work was partially supported by a grant from USEPA offic of Exploratory Research. However, this work has not been reviewed by USEPA.

8. REFERENCES

Burkhard, E.G. B.M. Ghauri, V.A. Dutkiewicz, and L. Husain, 1995: A multi-element tracer technique for the determination of SO_2 oxidation in clouds. *J. Geophys. Res.*, **100**, No. D12, 26,051-26,059, 1995.

Dutkiewicz, V.A., E.G. Burkhard, and L. Husain, 1995: Availability of H_2O_2 for oxidation of SO_2 in clouds in the northeastern United States. *Atmos. Environ.*, **29**, No 22, 3281-3292.

Husain, L., 1989: A technique for determining in-cloud formation of SO_4 Geophys. *Res. Lett.* 16, 57- 60.

Husain, L and V.A. Dutkiewicz, 1990: A long-term (1975-1988) study of atmospheric SO_4 regional contributions and concentration trends. *Atmos. Environ.* **24A**, 1175-1187.

Lazrus, A.L., G.L. Kok, J.A. Lind, S.N. Gitlin, B.G. Heikes, 1986: Automated fluorometric method for drogen peroxide in air. *Anal. Chem*, **58**, 594-597.

Mohnen, V.A., and J.A. Kadlecek, 1989: Cloud chemistry research at Whiteface Mountain, *Tellus*, **41B**, 79-91.

CHEMICAL MASS BALANCES IN MIXED PHASE CLOUDS

Margit Schwikowski[1], Olga Poulida[2], Urs Baltensperger[1] and Heinz W. Gäggeler[1,3]

[1] Paul Scherrer Institute, CH-5232 Villigen PSI, Switzerland
[2] Joint Research Centre, I-21020 Ispra, Italy
[3] Institute of Inorganic Chemistry, University of Bern, Freiestrasse 3, CH-3013 Bern, Switzerland

1. INTRODUCTION

Removal of aerosol particles from the air by precipitation is the most important cleansing mechanism of the earth atmosphere. A variety of processes are involved in the scavenging of aerosol particles in and below a cloud (see e.g. Pruppacher and Klett, 1980; Barrie, 1985). The most complex scavenging situation occurs in mixed phase or cold clouds, i.e. clouds containing ice crystals. This type of clouds is typically found in northerly climates and produces most of the precipitation there. After ice nucleation, ice crystals grow by water vapour deposition at the expense of the supercooled cloud droplets (Wegener-Bergeron-Findeisen mechanism) and/or by direct accretion of cloud droplets (riming) onto the surface of the crystal. The first mechanism is often the dominant physical process but insignificant with respect to the removal or transfer of pollutants resulting in very clean ice crystals. The latter mechanism determines to a great extent the chemical composition of the ice crystals by incorporation of activated aerosol particles.

In order to study scavenging processes of chemical species in precipitating clouds, high-elevation mountain sites are particularly suited since they are within the cloud during most of the precipitation events. The high-alpine research station Jungfraujoch, Switzerland (3450 m a.s.l.) was chosen as a suitable site for the simultaneous collection of aerosol particles, cloud droplets and ice crystals during snowfall events. In addition, cloud liquid water content and the mass concentration of ice crystals in air were measured. By this method, chemical mass balances between aerosol, cloud and ice phase could be obtained for the measured species. This is a new approach in order to understand overall air to snow scavenging efficiencies. In contrast to the conventional method of calculating scavenging ratios, where the concentration of a species in the deposited snow is related to the concentration of the respective species in the surrounding air, our concept allows to directly link the different phases in the same air parcel.

2. EXPERIMENTAL

In-cloud field experiments were carried out in October and November 1993. During snowfall, aerosol, cloud droplet and snow samples were simultaneously collected for subsequent chemical analysis. Aerosol samples were collected with a low-volume filter pack with an average time resolution of 2.5 h. The filter pack consisted of a teflon filter followed by a nylon filter (filter diameter 47 mm, 1.0 µm pore size, flow rate 2.6 $m^3 h^{-1}$). Bulk cloud water samples were collected by a single-stage cloud water impactor (Kruisz et al., 1993). The cloud water sampler was equipped with a large wind shield behind the impactor opening in order to stop cloud droplets up to 100 µm diameter in front of the shield. Thus, the droplets were sampled from a fairly stagnant flow. At a sampling rate of about 100 $m^3 h^{-1}$ the impactor had a lower cut diameter of about 7 µm and an upper cut of about 100 µm (A. Berner, personal communication). The supercooled cloud droplets froze on the plexiglass impaction plate. The time resolution varied between 29 and 211 min depending on the density of the cloud, with an average value of 84 min.

Time resolved samples of snow crystals were obtained by a collector designed after Borys et al. (1988). The sampling time varied between 20 min and 2.5 h with an average value of 1 h. This collector consisted of two plexiglass tubes (diameter: 14 cm) lined with polyethylene bags. The collection tube openings were automatically oriented into the wind. Wind speed was measured manually by an anemometer close to the snow collector. From the obtained average wind speed, the cross-sectional area of the collector tube openings and the sampling time, the volume of air was calculated for each snow sample. The weight of the snow samples was determined on site. A collection efficiency of the collector tubes for snow crystals of 65% was assumed according to Borys et al. (1988). The collection efficiency, the weight of the snow sample, and the volume of air were used to calculate the ice water content (IWC).

In addition, bulk samples of snow crystals were taken from a teflon surface exposed on the glacier after every snowfall event (Schwikowski et al., 1995). These bulk samples were also used to calculate mean precipitation rates (as mm water equivalent per hour).

Cloud water and snow samples were kept frozen until chemical analyses, which were carried out within a few weeks after the end of the field campaign. The major water soluble components Cl^-, NO_3^-, SO_4^{2-}, Na^+, NH_4^+, K^+, Mg^{2+}, and Ca^{2+} were determined by ion chromatography. The aerosol teflon filters were subjected to ultrasonic extraction, and the same components were determined. The nylon filter extracts were analysed for Cl^- and NO_3^- to determine gaseous HNO_3 and HCl.

The cloud liquid water content (LWC) was measured by a Particulate Volume Monitor (PVM-100, Gerber, 1984). LWC data were recorded on a one-minute time basis, and then averaged according to the collection time of the cloud water impactor.

3. RESULTS AND DISCUSSION

Altogether, eight snowfall events were investigated and the duration of observation varied between 6 and 12 h. The meteorological characteristics of these events are shown in Table 1. The ice water content ranged from 0.05 to 2.5 g m^{-3} during the eight snowfall events with a median of 0.37 g m^{-3} (+ 40%, -50%). The frequency distribution of the IWC is shown in Fig. 1. The relatively large error of the IWC is induced by uncertainties in determining the collection efficiency and the wind speed. Considering that our experimental site Jungfraujoch is located at the main ridge of the Bernese Alps which forms the first major obstacle for humid air masses approaching from the Northwest, precipitation forming clouds are expected to be of a convective type due to orographic lifting. This was confirmed by Doppler radar measurements conducted during most events (Poulida et al., 1994). Thus, the relatively high values of the IWC seem to be representative for convective clouds at such high elevations. These results were confirmed by comparing mean precipitation rates calculated from the IWC on an event basis to precipitation rates calculated from the bulk snow samples collected from the teflon surface and the duration of the snowfall event. Precipitation rates were typical for snow storms at high elevation sites (Table 1). Although the IWC was usually much higher than the LWC, it never exceeded the water vapour content. No direct relationship between IWC and water vapour content was found.

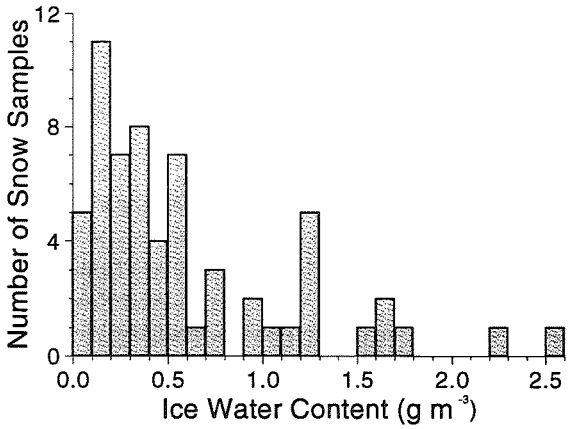

Figure 1: Frequency distribution of the ice water content during the eight snowfall events studied at Jungfraujoch in October and November 1993.

In Figure 2 the concentration of sulphate in snow is plotted versus the ice water content. Generally, the concentration in snow decreased with higher ice water contents. A similar behaviour was reported for the total ionic content in cloud water as function of the liquid water content (Möller, 1995). It is, however, interesting to note that for example the snowfall events on 6. and 11. November did not show such a dependence. These two events were characterised by a minor importance of riming on the concentration of sulphate in snow.

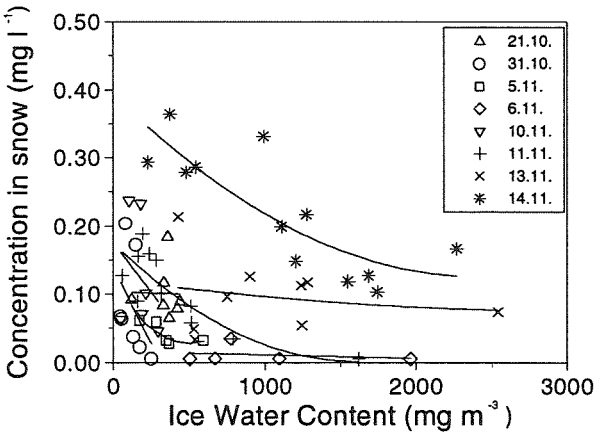

Figure 2. Concentration of sulphate in snow plotted versus the ice water content. The individual snowfall events are indicated by different symbols. Solid lines represent first order polynomial fits for single events.

Table 1: Meteorological characteristics of the snowfall events. The H_2O vapour content was calculated from the relative humidity and the air temperature on a 10 min basis and the precipitation rate from the IWC assuming a mean settling velocity of the ice crystals of 0.6 m s^{-1} (Pruppacher and Klett, 1980).

Event	Temp. (°C)	Wind (m s^{-1})	Wind Direction	Humidity (%)	H_2O Vapour (g m^{-3})	LWC (g m^{-3})	IWC (g m^{-3})	Prec. rate (mm h^{-1})
21 Oct.	-15	8.4	NW	86	1.4	0.09	0.35	0.76
31 Oct.	-7.8	11.3	SE	92	2.6	0.10	0.10	0.22
05 Nov.	-5.0	11.1	SE	95	3.4	0.12	0.35	0.76
06 Nov.	-6.1	6.6	SE	94	3.1	0.05	0.73	1.58
10 Nov.	-6.9	8.1	NW	91	2.8	0.08	0.19	0.41
11 Nov.	-10.0	6.4	NW	91	2.2	0.11	0.36	0.78
13 Nov.	-6.5	11.1	NW	94	3.0	0.09	0.97	2.10
14 Nov.	-13.5	8.8	NW	88	1.7	0.11	1.03	2.22

In order to illustrate our new approach to directly link the aerosol, cloud and ice phase within the same air parcel, the mass balances of sulphate are shown as an example in Figure 3a and 3b for two snowfall events. The mass concentration of sulphate in cloud water, e.g., is the mass of sulphate contained in the cloud water of one cubic metre of air. The experimental set-up was such that the cloud water sampler collected only the cloud droplets, whereas the filter pack sampled interstitial aerosol particles and cloud droplets at moderate wind speeds (< 10 m s^{-1}). Ideally, the cloud mass concentration of a species should therefore not exceed the aerosol mass concentration. The difference between both on 21.10.93 represents the uncertainty of the method. The two events exhibit a few main features that were generally valid for all events. 1. The mass concentrations in all three phases can increase during the event due to convection and entrainment. 2. Only a small amount of the total sulphate mass was associated with the snow. 3. This amount can vary significantly during one snowfall event.

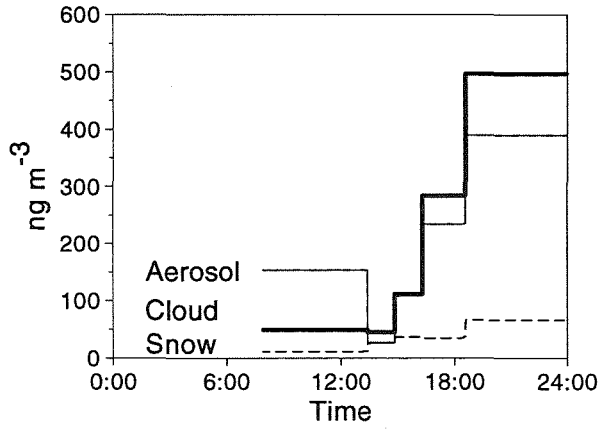

Figure 3a. Sulphate mass concentrations in the three phases aerosol, cloud water, and snow during the snowfall event on 21.10.1993.

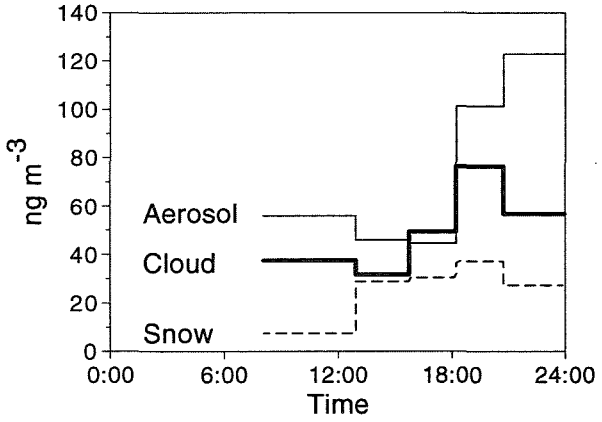

Figure 3b. Same as Figure 2a, but for the snowfall event on 11.11.93.

The chemical mass balances were calculated for the various chemical species. Table 2 gives the mass fractions of the species in the ice phase. The values are time weighted averages for the individual snowfall events. Additionally, time weighted means over all events are presented. The values are expressed as percentage of the total mass in one cubic metre of air which is the sum of the mass concentrations of the species in the aerosol, cloud, and ice phase. The mass balance calculations revealed that overall scavenging showed large variations from event to event and from species to species. In spite of these variations, the overall mass transfer from aerosol to snow was rather low with highest values of about 50% for nitrate. This seems to be caused by gas phase scavenging of nitric acid in addition to the scavenging of aerosol nitrate. The mass transfers for sulphate, sodium, ammonium, and magnesium were rather similar pointing at a common, dominant scavenging mechanism which could be riming. It is also obvious that the 13.11. and

14.11. snowfalls were generally more efficient in scavenging for most chemical components than the other events. These two events were characterised by high ice water contents (Table 1). In conclusion, the overall snow scavenging efficiency was rather low at the high alpine site Jungfraujoch and most of the aerosol-borne chemical mass remained in this phase after the precipitation event.

Table 2. Mass fractions of various species in the ice phase (%) calculated as time weighted averages of the individual snowfall events and as time weighted mean over all eight events.

Event	Cl^-	NO_3^-	SO_4^{2-}	Na^+	NH_4^+	Mg^{2+}
21 Oct.	18	61	15	29	19	34
31 Oct.	7	22	21	17	23	15
05 Nov.	12	46	58	29	45	13
06 Nov.	23	52	29	57	65	29
10 Nov.	6	27	38	13	47	40
11 Nov.	8	39	22	31	37	34
13 Nov.	19	73	72	32	75	63
14 Nov.	35	71	57	53	60	54
Mean	15	49	32	32	40	35

4. ACKNOWLEDGMENTS

This work was performed within the framework of the EUROTRAC subproject ALPTRAC and was supported by the Swiss Bundesamt für Bildung und Wissenschaft (BBW) and the Swiss National Science Foundation. The support of the staff and the facilities at the Jungfraujoch research station is highly appreciated.

5. REFERENCES

Barrie L.A., 1985: Atmospheric particles: their physical and chemical characteristics, and deposition processes relevant to the chemical composition of glaciers. *Annals of Glaciology*, **7**, 100-108.

Borys R.D., E.E Hindman and P.J. DeMott, 1988: The chemical fractionation of atmospheric aerosols as a result of snow crystal formation and growth. *J. Atmos. Chem.*, **7**, 213-239.

Gerber, H., 1984: Liquid water content of fogs and hazes from visible light scattering. *J. Climate Appl. Meteor.*, 23, 1247-1252.

Kruisz C., A. Berner and B. Brandner, 1993: A cloud water sampler for high wind speeds. In *Photo-oxidants: Precursors and Products.* Proc. EUROTRAC Symposium '92, Garmisch-Partenkirchen, 23-27 March, 1992 (edited by Borrell P.M., Borrell P., Cvitas T. and Seiler W.), pp. 523-525, SPB Academic Publishing, Den Haag.

Möller D., 1995: Cloud processes in the troposhere. In: *Ice Core Studies of Global Biogeochemical Cycles*, R.D. Delmas (ed.), Springer, Heidelberg, pp.39-63.

Poulida, O. M. Schwikowski, U. Baltensperger, J. Staehelin, and W. Henrich, 1994: Physical processes affecting the chemical composition of precipitation at the high alpine site Jungfraujoch, Switzerland. *Proc. EUROTRAC Symposium '94*, P.M. Borrell, P. Borrell, T. Cvitas, W. Seiler (eds.), SPB Academic Publishing bv, Den Haag, pp. 1225-1230.

Pruppacher H.R. and J.D. Klett, 1980: *Microphysics of Clouds and Precipitation*, D. Reidel, Dordrecht.

Schwikowski, M,. P. Seibert, U. Baltensperger, and H.W. Gäggeler, 1995: A study of an outstanding Saharan dust event at the high-alpine site Jungfraujoch, Switzerland. *Atmos. Environ.*, **29**, 1829-1842.

TRANSPORTS OF CHEMICAL CONSTITUENTS BY A FIELD OF TRADE-WIND CUMULI

Bruce Albrecht[1] and Terry Faber[2]

[1]MPO/RSMAS, University of Miami, Miami, FL 33149 USA
[2]Meteorology Dept., Penn State, University Park, PA 16802 USA

1. INTRODUCTION

Clouds can have a substantial impact on the vertical distribution of chemical constituents in the marine boundary layer. This is due to at least two possible mechanisms: 1) the vertical redistribution of chemical species by clouds and 2) the chemical processing of some species in the cloud. In this paper we address the issue of cumulus transports of chemical constituents in the trade wind boundary layer and develop a framework for including chemical processing within the parameterized cumulus cloud elements. Although we apply this model to ozone, other constituents could be treated in a similar manner.

The thermodynamic structure of the trade wind boundary layer can be represented as four distinct layers: 1) the subcloud layer, which is normally well mixed, 2) the cloud layer where water vapor mixing ratio decreases with height and potential temperature (or dry static energy) increases with height, 3) a weak inversion (the transition layer) that separates the subcloud and the cloud layer and regulates the convective transports from the subcloud into the cloud layer, and 4) an inversion (the trade inversion) that caps the cloud layer. Thus the application of simple mixed layer models to simulate chemical constituents in the trade wind boundary layer or interpret surface-based measurements may be inadequate.

In this paper we develop a model for simulating the boundary layer structure of chemical species. To consider the effects of clouds on the distribution, a mass-flux cumulus parameterization scheme is modified to include chemical constituents. This scheme is applied to a layered model of the trade-wind boundary layer (Albrecht et al., 1979; Albrecht, 1984; Albrecht, 1993; Bretherton, 1993). In this study we test the simulations using observations made during the Atlantic Stratocumulus Transition Experiment (ASTEX; Albrecht et. al., 1995).

2. THE MODEL

The layered model used in this study assumes conserved quantities in the subcloud layer are well mixed. In the cloud layer these quantities are assumed to have a linear variation with height. Thus the ozone concentration in the mixed layer is represented as $[O_3]_M$ and in the cloud layer it is represented as $[O_3]_A + \gamma_{O3}(\hat{p} - \hat{p}_A)$ where the subscript A represents an average over the layer, γ_{O3} is the slope of the ozone in the layer. The vertical coordinate $\hat{p}$ is defined as p_o-p where p_o is the surface pressure.

Ozone budgets for the layer are used to develop predictive equations for this simplified ozone representation following the approach described in Albrecht et. al. (1979). This gives

$$\frac{d[O_3]_M}{dt} = -\frac{g}{\hat{p}_B}\left[(F_{O3})_{B-} - (F_{O3})_0\right] - J[O3]_M \qquad (1)$$

$$\frac{d[O_3]_A}{dt} = \gamma_{O3}\frac{d\hat{p}_A}{dt} - \gamma_{O3}\hat{\omega}_A - \frac{g}{\delta\hat{p}}\left[(F_{O3})_{I-} - (F_{O3})_{B+}\right] - J[O_3]_A \qquad (2)$$

$$\frac{d\gamma_{O3}}{dt} = D\gamma_{O3} - \frac{4g}{\delta\hat{p}^2}\left[(F_{O3})_{I-} - 2(F_{O3})_A + (F_{O3})_{B+}\right] \qquad (3)$$

where J represents the net ozone decay rate $[-(1/[O_3])(d[O_3]/dt)]$, and $(F_{O3})_{B-}$ and $(F_{O3})_0$ are the fluxes of ozone just below the transition layer and at the surface respectively. The fluxes just below the trade inversion are designated by I-, just above the transition layer by B+, and at the midpoint of the cloud layer by A. The quantity $\delta\hat{p} = \hat{p}_I - \hat{p}_B$,

$\hat{\omega}$ is a pressure vertical velocity, and D is the average large-scale divergence in the layer. The time derivatives in (1)-(3) are horizontal total derivatives.

For the simulations described in this paper the ozone decay rate in (1) and (2) is specified as a constant. At the surface the ozone flux is defined as

$$(F_{O3})_0 = \rho V_{dep}(-[O_3]_M) \tag{4}$$

where ρ is density and V_{dep} is the deposition velocity for ozone. The other ozone fluxes needed in (1)-(3) are formulated using the same procedure as used for the other thermodynamic variables represented in the model. The flux at the top of the boundary layer is represented as

$$(F_{O3})_{B-} = -k((\Delta O_3)_B)(F_{sv})_0 / (\Delta s_v)_B \tag{5}$$

where (Δs_v) is the change in virtual dry static energy across the transition layer and k is a closure constant specified to be 0.2.

The ozone fluxes associated with cumulus transports in the cloud layer are represented using a mass flux parameterization to give

$$(F_{O3}) = \omega^*([O_3]_c - [\overline{O_3}])/g. \tag{6}$$

The subscript c refers to the ozone concentration in the parameterized cumulus elements, the overbar indicates area averaged values in the environment and ω^* is the cumulus mass flux. The fluxes given by (6) are formulated by expressing both ω^* and $([O_3]_c - [\overline{O_3}])$ as linear functions of $\hat{p}$ to give

$$F_{O3} = ((F_{O3})_{B+})(1+\mu p')(1+\lambda_{O3} p') \tag{7}$$

where $p' = \hat{p} - p_o$. The flux at cloud base is proportional to the product of the cumulus mass flux at cloud base and $(\Delta O_3)_B$. The factor μ defines a linear decrease in the mass flux and is parameterized as a function of an adjustment time scale τ_A that is specified externally. The coefficient λ_{O3} is obtained by using a lateral entrainment model to estimate in-cloud ozone concentrations with the assumption that the ozone concentration at cloud base is the mixed layer value. This coefficient depends on an entrainment factor E that is specified such that that the average difference between the cloud layer dry static energy, s_{vc}, and environmental virtual dry static energy, $\bar{s}_v$, satisfies the relationship

$$\frac{1}{c_p \delta \hat{p}} \int (s_{vc} - \bar{s}_v) d\hat{p} = b\Delta T_0 \tag{8}$$

where ΔT_0 is the value of the integral on the left with no entrainment and the buoyancy ratio b can vary from 0 to 1. Details of the closure are given in Albrecht et. al. (1984). In this study we consider the sensitivity of the ozone structure predicted with the model to the two critical closure parameters in the cumulus parameterization -- τ_A and b.

3. SIMULATIONS

The model simulations of ozone concentrations were evaluated using data obtained during ASTEX. On two occasions during ASTEX, instrumented aircraft and ships were used in a Lagrangian mode to study the evolution of boundary layer air masses moving downstream over the eastern Atlantic. Observations made during the second Lagrangian 18-20 June 1992 were used in this study to specify external parameters in the model and were made from about 38 °N to 31 °N at 22 °W. The downstream evolution of the boundary layer structure observed during the second Lagrangian is described in detail by Bretherton and Pincus (1995). They used aircraft soundings obtained from the NCAR Electra and the UK C-130 to construct time-height sections of temperature and moisture and use observations from the Electra to construct time-height sections of ozone. In addition, they provide estimates of sea surface temperature and large-scale divergence for the study area. We have supplemented the Bretherton and Pincus (1995) description of the Lagrangian boundary layer evolution using soundings from the R/V Oceanus as it followed the airmass downstream during the second Lagrangian. In addition, we have included additional ozone measurements from the NCAR Electra that were not included in the original analysis by Bretherton and Pincus (1995). Paluch et al. (1995) made a detailed analysis of the ozone budget during the

second Lagrangian. We use their results to specify a ozone deposition velocity of 260 μm s^{-1} and a ozone decay rate of 0.11 day^{-1} for the downstream ozone simulations. Except for the closure parameter sensitivity tests we specify τ_a = 1/3 day and b = 0.5.

The simulations were made by specifying the thermodynamic and ozone profiles above the inversion from the ASTEX observations. Based on the Bretherton and Pincus (1995) analysis we specify the sea surface temperatures to vary from about 18 °C to 21 °C, the surface wind speed to be 6 m s^{-1} and the large-scale divergence to be 3.0 × 10^{-6} s^{-1}. To minimize the effects of initial conditions on the downstream simulations, the model simulation is started 24 hours upstream from the 18 °C sea surface temperature location using initial conditions that give good model agreement with the observations at this point.

The ozone structure and corresponding ozone fluxes from the model are shown in Fig. 1 for various points in the simulations. These simulations show overall agreement with the observed ozone evolution and illustrate the sensitivity of the ozone structure to above-inversion ozone concentrations, which vary substantially during the ASTEX Lagrangian. The ozone fluxes in the cloud layer illustrate how the convective transports can in some cases increase cloud layer ozone while in other cases they result in a decrease. The fluxes above the surface are the principal modulators of simulated variations in the ozone since the flux due to deposition remains constant.

The sensitivity of the simulations to the specification of the closure parameters used in the parameterization are shown in Fig. 2. The specification of these parameters has very little impact on the ozone simulations.

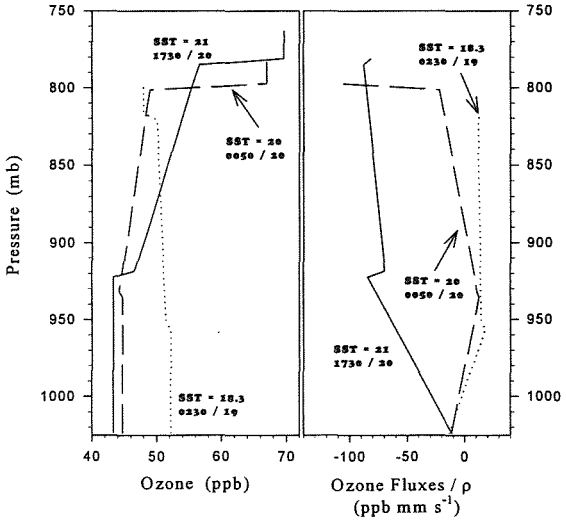

Figure 1. Ozone structure and corresponding ozone fluxes at different times within the downstream simulation.

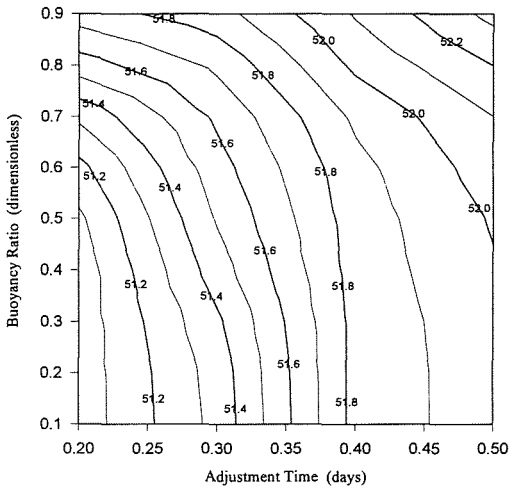

Figure 2. The sensitivity of the ozone concentration in the cloud layer for a wide range of specified adjustment times and buoyancy ratios.

4. CONCLUSIONS

A simple model of the thermodynamic structure of the trade-wind boundary layer was successfully modified to include ozone as a predicted variable. Simulations of the downstream evolution of the ozone structure agree well with observations made during ASTEX. This evolution is very sensitive to the large variations in ozone that are observed above the trade inversion. The simulated structure, however, is very insensitive to the specification of the closure parameters used to close the cumulus parameterization used in the model. The mass flux approach provides a very effective way of

treating chemical transports due to a field of cumuli. Other chemical species could easily be included with minimal modification. Furthermore, although no in-cloud chemical processing is included in the current model, these effects could be easily incorporated into the flux formulations.

5. ACKNOWLEDGMENTS

This work was supported the Office of Naval Research under Grant N00014-91-J-1992.

6. REFERENCES

Albrecht, B. A., A. K. Betts, W. H. Schubert, and S. K. Cox, 1979: A model of the thermodynamic structure of the trade-wind boundary layer. Part I: Theoretical formulation and sensitivity tests. *J. Atmos. Sci.*, **36**, 73-89.

Albrecht, B. A., C. S. Bretherton, D. Johnson, W. H. Schubert, and A. S. Frisch, 1995a: The Atlantic Stratocumulus Transition Experiment - - ASTEX. *Bull. Amer. Meteor. Soc.*, **76**, 889-904.

Albrecht, B. A., 1984: A model study of downstream variations of the thermodynamic structure of the trade winds. *Tellus*, **36A**, 187-202.

Albrecht, B. A., 1993: The effects of drizzle on the thermodynamic structure of the trade wind boundary layer. *J. Geophys. Res.*, **98**, 7327-7337.

Bretherton, C. S., 1993: Understanding Albrecht's model of trade cumulus cloud fields. *J. Atmos. Sci.*, **50**, 2264-2283.

Bretherton, C. S., and R. Pincus, 1995: Cloudiness and marine boundary layer dynamics in the ASTEX Lagrangian experiments. Part I: Synoptic setting and vertical structure. *J. Atmos. Sci.*, **52**, 2707-2723.

Paluch, I. R., S. McKeen, D. H. Lenschow, R. D. Schillawski, and G. L. Kok, 1995: Evolution of the subtropical marine boundary layer: photochemical ozone loss. *J. Atmos. Sci.*, **52**, 2967-2976.

Simulations of Maritime Stratiform Cloud Physico-Chemistry

*J A Lowe[1], S L Clegg[2], M H Smith[1] and C D O'Dowd[1].

[1]Physics Department, UMIST, Manchester, M60 1QD, UK
[2]School of Environmental Sciences, UEA, Norwich, UK

1. INTRODUCTION

Atmospheric aerosol particles, ubiquitous in the lower atmosphere, play an important role in global climate. These particles affect the radiation budget, both directly by scattering incoming solar radiation, and indirectly through their ability to modify cloud microphysics and albedo. Recently, a further important role of aerosol particles has been recognised. Aerosol particles can strongly influence the lifetimes of various trace gas species, such as SO_2 and NH_3, by providing them with a rapid removal mechanism (see, for example, Chameides and Stelson, 1992).

Measurements of maritime aerosol population under a variety of environmental conditions show several major features (Figure 1). The ultra-fine mode is highly transient, compared to the nucleation and accumulation modes in which particles have much longer lifetimes.

Figure 1 - Maritime Aerosol Spectrum

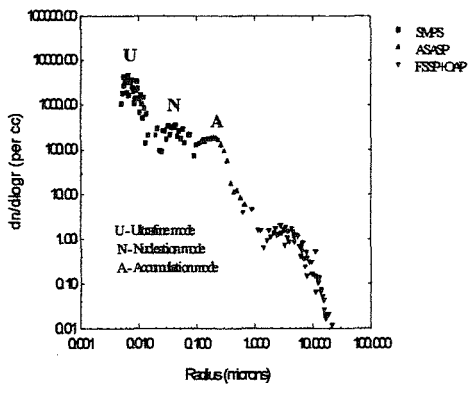

The nucleation mode, centred around 0.03μm radius, is dominated by particles formed by gas-to-particle conversion. The majority of these particles are thought to be composed of nss-sulphate and probably originate in the transient ultra-fine mode. Particles in the nucleation mode are generally too small to be activated in marine stratiform clouds, but may become activated in more vigorous cumulus clouds. Some nucleation mode particles grow to a size at which they can act as CCN in stratiform clouds. This occurs by a combination of growth mechanisms, including the condensation of low volatility vapours; processing in cumulus clouds; and to a much lesser extent, out of cloud chemical processing, and coagulation (Raes, 1992).

The accumulation mode is observed at sizes close to 0.1 μm dry radius. Particles in this mode have the longest residence times and their major removal processes are cloud related. Volatility analysis (O'Dowd and Smith, 1993) and morphological analysis (Meszaros and Vissey,1974) indicate that the majority of maritime accumulation mode particles are usually nss-sulphate based. These particles probably originate as nucleation mode particles which grow to a size where they can be activated in stratiform cloud. The local minimum between the nucleation and accumulation modes corresponds to the smallest size of nss-sulphate aerosol particle capable of being activated at the supersaturations typical of marine stratiform clouds. Once activated, the major growth mechanism for accumulation mode particles in the maritime environment is thought to be heterogeneous SO_4^{2-} production within non-precipitating clouds (for example Hoppel, 1986). The SO_4^{2-} particles are often either wholly or partially neutralised by the basic gas NH_3; the degree of neutralisation is highly dependent on the source of NH_3 within the region.

Other particle types also contribute to accumulation mode number and mass. Significant amounts of elemental carbon and sea-salt particles have both been observed in the accumulation mode (O'Dowd and Smith, 1993), as has organic material (Novakov and Penner, 1993).

At sizes above the accumulation mode, the major aerosol component is sea-spray, produced by the bursting of entrained air bubbles at the ocean-

atmosphere interface. Whilst the number of sea-salt particles at sizes above the accumulation mode may be relatively low, their surface area and mass can be significant. The contribution of sea-salt to the aerosol population is highly dependent upon wind speed (Smith et al, 1993). Some nss-sulphate and NO_3 is often found in the larger sizes, usually internally mixed with the sea-salt aerosol. This internal mixing may result from heterogeneous chemical reactions in sea-salt droplets, acid deposition onto sea-salt droplets, and/or scavenging of small aerosol during cloud cycles by cloud droplets formed upon sea-salt aerosol.

2. PURPOSE OF THIS STUDY

Under certain conditions, aqueous phase chemical reactions are thought to proceed particularly rapidly in cloud and in the least acidic aerosol droplets. This can provide a significant source of aerosol SO_4^{2-} and make soluble gas species, such as SO_2, no longer available for the formation and growth of new, small nss-sulphate aerosol particles.

A sub-section of the aerosol population evolution process has been modelled by linking a detailed chemical model to a Lagrangian representation of the updraught region of a stratiform cloud. The model is capable of dealing with the high ionic strength aqueous solutions found in unactivated aerosol solution droplets and even in some of the activated cloud droplets during part of their life cycle.

Early models of cloud chemical processes treated the physical development of the cloud and its droplet spectra in an oversimplified manner. Indeed, many workers treated the cloud as homogenous and monodisperse. Simple model calculations showed this to be unrealistic, with aqueous phase concentrations varying by several orders of magnitude across the droplet spectra (Twohy et al, 1989). Since then several researchers have tried to model cloud chemical processes with varying degrees of success (for instance, Ayers and Larson, 1990). The majority of such models have featured inadequate treatment of the non-ideal chemical aspects of the cloud droplets and the impact of these effects on the droplet growth law. Here, these techniques have been improved upon by using Pitzer's ion interaction approach to deal with the concentrated solution behaviour (Pitzer,1991).

3. MODEL DESIGN

The physical aspects of the simulation consist of a Lagrangian parcel model with explicit particle microphysics. The microphysical aspect utilises the dynamic growth equation to model the growth of aerosol solution droplets by the condensation of water vapour on to a size resolved spectrum of up to 100 size-resolved droplet classes. Rather than being fixed, the boundaries of these size channels move as the solution droplets grow. The growth law includes curvature and solution effects and is corrected for the breakdown of the continuum approximation close to the droplet surface (Pruppacher and Klett, 1978). Unactivated solution droplets are especially concentrated, with ionic strengths often much greater than unity. Under these conditions, the solution can no longer be treated as ideal. Non-ideal solution effects are taken into account in the calculation of water activity for each of the solution droplets. The water activity is then used to determine the supersaturation of water vapour just above the droplet surface, which in turn, controls the rate of condensational growth of the droplets.

The variations in liquid water content resulting from droplet growth or evaporation are supplied to equations describing the bulk thermodynamic parameters of the air parcel, such as temperature and relative humidity, which are then adjusted to represent the changes taking place during the movement of the air parcel through the boundary layer. The parcel updraught velocity is regulated to ensure it represents values typical of stratiform clouds, that is, of a few tens of centimetres per second.

The aqueous phase chemical aspects of the model comprise three separate elements, an equilibration module, a kinetic reaction module, and the non-ideal behaviour correction module.

The equilibration module is used to calculate the amount of soluble gaseous species dissolved in the aerosol, and, to apportion the aqueous aerosol species between associated and dissociated forms. This is achieved by solving the charge balance equation for each solution droplet. The aqueous activities of species equilibrating with the gas phase are calculated using Henry's law. The relationships between associated and dissociated aqueous species are written using appropriate equilibrium constants. Both the Henry's law and equilibrium constants are corrected for changes in temperature.

The non-ideal solution effects, previously mentioned in the context of droplet condensational growth, also effect aqueous phase chemical equilibria. Actual concentrations of dissolved species are related to their effective concentrations, or activities, appearing in the Henry's law expressions and equilibrium relationships by activity coefficients. The activity coefficients are functions of ionic strength, solution composition, and temperature. As a solution

becomes more concentrated, the activity coefficients deviate from unity, causing the activity to deviate from the concentration. The activity coefficients, and water activity as used by the growth law, are determined using the formulation of Pitzer. This formulation allows activity coefficients to be determined for a wide range of species in high ionic strength solutions and over a range of temperatures. Rather than using a look-up table of activity coefficient values, Pitzer's equations are built into the model (the non-ideal solution correction module) so that activity coefficients can be calculated as and when required.

The small surface to volume ratio of some of the solution droplets means that, at times, mass transport processes may limit the rate at which trace gas species can be scavenged from the gas phase, possibly reducing the rate of SO_4^{2-} production within the solution droplets. This effect is accounted for in a crude manner using the formulation of Schwartz (1981) to provide an upper limit on the amount of material that can be scavenged from the gas phase in a single time step.

The kinetic reaction module determines the rate of heterogeneous SO_4^{2-} production within the aqueous solution droplets. At present, SO_4^{2-} production may occur by the oxidation of SO_2 using dissolved H_2O_2 and/or O_3 as oxidant species. The reaction rates and their temperature dependence are taken from Ayers and Larson (1990) and references contained therein.

Within the model, a distinction is made between solution droplets formed on aerosol particles that contain no sea-salt material and those solution droplets that form on aerosol that were initially sea-salt based.

4. SIMULATIONS

A base case input deck was prepared to initialise the model. The pre-existing aerosol spectra consisted of a single nss-sulphate log-normal aerosol mode, sized at 0.075 μm dry radius with a geometric standard deviation of 1.4. The aerosol mode contained 158 particles cm^{-3}. The aerosol parameters were obtained by fitting a log-normal curve to an aerosol distribution measured during the BMCAPE campaign (Lowe et al, 1996a). Sea-salt aerosol was not included in these runs; the effects of the presence of sea-salt is the subject of a companion paper (Lowe et al, this issue). Gas phase concentrations for the species; SO_2, NH_3, O_3 and H_2O_2, were set at 0.5 ppb, 1.0 ppb, 30 ppb and 1 ppb respectively. The boundary layer structure was well mixed and a stratiform cloud, with updraft 40 cm s^{-1}, formed in the top 400m of the layer.

The base case simulation resulted in the production of 1.8 μg of SO_4^{2-} per kg^3 of air for a single passage through the cloud, a value consistent with observations (see for instance Hobbs, 1993).

The SO_4^{2-} produced per mole of pre-existing SO_4^{2-} and the droplet pH showed a wide variation across the aerosol spectrum as well as with height through the cloud, as illustrated in Figures 2 and 3.

Figure 2 - Efficiency of sulphate production

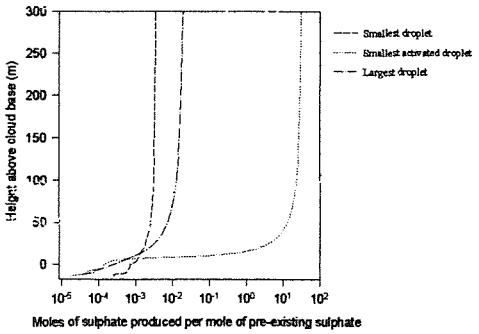

The peak cloud supersaturation was not large enough to activate the smallest aerosol solution droplets. These aqueous solutions were extremely acidic, and thus, did not provide effective sites for the aqueous production of SO_4^{2-} due to the less favourable dissociation of aqueous SO_2, the suppression of the O_3 driven oxidation pathway, and the small volume available for aqueous phase reactions provided by these droplets.

The smallest activated droplets provided the most effective SO_4^{2-} production environment, with the least acidic conditions and large solution volumes. The dry size of these droplets was close to that of the accumulation mode peak in which particles were most numerous. The combination of high SO_4^{2-} forming efficiency and the considerable aqueous volume provided by the large number of these rapidly growing droplets resulted in most SO_4^{2-} being produced in droplets formed upon particles in the accumulation mode peak.

Cloud droplets with the largest reactive volumes were formed upon the largest accumulation mode aerosol particles. However, the chemical conditions within these droplets were less conducive to aqueous SO_4^{2-} production than the faster growing droplets formed on accumulation mode particles.

The O_3 and H_2O_2 were both found to be important oxidants for cloud droplets formed on the SO_4^{2-} based aerosol population. The O_3 pathway was particularly important in the fastest growing droplets.

The partial pressures of SO_2 and oxidants were varied from the base case values, as were the number and mode radius of the aerosol distribution. Whilst the SO_2 concentration remained low compared to the NH_3 concentration, increases in SO_2 produced corresponding increases in SO_4^{2-} production. However, at higher SO_2 concentrations, increases in SO_2 did not produce such large increases in SO_4^{2-} production and a much lower consumption of available SO_2 resulted. This behaviour was a consequence of the less favourable, more acidic, conditions occurring when there was insufficient NH_3 to neutralise the large amounts of SO_4^{2-} produced during periods of high SO_2 concentrations. This resulted in the suppression of the O_3 driven oxidation reaction. The lack of sufficient H_2O_2 also reduced the potential SO_4^{2-} production in cases of high SO_2 concentration, particularly when NH_3 concentrations were low and the pH insensitive H_2O_2 oxidation pathways became particularly important.

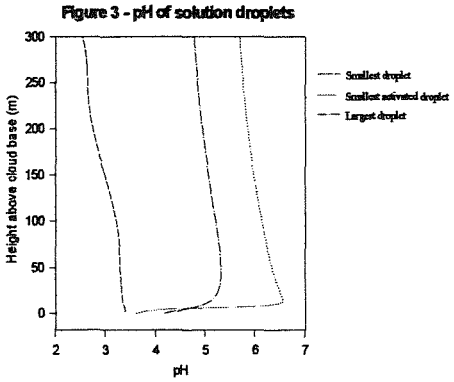

Aqueous SO_4^{2-} production in non-precipitating stratiform clouds provides an effective aerosol growth mechanism for accumulation mode particles. However, the mechanism becomes less effective at increasing aerosol particle size as the dry size of the particles become larger.

5. CONCLUSIONS

These simulations illustrate the rapid sink for SO_2 provided by chemical processing in non-precipitating stratiform clouds. The production of as much SO_4^{2-} as occurred during a single cloud cycle with base case input conditions (1.77 $\mu g\ kg^{-3}$) would take more than 100 hours by homogeneous means, even if favourable illumination conditions prevailed.

The in-cloud SO_4^{2-} production mechanism appears to be limited by a number of factors, namely, the availability of SO_2, the availability of oxidants (particularly H_2O_2), and the chemical behaviour of the evolving droplet spectra. The chemical behaviour of the droplets was found to be highly non-linear across the particle size range.

6. REFERENCES

Ayers G. P. & Larson T. V., 1990: Numerical Study Of Droplet Size Dependent Chemistry In Oceanic, Wintertime Stratus Cloud At Southern Mid-Latitudes. *J Atmos Chem* **11**, 143-167.

Chameides W. L. and Stelson A. C., 1992: Aqueous phase chemical processes in deliquescent sea-salt aerosols: A mechanism that couples the atmospheric cycles of sulphur and sea-salt. *J Geophys Res* **97(D18)**, 20565-20580.

Hobbs P.V., 1993: Aerosol-cloud interactions in Aerosol-cloud-climate interactions. *Academic Press.*

Hoppel W. A. , Frick G. M. and Larson R. E., 1986: Effect Of Nonprecipitating Clouds On The Aerosol Size Distribution In The Marine Boundary Layer. *Geophysical Research Letters* **13**, 125-128.

Lowe J.A., Smith M. H., Davison B. M., Benson S. E., Hill M. K., O'Dowd C. D., Harrison R. M. & Hewitt C. N., 1996a: Physico-chemical properties of atmospheric aerosol at South Uist. *Atmos. Environ.*, submitted

Lowe J. A., Clegg S. L., Smith M. H. and O'Dowd C. D., 1996b: Simulations of maritime stratiform cloud physico-chemistry. *This issue.*

Meszaros A. & Vissey K., 1974: Concentration, Size Distribution And Chemical Nature Of Atmospheric Aerosol Particles In Remote Oceanic Areas. *Aerosol Sci* **5**, 101-109.

Novakov T. & Penner J. E., 1993: Large Contribution Of Organic Aerosols To Cloud-Condensation-Nuclei Concentrations. *Nature* **365**,823-826.

O'Dowd C. D. and Smith M. H., 1993: Physico-chemical properties of aerosols over the northeast Atlantic: Evidence for wind speed related submicron sea-salt aerosol production. *J Geophys Res* **98(D1)**, 1137-1149.

Pitzer K. S., 1991: Ion Interaction Approach: Theory And Data Correlation in activity coefficients in electrolyte solutions, *CRC Press.*

Pruppacher H. R. & Klett J. D., 1978: Microphysics Of Clouds And Precipitation. *D. Reidel* .

Raes F., & Van Dingenen R., 1992: Simulations of condensation and cloud condensation nuclei from biogenic SO_2 in the remote MBL. *J Geophys Res.*, **97**, 12901-12912.

Schwartz S. E. & Freiberg J. E., 1981: Mass-transport limitation to the rate of reaction of gases in liquid droplets. Atmos Env 15, 1129-1144

Smith M. H., Park P. M. and Consterdine I. E., 1993: Marine aerosol concentration and estimated fluxes over the sea. *Q J R Met Soc* **119**, 809-824.

Twohy C. H. , Austin P. H. & Charlson R. J., 1989: Chemical Consequences Of The Initial Growth Of Cloud Droplets: A Clean Marine Case. *Tellus* **41B**,51-60.

CHEMICAL HETEROGENEITY AMONG CLOUD DROP POPULATIONS AND ITS EFFECTS ON SULFUR OXIDATION

J. Collett, Jr., X. Rao and A. Bator

Atmospheric Science Dept., Colorado State University, Ft. Collins, CO 80523 USA

1. INTRODUCTION

Traditional studies of cloud chemistry typically assumed clouds are comprised of a chemically homogeneous distribution of drops. Recent cloud models, however, predict substantial variations in cloud drop composition across the drop size spectrum. Such heterogeneity might be supposed simply on the basis of the chemically heterogeneous nature of the aerosol particles which serve as cloud condensation nuclei (CCN). Even for a chemically uniform aerosol composition, differences in growth rates between cloud drops nucleated on small and large CCN will yield a gradient in solute concentration across the drop size spectrum (Ogren and Charlson, 1992).

Early attempts to measure the size-dependence of cloud drop composition have revealed significant variations. Several studies have demonstrated total nonvolatile drop solute concentration varies with drop size (see e.g., Ogren et al., 1989). Other work has shown concentrations of individual ions and drop pH vary with drop size (Munger et al., 1989; Carter and Borys, 1993; Collett et al., 1993, 1994, 1995; Millet et al., 1995).

Variations in chemical composition across the cloud drop size spectrum can influence rates of aqueous phase sulfate production. While oxidation of S(IV) via hydrogen peroxide is essentially independent of pH in atmospheric water droplets, oxidation by ozone and by oxygen (catalyzed by Fe(III) and Mn(II)) is not. Differences in acidity between individual cloud drops can produce large differences in the amount of sulfur dioxide absorbed and oxidized by different drops. Due to the nature of the sulfur oxidation rate equations, chemical heterogeneity among cloud drop populations can enhance sulfate production relative to rates predicted from the average cloudwater composition (Collett et al., 1994). The modeling study of Hegg and Larson (1990) illustrates that S(IV) oxidation rates in clean environments might be underpredicted by a factor of 30 if the dependence of drop chemistry on drop size is ignored. The situation can be further complicated by variations in trace metal catalyst concentrations with drop size and by nonuniform formation of oxidation-resistant S(IV)-aldehyde complexes across the drop size spectrum.

2. EXPERIMENTAL

Ground-based cloud and fog sampling was conducted at several sites across the United States. Coastal sites in central and southern California and northern Oregon, mountain sites in North Carolina, New York, and Colorado, and valley sites in California were among the locations where measurements were made (see Fig. 1). The study included a number of cloud types (e.g., coastal stratus clouds, frontal/orographic clouds, and radiation fogs) and the sampled clouds and fogs possessed a wide range of pollutant loadings.

Figure 1. Cloud and fog sampling sites.

Cloud collectors used in the study included a two-stage ETH cloud impactor (Collett et al., 1993, 1995), a Caltech Active Strand Cloudwater Collector 2 (CASCC2) (Demoz et al., 1996), a Caltech Active Strand Cloudwater Collector (CASCC) with a size-fractionating inlet (Munger et al., 1989; Demoz et al., 1996), and a three-stage IESL cloud impactor (Collett et al., 1995). All but the CASCC2 are capable of simultaneous collection of two or more independent portions of the cloud drop size spectrum for chemical analysis.

3. RESULTS AND DISCUSSION

Significant differences in the chemical compositions of large and small cloud drop size fractions have been observed in all environments studied. These differences were observed using all of the size-fractionating cloud samplers. As expected, the compositions of the bulk samples collected by the CASCC2 tend to fall between the compositions of small and large drop fractions. Differences in acidity between small and large cloud drops were commonly observed at all locations and across a pH range from two to seven (see Figure 2). Smaller drops were typically, but not always, more acidic (up to two pH units) than large drops.

Species found in smaller aerosol particles formed from gas-to-particle conversion processes (nitrate, sulfate, and ammonium) tend to be enriched in the small drop fractions, while large cloud drops tend to be enriched in species found primarily in large, mechanically generated aerosol particles, including those derived from sea salt and soil dust (Bator and Collett, 1996). The preservation of the size-dependent chemical nature of atmospheric aerosols in the cloud drop population which forms on the aerosol is not entirely surprising, although some have speculated that this chemical signature would be lost in real clouds due to the complex combination of physical and chemical processes affecting cloud drops.

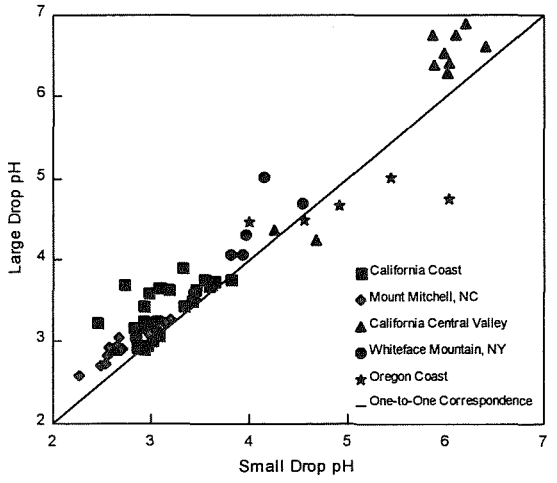

Figure 2. Large vs. small drop fraction acidities. The separation between small and large drops is made at 10 μm in the ETH impactor and at 23 μm in the size-fractionating CASCC.

Variations in drop acidity across the drop size spectrum suggest that predictions of the rate of aqueous phase sulfur oxidation by ozone are inaccurate in many instances (Collett et al., 1994). Due to the non-linear dependence of the ozone pathway's oxidation rate on acidity, use of the average cloud composition can lead to significant underprediction of the sulfate production rate. The extent of the underprediction increases as the pH difference increases between the two drop compositions.

Figure 3 depicts the calculated enhancement in sulfur oxidation by ozone, resulting from chemical heterogeneity within the cloud, for 105 cloudwater samples from numerous locations. The data is presented as a frequency distribution of samples with various ranges of oxidation rate enhancement. The average rate of sulfur oxidation in a cloud with two distinct drop compositions was divided by the rate of oxidation predicted using the average cloud drop composition to obtain the enhancement factor for each pair of large and small cloud drop fractions. Approximately one quarter of the samples considered were calculated to experience oxidation rate enhancements between 30% and 100%. Clouds with calculated sulfur oxidation enhancement exceeding 50% were sampled at nearly every location and covered a pH range nearly as wide as present in the entire data set.

Underprediction of sulfur oxidation rates resulting from use of average cloud acidity occurs for the trace metal catalyzed pathways as well. At times, the underprediction of oxidation rates for these pathways is made more severe by covariance of pH and catalyst concentrations.

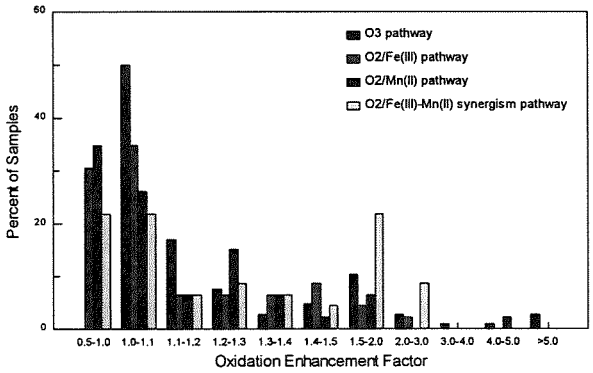

Figure 3. Calculated enhancement of sulfur oxidation for different chemical pathways due to the presence of chemical heterogeneity within the cloud. The data is presented as a frequency distribution of samples with various ranges of oxidation rate enhancement. The average rate of sulfur oxidation in a cloud with two distinct drop compositions is divided by the rate of oxidation predicted using the average cloud drop composition to obtain the enhancement factors. The rate in a cloud with two distinct drop compositions is calculated as a liquid water content weighted average of the rates associated with the two drop compositions. For purposes of these calculations, the fraction of total Fe assumed to exist as soluble Fe(III) was taken as 25% for all samples. Rate expressions from Hoffmann and Calvert (1985) for the ozone pathway and Ibusuki and Takeuchi (1987) for the metal catalyzed pathways were used in the calculations.

At some sites, we have observed iron enrichment in large cloud drops; at other locations, iron is enriched in small cloud drops (see Fig. 4). When higher than average iron

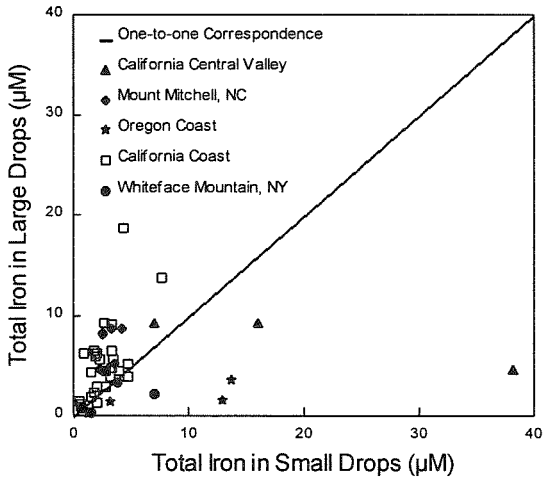

Figure 4. Iron concentrations measured in large and small cloud drop fractions. Two California Central Valley samples had small drop iron concentrations exceeding the range plotted here.

concentrations are found in drops with higher than average pH values, enhancement of the iron-catalyzed autooxidation of sulfur dioxide can exceed the enhancement calculated for the ozone pathway. When above average iron concentrations are found in drops with below average pH, iron-catalyzed autooxidation of sulfur dioxide is suppressed relative to the rate predicted from the average cloud drop composition.

Enhancement factors for the Fe-catalyzed autooxidation of S(IV) are depicted in Figure 3 for 46 sample pairs where pH and total iron concentrations are available for the large and small drop fractions. Note that negatively correlated pH and iron concentrations result in suppression of the S(IV) oxidation rate in approximately 30% of the samples, while positively correlated values of these two parameters result in enhancements of 30-100% in approximately 20% of the samples.

Differences in Mn concentrations were also observed commonly between large and small drops. As observed for Fe, Mn was sometimes enriched in large drops and at other times enriched in small drops. Calculations of the effect of different pH and Mn concentrations in large and small drops on Mn-catalyzed S(IV) oxidation are also included in Figure 3. The results are roughly similar to those observed for Fe: a mix of samples with suppression and enhancement of the oxidation rate relative to the rate expected from the average drop composition.

It is known that Fe and Mn catalysis of S(IV) oxidation exert a synergistic effect: the net oxidation rate in the presence of both catalysts is greater than can be explained from the sum of the individually catalyzed rates. Ibusuki and Takeuchi (1987) have demonstrated that the synergism can be rather large (factors of two to fifteen) for environmentally relevant conditions.

We evaluated the effect of the nonuniform cloud drop composition on the net rate of S(IV) oxidation as catalyzed by the presence of both Fe and Mn. As might be expected, oxidation rate enhancement was larger for this case than for the individual trace metal-catalyzed pathways. Approximately 30% of the samples were

calculated to experience oxidation rate enhancements of 50% or more for this pathway due to the presence of chemically distinct small and large droplet populations.

We have also observed formation of hydroxymethanesulfonic acid (HMS, a complex between S(IV) and formaldehyde), to differ between large and small cloud drops. HMS formation is relevant to understanding sulfate production in clouds and fogs because of its ability to compete with oxidation of S(IV) and to create a S(IV) reservoir in the drops that is relatively stable toward oxidation. The effect of S(IV)-aldehyde complex formation on sulfur oxidation is likely to be greatest in relatively large, high pH drops drops (Rao and Collett, 1995) where complex formation is relatively fast and mass transport of sulfur dioxide into the drop can limit the amount of S(IV) available for reaction.

4. CONCLUSIONS

Chemical heterogeneity among cloud drop populations can significantly enhance S(IV) oxidation by ozone and trace metal-catalyzed S(IV) autooxidation relative to rates predicted from the average droplet composition. The results presented here probably represent lower limits to the magnitude of the actual effect since we have considered the compositions of only two droplet size classes.

Further work is planned to examine the effect of the observed chemical heterogeneity on the total S(IV) oxidation rate in the sampled clouds and fogs. Effects are likely to be greatest at high pH and/or in the absence of significant hydrogen peroxide.

5. ACKNOWLEDGEMENTS

This material is based upon work supported by the Department of the Navy, Office of the Chief of Naval Research, the Midwestern Regional Center of the National Institute for Global Environmental Change, and the National Science Foundation (ATM-9509596). We are grateful to those individuals and organizations who provided access to sampling sites.

6. REFERENCES

Bator, A. and J. L. Collett, Jr., 1996: Cloud chemistry varies with drop size. *J. Geophys. Res.*, submitted.

Carter E. J. and R. D. Borys, 1993: Aerosol-cloud chemical fractionation: enrichment factor analysis of cloud water. *J. Atmos. Chem.*, **17**, 277-292.

Collett, Jr., J., B. Oberholzer, and J. Staehelin, 1993: Cloud chemistry at Mt. Rigi, Switzerland: dependence on drop size and relationship to precipitation chemistry. *Atmos. Environ.*, **27A**, 33-42.

Collett, Jr., J. L., A. Bator, X. Rao, and B. Demoz, 1994: Acidity variations across the cloud drop size spectrum and their influence on rates of atmospheric sulfate production. *Geophys. Res. Lett.*, **21**, 2393-2396.

Collett, Jr., J., R. Iovinelli, and B. Demoz, 1995: A three-stage cloud impactor for size-resolved measurements of cloud drop chemistry. *Atmos. Environ.*, **29**, 1145-1154.

Demoz, B., J. L. Collett, Jr., and B. C. Daube, Jr., 1996: On the Caltech Active Strand Cloudwater Collectors. *Atmos. Res.*, in press.

Hegg, D.A. and T. V. Larson, 1990: The effects of microphysical parameterization on model predictions of sulfate production in clouds. *Tellus*, **42B**, 272-284.

Hoffmann, M. R. and J. G. Calvert, 1985: *Chemical transformation modules for Eulerian acid deposition models. Volume II. The aqueous-phase chemistry.* National Center for Atmospheric Research, Boulder, Colorado.

Ibusuki, T. and K. Takeuchi, 1987: Sulfur dioxide oxidation by oxygen catalyzed by mixtures of manganese (II) and iron (III) in aqueous solutions at environmental reaction conditions. *Atmos. Environ.*, **21**, 1555-1560.

Millet, M., H. Wortham, and P. Mirabel, 1995: Solubility of polyvalent cations in fogwater at an urban site in Strasbourg (France). *Atmos. Environ.*, **29**, 2625-2631.

Munger, J.W., J. Collett, Jr., B. Daube, Jr. and M. R. Hoffmann, 1989: Chemical composition of coastal stratus clouds: dependence on droplet size and distance from the coast. *Atmos. Environ.*, **23**, 2305-2320.

Ogren, J.A. and R. J. Charlson, 1992: Implications for models and measurements of chemical inhomogeneities among cloud droplets. *Tellus*, **44B**, 208-225.

Ogren, J. A., J. Heintzenberg, A. Zuber, K. J. Noone, and R. J. Charlson, 1989: Measurements of the size-dependence of solute concentrations in cloud droplets. *Tellus*, **41B**, 24-31.

Rao, X. and J. L. Collett, Jr., 1995: The behavior of S(IV) and formaldehyde in a chemically heterogeneous cloud. *Environ. Sci. Technol.*, **29**, 1023-1031.

COMPARISON AND ANALYSIS OF THE CHEMICAL CHARACTERISTICS OF PRECIPITATION IN CHINA, JAPAN AND USA

Huang Meiyuan, Cheng Xinjin and Wang Zifa

Institute of Atmospheric Physics, Chinese Academy of Sciences, Beijing, China

1. INTRODUCTION

Acid rain is a very important regional environment phenomenon, its formation and spread is influenced by the distribution of pollution sources, geographical environment and meteorological conditions. In this paper, we focus on the different chemical characteristics of precipitation in China, Japan and USA.

World wide large-scale monitoring of precipitation chemistry began in the beginning of 1980's. From then on, most of the acid rain countries/regions have set up national/regional monitoring stations network of precipitation chemistry and accumulated a lot of valuable data. The data we use in this paper comes from Ref.[1-8] respectively.

2. AVERAGE VALUES OF CHEMICAL COMPOSITIONS OF PRECIPITATION IN CHINA, JAPAN AND USA

Table 1 provides the average chemical composition of precipitation $\bar{X}$ and its variation coefficient (variance /average value, $\zeta=s/\bar{X}$) in China, Japan and USA. From Table 1, it is shown that rain in the three countries is all acidic and the most acidic is in USA. Variation coefficient in China is the greatest (0.17). The differences of rain PH value in various places of China are very great. The rain is not acidic in northern China, such as Dalian where rain PH value is as large as 7.13, but PH value is very low in some regions of southern China, such as Chongqing where rain PH value is 4.21. This indicates that other than the emission of pollution gases, territorial, topographical and meteorological conditions have exerted great effects on the rain acidity. The lowest variation coefficient in Japan may be related to its smallest area.

From Table 1 it can also be found that the concentrations of three kinds of ions SO_4^{2-}, NH_4^+ and Ca^{2+} in China are especially high and about 3-6 and 6-25 times as high as those in Japan and USA respectively. It shows serious pollution of SO_2, NH_3 and soil particle in China. The concertinos of Cl^- and Na^+ are especially high in Japan and about 12/2 times high than that in USA and China respectively. This shows that chemical compositions of precipitation in Japan are affected greatly by sea salt. the total concentration in USA is much lower than that in China and Japan. It may be concluded that the air condition in USA is less pollutant.

Table 1. Average values of chemical compositions of precipitation in China, Japan and USA(μeq/L)

	PH	H^+	SO_4^{2-}	NO_3^-	Cl^-	NH_4^+	Ca^{2+}	Mg^{2+}	K^+	Na^+	Σ(-)	Σ(+)	Σ(-)+Σ(+)
CHINA X	4.83	14.8	166.7	23.9	46.4	100.7	155.4	36.1	22.7	32.6	237.1	362.5	599.5
ζ	0.17		0.66	0.67	1.00	0.43	0.93	0.85	1.51	0.81	0.56	0.65	
JAPAN X	4.69	20.4	48.7	15.7	86.4	19.9	24.7	19.3	3.7	68.1	150.7	156.1	306.8
ζ	0.06		0.25	0.45	0.99	0.32	0.88	0.84	0.76	0.93	0.62	0.54	
USA X	4.57	26.8	29.7	16.6	7.1	13.8	6.5	2.3	0.8	5.9	53.4	16.1	109.5
ζ	0.13		0.66	0.51	0.86	0.62	0.76	0.42	0.62	0.84	0.50	0.49	
Japan/USA		0.76	1.64	0.94	12.17	1.44	3.80	8.39	4.63	11.54	2.82	2.78	2.80
Japan/China		1.38	0.29	0.66	1.86	0.20	0.16	0.53	0.16	2.09	0.64	0.43	0.51
USA/China		1.81	0.18	0.69	0.15	0.14	0.04	0.06	0.04	0.18	0.22	0.15	0.18

3. CHEMICAL CHARACTERISTICS OF PRECIPITATION IN CHINA, JAPAN AND USA

Table 2 shows the typical chemical characteristics of precipitation in China, Japan ans USA. In China, the rate of SO_4^{2-} devided by total anion is much larger than that in Japan and USA. It is related to the combustion of coal. In China coal is widely used as a primary fuel for electricity generation, home heating and cooking. In other hand, the rate of NO_3^- and total anion in American is the largest in these three countries. A reasonable explation is that America has the greatest density of motor vehicles. In China some large cities such as Beijing and Shanghai share more and more similar rate of $NO_3^-/\Sigma(-)$ with the development of motor vehicles. In Japan the rate of $Cl^-/\Sigma(-)$ is the largest because Japan has the longest seashine line comapred to its area.

Table 2. Chemical Characteristics of Precipitation in China, Japan and USA

	PH	$\frac{Cl^-}{\Sigma(-)}$	$\frac{SO_4^{2-}}{\Sigma(-)}$	$\frac{NO_3^-}{\Sigma(-)}$	$\frac{NO_3^-}{SO_4^{2-}}$	$\frac{Ca^{2+}}{\Sigma(+)}$	$\frac{Na^+}{\Sigma(+)}$	$\frac{NH_4^+}{\Sigma(+)}$	$\frac{H^+}{\Sigma(+)}$	$\frac{Ca^{2+}}{NH_4^+}$
China	3.9~7.1	20%	70%	10%	0.14	43%	9%	28%	4%	1.54
Japan	4.5~5.1	57%	32%	11%	0.32	16%	44%	13%	13%	1.17
USA	4.2~5.6	13%	56%	31%	0.56	12%	11%	25%	48%	0.47

The rate of $Ca^{2+}/\Sigma(+)$ in China is much larger than that in Japan and USA. Three reasons follow: Calcareous soils (especially in the north), extensive use of calcareous building materials, lack particulate emission controls for the small and medium-sized furnaces. This is also the main reason for the high PH value of North China because Ca^{2+} will neutralize some of the precipitation acidity caused by H_2SO_4 and HNO_3 from fossil fuel combustion. We have a similar explanation for the high rate of $Na^+/\Sigma(+)$ to that of high rate of $Cl^-/\Sigma(-)$ in Japan. The value of Ca^{2+}/NH_4^+ maybe indicate the transparency of the air.

4. CONCLUSION

The chemical characteristics of precipitation is different in China, Japan and USA. Nowdays the average acidity of precipitation in China is not high, but in some southern regions acidification of precipitation is serious. Coal combustion as the preliminary fuel and high Ca^{2+} content in the soil of north China decide on the characteristics of precipitation of China. This is why the concentration of total ions is much larger than that of Japan and USA. Precipitation in America is most acidic with a comparative high NO_3^-, although the total ionic concentration is the lowest. In Japan, the differences of precipitation chemistry are not large from places to places. Sea salt and sulfur pollutant take an important part in the chemical characteristics of precipitation.

REFERENCES

[1] Huang Meiyuan et al,1993: Comparison and analysis of chemical characteristics of precipitation in China and Japan, *Chinese Journal of Atmospheric Sciences*, 17(1),21-34.

[2] Wang Ruibing et al, 1989: Studies on some characteristics of chemical components in precipitation in the south and north parts of China, *Collected Works on Acid Rain*, Chinese Publishing House Environmental Science, 227-240.

[3] Li Hongzhen, 1989: Studies on region of acid rain in China, *Collected Works on Acid Rain*, Chinese Publishing House Environmental Science, 208-216.

[4] Chen Panjing et al,1989: Present state and development trend of acid rain in Sichuan Province, *Collected Works on Acid Rain*, Chinese Publishing House Environmental Science, 250-264.

[5] Quan Wenzhe et al, 1989: Studies on present state of acid rain in area of Guangzhou, *Collected Works on Acid Rain*, Chinese Publishing House Environmental Science, 265-275.

[6] Cheng Chunming et al, 1989: Studies on chemical background value of precipitation in atmosphere in China, *Collected Works on Acid Rain*, Chinese Publishing House Environmental Science, 217-226.

[7] Result Report of National Investigation of Acid Precipitation in 1991, National Common Disaster Association of Japan (1993).

[8] NADP/NTN Annual Data Summary: Precipitation Chemistry in the United States 1990, Natural Resource Ecology Laboratory, Colorado State University.

[9] Environmental Agency of Japan, 1989: The result of the First Investigation of Acid Rain in Japan. Publishing data of Environmental Aegncy.

[10] Galloway, J.N. et al., 1987: Acid rain: China, United State and a remote area. Science, 26, 1559-1562.

SIZE-DEPENDENT STRATOSPHERIC DROPLET COMPOSITION IN MESOSCALE TEMPERATURE FLUCTUATIONS

Thomas Peter and Stefanie Meilinger

Max-Planck-Institut für Chemie, Mainz, Germany

1. INTRODUCTION

Under typical stratospheric conditions the stratospheric aerosol is known to consist of small ($r \simeq 0.1\,\mu$m) H_2SO_4/H_2O droplets with 60–80 wt% H_2SO_4. At very low temperatures ($T \leq 195$ K) HNO_3 dissolves in the droplets and, in combination with water uptake, leads to a massive volume growth of the aerosol [e.g. Carslaw *et al.*, 1994]. The freezing probability of these HNO_3-rich droplets is low, despite the strong supercooling with respect to several solid phases [Koop *et al.*, 1995]. Finally, when temperatures approach the frost point, the droplets form a liquid polar stratospheric cloud (PSC of type 1b).

Previous models of the stratospheric aerosol have assumed the HNO_3 and H_2O concentrations in the droplets to be always in equilibrium with the ambient gas phase. Recently, Meilinger *et al.* [1995] showed that temperature fluctuations characteristic for the stratosphere in orographically perturbed regions drive the aerosol particles away from their equilibrium state. In the following we also investigate cases with more extreme temperature histories, like synoptic cooling with a cooling rate of less than 0.7 K/h and gravity-wave-induced fluctuations of low amplitude with cooling rates of more than 8 K/h.

2. OROGRAPHICALLY-INDUCED EVENT

We briefly outline some of the results presented by Meilinger *et al.* [1995]. The development of an ensemble of lognormally distributed ternary $HNO_3/H_2SO_4/H_2O$ droplets is simulated with a Lagrangian trajectory box model. The lognormal distribution of droplet radii is represented by 26 size bins (denoted by B0-B25), see Fig.1. In all simulations we assume an amount of H_2SO_4 (involatile at these temperatures) typical for the background stratosphere. The growth and evaporation can be calculated from the time-independent diffusion equation in the gas phase [Pruppacher and Klett, 1978]. The solution is of the basic form

$$\frac{dc_l}{dt} = \frac{3D_g^\star}{a^2} \cdot \frac{p^\infty - Kp^{vap}}{RT}, \qquad (1)$$

where c_l is the liquid concentration (HNO_3 or H_2O) and a is the droplet radius. The partial pressure is denoted by p^∞ and the vapour pressures p^{vap} have been calculated according to Luo *et al.* [1995]. The effective diffusion constant $D_g^\star$ includes kinetic surface effects [Pruppacher and Klett, 1978], and the Kelvin term is calculated from $K = \exp(2\sigma v/RTa)$, where σ is the liquid/gas surface energy (assumed to be 90 erg/cm^2) and v is the partial molar volume. For the smallest droplets K reaches a value of 1.5 for HNO_3, which is sufficient to suppress their growth if either the cooling is too slow or if the temperature amplitude is not high enough.

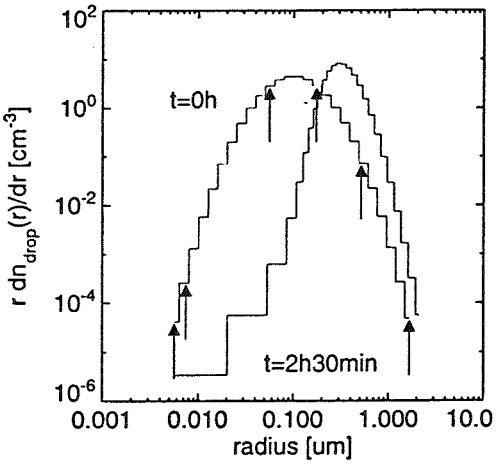

Figure 1: Radial distribution of ternary liquid particles moving through the temperature trough shown in Fig.2. Histograms show the 26-bin size distribution initially and after 2.5 hours. Arrows on the initial distribution mark the six bins (B0, B1, B10, B15, B20, B25) whose time evolution is shown in (c-e). The initial aerosol distribution is assumed to be lognormal at 230 K with a total particle number density $N = 10$ cm^{-3}, median radius $\bar{r} = 0.08\,\mu$m and width $\sigma = 1.8$ (typical of non-volcanic conditions).

Figure 2 shows the evolution of six of the 26 droplets (B0, B1, B10, B15, B20, B25 marked by arrows in Fig. 1) as the air first cools adiabatically along a smooth temperature ramp from 196 to 190 K

during one hour, remains constant for one hour, then increases again (Fig.2a). On the synoptic scale this temperature change corresponds to a very strong perturbation, but in a lee wave region this is still a rather mild cooling event. The development of the HNO_3 vapour pressures (solid lines) for bins B1 and B25 and the HNO_3 partial pressure (dotted line) are shown in Fig.2c. The small droplets (B1) quickly readjust their vapour pressure to partial pressure changes, but the large droplets (B25) are not able to maintain equilibrium. The limited rate of HNO_3 uptake by the large droplets during cooling means that wt%(HNO_3) rises very slowly, with a relaxation time of several hours. On the other hand, the small droplets (B1) reach 45 wt% HNO_3 and 55 wt% H_2O, with sulfuric acid concentrations well below 0.01 wt% (B1 in Fig.2d). Nitric acid concentrations reach even higher values upon subsequent warming: at 2.45 h the small droplets (B1) reach 51 wt% when H_2SO_4 is still below 0.1 wt%. Note that the particles in the smallest bin (B0) show less extreme behaviour due to the Kelvin effect, which is also apparent in the particle distribution function after 2.5 hours (Fig.2a). Finally, Fig.2b shows the development of the droplet radii: the radius of the small droplets (B1) grows by more than a factor of 20 and their

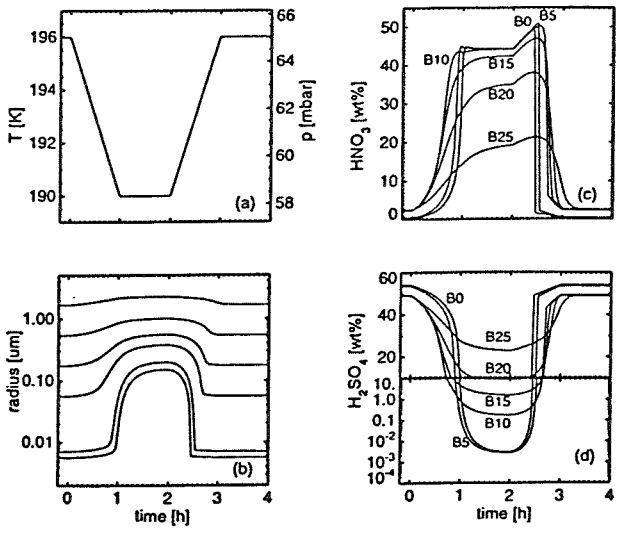

Figure 2: Time evolution of the droplet distribution when moving through the temperature trough (for the definition of bins see Fig.1). Assumed parameters are: mixing ratios of 5 ppmv H_2O, 10 ppbv HNO_3 and 0.53 ppbv H_2SO_4 (total mixing ratio). (a) Temperature (T, left ordinate) and pressure (p, right ordinate) evolution during an adiabatic cooling event. (c) Nitric acid weight percentages for bins B0, B1, B10, B15, B20, B25. (b) Particle radii associated with these bins. (d) Sulfuric acid weight percentages; note the change from linear to logarithmic scale below 10 wt%.

volume by four orders of magnitude. Clearly, this is due to the enhanced uptake of HNO_3 and H_2O and explains the dramatic change in wt%(H_2SO_4).

The long time constants reflect the time required to transfer substantial amounts of HNO_3 to the droplet surface by gas phase diffusion (which is much longer than the time required to attain steady state inside the droplet, thus allowing liquid phase diffusion to be treated as instantaneous). Meilinger *et al.* [1995] estimated the time constants for HNO_3 and H_2O uptake to be

$$\tau_{HNO_3} \approx 1\,\mathrm{h} \times a^2 \left(1+\frac{1.6}{a}\right) \approx \begin{cases} 7\,\mathrm{h} & \text{for } a = 2\mu\mathrm{m} \\ 10\,\mathrm{min} & \text{for } a = 0.1\mu\mathrm{m} \end{cases}$$

$$\tau_{H_2O} \approx 4\,\mathrm{s} \times a^2 \left(1+\frac{1.6}{a}\right) \approx \begin{cases} 29\,\mathrm{s} & \text{for } a = 2\mu\mathrm{m} \\ 0.7\,\mathrm{s} & \text{for } a = 0.1\mu\mathrm{m}. \end{cases} \quad (2)$$

As one would expect from the similar amounts of HNO_3 and H_2O that are transferred, their relaxation times differ by roughly the ratio of the partial pressures (note that the ratio $\tau_{H_2O}/\tau_{HNO_3} \approx [c_{H_2O}/p^{vap}_{H_2O}]/[c_{HNO_3}/p^{vap}_{HNO_3}] \approx p^{vap}_{HNO_3}/p^{vap}_{H_2O} \approx p^{\infty}_{HNO_3}/p^{\infty}_{H_2O} \approx 1 : 500$). Equation (2) shows that water is in equilibrium on a time scale of seconds, while nitric acid uptake, and hence the equilibration of the entire droplet, needs hours for micron-sized particles. Therefore, the non-equilibrium phenomenon outlined here is characteristic for the uptake of HNO_3 in the temperature range below 195 K, while the binary H_2SO_4/H_2O aerosol droplets above this temperature are practically always in equilibrium.

3. SYNOPTIC COOLING EVENT

In the absence of gravity wave activity temperature changes of individual air parcels proceed much slower. Such synoptic cooling and warming rates are typically between 0.1 and 1 K/h. In the light of the treatment given above, the question arises whether also these slow temperature changes can induce deviations from equilibrium. For example, the analysis by Carslaw *et al.* [1994] of type-1b PSCs in terms of liquid $HNO_3/H_2SO_4/H_2O$ particles was based on the assumption that the aerosol is in equilibrium. This analysis was applied to data from Dye *et al.* [1992] measured with a Forward Scattering Spectrometer Probe (FSSP) measurements aboard the American research aircraft ER-2.

During these ER-2 measurements orographically strongly perturbed regions were deliberately avoided. Figure 3 shows a trajectory calculation similar to Fig.1, but based on the synoptic trajectory given in the upper panel. The maximum cooling rate is 0.7 K/h. Only the last 18 hours of a ten-day trajectory are shown. At time t = 18 h the air parcel encounters the ER-2 aircraft. At time t = 0 the temperature is still high. Therefore the droplet ensemble is still almost in equilibrium with about 50

wt% H_2SO_4 and very little amounts of HNO_3. The droplets in bin B0 differ somewhat from the rest because of the Kelvin effect. After about $t = 4$ h, when the temperature drops below 194 K, HNO_3 uptake becomes substantial and the development of a non-equilibrium droplet distibution occurs despite the small cooling rate. At $t = 18$ h, when the measurment is taken, the equilibrium concentrations corresponding to the ambient temperature of 188.5 K would be 38 wt% HNO_3, 2 wt% H_2SO_4 and 60 wt% H_2O. In contrast, the kinetic calculation shows that the droplet ensemble is far from equilibrium. Nitric acid varies between 7 and 39 wt% and sulfuric acid between 1.5 and 25 wt% (ignoring particles in bin B0 which do not overcome the Kelvin barrier).

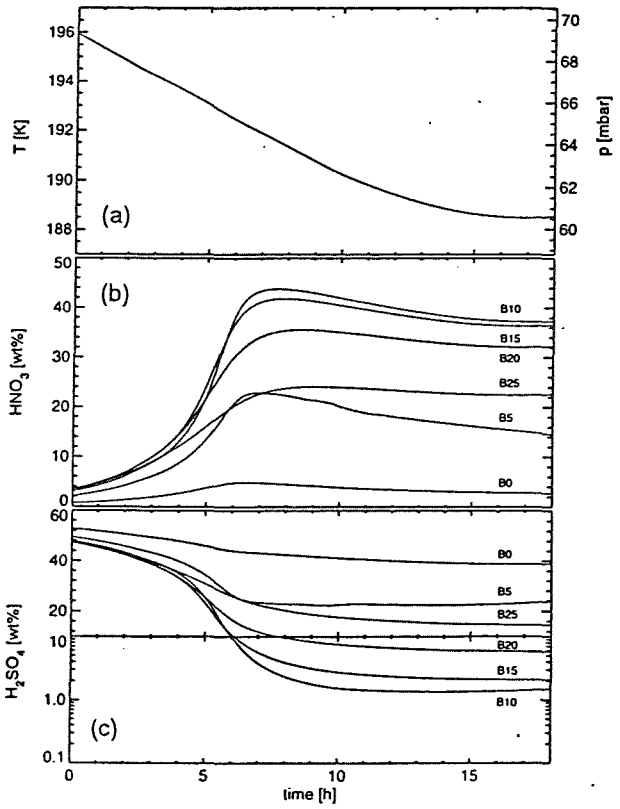

Figure 3: Development of the concentrations of liquid aerosol particles along a synoptic trajectory ending at 40.8 ksec of the ER-2 flight on 20/1/89 [K. Drdla, personal communication, 1995]. Particles are assumed to be lognormally distributed at 230 K with bins B0–B25 similar to Fig.1 (total number density 15 cm^{-3}, median radius 0.092 μm, width $\sigma = 1.8$ according to Dye *et al.* [1992]). (a) Temperature development during the last 18 hours before the encounter. (b,c) HNO_3 and H_2SO_4 concentrations in the same time window.

However, the response of the total particle volume ($\mu m^3/cm^3$) to the deviation from equilibrium is small. This is illustrated in Fig.2d (which may be compared with Fig.1 of Carslaw *et al.* [1994]). The reason for this is that the particles in bins B10 and B15 contribute most to the total volume, as can be seen from Fig.1a. For this mild cooling event these particles are still sufficiently small so that the diffusive resistance is not too high. Therefore, the total particle volume preserves the features of a liquid particle distribution in equilibrium, provided the cooling and heating rates are not too large. Also, this reconciles the equilibrium analysis by Carslaw *et al.* [1994] with the non-equilibrium approach presented here. The case considered by Carslaw *et al.* [1994] was sufficiently close to equilibrium, and the concentrations given in their work can be interpreted as mass-weighted averages.

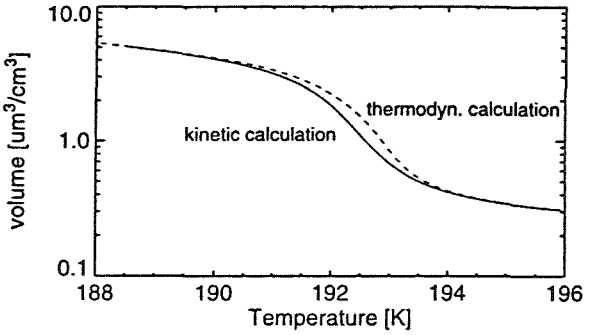

Figure 4: Comparison of calculated volumes for the aerosol in Fig.3 assuming thermodynamic equilibrium (dashed line, compare Fig.1 of Carslaw *et al.* [1994]) with kinetic calculation (solid line).

4. LOW-AMPLITUDE GRAVITY WAVES

Murphy and Gary [1995] report ER-2 *in-situ* temperature measurements showing strong mesoscale temperature fluctuations which are not considered in synoptic trajectory data. Figure 5 shows the influence of such rapid fluctuations on droplet composition for a small (B1) and a large droplet class (B25). We have superposed a mesoscale fluctuation of 8 K/h and an amplitutde of 1 K (typical values observed aboard the ER-2 [Murphy and Gary, 1995]) on a trajectory with a constant cooling rate of 0.5 K/h. Figure 5 shows that the small droplets follow almost instantaneously each mesoscale perturbation, whereas the large droplets are diffusively hindered and perform only a slight oscillation around their composition in the unperturbed case. Note that due to the Kelvin effect the small particles are not able to grow in the case without mesoscale fluctuations, whereas the Kelvin effect can be overcome due to the large temperature gradients in mesoscale fluctuations, which leads to high supersaturations. The intermittent changes in composition of the small droplets might raise the probability of PSC formation. Even though the periods in which the small droplets reach compositions close to the NAT stoi-

chiometry are very short for NAT to nucleate, there might still be an increase in the freezing probability.

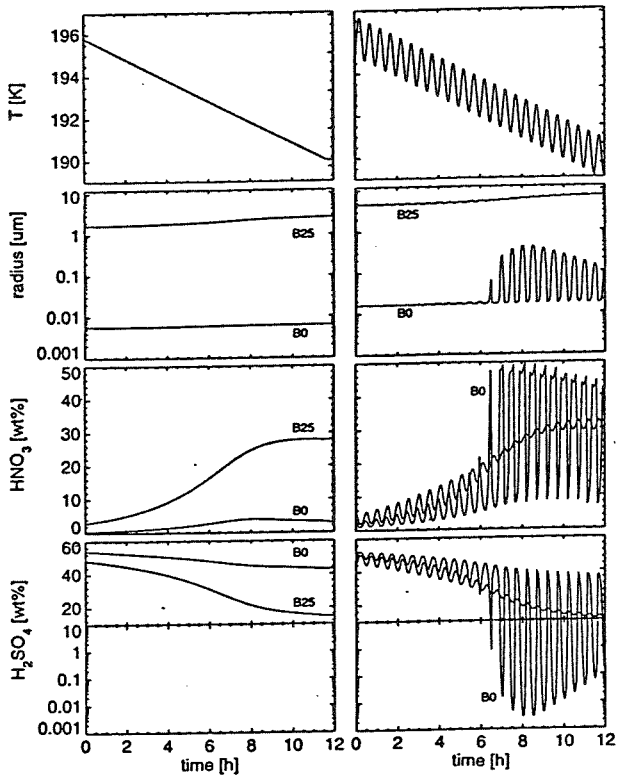

Figure 5: Left row: trajectory with a cooling rate of 0.5 K/h. Right row: same as left row but with a superposition of mesoscale temperature fluctuations with a cooling rate of 8 K/h and an amplitude of 1 K. Both Figures show the evolution of the smallest and largest droplets (B0 and B25 in Fig.1).

In summary, rapid temperature fluctuations in the vicinity of the NAT equilibrium temperature can lead to substantial deviations of the acid concentrations from the thermodynamic equilibrium values, even when the amplitude of the fluctuation is small (1 K). Stoichiometry of NAT can be reached in the smallest droplets, which possibly leads to nucleation of NAT. This size-selective NAT nucleation mechanism is in contrast to previous studies which postulated that the largest droplets would freeze first. This new mechanism would lead to the formation of two distinct radial modes, as the few frozen particles take up HNO_3 at the expense of the numerous larger droplets, which would finally revert back to almost binary H_2SO_4/H_2O. Clearly, further experiments will be necessary to determine whether cooling of stratospheric air in lee waves is an important pathway for the formation of frozen PSCs above the frost point. Whether they freeze or not, it is clear that mesoscale temperature fluctuations can strongly influence liquid aerosol composition and size distributions. Even synoptic temperature changes influence the composition of the droplets, whereas the total volume is hardly affected.

ACKNOWLEDGEMENTS

We thank Katja Drdla for providing the lee wave trajectory data and Jim Dye for valuable discussions. Support from the EU under contract number EV5V-CT93-0352 is gratefully acknowledged.

REFERENCES

Carslaw, K.S., Luo, B.P., Clegg, S.L., Peter, Th., Brimblecombe, P., Crutzen, P.J., Stratopsheric aerosol growth and HNO_3 gas phase depletion from coupled HNO_3 and water uptake by liquid particles, *Geophys. Res. Lett., 21*, 2479-2482, 1994.

Dye, J.E., Baumgardner, D., Gandrud, B.W., Kawa, S.R., Kelly, K.K., Loewenstein, M., Ferry, G.V., Chan, K.R., Gary, B.L., Particle size distributions in Arctic polar stratospheric clouds, growth and freezing of sulfuric acid droplets, and implications for cloud formation, *J. Geophys. Res., 97*, 8015-8034, 1992.

Koop, T., Biermann, U.M., Raber, W., Luo, B.P., Crutzen, P.J., Peter, Th., Do stratospheric aerosol droplets freeze above the ice frost point?, *Geophys. Res. Lett., 22*, 917-920, 1995.

Luo, B.P., Carslaw, K.S., Peter, TH., Clegg, S., Vapour pressures of $H_2SO_4/HNO_3/HCl/HBr/H_2O$ solutions to low stratospheric temperatures, *Geophys. Res. Lett., 22*, 247-250, 1995.

Meilinger, S., Koop, T., Luo, B.P., Huthwelker, Th., Carslaw, K.S., Krieger, U., Crutzen, P.J., Peter, Th., Size-dependent Stratospheric Droplet Composition in Mesoscale Temperature Fluctuations and their Potential Role in PSC Freezing, *Geophys. Res. Lett., 22*, 3031-3034, 1995.

Murphy, D.M., Gary, B.L., Mesoscale temperature fluctuations and polar stratospheric clouds, *J. Atmos. Sci., 52*, 1753-1761, 1995.

Pruppacher, H.R. and J.D. Klett, *Microphysics of Clouds and Precipitation*, D. Reidel, Dordrecht, 1978.

A WIND TUNNEL AND THEORETICAL INVESTIGATION OF THE UPTAKE OF NH_3, SO_2 AND CO_2 IN FALLING WATER DROPS

Anke Hannemann , S.K. Mitra, H.R. Pruppacher

Institut für Physik der Atmosphäre, Johannes–Gutenberg-Universität Mainz, Germany

1. INTRODUCTION

In this work scavenging experiments of NH_3, SO_2 and CO_2 have been performed using water drops of 2.9 mm radius, which were freely suspended in a vertical airstream containing a known concentration of these gases. Numerous experimental and theoretical studies have been carried out on the SO_2 uptake by individual water drops (Waltrop *et al.*, 1991; Walcek *et al.*, 1984; Walcek and Pruppacher, 1984; Mitra *et al.*, 1992; Beilke and Georgii, 1968; Beilke, 1970; Barrie and Georgii, 1976). Mitra and Hannemann (1993) compared experimental studies of the SO_2 desorption with different theoretical models. An experimental and theoretical investigation of the NH_3 uptake by falling drops was made by Hannemann *et al.* (1995).

The major results of these papers are summerized as follows:

(1) The amount of SO_2 taken up increases with increasing time of exposure and with increasing SO_2 concentration in air, usually reaching a limiting equilibrium value after long periods of time if SO_2 alone is involved. In the presence of oxidizing agents such as H_2O_2 or O_3 the concentration of total sulfur {[S(IV)] + [S(VI)]} in the liquid phase increases continuously with time.

(2) Drops with radii typically less than 20 μm reach their equilibrium concentration sufficiently quickly so that they may be assumed to be in equilibrium with their environment at all times. For larger drops the concentration of S(IV) in a drop has to be computed by using an appropriate gas diffusion model for inside and outside the drop.

(3) Diffusion models which assume that the drop is always well mixed with respect to the S(IV) taken up, are applicable only in the low ppbv range. At larger SO_2 concentrations the uptake has to be computed using a convective diffusion model which considers convective diffusion inside the drop as well.

(4) A well mixed drop model significantly overestimates the rate of desorption of SO_2. Desorption of SO_2 has therefore to be computed by a model involving transport inside the drop.

(5) At atmospheric concentrations the uptake of NH_3 is adequately described by a well mixed model, when the simultaneous uptake of atmospheric CO_2 is taken into account.

(6) To describe the uptake of NH_3 without the simultaneous presence of CO_2 it is necessary to consider diffusion outside as well as inside the drop.

(7) Desorption of NH_3 from drops can adequately be described by the well mixed model.

(8) Inclusion of CO_2 hydration kinetics is essential for explaining the uptake of CO_2 by water drops.

(9) Under conditions typical in the tropospheric boundary layer, CO_2 hydration kinetically limits the NH_3 uptake by rain drops.

(10) The experimental uptake rates of SO_2–NH_3–CO_2 confirm the uptake rates computed from the Kronig–Brink model, which in turn agrees with the well mixed model.

(11) In order to describe the uptake of CO_2 correctly the full CO_2 dissociation kinetics has to be taken into account.

So far no studies have been carried out to determine whether the uptake of each individual gas in a mixture of NH_3, SO_2 and CO_2 would exhibit the same scavenging characteristics as is exhibited by SO_2 and NH_3 alone. Here we investigate experimentally and theoretically the coupled scavenging behaviour of these compounds in a wind tunnel study.

2. THE EXPERIMENT

A water drop of 2.9 mm equivalent radius was freely suspended in the air stream of the Mainz vertical wind tunnel (see Waltrop *et al.*, 1991). In this tunnel

two vacuum pumps drive ambient air, free of particles with diameters larger than 0.3 μm by air filters, and with SO_2 and NH_3 concentrations less than 0.5 ppbv, through the observation section. The velocity of the air stream was adjusted to keep the drop at its terminal velocity in the vertical observation section of the tunnel. During a particular experiment, the temperature and humidity of the tunnel air stream were held constant at 20 °C and between 60 and 70 % relative humidity, respectively. This ensured that during the exposure of a drop to the trace gas the drop size remained practical unchanged. NH_3 and SO_2 where injected from a gas bottle into the mixing chamber of the tunnel at a metered rate. Mixing with the tunnel air yielded concentrations varying between 95 and 110 ppbv SO_2 and between 280 and 390 ppbv NH_3 in the observation section. The CO_2 content of the tunnel air was determined to be constant and near 350 ppmv. After exposure to the NH_3/SO_2 mixture, the drop was retrieved from its free floating position in the tunnel air stream by a drop retrieving system described in detail in Mitra and Hannemann (1993) and in Waltrop *et al.* (1991). Immediately following capture, the drop was transferred to a cuvette containing an accurately premeasured volume of spectroscopically pure H_2O_2 solution of sufficient concentration to convert all absorbed S(IV) to S(VI). The absorbed NH_3 was automatically converted to NH_4^+ in the drop due to the low pH in the drop. The solution was subsequently injected into cation and anion chromatographs to determine the concentrations of NH_4^+ and S(VI). From these values the amounts of NH_3 and SO_2 taken up by the drop were derived.

3. THE DIFFUSION MODELS

The major objective of the present study was to compare our experimental results with those predicted by the available diffusion theories. Walcek and Pruppacher (1984) showed that a correct and complete solution to the relevant transport problem would involve solving the convective diffusion equations for inside and outside the drop coupled by appropriate boundary conditions. However, such a procedure requires knowledge of the flow fields inside and around the drop. These flow fields are presently only available for drops up to about 500 μm radius (Pruppacher and Klett, 1978). In order to circumvent this problem, Walcek and Pruppacher (1984) showed that with satisfactory accuracy the process can be described by applying a model suggested by Kronig and Brink (1950). These authors assumed that the streamlines inside a drop of any size follow approximately those given by the Stokes solution of flow, an assumption which was independently verified by the results of Le Clair *et al.* (1972) who applied the complete steady state Navier–Stokes equation of motion to the exterior and interior of drops up to 500 μm radius. Further details of the Kronig–Brink model have been described by Hannemann *et al.* (1995). If it is assumed that the inside of a drop containing the dissolved gas is completely mixed at all times only diffusion of the gas outside the drop must be considered and the rate of gas uptake follows immediately from Fick's law of diffussion. Details of the equations used in the well mixed model are given by Waltrop *et al.* (1991) and by Mitra and Hannemann (1993).

4. THE CHEMICAL MODEL

The solution and dissociation equilibria for NH_3, SO_2 and CO_2 and the relevant chemical kinetics of the single drop uptake of NH_3 in the presence of atmospheric CO_2 and of SO_2 alone have been described in detail in our earlier article (Hannemann *et al.*, 1995; Waltrop *et al.*, 1991). They shall therefore not be repeated here.

Considering now the simultaneous uptake of NH_3, SO_2 and CO_2, the only additional complication is the solution of the electroneutrality equation, which noe reads

$$[H^+] + [NH_4^+] = [OH^-] + [HCO_3^-] + 2[CO_3^{2-}] + [HSO_3^-] + 2[SO_3^{2-}] + [HSO_4^-] + 2[SO_4^{2-}]. \quad (1)$$

This reduces to

$$[H^+] - \frac{k_w}{[H^+]} = [CO_2 dis]\,\frac{[H^+] + 2K_{CO_3^{2-}}}{[H^+] + K_{CO_3^{2-}}} + [S(IV)]\,\frac{K_{HSO_3^-}[H^+] + 2K_{HSO_3^-}K_{SO_3^{2-}}}{[H^+]^2 + K_{HSO_3^-}[H^+] + K_{HSO_3^-}K_{SO_3^{2-}}} + [S(VI)]\,\frac{[H^+] + 2K_{SO_4^{2-}}}{[H^+] + K_{SO_4^{2-}}} - [N(III)]\,\frac{K_{NH_4^+}[H^+]}{K_{NH_4^+}[H^+] + k_w}, \quad (2)$$

where $[CO_2 dis] = [HCO_3^-] + [CO_3^{2-}]$ and the K's are dissociation constants (taken from Seinfeld, 1986). In the numerical programs $[H^+]$ is calculated iterativly from Eq.(2).

5. RESULTS AND CONCLUSIONS

The results of our wind tunnel studies are plotted in Figures 1, 2 and 3 where they are compared with the theoretical predictions of the well mixed model and with the Kronig–Brink model.

These figures show that, for the conditions studied, the results of the well mixed model agree with the results of the Kronig–Brink model to such an extent that both results could be represented in terms of one single line. The three figures also demonstrate that our experimental wind tunnel results verify the

theoretically predicted simultaneous uptake of SO_2 and NH_3 in presence of CO_2. Our results imply that for gas concentration up to a few hundred ppbv the simultaneous uptake of SO_2, NH_3 and CO_2 can be described by the well mixed model. This finding parallels the finding of Waltrop *et al.* (1991) for the uptake of SO_2 alone and the uptake of SO_2 in presence of H_2O_2, and the finding of Hannemann *et al.* (1995) for the uptake of NH_3 in the presence of CO_2 if the full kinetics of the CO_2 uptake is taken into account.

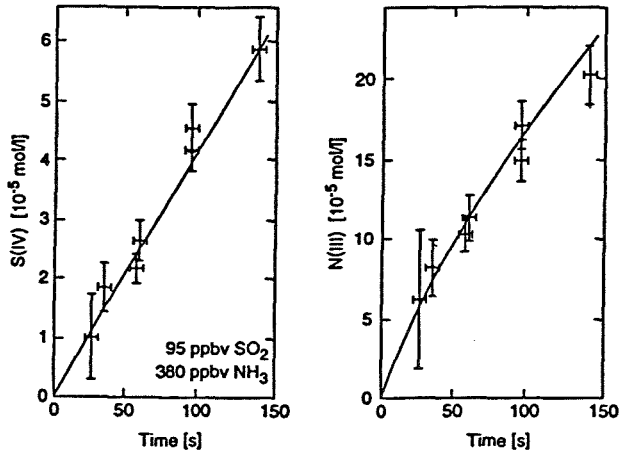

Fig.1.: Concentration of S(IV) and N(III) in a 2.9 mm drop at 15°C as a function of time for constant air concentrations of 95 ppbv SO_2 und 380 ppbv NH_3. Solid line: Results of the theoretical models (Kronig–Brink and well mixed model are almost the same at this concentrations).

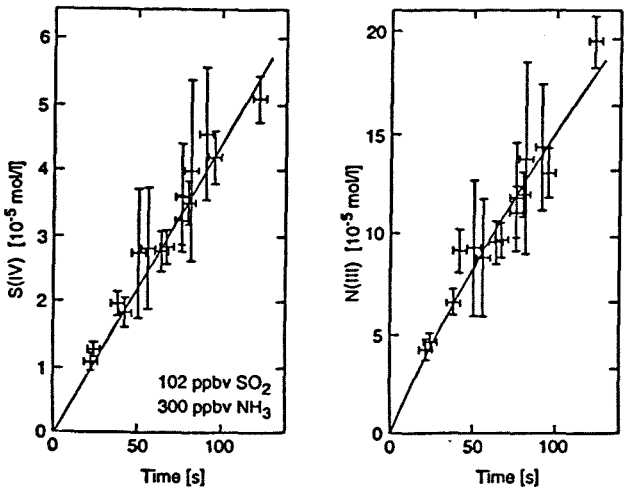

Fig.2.: Same as figure 1 but for absorption of 102 ppbv SO_2 and 300 ppbv NH_3.

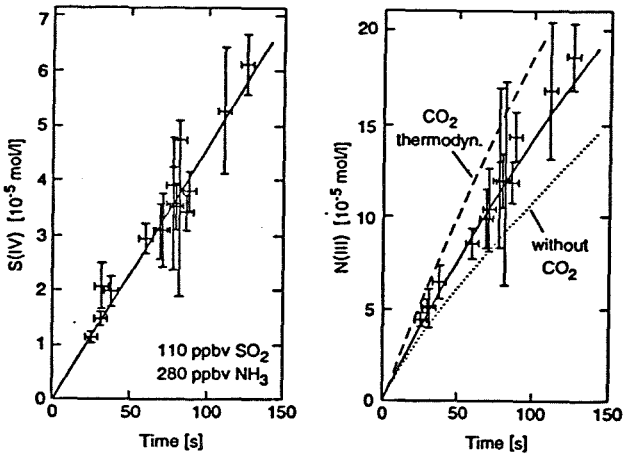

Fig.3.: Same as figure 1 but for absorption of 110 ppbv SO_2 and 280 ppbv NH_3. Dotted line: absorption curve without CO_2. Dashed line: absorption curve of uptake with CO_2 in thermodynamic equilibrium.

However, at higher concentrations deviations of the well mixed model from the Kronig–Brink model are found to occur (see Waltrop *et al.*, 1991, and Hannemann *et al.* 1995). Since the Kronig–Brink model has been shown to be the correct description of the diffusional gas uptake by a drop (see Mitra *et al.*, 1992 and Walcek and Pruppacher, 1984), the well mixed model should be applied to higher concentrations.

Interesting observations were made regarding the desorption of SO_2 and NH_3. Our studies (not shown here) indicate that from drops which previously had been simultaneously exposed to NH_3 and SO_2 neither gas desorps in significant quantities. This is in contrast to the desorption of NH_3 from a drop, previously exposed to NH_3 alone, which adequately can be described by the well mixed model (see Hannemann *et al.*, 1995). The results, in turn, are in contrast to the desorption of SO_2 from a drop, previously exposed to SO_2 alone, which cannot be described by the well mixed model but must be described by the Kronig–Brink model (see Mitra and Hannemann, 1993).

ACKNOWLEDGEMENTS

This work was supported by the German Science Foundation (DFG) from the research grant SFB 233 and also by the German Ministry of Education and Research (BMBF) from the research grant 0704580 B/9. In addition one of the authors (A. Hanne-

mann) wishes to express thanks to the Graduate College Program of DFG for providing personal financial support.

REFERENCES

Barrie, L.A. and H.W. Georgii, 1976: An Experimental Investigation of the Absorption of SO_2 by Water Drops containing Heavy Metal Ions; *Atmos. Environ.*, **10**, 743–749.

Beilke, S., 1970: Laboratory Investigation of Washout Trace Gases, *Precipitation scavenging – 1970*, US Atomic Energy Comission, National Techn. Info. Service. US Dept. of Commerce, Springfield, VA, 261–267.

Beilke, S. and H.W. Georgii, 1968: Investigation on the incorporation of SO_2 into fog and rain drops, *Tellus*, **20**, 435–442.

Hannemann, A.U., S.K. Mitra and H.R. Pruppacher, 1995, On the Scavenging of Gaseous Nitrogen Compounds by Large and Small Rain Drops I. A Wind Tunnel and Theoretical Study of the Uptake and Desorption of NH_3 in the Presence of CO_2, *J. Atmos. Chem.*, **21**, 293–307.

Kronig, R. and J.C. Brink, 1950: On the Theory of Extraction from Falling Droplets; *Appl. Sci. Res.*, **2**, 142–154.

Le Clair, B.P., A.E. Hamielec, H.R. Pruppacher, W.D. Hall, 1972: A theoretical and experimental study of the internal circulations in water drops falling at terminal velocity in air; *J. Atmos. Sci.*, **29**, 728–740.

Mitra, S.K. and A.U. Hannemann, 1993: On the Scavenging of SO_2 by Large and Small Rain Drops: 5. A Wind Tunnel and Theoretical Study of the Desorption of SO_2 from Water Drops Containing S(IV); *J. Atmos. Chem.* , **16**, 201–218.

Mitra, S.K., A. Waltrop, A. Hannemann, A. Floßmann and H.R. Pruppacher, 1992: A Windtunnel and Theoretical Investigation to Test Various Theories for the Absorption of SO_2 by Drops of Pure Water and Water Drops Containing H_2O_2 and $(NH_4)_2\,SO_4$; in: Schwartz S.E., Slinn W.G.N. (eds), *Precipitation Scavenging and Atmosphere - Surface Exchange*, Hemisphere Publishing Corporation, Washington, **1**, 123–141.

Pruppacher, H.R. and J.D. Klett, 1978: *Microphysics of Clouds and Precipitation*; D. Reidel Publishing Company, Dordrecht, 714 pp.

Seinfeld, J.H., 1986: *Atmospheric Chemistry and Physics of Air Pollution;* Wiley, New York, 738 pp.

Walcek, C.J. and H.R. Pruppacher, 1984: On the Scavenging of SO_2 by Cloud and Raindrops: I. A Theoretical Study of SO_2 Absorption and Desorption for Water Drops in Air; *J. Atmos. Chem.*, **1**, 269–289.

Walcek, C.J., H.R. Pruppacher, J.H. Topalian and S.K. Mitra, 1984: On the Scavenging of SO_2 by Cloud and Raindrops: II. An Experimental Study of SO_2 Absorption and Desorption for Water Drops in Air; *J. Atmos. Chem.*, **1**, 291–306.

Waltrop, A., S.K. Mitra, A.I. Floßmann and H.R. Pruppacher, 1991: On the Scavenging of SO_2 by Cloud and Rain Drops: IV. A Wind Tunnel and Theoretical Study of the Absorption of SO_2 in the ppb(v) Range by Water Drops containing H_2O_2; *J. Atmos. Chem.*, **12**, 1–17.

CALCULATION OF THE IN-CLOUD CONCENTRATION OF TRACE COMPOUNDS IN RAIN BY SAMPLING RAINDROPS AT THE GROUND

Thomas Prokop, Peter Ebert, Matthias Kibler, Antje Mainka, Birgit Tenberken and Knut Bächmann

Technische Hochschule Darmstadt; Fachbereich Chemie; Petersenstr. 18; D-64287 Darmstadt; Germany

1. INTRODUCTION

To calculate the contribution of in-cloud scavenging of different inorganic species (NH_4^+, Na^+, K^+, Ca^{2+}, Mg^{2+}, Cl^-, NO_3^- and SO_4^{2-}) it is necessary to know the concentration of these species in raindrops while leaving cloud base and at ground. No data concerning field experiments sampling simultaneously raindrops at these two places are known. Sampling size classified raindrops instead of bulk rain enables us to calculate the in-cloud concentration of trace compounds in rain by measurements at ground. A new method was developed which makes it possible to calculate the contribution of in-cloud scavenging without expensive aircraft measurements.

2. THEORY

We found in former studies an interdependence between the chemical content of raindrops and drop size (further shorten as c/r-dependence). Most inorganic anions and cations show a maximum concentration at a specific drop radius [Bächmann et al., 1993].

Calculation of the concentration of trace compounds in rain while leaving cloud base is only possible by assuming that at cloud base all raindrops show the same concentration. This assumption is based on the fact that the raindrop formation process through cloud drops leads to an almost complete disappearance of concentration differences of clouddroplets [Flossmann, 1994]. For large raindrops ($r > 1.4$ mm) the change in concentration from cloud base to ground is neglectable small. This assumption is based on the fact that (a) compared to small raindrops ($r < 0.8$ mm) a change in concentration by evaporation for large raindrops can be neglected, (b) terminal velocity of these drops is larger compared to small ones and therefore the resistance time of large raindrops in the atmosphere for below-cloud scavenging processes is smaller (c) the collision efficiency has a minimum for drop sizes larger than 1.4 mm radius [Pruppacher and K!ett, 1978]. Therefore it can be concluded that the concentration of trace compounds of large raindrops on ground is nearly the same as at cloud base.

Knowing the c/r-dependence far below the cloud it is possible to find a mathematical function describing the decrease of concentration for drops larger than 0.175 mm. Extrapolating this function to large raindrops ($r >$ 1.4 mm) a limit concentration was obtained which should not differ very much from the in-cloud raindrop concentration. To test this method field experiments were performed sampling simultaneously raindrops at cloud base and below the cloud [Bächmann et al., 1996]. The sample stations were located at the top and the bottom of a mountain which often lies with its top inside clouds. Therefore it was possible to compare our calculated in-cloud concentrations received by measurements of c/r-dependencies at the bottom of the mountain to the simultaneously measured in-cloud concentration at the top.

For the calculation of the contribution of in-cloud scavenging the areas above (below-cloud) and below (in-cloud) the calculated asymptote have to be measured. Furthermore the drop size distribution - measured simultaneously below the cloud - have to be taken into account.

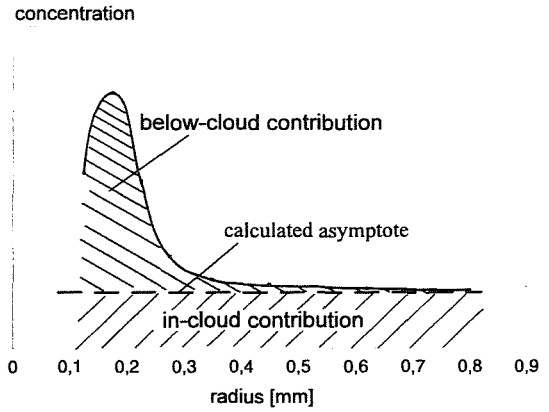

Fig.1: Calculation of the in-cloud and below-cloud concentration and scavenging contribution

3. EXPERIMENTAL

3.1 Location

Samples were taken at the mountain "Weisser Stein" (Dossenheim, Germany). Reasons for the choice of this place were:

- cloud base is often located at the top of the mountain
- horizontal distance between the two sample stations is less than 1500 m
- total height distance is 400 m
- both sample stations are situated in the same wind direction (south-west)

The upper station was located at the top of the mountain. The lower station was near Dossenheim.

3.2 Sampling Method

Raindrops are collected according to their size using the "Guttalgor" method (*Latin*: gutta - drop; *Latin*: algor - frost) described in detail elsewhere [Bächmann et al., 1993]. Size classification means that raindrops with similar sizes are put together to form one sample volume (size fraction). Drop size distributions were measured with a Waldvogel disdrometer (RD-69, Distromet Ltd., Basel, Switzerland). Analysis of size fractionated raindrops was carried out by capillary zone electrophoresis (CZE).

4. RESULTS AND DISCUSSION

4.1 Results

The measured c/r-dependencies at each station are similar for all rain events. During the sampling periods at mountain "Weisser Stein" we measured more than 150 c/r-dependencies for different inorganic species. There are only little differences for the c/r-dependencies regarding the relative values and not the absolute concentration. Two different c/r-dependencies were found depending on the sampling location:

- at the top of the mountain a constant concentration independent on drop radius is found (Fig.2).

- all samples taken at the bottom of "Weisser Stein" show a concentration maximum for a radius of about 0.175 mm (Fig.3). The shape of these curves is consistent with results obtained in former studies [Bächmann et al., 1993, 1995].

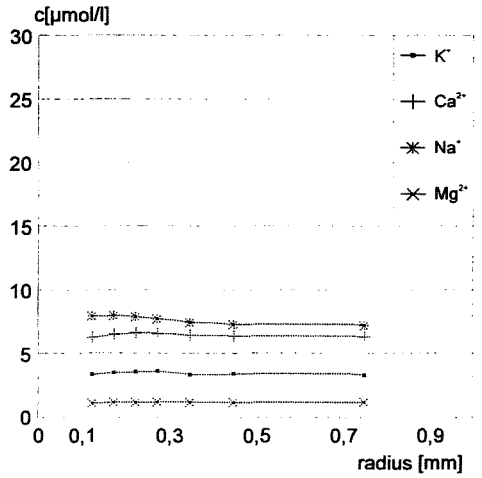

Fig.2: c/r-dependencies measured in-cloud

Table 1 and table 2 shows our calculated in-cloud concentrations received by measurements of the c/r-dependencies at the bottom of "Weisser Stein" and measured in-cloud concentration at the top of the mountain.

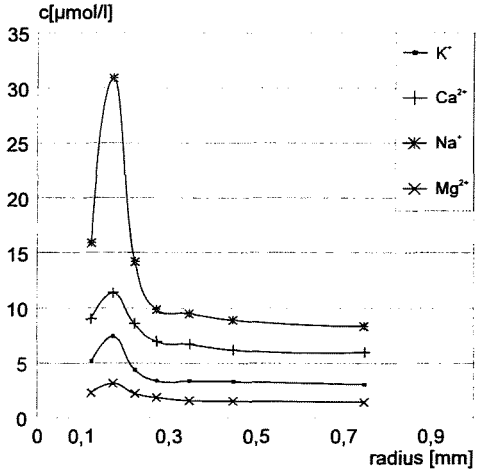

Fig.3: c/r-dependencies measured below-cloud

Tab.1: measured and calculated in-cloud concentration of different cations

ion [µM]	Na^+	K^+	Ca^{2+}	Mg^{2+}
measured	8.48	1.03	5.10	1.05
calculated	8.25	0.99	5.16	1.09

Tab.2: measured and calculated in-cloud conenctration of different anions

ion [µM]	Cl^-	SO_4^{2-}	NO_3^-
measured	7.29	7.49	7.18
calulated	7.10	7.10	6.95

4.2 Discussion and Interpretation

From literature it is known that cloud drops have different concentrations depending on their size [e.g. Noone et al., 1988]. This is due to nucleation and in-cloud scavenging of aerosol particles and gases. Our results clearly indicate that the raindrop formation process through cloud drops leads to an almost complete disappearance of these differences. This is consistent with theoretical predictions [e.g. Flossmann, 1994]. Flossmann (1994) assume a coalescence mechanism leading to raindrop formation and the existing differences in concentration for cloud drops disappear.

We conclude that all deviations from the constant concentration for all radii of raindrops at the cloud base to the measured c/r-dependencies in the plain of "Weisser Stein" are due to below-cloud influences (e.g. evaporation, particle scavenging or coalescence and breakup) [Bächmann et al., 1996].

An excellent agreement between calculated and measured values is obvious (Tab.1 and Tab. 2). Table 3 and Table 4 show the mean in-cloud contribution of different cations and anions. These values arise out of more than 70 rain events sampled at different locations. Most measurements were done in Darmstadt, Germany.

Tab.3: Mean in-cloud scavenging contribution of cations in rain

cation	NH_4 [%]	Na [%]	Ca [%]	Mg [%]	K [%]	Pb* [%]	Mn* [%]
in-cloud contribution	60.6	74.8	58.3	45.9	54.9	22.2	21.2

*from Steigerwald (1995)

Tab.4: Mean in-cloud scavenging contribution of anions in rain

anion	chloride [%]	sulfate [%]	nitrate [%]	nitrite [%]
in-cloud contribution	66.2	61.7	55.7	8.0

It is obvious that the main part of inorganic anions and cations is scavenged in-cloud. We found in-cloud contributions around 60 %. The low in-cloud value of sulphate compared to that of Flossmann (1994) is explained by the fact that the largest part of the measurements were done in Darmstadt where higher values of sulphate arise of industrial origin or combustion processes. Therefore a higher content of sulphate is in the air which was scavenged below-cloud.

The small in-cloud contribution of Pb and Mn is explained by other arguments. These two elements show a relative constant c/r-dependence nearly independent on precipitation time [Bächmann et al., 1995]. Only after long precipitation times a change for the c/r-dependencies was found. Their behaviour is contrary to what was found for other species (e.g. Na^+, Mg^{2+}, Cl^- or SO_4^{2-}) where changes from a continuous decrease to a maximum concentration occurred within one single rain event after very short precipitation times (15-20 minutes) [Bächmann et al., 1993]. These differences are explained by the fact that Mn and Pb are mainly located at aerosol particles of lower heights [Dannecker et al., 1981]. Our results show that the c/r-dependence of these two elements arise mainly of below-cloud scavenging processes. Evaporation or coalescence and break-up affects the c/r-dependencies the more the higher the fall distances of the raindrops from the clouds to the ground is. The c/r-dependencies of Pb and Mn are more affected by the scavenged size of aerosol particles where these elements are located at [Bächmann et al., 1995].

Determine the in-cloud contribution of nitrite as a function of temperature it is seen that with decreasing temperature the in-cloud contribution of nitrite becomes smaller (Fig.4). This can be explained by the fact that the oxidation of nitrite to nitrate is accelerated markedly when the freezing rate of clouddrops increases [Takenaka et al., 1992]. The reasons of the increase of the reaction rate is not quite clear but Takenaka et al. (1992) excluded thermochemical, photochemical and simple electrochemical reactions or catalysis on the ice surface. Our results are a strong hint that nitrite may be a source of nitrate in rain if the raindrops originate of "cold-rain" processes.

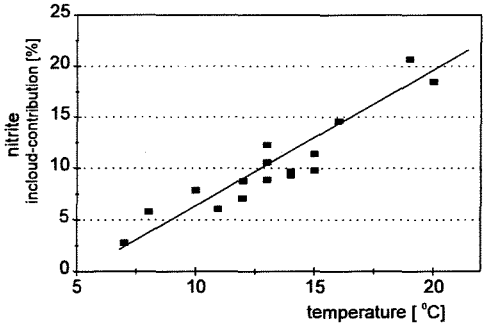

Fig.4: In-cloud contribution of nitrite as a function of temperature

5. SUMMARY

During several field studies performed at two different altitudes it was shown that different c/r-dependencies exist for raindrops at and far below the cloud base. Inside the clouds a uniform concentration independent of radius of the raindrops is

measured. In contrast to this we observed a concentration maximum for a middle drop radius for samples taken far below the clouds. We conclude that the existing concentration differences for cloud drops as a function of their size are levelled out by the raindrop formation process. This interpretation is consistent with predictions drawn from model calculations. Furthermore, we conclude that the measured c/r-dependencies are only caused by below-cloud influences such as evaporation, particle scavenging or coalescence and breakup.

A method is presented which enables us to calculate the in-cloud concentration of trace compounds in rain by sampling of size classified raindrops below the cloud. Raindrops were simultaneously measured in and below the cloud. The results of calculated in-cloud concentrations of trace compounds obtained by measurements of size-classified raindrops below the cloud and raindrops collected simultaneously at cloud base were compared and an excellent agreement was obtained. Encouraged by this agreement we investigated the in-cloud scavenging contribution of different inorganic species. Nucleation scavenging has been found to be the important removal mechanism for most species in rain whereas below-cloud scavenging is less effective. The presented method is a new way to get more detailed information about in-cloud and below-cloud scavenging processes without using aircraft measurements.

Acknowledgements - The authors acknowledge the financial support of the Deutsche Forschungsgemeinschaft (DFG) under Project SFB 233 ("Dynamik und Chemie der Hydrometeore").

6. REFERENCES

Bächmann, K., Haag, I. and Röder, A. (1993) A field study to determine the chemical content of individual raindrops as a function of their size, Atmospheric Environment 27A, 1951-1958.

Bächmann, K., Haag, I. and Steigerwald, K. (1995) Determination of transition metals in size classified rain samples by atomic absorption spectrometry, Atmospheric Environment 29A, 175-177.

Bächmann, K., Ebert, P., Haag, I. and Prokop, T. (1996) The chemical content of raindrops as a function of drop radius, Part I: Field measurements at the cloud base and below the cloud, Atmospheric Environment 30A, 7, 1019-1025.

Dannecker, W., Naumann, K. und Herbst, R. (1981) Zeitgleiche Schwebstaubprobennahme in verschiedenen Höhen im Ballungsraum Hamburg und die nachfolgende chemische Analyse, Staub-Reinhalt. Luft 41, 254-261.

Flossmann, A. (1994) A 2-D spectral model simulation of the scavenging of gaseous and particulate sulfate by a warm marine cloud, Atmos. Res. 32, 233-248.

Noone, K. J., Charlson, R. J., Covert, D. S., Ogren, J. A. and Heintzenberg, J. (1988) Cloud droplets: solute concentration is size dependent, J. Geophys. Res. 93, 9477-9482.

Pruppacher, H. R. and Klett, J. D. (1978) Microphysics of clouds and precipitation, D. Reidel, Dordrecht.

Roelofs, G. J. H. (1992) On the drop aerosol size dependence of aqueous sulfate formation in a continental cumulus cloud, Atmospheric Environment 26, 2309-2321.

Steigerwald, K. (1995) Messungen von Al, Si, Mn, Fe, Zn und Pb in größenklassifizierten und einzelnen Regentropfen, Ph. D. Thesis, Dept. Chemistry, Technische Hochschule Darmstadt, Germany.

Takenaka, N., Ueda, A. and Maeda, Y. (1992) Acceleration of the rate of nitrite oxidation by freezing in aqueous solution, Nature 358, 736-738.

FIELD EXPERIMENTAL DETERMINATION OF COLLISION EFFICIENCIES AS A FUNCTION OF RAINDROP AND AEROSOL PARTICLE SIZE

Peter Ebert[1], Gerhard Frank[2], Matthias Kibler[1], Antje Mainka[1], Thomas Prokop[1], Birgit Tenberken[1], Jochen Tschiersch[2] and Knut Bächmann[1]

[1]Technische Hochschule Darmstadt; Fachbereich Chemie; Petersenstr. 18; D-64287 Darmstadt; Germany
[2]GSF-Forschungszentrum für Umwelt und Gesundheit GmbH; Institut für Strahlenschutz; Ingolstädter Landstr.1; D-85764 Oberschleißheim; Germany

1. EXPERIMENTAL

Monodisperse aerosol particles (produced with a Sinclair LaMer generator, MAGE, Palas, Karlsruhe, Germany; mean radius varying from 0.19 µm to 1.8 µm) tagged by a fluorescent dye tracer were released during several precipitation events (Fig.1). Raindrops which scavenge these particles are collected with the "Guttalgor" method described in detail elsewhere [Bächmann et al., 1993]. Analysis of the raindrops is carried out by Capillary Electrophoresis (CE) with Laser-Induced Fluorescence (LIF) detection.

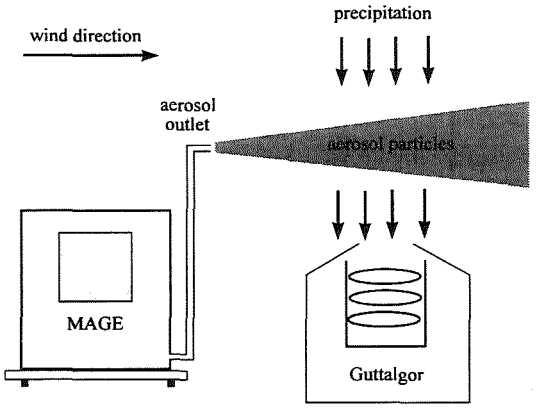

Fig.1: Experimental set-up of the field experiment

Collision efficiencies are calculated by formula (1):

$$\lambda_{D,i} = \frac{\Delta n * v}{Q * l * \tau} \qquad (1)$$

with $\lambda_{D,i}$: collision coefficient [s^{-1}]
Δn: number of scavenged particles
v : wind velocity [m/s]
Q : source strength of MAGE [s^{-1}]
l : length of sampling basin [m]
t : sampling time [s]

2. RESULTS

2.1 c/r-Dependence

An interdependence between the tracer concentration and raindrop size was found (further abbr. as c/r-dependence). The c/r-dependencies obtained by the scavenging of aerosol particles smaller than 1.8 µm radius show a maximum concentration at a specific raindrop radius. The maximum concentration shifted to a drop radius of 0.35 mm with decreasing scavenged aerosol particle size (Fig.2). A continuous decrease in concentration with increasing drop radius was measured for the scavenging of large particles (r_{AP}: 1.8 µm).

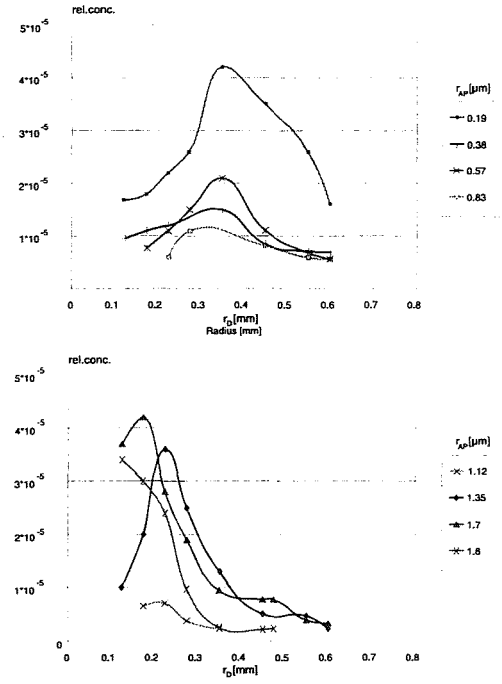

Fig.2: c/r-dependencies as a function of aerosol particle size (r_D: drop radius; r_{AP}: aerosol particle radius)

2.2 Collision Efficiencies *E* as a Function of Drop Radius

The collision efficiencies E range from 10^{-2} s^{-1} to $10^{-6}s^{-1}$. An increase of the collision efficiency with increasing raindrop size showing a maximum collision efficiency at a drop radius of 550 µm was obtained (Fig.3). With increasing scavenged particle radius the slope of *E* to larger raindrops becomes flat and lower values for *E* were found.

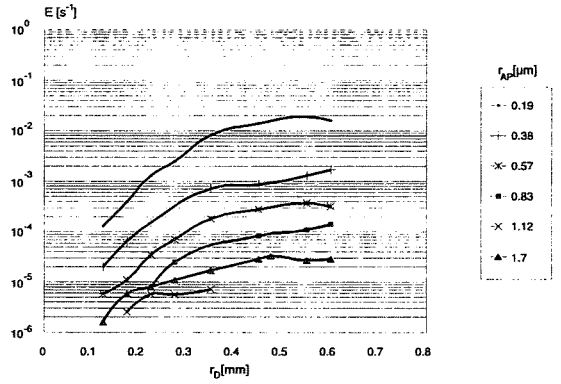

Fig.3: Collision efficiency as a function of drop size for different particle radii

In Fig.4 we show the obtained results of different tracer experiments for the same aerosol particle size. For aerosol particles with a radius of 0.19 µm the same collision efficiencies were measured at different rain events. For aerosol particles with a radius of 1.35 µm we found the same curve shape at both events but different absolute values for the collision efficiency. Below the figures we show meteorological parameters of the experiments.

a)

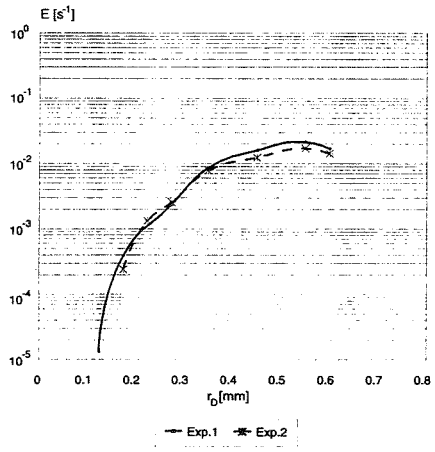

Nr.	T_0 [°C]	T_E [°C]	RH_0 [%]	RH_E [%]	p [mm/h]	clouds
1	24	22	72	87	1.1	1
2	22	-	87	-	1.7	1

b)

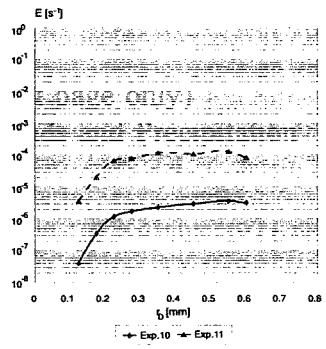

Nr.	T_0 [°C]	T_E [°C]	RH_0 [%]	RH_E [%]	p [mm/h]	clouds
10	16.6	16.6	94	-	2.0	3
11	17.2	17.4	100	100	4.4	2

Fig.4: Results of different tracer experiments for the same particle radius: a) r_{AP}: 0.19 µm; b) r_{AP}: 1.35 µm; T: temperature; RH: relative humidity; p: rain intensity; index 0: start of experiment; index E: end of experiment; clouds: 1: cumulus; 2: incomplete cloud cover; 3: stratus

2.3 Collision Efficiency as a Function of AP Size

The collision efficiency λ shows a decrease with increasing aerosol particle size from a particle radius of 0.19 µm to 1.35 µm (Fig.5).

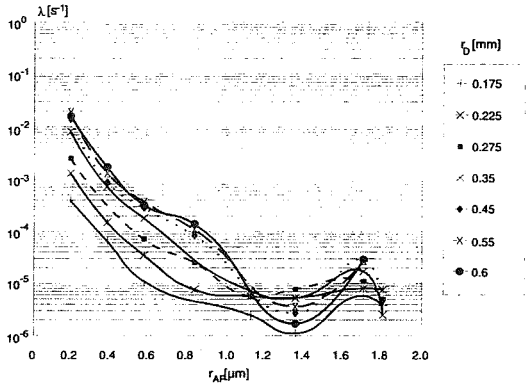

Fig.5: Collision efficiency (λ) as a function of aerosol particle size for different raindrop radii

For aerosol particles with a radius of 1.35 µm a minimum for the collision efficiency is seen for all raindrop sizes (only raindrops with 0.275 mm radius show a minimum scavenging efficiency at 1.12 µm). For aerosol particles larger than 1.35 µm an increase for the scavenging efficiency was found up to a radius of 1.7 µm showing a local maximum. Larger aerosol particles show a decrease in the scavenging efficiency which becomes stronger the larger the raindrop radius is. At an aerosol particle radius of 0.8 µm a bend for the collision efficiency is seen for all drop sizes.

3. DISCUSSION AND INTERPRETATION

3.1 c/r-Dependence

As the "Guttalgor" method [Bächmann et al., 1993] enables us to collect raindrops according to their size we are able to calculate mean collision efficiencies taking all raindrops of one sieve into account. Therefore each value is based on more than 100 single raindrops and represents a high statistic reliability.

The measured c/r-dependencies are in agreement with c/r-dependencies of trace compounds in rain found in former field experiments [Bächmann et al., 1993]. The results show that diffusional effects become stronger for aerosol particles with a radius smaller than 0.4 µm. Their curve shape is a consequence of diffusional effects by small scavenged aerosol particles.

3.2 Collision Efficiencies *E* as a Function of Drop Radius

In Fig.6 we present a comparison between our results, those of Wang and Pruppacher (1977) and Flossmann (1986).

In no case our results show an increase of *E* for drop sizes smaller than 230 µm which Flossmann (1986) and Wang and Pruppacher (1977) found. Taking into account that the concentration *c* is proportional to *E* and the inverse raindrop radius r_D it is not possible to calculate the obtained c/r-dependencies of this experiment by the calculated values of Flossmann (1986).

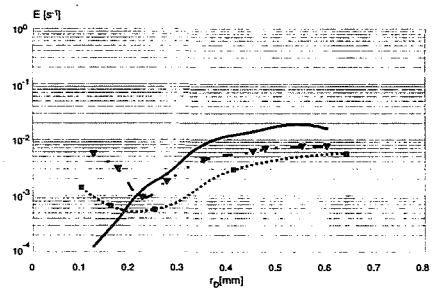

Fig.6: a) our results (r_{AP}: 0.19 µm; RH: 85 %)
b) Wang and Pruppacher (1977)(r_{AP}:0.25µm; RH:23%)
c) Flossmann (1986) (r_{AP}: 0.16 µm; RH: 75 %)

For small raindrops the increase of *E* calculated by theory leads always to an increase in concentration with decreasing drop radius as soon as the collision efficiency starts to increase for drop sizes smaller than 230 µm. Therefore for small particle sizes a c/r-dependence with an increase in concentration for raindrops smaller than 230 µm should arise. Since our results show a concentration maximum and no increase in concentration with decreasing drop radius the model calculations do not match with our results and previous measurements of c/r-dependencies of trace compounds in size classified raindrops [Bächmann et al., 1993]. Our results indicate that the minimum *E* must be at a drop radius smaller than 125 µm. We conclude that certain parameters not yet taken into account by theory are responsible for this discrepancy between theory and field experimental determined collision efficiencies.

For larger aerosol particle sizes we obtain the same curve shapes as Flossmann (1986). Only differences in the mean values for the collision efficiency which get larger the larger the scavenged particle radius becomes were obtained. These discrepancies can be a consequence of the used aerosol particles. The particles consist of di-2-ethylhexy-sebacate (DES). Problems can occur during the scavenging of the particles by raindrops because the density of this oil is smaller than water. This may be the reason for the discrepancies between the results of Flossmann (1986) and ours. Since the influence of impaction scavenging becomes stronger the larger the aerosol particles are the discrepancies for the relative values between theory and our results become stronger the larger the aerosol particles are. For small aerosol particles diffusional or electrical effects dominate the scavenging process. Since we obtain the same curve shapes as theory and only differences in the mean values our above mentioned interpretation for small raindrops is not influenced by this effect.

3.3 Collision Efficiencies λ as a Function of Aerosol Particle Radius

The results for the collision efficiencies λ are in agreement with similar field experiments but do not match with theoretical predictions. We find the minimum λ at a larger aerosol particle radius than theory predicts. The local maximum of the collision efficiency was not reported by theoretical predictions but measured by Volken and Schumann (1993).

The large aerosol particle size showing the minimum λ can be a consequence of the smaller density of the used aerosol particles compared to water. As described in 3.2 our values are to low for larger aerosol particles. Therefore our minimum λ is found at larger aerosol particle sizes. Our results show a bend at a particle radius of 0.8 µm. For this particle radius the minimum λ was measured by other authors.

3.4 Influence of Meteorological Parameters

It is obvious that our field experimental collision efficiencies are in contrast to theory. We find the local maximum at a constant particle size independent of

meteorological parameters as precipitation rate, temperature or relative humidity. Against that Schumann (1989) finds a local maximum scavenging efficiency at different particle sizes. Since both field experiments are done at different meteorological conditions we conclude that all these effects show no influence on the specific particle radius with the local maximum scavenging efficiency. There is only one difference our experiments and those of Schumann (1989). We used synthetic aerosol particles whereas Schumann (1989) measured the washout of atmospheric aerosol particles. Volken and Schumann (1993) concluded that particle shape may play an important role for the scavenging of aerosol particles. We conclude that phoretic forces of raindrops play an important role for below-cloud scavenging processes. Since our particles are uncharged and atmospheric particles may have an electric charge this should be the main difference between Schumann (1989) and our experiments. Electric effects are not negligible in the removal of particles as Schamberger et al. (1990) showed. They reported that for uncharged particles and a charged collector electrostatic torque's can lead to either increase or decrease in the collision efficiency, depending on the collector charge level. Since no in situ measurements of electrical charges of raindrops or aerosol particles have been performed their influence on particle scavenging in this study can not be excluded.

In Fig.4a we pointed out that the results obtained by our experiments with equal aerosol particle size are repeatable. It is obvious that for the equal particle radius the same collision efficiencies are obtained. An exception are the collision efficiencies measured for a particle radius of 1.35 µm radius (Fig.4b). Higher collision efficiencies are obtained for experiment Nr.11 compared to experiment Nr.10 but we found the same curve shapes in both cases. At experiment Nr.10 the rain arises out of stratus clouds. At all other experiments cumulus cloud or an incomplete cloud cover takes place. It seems that the raindrops creation process influences the scavenging processes.

Schumann (1989) pointed out that an increase of phoretic forces of raindrops and/or aerosol particles can be explained by the fact that in winter raindrops reaching the ground are melted a few hundred meters above the ground. These drops may not have reached the ambient temperature and may even be colder than the dewpoint temperature. In this case the thermophoretic forces increase considerably and at dewpoint temperature the diffusiophoretic forces exceed the thermophoretic force. As the rain in our case originates from "cold rain" process - i.e. cloud- droplets are passed through an ice phase stage - an electric charge of the raindrops is possible.

4. SUMMARY

It seems that for small raindrops some processes which have not been taken into account by theory have an important influence on below-cloud particle scavenging. The collision efficiency shows a strong dependence on several parameters which explains the different results of field experiments and theoretical calculations. At the moment these parameters are not totally taken into account by models and can not represent the observed effects of the interaction between aerosol particles and raindrops correctly. Therefore it is necessary to perform further field experiments to get a more detailed data base which allow reliable statistics for new theoretical models.

Acknowledgements - The authors acknowledge the financial support of the Deutsche Forschungsgemeinschaft (DFG) under Project SFB 233 ("Dynamik und Chemie der Hydrometeore") and the team of Prof. H.R. Pruppacher, Dept. Meteorology, Johannes-Gutenberg Universität Mainz, Germany for their helpful suggestions.

5. REFERENCES

Bächmann, K., Haag, I. and Röder, A. (1993) A field study to determine the chemical content of individual raindrops as a function of their size, Atmospheric Environment 27A, 1951-1958.

Flossmann, A. I. (1986) A theoretical investigation of the removal of atmospheric trace constituents by means of a dynamical model, Ph. D. Thesis, Dept. Meteorology, Johan.-Gutenberg-Universität Mainz, Germany.

Schamberger, M. R., Peters, J. E. and Leong, K. H. (1990) Collection of prolate spheroidal aerosol particles by charged spherical collectors, J. Aerosol. Sci. 21, 539-554.

Schumann, T. (1989) Large discrepancies between theoretical and field-determined scavenging coefficients, J. Aerosol Sci. 20, 1159-1162.

Volken, M. and Schumann, T. (1993) A critical review of below-cloud aerosol-scavenging results on Mt. Rigi, Water, Air, Soil Pollution 68, 15-28.

Wang, P.K. and Pruppacher, H.R. (1977) An experimental determination of the efficiency with which aerosol particles are collected by water drops in subsaturated air, J. Atmos. Sci. 34, 1664-1669.

EFFECTS OF CLOUDS COVER IN GAS PHASE CHEMICAL REACTIONS

Wang Tijian

Dept. of Atmos. Sci. ,Nanjing Univ. ,210093,P. R. China

1. INTRODUCTION

Clouds play an important role in gas phase chemical reactions. The clouds cover can make the photodissociation rates of chemical species changed by their influence on solar radiation, therefore, the chemical balance between all reacting species are changed correspondingly. Finally,they will have influence on the conversion rates of transformation of SO_2 and NO_x to H_2SO_4 and HNO_3. This procedure is very important in study of gas phase chemical reactions. In this paper, a parameterization scheme considering effects of clouds cover is adopted based on the CBM—I mechanism (Whritten,1980),and some satisfied results are obtained.

2. GAS PHASE CHEMICAL MECHANISM

The famous CBM — I mechanism was chosen for our work with a few improvements,in which SO_2 oxidation by OH and HO_2 radicals are taken into account and some rate constants are altered according to our experiments so that the mechanism can better describ the transformation process of SO_2 and NO_x. The improved mechanism includes 20 chemical species and 36 reactions.

3. CONSIDERATION OF CLOUDS COVER

There are four photolysis reactions in the mechanism. A parameterization method,which originates from RADM(J. S. Chang,1987) is applied to consider the effect of clouds cover on photodissociation coefficients.

4. CHEMICAL KINETIC SOLVERS

A set of ordinary differential equations describing how the pollutants react chemically are coupled, nonlinear and stiff. The Hybrid (Young and Boris, 1977) scheme,which is a fast solver with high accuracy is applied with a mass conservation technique of redistributing the conservation errors proportionally among various species(Odman,1992).

5. RESULTS AND ANALYSES

5. 1 Photodissociation rate

Photolysis rates of NO_2,HNO_3,H_2O_2,CAR at various conditions are listed in table 1. The cloud depth is set 1000m, condensed water content $1g/m^3$ and solar zenith angle 45° for calculations.

Table 1. Photodissociation rates in clear — sky (s^{-1}) and ratio of cloudy—sky rates to clear—sky ones(%)

species	clear sky	above cloud	in cloud	below cloud
NO_2	2. 99E-1	139	99	54
HNO_2	5. 68E-2	133	99	54
H_2O_2	7. 35E-5	133	99	54
CAR	1. 79E-3	133	99	54

Table 1 shows that,when solar zenith angle is set 45°,the existence of clouds makes the photodissociation rates below clouds decrease 46 percent, above clouds increase 33—39 percent and in clouds decrease only 1 percent. Further calculations indicate that, when solar zenith angle is variated around 45°, dissociation rates decrease below clouds,increase above clouds and either increase or decrease in clouds,depending on solar zenith angle. The reason is that, above clouds, the photodissociation rates increase compared to a clear — sky situation due to reflections from the clouds below. The radiation is efficiently scattered in the clouds. Increased scattering results in a substantial increase in photodissociation rates in the clouds. Below the clouds, where only diffuse radiation will penetrate, photodissociation rates are much lower than corresponding clear—sky rates.

5. 2. Concentration of gas species

In this section,the gas phase chemistry model is integrated for 600 minutes and a hypothesis is made that the life time of the clouds is 120 minutes during the period of intergration. The initial concentrations of gas species are listed in table 2. Fig. 1 gives the variations of concentrations with time for each chemical species.

Fig. 1 shows that,the concentrations of main gas species enhance above clouds,reduce below clouds and

change little in clouds. That is to say, photolysis reactions are strengthened above clouds, weaken below clouds and almost change little in clouds. This is generally consistent with the results in table 1.

The responses from different species to effects of clouds are differet too. The variations of NO and NO_2 concenerations is small although NO_2 is a photodissociation species, which shows that NO_2' s reaction with other nitrogen oxidants are more important than its photolysis reaction. The "windows" in Fig. 1(4)(5)(7)(9) indicate that, during the life time of clouds, concentrations of OH, HO_2, HNO_2, PAN increase above clouds, decrease below clouds and change small in clouds. This variation tendacy distinguished with the disappearance of clouds. But, for O_3, HNO_3, H_2O_2 and hydrocarbon compounds, the effects of clouds will be continuous when clouds are disappeared. All in all, the chemical balance will be transformed because of the existence of clouds and each chemical species responsed differently to clouds cover.

Table 2. Initial concentration for calculations

species	concentration (ppm)
NO	0.075
NO_2	0.025
CO	1.0
HNO_2	0.005
PAR	0.1368
OLE	0.0978
ARO	0.057
CAR	0.086
SO_2	0.1

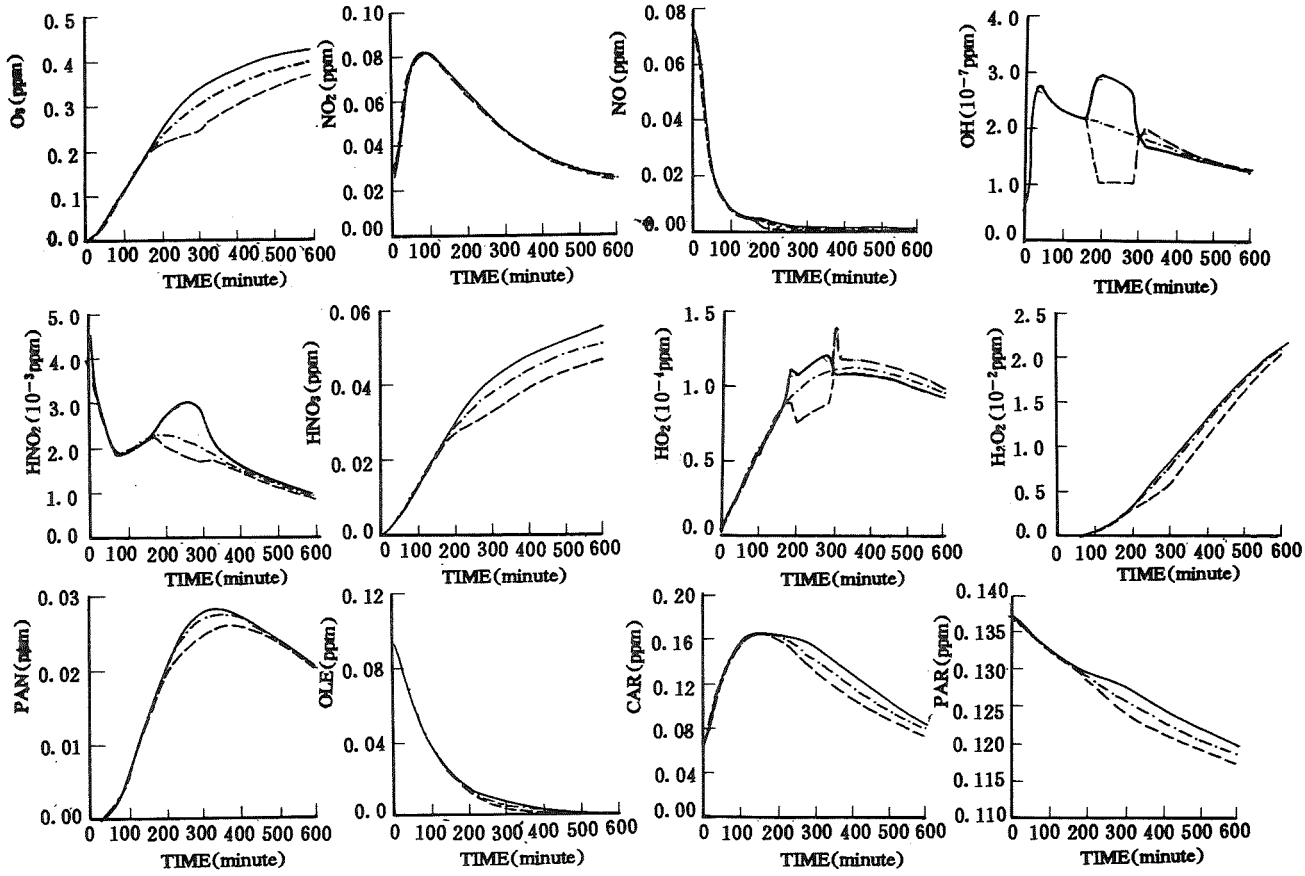

Fig 1. Effects of clouds on concentrations of chemical species
no cloud — above cloud —— in cloud ····· below cloud – – –

5.3 Conversion rate

Conversion rates of SO_2 and NO_x are estimated. The results are listed in table 3.

Table 3 shows that, the average conversion rates of SO_2 and NO_x are 1.5%/hr and 13.8%/hr respectively in clear—sky. When the clouds appear, the conversion rates of SO_2 and NO_x are enhanced above clouds, reduced below clouds and change small in clouds. Further studies show that the variation of conversion rates with

in clear—sky. When the clouds appear, the conversion rates of SO_2 and NO_x are enhanced above clouds, reduced below clouds and change small in clouds. Further studies show that the variation of conversion rates with solar zenith angle in cloudy—sky is similar to that of photodissociation rates with solar zenith angle.

Table 3. Conversion rates of SO_2 and NO_x in day time at different cloud situation (%/hr)

species	no cloud	cloud+			cloud depth*			cloud amount*			condensed water content*		
		above	in	below	5000	3000	1000	10/10	5/10	0/10	10	1	0.1
SO_2	1.46	2.02	1.45	0.77	2.05	2.04	2.02	2.54	2.02	1.46	2.06	2.02	1.77
NO_x	13.83	14.75	13.82	12.02	14.79	14.78	14.75	14.89	14.75	13.83	14.80	14.75	14.39

+ cloud depth 1000m, cloud amount 5/10, condensed water content 1 g/m^3

* conversion rates are calculated above cloud

6. CONCLUSIONS

Based on CBM—I mechanism, SO_2 oxidation by OH and HO_2 radicals is added and influence of clouds on photodissociation rates is parameterized. On the basis of gas phase chemistry model improved, variations on photodissociation rates, concentrations of chemical species and conversion rates of SO_2 and NO_x cloudscover are checked. The following conclusions are obtained.

(1) Both photodissociation rates of NO_2, HNO_2, H_2O_2, CAR and conversion rates of SO_2, NO_x may be enhanced above clouds, reduced while below clouds. In clouds, they may be either enhanced or reduced, depending on solar zenith angle.

(2) The responses of chemical species to clouds cover are nonlinear. The previous chemical balance will be destroyed and a new one will be constructed due to the existence of clouds.

(3) The physical parameters, such as cloud depth, cloud amount, condensed water content in cloud, have some influence on conversion rates. Espeically, it is obvious that clouds amount and condensed water content have significant effects on conversion rate of SO_2.

7. REFERENCES

Jan E. Jonson, 1993: Troposheric ozone chemistry. The impact of cloud chemistry. J. Atmos. Chem., 16 (2), 99—122.

J. S. Chang, 1987: A three—dimensional eulerian acid deposition model: physical concepts and formulation. J. Geophys. Res., 92(D12), 14681—14700.

Mehmet T. Odman, 1992: A comparison of fast chemical kinetic solvers for air quality modeling. Atmos. Environ., 26A(9), 1783—1789.

Whritten G. Z. et al, 1980: The carbon bond mechanism: a condensed kinetic mechanism for photochemical smog. Envir. Sci. Technol., 18, 280—287.

Young T. R. and Boris J. P., 1977: A numerical technique for sloving stiff ordinary differential equations associated with the chemical kinetics of reactive flow problems. J. Phys. Chem., 81, 2424—2427.

ANALYSES OFSEVERALCHEMICAL COMPOSITION OF THE STRATIS IN NORTH ALONG Mt. TIANSHAN IN XINJIANG IN WINTER

Li Bin Shi Wenquan

(Xinjiang Weather Modification Office,Urumqi,Xinjiang,P.R.China)

1.INTRODUCTION

A strong lasting and firm inversion layer often arises in Zhunger Basin and north along Mt.Tianshan in Xinjiang in winter,under which (about 850hpa) is of great advantage to the vapour's accumulation. Moreover,the cold air invades northern Xinjiang from west to east so frequently that there usually are lower clouds and overcast fog and stratis' precipitations in Zhunger Basin and north along Mt. Tianshan in Xinjiang in winter.

The observation of aerosol particles in the lower atmophere in Xinjiang in winter shows that a large number of accmulations of aerosol particles often exist under the strong inversion layer. Especially at the dense industrical and population areas of both sides of Mt. Tianshan , the lower atmosphere pollution is very serious.The main source of these aerosol particles is the smoke given off by industries for production and citizens in cities and towns burning coal for heat. When the lower clouds and overcast fog or the systematic frontal rainfall emerge,the aerosol particles will be absorbed by cloud water or washed out by precipitations. The knomledge of the chemical composition and the concentrations of ions in cloud water is significant to research the pollutant absorption and purges by clouds and precipitations , and the pollutant influence on cloud physics processes and environments.

2.COLLECTION OF CLOUD WATER AND DETERMINATION OF CHEMICAL COMPOSITION

The ice layers which were the cloud water samples were formed at the wings of the aircraft and the heads of PMS measurement instruments by collisions when the artifical snow aircraft flew in the supercooling clouds (They are mainly lower clouds.). These ice layers were taken out and put into a clean plastic bag as soon as the aircraftlanded, then washed down with distilled water indoors and put in another clean bag.After melting, they were loaded in a clean bottle, and then sealed up, kept at lower temperature.

The chemical analyses of all the cloud water samples co-operated with Xinjiang Institute of Environment Protection, chiefly include 5 chemical composition Na^+,K^+,Ca^{++}, Mg^{++} and Ag^+.

3.ANALYSES

3.1 The mean concentrations of ions in the cloud water samples of stratis

The analysis results of the chemical composition of the cloud water of stratis from the mearsurement of 7 flights in winter of 1987, are given in Table 1.By the table we can know that the average concentrations of 5 ions, Na^+,K^+,Ca^{++},Mg^{++} and Ag^{++} differently are 2.46ppm, 2.64ppm, 4.29ppm, 0.97ppm and 0.0018ppm. With different weather conditions, the change ranges of the concentrations of all ions are small. Except Ag^+,the concentrations of the other 4 ions change at the same quantity level.

Table1. The measurement concentrations of ions in cloud water of stratus in winter of 1987 (ppm).

Figures	Na^+	K^+	Ca^{++}	Mg^{++}	Ag^+
Mean	2.46	2.64	4.29	0.97	(0.0018)
Maximum	3.23	4.00	7.81	1.59	0.0048
Minimum	1.94	1.59	1.56	0.41	<0.0002

Comparing the concentrations of Ca^{++} and Mg^{++} in the cloud water samples in winter of 1987 with the measurement of those of the cloud water and the snow water obtained in winter of 1984-1986 (Table 2), we can obtain the following results:

(1). The mean concentrations of ions in the cloud water samples in winter of 1987 are basically identical with those in winter of 1984-1986.

(2).The mean concentrations of Ca^{++} and Mg^{++} in the cloud water samples are slightly higher than those in the snow water samples (In fact they are solid precipitions' samples of stratis.). But the change ranges of the concentrations of Ca^{++}, Mg^{++} in the cloud water samples all are bigger than that in the snow water samples. This indicates that the concentrations of ions in the snow water samples comparatively are quite even with different weather conditions.

Table2.The measurementconcentrations ofions in cloud water samples and in snow watersamples (ppm).

Ions	Cloud water				Snow water	
	Winter of 1987		Winters of 1984-1986		Winters of 1984-1986	
	Measurement	Mean	Measurement	Mean	Measurement	Mean
Ca^{++}	1.56-7.81	4.29	0.95-27.20	8.9	2.83-5.10	4.04
Mg^{++}	0.41-1.59	0.97	0.31-2.14	0.85	0.47-0.85	0.72

3.2 The concentrations of ions in the cloud water with different weather conditions

Depended upon the influence weather systems, the stratis in northern Xinjiang in winter can be classfied into two basic types: frontal clouds and topographic lower clouds. In winter the majorities of frontal clouds are stratis, whose main characteristics are thequick weather processes, the short keeping time,the thicker cloud layer and the several layers structure, but the supercooling clouds generally are lower layers. The topographic lower clouds are St or Sc clouds shaped under the strong inversion in the same air mass (usually at the bottom of a high),which are special topographic clouds in Zhunger Basin and north along Mt.Tianshan in Xinjiang inwinter.Their main characteristics are the thin cloud layer (300-500m), lower altitude (850hpa orso), large ranges,long keeping time and stability.

The analysis results of the chemical composition of the cloud water of stratis in winter of 1987 indicates that the concentrations of Na^{+}, K^{+}, Ca^{++}, and Mg^{++} in the cloud water of the topographic lower clouds are nearly one times higher than those of the frontal clouds (Table 3). This result is consistent with the measurement observed by professor You Laiguang etc. in northern Xinjiang in 1982-1984.

Table3.The mean concentrations ofions in cloud water of different stratis (ppm).

Cloud types	Cloud shapes	Na^{+}	K^{+}	Ca^{++}	Mg^{++}
Topographic lower clouds	St Sc	2.86	4.00	7.42	1.56
Frontal clouds	St Sc Ns	2.30	2.10	3.04	0.73

The observation indicates that the chemical composition and the concentrations ofions in the cloud water of stratis in northern Xinjiang in winter are mainly influenced by local pollution sources. Becouse of low altitude,keeping long time and stability, the topographic lower clouds obviously are subject to the local pollution sources from the earth's surfaces and the layers near the earth.

3.3 The concentrations of ions in cloud water of stratis influenced with different regions and ground layer's features

The sampling areas of the aircraft consisted of three regions: Urumqi(including Miquan, Fukang etc.),the west to Urumqi (from Hutubi to Wusu) and the east to Urumqi (from Jimuser to Mulei).The measurement of the concentrations of ions in the three regions is given in Table 4. The table shows that the mean concentrations of 4 ions in the cloud water in Urumqi region are higher than those in the other regions. This obviously is concerned with the quite dense populations and industries in Urumqi region.

Table4.The mean concentrations of ions in cloud water of stratis in different areas (ppm).

Areas	Na^{+}	K^{+}	Ca^{++}	Mg^{++}
Urumqi	2.62	3.50	6.30	1.33
The west to Urumqi	2.44	2.00	2.60	0.69
The east to Urumqi	2.04	2.00	3.12	0.71

The measurement of the mean concentrations of ions in cloud water of stratis obtained at

different periods and with different ground layer features is listed in Table 5.The table indicates that the concentrations of Na^+,K^+, Ca^{++} and Mg^{++} in the cloud water of stratis sampled in November 9-21 when the erath's surfaces were covered without snow are sharply higher than those sampled in December 16-18 when the earth's surfaces were covered with snow. This proves that the snow covering the earth's surfaces can restrain the diffusion of the silt and dust from the ground layer and reduce the pollution of clouds and the lower atmospheres

Table5. The mean concentrations of ions in cloud water of stratis with snow covering the earth's surface and without snow covering the earth's surface (ppm).

Ground layer qualities	The time of sampling	Na^+	K^+	Ca^{++}	Mg^{++}
Without snow	November,9-21	2.86	4.00	7.42	1.56
With snow	December,16-28	2.30	2.10	3.04	0.73

Depending on these analyses , we can understand that the local factors influencing the concentrations ofions in the cloud water of stratis in northern Xinjiang in winter first are the smoke given off by industries for production and citizens in cities and towns burning coal for heat,second maybe the dust and silt raised from the earth. The snow covering the earth can prevent the ground layer from pollutingthe lower atmospheres and clouds.

4.CONCLUSIONS

Based on above analyses of the chemical composition of stratis in northern Xinjiang in winter of 1987, the following conclusions are obtained

(1).The mean concentrations of 5 ions, Na^+, K^+, Ca^{++}, Mg^{++},Ag^+ in the cloud water of stratis in north Xingjiang in winter differently are 2.46ppm, 2.64ppm, 4.29ppm, 0.97ppm and 0.0018ppm . Except Ag^+ , the concentrations of other ions have a fewer change.

(2).Becouse of low altitude,keeping long time and being stable, the topographic lower clouds are subject to local pollution sources .So the concentrations of Na^+,K^+,Ca^{++} and Mg^{++} in the clouds water of topographic lower clouds are higher than those of frontal clouds.

(3).The local factors which influence the concentrations of the ions in clouds water of stratis in north Xinjiang in winter,first are the smoke given off by industries for production and citizens of cities and towns burning coal for heat, second maybe the dust raised from the bareearth.It isindicated that the snow covering the earth's surfaces can prevent the ground layer from polluting the lower atmophere and cloud layers.

REFERENCES

You Leiguang,and Ma Peimin,1985: The research development of the natural resources for artificial precipitations in northern China.J.Meteor.Sci.Tech.China,9,1-10.

Wan Qian,You Leiguang,and Hu Zhijin,1987: The research of Sc clouds in Urumqi,Xinjiang in winter.J.Meteor.China,45,2-11.

Guan Fuyin, Ma Peimin, and You Leiguang,1986: The research of lower clouds in Zhunger Basin.Documents of National Conference on Cloud Physics and Weather Modification,18-23.

You Leiguang, Lin Yangang,and Li Yanhui,1987: The analyses of the chemical composition and the acid of cloud water and precipitation in Urumqi , Xinjiang in winter. J.Insti.Meteor.China,2,60-65.

MEASUREMENT AND RESEARCH ON CLOUDWATER CHEMISTRY OVER SEVERE ACID RAIN AREAS OF CHINA

SHEN Zhilai, WU Yuxia, HUANG Meiyuan, XIAO Hui, and LEI Henchi

Institute of Atmospheric Physics,Academia Sinica,Beijing,100029

1. INTRODUCTION

Cloud chemistry is one of important parts of environmental sciences and atmospheric chemistry. The measurements of cloudwater chemistry are causing growing concern. It is the purpose of the paper to present some results and discussion of measurements of the cloudwater chemistry in severe acid rain regions of China. Plane was used as sampling platform and two passivity rod-slot cloudwater collectors made in our institute were used for collecting cloudwater[1].

The sampling method was introduced by Shen (1988). The object clouds measured are mostly precipitous stratiform clouds, and the sample altitude is from 1 Km to 4 Km over sea surface.

2.RESULTS AND DISCUSSION

2.1 Acidity of Cloudwater

The acidity of cloudwater in different areas is shown in table 1.

a).In most areas the acidity variation of cloudwater is large with more than one pH unit and even 3.5 pH unit in some places. However, the difference of mean values of pH in different areas is not obvious and no more than one pH unit from 3.86 to 4.86 except for Chongqing area in 1985.

b).The cloudwater has been acidified in severe acid rain regions of China since 1988. The average value of pH is less than 4.9. The annual variation of pH average values is large in some areas, for example,i t has been acidified from the value 6.15 of pH in 1985 to 4.56 in 1989 in Chongqing area.

2.2 Ion Concentrations of Cloudwater

As shown in table 1, the change range of total average ion concentrations of cloudwater is large over severe acid rain regions of China. It is from 164 to 1043 μ eqL^{-1},and the maximum is six times more than the minimum. There is unlinear relationship between total ion concentration and acidity of cloudwater. For example, the ion concentration in Guiyang area is only 64.1μ eqL^{-1} and only a small part of other places, but their acidity is similar. Sulfate($SO_4^=$) is a dominant anion in cloudwater and the ratio of $SO_4^=$ to nitrate(NO_3^-), $SO_4^=/NO_3^-$, is very large from 8.4 to 12.7,such as Southwest of China. The cloudwater is called as sulfuric acid- type, in which the precursor is mainly sulfur dioxide(SO_2).The other kind of cloudwater is called as mixed-type of sulfuric and nitric acid with the ratio of $SO_4^=$ to NO_3^- is nearly one or less than one, in which the precursor is SO_2 and NO_x. Similiar observation of overseas showed that NO_3^- is as importance as $SO_4^=$ in severe acid rain regions.

For example, the ratio of the concentration of $SO_4^=$ to NO_3^- is 1.8(Issac,1987). Ca^{2+} and NH_4^+ are the main cation in cloudwater. The ratio of Ca^{2+} to NH_4^+,Ca^{2+}/NH_4^+ is less than one in LiangGuang and XiangGan regions,but it is more than one in other places.

The concentration of $SO_4^=$ and NO_3^- has been increased from 103. 4 in 1985 to 215.3 μ eqL^{-1} in 1989, about 108 percent. Otherwise, the concentration of NH_4^+ and Ca^{2+} only increased 14 percent from 120.5 to 137.9μ eqL^{-1}, and the concentration of H^+ increased accordingly 26μ eqL^{-1}. In recent years the increase of coal consumption resulted in the raise of emission of SO_2 and NO_X. On the other hand,the emission of smoke decreased because of the more elevated point source. These facts lead to the great variation cloudwater acidity and ion concentrations from 1985 to 1989 over Chongqing area.

2.3. Contribution of process below-cloud to the acidification of cloudwater

The process of acidification can be divided into washout and rainout.In the latter,when raindrops fall from cloud base to the surface, if the acidity of raindrop raises, it is called as acidification process, otherwise called as alkalinized process. Comparing the H^+ and total ion concentrations of cloudwater with those of rain water in table 1, it is easily found that H^+ concentration of rainwater is larger than that of cloudwater in Southwest of China and Guiling area of LiangGuang area. Naturally there is a acidification process. Other measured examples of cloud and rain water collected at the same

Table.1 Average state of chemical composition of cloudwater and rainwater, μeqL^{-1}

Area	Aircraft type	Water type	Range of pH	Mean of pH	NO_3^-	$SO_4^=$	NH_4^+	Ca^{2+}	$\Sigma(+,-)$	$SO_4^=/NO_3^-$	Ca^{2+}/NH_4^+
Chengdu	TwinOtter	Cloud	3.18-6.76	4.58	24.2	306.9	94.6	125.2	785.7	12.7	1.3
(1989)	[8,58]	Rain	3.31-6.99	4.44	30.4	431.5	250.7	192.0	1069.2	14.2	0.8
Chongqing	TwinOtter	Cloud	4.88-7.82	6.15	7.8	95.6	34.1	86.4	425.1	12.3	2.5
(1985)	[7,16]	Rain	3.08-5.18	4.44	19.3	195.2	138.3	87.2	712.1	10.1	0.6
Chongqing	TwinOtter	Cloud	3.17-6.02	4.56	22.9	192.4	40.6	97.3	504.9	8.4	2.4
(1989)	[6,46]	Rain	3.53-4.57	4.03	43.2	421.8	386.6	207.2	1316.8	9.8	0.5
Guiyang	TwinOtter	Cloud	3.40-5.96	4.62	5.3	49.6	0.0	31.9	164.1	9.3	-
(1989)	[5,48]	Rain	3.63-5.76	3.99	9.7	122.4	15.8	36.9	344.7	12.9	2.3
Guilin	Yi-14	Cloud	3.33-5.24	3.89	116.7	127.6	196.3	102.5	891.7	1.1	0.5
Guangzhou	Yi-14	Cloud	3.40-6.27	3.86	97.6	134.3	111.9	46.3	725.6	1.4	0.4
(1988)	[7,47]	Rain	3.43-4.64	4.34	20.6	66.2	46.1	41.3	316.4	3.2	0.9
Nanchang	Yun-12	Cloud	3.36-6.46	4.67	69.8	157.6	163.3	88.5	1043.1	2.3	0.5
(1993)	[8,51]	Rain	4.27-5.13	4.13	17.3	122.9	74.8	32.5	377.3	7.1	0.4
Changsha	Yun-12	Cloud	4.40-5.60	4.86	71.9	254.0	91.7	63.0	775.1	3.5	0.7
(1993)	[3,13]	Rain	4.60-5.39	4.99	10.9	130.0	26.1	37.5	284.3	13.0	1.4

Notice: 1.The numbers in brackets[,] represent the number of flight and the number of samples, respectively
2. $\Sigma(+,-)$ is the total concentration of anion and cation(μ eqL^{-1}),
3. $SO_4^=/NO_3^-$和Ca^{2+}/NH_4^+ are the mean ratio of equivalent concentration,
4.The range of pH and average pH are obtained respectively from all samples and the ion concentration is averaged by the samples which can be enough to be chemical analysis

period also proved this fact. The result of aircraft measurement of pollution gas such as SO_2 and NO_x shows these pollutants almost accumulate in the layer from 600 to 800m in October, 1989 in Chongqing area. The concentrations of H_2O_2 and S(IV) are respectively 19.5μ M and 2.49 mgL^{-1} in cloud water and 0.4μ M and 1.18 mgL^{-1} in rain water. Falling from cloud base to the surface, rain drops absorbed SO_2 below the cloud, then S(IV) is oxidized into S(VI) by aqueous reaction with H_2O_2 , in which S(IV) and H_2O_2 are consumed and $SO_4^=$ in rain water increased. Modeling calculation has proved the result (Liu,1988).

2.4. Influence of cloud microphysical process on cloud and rain water chemistry

In contrast with the result from Southwest area, in Guangzhou of LiangGuang and XiangGan regions these parameters in rainwater are two times less than those in cloud water. One probable reason is that in falling period some soluble substance changed into insoluble ones by chemical reaction and led to the decrease of the ion concentration. The other reason is probably the influence of microphysics processes of cloud and rain. The object clouds measured are mostly mixing cloud of cold and warm or two layer clouds with warm and cold. In cold cloud most ice crystal form and grew from vapor on non-hygroscopic nuclei by sublimation. Furthermore, the ice crystal formed from vapor only by sublimation is very pure[6] . However, cloud-particles condensed from vapor on soluble aerosol particles and obtained a great amount of ion during nucleation process. As a result, the ion concentration in cloud water is more larger not only than the ion concentration of rain in cloud when the rain has formed by classic seeder-feeder mechanism but also than that of rain on surface, although the ion concentration of raindrop increased while falling to the surface. Similar results can be seen in Isaac(1987) and Parungo(1987). Of course, it needs more research to explain the fact that the ion concentration of cloud water is large than that of rain water.

REFERENCE

1.SHEN Zhilai, NING Tianshan, HUANG Meiyuan et al. , A cloud water collector and the brief analysis of some measurements, SCIENTIA ATMOSPHERIC SINICA, 1988,Vol.12,No.1,99-102
2.SHEN Zhilai,WU Yuxia, XIAO Hui et al. , Some basic features of cloudwater chemistry in Southwest China, SCIENTIA ATMOSPHERICA SINICA, 1993,Vol.17,No.1,87-96
3.Isaac G.A.,Daum P. H.,A winter study of air,cloud and precipitation chemistry in Ontario,Canada,Atmos. Environ.,1987,Vol.21,No.7,1587-1600
4.Annual variation of chemical characteristics of cloudwater in Chongqing area, ACTA SCIENTIAE CIRCUMSTANTIAE,1992,VOl.12,No.2,193-199
5.A numerical simulation of the acidification process of rainwater below the cloud and the mechanism of acid rain formation in Chongqing area,SCIENTIA ATMOSPHERICA SINICA(Special Issue),1988,245-257
6.Borys R.D.,Demott P.I.,et al.,The significance of snow crystal andmountain- surface riming to the removal of atmospheric tracedy concentration from cold cloud, Proceeding 4th Con. Precipitation Scavenging,Dry Deposition,and resuspension,Elsevier Press, 1983: 181-189
7.Parungo F.,et al.,A study of the mechanisms of acid rain formation, J.Atmos.Sci., 1987, 44(21):3162-3174

SCAVENGING OF SO_2 AND NH_3 DURING GROWTH OF ICE

G.Santachiara[1], F.Prodi[1,2] and R.Udisti[3]

[1] Institute FISBAT-CNR, Clouds and Precipitation Group, Bologna, Italy

[2] Department of Physics, University of Ferrara, Italy

[3] Department of Public Health and Environmental Analytical Chemistry, University of Florence, Italy

1. INTRODUCTION

Gases and vapours can be scavenged in the atmosphere by different mechanisms, in clouds, during hydrometeor fall or at the ground. Sublimation of water vapour onto growing ice and riming of ice crystals are significant chemical-physical processes involving the removal of gases . Riming occurs commonly in cold clouds, where ice particles have grown large enough to sediment significantly with respect to small cloud drops. Theoretical considerations have shown that riming can increase the concentration of gaseous pollutants in precipitation compared to that forming through diffusional growth (Scott, 1978). Although some studies (Borys *et al.*, 1988; Mitchell and Lamb, 1989) have shown a connection between the degree of riming and the transfer of gaseous species from cloud water to snow, Mitchell and Borys (1992) found that the ratio of gas content in the precipitation to that in cloud water was only slightly correlated to the rimed mass fraction.

The interaction of trace gases (SO_2 , HNO_3, HCl) with ice crystals during their growth from water vapour has been studied in the laboratory (Mitra *et al.*, 1992 ; Santachiara *et al.*, 1995) and in field experiments. At the ground, gases are scavenged by dry deposition on vegetation, on liquid surfaces (sea, lakes, etc.), on snowpacks, by riming of supercooled droplets on obstacle surfaces (e.g. vegetation), adsorption on ice covered ground or during hoarfrost formation. The last of these phenomena occurs on clear nights, while surfaces cool rapidly due to long-wave radiation emission and light winds, that promote cooling by carrying heat away. If the surface temperature cools below 0°C, hoarfrost forms, so gases present in the atmosphere (e.g. SO_2) tend to be incorporated into ice while water vapour diffuses to the surface. Little knowledge is available on the uptake of gases by an ice surface growing through water vapour diffusion as a function of temperature and with the interaction of mixed gases. Thus, an experimental study has been performed in the laboratory in order to increase our knowledge on gas scavenging in the atmosphere.

2. EXPERIMENTAL SET-UP

The core of the experimental device is essentially a rectangular section (5x1 cm) diffusion chamber, 10 cm in length, located in a cold room. An ice surface (0.3 cm thickness) is previously prepared by freezing distilled water on the upper plate and then maintained at -1.0°C. The temperature of the bottom plate is kept constant at the test temperature by an electrically controlled Peltier device. Runs were made at -6.0 and -15.0°C in the present work. Water vapour diffuses from the upper to the bottom plate, while the gases to be inspected for scavenging efficiency flow at about $5x10^{-3}$ m s^{-1}. The gas tested were SO_2 at concentrations

ranging from 0.07 to 6 ppmv and NH_3 from about 0.02 to 5 ppmv , which were supplied in compressed gas-cylinders, with nitrogen as carrier. The concentration was controlled by a calibrating and metering valve.

The SO_2 and NH_3 concentrations at the outlet of diffusion chamber were measured with the gases flowing successively through two bubblers containing 40 cc of 5% H_2O_2 solution and 10^{-2} N of H_2SO_4, respectively. The thick deposit of ice formed by vapour diffusion on the bottom plate (lasting about six hours) was scraped away at the end of each run ; it was then melted, diluted with Milli-Q water and stored in a plastic vessel. A known volume of H_2O_2 solution was added to convert S(IV) to S(VI). The chemical concentrations of S(VI) and NH^+_4 in the samples were analyzed with an ion chromatograph.

3. RESULTS AND DISCUSSION

The SO_2 test data are reported in Fig.1. In our experimental conditions the crystal growth occurs at a nearly constant SO_2 concentration in the diffusion chamber. The absence of sulphate aerosol in the carrier gas is ensured by filtration through an absolute filter.

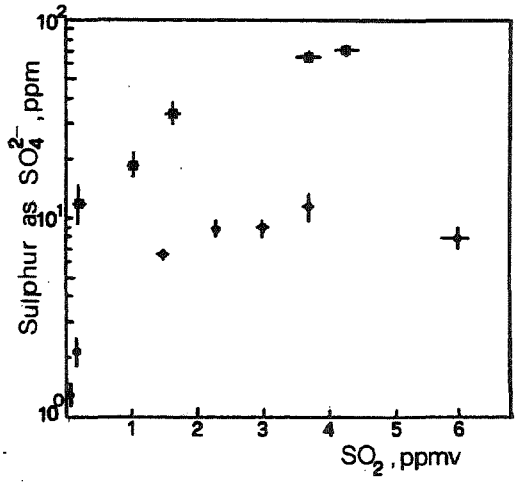

Fig.1. Sulphur as sulphate in the ice as a function of SO_2 concentration in the gas phase: ■ T=-6°C ; ● T=-15°C

At both temperatures (-6.0 and -15.0°C) we observe an increase of sulphur as sulphate within the ice for SO_2 concentrations up to about 3 ppmv. At higher SO_2 concentrations an effect of saturation in the ice-phase is reached. Highest S(VI) concentrations measured at T=-6 and -15°C are about 70 and 10 ppm respectively.

Present values at T=-15°C agree with those obtained in a previous experiment (Santachiara *et al.*, 1995) , in which cloud crystals freely grew in column at T=-13°C, in presence of supercooled droplets, following the Wegener-Bergeron process. In this case SO_2 concentrations in air ranged from 1 to 7 ppmv. We also observe that the SO_2 uptake at -6.0°C is higher than at -15.0°C. Valdez *et al.*(1989) found that SO_2 was captured in deposited ice at -15°C, in concentrations comparable to those given by the SO_2/S(IV) equilibrium at 0°C. While our experiment at T=-6.0 °C confirms this result , in the test at -15°C we find that S(IV) $_{exp.}$ is much lower than the theoretical S(IV) equilibrium value at T=0°C.

Concerning experiments with NH_3 (Fig.2) , in concentrations ranging from about 0.02 to 5 ppmv, we obtain at T=-15°C a mean value of NH^+_4=(0.66±0.42)ppm, regardless of the gas phase concentration. Runs made at T=-6°C give NH^+_4

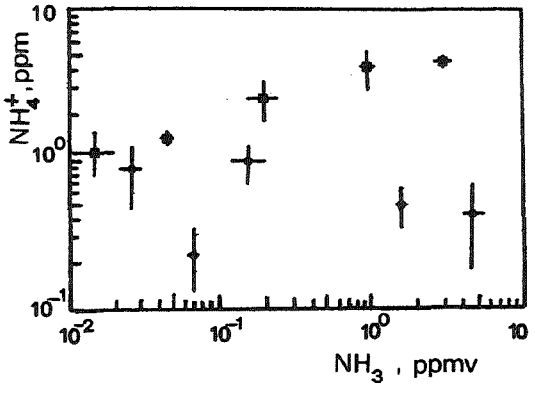

Fig.2 . NH_3 concentration in the gas phase as a function of NH^+_4 in the ice : ■ T=-6°C ; ● T=-15°C

concentrations higher than at T=-15°C and show an increase of NH^+_4 with increasing NH_3. By considering mixed runs at T=-15°C (Fig.3) and -6°C (Fig.4) , we observe an increase in both NH^+_4 and SO_4^{2-} in the ice phase, compared to experiments at the same temperature but with separate gases. We obtain higher values at T=-6°C than with T=-15°C, as in the experiments with separate gases.

To explain these findings, we assume the existence of a liquid-like surface layer during ice-growth, so that water vapour molecules change to ice not directly, but passing through the liquid phase. This film is in equilibrium with water vapour on one side and with bulk ice on the other. It is neither liquid water nor ordinary ice, but a transition film which has thermodynamic properties between those of ice and water. Previous studies on the surface electrical conductivity of ice and gas adsorption (Maeno, 1973 ; Sommerfeld and Lamb, 1986) provide indirect evidence of the presence of a liquid film at the ice-air interface even at temperatures below 0°C. The thickness of this layer is strongly dependent on temperature and the ionic content of ice.

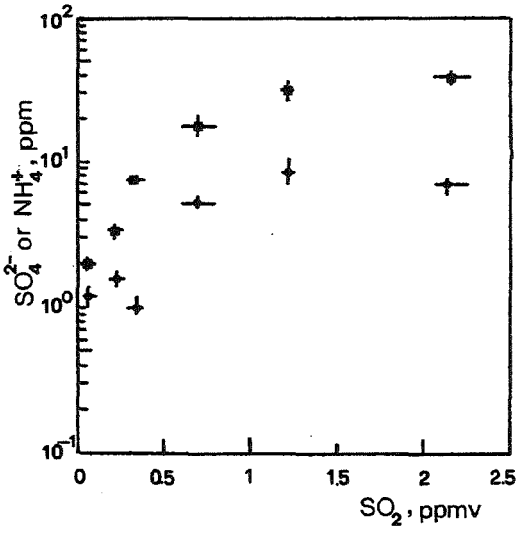

Fig.3. S(VI) or NH^+_4 in the ice phase as a function of SO_2 concentration at T=-15°C : ■ SO_4^{2-} ; ● NH_4^+
NH_3 = (0.12±0.02) ppmv

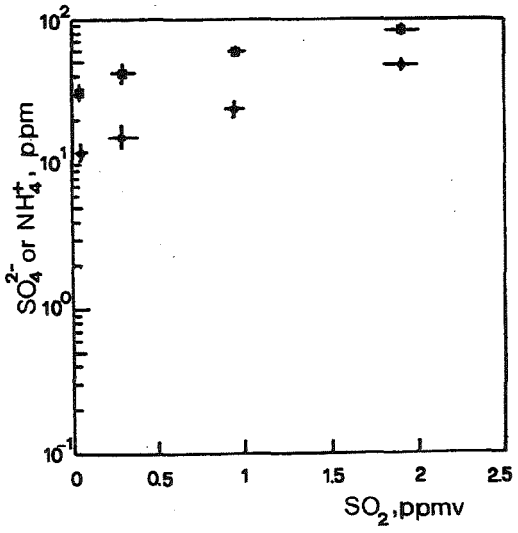

Fig.4. S(VI) or NH^+_4 in the ice phase as a function of SO_2 concentration at T=-6°C : ■ SO_4^{2-} ; ● NH_4^+
NH_3 =(0.10±0.02)ppmv

Experiments on freezing water containing low concentrations of ionizable salts (Workman and Reynolds, 1950 ; Cobb and Gross, 1969) indicate the development of electrical potential across the growing ice interface, due to differentiated incorporation of foreign atoms or ions into the ice lattice. The sign and magnitude of freezing potential depend on the ionic species present, their concentration and freezing rate. The existence of a liquid layer and freezing potential has also been postulated by Finnegan and Pitter (1990) in their experiments on the effects of different solutes in cloud water on ice crystal shape due to vapour diffusion, i.e. a growth similar to our one. As far as our experiments are concerned, NH_3 and SO_2 probably dissolve and ionize in the liquid layer present during ice growth and subsequently move into the ice lattice, with a differentiated incorporation.

Experimental results show that solubility of NH^+_4 in the ice phase is lower than that of S(IV), a behaviour opposite to the one observed in the bulk liquid phase. Previous experiments indicate that the incorporation of ions into the ice depends on several parameters (ion size and electronegativity, pH and counter-ion in

solution, etc). For example, Cobb and Gross (1969) , in experiments with ammonium salts (Chloride, bromide, formate) find that ammonium ion has a greater tendency to enter the solid phase than any anion constituent except fluoride, and that incorporation of NH^+_4 is different for NH_4F and NH_4Cl (influence of counter-ion). Gross *et al.*, 1975 , found for ammonium hydroxide (the compound that is expected to form in the liquid layer in the presence of NH_3), a very sharp ice solubility limit of about $5x10^{-6}$ M and an insignificant freezing potential. Ammonium ice concentrations obtained in our experiments with NH_3 seem to confirm a low ice solubility of NH_4OH.

Experimental results, in showing an increase of NH^+_4 and S(IV) in the ice phase with increasing temperature, can be explained if we take into account that temperature influences liquid-layer thickness, reaction rates and diffusivity of all species present in the transition layer. Thus the transfer of SO_2 and NH_3 from the gas to ice phase can increase with temperature. Experiments with mixed gases (SO_2 and NH_3), showing an increase in both ions NH^+_4 and S(IV) in the ice phase compared to runs made with single gases at the same temperature, indicate that SO_2 and NH_3 infuence each other in term of solubility in the liquid layer and incorporation in the ice. The presence of SO_2 enhances the hydrogen ion content in the transition layer, thus influencing the freezing potential during ice growth, distribution coefficient and ice conductivity .

4. REFERENCES

Borys , R.D., E.E. Hindman, and P.J. Demott, 1988 : The chemical fractionation of atmospheric aerosol as a result of snow crystal formation and growth. *J.Atmos.Chem.*, 7, 213-239.

Cobb, A.W., and G.W.Gross, 1969 : Interfacial electrical effect observed during the freezing of dilute electrolytes in water. *J.Electrochem.Soc.*, **6**, 796-804.

Gross,G.W., Chen-ho Wu, L.Bryant, and C.McKee, 1975 : Concentration dependent solute redistribution at the ice/water phase boundary. II .Experimental investigation. *J.Chem.Physics*, **8**, 3085-3092.

Maeno, N., 1973 :*Proc. Conf. Phys. Chem. Ice*, p.140, Ottawa

Mitchell, D.L., and R.D Borys, 1992 : A field instrument for examining in-cloud scavenging mechanism by snow, in *Precipitation Scavenging and Atmosphere-Surface Exchange*, Vol.I, pp.239-255, edited by S.E.Schwartz and W.G.N.Slinn.

Mitchell, D.L., and D.Lamb, 1989: Influence of riming on the chemical composition of snow in winter orographic storms. *J.Geophys. Res.*, **94**, 14831-14840.

Mitra, S.K., C.Diehl, and H.R.Pruppacher, 1992 : A laboratory study of the uptake of SO_2 and HNO_3 by snow crystals. *11th Int. Conf. on Clouds and Precipitation*, Montreal, pp.851-854.

Pitter, R.L., and W.G.Finnegan, 1990 : An experimental study of effects of soluble salt impurities on ice crystal processes during growth. *Atmos. Res.*,**25**, 71-88.

Santachiara,G., F.Prodi, and F.Vivarelli, 1995 : Scavenging of SO_2 and HCl during growth of ice crystals by vapour diffusion. *Atmos.Environ.*, **9**, 983-987.

Scott , B.C., 1978 : Parameterization of sulfate removal by precipitation. *J.Appl.Meteorol.*, **17**, 1375-1389.

Sommerfeld , R.A., and D.Lamb, 1986: Preliminary measurements of SO_2 adsorbed on ice. *Geophys.Res.Lett.*, **13**, 349-351.

Valdez , M.P., G.E.Dawson, and R.C.Bales, 1989 : Sulfur dioxide incorporation into ice depositing from the vapor. *J.Geophys.Res.*, **94**, 1095-1103.

Workman , E.J., and S.E.Reynolds, 1950 : Electrical phenomena occurring during the freezing of dilute aqueous solution and their possible relationship to thunderstorm electricity. *Phys.Rev.*, **78**, 254-259.

THE EFFECTS OF CLOUD MICROPHYSICAL PARAMETRIZATION ON MODEL PREDICTIONS OF GAS SCAVENGING BY WARM CONVECTIVE CLOUDS

Sabine Wurzler

Institut für Physik der Atmosphäre, Johannes Gutenberg-Universität Mainz, Germany

1. INTRODUCTION

The dynamic, microphysical, gas and particle scavenging processes of clouds are very complicated. Even the interactions of the known processes are an enormeous challenge for modelling purposes. Thus, it must be appreciated that all models include some kind of simplifications. Cloud microphysics are often parameterized in long range transport models, which address among other topics the problem of acid deposition (Hegg and Larson, 1990). Anthropogenic aerosols and trace gases contribute to enhanced shortwave cloud radiative forcing, but even the most detailed of the present climate models can represent cloud microphysical processes only in a highly parameterized manner, if at all (Schwartz and Slingo, 1996). In many models monodisperse cloud drop spectra with radii of 5 or 10 μm were assumed (Wurzler, 1995). More detailed approaches are still restricted by the computer resources available. It is well known from field experiments, laboratory studies and model studies, that the scavenging of gases and particles proceeds drop size dependent. This arises the question, if, and to what extent, the scavenging behaviour of models and, thus, all related processes are influenced by cloud microphysical parametrizations. Hegg and Larson (1990) compared the predictions of the sulfate production in a bulk model to those of a more explicit model and found a higher sulfate production in the explicit model. The scavenging of HNO_3 proceeds quite differently than the scavenging of sulfur compounds (Wurzler et al., 1995). This encouraged to study the behaviour of HNO_3 scavenging by cloud drops by employing an air parcel model (Wurzler et al., 1995) as well as a dynamic 2D–cloudmodel with explicit and with parameterized cloud microphysics (Wurzler, 1995). The cloud parcel model was employed to estimate the extent to which the scavenging behavior of nitrate is influenced by the treatment of cloud microphysics. With the 2D–model an estimate for a marine situation was tried in order to find out to which extent the different developement of a numerical cloud with parameterized and with detailed microphysics influences the scavenging of HNO_3 and, thus, the wet deposition.

2. THE CLOUD MODELS

The air parcel model including explicit microphysics has been discussed in detail by Flossmann et al. (1985). In order to guarantee the same environmental conditions and to exclude dynamic or other effects derived from the parametrization, the bulk liquid water content obtained by our model with detailed microphysics was assigned to monodisperse drop size populations. This guarantees the same liquid water content and the same amount of HNO_3 available for scavenging in the detailed as well as in the parameterized case.

The basic dynamic frame work of the two-dimensional cloud model is a slab-symmetric version of the three-dimensional cloud model of Clark (1977,1979), Clark and Gall (1982), Clark and Farley (1984) and Hall (1980). The detailed microphysical processes are incorporated into this two dimensional, anelastic dynamic frame work in the manner described by Flossmann and Pruppacher (1988).

The air parcel model and the 2D–model have been extended to the scavenging of HNO_3 by Wurzler et al (1995) and Wurzler (1995). In the models with detailed microphysics, HNO_3 gas and two aerosol particle types are assumed, whose size distribution change with time due to activation to drops, impaction on drops and entrainment. The nucleation scavenging and condensational growth of the aerosol particles considered and their scavenging by drops are described by the relations given in Flossmann et al. (1985) and Flossmann (1991). The size distribution of the corresponding cloud drops changes in time due to condensation, evaporation, collision and coalescence, and break–up. The concentration of the gaseous species is assumed to change in concentration with time by mass transport to and into the drops and by mixing with environmental air. The model follows the aerosol particle mass and gas mass inside each drop size category in time as materials are scavenged and re–distributed inside the changing drop size spectrum.

The uptake and redistribution of HNO_3 by drops inside a warm convective cloud with explicit microphysics has been considered in detail by Wurzler et al. (1995) and Wurzler (1995). The mass transport of nitric acid from the gas phase to the solution droplets is described by

$$\frac{d[N(V)]}{dt} = \frac{k_{mt}}{R^*T} \cdot (p_{HNO_3,\infty} - p_{HNO_3,S}) \cdot F_g \quad (1)$$

with:

$$k_{mt} = \left(\frac{a^2}{3D_g \cdot F_g} + \frac{4a}{3\bar{v}\alpha} \right)^{-1} \quad (2)$$

where k_{mt} is the mass transfer rate coefficient that incorporates interfacial and gas phase mass transport, $p_{HNO_3,\infty}$ is the partial pressure of nitric acid in the bulk gas phase of the cloud, $p_{HNO_3,S}$ is the nitric acid partial pressure in equilibrium with the aqueous phase concentration and F_g is the ventilation coefficient for HNO_3. R^* is the universal gas constant and T is the temperature. a is the drop radius, D_g the gas-phase diffusion coefficient, $\bar{v}$ the mean molecular speed and α the mass accomodation coefficient. The drops were considered to be well mixed. The HNO_3 uptake by the drops was calculated for the detailed microphysics as well as for the parametrizations time dependent according to Eq. (1).

3. INITIAL CONDITIONS

We have chosen marine situations as initial conditions. As in Flossmann et al.(1985) the temperature and humidity distribution assumed for the simulation with the air parcel model were those used by Lee et al.(1980). For the simulation with the 2D–cloud model the vertical temperature and humidity profile of September 22nd 1991 observed by Schulz and Larson (1992) over the North Sea was assumed. For the marine aerosol particle size distribution a fit (Wurzler et al, 1995) to a marine distribution observed by Hoppel et al.(1990) was chosen. Particles in the submicrometer size range were assumed to consist of $(NH_4)_2SO_4$ while the particles in the size range above 1 μm were assumed to consist of sea salt. The size dependent decrease of the aerosol particles with height, was described by exponential vertical profiles with different scale heights. The submicrometer particles were assumed to have a scale height of 5 km and the particles covering mainly the size range above 1 μm were assumed to have a scale height of 3 km. The concentration of HNO_3 in the air was assumed to be 0.5ppb(v) and to decrease with height as the total air pressure. For the mass transfer coefficient a mass accomodation coefficient α of 0.1 (J.L.Ponche, 1993) was chosen.

4. RESULTS AND CONCLUSIONS

Air parcel model results:

Fig. 1 displays the increase of the liquid water content inside the model cloud due to condensation.

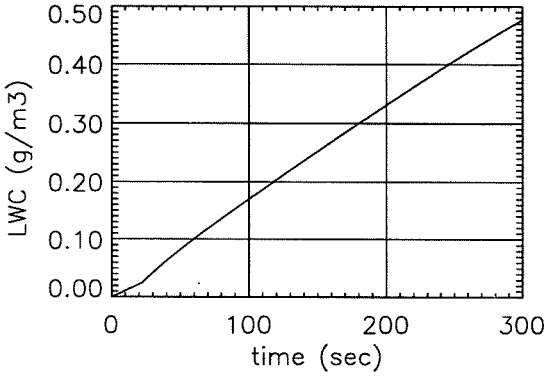

Fig. 1: Time evolution of the bulk liquid water content LWC in the parcel model.

The HNO_3 scavenging by the monodisperse drop size populations was calculated for drop radii ranging from 1 μm to 10 μm. Fig.2 displays the time evolution of the percentage of the HNO_3 mass scavenged by the monodisperse drop populations in comparison to the HNO_3 mass scavenged by the drop population with explicit microphysics.

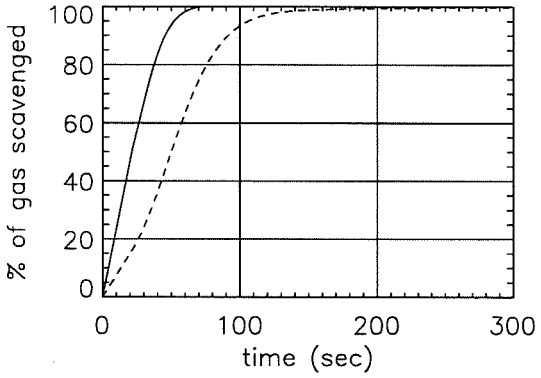

Fig. 2: Time evolution of the percentage of the HNO_3 mass scavenged by the monodisperse drop populations with radii of 5 μm (solid line) and 10 μm (dashed line) in comparison to the HNO_3 mass scavenged by the drop population with explicit microphysics in the parcel model

A monodisperse drop population with an assumed drop radius of $a = 1\mu m$ has scavenged at the same time the same amount of gas as the detailed drop spectrum. This is obvious because in the model with the detailed microphysics all cloud drops have originated from very small drops with radii in the range of 1 μm, due to the nucleation of aerosol particles to drops. We also see from Fig. 2 that the gas uptake becomes slower with increasing radius chosen for the monodisperse drop population. The drop population with $a = 5\mu m$ has scavenged after 70 seconds of modelling time the same amount which the de-

tailed model had already scavenged after 8 seconds. The population with $a = 10\mu m$ has scavenged about 270 seconds later the same amount of HNO_3 as the detailed drop population. This behaviour can be explained by the inverse drop radius dependency of the mass transfer coefficient k_{mt}, which is defined in Eq. (2). This implies that the larger the drop size the slower the mass transfer, as predicted by Levine and Schwartz (1982). Please note, that these time delays are direct results of the assumption that all drops present in the parameterized model cloud are of the same size.

2D–model results:

Comparison of the results of the detailed model and the parameterized solution revealed that the parameterized model cloud developed, rained but also dissipated faster than the detailed model cloud. The lifetime of the parameterized cloud was approximately 30 % lower than the lifetime of the detailed model cloud. In addition, the parameterized model predicted a 50 % lower water mass deposited as rain on the ground than the detailed model. In a previous study with the detailed model (Wurzler, 1995) has been demonstrated that approximately 50 % of the HNO_3 gas mass scavenged by the cloud is deposited with the rain on the ground. This is about 20 % of the total HNO_3 mass transported trough the cloud. The parameterized model predicted that approximately 15 % of the total HNO_3 mass transported through the cloud is deposited with the rain on the ground. Comparison of the gas scavenging and wet deposition behaviour of both models reveals that the parameterized model removed approximated 60 % less HNO_3 from the atmosphere and, thus, underestimates the wet deposition of gases.

Summarizing we found that the gas uptake proceeds slower in the parameterized model than in the model with detailed micropysics. A delay of approximately 70–270 seconds in the gas scavenging for average drops sizes of 5–10 μm, which are in general employed in parameterized models, does not seem to be much, but has certainly a serious impact on the gas scavenging behaviour of a cloud. In a rapidly developing cumulus cloud with high updraft velocities the location of a cloud drop can change in this time span from near the cloud border to the center of the cloud. In the center of the cloud the gas reservoir of highly soluble gases like HNO_3 has already been depleted (Wurzler, 1995). Therefore the gas concentration of the drop will stay too low. The result is an underestimation of the wet removal of HNO_3 and presumably all other highly soluble gases. Hegg and Larson (1990) compared results of an explicit cloud chemistry parameterization with corresponding predictions of a bulk chemistry model for the scavenging of SO_2 and H_2O_2. They found that the aqueous concentrations found with the bulk model are 3–30 times lower than the aqueous concentrations predicted by the explicit model. Combining these findings with the results of the present study, we may conclude that in comparison to models including detailed microphysics, the parameterized models are straggelers in the gas scavenging and that the gas mass scavenged as well as the wet deposition of scavenged gases is presumably underestimated by all parameterized models. These effects of cloud microphysical parametrizations will certainly also affect predictions of acid deposition by long range transport models and of the influence of scavenged gases on cloud radiative forcing by climate models.

ACKNOWLEDGEMENTS

Fundings for the present study were provided by the Johannes Gutenberg–University in collaboration with the SFB 233 and, thus, by the DFG. The computer capacity for the 2D-model has been provided by the HLRZ, Forschungszentrum Jülich.

REFERENCES

Clark, T.L., and R.D.Farley, 1984: Severe downslope windstorm calculations in two and three spatial dimensions using anelastic interactive grid nesting. *J. Atmos. Sci.*, **41**, 329–350.

Clark, T.L. and R.Gall, 1982: Three dimensional numeric model simulations of air flow over mountainous terrain: A comparison with observation. *Mon. Wea. Rev.*, **110**, 766–791.

Clark, T.L., 1979: Numerical simulations with a three dimensional cloud model. *J. Atmos. Sci.*, **36**, 2191–2215.

Clark, T.L., 1977: A small scale dynamic model using a terrain–following coordinate transformation. *J. Comput. Phys.*, **24**, 186–215.

Flossmann, A.I., 1991: The scavenging of two different types of marine aerosol particles calculated using a two–dimensional detailed cloud model. *Tellus*, **43B**, 301-321.

Flossmann, A.I. and H.R. Pruppacher, 1988: A theoretical study of the wet removal of atmospheric pollutants. Part III: The uptake, redistribution of $(NH_4)_2SO_4$ particles by a convective cloud using a two–dimensional detailed cloud model. *J. Atmos. Sci.*, **45**, 1857-1871.

Flossmann, A.I., W.D. Hall, and H.R. Pruppacher, 1985: A theoretical study of the wet removal of atmospheric pollutants. Part I: The redistribution of aerosol particles captured through nucleations and impaction scavenging by growing cloud drops. *J. Atmos. Sci.*, **42**, 582-606.

Hall, W.D., 1980: A detailed microphysical model within a two–dimensional dynamic framework: model description and preliminary results. *J. Atmos. Sci.*, **37**, 2486–2507.

Hegg, D.A., and T.V. Larson, 1989: The effects of microphysical parameterization on model predictions of sulfate production in clouds. *Tellus* **42B**, 272-284.

Hoppel, W.A., J.W. Fitzgerald, G.M. Frick, R.E. Larson, and E.J. Mack, 1990: Aerosol Size distributions and optical properties found in the marine boundary layer over the atlantic ocean. *J. Geophys. Res.*, **95**, 3659–3686.

Lee, I.Y., G. Hänel, and H.R. Pruppacher, 1980: A numerical determination of the evolution of cloud drop spectra due to condensation on natural aerosol particles. *J. Atmos. Sci.*, **37**, 1839–1853.

Levine, Z.S., and S.E. Schwartz, 1982: In–cloud and below–cloud scavenging of nitric acid and acid vapor. *Atmos. Environ.*, **16**, 1725–1734.

Ponche, J.L., Ch. George, Ph. Mirabel, 1993: Mass transfer at the air/water interface: Mass accomodation coefficients of SO_2, HNO_3 and NH_3. *J. Atmos. Chem.*, **16**, 1–21.

Schulz, M. and S. Larsen, 1992: Overview of the meteorological conditions during the North Sea experiment 1991. in: *NOSE-report to The Department of the Environment.*, School of Environmental Sciences, UEA, Norwich NR4 7TJ.

Schwartz, S.E. and A. Slingo, 1996: Enhanced shortwave radiative forcing due to anthropogenic aerosols. *NATO ASI Series*, Vol. I 35, *Clouds, Chemistry, Climate. Springer-Verlag Berlin Heidelberg*, 191-236.

Wurzler, S., A.I. Flossmann, H.R. Pruppacher and S.E. Schwartz, 1995: The scavenging of nitrate by clouds and precipitation: I. A theoretical study of the uptake and redistribution of $NaNO_3$ particles and HNO_3 gas by growing cloud drops using an entraining air parcel model. *J. of Atm. Chem.* 20, 259-280

Wurzler, S., 1995: The scavenging and wet deposition of nitrogen compounds by a warm convective cloud using two cloud dynamic models. PhD-Thesis, *Shaker Verlag Aachen, Berichte aus der Physik*, 160 pp.

Perturbation Induced by Clouds on Ozone Diurnal Variations in the Marine Boundary Layer over the Indian Ocean: Measurements and Simulations.

P. J. BREMAUD,[1] A. M. THOMPSON,[2] F. TAUPIN,[1] AND N. CHAUMERLIAC[3]

[1] Laboratoire de Physique de l'Atmosphère, Université de la Réunion, Saint-Denis, Ile de la Réunion, France.
[2] NASA Goddard Space Flight Center, Greenbelt, Maryland, USA.
[3] Laboratoire de Météorologie Physique, Université Blaise Pascal-CNRS, Clermont-Ferrand, France.

1. INTRODUCTION

At Réunion Island (21.5° South, 55° East), during austral winter we observe a strong temperature inversion marking the top of the marine boundary layer, which is characterized by an elevated relative humidity and a low concentration of ozone. During the day the warming of the air combined with the interaction between trade winds and mountains leads to the formation of a cloud layer, which has a critical impact on the diurnal cycle of ozone in the marine boundary layer. This impact can take place through many forms:

1-These clouds perturb the radiation field and then modify the photolysis rate of the key reactions governing the ozone concentration.

2-The presence of clouds reduces the diurnal variation of temperature and then modifies many reaction rates which are temperature dependent.

3-Through the aqueous phase the gas phase equilibrium is perturbed since many trace gases are highly soluble.

4-The clouds act directly in the exchange between the ozone-rich free troposphere and the ozone-poor marine boundary layer.

Here we present the relative importance of each of these influences on the diurnal cycle of ozone in the marine boundary layer using a OD time dependent model. In order to support the results of the simulations, measurements of diurnal variations of ozone concentration are presented.

2. MODEL DESCRIPTION

We use a time-dependent box model in order to simulate the photochemistry of the marine boundary layer. This model describes the oxidation chains of carbon monoxide and methane in the presence of N_xO_y and H_xO_y gaseous species (Brémaud *et al.*, 1996) and includes also the aqueous phase using the Edy *et al.* (1996) reaction scheme with the reaction $N_2O_5+H_2O \rightarrow 2HNO_3$ in addition. In these reaction schemes sulfur chemistry has been excluded as well as the chemistry of NMHCs since their total concentration is expected to be small for pristine oceanic air. But we simulate the chemistry of formic acid since it has been identified as an important acid for remote locations and in cloudy conditions.

In order to calculate photodissociation rates of each photoactive molecule (the J value) we use a photochemistry model developped by Madronich (1987). For our location of interest photodissociation rates are calculated using the date of the beginning of the simulation, i.e. October 10, 1992, and the latitude and longitude of Réunion Island (21°South, 55°East). Both clear sky and cloudy conditions are examined, and the radiation calculation includes an above-troposphere total ozone column of 270 Dobson Units (DU), routinely obtained using a Zenithal Observations Analysis Spectrometer (SAOZ) installed at Réunion Island, and a sea surface albedo of 0.07, a value characteristic of water surfaces (Jacob, 1986).

Since several reaction rate coefficients are temperature dependent we have simulated a diurnal cycle of temperature with a minimum of 282K just before sunset and a maximum of 291K at the beginning of the afternoon in clear sky conditions. Under cloudy conditions the temperature is assumed to be constant at 289K.

Table 1 shows the gaseous concentrations of the chemical species assumed by the model. These concentrations are those observed on TRACE-A flight number 11 near 23° south latitude (Heikes *et al.*, 1996). They are assumed to be pertinent to study the photochemistry at Réunion Island (Brémaud *et al.*, 1996). In order to simulate these concentrations different sources and sinks are defined. Thus sea surface deposition is assumed for all species except for CO and NO and the radicals OH, HO_2, and CH_3O_2, which are considered to be in photochemical equilibrium. The deposition velocities that we use are those described by Thompson and Zafiriou (1983). Besides a first order rate coefficient corresponding to rainout and particulate removal is assumed for H_2O_2, CH_2O, CH_3O_2H, HNO_3, and HCO_2H. We consider an oceanic source for NO, whose flux is equal to 2.5×10^8 molecules cm^{-2} s^{-1} (diurnally averaged) if we assume a mixing layer of 1.5 km during the night and 2.0 km during the day. For carbon monoxide the usually weak oceanic source is negligible relative to the free tropospheric one. Indeed, in our simulations the exchange between the free troposphere and the marine boundary layer is fundamental in order to reproduce the observed concentrations. The origin of this exchange is discussed in the following part.

Table 1. Model conditions:

Species	TRACE-A Observed Mixing Ratio
O_3	28-31 ppbv
H_2O_2	0.9-1.4 ppbv
NO	3.0-4.5 pptv
HNO_3	160-200 pptv
HCO_2H	0.34-0.68 ppbv
CO	67-74 ppbv
CH_2O	130-160 pptv
CH_3O_2H	0.71-0.73 ppbv

Regarding the aqueous phase we will focus on the chemistry of a remote marine tropical orographic cloud, which in addition do not precipitate. This cloud is assumed to develop between 1500 meters and 2000 meters high in agreement with local observations. As Grégoire *et al.* (1994), Jacob (1986), Chameides (1984) and Lelieveld and Crutzen (1991) do, we consider a monodisperse chemically homogeneous distribution of droplets having a radius equal to 10 μm. We assumed that the studied cloud is characterized by a low level of turbulence and fairly constant liquid water content and temperature. So we deduce a 0.5 gm^{-3} LWC and a 289 K temperature inside the whole cloud from our soundings.

3. RESULTS AND DISCUSSIONS

The base of this discussion is Figure 1 which represents the diurnal variations of ozone gaseous concentration both measured near the

coast of Réunion Island (dashed line) and simulated using only the gaseous reaction scheme (solid line). Our measurements show a clear diurnal cycle of ozone concentration with a maximum near sunrise, a minimum in late afternoon and a diurnal variation of approximately 4 ppbv. Such a diurnal cycle has already been observed over the Indian ocean by Johnson *et al.* (1990) during the SAGA 87 Indian cruise. The key point in order to reproduce this diurnal variation of concentration is the vertical exchange between the lower free troposphere and the marine boundary layer (Brémaud *et al.*, 1996). We use a daytime entrainment velocity of 1 mm s^{-1} comparable with the those deduced by Kawa and Pearson (1989) during the day and under cloudy conditions, and a nighttime entrainment velocity of 14 mm s^{-1}. Thus both the ozone nighttime recovery and daytime photochemical destruction are simulated well.

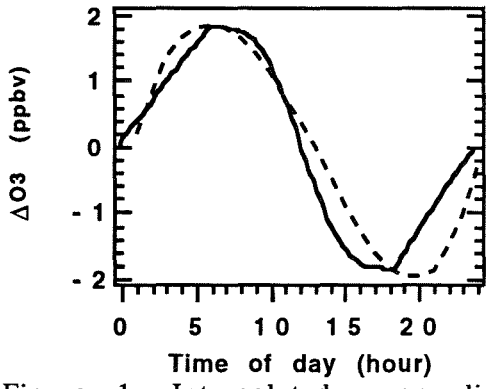

Figure 1: Interpolated mean diurnal variation of measured concentration of ozone (dashed line); Simulated diurnal variation of ozone concentration (solid line).

Since clouds are present during most of the daytime on the slopes of Réunion Island, the question is: what is the influence of clouds on the diurnal cycle of ozone concentration? The meteorological conditions leading to the formation or the dissipation of clouds observed in the northern part of Réunion Island, where the measurements of ozone were done, are characterized by a sea breeze during the day and a land breeze during the night embedded within trade winds. Then during the day the sea breeze forces the air to go up along the slopes allowing the formation of clouds between the condensation level (1.5 km high approximately) and the top of the marine boundary layer, i. e. 2.0 km. At their levels these clouds have two major influences. First they greatly limit the exchange between the lower free troposphere and the marine boundary layer. Indeed, Betts and Boers (1990) suggest that vertical mixing across the inversion should be more efficient in clear sky conditions than in cloudy conditions. This is due to a gradual temperature inversion in clear sky conditions versus a sharp one in the presence of clouds due to the enhancement of turbulence in the upper part of the boundary layer. A decrease of the potential temperature gradient below the inversion results from this mixing, leading to sharp temperature jumps at the inversion (Paluch and Lenschow, 1991).

Moreover through the aqueous phase ozone is destroyed in great quantities as highlighted by Lelieveld and Crutzen (1991), who estimated that the ozone destruction in NO_X-poor regions (such as Réunion Island) can be enhanced by a factor 1.7 to 3.7, especially in the tropics. Thus our simulations show that this enhancement factor of ozone destruction is 3.5.

Nevertheless, below the clouds the photolysis rates are greatly reduced. The photolytic destruction of ozone is less efficient (Thompson, 1984). Thus below our 500 meter thick cloud we simulate a 2 ppbv destruction of ozone against the 4 ppbv in clear sky conditions. But this influence is spatially limited since the orographic clouds generally observed do not extend horizontally as far as the vertical of the coast.

In our simulations the modification of temperature induced by the presence of clouds is negligible relative to the other perturbations for the diurnal cycle of ozone.

4. CONCLUSION

The diurnal cycle of ozone concentration in the marine boundary layer at Réunion Island is

critically dependent on dynamical aspects related to the high mountains. This dynamic leads to the formation of clouds on the slopes of the mountains. These clouds influence directly the variation of ozone concentration mainly by limiting the exchange between the lower free troposphere and the marine boundary layer. But they equally modify the ozone concentration in the marine boundary layer through the aqueous phase since the air going up along the slopes penetrates into the clouds. Then ozone, after being passed below the clouds where it is less destroyed, is greatly destroyed into the clouds. The evaluation of the exact impact of this process on the diurnal cycle of ozone concentration requires 2D simulations taking into account both dynamical and chemical aspects. This will be the goal of our next study.

5. ACKNOWLEDGEMENTS

We are indebted to Drs. J. Leveau and S. Baldy for their confidence and their support. The edition of this extended abstract owes much to Thierry Portafaix.

6. REFERENCES

Betts, A. K., and R. Boers, 1990: A cloudiness transition in a marine boundary layer, *J. Atmos. Sci.*, **47**, 1480-1497.

Brémaud, P. J., F. Taupin, A. M. Thompson, and N. Chaumerliac, 1996: Ozone nighttime recovery in the marine boundary layer over the Indian ocean: measurements and simulated influence on ozone diurnal cycle, *submitted to J. Geophys. Res.*

Chameides, W. L., 1984: The photochemistry of a remote marine stratiform cloud, *J. Geophys. Res.*, **89**, 4739-4755.

Edy, J., S. Cautenet, and P. Brémaud, 1996: Modeling ozone and carbon monoxide redistribution by shallow convection over the Amazonian rain forest, *submitted to J. Geophys. Res.*

Grégoire, P. J., N. Chaumerliac, and E. C. Nickerson, 1994: Impact of cloud dynamics on tropospheric chemistry: advances in modeling the interactions between microphysical and chemical processes, *J. Atmos. Chem.*, **18**, 247-266.

Heikes, B., M. Lee, D. Jacob, R. Talbot, J. Bradshaw, H. Singh, D. Blake, B. Anderson, H. Fuelberg, A. M. Thompson, 1996: Ozone, hydroperoxides, oxides of nitrogen, and hydrocarbon budgets in the marine boundary layer over the south Atlantic, *to be published* in *J. Geophys. Res.*

Jacob, D. J., 1986: Chemistry of OH in remote clouds and its role in the production of formic acid and peroxymonosulfate, *J. Geophys. Res.*, **91**, 9807-9826.

Johnson, J. E., R. H. Gammon, J. Larsen, T. S. Bates, S. J. Oltmans, and J. C. Farmer, 1990: Ozone in the marine boundary layer over the Pacific and Indian Oceans: latitudinal gradients and diurnal cycles, *J. Geophys. Res.*, **95**, 11, 847-11,856.

Kawa, S. R., and R. Pearson, Jr., 1989: An observational study of stratocumulus entrainment and thermodynamics, *J. Atmos. Sci.*, **46**, 2649-2661.

Lelieveld, J., and P. J. Crutzen, 1991: The role of clouds in tropospheric photochemistry, *J. Atmos. Chem.*, **12**, 229-267.

Madronich, S., 1987: Photodissociation in the atmosphere, 1. actinic flux and the effects of ground reflections and clouds, *J. Geophys. Res.*, **92**, 9740-9752.

Paluch, I. R., D. H. Lenschow, 1991: Stratiform cloud formation in the marine boundary layer, *J. Atmos. Sci.*, **48**, 2141-2158.

Thompson, A. M., 1984: The effect of clouds on photolysis rates and ozone formation in the unpolluted troposphere, *J. Geophys. Res.*, **89**, 1341-1349.

Thompson, A. M., and O. C. Zafiriou, 1983: Air-sea fluxes of transient atmospheric species, *J. Geophys. Res.*, **88**, 6696-6708.

SCAVENGING ALONG A MOUNTAIN SLOPE: EXPERIMENTAL AND MODEL COMPARISON

J. ORB, J. STAEHELIN AND A. WALDVOGEL

Inst. Atmospheric Science, ETH Hönggerberg, 8093 Zürich, Switzerland

1. INTRODUCTION

Cloud and precipitation chemistry are strongly related to microphysical processes. At the initial stage of the cloud, nucleation scavenging of heterogeneous cloud condensation nuclei (CCN) generates droplets both varying in size and chemical composition. Different sizes of droplets once formed influence the droplet's chemistry (e.g. by means of size-dependent uptake of gases of the interstitial gas phase).

Not only microphysics affects cloud chemistry, also the reverse is true. Condensational growth for example depends on the droplet solute concentration. The vapour pressure over a solute is lower than over a droplet of pure water of the same size. Highly concentrated droplets tend to grow faster and shrink slower than more diluted of the same size and at the same thermodynamical conditions.

These coupled cloud-forming processes lead to strong chemical heterogeneities within the cloud. Several authors (Twohy *et al.*, 1989; Ogren and Charlson, 1992) pointed out, that not only the droplet's chemistry is varying with size (which can be accented by condensation), but it can also vary in concentration and composition from droplet to droplet within the same size. This is due to the fact that drops grow up on internal and external mixed CCN. Obviously the simplifying point of view that clouds are an accumulation of liquid water in the atmosphere transforming aerosols to precipitation chemistry cannot be maintained (Hegg and Larson,1990; Pandis *et al.*,1990).

The once formed heterogeneities in clouds can even be accentuated by the formation of precipitation. Precipitation formation in mid-latitudes is mainly controlled by the BERGERON-FINDEISEN-process. Ice crystals grow at the expense of liquid cloud particles. Since the equilibrium vapour pressure of ice is for negative temperatures (in °C) lower than that of liquid water, cloud droplets evaporate while water vapour condensates on ice crystals. This process causes low pollutant concentrations in ice crystals while concentrations in cloud droplets remain large. Hence the precipitation formed by the BERGERON-FINDEISEN-process tends to low pollutant concentrations. Yet there's a need to explain high solution concentrations in precipitating particles. Collet *et al.* (1991) have illustrated the important influence of riming on precipitation chemistry. Riming is a very efficient removal mechanism for highly concentrated cloud droplets.

The process of riming is dependent on sizes of the cloud drops. Experiments (Pruppacher and Klett, 1980; Borys *et al.*, 1988) revealed that cloud drops with diameters below 10 μm are not efficiently captured by ice particles. At the Mt. Rigi cloud droplets attached to rimed ice crystals varied from 30-45 μm in diameter (Collet *et al.*, 1992). Hence there is no 1:1 relationship of cloud chemistry and precipitation chemistry. This will be even further accentuated by heterogeneous cloud properties.

Thus to describe precipitation chemistry one has to take into account cloud heterogeneities (proceeding from internal and external mixing of cloud forming aerosol particles, being emphasized or mitigated by microphysical processes) and the size dependent process of transferring cloud chemistry components to the precipitation (*i.e.* riming).

2. MODEL DESCRIPTION

In a first step a zero dimensional model was developed in order to describe the size-dependent evolution of solute concentrations in cloud drops grown up on CCN of different sizes. The model contains a droplet size dependent description of the condensational process. Following several authors (Twohy *et al.*, 1989; Hegg and Larson, 1990; Pandis *et al.*, 1990) aerosol particles and droplets are considered in the same size distribution (opposite to models where aerosol particles and droplets are separated, e.g. Flossmann, 1985; Roelofs, 1993). As we intend to study cloud droplet concentrations a continuous model seems to be more adequate. The dry aerosol particles are first brought to equilibrium by applying the KÖHLER-equation. The wetted particles are redistributed into wet aerosol particle/droplet classes (following Roeloffs, 1993). Changes in the humidity of the air surrounding the aerosol alter its size distribution. The time rate change of the number density function due to condensation growth

of water droplets is expressed following Hall, 1980 and Flossmann *et al.*, 1985 by

$$\frac{\partial f(a)}{\partial t} = -\frac{\partial}{\partial a}(\dot{a}f) \qquad (1)$$

with

$$\dot{a} = \frac{4D}{a}(rH - rH_a) \qquad (2)$$

determining the droplet growth velocity (Volken, 1994). The aerosol particle mass change in the droplets with time is calculated by a similar equation.

$$\frac{\partial g(a)}{\partial t} = -\frac{\partial}{\partial a}(\dot{a}g) \qquad (3)$$

(Flossmann, 1985).

After each time-step the new dry particle diameter is calculated by using the aerosol particle mass density per class:

$$d_p = \sqrt[3]{\frac{6 \cdot g(a)/f(a)}{\pi \rho_p}} \qquad (4)$$

This is required to force the drops to converge to the equilibrium size and equilibrium concentration of solute. The aerosol mass mixing ratio distribution function is calculated following Flossmann *et al.*, 1985 by

$$Q(a) = \frac{g(a)}{m(a) \cdot f(a)} \qquad (5)$$

The advection-like equations are solved by a flux-corrected transport scheme (FCT) suggested by Boris and Book, 1971. This method is conservative and it strictly maintains positive values. Numerical instabilities caused by multiplying the dependent variables da/dt and g are smoothed by a numerical filter applied on the calculated growth velocity after each time step.

3. RESULTS AND DISCUSSION

To initialize the model we apply a trimodal dry aerosol particle distribution used by Flossmann (1991). The wet aerosol particle distribution is first initialized by applying a relative humidity of 0.98. After this initializing step, the relative humidity was risen to a value of 1.002. This value was chosen to activate droplets with a diameter approximately greater than 1µm while smaller particles remaining not activated. The model run was set to 5 minutes. After that period the wet aerosol particles reached their equilibrium size and the droplets' growth velocities has decreased to a maximum speed of about 0.002µm/s for droplets with a diameter of about 10µm.

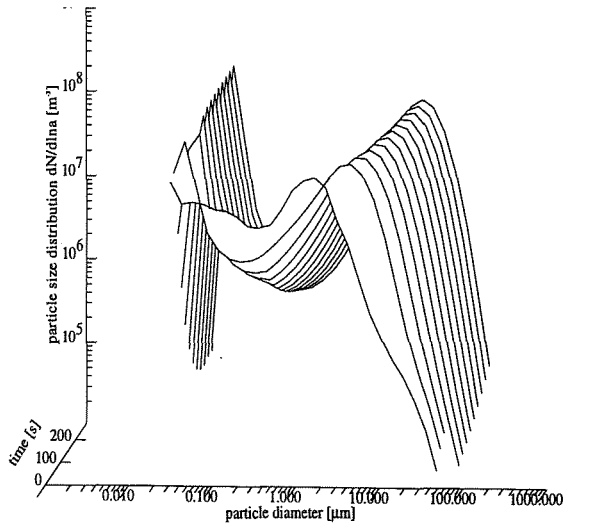

FIG. 1. Evolution in time of the droplet number distribution function *f(a)*

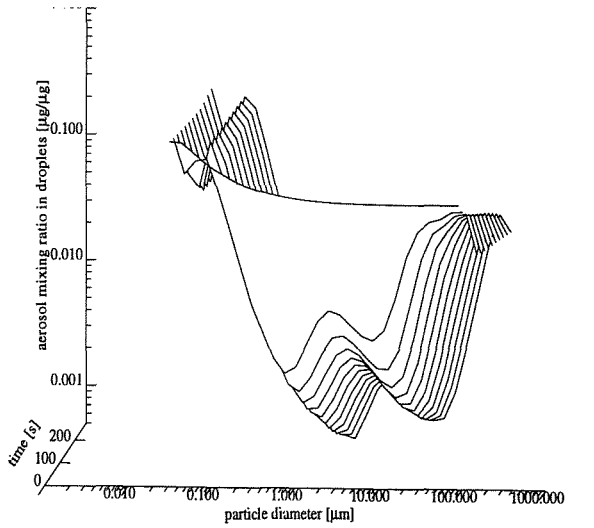

FIG. 2. Time evolution of the aerosol mass mixing ratio distribution *Q(a)*.

Fig.1 shows the number distribution change with time. Concordant with other authors (e.g. Hegg and Larson, 1990) we also find a size separation of (non-activated) aerosol particles and (activated) droplets. This behaviour can easily be explained by the KÖHLER-equation. The non-activated aerosol particles will grow until their branch of the KÖHLER-curve will reach the value of the supersaturation of the surrounding atmosphere. The drops, once having passed their activation diameter will go on growing.

The time change of the aerosol mass mixing ratio distribution, i.e. a measure for the solute concentration in the aerosol particles/droplets is displayed in Fig.2. The temporal development reflects the growth history of the particles. While the concentration of the particles smaller than 0.1µm varies little with the change in supersatura-

tion, the droplets just being activated (0.1μm<a<10μm) dilute very efficiently. This is due to the fact, that these particles have the largest relative growth velocity. Droplets larger than 10μm reveal increasing concentration with drop-size because they grow up on the largest CCN and their relative growth velocity is much lower than that of the droplets just being activated. The little elevated values between 1μm and 10μm (remind the logarithmic-scale of the z-axis) arise from numerical inaccuracies dividing two values calculated separately. The low concentrations for diameters of about 0.05μm are probably also a numerical artefact resulting from high values of f due to initial conditions.

In general our results are in good agreement with other theoretical studies (e.g. Twohy *et al.*, 1989; Pandis *et al.*, 1990; Ogren and Charlson, 1992) where aerosol particles and cloud droplets were treated also in the same size-distribution.

4. OUTLOOK

In a first step the developed model will be used to study the significant processes leading to cloud chemistry heterogeneities. For that purpose we want to connect a model for S(IV)-oxidation with a time dependent box-model for cloud microphysics. Emphasize will be put on studying differences in chemical composition of cloud droplets of different sizes. Further on the tested chemical scheme is intended to be coupled to a 1D-precipitation model with spectral particle distributions and including ice phase microphysics. This way we hope to assess the characteristic influence of riming on some chemical species in the cloud droplet. Finally it is intended to compare the results of this precipitation chemistry model with an extended data set of field measurements, which took place at Mt. Rigi in Central Switzerland from 1985 until 1992.

APPENDIX

SYMBOLS

a	droplet/aerosol particle diameter
D	diffusivity of water vapour in air
$f(a)$	number density distribution of aerosol particles/ droplets
$g(a)$	aerosol particle mass distribution in the droplets
$m(a)$	mass of droplet
$Q(a)$	aerosol mass mixing ratio distribution function
rH	relative humidity of the surrounding atmosphere
rH_a	relative humidity on the surface of the droplets
ρ_p	density of dry aerosol particle

REFERENCES

Boris, J. P. and Book, D. L. 1973. Flux-Corrected Transport. I. SHASTA, A Fluid Transport Algorithm That Works. *J. Comput. Phys.* **11**, 38-69.

Bower, K. N., Hill, T. A., Coe, H. and Chourlaton, T. W. 1991. SO_2 oxidation in an entraining cloud model with explicit microphysics. *Atmos. Environ.* **25A**, 2401-2418.

Collet, J. Jr, Oberholzer, B. and Staehelin, J. 1993. Cloud chemistry at Mt Rigi, Switzerland: Dependence on drop size and relationship to precipitation chemistry. *Atmos. Environ.* **27A**, 33-42.

——, Prevot, A. S. H., Staehelin, J. and Waldvogel, A. 1991. Physical factors influencing winter precipitation chemistry. *Envir. Sci. Technol.* **25**, 782-606.

Dixon, R. W., Mosimann, L., Oberholzer, B., Staehelin, J., Waldvogel, A. and Collet, J. L. Jr. 1995. The effect of riming on the ion concentrations of winter precipitation. 1. A quantitative analysis of field measurements. *J. Geophys. Res.* **100**, 11517-11527.

Flossmann, A. I., Hall, W.D. and Pruppacher, H. R. 1985. A theoretical study of the wet removal of atmospheric pollutants. Part I: The redistribution of aerosol particles captured through nucleation and impaction scavenging by growing cloud drops. *J. Atmos. Sci.*, **42**, 582-606.

——. 1991. The scavenging of two different types of marine aerosol particles calculated using a two-dimensional detailed cloud model. *Tellus* **43B**, 301-321.

Hegg, D. A. and Larson, T. V. 1990. The effects of microphysical parameterization on model predictions of sulfate production in clouds. *Tellus* **42B**, 149-160.

Ogren, J. A. and Charlson, R. J. 1992. Implications for models and measurements of chemical inhomogenities among cloud droplets. *Tellus* **44B**, 208-225.

Pandis, S. N., Seinfeld, J. H. and Pilinis, C. 1990. Chemical differences in fog and cloud droplets of different sizes. *Atmos. Environ.* **24A**, 1957-1969.

Pruppacher, H.R. and Klett, J.D. 1987. *Microphysics of clouds an precipitation.* D. Reidel, 714 pp.

Roelofs, G. J. H. 1993. A cloud chemistry sensitivity study and comparison of explicit and bulk cloud model performance. *Atmos. Environ.* **27A**, 2255-2264.

Svenningsson, I. B., Hansson, H.-C., Wiedensohler, A., Ogren, J. A., Noone, K. J.and Hallberg, A. 1992. Hygroscopic growth of aerosol particles in the Po Valley. *Tellus* **44B**, 556-569.

Twohy, C. H., Austin, P. H. and Charlson, R. J. 1989. Chemical consequences of the initial diffusional growth of cloud droplets: a clean marine case. *Tellus* **41B**, 51-60.

Volken, M. A. 1994. *A model for below-cloud scavenging of aerosols and trace gases: Results and observations.* PhD. Thesis, ETH Zürich.

A STUDY OF THE AEROSOL MODIFICATION GENERATED BY PASSAGE THROUGH AN OROGRAPHIC CLOUD

T.W. Choularton[1], K.N. Bower[1], M.W. Gallagher[1], C. Bradbury[1], M. Wells[1], A. Weidensohler[2], W. Birmili[2]

[1]Physics Dept, UMIST, Manchester M60 1QD, UK
[2]Institute of Tropospheric Research, Leipzig, Germany

INTRODUCTION

During the spring of 1993 and again during 1995 field experiments were conducted in which the Great Dun Fell cap cloud was used as a natural flow through reactor to study the processing of the ambient atmospheric aerosol by passage through cloud. The aim was to study the modification of those accumulation mode particles which act as cloud condensation nuclei (CCN). This will occur as a result of aqueous phase chemical processes which are expected to increase their soluble mass and decrease their critical supersaturation. This can be important for the indirect radiative forcing of aerosol (Jones et al 1994). In addition, by measuring the size distribution of Aitken Mode Particles, which remained interstitial to the cloud droplets, before and after the cloud possible chemical reactions on these particles were investigated. Finally the generation of new ultra-fine particles on exit from cloud was investigated.

The results from the field experiment were compared to the predictions of a model of the airflow, cloud formation and cloud chemical processes (Bower and Choularton 1993).

THE FIELD EXPERIMENTS

These were performed at the UMIST field station on Great Dun Fell in Cumbria, UK. Great Dun Fell forms part of a long ridge running from NW to SE. The prevailing winds in the area are from either the SW or NE, hence the site is ideal for a flow through reactor study as air is forced to rise over the ridge. The site has been used extensively for cloud chemistry studies (eg Colvile et al 1994).

The ridge is frequently enveloped by a capping cloud. The 1993 experiment was performed at 5 major sites. These were as follows:-

SITE 1 Wharley Croft (elevation 206m)
SITE 2 Fell Gate (elevation 430m)
SITE 3 Mine Road (elevation 670m)
SITE 4 Great Dun Fell Summit (elevation 847m)
SITE 5 Moor House (elevation 550m)

Sites 1 and 2 are generally below cloud base on the SW side of the ridge. Site 3 is generally close to or rather above cloud base, site 4 is at the hill summit and site 5 is close to cloud base on the NE side of the ridge. In order to investigate the aerosol processing comprehensive measurements were made of oxides of nitrogen, ammonia, sulphur dioxide and the principal oxidants upwind and downwind of the hill. Detailed measurements of the aerosol size distribution, aerosol chemistry as a function of particle size and hygroscopic properties (using a Tandon Differential Mobility Particle Sizing instrument, TDMA) were made. At the hill summit measurements of the cloud microphysics and cloud chemistry were made.

The main measurements made at each of the sites are summarised in table 1. Contributions to these measurements were made by all Ground Based Cloud Experiment (EUROTRAC Sub project GCE) member groups and the other UK groups.

The most important measurements for the work presented in this paper were the measurements of aerosol size distribution using three Differential Mobility Particle Sizing Instruments (DMPS) located upwind of the cloud, at the hill summit (measuring the interstitial size distribution) and downwind of the cloud. These instruments cover the size range 3 nm to 600 nm and hence they measure from ultra-fine newly formed aerosol particles through to the accumulation mode.

Table 1 List of the Measurements made during the GCE campaign at Great Dun Fell

Gas Phase Species		Aerosol Physics		Cloud measurements	
NO_x NO_y	1 3 4 5	size dist'n DMPS	2 4(i/s) 5	M/physics FSSP/PVM	3 4
SO_2	1 3 4 5	size dist'n ASASPX	1 5	CVI	4
O_3	1 3 4 5	CN ultrafine 3025	1 5	DAA	4
NH_3	1 3 4 5	Hyg'ic growth TDMA RHP	2	Continuous Chemistry	
HNO_3	1 2 3 4 5	LAMMA	2 4 5	cloud collector (active)	3 4
NMHC	1	Aerosol Chemistry		cloud collector (passive)	4
PAN	5	4 stage impactors (x2)	1 5	pH	3 4
HNO_2	2	8 stage impactors (x2)	4	S(IV)	3 4
H_2O_2 (g)	2 3 4	Bulk aerosol (R&M)	1 5	H_2O_2	3 4
Organics acids (Formic/Acetic +)	2 4	Bulk interstitial aerosol	3	NO_2^-	4
HCHO	4	Aethelometer	1 4	Cloud droplet size chemistry	4
AWS	all sites	Hi-Vol....organics	2 4	Bulk chemistry	3 4
SODAR	1	UVB/radiation	2 4	Transition metals	4
		JNO_2	2 5		

RESULTS FROM THE FIELD EXPERIMENTS

Figure 1 shows data obtained from the three DMPS instruments operated upwind of the cap cloud, within the cap cloud and downwind of the hill cap cloud. This diagram illustrates features which are found in much of the data set when the airflow between the three sites is connected and aqueous phase oxidation of S(IV) to sulphate is occurring in the cloud water. At the largest sizes the aerosol particles are activated to form cloud droplets. The DMPS at the summit is only measuring interstitial particles. At the downwind site the cloud droplets evaporate returning the CCN to the aerosol phase with some growth due to sulphate production. Careful analysis of the full data set suggests that in conditions where sulphate production by aqueous phase oxidation is occurring, some growth of the interstitial aerosol also occurs although this is much less than for the particles which are nucleation scavenged. At the smallest sizes in the 'new nucleation mode' it is sometimes observed that new particles are produced on

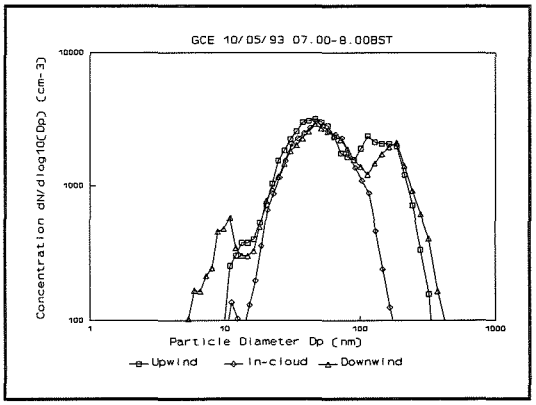

Figure 1 Measurements of the aerosol size distribution before cloud, at the hill summit and after cloud.

leaving the cloud as shown in figure 1. The number of particles produced is very variable, sometimes much larger than shown. On other occasions small particle loss is observed as the air flows across the hill and through the cap cloud. This is probably due to the Brownian capture of small particles which are in the interstitial air within the cloud, to the cloud droplets.

The mechanism of the formation of the small particles is of interest. The measurements of ammonia concentrations made by our collaborators from the Institute of Terrestrial Ecology are probably relevant. They show that ammonia does outgas from evaporating cloud droplets as the airstream leaves the cloud. The aerosol and cloud water chemistry measurements show that some droplets form on large sea-salt aerosol whilst the majority form on ammonium sulphate aerosol. Sulphate production within those droplets forming on sea-salt aerosol is predicted to result in the out-gassing of HCl as these droplets evaporate. Preliminary modelling studies performed by Kulmala (private communication) suggest that the nucleation of Ammonium chloride and water aerosol may explain the new particle production which is observed.

THE CLOUD MICROPHYSICS

In this experiment detailed measurements of the size distribution of the aerosol entering the cloud were available along with measurements of the hygroscopic properties of the particles (from the TDMA). The predicted droplet size distribution from our model, using this data as input along with a description of the airflow over the hill was compared to the observed size distribution. Generally reasonable agreement was obtained. The model tended to overestimate the number of activated droplets observed at the hill top by typically 20%. A complex supersaturation history was often predicted when the wind was blowing from the NE with a trajectory to the summit over complex terrain. This history produced several supersaturation peaks within the cloud and hence CCN activation occurred at more than one level. The result was a broad droplet size distribution in agreement with observations.

On a few occasions a larger discrepancy was observed but usually the differences were less than at Kleiner Feldberg. The possibility exists that some component of the droplet chemistry is affecting the properties of the particles during the activation process. Recent studies performed by Schulman et al 1996 suggest that the organic component of the aerosol may be responsible for this.

MODELLING OF THE AEROSOL PROCESSING

Simulations of the modification of the size distribution of the aerosol resulting from the cloud processing have been performed. Generally good agreement between the observations from the field studies and the model predictions was obtained. The change in the aerosol size distribution observed was due to sulphate production with hydrogen peroxide and ozone the dominant oxidants.

Figure 2 shows model results of the effect of the processing of the aerosol on the CCN activity spectrum. The input activity spectrum was deduced from the observed size distribution, chemical composition and hygroscopic properties of the input aerosol. The results are presented for a range of sulphur dioxide concentrations entering the cloud. The cloud droplet chemistry is seen to have the largest effect on the smallest activated CCN. This enables such particles to activate much more readily after cloud processing at critical supersaturations up 20 times lower than originally required. A simple cloud model is used to investigate the sensitivity of this secondary activation.

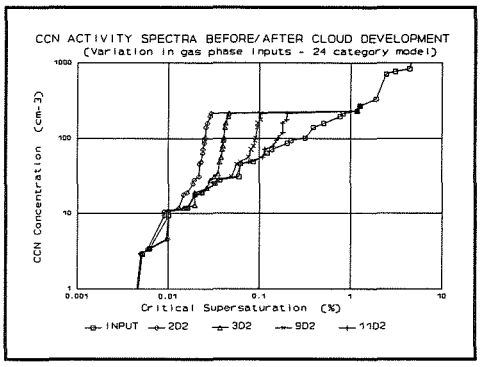

Figure 2 Change in CCN activity spectrum for 5ppv, 2ppv, 0.5ppbv, 0.01ppbv SO_2 respectively.

With updraughts typical of a stratocumulus type cloud, droplet effective radii are seen to be lowered by up to 3μm, 500m above cloud base. This result is insensitive to the concentration of SO_2 present in the processing cloud down to very low concentrations.

CONCLUSIONS

1. A broad droplet size distribution is often observed near the hill summit produced by a complex supersaturation profile and by mixing between parcels with different ascent trajectories.

2. The model produces several supersaturation peaks as the airstream ascends the hill.

3. When sulphate production occurs due to the oxidation of S(IV) by hydrogen peroxide and ozone a marked evolution of the chemical properties of the aerosol particles on which the droplets forms occurs.

4. A significant modification of the aerosol size distribution and hygroscopic properties is modelled and observed.

5. Generally sulphate production reduces the critical supersaturation of processes aerosol particles. On some occasions, however, outgassing of ammonia causes an increase in the critical supersaturation.

6. The growth of interstitial haze particles is also observed.

REFERENCES

K.N. Bower and T.W. Choularton
1993 Cloud processing of the Cloud Condensation Nucleus Spectrum and its Climatological Consequences. Quart. J.R. Met. Soc. Vol 119, pp 655 - 680

R.N. Colvile, T.W. Choularton, M.W. Gallagher, A.J. Wicks, R.M. Downer, B.J. Tyler, K.J. Hargreaves, R. Storeton-West, D. Fowler, J.N. Cape, G.J. Dollard, T.J. Davies, B.M.R. Jones, S.A. Penkett, B.J. Bandy and R. Burgess
1994 Field Observation of the pathways by which nitric oxide and nitrogen dioxide are converted to nitric acid in cloud.
Atmospheric Env. Vol 28, No. 3 pp 397-408

A. Jones, D.L. Roberts and A. Slingo
1994 A climate model study of indirect radiative forcing by anthropogenic sulphate aerosols. Nature, 307, pp 450-4533.

M. L. Shulman, M.C. Jacobson, R.J. Charlson, R.E. Synovec and T.E. Young 1996 Dissolution behaviour and surface tension effects of organic compounds in nucleating cloud droplets
Geophys. Res. Lett. Vol 23 pp 277-280.

ACKNOWLEDGEMENTS

This work was supported by the Natural Environment Research Council and by the European Union Environment Program

PRECIPITATION SCAVENGING IN A COUPLED CHEMISTRY/CLIMATE MODEL OF SULFATE AEROSOL

Charles R. Molenkamp, Joyce E. Penner, John J. Walton, Charles J. O'Connor

Atmospheric Sciences Division
Lawrence Livermore National Laboratory, Livermore, CA 94550

1. INTRODUCTION

Knowledge of the spatial distribution of sulfate aerosol over the globe is important because sulfate aerosols affect global climate directly by scattering solar radiation and indirectly by altering the cloud drop size distributions. The resulting negative climate forcing due to scattering by aerosols counteracts the warming associated with increased greenhouse gas concentrations; however, the pattern of forcing is quite different because the distribution of sulfate aerosol is regionally inhomogeneous (Charlson, et al., 1992; Kiehl and Briegleb, 1993). Furthermore, changes in cloud drop size distributions induced by aerosols can change the back-scattering of solar radiation by clouds and the cloud life cycle, thereby affecting global temperature and precipitation patterns.

We have previously examined the climate effects of sulfate aerosols and greenhouse gases using the Lawrence Livermore National Laboratory tropospheric chemistry model (GRANTOUR) in conjunction with CCM1 and concluded that representation of the regional distribution of atmospheric aerosols was essential for reliable prediction of climate change (Taylor and Penner, 1993). Using CCM1 meteorology, GRANTOUR has also been use to simulate the global transport and deposition of ^{222}Rn and ^{210}Pb (Dignon, et al., 1993), O_3 and OH (Atherton, 1993; Atherton et al., 1993; Penner et al., 1993a), organic nitrates (Atherton, 1989), anthropogenic aerosols (Taylor and Penner, 1993), smoke (Ghan et al., 1988), soot aerosols from biomass burning (Penner et al., 1991b), and black carbon (Penner et al., 1993b). We have also used GRANTOUR to simulate the global nitrogen budget (Atherton et al., 1991; Penner et al., 1991a) and the global sulfur cycle (Erickson et al., 1991).

Recently we have coupled GRANTOUR with the ECHAM global climate model. This provides several enhanced capabilities in the representation of aerosol interactions compared to the previous simulations with GRANTOUR coupled to CCM1. ECHAM includes a specific representation of liquid water in large-scale clouds that permits a parameterization of wet phase gas-to-particle conversion of SO_2 to sulfate. It also includes a large-scale precipitation module that we are using to improve the parameterization of scavenging by these clouds. The convective parameterization (Tiedke, 1989) includes a precipitation component that can be used to represent scavenging of aerosols by convective precipitation.

2. COUPLED MODEL

The current ECHAM/GRANTOUR model is only coupled in one direction. ECHAM is used as a meteorological driver for GRANTOUR. This has the advantage of allowing us to run ECHAM once to generate the meteorological data and then developing parameterizations for GRANTOUR with a constant set of meteorology. It has the disadvantage of not allowing feedback of the aerosols on the evolution of the weather and climate system.

We generated one year of meteorological data from ECHAM at T21 resolution. Four hour averages of the 12 variables in Table 1 were saved and constitute the meteorological data set; all are three dimensional variables defined on the ECHAM grid. GRANTOUR interpolates the variables to a constant sigma vertical coordinate that corresponds with the ECHAM variable grid for a surface pressure of 10^5Pa. Both models use the same horizontal grid. Vertical velocity is derived from U and V using the continuity equation. The parameterizations of large-scale scavenging and of convective mixing and scavenging and are actually performed on the ECHAM vertical grid with trace species mixing ratios interpolated from the GRANTOUR grid.

In the future we will provide four hour average trace species mixing ratios and/or aerosol optical properties to

ECHAM. This will permit us to evaluate some of the feedback effects of sulfate aerosols.

The aerosol precipitation scavenging parameterizations we have developed for GRANTOUR depend on the representations of the corresponding precipitation processes in ECHAM and the variables we have saved. The parameterizations are simple extrapolations of the ECHAM precipitation processes based on the assumption that sulfate aerosols are soluble, and therefore, when liquid water is present, all the sulfate mass is associated with cloud drops and precipitation.

3. LARGE-SCALE CLOUD SCAVENGING

Large-scale or stratiform precipitation in ECHAM is represented by a modified version of Sundquist's (1978) formulation (Deutsches Klimarechenzentrum, 1993). From the ECHAM simulation we save the large-scale precipitation rate, P_{LS}, and large-scale cloud fraction, F_c, and we assume all aerosol in the cloudy region is in cloud droplets. The calculation works from the top of each atmospheric column down. If P_{LS} increases downward there must have been accretion of cloud droplets and scavenging of aerosol. If we assume a cloud drop size distribution we can define an accretion (scavenging) rate as a function of P_{LS}. For simplicity we used a Marshall-Palmer size distribution,

$$n(D) = n_0 \exp^{-\Lambda D} \qquad (1)$$

where D is drop diameter, n_0 is a constant parameter, and Λ is the mean drop diameter. We specified the drop terminal velocity, V_t, with the simple expression,

$$V_t(D) = kD^{1/2}. \qquad (2)$$

Then the precipitation rate, P_{LS}, is given by

$$P_{LS} = \frac{n_0 \pi \rho_l k}{6} \frac{\Gamma(4.5)}{\Lambda^{4.5}} \qquad (3)$$

and the rate of accretion is

$$\lambda = \frac{E n_0 \pi k}{4} \frac{\Gamma(3.5)}{\Lambda^{3.5}} \qquad (4)$$

where ρ_l is air density and E is the collection efficiency. Using standard values for the constants of

$$\begin{aligned} E &= 1 \\ n_0 &= 10^7\ m^{-4} \\ k &= 130\ m^{1/2} s^{-1} \\ \rho_l &= 10^3\ kg\, m^{-3} \end{aligned} \qquad (5)$$

gives the necessary relationship between P_{LS} and λ,

$$\lambda\ [hr^{-1}] = 1.94\ P_{LS}[mm/hr]^{\frac{7}{9}}. \qquad (6)$$

Table 1. ECHAM Variables Passed to GRANTOUR

Name	Variable	Units
U	Zonal Velocity	km/hr
V	Meridional Velocity	km/hr
T	Air Temperature	K
q_v	Water Vapor Mixing Ratio	
q_l	Liquid Water Mixing Ratio	
P_{LS}	Large-Scale Precip. Rate	cm/hr
P_{CV}	Conv. Precip. Production Rate	cm/hr
M_u	Convective Mass Flux Up	kg/m^2/s
M_d	Convective Mass Flux Down	kg/m^2/s
P_h	Half-Level Pressure	Pa
F_c	Large-Scale Cloud Fraction	
K_z	Vertical Diffusion Coefficient	m^2/s

In time dt [hr], the amount of aerosol scavenged in layer j, S_{aj}, is given by

$$S_{aj} = (1 - \exp^{-dt\lambda})\ F_{cj} \chi_{aj} \frac{\Delta p_j}{g}, \qquad (7)$$

where χ_{aj} is the aerosol mixing ratio, Δp_j is the pressure thickness of layer j, and g is the acceleration of gravity.

If P_{LS} decreases downward, there must have been evaporation of rain and possible resuspension of aerosol. The fraction of rain that evaporates in layer j, f_e, is

$$f_e = \frac{P_{LS(j-1)} - P_{LS(j)}}{P_{LS(j-1)}} \qquad (8)$$

(j increases downward). Since most of the evaporated water comes from drops that only partially evaporate and do not resuspend aerosol, we assume that the fraction of rain in drops that evaporate completely, f_{ec}, is given by

$$f_{ec} = f_e^n \qquad (9)$$

where n is currently 2. Therefore, the amount of aerosol resuspended in layer j is

$$R_{aj} = f_{ec} A_{j-1} \qquad (10)$$

where A_{j-1} is the amount of aerosol in rain in layer j-1.

Working from the top down

$$A_j = A_{j-1} + S_{aj} - R_{aj} \qquad (11)$$

and

$$\chi_j^{(t+dt)} = \chi_j^{(t)} - (S_{aj} - R_{aj}) \frac{g}{\Delta p_j}. \qquad (12)$$

4. CONVECTIVE CLOUD SCAVENGING

The parameterization of scavenging by convective clouds in GRANTOUR is a part of the convective mixing algorithm just as in ECHAM. We save the rate of formation/evaporation of convective precipitation from ECHAM and have available in the parameterization the upward and downward fluxes of aerosol (all of which is assumed to be in cloud water because the convective updrafts are saturated). If a layer has an increase in convective precipitation, aerosol is assumed to be accreted at the same rate as cloud water, G_P, which is given in ECHAM by

$$\overline{\rho} G_P = K l M_u \qquad (13)$$

where ρ is air density, K is a constant, 2×10^{-3} m^{-1}, l is the cloud water mixing ratio in the convective updraft, and M_u is the updraft mass flux. Therefore the accretion rate of aerosol, G_a, is

$$\overline{\rho} G_a = K \chi_l M_u \qquad (14)$$

where χ_l is the mixing ratio of aerosol in cloud water. The upward mass flux of aerosol in cloud water is given by

$$\frac{\partial}{\partial z}(M_u \chi_l) = E_u \chi_e - D_u \chi_l - \overline{\rho} G_a \qquad (15)$$

where E_u and D_u are the entrainment and detrainment rates for the convective updraft and χ_e is the aerosol mixing ratio in the environment. Using (14) in (15) the new mixing ratio for layer j due to accretion of aerosol by rain can be approximated by

$$\chi_l^{t+dt} = \chi_l^t \frac{1}{1 + K\Delta z} \qquad (16)$$

and the convective scavenging rate, S_c, by

$$S_c = \frac{K\Delta z}{1 + K\Delta z} M_u \chi_l. \qquad (17)$$

Resuspension of aerosol in convective precipitation due to evaporation of rain in convective downdrafts is parameterized by assuming the rate of resuspension is equal to the evaporation rate. If f_{ce} is the fraction of rain evaporated, then the new mixing ratio of aerosol in the convective downdraft, χ_d, is given by

$$\chi_d^{t+dt} = (1 + f_{ce}) \chi_d^t \qquad (18)$$

and the rate of resuspension, R_c, is

$$R_c = f_{ce} \chi_d M_d. \qquad (19)$$

5. SIMULATION RESULTS

Results from the simulations will show the global distribution of sulfate scavenged by large-scale and convective clouds and the spatial distributions of suspended sulfur species. We also plan to calculate the climate forcing due to anthropogenic sulfate.

6. REFERENCES

Atherton, C. S., 1989: Organic nitrates in remote marine environments--evidence for long-range transport. *Geophys. Res. Lett.*, **16**, 1289-1292.

Atherton, C. S., 1993: Ph. D. Dissertation, University of California, Davis.

Atherton, C. S., J. Dignon, J. E. Penner, S. Sillman, and J. J. Walton, 1993: Man's impact on tropospheric O_3 and OH: Global model results. Presented at the IAMAP-IAHS International Scientific Meeting, session on Major Advances of Atmospheric Chemistry over the Past Decade and Their Impact on Public Welfare, Yokohama, Japan, July 11-23.

Atherton, C. S., J. E. Penner, and J. J. Walton, 1991: The role of lightning in the tropospheric nitrogen budget: Model investigations. LLNL Report UCRL-JC-107223.

Charlson, R. J., S. E. Schwartz, J. M. Hales, R. D. Cess, J. A. Coakley Jr., J. E. Hansen, and D. J. Hoffman, 1992: Climate forcing by anthropogenic aerosols. *Science*, **255**, 423-430.

Deutsches Klimarechenzentrum, 1993: *The ECHAM 3 Atmospheric General Circulation Model.* Report No. 6, Hamburg, 189 pp.

Dignon, J., J. E. Penner, and J. J. Walton, 1993: Simulation of ^{222}Rn and ^{210}Pb in a three-dimensional chemical transport model. LLNL Report.

Erickson III, D. J., J. J. Walton, S. J. Ghan, and J. E. Penner, 1991: Three-dimensional modeling of the global atmospheric sulfur cycle: A first step. *Atmos. Environ.*, **25A**, 2513-2520.

Ghan, S. J., M. C. MacCracken, and J. J. Walton, 1988: Climatic response to large atmospheric smoke injections: Sensitivity studies with a tropospheric general circulation model. *J. Geophys. Res.*, **93**, 8315-8337.

Kiehl, J. T. and B. P. Briegleb, 1993: The relative roles of sulfate aerosols and greenhouse gases in climate forcing. *Science*, **260**, 311-314.

Penner, J. E., C. S. Atherton, J. Dignon, S. J. Ghan, J. J. Walton, and S. Hameed, 1991a: Tropospheric nitrogen: A three-dimensional study of sources, distribution, and deposition. *J. Geophys. Res.*, **96**, 959-990.

Penner, J. E., S. J. Ghan, and J. J. Walton, 1991b: The role of biomass burning in the budget and cycle of carbonaceous soot aerosols and their climate impact. In *Global Biomass Burning* , Ed. J. Levine, MIT Press, Cambridge, MA, 387-393.

Penner, J. E., C. S. Atherton, and T. Graedel, 1993a: Global emissions and models of photochemically active compounds. In Global Atmospheric-Biospheric Chemistry: The First IGAC Scientific Conference, OHOLO Conference Series Books, Plenum Publishing, New York, in press.

Penner, J. E., H. Eddleman, and T. Novakov, 1993b: Towards the development of a global inventory of black carbon emissions. *Atmos. Environ.*, **27A**, 1277-1295.

Sundquist, H., 1978: A parameterization scheme for non-convective condensation including prediction of cloud water content. *Quart. J. Roy. Meteor. Soc.*, **104**, 677-690.

Taylor, K. E. and J. E. Penner, 1993: Response of the climate system to atmospheric aerosols and greenhouse gases. *Nature*, **369**, 734-737.

Tiedke, M., 1989: A comprehensive mass flux scheme for cumulus parameterization in large-scale models. *Mon. Wea. Rev.*, **117**, 1779-1800.

6. ACKNOWLEDGEMENTS

This work was performed under the auspices of the U. S. Department of Energy by the Lawrence Livermore National Laboratory under contract No. W-7405-ENG-48.

ORGANIC AEROSOLS AS CCN IN CARIBBEAN TRADE WINDS

T. Novakov [1], C.E. Corrigan [1], J.E. Penner [2], C.C. Chuang [2], O. Rosario [3] and O.L. Mayol Bracero [3]

[1] Lawrence Berkeley National Laboratory, Berkeley, California 94720
[2] Lawrence Livermore National Laboratory, Livermore, California 94551
[3] University of Puerto Rico, Rio Piedras, Puerto Rico 00931

1. INTRODUCTION

The cloud condensation nucleus (CCN) activity of aerosol particles depends on the physical and chemical properties of all aerosol components, inorganic and organic. Most studies have been on inorganic aerosols, especially sulfate, because their nucleation properties are well known. As sulfate species are not always the principal component of submicron aerosol mass, it can be expected that non-sulfate components will contribute to the CCN and total aerosol number concentrations. Indeed, comparisons of CCN number and sulfate mass concentrations in the North Atlantic (Hegg et al., 1993) and in the Caribbean (Novakov et al., 1994) suggest that a substantial fraction of measured CCN concentrations cannot be explained by sulfate species alone. Our experiments in the Caribbean data set (El Yunque peak, Puerto Rico) demonstrate that the organic aerosol fraction may account on the average for 60% of CCN number concentrations (Novakov and Penner, 1993; Rivera-Carpio et al., 1996).

Although El Yunque peak (located on the eastern end of Puerto Rico) is exposed to tropical trade winds non-marine aerosols, from rain forest biogenic emissions below the site and from human activities in the area between the peak and the ocean may also contribute to the aerosol concentrations at this site. This possibility raises the question of how representative the El Yunque results are of marine trade wind aerosols. To resolve this question, we have conducted a study at Cape San Juan, a coastal site located on the extreme northeastern tip of Puerto Rico, during days when the wind direction was consistently from the Northeast to the East sector. Under these conditions, the collected aerosol should be representative of tropical marine trade winds.

2. SAMPLING AND ANALYSES

The aerosol sampling platform was located about 150 m from the seashore and 20 m above sea level. A cascade impactor was used to sample particles with aerodynamic diameters below 0.6 μm. This size range was chosen to exclude seasalt and mineral dust particles and to sample only particles that contribute most to the aerosol and CCN number concentrations. Twenty-four-hour (noon to noon) and 12-h daytime samples were collected. The carbonaceous material was characterized by thermal Evolved Gas Analysis (EGA) (Novakov, 1981, 1982). Aliquots taken from the same filter samples were extracted in deionized water and analyzed for major inorganic anions by ion chromatography.

3. RESULTS

Derivation of mass concentrations of aerosol organic carbon from analyses of filter-collected samples is complicated because the sampled air contains organic material in both the particle phase and the gaseous phase. During sampling the filterable particulate organic species (OC_F) are retained on the filter together with gaseous species adsorbed on the fibrous filter material, such as quartz, the preferred filtration medium for carbonaceous aerosols (McDow and Huntzicker, 1990; Fitz, 1990). Furthermore, aerosol particles may contain semivolatile aerosol organic (OC_{SV}) species. Although OC_{SV} is associated with suspended particles, these organic species may be desorbed from the particulate phase during sampling (Eatough et al., 1993). To derive mass concentrations of organic aerosols the organic content of filter collected material must be corrected for these sampling artifacts.

In this study the sampling was done with two back-to-back quartz filters and with quartz filters

preceded by Teflon filters. This filter arrangement, when used in conjunction with an analytical method that provides a separation of organic materials by thermal volatility such as EGA, can be used to estimate both filterable and semivolatile organic aerosol concentrations (Novakov et al., 1996).

The mass concentrations of particulate (OC_P) and semivolatile (OC_{SV}) organic material, together with water-soluble sulfate and chloride concentrations are listed in Table 1. Nitrate concentrations and black carbon were below detection. The maximum possible concentration of black carbon, estimated from the EGA thermograms, is about 30 ng m^{-3}.

Table 1. Concentrations (in ng m^{-3}) of semivolatile (OC_{SV}), filterable organic carbon (OC_P), SO_4^{2-}, and Cl^-.

Date[a]	OC_{SV}	OC_P	SO_4^{2-}	Cl^-
2/12-13	562	431	375	127
2/13-14	506	733	292	<40
2/14-15	509	562	208	<40
2/15-16	643	511	204	<40
2/16-17	575	309	204	<40
3/13-14	708	458	250	48
3/14-15	536	336	250	<40
3/15-16	551	632	229	56
3/16-17	623	525	333	<40
5/30	1420	932	254	139
5/31	813	637	n.m.[b]	n.m.
6/1	1235	898	296	<40
6/2	1284	628	400	<40
Average[c]	776	617	274	
	±325	±232	±66	

[a] February and March samples collected for 24-h, May and June samples collected for 12-h during daytime.

[b] Not measured.

[c] ± denotes standard deviation of the mean.

A comparison of these data with the results obtained at El Yunque (Novakov and Penner, 1993; Rivera-Carpio et al., 1996) show that average OC_p mass concentrations of 620 ng m^{-3} observed at the coastal site are comparable to the average OC concentration of 660 ng m^{-3} at the El Yunque site. In contrast, the average SO_4^{2-} concentrations at El Yunque (1060 ng m^{-3}) are 3.8 times higher than the average SO_4^{2-} concentrations of 275 ng m^{-3} measured in this study. As this comparison indicates the SO_4^{2-} at El Yunque is largely derived from local sources. However, the organic aerosol fraction at El Yunque does not appear to be significantly influenced by local anthropogenic or biogenic emissions.

We have tested a number of Cape San Juan samples to determine if their organic content is water soluble. Aliquots taken from the exposed filters were immersed in 250 ml deionized water for about 20 min without agitation, then dried and analyzed by EGA. The results show that about 70% of the organic carbon mass of these samples is water soluble. The water-soluble nature of the trade wind organic aerosols is consistent with our previously inferred contribution of El Yunque organic aerosol to CCN concentrations (Novakov and Penner, 1993; Rivera-Carpio et al., 1996).

3. DISCUSSION

Because the Cape San Juan samples were collected under trade wind conditions, the aerosols either originate in these oceanic air masses (Hoffman and Duce, 1974, 1976; Eichman et al., 1979, 1980) or are generated in upwind, perhaps continental, locations (Cachier et. al, 1986; Cachier, 1989) and are carried to the site by the trade winds. Because black carbon is a tracer for combustion, its virtual absence suggests that combustion is not the main source of the sub-0.6 μm aerosol at this site. It is also unlikely that water-soluble organic aerosols will reach the sampling site by long-range transport without being efficiently removed from the atmosphere by nucleation or other wet-scavenging mechanisms. These observations and the fact that sulfate concentrations are in the range close to that expected from natural sources (generally less than 300 ng m^{-3}) (Savoie et al., 1989) tend to support the possibility that organic aerosols are derived from oceanic sources. One potential oceanic source – seasalt – can be ruled out because of the low Cl^- concentrations detected in sub-0.6 μm samples (Table 1). The presence of semivolatile organic species at concentrations similar to filterable particulate OC suggests that organic aerosols are formed by a process involving the condensation of either secondary or primary organic gases and vapors. Finally, preliminary results of high resolution mass spectrometric analyses of Cape San Juan aerosol samples show that the organic mass is dominated by naturally occurring compounds such as fatty and carboxylic acids (Mayol and Rosario, unpublished data). With the other evidence discussed above, this leads us to the conclusion that the background aerosols in the tropical trade winds have a large organic component, most likely of natural origin.

If natural organic species significantly contribute to the oceanic background aerosols as our results suggest, they should affect estimates of indirect forcing by anthropogenic sulfate aerosols. Because of the nonlinear relationship between CCN and cloud drop number concentrations, the presence of substantial concentrations of natural background particles that are able to act as CCN must lower

estimates of indirect forcing by anthropogenic SO_4^{2-}. To illustrate this possibility, we have calculated the response of drop concentration and albedo of a hypothetical stratus cloud (1000 m thick, 0.2 g m^{-3} liquid water content) to changing anthropogenic SO_4^{2-} concentrations in the presence of natural SO_4^{2-} and organic aerosols. In these calculations we assumed that the natural aerosol is composed of 300 ng m^{-3} of SO_4^{2-} and OC of 500 and 1000 ng m^{-3}. These values approximately correspond to measured mass concentrations of SO_4^{2-}, OC_P, and the sum of OC_{SV} and OC_P.

The calculations were performed by assuming that the natural organic and sulfate aerosol components are distributed over the typical size distribution measured in marine situations, adopted by Chuang et al. (1995a), and that 75% of anthropogenic SO_4^{2-} is produced by aqueous, in-cloud oxidation and the remainder is in the form of sulfuric acid deposited on the pre-existing natural aerosols.

We calculated dependencies of cloud drop concentrations, cloud albedo, and the albedo change on increasing anthropogenic sulfate aerosol mass concentrations for vertical velocities of 10 and 50 cm sec^{-1} by following the procedure and assumptions in Chuang et al. (1995b). Changes in drop concentrations due to inclusion of anthropogenic sulfate strongly depend on the assumed pre-existing aerosol concentrations. For example, increasing the anthropogenic sulfate mass concentrations from zero to 600 ng m^{-3} results in about 70% increase in drop concentrations (for 10 cm sec^{-1} vertical velocity) if natural sulfate were the only pre-existing aerosol species. In contrast, the same increase in anthropogenic SO_4^{2-} would result in only about 25% increase in drop concentrations if 500 ng m^{-3} of natural organics are part of the pre-existing particles.

The cloud albedo would increase (depending on the updraft velocity) by about 2–3% if the anthropogenic SO_4^{2-} concentrations were to increase from zero to 600 ng m^{-3} and if the pre-existing aerosol was composed entirely of natural SO_4^{2-}. If natural organic and sulfate species together comprise the pre-existing aerosols, then the albedo values are expected to be higher than if the natural aerosol is composed of sulfate only but the albedo change due to an increase in anthropogenic sulfate will be considerably smaller. For a natural OC of 500 ng m^{-3}, albedo changes will be about 0.05% or less for a similar anthropogenic sulfate concentration increase. Consequently, the addition of a source of natural organic aerosols should reduce the estimated indirect aerosol forcing compared to the estimates that assume only a natural sulfate source.

4. CONCLUSIONS

Analyses of sub-0.6-μm aerosol samples collected in the Caribbean trade winds show that (1) sulfate mass concentrations are close to expected natural levels (average $\approx$ 250 ng m^{-3}); (2) organic aerosol mass concentrations (average $\approx$ 600 ng m^{-3}) significantly exceed sulfate concentrations; and (3) this organic aerosol material is water soluble, a fact consistent with our earlier findings that organic aerosol material is a major contributor to CCN number concentrations.

The virtual absence of black carbon (a unique tracer for combustion) suggests that combustion is not the main source of the sub-0.6-μm aerosol at this site. Because of its water solubility, the organic aerosol material will not likely survive long-range transport. Our results suggest the possibility that trade wind organic aerosol formation involves natural oceanic emissions.

A model was used to estimate the effect on cloud albedos due to the addition of anthropogenic sulfate aerosol to the marine background aerosol concentration. Results imply that the indirect forcing of climate that results from changing cloud albedo by anthropogenic sulfate aerosol could be substantially overestimated if the natural sources of background organic marine aerosol are not included. It is, therefore, important to quantify the sources of these aerosols as well as their spatial and temporal distribution.

Acknowledgments. This work was supported by the U. S. Department of Energy, Office of Health and Environmental Research, Environmental Sciences Division under contract DE-AC03-76SF00098 at Lawrence Berkeley National Laboratory, and contract W-7405-Eng-48 at Lawrence Livermore National Laboratory. The work at University of Puerto Rico was supported the NASA-EPSCoR program and the support for instrumentation facilities provided by the NIH-RCMI program Grant Number RR03641.

REFERENCES

Cachier, H., P. Buat-Ménard, M. Fontugne, and R. Chesselet, 1986: Long-range transport of continentally-derived particulate carbon in marine atmosphere: Evidence from stable carbon isotope studies, *Tellus*, **38B**, 161-177.

Cachier, H., 1989: Isotopic characterization of carbonaceous aerosols, *Aerosol Sci. Technol.*, **10**, 379-385.

Chuang, C.C. and J.E. Penner, 1995a: Effects of anthropogenic sulfate on cloud drop nucleation and optical properties, *Tellus*, **47B**, 566-577.

Chuang, C.C., J.E. Penner, K.E. Taylor, A.S. Grossman, and J.J. Walton, 1995b: An assessment of the radiative effects of anthropogenic sulfate on climate, submitted to *J. Geophys. Res.*

Eatough, D.J., A. Wadsworth, D.A. Eatough, J.W. Crawford, L.D. Hansen, and E.L. Lewis, 1993: A multiple-system, multi-channel diffusion denuder sampler for the determination of fine-particulate organic material in the atmosphere, *Atmos. Environ.*, **27A**, 1213-1219.

Eichmann, R., P. Neuling, G. Ketseridis, J. Hahn, R. Jaenicke, and C. Junge, 1979: N-alkane studies in the troposphere - I. Gas and particulate concentrations in North Atlantic air, *Atmos. Environ.*, **13**, 587-599.

Eichmann, R., G. Ketseridis, G. Schebeske, R. Jaenicke, J. Hahn, P. Warneck and C. Junge, 1980: N-alkane studies in the troposphere - II. Gas and particulate concentrations in Indian Ocean air, *Atmos. Environ.*, **14**, 695-703.

Fitz, D.R., Reduction of the positive organic artifact on quartz filters, 1990: *Aerosol Sci. Technol.*, **12**, 142-148.

Hegg, R.D., J. Ferek and P.V. Hobbs, 1993: Light scattering and cloud condensation nucleus activity of sulfate aerosol measured over the northeastern Atlantic Ocean, *J. Geophys. Res.* , **98**, 14887-14894.

Hoffman, E.J., and R.A. Duce, 1974: The organic carbon content of marine aerosol collected on Bermuda, *J. Geophys. Res.*, **79**, 4474-4477.

Hoffman, E.J., and R.A. Duce, 1977: Organic carbon in marine particulate matter: Concentration and particle size distribution, *Geophys. Res. Letters*, **4**, 449-452.

McDow, S.R., and J.J. Huntzicker, 1990: Vapor adsorption artifact in the sampling of organic aerosol, *Environ. Sci. Technol.*, **23**, 688-699.

Novakov, T., 1981: Microchemical characterization of aerosols, in *Nature, Aim and Methods of Microchemistry* , edited by H. Malissa, M. Grasserbauer, and R. Belcher, Springer, Vienna, 141-165.

Novakov, T., 1982: Soot in the atmosphere, in *Particulate Carbon: Atmospheric Life Cycle*, edited by G.T. Wolff and R. L. Klimish, Plenum, New York, 19-41.

Novakov, T., C. Rivera-Carpio, J.E. Penner, and C.F. Rogers, 1994: The effect of anthropogenic sulfate aerosols on marine cloud droplet concentrations, *Tellus*, **46B**, 132-141.

Novakov, T., C.E. Corrigan, J.E. Penner, C.C. Chuang, O. Rosario, and O.L. Mayol Bracero, 1996: Organic Aerosols in the Tropical Trade Winds: A Natural Source?, Submitted to *J. Geophys. Res.*

Novakov, T., and J.E. Penner, 1993: Large contribution of organic aerosols to cloud-condensation-nuclei concentrations, Nature, **365**, 823-826.

Rivera-Carpio, C.A., C.E. Corrigan, T. Novakov, J.E. Penner, C.F. Rogers, and J.C. Chow, 1996: Derivation of contributions of sulfate and carbonaceous aerosols to cloud condensation nuclei from mass size distributions, *J. Geophys. Res.*

Savoie, D.L., J.M. Prospero, and E.S. Saltzman, 1989: Nitrate, non-seasalt sulfate and methanesulfonate over the Pacific Ocean, *Chem. Oceanogr.*, **10**, 219-250.

SEASONAL VARIATION OF CLOUD LIQUID WATER CONTENT AND ACTIVATED AEROSOL FRACTION AT A HIGH-ALPINE SITE

Urs Baltensperger[1] Margit Schwikowski[1], Dieter T. Jost[1], Stephan Nyeki[1] and Heinz W. Gäggeler[1,2]

[1] Paul Scherrer Institute, CH-5232 Villigen PSI, Switzerland
[2] Institute of Inorganic Chemistry, University of Bern, Freiestrasse 3, CH-3013 Bern, Switzerland

1. INTRODUCTION

Anthropogenic aerosol particles acting as cloud condensation nuclei (CCN) are believed to increase the number concentration of cloud droplets, increasing cloud albedo (see e.g. Charlson and Heintzenberg, 1995). The actual value of this indirect effect of radiative forcing by aerosols is however associated with a large uncertainty, which calls for more detailed research on the aerosol - cloud relationship.

The high-alpine site Jungfraujoch, Switzerland (3450 m asl) is very well suited for such investigations, since this site is quite often within clouds during all seasons.

2. EXPERIMENTAL

Long-term measurements of the aerosol concentration as well as the cloud liquid water content (LWC) were performed at the Jungfraujoch. For the aerosol measurements, an epiphaniometer (Gäggeler et al., 1989) has been operated since 1988. This instrument determines the Fuchs surface area of the aerosol particles. LWC has been measured by a particulate volume monitor (Gerber, PVM-100) since April, 1995 (Gerber, 1984).

Furthermore, extensive field campaigns were performed during different seasons. This paper reports data from two campaigns, i.e. in April/May, 1992 and October/November, 1993. In addition to the parameters mentioned above, the aerosol number concentration for particle diameters d_p > 0.01 µm and the size distribution for particles with 0.1 < d_p < 7 µm were measured by a condensation particle counter (CPC, TSI, 3022) and an optical particle counter (OPC, PMS, LAS-X). A filter pack was used to sample aerosol-borne as well as gaseous species (i.e. Cl^-, NO_3^-, SO_4^{2-}, Na^+, NH_4^+, K^+, Mg^{2+}, Ca^{2+}, and HNO_3 and HCl, respectively). Cloudwater samples were obtained by a Berner cloudwater impactor, for the determination of the ions mentioned above as well as H^+. The droplet size distribution was determined by a forward scattering spectrometer probe (PMS, FSSP-100). More information is given in Schwikowski et al. (1995).

The experimental set-up was such that the cloudwater sampler collected only the cloud droplets, whereas the filter pack sampled aerosol particles and cloud droplets at moderate wind speeds (<10 m s^{-1}). Thus, the cloudwater to filter pack ratio directly represented the activated mass fraction of a certain chemical species (Baltensperger et al., 1994). The cloud droplets did not enter the inlet of the optical particle counter. Thus, only non-activated particles were measured with the OPC.

3. RESULTS AND DISCUSSION

Figure 1 shows the monthly means of the aerosol concentrations as measured by the epiphaniometer. It can be seen that large variations are found, with values typically a factor of ten higher in summer than in winter (Baltensperger et al., 1991, 1996). This variation is due to the seasonal variation of thermal convection, which during summer often induces transport of planetary boundary layer air to the Jungfraujoch. In contrast, during winter the site represents the free troposphere most of the time (Baltensperger et al., 1996).

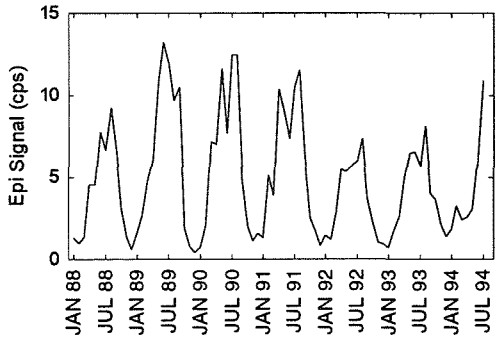

Figure 1. Annual variation of the aerosol signal as measured by the epiphaniometer (monthly means).

In contrast, the liquid water content did not vary significantly with season. Figure 2 shows the LWC frequency distributions, averaged over each month

since April, 1995. Evidently, there is no significant seasonality, and the median LWC for the whole time period (0.085 g m^{-3}) is very similar to the value obtained for fogs and low clouds of the Swiss plains (0.09 g m^{-3}) (Joos and Baltensperger, 1991). This is remarkable, since higher LWC values are usually found at mountain stations. As an example, Mohnen and Vong (1993) report an LWC of 0.44 g m^{-3} for Whiteface mountain, USA (1483 m asl).

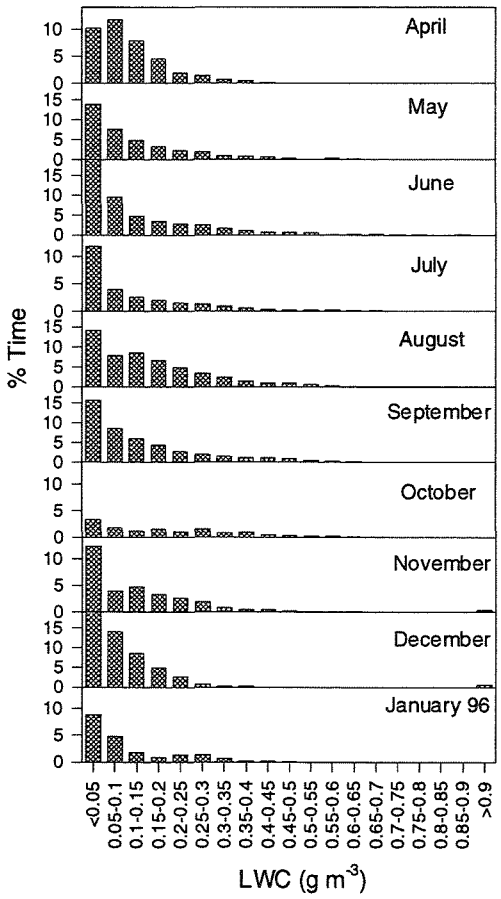

Figure 2. Frequency distributions of the cloud liquid water content for each month between April, 1995 and January, 1996, determined from 10-min averages.

The consequences of this different seasonal behavior are revealed in more detail by the results of the field campaigns. The OPC data showed that the formation of a cloud was often accompanied by a nearly complete elimination of the accumulation mode particles (0.1-1 μm) indicating that a large fraction of this particle size range was activated (Baltensperger et al., 1995).

The same observation was true regarding selected chemical species. As an example, Fig. 3 shows the sulfate load of cloudwater as a function of filter pack sulfate load (which included both, the cloudwater and the interstitial aerosol). Winter as well as spring data are given. The open circles represent cases with Southerly wind conditions: the strong winds from the South caused a large updraft at the sampling site, which was situated on a rocky crest. Under these conditions, the sampling efficiency of the Berner cloudwater collector dropped significantly, especially for the larger droplets, which often resulted in Gerber to Berner LWC ratios of greater than 10. Therefore, the Gerber LWC value was assumed to represent the correct values, and these data were used for the calculation of the load. However, when large droplets were present, this procedure yielded loads that were too high, since large droplets often have lower concentrations (Ogren et al., 1992). Indeed, it can be seen from Fig. 3 that most values which are significantly above the 1:1 line belong to these Southerly wind conditions.

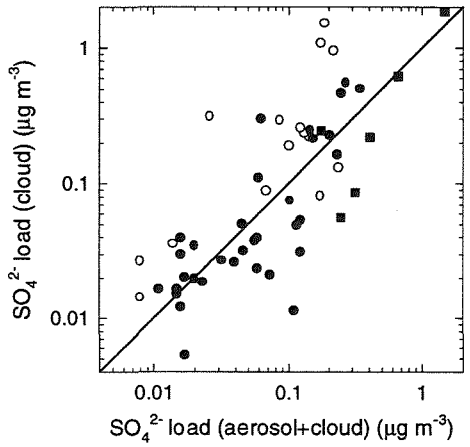

Figure 3. Sulfate load of cloudwater (determined from the concentrations of cloudwater samples and the LWC signal of the Gerber instrument) as a function of the sulfate load of cloudwater and interstitial aerosol (determined from the filter pack measurements). ●: winter cases; O: winter cases with Southerly wind conditions (see text); ■: spring cases. The solid line depicts the 1:1 relationship.

The other cases yielded values that were remarkably close to the 1:1 line indicating that the fraction of activated sulfate was often close to 1. Eliminating the cases with Southerly winds the mean activated sulfate fraction is about 1. This is in qualitative agreement with data by Heintzenberg and Leck (1994) who reported an activated sulfate fraction of about 0.8 for a remote marine atmosphere (sulfate concentrations between 0.2 and 2 μg m^{-3}). In highly polluted atmospheres, this value is much lower (about 0.2, see Heintzenberg and Leck, 1994, and references therein). Note that up to a total load of 1 μg m^{-3} sulfate, no dependence of the activated fraction on the sulfate concentration was found. Thus, the decrease of the activated fraction with sulfate load seems to occur only at concentrations > 1 μg m^{-3}.

Table 1 gives the mean ion concentrations (weighted by the liquid water content) for the October/November 1993 campaign. The total ion concentration (sum of anions and cations) is 98 μeq l^{-1}, which is much lower than e.g. on Mount Brocken, Germany, which is the highest mountain in the northern part of Middle Europe (1142 m asl, Möller et al., 1995). Mohnen and Vong (1993) also report higher values for Whiteface mountain, with a total ion concentration of about 600 μeq l^{-1}. Thus, our data from October/November 1993 are actually winter values, representative for the free troposphere. In contrast, the concentrations of the April/May 1992 campaign were about a factor of 6 higher (Schwikowski et al., 1994), and comparable to the annual average of Whiteface mountain (Mohnen and Vong, 1993).

Table 1. Liquid water weighted mean concentrations of the measured anions and cations (n= 72).

Ion	Concentration (μeq l^{-1})
Cl^-	5.5
NO_3^-	10.3
SO_4^{2-}	27.5
H^+	12.0
NH_4^+	16.7
Na^+	6.1
K^+	2.7
Mg^{2+}	2.3
Ca^{2+}	14.9

The best way in which to evaluate the relationship between the cloud droplet size and the aerosol number concentration would be through use of the FSSP-100. However, at the low temperatures usually encountered at this site excessive riming due to supercooled droplets occurred at the FSSP inlet, despite an installed heating unit. Thus, with the exception of a few cases the instrument did not yield reliable data. Since large variations of the aerosol concentrations occurred during a cloud event (Poulida et al., 1994), the OPC values just before the cloud were not necessarily representative for the whole time period. During the cloud event, the cloud droplets did not enter the inlet of the OPC so that the OPC did not yield a total number concentration either.

Therefore, an indirect approach was used to investigate the dependence of the cloud drop size on the aerosol number concentration. It has recently been shown that the size distribution of the accumulation mode aerosol at the Jungfraujoch is remarkably constant and independent of the aerosol concentration (Baltensperger et al., 1996). Therefore, the total sulfate load (i.e. the filter pack data) were chosen as a relative number of the aerosol particle concentration in the accumulation mode, taking the cube root of LWC divided by the sulfate load. Figure 4 shows that this nominal drop size decreases significantly with the sulfate load.

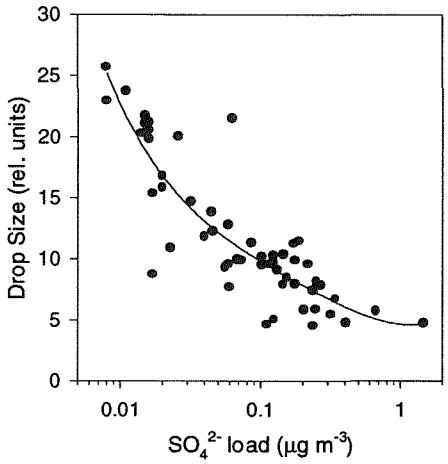

Figure 4. Calculated nominal drop size (relative units) as a function of the aerosol sulfate load.

Thus, higher aerosol concentrations on the Jungfraujoch during summer are most probably associated with smaller drop sizes, giving additional evidence for the impact of anthropogenic aerosols on cloud albedo.

4. ACKNOWLEDGMENTS

The support of the staff and the facilities at the Jungfraujoch research station is highly appreciated. This work was supported by the Swiss Bundesamt für Bildung und Wissenschaft (BBW) and the Swiss National Science Foundation.

5. REFERENCES

Baltensperger, U. H.W. Gäggeler, D.T. Jost, M. Emmenegger, and W. Nägeli, 1991: Continuous background aerosol monitoring with the epiphaniometer. *Atmos. Environ.*, **25A**, 629-634.

Baltensperger, U., M. Schwikowski, and H.W. Gäggeler, 1994: Scavenging of atmospheric constituents by snow. *Proc. EUROTRAC Symposium '94*, P.M. Borrell, P. Borrell, T. Cvitas, W. Seiler (eds.), SPB Academic Publishing bv, Den Haag, pp. 973-977.

Baltensperger, U., M. Schwikowski, H.W. Gäggeler, and O. Poulida, 1995: On the aerosol-cloud relationship at a high-alpine site. *J. Aerosol Sci.*, **26**, Suppl. 1, S899-S900.

Baltensperger, U., H.W. Gäggeler, D.T. Jost, M. Lugauer, M. Schwikowski, and P. Seibert, 1996: Aerosol climatology at the high-alpine site Jungfraujoch. *J. Geophys. Res.*, submitted.

Charlson, R.J., and J. Heintzenberg (eds.), 1995: *Aerosol Forcing of Climate*, John Wiley, Chichester.

Gäggeler, H.W., U. Baltensperger, M. Emmenegger, D.T. Jost, A. Schmidt-Ott, P. Haller, and M. Hofmann, 1989: The epiphaniometer, a new device for continuous aerosol monitoring. *J. Aerosol Sci.*, **20**, 557-564.

Gerber, H., 1984: Liquid water content of fogs and hazes from visible light scattering. *J. Climate Appl. Meteor.*, **23**, 1247-1252.

Heintzenberg, J., and C. Leck, 1994: Seasonal variation of the atmospheric aerosol near the top of the marine boundary layer over Spitsbergen related to the Arctic sulphur cycle. *Tellus*, **46B**, 52-67.

Joos F., and U. Baltensperger, 1991: A field study on chemistry, S(IV) oxidation rates and vertical transport during fog conditions. *Atmos. Environ.*, **25A**, 217-230.

Mohnen, V.A., and R.J. Vong, 1993: A climatology of cloud chemistry for the eastern United States derived from the mountain cloud chemistry project. *Environ. Rev.*, **1**, 38-54.

Möller, D., K. Acker, W. Wieprecht, S. Naumann, R. Auel, A. Oestreich, 1995: Preliminary results from the long-term Cloud Chemistry Monitoring at Mt. Brocken, Harz. *Proc. WMO-IGAC Conference on the Measurement and Assessment of Atmospheric Composition Change*, World Meteorological Organization, Global Atmosphere Watch No. 107, WMO, Geneva, pp. 31-35.

Ogren, J.A., K.J. Noone, A. Hallberg, J. Heintzenberg, D. Schell, A. Berner, I. Solly, C. Kruisz, G. Reischle, B.G. Arends, and W. Wobrock, 1992: Measurements of the size dependence of the concentration of non-volatile material in fog droplets. *Tellus*, **44B**, 570-580.

Poulida, O. M. Schwikowski, U. Baltensperger, J. Staehelin, and W. Henrich, 1994: Physical processes affecting the chemical composition of precipitation at the high alpine site Jungfraujoch, Switzerland. *Proc. EUROTRAC Symposium '94*, P.M. Borrell, P. Borrell, T. Cvitas, W. Seiler (eds.), SPB Academic Publishing bv, Den Haag, pp. 1225-1230.

Schwikowski, M., O. Poulida, U. Baltensperger, and H.W. Gäggeler, 1994: In-cloud scavenging of aerosol particles by cloud droplets and ice crystals during precipitation at the high alpine site Jungfraujoch. *Proc. EUROTRAC Symposium '94*, P.M. Borrell, P. Borrell, T. Cvitas, W. Seiler (eds.), SPB Academic Publishing bv, Den Haag, pp. 1221-1224.

Schwikowski, M,. P. Seibert, U. Baltensperger, and H.W. Gäggeler, 1995: A study of an outstanding Saharan dust event at the high-alpine site Jungfraujoch, Switzerland. *Atmos. Environ.*, **29**, 1829-1842.

CLOUD PROCESSING OF AEROSOL IN THE STRATOCUMULUS-CAPPED MARINE BOUNDARY LAYER

Sonia M. Kreidenweis[1], Graham Feingold[2], Bjorn Stevens[1] and William R. Cotton[1]

[1]Department of Atmospheric Science, Colorado State University, Fort Collins, CO, USA
[2]Cooperative Institute for Research in the Atmosphere / NOAA, Colorado State University, Fort Collins, CO, USA

1. INTRODUCTION

The effects of two aerosol processing mechanisms, both active in nonprecipitating clouds, upon the mass mean radii of cloud condensation nuclei (CCN) are examined. Repeated cycling of aerosol particles through nonprecipitating clouds is believed to be the mechanism by which the frequently-observed bimodal marine aerosol distribution is created (Hoppel, 1989). This distribution has peaks in the number concentration at radii near 0.02 and 0.09 μm, with a relatively sparse population of particles with radii near 0.06 μm. Such bimodal distributions are generally observed in air masses which have resided over the ocean for a number of days, and which have encountered clouds along their trajectories.

As discussed by Hoppel (1989), aqueous-phase S(IV)-to-S(VI) oxidation adds nonvolatile solute to each cloud droplet. If the drop is not removed by precipitation, but instead evaporates as the cloud dissipates, this nonvolatile mass is added to the CCN particle upon which the drop was formed. This chemical mechanism thus increases the mass mean size of that portion of the original aerosol spectrum which served as CCN; for typical marine stratus supersaturations, this corresponds to particles with radii larger than about 0.06 μm. The distribution minimum is produced by growth of the smallest CCN into the larger mode.

Droplet collision-coalescence acts to deplete the droplet number concentration (Ackerman *et al.*, 1993), and in nonprecipitating clouds will thus also increase the mass mean radius of CCN (Hudson, 1993). If significant collision–coalescence has occurred over the nonprecipitating cloud cycle, fewer particles are regenerated upon evaporation than were activated, thus leading to a larger mass mean CCN size.

During the lifetime of a natural cloud, it is likely that both mechanisms contribute to increases in CCN mass mean radii, although these changes may be small for a single cloud encounter. Several previous workers have investigated the role of short-term processing of aerosol. For example, Bower and Choularton (1993) and Flossmann (1994) have modeled hill-cap clouds and precipitating cumulus, respectively. The former study focused on chemical processing, while the latter included both chemistry and collision–coalescence. Both studies found substantial effects on the initial CCN spectrum for a single cloud processing event.

The focus of this work is an examination of the extent of CCN mass mean radius modification, via drop collision–coalescence and aqueous S(IV)-to-S(VI) conversion, that may occur in a nonprecipitating stratocumulus cloud, and the conditions under which either mechanism may play the dominant role in aerosol processing during such an event. Repeated cycling through clouds, in addition to other factors such as local particle sources and precipitation removal of CCN number and mass, is probably necessary to produce the dramatic shift from monomodal, continental-type aerosol distributions to the marine bimodal distribution.

2. MODEL FRAMEWORK

The role of drop collision–coalescence as a means of reducing drop number concentrations and thus CCN concentrations in a non-drizzling, stratocumulus–capped marine boundary layer is investigated in two types of modeling framework. The first is a two-dimensional eddy resolving model (ERM) that includes explicit treatment of aerosol and drop spectra, as well as the solute transfer between drop size bins. The second model framework is a box model representation which uses the same drop microphysics scheme to compute time-dependent drop spectra, but for which liquid water content (LWC) is specified.

The box model reasonably reproduces the drop number concentration depletion predicted in the ERM simulation, if similar LWC and initial drop number concentrations are assumed, and if, most importantly, the time available for collision–coalesence processing is weighted by the time spent continuously in–cloud along typical parcel trajectories. The box model, together with information on in–cloud residence time, has the advantage of numerical simplicity and speed and serves as a convenient framework for examining aerosol processing by

aqueous chemistry. The latter formulation is therefore focused on here, and the ERM and results derived from it discussed only briefly.

2.1 The Eddy Resolving Model (ERM)

This study employed the explicit–microphysics (EM), two-dimensional ERM version of the Regional Atmospheric Modeling System (RAMS), developed at Colorado State University. This model, and a three-dimensional large eddy simulation version, have been applied to stratocumulus studies in a number of works (Feingold *et al.*, 1994; Stevens *et al.*, 1996) that have investigated various aspects of CCN–cloud interactions and drizzle formation.

2.2 The Box Model

A box model was used to compute time-dependent drop number concentration depletion by the collision–coalescence mechanism only. The explicit microphysical scheme used, which is described in the next section, is the same as that in the ERM. Simulations were initiated with a lognormal drop distribution, defined by specified LWC and drop number concentration, with a geometric standard deviation of 1.5.

2.3 The Explicit Microphysics (EM) Model

The EM model employs a moment-conserving approach whereby moments of the drop, solute, and aerosol distribution functions are predicted. Changes in drop spectra due to activation, drop condensation and evaporation, stochastic collection and sedimentation are calculated explicitly following the moment-conserving techniques of Tzivion *et al.* (1987). The explicit microphysical routines solve for both number and mass concentrations of drops in each of the 25 drop bins, which span the radius space from 1.5625 to 500 μm, and of particles in each of 14 size bins, spanning the radius space 0.0056 to 7.3 μm. The aerosol is assumed to be chemically homogeneous, and particles are activated to droplets based on the assumed particle thermodynamic properties and on the local cloud supersaturation, calculated as in Stevens *et al.* (1996).

The major modification in this study is the inclusion of algorithms that predict the mass concentration of solute within the drops following the activation of CCN. Solute mass is transferred between bins via the processes of condensation / evaporation and stochastic collection, again using the techniques of Tzivion *et al.* (1987). The solute number concentration, which represents the potential number concentration of CCN that can be regenerated upon evaporation, is assumed equal to the drop number concentration. Thus, the total mass and number concentrations of the CCN regenerated from drop evaporation over a timestep are known.

3. COLLISION–COALESCENCE SIMULATIONS

3.1 Number Depletion in the ERM

The ERM was initiated with the July 7, 1987 sounding from the First ISCCP Regional Experiment (FIRE) held off the coast of CA (Betts and Boers, 1990). The domain size was 3000 m in the horizontal and about 1400 m in the vertical, with a Δz of 25 m and a Δx of 50 m. A time step of 2 s was used for all but the acoustic terms. In addition, the initial CCN field was chosen to produce little precipitation in the early stages of the simulation, in order to eliminate the effects of precipitation removal on the CCN spectrum.

Results from this simulation are summarized in Table 1, which reports the domain-averaged change in drop number concentration, $N_d(t)/N_d(0)$, where $N_d(t)$ is the drop number concentration at time t, and the corresponding change in aerosol mass mean radius, $r_a(t)/r_a(0)$, computed from Equation (1), where the subscripts a and d refer to the aerosol and the drops, respectively:

$$\frac{r_a(t)}{r_a(0)} = \left(\frac{N_a(t)}{N_a(0)}\right)^{-\frac{1}{3}} = \left[1 - \frac{N_d(0)}{N_a(0)}\left(1 - \frac{N_d(t)}{N_d(0)}\right)\right]^{-\frac{1}{3}} \quad (1)$$

The first hour of the simulation was a spin-up period, after which the steady-state LWC of approximately 0.25 g m^{-3} was achieved and collision–coalescence processing commenced. During the second hour of the simulation, the drop number concentration is depleted to 77.5% of its original value, with a corresponding 6.8% increase in the mass mean radius of the CCN.

Time (min)	$N_d(t)/N_d(0)$	$r_a(t)/r_a(0)$
0	1	1
60	1	1
90	0.915	1.024
120	0.775	1.068
150	0.558	1.157
180	0.390	1.250

Table 1. Domain-averaged drop number concentrations (N_d) at six times in ERM simulation, with corresponding change in aerosol mass mean radius, r_a.

3.1 Number Depletion in the Box Model

The box model was initialized as described in Section 2.2, and a series of computations performed for LWC ranging from 0.1 to 0.8 g m^{-3} and initial drop number concentrations ranging from 10 to 200 cm^{-3}. The time-dependent change in drop number concentration by collision–coalescence was then weighted by the probability density function (PDF) for the amount of time per hour that parcels spend continuously in cloud (Figure 1), as

determined by Stevens *et al.* (1996) from two- and three-dimensional ERM simulations.

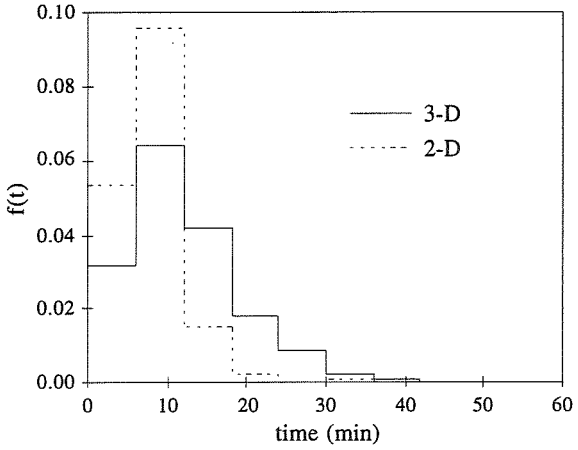

Figure 1. PDFs of parcel in-cloud residence time, in min per hour, from two- and three-dimensional ERMs. Adapted from Stevens *et al.* (1996).

The normalized mean drop number concentrations after one hour, shown in Figure 2, were generated by applying the PDFs for the two-dimensional case to the results for the box model simulations, using Equation (2):

$$\left(\overline{N_d(t)/N_d(0)}\right) = \frac{\int \left(N_d(t)/N_d(0)\right) f(t)dt}{\int f(t)dt} \quad . \qquad (2)$$

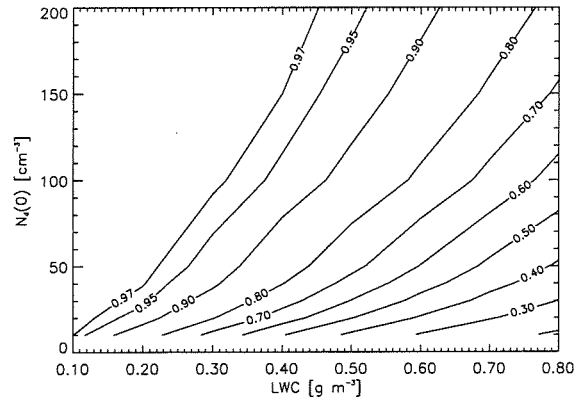

Figure 2. Contours of normalized mean drop number concentration, $\overline{N_d(t)/N_d(0)}$ after one hour, as a function of initial number concentration (cm^{-3}) and liquid water content ($g\ m^{-3}$) and using the two-dimensional PDF as the weighting function for in–cloud residence time.

From Figure 2, for a fixed initial drop number concentration, increasing the LWC will result in increased drop number depletion; at a specified LWC, decreasing initial drop number concentrations enhances the number depletion. At 60 min in the ERM, $N_d(0)$ was 40 cm^{-3} and the average LWC 0.25 $g\ m^{-3}$; after 60 further min of processing, $\overline{N_d(t)/N_d(0)}$ was found to be 0.775 (Table 1). From Figure 2, the same initial conditions yield a value of approximately 0.95. Since many of the trajectories spend greater amounts of time near cloud top, where the LWC is closer to 0.5 $g\ m^{-3}$, this estimate is too conservative. Using a LWC of 0.4 $g\ m^{-3}$ in Figure 2, $\overline{N_d(t)/N_d(0)}$ is estimated to be 0.8, in good agreement with the ERM.

The residence-time-weighted drop depletion and corresponding increase in aerosol mass mean radius were determined for a range of initial drop number concentrations and LWCs, assuming $N_d(0)/N_a(0)$=0.8, which was the average for the ERM simulation. The results for one hour of cloud processing are shown in Table 2. The three-dimensional simulations predict more depletion, and hence a larger impact on particle radius, because of the weighting toward longer in–cloud times evident in Figure 1. The predicted impacts on aerosol mass mean radius range from negligible, at low LWC, to about a 10% increase for higher LWC.

	2-D		3-D	
	$N_d(0)$		$N_d(0)$	
LWC ($g\ m^{-3}$)	50	100	50	100
0.1	1.0008	1.0003	1.0013	1.0005
0.2	1.0054	1.0019	1.0109	1.0035
0.5	1.0860	1.0354	1.1668	1.0893

Table 2. Ratio of aerosol mass mean radius to its initial value, after one hour of collision–coalescence processing in the residence time / box model.

4. CHEMICAL PROCESSING OF AEROSOL

4.1 Mass Addition in Box Model

The next step is to produce a table which is the analogue of Table 2, but which shows the increase in mass mean particle radius due to the addition of nonvolatile mass by aqueous-phase S(IV)-to-S(VI) conversion. The following equation, similar to that applied to compute the mean extent of drop depletion, was used to determine the mean extent of chemical conversion of SO_2, $\bar{c}$:

$$\bar{c} = \frac{\int c(t)f(t)dt}{\int f(t)d(t)} \quad . \qquad (3)$$

Estimates of $c(t)$, the time-dependent chemical conversion of SO_2, were obtained from the work of Chameides (1984), who reported the results of simulations of the aqueous-phase chemistry in a marine stratus cloud as the percent conversion of SO_2 for several LWCs. His base-case initial gas-phase concentration of SO_2 was 55 pptv, which was also adopted here to determine the mass converted. Results from the application of Equation (3) are summarized in Table 3. Determination of $c(t)$ from Chameides' (1984) results required interpolation between the limited data he reported; thus the estimates of $\bar{c}$ shown in Table 3 are approximate, and will also vary with the chemical environment chosen.

LWC (g m^{-3})	$\bar{c}$, 2-D	$\bar{c}$, 3-D
0.1	11	17
0.2	28	37
0.5	45	54

Table 3. Estimated mean percent SO_2 conversion, after one hour of processing in residence time / box model.

The impact on mass mean particle size was next computed from Equation (4), where the mass added over one hour by aqueous chemistry, M_{aq}, was determined from the mean conversion from Table 3 and the assumed initial gas-phase concentration:

$$\frac{r_a(t)}{r_a(0)} = \left(1 + \frac{M_{aq}(t)}{M_a(0)} \right)^{\frac{1}{3}} . \qquad (3)$$

Table 4 summarizes values computed for the assumption that the initial aerosol mass, $M_a(0)$, is that of a lognormal initial aerosol with the particle number concentrations indicated, a geometric mean radius of 0.08 μm, and a geometric standard deviation of 1.8.

	2-D		3-D	
	$N_a(0)$		$N_a(0)$	
LWC (g m^{-3})	50	100	50	100
0.1	1.0078	1.0039	1.0116	1.0058
0.2	1.0189	1.0096	1.0249	1.0126
0.5	1.0301	1.0153	1.0359	1.0183

Table 4. Ratio of aerosol mass mean radius to its initial value, after one hour of chemical processing in the residence time / box model.

Comparison of Tables 2 and 4 suggests that, at low to moderate LWCs, aqueous chemistry plays a dominant role in modifying the mean particle size, whereas the impact of collision–coalescence is comparable to, or even larger than, that of chemistry for LWC = 0.5 g m^{-3}. Chemical conversion may occur more strongly in the initial stages of the cloud, until reagents are consumed, whereas the effectiveness of collision–coalescence is expected to increase with time as drop number concentrations are depleted (Feingold *et al.*, 1996).

5. SUMMARY

Both collision–coalescence and aqueous chemical reactions increase the mean size of CCN regenerated from nonprecipitating clouds, and thereby also enhance the cloud-nucleating activity of the CCN in subsequent cloud cycles. Collision–coalescence has been explored in an eddy resolving model and found to have a potentially large impact on the mass mean size of CCN. To explore parameter space more extensively, and to examine the relative importance of collision–coalescence and aqueous chemistry, a box model that treats each process independently was developed. The results suggest that the impacts of collision–coalescence on the CCN spectrum regenerated from nonprecipitating clouds can, under some circumstances, be as substantial as those resulting from aqueous chemical processes, with the relative importance of the two mechanisms varying with environmental conditions.

6. ACKNOWLEDGMENTS

This work was supported by the National Science Foundation under Grant No. ATM-9215951, by the Office of Naval Research under Grant No. N00014-93-0420-P00001, and by the NOAA Climate and Global Change Program.

7. REFERENCES

Ackerman, A. S., O. B. Toon, and P. V. Hobbs, 1993: Dissipation of marine stratiform clouds and collapse of the marine boundary layer due to depletion of cloud condensation nuclei by clouds. *Science*, **262**, 226–229.

Betts, A. K., and R. Boers, 1990: A cloudiness transition in a marine boundary layer. *J. Atmos. Sci.*, **47**, 1480–1497.

Bower, K. N., and T. W. Choularton, 1993: Cloud processing of the cloud condensation nucleus spectrum and its climatological consequences. *Quart. J. R. Meteor. Soc.*, **119**, 655–679.

Chameides, W. L., 1984: The photochemistry of a remote marine stratiform cloud. *J. Geophys. Res.*, **89**, 4739–4755.

Feingold, G., B. Stevens, W. R. Cotton and R. L. Walko, 1994: An explicit cloud microphysical / LES model designed to simulate the Twomey effect. *Atmos. Res.*, **33**, 207–233.

Feingold, G., S. M Kreidenweis, B. Stevens, and W. R. Cotton, 1996: Numerical simulations of stratocumulus processing of cloud condensation nuclei. *J. Geophys. Res.*, submitted.

Flossmann, A. I., 1994: A 2-D spectral model simulation of the scavenging of gaseous and particulate sulfate by a warm marine cloud. *Atmos. Res.*, **32**, 233–248.

Hoppel, W. A., 1989: in *Aerosols and Climate*, P. V. Hobbs and M. P. McCormick, Eds. A. Deepak Publishing, 9–19.

Hudson, J. G., 1993: Cloud condensation nuclei near marine cumulus. *J. Geophys. Res.*, **98**, 2693–2702.

Stevens, B., G. Feingold, W. R. Cotton, and R. L. Walko, 1996: On elements of the microphysical structure of numerically simulated nonprecipitating stratocumulus. *J. Atmos. Sci.*, **53**, 980–1006.

Tzivion, S., G. Feingold and Z. Levin, 1987: An efficient numerical solution to the stochastic collection equation. *J. Atmos. Sci.*, **44**, 3139–3149.

THE INFLUENCE OF CONVECTIVE CLOUDS ON THE TRANSPORT OF GASES AND PARTICLES

Andrea I. Flossmann

Laboratoire de Météorologie Physique, Université Blaise Pascal - CNRS - OPGC
63177 Aubière Cedex, France

1. INTRODUCTION

Numerous atmospheric pollutants have their sources (natural or anthropogenic) at the earth's surface. There, they are emitted and then distributed evenly in the well-mixed boundary layer. As long-range horizontal transport in the boundary layer is rather limited and the life times of some of the species are only on the order of a few days, the species would stay close to the source in the absence of vertical transport. However, it has been argued that convection would provide an efficient means of transporting these chemical species from the boundary layer to the free troposphere. Due to this transport of gaseous matter and aerosols from the boundary layer to the free troposphere, the pollutants can not only participate in the long range transport, which takes predominantly place in these higher altitudes. There, they can sometimes also experience longer residence times due to the changed temperatures and participate in the free tropospheric chemistry.

We will thus study the transport of trace gases and aerosol particles from the well mixed boundary layer to the free troposphere by a moderate convective cloud. As we can expect the amount of trace gases present in and transported through the cloudy air to be strongly influenced by the solubility of the considered trace gases we choose to study the behavior of three different gases (inert tracer, SO_2, and H_2O_2) covering the range of Henry constants commonly found in the atmosphere. As an inert tracer we have also used SO_2 by artificially suppressing any uptake by the cloud drops.

2. MODEL DESCRIPTION

As discussed in detail by Flossmann and Pruppacher (1988) the basic framework employed in the present study is a two-dimensional slab-symmetric version of the three-dimensional model developed by Clark and coworkers (e.g. Clark, 1977, 1979; Clark and Gall, 1982; Clark and Farley, 1984; Hall, 1980). DESCAM, i.e., the *de*tailed *sca*venging and *m*icrophysical model is discussed in Flossmann et al (1985, 1987). There, the aerosol particles are treated in a spectral form and apart from dynamical processes the number of particles of a certain size changes due to activation to drops, due to size changes resulting from humidity changes, and due to impaction scavenging by drops. The nucleated drops then grow by condensation or evaporate, collide and coalesce, and eventually break up. During their lifetime they further scavenge particles and the scavenged pollutant mass is redistributed through the microphysical processes.

3. INITIAL CONDITIONS

The initialization of the present model is the same as that in Flossmann (1991, 1994) with the exception of the initial concentrations of SO_2 and H_2O_2. The sounding was taken at Day 261 (September 18, 1974) of the GATE campaign at 12 GMT. Our 2-D model domain was oriented north-south, as this was the main wind direction. In the lowest 2km and above 6km the wind was southerly while in between the wind was northerly.

The initial aerosol particle spectrum was assumed to be of maritime type consisting of a superposition of three log-normal distributions. The two small modes were assumed to consist of $(NH_4)_2SO_4$ particles and the large mode was set to hold only NaCl particles. The particle spectra were assumed to decrease exponentially with height taking into account that practically no NaCl exists above 2.5km (scale height of 1km, compare Flossmann, 1991). The $(NH_4)_2SO_4$ particles were assumed to decrease with a scale height of 3km as described in Flossmann (1991).
The SO_2, H_2O_2 and O_3 initial concentrations were assumed to 0.5ppb, 0.5ppb, and 30ppb, respectively, in agreement with marine observations. In order to be able to calculate the transport of SO_2 and H_2O_2 produced at the surface we prescribed constant values for SO_2 and H_2O_2 in the first 400m above ground (two gridlevels), above which the concentrations were set to zero. O_3 was prescribed constant with height. In a first simulation (*case 1*) the uptake of SO_2 and its oxidants into the liquid phase was purposely inhibited, thus considering as an inert tracer. In *case 2* all three gases were scavenged by the cloud drops where H_2O_2 and O_3 served as oxidizing agents

converting S(4) to S(6). This was done to be able to identify the role of cloud gas uptake for the vertical redistribution of atmospheric pollutants by convection.

In order to test the role of the aerosol particles in the vertical transport by convective clouds the *case study 3* was performed. Here, all aerosol particels above 400m altitude were set to zero.

4. MODEL RESULTS

The simulations started at 12 GMT. After 26 min. of model time a cloud had formed. After 14 min. of cloud life time the first rain fell from cloud base and after 19min of cloud life time the first rain reached the ground. The rain lasted for about 25 min, the last 10 min. being only an insignificant drizzle (precipitation rate below 1mm/h). Therefore, we terminated the simulation after 60 min. The dynamical and microphysical results compared quite well with observations made during that day (Table 2 of Flossmann, 1991).

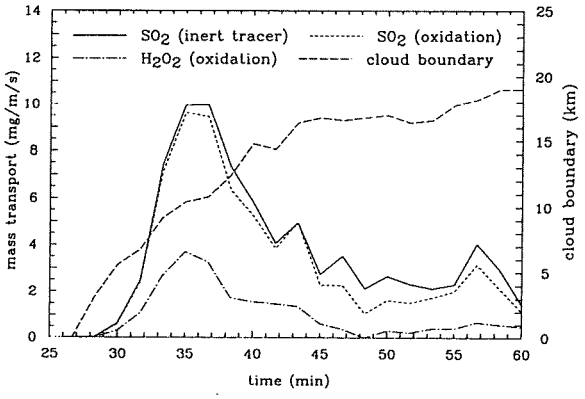

Fig.1: Net transport of mass in mg/m/s into the cloud. The long-dashed line gives the length of the cloud boundary through which the transport occurred.

The mass transport of the considered gases through the cloud boundaries is displayed in Fig.1. In addition also the "length" of the associated cloud boundary is given by the long-dashed line. In general, we can see from Fig.1 that at all times the time evolution for the three gases displayed shows the same qualitative behavior. Quantifying the mass transport across the boundaries, we can see that the case of the inert tracer (solid line) shows the strongest transport, and the weakest transports are found for H_2O_2 (dash-dotted line). In the middle, we find SO_2 with uptake into the liquid phase and subsequent oxidation processes considered. The difference between the curves for SO_2 as a scavenged and oxidized gas and H_2O_2 results from two facts. The first is, that 0.5 ppb(v) SO_2 and 0.5 ppb(v) H_2O_2 give a higher mass concentration (about a factor of 2) for SO_2 than for H_2O_2 (initial boundary layer mass concentrations: 1.4mg/m^3 for SO_2 and 0.76 mg/m^3 for H_2O_2). The second difference results from the fact that H_2O_2 is much more soluble than SO_2. We find here, that it is mainly determined by the mass transport through cloud base as the transports through the sides and the top are generally much smaller and often compensate each other.

	SO_2 (inert)	SO_2(ox)	H_2O_2(ox)
$T^{total}_{cl\ base}$	7.4	6.8	2.3
$T^{total}_{cloud\ top}$	1.0	0.6	0.1
T^{total}_{left}	0.7	0.8	0.4
T^{total}_{right}	-1.3	-1.3	-0.7
$T^{total}_{(2\text{-}D)}$	7.8	6.9	2.1

Table 1: total masses in g/m^3 transported through the 2-D boundaries

The total masses associated with the transport through the four different cloud boundaries and the net transport are given in Table 1. These variables pertain to a 2-D cloud with unit depth. Considering an average cloud base length of 5km we can estimate from Table 2 the total mass transfer of a 3-D cloud from the boundary layer to the free troposphere to be 37 kg for SO_2 as an inert tracer, 34 kg for SO_2 as a scavenged species and 12 kg for H_2O_2. This corresponds to roughly 60% of the pollutant mass initially present in the boundary layer (this number depends on the size of the computational domain). However, not all this material will be found at a given time in the air. This will only apply to the case of the inert tracer. SO_2 will be taken up into the cloud where it will be oxidized and transported to the ground with precipitation. Consequently, the fraction remaining in the air will vary but generally ranges around 75%. As H_2O_2 has a much higher solubility only about 30% of the material transported upward will actually be found in the air. The rest is scavenged rather efficiently by the cloud drops whereby the scavenging is almost complete in the center of the cloud. Gaseous H_2O_2 can only be found at the cloud edges where the liquid water content is rather small.

In Fig.2 we see the transport and uptake of SO_2 by the cloud. Note the reduction in the boundary layer and the accumulation in the cloud regions. However, the resulting SO_2 concentrations in the cloud are smaller in case 2 (scavenged gas) than case 1 (inert tracer) due to the scavenging of part of the SO_2 into the liquid phase. This becomes even more prominent for H_2O_2. The high Henry's law constant is responsible for the fact that we see almost no H_2O_2 (concentrations below 0.01 ppb(v) in the center of the cloud and concentrations below 0.1 ppb(v) at the edges) above 1km. We find this effect also in the curves for the net mass transport (Fig.1). For the transport through cloud base we still find roughly a factor of 2 to 3 between H_2O_2 and SO_2 maintained.

The transport through cloud top, however, differs by roughly a factor of 8 as almost no H_2O_2 is found at cloud top.

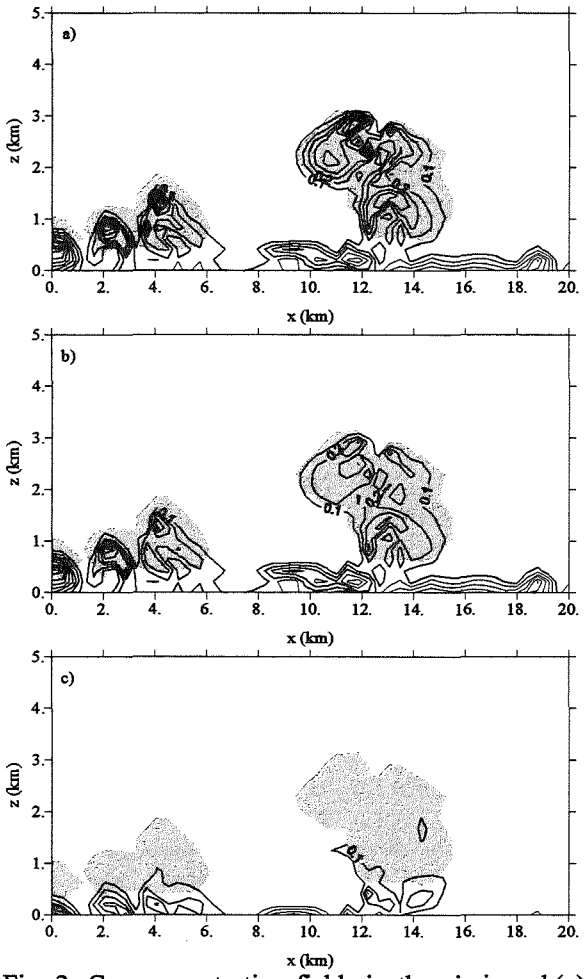

Fig. 2: Gas concentration fields in the air in ppb(v) after 45 min. of model time (19 min. of cloud life time). (a) SO_2 concentration from case 1, (b) SO_2 concentration from case 2, (c) H_2O_2concentration from case 2; contour spacings: 0.1 ppb(v); the shaded area is the visible cloud ($q_c>10^{-4}$ g/kg).

A similar transport can be found for the aerosol particles. In Fig.3 we see the vertical transport of aerosol particles. Initially, the particles have only been present below 400m. Convection has transported them to higher altitudes where they served as CCN and formed the cloud. However, not all particles were taken up by nucleation scavenging. Numerous particles, among those also particles larger than 0.1μm in radius (see Fig.3b) exist now at higher altitudes. The evolving cloud is similar to the one which formed on the complete spatial distribution of aerosol particles assumed for case 1 and 2. Differences, however, can be noted, e.g., concerning the faster formation of precipitation in case 3. This indicated that clouds form mainly on the aerosol particles present in the boundary layer which are vented up in the process of cloud formation.

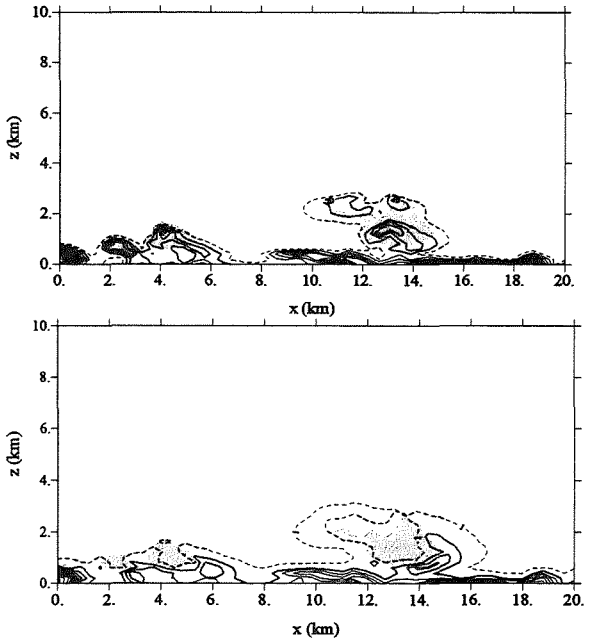

Fig.3: Venting of aerosol particles by convective clouds: for small particles (upper fig; a<0.1μm) and large particles (lower fig.; a>0.1μm) in no./cm^3; the shaded area gives the cloud after 20min of life time (Flossmann, 1996); initially the particles were only at z<400m

5. SUMMARY AND CONCLUSIONS

We have used the DESCAM model in a 2-D dynamic framework. Assuming a local pollution layer of SO_2 and H_2O_2 due to emission at the ground and an even mixture in a marine boundary layer of 400m, we have calculated the vertical and horizontal redistribution of these gases caused by a warm convective cloud. In order to cover the different solubilities of atmospheric gases we have performed two case studies. In the first case we have used SO_2 as an inert tracer by artificially suppressing any uptake by the cloud drops. Even though this is an unrealistic scenario it is nevertheless useful. First, as SO_2 is not interacting with the cloud it can also be considered as a generic inert tracer as the results obtained would apply to any inert gas with similar distribution, taking into account the differences in molecular weight. Secondly, the run is useful as it allows a comparison with the second case study where SO_2 and H_2O_2 are scavenged by the cloud drops. In the cloud S(4) is oxidized to S(6) with the help of H_2O_2 and O_3 which are simultaneously present. The comparison between SO_2 from case 1 (inert tracer) and case 2 (scavenged gas) gives information on the contribution of cloud chemistry to the process of cloud venting. Studying the vertical fluxes of the gases in the two cases, as well as the mass transport

and the development of the vertical distribution of the gases we can draw the following conclusions:

(1) An inert tracer is depleted from the boundary layer and transported upward by a convective cloud. For the medium-sized warm cumulus cloud considered 37 kg were transported through cloud base (initial MBL concentration: 1.4 mg/m^3) corresponding to 60% of the initial pollutant mass in the MBL surrounding the cloud. The upward and downward flux at cloud top is at least a factor of 5 smaller than the inflow at cloud base. The transport through the sides is strongly influenced by the ambient meso-scale flow influencing cloud circulation.

(2) The results showed little sensitivity using SO_2 as an inert tracer or as a gas scavenged and oxidized by the cloud drops. The mass of SO_2 transported through the cloud boundaries differs only marginally at cloud base. However, at cloud top the two cases differ by a factor of 2 which reflects the integrated history of the SO_2 uptake by the cloud. The total mass transport across cloud base introduces 34 kg of SO_2 into the free troposphere which corresponds again to 60% of the SO_2 mass initially present in the surrounding MBL. Due to the uptake into the cloud drops, however, after half an hour of cloud life time only about 75% of the gas is actually in the air ready to participate in long range transport if the cloud would suddenly disappear. Part of the scavenged SO_2 is present as S(6) in the cloud drops and part as S(4) which could eventually desorb again. Of this scavenged SO_2 a certain fraction has already left the atmosphere because it has been redistributed through collision and coalescence into the large drops which have dropped to the ground as precipitation (compare Flossmann, 1994).

(3) As an example for a highly soluble gas H_2O_2 was considered. Taking into account the fact that 0.5ppb H_2O_2 results in a factor of 2 lower mass concentration than SO_2 (MBL concentration 0.76 mg/m^3), the mass transport of H_2O_2 across cloud base has the same magnitude as for SO_2. Actually, about 12 kg (60% of the mass initially present in the surrounding MBL) were transported out of the boundary layer through a cloud base of roughly 25km^2 as compared to 34kg for SO_2. The fluxes through the other boundaries are rather small as almost all H_2O_2 (70%) was scavenged by the cloud drops and partly used up during the sulfur oxidation process.

(4) Clouds are mainly formed on the aerosol particles they vent up from the boundary layer. Thereby, they don't use up all these particles as CCN. Numerous particles, some of these also larger than 0.1mm, stay unactivated in the vincinity of the cloud. These particles will make it difficult to identify in real clouds the formation of new particles.

6. ACKNOWLEDGMENTS

The author acknowledges with gratitude the support by the European Community under EV5V-CT93-0313. The calculations have been done on the CRAY C98 and C94 of the "Institut du Développement et des Ressources en Informatique Scientifique" (IDRIS, CNRS) in Orsay (France) under project no. 940180. The author acknowledges with gratitude the hours of computer time and the support provided. Furthermore, the author acknowledges the support provided by the French national program PATOM.

7. LIST OF REFERENCES

Clark, T.L., 1977: A small scale dynamic model using terrain-following coordinate transformation. *J. Comput. Phys.*, **24**, 186-215.

Clark, T.L., 1979: Numerical simulations with a three dimensional cloud model. *J. Atmos. Sci.*, **36**, 2191-2215.

Clark T.L., and Gall, R., 1982: Three dimensional numerical model simulations of air flow over mountainous terrain: A comparison with observation. *Mon. Weather Rev.*, **110**, 766-791.

Clark, T.L and Farley, R.D., 1984: Severe downslope windstorm calculations in two and three spatial dimensions using anelastic interactive grid nesting. *J. Atmos. Sci.*, **41**, 329-350.

Flossmann, A.I., 1991: The scavenging of two different types of marine aerosol particles using a two-dimensional detailed cloud model. *Tellus*, **43B**, 301-321.

Flossmann, A.I., 1994: A 2-D spectral model simulation of the scavenging of gaseous and particulate sulfate by a warm marine cloud. *J. Atmos. Res.*, **32**, 255-268.

Flossmann, A.I., 1996: Interaction of aerosol particles and clouds, in preparation.

Flossmann, A.I., W.D. Hall, and H.R. Pruppacher, 1985: A theoretical study of the wet removal of atmospheric pollutants. Part I. *J. Atmos. Sci.*, **42**, 582-606.

Flossmann, A.I., H.R. Pruppacher, J.H. Topalian, 1987: A theoretical study of the wet removal of atmospheric pollutants. Part II. *J. Atmos. Sci.*, **44**, 2912-2923.

Flossmann, A.I., and H.R. Pruppacher, 1988: A theoretical study of the wet removal of atmospheric pollutants. Part III. *J. Atmos. Sci.*, **45**, 1857-1871.

Flossmann, A.I. and W. Wobrock 1996:Venting of gases by convective clouds. *J. Geophys. Res.*, submitted.

Hall, W.D., 1980: A detailed microphysical model within a two-dimensional dynamic framework: Model description and preliminary results. *J. Atmos. Res*, **37**, 2486-2507.

AEROSOL-CLOUD INTERACTIONS IN THE CLOUDY MARINE BOUNDARY LAYER

Raif Majeed[1], Dean A. Hegg[2], Pofat Yuen[2] and Marcia B. Baker[1]

[1] Geophysics Program, University of Washington, Seattle, WA 98195-1650, USA
[2] Dept. of Atmospheric Sciences, University of Washington, Seattle, WA 98195-1640, USA

1. INTRODUCTION

A particularly interesting example of aerosol-cloud interaction is the impact of cloud processing on the aerosol size distribution. One consequence of this size modulation by clouds is that the integral properties of the aerosol size distribution, for example aerosol light scattering, may also be modulated by cloud processing. Indeed, Lelieveld and Heintzenberg (1992) have suggested that cloud processing will much enhance the scattering efficiency of aerosol. Another consequence of the impact of cloud processing on the aerosol size distribution is the potential enhancement in the Cloud Condensation Nucleus (CCN) activity of the aerosol. This, in principle, can alter the microstructure of succeeding clouds which form on the processed aerosol, thus establishing an interesting feedback (cf., Hoppel *et al.*, 1990; Hegg, 1990; Kaufman and Tanre, 1995).

To explore these issues further, we have undertaken a modeling study of the impact of clouds—including multiple cloud cycles—on the light-scattering and CCN properties of the aerosol processed by them. Our main tool for this study is a Lagrangian parcel model (LTM) which we use in a kinematic framework, the parcel trajectory and cloud-interaction history being (in general) prescribed by a combination of back trajectory analysis, the satellite-based cloud encounter scheme of Bretherton *et al.* (1995), and the output of an Eulerian Large Eddy Simulation (LES) model (Rand, 1994). For the simulations presented here, which are preliminary in nature, the prescribed kinematic profiles are ad-hoc, designed to address a limited set of specific issues.

2. RESULTS

2.1 Impact of cloud processing on aerosol light-scattering

Simulation with a predecessor parcel model to the LTM demonstrated the impact of heterogeneous cloud chemistry on the light-scattering properties of cloud processed marine aerosol (Hegg *et al.*, 1992), in particular, the impact of sea salt particles. Sievering and his colleagues (e.g., Sievering *et al.*, 1995) have shown that SO_2 oxidation in "dry" salt haze can have a significant impact on the sulfur budget of the MBL, thus suggesting the possibility of such oxidation impacting the aerosol size distribution and consequent aerosol light-scattering properties in a manner analogous to that which occurs in clouds (i.e., activated aerosol). To explore this issue, we have run the LTM model under both saturated and subsaturated conditions to compare the effects of SO_2 oxidation in clouds and haze on the particle size distribution and the aerosol light-scattering. We have done this for two different scenarios, background marine air and polluted air such as that found just off shore of the east coast of the United States. We have also conducted a model run involving multiple cloud cycles (three) to simulate the repeated cycling of MBL air through cloud in an MBL topped by a stratocumulus deck. The initial conditions for this run were taken from data collected during ASTEX. To date, all cloud runs which have examined chemical effects have been for non-precipitating clouds.

Sulfate production as a function of time for the two "dry" runs are shown in Figure 1. While the time dependencies of the sulfate production for the two different scenarios (polluted and background) are distinct and interesting, the important point to note here is that both suggest an average of ~15% SO_2 conversion during the ~8 hr time scale of the runs. Thus, in both cases, significant SO_2 oxidation has occurred, confirming the work of earlier investigations. However, the impact of this oxidation on the aerosol

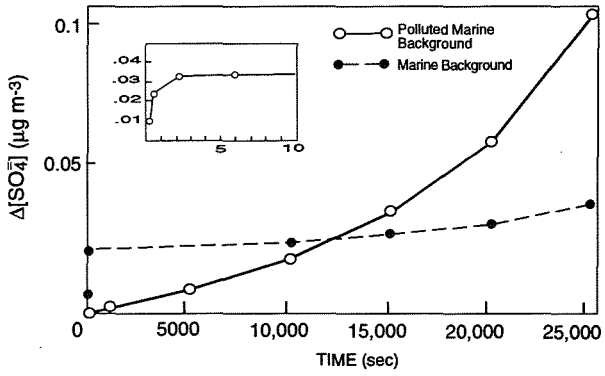

Figure 1: Sulfate production as a function of time for subsaturated runs at an initial RH of 93%. Background marine scenario (—). Polluted marine scenario (---).

size distribution was negligible. Initial and final size distributions were essentially identical. Hence, the impact of the cloud processing on the aerosol light scattering and aerosol optical depth was also negligible.

In contrast to the dry runs, the cloud-processed size distributions showed significant differences with the initial spectra. Initial and final aerosol volume distributions for the background and polluted scenarios are shown in Figures 2 and 3, respectively. However, for the background case, the volume change was outside of the efficient light scattering range and hence the impact on aerosol light scattering was still only slight. On the other hand, the volume change for the polluted scenario occurs predominantly in the efficient light-scattering range and thus produces an appreciable change in the aerosol light-scattering and optical depth.

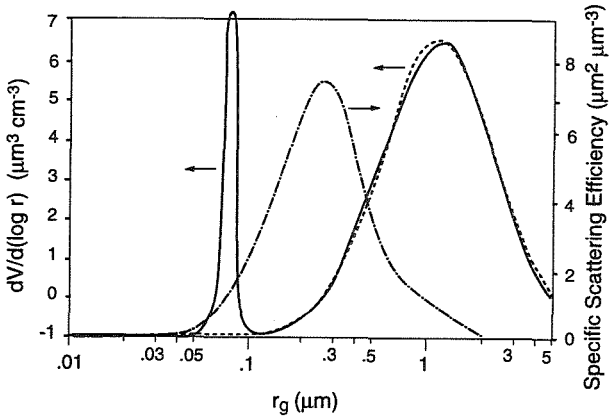

Figure 2: Particle size distributions before (---) and after (—) cloud processing for the background marine scenario. Also shown in the specific scattering efficiency for Mie scattering (-•••-).

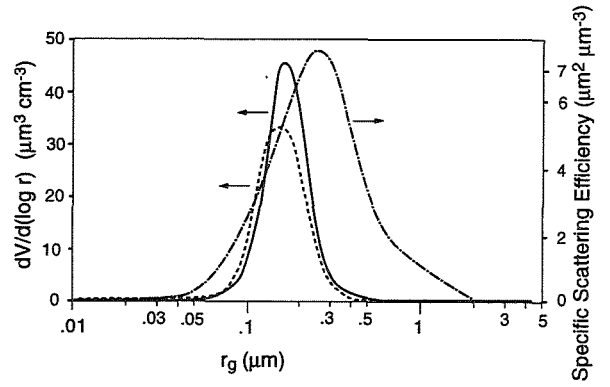

Figure 3: Particle size distributions before (---) and after (—) cloud processing for the polluted marine scenario. Also shown is the specific scattering efficiency for Mie scattering (-•••-),

Optical depths calculated for each of the four scenarios described above (assuming an MBL depth of 1 km) are shown in Figure 4. Observations of gradients in optical depth over trajectories with time scales on the order of 8 hrs suggest that variation in

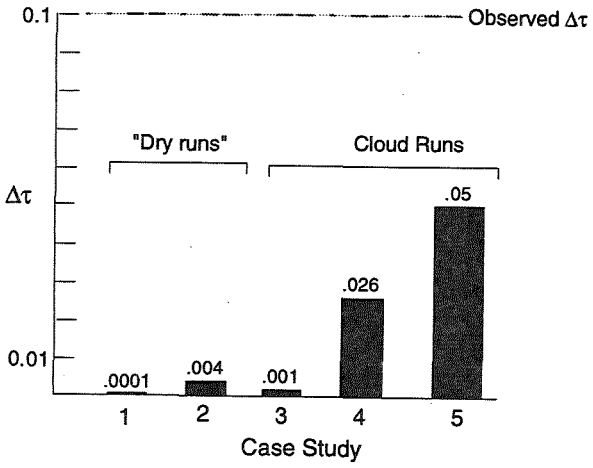

Figure 4: Aerosol optical depth changes ($\Delta\tau$) for five different model runs. Case 1: background marine, undersaturated, 8-hr run. Case 2: polluted, subsaturated, 8-hr run. Case 3: background marine, 30-min cloud run. Case 4: polluted, 30-min cloud run. Case 5: ASTEX, 3-cycle cloud run.

optical depth are on the order of 0.05 to 0.1. Hence, the cloud processing scenarios appear to provide a viable explanation for observed variation while the dry runs do not. This is particularly striking when one considers that the cloud runs are for a single cloud cycle of ~0.5 hrs, i.e., the effect produced would assume only a single 0.5 hr cloud encounter over an 8-hr period.

The final scenario analyzed was based on data from the ASTEX experiment. In this run, three consecutive cloud encounters are postulated of ~0.5 hrs each, with inter-cloud time scales essentially equivalent to the boundary layer turn-over time of ~one hour. Thus, the total run time is on the order of 4 hrs. The initial and final aerosol size distributions for this run are shown in Figure 5. The multiple cloud processing has markedly increased the aerosol volume in the efficient light-scattering range. The optical depth change associated with this spectral modification is shown in Figure 4. The optical depth change of ~0.05 is clearly of great significance.

2.2 Impact of cloud processing of aerosol on droplet spectra in subsequent clouds

Because of its impact on CCN activation spectra, cloud processing of aerosol is known to have an impact on the sizes of cloud droplets which subsequently form on those aerosol particles. Bower and Choularton (1993) reported a significant decrease in simulated droplet radius as a result of such processing; however they did not consider the effect on the initiation of precipitation, a process that we include in our model.

Our preliminary results indicate a complex parameter space within which microphysical effects of cloud processing are significant. Figure 6 shows droplet-size distributions after two cloud cycles,

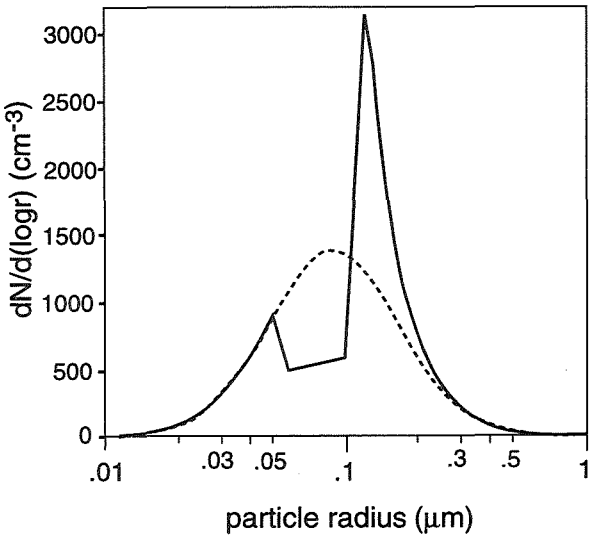

Figure 5: Particle size distributions before (---) and after (—) three cloud interaction cycles for the ASTEX scenario.

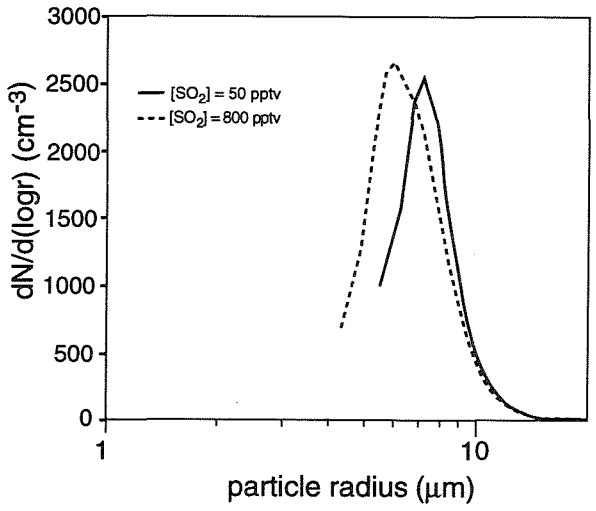

Figure 6: Cloud droplet size distributions for the ASTEX scenario for two different initial SO_2 concentrations.

modeled using typical chemical and dynamical conditions of ASTEX Lagrangian 2 (L2). In order to establish sensitivity of droplet size to SO_2 concentration, sensitivity-test runs are shown for two extreme cases: 50 pptv SO_2 and 800 SO_2 pptv. Droplet sizes are on the order of 1 micron higher in the 50 pptv case. This sensitivity arises because the SO_2 oxidation which produces additional soluble mass, and thus lowers the activation supersaturation of the aerosol particles, occurs preferentially in droplets which form on the smaller CCN. Hence, the higher the SO_2 concentration, the more CCN which will be active at a given supersaturation and thus the higher the initial cloud drop number concentration. This, of course, results in smaller drop radii.

Although no precipitation is predicted for these conditions, it is clear that such droplet-size modification might lead to effects on precipitation in certain cases. Evaluating the contribution of such size sensitivities, in various parameter regimes, to precipitation is a present focus of this investigation.

3. ACKNOWLEDGMENTS

This research was supported by NASA Grant No. NAGW-3754.

4. REFERENCES

Bower, K. and T. Choularton. 1993. A model of the development of droplet effective radius in convective clouds. *Quart. J. Roy. Meteor. Soc., 119*, 443-456.

Bretherton, C. and R. Pincus. 1995. Cloudiness and marine boundary layer dynamics in the ASTEX Lagrangian experiments. Part I: Synoptic setting and vertical structure. *J. Atmos. Sci., 52*, 2707-2723.

Hegg, D. A. 1990. Heterogeneous production of cloud condensation nuclei in the marine atmosphere. *Geophys. Res. Lett., 17*, 2165-2168.

Hegg, D. A., P. F. Yuen and T. V. Larson. 1992. Modeling the effects of heterogeneous cloud chemistry on the marine particle size distribution. *J. Geophys. Res., 97*, 12927-12933.

Hoppel, W. A., J. W. Fitzgerald, G. M. Fick and R. E. Larson. 1990. Aerosol size distribution and optical properties found in the marine boundary layer over the Atlantic Ocean. *J. Geophys. Res., 95*, 3659-3686.

Kaufman, Y. J. and D. Tanre. 1994. Effect of variations in supersaturation on the formation of cloud condensation nuclei. *Nature, 369*, 45-48.

Lelieveld, J. and J. Heintzenberg. 1992. Sulfate cooling effect on climate through in-cloud oxidation of anthropogenic SO_2. *Science, 258*, 117-120.

Rand, H. A. 1994. Mesoscale dynamics of the marine boundary layer. Ph.D. Dissertation, Dept. of Atmospheric Sciences, Univ. of Washington, 136 pp.

Sievering, H., E. Gorman, T. Ley, A. Pszenny, M. Springer-Young, J. Boatman, Y. Kim, C. Nagamoto and D. Wellman. 1995. Ozone oxidation of sulfur in sea-salt aerosol particles during the Azores marine aerosol and gas exchange experiment. *J. Geophys. Res., 100*, 23075-23081.

OBSERVATIONS AND MODELLING STUDIES OF CHEMICAL CLOUD PROCESSING BY MARINE STRATOCUMULUS

Colin D. O'Dowd , Jason A. Lowe, and Michael H. Smith

Physics Department, UMIST, Manchester, M60 1QD, UK

1. INTRODUCTION

The atmospheric aerosol size distribution is normally multi-modal in shape, reflecting the different formation mechanisms of primary (mechanically produced) and secondary aerosol (formed through gas-to-particle conversion processes). The background secondary aerosol distribution, particularly in the marine environment, generally comprises two sub-micron modes: the nucleation mode (r≈0.01-0.05 μm) and the accumulation mode aerosol (r≈0.05-0.5 μm). These two mode are separated by a local minimum in the distribution at r≈0.05μm. The primary composition of these background secondary aerosol modes is generally in the form of non-sea-salt (nss)-sulphate derived from the oxidation of SO_2.

Condensation growth and coagulation growth processes are capable of producing aerosol in the nucleation mode by growing recently formed nuclei (r<10 nm) into this size range, however, these processes can not account for accumulation mode aerosol formed from the gas phase. Both modelling studies (Raes and Van Dingenen, 1992, Hoppel *at al.*, 1986) and growth law analysis studies (Kerminen and Wexler, 1995; Smith *et al.*, 1996) illustrate that the only plausible mechanism which can account for accumulation mode aerosol formed from the gas phase is aqueous phase oxidation of SO_2 which has dissolved in cloud droplets. The primary oxidants are O_3 and H_2O_2 with O_3-oxidation proceeding more rapidly at high values of pH whilst H_2O_2-oxidation dominates at low pH values (Lin *et al.*, 1992). Due to the much higher values of pH in cloud droplets compared with that encountered in wet aerosol particles, and thus, higher reactions rates, the growth of nucleation mode particles into accumulation mode aerosol is thought to require the aid of clouds. This growth results in a minimum in the size distribution at r≈0.05 μm which separates the two modes and is thought to correspond to the critical size of CCN which are activated in stratocumulus clouds (Hoppel *et al.*, 1986; Kerminen and Wexler, 1995).

We present observations of the growth of the accumulation mode aerosol after repeated cycling through a non-precipitating stratocumulus cloud in clean marine air over the Pacific Ocean, off the Californian coast. Simulations of cloud-induced growth of the accumulation mode, using an lagrangian aerosol-cloud-chemistry model containing explicit micro-physics and possessing the capability dealing with of high-ionic strength aqueous solutions and non-ideal solution effects, are presented.

2. INSTRUMENTATION

Accumulation mode aerosol measurements were taken using a PMS ASASP-X optical particle counter (covering sizes 0.05 - 1.5 μm radius) onboard the Meteorological Research Flight C-130 research aircraft. An airborne volatility system was deployed to infer aerosol composition and its variation with size (O'Dowd *et al.*, 1996). Cloud droplet and sea-spray concentrations and size were measured by using a PMS FSSP optical particle counter.

3. OBSERVATIONS

3.1 Cloudy and cloud-free characteristics

A characteristic aerosol spectral-difference was observed between cloud-free and cloudy conditions. Figure 1 illustrates the spectral characteristics, for distributions normalised to N=100 cm^{-3}, between that observed under cloud-free conditions and that observed under cloudy conditions. Generally, the aerosol distributions observed under cloud-free conditions possess a mode radius, or peak concentration, at sizes of ≈0.05μm or less (the actual peak may occur below the measurement range used here) whilst, by comparison, aerosol observed under cloudy conditions in the boundary layer exhibit a mode radius at sizes of ≈0.1 μm. Aerosol observed under cloudy conditions clearly possess radii approximately twice that of cloud-free aerosol, and thus, significantly greater mass. This difference is attributed to aerosol growth in clouds.

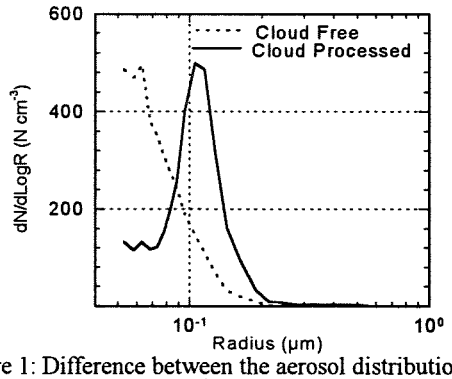

Figure 1: Difference between the aerosol distribution observed under cloudy and cloud-free conditions.

3.2 Specific Case : 27th June 1994

During the 27th June, 1994, measurements of aerosol and cloud properties were undertaken in a moderately-clean air mass off the Californian coast in a north-westerly air flow. The boundary layer was well mixed with a boundary layer height extending to ≈ 550 m and a solid stratocumulus cloud deck ≈ 250 m thick. During this flight, measurements of the accumulation mode aerosol size distribution were undertaken just below cloud base at various distances down-wind after the air had undergone cycling in and out of cloud. Four distributions are shown in Figure 2 which correspond to the evolution of the air over a period of ≈ 155 minutes. During this period, simple calculations suggest that the aerosol is likely to have undergone three cycles through cloud - one between each consecutive distribution observation.

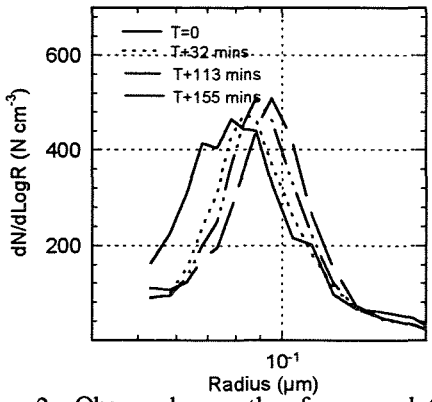

Figure 2: Observed growth of accumulation mode aerosol after successive cloud cycles.

A progressive increase in the accumulation mode radius from 0.078 μm to 0.094 μm is observed over the time scale involved, concomitant with a narrowing of the distribution. The number concentration at T=0 is 120 cm^{-3}, falling to 95 cm^{-3} at T=32 minutes (thought to correspond to one cloud cycle), and thereafter, remains relatively constant at 99 cm^{-3} and 97 cm^{-3} for the following two distributions (each thought to correspond to one further cloud cycle).

4. MODEL DESCRIPTION

The physical aspects of the simulation consist of a lagrangian parcel model with explicit particle micro-physics. The micro-physical aspect utilises the dynamic growth equation (Pruppacher and Klett, 1978) to model the growth of aerosol solution droplets by the condensation of water vapour on to a size resolved spectrum of up to 100 size-resolved droplet classes. Rather than being fixed, the boundaries of these size channels move as the solution droplets grow. The growth law includes curvature and solution effects, and, is corrected for the breakdown of the continuum approximation close to the droplet surface (Pruppacher and Klett, 1978). Un-activated solution droplets are especially concentrated, with ionic strengths often much greater than unity. Under these conditions, the solution can no longer be treated as ideal. Non-ideal solution effects are taken into account in the calculation of water activity for each of the solution droplets. The water activity is then used to determine the supersaturation of water vapour just above the droplet surface which in turn controls the rate of condensational growth of the droplets. Inclusion of mass-transport limitations follows the formulation of (Schwartz 1986).

The aqueous phase chemical aspects of the model comprise three separate elements, an equilibration module, a kinetic reaction module, and the non-ideal behaviour correction module. The equilibration module is used to calculate the amount of soluble gaseous species dissolved in the aerosol, and, to apportion the aqueous aerosol species between associated and dissociated forms. This is achieved by solving the charge balance equation for each solution droplet. The aqueous activities of species equilibrating with the gas phase are calculated using Henry's law. The relationships between associated and dissociated aqueous species are written using appropriate equilibrium constants. Both the Henry's law and equilibrium constants are corrected for changes in temperature.

The non-ideal solution effects, previously mentioned in the context of droplet condensational growth, also effect aqueous phase chemical equilibria. Actual concentrations of dissolved species are related to their effective concentrations, or activities, appearing in the Henry's law expressions and equilibrium relationships by activity coefficients. The activity coefficients are functions of ionic strength, solution composition, and temperature. As a solution becomes more concentrated, the activity coefficients deviate from unity, causing the activity to deviate from the concentration. The activity coefficients, and water activity as used by the growth law, are determined using the formulation of Pitzer (1991). This formulation allows activity coefficients to be determined for a wide range of species in high ionic strength solutions and over a range of temperatures. Rather than using a look-up table of activity coefficient values, Pitzer's equations are built into the model (the non-ideal solution correction module) so that activity coefficients can be calculated as and when required.

The kinetic reaction module determines the rate of heterogeneous sulphate production within the aqueous solution droplets. At present, sulphate production may occur by the oxidation of SO_2 using either dissolved H_2O_2 and/or O_3 as oxidant species. The reaction rates and their temperature dependence are taken from Ayers and Larson (1990) and references contained therein. Droplet growth and droplet chemistry takes place on both sea-salt and sulphate nuclei.

5. MODEL INPUT CONDITIONS.

Since the aqueous phase oxidation rate of SO_2 is strongly dependent on the solution pH, which is, in turn, influenced by the dissolved cloud droplet nuclei (Lowe *et al.*, 1996), an accurate knowledge of the CCN composition must be known. Information on the chemical composition and its variation with size was

derived from volatility measurements which allowed inference of chemical composition. At the start of the evolution study, three primary aerosol species where observed: sulphuric acid, ammonium bisulphate, and sea-salt. The ammonium-to-sulphate molar ratio was inferred, from volatility analysis, to be 0.8, and, its spectral shape was in the form of a log-normal distribution possessing a mode radius (r_m) of 0.078 μm and a standard deviation (σ) of 1.3. The sea-salt aerosol distribution was bi-modal in shape due to the contribution from film and jet drops (O'Dowd *et al.*, 1996) and also were log-normal in shape with parameters N_{film}= 20 cm^{-3}, r_{m_film}=0.1 μm, σ_{film}=1.9; and, N_{jet}=0.8 cm^{-3}, r_{m_jet}=0.9 μm, σ_{jet}=2. Both the nss-sulphate mode radius and the sea-salt mode radii correspond to a 'dry-size' radius.

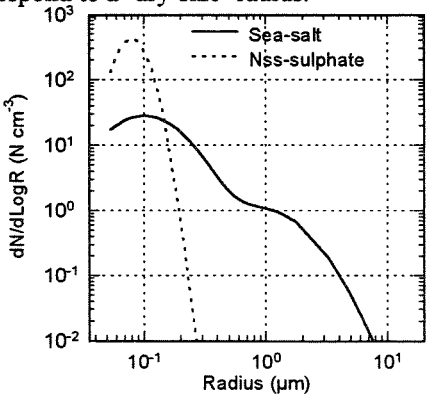

Figure 3: Initial nss-sulphate and sea-salt aerosol model input at T=0.

Initial gas phase concentrations of SO_2, H_2O_2, O_3, and NH_3 used are 22 nmoles kg^{-1} air (0.56 ppb), 40 nmoles kg^{-1} air (1 ppb), 1.03 x 10^3 nmoles kg^{-1} air (26 ppb) and 40 nmoles kg^{-1} air respectively. Boundary layer observations of thermodynamics and cloud droplet structure are used to initialise the model.

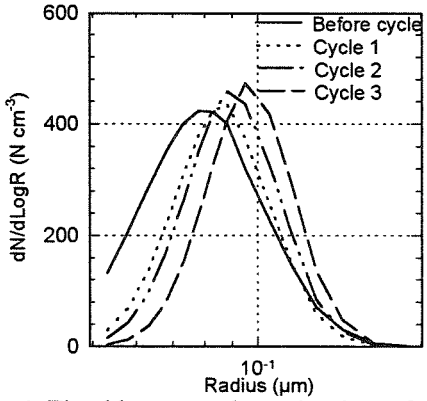

Figure 4: Fitted log-normals used as input for each consecutive simulation.

The model is started just below cloud base and cycled through the cloud - once for each simulation. The predicted aerosol distribution, after undergoing chemical processing in-cloud, is then compared with the observed distribution after that cloud cycle. For the following cloud cycle, the log-normal curve fit to the observed data on cycling out of cloud was then used as the input data for the next cloud cycle. The log-normal curves fitted to the observed data are shown in Figure 4 and the associated parameters are displayed in Table 1. For all simulations of the model, the initial gas-phase concentrations and sea-salt aerosol input conditions were keep constant.

6. SIMULATIONS AND RESULTS

Four model runs were performed, three to compare with the observations after three cloud cycles, and one to predict the aerosol growth after a fourth cycle. The spectral nss-sulphate output from the four model simulations are shown in Figure 5 where it can be seen to replicate the observations in Figure 4 with close agreement (Cycles 1-3). The log-normal parameters for the model output size distributions are compared with the observed distribution parameters in Table 1. In Table 1, comparison can be made by comparing the model output of one cycle with the observed input for the following cycle.

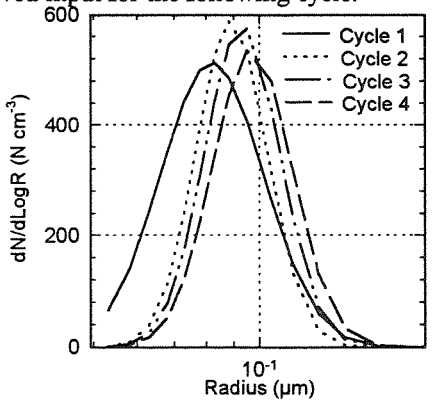

Figure 5: Model aerosol output after four cycles through cloud.

The agreement between the predicted mode radii by the model and those observed in the measurements exhibit excellent agreement to within ≈3%. As there are no loss mechanisms such as coagulation loss or coalescence included, the number concentrations from the first cycle output are higher than the observations since the input number concentration is higher. For the latter three cycles, the observed concentration is constant, thus, leading to good agreement between the model results and the measurements

Table 1. Comparison of model output with observations

	Input spectra (data)			Output spectra (model)		
Cycle	N cm^{-3}	r_m μm	σ	N cm^{-3}	r_m μm	σ
1	120	0.079	1.3	120	0.082	1.24
2	95	0.084	1.22	95	0.089	1.16
3	99	0.089	1.221	99	0.093	1.17
4	97	0.094	1.225	97	0.097	1.18

The dominant features associated with the model runs is that after every cloud cycle, the mode radius, and thus, mass of the distribution has increased, and, a narrowing of the distribution, relative to the input distribution, results. This narrowing is brought about by the fact that the smaller nuclei grow most rapidly (Lowe *et al.*, 1996). We should note that whilst the observations indicate a reduction in σ for the first cloud cycle, σ remains more or less constant after the

following cycles. It is not clear why this was observed, however, activation of a small number of particles at sizes below our measurement range, and their subsequent growth in cloud, may tend to result in a slightly broader distribution. This effect is not reproduced in the model since the updraft (40 cm^{-3} s^{-1}) was selected to only activate aerosol with r>0.05 μm.

In Figure 6, the observed output distribution is compared with the model output distribution for the second cloud cycle. As seen earlier, the agreement between the mode radius is within a couple of percent, whilst the difference between σ is somewhat higher (about 5%). If the model output value of σ is forced to that observed by the measurements (i.e. 1.22), the agreement between the model output and the observations is near-perfect. This forcing of σ results in an increase in the predicted mass of only 6%.

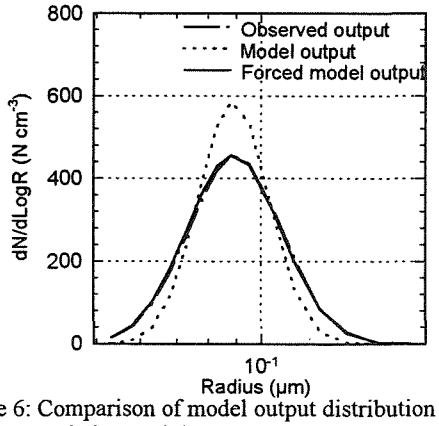

Figure 6: Comparison of model output distribution (σ=1.16) and observed data (σ=1.22). Also shown is model output with σ forced to 1.22.

The amount of sulphate aerosol produced on both sulphate and sea-salt nuclei is displayed in Table 2. Although sea-salt aerosol contributed approximately 20% to the activated CCN, cloud droplet concentration, the total amount of sulphate produced on these nuclei is typically twice the total produced on sulphate nuclei. The primary reason for this effect is due to the much higher pH associated with droplets activated on sea-salt nuclei, thereby allowing oxidation by O_3 to proceed more rapidly than in sulphate nuclei.

Table 2: Sulphate produced on activated nuclei

Nuclei	Sulphate produced (nmoles Kg^{-1} air)			
	cycle 1	cycle 2	cycle 3	cycle 4
sulphate	1.51	1.46	1.48	1.49
sea-salt	3.11	3.15	3.17	3.17

7. CONCLUSIONS

Measurements of the marine accumulation mode distribution, after repeated cycles through a stratiform cloud deck, exhibit a progressive growth in the mode radius from 0.078 μm radius to 0.093 μm. This growth was attributed to aqueous phase oxidation of SO_2 in cloud droplets. A high ionic strength aerosol-cloud-chemistry model was used to simulate the observed growth. The mode radius growth predicted by the model was within 2-3% of the mode radius observed in the measured aerosol distribution. Approximately 1.5 nmoles Kg^{-1} air of sulphate was produced on sulphate nuclei during each cloud cycle, whilst ≈ 3.2 nmoles Kg^{-1} air was produced on sea-salt nuclei due to its higher pH.

8. ACKNOWLEDGEMENTS

This work was supported by NERC under contracts GST/02/659 and GR3/9416.

9. REFERENCES

Ayers, G.P., and T.V. Larson, 1990: Numerical study of droplet size dependent chemistry in oceanic, wintertime stratus cloud at southern mid-latitudes. *J. Atmos. Chem.*, **11**, 143-167.

Hoppel , W.A., G.M. Frick, and R.E. Larson, 1986: Effect of non-precipitating clouds on the aerosol size distribution. *Geophys. Res. Lett.*, **13**, 125-128.

———, G.M. Frick, and J.W. Fitzgerald, 1995: Marine boundary layer measurements of new-particle formation and the effects of nonprecipitating clouds have on aerosol size distribution, *J. Geophys. Res.*, **99**, 14,443-14,459.

Kerminen, V. and A.S. Wexler, 1995: Enhanced formation and development of sulphate particles due to marine boundary layer circulation. *J. Geophys. Res.*, **100**, 23,051-23,062.

Lin, X., W.L. Chameides, C.S. Kiang, A.W. Stelson, and H. Berresheim, 1992: A model study of formation of cloud condensation nuclei in remote marine areas. *J. Geophys. Res.*, **97**, 18,161-18,171.

Lowe, J.A., S.L. Clegg, M.H. Smith, and C.D. O'Dowd, 1996: Simulations of maritime stratiform cloud physico-chemistry, *This issue.*

O'Dowd, C.D., M.H. Smith, A.D. Kaye and J.A. Lowe, 1996: The relative importance of nss-sulphate and sea-salt aerosol to the marine cloud condensation nuclei population. *This issue.*

———, M.H. Smith, I.E. Consterdine, and J.A. Lowe, 1996: Marine aerosol, sea-salt, and the marine sulphur cycle: A short review. *Atmos. Environ.* **in press.**

Pitzer, K.S., 1991: *Activity coefficients in electrolyte solutions*, **CRC Press,** Ann Arbor.

Pruppacher, H.R., and J.D. Klett, 1978: *Microphysics of Clouds and Precipitation.* **D. Reidel**, Dordrecht.

Raes, F., and R. Van Dingenen, 1992: Simulations of condensation and cloud condensation nuclei from biogenic SO_2 in the remote marine boundary layer. *J. Geophys. Res.*, **97**, 12,901-12,912.

Smith, M.H., C.D. O'Dowd and, J.A. Lowe, 1996: Observations of cloud-induced aerosol growth. Proceedings of the 14th *International Conference on Atmospheric Aerosols and Nucleation.* **In press.**

Schwartz, S.E., (1986): Mass-transport considerations pertinent to aqueous phase reactions of gases in liquid-water clouds. *In Chemistry of Mutli-phase Atmospheric Systems*, **NATO ASI ser.**, edited by W. Jeaschke, Springer-Verlag, New Yorf, 415-471.

CHEMICAL AND MICROPHYSICAL PROPERTIES OF CLOUD DROPLET RESIDUAL PARTICLES IN MARINE STRATOCUMULUS CLOUDS OBSERVED DURING THE MAST EXPERIMENT

Kevin J. Noone[1], Elisabeth Öström[1], Robert A. Pockalny[2], Lieve De Bock[3] and René Van Grieken[3]

[1]Department of Meteorology, Stockholm University, S-106 91 Stockholm Sweden
[2]Graduate School of Oceanography, URI, Narragansett, RI 02882, USA
[3]Department of Chemistry, University of Antwerp, 2610 Wilrijk, Belgium

1. INTRODUCTION

Marine stratocumulus clouds have been recognized as an important ingredient in the Earth's radiative balance. The albedo of these clouds is an important parameter in determining what influence they have in a climatic sense. The Monterey Area Ship Tracks Experiment (MAST) was carried out in June, 1994 to determine the mechanisms behind the observations that effluents from ships modify marine stratocumulus cloud albedo. The larger aim of the MAST experiment was to investigate the mechanisms by which anthropogenic injection of aerosol into the atmosphere can alter cloud radiative properties [*Durkee and Noone*, 1994].

As part of this experiment, a Counterflow Virtual Impactor (CVI) was operated onboard the University of Washington C131 research aircraft [*Noone et al.*, 1988b; *Ogren et al.*, 1985]. The CVI was used to sample cloud droplets and examine the properties of the *residual aerosol* - particles left behind after the droplets were evaporated in the CVI.

2. MEASUREMENTS

The CVI sampled droplets larger than 2-3μm radius. After sampling, the droplets were evaporated in the CVI. Water and any volatile material dissolved in the droplets was driven into the gas phase, while the non-volatile material in the droplets was left behind as residual aerosol particles. The residual particles between 0.055 - 4.5μm radius were counted and sized using a PMS PCASP optical particle counter (PMS, Boulder, CO, USA).

The residual particles were also collected on filters for subsequent chemical analysis. Chemical analysis of individual particles was performed using an electron probe X-ray microanalysis/scanning electron microscope technique [*Jambers et al.*, 1995]. This technique yields qualitative information on the size, morphology, and elemental composition of the individual aerosol particles. Information about the presence of organic material in the particles is also obtainable with this technique.

A total of 12 research flights with the UW C131 were carried out during the experiment to investigate differences between the unperturbed clouds and ship tracks. In this presentation we will focus on the nature of cloud droplet residual particles from the background clouds, rather than on contrasting ship tracks and background clouds.

3. RESIDUAL PARTICLE MICROPHYSICS

Clean Marine Boundary Layer

Figure 1 shows residual particle size distributions obtained on June 30th when the marine boundary layer was relatively clean. Total boundary-layer particle concentrations were between 200-500cm^{-3}, while accumulation-mode particle concentrations were typically near 100cm^{-3}.

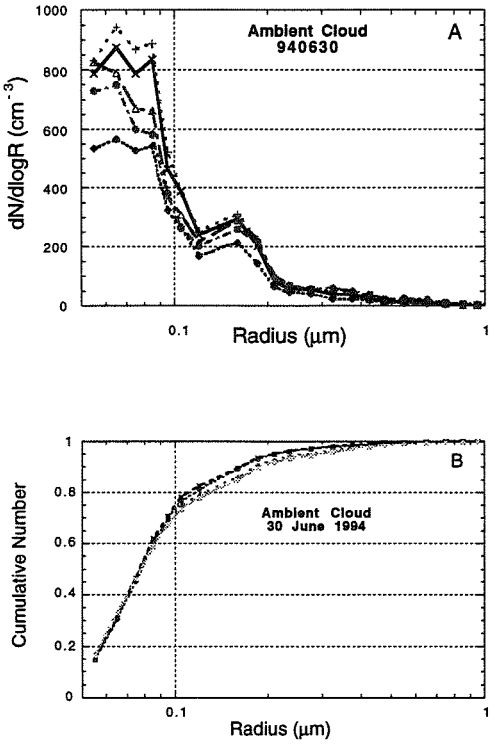

Figure 1. Residual particle size distributions in a clean boundary layer. Panel A shows a number size distribution. Panel B shows a cumulative number size distribution.

The residual particle number size distribution shows two modes: one between 0.1-0.2μm radius and one smaller than 0.1μm. The larger mode was composed

primarily of sea salt particles. The smaller mode in the residual particle size distribution is not resolved, indicating that in this clean boundary layer, a substantial fraction of the droplets in the clouds formed on particles smaller than 0.055μm radius.

This observation is supported by the cumulative size distribution shown in panel B. This figure indicates that 80% of the residual particles were below 0.1μm radius. This is an underestimate of the true 80th percentile size, since the lower size resolution of the OPC was 0.55μm, and there were clearly residual particles present below this size.

Polluted Boundary Layer

A moderately polluted boundary layer was encountered on June 11th. Total particle concentrations were typically ca. 1000cm^{-3}, and accumulation-mode particle concentrations were between 200-300cm^{-3}.

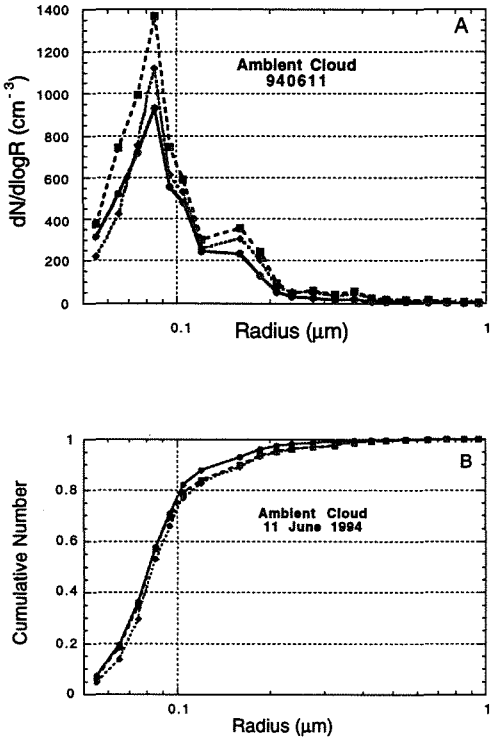

Figure 2. Residual particle size distributions in a moderately polluted boundary layer. Panel A shows a number size distribution. Panel B shows a cumulative number size distribution.

The number size distribution in this case again shows two modes. In this case the smaller mode is clearly resolved, in contrast to the clean case. Here we observe that the mode size of residual particles was larger in a polluted boundary layer than in a clean one. One possible explanation for this observation is that the higher concentration of accumulation-mode particles in the polluted boundary layer increases the competition for the available water vapor. For a given dynamic forcing, having more particles able to acquire water may reduce the peak supersaturation in the clouds relative to the clean case. Given similar chemical composition for the aerosol, a reduction in peak supersaturation would lead to an increase in mode size for the residual particles.

Interestingly, the cumulative size distributions for the polluted case are quite similar to the clean case. As in the clean case, 80% of the residual particles were below 0.1μm diameter. This 80th percentile size was consistent for all of the flights examined to date.

The 80th percentile for the cumulative volume (mass) distributions for these cases was typically between 0.8-1μm radius. These observations indicate that cloud parameters based on number (e.g., cloud droplet concentration, effective radius, albedo) will be determined by submicrometer aerosol particles. The bulk chemical composition of the droplets in these clouds, a mass-based parameter, was determined by a different size range of particles; namely those between ca. 0.1-1μm. The observations further indicate that bulk cloudwater composition can a rather poor description of the true chemical composition of the cloudwater, since bulk composition smears out the heterogeneity in cloudwater composition and concentration across droplet size [*Noone et al.*, 1988a].

4. SINGLE PARTICLE ANALYSIS

Single particle analysis of residual particles yielded information on the chemical composition of the aerosol which formed droplets in the clouds we encountered.

Table 1 summarizes the groups of particle composition observed from a residual particle sample taken on June 27th in moderately polluted boundary layer clouds.

Cluster	% of Total	Mean Radius	Composition
1	43.0	0.2	Cl, Na
2	25.0	0.25	Cl, Organic
3	19.4	0.25	Cl, S, Na
4	11.4	0.2	Organic
5	1.2	0.15	S, Ca, Cl

Table 1. Hierarchical cluster analysis results for ambient cloud droplet residual particles. A total of 500 particles were analyzed.

Cluster 1 reflects the presence of sea salt particles in the residual aerosol. Cluster 3 appears to be a combination of sea salt and sulfate; perhaps cloud-processed aerosol or a well-aged particles which have had time to coagulate.

There are two clusters containing organic material. Cluster 2 contains chlorine and organic material, while cluster 4 is exclusively organic material. These two clusters accounted for 182 of the 500 particles analyzed. Polyaromatic hydrocarbon material was found in both bulk interstitial and residual aerosol particle samples during MAST (L.Russell, et al., manuscript in preparation.) While it is not possible to distinguish which organic species were present with the EPXMA technique, it is interesting to note that particles

containing organic material accounted for more than 36% of the 500 particles analyzed in this sample. Clearly, organic particles were acting as cloud condensation nuclei in the clouds sampled on this day.

Table 2 shows clusters from an ambient cloud residual particle sample taken in a clean boundary layer on June 30th.

Cluster	% of Total	Mean Radius	Composition
1	57.6	0.2	Cl, Na
2	29.8	0.2	Cl, Na, S
3	10.6	0.25	Cl, S, Na, Ca
4	2.0	0.15	S, Ca, Cl

Table 2. Hierarchical cluster analysis results for ambient cloud droplet residual particles. A total of 500 particles were analyzed.

These clusters are consistent with a particle composition of sea salt and sulfate, typical of the clean marine boundary layer. No organic components were observed in the single particle analysis from this flight.

Submicrometer sea salt particles were observed in all of the flights analyzed to date. Wind speeds were generally fairly high throughout the campaign (10-20m s^{-1}) allowing small sea salt particles to be generated. The single particle analysis results are consistent with determinations of particle composition using a thermal volatility technique (C. O'Dowd, personal communication.)

5. CONCLUSIONS

Measurements of cloud droplet residual particle microphysics and chemistry were made in marine stratocumulus clouds off the central California coast during the MAST experiment in June, 1994.

Typically, 80% or more of the residual particles were below 0.1μm radius. While the mode size of residual particles was slightly higher in polluted clouds than in clean ones, the droplet population in both cases was determined by the submicrometer aerosol. One explanation for the shift towards larger sizes in the residual particle size distributions for polluted versus clean clouds is a reduction of the peak supersaturation in the polluted clouds due to an increase in the rate at which water vapor is taken up by the larger number of particles present in the polluted clouds.

Single particle analysis for samples taken in a clean marine boundary layer showed the residual particles larger than 0.1μm radius to have been composed of sea salt and a combination of sea salt and sulfate. This composition is typical of the background marine boundary layer aerosol. Residual particles containing exclusively organic material and also organic material plus Cl were observed in a sample from a moderately polluted cloud. These clusters accounted for 182 of the 500 particles analyzed, indicating that organic particles were a substantial fraction of the cloud condensation nuclei in these particular clouds.

6. ACKNOWLEDGMENTS

Phil Durkee, Kurt Nielsen and Chuck Skupniewicz, as well as scientists and staff at the Naval Postgraduate School were a tremendous help during the campaign. We are also indebted to the UW team, especially Ron Ferek, for their invaluable help during the campaign. This research was supported by the Office of Naval Research.

7. REFERENCES

Durkee, P.A., and K.J. Noone, Editors, The Monterey Area Ship Tracks Experiment (MAST) Science Plan, Technical Report NPS-MR-94-004, Naval Postgraduate School, Monterey, CA, 1994.

Jambers, W., L. De Bock, and R. Van Grieken, Recent Advances in the Analysis of Individual Environmental Particles, *Analyst, 120*, 681-692, 1995.

Noone, K.J., R.J. Charlson, D.S. Covert, J.A. Ogren, and J. Heintzenberg, Cloud droplets: Solute concentration is size dependent, *J. Geophys. Res., 93D*, 9477-9482, 1988a.

Noone, K.J., J.A. Ogren, J. Heintzenberg, R.J. Charlson, and D.S. Covert, Design and calibration of a counterflow virtual impactor for sampling of atmospheric fog and cloud droplets, *Aerosol Sci. Tech., 8*, 235-244, 1988b.

Ogren, J.A., J. Heintzenberg, and R.J. Charlson, In-situ sampling of clouds with a droplet to aerosol converter, *Geophys. Res. Lett., 12*, 121-124, 1985.

EFFECT OF DROP BREAK UP ON THE SUBCLOUD SCAVENGING OF AEROSOLS OF 1 TO 5 μm

Gustavo G. Carrió

Dto. de Cs. de la Atmósfera, F.C.E.y N.
Universidad de Buenos Aires (UBA), Argentina

1. INTRODUCTION

Wet removal of aerosol particles by precipitation plays an important role in mantaining a balance between their sources and sinks in the lower atmosphere. These particles are scavenged by colliding with drops through the mechanisms of Brownian diffusion, inertial impactation and through phoretic and electric effects. The various processes other than the inertial impactation are of little importance for aerosol with radii greater than one micron if electric effects are ignored.

A rainshaft model has been used to study the effect of drop break-up on the subcloud scavenging behavior for aerosol with radii between 1 to 5 microns. The model computes the time and vertical drop distribution changes because of evaporation, collision-coalescence, break-up and sedimen-tation. Drop spectrum is discretized in 34 size categories between .1 and 7 millimeters in diameter and collisional break-up has been modelated using a formulation based on the Low and List (1982) coalescence efficiencies and fragment distributions.

When a drop size distribution constant in time is imposed at the top of the shaft, a steady state (SS) is reached after a certain time of evolution and the spectra at each level remain constant. Tzivion (1989) calculated the corresponding scavenging coefficient vertical profile using an impactation efficiency of unity for a some initial distributions.

In this study size the SS scavenging profiles have been studied under saturated and unsaturated conditions, and considering the collision efficiency dependence with the particle and drop sizes.

2. RESULTS

The SS spectra corresponding to fall distances within a 2000 m tall shaft have been simulated under a wide variety of conditions. Drop size distributions with precipitation rates between 20 and 150 mm/h has been considered as rain sources at the top of the shaft and relative humidity varied between 20 to 100 %.

Results can be briefly summarized as follows:

When the collisional break-up is the dominant mechanism, for increasing fall distance, the scavenging rates decreased for small particles and decreased for larger aerosol size. When the collision-coalescence is dominant an opposite behavior was observed.

As an example, the SS scavenging rates relative to the corresponding value at the top of the modelated layer are shown for Marshall-Palmer (1948) initial spectra with liquid water content of 2 and 5 g/m3 in Figs. 1 and 2, respectively.

For the larger particles, the scavenging rate is governed by the number concentration of small drops which decreases monotonically due to the fast evaporation in Fig 1. When the liquid water content is rather large, it increases due to the high efficiency the break-up and

then decreases as L is depleted (Fig 2).

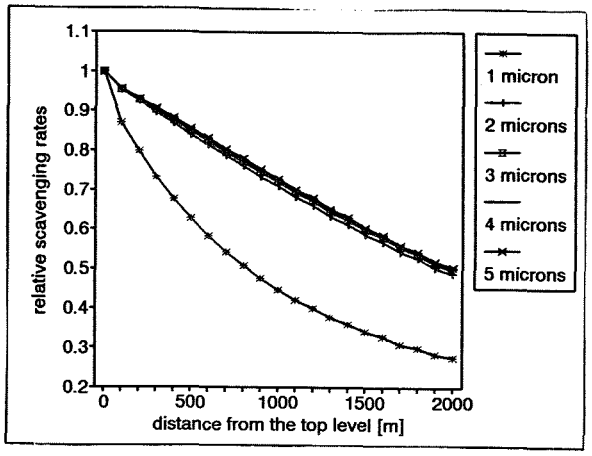

Fig 1. Scavenging rates relative to the corresponding values at the top of the shaft, for an initial Marshall-Palmer distribution with L = 2g/m^3.

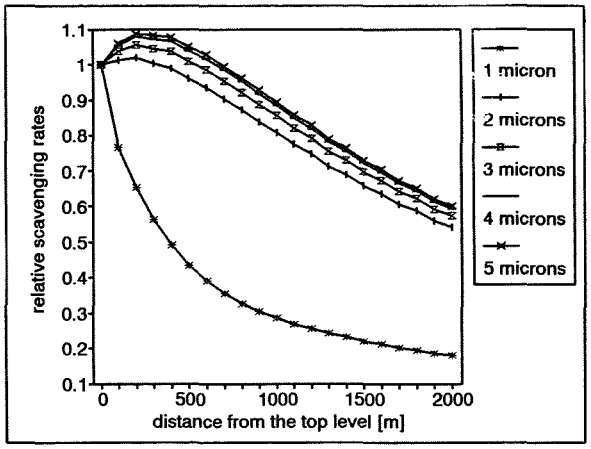

Fig 2. Scavenging rates relative to the corresponding values at the top of the shaft, also for an initial Marshall-Palmer distribution but for L = 5g/m^3.

On the other hand for the smaller sizes the scavenging rates tends to monotonically decrease as the concentration of small drops does in both cases.

3. COMMENTS

Results show a selective impact of the collisional processes for aerosols of different radii. The scavenging of the smaller particles vary in the vertical as does the large drop end of the spectrum. On the other hand, the capture of larger aerosols is governed by the magnitude of the mode centered about 200 microns in diameter.

The large aerosol capture tends to decrease for low relative humidity due to the fast evaporation of small drops. For large L this decrease tends to be compensated by higher efficiency of the collisional break-up to generate small fragments.

The behavior of vertical profiles for large aerosols is in agreement with that observed by Tzivion (1989) using collision efficiencies of unity, although for the smaller particles of the studied range, the sensibility of scavenging rates to relative humidity is substantially weaker.

ACKNOWLEDGMENTS

The author wishes to thank Drs. Laura Levi and Matilde Nicolini for useful discussions and UBA for financial support.

REFERENCES

Low, T. B., and R. List, 1982: Collision, coalescence and breakup of raindrops. Part II: Parameterization of fragment size distributions. J. Atmos. Sci., **39**, 1607-1618.

Marshall, J. S., and W.M. Palmer, 1948: The distributions of raindrops with size. J. Meteor., **9**, 327-332.

Tzivion, S., G. Feingold and Z. Levin, 1989: Evolution of raindrop spectra. Part II collisional collection/breakup and evaporation in a rainshaft. J. Atmos. Sci., **46**, 3312-3327.

SULFUR CHEMISTRY IN THE NCAR COMMUNITY CLIMATE MODEL

Mary C. Barth, Phil J. Rasch and Jeffrey Kiehl

National Center for Atmospheric Research
Boulder, Colorado

1. INTRODUCTION

Understanding the global sulfur cycle is necessary for learning what processes are important to the production of aerosol sulfate which can influence the global climate both radiatively and hydrologically. When more aerosol sulfate is present than natural background concentrations, the aerosol can scatter more solar radiation thus effectively cooling the atmosphere. Aerosol sulfate is a major source of cloud condensation nuclei. When more aerosol sulfate is present than natural background concentrations, more cloud drops that are smaller in size may form. This leads to a higher albedo from clouds thus effectively cooling the atmosphere and this also leads to a decrease in precipitation formation since the drops are not large enough to fall to the ground.

We present here a global model that accounts for the processes that influence the mass of sulfur, but does not yet include the processes that influence the number of aerosol particles nor the interactions of aerosols with clouds. Another presentation (Kiehl *et al.*, this issue) discusses the interactions of aerosol sulfate on the direct effect of solar radiation.

2. DESCRIPTION OF SULFUR CHEMISTRY

The sulfur chemistry is incorporated in a version of the NCAR Community Climate Model (CCM) that has recently been updated. The sulfur chemistry described in the CCM includes emissions, transport, gas and aqueous chemistry, and wet and dry deposition of dimethyl sulfide (DMS), sulfur dioxide (SO_2), and aerosol sulfate ($SO_4^=$).

2.1 Emissions

Emissions of DMS, SO_2, and $SO_4^=$ were obtained from the GEIA emissions inventory which provided data of biogenic sulfur emissions and anthropogenic sulfur emissions. The seasonally averaged emissions data were provided at the surface and at 100 m and above to accomodate emissions from industry stacks. The biogenic emissions occurred only at the surface. DMS emissions were obtained from the biogenic emissions data by choosing the biogenic emissions from the oceans. The anthropogenic emissions were assumed to be 98% SO_2 and 2% $SO_4^=$.

2.2 Gas Chemistry

In the model, two reactions in the gas phase are described in a manner similar to Benkovitz *et al.* (1994). These reactions are,

$$SO_2 + OH \rightarrow SO_4^= \quad (1)$$
$$DMS + OH \rightarrow \alpha\ SO_2 + (1\text{-}\alpha)\ MSA \quad (2)$$

where MSA is methane sulfonic acid whose concentration is not tracked in our model and α is the yield of SO_2 formed from reaction 2. In reaction (1), it is assumed that the SO_2 + OH reaction is the rate limiting step of the multi-step process of forming aerosol sulfate. Concentrations of OH were prescribed using zonally mean, monthly averaged concentrations obtained from the IMAGES model (Müller and Brasseur, 1995). The rates of these reactions are determined by finding the first order rate coefficient and using a quasi-steady-state approximation (Hesstvedt *et al.*, 1978).

2.3 Aqueous Chemistry

In addition to the gas-phase chemistry, oxidation of aqueous SO_2 to form $SO_4^=$ aerosol is described by the following reactions,

$$HSO_3^- + H_2O_2 + H^+ \rightarrow SO_4^= + 2H^+ + H_2O \quad (3)$$
$$HSO_3^- + O_3 \rightarrow SO_4^= + H^+ + O_2 \quad (4)$$
$$SO_3^= + O_3 \rightarrow SO_4^= + O_2 \quad (5)$$

Concentrations of H_2O_2 were allowed to deplete according to (3) and to replenish based on a 1.5 day relaxation time to reach its zonally mean, monthly averaged concentrations. The concentrations of O_3 were prescribed using zonally mean, monthly averaged concentrations obtained from the IMAGES model. The pH of the drops was set to 4.5. The mixing ratio of cloud water is a prognostic variable in the model and the mixing ratio of rain was diagnosed from the precipitation rate assuming a fallspeed of 4 m s^{-1}. SO_2 and H_2O_2 were depleted and $SO_4^=$ was produced only in the cloudy region of the grid box. The grid box concentration of these species was found by combining the cloudy region concentration times the cloud fraction and the clear

air concentration times the fraction of clear air in the grid box.

Since the rate of oxidation of S(IV) (= SO_2-H_2O+ HSO_3^- + $SO_3^=$) by H_2O_2 is faster than the rate of oxidation by O_3 at a pH of 4.5, we first calculated the rate of S(IV) oxidation by H_2O_2. This reaction has a good chance of going to completion during the 40 minute timestep and therefore may be limited by the amount of reactant available. Therefore, we first check to see if reaction 3 is SO_2 limited or H_2O_2 limited. If the reaction is SO_2 limited and it does go to completion, SO_2 in the cloudy region is set to zero, $SO_4^=$ and H_2O_2 in the cloudy region are modified according to the amount of SO_2 that was available. If the reaction is H_2O_2 limited, H_2O_2 in the cloudy region is set to zero, and $SO_4^=$ and SO_2 in the cloudy region are modified according to the availability of H_2O_2. Since there is SO_2 still in the cloud or rain drops after this H_2O_2-limited step, SO_2 is allowed to react further with O_3.

The rate of oxidation of S(IV) by O_3 was calculated using the quasi-steady-state approximation (Hesstvedt *et al.*, 1978) where the concentrations of aqueous O_3, HSO_3^-, and $SO_3^=$ are assumed to be in Henry's Law equilibrium.

2.4 Wet Deposition

Wet deposition rates are determined using a flux method which allows precipitation to evaporate. This calculation is consistent with the hydrologic cycle of the CCM. The microphysics in the CCM allows both cloud water and ice to exist at temperatures below freezing, but only snow to precipitate at these temperatures. At temperatures above freezing, only cloud water and rain exist. SO_2 and H_2O_2 are treated as soluble gases and are scavenged only in the liquid phase using a Henry's Law calculation. Aerosol sulfate is treated as a highly soluble aerosol and is scavenged in-cloud in the liquid phase only, but is scavenged by snow or rain below cloud.

2.5 Dry Deposition

Calculation of dry deposition rates follows that described by Benkovitz *et al.* (1994). The deposition velocities of SO_2 and H_2O_2 are determined following the series resistance method outlined in Wesely (1989) where the deposition velocity is inversely proportional to the sum of the aerodynamic resistance, the resistance to transport across the atmospheric sublayer in contact with surface elements, and the surface resistance. The aerodynamic and sublayer resistances are determined using boundary layer meteorological parameters. The surface resistance is found through a parameterization outlined by Wesely (1989). The deposition velocity of aerosol sulfate is determined similarly to Walcek *et al.* (1986).

3. RESULTS

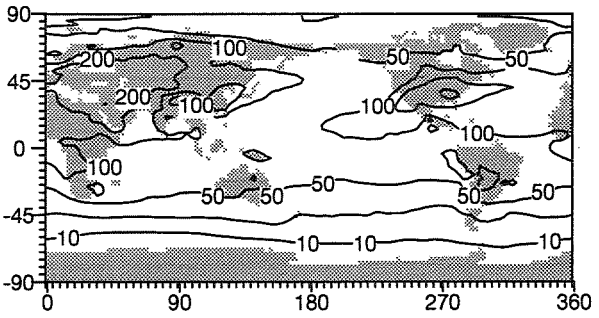

Fig. 1. Monthly-mean aerosol sulfate column burden (μmol m^{-2}) for the month of July.

Driven by sea surface temperatures obtained from AMIP data, the model was integrated for 17 months from September to the following February. Figure 1 shows the monthly-mean aerosol sulfate column burden for the month of July. The aerosol sulfate is located primarily near source regions, but there is a widespread concentration of sulfate throughout the northern hemisphere. The column burdens shown here are consistent with those illustrated in Benkovitz *et al.* (1994) for their regional model. Furthermore, concentrations of aerosol sulfate and SO_2 at the surface are in general agreement with observations especially for monthly-mean July concentrations.

The aerosol sulfate concentration in the model was tagged according to whether the sulfate was derived from primary emissions, gas-phase chemistry, or aqueous-phase chemistry. Figure 2 shows the column burden of aerosol sulfate from these three sources for the month of July. It is clear that most of the aerosol sulfate is derived from aqueous-phase chemistry. This result contrasts with Benkovitz *et al.* (1994) who showed that these three processes contributed fairly equally to the total sulfate concentration. However, since their model used ECMWF analyzed precipitation rates to determine the liquid water content in the troposphere, the aqueous chemistry that Benkovitz *et al.* calculated could be underestimated because the precipitation rates from ECMWF could not possibly account for all clouds observed. The large contribution by aqueous chemistry to the aerosol sulfate burden indicates that reaction (3) is probably the important process to consider. Thus, when modeling sulfur chemistry in the atmosphere, the skill in modeling cloud and rain water mixing ratios and H_2O_2 concentrations must be considered.

4. SUMMARY

We have incorporated sulfur chemistry into a version of NCAR's Community Climate Model. This chemistry includes emissions of sulfur species, gas-phase production of sulfate, aqueous-phase production of sulfate, and wet and dry deposition of sulfate,

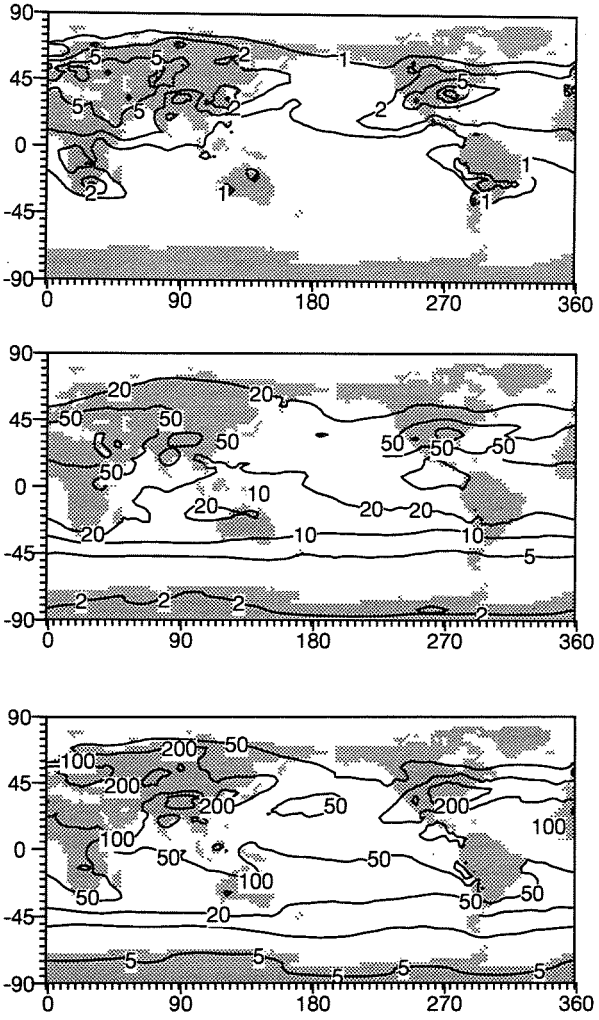

Fig. 2. Monthly-mean aerosol sulfate column burden (μmol m^{-2}) (a) derived from primary emissions, (b) derived from gas-phase chemistry, and (c) derived from aqueous-phase chemistry for the month of July.

SO_2, and H_2O_2. The distribution of aerosol sulfate and SO_2 are in accord with other sulfur modeling studies. The concentrations of aerosol sulfate and SO_2 at the surface are in general agreement with observations. The process that controls the concentration of aerosol sulfate is aqueous-phase chemistry.

5. ACKNOWLEDGMENTS

The National Center for Atmospheric Research is sponsored by the National Science Foundation.

6. REFERENCES

Benkovitz, C. M., C. M. Berkowitz, R. C. Easter, S. Nemesure, R. Wagener, and S. E. Schwartz (1994) Sulfate over the north Atlantic and adjacent continental regions: Evaluation for October and November 1986 using a three-dimensional model driven by observation-derived meteorology, *J. Geophys. Res.*, **99**, 20,725-20,756.

Hesstvedt, E., O. Hov, and I. S. A. Isaksen (1978) Quasi-steady-state approximation in air pollution modeling: Comparison of two numerical schemes of oxidant prediction, *Int. J. Chem. Kinet.*, **10**, 971-994.

Müller, J-F, and G. Brasseur, (1995) IMAGES: A three-dimensional chemical transport model of the global troposphere, *J. Geophys. Res.*, **100**, 16,455-16,490.

Walcek, C. J., R. A. Brost, J. S. Chang, and M. L. Wesely (1986) SO_2, sulfate and HNO_3 deposition velocities computed using regional landuse and meteorological data, *Atmos. Environ.*, **20**, 949-964.

Wesely, M. L. (1989) Parameterization of surface resistances to gaseous dry deposition in regional-scale numerical models, *Atmos. Environ.*, **23**, 1293-1304.

A MODELLING STUDY OF AEROSOL PROCESSING BY STRATOCUMULUS CLOUDS

Keith N.Bower and Tom W.Choularton

Physics Dept, UMIST, PO Box 88, Manchester M60 1QD, UK.

1. INTRODUCTION

Aerosol particles in the atmosphere play an important role in the earths radiation budget. They have a direct effect by back-scattering or absorbing incoming solar radiation, but they also contribute indirectly by acting as cloud condensation nuclei (CCN). The CCN distribution (along with other factors such as cloud dynamics) regulates the number and size of droplets which activate within clouds, and so significantly affects the radiative properties of clouds. It is therefore important to investigate the processes which control or affect the properties of the atmospheric aerosol population. This will improve our understanding of the possible feedback role played by aerosols (and clouds) in offsetting the climate change which has been predicted will accompany increases in greenhouse gases and other anthropogenic precursors.

The changes in aerosol properties resulting from a single processing cycle through a cloud system (including observations from a cap cloud experiment and the results from a modelling study) are presented in Choularton *et al.* (1996 - this issue). In this paper, a simple model of the stratocumulus (Sc) capped boundary layer is used to examine the aerosol modification resulting from multiple processing cycles through a shallow cloud filled layer, and the effect this has on the cloud microphysics. Such clouds generally cover a large fraction of the earths surface and so are important climatologically.

2. THE STRATOCUMULUS MODEL.

The model used is based on the cloud microphysics and chemistry model of Bower *et al.* 1991. It consists of sub-routines which calculate separately the microphysical and chemical development of a droplet distribution as the air parcel in which they reside is subjected to adiabatic cooling (or warming) as it is forced to rise (or fall) through the layer between cloud base (CB) and cloud top (CT). Vertical velocities ($\sim$ a few tenths $m\,s^{-1}$ - based on observed profiles) are prescribed. Within 20m of cloud top, the effects of entraining heat, moisture, fresh aerosol and tropospheric gases into the cloud through the boundary layer top (and the detrainment of cloud drops and interstitial aerosol) are considered. Once at cloud top the updraught profile is reversed, and the droplets begin to evaporate, eventually reforming a modified aerosol distribution at cloud base. The modified distributions (and gases) are then used as input to further cloud processing cycles.

The initial aerosol distribution is divided up into a number of size categories and is input to the model at its equilibrium wet size at 99% relative humidity (RH). The soluble fraction and chemical composition of the aerosol is prescribed (based on measured or previously calculated values), and the nucleation scavenging calculated as the parcel ascends towards cloud base. The developing super-saturation activates those aerosol which are able to act as CCN, but eventually, efficient growth of the activated drops is such as to reduce the peak supersaturation preventing further activation. The model then calculates the continuing growth and chemical development of the embryo cloud drops. Changes in the soluble component of the initial aerosol mass (i.e. the effective CCN mass) due to aqueous phase chemistry are calculated at each timestep.

The chemistry model considers the aqueous phase oxidation of S(IV) to S(VI) (predominantly by the oxidants O_3 and H_2O_2) within cloud drops (when $r > 0.5\mu m$), as well as the uptake or out-

gassing of soluble gases (which include H_2O_2, O_3, SO_2, CO_2, NH_3, HNO_3 and higher oxides of N) and the repartitioning of such species between droplets of different initial composition. Equilibrium concentrations of gases in solution are not assumed to be attained instantaneously, the uptake/outgassing being limited kinetically. Presently, the chemistry model is activated only after the liquid water content exceeds 0.01 g m^{-3}. This avoids problems associated with the non-ideal strong solutions present in small droplets/aerosol (however the model is currently under development to include the chemistry of such drops).

3. MODEL INITIALISATION.

In the studies presented, the aerosol size distributions used as input were based on measured spectra from a hillcloud experiment at Mt. Kleiner Feldberg (by DMPS) in central Germany (Wobrock *et al.* 1994), or as measured aboard the MRF C130 aircraft (in ship track plumes) off the coast of California in 1994 (by PCASP). The soluble fractions of the input aerosol were prescribed to vary from 50% by volume for the smallest aerosol, up to 100% for the largest aerosol (which for DMPS spectra were added to extend the distributions to beyond their upper cut-off size). For simplicity an initial standard ammonium sulphate aerosol composition was prescribed.

Initial concentrations of the major gas phase species at the start of the first cycle (set to simulate dirty continental or ship plume conditions for all runs) were: SO_2=10ppbv; NH_3=0.1ppbv; O_3=30ppbv (boundary layer and free troposphere); H_2O_2=1ppbv (2ppbv in tropospheric air when entrained). Prescribed vertical velocities of 0.2ms^{-1} were used throughout, and the tropospheric air was approximately 4°C warmer than cloud top (with an RH of 85%). Cloud base was fixed at 300m (12.5°C) and the cloud layer was 300m deep.

4. MODEL SIMULATION CASES

For each series of model runs, up to ten processing cycles up and down through the cloud layer were performed. In successive series, the sensitivity of the results obtained to parameters such as input gas phase concentrations (e.g. see Choularton *et al.*), or to the entrainment rate at cloud top e.t.c. were examined. Some of the essential results obtained from these studies will now be presented.

Figure 1 shows a comparison of the dry aerosol size distribution input to run series 3 with the modified spectra generated following 1, 5 and 10 processing cycles through the cloud layer. In this series, entrainment of fresh H_2O_2 into cloud top was simulated by restoring the parcel concentration to 1ppbv in this region. No other entrainment was allowed.

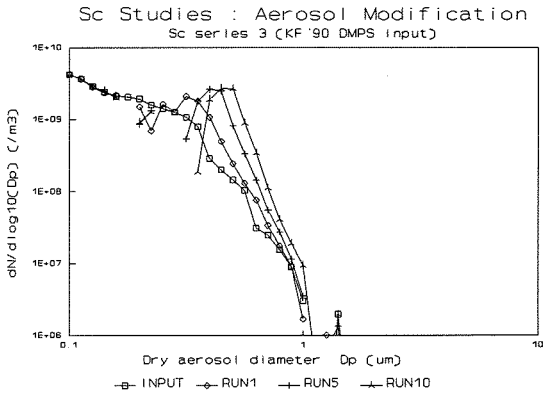

Figure 1 : The input and output dry aerosol spectra after 1, 5 and 10 passes through the Sc layer - Series 3

In this case, significant modification of the size distribution occurs after each cycle, generated as a result of sulphate production. A characteristic bimodal spectrum is produced, which becomes steadily more pronounced as the smallest CCN activated gain soluble material. Figure 2 illustrates how this significantly reduces the critical supersaturation required to activate these CCN in

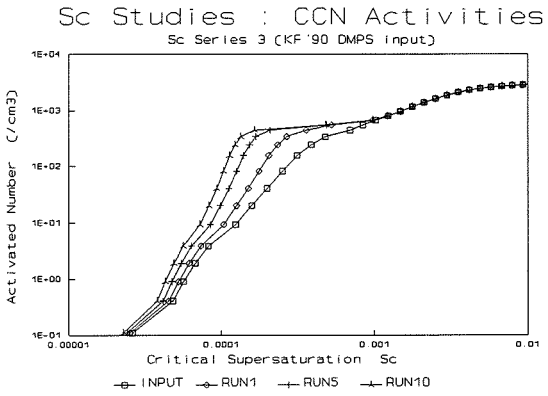

Figure 2 : The input and modified CCN activity spectra after 1, 5 and 10 cycles through the Sc layer - Series 3

subsequent cloud cycles. With updraughts fixed at

0.2 m s^{-1}, the droplet number at cloud top remains unchanged. However, the modified CCN take up water vapour at an increased rate causing a reduction in the peak supersaturation (S) attained in successive cycles (figure 3). This could also stabilise the droplet number concentration in Sc cloud layers. In these model runs, the more efficient removal of water vapour early on (which delays and reduces the peak S) delays the activation of the smallest CCN causing an initial increase in the effective cloud droplet radius. This effect becomes less significant after run 2, as shown in figure 4 for run series 5 (using PCASP ship track aerosol as input).

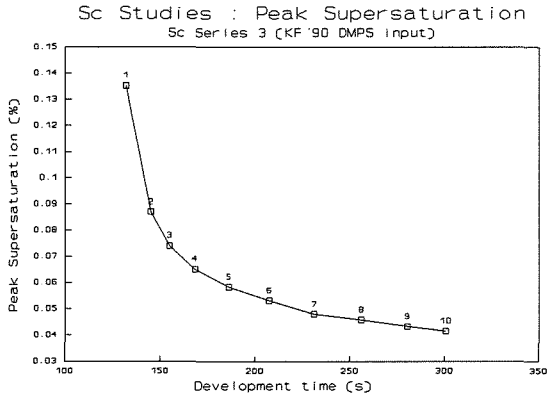

Figure 3 : The peak supersaturation attained in successive Sc cycles - Series 3

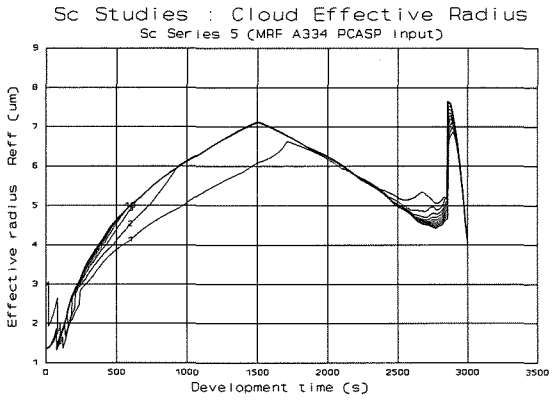

Figure 4 : The effective radius profile in successive Sc cycles - Series 5 (as Series 3 except ship track aerosol)

In these studies, the oxidation of S(IV) to S(VI), and hence the aerosol modification, is highly H_2O_2 oxidant limited. Although there is an ample supply of O_3 oxidant, with the input conditions used, the droplet pH (generally 3.5 or less) is too low to allow any significant sulphate production via this pathway. This is illustrated in figure 5, which shows the aerosol modification generated in successive cycles for run series 0. Series 3 inputs were used, but no attempt was made to simulate entrainment of H_2O_2 at CT. After the initial CB concentration of H_2O_2 is consumed in run 1, no significant further growth of aerosol occurs in successive cycles. However, with an adequate supply of ammonia available in the boundary layer (BL) to neutralise droplet acidity, further sulphate growth via the ozone reaction would be possible. NH_3 concentrations of a few ppbv are present over many continental and some oceanic regions, and recent evidence (Wells *et al.* 1996) suggests that ammonia can be transported large distances, trapped in dry aerosol as ammonium, before being released into the gas phase again at high RH. This result can be simulated in the model by prescribing higher BL NH_3 concentrations and/or by using a more complex (and realistic) mixed aerosol composition at input.

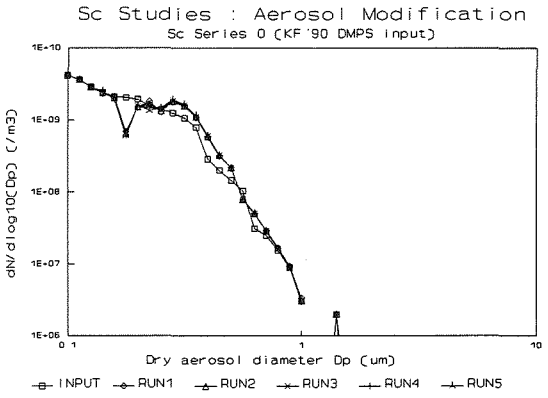

Figure 5 : The aerosol modification generated in Series 0, in the absence of entrained H_2O_2.

With the importance of replenishing the cloud parcel with fresh oxidant rich air highlighted, an attempt was made to simulate more realistically the effects of entrainment of tropospheric air into the system at cloud top (as described in §2). In series 9, an entrainment rate of $\mu = 10^{-3} m^{-1}$ was set for the entrainment region. Heat, moisture and oxidants were entrained (and cloud drops and interstitial aerosol detrained), but the tropospheric air was assumed to be devoid of fresh aerosol. This entrainment rate was sufficient to reduce the CT liquid water content by about 10%, but the additional sulphate generated by entrained peroxide was insufficient to produce a large modification of the aerosol size spectrum after the first cycle.

Figure 6 shows the CCN activity spectra for this series. The removal of drops enables the peak

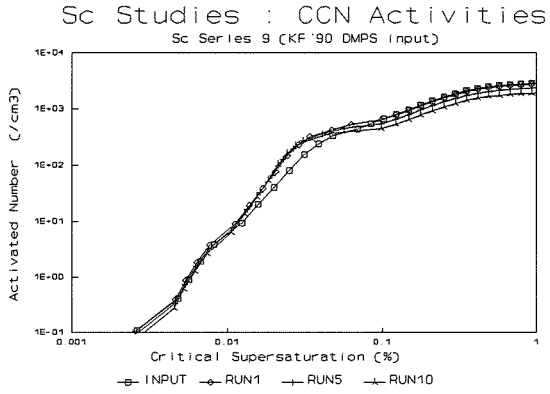

Figure 6 : CCN modification in successive runs with entrainment (not fresh aerosol) - Series 9

supersaturation attained in successive cycles to increase slightly, but not to the run 1 maximum. With fixed updraughts, the main effect of entrainment in series 9 is to reduce the aerosol number and increase the cloud effective radius in successive cycles, even though the concentration of H_2O_2 in entrained air, and the entrainment rate, are realistic.

In series 8, the entraining model was rerun, but with an aerosol population (identical properties to the CB spectrum) entrained in a single event (to limit the total number of categories and hence computation times). The concentration of entrained aerosol was assumed to be half that at CB. The main effect of this was to offset the increase in peak S and the increase in cloud effective radius, and to halve the decrease in cloud droplet number in successive cycles.

5. CONCLUSIONS

(i) Sulphate production in cloud droplets leads to a marked evolution of the chemical properties of the aerosol particles on which they form.

(ii) A significant modification of the aerosols size distribution and hygroscopic properties is nearly always predicted for the first cycle through a cloud.

(iii) Modification of aerosols in successive cycles through Sc cloud layers is highly oxidant limited unless a strong source of ammonia is present. In the absence of ammonia, entrainment of hydrogen peroxide from the free troposphere is rate limiting for the S(IV) oxidation process and hence for the continued modification of the aerosol.

(iv) The microphysics of the stratocumulus is fairly insensitive to the trace gasses entering the cloud, the system appearing to self compensate for the aerosol modification generated.

(v) The reduction of the critical supersaturation of processed CCN will, however, make them much more efficient CCN if mixed into much less vigourous clouds.

6. FUTURE WORK

To further examine sensitivities to: the input gas chemistry (particularly NH_3); the properties and composition of the input aerosol; the degree of entrainment and properties of entrained air and aerosol, and to develop the model to take account of the effects of coalescence and high ionic strength chemistry during activation and evaporation phases (and to examine the modification of interstitial aerosol).

7. ACKNOWLEDGEMENTS

This work was supported by the Natural Environment Research Council, the UK Department of the Environment, the Hadley Centre and by the European Union Environmental Program. We should also like to thank the Meteorological Research Flight for supplying data from stratocumulus flights.

8. REFERENCES

Bower,K.N., Hill,T.A., Coe,H. and Choularton, T.W. 1991. Sulphur Dioxide Oxidation in an Entraining Cloud Model with Explicit Microphysics. *Atmospheric Environment.* **25A, No10**, 2401-2418.

Choularton,T.W. *et al.* 1996. A study of the aerosol modification generated by passage through an orographic cloud. *Proc. 12th International Conf. on Clouds and Precipitation, Zurich, Switzerland.*

Wells,M. *et al.* 1996. The reduced nitrogen budget of an orographic cloud. The Great Dun Fell, GCE 1993 special edition of: *Atmospheric Environment.*

Wobrock,W. *et al.* 1994. The Kleiner Feldberg Cloud Experiment 1990. An overview. *J.Atmos.Chem.* **19, Nos. 1 & 2,** 3-35.

CLOUD-PROCESSING AND MORPHOLOGICAL RESTRUCTURING OF SOOT AGGREGATES SAMPLED AT THE JUNGFRAUJOCH HIGH-ALPINE RESEARCH STATION (3454 M), SWITZERLAND

Stephan Nyeki[1,2], Vincent Lavanchy[3], David Lewis[2], Urs Baltensperger[1], Ian Colbeck [2] and Heinz W. Gäggeler[1,3]

[1]Paul Scherrer Institute, CH-5232 Villigen-PSI, Switzerland
[2]Institute for Environmental Res., University of Essex, Colchester CO4 3SQ, UK
[3]Institute of Inorganic Chemistry, University of Bern, CH-3013 Bern, Switzerland

1. INTRODUCTION

Soot combustion aggregates have been shown in laboratory studies to exhibit compaction or restructuring of their morphology when subjected to evaporation/condensation processing otherwise known as humidity cycling (Colbeck *et al.*, 1990; Huang *et al.*, 1994). Such processing is also postulated to occur within clouds, where the number of cloud-processing cycles has been estimated variously from ~3 (Pruppacher and Jaenicke, 1995) to 10 - 20 (Charlson and Ogren, 1982). As a result, the aggregate atmospheric lifetime and optical properties may be altered. The significance of this effect, when considering the ubiquitous nature of soot, remains to be assessed.

Atmospheric observations of restructuring induced by cloud-processing are difficult to obtain and remain sparse. This study presents results from an aerosol campaign running continuously since July 1995 at the Jungfraujoch high-alpine research station (3454 m), Switzerland. The station is influenced mainly by free tropospheric "background" air and is often under in-cloud conditions, hence providing a suitable site for studying soot morphology amongst other parameters.

Soot samples from the measurement of black carbon (BC) concentration, using an optical method, are analysed by correlation with the cloud liquid water content (LWC) and ambient relative humidity (RH). Scanning electron microscope (SEM) studies allow the soot morphology to be studied as a function of the above parameters. In addition to these measurements, the elemental/total carbon ratio (EC/TC) was determined to investigate its influence on the aerosol hygroscopicity and hence the morphology.

2. EXPERIMENTAL

The present campaign has included the measurement of the following aerosol parameters: the light scattering coefficient (integrating nephelometer, TSI 3563), the BC concentration (aethalometer, AE-10), the surface concentration (epiphaniometer), the number concentration (condensation nucleus counter, TSI CNC 3025) and the size distribution (optical particle counter, PMS Las-X). Additional supplementary data includes the cloud LWC (Gerber, PVM-100) and meteorological data from the Swiss Meteorological Institute. All instruments sampled ambient air from a common stainless-steel inlet (total length 3.5 m of which 1.5 m protruding into the laboratory; and 4.0 cm diameter) fitted with a snow-hood to prevent the ingress of snow or precipitation. Further aspects of the campaign and experimental details may be found elsewhere (Nyeki *et al.*, 1996).

Under the conditions prevalent at a high-alpine site, humidity control of the aerosol sample was initially considered necessary using a heating-tape, wrapped on the 1.5 m length of inlet in the laboratory. Global Atmosphere Watch (GAW) recommendations for relative humidity stipulate a value < 50 % to prevent the erroneous measurement of aerosol light scattering in the deliquescent phase (Ogren *et al.*, 1993). Throughout the campaign it has however, been found that the ambient conditions in the laboratory (22 - 23°C) and the relatively low flowrate through the sample inlet always ensured an RH < 20 %, which has so far removed the need to operate the heating-tape. This is fortuitous as during the sampling process and subsequent filter handling, large variations in humidity are avoided. Such variations in the RH may introduce additional artefact restructuring, however, it is considered that any such artefact is

probably minimal due to careful storage of the filters and the low RH experienced within the buildings.

The morphological and chemical study of BC aerosols was conducted on filter samples from the continuous measurement of BC with a 30 minute temporal resolution (60 minutes in winter). The filter disc (1.1 cm diameter) was geometrically cut in half and weighed to account for any deviation during cutting. One half was used for SEM studies and the other for the determination of the EC/TC ratio.

SEM samples were prepared in the standard way by sputtering a gold layer onto the filter sample. One drawback involved in such SEM studies is the physical handling involved in preparing the sample i.e. evacuation in the sputtering and SEM chambers. As a consequence, whether additional artefact restructuring also occurs during sample preparation cannot be answered. Literature studies suggest in-situ and SEM results to be in good agreement, and hence the effect is again tentatively considered minimal.

Measurement of the EC/TC ratio was conducted based on a two-step combustion technique (Cachier *et al.*, 1989). During the first combustion step the organic carbon (OC) component is oxidised to CO_2 by passing analytical grade O_2 over the sample at an optimised temperature of 340°C. Upon increasing the temperature to 900°C complete oxidation of the remaining carbon component, defined as EC, occurs. The experimental apparatus consists of two units. In the first stage a combustion unit is followed by a catalyser to ensure the complete oxidation of the combustion products. In the second stage a Total Organic Carbon 700 Analyser (O. I. Analytical) accumulates the derived CO_2 from the combustion process, which is then measured using a Non-Dispersive Infrared Analyser (NDIR).

3. RESULTS AND DISCUSSION

A comparison of daily average values of cloud LWC and BC concentrations for the period July 1995 - January 1996 appears in Figures 1 and 2, respectively. As the cloud LWC has only been measured since April 1995 a clear seasonal variation has not manifested itself, a point further substantiated by statistical analysis (Baltensperger *et al.*, 1996a). In contrast, the BC concentration for the same period exhibits a seasonal peak in the summer (e.g. July average 197 $ng.m^{-3}$) and a trough in winter (e.g. December average 21 $ng.m^{-3}$).

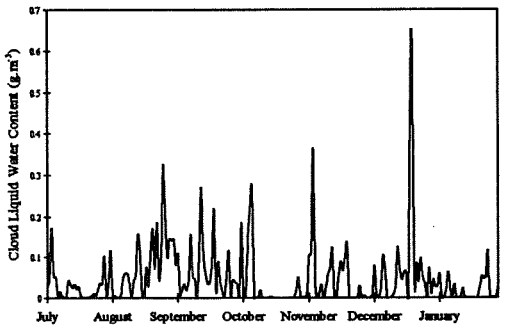

Figure 1. Daily Average Values of Cloud LWC at the Jungfraujoch Station from July 1995 - January 1996

These results are similar to the seasonal cycles observed continuously since 1988 by the epiphaniometer, which measures a quantity proportional to the aerosol surface concentration (Baltensperger *et al.*, 1991).

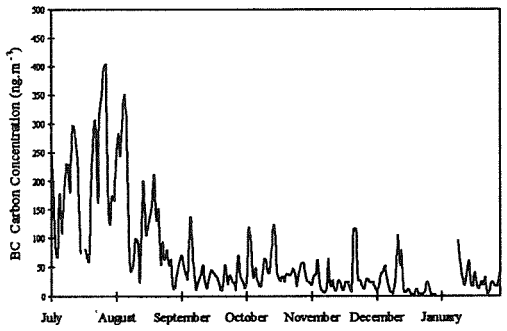

Figure 2. Daily Average Values of BC Concentration at the Jungfraujoch Station from July 1995 - January 1996

Correlation analysis of the cloud LWC and the BC concentration reveals a weak negative value at -0.16, while -0.26 is obtained for an evaluation of the aerosol number concentration (diameter d > 0.01 μm) against cloud LWC. It should be mentioned that these values only include paired data points for which the cloud LWC is non-zero i.e. only in-cloud conditions are considered. In this manner the "bias" on the correlation coefficient from cloud LWC zero values (out-of-cloud conditions) is removed. While the scavenging of aerosols within clouds is expected, the low correlation coefficients cannot be interpreted either way to any degree. A plot of hourly average values of aerosol number concentration against cloud LWC in Figure 3, however, reveals a confinement of the majority of points behind the indicated solid line. The line only represents an approximate guide

for the eye. While such an analysis requires further data, it would seem to demonstrate that a particular cloud LWC content allows a range of aerosol concentrations up to a certain maximum value.

SEM samples are to be presented. By using fractal analysis, a quantitative measurement of the aggregate morphology from SEM images may be obtained. The fractal dimension D is a measure of the physical space occupied by an aerosol. As an example, D = 3 represents a compact sphere, D = 1 a chain-like linear morphology and an intermediate value a distended morphology. Representative values for freshly emitted soot aggregates lie in the range 1.8 - 1.9, while humidity processed aggregates have been variously restructured to values as high as 2.5.

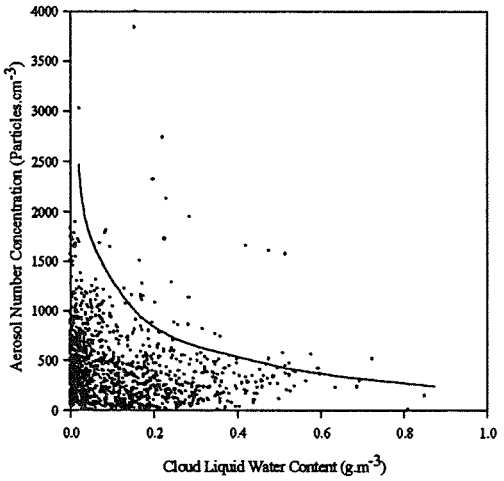

Figure 3. Hourly Average Values for Aerosol Number Concentration (d > 0.01 μm) vs. Cloud LWC from July 1995 - January 1996

To obtain statistically significant values of D, numerous aggregates from each filter sample will have to be analysed. Temporal analysis of the SEM images with respect to cloud LWC and ambient humidity will allow those periods to be identified in which sampling occurred under in-cloud conditions.

Independent determination of the EC and OC values provides not only a calibration cross-reference for the aethalometer, but also an insight into the influence of chemical composition on the hygroscopicity of aerosols. As the aethalometer calibration is based on a chemical method, the terms BC and EC are essentially equivalent but are used to differentiate between the two methods. However, discrepancies do occur for instance during Saharan dust events when aeolian dust containing haematite (Fe_2O_3) and carbonate, among other constituents, are sampled. Haematite is the only major optically absorbing aerosol species beside soot and will thus cause only aethalometer readings to be overestimated. In comparison, the carbonate component may cause a small artefact in the EC/TC method due to the liberation of CO_2 and can be removed by pre-treatment of the filter with HCl fumes. In these experiments, Saharan dust episodes were identified from the twice daily measurement of the calcium ion concentration. Only aethalometer filter samples from such episodes were treated for carbonate.

Preliminary results for the determination of the EC/TC ratio indicate values ranging from ~ 0.15 - 0.45, comparing favourably to an average value 0.20 reported for urban aerosols in temperate latitudes (Cachier *et al.*, 1989). The significance of this ratio in relation to the total aerosol number and the LWC concentration at the Jungfraujoch will be further analysed.

The chemically inert nature of black carbon aerosols and their accumulation mode size (~ 0.1 - 1.0 μm), results in an elevated atmospheric lifetime (average 3 - 7 days). During this period, long-range transport may occur which, according to season results in the annual cycle of aerosol concentration at the Jungfraujoch station. In addition, a superimposed diurnal cycle of aerosol has also been observed. The convective transport of polluted air from the planetary boundary layer (PBL) by convection, is attributed to this effect and occurs mainly during the summer (Baltensperger *et al.*, 1996b).

The diurnal cycle may be approximately divided into two periods, when the station is in the free troposphere 01:00 - 11:00 (Local Standard Time, LST) and influenced by long-range transported aerosol and 11:00 - 01:00 when the Jungfraujoch station is influenced by "fresh" aerosol from the PBL. Hence, further interpretation is possible by considering the age and origin of the sampled air masses.

4. CONCLUSIONS

An investigation of the effect of cloud-processing on soot morphology at a high-alpine site has been considered and will be further presented using fractal dimension analysis of SEM images of aggregates. Preliminary results indicate that different degrees of restructuring induced by cloud-processing provisionally appear to depend on

a number of factors: the origin of the air mass i.e. free tropospheric or polluted air from the PBL, the humidity history of the air mass and the aerosol chemical composition evidenced by the EC/TC ratio. A detailed study of the influence of such aspects on the soot morphology will be examined.

5. ACKNOWLEDGEMENTS

This work was supported by the NERC. The support of the staff and facilities at the Jungfraujoch research station and the PSI are gratefully acknowledged.

6. REFERENCES

Baltensperger U., H. W. Gäggeler, D. T. Jost, M. Emenegger and W. Nägeli, 1991: Continuous background aerosol monitoring with the epiphaniometer. *Atmos. Environ.* **25A**, 629 - 634.

Baltensperger U., M. Schwikoski, D. T. Jost, S. Nyeki and H. W. Gäggeler, 1996a: Seasonal variation of cloud liquid water content and activated aerosol fraction at a high-alpine site. ICCP Conference, Zürich 1996.

Baltensperger U., H. W. Gäggeler, D. T. Jost, M. Lugauer, M. Schwikowski and P. Seibert, 1996b: Aerosol climatology at the high-alpine site Jungfraujoch, Switzerland. *J. Geophys. Res. Submitted.*

Cachier H., M. -P. Bremond and P. Buat-Ménard, 1989: Determination of atmospheric soot carbon with a simple thermal method. *Tellus* **41B**, 379-390.

Charlson R. J. and J. A. Ogren, 1982: The atmospheric cycle of elemental carbon. In *Particulate Carbon* (Edited by Wolff G. T. and Klimisch R. L.), Plenum, New York.

Colbeck I., L. Appleby, E. J. Hardman and R. M. Harrison, 1990: The optical properties and morphology of cloud - processed carbonaceous smoke. *J. Aerosol Sci.* **21**, 527 - 538.

Huang P-F., B. J. Turpin, M. J. Pipho, D. Kittelson, and P. H. McMurry, 1994: Effects of water condensation and evaporation on diesel chain-agglomerate morphology. *J. Aerosol Sci.* **25**, 447 - 459.

Nyeki S., U. Baltensperger, I. Colbeck, M. Schwikowski, D. T. Jost, 1996: The Jungfraujoch high-alpine site (3453 m) as a background continental site for the measurement of aerosol parameters. *In Preparation*

Ogren J. A., D. Hegg, T. Clarke and J. Gras, 1993: Sampling considerations for the aerosol component of GAW. *Draft Copy.*

Pruppacher H. R. and R. Jaenicke, 1995: The processing of water vapor and aerosols by atmospheric clouds, a global estimate. *Atmos. Res.* **38**, 283 - 295.

ON THE INFLUENCE OF ACTIVITY COEFFICIENTS ON THE SIZE DEPENDENT CLOUD DROP CONCENTRATION DEVELOPMENT

Frank Müller

Laboratory for Air and Soil Pollution, EPFL, 1015 Lausanne, CH

1. INTRODUCTION

The transition of wet aerosols to solution droplets is described by the activation process. On one hand, the size dependent physico-chemical properties of the aerosols are determining the subsequent growth processes (condensation, coagulation, break-up, aerosol scavenging) of the newly formed cloud droplets. On the other hand, multi-phase chemical processes (chemical reactions, mass transfer between the gas and the aqueous phase) are supported in the droplets due to the presence of chemical substances originated from the aerosol phase. The initial drop concentration as well as their evolution are also size dependent processes which are determined by the simultaneous interaction of cloud micro-physical and multi-phase chemical processes. Beside the size dependency, condensation as well as chemical processes are concentration dependent processes, whereas both size and concentration dependency, respectively, are non-linearly interrelated.

Since the aerosol particles mass is size dependent distributed one finds for the wet aerosol particles, which are thought to be in equilibrium with respect to water vapor, the highest solute concenteations for the smallest aerosol particles according to the Köhler equilibrium curves. Therfore one finds for the newly formed cloud droplets a size dependent distribution of chemical matter inside the size distributed droplets, whereas the highest solute concentrations are related to the smallest droplets.

The presence of soluble substances has two consequences: On one hand, the solute concentration of the cloud droplest is influencing the water vapor flux between the surface of the droplets and their environment via Raoult's law. This is expected to be a size dependent effect. On the other hand, more complex relations exist with respect to the influence of the ion concentration in the droplets due to the interaction between the pH and other parameters like solubility of gaseous species or reaction rates. In turn, this interactions affect the the water wapor flux and the solution concentration of the cloud droplets.

In order to account for the different effects of solute concentration generally the mole ratio of water is used. This approach is only valid for solute concentrations smaller than about 10^{-3}mole/l. For higher solute concentrations considerable deviations from Raoult's law appear due to non-linear interactions between the ions in the solution. The use of the water activity a_w instead of x_w is preferenced under such conditions, whereas the aqueous phase concentrations are expressed in terms of the ion-specific activity coefficients f_i.

3. MODEL DESCRIPTION

The applied model is focussed on the simulation of the generation and evolution of a cloud in the first few minuts. Starting point is an aerosol distribution of rural background type according to Jaenicke (1987). The main constituents of the aerosol are NaCl, $(NH_4)_2SO_4$, and SiO_2, whereas the composition is a size dependent, internal mixture according to Müller (1994).

3.1. THE ACTIVITY MODEL

Based on the Gibbs-Duhem equation of a multi-component solution

$$c_W \, dln\, a_W + \sum_{k=1}^{K} c_k \, dlna_k = 0 \qquad (1)$$

one can derive an expression for the water activity a_w as a function of the solute concentration c_k, whereas the solute can be subdivided into soluble and non-soluble substances, respectively. The soluble substances can be splitt off further into electrolytes and non-electrolytes with concentrations c_e and c_n, respectively. Only the electrolytes in the solution are causing non-linear deviations from Raoult's law, whereas the other fractions of the solute can be treated as in ideal solutions. Therefore one finds:

$$\ln a_w = \frac{1}{c_w}\left[\sum_{n=1}^{N}\frac{c_n}{x_n}dx_n - \sum_{e=1}^{E}\nu_e c_e\left(1+\int_0^{c_e}\frac{\bar{c}_e}{\bar{\gamma}_e}\frac{\partial\bar{\gamma}_e}{\partial c_e}dc_E\right)\right] \qquad (2)$$

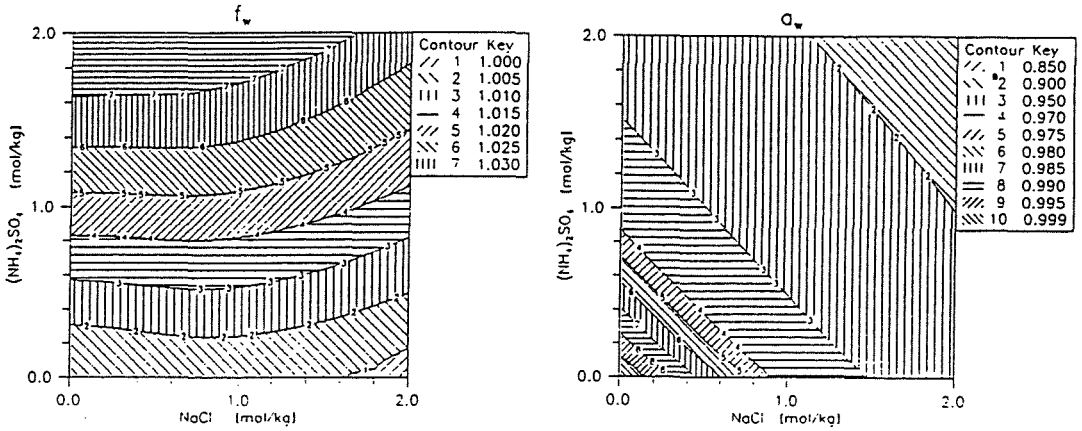

Fig. 1: Activity coefficient (left) and activity (right) of water for a NaCl-$(NH_4)_2SO_4$-H2O system

To solve the integral in eq. (2) the non-linear dependence of the average activity coefficient $\bar{\gamma}_e$ on the electrolyte concentration c_e must be known, especially for the simultaneous interaction of all other electrolytes present in the solution. In general, the calculation of the activity coefficients in multi-component solutions is based on the activity coefficients of binary solutions (e.g. Tang et al., 1993), whereas the activity coefficients for the binary solutions are often calculated according to Pitzer and Mayorga (1973). This method does not allow the calculation of the activity coefficients for the different types of anions and cations, $\gamma_{+/-}$, resulting from the dissociation of the aerosol salt particles or volatile compounds, or which are originated from chemical reactions in the aqueous phase like. The ion-specific activity coefficients $\gamma_{+/-}$ are used for the chemical reaction system. Further, this mehtod is not capable to take into account the ionic cross interactions. Since there exists no theory which is describing the ionic cross interactions for multi-component solutions at present time, those values are only accessable by laboratory measurements.

In the present study the $\gamma_{+/-}$ and the $\bar{\gamma}_e$ are calculated using the so-called 'Davis approximation' (cp. Stumm and Morgan, 1981). This approximation is valid for solution concentrations less then c<0. 05M' (M'=mole/1kg water)(Young and Warren, 1992). Therefore, it follows for the $\gamma_{+/-}$ and $\bar{\gamma}_e$:

$$\log \gamma_{+/-} = -A z^2_{+/-} \left(\frac{I^{1/2}}{1 + I^{1/2}} - 0.2I \right) \qquad (3)$$

$$\text{with } A = 1.83 \cdot 10^6 (\varepsilon T)^{-\frac{2}{3}}, \quad I = \frac{1}{2} \sum_{j=1}^{J} z^2_j c_j$$

$$\bar{\gamma}_e = \left(\gamma_+^{\nu_+} \gamma_-^{\nu_-} \right)^{\frac{1}{\nu_e}} \quad \text{with } \nu_e = \nu_+ + \nu_-$$

where $z_{+/-}$, $\nu_{+/-}$, and ν_e are the charge of the cations and anions, the number of cations and anions per aerosol salt molecule, and the total number of ions of a certain salt molecule, respectilvely. For solute concentrations c>0.05M' measured average activity coefficients of binary solutions (Weast (1984), Stumm and Morgan (1981)) are fitted according to eq. (4).

$$\bar{\gamma}_e = \sum_{n=1}^{N} a_n c_e^n \qquad (4)$$

The polynom coefficients for the used aerosol composition can be found in Müller (1994).

As an example of the calculations using eq. (2) the activity coefficient f_w of water and the water activity a_w for a NaCl-$(NH_4)_2SO_4$-H_2O system are shown in Fig. 1, which is used throughout this study. The contours of f_w show clearly the dominant influence of ammonium sulfate as a strong electrolyte on the activity of water compared to NaCl.

3.2. MICRO-PHYSICAL MODEL

To investigate the principle influence of the water activity and of the ion specific activity coefficients on the size dependent concentration development, activation of wet aerosols of rural background type and droplet growth by condensation/evaporation are considered. The activation process is parameterized according to the so-called 'Köhler equilibrium curves' taking into account an assumed size dependent chemical composition of the aerosols. The treatment of the diffusional droplet growth considers the Kelvin, the Raoult, and the temperature effect, respectively. To avoid numerical discretization errors, Lagrangian water mass co-ordinates are used to describe the droplet growth. For a detailled description see Müller (1994) and Müller and Mauersberger (1994).

3.3. CHEMICAL MODEL

The used chemical model describes the dominant acidity formation processes taking into account the fluxes of volatil compounds between the gas and the aqueous phase as well as aqueous phase chemical

reactions. The description of the mass transfer coefficients follows Schwartz (1986), whereas the formulation of the aqueous phase reaction system is similar to the one in Lin and Chameides (1991). It is assumed that electroneutrality and dissoziation equilibria are instantaneously established. The initial gas phase concentrations are given in Tab.1.

Gas	CO_2	H_2O_2	O_3	HNO_3	NH_3	SO_2	HCl
ppb(v)	$3.3 \cdot 10^5$	1.0	30.0	0.5	5.0	30.0	0.5

Tab.1: Initial gas phase concentrations

4. RESULTS

Two sets of simulations were performed: The first set without activity coefficients, i.e. $\gamma_{+/-}=1$ and $f_w=1$ (case A), and a second set considering the activity effects (case B). The initial environmental conditions for temperature, pressure, and relative humidity are set to T=280K, P=800hPa, and RH=100.1%, respectively. Deviations are considered with respect to case A.

4.1. INFLUENCE ON THE LIQUID WATER CONTENT AND ON THE MASS OF SOLUTE IN THE DROPLETS

Basically, the Raoult's law accounts for the effect of the substitution of water molecules on the droplet surface by solute molecules in ideal solutions. Therefore, the reduction of the saturation water vapour pressure on the droplet surface depends on the solute concentration in the droplet, and hence, on the droplet surface (presuming a homogeneous solute distribution within the droplets). This effect is partely neutralized due to the non-linear ion interactions, which lead to a renewed increase of water molecules on the droplet surface. An increase of the saturation water vapour pressure results in a decrease of the mass growth rate of the individual droplets. Hence, one can expect a decrease of the droplet water mass due to the consideration of water activities a_w or the water activity coefficients f_w. The dominant influence of $\gamma_{+/-}$ can be seen in the shifting of the solution equilibria towards the ionic components. This, in turn, increases both the overall solute concentration and the formation of irreversibly produced solute components (SVI in this particular case). An increase of the solute concentration increases the Raoult effect, and therefore the water content in the case of the use of ionic activity coefficients. Generally, this effect is very small (about 1%) and is of the same order of magnitude as the increase of solute due to the consideration of $\gamma_{+/-}$. For a comparison, the water content is increased by about 20% only due to the consideration of chemical processes. This increase is especially pronounced in the small droplet size range too.

The result of the superposition of both activity effects is shown in Fig. 2. As one could expect from the results described above, the overall behaviour of liquid water mass in the coupled micro-physical/chemistry system is controlled by the water activity a_w, whereas the solute mass is only little affected due to the consideration of the ion specific activity coefficient. Therefore, the total solute concentration shows the opposite behaviour as the water mass of the droplets: The activity case B shows higher concentrations, especially in the size range of the small droplets.

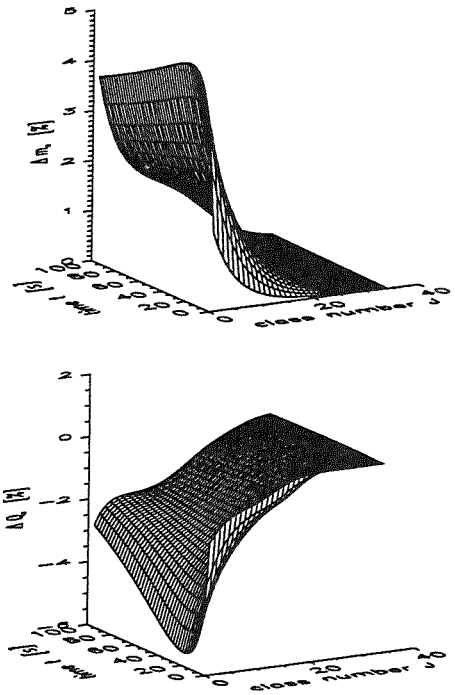

Fig. 2: Percental differences of the drop water mass (top) and of the total solute mixing ratio Q_s (bottom) due to the combined effect of f_w and $\gamma_{+/-}$

4.2. THE BEHAVIOUR OF SINGLE AQUEOUS PHASE COMPONENTS

One effect of the consideration of f_w on the concentration of the aqueous phase species can be seen in the reduced dilution. This causes slightly increased acidities in the activity case B. As a result one can expect a reduced solubility of gaseous species which undergo further dissoziation or which do not dissoziate (reduced liquid water content). Further, the decreased availability of the corresponding reactants in the aqueous phase is also reducing the S(IV) oxidation.

The use of the ion specific activity coefficients is directly affecting the dissoziation equilibria and is, therefore, increasing the ion concentrations. Morover, the $\gamma_{+/-}$ are indirectly affecting the pH via the electroneutrality equation and the mass fluxes between the gas and the aqueous phase, respectively. Hence, one can recognize an increase of $[H^+]$, which causes an

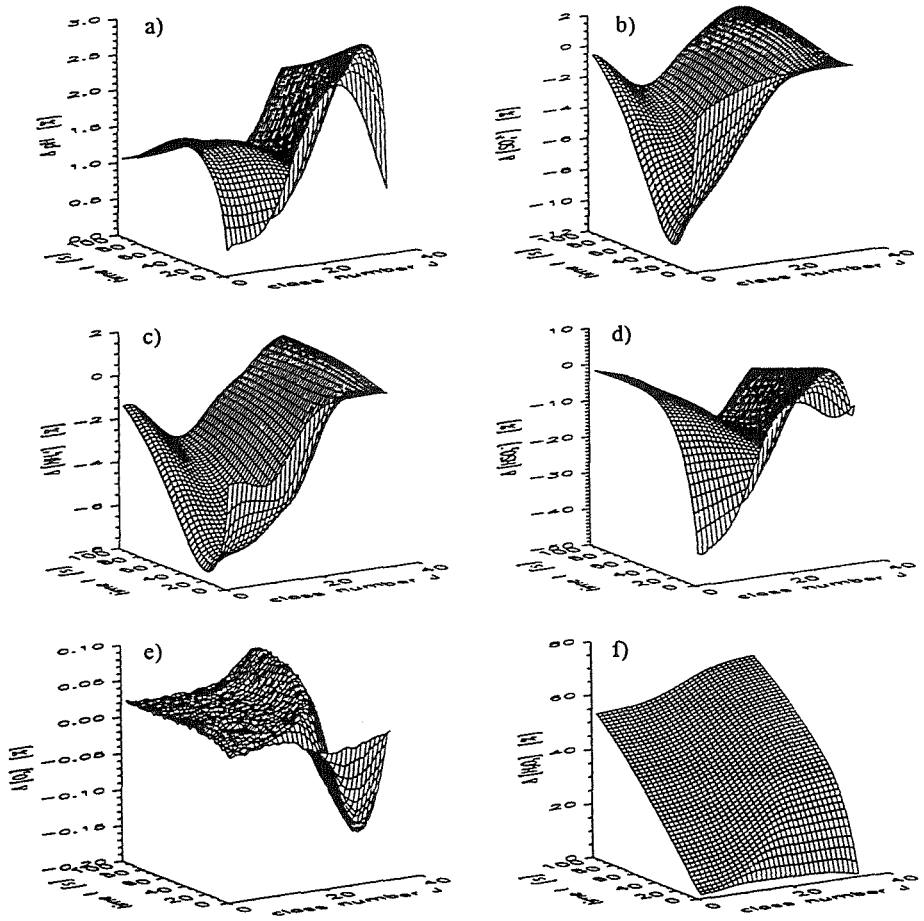

Fig. 3: as Fig. 2, but for chosen aqueous phase components

acceleration of the S(IV) oxidation via the increased HSO_3^- concentration. This leads to a further increase of the acidity. The positive feedback is regulated by the pH itself due to a decreasing solubility of SO_2 and an increasing solubility of NH_3. These relations can be seen for some selected aqueous phase species in Fig. 3. Fig. 3a shows that the acidity is slightly increased in case B ($\Delta pH>0$). Distinctly marked is also the increase of [HSO_3^-] (50%) and the strong decrease of [H_2O_2] (60%) in case B (Fig. 3f). This is related to the pronounced S(VI) production with a maximum of about 12% in the small droplet size range (Fig. 3d,f,b). The development of $\Delta[NH_4^+]$ goes along with $\Delta[SO_4^{2-}]$. $\Delta[O_3]$ is very small due to the abundance in the gase phase. The change of the sign of $\Delta[O_3]$ is following the competing effects of ΔpH and $\Delta S(IV)$: In the range of low ΔpH the effect of the S(IV) oxidation via O_3 is dominant due to higher [S(IV)] in case B -> $\Delta[O_3]>0$. For increasing acidities in case B (bigger ΔpH) one finds a reduction of the S(IV) oxidation via O3 -> $\Delta[O_3]<0$. The range of the change of sign in $\Delta[O_3]$ is related to the ranges of highest ΔpH.

5. CONCLUSIONS

The consideration of activities leads to non-neglectable deviations in both the water mass of the droplets and the total solute concentration especially in the size range of small droplest (<10mm). The consideration of ion specific activity coeffients partially induces drastic changes the development of the aqueous phase species concentration in time and over the whole drop size spectrum.

6. REFERENCES

Jaenicke, R., 1987: Aerosol physics and chemistry, Landolt-Börnstein Neue SERIE; Gruppe V, 46, Physical and chemical properties of the air, Springer Verlag, Berlin

Lin, X., Chameides, W.L., 1991: Model studies of the impact of chemical inhomogeneity on the SO2 oxidation, J. Atm. Chem. **13**, 109-129

Müller, F., 1994: Zur spektralen Modellierung der Wechselwirkung wolkenchemischer und mikrophy-sikalischer Prozesse, FhG-IFU Schriftenreihe, Bd. **30-94**, PhD-Thesis (German)

Müller, F.,Mauersberger, G., 1994: On the interaction of cloud chemical processes and micro-physics, Atmosph. Res. **32**, 273-288

Pitzer, K.S., Mayorga, G., 1973: Thermodynamics of Electrolytes - II: Activity and osmotic coefficients for strong electrolytes with one or both ions univalent, J. Phys. Chem. 77, 2300-2308

Schwartz, S., 1986: Mass transfer considerations pertinent to aqueous phase reactions of gases in liquid water clouds, in Chemistry of Atmospheric Systems, ed. by Jaeschke, W., NATO ASI Series G, Vol. 6, pp. 415-472

Stumm, W., Morgan, J.J., 1981: Aquatic Chemistry: An introduction emphasizing chmecal equilibria in natural water, Wiley and Sons, New York

Tang, I.N., Munkelwitz, H.R., 1993: Composition and temperature dependence of the deliquescence properties of hygroscopic aerosols, Atmos. Env. **27A**, 467-473

Young, K.C., Warren, A.J., 1992: A reexamination of the deviation of the equilibrium saturation curve of soluble particles, J. Atm. Sci. **49**, 1138-1143

The Effects of Sea-Salt Aerosol on the Production of Sulphate in the Marine Atmospheric Boundary Layer and its Effect on Stratiform Clouds

*J A Lowe[1], M H Smith[1], C D O'Dowd[1], and S L Clegg[2]

[1] Physics Department,UMIST, PO Box 88, Manchester, M60 1QD, UK
[2] School of Environmental Sciences, UEA, Norwich, UK

1. INTRODUCTION

In the remote maritime atmosphere, aerosol particles play a direct and significant role in determining the net radiative forcing. Accumulation mode aerosol particles, composed mainly of nss-sulphate and sea-salt material, interact efficiently with solar radiation due to the similarity of their size with the wavelength of the solar radiation. Low level maritime stratiform clouds make an even greater contribution to the radiation budget (Charlson et al, 1987, 1991). These clouds cover a large proportion of the globe, and, due to their low droplet number concentration and low optical thickness, their radiative behaviour is particularly sensitive to changes in droplet microphysics (Hobbs, 1993).

Occasionally, sea-salt aerosol particles dominate the accumulation mode number concentration (O'Dowd, 1993); however, it is more common for the nss-sulphate particles to be the most numerous in this size range. In terms of mass and surface area, the aerosol population is often dominated by sea-salt, originating in both the accumulation mode and in the larger coarse mode. Thus, even when a minority contributor to aerosol number, sea-salt aerosol particles may play a large role in shaping the aerosol distribution, including strongly affecting the development of small nss-sulphate based particles by providing a sink for their precursor materials (O'Dowd et al, 1996).

Outside of clouds, solution droplets formed on sea-salt aerosol provide effective sites for aqueous phase SO_4^{2-} production. The sea-salt solution droplets are buffered to a high pH by the presence of carbonate buffer, providing an environment where the O_3 driven oxidation of dissolved SO_2 can proceed rapidly (Chameides and Stelson, 1992). Thus, these aqueous sites provide a rapid sink for gaseous SO_2 and a significant source of aerosol SO_4^{2-}.

Accumulation mode sea-salt particles, and a fraction of the jet mode sea-salt particles found in the coarse aerosol fraction, may be well mixed within the boundary layer, often being measured at cloud height (Warneck, 1988). If thermodynamic conditions are such that air becomes saturated with respect to water vapour then cloud droplets form. The activated droplets tend to form on sea-salt aerosol in preference to nss-sulphate aerosol particles. This favoured activation of sea-salt is a consequence of sea-salt aerosol often having a larger mode radius than nss-sulphate aerosol, and because the chemical composition of sea-salt results in a lower energetic barrier to their activation as cloud droplets. Incorporation of sea-salt aerosol into cloud droplets is thought to result in an enhancement of their chemical processing ability and to suppress the incorporation into cloud droplets of the less active nss-sulphate based aerosol particles. Thus, the chemical nature of sea-salt and its preferential activation in clouds has the potential to reduce the importance of sulphur species in the marine atmosphere.

2. METHODOLOGY

Two versions of a Lagrangian air parcel model with explicit droplet microphysics were used to simulate the growth of a droplet distribution in a parcel of moist air. The first model version featured no aqueous phase chemical processes and was used to examine the suppressing effect of sea-salt on the activation of nss-sulphate aerosol particles (The model is described in Pruppacher and Klett, 1978). The second model version was more elaborate, having the cloud microphysical aspects coupled to a state of the art chemistry model (Lowe et al, this issue). The chemical aspects of the model simulate the dissolution and dissociation of soluble trace gas species and, with sulphur species, the chemical kinetics. Aqueous

aerosol solutions are often extremely concentrated and their behaviour deviates from that of an ideal solution. The non-ideal solution behaviour encountered in concentrated aerosol solution droplets was dealt with using the formulation of Pitzer (1991).

Nss-sulphate and sea-salt aerosol spectra are required as input for the model (Figure 1). The nss-sulphate aerosol particles were represented by a log-normal distribution function of mode radius 0.075 μm and a standard deviation 1.4. The nss-sulphate aerosol parameters were derived from curves fitted to data collected, using a volatility technique, during the BMCAPE campaign (Lowe et al, 1996). The sea-salt aerosol distribution was represented by the sum of two log-normal curves. The first log-normal curve represents the film mode, with mode radius 0.1 μm and standard deviation 1.9; the second log-normal curve represents the jet mode and has a mode radii of 1 μm and standard deviation of 2.0. The number concentration of sea-salt aerosol is wind speed dependent, ranging from 6.5 cm^{-3} at 5 m s^{-1} up to 53 cm^{-3} at 15 m s^{-1}. The sea-salt spume mode was not included in this study as these particles, whose dry mode radius is larger than 5 μm, are short lived and probably not mixed up to cloud height. The sea-salt aerosol particle parameters were derived from measurements made during a campaign in the north east Atlantic ocean (O'Dowd and Smith, 1993).

Figure 1 - Aerosol Input Spectra

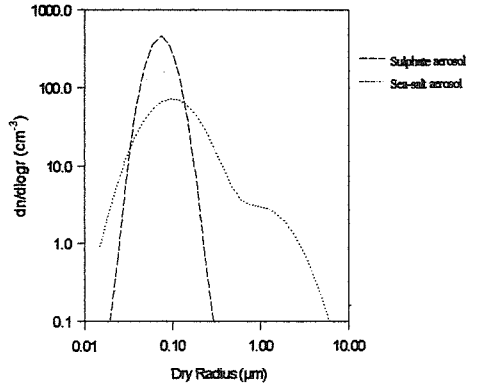

Two well mixed boundary layer scenarios were modelled. In the first, a stratiform cloud occupied the upper 400m of the boundary layer, whereas the second scenario was cloud free.

Gas phase concentrations of SO_2, NH_3, O_3, and H_2O_2 were initially set to 0.5 ppb, 1 ppb, 30 ppb and 1 ppb respectively. The partial pressure of HCl was adjusted so as to be in equilibrium with the initial form and distribution of jet mode sea-salt particles.

3. ACTIVATION IN CLOUD

Within the cloudy boundary layer, the sea-salt and nss-sulphate aerosol particle number concentrations were varied. The total number of cloud droplets formed within 100m of cloud base was determined in each case.

Above cloud base, as the supersaturation increased, sea-salt aerosol was preferentially activated. The presence of these sea-salt based cloud droplets then acted to reduce the peak supersaturation, by providing a large effective sink for the condensing water, and prevented the smaller, less effective, nss-sulphate aerosol particles from becoming activated.

The total number of activated droplets within the cloud was controlled by the atmospheric thermodynamics and the sea-salt and nss-sulphate aerosol particle populations. A relationship between the number of sub-cloud aerosol particles and the number of activated droplets within the cloud has been developed from the results of the simple parcel model simulations. Each simulation, which used a different sub-cloud aerosol concentration, resulted in a different number of cloud droplets. A curve was fitted to the results using non-linear regression techniques.

$$N_{drops} = a_0 + a_1 N_{sulp} + a_2 N_{sulp}^2$$

N_{drops} is the number concentration of cloud droplets (cm^{-3}) and N_{sulp} is the number concentration of nss-sulphate aerosol particles (cm^{-3}). The parameters a_0, a_1, and a_2 are functions of the sea-salt concentration and are written in terms of horizontal wind speed (U m s^{-1}), on which the sea-salt concentration depends.

$$a_0 = 11.60 - 2.51U + 3.25x10^{-1}U^2$$

$$a_1 = 1.108 + 6.80x10^{-2}U - 5.99x10^{-3}U^2$$

$$a_2 = -6.6x10^{-4} - 2.53x10^{-4}U + 1.64x10^{-6}U^2$$

Due to the nature of the aerosol spectra, this semi-empirical relationship is only valid in the clean maritime regime and for horizontal 10m wind speeds in the range 2.5 to 15 m s^{-1}. However, similar droplet relationships can be derived for more unstable conditions and more polluted environments. Such parameterisations will provide an essential component of a large climate model in which aerosol-cloud processes are parameterised (Smith et al, this issue).

It is planned to refine this relationship using a dynamically more realistic entraining cloud model.

4. HETEROGENEOUS SULPHATE PRODUCTION IN CLOUDY AIR

In the cloudy boundary layer, the SO_4^{2-} produced by a single cycle through a non-precipitating cloud was found to be 0.7 μg of SO_4^{2-} per kg of air, for base case gas concentrations, and for nss-sulphate aerosol and sea-salt aerosol particle concentrations of 158 cm^{-3} and 44 cm^{-3} respectively. Approximately 85% of the SO_4^{2-} was produced in cloud droplets formed on sea-salt aerosol.

As the SO_2 concentration was increased from 0.5 ppb to 1.5 ppb the production of SO_4^{2-} increased by a factor of 6. Again, the majority (77%) of SO_4^{2-} was produced in cloud droplets formed on sea-salt based aerosol particles. Reducing the sea-salt aerosol particle concentration to 6.5 cm^{-3} tended to reduce the SO_4^{2-} produced in a single cloud cycle to 44% of that produced with the higher sea-salt aerosol with the lower SO_2 concentration. Varying the initial nss-sulphate aerosol concentration had little effect on the amount of SO_4^{2-} produced, but did effect its distribution across the aerosol spectrum.

Figure 2a - pH profile for sea-salt based droplets

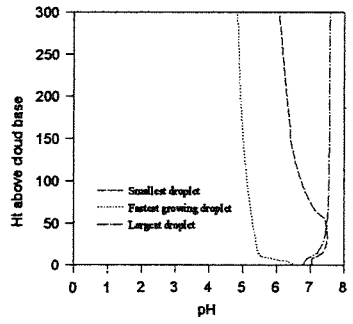

The variation of pH in the sea-salt droplets and in the nss-sulphate droplets for one cycle through the cloud is shown in Figure 2. The sea-salt droplets are less acidic than nss-sulphate droplets through a large fraction of the cloud, making them more efficient sites for the rapid O_3 driven oxidation of dissolved SO_2.

Figure 2b - pH profile for sulphate based droplets

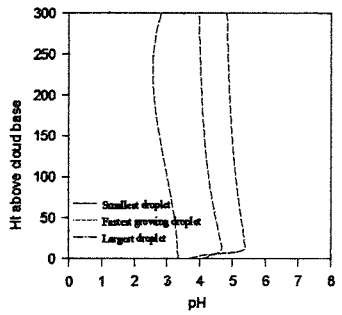

The dry size at which most SO_4^{2-} is produced is around 1 μm. This corresponds to the jet mode peak in the sea-salt aerosol spectrum. It is these particles that provide a large reactive volume, favourable chemical conditions, and a sufficiently high surface to volume ratio. The smallest activated sea-salt particles provide a less favourable environment for SO_4^{2-} production and a lower reactive volume. The largest droplets have such a small surface to volume ratio that mass transport effects limit the rate at which gaseous material can be scavenged from the gas phase. In nss-sulphate based droplets most of the SO_4^{2-} is produced at a dry size corresponding to the accumulation mode peak in the sulphate spectrum. The variation of SO_4^{2-} forming efficiency in nss-sulphate and sea-salt droplets is shown in Figure 3.

Figure 3a - Efficiency of sulphate production

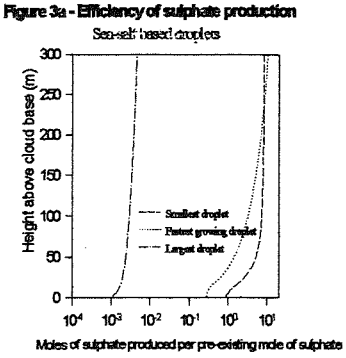

Both O_3 and H_2O_2 are found to be important oxidants. However, the O_3 driven oxidation pathway is favoured in the less acidic sea-salt droplets and becomes increasingly dominant as the SO_2 concentration is increased.

Figure 3b - Efficiency of sulphate production

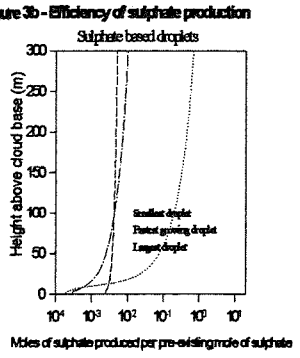

The exchange of the trace gas species, HCl, is closely related to the pH of the sea-salt solution droplet spectra. The fastest growing sea-salt aerosol droplets tended to "suck in" gaseous HCl, increasing their chloride component and tending to hold the pH of the droplets at a value lower than one might expect. Much of the chloride is sourced from the larger, slower growing droplets, which volatilise HCl.

5. HETEROGENEOUS SULPHATE PRODUCTION IN CLOUD FREE AIR

Processing of sea-salt aerosol in the cloud free boundary layer has also been considered. Significant amounts of SO_4^{2-} are produced in the larger sea-salt droplets. However, since these have the shortest lifetimes, sulphur material is quickly removed from the atmosphere.

If sea-salt aerosol is pre-processed in the cloud free boundary layer prior to incorporation in a cloud, the SO_4^{2-} forming ability in the cloud is slightly reduced. However, the total SO_4^{2-} produced by pre-processing below cloud plus cloud processing is similar to that obtained by cloud processing of non pre-processed sea-salt aerosol.

Within an unactivated sea-salt solution droplet, the initial rate of production of SO_4^{2-} is high. In these early stages, the pH of the droplet is maintained at a high value by the carbonate buffer allowing the ozone driven oxidation of aqueous SO_2 to proceed extremely rapidly. Later, when the carbonate buffer has been consumed and the pH falls, the rate of SO_4^{2-} production decreases. However, the volatilisation of HCl and the dissolution of NH_3 may keep the pH of the droplet high enough for the O_3 driven reaction to still be important. The H_2O_2 driven reaction becomes increasingly important as the pH drops.

Nitric acid is often present in the marine boundary layer and tends to migrate to the larger sea-salt particles (Fitzgerald, 1991). Its presence, and that of other acidic species, is likely to reduce the amount of SO_4^{2-} produced in the sea-salt solution droplets. Nitric acid has not been included in these results and so the amount of SO_4^{2-} predicted by the present model out of cloud represents an over estimate. It is planned to refine the results by including nitric acid.

6. CONCLUSION

These results illustrate the importance of including sea-salt in cloud chemistry models and in calculations of sulphur species life cycles. The consumption of sulphur aerosol precursors may reduce the number and rate of growth of smaller nss-sulphate aerosols and ameliorate their potential role in governing global climate.

7. REFERENCES

Chameides W. L. and Stelson A. C., 1992: Aqueous phase chemical processes in deliquescent sea-salt aerosols: A mechanism that couples the atmospheric cycles of sulphur and sea-salt. *J Geophys Res* **97(D18)**, 20565-20580.

Charlson R. J., Lovelock J. E., Andreae M. O. and Warren S. G., 1987: Oceanic phytoplankton, atmospheric sulphur , cloud albedo and climate. *Nature* **326**, 665-661.

Charlson R. J., Langer J., Rodhe H., Leovy C. B. and Warren S. G., 1991: Perturbation of the northern hemisphere radiation balance by back scattering from anthropogenic sulphate aerosols. *Tellus* **43AB**, 152-163.

Fitzgerald J. W., 1991: Marine aerosols : A review. *Atmospheric Environment* **25A**, 533-545.

Hobbs P.V., 1993: Aerosol-cloud interactions in Aerosol-cloud-climate interactions. *Academic Press.*

Lowe J. A., Clegg S. L.,Smith M. H. and O'Dowd C. D., 1996a: Simulations of maritime stratiform cloud physico-chemistry. *This issue.*

Lowe J.A., Smith M. H., Davison B. M., Benson S. E., Hill M. K., O'Dowd C. D., Harrison R. M. & Hewitt C. N., 1996b: Physico-chemical properties of atmospheric aerosol at South Uist. *Atmos. Environ.*, submitted

O'Dowd C. D. and Smith M. H., 1993: Physico-chemical properties of aerosols over the northeast Atlantic: Evidence for wind speed related submicron sea-salt aerosol production. *J Geophys Res* **98(D1)**, 1137-1149.

O'Dowd C. D., Smith M. H., Consterdine I. E. and Lowe J. A., 1996: Marine aerosol, sea-salt and the marine sulphur cycle. *Atmos. Environ.*, in press

Pitzer K. S., 1991: Ion Interaction Approach: Theory And Data Correlation in activity coefficients in electrolyte solutions, *CRC Press.*.

Pruppacher H. R. & Klett J. D., 1978: Microphysics Of Clouds And Precipitation. D. Reidel

Smith M. H., Jones A., Lowe J. A., and O'Dowd C. D., 1996: Role of atmospheric aerosol in the indirect climate cooling mechanism. *This issue.*

Warneck P., 1988: The chemistry of the natural atmosphere. Academic Press, London.

CLOUD CYCLING OF SOLUBLE AND INSOLUBLE SUBSTANCES: FIELD STUDIES ON MOUNTAIN KLEINER FELDBERG, FRG

Martina Krämer[1], Cornelia Eichel[1],
Matthias Schüle[1], Lothar Schütz[1] and Dieter Schell[2]

[1]Institute for Atmospheric Physics, University of Mainz, 55099 Mainz, Germany
[2] Centre of Environmental Research, University of Frankfurt, 60325 Frankfurt, Germany

1. INTRODUCTION

In the atmosphere, cloud formation and dissipation is taking place continuously. During its formation and over its lifetime, a cloud represents a sink for a part of the aerosol particle spectrum as well as for water-soluble trace gases, while during cloud dissipation it is a source for new aerosol particles released to the atmosphere when the cloud droplets evaporates (Pruppacher and Jaenicke, 1995). The newly formed particles differ from those nucleated to cloud drops in the ratio of insoluble to soluble substances, because the cloud drops take up water-soluble trace gases during their lifetime (Frick and Hoppel, 1993). This process, leading to an increase of the soluble material, is called cloud processing. Here, a method is presented to estimate the magnitude of nucleation and gas scavenging in cloudwater and thus the growth factor of a cloud processed particle from the measurement of insoluble and soluble material in cloud water and in aerosol particles. Data of cloudwater concentrations of soluble and insoluble substances, nucleated and scavenged mass and particle growth are shown for three drop size classes from several field studies.

2. FIELD EXPERIMENTS

Three groundbased experiments, where cloudwater from low stratus clouds was sampled, took place at the Mountain Kleiner Feldberg, Germany (30 km westerly of Frankfurt/Main, 825 m asl), in 1990, 1993 and 1995. The field studies, sponsored by the German Resaerch Foundation (through its 'Sonderforschungsbereich 233': Dynamics and Cemistry of Hydrometeors) were carried out to measure, among other parameters, the insoluble and the soluble material in clouds and in aerosol particles.

3. SAMPLING

During 1990 cloud drops $\geq 7\mu m$ radius were sampled using the **R**otating **A**rm **C**ollector (RAC; Krämer and Schütz, 1994). In 1993 and 1995 cloudwater samples were taken in several size classes using the RAC and in addition the **T**wo–stage **F**ogwater Impactor (TFI2; Schell et al.,1994) for drops in the size ranges 2.5–5.0μm and $\geq 5\mu m$ radius. The samples were taken hourly.

Aerosol particles were sampled in five narrow size bands using two–stage cascade impactors (Eichel et al., 1996).

4. ANALYSIS

The pH–value and the electrical conductivity of the cloudwater samples were measured immediately after sampling. Until the analysis of the insoluble particles the samples were stored at about -18°C.

From the measurement of pH and electrical conductivity σ the soluble mass (M_{sol}) in cloudwater can be determined (Krämer et al., 1996)

$$M_{sol} = \frac{\sigma - [H^+]\Lambda_{eq_{H^+}}}{\overline{\Lambda}_m} \qquad (1)$$

where $[H^+]$ and $\Lambda_{eq_{H^+}}$ are the equivalent concentration and conductivity of the H^+–ions. $\overline{\Lambda}_m$ is the mean mass conductivity of all other ions present in atmospheric hydrometeors (see Tab. 1).

The concentration of the insoluble mass in cloudwater (M_{insol}) results from integration over the size spectrum of the insoluble particles in cloudwater, measured with a Coulter Multisizer in the size range 0.3–10.0μm radius.

The mean water-soluble fraction of aerosol particles was analysed with the newly developed system SoFA (water-SOluble Fraction of Aerosol particles; Eichel et al., 1996).

5. CALCULATIONS

The mass entering cloud drops via particle nucleation (M_{nucl}) and gas scavenging (M_{scav}) can be calculated following the notion that nucleation scavenging is the major pathway for insoluble material

σ	$\frac{\mu S}{cm}$	electrical conductivity
$[H^+] = 10^{-pH} \times 10^6$	$\frac{\mu eq}{l}$	concentration of H^+
		concentration of →
M_{insol}	$\frac{mg}{l}$ or %	→ insoluble mass in drops
M_{sol}	$\frac{mg}{l}$ or %	→ soluble mass in drops
$(M_{sol})_{AP}$	$\frac{mg}{l}$ or %	→ sol. mass from nucl.
$(M_{sol})_{gas}$	$\frac{mg}{l}$ or %	→ sol. mass from scav.
M_{liq}	$\frac{mg}{l}$ or %	→ total mass in drops
M_{nucl}	$\frac{mg}{l}$ or %	→ nucleated mass
M_{scav}	$\frac{mg}{l}$ or %	→ scavenged mass
$M_{AP,sol}$	%	→ insoluble mass in APs[1]
$M_{AP,insol}$	%	→ insoluble mass in APs
$M_{AP} = 1$	%	→ total mass of APs
gf	-	growth factor AP
		equiv. conductivity of →
$\Lambda_{eq_{H^+}} = 0.35$	$\frac{\mu S\ cm^{-1}}{\mu eq\ l^{-1}}$	→ H^+
$\overline{\Lambda}_m = 1.88$ (clouds[2])	$\frac{\mu S\ cm^{-1}}{mg\ l^{-1}}$	mean mass conductivity
$\overline{\Lambda}_m = 1.91$ (rain[3])	$\frac{\mu S\ cm^{-1}}{mg\ l^{-1}}$	mean mass conductivity

Table 1: List of symbols. [1]aerosol particles, [2]for clouds at Mountain Kleiner Feldberg, calculated from Wobrock et al.(1994), [3]for rainwater at Mainz, FRG, from Krämer et al.(1994).

to the liquid phase. Therefore, as long as no gas scavenging occurs, the ratio of soluble to insoluble material inside a drop remains constant. Scavenging of atmospheric trace gases such as NH_3, SO_2 and HNO_3 and subsequent chemical reactions increase the soluble material and therefore the ratio M_{sol}/M_{insol}.

Thus, if the ratio of soluble to insoluble material in aerosol particles ($M_{AP,sol}/M_{AP,insol}$) and in the liquid phase is known, M_{nucl} and M_{scav} can be calculated –without any measurement of concentrations of trace gases– from the equations

$$M_{AP} = M_{AP,sol} + M_{AP,insol} = 1 \quad (2)$$

$$M_{liq} = M_{sol} + M_{insol} = M_{scav} + M_{nucl} = 1 \quad (3)$$

$$M_{nucl} = (M_{sol})_{AP} + M_{insol} \quad (4)$$

$$M_{scav} = (M_{sol})_{gas} \quad (5)$$

and

$$\frac{M_{AP,sol}}{M_{AP,insol}} = \frac{(M_{sol})_{AP}}{M_{insol}} \quad (6)$$

Eq. 6 describes the simple fact that the ratio of soluble to insoluble material of the original aerosol particles is equal to the ratio of soluble to insoluble material –originating from nucleation– in the resulting drop.

Following Eqs. 3, 4 and 6 leads to

$$M_{nucl} = \left(\frac{M_{AP,sol}}{M_{AP,insol}} + 1\right) \cdot M_{insol} \quad (7)$$

$$M_{scav} = 1 - M_{nucl} \quad (8)$$

If the drop evaporates, the growth factor (gf) of the processed particle can be calculated as

$$\text{gf} = \frac{M_{liq}}{M_{nucl}} = \left(\frac{1}{M_{nucl}}\right)^{\frac{1}{3}} \quad (9)$$

In a strict sense, these equations are only valid for the cloud cycle of a single particle. However, application on bulk cloudwater samples on the basis of the mean ratio of soluble to insoluble material in the aerosol particles provides information on the magnitude of nucleation and gas scavenging in cloudwater and the growth factor of a cloud processed particle.

6. RESULTS

In the course of the field experiment in 1993, aerosol particles are found to have an average composition of about 62% soluble and 38% insoluble mass in the size range 0.4–5.0μm (Eichel et al., 1995). In 1990, aerosol particles were not analysed and the data from the experiment in 1995 are not yet available.

The results of all field experiments are shown in Fig. 1 as absolute mean values for the different years and in Tab. 2 as relative mean values for the different size classes.

	M_{sol} | M_{insol} %	M_{nucl} | M_{scav} %	gf
KLEINER FELDBERG CLOUDWATER			
$r_d : 2.5 - -5.0\mu m$			
1993	83 | 17	45 | 55	1.3
1995	98 | 2	? 6 | 94 ?	2.7 ?
$r_d \geq 5\mu m$			
1993	90 | 10	26 | 74	1.6
1995	95 | 5	? 14 | 86 ?	2.0 ?
$r_d \geq 7\mu m$			
1990	88 | 12	? 32 | 68 ?	1.5 ?
1993	85 | 15	41 | 59	1.4
1995	92 | 8	? 20 | 80 ?	2.3 ?
RAINWATER MAINZ			
92/93	96 | 4	? 11 | 89 ?	-

Table 2: Mean values (in %) of the ratio of • soluble (M_{sol}) to insoluble (M_{insol}), • nucleated (M_{nucl}) to scavenged (M_{scav}) mass and the resulting • growth factor (gf) of cloud processed aerosol particles. (r_d: drop radius; ?: values are calculated on the basis of particle analysis for 1993).

Comparison of 1993 and 1995 (1990 can be compared with 1993 and 1995 only for the drops > 7μm)

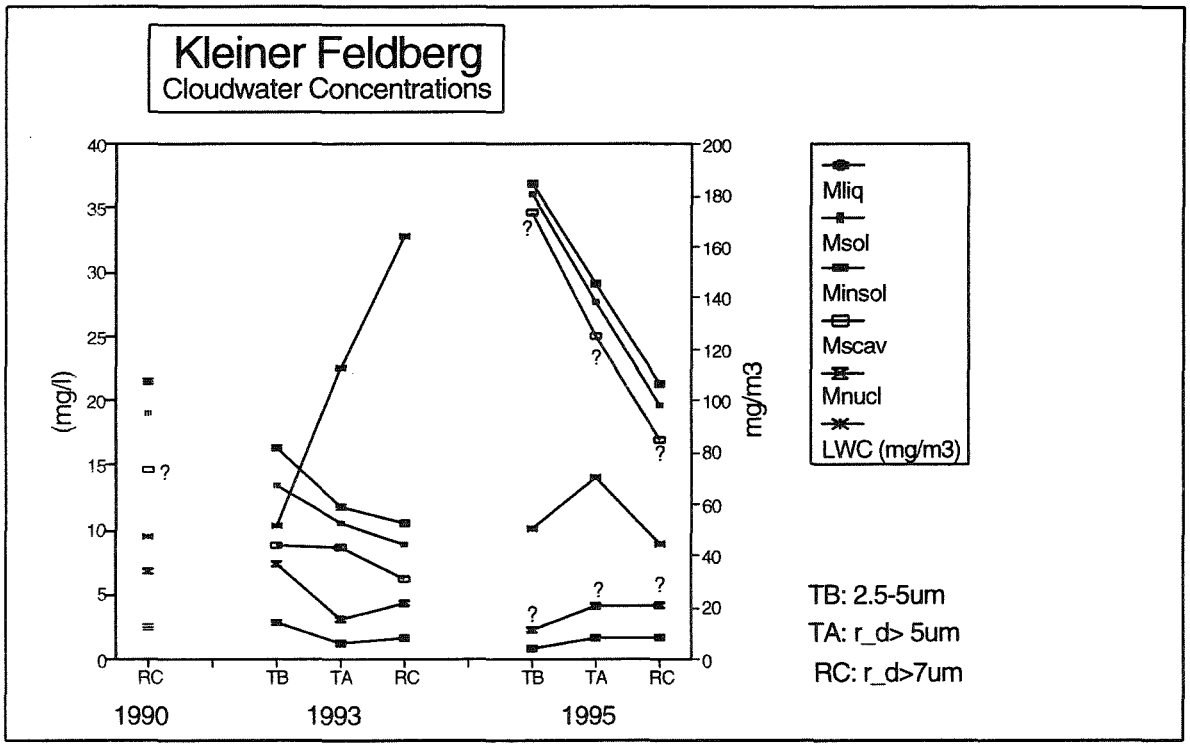

Figure 1: Mean values of the concentrations (in mg/l) of • total mass (M_{liq}), • soluble mass (M_{sol}), • insoluble mass (M_{insol}), • scavenged mass (M_{scav}), • nucleated mass (M_{nucl}) and the Liqiud Water Content (LWC, in mg/m^3) (?: values are calculated on the basis of particle analysis for 1993).

reveals that the insoluble mass concentration in cloudwater (Fig. 1) does not vary to a great extent, neither in the different size classes nor with time. It ranges between 1–3 mg/l. The soluble mass behaves different: it decreases with increasing drop size for 1993 and 1995, but the concentrations are much higher –and show a stronger gradient between the different size classes– in 1995 (36–20 mg/l) than in 1993 (14–9 mg/l).

The question arises, which mechanisms are responsible for this behaviour (especially if the composition of the aerosol particles is not yet known) and if it is possible to obtain a –preliminary– answer only based on the presently available parameters?

The liquid water distribution (the LWC for the different size classes is determined from the water mass sampled with the corresponding cloudwater collectors) of the clouds is very different in 1993 in comparison to 1995 and 1990 in the sense that in 1993 the main water mass is found in the range of the largest drops, which is unusual at the Mountain Kleiner Feldberg. But it seems unlikely that the LWC is the cause of the low concentrations of soluble material in 1993, because for the smallest drops it is similar for the two years and nevertheless the soluble mass differs by a factor of three.

Enhanced aerosol particle concentration increases the number of CCN and leads to a drop spectrum with more, but smaller drops (Charlson et al., 1992). In a bulk sample of droplets the concentration of both soluble and insoluble material is therefore expected to increase with enhanced particle number. From the fact that the insoluble mass is in the same range for all three years we conclude that nucleation scavenging is not the reason for the differences between 1993 and 1995. Indeed, the total concentration of aerosol particles is similar for both years (Uhlig, 1996).

An enhanced soluble fraction of particles also leads to more available CCN and therefore also to a drop spectrum shifted to smaller sizes with a larger number of drops (Eichel et al., 1996). The effect on the concentration of soluble and insoluble substances is more complicated: On the one hand a smaller insoluble fraction of particles would lead to a lower concentration of insoluble material, but on the other hand the changed drop spectrum would tend to increase the concentration of insoluble substances. These two mechanisms may balance the concentration of insoluble material whereas the solute concentration would strengthen twice. This could have an influence on the observed concentrations in 1995. However, we do not believe that the soluble concentrations can be trebled only by changing the water-soluble fraction of the aerosol particles. Enhanced scavenging of trace gases seems much more likely to

be the reason for the strongly increased concentration of the soluble substances in 1995. Therefore, M_{nucl} and M_{scav} are calculated on the basis of the ratio $M_{AP,sol}/M_{AP,insol} = 62/38$ found in 1993. The values of M_{nucl} and M_{scav} calculated on the basis of this ratio for 1990 and 1995 are marked with a ? in Fig. 1 and Tab. 2.

For the mass entering cloud drops by nucleation scavenging no pronounced size dependance is seen (see Fig. 1); it ranges from 2–7 mg/l for all experiments and in all size classes. This is caused by the fact that no size dependance of the water-soluble fraction of aerosol particles was found.

The mass originating from gas scavenging decreases with increasing drop size and ranges on average between 9–6 mg/l (75–55%, see Tab. 2) in 1993 and 35–15 mg/l (95–68%) in 1990 and 1995. This means that trace gas scavenging plays a minor role in 1993 than in 1990 and 1995, possibly caused by lower gas phase concentrations.

The growth factor of aerosol particles passing a cloud cycle shows no dependance on drop size and ranges between 1.3–1.6 (see Tab. 2) in 1993 and 1990. Due to the enhanced gas scavenging it raises to values between 2.0–2.7 in 1995.

Finally, the concentrations found in cloudwater are compared to those found in rainwater sampled at Mainz, FRG (see Tab. 2), with a wet–only sampler during one year (August 1992–July 1993) on a daily basis. The rainwater underwent the same analysis procedure as the cloudwater. Though the absolute concentrations are much lower (M_{sol}= 7.7 mg/l, M_{insol} = 0.3 mg/l), the ratios of M_{sol}/M_{insol} and M_{nucl}/M_{scav} are comparable to those in cloudwater from 1995. In Krämer et al. (1995) we speculated that the high value for gas scavenging in rainwater is caused by the –in comparison to cloudwater– additional uptake of trace gases below the clouds. This hypothesis is not supported by the new data.

Summarising, it can be stated that for the low stratus clouds discussed here, decreasing concentrations of soluble and insoluble material are found with increasing drop size. This size dependance is caused by scavenging of trace gases, whereas concentrations due to nucleation scavenging and the growth factor of cloud processed particles are not dependant on drop size.

7. REFERENCES

Charlson R.J.; Schwartz, S.E.; Hales, J.M.; Cess, R.D.; Coakley, J.A.; Jr.; Hansen, J.E. and D.J. Hofmann (1992): Climate forcing by anthropogenic aerosols. *Science, 255,* 423-430.

Eichel, C.; Krämer, M.; Schütz, L. and S. Wurzler (1996): The Water-Soluble Fraction of Atmospheric Aerosol Particles and its Influence on Cloud Microphysics. *Submitted to J. Geophys. Res.*

Frick, G.M. and W.A.Hoppel (1993): Airship measurements of aerosol size distributions, cloud droplet spectra, and trace gas concentrations in the marine boundary layer. *Bull. Am. Met. Soc. 74,* 2195-2202.

Krämer, M. and L. Schütz (1994): On the collection efficiency of a Rotating Arm Collector and its applicability to cloud– and fogwater sampling. *J. Aerosol Sci. 25,* 137-148.

Krämer, M.; Brinkmann, J.; Eichel, C.; Jaenicke, R.; Schell, D.; Schüle, M. and L. Schütz (1995): Field studies on the cloud processing of atmospheric aerosol particles and trace gases. *J. Aerosol Sci. 26,* S893-S894.

Krämer, M.; Schüle, M. and Lothar Schütz (1996): A Method to Determine Rainwater Solutes from pH and Conductivity Measurements. *in press, Atmos. Envir.*

Pruppacher, H.R. and R. Jaenicke (1995): The Processing of Water Vapor and Aerosols by Atmospheric Clouds, a Global Estimate. *Atmos. Res. 38,* 283-295.

Schell, D.; Maser, R.; Preiss, M.; Wobrock, W.; Acker, K.; Wieprecht, W.; Pahl, S.; Georgii, H.-W. and W. Jaeschke (1994): The Dependence of Cloud Water Chemical Concentrations on Drop Size and Height above Cloud Base at Great Dun Fell: Instrumentation and First Results. In: P.M. Borrell et al. (eds.): *The Proceedings of EUROTRAC Symposium '94,* SPB Academic Publishing bv, The Hague, 1133-1137.

Uhlig, E.-M. (1996): Personal communication.

Wobrock, W. et al. (1994): The Kleiner Feldberg Cloud Experiment 1990. An overview. *J. Atmos. Chem. 19,* 3-35.

SENSITIVITY OF CLOUD MICROPHYSICS ON THE SOLUBILITY OF ATMOSPHERIC AEROSOL PARTICLES: NUMERICAL CASE STUDIES USING NEW EXPERIMENTAL DATA

Sabine Wurzler, Cornelia Eichel, Lothar Schütz and Martina Krämer

Institut für Physik der Atmosphäre, Johannes Gutenberg-Universität Mainz, Germany

1. INTRODUCTION

Atmospheric aerosol particles (AP) are the building blocks of clouds. Already Twomey (SCEP 1970) pointed out that increasing AP-number concentration results in an increased number concentration of cloud droplets. This leads to an enhanced multiple scattering of light within clouds and to an increase in cloud albedo, thereby exerting a radiative influence upon climate. According to Schwartz et al. (1996) a 10% relative increase in cloud droplet number concentration yields an increase in absolute cloud top albedo by nearly 1%. In addition, an increased number concentration of cloud droplets causes –provided that the amount of water vapour available remains unchanged– a decrease in drop size, which may inhibit precipitation development. This in turn would increase cloud liquid water content and cloud lifetime, thus contributing further to the cloud albedo (Schwartz et al. 1996).

Ahr et al. (1989) showed that nucleation scavenging, cloud interstitial aerosol and drop size population also depend sensitively upon the water-soluble fraction of the particles. So there is evidence that not only the number of particles, but also the amount of soluble material in particles has an influence upon climate.

Nevertheless, experimental studies are rare. Therefore the particle number size distributions as well as the composition of the particles and the related scavenging processes via nucleation have often been parameterised or simplified in model studies. Bott (1991), for example, used the water-soluble fractions determined by Winkler (1974), even though Winkler investigated only a *mean* water-soluble fraction of particles in three size classes. However, recent investigations (e.g. Svenningsson et al. 1992 and 1994; Eichel et al. 1996) revealed that not all particles within one size class have the same amount of water-soluble material.

To point out the sensitivity of nucleation scavenging, cloud microphysics and thus, radiative forcing, on the water-soluble fractions of APs, two cloud situations were modeled, differing only by the water-soluble fractions of the initial APs (Wurzler 1995). Cloud I includes APs with water-soluble fractions after Winkler (1974), for cloud II new experimental data (Svenningsson et al. 1994; Eichel et al. 1996) for the water-soluble fractions of the initial APs are used. An air parcel model including detailed microphysics was employed for this purpose.

2. THE WATER-SOLUBLE FRACTIONS OF ATMOSPHERIC AEROSOL PARTICLES – EXPERIMENTAL DATA

Winkler (1974) investigated the mean water-soluble fraction of APs in three size-classes ($0.1\mu m < r_p < 0.3\mu m$; $0.3\mu m < r_p < 1.0\mu m$ and $r_p > 1.0\mu m$, r_p: particle radius). In Deuselbach, Germany, he observed an average of 61% water-soluble material for particles larger than $0.3\mu m$ and 67% for those larger than $0.1\mu m$. The water-soluble fraction varied between 80% in the smallest and 48% in the largest size class.

Recently, the water-soluble fractions of small APs ($25nm \leq r_p \leq 150nm$) have been determined using a TDMA ('Tandem-Differential-Mobility-Analyser'; Svenningsson et al. 1994), those of large APs ($0.4\mu m \leq r_p \leq 2.3\mu m$) were investigated with the newly developed method SoFA (Soluble Fraction of Large and Giant Atmospheric Aerosol Particles; Eichel et al. 1996). The results of both studies are summarised in Fig. 1: Svenningsson et al. (1994) found two types of small continental APs, having a water-soluble fraction of 5% (type I) and 50% (type II). However, the results of Eichel et al. (1996) show three types of larger particles with water-soluble fractions of 9% (type I), 50% (type II) and 88% (type III). The new type III-particles are assumed to arise during the dissipation of cloud droplets ('cloud processed particles'). This hypothesis is supported by the investigation of water-soluble material in cloud water at the same location and time period, resulting in an identical average value (88%, Krämer et al. 1995). Therefore, it is consequent that type III

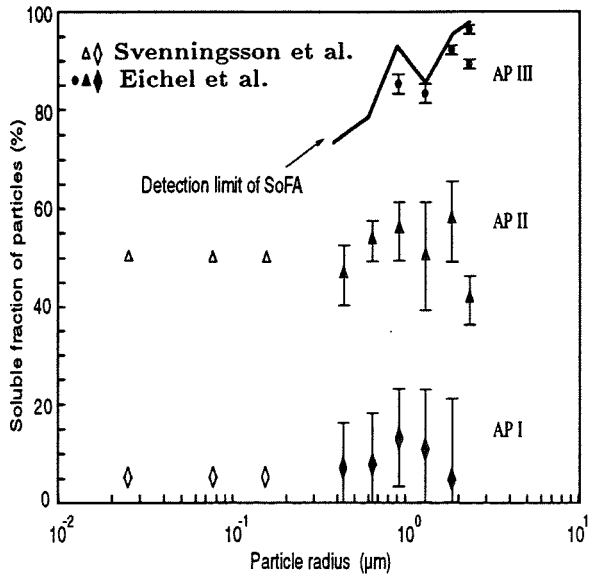

Figure 1: Water-soluble volume fractions of atmospheric aerosol particles. The measurements were both carried out on Mount Kleiner Feldberg, Taunus, Germany, those of Svenningsson et al. (1994) in November 1991 employing a TDMA, those of Eichel et al. (1996) in November 1993 with the help of SoFA.

was not found by Svenningsson et al. (1994), because if small particles become activated to cloud drops, they will grow to larger sizes beyond the upper detection limit of the TDMA during cloud formation. In agreement with Svenningsson et al. (1994), type I and II were roughly of the same frequency. Type III–particles were the most frequent and comprised about 50% of the particles of one size class. Because of the detection limits of both methods the threshold for the appearance of type III-particles could not be detected.

3. THE PARCEL MODEL

The dynamic framework employed in the present study is the entraining air parcel model with detailed microphysics as discussed by Flossmann et al. (1985 and 1991). Activation of APs to drops, condensation and evaporation of drops and deactivation of drops to APs are simulated together with the collision, coalescence and break up of drops as well as impaction scavenging of particles by drops. Precipitation is not regarded. The model treats 69 droplet and 81 AP size categories. The radius of the APs ranges between $10^{-3}\mu m$ and $10\mu m$, that of the drops between $1\mu m$ and $2600\mu m$. The time step for the simulations is 2s. The general initial conditions for the parcel's environment are as follows: The initial updraft radius of the air parcel is assumed to be $350m$, the initial impulse for the simulation is given by an updraft velocity of $1ms^{-1}$. The simulation starts at a height of $1km$, where the relative humidity is assumed to be 99%. The vertical temperature and humidity profiles have been observed during the field experiment CLEOPATRA (Meischner et al. 1993; Wurzler et al. 1994) and represent the environmental air which enters the air parcel via entrainment. The AP size spectra are fitted by superimposing three log-normal distributions according to Jaenicke (1988). The number density of the particles is assumed to decrease exponentially with height as given by Wurzler (1995) and Eichel et al. (1996).

The water-soluble material of the aerosol particles is assumed to consist of 50% NH_4NO_3 and 50% $(NH_4)_2SO_4$. The different water-soluble fractions of the particles employed for the two cloud situations are given in Tab. 1: Cloud I is roughly based on observations of Winkler (1974). The water-soluble fraction of the particles decreases with increasing particle size. All particles of the first and second mode of the three log-normal particle spectra are assumed to consist of 50% water-soluble material, while all particles of the third mode have a water-soluble fraction of 10%. Cloud II, by contrast, is based on the new results of Eichel et al. (1996) and Svenningsson et al. (1994) (see section 2). For particles $< 0.15\mu m$ radius in each mode of the spectrum half of the APs consists of 9% and the remainder of 50% water-soluble material. For particles $\geq 0.15\mu m$ radius a third particle type arises. In all three modes 45% of the total particle number are assumed to be of this highly soluble particle type, whereas 25% of the particles have a water-soluble fraction of 50% and the remaining 30% consist of 9% water-soluble material. As threshold size for the appearance of type III a radius of $0.15\mu m$ is chosen, because Hallberg et al. (1994) found at the same site that particles larger than $0.1\mu m$ are efficiently incorporated in cloud drops. Note that on average the soluble fraction of particles in Cloud I is smaller than in Cloud II.

4. MODEL RESULTS

To demonstrate the importance of the fractions of water-soluble material in atmospheric APs with regard to cloud microphysics, two different cloud situations with the same general initial conditions, the same AP-number density and vertical distribution and chemical composition of the water-soluble material, but different water-soluble fractions of the particles were simulated (see section 3).

Concerning cloud interstitial aerosol, the model results reveal that the development of mass as well as number size distribution is similar for both clouds.

However, cloud drop number and related water mass behave quite different (see Fig. 2): Eventhough the same liquid water content is present in both

Cloud I	
Mode	$n : \epsilon$ (%:%)
1–2	100:*50*
3	100:*10*
Cloud II	
Mode	$n : \epsilon$ (%:%)
1–3 ($r_p < 0.15\mu m$)	50:*9* ; 50:*50*
1–3 ($r_p \geq 0.15\mu m$)	30:*9* ; 25:*50* ; 45:*88*

Table 1: Parameters of the two parcel model simulations of cloud formation: relative number n of aerosol particles having water-soluble fractions ϵ in the rural size distribution after Jaenicke (1988).

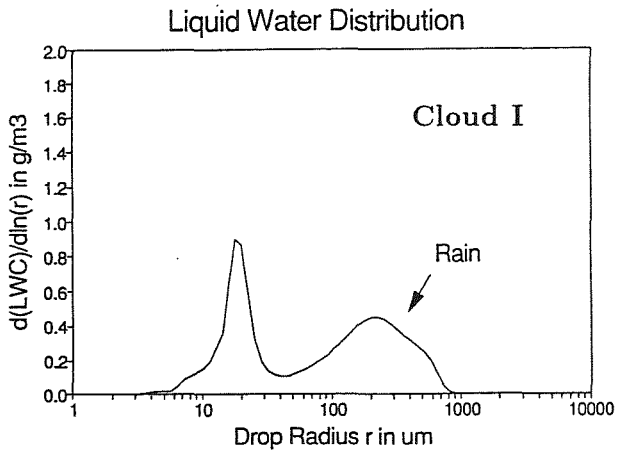

Figure 2: Mass density distributions of the droplets of Cloud I and Cloud II after 1000sec of modelling time (Wurzler 1995 and Eichel et al. 1996).

cases, the distribution of the water content among the drop sizes is quite different. In Cloud I there are two maxima for the liquid water mass, one of them in the range of precipitation-sized drops. In Cloud II there is no real second maximum for drops larger than $50\mu m$. This is caused by the fact that in Cloud II the water-soluble fraction of the initial aerosol particles is higher, leading to a larger number of cloud condensation nuclei. Therefore in Cloud II almost twice as many droplets than in Cloud I are in competition with each other for the same amount of water vapour available. Consequently, the average drop sizes of Cloud II are smaller than those of Cloud I, which hinders the collision and coalescence process in Cloud II. Thus, in Cloud II only 20% of the water mass, which can be found in the precipitational drop size range of Cloud I, have reached the large drop size categories via collision and coalescence. Therefore, Cloud I will presumably rain, whereas Cloud II will produce no rain.

Summarising it can be deduced that clouds of the same liquid water content and the same AP-number density distribution show different drop size populations depending only on the water-soluble fraction of the initial APs. Inspection of the model results reveals that, for the meteorological scenario assumed here, the concentration of drops raises and the mean drop sizes and therefore the probability of rain decreases with an increasing number of large and highly soluble particles. As the droplet concentration and size is influencing the radiative properties of clouds and thus, has an impact on climate (Schwartz et al. 1995), we conclude in agreement with Kulmala et al. (1995) that the soluble fraction is a particle characteristic affecting the indirect aerosol forcing of climate.

ACKNOWLEDGEMENTS

Fundings for this experiment were provided by the German Research Foundation through its 'Sonderforschungsbereich 233': Chemistry and Dynamics of Hydrometeors.

REFERENCES

Ahr, M., A.I. Flossmann and H.R. Pruppacher, 1989: On the effect of the chemical composition of atmospheric aerosol particles on nucleation scavenging and the formation of a cloud interstitial aerosol. *J. Atmos. Chem.*, **9**, 465-478.

Bott, A., 1991: On the influence of the physicochemical properties of aerosols on the life cycle of radiation fogs. *Bound. Layer Met.*, **56**, 1-31.

Eichel, C., M. Krämer, L. Schütz and S. Wur-

zler, 1996: The Water-Soluble Fraction of Atmospheric Aerosol Particles and its Influence on Cloud Microphysics. subm. to *J. Geophys. Res.*

Flossmann, A.I., W.D. Hall and H.R. Pruppacher, 1985: A theoretical study of the wet removal of atmospheric pollutants. Part I: The redistribution of aerosol particles captured through nucleation and impaction scavenging by growing cloud drops. *J. Atmos. Sci.,* **42**, 583-606.

Flossmann, A.I., 1991: The scavenging of two different types of marine aerosol particles calculated using a two–dimensional detailed cloud model. *Tellus,* **43B**, 301-321.

Hallberg, A., K.J. Noone, J.A. Ogren, I.B. Svenningsson, A. Flossmann, A. Wiedensohler, H.C. Hansson, J. Heintzenberg, T. Andersson, B. Arends and R. Maser, 1994: Phase Partitioning of Aerosol Particles in Clouds at Kleiner Feldberg. *J. Atmos. Chem.,* **19**, 107-128.

Jaenicke, R., 1988: Aerosol physics and chemistry. In: Landolt–Boernstein: *Zahlenwerte und Funktionen aus Naturwissenschaften und Technik,* **V 4b**, G.Fischer, Editor, Springer, 391-457.

Krämer, M., J. Brinkmann, C. Eichel, R. Jaenicke, D. Schell, M. Schüle and L. Schütz, 1995: Field studies on the cloud processing of atmospheric aerosol particles and trace gases. *J. Aerosol Sci.,* **26**, 5893-5894.

Kulmala, M., A. Laaksonen, P. Korhonen, T. Vesala A. Ahonen, 1993: The effect of atmospheric nitric acid vapor on cloud condensation nucleous activation. *J. Geophys. Res.,* **98**, 949-958.

Meischner, P.F., M. Hagen, T. Hauf, D. Heimann, H. Höller, U. Schuhmann, W. Jaeschke, W. Mauser and H.R. Pruppacher, 1993: The field project CLEOPATRA, May-July 1992 in Southern Germany. *Bull. Am. Met. Soc.,* 401-412.

SCEP (Study of Critical Environmental Problems, 1970). *Man's Impact on the Global Environment.* MIT Press, Cambridge, MA, 319pp.

Schwartz, S.E., F. Arnold, J.P. Blanchet, P.A. Durkee, D.J. Hofmann, W.A. Hoppel, M.D. King, A.A. Lacis, T. Nakajima, J.A. Ogren, O.B. Toon and M. Wendisch, 1995: Group report: Connections between aerosol properties and forcing of climate. In: R.J. Charlson and J. Heintzenberg (eds.): *Aerosol Forcing of Climate,* J. Wiley & Sons, 251-280.

Schwartz, S.E. and A. Slingo, 1996: Enhanced Shortwave Cloud Radiative Forcing due to Anthropogenic Aerosols.*NATO ASI Series, Vol. I 35, Clouds, Chemistry and Climate.* Springer-Verlag Berlin Heidelberg.

Svenningsson, I.B., H.C. Hansson, A. Wiedensohler, J.A Ogren, K.J. Noone and A. Hallberg, 1992: Hygroscopic growth of aerosol particles in the Po Valley. *Tellus,* **44B**, 556-569.

Svenningsson, I.B., H.C. Hansson, A. Wiedensohler, K.J. Noone, J. Ogren, A. Hallberg and R. Colvile, 1994: Hygroscopic growth of aerosol particles and its influence on nucleation scavenging in cloud: Experimental results from Kleiner Feldberg. *J. Atmos. Chem.,* **19**, 129-152.

Winkler, P., 1974: Die relative Zusammensetzung des atmosphärischen Aerosols in Stoffgruppen (The relative composition of the atmospheric aerosol). *Meteorol. Rdsch.* **27**, 129-136.

Wurzler, S., P. Respondek, A.I. Flossmann and H.R. Pruppacher, 1994: Simulation of the dynamics, microstructure and aerosol particle scavenging of a precipitating and a non–precipitating cloud by means of a detailed 2–D cloud model. *Beitr. Phys. Atmos.* **67**, 313-319.

Wurzler, S., 1995: The scavenging and wet deposition of nitrogen compounds by a warm convective cloud using two cloud dynamic models. PhD-Thesis, Shaker Verlag Aachen, Berichte aus der Physik, 160 pp.

COMING INTO THE QUESTION OF AEROSOLS CHEMICAL-AND-PHYSICAL PROPERTIES INFLUENCE UPON DISASTROUS HAIL FORMING

M.R. Vatiashvily,

I.R. Preis

Scientific and Production Geophysical Center, Stavropol, Russia

H.M. Kalov

High - Mountain Geophysical Institute, Nalchik, Russia

During the last decades a new researching trend appeared in meteorology - chemistry of atmosphere which is connected with the study of aerosols chemical - and- physical properties influence upon climate.

The obtained qualitative and quantitative evaluations made it possible to reveal the following; the value of ions sums electric conductance, PH and SO_4^{--}/Na^+ ratio get increased while moving from the coastal areas inside the continent, and Cl^-/Na^+ ratio of ions concentration values gets decreased; the probability of hail fall- out grows over sea area from summer to winter and from the sea coast to the continent during a year.

The sea and continental clouds microstructure differences are caused not by vertical currents speeds, turbulence and duration of their existance only, but also by the difference of the aerosols physical - and - chemical properties included in them. The contribution of chlorides with a definite spectrum of particles dimensions into the formation of liquid - drops precipitation is the greatest one at the coastal regions, and it considerably drops down on the continents due to their decrease. However, at some optiumum concentrations of them hail - stones of various dimensions may form.

The purpose of this work is to study the influence of aerosols chemical - and - physical properties (hydroscopicity) uron the forming of catastrophical hail - stones.

To evaluate the substance hydroscopicity use was made of air temperature and relative humidity with respect to real solutions.

The equation has the next form

$$U = U_e \, (R_e / R)^n, \qquad (1)$$

where R_e and U correspondently the salts solubility and the air

relative humidity at the eutectic temperature t_e the lowest temperature of the solution on the freezing curve.

The equation (1) holds true for the temperature range from the eutectic temperature to 60°C of saturated solution.

The calculations results n and U, as well as table values t_e for various hygroscopic substances are presented in Table 1.

For example, for K_2SO_4 salt having t_e = - 1,6°C drops formation in the atmosphere may take plase at U = 96 %, and for MgCl salt (t_e = = -33,5°C) - at U > 33 %. With these results in view we may conclude: the lower is the eutectic temperature of salts aqueous solutions, the higher is the degree of their hygroscopicity; aerosols hygroscopicity, depending on their eutectic temperature, can favour the formation of cloud elements of various states of aggregation.

At the present time known are two mechanisms of hail stones growth:

Table 1

SOLUBLE SALTS HYGROSCOPICITY DISTRIBUTION DEPENDING ON THE VALUES OF EUTECTIC TEMPERATURE

SALT	K_2SO_4	KNO_3	KCl	$(NH_4)_2SO_4$	NaCl	$Mg(NO_3)_2$	$MgCl_2$
t_e°C	-1,6	-2,9	-10,6	-18,5	-21,2	-31,9	-33,5
n	0,030	0,093	0,201	0,247	0,406	0,296	1,054
Ut (20°C)	96	93	85	80	75	52	33

around crystallization centres (small hail grown on icy dendrites) and freezing of large (of millimeters dimensions) drops.

Hail formation around crystallization nuclei evidenly may ake plase on soluble aerosols of local origin (for example KNO_3) having comparatively low hygroscopicity and high eutectic temperature as compared with the ambient air temperature t_e = -2,9°C, i.e. $t_e > t$.

Hail formation around the frozen drops can be observed in highly hygroscopic, having low eutectic temperature sea aerosols (chlorides): KCl, NaCl, LiCl, MgCl.

The drops will not get frozen if the values of the corresponding eutectic temperatures of solutions prove to be lower than the temperature of the ambient air ($t_e < t$). In this case due to coalescence (mergence) the drops undergo intensive growth and, depending on

their dimensions and the speed of the ascending currents, reach various altitudes. The solutions drops reach their maximum altitudes above the level of the ascending currents maximum speeds, i.e. at the altitude of 6-9 km, where the air temperature is below -20 -35°C. At these levels the probability of the drops freezing is rather high because $t \ll t_e$ of the corresponding solutions. The hail stones formed around the frozen drops start moving down under the action of the gravitation force, and at the result of gravity coagulation they grow during a short period of time up to catastrophical dimensions (2 - 4 cm and more).This is proved by the fact that catastrophic hail is noted in 70 - 80 % of cases when first echo signal reflected from a cloud is registered within the subzero range of temperatures.

Taking into consideration the physical-and-chemical properties of sea aerosols we've carried out numerical experiments with hail-stones coagulation growth on the frozen drops.

A coagulation equation is as follows:

$$R_f = R_i + [EqV \quad H : 4 (\bar{V} + \bar{W})], \quad (2)$$

where $\Delta H = H_i - H_f$ -the thickness of the cloud overcooled part (km); the values of the corresponding H_i- the height of the given salt he ascending solution eutectic temperature value location, H_f - the isothermic line (0 °C) altitude; R_i and R_o- hail stones radii at H_i and H_f (cm) accordingly; E - a hail stone capture coefficient (E = 1,0); q - water content of a cloud (gm^{-3}); ρ - hail density ($g \cdot cm^{-3}$); $\bar{V}$ - average speed of a hail stone falling down ($m \cdot s^{-1}$); $\bar{W}$ - average speed of air currents ($m \cdot s^{-1}$).

The calculations were done for chloride of various hygroscopicity at water contents within the values range of $q = 2 - 15\ g \cdot m^{-3}$ and at the thicknesses of the cloud overcooled part: $\Delta H = 2$ km for KCl with $t_e = -10.6$°C; $\Delta H = 4$ km for NaCl with $t_e = -21.2$°C; $\Delta H = 5.5$ km for $MgCl_2$ with $t_e = -33.5$°C. The thickness of the layer ΔH, the speed of hail falling down in the overcooled part of a cloud were taken with due regard for the salts eutectic temperature: 2 km - for KCl, 4 km - for NaCl and 5.5 km - for $MgCl_2$.

The calculations results of a hail stone final diameter (D_f) dependence on the initial dimensions of the salts solution frozen drops (D_i), their eutectic temperature (t_e) and the water content of a cloud are represented in Table 2. From this table it follows that as the water content and the initial dimensions of the frozen drops increase and as the chlorides eutectic temperature gets down, the calculated dimensions of hail stones get increased. The greater values of these quantities, the greater is the probability of hail stones formation of dangerous dimensions. Large hail stones (> 2 cm) leading to catastrophical hail - damage may be formed when $t < t_e = -10,6$ °C, $q > 15\ g \cdot m^{-3}$ and $D_i > 0,6$ cm if a nucleus drop

Table 2

DEPENDENCE OF HAIL STONES FINAL DIAMETER D_f (AT THE LEVEL OF ZERO ISOTHERMIC LINE) ON THE CLOUD WATER CONTENT, INITIAL DIAMETER OF THE FROZEN DROP D_i, AND ON EUTECTIC TEMPERATURE OF THE SALTS DISOLVED IN A DROP

Salt	D_i [cm]	q [g m^{-3}]					
		2,0	3,5	5,0	7,0	10,0	15,0
KCl	t_e = - 10,6°C,			ΔH = 2 km,		ρ_h = 0,7	g·cm^{-3}
	0,4	0,60	0,74	0,89	1,0	1,38	1,87
	0,6	0,80	0,94	1,09	1,20	1,58	2,07
	0,8	1,00	1,14	1,29	1,40	1,78	2,27
NaCl	t_e = - 21,2°C,			ΔH = 4 km,		ρ_h = 0,7	g·cm^{-3}
	0,4	0,78	1,08	1,38	1,76	2,34	3,31
	0,6	0,98	1,28	1,58	1,96	2,54	3,51
	0,8	1,18	1,48	1,78	2,16	2,74	3,71
MgCl	t_e = - 33,5°C,			ΔH = 5,5 km,		ρ_h = 0,7	g·cm^{-3}
	0,4	0,94	1,34	1,74	2,28	3,08	4,42
	0,6	1,14	1,54	1,94	2,48	3,28	4,62
	0,8	1,34	1,74	2,14	2,68	3,48	4,82

comprises KCl solution; when $t < t_e$ = 21,2°C, $q > 7$ g·m^{-3} and $D_i > 0,8$ cm or when $q > 10$ g·m^{-3} and $D_i > 0,4$ cm if a nucleus drop comprises NaCl solution: when $t < t_e$ = 33,5°C, $q > 5$ g·m^{-3} and $D_i > 0,8$ cm or when $q > 7$ g·m^{-3} and $D_i > 0,4$ cm if a nucleus drop comprises $MgCl_2$ solution.

AEROZOL EXCHANGE IN THE SYSTEM A CLOUD - AMBIENT AIR

N.A. Berezinsky
Scientific and Production Geophysical Center, Stavropol,Russia

G.V. Stepanov
High-Mountain Geophysical Institute, Nalchik, Russia

An aerosol struckture researches of a cloud and its environment have been carried out from a plane. Particles were traped with a cascade impactor . A deposit carrying base at the first stage was a filter with local suction of the air from under the aerosol stream falling down on it. Water was sucked through the filter and aerosol deposit remained on the surface. After determination of particles dimensions and concentrations the aerosol samples were placed into a thermo-diffusion chamber . The worked-out method made it possible to study their condensational and ice-forming properties and nucleation mechanism on separate particles.

Averaged data on particles concentration in the base Cu med and under it are represented in Tabl 1. Already judging by them one can note the transformation of particles spectrum in the cloud.

Table 1

PARTICLES CONCENRATIONS RELATIONSHIP IN THE BASE Cu med AND UNDER IT, cm^{-3}

H, m	d, mcm					Sum
	0,05-0,5	0,5-1,0	1,0-10	10-30	> 30	
800	1228	14,5	14,7	0,08	-	1257,3
1000	922	26,7	16,1	0,3	0,05	965,2
Difference	306	-12,2	-1,4	-0,05	-0,05	292,1

The curves of aerosol particles distribution in St and Cu various altitudess are represented in Fig.1, from which one can see that with the altitude growth the particles concentration in a cloud decreases, and the curves inclination increases mainly due to the loss of small particles-meteorological nuclei of condensation and Aitken nuclei.

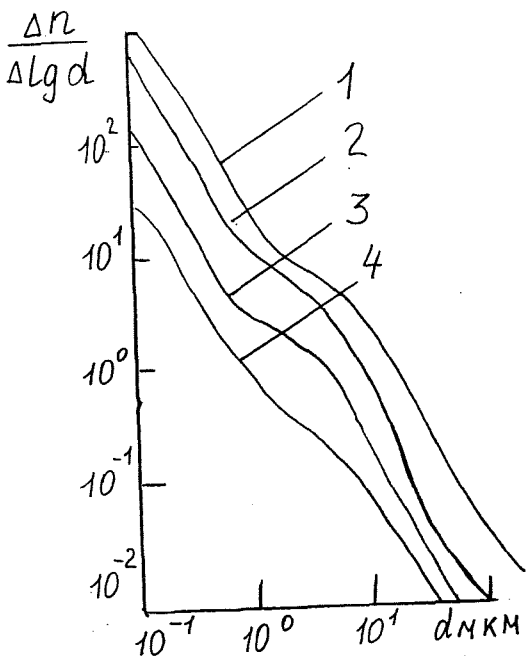

Fig.1. The curves of aerosol particles distribution in dimension in a heap cloud:
1 - under the low boundary (H=800); 2,3,4 - in a cloud at the heigts of 1000, 2100 and 3000 m accordingly

Supergigantic particles are found only in aerosol remainders of drops of 200-800 m diameter. Most of all the particles spectrum is deformed in the subinversional cloudiness due to the process duration and small vertical extent.

As it seen from Table 2 the aerosols concentration, especially those of supergigantic ones, are considerably higher under the convective clouds, than aside from them at the same level.

When the cloud thickness is getting increased the particles concentration in its ascending current grows, the second distribution maximum disappears, the curves inclination grows approaching the youngue distribution for the adjoining the ground surface atmosphere.

Table 2

Concentration of aerosol particles under Cu and outside the cloud at the same level, cm^{-3}

Sampling spot	d, mcm				Sum
	<1,0	1,0-10	10-30	>30	
1000m under the cloud	2025	0.865	0.15	0.002	2026
1000m outside the cloud	1991	0,325	0,01		1991

The transforming influence is particularly noticeable under the conditions when the leading stream speed is higher that of the front spreading. A great number of large and gigantic particles having changed physical-and-chemical properties are ejected from the Cu cong peaks into the upper and middle troposphere and carried over at great distances.

A vertical temporarry sectional

view of a cold anafront is shown in Fig.2.

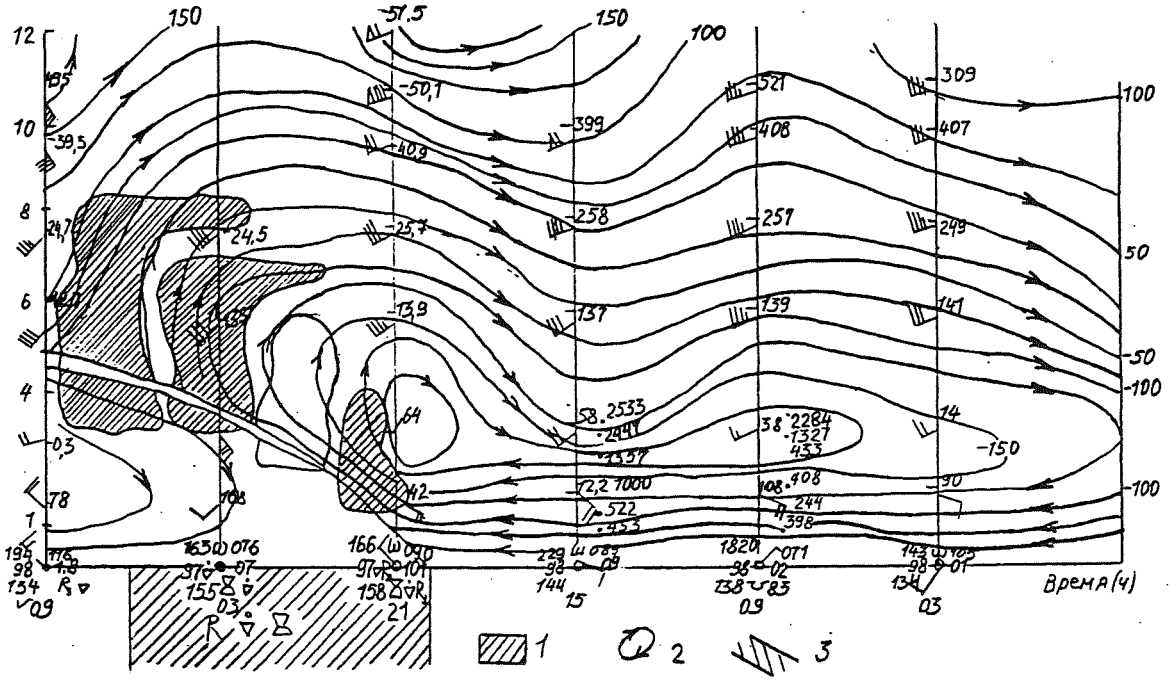

Fig.2. A vertical section view of a cold front: 1 - cloudiness zone; 2 - current line; 3 - front zone, the on-line figures - the current function value.

and represented here are the lines of current function, temperature, wind distribution in height, of the actual weather conditions within the sounding term, the cloud system on the frontal boundary line, and vertikal distribution of aerosols concentrations.

From the figure one can see that in the lower troposphere the current lines are directed towards the front. At the frontal boundary line vertikal ordered air motion is formed. At the level of the leading current and above the leading current lines are directed from the front. At the height of the change of motion direction sites with closed current lines are noted. The measurement of aerosols concentrations reveals (Fig.3) that just in the centre

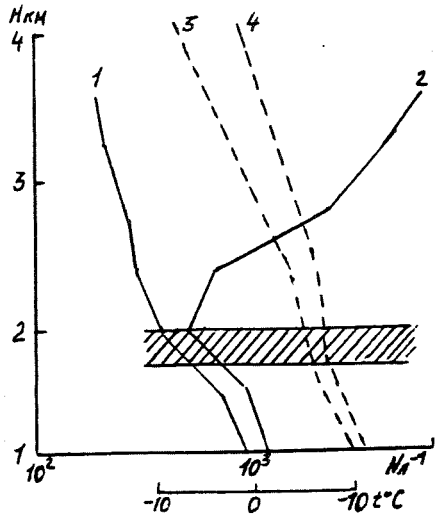

Fig.3. Vertical profile of natural aerosol concentration on 21 June (1) and 22 June (2) 1985 and temperature stratification at 03.00 a.m. on 21 June (3) and at 03.00 a.m. on 22 June 1985 (4)

of these sites the aerosols abnormal distribution over the layers of inversions and isothermies is observed.

At the interaction of aerosol with the cloud environment rtansformation of the microstructure and particles physical-and-chemical properties takes place. The aerosol particles which passed through an ice-formation stage get preactivated and initiate recrystallization at already higher temperature and at greater speed. The aerosol residual of the evaporated drops and crystals is of a compound composition. This makes them highly active in the subsequent condensation and ice accretion processes. At the repeated involvement of such particles into a cloud all the microphysical processes of the cloud development and precipitation formation are internsified.

PARAMETERIZATION OF IN-CLOUD SULPHATE PRODUCTION

Qingyuan Song, Henry Leighton

Department of Atmospheric and Oceanic Sciences
McGill University
Montreal, H3A 2K6, Canada

1. Introduction

Clouds not only play an important role in transforming and redistributing chemical species, but they also modify the size distribution of atmospheric aerosol particles through heterogeneous chemical reactions. The latter effect may significantly enhance the number of CCN available for subsequent cloud formation (Charlson et al, 1992) and may also significantly increase aerosol light-scattering efficiency (Lelieveld and Heintzenberg, 1992), both processes having implications for global climate change. However, it is computationally impractical to include an explicit aqueous oxidation scheme in general circulation models or regional models to obtain even a total column amount of in-cloud sulphate production. A parameterization of the process is essential.

2. Approach

Much effort has gone into parameterizing aqueous-phase oxidation of SO_2. Langner and Rodhe (1991) based their estimate of S(IV) oxidation on the magnitude of some characteristic time scales: the average time it takes between successive cloud encounters for an air parcel; the average time the air parcel stays inside a cloud once a cloud is reached; and the average chemical life time due to transformation inside the cloud. However, in such a parameterization, the ambient chemical concentrations are not accounted for explicitly but instead are included implicitly in the chemical transformation time scale.

We have developed a parameterization that describes oxidation of S(IV) by hydrogen peroxide and ozone in convective clouds. Based on the equilibrium and reaction rate equations describing dissolution, dissociation and oxidation processes (e.g. Leighton et al, 1990), the parameterization scheme is an explicit function of the concentrations of ambient chemical species such as sulphur dioxide, sulphate aerosol, hydrogen peroxide, ozone, ammonia and nitric acid.

The parameterization is formulated in terms of static gross cloud parameters such as average cloud water content, cloud base height, cloud thickness, average cloud lifetime and cloud total water content, which may, in principle, be extracted from GCMs or regional models. During the cloud lifetime, the ambient chemical concentrations are assumed to remain constant. Thus, given ambient chemical profiles and these cloud parameters, the parameterization may be applied in large scale models to obtain the in-cloud sulphate production.

In the parameterization scheme, there are two correction factors which depend on cloud pH value and cloud lifetime. The former accounts approximately for the rapid increase in oxidation rate by ozone with increasing pH. The second correction factor accounts for the reduction in the rate of injection of gases and aerosol into the cloud during its decaying phase.

3. Model description

The parameterization has been formulated and tested by comparisons with a well-established 3-D cloud chemistry model (Tremblay and Leighton, 1986). Many cloud chemistry simulations have been performed with the chemistry model (e.g. Tremblay, 1987; Leighton et al, 1996), and the results have been found to agree with observational data reasonably well.

The chemistry model has been modified to include the ice phase. The cloud dynamics and microphysics fields are provided by a 3-D cloud dynamics model that includes ice in the form of crystals or snow, and graupel or hail (Kong, 1992). Chemicals reactions in ice are not considered. Chemicals are transported between the different ice forms and are scavenged by snow and graupel.

Table 1. Ambient chemical concentrations at the surface (10^{-8} mol/m^3)

Case	1	2	3	4	5	6	7	8	9	10	11	12
SO_2	1.75	1.75	1.75	1.75	1.75	1.75	1.75	1.75	1.75	1.75	1.0	1.75
HNO_3	4.5	4.5	3.5	4.5	4.5	3.5	4.5	4.5	4.5	4.5	4.5	4.5
NH_3	4.5	4.5	4.5	4.5	4.5	4.5	4.5	4.5	4.5	4.5	4.5	4.5
H_2O_2	9.	9.	9.	18.	18.	9.	18.	9.	9.	9.	18.	18.
$SO_4^=$	3.1	3.1	3.1	3.1	3.1	3.1	3.1	3.1	3.1	3.1	3.1	3.1
O_3	10.	5.	5.	10.	5.	5.	5.	5.	5.	5.	5.	10.
Relative acidity	0	0	0	0	0	1	1	0	1	1	0	0
Profile	U	U	U	U	U	U	U	L	L	L	L	L

U and L refer to uniform and linearly decreasing vertical chemical profiles respectively.

In the freezing and riming processes, strong soluble solutes such as HNO_3, NH_3, H_2O_2, SO_4 are considered to totally remain in the ice phase. SO_2 (Iribarne and Pyshnov, 1990) and H_2O_2 (Snidder et al, 1992) are partially released into the air.

4. Results and discussion

Aqueous phase sulphate production from the 3-D model and from the parameterization are compared. A series of cases with different chemical and dynamical conditions (Tables 1 and 2) have been used to test the parameterization. The cloud parameters in Table 2, which are required for the calculations with the parameterization, are extracted from results of the 3-D cloud model. For each pair of simulations, the chemical profiles are the same and are assumed to be either uniform or to decrease linearly with height from surface to 10km. In Table 1, cases 1-9 are the chemical profiles for the warm cloud, and cases 10-12 are for the cold cloud chemistry simulations.

The comparisons of the sulphate production by H_2O_2 and O_3 are investigated separately. Results from the warm cloud case (Figs. 1 and 2) and cold cloud case (Figs. 3 and 4) are also shown separately.

The agreement between the parameterization and the 3-D model for production by H_2O_2 is very good (Figs. 1 and 3), being within 30% for all cases.

Table 2. Cloud parameters

parameters	warm cloud	cold cloud
average cloud water content (g/m^3)	0.29	0.26
cloud life time (mins)	23	42
average temperature (K)	273	265
total water content (10^6×kg)	0.89	78.
cloud base height (m)	2,500	4,300
cloud depth (m)	4,000	13,000

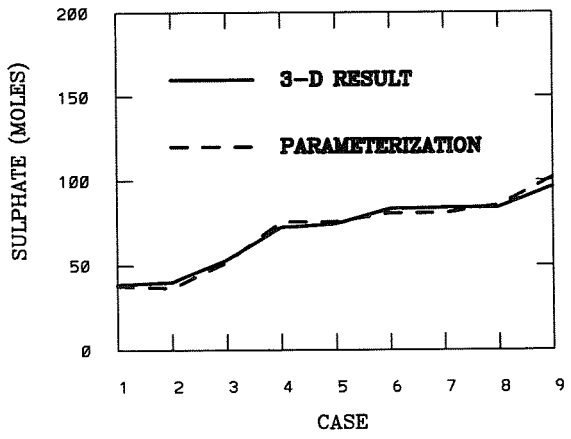

Fig. 1. Sulphate production by H_2O_2 in warm cloud

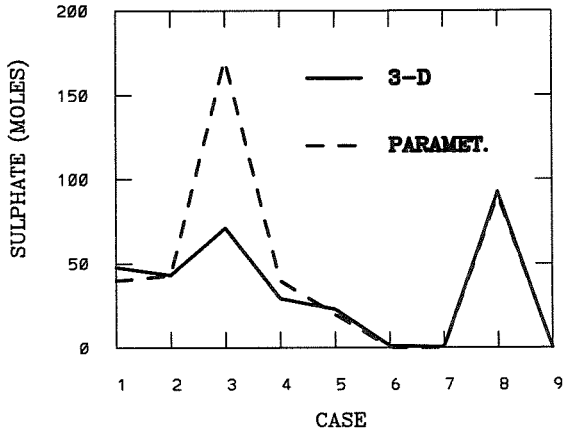

Fig. 2. Sulphate production by O_3 in warm cloud

The agreement for sulphate production by O_3 (Fig. 2 and Fig 4) is not as good as by H_2O_2 but is still acceptable. Except for one case, the differences are also less than 30%.

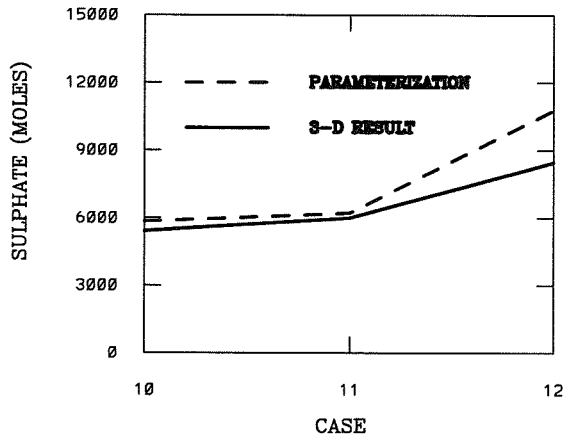

Fig. 3. Sulphate production by H_2O_2 in cold cloud

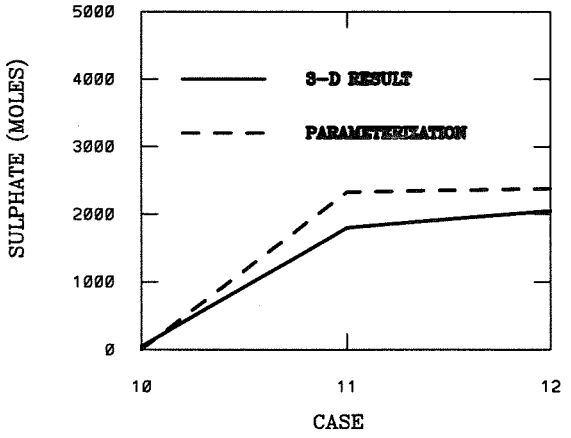

Fig. 4. Sulphate production by O_3 in cold cloud

As an indication of a potential application of the parameterization, we compare the sulphate production by the parameterization with results from the cloud module of the Acid Deposition and Oxidant Model (ADOM) and the 3-D cloud model (Glazer and Leighton, 1994) for identical initial conditions. In this comparison, the 3-D chemistry model is driven by the dynamical cloud model of Yau (1980). Two cloud cases (the Cloud A and Cloud B of Glazer and Leighton, 1994) with 12 different chemical conditions were simulated. As shown in Fig. 5 and Fig. 6, the cloud module of ADOM tends to overestimate the amount of sulphate production compared to the results of the 3-D cloud chemistry model. However, the agreement between the parameterization and the cloud chemistry model is very good indeed.

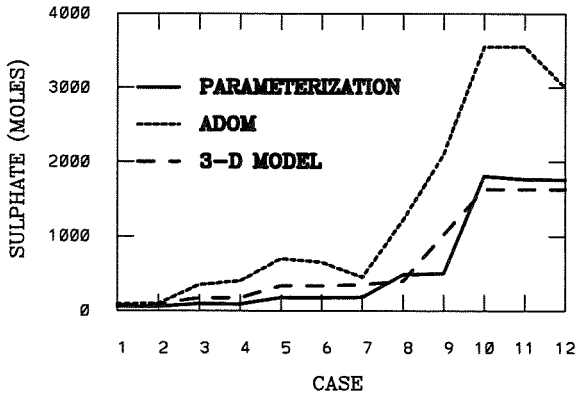

Fig. 5. Comparison between sulphate production from the 3-D cloud chemistry model, the parameterization, and the ADOM cloud module, for Cloud A. The numbers 1-12 identify 12 cases with different chemical profiles.

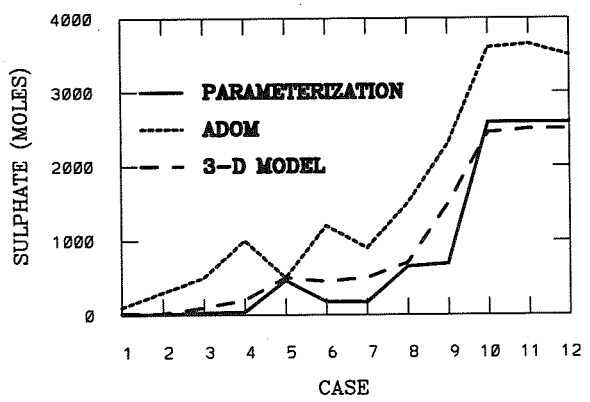

Fig. 6. As Fig. 5 but for Cloud B.

5. Conclusion

Results have shown a satisfactory agreement between the parameterization scheme and the 3-D model. The parameterization holds considerable promise for use in large- scale cloud chemistry models.

6. Acknowledgement

The authors acknowledge Dr. Fanyou Kong for his help in running his cloud dynamics model. Financial support from the Canada/McGill International Fellowship and the Atmospheric Environment Service are also gratefully acknowledged.

7. Reference

Charlson, R.J., S.E. Schwartz, J.M. Hales, R.D. Cess, J.A. Coakley, J.E.Hansen and D.J. Hofmann, 1992: Climate forcing by anthropogenic aerosols. *Science*, 255, 422-430

Glazer, A. and H.G. Leighton, 1994: An Evaluation of the ADOM cloud module. *Atmos. Ocean.* 32 (4) 1994, 645-661.

Iribarne, J. V. and T. Pyshnov, 1990: The effect of freezing on the composition of supercooled droplets--I. retention of S(IV). *Atmos. Environ.* 24A, 389-398

Kong, F. Y, M. Y. Huang, H. Y. Xu, 1992: Three-dimensional numerical simulations of the effects of ice phase processes on evolution of convective storms. *Sci. of China.* 35, 834-846

Langer, J., H. Rodhe, 1991: A global three-dimensional model of the tropospheric sulfur cycle. *J. of Atmos. Chem.* 13, 255-263

Leighton, H. G., M. K. Yau, A. M. Macdonald, J. S. Pitre and A. Giles, 1990: A numerical simulation of the chemistry of a rainband, *Atmos Environ.* 24A, No. 5, pp. 1211-1217

Leighton, H.G., L. Lauzon, W. R. Leaitch, 1996: Evaluation of a three-dimentional cloud chemistry model. *Atmos. Environ* (in press).

Lelieveld, J., J. Heintzenberg, 1992: Sulfate cooling effect on climate through in-cloud oxidation of anthropogenic SO_2. *Science*, 258, 117-120

Snider, J.R., D.C. Montague and G.Vali, 1992: Hydrogen peroxide retention in rime ice. *J. Geophys. Res.* 97, 7569-7578

Tremblay, A. and H. Leighton, 1986: A three-dimensional cloud chemistry model. *J. Clim. Appl. Meteorol.*, 25, 652-671

Tremblay, A. 1987: Cumulus cloud transport, scavenging and chemistry: Observation and simulations. *Atmos. Environ.* 21: 2345-2364.

Yau, M. K. 1980: The effects of evaporation, water load and wind shear on cloud development in a three-dimensional numerical model. *J. Atmos. Sci.* 37,

PARAMETERIZATION OF THE DROPLET EFFECTIVE RADIUS OF WARM CLOUDS

Constantin A. Pontikis and Elizabeth M. Hicks

Météo-France/Université des Antilles et de la Guyane, U.F.R. Sciences
97159, Pointe à Pitre Cedex, Guadeloupe, France (F.W.I.)

1. Introduction

The evaluation of the warm cloud contribution to the earth's radiation budget is a necessary step in the GCM calculations in order to predict climatic changes. This evaluation requires the knowledge of the warm cloud optical characteristics (i.e. optical thickness and single-scatter albedo) that can be expressed as a function of the cloud droplet effective radius R_e. For a given cloudy air parcel, Pontikis and Hicks (1992) have derived a theoretic expression showing that R_e depends upon both the droplet concentration and the liquid water content. Since microphysical cloud characteristics are not predicted in GCM's, the droplet effective radius is represented by using parameterizations depending upon either the model predicted liquid water path (Stephens, 1978b) or liquid water content (Fouquart, 1989). These parameterizations are independent of the cloud character (maritime or continental). Further, in some cases, constant effective radius values are used (Ingram, 1990). The above mentioned parameterizations have been obtained on the basis of intuitive arguments combined to a limited number of observational results. The absence of a clear theoretical basis in the derivation of these R_e parameterizations does not allow the argumented choice of one of them. Further, according to the parameterization used, different R_e values are obtained for a given liquid water path, thus most probably affecting the predictive skill of GCM's since the latter are very sensitive to the R_e values. Slingo (1990) has estimated that a relatively small decrease of this parameter could offset the greenhouse effect resulting from the doubling of the CO_2 concentration in the atmosphere. The goal of this paper is to infer pertinent cloud droplet effective radius parameterizations for both stratiform and convective warm clouds based upon a clear theoretical procedure and to validate them by using appropriate observational data.

2. Effective radius parameterization for layer clouds

Since layer clouds may be considered as adiabatic except in a very thin layer close to cloud top (Bower and Choularton, 1992; Martin et al., 1994; Garett and Hobbs, 1995), the mean adiabatic cloud droplet effective radius $\overline{R}_{ea}$ may be used to infer a parameterized expression valid for layer clouds. The $\overline{R}_{ea}$ expression determined by Pontikis (1995) may be written as :

$$\overline{R}_{ea}=\frac{3K(d)}{4}\left(\frac{9A}{8\pi^2\rho_l^2\overline{\rho}_A N_a^2}\right)^{1/6}L_a^{1/6} \qquad (1)$$

where K(d) is a function of the droplet spectral dispersion d, A the coefficient that relates linearly the liquid water content Q_l (expressed in terms of mixing ratio) to the height h above cloud base (Q_l=Ah), ρ_l the liquid water density, $\overline{\rho}_A$ the mean air density, N_a the droplet concentration, L_a the liquid water path and the index "a" denotes the adiabatic cloud character. Since the parameters N_a, K(d) and A involved in equation (1) are not predicted by GCM' s, climatological values of these parameters have been used in order to infer a pertinent parameterization of the droplet effective radius of warm layer clouds as a function of L_a exclusively. In maritime and continental clouds, N_a varies respectively between $50mg^{-1}$ and $200mg^{-1}$, and $400mg^{-1}$ and $800mg^{-1}$. Thus, pertinent climatological values of the adiabatic droplet concentration in such clouds could be $N_{amar}=100mg^{-1}$ and $N_{acont}=600mg^{-1}$. Further, the K(d) value may vary between 1.05 and 1.09 for maritime clouds (Pontikis and Hicks, 1993), thus K(d)=1.07 seems a reasonable value for such clouds. For continental clouds, K(d)=1.14 has been used (Martin et al., 1994). The coefficient A depends exclusively upon the cloud base characteristics (Pontikis, 1993) and can be represented by the following expression (Pontikis, 1996) :

$$A=\frac{g\,Q_{vs}(0)}{c_pT(0)}\,\frac{\frac{L'}{R_wT(0)}-\frac{1}{\kappa}}{1+\frac{Q_{vs}(0)L'^2}{c_pR_wT(0)^2}} \qquad (2)$$

where g is the gravity acceleration, c_p the specific heat for air, κ = 0.286, L' the latent heat of condensation, R_w the specific gaz constant for water vapor, and Qvs(0) and T(0) are respectively the mixing ratio and temperature at cloud base. A climatological value of A

may be determined with the assumption that the climatological cloud base characteristics (i.e. pressure, temperature and mixing ratio) can be obtained by raising a clear air parcel with standard atmosphere characteristics from ground level up to the corresponding condensation level. In this work, three different ground air parcels corresponding respectively to the mid-latitude winter and summer standard atmospheres and to the tropical standard atmosphere have been taken into consideration. These parcels have the following characteristics : p=1018mb, t=-1°C, Q=2.7gkg^{-1} (mid-latitude winter), p=1013.5mb, t=21.1°C, Q=12gkg^{-1}(mid-latitude summer), p=1013mb, t=27.2°C, Q=16gkg^{-1} (tropical). They lead respectively to the following condensation level characteristics : p_c=969.9mb, t_c=-4.8°C, Q_c=2.7gkg^{-1}(mid-latitude winter), p_c=952.9mb, t_c=15.9°C, Q_c=12gkg^{-1}(mid-latitude summer), p_c=935.0mb, t_c=20.1°C,Q_c=16gkg^{-1}(tropical). By introducing the above characteristics into expression (2) one obtains respectively for A :

$A_{mlwinter}=1.09\times10^{-6}m^{-1}$

$A_{mlsummer}=2.0\times10^{-6}m^{-1}$

$A_{tropic}=2.27\times10^{-6}m^{-1}$.

Note that the A value for tropical latitudes is in excellent agreement with the value of $A=2.3\times10^{-6}m^{-1}$ used by Austin et al. (1995) to fit FIRE observed liquid water contents in marine stratocumulus clouds. The climatological A value may be obtained by calculating a weighted mean A value : $A=0.25A_{mlsummer}+0.25A_{mlwinter}+0.50A_{tropic}=1.91\times10^{-6}m^{-1}$. By introducing in equation (1) the above climatological values, one obtains the following parameterized R_e expressions respectively representative of maritime and continental warm layer clouds :

$$R_{epmar}=4.16L_a^{1/6} \quad (3)$$

$$R_{epcont}=2.41L_a^{1/6} \quad (4)$$

where L_a=L, the model predicted liquid water path. For coastal clouds that develop in air masses that are neither clearly continental nor clearly maritime, adiabatic droplet concentrations may vary between 100mg^{-1} and 300mg^{-1}. An appropriate parameterization for such clouds may be obtained by using a "standard" concentration N_a=200mg^{-1} :

$$R_{epcoast}=3.25L_a^{1/6} \quad (5),$$

where L_a is in g m^{-2} and R_{ep} in μm. Expression (3) has been compared to the experimental effective radii of maritime layer clouds reported by different authors. This comparison is presented in Fig. 1. The equation of the power regression line that fits the experimental (L, R_e) points, $R_e=4.1786L^{0.16656}$, is in excellent agreement with equation (1). This constitutes a confirmation of the pertinent character of the above parameterizations. Note that for GCM's using constant effective radius values, two pertinent R_e values may be obtained by integrating the above parameterizations (3) and (4) with the assumption that for a given layer cloud field all H values between 0m and 500m are equally probable. This leads to : R_{epmar}=9.1μm and R_{epcont}=6.1μm.

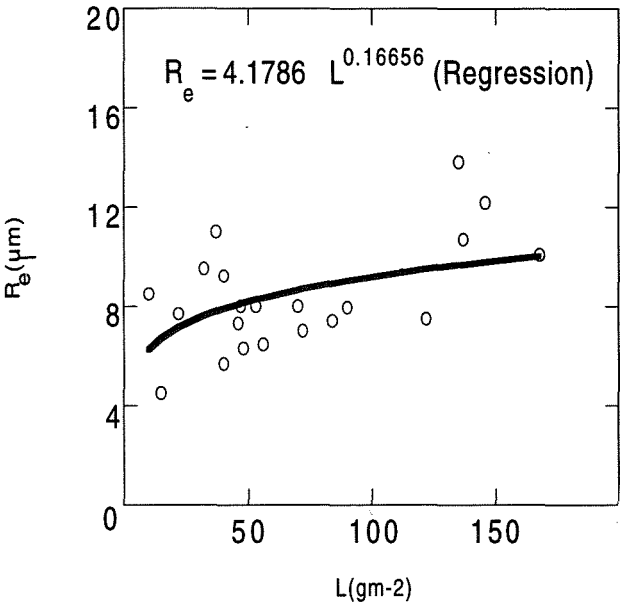

Figure 1 : Comparison between calculated (full line) and experimentally determined R_e values (o) presented as a function of L. The experimental points correspond to values reported by Albrecht et al. (1988), Austin et al. (1995), Garrett and Hobbs (1995), Hermann and Curry (1984), Noonkester (1985), Slingo et al. (1982), Spinhirn et al. (1989), Stephens and Platt (1987).

3. Effective radius parameterization for convective clouds

Convective clouds are submitted to the effects of clear air entrainment and mixing. The effects of these processes on the liquid water content, the droplet concentration and the droplet effective radius have been extensively discussed by Pontikis and Hicks [1993]. Pontikis [1995] suggests that a reasonable R_e parameterization for convective clouds that takes into account the clear air entrainment and mixing effects could be :

$$R_{ep}=\frac{1}{2}\left[1+\left(\frac{L}{L_a}\right)^{1/3}\right]\overline{R}_{ea} \quad (6)$$

with $L/La \sim (\overline{F}-\overline{F}_s)/(1-\overline{F}_s)$, where $\overline{F}$ is the mean cloud dilution fraction (Jensen et al., 1985). Note that F=1 for an adiabatic cloudy air parcel and F=Fs for a just saturated diluted parcel in which all droplets have evaporated to maintain saturation. Simple numerical

tests made with an entraining cloud parcel model (constant entrainment rate) associated to experimentally determined $\overline{F}_s$values reveal that the mean dilution fraction $\overline{F}$ is roughly equal to the arithmetic mean $(1+\overline{F}_s)/2$. This implies an L/L_a ratio roughly equal to 1/2. By introducing this value and expression (1) into (6) and by using the climatological values for A, N_a and K(d), one obtains three parameterized expressions for warm convective clouds :

$$R_{epmar}=4.19L^{1/6} \quad (7)$$

$$R_{epcont}=2.43L^{1/6} \quad (8)$$

$$R_{epcoast}=3.27L^{1/6} \quad (9),$$

where L is the model predicted liquid water path. These expressions are almost identical to the parameterized expressions (3), (4) and (5) obtained for layer clouds. The validity of this expressions has been tested by using ten clouds sampled on 10, 11 and 19 July 1985 during the Joint Hawaii Warm Rain Project (1985). These coastal clouds had mean droplet concentrations ranging between 100 and 300 mg^{-1}. Thus, R_{ep} has been calculated by using expression (9). Further, the mean cloud droplet effective radii, R_{em}, have been calculated by using observed spectral distributions. The agreement between the R_{ep} and R_{em} values is good, thus attesting for the pertinent character of the above parameterizations.

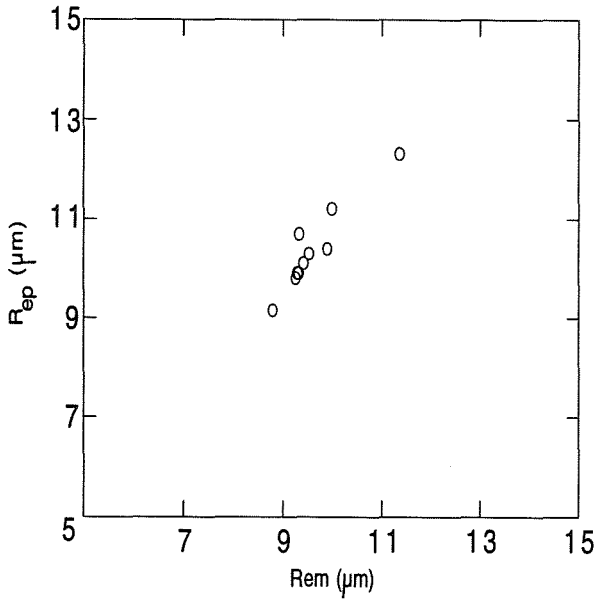

Figure 2 : Comparison between the Rep and Rem values for clouds observed offshore the east coast of Hawaii.

4. Discussion and conclusion

Two parameterized expressions of $\overline{R_e}$ depending exclusively upon the liquid water path, valid respectively for warm maritime and continental clouds, have been derived. It appears that these expressions are independent of the cloud type (stratiform or convective). The "standard" droplet concentrations used to obtain these expressions correspond to typical maritime clouds and continental clouds. However, intermediate droplet concentrations ($100mg^{-1}$-$400mg^{-1}$) may be observed in layer clouds developing close to coastal regions as well as in clouds developing in originally continental air masses submitted to oceanic influences. Further, in very polluted continental air masses, droplet concentrations as high as $1000mg^{-1}$ may be observed. It is clear that the "standard" N values used in this work have been chosen in order to represent general conditions and should be reconsidered in the case of studies implying specific conditions. Since the experimental R_e values used to validate the parameterized R_e expressions correspond to maritime and coastal observations, further investigations are necessary in order to confirm the validity of the proposed parameterizations for continental warm clouds.

Refferences

Albrecht, B. A., D.A. Randall and S. Nicholls, 1988 : Observations of marine stratocumulus clouds during FIRE. Bull. Amer. Meteor. Soc., 69, 618-626.

Austin, P., Y. Wang, R. Pincus and V. Kujala, 1995 : Precipitation in stratocumulus clouds : Observational and modeling results. J. Atmos. Sci., 52, 2329-2352.

Bower, K. N., and T. W. Choularton, 1992 : A parameterization of the effective radius of ice-free clouds for use in global climate models. Atmos. Res., 27, 305-339.

Fouquart, Y., J. C. Buriez and H. Herman, 1989 : The influence of boundary layer clouds on radiation : A review. Atmos. Res., 23, 203-228.

Garrett, T. J., and P. V. Hobbs, 1995 : Long-Range transport of continental aerosols over the Atlantic ocean and their effects on cloud structures. J. Atmos. Sci., 52, 2977-2984.

Hermann, G. F., and J. A. Curry, 1984 : Observational and theoretical studies of solar radiation in arctic stratus clouds. J. Climate Appl. Meteor., 23, 5-24.

Ingram, W.J., 1990: Unified model documentation paper no. 23 : Radiation. U. K. Meteorological Office internal note.

Jensen, J., P.H. Austin, M.B. Baker and A.M. Blyth, 1985 : Turbulent mixing, spectral evolution and dynamics in awarm cumulus cloud. J. Atmos. Sci., 42, 173-192, 1985.

Martin, G. M., D. W. Johnson and A. Spice, 1994 : The measurement and the parameterization of effective radius of droplets in warm stratocumulus clouds. J. Atmos. Sci., 51, 1823-1842.

Noonkester, V. R., 1985 : Profiles of optical extinction coefficients calculated from droplet spectra observed in marine stratus cloud layers. J. Atmos. Sci., 42, 1161-1171.
Pontikis, C., and E. Hicks, 1992 : Contribution to the cloud droplet effective radius parameterization. Geoph. Res. Letters, 19, 2227-2230.
Pontikis, A. C., and E. M. Hicks, 1993 : The influence of clear air entrainment on the droplet effective radius of warm maritime clouds. J. Atmos. Sci., 50, 2889-2900.
Pontikis, C., 1993 : Parameterization of the cloud optical thickness : influence of clear air entrainment. Geoph. Res. Letters, 20, 2655-2658.
Pontikis, C., 1995 : Contribution to the droplet effective radius parameterization of warm convective clouds : Clear air entrainment effects. Geoph. Res. Letters, 22, 795-798.
Pontikis, C., 1996 : Parameterization of the droplet effective radius of warm layer clouds. Submitted to the Geoph. Res. Letters.
Slingo, A., S. Nichols and J. Smetz, 1982 : Aircraft observations of marine stratocumulus during JASIN. Quart. J. Roy. Meteor. Soc., 108, 833-856.
Slingo, A., 1990 : Sensitivity of the earth's radiation budget to changes in low clouds. Nature, 343, 49-51.
Spinhirn, J. D., R. Boers and W. D. Hart, 1989 : Cloud top liquid water from lidar observations of marine stratocumulus. J. Appl. Meteor., 28, 81-91.
Stephens, G. L., 1978b : Radiation profiles in extended water clouds. II : Parameterization schemes. J. Atmos. Sci., 35, 2123-2132.
Stephens, J. L., and C. M. R. Platt, 1987 : Aircraft observations of the radiative and microphysical properties of stratocumulus and cumulus cloud fields. J. Climate and Appl. Meteor., 26, 1243-1269.

THE EFFECTIVE RADIUS OF STRATIFORM CLOUD PARTICLES IN MIDDLE LATITUDES (EMPIRICAL DATA)

Ilia P.Mazin, Victor F. Shugaev and Nadezhda A. Monakhova

Cloud Phys. Lab., Central Aerological Observatory, Dolgoprudny, Moscow Region, 141700, Russia

1. INTRODUCTION

The numerical simulation of climate by no means implies a parametric description of radiation processes and needs a higher level of accuracy of cloud parameterization. An ample material of aircraft observations has been accumulated in the CAO in 1977-1984, which is only partially generalized in the empirical Handbook of Clouds and Cloudy Atmosphere /Mazin & Khrgian,1989/. Any cloud represents an extremely inhomogeneous medium, continuously changing in space and time and "we still do not know how to generalize our understanding of cloud microphysics" /Qingjuan et al.,1994/, An attempt to overcome these difficulties is made in this report.

2. THE MAIN DEFINITIONS AND RELATIONS

The optical and radiative properties of clouds mainly depend on their optical thickness τ. For a small cloud element they depend on the cloud extinction efficiency ε. For liquid clouds, ε is connected with the liquid water content (w_l) and effective droplet radius (r_e) by the relation:

$$\varepsilon = (3w_l) / (2r_e \rho_w), (1)$$

where /Hansen & Travis,1974/

$$r_e = \overline{r^3} / \overline{r^2}. (2)$$

Here ρ_w is water density and $\overline{r^k} = \int r^k f(r)dr$. The eq.(1) follows from evident equations: $w_l = (4/3)\pi\rho_w \overline{r^3} N$ and $\varepsilon = 2\pi \overline{r^2} N$, where f(r) is droplet size spectra normalized to 1 and N is the droplet concentration. For the water path P_l and the optical thickness τ_l in a liquid cloud , we may write

$$\tau = \int_0^H \varepsilon dz = 2\pi < \overline{r^2} N > H, (3)$$

$$P_l = \int_0^H w_l dz = (4/3)\pi\rho_w < \overline{r^3} N > H, (4)$$

where H is the cloud thickness, z is the height above cloud base. French quotes here denote averaging over the whole cloud layer. The effective cloud droplet radius $r_{e,cl}$ for the whole cloud layer may be analogously to r_e defined as

$$r_{e,cl} = \frac{<\overline{r^3}N>}{<\overline{r^2}N>} = \frac{\int_0^H \overline{r^3}(z)N(z)dz}{\int_0^H \overline{r^2}(z)N(z)dz} = \frac{3}{2}\frac{P_l}{\tau_l}\frac{1}{\rho_w}. (5)$$

It is evident that

$$r_{e,cl} \neq < r_e > = \overline{r^3} / \overline{r^2}. (6)$$

In order to parameterize mixed or ice clouds, it is convenient to introduce the notion of "an equivalent liquid cloud" (ELC). That means liquid cloud with P_l equal to the cloud water

path P for the considered mixed (ice) cloud, the same optical $\tau_l=\tau$ and geometrical $H_l=H$ cloud thickness . The effective radius $r_{e,cl}$ for ELC is one of the helpful parameter to describe the radiative properties of any cloud, independent of its phase structure.

The generalization of the empirical data of cloud water content W and cloud extinction ε and parameterization of the dependences of their mean values (as well as for τ , P and $r_{e,cl}$) on H for clouds of different types is the main goal of this paper.

3. AIRBORNE OBSERVATIONAL DATA

Some information about the used aircraft instrumentation, their accuracy and measurement techniques can be found in refs /Nevzorov, 1996, and Mazin et al.,1992/. Here we only emphasize that the summary effects of ice and water particles were measured (i.e. total water content W and total extinction efficiency ε). Empirical data were obtained mainly in the Europian part of the former USSR.The values of W and ε averaged over 0,5 s, are kept in the CAO archives, an idea of an amount of which is given in Table 1.

Cloud group	T_{base} (°C)	Cloud thickness (km) <.2	.2–.4	.4–.6	>.6	Total	Total length of incloud flights (km)
St	⊂(0,-10)	8	10	4	0	22	$16\cdot10^3$
	∝(0,-10)	1	4	5	1	11	
Ac	⊂(0,-10)	4	6	2	2	14	$7\cdot10^3$
	∝(0,-10)	1	6	1	1	9	
Ns	⊂(0,-10)	0	0	4	4	8	$55\cdot10^3$
	∝(0,-10)	0	0	0	0	0	
As	⊂(0,-10)	2	4	4	6	16	$28\cdot10^3$
	∝(0,-10)	2	2	2	7	13	
Total		18	32	22	21	93	$106\cdot10^3$

Table 1. The amount of aircraft cloud soundings

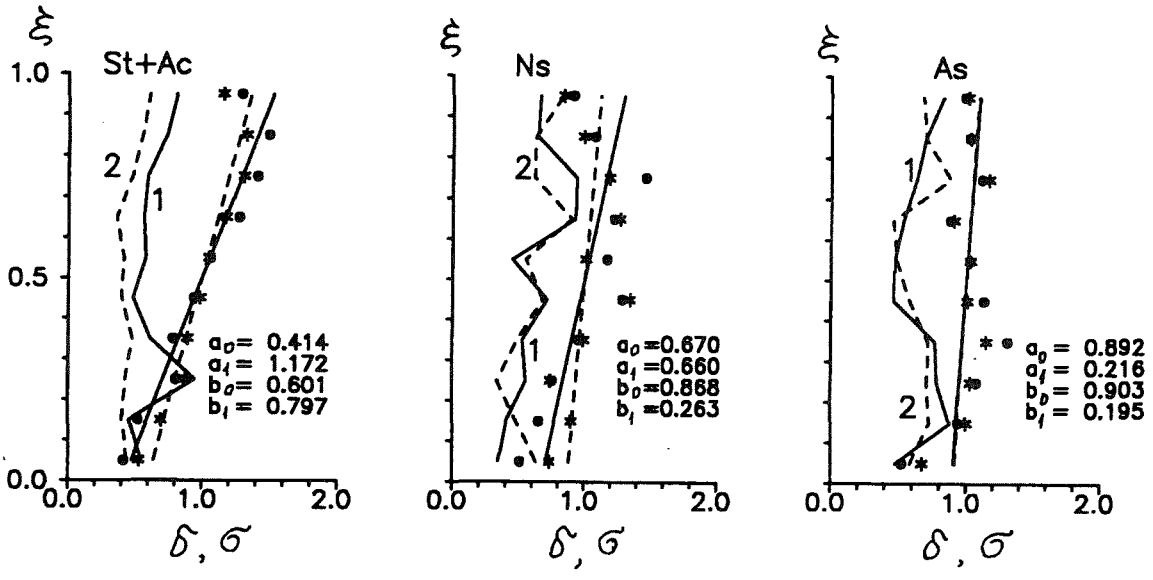

Fig.1. Mean vertical profiles of relative cloud water content $\delta_w(\xi)$ (solid lines), and relative extinction efficiency $\delta_\varepsilon(\xi)$ (dashed lines) for different cloud groups. Here $\xi=z/H$ is relative height, z is the height above cloud base and H is cloud thickness. Solid circles and asterisks are mean values of δ_w and δ_ε for each tenths of cloud thickness. Straight lines are linear least square fit parameterization for $\xi\subset(0.1–0.9)$. $\delta_w=a_0+a_1H$ and $\delta_\varepsilon=b_0+b_1H$. σ_w (1 on the figure) and σ_ε (2 on the figure) are standard deviations of individual (single) profiles.

Low level stratiform clouds like St, Sc and their modifications in Table 1 are denoted as St, modification of altostratus as As, that of altocumulus or nimbostratus as Ac or Ns, respectively.

In each of 93 cases of cloud sounding mentioned in Table 1, the vertical profiles of W and ε were found and P and τ were calculated. Individual profiles W(z) and ε(z) exhibit a great scattering. The relative profiles $\delta_\varepsilon(\xi) = \varepsilon(\xi)/ < \varepsilon >$, where ξ=z/H, and $\delta_\varepsilon(\xi) = \varepsilon(\xi)/ < \varepsilon >$ are less variable. Fig.1 presents the mean values of δ_w and δ_ε, the curves of standard deviations $\sigma_w(\xi)$ and $\sigma_\varepsilon(\xi)$ as well as found in the interval $\xi \subset (.05,.95)$ linear least square fit parameterization. Closer to the cloud boundaries all values sharply fall to zero. The scatter plots for <w>, P, τ and $r_{e,cl}$ via H for different cloud groups are presented in Fig.2.

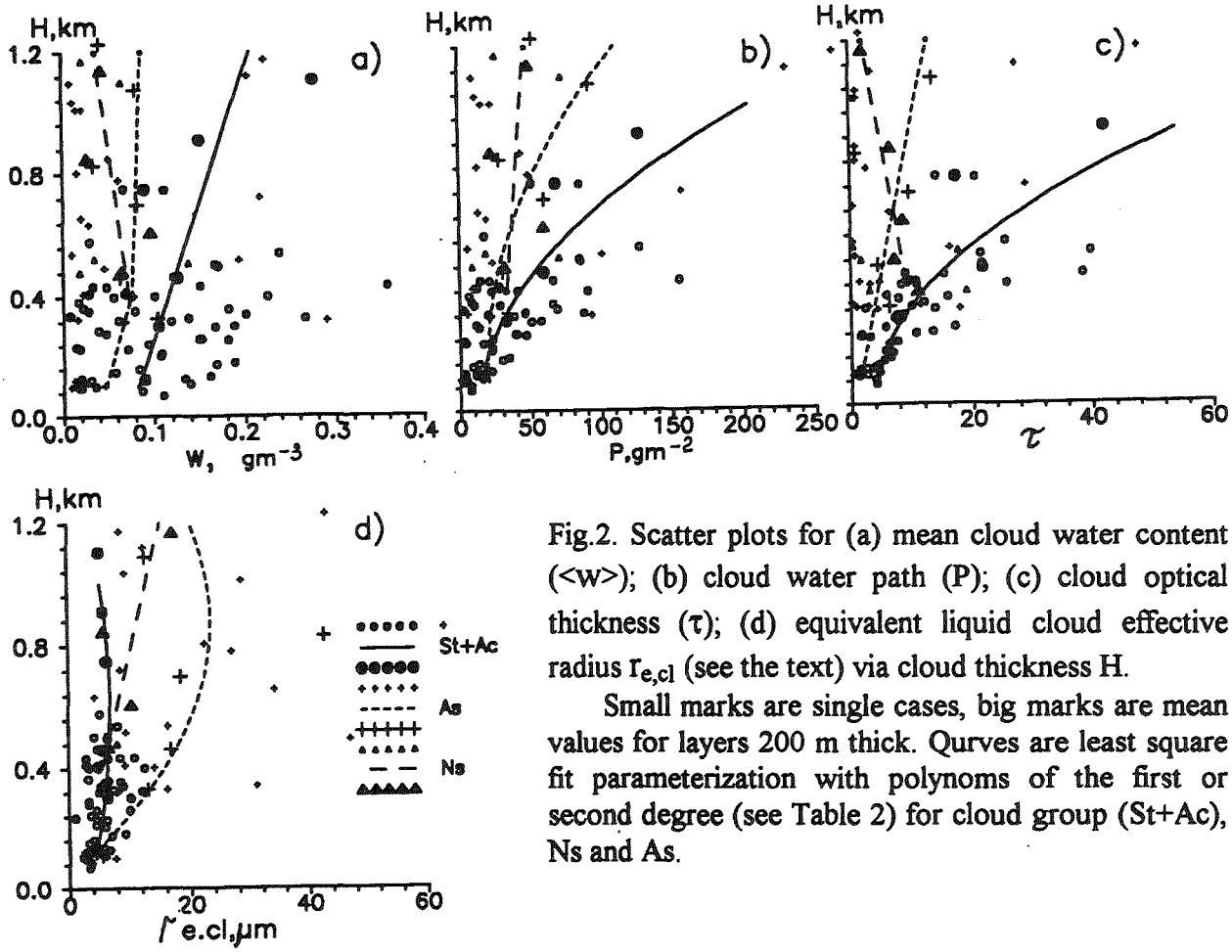

Fig.2. Scatter plots for (a) mean cloud water content (<w>); (b) cloud water path (P); (c) cloud optical thickness (τ); (d) equivalent liquid cloud effective radius $r_{e,cl}$ (see the text) via cloud thickness H.

Small marks are single cases, big marks are mean values for layers 200 m thick. Qurves are least square fit parameterization with polynoms of the first or second degree (see Table 2) for cloud group (St+Ac), Ns and As.

According to our experience, there is no large difference between microphysical properties in St and Ac cloud groups, all other factors being the same. Thus, to improve the statistics, we summarize the data for both cloud groups.

The averaged dependence of <w> on H shows its growth in the first 500 m (St + Ac, As) and only weakly depends and even decreases with farther increasing of cloud thickness H. Cloud particle size spectra and phase transformation with increasing H may be the reason for such a behavior. All relations were parameterized with polynoms of no more than the second degree (or broken lines) and their factors A_i found with least square fit method, are given in Table 2. Because of poor statistics the values of found factors to some degree, may be refined in the future.

Table 2. Factors A_i in the relation $(Y)_{aver} = A_0+A_1H+A_2H^2$, T = -5 °C, n is the number of soundings, $(H_1–H_2)$ is the interval (in km) of the definition area.

Y	Cloud group	n	A_0	A_1	A_2	$H_1–H_2$
<W> (gm^{-3})	St+Ac	56	0.071	0.113	0	0.1–1.0
	Ns	8	0.091	-0.045	0	0.4–1.2
	As	13	0.036	0.096	0	0.1–0.4
	As	15	0.070	0.015	0	0.4–1.2
P (gm^{-2})	St+Ac	56	13.5	-9.32	200.16	0.1–1.0
	Ns	8	26.02	17.19	0	0.4–1.2
	As	28	-2.35	58.56	-33.16	0.1–1.2
τ	St+Ac	50	4.53	-6.43	68.19	0.1–1.0
	Ns	9	12.81	-8.84	0	0.4–1.2
	As	28	0.59	10.20	0	0.1–1.2
$r_{e,cl}$ (μm)	St+Ac	53	3.26	11.92	-9.84	0.1–1.0
	Ns	6	0.58	12.31	0	0.4–1.2
	As	27	-2.35	58.56	-33.16	0.1–1.2

4. CONCLUSIONS

Based on the microphysical data collected in the CAO archives, the parameterization of the dependencies of the cloud optical thickness τ, cloud water path P, and cloud particles effective radius $r_{e,cl}$ for the cloud layer as a whole on the cloud thickness H, is suggested. The parameterization is restricted to the continental stratiform clouds of middle latitudes with the temperature of their base being approximately equal to -5°C. The temperature effect, as a first approximation, may be taken into account using the relation found by Mazin, 1995, for W. Thus,

$$(T) = Y(T_0)\exp[0{,}03832(T - T_0)], \quad (7)$$

where Y is any of parameters W, P, $r_{e,cl}$. The parameters ε and τ to a first approximation, are independent of T.

5. REFERENCES

Hansen J.E. and L.D. Travis, 1974: Light scattering in planetary atmospheres. *Space Sci. Rev.*, **16**, 527-610.

Mazin I.P., 1995: Cloud water content in continental clouds of middle latitudes, *Atm. Res.* **35**, 283-297.

Mazin I.P. and A.Kh.Khrgian (eds), 1989: Clouds and Cloudy Atmosphere (Handbook).*Gidrometeoizdat*, Leningrad, 646 p.

Mazin I.P.,Nevzorov A.N.,Shugaev V.F. and Korolev A.V. Phase structure of stratiform clouds. *11th ICCP*, Montreal, 1992,**1**, 332-335.

Nevzorov A.N., 1996: CAO aircraft instrumentation for cloud physics. This issue.

Nevzorov A.N., Shugaev V.F. Experimental studies of the phase-disperse structure of stratiform clouds at negative temperatures. Soviet *Meteorology and Hydrology*. 1992, 8, 41-51.

Qingyuan H., Rossow W.B. and A.A.Lacis, 1994: Near-global survey of effective droplet radii in liquid water clouds using ISCCP data, *Journal of Climate*, 7, 465-497.

INFLUENCE OF DIFFERENT PARAMETERIZATIONS OF ICE CLOUDS ON CLIMATE SENSITIVITY IN A GENERAL CIRCULATION MODEL

Ulrike Lohmann and Erich Roeckner

Max Planck Institute for Meteorology, Hamburg, Germany

1. INTRODUCTION

The response of the climate system to a radiative perturbation resulting from, for example, increasing levels of atmospheric CO_2 concentrations depends on a variety of poorly understood feedback mechanisms. One of the most complex and uncertain processes is the cloud-radiation-temperature feedback which involves large but partly compensating changes in the radiative fluxes. In a climate change study Cess et al. (1990) show that even the sign of the cloud feedback varies among the participating general circulation models.

In this paper we analyze the impact of different ice phase parameterizations on the global climate sensitivity using the same experimental setup and analysis method as in Cess et al. (1990). Climate sensitivity is defined here as the radiative response at the top of the atmosphere (TOA) to a global increase in sea surface temperature of 4 K which can be regarded as a surrogate climate change.

2. MODEL AND EXPERIMENTS

For this study two different ice phase schemes for stratiform clouds used in the Hamburg climate model ECHAM (Roeckner et al., 1992) are used. The first scheme (CTL) prognoses the sum of cloud water and cloud ice (Roeckner, 1995). The second scheme (PCI) considers cloud water and cloud ice as separate prognostic variables (Lohmann and Roeckner, 1996). The most important difference between both schemes in terms of changes of cloud properties in the warmer climate is the precipitation formation in the ice phase. While in CTL the precipitation formation is parameterized in terms of the sedimentation flux of ice crystals, in PCI ice crystals are assumed to have no terminal velocity, but aggregate to snow crystals and snow crystals further remove ice crystals by accretion following Levkov et al. (1992).

The precipitation formation rate in the ice phase multiplied with the model time step (Δt = 30 min) of both schemes as a function of cloud ice is shown in Figure 1. The aggregation rate of PCI increases faster with increasing cloud ice than the sedimentation flux of CTL does. At approximately 0.1 g kg^{-1} the aggregation is as large as the cloud ice itself, so that all cloud ice in PCI will be transferred into snow within one time step. On top of that if not all cloud ice aggregates to snow, the subsequent accretion of cloud ice by snow is a further sink of cloud ice in PCI.

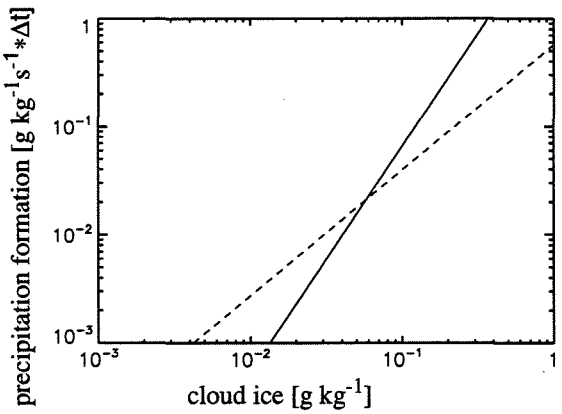

Figure 1: Different precipitation formation rates in the ice phase multiplied with the model time step as a function of cloud ice for CTL (– –) and PCI (—).

Additionally two sensitivity experiments are carried out. In the first one the parameterization of the aggregation and accretion rate of PCI replaces the parameterization of the sedimentation flux of CTL (CAGG) and in the second one the parameterization of the sedimentation flux of CTL replaces the one of the aggregation and accretion rate of PCI (PSED). Both experiments are carried out in such a way, that the cloud forcing is afterwards again in agreement with the ERBE data as it is in CTL and PCI.

3. CLIMATE SENSITIVITY

In all reference experiments the climatological July SST of the perpetual July integration is cooled globally

by 2K, while it is heated by 2K in the respective climate warming experiments. The simulation time of each experiment is 540 days, but the initial spin-up period of 90 days is not considered in the analysis. Following Cess et al. (1990), the climate sensitivity parameter λ is defined as

$$\lambda = \left(\Delta F/\Delta T_s - \Delta Q/\Delta T_s\right)^{-1}$$

where ΔT_s is the change in global mean surface temperature and ΔF and ΔQ are the changes of the global mean TOA longwave emission F and net solar radiation Q, respectively. A clear-sky parameter can be defined with the radiative responses ΔF and ΔQ replaced by their respective clear-sky values (cs).

Thus λ/λ_{cs} can be regarded as a measure of cloud feedback with λ/λ_{cs} larger (smaller) 1 denoting a positive (negative) feedback. It was further shown by Cess et al. (1990) that λ/λ_{cs} is proportional to the change in cloud forcing ΔCF:

$$\lambda/\lambda_{cs} = 1 + \Delta CF\,(\Delta F - \Delta Q)^{-1}$$

4. RESULTS

	CTL	PCI	PSED	CAGG
ΔLWP	9.2±1.3	5.5±1.0	8.7±1.0	7.2±1.9
ΔIWP	2.7±0.3	-2.2±0.3	5.1±0.5	-1.2±0.2
ΔCC	0.5±0.7	-1.9±0.7	-0.7±0.6	-3.5±0.6
ΔSCF	-2.6±0.7	0.6±0.6	-1.1±0.4	0.8±1.1
ΔLCF	4.0±0.3	0.1±0.5	1.9±0.6	-0.7±0.4
ΔCF	1.4±0.7	0.7±0.4	0.8±0.5	0.2±1.1
λ_{cs}	0.54	0.51	0.53	0.49
λ	0.67±0.1	0.56	0.60±0.1	0.51±0.1
λ/λ_{cs}	1.24±0.1	1.10±0.1	1.13±0.1	1.04±0.2

Table1: Differences in liquid water path (ΔLWP) [gm^{-2}], ice water path (ΔIWP), cloud cover (ΔCC) [%], short-wave (ΔSCF), longwave (ΔLCF) and net cloud forcing (ΔCF) [Wm^{-2}] between the SST+2K and SST-2K experiment and climate sensitivity parameter λ [$Km^{-2}W^{-1}$], λ_{cs} and λ/λ_{cs}. Standard deviations below 0.1 are not listed.

The results are summarized in Table 1. The most striking result is the different change in ice water path between CTL and PCI. The climate warming leads to an increase in ice water path in CTL by 2.7 gm^{-2}, while the ice water path decreases by 2.2 gm^{-2} in PCI. If the sedimentation flux of CTL is implemented in PCI (PSED) the ice water path increases by 5.1 gm^{-2}, while it decreases by 1.2 gm^{-2} in CAGG.

The ice water content for all experiments in the SST-2K experiment is shown in Figure 2. In CTL cloud ice has a distinct maximum in the tropics and secondary maxima in the extratropics. In PCI the ice water path is 40% higher and the maxima in the extratropics are as large as in the tropics. Especially in the winter hemisphere cloud ice is higher than in CTL. Additionally cloud ice is confined to higher altitudes.

While the gross features of CAGG and CTL are similar, the ice water path is 30% lower in CAGG than in CTL. The main difference between them is that the maximum cloud ice in CAGG is located in the extratropics on the Southern Hemisphere and not in the tropics as in CTL. Secondly, cloud ice has increase in the middle atmosphere at 60°S, which both are features more typical of PCI. Conversely the ice water path is 65% higher in PSED than in PCI, but the overall pattern are similar. The large maximum of cloud ice in the tropics in PSED and the decrease of cloud ice in the middle atmosphere of high latitudes in the Southern Hemisphere is in better agreement with CTL than with PCI.

Figure 3 shows the change in cloud ice between the SST+2K and SST-2K experiment. All changes in cloud ice have in common that the sources of cloud ice, mainly the detrainment of convective cloud ice have decreased in the warmer climate by 5% to 10% (not shown). Secondly as a result of tropopause lifting clouds in the lower and mid troposphere have decreased and high clouds have increased. In CTL and CAGG cloud ice decreases for temperatures above 258 K and increases below. In PCI and PSED the decrease of cloud ice is confined to the whole mixed phase region. The different vertical displacement is caused by the diagnostic separation of cloud water and cloud ice in CTL and CAGG as compared to the prognostic treatment of both phases in PCI and PSED. I. e., in CTL the ice fraction in mixed clouds at 258 K is 50%. If all cloud ice would be removed within one time step while no cloud water precipitates, the diagnostic relation would afterwards create again 50% cloud ice with half of its amount. Therefore cloud ice can never be totally removed in the mixed phase in CTL.

A similar behavior in CTL and PSED is the large increase in cloud ice in the tropics, the increase of cloud ice in the subtropics and the increase in life time of ice clouds in the warmer climate. CAGG and PCI agree in a less pronounced and separated increase in cloud ice in the tropics and a small decrease in life time of ice clouds

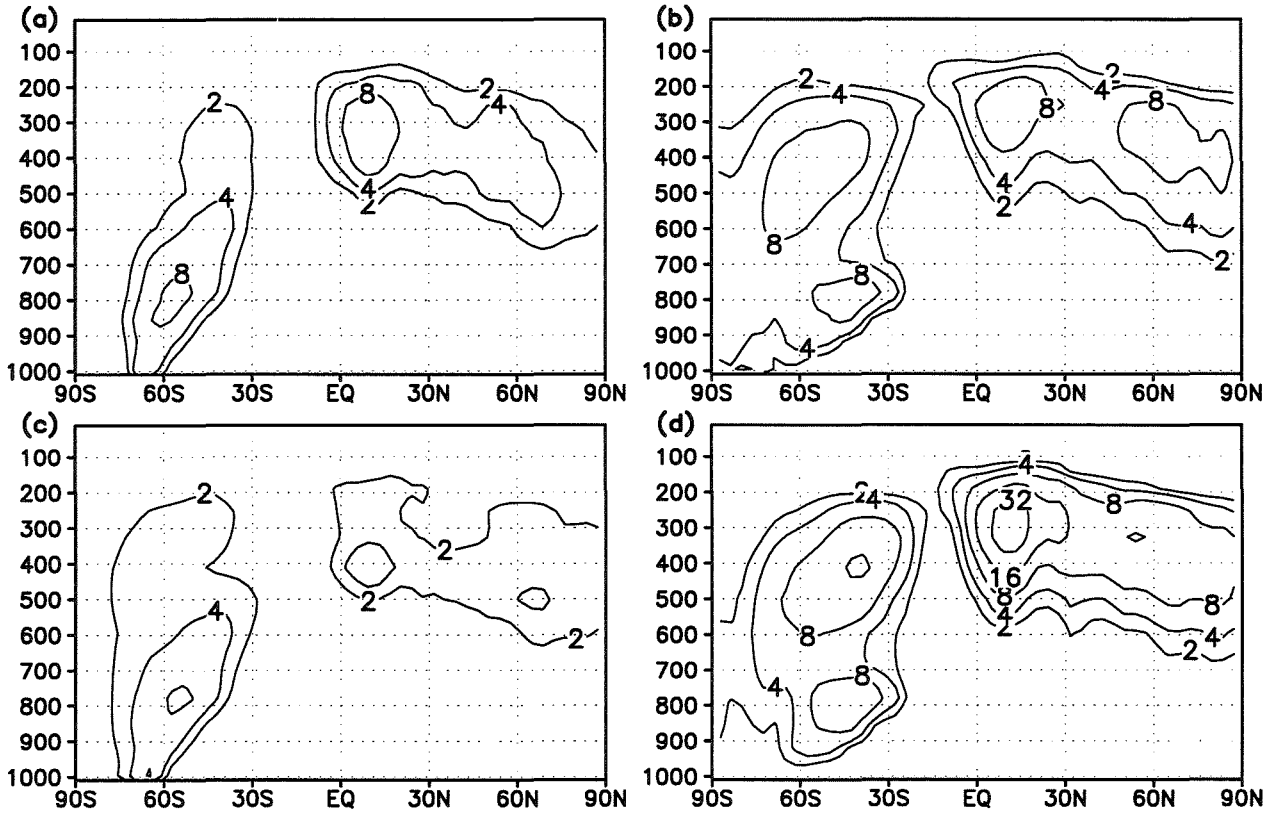

Figure 2: Latitude height cross section of cloud ice in the SST-2K experiments for CTL (a), PCI (b), CAGG (c), PSED (d). Contour spacing is 2, 4, 8, 16, 32 mg kg^{-1}.

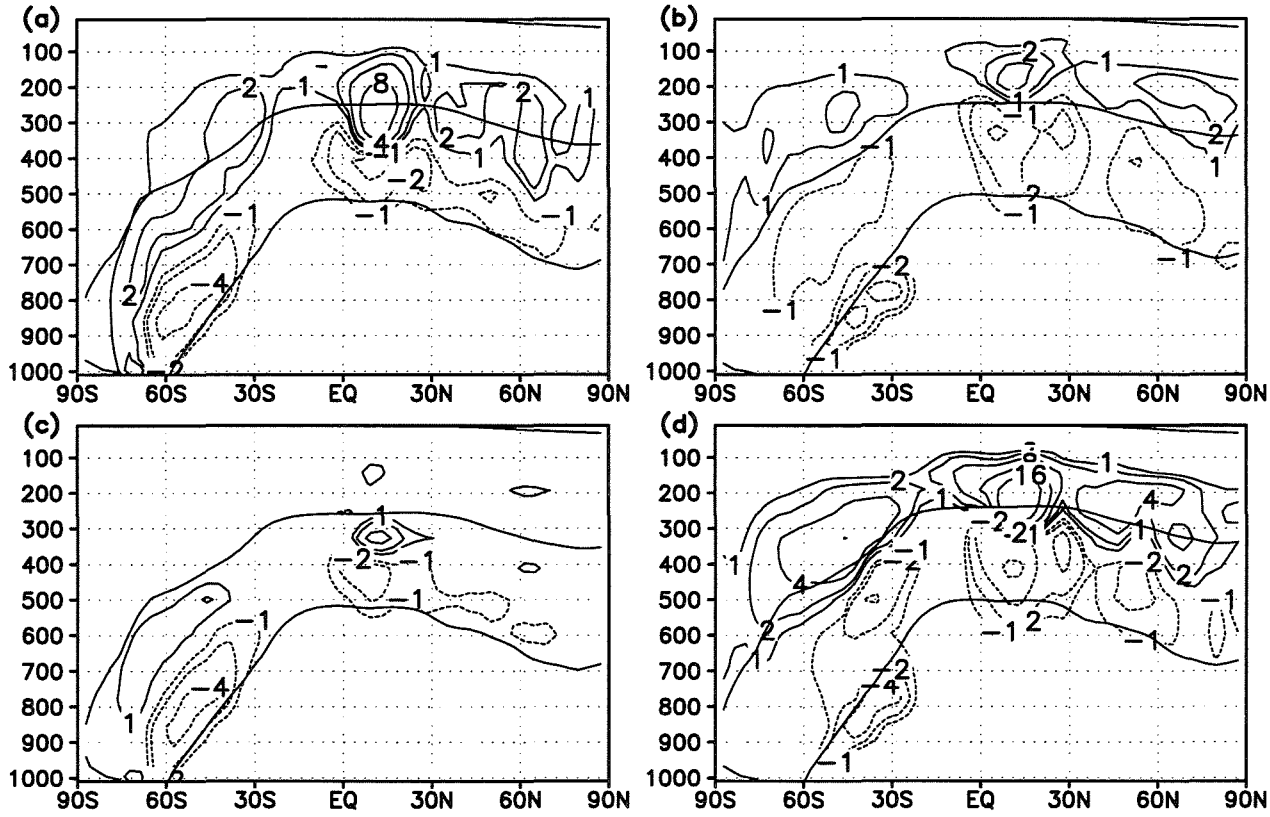

Figure 3: Latitude height cross section of the difference in cloud ice between the SST+2K and SST-2K experiment for CTL (a), PCI (b), CAGG (c), PSED (d). Contour spacing is ±1, ±2, ±4, ±8, ±16 mg kg^{-1}.

in the warmer climate. The decrease in life time of ice clouds results from a more frequent transformation of cloud ice into snow within one time step.

The resulting changes in cloud forcing are much larger in CTL than in PCI. In CTL, clouds enhance the global sensitivity by 24%. Water and ice clouds have been lifted into higher altitudes in the warmer atmosphere and their paths have increased by 9.2 gm^{-2} and 2.7 gm^{-2}, respectively. This is particularly relevant for non black cirrus, because its emissivity increases as the ice water content increases. Additionally the shift of cloud ice in higher altitudes of colder temperatures yields an increase in LCF. The total cloud cover has also increased by 0.5%. As a result, the longwave cloud forcing (LCF) is 4 Wm^{-2} larger in the warmer climate. The negative change in shortwave cloud forcing (ΔSCF) of -2.6 Wm^{-2} is caused by the increase in liquid water path and optical depth resulting in a higher cloud albedo. Since the changes in SCF and LCF are of opposite sign, they partly cancel each other yielding an increase in net cloud forcing of only 1.4 Wm^{-2}.

In PCI the radiative effect of the decrease in cloud ice is offset by the effect of the shift of ice clouds in higher altitudes which itself would enhance LCF. Therefore LCF remains virtually unchanged in the warmer climate. The increase in liquid water path in PCI is only 60% of that in CTL, and the total cloud cover decreases by roughly 2%. SCF slightly decreases in the warmer climate as a result of the larger effect of the decrease in low level clouds than the increase in liquid water path. The change in net cloud forcing of 0.7 Wm^{-2} is approximately the same as in SCF. Clouds enhance the global climate sensitivity by only 10% significantly less than in CTL.

In PSED the increase in cloud ice is about twice as large as in CTL but the increase in LCF is only half of that in CTL. A similar increase in liquid water path in the warmer climate in CTL and PSED leads to a much smaller increase in SCF in PSED. One reason for the smaller changes in cloud forcing in PSED is that cloud cover decreases in PSED but increases in CTL. Another reason is the different geographical distribution of water and ice clouds in both simulations. The resulting change in net cloud forcing is similar to the one in PCI.

The difference between CAGG and PCI is not a mirror image of the difference between CTL and PSED. The changes in CAGG are much more similar to the ones in PCI than those of CTL and PSED are. The decrease in cloud ice in CAGG yields a decrease in LCF in the warmer climate. Compared to PCI, this is caused by a larger decrease in cloud cover in CAGG and a smaller decrease in cloud ice. The changes of the liquid water path and SCF are comparable in PCI and CAGG. The enhancement of the global climate sensitivity due to clouds of 4% is smallest in this experiment.

To conclude, the difference in climate sensitivity between CTL and PCI is mainly caused by the different parameterizations of the precipitation formation in the ice phase. This leads to an increase in ice water path in CTL and a decrease in PCI in the warmer climate. Consequently the changes of both components of the cloud forcing and the cloud feedback are smaller in PCI than in CTL.

5. REFERENCES

Cess, R. D. et al., 1990: Intercomparison and interpretation of climate feedback processes in 19 atmospheric general circulation models. *J. Geophys. Res.* **95,** 16601-16615.

Levkov, L., B. Rockel, H. Kapitza, E. Raschke, 1992: 3D mesoscale numerical studies of cirrus and stratus clouds by their time and space evolution. *Contr. Phys. Atmos.* **65,** 35-58.

Lohmann, U, E. Roeckner, 1996: Design and performance of a new cloud microphysics scheme developed for the ECHAM general circulation model. *Clim. Dyn.* (accepted).

Roeckner, E. et al., 1992: Simulation of the present-day climate with the ECHAM model: Impact of model physics and resolution. *Report No* **93,** *Max Planck Institute for Meteorology,* 172 pp.

Roeckner, E., 1995: Parameterization of cloud radiative properties in the ECHAM4 model. In WCRP workshop on „*Cloud microphysics parameterizations in global atmospheric circulation models*", 23-25 May 1995, WCRP-90, Kananaskis, Canada, pp 105-116.

PARAMETERIZATION OF TROPICAL ICE CRYSTAL SPECTRA AND IMPLICATIONS FOR RADIATIVE PROPERTIES

Greg M. McFarquhar and Andrew J. Heymsfield

National Center for Atmospheric Research
Boulder, CO., USA

1. INTRODUCTION

Ice clouds, especially tropical cirrus, have a major effect on the earth's radiation balance and climate as the result of the reflection and absorption of solar and infrared radiation. The radiative properties of ice clouds are influenced to a large extent by cloud microphysics. However, realistic parameterizations of convectively generated or tropical cirrus microphysical and radiative properties are largely unavailable.

Data upon which parameterizations can be based have been lacking since tropical cirrus are usually inaccesssible because they are far removed from aircraft landing sites and because they extend to high heights. In this paper, data collected during the Central Equatorial Pacific Experiment (CEPEX), reported by Heymsfield and McFarquhar (1996), hereafter HM, and McFarquhar and Heymsfield (1996), hereafter MH, are used to parameterize tropical ice crystal spectra in terms of ice water content, IWC, and temperature, T.

2. DATA SET

All data used here were collected during CEPEX, conducted to quantify the energy budget of the atmosphere and ocean over the warm pool where sea surface temperatures exceed 300 K. Microphysical data were obtained using a Learjet which flew in anvils, and occasionally in convective regions, with ambient temperatures between -70°C and -20°C, and within the area bounded by 160°E to 160°W and 2°N to 18°S. The Learjet flew 35 hours in cloud, approximately one third of which was spent near cloud tops.

Ice crystals with maximum dimensions larger than 100 μm were measured by a Particle Measuring Systems's (PMS) two-dimensional cloud probe (2DC); in addition, particles with maximum dimensions from 5 to greater than 100 μm were measured with a Video Ice Particle Sampler (VIPS), an instrument deployed in a wing-mounted cannister which videophotographs crystals that impact upon a 0.5 cm transparent moving belt exposed to the airflow.

Corresponding author address: Greg M. McFarquhar, NCAR/MMM, P.O. Box 3000, Boulder, CO. 80307-3000, mcfarq@ncar.ucar.edu

A number of microphysical properties can be derived from these data, including IWC, cross-sectional area (A_c), cross-sectional area from equivalent melted spheres (A_s), effective radius (r_e), and number concentration (N). Radiative properties are calculated using anomalous diffraction theory (ADT) following the equations outlined by Mitchell and Arnott (1994). The volume extinction coefficient, β_{ext}, is proportional to the cross-sectional area of the particles and the volume absorption coefficient, β_{abs}, is proportional to the volume of the particles to first order.

3. PARAMETERIZATION

This study is modeled after that of Heymsfield and Platt (1984), hereafter HP, who parameterized cirrus particle size spectra for crystal dimensions greater than 20 μm as a function of T. MH showed that although the HP parameterization gives an adequate representation of tropical cirrus spectra for temperatures warmer than -40°C, it is inadequate at cooler temperatures because it is principally based on measurements made in mid-latitude cirrus typically produced by in-situ lifting or localized convection. In the tropics, tropical cirrus frequently originate as the outflow of vapor and condensate from below deep convective cores.

To maximize the parameterization's utility for cloud resolving and climate models, four major requirements were identified: 1) the optical and radiative properties from the parameterized spectra had to closely replicate those from observed spectra; 2) the parameterized mass had to equal the observed mass; 3) small ice crystals had to be realistically represented; and 4) the parameterization had to be easily integratable and converge.

This parameterization depends on the diameter of melted equivalent spheres, D_m, rather than on maximum crystal length to more easily force mass conservation. However, the radiative properties obtained from this parameterization do not assume equivalent melted spheres or equivalent area spheres.

The distributions of large and small ice crystals are represented separately. Large ice crystals, with D_m >100 μm, were measured by the 2DC, and small ice crystals, with D_m <100 μm, were measured by the VIPS.

All 2DC spectra, each representing a 10 s or 2 km average, were grouped into 6 temperature

bins, spaced every 10°C, and into 10 IWC bins, logarithmically spaced. The temperatures at which the measurements were made are not necessarily those at which the ice crystals grew because crystals may have been lifted or fallen to that height. As only 37 VIPS spectra have been processed, each VIPS spectra, representing a 6 s average, was fit independently and the variation of fit parameters with IWC examined; there are not sufficient data to examine trends with T.

Tests determined that exponential distributions best characterized small crystals and lognormals well represented large crystals. The exponential function is given by

$$N(D_m) = \frac{6\ IWC_{<100}\alpha_{<100}^4}{\pi\rho_{ice}\Gamma(4)}\ exp(-\alpha_{<100}\ D_m) \quad (1)$$

where ρ_{ice} is the density of solid ice (0.91 g cm^{-3}), $\alpha_{<100}$ the exponential slope and $IWC_{<100}$ the mass of all crystals with $D_m < 100$ μm in the observed spectra. The lognormal function is given by

$$N(D_m) = \frac{6\ IWC_{>100}}{\pi^{3/2}\rho_{ice}\sqrt{2}(e^{3\mu_{>100}+9/2\sigma_{>100}{}^2})D\sigma_{>100}}$$
$$exp\left[-\frac{1}{2}\left(\frac{logD-\mu_{>100}}{\sigma_{>100}}\right)^2\right] \quad (2)$$

where $\sigma_{>100}$ is the standard geometric deviation of the distribution, $\mu_{>100}$ the mode, and $IWC_{>100}$ the mass of all crystals with $D_m > 100$ μm in the observed spectra.

To determine the fit parameters, the chi-squared function, given by

$$\chi^2 = \sum_{i=1}^{N}\left(\frac{N_i - N(D_{m_i};a_1...a_M)}{\sigma_i}\right)^2 \quad (3)$$

must be minimized. N_i represents the observed number distribution function at mass-equivalent diameter D_{m_i}, and a_1 through a_M represent the fit parameters of the exponential (M=1; $a_1 = \alpha_{<100}$) or lognormal distribution (M=2; $a_1 = \mu_{>100}$; $a_2 = \sigma_{>100}$). The uncertainties, σ_i, were chosen to force the parameterized optical properties to match the observed optical properties as closely as possible. Since the contributions of particles to radiative properties, such as β_{ext}, are proportional to projected area, the weight of each bin is set to the directly measured A_c for that bin.

The downhill simplex method described by Press et al. (1992) is used to determine $\alpha_{<100}$, $\mu_{>100}$, and $\sigma_{>100}$. The bootstrap method (Efron and Tibshirani 1993), a modified Monte Carlo technique, gives uncertainty estimates. This method is commonly used when not enough is known about the underlying process or nature of the measurement errors, and is statistically robust.

4. RESULTS

The weightings of the lognormal and exponential function are proportional to the mass of crystals with D_m greater than or less than 100 μm. Figure 1 plots $IWC_{<100}$ as a function of total IWC. The solid line represents the best fit given by

$$IWC_{<100} = a\ IWC^b \quad (4)$$

where $a = 0.252 \pm 0.068$ and $b = 0.837 \pm 0.054$. As expected, smaller crystals make larger contributions to the total mass for lower IWCs.

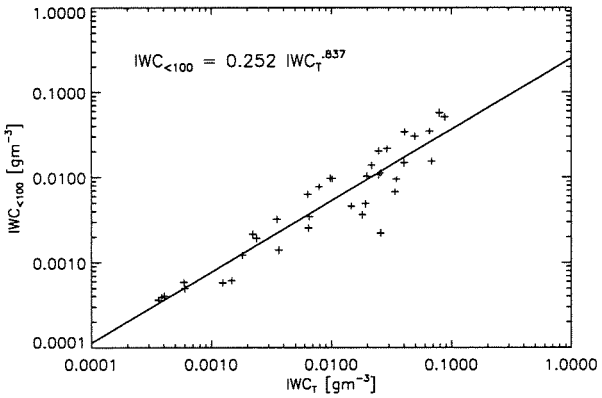

Figure 1. $IWC_{<100}$, versus total $IWC_T = IWC_{<100} + IWC_{>100}$. Solid line represents best fit to data.

Figure 2 shows the best exponential fit to a small crystal spectrum measured during CEPEX. $N(D_m)$ for $D_m < 10$ μm is overestimated by the fit, but only 4% of the fit mass is found in such small sizes.

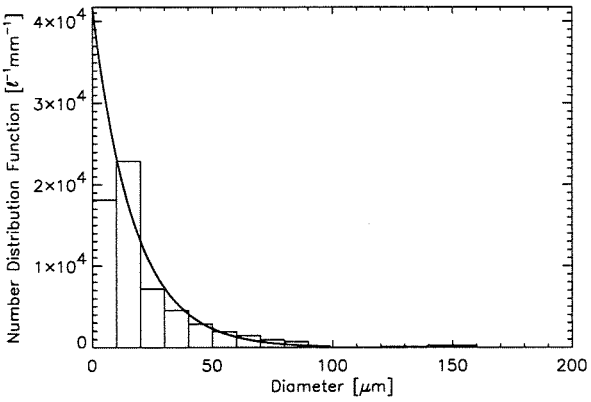

Figure 2. Ice crystal spectrum measured by VIPS, April 1, 23:03:54. Horizontal axis is melted equivalent diameter. Temperature -49.3°C. Solid line represents best fit to data conserving mass. Only crystals with $D_m < 100$ μm used in fit.

The best fit for the variation of $\alpha_{<100}$ with $IWC_{<100}$ is given by

$$\alpha_{<100} = b - m\, log(IWC_{<100}). \quad (5)$$

where b = -3.02 x 10^{-3} ± 3.74 x 10^{-3} and m = 0.0324 ± .0020. On average, the total area calculated is 1.02 times that obtained from the VIPS measurements, further indicating that ice crystal spectra and their radiative properties are adequately represented.

Figure 3 shows the average spectra measured by the 2DC for T between -50 to $-40°C$ and for $IWC_{>100}$ between 10^{-1} and $10^{-0.5}$ g m^{-3}, together with the best fit. The numbers of crystals with D_m larger than about 400 μm are somewhat underestimated, and also the IWC and area from crystals in these size ranges. No alternate parameterizations were found that provided as good of a fit while meeting all the required criteria.

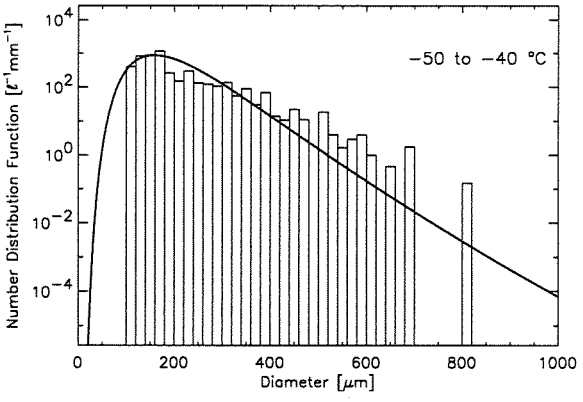

Figure 3. Average ice crystal spectra observed during CEPEX with IWC between 10^{-1} and $10^{-0.5}$ g m^{-3} and T between -50 and -40°C. Horizontal axis melted equivalent diameter. Solid line represents best fit of mass conserving lognormal distribution. Points with D_m < 100 μm do not contribute to fit.

For a given temperature, $\mu_{>100}$ may be characterized as

$$\mu_{>100} = a_\mu(T) + b_\mu(T)IWC \quad (6)$$

where $a_\mu(T)$ and $b_\mu(T)$ are given by

$$a_\mu(T) = a_{a_\mu} + b_{a_\mu}T \quad (7)$$

$$b_\mu(T) = a_{b_\mu} + b_{b_\mu}T \quad (8)$$

with a_{a_μ} = 5.27 ± .02, b_{a_μ} = 0.0024 ± .0005, a_{b_μ} = 0.026 ± .024, and b_{b_μ} = -9.9 ± 5.3 x 10^{-4}. $\sigma_{>100}$, can also be represented by Eqs. (6) through (8) by replacing μ with σ. Here, a_{a_σ} = 0.39 ± .02, b_{a_σ} = 2.1 ± .5 x 10^{-3}, a_{b_σ} = 0.022 ± .023, and b_{b_σ} = -1.3 ± 4.1 x 10^{-4}. Both $\sigma_{>100}$ and $\mu_{>100}$ increase as T and IWC increase, consistent with HM's (1996) analysis showing larger crystals and consequently broader spectra at higher IWC and T.

MH describe in more detail the adequacy of the representation of the observed data by the fits. They also show that the fit uncertainties are larger than the observed errors, showing that the fits are only valid on the average.

To calculate radiative properties, β_{ext}, determined from the distribution of equivalent melted spheres, is multiplied by the actual cross-sectional area divided by the cross-sectional area of equivalent melted spheres, A_c/A_s, a correction factor based on observations to force β_{ext} to represent non-spherical ice crystals. For crystals with D_m <100 μm, no correction is necessary because there is a 4% difference between A_c and A_s on average. However, for crystals with D_m>100 μm there is a 27% difference, and A_c/A_s is expressed by

$$A_c/A_s = a(T) + b(T)IWC_{>100} \quad (9)$$

where a(T) and b(T) are linear functions of T in °C with respective intercepts of 2.371 ± .013, and 0.216 ± .023 m^3g^{-1}, and respective slopes of 0.0133 ± .0006, and 2.2 ± 5.1 x 10^{-4}.

5. PARAMETERIZATION IMPLICATIONS

Optical properties calculated from this parameterization using ADT are compared with optical properties predicted from Ebert and Curry's (1992) parameterization, hereafter EC. Figure 4 shows the ratio of τ calculated by EC compared to that calculated from CEPEX; the ratio decreases as temperature increases because A_c/A_s is larger at warmer T. Agreement is especially good for larger τ, the most radiatively significant cases, at cooler temperatures. Under such conditions, the CEPEX τ is a little larger, suggesting that the CEPEX spectra have more smaller crystals, providing greater surface area. EC based their parameterization principally on mid-latitude observations where there are fewer small crystals and different growth mechanisms. Good agreement was also obtained between the longwave emissivities derived here and by EC. This agreement is not surprising as EC require knowledge of r_e, which is calculated from the CEPEX spectra.

A separate investigation on the importance of small crystals for causing high reflectances of tropical cirrus was made. During the Stratospheric-Tropospheric Exchange Project (STEP), Knollenberg et al. (1993), hereafter KKW, found particle mass modes at sizes of 20–40 μm in the tops of cirrus, with IWCs as high as 0.07 g m^{-3}, complimenting previous suggestions that small ice crystals cause high reflectances. On the contrary, HM determined that the predominantly large particles in the lower, warmer parts of the cirrus contain at least an order of magnitude greater mass than those crystals in the colder tops, and are at least equally as important in producing high albedos.

As an extension of Zender and Kiehl (1994), the radiative transfer code of CCM2 is used with the CEPEX and KKW spectra to investigate the contributions of ice crystals between 3 and 20 μm to radiative properties. Their importance varies substantially. For an IWP of 100 g m^{-2} with KKW, the albedo decreases from 0.345 to 0.251, and τ from 7.4 to 4.8 when small crystals are omitted. However, with CEPEX under similar conditions, the albedo only decreases from 0.26 to 0.25 (τ from 5.1 to 4.8). The measurements of KKW may be an exception to general trends because they were made close to convection at temperatures as cold as -90°C; the coverage of convective cores is small compared to that of anvils in the tropics.

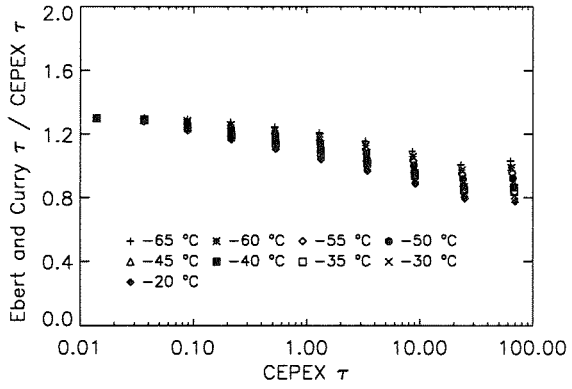

Figure 4. Ratio of τ calculated using Ebert and Curry (1992) against τ calculated using current parameterization as function of τ calculated using this parameterization. A_c/A_s correction factor included. Different symbols represent different temperatures.

6. CONCLUSIONS

This parameterization that characterizes the average properties of tropical ice crystal spectra, dependent on T and IWC, is mass conserving, provides easily integrable expressions for optical properties, and accurately represents small ice crystals. The number distribution function is expressed as the sum of an exponential distribution describing small ice crystals (D_m <100 μm) and a lognormal distribution describing larger ice crystals (D_m >100 μm); the coefficients of the fit are chosen to force the parameterized radiative properties to replicate the observed radiative properties as closely as possible. Uncertainty estimates on the fit parameters are obtained using the bootstrap technique. The use of this parameterization in climate and cloud-resolving models is possible, and is encouraged to better see the effects of outflow cirrus on cloud mass and radiative properties.

7. ACKNOWLEDGMENTS

The authors are grateful for the advice and contributions of S. Aulenbach, W. Grotewold, R. Hobbs, B. Jones, J. Kiehl, L. Miloshevich, D. Rusk, R. Srivastava, R. Wallin, and C. Zender.

8. REFERENCES

Ebert, E. E., and J. A. Curry, 1992: A parameterization of ice cloud optical properties for climate models. *J. Geophys. Res.*, **97**, 3831–3836.

Efron, B., and R.J. Tibshirani, 1993: *An introduction to the bootstrap.* Chapman & Hall, 436 pp.

Heymsfield, A. J., and C. M. R. Platt, 1984: A parameterization of the particle size spectrum of ice clouds in terms of ambient temperature and the ice water content. *J. Atmos. Sci.*, **41**, 846-855.

Heymsfield, A.J., and G.M. McFarquhar, 1996: On the high albedos of anvil cirrus in the tropical Pacific warm pool: microphysical interpretations from CEPEX. *J. Atmos. Sci.*, in press.

Knollenberg, R. G., K. Kelly, and J. C. Wilson, 1993: Measurements of high number densities of ice crystals in the tops of tropical cumulonimbus. *J. Geophys. Res.*, **98**, 8639–8664.

McFarquhar, G. M., and A. J. Heymsfield, 1996: Parameterization of tropical cirrus ice crystal spectra and implications for radiative transfer: results from CEPEX. *J. Atmos. Sci.*, submitted

Mitchell, D. L., and W. P. Arnott, 1994: A model predicting the evolution of ice particle size spectra and radiative properties of cirrus clouds. Part II: Dependence of absorption and extinction on ice crystal morphology. *J. Atmos. Sci.*, **51**, 817–832.

Press, W.H., S.A. Teukolsky, W.T. Vetterling, and B.P. Flannery, 1992: *Numerical Recipes in FORTRAN. The Art of Scientific Computing Second Edition*, Cambridge University Press, 963 pp.

Zender, C.S., and J.T. Kiehl, 1994: Radiative sensitivities of tropical anvils to small ice crystals. *J. Geophys. Res.*, **99**, 25869–25880.

The Modelling of Secondary Ice Production in Stratiform Clouds by the use of a One Dimensional Mixed Layer Model

D.S.Morris and T.W. Choularton

Atmospheric Physics Department, UMIST, Manchester, UK;
1 944 161 200 3970; e-mail:daniel@jc.phy.umist.ac.uk

1. INTRODUCTION

Stratiform clouds play an important role in regulating the Earths climate. The microphysics of these clouds has an important effect on their radiation balance and hence on global radiation balance.

Traditionally, the ice crystal concentrations of these clouds has been estimated using the empirical relationship derived by Fletcher (1962). However, more recent studies have shown that many mixed phase stratiform clouds exhibit ice enhancement. Ice crystal concentrations have been found to far exceed the concentrations that would be predicted by the Fletcher curve, Harris-Hobbs and Cooper (1986), Bower *et al.*, (1996). It is thought that much of this ice enhancement may be caused by the Hallett-Mossop process, Hallett and Mossop (1974).

Changes to the predicted ice crystal concentrations will have a direct effect on the precipitation efficiency, the water budget and the radiative properties of the cloud. Applied globally, to all stratiform clouds, it may significant affect the radiation budget of the planet. Gregory and Morris (1996), produced evidence that indicated that General Circulation Model's (GCM's) are already sensitive to the specification of mixed phase layer clouds.

GCM's, however, are currently unable to predict the effect of these high ice crystal concentrations on the global radiation budget. Mixed phase clouds, in UK Meteorological Office's GCM for example, linearly partition the liquid and ice water contents such that the cloud is all liquid water at 0°C and all ice at -9°C.

An explicit microphysics routine is currently being developed for inclusion in the next version of the Unified Model. Ballard and Hutchinson, (1995), describe preliminary tests using the Meteorological Office's non hydrostatic model that includes explicit microphysics for stratiform clouds based on the parameterization scheme developed by Rutledge and Hobbs, (1983). The scheme includes ice and snow formation, the depositional growth of snowflakes, their growth by riming, together with a full treatment of the liquid phase process.

A parameterization of the Hallett-Mossop process is also to be included in the new microphysics routines. However, it is desirable to test such a parameterization, in a high resolution stratiform cloud model, where diagnostics can be compared directly with sampled cloud data.

2. THE HALLETT-MOSSOP PROCESS

The Hallett-Mossop process is a mechanism by which a large number of secondary ice crystals can be nucleated at

temperatures higher than -9°C. Much work has been published on the microphysics that leads to the production of the crystals and there is a good understanding of the environmental conditions that are required before the process can take place.

The Hallett-Mossop process occurs at temperatures between -3°C and -8°C when a droplet spectrum exists such that both droplets <13μm and >24μm are present.

Although the process has never been observed directly, a number of theories have been put forward to describe the actual mechanism. As a graupel particle falls through the cloud, small droplets (<13μm) may become attached to it causing a roughening of its surface. Larger droplets (>24μm) may then become attached to the smaller droplets. The attached droplets have a poor thermal contact with the graupel so they may freeze symmetrically from the outside in. This causes the pressure at the centre of the droplet to increase which in turn causes unacceptable stresses at the crystalline or near crystalline surface. The pressure build up may induce a spike of water to 'erupt' from the surface which will again freeze symmetrically from the outside inwards. The ice shell that develops around this protuberance is thin in comparison to the shell that develops around the droplet. It is thought that the protuberance may then shatter explosively causing splinters of ice to be produced, (Griggs *and* Choularton 1983). These splinters can then in turn become sources for further ice nucleation, thus the ice population of a cloud can rise rapidly; measurements of ice production rates by the Hallett-Mossop process have been recorded at orders of 1000 crystals/m^3/s, Harris-Hobbs and Cooper (1987).

3. THE STRATIFORM CLOUD MODEL

The Stratiform Cloud Model is a one dimensional and initially well mixed model. Ice is initialized using the Fletcher curve and is grown by both vapour deposition and riming. As the ice sediments it eventually passes through the Hallett-Mossop temperature regime.

The Hallett-Mossop process in this model is a parameterization as developed by Hallett *et al*, (1978), and further used by Willis and Hallett, (1991), that does not require a droplet spectrum and gives a secondary ice production rate described by

$$S_i = \frac{N_g N_d V_g \pi D^2 E}{4} \qquad (1)$$

where $\mathbf{S_i}$ is the number of splinters produced in 1 second; $\mathbf{N_g}$ is the concentration of ice crystals of diameter **D**, falling with velocity $\mathbf{V_g}$, and $\mathbf{N_d}$ is the concentration of cloud droplets greater than 25μm in diameter collected with an efficiency **E**; 200 droplets produce one splinter, however, this number is provisional. It was Hallett and Mossop that found that the splinter production rate was approximately 1 splinter for every 200 drops accreted. However, they further found that in some circumstances the splinter production rate could rise so that 1 splinter was produced for every 50 drops accreted. In our case we are dealing with layer clouds where large numbers of snow crystals are growing by riming, rather than small numbers of graupel particles. It is therefore not obvious that 1 splinter produced per 200 drops rimed will still be appropriate. In this abstract comparisons are made between data produced by model runs with 400 rimed drops per splinter, 200 rimed drops per splinter, 50 rimed drops per splinter and MRF data Bower *et al.*, (1996).

4. RESULTS

Comparing the results, from the model runs, with the measured aircraft data, indicates that the best parameterization of the Hallett-Mossop process will incorporate a splinter production rate of 1 splinter per 200 rimed drops >24μm.

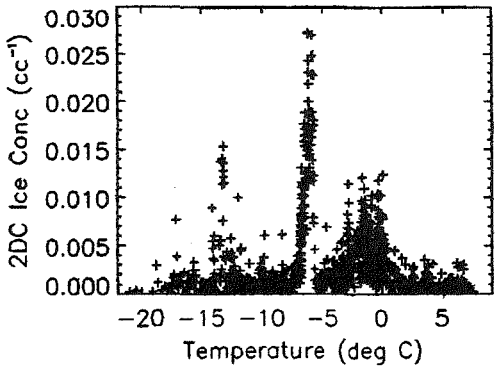

Figure 2. Recorded aircraft data of a Nimbostratus ice crystal concentration (>125μm), Bower *et al.*, (1996).

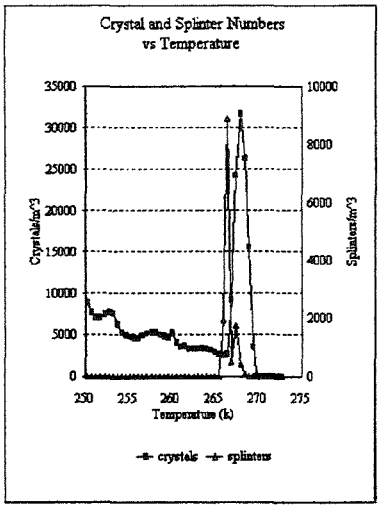

Figure 1. Model data. All crystal and splinter numbers.

The above figures illustrate this. The model considers all splinters that have grown to 100μm to be crystals. It can be seen that the concentration of crystals in the Hallett-Mossop region is directly comparable with the recorded measurements from the MRF flight, of around 30000 crystals/m^3.

5. THE UNIFIED MODEL HALLETT-MOSSOP PARAMETERIZATION

The results from the stratiform cloud model now enable us to complete the parameterization of the Hallett-Mossop process that is to be included in the next version of the UK Meteorological Office GCM.

The parameterization of the rate of production of splinter numbers by the Hallett-Mossop process which is to be added to the Rutledge and Hobbs parameterization is given by

$$N_{hm} = (PGACW + PSACW) * f * 1/m_{25} \,, \quad (2)$$

where **PGACW** is the rate of collection of cloud liquid water by graupel, (**kgm^{-3}s^{-1}**); **PSACW** is the rate of collection of cloud liquid water by snow, (**kgm^{-3}s^{-1}**); **f** is the fraction of droplets greater than 25μm in diameter; $\mathbf{m_{25}}$ is the average droplet mass for droplets > 25μm in diameter; and **s** is the number of droplets rimed for the production of 1 splinter, (set to 200).

The Rutledge and Hobbs parameterization will then grow the splinters by vapour deposition, riming, capture by raindrops, aggregation and capture by graupel.

6. ACKNOWLEDGEMENTS

This work was supported by the United Kingdom Meteorological Office and The

Department of the Environment.

7. REFERENCES

Ballard S.P. and Hutchinson M.G. Parameterization of mixed-phase cloud and precipitation. ***Proceedings of ECMWF/GEWEX workshop on modelling, validation and assimilation of clouds.*** (1994).

Bower K.N., Moss S.J., Johnson D.W., Choularton T.W., Latham J., Brown P.R.A., Blyth A.M. and Cardwell J. A parameterization of the ice water content observed in frontal and convective clouds. submitted to ***Q. J. R. Meteorol. Soc.*** (1996).

Fletcher N.H. The physics of rainclouds. ***Cambridge University Press*** (1962).

Gregory D. and Morris D. The sensitivity of climate simulations to the specification of mixed phase clouds. ***Climate Dynamics*** (1996).

Griggs D.J. and Choularton T.W. Freezing modes of riming droplets with application to ice splinter production. ***Q. J. R. Meteorol. Soc.*** 109 pp. 243-253 (1983).

Hallett J. and Mossop S.C. Production of secondary ice particles during the riming process. ***Nature*** 249 pp. 26-28 (1974).

Hallett J., Sax R.I., Lamb D. and Murty A.S.R. Aircraft measurements of ice in Florida cumuli. ***Q. J. R. Meteorol. Soc.*** 104 pp. 631-651 (1978).

Harris-Hobbs R.L. and Cooper W.A. Field evidence supporting qualitative predictions of secondary ice production rates. ***American Meteorological Society*** 44 pp. 1071-1082 (1987).

Rutledge S.A. and Hobbs P.V. The mesoscale and microscale structure and organization of clouds and precipitation in midlatitude cyclones. VIII: a model for the 'seeder-feeder' process in warm-frontal rainbands. ***Journal of the Atmospheric Sciences*** 40 pp. 1185-1206 (1983).

Willis P.T. and Hallett J. Microphysical measurements from an aircraft ascending with a growing isolated maritime cumulus tower. ***Journal of Atmospheric Sciences*** 48 pp. 283-300 (1991).

A PARAMETERIZATION FOR PREDICTING FRACTIONAL CLOUDINESS IN THE TRADE CUMULUS BOUNDARY LAYER

Alistair M Fraser and Christopher S. Bretherton

Atmospheric Sciences, University of Washington, Seattle, WA 98195, USA

1. INTRODUCTION

Boundary layers capped with shallow cumuli are an ubiquitous feature of the subtropical and tropical oceans, and are common in many other regions of the world. Their typical structure consists of a turbulent subcloud layer (typically 500m deep), a weak shallow stable layer (near the lifting condensation level (LCL) of the subcloud air), a conditionally unstable cumulus layer (typically 500-2000m deep), and a strongly stable layer called the trade inversion (Augstein et al 1974). This boundary layer structure is also observed in a transitional regime between stratocumulus and cumulus (Albrecht et al 1995).

Our goal is to develop an improved physically based boundary layer parameterization that predicts the cloud fractional area (CFA), and boundary layer structure that incorporates recent insights into the dynamics of these boundary layers. Current schemes for this purpose have several shortcomings. For example, reasonable changes in ad hoc internal parameters governing the lateral entrainment rate and updraft fraction in Albrecht's (1984) two layer cumulus-capped boundary layer model can drastically affect the mean structure (Bretherton 1993). Other parameterizations treat cumuli as laterally entraining plumes with no detrainment below cloud top. Tiedtke (1991) assumes that detrainment and entrainment per unit of cloud base vertical mass flux are equal to each other. None of these assumptions are consistent with recent results of three dimensional large eddy simulations (Siebesma and Cuijpers 1995; hereafter SC).

Mixing processes at the trade inversion also have a strong impact on the vertical humidity profile in the boundary layer (see x). Wyant et. al. (1996) suggest that penetrative entrainment of above-inversion air by overshooting cumuli regulates the liquid water content of air detrained from cumuli at the inversion and feeds back on the cloud fraction. Of current parameterizations, only Tiedtke's (1993) cloud parameterization scheme explicitly couples stratocumulus 'anvil' cloud properties to the liquid water detrained from their feeding cumuli.

The parameterization we propose here combines improved representations of cumulus lateral entrainment and detrainment, penetrative entrainment and clouds formed by the detrainment of liquid water from cumuli. To test our approach, we first compare our results with the BOMEX case used in SC. We then compare the model to the first ASTEX Lagrangian experiment and a week long composite of observations taken at the R/V Valdivia during ASTEX. We can reproduce the temperature and moisture soundings as well as the diurnal variation of the cloud fraction quite well in all of these cases.

2. MODEL PHYSICS

The model is divided into equations governing the evolution of the sub-cloud mixed layer, and equations governing the conditionally unstable cloudy layer.

The mixed layer's depth and thermodynamic evolution is determined following the approach of Albrecht (1984) and Bretherton (1993) from surface fluxes, entrainment of air from the base of the cumulus layer, and a cloud base mass flux. The top of the mixed layer is constrained to be the LCL of mixed layer air. This determines the updraft mass flux at cloud base.

The cloudy layer thermodynamically evolves in response to imposed large-scale subsidence, horizontal advection, internally calculated radiative warming, the compensating mass flux of cumulus convection, and the convective thermodynamic source terms. The convective source terms and the compensating mass flux are determined as described below. The model is discretized on a fixed vertical grid with spacing $\Delta z = 75$m.

3. CONVECTIVE SCHEME

Our representation of a cumulus cloud is best described as a buoyancy-sorting, entraining plume model. Starting with the cloud base mass flux as computed by the mixed layer formulation, we compute the

lateral entrainment E into the cumulus updraft at each grid level as it rises to the trade inversion assuming a constant fractional entrainment rate $\varepsilon = 3*10^{-3}$ m^{-1} to match the diagnosed entrainment of SC (using their updraft decomposition).

The entrained air $E(z)$ is combined and divided into a uniformly distributed spectrum of mixtures ranging from undilute updraft to pure environmental air (following Raymond & Blyth (1986)). All positively buoyant mixtures remain in the rising updraft while negatively buoyant mixtures sink without further mixing to their level of neutral buoyancy (LNB). When the updraft reaches the trade inversion (where it is neutrally buoyant), it is composed of a mixture of undilute mixed-layer air and all the positively buoyant mixtures formed at grid levels below.

The updraft is then assumed to overshoot by one grid point above its LNB, where it entrains penetratively as suggested by the LES simulations of the stratocumulus to trade cumulus transition of Wyant et al (1996). The penetrative entrainment mass flux is proportional to the inverse of the bulk convective Richardson number, the updraft mass flux and an entrainment efficiency A. We set the value of A to be 0.45 as determined from their numerical simulations. After entrainment, which substantially dries the overshooting updraft air, it settles to its LNB.

Our model produces a two gridpoint thick detrainment layer in the trade inversion. If this detrained air is saturated, it is identified as stratocumulus cloud and can contribute to the CFA. After a specified "anvil lifetime" $L_t = 2800$ seconds, the air undergoes radiative cooling for a specified length of time after which it mixes with just enough environmental air from the vicinity of the parcel to evaporate all the liquid water. This air then settles to its LNB. We plan in the future to use a radiative-convective mixed layer model to predict L_t instead of specifying it.

The CFA is the ratio of the mass of saturated air detrained into the base of the inversion in the last L_t seconds to the overall mass of air at that grid level.

4. RADIATION

We use a two-stream longwave emissivity scheme and a 3-band shortwave scheme (Wyant et al. 1996). Two radiational profiles are calculated, one for the 150m thick stratocumulus 'anvil', and one for the remaining environmental air. The two radiational profiles are then linearly combined according to the fractional cloudiness.

5. COMPARISON WITH BOMEX AND LES

We compare our model with SC's BOMEX trade cumulus simulations, using the same initial soundings and forcings with two exceptions. We increase the subsidence rate above the inversion so as to remain constant above the inversion base. This helps to stabilize the inversion height allowing the model to create a comparable steady state to their LES simulation. We also keep the radiational cooling uniform above the inversion instead of decreasing it to zero.

Our steady state differs from the initial conditions by less than one degree K and one g kg^{-1} at all points in the cloudy layer. Our CFA stays at approximately 20%, in agreement with SC. A comparison of our modeled detrainment profiles to those of SC is shown in figure 1, while our modeled entrainment profiles are shown in figure 2. That our entrainment is similar near cloud base indicates that the mixed layer scheme is producing an acceptable cloud base mass flux. Excess entrainment over SC above 1500m could be because SC's measured lateral entrainment rate ε decreases above 1500 m while our's remains constant..It could also mean that some *negatively* buoyant mixtures should be mixed into the updraft.

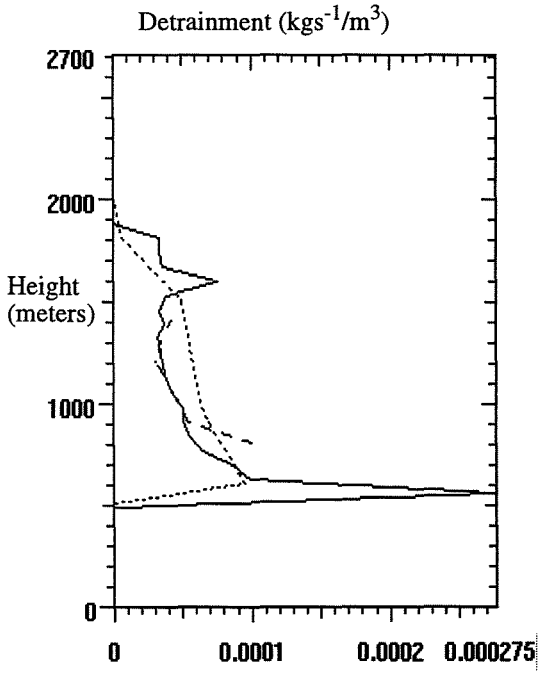

Figure 1: Modeled detrainment (solid), LES detrainment (dotted), and Observed detrainment (dashed) for the BOMEX steady state of SC.

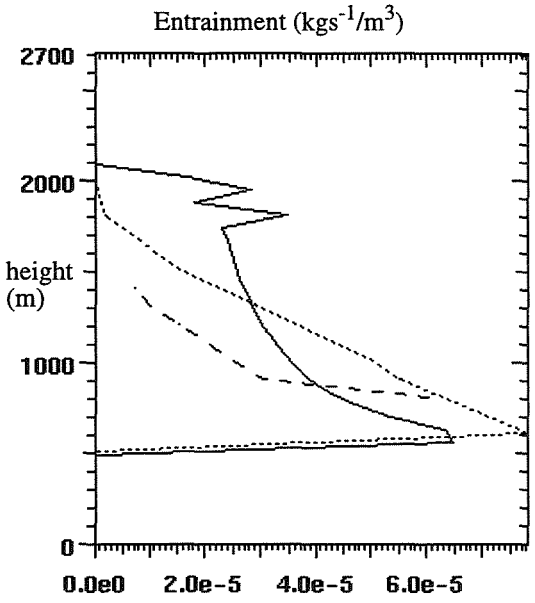

Figure 2: Modeled entrainment (solid), LES entrainment (dotted) and observed entrainment (dashed) for the BOMEX steady state of SC

6. COMPARISON OF MODEL WITH ASTEX EXPERIMENTS

The model was used to simulate the average diurnal cycle observed by the R/V Valdivia during June 8-15, 1992 in ASTEX (Betts et al. 1995), and the transition from stratocumulus to trade cumulus observed in the first ASTEX Lagrangian experiment (Bretherton 1995a), (Bretherton 1995b).

Both cases involved relaxing the above inversion air to different observed soundings over time. The start of the relaxation was 150m above the height of the inversion. We can reproduce the mean temperature and moisture soundings to within 1K and 1 g kg^{-1}, predict the height of the inversion within 200m, and produce the correct variation in CFA.

In simulating the observations of the R/V Valdivia, the aim was to capture the diurnally varying CFA while simultaneously keeping the soundings in steady state. Modeling this case involved adding thermodynamic source terms as described in Betts et al (1995) Figure 3 shows the modeled and observed variation in CFA for the R/V Valdivia observations during a cycle of two days in the simulation.

Figure 4 shows the modeled and observed θ_v for hour 42 of the first ASTEX Lagrangian experiment. The simulation was started at the first hint of decoupling

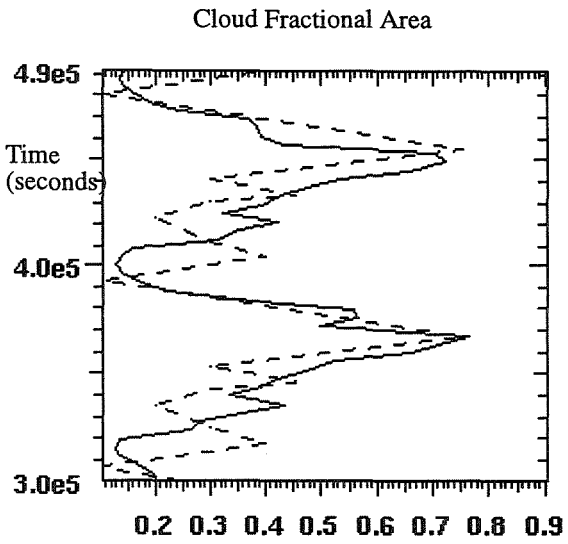

Figure 3: Observed (dashed) and modeled (solid) CFA for the diurnally varied steady state for 2 days. Observations were taken by the R/V Valdivia during ASTEX.

(hour 16). As the boundary layer deepened, the CFA decreased from 100% to 50% which is consistent with observation..

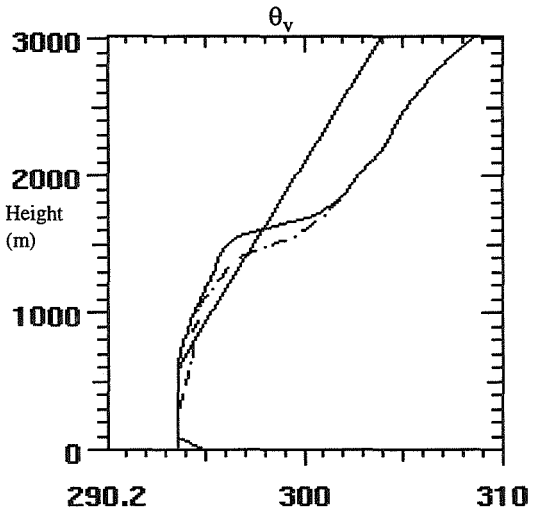

Figure 4: Observed (dashed) and modeled (solid) soundings of θ_v (K) at hour 42 in the first ASTEX lagrangian experiment.

7. SENSITIVITY EXPERIMENTS

We looked at how the temperature, moisture and CFA vary over a broad range of values of the lateral entrainment coefficient ε, the entrainment efficiency A,

and the anvil lifetime L_t. The temperature and moisture soundings were not sensitive (to within 1 K and 1 g kg^{-1}) when varying ε between 0..007 and 0..0007, L_t between 2300 and 3360 seconds, and A between 0 and 1. The CFA, on the other hand showed significant sensitivity to these parameters.

Decreasing ε caused an increase in the CFA by as much as 40% (and vice versa). Increasing L_t increased the CFA for all values of ε and A. With ε =0.003 and A=0.45, varying L_t by 560 seconds can cause a change in the CFA by as much as 30%. The sensitivity to A is largest when ε is lowest, where it can cause the CFA to vary by 80%.

8. REFERENCES

Albrecht, B. A., 1981: Parameterization of trade-cumulus cloud amount. *J. Atmos. Sci.,* **38**, 73-89.

---------, A.K. Betts, W. Schubert, and S.K. Cox. 1979a: A model of the thermodynamic structure of the trade-wind boundary layer: Part I: Theoretical formulation and sensitivity tests. *J. Atmos. Sci.*, **36,** 73-89.

----------, C. S. Bretherton, D. Johnson, W. Schubert and A. S. Frisch, 1995: The atlantic stratocumulus transition experiment (ASTEX). *Bull. Amer. Meteor. Soc.*, **76**, 889-903.

Arakawa, A., and H. Schubert, 1974: Interaction of a cumulus cloud ensemble with the large-scale environment. Part I: Theoretical formulation and sensitivity tests. *J. Atmos. Sci*, **31**, 674-701.

Augstein, E., H. Schmidt, and F. Ostapoff, 1974: The vertical structure of the atmospheric planetary boundary layer in undisturbed trade winds over the Atlantic Ocean. *Bound.-Layer Meteor.*, **6**, 129-150.

Betts, Alan K., C.S. Bretherton, E. Klinker, 1995: Relation between mean boundary-layer structure and cloudiness at the R/V Valdivia during ASTEX. *J. Atmos. Sci.*, **52**, 2752-2762.

Bretherton, C. S., 1993: Understanding Albrecht's model of trade cumulus cloud fields. *J. Atmos. Sci.*, **50**, 2264-2283.

----------, R. Pincus, 1995: Cloudiness and marine boundary layer dynamics in the ASTEX lagrangian experiments. Part I Synoptic setting and vertical Structure. *J. Atmos. Sci.*, **52**, 2707-2723.

----------, P. Austin, S.T. Siems, 1995:Cloudiness and marine boundary layer dynamics in the ASTEX lagrangian experiments, Part II: Cloudiness, drizzle, surface fluxes and entrainment. *J. Atmos. Sci.*, **52**, 2724-2735.

Raymond, D. J. and A. M. Blyth, 1986: A stochastic model for nonprecipitating cumulus clouds. *J. Atmos. Sci.*, **43,** 2708-2718.

Siebesma A. P. and J. W. M. Cuijpers., 1995: Evaluation of parametric assumptions for shallow cumulus convection. *J. Atmos. Sci*, **52**, 650-666.

Tiedtke, M., 1989: A comprehensive mass flux scheme for cumulus parameterization in large-scale models. *Mon. Wea. Rev.*, **117**, 1779-1800.

Wyant, M. C., C. S. Bretherton, H. A. Rand, and D. E. Stevens, 1996: Numerical simulations and a conceptual model of the stratocumulus to trade cumulus transition. *J. Atmos. Sci.*, accepted for publication.

Parameterisation of Cloud Droplet Condensational Growth

Alan M. Gadian[1], Jean-Louis Brenguier[2] and Wojciech W. Grabowski[3]

[1] Physics Dept, UMIST, Manchester, M60 1QD, UK
[2] METEO-FRANCE (CNRM/GMEI), Toulouse, France
[3] MMM/NCAR, Boulder, Colorado, USA

1. INTRODUCTION

Complete numerical simulation of the coupling between the condensation process and the dynamics in convective clouds is still not feasible because of the range of scales needed to represent explicitly, from the cloud scale (km) to the microphysical scale (cm). Multi-dimensional Eulerian models are suitable for the simulation of a complete cloud, but small scale microphysical processes must be parameterised at the sub grid scale. Inversely, Lagrangian parcel models can be run with very short time steps, but they represent a unique parcel in the cloud.

Eulerian simulations represent an ensemble average of the processes that are not explicitly represented by the model. For example, the dynamics at the sub-grid scale is treated as turbulence and the mean effect of this turbulence must be parameterised. There is no parameterisation of the coupling between the turbulence and the microphysics, and thus the droplet growth is calculated from the mean values of the thermo-dynamical parameters.

Lagrangian schemes, where individual droplets can be followed, are more suited for the calculation of the Lagrangian integral of supersaturation encountered along the droplet trajectory, whose variability determines the spectrum broadening. The fluctuations in supersaturation can be derived from the thermodynamics and the droplet concentration in the air surrounding the droplet. Except for the simplest case of an adiabatic parcel, it is not clear what these conditions can be along the trajectory of a droplet in an actual cloud.

The approach here aims at the coupling between an Eulerian model, that provides air parcel trajectories in a realistic environment, and a Lagrangian microphysical model running along these trajectories. The trajectories are chosen by selecting a location in the Eulerian simulated field and calculating a series of trajectories ending at this location. The variability in the trajectories is obtained by adding a stochastic component to the Eulerian velocity field. If this process is consistent, the ensemble average of the Lagrangian simulations must be similar to the Eulerian result at the selected location. After this condition has been verified, the Lagrangian scheme can then be used for testing various parameterisations of the coupling between the turbulence and the microphysics.

The similarity between the two representations is strongly dependent upon the statistics of the stochastic components of the velocity field that must be consistent with the parameterisation of the turbulence in the Eulerian frame. This presentation shows the tests of the methodology.

2. APPROACH

2.1 Eulerian

A two-dimensional Eulerian model based on Smolarkiewicz et al (1990) is used as a dynamical framework in which the droplet microphysical scheme of Brenguier et al. (1993) is applied. The Eulerian computed data for the temperature, droplet (b^2) spectra, the velocity, vapour mixing ratio, cloud water mixing ratio and the Turbulent

Kinetic Energy fields were stored for later use in the Lagrangian trajectory analysis.

2.2 Lagrangian

To determine the ensemble of paths which are required to represent the various origins of the air ending at a particular point in space and time, back trajectories are calculated using the Eulerian dynamical fields. The stochastic process of turbulence in the Eulerian frame, is simulated with a random velocity component of magnitude determined by the Turbulent Kinetic Energy (Klemp et al., 1978) and applied at each time step on the trajectory. Two hundred paths in the backward direction were created for use in the forward trajectory ensemble calculation required for a Lagrangian simulation. Inhomogeneous and homogeneous activation was enabled when supersaturation was attained, and the droplet spectra growth was obtained by integration of the supersaturation (b^2)

3. RESULTS

Eulerian simulations were completed for 1500 seconds using the Hawaiian warm cloud measurements of Raga et al. (1990). In summary, the observations showed that warm clouds developed in the unstable boundary layer, but that the convection had difficulty in penetrating the stable layer above 1.7km, causing the clouds to spread horizontally. For the model computations, a spatial resolution of 20 metres and a time-step of 2.5 seconds was used. A comparison was directly made between the Eulerian b^2 distribution and the frequency distribution of the b^2 values calculated in the Lagrangian frame.

The computations were made for many different parts of the cloud, but only one is presented below to demonstrate the technique.

4. DISCUSSION

Figure 1 shows the background cloud water field at 1500 seconds and the ensemble of trajectories. The ending trajectories' location has been chosen in a region that should be affected by mixing. In a sense, the figure is misleading because the trajectories correspond to all the time steps from the beginning of the simulation, while the LWC field is represented only at the last time step. For this reason, the trajectories are apparently crossing a region void of cloud while, at this time, earlier in the simulation, the cloud was in fact at the level of the trajectories. Figure 2 shows the b^2 distributions for the Eulerian calculations (x) and the frequency distribution of the Lagrangian b^2 values (o).

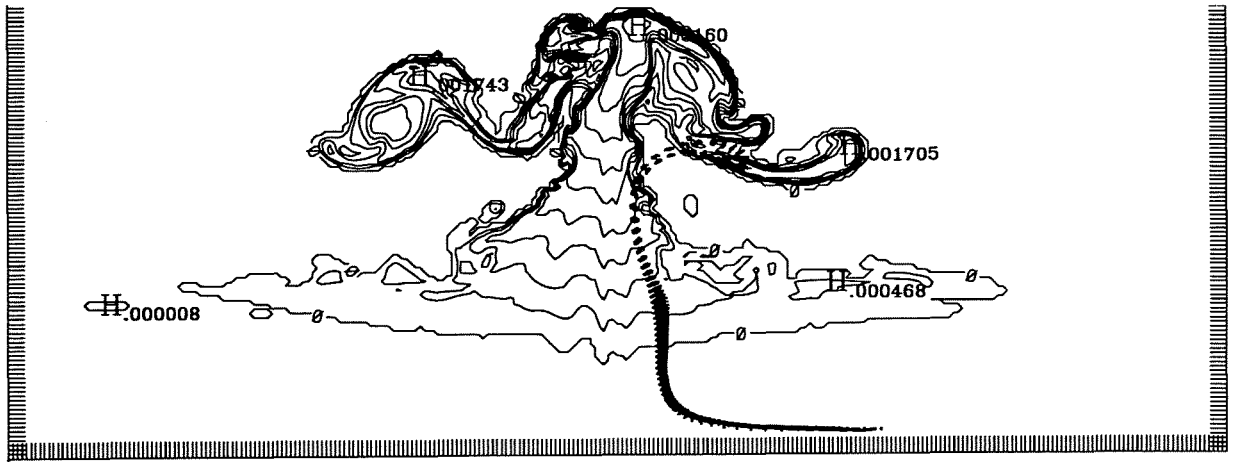

Fig. 1 Two hundred trajectories super-imposed on the 1500s. field of cloud water contours at 0.003 kg/kg intervals. The horizontal ticks are at 20 m. intervals

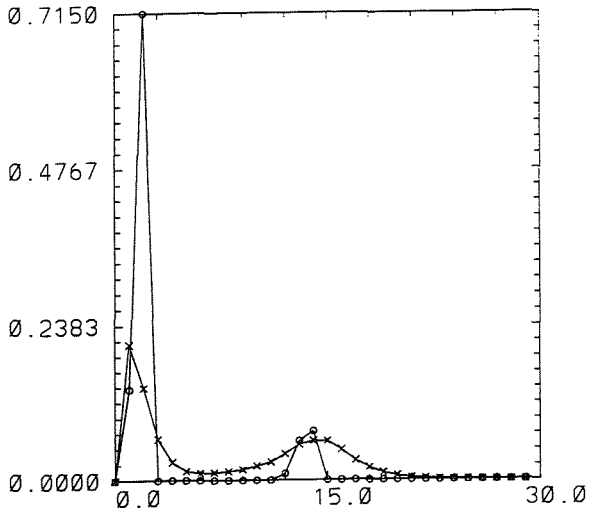

Fig. 2 Comparison between the Eulerian x, and the Lagrangian o, b^2 spectra. The curves (with normalised integrals) display the b^2 class, $(r + 2\ \mu m)^2$, on the abscissa, corresponding to a radius, r, varying from 0 to 15 μm

The validation step shows that the ensemble of the values of the integral of supersaturation for populations of droplets following various trajectories ending at the same point, produces a frequency distribution similar to the b^2 distribution calculated in the Eulerian frame.

The main feature of the chosen location is the bimodality of the b^2 spectrum that shows that at this location there are droplets ascending from the cloud base mixed with droplets originating from a higher source of activation. This secondary source of activation has been discussed in Brenguier and Grabowski, 1993. Fig. 2 shows that the calculation of the backward trajectories allows reproducing these two origins and partially preserves the proportion of droplets from each one. Considering the mode corresponding to the droplets from the cloud base, it can be noted that the Lagrangian scheme produces a narrower distribution than the Eulerian one.

In the Eulerian frame, the broadening results from turbulent mixing between adjacent boxes and numerical broadening of the advection scheme in the b^2 scale. In the Lagrangian frame, the broadening results only from the variety of the trajectories since, by definition, each trajectory contributes to the frequency distribution, a single value of b^2. This results suggests that the variance in the distribution of the random components of the velocity field that are used for the calculation of the backward trajectories is slightly underestimated.

This study shows how the Eulerian and Lagrangian frames can be coupled and how the method can be validated. It is now planed to use the Lagrangian frame for studying various contributions to the variability of the integral of supersaturation and their effects on droplet spectra broadening.

ACKNOWLEDGEMENTS

This research was supported by Meteo-France and INSU under grant D13570

REFERENCES

Brenguier, J-L. and Grabowski, W. W. 1993, Cumulus Entrainment and Cloud Droplet Spectra; A Numerical Model within a Two-dimensional Framework, J. Atmos. Sci. 50, pp120-56

Klemp, J.N. and Williamson, R. 1978, The Simulation of Three Dimensional Convective Storm Dynamics, J. Atmos. Sci. 35, pp1071-96

Raga, G , Jenson, J and Baker, M. 1990, Characteristics of Cumulus Band Clouds off the coast of Hawaii, J. Atmos. Sci, 47, pp338-55.

Smolarkiewicz, P. et al. 1990, The multi-dimensional positive definite advection transport algorithm, J. Comp. Phys. pp355-75

PARAMETERIZATION OF CCN CONCENTRATION BASED ON THE CALCULATION OF THE VERTICAL PROFILE OF AEROSOL PARTICLES

Julia Phelps, M. H. Smith and Colin D. O'Dowd

Physics Dept., UMIST, Manchester, M60 1QD, UK

1. INTRODUCTION

Aerosol particles can, under certain conditions, be activated to form cloud droplets; particles which are activated are known as cloud condensation nuclei (CCN). The CCN concentration directly influences the concentration of cloud droplets in a cloud, Twomey (1974). An increase in aerosol concentration, perhaps due to an increase in anthropogenic particle releases, can increase the number of cloud droplets formed, which will decrease the effective radius of the droplets. This inhibits precipitation development and increases cloud lifetime, which affects the radiative properties of cloud, Charlson et al (1992). Thus it is important to know aerosol concentration at cloud base, during cloud formation, to better understand the cloud's properties.

It is common when modelling cloud formation to assume a well-mixed boundary layer; in which case a surface measurement of aerosol distribution is often sufficient to calculate the CCN concentration at cloud base. However this is not always a valid assumption as the boundary layer is not always well-mixed and can also be composed of various sub-layers, with different thermodynamic characteristics, that can markedly affect the aerosol profile, Turton and Nicholls (1987) and O'Dowd and Smith (in press).

A semi-empirical model is outlined here, which calculates the total aerosol profile in the boundary layer from the thermodynamic structure and aerosol concentration at ground level, and thus, takes into account the amount of mixing that may be taking place. The aerosol size distribution is then derived according to the air mass history, using a parameterization based on inferred chemical composition using volatility measurements. From the derived spectra the CCN concentration at cloud base can be estimated.

2. FIELD MEASUREMENTS

Field measurements were used to both develop and test the one-dimensional semi-empirical model. Data from four measurement campaigns were used. These comprise airborne measurements taken at Carlisle in December 1991 and June 1992, and at Gamston and Woodford, in NW England, in March 1991, as well as ground based measurements taken at Westcott, Berkshire, in 1993.

The airborne measurements include accumulation mode aerosol (readily activated as CCN in stratiform clouds) concentrations and size distributions throughout the vertical extent of the boundary layer, under different meteorological conditions. Also, extensive measurements have been taken using an airborne volatility system to determine the volatile properties of aerosol, from which the chemical composition can be inferred. Typically, the aircraft, a Cessna 182, would obtain vertical profiles of the meteorological parameters, such as temperature, pressure and relative humidity and total aerosol loading. Then a series of horizontal flights made at selected heights collected aerosol size distributions and volatility data.

Aerosol measurements were made using a PMS ASASP-X optical particle counter in the radius range 0.05 - 1.5μm. The probe was mounted in the cabin of the plane, and air supplied to it via a duct from a nozzle which protruded forward from the port wing. This intake tube was kept 20-30°C above the ambient temperature and hence all the spectra recorded by it are considered 'dry'. For a full description of the instruments and the methods used to obtain all the data, see O'Dowd and Smith (1996).

The volatility technique used to collect the data outlined here is similar to that described in O'Dowd et al (1993), but modified for airborne use. The temperature response of atmospheric aerosol in the volatility instrumentation is interpreted by comparison with a range of polydisperse laboratory generated aerosol. Table 1 shows examples of

aerosol species and their evaporation/ decomposition temperatures, O'Dowd et al (1993).

Aerosol	Volatility Temp °C
H_2SO_4	≈100
$(NH_4)_2SO_4$	≈200
NaCl	≈650
soot	≈820

Table 1: Common aerosol constituents and their decomposition temperatures

The volatility measurements were made using the PMS ASASP-X equipped with four temperature-controlled heated inlet tubes each operating at a different temperature. Four tubes were used to reduce the sampling time of the ground based version with its single tube. The temperatures were selected to be 40°C, 80°C, 160°C and 350°C. Thus the 40°C tube resulted in a dry ambient reference spectra, the spectra from the 80°C tube is due to the loss of, predominantly, volatile organics, the 160°C tube sulphuric acid aerosol, and from the 350°C tube an ammonium sulphate/bisulphate spectra results. Aerosol remaining above 350°C is generally thought to be soot carbon or sea-salt depending on the underlying air mass characteristics.

3. VERTICAL PROFILES

The aerosol concentration at cloud base is dependent not only on the column total of aerosol within, but also how it is distributed vertically throughout, the boundary layer. Therefore, whether mixing is taking place, and if so how much, is of vital importance in estimating the number of aerosol that will be activated to form cloud droplets. The degree of mixing can be ascertained by examining the stability of the boundary layer.

The model takes into account the thermodynamic structure of the boundary layer, thus incorporating the amount of vertical mixing due to turbulence into the aerosol profile. The boundary layer is examined by looking at the virtual potential temperature, θ_V, profile to find the depth and position of the various layers and any inversions, and also the stability of these layers. Once this initial assessment has been made and the boundary layer structure determined, calculation of the aerosol profile is carried out as described below.

3.1 Unstable Conditions

For conditions to be well-mixed the boundary layer must be unstable, or neutral, and the temperature lapse rate sub-adiabatic. In well-mixed conditions, the aerosol concentration becomes uniform with height, thus if the surface concentration is known then so is the concentration at cloud base.

3.2 Stable Conditions

In the stable case, it is not sufficient to know only the surface concentration of aerosol in order to estimate the CCN at cloud base. Under stable conditions, when the lapse rate is superadiabatic, turbulent mixing is inhibited by opposing buoyancy forces, surface generated aerosol will not be able to progress very far beyond the surface layer. How much, or how little, mixing takes place depends on the strength of these buoyancy forces. Equation 1 shows how the buoyancy force at any point in the stable layer can be calculated from the θ_V profile.

$$F_B = -\frac{g}{\theta_V}\frac{\partial \theta_V}{\partial z} \qquad (1)$$

The θ_V profile is modelled using an exponential expression as described by Carlson and Stull (1986), and is shown in equation 2. $H_{\Delta\theta}$ is the e-folding depth and $\Delta\theta_S$ is the difference in potential temperature of the surface temperature and the temperature at the top of the stable layer.

$$\Delta\theta(z) = \Delta\theta_S \exp\left(\frac{-z}{H_{\Delta\theta}}\right) \qquad (2)$$

From this simple representation, plots of the buoyancy force against aerosol concentration were plotted for all the stable cases in the Carlisle

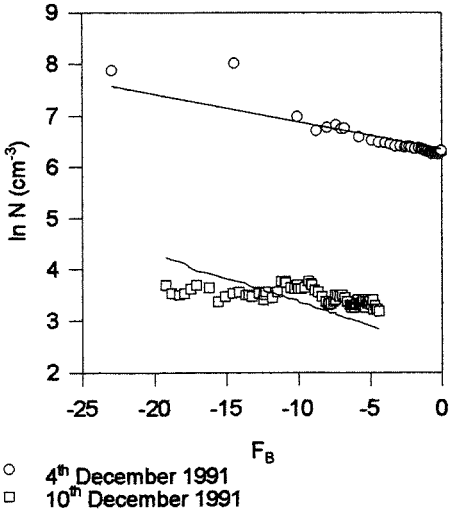

Figure 1: Plot showing the variation of total aerosol concentration, N, with buoyancy force, F_B, for two different days during the Carlisle field project. Also shown, solid line, is the empirical fit as described by equation 1.

project. It was found that these plots could be well fitted by an exponential equation of the form of equation 3, see Fig. 1. N_S is the aerosol

concentration at the bottom of the surface layer, b is the buoyancy force at the height the aerosol concentration is measured at and c is an e-folding parameter.

$$N = N_S \exp\left(\frac{F_B + b}{c}\right) \qquad (3)$$

A typical result from the total aerosol concentration profile calculation, is shown in Fig. 2. Near the surface there is a stable layer which becomes more well-mixed with increasing altitude until a capping inversion is reached at around 1km, when conditions become more stable again. The model takes these changes in stability into account and calculates the aerosol profile in each of the sub-layers of the boundary layer. Good agreement between model and measurements is found on those days where total aerosol profiles were measured, with the main features of the changes in concentration due to atmospheric stability duplicated.

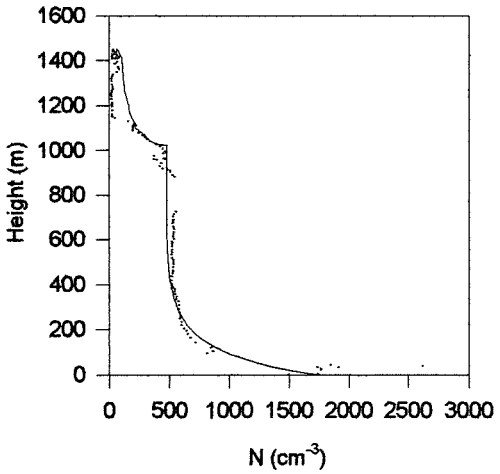

Figure 2: Graph showing measured total aerosol profile (dots) and the results of the model (solid line) for 4/12/1991, Carlisle project

4. AEROSOL SIZE DISTRIBUTION

These schemes above only calculate the total aerosol profile and say nothing about the aerosol size distribution, which is of importance in determining the number of CCN.

Size spectra of the sulphuric acid, ammonium sulphate and soot carbon fractions of the total aerosol size distributions, were inferred from a large collection of volatility measurements made during the Carlisle and Westcott campaigns. These field projects were involved in mainly measuring rural air, although recent air mass history influences the exact chemical composition of the aerosol particles and their evolution with time as the air mass traverses over land and sea.

Background spectra, taken as clean air uncontaminated by anthropogenic releases, were compared and used to derive a base spectra. This base spectra could then be modified according to air mass history to produce a spectra representative of the prevailing conditions. The modification factors were derived empirically from the rest of the data set, and the results of the total aerosol concentration profiles were incorporated to produce aerosol spectra at any height in the boundary layer.

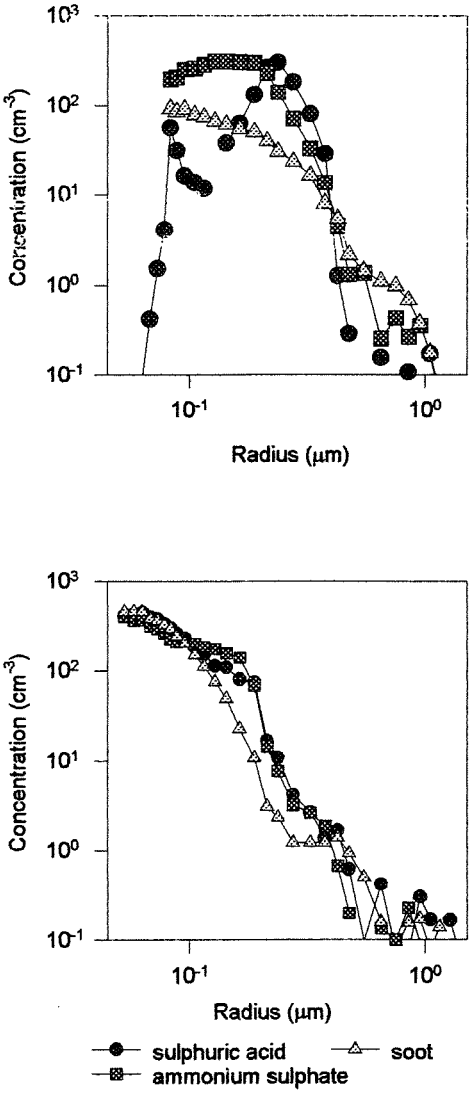

Figure 3: Graphs showing number concentration of sulphate, ammonium sulphate and soot for clean polar air (top), and continentally modified air (bottom).

Figure 3 shows a comparison between spectra showing clean polar air, newly arrived above the UK, and a modified air mass that had spent five days over the UK. It can be seen from these results that the polar air has generally fewer aerosol, as would be expected. Formation of sulphate aerosol can be seen in the continentally modified air by the presence of increased concentrations at low radii. The soot concentration also increases. These graphs

show how an air mass can be modified and are the basis of a parameterization scheme which calculates the aerosol distribution according to air mass history.

5. CCN CALCULATION

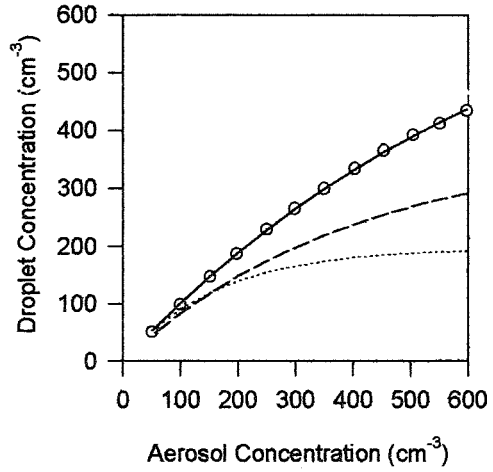

Figure 4: Droplet concentration plotted against aerosol concentration (o), and fit shown in equation 6 (solid line). Also shown are the Jones et al (1994), dashed, and O'Dowd et al (1996), dotted, relations.

The number concentration of CCN at cloud base is derived from the aerosol spectra from the model using the Kohler curve equation, (Equation 4). The Kohler curve describes the growth of a solution droplet as the relative humidity, and then supersaturation, increases, where a/r is the curvature term and b/r^3 is the solution term of the aerosol and b is a function of the dry radius. The curve shows that for a particular value of the supersaturation the growth of the aerosol droplet is no longer dependent on the increase in humidity. This supersaturation is known as the critical supersaturation and the corresponding radius, the critical radius. Any aerosol particle equal or greater than this critical radius is considered to be activated as a cloud droplet.

$$\frac{e_s'(r)}{e_s(\infty)} = 1 + \frac{a}{r} - \frac{b}{r^3} \qquad (4)$$

The critical supersaturation, S_c, is the peak supersaturation of the Kohler curve and is therefore found to be expressed as in equation 5. By substituting for a and b, for a particular aerosol chemical composition, in equation 5, the critical radius, r_c, can be found. If it is then assumed that all the non-soot aerosol act as CCN, the aerosol number spectra can be integrated from r_c upwards, thus giving the number of CCN in the cloud. The peak supersaturations were calculated using the results of a Lagrangian parcel model, Lowe et al (this issue).

$$S_c = \sqrt{\frac{4a^3}{27b}} \qquad (5)$$

Figure 4 shows the results of calculating the number of activated aerosol particles from the same spectra for different critical supersaturations and therefore different critical radii, compared with the total number of aerosol particles present. The fit through the data points is shown in equation 6,

$$N_C = 752\left(1 - \exp\left(-1.45 \times 10^{-3} N_A\right)\right) \qquad (6)$$

where N_A is the total number of aerosol particles present and N_C is the number activated to be CCN.

6. REFERENCES

Carlson M.A. and Stull R.B.,1986: Subsidence in the nocturnal boundary layer. *J. Climate Appl. Meteor.*, **25**, 1088-1099

Charlson R.J. et al, 1992: Climate Forcing by anthropogenic aerosols. *Science*, **255**, 423-430

Jennings S.G. and O'Dowd C.D., 1990: Volatility of aerosol at Mace Head, on the west coast of Ireland. *J. Geophys. Res.* **95**, D9, 13 937-13 948

Jones A. et al, 1994: A climate model study of indirect radiative forcing by anthropogenic sulphate aerosols. *Nature*, **370**, 450-453

Lowe J.A. et al, 1996: The effects of sea-salt aerosol on th eproduction of ulphate in the marine atmospheric boundary layer and its effect on stratiform clouds. *This issue*

O'Dowd C.D. et al, 1993: Physicochemical Properties of aerosols over the Northeast Atlantic: evidence for wind-speed related sub-micron sea-salt production. *J. Geophys, Res.*, **98**, 1137-1149

O'Dowd C.D. and Smith M.H. 1996: The vertical structure of aerosol in boundary layer thermodynamics. *Q. J. R. Meteorol. Soc.* in press

O'Dowd C.D. et al, 1996: The relative importance of NSS-sulphate and sea-salt aerosol to the marine CCN population. *This issue*

Smith M.H., 1988: Air parcel thermodynamic properties and aerosol particle concentrations in the maritime atmospheric boundary layer. *Q. J. R. Meteorol. Soc.*, **114**, 771-780

Turton J.D. and Nicholls S., 1987: A study of the diurnal variation of stratocumulus using a multiple mixed layer model.. *Q.J.R.Met.Soc.*, **113**, 969-1009

Twomey S.A., 1974: Pollution and the planetary albedo. *Atmos. Environ.*, **8**, 1251-1256

THE SENSITIVITY OF A LAM MODEL TO AN INCLUSION OF A CLOUD FRACTION IN AN EXPLICIT REPRESENTATION OF CONVECTION: PRELIMINARY RESULTS

A. Celeste Saulo - Matilde Nicolini
Depto de Ciencias de la Atmósfera. Universidad de Buenos Aires (UBA)
Centro de Investigaciones del Mar y la Atmósfera (CIMA)- UBA/CONICET
Buenos Aires, Argentina

1. INTRODUCTION

Cumulus parameterization has been widely recognized as a fundamental problem in numerical modeling. Also, it was shown that different parameterization schemes have different performance depending (among others) on grid spacing, model characteristics, and phenomena being modeled (Molinari and Dudek, 1992). This study presents some results using the LAHM/GFDL (Limited Area Hibu Model / Geophysical Fluid Dynamic Laboratory - CIMA version), with an explicit representation of convection, combined with a vertical diffusion scheme. This kind of representation was chosen because it has been previously shown (Saulo and Nicolini, 1994 and Nicolini and Saulo, 1995) that it provides a reasonably good representation of the precipitation pattern associated with deep convective events, compared with Arakawa and Schubert (1974) cumulus parameterization scheme. It also has the main advantage of solving a prognostic equation for cloud water, which is a fundamental variable in the feedback mechanism of clouds into the atmosphere.

The main purpose of this work is to test the sensitivity of the predicted precipitation fields to the inclusion of a cloud fraction (from now on CF) as it was formulated by Orlanski and Polinsky (1984). In this case, a heavy precipitation event associated with a squall line over Central Argentina was chosen. This situation was previously studied in Nicolini and Saulo (1995). The CF formulation will be presented in Section 2. The experiments designed for this study are described in Section 3 together with the analysis of the results. The effect of the different terms acting on the specific humidity tendency equation is discussed in Section 4. Finally, the conclusions and guides for future work are presented in Section 5.

2. THE CLOUD FRACTION REPRESENTATION

As it was mentioned in the previous section, an explicit representation of convection, as it was used by Ross and Orlanski (1982), has been chosen. In a later work, Orlanski and Polinsky (1984) pointed out that subgrid convection in a three dimensional mesoscale model, could be better represented if a coefficient suitable to modulate the condensation term (CF) was incorporated. In order to test the sensitivity of our model to the inclusion of a CF, the original condensation term in the thermodynamic and water substance conservation equations was modified as follows:

$$T(n+1) = T'(n+1) + \delta t * CD * \frac{L}{Cp * \pi} * CF$$

$$q(n+1) = q'(n+1) - \delta t * CD * CF$$

$$c(n+1) = c'(n+1) + \delta t * CD * CF$$

where T is temperature, q specific humidity, c cloud water, CD condensation, π Exner function, and primed variables indicate tentative values obtained for the time $t+\delta t$ with the assumption that no condensation or evaporation takes place. As it was stated by Orlanski and Polinsky (1984), CF(z) is a coefficient that represents the probability distribution of clouds in an area defined by the grid scale of the model. Viewed as the probability for a cloud fraction to occur at a given height, they've found that the following formulation for CF(z) was adequate:

$$CF(z) = 1 - \left(\frac{z}{H}\right)$$

Though it can be argued whether this is the best form for CF or not, it is an easy representation to test the sensitivity of a model to an inclusion of such formulation. If this can be shown, then further work will be needed in order to find a better expression for CF.

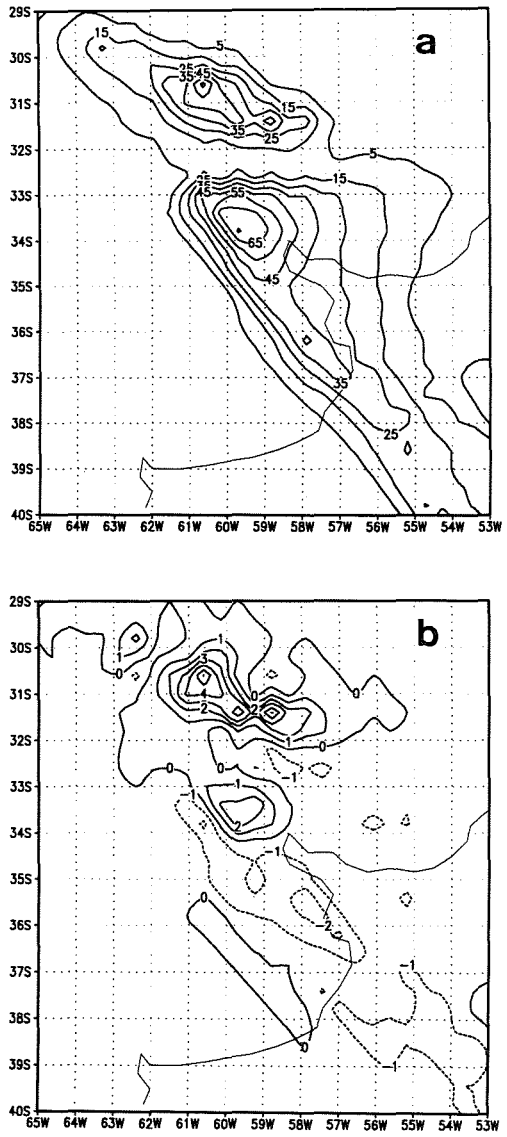

Figure 1: *a) Predicted precipitation amounts (contour interval 10 mm) for the period 12 UTC, 12 April 1983 to 0 UTC, 13 April 1983; CF1 experiment. b) CFZ precipitation amounts for the same period subtracted from the CF1 values (each mm).*

3. EXPERIMENTS DESIGN

The LAHM/GFDL model can be used with variable horizontal resolution, with a limit imposed by the hydrostatic assumption. In this case, the model was run with a grid spacing of 0.4° in latitude and 0.45° in longitude, over an area of approximately 2500 km on each side. The telescoping nesting technique was used in order to minimize the impact of the sudden change in resolution from coarser analyses (used to initialize and to provide boundary conditions) to a finer model grid. In the vertical, 9 sigma levels where first used, and two experiments where carried out: CF1, in which CF was one, i.e., no cloud fraction, and CFZ for which the CF formulation presented in Section 2, was used. Then, two more experiments where done, in which vertical resolution was doubled (i.e.18 levels) while horizontal resolution was reduced in order not to increase computation requirements. This experiments are referred to as 18-CF1 and 18-CFZ.

Figure 1a shows 12 hours accumulated precipitation obtained for CF1, and in Figure 1b, the difference between CF1 and CFZ for the same field is depicted (CFZ is subtracted from CF1). As it was expected, there is a decrease in precipitation amounts when CF(z) is included. Nevertheless, the impact is not significant in the area of maximum rain, being more intense in the secondary maximum surroundings. In the following section, this response will more carefully analyzed.

A similar comparison was performed between 18-CF1 and 18-CFZ, but the signal was even lower (not shown).

4. ANALYSIS OF THE WATER VAPOR CONSERVATION EQUATION

The relative magnitude of the different terms acting in the water vapor conservation equation will be analyzed to better understand the low sensitivity of the precipitation field to a change in the condensation/evaporation term, which is expected to be the most important contributor to changes in water vapor

amounts.

If the conservation equation for specific humidity is expressed as follows:

$$\frac{\partial q}{\partial t} = -V\cdot\nabla q - w\frac{\partial q}{\partial z} - CD + F_h + F_v$$

where the notation is as usual, then each of this terms can be measured individually at each time step, at any desired level.

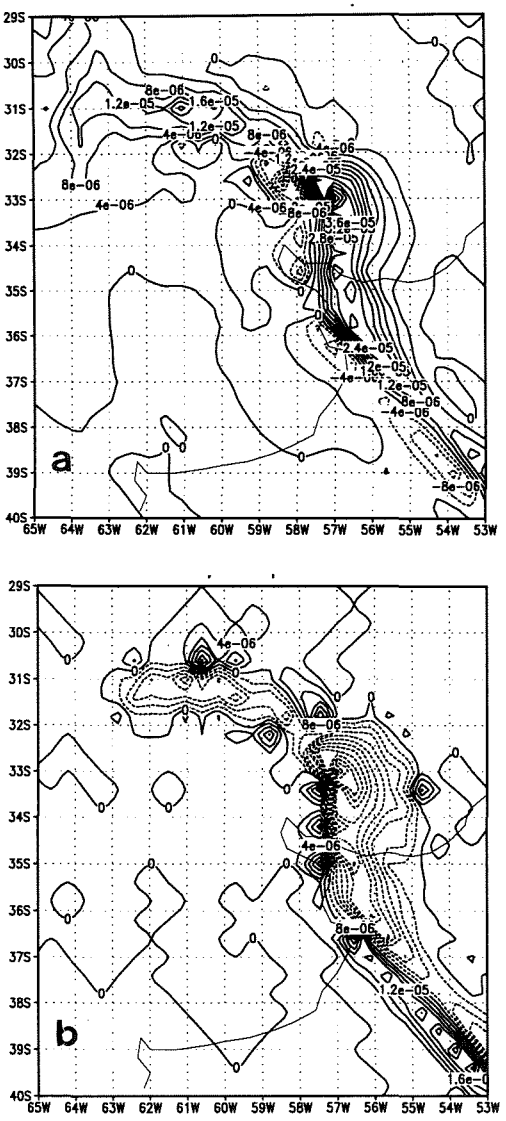

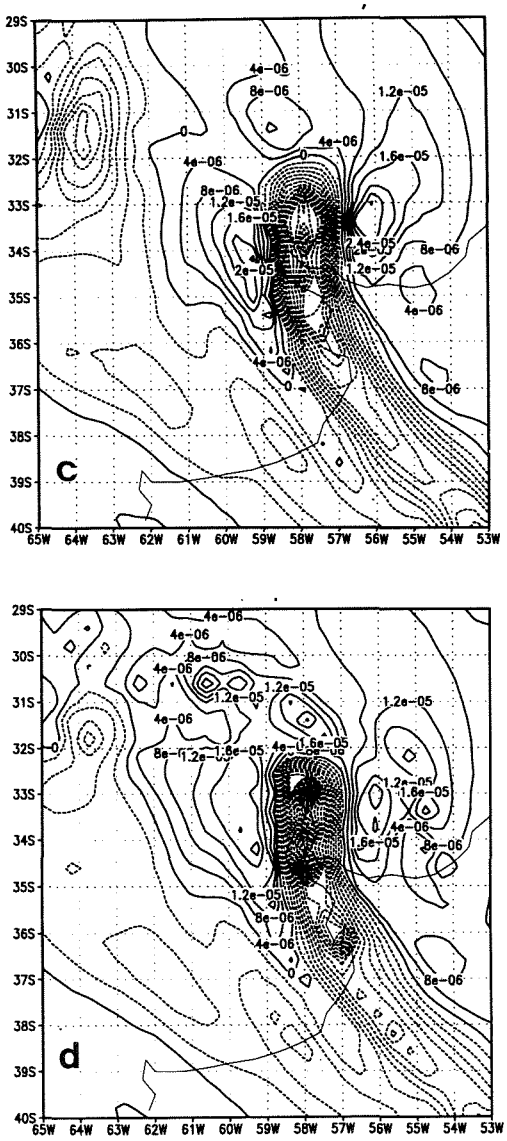

Figure 2: *Different terms of the specific humidity equation at 18 UTC, 12 April 1983, at the sigma level 0.5 a) vertical advection, b) condensation /evaporation, c) horizontal advection, d) tendency .Contour intervals are 2 10^{-6}.*

This analysis provides some interesting information. Both advective terms are of the same order of magnitude over medium and low atmosphere. Condensation/evaporation is locally as important as the others, but behaves opposite to vertical advection, so, at convective active areas, it can be thought as if they cancel each other, being the whole pattern dominated by horizontal advection effects. This can be seen in Figure 2, where this three terms together with the local variation of specific humidity are shown at sigma level 0.5 (approximately 550 hPa) at a time when convection is active. Both diffusivities are secondary terms, though vertical one has a greater order of magnitude in moist

convective areas because of its formulation (Saulo and Nicolini, 1995). This pattern is observed for both, CF1 and CFZ. Again, condensation and vertical advection effect the specific humidity local changes by comparable but opposite amounts. Accordingly, the net effect of including of including a CF(z) seems to be minimized.

6. DISCUSSION OF RESULTS

Four experiments were carried out in order to test the sensitivity of a regional model to the inclusion of a coefficient (CF(z)) which could modulate the intensity of convection in a explicit representation of this process. It was found that, when high horizontal resolution and 9 sigma levels are used, the response to the inclusion of a CF(z), is not as significant as it was expected to be. The condensation/evaporation term is diminished by CF(z), resulting in a relative increase of specific humidity. The decrease in vertical velocity produced by CF(z) effect on temperature, seems to be less important, but vertical advection (increased specific humidity but less vertical velocity) is not significantly modified, and the relation between vertical advection and condensation (being of similar magnitude but opposite sign) remains little affected.

An experiment with increased vertical resolution was performed in order to find out to what extent a better vertical representation could be more sensitive to CF(z). However, as horizontal resolution had to be lowered, even less response was found. In this sense, it seems clear that in order to better represent mesoscale characteristics of moist convective areas, both, high horizontal and vertical resolution are needed. The relative low sensitivity to CF(z) found in 9 and 18 levels, partially depicts the lack of representation of lower scale patterns associated with deep convection. It seems that, with the resolution used, only large scale patterns are captured, which remain unaffected by the present formulation of CF(z) (i.e. mainly stratiform precipitation is simulated, which is essentially the same profile proposed by CF).

Further work is needed to assess the impact of CF(z) in high both horizontal and vertical resolution. Preliminary studies, however, show a greater sensitivity when these conditions are implemented. This result is encouraging and justifies future research in this direction.

7. REFERENCES

-Arakawa, A. and W. H. Schubert, 1974: Interaction of a cumulus cloud ensemble with large-scale environment: Part I. J. Atmos. Sci., vol. 31, págs. 674-701.

-Molinari, J., y M. Dudek, 1992: Parameterization of convective precipitation in mesoscale numerical models: A critical review. *Mon. Wea. Rev.*, vol. 120, 326-343.

-Nicolini M. and A. C. Saulo 1995: "Experiments using the LAHM/CIMA model over Argentina in convective situations: preliminary results of precipitation fields". PWPR No. 7 - WMO/TD No. 699 - International Workshop on Limited-Area and Variable Resolution Models, October 1995, Beijing, China.

-Orlanski, I. and Polinsky, 1984: Predictability of mesoscale phenomena. Proc. Int. Symp. Nowcasting, 2nd, 1984. Norrkoping, Sweden, pp 271-280.

-Ross, B. B. and I. Orlanski, 1982: The evolution of an observed cold front. Part I: Numerical Simulation. J. Atmos. Sci., vol. 39, No. 2, pp 296-327.

-Saulo, A. C. y M. Nicolini, 1994: Numerical simulation of a mesoscale convective complex over South America: Sensitivity to different convective parameterizations. AMS Extended abstracts-Tenth Conference on Numerical Weather Prediction.

-Saulo, A. C. and M. Nicolini (1995): "Inclusión de la difusión vertical en un modelo regional de pronóstico: efecto sobre la precipitación" , *Meteorológica*, vol. 20, pp 25-36.

CALCULATION AND PARAMETRISATION OF THE EFFECTIVE RADIUS OF ICE PARTICLES USING AIRCRAFT DATA.

Sarah J. Moss, Peter N. Francis and Doug W. Johnson

Met. Research Flight, Y46, DERA, Farnborough, Hants GU14 6TD, U.K.

1. INTRODUCTION

Ice clouds are present around the globe at all altitudes and during all seasons, and they can have a large effect on the heating and cooling of the middle and upper troposphere. Therefore, for accurate climate prediction it is essential that they are adequately represented in numerical models. The grid spacing in these models is too large to explicitly resolve the microphysical processes occurring within these clouds. To produce more realistic model predictions, improved parametrisations of the microphysical effects in terms of the bulk model variables, have to be developed.

Slingo and Schrecker (1982) showed that the important parameters needed to describe the radiative properties of liquid water clouds i.e. the single scattering albedo, the extinction coefficient, and the asymmetry parameter, can be parametrised in terms of the liquid water content and effective radius r_e of the droplet size spectrum where

$$r_e = \frac{\sum_{n=1}^{15} r_n^3 N_n}{\sum_{n=1}^{15} r_n^2 N_n}$$

where r is the droplet radius and N is the droplet concentration. However, the range of particle habits present in ice clouds makes it much more difficult to determine an effective radius which can be used in the parametrisation of cloud radiative properties. Foot (1988) defined the effective radius of an ice particle to be the following:

$$r_e = \frac{\sum_{j=1}^{n} N_j \left(\frac{D_j}{2}\right)^3}{\sum_{j=1}^{n} N_j \left(\frac{A_j}{\pi}\right)}$$

where D is the diameter of a water drop of the same mass as the ice particle and A is the the ice particle's cross-sectional area. It has been shown that, for large irregular particles, the absorption coefficient depends on the volume of the particle and the scattering coefficient depends on the cross-sectional area. Therefore, it can be seen that r_e is proportional to the ratio of the absorption coefficient to the scattering coefficient, and this definition of r_e is consistent with the definition of effective radius for water cloud.

Observations of the microphysical characteristics of ice clouds from the Meteorological Research Flight's (MRF) C-130 aircraft have been analysed to investigate the variation of the r_e of ice particles. Results from experiments carried out around the U.K. and over the Sierra Nevada in frontal and orographic clouds will be presented. 18 flights in all were used nine of which came from the European Cloud and Radiation Experiment (EUCREX) that took place from 17 September to 9 October 1993, mainly over the Atlantic to the north and west of Scotland.

2. MEASUREMENTS.

The instruments used to obtain the microphysical data analysed were the Particle Measuring Systems (PMS) 2-dimensional cloud probe (2-DC) which measures cloud particles in the size range 12.5 to 400μm radius; the PMS 2-dimensional precipitation probe (2-DP) which measures particles in the size range 100 to 3200μm radius and the PMS Forward Scattering Spectrometer Probe (FSSP) which counts and sizes cloud droplets in the size range 1.5 to 21μm radius. These instruments are described fully in Baumgardner (1989). Temperature measurements were made with a de-iced Rosemount platinum resistance thermometer, and the liquid water content was measured with a Johnson-Williams hot wire probe. Broad-band long-wave (4-50μm) irradiances were measured using modified Eppley pyrgeometers (Foot 1986), and the broad-band short-wave (0.3-3.0μm) irradiances were measured using standard Eppley clear-domed pyranometers. Full details of the instruments mounted on the MRF C-130 are given in Rogers et al. (1995).

The data from the 2-D probes were processed according to the method described in Moss and Johnson (1994). A for each particle is calculated by counting the number of shaded pixels in its image. The particle is then assigned to a size-bin, where each bin represents particles which have cross-sectional areas within

a certain range. D can be derived from A by equations of the form:

$$D = aA^b$$

where a and b are constants similar to those used by Cunningham (1978) and are dependent on particle habit and size. Unfortunately, the 2-D probes have the severe limitation in that they cannot measure particles smaller than 12.5μm radius. It has been shown that small ice particles can play an important role in the radiative properties of cirrus, so it is important that the small end of the spectrum should not be ignored. An attempt has been made to take account of the small particles by using data from the FSSP. The FSSP was designed for use in water cloud. It measures the amount of light scattered by the particles passing through its laser beam, and, by application of Mie theory, it is possible to determine the size of the particle. Knollenberg (1993), however, used an FSSP to measure small ice particles in tropical cumulonimbus. In order to make use of the data, they set the FSSP pulse-height-analyser curves to the instrument's expected response to ice spheres, based upon theoretical calculations and empirical tests. In the C-130 data discussed in this study, the FSSP was calibrated for water drops throughout all of the flights, so a slightly different approach to that made by Knollenberg had to be used. In this case, the theoretical Mie calculations for water were compared with those for ice spheres and the FSSP bins were re-sized. In order to create a complete size spectrum the FSSP and two 2-D spectra were appropriately merged. Figure 1 shows a typical example of the spectra from the 3 probes and the resulting merged spectra.

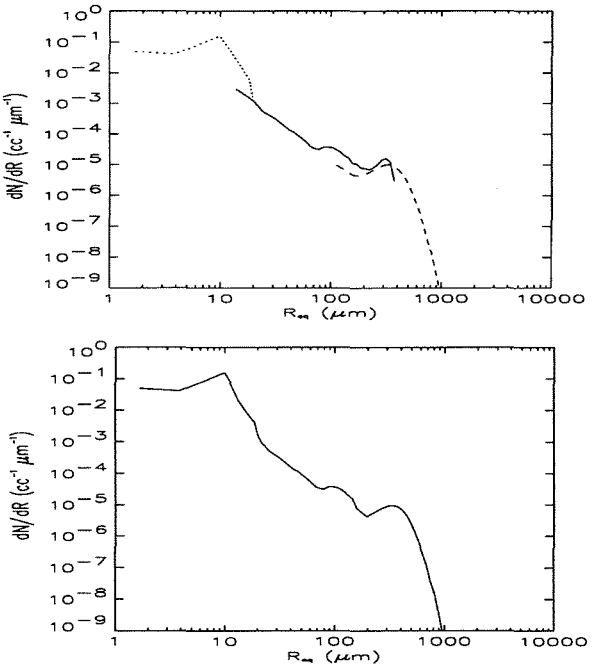

Figure 1 - An example of the merging of spectra from 3 probes, FSSP (dotted), 2D-C (solid) and 2D-P (dashed) Merged spectra is in lower graph.

3. RESULTS.

The effective radius has been calculated, from the merged spectra averaged over 5~seconds of data from straight and level runs from all the flights analysed. Five second averages were required in order to get a representative spectrum from the 2-D probes, since the concentrations of the 2-D sized particles were often low. Figure 2 shows the distribution of calculated r_e values in different temperature ranges for all the frontal flights. The graphs show that where the temperature is low (T<220K), the r_e lies within the range 8-22μm, with the peak at around 15μm. As the temperature increases, the value at which the frequency peaks increases, and the distribution of r_e values broadens. Where the temperature is high (T>260K), the distribution changes greatly. There is a peak at around 17μm, but there is also a large number of particles with r_e greater than 60μm. Since these temperatures are very close to the freezing level, the higher values of r_e encountered are likely to be a consequence of ice crystals aggregating, and falling into this region from above. It is possible that the lower r_e values are a result of the presence of water droplets, or a large number of small ice crystals produced by the Hallett Mossop ice multiplication mechanisms which operates in the temperature range 265 to 270K. Figure 3 shows frequency distributions of the ice particle concentrations for different temperature bands measured during the frontal flights. It can be seen that, throughout the whole temperature range, a broad range of ice particle concentrations were measured, spanning several orders of magnitude. The histograms peak at ice particle concentrations between 0.13cm^{-3} and 0.16cm^{-3}, and the mean concentration values range from 0.51cm^{-3} at the lowest temperature range, to 2.6cm^{-3} at the highest temperature range. The shape of the frequency distribution changes when the temperature is higher than 260K. Here the concentration of particles is likely to be affected by ice multiplication processes and the breakup of ice crystals on melting. The mean ice particle concentration measured for all the frontal cloud cases, where the temperature is less than 260K, was found to be 1.0cm^{-3}.

Before we discuss how the effective radius can be parametrised, it is worth asking how valid are the r_e values we have measured. Since the main purpose of this work is to improve the treatment of cirrus cloud radiative transfer in numerical models, we need to see how well the radiation fields measured in the vicinity of real cirrus clouds compare with those modelled using the r_e measurements. To do this, we have followed the approach of Francis et al (1994), i.e. for a particular EUCREX cirrus case study, run-averaged measurements of ice water content and r_e, are used to construct a model cloud and then this cloud is input to a number of recent broad-band radiation parametrisations, both in the shortwave (0.3-3.0μm) and longwave (4-50μm)

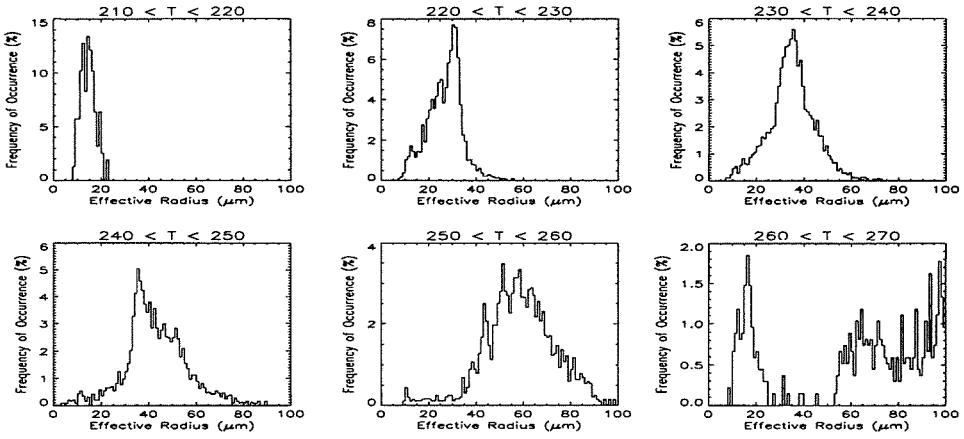

Figure 2 - Frequency distribution of the effective radius of ice particles in frontal clouds over different temperature ranges.

regions of the spectrum. The calculated irradiances are then compared with the irradiances which were measured simultaneously from the aircraft. Figure 4 shows this comparison. The agreement is seen to be reasonable with all three schemes and shows that, using the values of r_e measured from the aircraft, one can model the radiation field in and around cirrus clouds reasonably well.

Different formulations of a parametrisation of r_e have been attempted. the best we have found with our limited data set is one that makes r_e a function of ice water content (IWC) alone:

$$r_e = 83.8IWC^{0.216}$$

Figure 5 shows a scatter plot of the measured r_e against IWC with the parametrisation plotted as a solid line.

Sun and Shine (1995) have recently developed a parametrisation for the single scattering parameters β_{ext}, ω_o and g in terms of the ice water content only. This parametrisation, therefore, contains an implicit relationship between ice water content and effective radius, since one would expect the single scattering parameters to depend on both quantities. If we assume the particles are hexagonal columns the explicit form of this relationship is: is:

$$r_e = \frac{45.9+382.2IWC}{F_a}$$

where F_a is a small particle correction factor which is a function of temperature. This has also been plotted on figure 5 as a dashed line.

It can be seen that the Sun and Shine parametrisation has a tendency to underestimate effective radius at the smaller sizes and overestimate at the larger sizes.

4. SUMMARY.

Microphysical measurements, made by the MRF C-130, in ice clouds around the U.K. have been analysed. Using data from the PMS FSSP and 2-D probes, an ice particle size spectrum was calculated, and from this spectrum, an effective radius was derived. These measurements have enabled us to develop a parametrisation of effective radius of ice particles in frontal clouds, based on the ice water content. The uncertainties in the reliability of the data from the FSSP when it is operated in ice or mixed-phase cloud should not be ig-

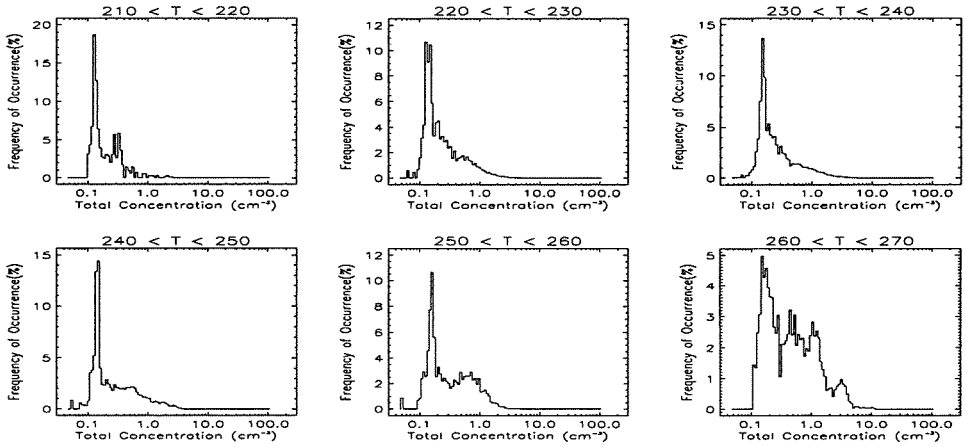

Figure 3 - Frequency distribution of the concentration of ice particles in frontal clouds over different temperature ranges.

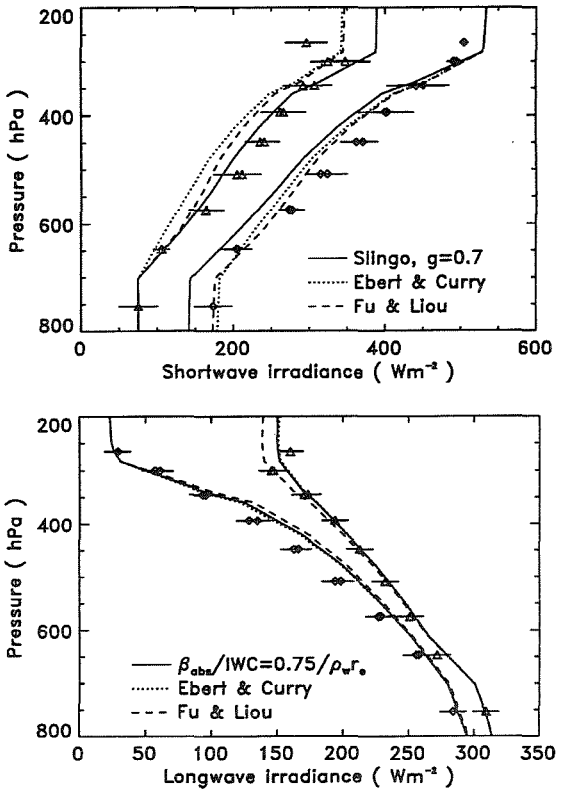

Figure 4 - Comparisons between measured upwelling (triangles) and downwelling (diamonds) short wave (top) and longwave (lower) irradiances with 3 different models.

nored. An attempt has been made to recalibrate the probe for use in ice cloud. Confidence in the FSSP data is enhanced by the consistently good agreement between the higher FSSP channels and the overlapping 2-DC size bins. This good agreement meant that the spectra could be merged together without introducing discontinuities in the slope of the spectra in the overlap region. Significant differences were found in the variation of r_e with IWC between frontal and orographic (not shown here) clouds. This is likely to be due to the different microphysical development of the clouds. In the case of the orographic clouds, all the ice particles must be nucleated within the relatively narrow cloud band, and, hence, within a narrow temperature range; whereas in the frontal clouds, the deeper cloud systems make it possible for particles to be transported from deep within the cloud to the cirrus levels. For this reason a wide range of particle habits are likely to be found in the frontal cloud, whereas the orographic clouds are likely to be dominated by one or two habits. The particles in the frontal cloud will encounter a much wider range of temperatures, and, since they are transported through the cloud in the up and down draughts, they are more likely to collide with other particles, making aggregation very important. For these reasons, the size spectra of the two cloud types will develop in very different ways.

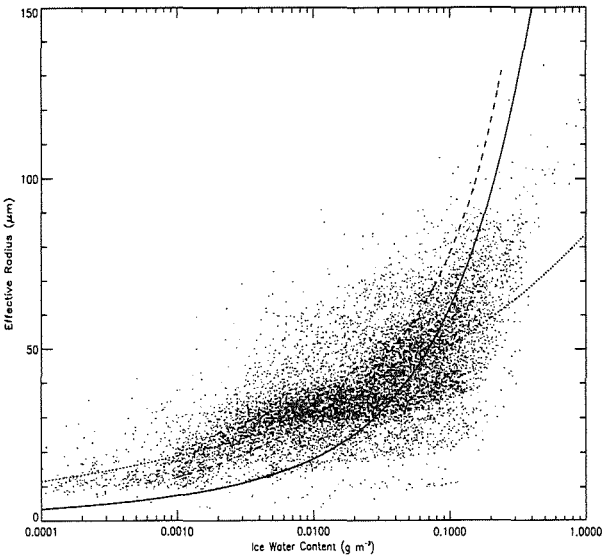

Figure 5 - Scatter plot of measured r_e against measured IWC. Dotted line is best fit to the data and dashed line is Sun and Shine's parametrisation.

5. REFERENCES

Baumgardner, D. 1989: Airborne measurements for cloud microphysics. NCAR Research Aviation Facility Bulletin No. 24. NCAR.

Francis, P.N., Jones, A., Saunders, R.W., Shine, K.P., Slingo, A. and Sun, Z. 1994: An observational and theoretical study of the radiative properties of cirrus: Some results from ICE'89. Q.J.R.Meteorol. Soc., 120, 809-848

Knollenberg, R.G., Kelly, K. and Wilson J.C. 1993: Measurements of high number densities of ice crystals in the tops of tropical cumulonimbus. J. Geophys. Res., 98, 8639-8665

Moss, S.J. and Johnson, D.W. 1994: Aircraft measurements to validate and improve numerical model parametrisations of ice to water ratios in clouds. Atmos. Res., 34, 1-25.

Rogers, D.P., Johnson, D.W. and Friehe, C.A. 1995: The stable internal boundary layer over a coastal sea I. Airborne measurements of the mean and turbulence structure. J. Atmos. Sci., 52, 667-683.

Slingo, A. and Schrecker, H.M. 1982: On the short wave radiative properties of stratiform water clouds. Q. J. R. Meteorol. Soc., 108, 407-426.

Sun, Z. and Shine, K.P. 1995: Parametrisation of ice cloud radiative properties and its application to the potential climatic importance of mixed phase clouds. J. Climate, 8, 1874-1888.

A Comparative Analysis of Two Bulk-Parameterization Schemes of Cloud Microphysics Used in a Meso-β-Scale Non-Hydrostatic Meteorological Model

N. Mölders[1], A. Raabe[1], G. Kramm[2] and M. Laube[3]
[1]LIM - Institut für Meteorologie, Universität Leipzig, D-04103 Leipzig, Germany
[2]IFU - Fraunhofer Institut, D-82467 Garmisch-Partenkirchen, Germany
[3]Institut für Geophysik und Meteorologie, Universität zu Köln, D-50923 Köln, Germany

1. Introduction

Clouds strongly influence the Earth's energy, water and trace species budget via radiation and thermodynamic forcing, liquid phase chemistry, scavenging and the redistribution of trace species. Due to these modifications the incorporation of cloud and precipitation processes in numerical atmospheric models has recently received increasing attention. Unfortunately, clouds vary over large temporal and spatial ranges. Moreover, clouds and cloud processes are of subgrid scale and have to be parameterized. Such parameterizations require a lot of simplifications and are often derived semi-empirically. It has to be expected that the predicted cloud and precipitation pattern may depend on the bulk-parameterization schemes. Two different bulk-parameterization schemes are, therefore, compared and evaluated with respect to their effect on predicted cloud and precipitation formation. The first scheme, referred to hereafter as J-scheme, was designed and evaluated for clouds associated with land-sea-breeze (Jacob 1991, Eppel et al. 1995). The second scheme, denoted as M-scheme, was developed and evaluated for a meso-α-scale model (Mölders et al. 1994a) and further developed for a meso-β-scale model (Mölders et al. 1994b).

2. Description of the model and bulk microphysics

The unelastic and non-hydrostatic model used in our study is a modified version of GESIMA (e.g., Eppel et al. 1995). The condensation/evaporation and deposition/sublimation are determined by the same saturation adjustment scheme in both the parameterization schemes. Herein, mass-weighted saturation mixing ratios and a temperature-dependent partitioning of the excess water vapor between condensation and deposition rates are used (e.g., Lord et al. 1984). It is assumed that under subsaturated conditions cloud water evaporates before ice sublimates. Both the schemes consider homogeneous freezing of cloud drops at temperatures lower than -35°C (Lord et al. 1984), and autoconversion (Kessler 1969). The fall velocities of cloud drops are assumed to be zero. Sedimentation of ice immediately starts after ice has been formed. Assuming a Marshall-Palmer-distribution for the spectral density of precipitation particles mass-weighted mean terminal velocities are calculated for rain drops, ice crystals and graupel by the M-scheme and only for ice by the J-scheme. Note that different ice crystal types, interception values and densities of ice are applied.

The J-scheme is a four water class scheme (*water vapor, cloud water, rainwater, ice*) which, in addition to the processes mentioned above, considers coalescence (Kessler 1969), melting of ice, accretion (Lin et al. 1983), homogeneous freezing of rain drops to ice (Wisner et al. 1972), and evaporation of rainwater (Ogura and Takahashi 1971). Sedimentation of rainwater is parameterized similarly to Kessler (1969).

The M-scheme is a five water class scheme (*water vapor, cloud water, rainwater, ice and graupel*) which considers in addition to the processes already mentioned, evaporation of rainwater, coalescence (Orville and Kopp 1977), melting of ice and graupel, freezing of rain drops to graupel (Wisner et al. 1972), sublimation of graupel, deposition of water vapor onto graupel (Lin et al. 1983), riming of supercooled cloud water onto ice crystals and graupel, conversion from ice crystals to graupel (Cotton et al. 1982). Note that in the M-scheme the class *ice* reaches from cloud ice to lightly rimed graupel of hexagonal type and the class *graupel* encompasses all spherical frozen particles.

The model domain encompasses the troposphere over the mouth of the river Elbe and parts of the western Baltic Sea from the surface to 11.5 km height with a horizontal extension of 128 km in the North-South and 200 km in the West-East direction and with a horizontal grid resolution of 4 x 4 km^2. The vertical resolution varies from 20 m close to the ground to 1 km at the upper model domain with 8 levels below 2 km and 7 levels above that height.

3. Results of 3D-simulations

In nature, cloud and precipitation formation processes are affected by microphysical-dynamical interaction, updrafts and downdrafts, and the water availability from advection or from local recycling of water. In our studies all processes, except those of cloud and precipitation formation, are kept up. Therefore, the predicted cloud and precipitation formation are affected primarily by differences resulting from the different parameterizations and parameters which lead to differences in phase transition processes, and, hence, in the mixing ratios of the water substances. Consequently, differences in the predicted tempera-

tures and vertical motions occur due to the release and consumption of heat again enhancing the differences in phase transition processes. Secondary effects evolve by the different recycling of water caused by different cloudiness, precipitation pattern and available energy.

The clouds predicted by the simulation with the J-scheme (J-run) are stratiform (Fig. 1) while the M-run generates broken cloud fields (Fig. 2). The interception value, which was derived from convective clouds (Leary and Houze 1979), in combination with the assumed ice crystal types, which more frequently occur in convective than in stratiform clouds, may contribute to this. Generally, there is a higher probability for larger cloud water mixing ratios in the M-run than in the J-run. The horizontal distribution of the predicted fields of clouds is more or less similar in the ABL, but the cloudy areas extend slightly larger in the horizontal direction for the J-run than for the M-run. Differences in the cloud water mixing ratios especially exist at temperatures colder than 0°C which can be explained by differences in vertical motions, temperatures, water vapor and saturation mixing ratios. Differences in the predicted mixing ratios of ice and cloud water as well as in water vapor and temperature again lead to different condensation and deposition rates due to the use of a mass-weighted saturation mixing ratio and a temperature-dependent partitioning of the excess of water.

The larger ice mixing ratios in the mid-troposphere in the J-run may partly be attributed to the fact that the accretion process implemented in the J-run only requires the presence of both the ice and cloud water while the riming process used in the M-run depends on saturation and ice crystal type (Mölders et al. 1995). The mass-weighted saturation mixing ratio will shift towards that of ice in the J-run if more ice is present leading to enhanced ice mixing ratios. In the upper model troposphere the J-run predicts a nearly closed thin layer of cirrus while the M-run predicts fields of broken cirrus. This results in 1 K (and more) stronger radiative cooling during the daytime in the J-run than in the M-run. On the contrary, the mid-troposphere is slightly warmer for the J-run than for the M-run.

Since in the M-run more cloud water remains for competitive microphysical processes more rainwater exists at temperatures below 0°C than in the J-run if clouds and rainwater are predicted at the same level and location in both the simulations. The settling of precipitation particles is larger and the onset of precipitation at the ground is earlier in the M-run than in the J-run due to the locally larger rainwater mixing ratios which, among others, go along with larger terminal velocities and differences in melting rates. Below the cloud bases the predicted rainwater mixing ratios largely differ (Figs. 1, 2) due to the different parameterization of evaporation and the differences in predicted water vapor deficit. At temperatures above 0°C the predicted rainwater mixing ratios are additionally influenced by the differences in the melting rates. In the ABL the evaporative cooling and cooling by melting alter the air temperatures, locally leading to 1 K (and more) lower values in the M-run than in the J-run. Rainwater is found at higher levels in the J-run than in the M-run because the coalescence rates are larger for the J-run. Only the M-run is able to provide *graupel*. In our case study, however, the predicted amount of *graupel* was small so that differences resulting from this additional ice class are negligible.

The domain-averaged 24h-accumulated precipitation is a factor of two larger for the M-run than for the J-run. The peaks in the domain averaged precipitation occur in the afternoon for the M-run and in the evening and nighttime for the J-run. This temporal offset causes that in the M-run evapotranspiration can reprovide more of the precipitated water to the atmosphere than in the J-run because of the larger available energy. As a consequence of the more convective-like habit of the clouds the precipitation pattern predicted by the M-run also show a more shower-like character with larger intensities. Whereas, a more stratiform and homogeneous precipitation with lower intensities is predicted by the J-run. These differences may significantly affect the predicted water cycle and removal of trace species. Large precipitation intensities over a short time tend to enhance runoff while long-lasting lower intensities (even if they accumulate to the same amount) may lead to a larger infiltration and, hence, to a reduced runoff. Large precipitation events tend to have higher pH-values than smaller precipitation events.

Besides the different cloud coverage, differences in the characteristics of precipitation may significantly affect evapotranspiration, and soil wetness. The more shower-like precipitation in the M-run than in the J-run leads to a stronger heterogeneity of soil wetness. This again alters water availability and the recycling of water by evapotranspiration, again enhancing the more convective-like habit of the clouds in the M-run as compared with the J-run.

Generally, vertical motions are mainly affected by clouds in several ways. In cloudy regions the various paths of the parameterized cloud microphysics may alter the vertical wind components due to their thermodynamical forcing associated with the phase transition processes. The cooling, for example, by melting or evaporation may initiate downdrafts. In the lower troposphere the additional condensate from sedimentation may turn a thermally buoyant upward motion into a downward directed motion. Since cloudiness affects insolation, changes in the ABL, low level convergence, and, hence, in vertical motions may also occur by surface heating and evapotranspiration. Especially in cloudy regions and in the ABL in the afternoon the horizontal wind fields predicted by the M-run vary stronger than those obtained by the J-run due to the horizontally larger heterogeneity of insolated and shaded, wet and dry surface.

The local maxima of vertical wind speed coincide reasonably well with the local maxima of cloud water and ice in both the runs. The lower temperatures pre-

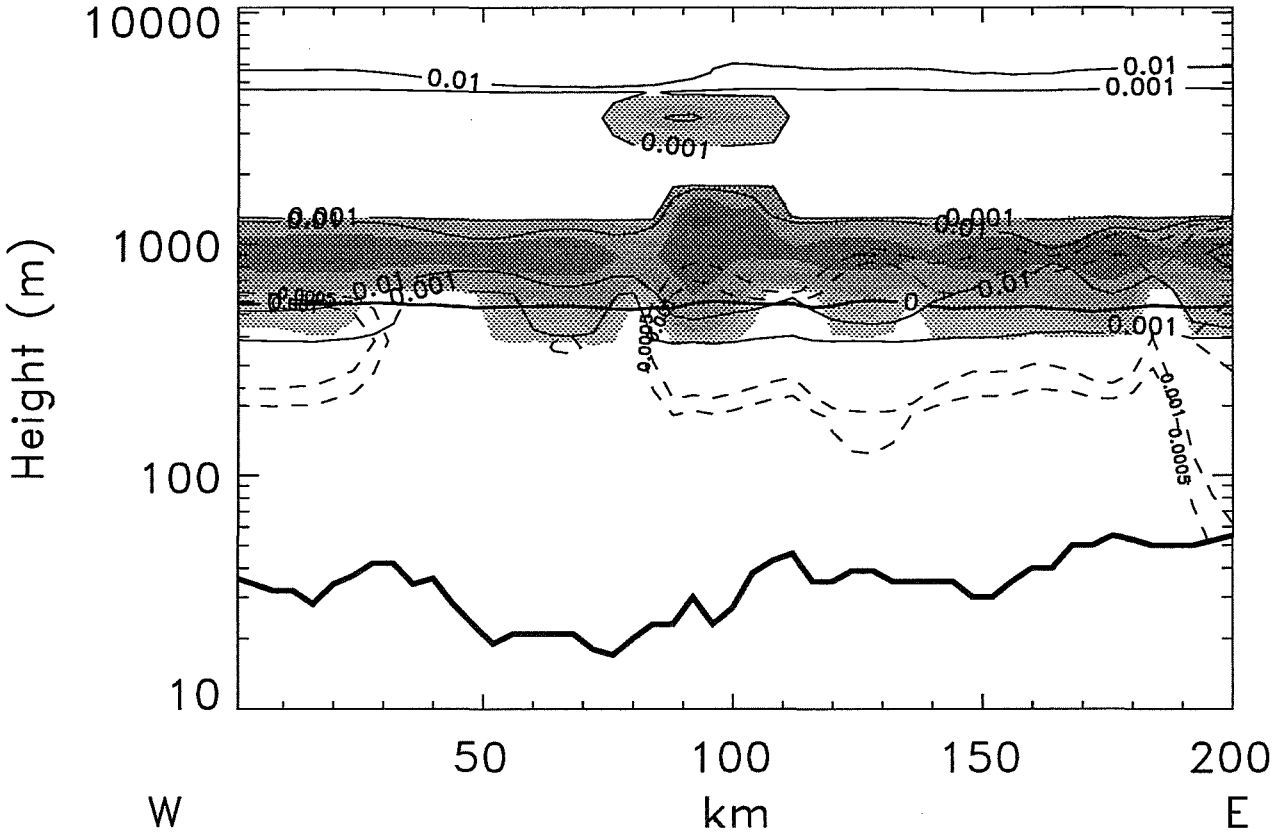

Fig. 1 Mixing ratios of cloud water (grey levels at 0.001, 0.005, 0.01, 0.05, 0.1, 0.5), rainwater (dashed) and ice (solid lines) in g/kg as obtained by the J-run at 12 LT after 12 h of simulation.

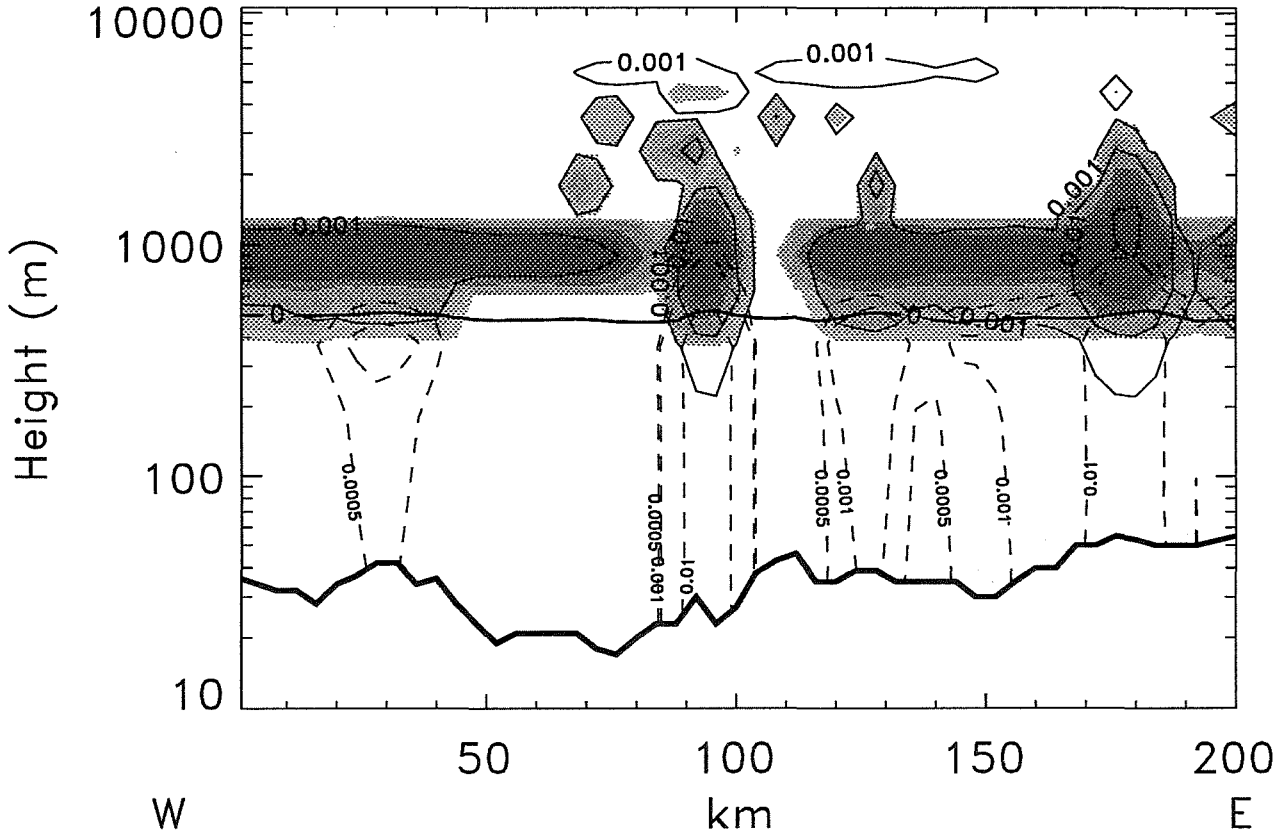

Fig. 2 As Fig. 1 but for the M-run.

dicted for the ABL by the M-run may also contribute to the stronger but horizontally less extended updrafts as compared with the J-run. This leads to a stronger cloud formation in the updraft regions and a slight depletion in the downdraft regions in the M-run as compared with the J-run. Although the updrafts are slightly weaker in the J-run they are more long-lasting and horizontally more extended than in the M-run. This, among others, contributes to the rapid glaciation of the clouds, especially in the upper troposphere (Fig. 1).

4. Summary and conclusions

A four and a five class bulk-microphysics parameterization scheme were investigated with respect to their impact on predicted cloud and precipitation formation. The main differences in the parameterizations are the assumptions made on the heterogeneous ice forming processes, on the form and density of the ice as well as on the terminal velocities of the water substances. The numerical experiments with the two bulk-parameterization schemes show that the dynamics, the spatial distribution as well as the temporal development of clouds, precipitation, evapotranspiration, and soil wetness differ largely. Altogether, the simulations substantiate that primary the differences mainly result from the different formulations of the microphysical processes mentioned above, especially form those processes which compete with each other for the available cloud water. Small differences in the predicted rates of transition processes and terminal velocities accumulate with time, finally leading to relative large differences in the predicted cloud fields and precipitation pattern. Due to the different partitioning between the cold and the warm path of precipitation formation the release and consumption of heat differ for the two schemes causing differences in the temperature fields, and hence, in vertical motions, redistribution and availability of water vapor. Since the parameter and parameterizations used lead to broken clouds and a more shower-like precipitation in the M-run and to stratiform-type clouds and precipitation in the J-run, we may conclude that more general schemes with more classes of ice crystals of smaller sizes are required for hydrological and chemical-dynamical modeling.

An essential point for the differences is also that assumptions for the initiation of a cloud as well as for the partitioning between cloud water and ice are required. The saturation adjustment scheme, which is identically in both the runs, causes differences as a secondary effect of the differences in the microphysical processes mentioned above, because a mass-weighted saturation mixing ratio and a temperature-dependent partitioning of the excess of water is not only affected by the water vapor availability and the temperature distribution but also by the amounts of cloud water and ice already present. Consequently, more reliable saturation adjustment schemes are required.

5. Acknowledgment

We would like to thank to the Minister of education, science, research and technology (BMBF) of Germany for the support of this study by contract 521-4007-07 VWK 01.

References

Cotton, W.R., M.A. Stephens, T. Nehrkorn, G.J. Tripoli, 1982: The Colorado State University three-dimensional cloud mesoscale model 1982. Part II: An ice phase parameterization. *J.Rech.Atmos.* **16**, 295-320.

Eppel, D.P., H. Kapitza, M. Claussen, D. Jacob, W. Koch, L. Levkov, H.-T. Mengelkamp, N. Werrmann, 1995: The non-hydrostatic mesoscale model GESIMA. Part II: Parameterizations and applications. *Contr.Atmos.Phys.* **68**, 15-41.

Jacob, D., 1991: Numerische Simulation der Wolkenbildung in einer Land-Seewind-Zirkulation. GKSS 91/E/40.

Kessler, E., 1969: On the distribution and continuity of water substance in atmospheric circulation. *Met. Monogr.* **27**, Amer. Met. Soc., 84.

Leary, C.A., R.A. Houze, 1979: Melting and evaporation of hydrometeors in precipitation from the anvil clouds of deep tropical convection. *J.Atmos.Sci.* **36**, 669-679.

Lin, Y.-L., R.D. Farley, H.D. Orville, 1983: Bulk parameterization of the snow field in a cloud model. *J.Clim.Appl.Met.* **22**, 1065-1092.

Lord, St.J., H.E. Willoughby, J.M. Piotrowicz, 1984: Role of a parameterized ice-phase microphysics in an axissymetric, nonhydrostatic tropical cyclone model. *J. Atmos. Sci.* **41**, 2836-2848.

Mölders, N., H. Hass, H.J. Jakobs, M. Laube, A. Ebel, 1994a: Some effects of different cloud parameterizations in a mesoscale model and a chemistry transport model. *J.Appl.Met.* **33**, 527-545.

Mölders, N., M. Laube, G. Kramm, 1994b: A scheme for parameterizing ice and water clouds in regional models. In: Borrell et al. (eds.). *The proceedings of the EUROTRAC symposium'94*, SPB Academic Publishing, The Hague, 839-844.

Mölders, N., M. Laube, G. Kramm, 1995: On the parameterization of ice microphysics in a mesoscale α weather forecast model. *Atmos.Res.* **38**, 207-235.

Ogura, Y., T. Takahashi, 1971: Numerical simulation of the cycle of a thunderstorm cell. *Mon.Wea.Rev.* **99**, 895-911.

Orville, H.D., F.J. Kopp, 1977: Numerical simulation of the life history of a hailstorm. *J.Atmos.Sci.* **34**, 1596-1618.

Wisner, C., H.D. Orville, C. Myers, 1972: A numerical model of a hail-bearing cloud. *J.Atmos.Sci.* **29**, 1160-1181.

APPLICATION OF CLOUD MODEL TO PREDICTING THE TORRENTIAL RAIN IN CENTRAL CHINA

Hu Zhijin Liu Gongbo

China Academy of Meteorological Sciences, CMA, China

1.INTRODUCTION

Torrential rain occur frequently in the Yangzi River basin in summer, sometimes leading to catastrophic floods. The heavy rainfalls are mainly generated by the stratiform cloud systems (sometimes with embedded convection) associated with the quasi-stationary 'Meiyu' front. It is a challenge to use the stratiform cloud model for predicting the heavy rainfall events during 'Meiyu' period.

2. MODEL DESCRIPTION

A three dimensional mixed-phase stratiform cloud model (SCM) developed by Liu et al (1993) is used in this study. The dynamic equations and differential schemes are mainly taken from Anthes et al (1978). In the hydrostatic geopotential equation the load of hydrometeors is added. The diabetic heating by phase change of water substances is also considered.

The cloud microphysical equations are mainly taken from Hu and Yan (1986). Seven microphysical variables are calculated: the specific mass of cloud, rain, ice and snow and the concentration of particles of rain, ice and snow. Eleven microphysical processes are considered. A hybrid calculation scheme is used considering the different characteristic times of various processes. The grid points are 31x31x11 and $\Delta x=\Delta y=70$km. Model is initialized based on observational data, and all microphysical variables are set to be zero at the beginning.

3. EXPERIMENTAL PREDICTION OF TORRENTIAL RAINFALL EVENTS

Model was run for 5-14 July 1991, when the 'Meiyu' rainfall caused severe floods in Central China. The PSU/NCAR-MM4 model of Anthes et al (1987) with explicit scheme of warm cloud (MM4E) was run in parallel for comparison. Predicted results by using MM4 model with convective parameterization scheme (MM4C) were kindly provided by Mr. Zhu Tong from Institute of Mesoscale Meteorology, CAMS, but only for five days-5,6,7,9,13 July. Results showed that all three models were able to predict the general evolution and movement of the

weather systems, but SCM was a litter worse in some days. The locations of the observed centres of rainfall more than 20 mm/day and the predicted centres by all models were listed to examine their prediction skill. Assuming that the prediction is adopted as correct one when the distance between the observed and predicted centres are smaller than one degree of latitude or longitude, the number of correctly predicted events (N_1), number of observed but not predicted events (N_2) and number of incorrectly predicted events (N_3) are summarized for each model in Tab.1. A criteria of prediction skill $TS=N_1/(N_1+N_2+N_3)$ was used for comparison. As shown in Tab.1, the skills of prediction of the heavy rainfall events are not very high for all 3 models. Besides, the values of TS are not stable due to the small sample, e.g. SCM is worse than MM4E in ten-days' comparison, but it is contrary in five-days' comparison. The average daily rainfall amount at the observed and predicted centres (R) were also listed in Tab.1. In average, the predicted rainfall is much smaller than the observed one. Models with explicit scheme are worse than MM4C in this aspect.

Tab. 1 Summary of the prediction of heavy rain events

	Obs.	SCM	MM4E	MM4C	S+C
10days (5-14 July 1991)					
R(mm)	101	27	30		
N_1	39	11	14		
N_2		28	25		
N_3		8	11		
TS(%)		23	28		
5days (5-7,9,13 July 1991)					
R(mm)	110	37	49	61	
N_1	19	6	5	7	10
N_2		13	14	12	9
N_3		3	7	9	11
TS(%)		27	19	25	33

It is worth noting that the cloud model is stronger in cloud microphysics, but is weaker in other aspects in comparison with MM4, so it takes less computer time and might be improved.

4. TEST OF THE INITIALIZATION OF THE CLOUD VARIABLES

In cloud model zero is set initially for all cloud variables due to the lack of the observed values. The initial water vapour in cloud-precipitation zone usually is not saturated because of the errors in observation or/and objective analysis. In cloud model the cloud formation and precipitation development take a period of time, which leads to a systematic delay and under-estimation of the rainfall, especially in the first 6 hours. An example is shown in Tab.2, where observed and calculated rainfalls in every 6 hours are presented. A scheme of initialization of the water substances is suggested: Model starts run for a time period of cloud initialization with unchanged thermodynamic structures to get the initial field of water vapour and cloud variables. After then the model begins prediction. The time period of cloud initialization of 30 min, 60 min. and 180 min are taken for test, calculation results are given in Tab.2 named I30, I60, and I180

respectively. Calculation results of convective parameterization (CPM) and cloud model without cloud initialization (SCM) are also listed for comparison. As shown in Tab.2, the rainfall prediction after initialization was significantly improved. The effect is greater for longer time of initialization. Another experiment I180A is also done by using 180 min of initialization but setting zero values for all cloud variables except the vapour. Comparison of this case (I180A) with SCM and I180 shows that the rainfall prediction is sensitive to the initial values of both the vapour and cloud variables.

Tab.2 Influence of cloud initialization on rainfall

Period(h)	0-6	6-12	12-18	18-24
Observ.	48	129	132	44
CPM	33	21	22	16
SCM	11	34	59	43
I30	16	38	54	34
I60	19	40	54	37
I180	21	54	61	38
I180A	15	49	61	34

5. A COMPLEX CLOUD MODEL

The stratiform cloud model (SCM) deals with the grid-scale cloud-precipitation processes while the convective parameterization scheme deals with the subgrid cloud-convection process and may be a complement to the former. Taking together the centres predicted by SCM and MM4C for July 1991, the predicting skill (TS) increased significantly as expected (see Tab.2 for S+C). A complex cloud model (CCM) was designed by including the Kuo-Anthes convective parameterization scheme into the cloud model. Calculation of the grid-scale advection and condensation of vapour is preferential to the convective parameterization considering the characteristic times of these processes. Instead of the summarized in vertical value of horizontal convergence of the vapour M_t in K-A scheme, the difference between the horizontal convergence and microphysical sinks of the vapour (M_e) is used in this model to start the convective parameterization, if M_e is greater than some threshold value. Two schemes are identical in case where the microphysical sinks of vapour (condensation etc.) are absent.

Experimental prediction was made for torrential rainfall 5-6 July 1991 by using SCM, CPM, and CCM. The observed and predicted rainfall distribution (see figure) showed that SCM predicted the major rainfall region only; CPM predicted both rainfall regions, but the maximum intensity of the major rainfall is much under-estimated; The prediction of CCM was the best in the given case.

The profiles of the summarized values of the calculated latent heat release along x=18 (near 31^0N) in a period of 18 hours by using SCM,

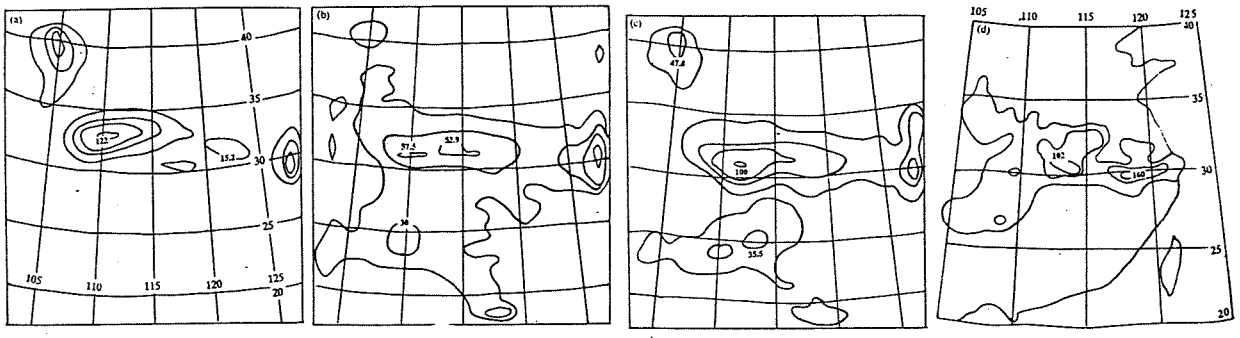

图 2 1991 年 7 月 5 日 8 时至 6 日 8 时雨量分布

Fig.1 Distribution of rainfall during 5-6 July 1991
(a)SCM (b)CPM (c)CCM (d)Obs. Lines in (a) (b) (c) denote isohyet of 10, 30, 50, 100mm. Lines in (d) denote isohyet of 10, 50, 100mm.

CCM and CPM are compared. It is shown that the maximum warming in the major rainfall area located at 530, 460 and 410 hPa for SCM, CCM and CPM respectively. The distribution of air warming in SCM isnot presumed as in CPM but is determined by the advection of vapour and the cloud processes. In the given case air warmed in SCM mainly in the middle troposphere, which influenced the weather system more at lower layer and had stronger feedback, leading to a torrential rainfall.

6.ACKNOWLEDGMENT

This research was a part of the National Scientific-technical Research Program 85-906 and was also supported by National Natural Science Foundation of China.

References

Anthes R. A. and Warner T. T., 1978: Development of hydro-dynamic models suitable for air pollution and other meso-meteorological studies, Mon. Wea. Rev.,106,1045-1078.

Anthes R. A. Hsie E-Y and Kuo Y-H, 1987: Description of the PSU/ NCAR Mesoscale Model Version 4 (MM4) NCAR Tech. Note-282.

Hu Zhijin & Yan Caifan,1986: Numerical simulation of microphysical processes in stratiform clouds-PartI: Microphysical model, Annual Report 1986, Academy of Meteorological Science, SMA, China, 64-73, China Meteorological Press, Beijing.

Liu Gongbo, Hu Zhijin and You Laiguang, 1993: Mixed-phase stratiform cloud system model and case modelling on two low-level mesoscale vortices, Acta Meteorologica Sinica, 7,4,454-468.

APPLICATION OF CLOUD AND PRECIPITATION IN SCIENTIFIC SYSTEM ON NATURAL DISASTER REDUCTION

Wang Angsheng, Liang Bijun, Dong Jiarui, Feng Qiang, Wang zhou
(Institute of Atmospheric Physics,Chinese Academy of Sciences, Beijing,China)

1. INTRODUCTION

China is one of the few countries where natural disasters strike frequently and cause heavy damages. During recent years, the direct pecuniary loss in China per year is over 100 billion yuan (RMB), about 3%–6% of our GNP,which equals to 17%–35% of our national revcnue[1]. Among these hazards, heavy–rain flood, drought, typhoon, stormy surge, thunderstorm,hailstorm, snowstorm etc. are more destructive which belong to atmospheric hydrospheric disasters. In China, 69–70% disastrous losses were caused by the meteorological disasters mentioned above. As well known, all the disaters above are in close relationship with clouds and precipitation, especially with severe convective clouds[2].

2. CLOUD–PRECIPITATION AND DISASTER REDUCTION

Due to severe or long–time heavy rain, flood appears; due to little rainfall for a long time, drought happens; if typhoon comes, stormy surge and typhoon disaster emerges; when thunderstorm, hailstorm or snowstorm happen, they will badly hurt mankind;and so on. So, cloud(specially the severe convective cloud) and precipitation is in close relationship with disasters.

Chinese Government has long regarded disaster reduction as one of the basic state policies for promoting social stability and sustainable economic development, and has attached importance to diasater reduction undertakings, thus scoring great achievements over the past dozens of years. Besides China's construction works in disaster reduction engineering, China's natural hazards monitoring and early warning systems are very important. By the way, disaster assessment and the policy –decision of disaster reduction are new important works.

According to the necessary of our country and the strategy of disaster reduction in China[3], a Sythetical Scientific System of Disaster Reduction (SSSDR) on Atmospheric and Hydrospheric Disasters was studied and established in the Centre of Disaster Reduction, Chinese Academy of Sciences (CDR, CAS) and the Meteorological Centre, Chinese Meteorological Administration(MC, CMA).

3. SCIENTIFIC SYSTEM(SSSDR)

From 1991 to 1995, project of SSSDR was studied by over 200 scientists and engineers who came from more than 20 institutes and universities. Professor Wang Angsheng was the director of this project. The system(SSSDR) consists of State Warning and Service System (SWSS),Information System on Disaster Reduction (ISDR), Synthetical Data –base and Assessment (SDBA) and Local Demonstration System of Warning and Service (LDSWS) etc. LDSWS

includes six sub–systems respectively in Hubei, Sichuan, Henan, Jiangsu,Guangdong provinces and Shanghai city[4].

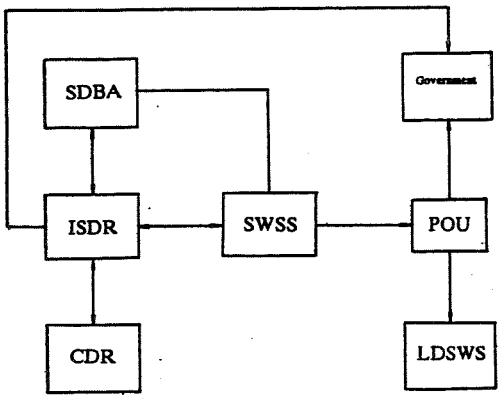

Fig. 1. The Structure of SSSDR

The structure of SSSDR is given in Fig.1. All information is transmited on real time by local net and remote net among all systems. In this system, we must do Countermeasure to Disaster Reduction (CDR) , then, SWSS, ISDR, SDBA and CDR get a lot of products togther. All products of this system are transmited to Governments and LDSWS by Products Output Unit (POU). All products are very useful for disaster Reduction[5].

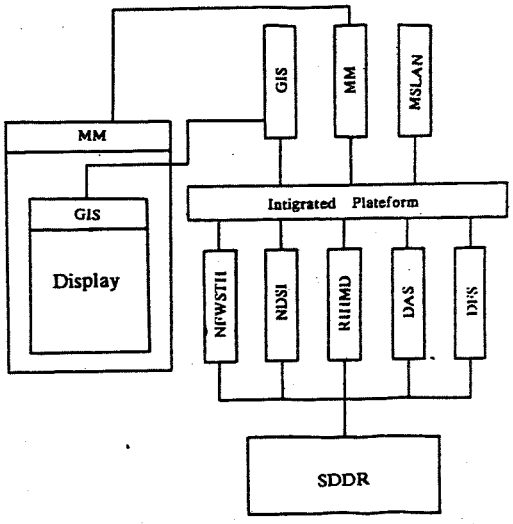

Fig. 2. Software Archpicture of SSSDR

Fig.2 is the software archpicture of SSSDR. It consists of nine models which are National Forecasting and Warning System of Typhoon and Heavy rain (NFWSTH), National Disaster Situation Information (NDSI), Real–time Information Handling of Making disaster (RIHMD), Disaster Assessment System (DAS), Disaster Forcasting System (DFS), Synthetical Database of Disaster Reduction (SDDR), Geographical Information System (GIS), Main Menu (MM), Management System of Local Area Network (MSLAN). They are intigrated on Windows Plateform. Thereof[6], we can share the data and information.

The characteristic of the system is that it can carry out real –time monitoring of disaster in a movable state, assessment of disaster situation for one to three days, and can assess disaster situation after disaster. For example, in summer of 1995,disater prediction was made about the serious floods happening in the middle valley of Yangtse river and in the northeastern China.The theoretical results of the prediction complied very well with the practical results.

4. SOME RESULTS FROM RESEARCH ON THE RELATIONSHIP BETWEEN CLOUD –PRECIPITATION AND SEVERE FLOODS IN CHINA

By means of the system mentioned above and through its comprehensive analysis, a geat deal of data were gained, such as satellite data, radar data, precipitation data, and so on. Fartherly, on basis of the products of weather prediction, data from atmospheric sounding, hydrological data, disastrous data, and geographical information, etc., the atmospheric hydrospheric disasters have been studied in China[1]. Perticularly, the relationship between cloud precipitation and severe disasters has been studied rather extensively. Here are some results of the study.

(1). The shift of the main floods–striken area in China[7]

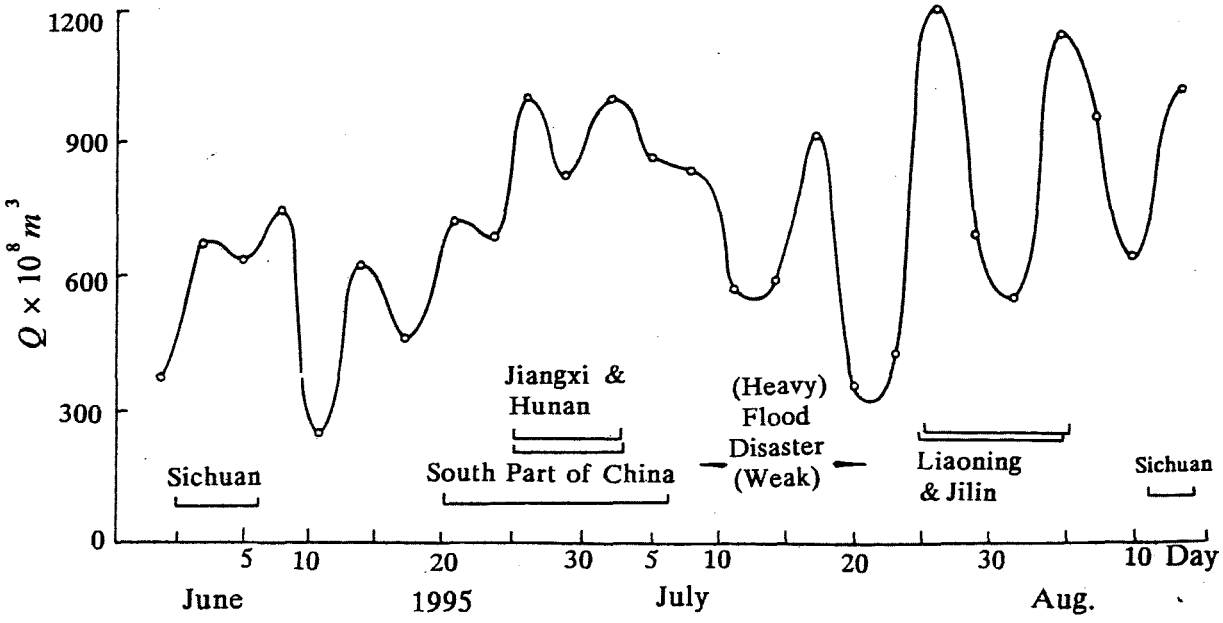

Fig. 3. Total Rainfall of the Whole Country for 3 Days (1995)

From 1950 to 1966, the main floods–striken area in China was Northern China Plain and part of Yangtse River–Huihe River valley(Henan, Shangdong, Jiangsu, Anhui Province); but from 1978 to 1993, it shifted to Yangtse River Valley and Northeastern China. One of the most possible reasons is that Northern China Plain has had less rainfall since mid 1960s, its climate becomes drier.

(2). The relationship between the generel precipitation of the whole country and severe floods in China

Fig.3 is the carve of the generel rainfall of the whole country for 3 days from June to August in 1995. The ranges of pinnacle value are exactly relevant to the periods when floods happening in different parts of China.

(3). The relationship between the precipitation of typhoon and floods in China[8,9]

Most of the time,typhoon strikes the coastal area in our country. Therefore, the floods caused by typhoon often happens in the coastal area of Southeastern China. Otherwise,typhoon may invade the internal area of China and may result in severe floods, for example, the flood disater in August 1975.

(4). The relatinship between the cloud precipitation belt and floods disaster belt in the annual rainy season in China[9]

In China, from April to September, the distribution of cloud precipitation is belt–like. The cloud precipitation belt skips from south to north with season. Thereupon, there exist four rainy periods: the primary rainy period and poster rainy period in Southern China,Mei Yu rainy period in Yangtse River–Huihe River valley, the rainy period in Northern and Northeastern China. Relatinng to this, the distribution of floods caused by heavy–rain in rainy season in China is belt–like, and it also has seasonal variation characteristics, jumping from south to north. Besides above, the cloud precipitation has intraseasonal variation, according to this, floods has intraseasonal variation. During a rainy period, the damage resulted from floods at a spot explosively increases in the final stage of the disaster development.

5. SOME RESULTS AND ENLIGHTMENTS FROM THE REAL–TIME OPERATION OF THE SYSTEM IN 1995

From June 1 to the middle period of September 1995, the Centre of Disaster Reduction, Chinese Academy of Sciences, the Meteorological Centre of Chinese Meteorological Administration, China Natural Committee of International Decade for Natural Disaster Reduction(CNCIDNDR) collaborated to carry out the real–time operation of the system. They obtained a great deal of data, completed disaster prediction and warning pre–assessment for 1 to 3 days and periodical assessment in time, which turned the disaster reduction undertaking into operative scientific system and brought about fairly good results.

(1). The synthetical scientific system of disaster reduction is quite important. Its successful real–time operation has set up a good example[6].

(2). The most severe atmospheric hydrospheric disasters were virtually pedicted in 1995 .

(3). It can be used extensively against other kinds of disasters in atmosphere hydrosphere. The job has popular meaning to our national disaster reduction undertaking.

(4). It has basically founded the scientific and technological base for the disaster reduction framework of Chinese Disaster Reduction Centre[3,6].

References

[1]. Wang Angsheng, 1995: Speech on the Inaugural Meeting of Disaster Reduction Centre of Chinese Academy of sciences. Natural Disaster Reduction in China, 1995 Vol.4, No.4, P145–149.

[2]. Wang Angsheng, Fan Zhen et al., 1992: The Application of Cloud and Precipitation study on IDNDR. Proceedings of 11th International Conference on Cloud and precipitation, 17–21, August 1992, Montreal, Canada, P736–739.

[3]. Wang Angsheng, 1991: A Brief Discussion on the Strategy of sreious Natural Disaster Reduction. Natural Disaster Reduction in China, 1991, Vol., No.2, P12–15.

[4]. Wang Angsheng, Li Jishun, Xu Naizhang et al., 1995: Advances on Forecasting Warning system, Disaster Assessment and Countermeasure Study of Typhoon and Heavy Rain. Forecasting Warning System and Disaster Reduction Study of Typhoon and Heavy Rain. Meteorological Press, Beijing. P1–6.

[5]. Liang Bijun, Wang Angsheng, et al., 1995: The Study of Information System for Disaster Reduction of Typhoon and Heavy Rain. Forecasting Warning System and Disaster Reduction Study of Typhoon and Heavy Rain. Meteorological Press, Beijing. P32–37.

[6]. Wang Angsheng et al., 1995: Forecasting Warning System and Disaster Reduction Study of Typhoon and Heavy Rain. Meteorological Press, Beijing. 1–354.

[7]. Zhen Shuangzhi et al., 1995: Research on the Changing Features of Floods in China. Forecasting–Warning System and Disaster Reduction Study of Typhoon and Heavy Rain. Meteorological Press, Beijing. P133–138.

[8]. Wang Zhuo et al., 1995: Typhoon Disaster and Its Risk Assessment in China. Forecasting Warning System and Disaster Reduction Study of Typhoon and Heavy Rain. Meteorological Press, Beijing. P215–221.

[9]. Feng Qiang et al., 1995: Summary on Heavy–rain Floods in CHina. Forecasting Warning System and Disaster Reduction Study of Typhoon and Heavy Rain. Meteorological Press, Beijing. P126–132.

RAINBAND PRECIPITATION PROCESSES IN DIFFERENT CLIMATOLOGICAL AREAS

Tsutomu Takahashi

Dept. of Earth and Planetary Sciences, Kyushu University, 33, Fukuoka 812–81, Japan

1. INTRODUCTION

One of the most important goals in the field of cloud physics is to understand the processes through which precipitation is formed. Its importance is further enhanced by consideration of climate change and the question of global circulation of water. Climate models require identification of precipitation processes, particularly in rainbands, since they are the primary rain producers. Identification requires knowledge of the spatial distribution of particles in the clouds of interest. Although aircraft platforms are powerful tools in investigations of the phenomena, they are unable to fly into those areas of intense radar echoes where important precipitation processes occur. A new method using a videosonde system has recently been developed to overcome this difficulty (Takahashi, 1990). Data from more than 80 such videosondes have shown that precipitation processes vary widely in different climatological areas. When used in a numerical cloud model the data suggest that different processes significantly affect not only the amount of precipitation, but other characteristics as well.

2. VIDEOSONDE SYSTEM

In order to make the necessary in–cloud measurements a special radiosonde, the Precipitation Particle Image Sensor (PPIS) was designed and is illustrated in Fig. 1a. Its primary features are a video camera that records images of falling precipitation particles and an induction ring that measures their electric charge. An infra–red light with a beam 15 mm above and parallel to the line of sight of the camera is interrupted by any particle larger than 0.5 mm in diameter which then triggers a flash lamp mounted above the camera lens. The lamp has a pulse duration of 1/22000 sec and may be triggered a maximum of twice a second. A delay circuit between the infra–red sensor and the flash trigger make it possible to record images of particles even if their fall velocity is zero (Fig. 1b).

Another, circular flash lamp, with a longer pulse duration of 1/6000 sec is mounted so as to encircle

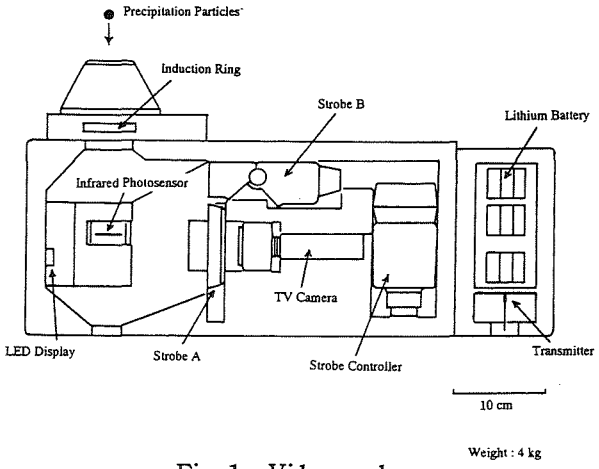

Fig. 1a. Videosonde.

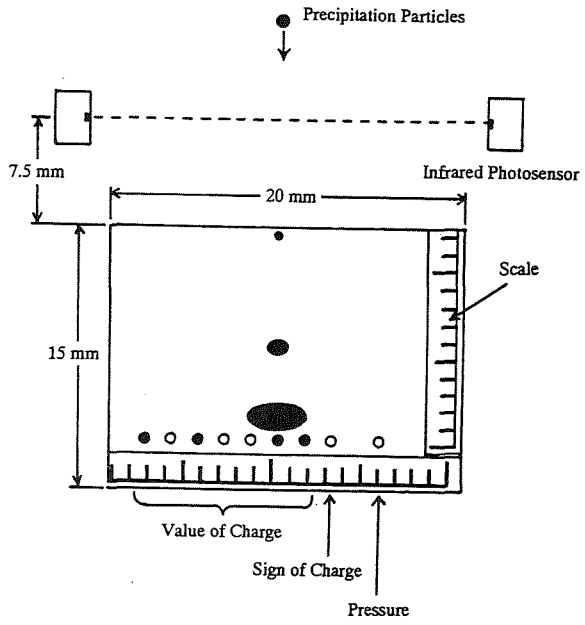

Fig. 1b. Particles on the TV Screen.

the camera lens. The lamp flashes continuously three times a second. Particle image signals are converted to frequencies between 10Hz and 1 MHz and sent to the ground station by 1680 MHz carrier wave.

The induction ring used to measure charges on the particles is located on top of the radiosonde. The sign and magnitude of the charges are

logarithmically amplified and transmitted to the ground station.

The PPIS has an effective volume area of 20 × 15 × 29 mm ^{3}. At the ground station the particle images are projected on a TV screen at 10 × magnification and are recorded on video tape. Atmospheric pressure data from the radiosondes as well as the sign and magnitude of the particle charges are displayed on a series of LEDs at the bottom of the screen; the rightmost LED flashing at preset reference pressures, the next indicating the sign of the charge on the particle, and the remaining LEDs the magnitude of the charge through preset reference voltages.

The absolute values for ice crystal concentrations given herein are derived from the number of images observed in a fixed time interval. Supercooled raindrops and frozen particles are differentiated by differences in transparency, air bubbles, and shape.

3. OBSERVATIONS

Videosondes have been launched in different climatological areas (Fig. 2): Manus Island, Papua, New Guinea; Ponape, Micronesia; Pingliang, China; Songkhla and Surat Thani, Thailand; Hokuriku and Kagoshima, Japan; and Melville Island, Australia (Takahashi & Kuhara 1993, Takahashi et al 1995a, b). Typical precipitation particle distributions from

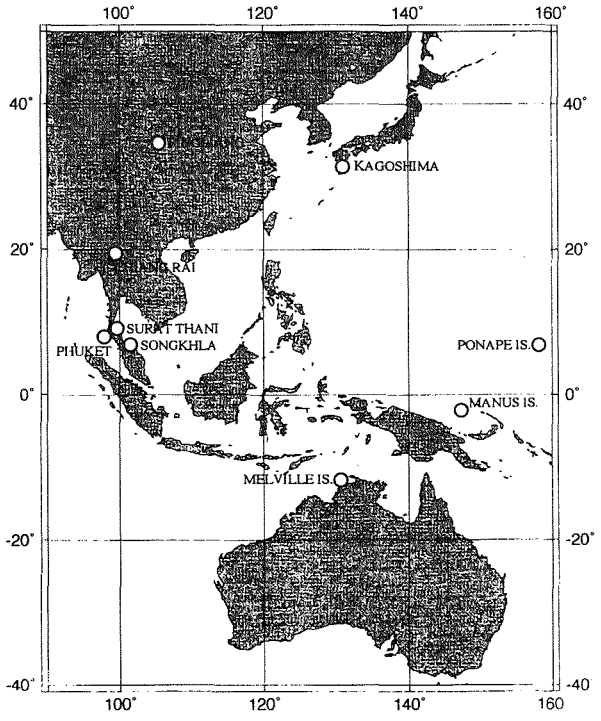

Fig. 2. Videosonde launching sites.

rainbands were selected from each region for comparison.

Precipitation processes varied greatly in different climatological areas (Fig. 3, 4). Near the equator the major particle types were raindrops and frozen particles with very few ice crystals. The warm rain process predominated, probably because of low concentrations of both ice and condensation nuclei. In contrast, over the continent in a semi-arid area of China, the primary precipitation particles were graupel. The warm rain process probably could not work efficiently there because of the expected high concentration of cloud condensation nuclei. A third process was observed along the East Asian monsoon belt where raindrops formed through both warm rain and graupel formed by riming on ice crystals.

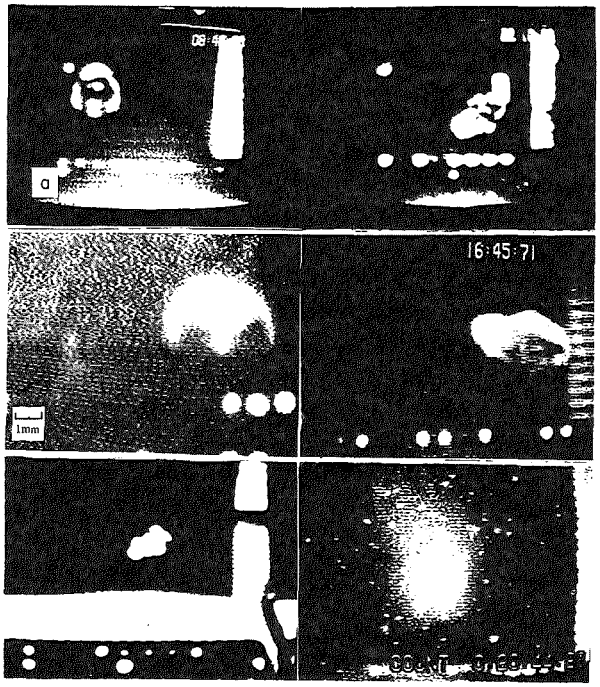

Fig. 3. Images of precipitation particles.
(Upper Left) Raindrop at Manus, 10.2 ℃, scale 1 mm
(Upper Right) Frozen particle at Manus, 14.9 ℃
(Middle Left) Raindrop at Songkhla, 22 ℃
(Middle Right) Hail at Melville, 2.3 ℃
(Lower Left) Graupel–aggregate, 2.4 ℃ from thick layered cloud
(Lower Right) Ice crystals at Melville, –22.9 ℃

A surprising observation is the almost two orders of magnitude fewer ice crystals in clouds along the equator in the Western Pacific. However in the Hector clouds over Melville Island, ice crystal concentrations occasionally increased up to 10 per cm ^{3} associated with the appearance of graupel. Another interesting finding is that in clouds over Manus Island graupel aggregates were first observed in thick, upper layered cloud.

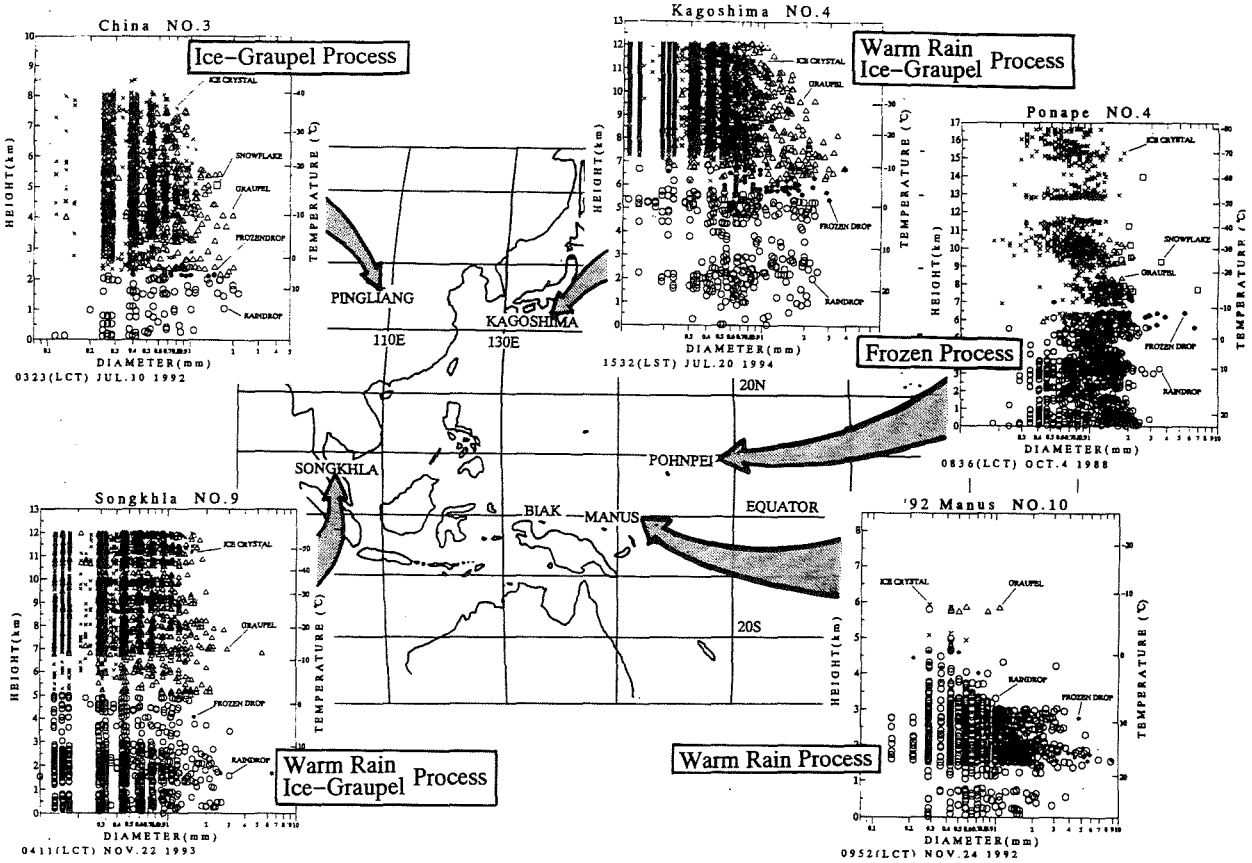

Fig. 4. Typical precipitation particle distributions from rainbands in different climate areas.

4. CLOUD MODEL

A cloud model was used to examine how such different precipitation processes affected the amount of precipitation and the properties of the clouds. The model used was deep, two-dimensional, non-hydrostatic, and anelastic, and included detailed microphysics from Takahashi, 1976. In order to simulate a self-sustaining rainband, a linear wind shear was used in the lower levels of the cloud. An initial impulse was given in the lower left corner of the cloud. Different number concentrations of both cloud and ice nuclei were used in each model run and in one run simulating rainbands over the equator in the Western Pacific, raindrop freezing was accelerated.

Rain fell from two locations in the modelled clouds. A warm rain process produced rain from the forward area of the cloud. In that process raindrop growth was enhanced by drop recirculation. When there was sufficient ice crystal growth, the release of additional latent heat enhanced higher growth on the cloud's lee side and rain was then formed through graupel and hail.

Since rain originating from ice phase is missing in warm clouds, the rainfall totals were less and the cloud less active. Over time the maximum rainfall accumulated in the maritime-ice rainband and the minimum in the continental-warm band (Figs. 5a, b).

The cloud model results suggest that the precipitation process is rather weak in equatorial rainbands over the Western Pacific. The results also show that the most productive rain process occurs in rainbands over the East Asian monsoon area.

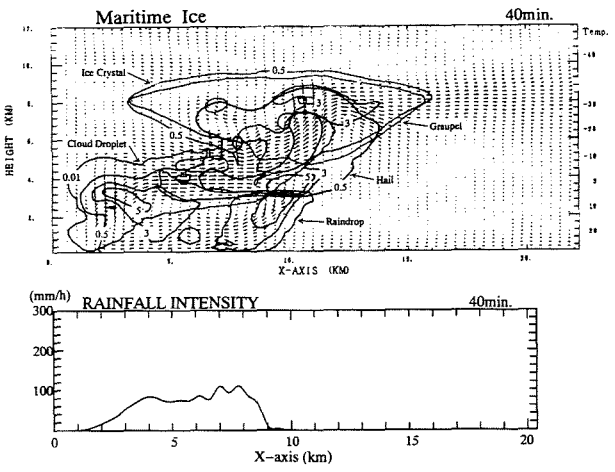

Fig. 5a. Model calculated airflow and mixing ratio after 40 minutes in maritime ice case.

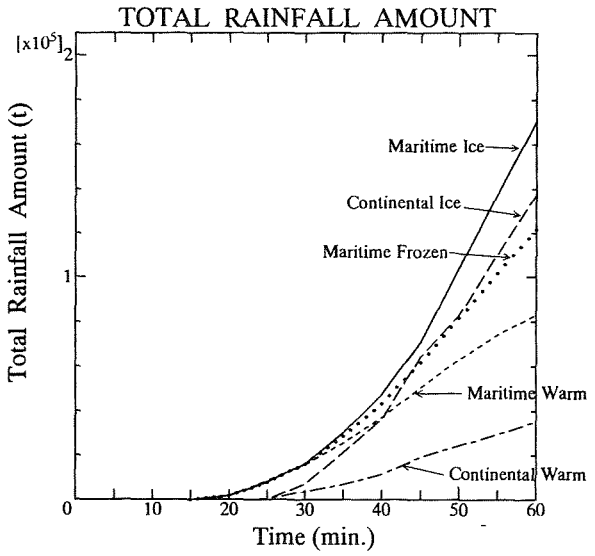

Fig.5b. Model calculated total rainfall over time.

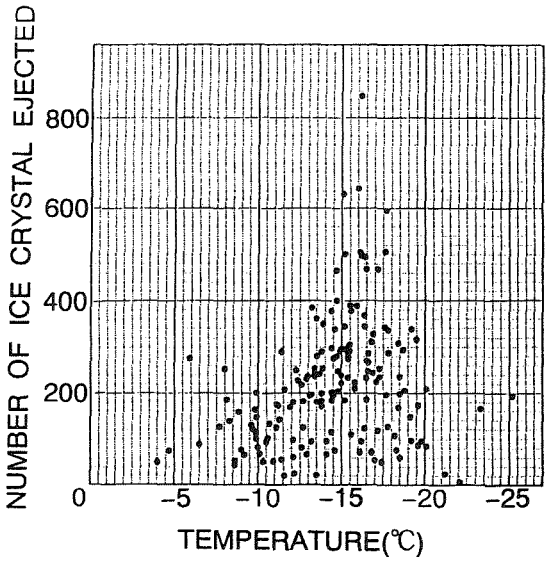

Fig. 6. Ejected ice particles during graupel–graupel collisions.

5. LABORATORY EXPERIMENTS

Videosonde data occasionally showed very high concentrations of ice crystals in the clouds, usually accompanied by graupel. Since the temperature of the region where such high ice crystal concentrations were observed was much colder than that of the region where the Hallett–Mossop ice multiplication process occurs, another process must be responsible. It was assumed that new ice crystals were produced during graupel–to–graupel collisions; especially when large graupel grown mainly by riming collide with small graupel grown by deposition. In such collisions large graupel having a solid surface will break branches growing on the smaller graupel.

The experiments were conducted in a cold box in which graupel were simulated by rotating ice spheres (Takahashi et al, 1995c). Spheres rotating at higher speeds were assumed to correspond to large graupel whilst more slowly rotating spheres were assumed to simulate small graupel. The experimental results showed the highest rate of crystal production at −16℃ (Fig. 6.). Thus, production of crystals through graupel–to–graupel collisions seems sufficient to explain the high concentrations of ice crystals in some rainbands.

6. SUMMARY

Videosonde data have shown the existence of different precipitation processes in rainbands in different climatological areas. The cloud model results suggest that maximum rain production occurs in monsoon area rainbands. Many ice crystals may be newly formed during graupel–to–graupel collisions according to laboratory work.

REFERENCES

Takahashi, T., 1990: Near absence of lightning in torrential rainfall producing micronesian thunderstorms. Geophys. Res. Lett., 17, 2381–2384.

Takahashi, T., and K. Kuhara, 1993: Precipitation mechanisms of cumulonimbus clouds at Pohnpei, Micronesia. J. Meteor. Soc. Japan, 71, 21–31.

Takahashi, T., K. Suzuki, M. Orita, M. Tokuno and Robert de la Mar, 1995a: Videosonde observations of precipitation processes in equatorial cloud clusters. J. Meteor. Soc. Japan, 73, 509–534.

Takahashi, T., K. Suzuki, C. Wang and C. Guo, 1995b: Precipitation mechanisms of cloud systems developed in semi–arid area of Pingliang, China–Videosonde observation. J. Meteor Soc. Japan, 73, 1191–1211.

Takahashi, T., Y. Nagao and Y. Kushiyama, 1995c: Possible high ice particle production during graupel–graupel collisions. J. Atmos. Sci., 52, 4523–4527.

PHYSICAL CHARACTERISTICS OF HAIL FROM NATURALLY DEVELOPED AND SEEDED CLOUD PROCESSES. RECOMENDATIONS ON MODIFICATION OF PRESENT HAIL SUPPRESSION METHODS

M.I. Tlisov, B.M. Khuchunaev

Hiqh−Mountain Geophysical Institute, Lenin 2, Nalchik, 360030, RUSSIA.

Despite of the hail suppression activities on the productional base in many countries are carried out during several decades there is no unambiguous point of view on the degree of successfulness of hail suppression operation among the specialists, occupied this problem. It is due to that the physical characteristics of hail undergo the considerable natural varia− tions and it is difficult to identify the seeding effect. From another hand this estimate re− mains to be very tedious and thankless task.

In High−Mountain Geophysical Institute (VGI) one of the largest in the world hail− measuring network is functioning since 1983 for hail investigation and estimation of the effect of hail suppression activities on the hail precipitation regime. Its area is 3500 km^2. The network contains 600 passive indicators of hail, 12 automatic hail collectors, 5 recorders, 36 pluviographs.

The analysis results of 12−year data set of microphysical, spectral and energetic hail characteristics from more than 100 hailstorms showed the similarity of samples with and without seeding. The differences between the sets of physical characteristics of hail with and without seeding are negligible. If the proc− esses with kinetic energy with $E < 50$ J m^{-2} refer to the first category, with $50 < E < 600$ J m^{-2} refer to the second category, of $600 < E < 100$ J m^{-2} to the third category and with $E > 100$ J m^{-2} to the fourth category, comparison of areal distribution of processes of 1 and 2 categories showed the considerable differences for hailfall with and without seeding (Fig.1).

It is worth to note that the processes of one category do not damage the agricultural crops and processes of 3 and 4 categories bring 100% damage (Tlisov, et al., 1989).

The analysis and comparison of spectral and energetic characteristics of hailfalls with and without seeding show necessity for improvement of the present methods of hail suppression. In VGI durign the last 12 years

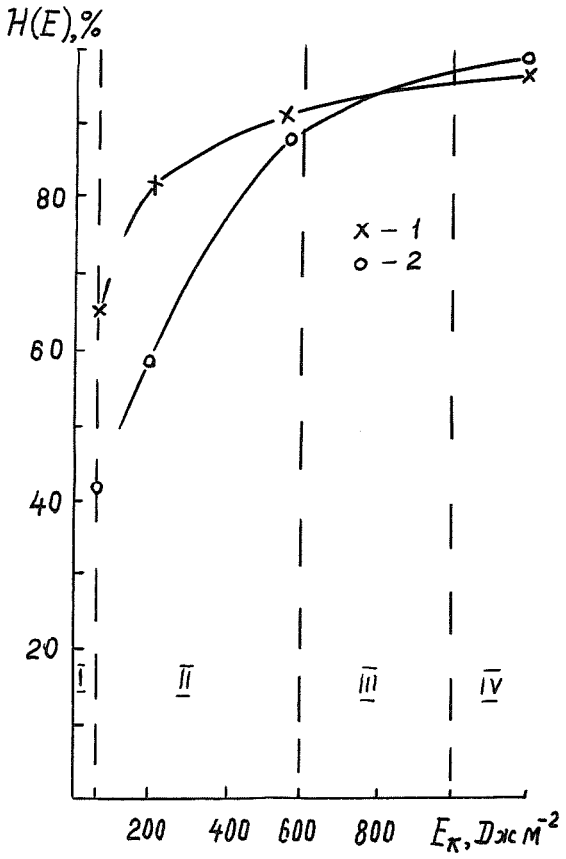

Fig. 1. Some frequencies of areas with defined kinetic energy.

1 − processes without seeding;
2 − processes with seeding;
I − relative number of areas with kinetic energy of 50 J m^{-2};
II − relative number of areas with kinetic energy of 600 J m^{-2};
III − relative number of areas with kinetic energy of 100 J m^{-2};
IV − relative number of areas with kinetic energy more 1000 J m^{-2}.

the microphysical characteristics of hailfalls were obtained and generalized, which can be used for these aims. We found out that in hail cloud two known mechanisms of Bergeron – Fundizen (the ice phase mechanism and warm rain mechanism (Tlisov, 1989).

The formation of droplet and grauple embryos is separated in space. The investigation results of bubble structure and isotopic composition showed that the predominant part of droplet embryos formed at the temperature levels of -8 ... -12 °C and their formation mainly occurred along the upward trajectory. The formation of grouple embryos usually took place during the descend from the upper layers of cloud into the zone of hail growth.

During the crystallizataion of droplet embryos the explosion–like splitting of drops occurs with the formation of ice crystals, which in the future can initiate the crystallization of another drops and become the embryos.

The formation probability of droplet embryos in hail cloud increases with the increase of maximum velocities, Wmax, of updrafts and the height of level of maximum velocities, Hw, and has the form:

$$P = -0.47 + 0.011 \text{ c m}^{-1}\text{Wmax} + 0.14 \text{ km}^{-1}\text{Hw},$$

where P is a fraction of droplet embryos.

With the increase of updraft velocities the turbulent zone increases on the boundaries of updrafts and downdrafts and the increase of height of maximum–velocity levels increases the temperature difference of updrafts and downdrafts of air, thereby the more favourable conditions are created. The decrease of temperature at this level increases a probability of drop freezing and their transformation into the hail embryos.

In the cloud under the effect of updraft the hail separation takes place, the large hailstones, formed on the droplet embryos, fall out near the updraft on the right side of hail streak. A part of grauple and rain drops, which was not used in hail formation , falls on the left side of hail streak. The study of spectral and microphysical characteristics of hailfalls leads us to the conclusion that the boundary of updrafts and downdrafts limited by isotherms of -4... -10 °C, where the droplet embryos form, is the most favourable for the ejection of crystallizing agent in order to decrease the hail damage.

REFERENCES

1. Tlisov M.I. et. al., 1989: Kinetic characteristics of hail and agricultural crops losses/M.I. Tlisov, A.Kh. Taumurzaev, L.M. Fedchenko, B.M. Khuchunaev. Pap. 5th. WMO, Conf. on Weath. Modif. and Appl. Cloud. Phys., Beijing, 1, 339–340.

2. Tlisov M.I., 1989: Physical characteristics and mechanism of hail formation. Pap. 5th WMO Sci. Conf. on Weath. Modif. and Appl. Cloud Phys., Beijing, 337–338.

THE GLOBAL PROPERTIES AND ENVIRONMENT OF MESOSCALE CONVECTIVE COMPLEXES

Arlene G. Laing and J. Michael Fritsch

Department of Meteorology, Pennsylvania State University, USA

1. INTRODUCTION

During the past decade, much research has focussed on mesoscale convective systems (MCSs), especially the subset of MCSs termed mesoscale convective complexes (MCCs). The MCC is characterized and defined by its large ($> 10^5$ km^2), long-lasting (> 6h), quasi-circular cold-cloud shield readily observed in enhanced infrared satellite imagery (Maddox, 1980; Fig. 1). Known for its production of severe weather and copious rainfall (Fritsch et al., 1986), the MCC typically forms in association with a weak mid-tropospheric short-wave trough and a weak surface front or outflow boundary. Its environment often exhibits pronounced low-level temperature and moisture advection in association with a well-defined low-level jet (Maddox, 1983; Cotton et al., 1989). It is widely recognized that MCCs greatly modify the environment in which they develop (Fritsch and Maddox, 1981; Johnson and Bartels, 1992) and that they can be instrumental in initiating subsequent convective weather systems (Fritsch et al., 1994). Under certain slowly-evolving large-scale conditions, series of MCCs develop in roughly the same location and follow similar tracks, thus enhancing the flood potential. This characteristic was recently observed during the 1993 floods in the mid-western United States (Junker et al., 1995).

Since populations of MCCs have been documented in practically all regions of the world it is now possible to assemble a global climatology of MCCs. This study constructs such a global set, and uses it to identify some of the global properties of these important weather systems. The environment of a subset of the global MCC population is compared to other deep convective environments.

2. DATA and METHODS

A global data set was compiled from the MCC populations in Central and South America (Velasco and Fritsch, 1987), the Western Pacific region (Miller and Fritsch, 1991), the Indian monsoon region (Laing and Fritsch, 1993a), Africa (Laing and Fritsch, 1993b), and Europe (added in this study). Seven hundred and fourteen MCC occurrences were used in the study, 475 from the northern hemisphere and 239 from the southern hemisphere. All climatologies included the date of MCC occurrence, time of first storms, initiation, maximum extent, termination, duration, cold-cloud shield areas, and tracks from initiation to termination. The European systems were identified from digitized images from the European geostationary satellite (METEOSAT). Images are products of the International Satellite Cloud Climatology Project (ISCCP) B3 stage radiance data, have a spatial resolution of 30km, and are available at three-hourly synoptic intervals (Rossow et al., 1985). Geographic, seasonal, diurnal, size and duration distributions are presented in Section 3.

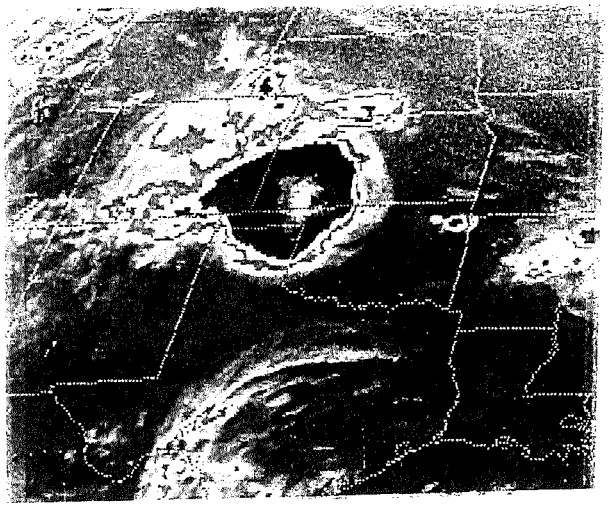

Fig 1. Enhanced infrared image of a mature US MCC, 0130UTC 1 May 1984. Enhancement levels correspond to -33 °C, -42°C, -54°C, -58°C, -64°C, and -70 °C.

Synoptic-scale composites of a subset of the global MCC population were constructed using the 2.5° grid ECMWF Global Analyses. MCCs from regions of maximum occurrences in the US, China, S. America, Africa and Australia were composited on an MCC-centred grid similar to those used by Maddox (1983) and Cotton (1989).

A set of Non-MCC deep convective systems (Table 1) were similarly analysed. The MCC composites contain twelve systems, and the Non-MCC composites nine systems. Horizontal analyses of the MCC and Non-MCC environments in the US are compared in Section 4.

Table 1. Non-MCC deep convective systems

Squall lines:	Area of -54°C cloud area ≥ 50,000km^2 Minor/major axis ≤ 0.4 Size criteria met for at least 2 obs.
Air mass clusters:	Cumulative non-contiguous -54°C cloud area within 5°x 5°box ≥ 50,000km^2, individual elements ≤ 35,000km^2 Size criteria met for at least 2 obs.

3. RESULTS

Figure 2 presents a plot of the geographic distribution of the

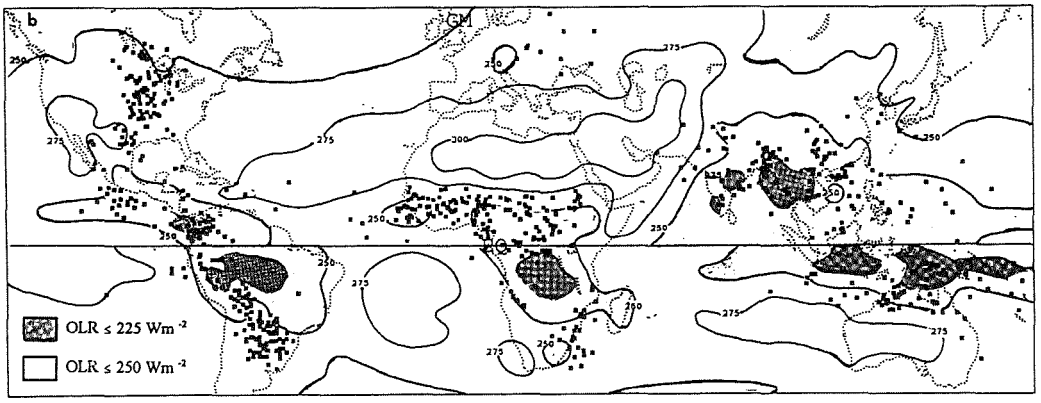

Fig 2. Global distribution of MCCs and regions of widespread frequent deep convection as inferred by outgoing longwave radiation (OLR) minima (shaded). OLR in Wm^{-2} (Winston et al., 1979).

global population of MCCs. It is evident that MCCs occur frequently (~ 364 annually) and are a predominantly continental phenomenon; 91.6% of all systems are land-related[1]. It is also clear that they occur mainly in certain regions of the world, namely:

. In the gradient zones between outgoing-long-wave radiation (OLR) maxima and minima, especially along the periphery of significant OLR minima, and

. In the lee (relative to prevailing mid-level flow) of elevated terrain (Fig. 3)

Since deep convection occurs frequently in many areas other than the MCC regions, it is clear that there must be special thermodynamic and/or dynamic conditions that are conducive to organization of deep convection into the MCC mode.

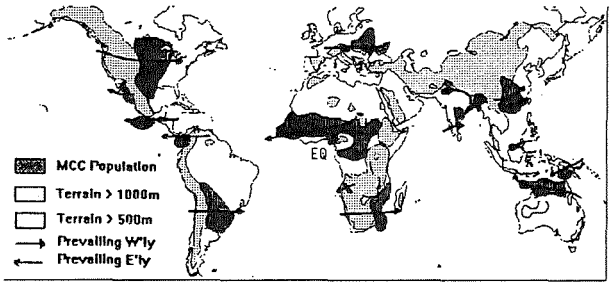

Fig. 3. Relationship among MCC population centers, elevated terrain, and prevailing mid-level flow.

3.1 Diurnal Variability

Since all of the previously documented regional populations of MCCs were found to be nocturnal, it follows that the global population is also predominantly nocturnal. The first thunderstorms usually develop in the mid-to-late afternoon and, by around sunset, their individual cold cloud shields have amalgamated into a coherent mesoscale structure. The cold-cloud shield typically attains MCC initiation size in the early nighttime hours, reaches maximum extent after midnight, and dissipates a few hours after sunrise. The nocturnal nature of MCCs is also evident when the population is stratified into northern and southern hemisphere events and into land and oceanic events. There are, however, some notable differences: 1) most oceanic MCCs end much later in the morning than continental systems, and 2) southern hemisphere MCCs initiate and end slightly later than northern systems. These differences indicate that the lifecycles are not totally dictated by the diurnal radiation cycle.

3.2 Seasonal Influences

MCCs are also influenced by the seasonal radiative cycle, i.e., they tend to follow the sun. This is clearly indicated by the shift in activity from 35S in early January, to poleward of 50N at the height of the boreal summer, and then back to 35S by late December (Fig. 4). Although not evident from Fig. 4, it is important to note that this latitudinal progression of MCC activity tends to be related to the seasonal migration of large scale circulation patterns. For example, in China and the US, where there are pronounced poleward shifts in the jet stream accompanying the boreal summer, the MCC activity shifts strongly poleward (Miller and Fritsch, 1991). While, in South America, where the MCC population is closely related to the quasi-stationary subtropical jet stream, the location of MCC activity changes relatively little (Velasco and Fritsch, 1987).

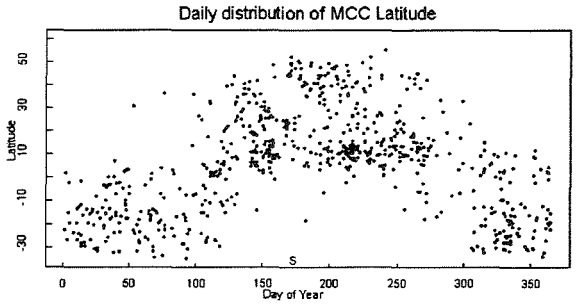

Fig. 4. Daily distribution of MCC latitude.

3.3 Size and Duration

The global MCC population has a mean cloud-top area of 3.54 x 10^5 km^2 and mean duration of 10.8h. Systems in the SH are slightly larger than those in the NH but have a shorter duration. Oceanic systems, although small in number, are, on average, slightly larger and longer lasting than other systems.

There is a tendency for the duration and maximum area in the global population to be positively correlated (correlation coefficient r = 0.385). This simply indicates that systems which generate large cold-cloud shields tend to persist longer than those which produce small shields. Although the relationship is weak, it appears to be ubiquitous with positive correlations in both hemispheres and for the relatively sparse oceanic systems as well.

[1]Land-related MCCs formed over or within 250km of land

4. SYNOPTIC-SCALE COMPOSITES

As expected, the large-scale MCC environment strongly resembles that found by Maddox (1983). Notable features in the MCC genesis zone include a low level jet of high θ_e air and a pronounced north-south temperature gradient with strong warm advection throughout the lower troposphere. The strong warm advection is characteristic of MCC environments (Augustine and Howard, 1991). The height, wind and thermal patterns suggest the presence of a weak cyclonic disturbance on a warm or stationary front that stretches east-west through the genesis zone. Typically, the MCC develops just to the east or northeast of the weak cyclone in the vicinity of the strong warm advection at 850 and 700mb. In contrast to the MCC environment, the squall line environment exhibits a shallow, surface-based layer of warm advection with little or no advection at 850 and 700 mb. The temperature, wind and height patterns indicate the presence of a north-south oriented cold front along the western border of the squall line genesis zone. Convection develops in the warm airmass ahead of the north-south oriented cold front in an environment which appears to be locally more barotropic than the MCC environment. The environment of the airmass convective events is similar in some respects to both the MCC and squall line environments, but there are important differences as well. For example, magnitudes of the K-index and θ_e are about the same as for MCCs and squall lines, however the wind speeds and shear are noticeably weaker. Of particular note is that there is no low-level jet nor are there any pronounced frontal boundaries or warm advection in the near vicinity of the region of convective activity.

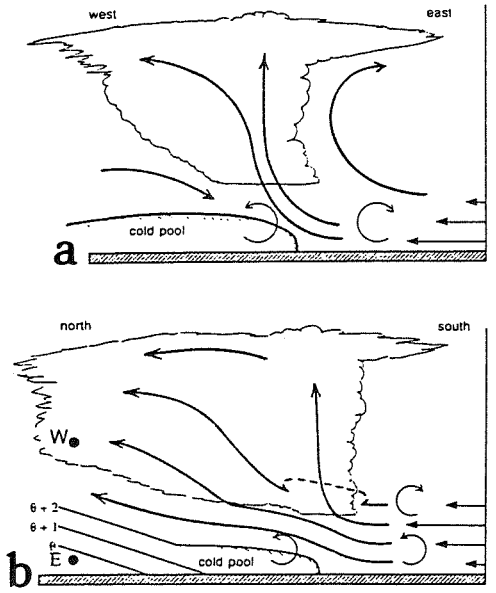

Fig. 5 Schematic of: a) squall line environment (adapted from RKW). Bold arrows indicate flow relative to an eastward propagating convective line. Horizontal arrows indicate vertical distribution of horizontal wind. b) As in (a) except for MCC environment and flow is relative to an east-west oriented convective line. Large dots labelled W and E indicate westerly and easterly flow, respectively, of large scale environment.

It is interesting to compare the MCC and squall line environments within the framework of the Rotunno et al. (1988) (RKW) conceptual model for long-lived convective systems. Recall that, within this framework, the vorticity of the ambient shear opposes the vorticity of the convectively- generated surface-based cold pool. For a north-south oriented line, the RKW configuration of shear and cold pool would fit the environment found in the squall line composite (Fig. 5a). On the other hand, the MCC environment exhibits a very different configuration of vertical wind shear relative to the orientation and direction of propagation of the deep convection (Fig 5b). In particular, the shear-induced vorticity has the same sign as that which would be expected from any convectively-generated cold pool that would develop. Moreover, the presence of the strong warm advection suggests that there is an additional mechanism, other than the convectively-generated cold pool, that can provide the sloping lift necessary for producing the stratiform region of many mesoscale convective systems, especially MCCs. Specifically, the warm advection implies that there is sloping isentropic lift as an inherent part of the MCC environment. Thus, considering the sign of the environmental shear and the presence of the sloping isentropic lift, the MCC environment is more conducive to producing large stratiform anvils which, of course, are characteristic of MCCs and distinguish them from other modes of organized convection.

5. SUMMARY AND CONCLUDING REMARKS

An estimate of the global population of MCCs was compiled. The global population was constructed by combining the regional populations documented in the literature and by examining two years of enhanced infrared satellite imagery for regions not included in the published literature. A total of 714 MCCs, 475 from the northern hemisphere and 239 from the southern, were included in the data set. The typical MCC exhibits a maximum cold-cloud shield area of about 3×10^5 km^2 and persists for about 10 h. Examination of the global population indicates that MCCs occur frequently (> 300 per year) and are found over all continents (except Antarctica) and tropical oceans. Since the populations used in this study included the 1982-83 and 1986-87 El Niños, as well as part of the 1988-89 La Niña, there is a possibility that the MCC totals reported here may differ from the long-term average. Although they occur in many places around the world, they are a predominantly land-based phenomenon and tend to be concentrated into certain limited regions, especially on the periphery of OLR minima and in the lee of major terrain features.

The majority of MCCs exhibit a nocturnal lifecycle that begins in the mid to late afternoon, peaks after midnight, and ends shortly after daybreak. Nocturnal development is indirectly tied to the diurnal radiative cycle. For example, studies of MCC populations in the US indicate that a nocturnal low-level jet is typically present during their development and is an important feature because it provides a continuous supply of high θ_e air to the intense and long-lived convection. According to Blackadar (1957), the nocturnal low-level jet in over-land MCC regions is a consequence of terrain-related differential radiative processes and decoupling of daytime well-mixed boundary layers from the friction layer as afternoon solar radiation diminishes. Interestingly, recall that most MCC populations are immediately downwind (relative to prevailing

mid-level flow) of significant terrain features.

The lifecycle of oceanic MCCs was found to be slightly different from the general MCC population in that the diurnal modulation is weaker and many systems persist until much later in the morning. This difference suggests that lifecycles are not totally dictated by the diurnal radiation cycle, but may also be affected by such factors as regional physiography and/or local dynamical processes. It was found that the global MCC population is strongly influenced by the seasonal radiative cycle. In particular, activity shifts from 35S in early January to beyond 50N at the peak of the boreal summer and then returns to 35S by December. This shift is most pronounced in the northern hemisphere and occurs concomitantly with the poleward migration of the jet stream. In the ocean-dominated southern hemisphere, where jet streams are quasi-stationary, poleward migration is not as readily evident.

Not surprisingly, MCCs with large cold-cloud shields last longer than those with small shields. McAnelly and Cotton (1992) identified a meso-β-scale convective scale cycle that occurs early in the meso-α-scale growth phase and argue that it distinguishes the relatively long-lived MCCs from other shorter-lived MCSs. The critical importance of early explosive growth was noted previously by Tollerud et al. (1992). Thus, strong early growth may be the distinguishing factor in the longevity and size distributions of MCCs.

Very few MCCs developed in Europe for reasons which may be related to interference of the low-level flow by the mountainous terrain or the fact that the air mass feeding these systems is not as moist as the air flowing from the Gulf of Mexico or the Amazon Basin. In their radar-based study of mesoscale precipitating systems in Switzerland, Schiesser et al. (1995) found that instability was weaker in this region and that systems were not as well organized as those in the Central Plains of the US.

Since deep convection is common in many areas other than MCC-active regions, clearly, there must be special conditions necessary for the organization of deep convection into the MCC mode. Fundamental differences were found among the composite environments of MCCs, squall lines and air mass clusters in the US. Most notable were that the relationship between the vorticity of the ambient shear and that of the convectively-produced surface-based cold pool is reversed in MCC environments compared to squall line environments. Also, unlike the squall line environment, the MCC environment contains a large-scale lifting mechanism that favors the development of large stratiform precipitation regions, a feature characteristic of MCCs.

Finally, the results presented here raise many questions about the factors and processes that dictate the location, frequency, and seasonal distribution of MCCs. Most important, considering their predominantly nocturnal lifecycles, copious rainfall, large and deep cloud shields, and great frequency, the global population of MCCs maybe a significant component of the global hydrologic cycle and heat budget.

Acknowledgements

Thanks to Dr. Ines Velasco for providing Central and South America MCC data and to Dr. Robert Vislocky for statistical assistance. This research was supported by NSF Grant ATM-92-22017.

REFERENCES

Augustine, J. A. and K. W. Howard, 1991: Mesoscale convective complexes over the United States during 1986 and 1987. *Mon. Wea. Rev.*, **119**, 1575-1589.

Blackadar, A. K., 1957: Boundary layer wind maxima and their significance for the growth of nocturnal inversions. *Bull. Amer. Meteor. Soc.*, **38**, 283-290.

Cotton, W. R., M.-S. Lin, R. L. McAnelly and C. J. Tremback, 1989: A composite model of mesoscale convective complexes. *Mon. Wea. Rev.*, **117**, 765-783.

Fritsch, J. M. and R. A. Maddox, 1981: Convectively-driven mesoscale pressure systems aloft, Part I: Observations. *J. Clim. Appl. Meteor.*, **20**, 9-19.

Fritsch, J. M., R. J. Kane and C. H. Chelius, 1986: The contribution of mesoscale convective weather systems to the warm season precipitation in the United States., *J. Clim. and Appl. Meteo.*, **25**, 1333-1345.

Fritsch, J. M., J. D. Murphy and J. S. Kain, 1994: Warm core vortex amplification over land. *J. Atmos. Sci.*, **51**, 1781-1806.

Johnson, R. H. and D. L. Bartels, 1992: Circulations associated with a nature-to-decaying mid-latitude mesoscale convective system. Part II: Upper-level features. *Mon. Wea. Rev.*, **120**, 1301-1320.

Junker, N. W., R. S. Scheidner, and R. A. Scofield, 1995: The meteorological conditions associated with the Great Midwest Flood of 1993. *Preprint, 14th Conference on Weather Analysis and Forecasting,* Amer. Meteor. Soc., 15-20 Jan, Dallas, Texas, (J4) 13-17.

Laing, A. G. and J. M. Fritsch, 1993a: Mesoscale convective complexes over the Indian monsoon region. *J. Climate,* **6**, 911-919

Laing, A. G. and J. M. Fritsch, 1993b: Mesoscale convective complexes in Africa. *Mon. Wea. Rev.*, **121**, 2254-63.

Maddox, R. A., 1980: Mesoscale convective complexes. *Bull. Amer. Meteor. Soc.*. **61**, 1374-1387.

Maddox, R. A., 1983: Large-scale meteorological conditions associated with mid-latitude, mesoscale convective complexes. *Mon. Wea. Rev.*, **111**, 1475-1493.

Mapes, B. E. and R. A. Houze, 1993: Cloud clusters and superclusters over the oceanic warm pool. *Mon. Wea. Rev.*, **121**, 1398-1415.

McAnelly, R. L. and W. R. Cotton, 1989: The precipitation life cycle of mesoscale convective complexes over the central United States. *Mon. Wea. Rev.*, **117**, 784-808.

McAnelly, R. L. and Cotton, W. R. , 1992: Early growth of mesoscale convective complexes: A meso-β-scale cycle of convective precipitation? *Mon. Wea. Rev.*, **120**, 1851-1877.

Miller, D. and J. M. Fritsch, 1991: Mesoscale convective complexes in the western Pacific region. *Mon. Wea. Rev.*, **119**, 2978-2992.

Rossow, W. B., E. Kinsella, A. Wolf, L. Garder, 1985: International Satellite Cloud Climatology Project description of reduced radiance data. WMO TD-No 58, World Meteorological Organization/International Council of Scientific Unions.

Schiesser, H. H., R. A. Houze, and H. Huntrieser, 1995: The mesoscale structure of severe precipitation systems in Switzerland. *Mon. Wea. Rev.*, **123**, 2070-2097.

Tollerud, E. I., J. A. Augustine and B. D. Jamison, 1992: Cloud top characteristics of mesoscale convective systems in 1986., *Preprints, Sixth Conf. on Satellite Meteorology and Oceanography,* Amer. Meteor. Soc., 4-10 Jan 1992, Atlanta, GA.

Velasco, I. and J. M. Fritsch, 1987: Mesoscale convective complexes in the Americas. *J. Geophys. Res.*, **92**, 9591-9613.

Winston, J. S., A. Gruber, T. I. Gray Jr., M. S. Varnadore, C. L. Earnest, L. P. Mannello, 1979: Earth-Atmosphere Radiation Budget analyses derived from NOAA satellite data, June 1974-February 1978.

VALIDATION OF SATELLITE-DERIVED CLOUD PROPERTIES DURING TOGA/COARE

David R Doelling[1], Patrick Minnis[2], Rabindra Palikonda[1],
J Kirk Ayers[1], Thomas P Ackerman[3], James D Spinhirne[4], and C Martin R Platt[5]

[1]Analytical Services and Materials, Inc., Hampton, VA 23666, USA
[2]NASA Langley Research Center, Hampton, VA 23681, USA
[3]Dept. of Meteorology, Penn State University, University Park, PA 16802, USA
[4]NASA Goddard Space Flight Center, Greenbelt, MD 20771, USA
[5]CSIRO Division of Atmospheric Research, Aspendale, Victoria, Australia

1. INTRODUCTION

The tropical maritime atmosphere is one of the most important, but least understood parts of the global climate system. Tropical clouds play an important role in the hydrological cycle, radiation budget, and general circulation. Thus, the accurate quantification of tropical cloud properties is required to better understand and model atmospheric processes in the tropics. Tropical cloud systems have been monitored with satellites for over a decade. However, minimal attention has been given to the validation of satellite retrievals of cloud properties in the equatorial regions. This paper presents the results and verification of an analysis of satellite data taken during the Tropical Ocean Global Atmosphere Coupled Ocean-Atmosphere Response Experiment (TOGA/COARE) conducted from November 1992 through February 1993 over the tropical western Pacific.

2. DATA AND ANALYSIS

Cloud properties were derived at three different scales from hourly, 5-km Geostationary Meteorological Satellite (GMS) visible (VIS; 0.65 μm) and infrared (IR; 11 μm) data taken over the TOGA/COARE area from November 1992 through February 1993. The largest domain consists of a 2.5° grid extending from 137.5°E to 180°E and 10°N to 12.5°S. The 1°-grid is bounded by 6°N, 162°E, 8°S, and 148°E; the 0.5°-grid by 4°N, 160°E, 6°S, and 150°W. The GMS data were calibrated against collocated Advanced Very High Resolution Radiometer data from NOAA-11. The methods of Minnis et al. (1987) were used to determine clear-sky reflectance and IR temperature at each hour and grid box. The layer bispectral threshold method (LBTM) of Minnis et al. (1995) was used to derive amount, height z_c, and optical depth t at three levels: low ($z_c < 2$ km), middle (2-6 km), and high ($z_c > 6$ km). Temperature is converted to altitude using temperature profiles from the National Meteorological Center analyses. Cloud temperature is adjusted in LBTM using the values of τ. This adjustment only affects optically thin clouds and decreases (increases) the cloud temperature (altitude). A simple hexagonal-column cirrostratus model is used to retrieve τ. The satellite analyses are available via the Internet at http://vikranth.larc.nasa.gov/larc_ toga_twp.html.

Cloud top and base heights were derived along the flight paths of the NASA ER-2 from the nadir-viewing cloud lidar system (CLS) data (available on the Internet at http://virl.gsfc.nasa.gov/). Cloud-base height is uncertain for optically thick clouds. Cloud center altitude z_a is the mean of the top and base heights. Cloud thickness Δz_a was determined by averaging the summed thicknesses of all cloud layers in a given height category and time interval. The thicknesses between the cloud layers were not included in the averaging. Similar quantities were determined from micropulse lidar (MPL) data taken from the surface at the Kavieng Atmospheric Radiation Measurement Pilot Radiation Observation Experiment. Kavieng (2.35°S, 150.48°E) is located near the northern border of a 0.5° grid box. Cloud optical depths τ_s derived from Kavieng sun photometer data were averaged at 1-hour intervals centered at the UTC half hour. The Kavieng data can also be accessed electronically at http://www.arc.essc.psu.edu/datasets/togac/b4.html.

The satellite and aircraft data were compared at the three grid scales. Only four ER-2 flights (Jan. 18, Feb. 20, 23, and 24) entered one of the three grids when both GMS VIS and ER-2 lidar data were acquired. The average lidar cloud heights were computed for each grid box during a leg of the flight. Thus, there may be two lidar datasets for a given box: one during the outward leg and another during the return leg. The heights in a given box are compared to the LBTM results closest in time to the ER-2 overpass.

Kavieng is at the northwestern tip of the relatively large island of New Ireland. Because of Kavieng's location, the surface-based data are compared to the LBTM results from the 0.5° regions containing the island and immediately north of the island. Some land effects may dominate the clouds in the island region, whereas the Kavieng data may be more representative of the surrounding ocean.

3. RESULTS

The February mean total cloud amounts and high-cloud amounts, optical depths, and heights are shown in Fig. 1 for the 1° grid. Most of the satellite-observations are classified as high clouds. Near Kavieng, there are north-south cloud amount and optical depth gradients with greater values south of the island. The high- cloud maxima are associated with the areas having the most convective activity. The relatively low optical depths and large cloud cover suggest that the high clouds in this domain contain only small amounts of ice water.

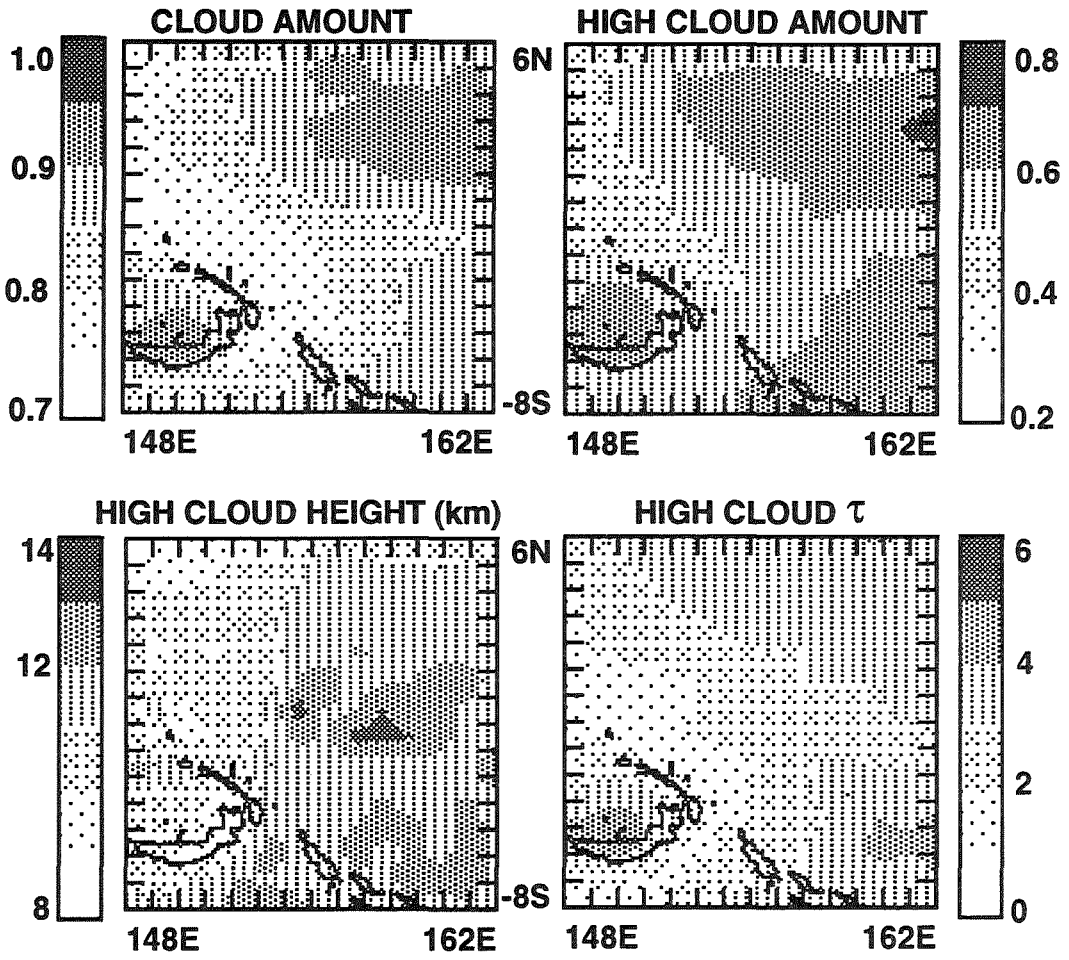

Fig. 1. Mean cloud properties from 1° gridded LBTM analyses for February, 1993.

3.1 Aircraft comparisons

The ER-2 typically flew northwestward between the islands into the center of the grid from Townsville, Australia and returned along much the same path. The average February high-cloud amounts and optical depths are ~ 55% and 2, respectively (Fig. 1). The mean cloud-center altitude is ~11 km. Agreement between the CLS and satellite for the 4 ER-2 flights is very good if the LBTM high-cloud center heights in the 1° grid are compared (Fig. 2). Of the 30 cases, only 4 differ by more than 2 km. The high-cloud results for two grids are summarized in Table 1. Sampling for the 0.5° grid was limited because of its distance from Townsville. Most of the 0.5° data correspond to one or two 1° boxes. Because of this limited sampling, the 0.5° results are not considered here. Table 1 includes the number of samples n, the mean LBTM high-cloud fraction in the sampled regions, the standard deviations of the differences σ, the lidar cloud thickness Δz_a, and the mean differences in the thicknesses Δz_c - Δz_a. The LBTM cirrus thickness Δz_c was computed using an empirical formula based on midlatitude cirrus clouds (Minnis et al., 1995).

The greatest number of samples were obtained using the 1° grid. Nearly overcast high cloud conditions prevailed during most of the flight legs. The average optical depths are greater than the means shown in Fig. 2 because the flights were generally planned for disturbed conditions when thick anvil formation was likely. The LBTM high-cloud center heights are lower than the CLS values by the same amount (~ -0.3 km) for both thick and thin clouds. The standard deviations in the differences are slightly larger for the thin clouds as would be expected. Overall, this comparison suggests that the optical depth corrections for the thin clouds are relatively accurate for these cases. Although the center

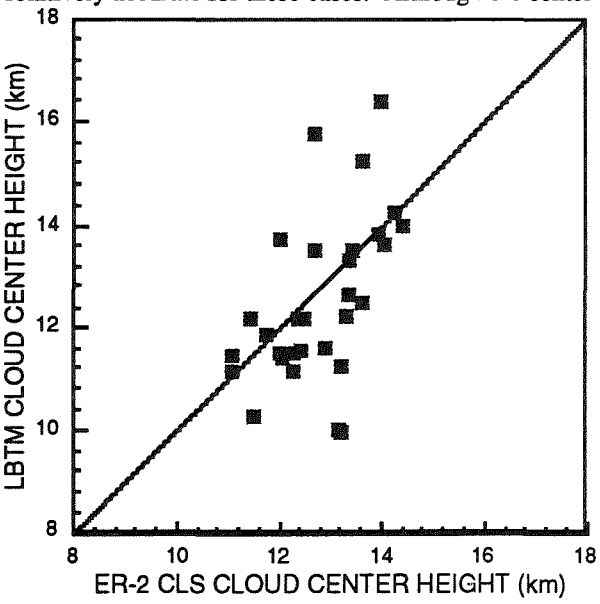

Fig. 2. Mean high-cloud center heights for 1° grid data.

Table 1. Summary of matched CLS and LBTM high-cloud properties for four ER-2 flights during TOGA/COARE.

GRID	τ range	mean τ	n	C	z_a (km)	$z_c - z_a$	$\sigma(z_c - z_a)$ (km)	Δz_a (km)	$\Delta z_c - \Delta z_a$ (km)
1°	all	6.5	30	.95	12.9	-0.4	1.3	3.7	-1.0
	0 - 6	2.8	15	.91	12.5	-0.3	1.8	4.0	-1.4
	> 6	10.2	15	1	13.3	-0.4	0.8	3.4	-0.6
2.5°	all	6.1	27	.87	13.3	-1.5	1.5	3.5	-0.5
	0 - 6	3.9	13	.78	12.9	-1.7	1.8	3.9	-0.9
	> 6	8.2	14	.95	13.6	-1.2	1.3	3.2	-0.2

heights are well-placed by the LBTM, the cloud thickness estimates are too low.

Agreement between the 2.5° satellite and lidar cloud heights is not as good as that for the 1° data. In these cases, the LBTM underestimates z_a by more than 1 km. The fact that the high-cloud centers for the thicker clouds are underestimated by 1.2 km suggests that the clouds sampled by the lidar are probably not representative of the 2.5 region. Thus, it may be concluded that the 1° grid is more relevant for comparison of the satellite and aircraft results in this study.

3.2 Surface comparisons

The values of τ for high clouds are plotted with τ_s in Figs. 3 and 4 for the 0.5° regions 262 and 242 containing Kavieng and north of Kavieng, respectively. Although the data are not well correlated for either region, they appear to be evenly distributed about the line of agreement for region 242. The mean region-262 high-cloud optical depth is 2.3 compared to 1.4 for the sun photometer. These averages are consistent with the monthly means in Fig. 1. The rms difference is 2.3. If the total τ for the matching times is considered for region 262, the mean and rms differences are 1.9 and 3.4, respectively, indicating that a significant amount of low and midlevel clouds were over the region during some of the matched times. Moving to region 242 reduces the mean optical depth differences to 0.0 and 0.6 for high and total cloud cover, respectively. The respective rms differences are 1.4 and 3.1 for 40 and 42 samples.

As seen in Fig. 1, Kavieng is on the edge of a gradient in τ. Clouds directly over the island tend to have slightly larger optical depths than the surrounding water due to deeper convective processes over the island center. If it is assumed that the atmosphere over Kavieng at 3 m above mean sea level is more like the surrounding waters than the island interior, then it is likely that region 242 is more like the site than region 262. If all 4 months are considered together, the high-cloud optical depth from the LBTM in region 242 is 2.4 compared to 2.0 from the sun photometer, a difference of 17%. From the standard deviation of 3.8 in the 130 differences, it can be concluded that τ is accurate in the mean to within 0.4 $\pm$ 0.3 relative to τ_s. The large scatter seen in Figs. 3 and 4 and quantified by the rms

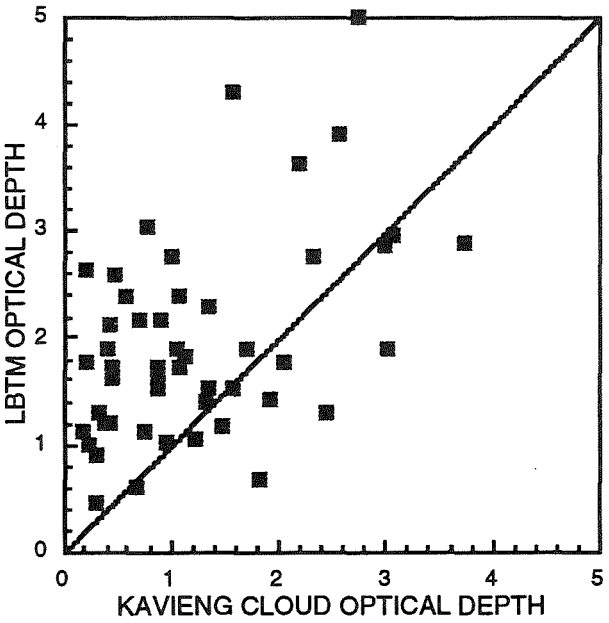

Fig. 3. February surface and region-262 hourly high-cloud optical depths.

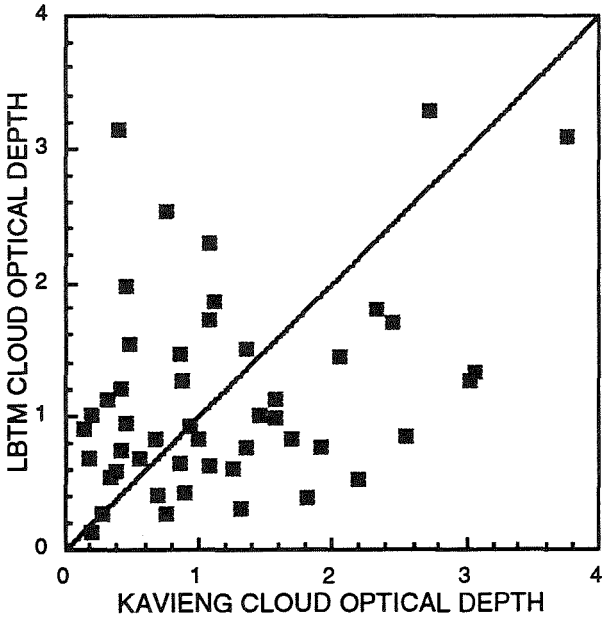

Fig. 4. February surface and region-242 hourly high-cloud optical depths.

errors is most likely the result of the large differences in spatial sampling between the two methods. A complete evaluation of both the mean and rms differences will require matching the GMS pixels with the sun photometer field of view. While that technique will minimize spatial sampling differences, it will not eliminate them entirely.

The cloud-height comparisons using the MPL at Kavieng differ from the aircraft results. The region-242 LBTM high-cloud centers were almost 3 km higher than the MPL centers, while the mid-cloud centers were only 0.2 km higher. This apparent overestimate from the satellite data is most likely due to two aspects of the MPL data taken during TOGA/COARE. First, the surface lidar cannot penetrate thick clouds, so that the true cloud top cannot be discerned in thicker clouds. Thus, MPL cloud top height will be too low if the cloud is thick. The maximum optical depth that can be penetrated with the MPL has not yet been established. The cloud heights were determined manually from the low-resolution MPL imagery. The first tropical MPL data arre quite noisy, especially in the upper levels. The noise level is so great in some images that thin cirrus clouds cannot be discerned with any confidence. Thus, there are significant problems in determining the top heights for both thick and thin cirrus clouds.

The CSIRO lidar (Platt et al., 1995), at Kavieng during January February 1993, is more powerful and produces a much cleaner set of lidar returns than the PROBE MPL. The mean cloud-center heights from the 12 matching LBTM-CSIRO lidar data points for region 242 differ by almost 2 km. In this case, the lidar tops are greater than the satellite values. Although this comparison has very few data points, it indicates that the MPL may not be detecting the higher layer clouds.

Initial estimates of the visible optical depths derived from the CSIRO lidar are 0.2 ± 0.2 less than τ(LBTM), differences quite similar to those from the sun photometer-satellite comparison. Again, the number of samples is prohibitively small for drawing conclusions.

4. DISCUSSION

Overall, cloud-center heights for the tropical cirrus appear to be underestimated from the satellite perspective. Cirrus cloud thickness from the aircraft data is substantially greater (~1 km) than estimated by the LBTM. The LBTM thickness parameterization is based on measurements of midlatitude cirrus using τ and cloud temperature as independent variables. The thickness differences suggest that the tropical cirrus may be more diffuse and have a smaller ice water content than the typical midlatitude cirrus clouds. The diffuse nature of these clouds can affect the satellite determination of cloud-center height, especially if the ice is concentrated in the lower portion of the clouds.

In the aircraft data, a cloud layer between 0.5 and 2.5 km thick with very low intensity lidar backscatter often occurred between 15 and 18 km above more reflective clouds between 9 and 15 km. These nebulous upper-layer clouds may be the subvisual cirrus that is frequently observed in this area (e. g., Wang et al., 1996). If so, the optical depth is extremely small and virtually undetectable with passive reflected visible techniques. Thus, the subvisual cirrus has minimal impact on the retrieval which, in this event, will depend entirely on the optical depth of the lower cloud. Because these top-level clouds are ~ 1-km thick, on average, for this dataset and occur in roughly 80% of the relevant returns, their presence can explain much of the thickness difference observed for the 1° data. The presence of subvisual clouds in the CSIRO dataset over Kavieng may help account for the discrepancies in that LBTM-lidar cloud height comparison. The cloud tops occurred at 16-17 km on several of the sampled days. Because only thin cirrus were observed in that comparison (τ ~1.6) and the clouds were 4-5 km thick when the tops were at 17 km, it is quite likely that a layer of subvisual cirrus was present above the main cirrus cloud.

In addition to the spatial differences between the satellite and other sensors, other causes for the discrepancies in the cloud heights may be the models used to deterive the optical depths. The ice crystals in these clouds may have a different shape and/or size that the assumed cirrostratus model. The optical depths of the stratospheric aerosol layer from the June, 1991 Mt. Pinatubo eruption ranged from 0.05 to 0.15 over the tropics and may have biased one or all of the datasets.

5. CONCLUDING REMARKS

These initial results reveal that the satellite-derived cirrus properties in the tropics are quite reasonable. Subvisual clouds may be an important consideration in the comparisons. A more complete and accurate comparison will be performed by matching the satellite and correlative data fields of view. Such an analysis should diminish the rms errors and may affect the bias errors.

6. REFERENCES

Minnis, P., E. F. Harrison and G. G. Gibson, 1987: Cloud cover over the equatorial eastern Pacific derived from July 1983 ISCCP data using a hybrid bispectral threshold method. *J. Geophys. Res.*, **92**, 4051-4073.

Minnis, P., W. L. Smith, Jr., D. P. Garber, J. K. Ayers, and D. R. Doelling, 1995a: Cloud properties derived from GOES-7 for the spring 1994 ARM Intensive Observing Period using Version 1.0.0 of the ARM Satellite Data Analysis Program. *NASA RP 1366*, August, 59 pp.

Platt, C. M. R., S. A. Young, P. J. Manson, and G. R. Patterson, 1995: Observations of tropical cirrus properties in the Pilot Radiation Observation Experiment using lidar and the CSIRO ARM filter radiometer. *Proc. 4th ARM Sci. Team Mtg., Feb. 28-Mar. 3, 1994, Charleston, South Carolina.* CONF-940277, U.S. Dept. of Energy, Washington, D.C., pp. 247-252.

Wang, P.-H., M. P. McCormick, P. Minnis, G. S. Kent, and K. M. Skeens, 1996: A 6-year climatology of cloud occurrence frequency from SAGE II observations (1985-1990). Submitted to *J. Geophys. Res.*

NUMERICAL SIMULATIONS OF HYGROSCOPIC SEEDING FOR RAINFALL ENHANCEMENT

ZAILIANG HU[1], ROELOF T. BRUINTJES[2] AND ERIC A. BETTERTON[1]

[1]Institute of Atmospheric Physics, University of Arizona, Tucson, AZ 85721, USA
[2]MMM Division, National Center for Atmospheric Research, Boulder, CO 80307, USA

1 Introduction

This paper describes some preliminary microphysical modeling of hygroscopic seeding of convective clouds in central Arizona with the objective to enhance precipitation. Input data were collected during the two month field experiment of the Arizona Program from 15 January through 15 March 1995. One of the objectives was to understand the natural precipitation of central Arizona winter storms and to investigate the feasibility of cloud seeding to enhance precipitation.

2 Numerical Model Experiments

The microphysical parcel model, an update of Hall (1980), includes CCN activation, condensation and droplet collection. Numerical diffusion is inevitable for numerical methods such as Berry and Reinhardt (1972) (for collection process) and Smolarkiewicz (1980) (for condensation process) when low resolutions are used. Reasonably high resolutions are generally applied to control the artificial spreading of the numerical solutions (Hu and Srivastava, 1995). For mass doubling every 6 bins in the parcel model, the tests showed that numerical diffusion was reduced substantially compared with solutions generated by mass doubling every 2 bins; further improvement by using mass doubling every 8 bins was very small. The smallest droplet is 0.01 μm and the largest droplet is over 3000 μm in radius. Condensation and collection schemes were similar to those described in Hall (1980), but the collection efficiencies were from Boehm (1990 and 1992) and coalescence efficiencies were from Beard and Ochs (1985).

The major difference between the current model and Hall (1980) is that drop nucleation is treated explicitly in the current version, while Hall used a simplified approach. Because of the focus on hygroscopic seeding, activation is the root of precipitation and it has to be understood properly. When investigating the hygroscopic seeding effect in a convective cloud, Tzivion et al (1994) distributed the newly activated drops at every time step into a Gamma function, this simplified the calculation but could bias the results. For example, at very low supersaturations, when only giant or ultra giant particles are activated, newly activated drops should not be distributed to very small drops.

We calculate the nucleation process according to classic theory. A salt particle is activated only if the local supersaturation exceeds its critical supersaturation. This suggests that, at every time step when activation is effective, the distributions of activated droplets do not have the same shape but are fragments of a complete distribution. One simplification made in this study is based on Fitzgerald (1972). Droplets grow from their equilibrium sizes at a fixed relative humidity of 95% and cloud base temperature. Unactivated particles do not participate in diffusional growth but stay in their equilibrium sizes at the pre-determined relative humidity and cloud base temperature. The smallest radius of dry particle (natural and seeded) is 0.01 μm. Dry CCN distribution for s $\leq s_{cut1}$ is determined by the profile of $293s^{0.81}$, which was the observed CCN spectrum at cloud base in a convective system on 22 Febuary 1995 in the Verde Valley, AZ and $s_{cut1} = 0.4\%$ according to Cooper et al (1994). Dry particle distribution is extended to giant and ultra giant sizes by two power laws according to Cooper et al. Hobbs et al (1985) showed more abundance of CCN in natural ultra giant sizes.

The spikes near the truncation sizes are smoothed out by allowing the CCN spectrum to go further to intercept the large particle distribution. The connection between large and giant particles is similar. This results in loss of CCN concentration, a constant factor is applied to the whole size spectrum to adjust for this. This approach works as long as r_{cut1} (corresponding to s_{cut1}) $\gg 0.01$ μm, but when r_{cut1} is close to 0.01 μm, it results in substantially increased slope for the CCN spectrum and therefore violates the measurements.

Vertical air velocity, W, was prescribed as a function of height, 2 m/s at cloud base, increasing linearly to 5 m/s at z = 2 km and then dropping to

0 at z = 5 km. At cloud base, P = 710 mb, T = 3 °C. P and T above cloud base were determined by thermodynamic (hydrostatic and adiabatic) equations.

The supersaturation profile, especially the maximum supersaturation s_{max}, depends on a detailed treatment of the condensational growth equation (dm/dt). The equation in Hall (80) was modified to include adjustment to both the diffusivity and thermal conductivity. Vapor and thermal jumps were 0.1 and 0.2 μm (Young, 93). The condensation and accommodation coefficients were 0.04 and 1, respectively. This change was necessary since r(1) was 0.01 μm instead of 1 μm. It was difficult to include the solution effect in the condensational growth equation for individual drops because these are not tracked in the Eulerian model. Applying the curvature effect after the maximum supersaturation results in a slightly higher supersaturation. However, this had very little effect on the droplet size distribution, rain water content (RWC) and radar reflectivity factor (Z) profiles. Therefore, solution and curvature effects were not considered. As in Hall (1980), the supersaturation was calculated by using an implicit scheme which is dynamically and microphysically consistent.

The seeding particle profile was provided by measurements from airborne PCASP and FSSP in a clear air situation in South Africa (RH < 50% and T = 10 °C). The distribution was fitted by a 5th order polynomial and diluted to allow for mixing and dispersion. The seeding particle distribution is valid for 0.066 $\mu m \leq$ r $\leq$ 15.25 μm. According to Cooper et al (1994), natural CCN were taken to be ammonium sulfate, and seeded particles potassium chloride.

3 Results

Figure 1 shows that the seeding particles with total concentration 150 cm^{-3} and seeding mass 5.1×10^{-5} g m^{-3} outnumber the natural CCN particles in the giant and ultra giant sizes. Small CCNs as represented by the power law $293s^{0.81}$ would be activated only at high supersaturations (> 1%), otherwise, the cumulative number distribution was dominated by the seeded CCNs.

Figure 2 demonstrates that hygroscopic seeding substantially enhanced the droplet growth. By comparing Z, it shows that coalescence started at least a half kilometer lower in the seeded case. Even though the addition of seeding particles reduced the supersaturation in the cloud and resulted in reduced condensational growth, this difference was negligible compared with the enhanced coalescence

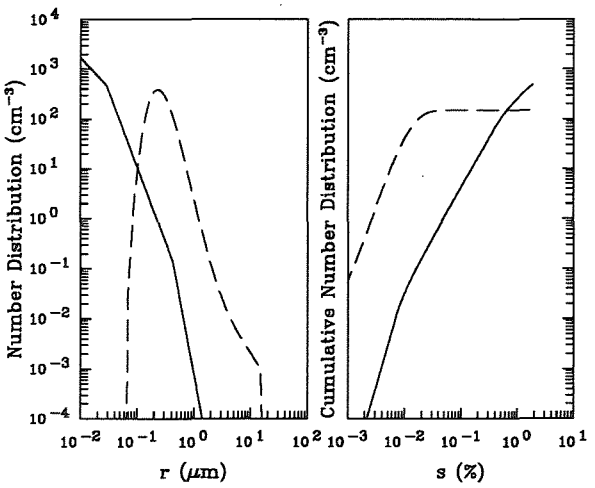

Figure 1: Dry particle number and cumulative number distributions for natural CCN (solid line) and seeding particles (dash line).

growth. RWC was not increased by much due to seeding and eventually RWCs in seeded and natural cases tend to approach the same values, total cloud water content. This is to be confirmed further in Figure 4.

Figures 3 and 4 display the detailed structures of drop size distributions for both natural and seeded cases, (a) near the cloud base, where coalescence is not involved and (b) near cloud top, where coalescence dominates. f<r>dr is the number concentration for droplets with radii between r and r+dr, while g<lnr>dlnr is the mass for droplets with radii between r and r+dr. Figure 3 further demonstrated that initially the seeding particles slowed the condensational growth process, but there were small amounts of ultra giant seeding particles activated immediately after the parcel left the cloud base. They remain in the parcel until the establishment of enough small cloud droplets generated by condensation. Those ultra giant seeding particles were termed coalescence nuclei in Beard and Ochs (1993) since they were able to participate in the coalescence process immediately after nucleation. A very interesting feature (Figure 4) was that seeding brought in more large raindrops and substantially fewer drizzle drops (r around 100 μm). This further confirmed that seeding does not produce more rain water, rather it tends to produce rain water earlier, but eventually if the cloud has long enough lifetime, it will produce the same amount of rain water as in the natural case. This was also illustrated in Figure 2. The sharp decrease of f<r> and g<lnr> at large sizes correspond to the dry size cutoff of seeding particles. Further numerical calculations indicated that the seeding effect demonstrated above

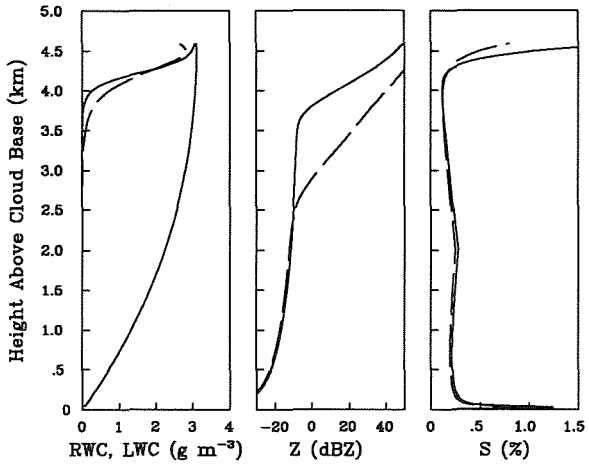

Figure 2: Evolution of cloud water content, rain water contents, radar reflectivity factor and supersaturation for the natural (solid) and seeded (dash) cases.

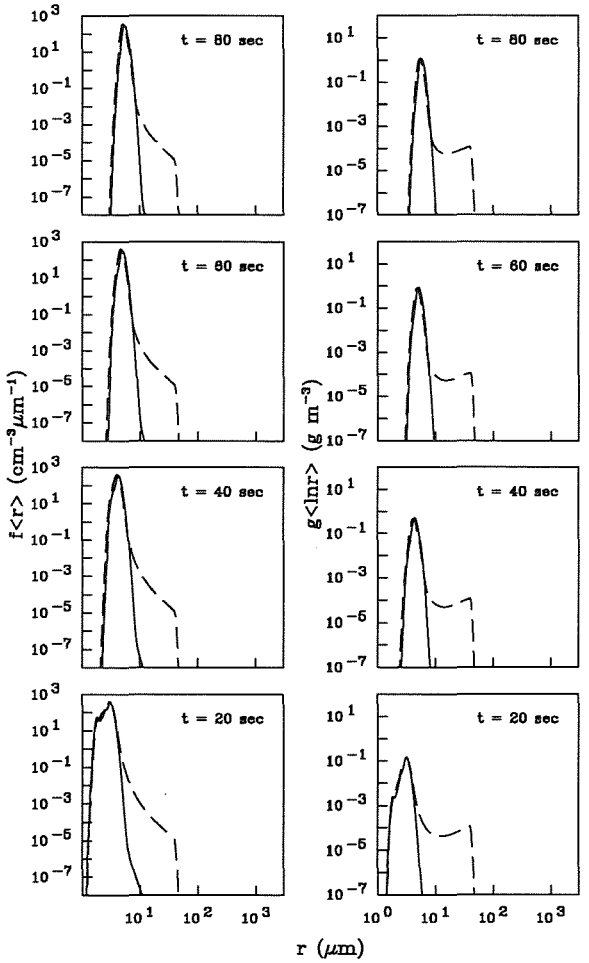

Figure 3: Number and mass density distributions for the natural (solid lines) and seeded (dash lines) cases in early times t = 20, 40, 60 and 80 minutes after the parcel leaving cloud base.

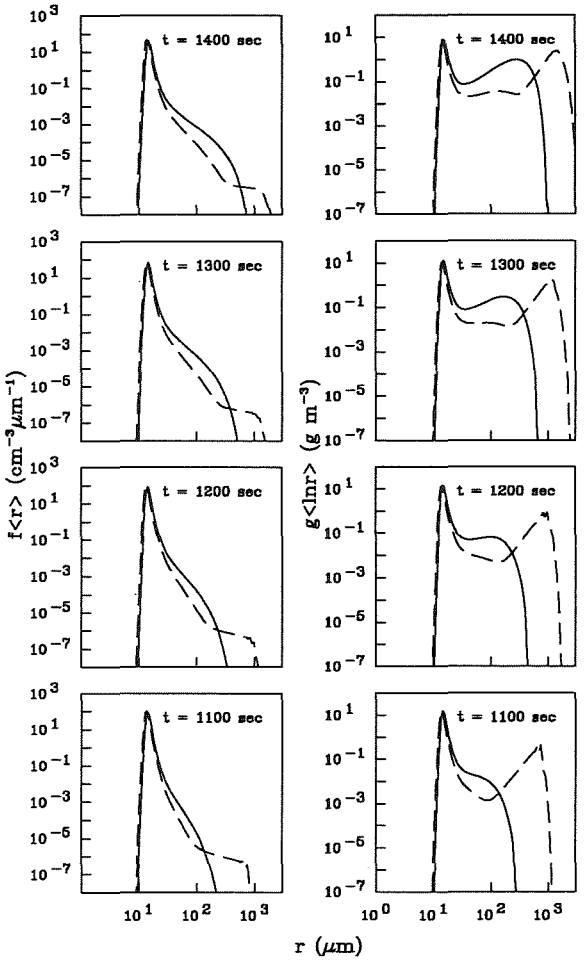

Figure 4: Number and mass density distributions for the natural (solid lines) and seeded (dash) cases in later times t = 1100, 1200, 1300 and 1400 minutes after the parcel leaving cloud base.

was produced by the ultra giant seeding particles ($r_d > 1$ μm) only. By truncating the seeding particle distribution at $r_d = 1$ μm (total seeding mass 2.8×10^{-5} g m^{-3}) rather than 0.066 μm, we got slightly faster growth. This is understandable since the small seeding particles consumed a lot of water vapor and resulted in slower condensation growth for the whole drop size distribution. This conclusion suggests that the coalescence nuclei are responsible for the seeding effect, even though they have substantially low counts compared to the high concentrations of sub micron sized particles. Those sub micron particles cannot enhance droplet growth; rather they have a negative effect in droplet growth.

The above calculation was also run under the Hobbs et al (1985) CCN profile, which showed abundant ultra giant natural CCN. Not surprisingly, the conclusions were totally different. The seeding particle distribution in Figure 1 was not able to accelerate droplet growth compared with the natural case. Since at this time, the natural CCN profile contained sufficient coalescence aerosols and the natural cloud itself was able to grow fast enough and the seeded coalescence aerosols did not make any appreciable difference. Therefore it is crucially important to understand ultra giant CCN distributions before trying to seed clouds. It is strongly recommended that in future field weather modification attempts, CCN counters capable of measuring very low supersaturations should be used.

Acknowledgments. This work was supported by the NOAA Cooperative Agreement IGA 91 - 6111 - 189 - 1085.

References

Beard, K. V., and H. T. Ochs, 1993: Warm rain initiation: An overview of microphysical mechanisms. *J. Appl. Met.* **32**, 608-625.

Berry, E. X, and R. Reinhardt, 1974a: An analysis of cloud drop growth by collection. Part I. Double distributions. *J. Atmos. Sci.*, **31**, 1814-1824.

——, and ——, 1974b: An analysis of cloud drop growth by collection. Part II. Single Initial distributions. *J. Atmos. Sci.*, **31**, 1825-1831.

Boehm, J. P., 1992: A general hydrodynamic theory for mixed-phase microphysics . Part II: collision kernels for coalescence. *Atmos. Res.*, **27**, 275-290.

——, 1990: On the hydrodynamics of cloud and precipitation particles. Ph.D. Thesis, Swiss Federal Institute of Technology. 159 pp.

Cooper, W. A., R. T. Bruintjes and G. K. Mather, 1994: Some calculations pertaining to hygroscopic seeding with flares. Proc. Sixth Int. WMO Conf. on Weather Modification. 30 May - 4 June 1994, Paestum, Italy, 667-680.

Fitzgerald, J. W., 1972: A study of the initial phase of cloud droplet growth by condensation and comparison between theory and observation. Ph.D. Thesis, University of Chicago, 144 pp.

Hall, W. D., 1980: A detailed microphysical model within a two dimensional dynamic framework: Model description and preliminary results. *J. Atmos. Sci.*, **37**, 2486-2507.

Hobbs, P. V., D. A. Bowdle and L. F. Radke, 1985: Particles in the lower troposphere over the high plains of United States. Part I: Size distributions, elemental compositions and morphologies. *J. Clim. Appl. Met.*, **24**, 1344-1357.

Hu, Z., and R. C. Srivastava, 1995: Evolution of raindrop size distribution by coalescence, breakup, and evaporation: Theory and observations. *J. Atmos. Sci.*, **52**, 1761-1783.

Ochs, H. T., and K. V. Beard, 1984: Laboratory measurements of collection efficiencies for accretion. *J. Atmos. Sci.*, **41**, 863-867.

——, and ——, 1985: Effect of coalescence efficiencies on the formation of precipitation. *J. Atmos. Sci.*, **42**, 1451-1454.

Smolarkiewicz, P. K., 1983: A simple positive definite advection scheme with small implicit diffusion. *Mon. Wea. Rev.*, **111**, 479-486.

Tzivion, S., T. Reisin, and Z. Levin, 1994: Numerical simulation of hygroscopic seeding in a convective cloud. *J. Appl. Met.*, **33**, 252-267.

Young, K. C., 1993: *Microphysical Processes in Clouds.* Oxford University Press. 421 pp.

THE STRUCTURAL CHARACTERISTICS OF THE CLOUD AND PRECIPITATION FIELDS IN CENTRAL ASIA (TURAN CLIMATIC REGION)

B.Sh. Kadyrov, V.P. Kurbatkin, V.Ph. Ushintseva
Central Asian Research Hydrometeorological Institute, Tashkent,
Republik of Uzbekistan

The Turan climatic zone which is well known in scientificc community occupies the climatic zone wthin 35 - 46 N and 52 -80 E.

It presents flow-free zone where the water resources are composed by the rainfall over its territory. Thats why the value of clouds and precipitation was always highly estimated in the Central Asia and, mainly, from the point of view of the solution of applied problems.

At present we have suffisient information on fairly comprehensive view on the structural characteristics of precipitation fields and regional precipitation. The summarized review of such characteristics is presented below.

1. Large-scale characteristics of the cloud fields

The largest spatial scale of the cloud field is determined by region size. As it is seen from the region location, it can bbe framed into rectangular with the linear dimensions of 1000 km extension from south to north and 3000 km extension from west to east. (Referenz book, 1967) demonstrates, that the value of 0.70 is characteristic really observed value of the relationship of the sunshine duration. Its territorial variations are about 0.1 from which it follows that by the total time during a year the territory is fairly unifomrly covered by the cloud fields. But precipitation fields (quantity) have no such uniformity (Balashova E.N., 1960, Dzhuraev A.D., et.al., 1977). From the consideration of territorial distribution of the first chractetistics it is seen that cloud situations are more frequently observed in the areas of initiated uplight of the air flow with the available suffiecient moisture. But the later factor is more frequently manifested more in the increased intensify of the process than in its prolongation (Kurbatkin V.P., et.al., 1981). It can be explained by the cloud densification, which is particularly manifested by signicant water content values and sizes of the cloud particles (Ushintseva V.Ph., 1971, pp. 48-53, 54-59).

During individual synoptical processes the region is at one time covered for 1/3-1/2 by clouds during the outbursts of the south cyclones and, to the greater extent, up to the complete coverage of the whole territory with the subsequent western, north-western intrusions. In our region we observe specific synoptic process, which is like the (previous ones) well presented in (Djordjio V.A., et.al., 1957) where the cloud process is traced along the mountainous system. Its duration can reach 180 hours whereas the average duration of the main processes determining dull weather in Tien Shan is 2-5 days (Kurbatkin V.P. et.al., 1989).

For the whole region this period equals 2-11 days. It is evident that in linear dimensions this value correponds to the sizes of region.These are the scales of the cloud fields. The precipitation processes (except the shower, short and intermittent ones) are observed for the 1/3-1/2 synoptic processes duration. By the duration the average precipitation value in the piedmont north-eastern area of Uzbekistan is 20-26h with mean square deviation of 16-19h, which is consistent with the spatial scale of 700-900 km at the mean square deviation of 600-700 km (Kadyrov B.Sh., et.al.,1990).

2. Structural characteristics of the precipitation fields on the mezo-polygon

In the central part of the piedmont area of the region the precipitation measuring mezo-polygon with the area of 2500 km was founded where in the heigth zone of 50-1400m 34 raingauges were fairly evenly distributed. Description of polygon is given, and results of analysis are presented in (Ushintseva V.Ph., 1989). The precipitation distribution even on such small territory is relativelly uneven. The mean monthly precipitation recorded by these sites, can differ two times. One of the reasons of the eneven precipitation distribution is that during some cloud processes the precipitation is recorded only on the part of this piedmont territory. The table presents the degree of simultaneous precipitation event on the area of the whole polygon depending on precipitation value for 12 hours and on its form (tabl.1).

The data of the analysis shows that at considerable precipitation the levelling of precipitation inhomogeneity is observed, and they occur over major part of polygon. This is also can be attributed to precipitation events of snow (tabl.1).

3. Inner inhomogeneity of cloud fields

The precipitation distribution registered both by the available hydrometeorological network and by airborne measurements testifield to the existence of inner inhomogeneity of cloud. In the airborne measurements separate changes were smoothed when averaging in order to get stable values.Radar measurements revealed the mezoinhomogeneities. The data on inhomogeneity and number of values were no-

Table 1. The occurence (%) of the raingauges number where the simultaneous precipitation is recorded depending on the quantity, and their type

Quantity (mm) and type of precipitation	Number of raingauges simultaneously registering precipitation						
	1-5	6-10	11-15	16-20	21-25	26-30	31-34
0,5	73	13	7	7	-	-	-
0,5-6,0	18	16	12	16	10	12	16
5,1-10,0	14	6	3	15	10	26	26
10,0-15,0	11	4	-	7	35	27	16
15,1	5	5	-	-	13	30	47
Drizzling rain	-	67	17	16	-	-	-
rain	-	5	5	5	10	35	40
snow	-	-	9	8	8	35	40
torrentail rain	30	25	20	20	5	-	-

ted in (Kurbatkin V.P., et.al., 1975, Dzhuraev A.D., et.al., 1977). Futher for substantiation of the fact the installation was made (Rashidov R.R., 1988) which eliminated the measurement error related to the less of simultaneous intensity with the increase of distance. The discrepancy values in meteoelements obtained before. were rechecked up. The works (Kadyrov B.Sh., 1981, Philippov S.G., 1988) testified to that fact and also added to the reason of the cloud turbulence by the relief mezo-inhomogeneity. Now it can be concluded that inhomogeneities in clouds are of ellipsoid form. Its linear horizontal dimension is 1,5-1,8 times as the vertical one. The dimensions of such inhomogeneities increase with the height. Thus, in 2,0-4,0 km layer the horizontal dimension of inhomogeneities is 1,3-1,4 times as in 0 - 2,0 km layer,which in 5,0-8,0 km layer it is 1,6-1,8 times as the value in surface 2,0 km layer. The linear horizontal dimensions of inhomogeneities recorded by the radar, are within the range of 0-15,0 km. They usually reach hundreds meters-kilometes; while the vertical ones from hundreds meters up to 1,5-2,0 km. These inhomogeneities are frequently unstable in time. In this case the time of their duration is 20 min (Philippov S.G., 1988). There are also homogeneous layers in the clouds.

REFERENCES

Balashova E.N. , *et.al.*, 1960: Climatic descripstion of the republics of the Central Asia. L., Gidrometeoizdat, 241 pp.

Djordjio V.A. , *et.al.*, Synoptical processes of the Central Asia. Ac. Sc. UzSSR, Tashkent, 1957, 310 pp.

Dzhuraev A.D. , *et.al.*, 1975: On inhomogeneity of the stratiform clouds. *Proceed. of SANIGMI*, **30(111)**, 71-77.

———, *et.al.*, 1977: Cloud resources and possibility of precipitation enhancement in the Central Asia (monograph). *Proceed. of SANIGMI*, **46(127)**, 54 pp.

Philippov, S.G., 1988: Spectral analysis of stratiform cloudiness. *Proceed. of SARNIGMI*, **126(207)**, 25-32.

Kadyrov B.Sh. , *et.al.*, 1990: Structural characteristics of cloud and precipitation fields. Weather modification. Proceed. of All-Union Conference, 371-375.

Kadyrov B.Sh. , and V.Ph. Ushintseva, 1995: Radar and thermal parameters of stratiform clouds on the north of Kashkadarja. *Proceed. of SANIGMI*, **148(229)**, 37-44.

Kadyrov, B.Sh., 1989: Indication of the wave movements using meteorological radar. *Proceed. of Glavgidromet SANII*, **79(160)**, 56-58.

Kurbatkin V.P. , *et.al.*, 1989: Characteristics of synoptical processes in Kirgizia. *Proceed. of SARNIGMI*, **75(156)**, 61-73.

Kurbatkin V.P. , and V.Ph. Ushintseva, 1989: Qualitative pattern for the transformation of precipitation fields. *Proceed. of Glavgidromet SANII*, **79(160)**, 3-17.

———, ———, 1977: Geometrical parameters of radar echo of the stratiform clouds and inhomogeneities on the boundary interfaces (on the north of Fergana valley). *Proceed. of SARNIGMI*, **48(129)**, 125-132.

Rashidov, R.R., and S.H. Tulabaev, 1988: Multichannel device for the measurement and registration of the moderate power of meteorological radar signal. *Proceed. of SARNIGMI*, **126(2207)**, 142-144.

Reference book on USSR climate, 1967: **19**, part 1. L., Gidrometeoizdat, 69 pp.

Ushintseva, V.Ph., 1971: Water content of stratiform clouds in different orographic conditions of Central Asia. *Proceed. of SANIGMI*, **53(68)**, 54-59.

———, 1971: Results of cloud elements studies in the Central Asia. *Proceed. of SANIGMI*, **53(68)**, 48-53.

———, 1989: Atmospheric precipitation field on the north of Kashkadarja region. *Proceed. of Glavgidromet SANII*, **126(207)**, 3-17.

Rasulova, L.S., and S.G. Philippov, 1990: Research of structural of stratiform cloids in mountainous valley by means of the apparatus "Vertikal". *Proceed. of SANIGMI*, **110(191)**, 8-13

Kurbatkin V.P., et.al., 1994: The results of cloud modification aimed at precipitation enhancecement in the target area of Uzbekistan (1985-1991). Sixth WMO scientific conference on weather modification. WMO/TD-N° 596, p.641-644.

NUMERICAL SIMULATION OF NDTP CASE 3.1 (JUNE 28,1989)

Xiong Huanan, Feng Shuchang, and Chen Yuan

Meteorological Institute of Hunan, 410007, CHINA

1. GENERAL DESCRIPTION OF THE CLOUD MODEL

The model used in the case 3.1 (NDTP) is a two-dimensional,time-dependent (2DTD) Slab-symmetric model. It originated from the work of Xu Huaying et al (1986) . Further improvement of taking ice- phase process into account to the model has been made by Xiong Huanan et al. (1990).

The model has used bulk water microphysics to simulate precipitation processes. Water substance is divided into four classes: water vapor,cloud liquid, rain and ice water without dividing ice into three classes (cloud ice,hail/graupel and snow).

The basic model covers 20 km x 20 km. Grid sizes are both 500 m in the horizontal and vertical directions. Time step is adjustable and maximum time step is not beyond 30 seconds. Method of explicit upstream difference is used.

The boundaries are open. Natural ice nucleation occurs at -18 °c in the model without concerning environment wind field.

The sounding adopted by the model are the temperature, moisture and the lapse rate of pressure at 14:35 Z on 28, June 1989 in GDH provided by Dr.H.D.Orville with their horizontal homogeneity, which temperature and moisture on the ground are replaced with which they are at 21:35 Z on the same day.

In order to initiate a cloud we assume that there is an area of initial fluctuating humidity and fluctuating temperature with the scope of 1 km x 2 km which is 1 km high above the ground with the central humidity (100%) and central fluctuating temperature 2.5°c.

The local variation of density is assumed to be zero so as to calculate density -weighted stream function.Also we assume that distribution of precipitation follows M-P exponential law.

The model simulates clouds' complete life history and the time- variation of stream field, temperature deviation, water vapor, cloud liquid, rain and ice water.

2. MODEL RESULTS

2.1 General Description of The Model Results

After running the model, a cloud first forms at about 2 km high above the ground where is given a fluctuating of temperature and humidity. The cloud top grows rapidly. During the integrating time of 23 to 43 min the average growth rates of the top is 3. 3 m/s and from 70 min to 75 min it is 6. 7 s/m. The updraft velocity maximum reaches 19.7 ms at 117 mim, after appearing the condensation ratio maximum 0.044 g/kgs 5 min. At 43 min the top reaches the first maximum 11.0 km.

After integrating 23 min, ice phase begins to form above 6.0 km. When in 51 mim rain drops down to the ground. Warm rain process is not obvious.At simulating time

peak value 157 mm/h and its maximum 177 mm/h occurs at 133 min. The first ice water maximum 4.8 g/kgs occurs near the ground at 56 min. Hail shooting also emerges in the case. Since then hail shootings occurs at other places several times. The precipitation process lasts over 3 hours. The rainfall intensity presents multi- peak pattern. The maximum rainfall of single station is 40.8 mm and then 33.1 mm and 26 .3 mm in other two stations.

2.2 X-Z plots in Stages of development, mature and dispertion of cloud life history

Three new cells grow again above near ground at 35 min, which one called B lay just under the initial cell A and other two cells called C and D are respectively near the boundaries of right and left. These celles(A,B,C and D) are all isolated each other. The cell A looks vertically axisymmetric.Its top reaches 11.5 km. There is a centre of maximum cloud water substance near 7.0 km level with the mixing ratios 6.1 g/kgs. As Fig. 1 shows.

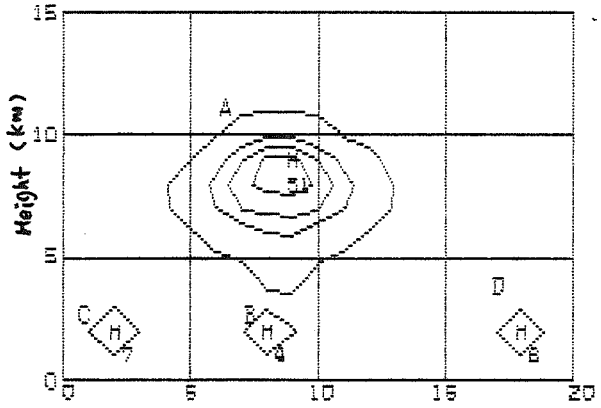

FIG. 1 Cloud content in g/kg. Gap of contour is 1.5 g/kg. There are 4 individual clouds.

At 43 min cell A joints with cell B in the vertical direction,which is called AB with the top 13.0 km. The maximum mixing ratios keeps 6.0 g/kgs, but its central position falls down to 4.0 km where is just the joint of cell A and B.

When in 51 min, precipitation from cloud AB drops down to the ground. Rainwater is majority derived from ice phase substance.

At 65 min cell C and D develop vigorously and cell C is little intenser than D, but cell D is a little higher than cell C. Updraft velocity appears first maximum value 16.1 m/s near 4.5 km level in the cell C. The cloud body AB and cell D have merged into one, but they still maintain their respective core.

From the mergence AB and D to 71 min, cloud AB merges with cell C subsequently. Cloud bridge lies above 7. 0 km. However, they have their respective core. There is a core whose value reaches 11.0 g/kg with ice water 7.0 g/kg at 7.0 km level in the cell C.It is the most intensive one among these cores.

Fig. 2 shows top 13. 0 km when at calculating 86 min.Maximum value 157 mm/h of the first rainfall intensity can be seen on the ground. Under the cell C hail shootings occurs. Ice mixing ratios reaches 5.0 g/kgs near the surface.

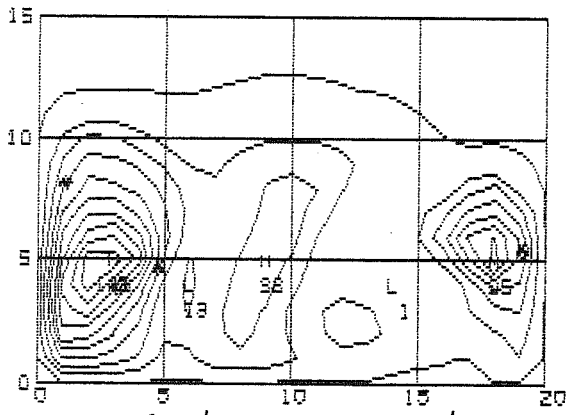

FIG. 2 Similar to Fig.1, but those clouds have merged.

At 105 min the intensity of the cell C decreases because of falling hail. The top drops down to 12.5 km. All clouds have

merged completely,bue there are still three cores in the cloud body and the core of cloud AB is 11.0 g/kg with 9. 0 g/kg ice water above 7.0 km.

At 117 min top rises up to 13. 5 km again, the core of cell C has disappeared and there are only two cores in the cloud body. The core of the merged cloud AB is about 13.0 g/kg and the ice water is 10. 0 g/kg. Vertical velocity maximum value 19 .7 m/s appears. The heavier rainfall and hail -shower are being brewed.

After 6 min (at simulating 123 min) heavy precipitation with hail- shower falls down to the ground, but the top of the cloud body rises up to 14.0 km.

After 10 min (at 133 min heavy precipitation still remains under the cloud AB and the intensity increased to 177 mm/h, and also there is only a core (11.0 g/kg) at 1.0 km level in the huge cloud body. The top of the cloud falls down to 13.5 km.

At simulating 163 min hail shootings come into an end and the intensity of the rainfall decreases continually.

When integrating to 224 min, precipitation process is coming into an end. The cloud body appears to be huger and looser and water of rain and ice decreases obviously in the cloud body. Cloud water drifts at high level and cloud body disappears slowly.

3. CONCLUDE

The model don't consider environment wind field and simulating for the ice phase process is a bit rough.Simulated cloud is only one of which is possible to be the most intensive cloud appearing in the sky on the just day. On the just day there are cloud system. Clouds' mergence enhances development and precipitation. In adition, isolated cell was simulated by authors, results shows that maximum value of rainfall account of single station from isolated cell is less than a half of cloud merged.

ACKNOWLEDGEMENTS

The authors wish to thank Dr. H. D. Orville for providing a floppy disk with digited class data for EGN & GDH .We would like to thank Mis. Xiaotie for typing the manuscript. The simulations were performed on AST 486/33 computer at Meteorological Institute of Hunan Province of China.

REFERENCES

Orville,H.D.,F.J.Kopp,R.D.Farley, and R.B. Hoffman, 1989: The Numerical Modeling of Ice-Phase Cloud Seeding Effects in A Warm-Base Cloud, *WMA*. ,21,1.

Hu Zhijin and He Guanfang,1987: Numerical Simulation of Microphysical Processes in Cumulonimbus: I. Microphysical Model, *ACTA METEOROLOGICAL SINICA*,45, 4.

Xu Huaying ,Li Guishen, and Hao Jingpu, 1986:Papers on Cloud Physics And Weather Modification in Southern China, The Meteorological Pressing House, 110-120.

NUMERICAL SIMULATION OF THE PRECIPITATION DEVELOPMENT ON CUMULUS MERGERS IN CHANGSHA OF CHINA

Xiong Huanan, Feng Shuchang and Han Siying

Meteorological Institute of Hunan, Changsha, CHINA, 410007

1. INTRODUCTION

Huang et al (1980) and Simpson et al (1980) indicated that when clouds are merged cloud growth is urged, as a result, cloud lifetime is extended, rain intensity is strengthened and precipitation is largely increased. Orville et al (1980) simulated clouds mergers and found that clouds mergers are possible when two near clouds which have insymmetric stream field are in different development stage. Total precipitation of clouds mergers is 1.5-2.0 times than that of individual cloud. Huang et al(1987) simulated the precipitation of the convective- stratiform mixed cloud system and considered that the existence of stratiform cloud has significant effect on the development of cumulus cloud owing to offer plenty vapour in rainty season and rainfall amount of them is several- tens times than that of cumulus.

In this paper a two- dimensional time -dependent model of cumulus clouds is used for simulating development on cumulus mergers in summer- autumn in Changsha of China. The data of sounding in Changsha are put into the model and the results are compared not only with the data of radar echos, but also that of rainfall on the ground. The development of seeding clouds is also simulated in this paper.

2. THE MODEL

2.1 General Model Characteristics

The dynamic framework of a cumulus cloud used in this paper is based on a cloud model developed by Hu Huaying et al (1986). The ice phase process is added by Xiong Huanan et al (1990).

The model includes vorticity equation, stream function equation, thermodynamic and four continuity equations for the water substance (mixing ratios of water vapour, cloud water, rain water and cloud ice).

Integration domain is 20 km in the horezontal and 15-20 km in the vertical direction. Space steps in the both directions are 0.5 km. The large time step is 30 s and the small is 2 s.

2.2 Microphysical Processes

In this paper used methods are proposed by Ogura et al (1971) and Shiino (1978) . Bulk water parameterizations are used for simulation of microphysical processes. Four classes of water substance are considered: water vapour, cloud water, rain and cloud ice. Cloud water is assumed to be monodisperse with zero terminal velocities. Rain and cloud ice have the Marshell-Palmer type size distributions with fixed intercept parameters.

In this model supersaturation is assumed not to be realized in any stage of the life cycle of the cloud. The condensasion rate is calculated by Newton iteration. The evaporation process of cloud drops is a reverse process of condensation of water vapour. Both the processes of autoconversion and collection, which produce rain drop, are combined into one in this study and treated

as a step function. Other processes, glaciation, sublimation, melting, riming, and evaporation process of raindrops and melting ice crystals used a simple paramerization by Ogura et al (1971), except the evaporation process of ice crystals owing to it is too small to be considered.

2. 3 Initial and Boundary Conditions

The sounding at 07:00 in local time is interpolated vertical into grids and first the values of the horizontal direction are considered to be identical. The ground temperature and dew-point temperature are the data sampled at 14:00 in local time.

The upper and lateral boundaries are assumed to be open and time- dependent so that disturbance can pass through with minimal reflection. Both vertical and horizontal velocities vanish on the ground surface. Water of rain and ice at the ground computed by the linear extrapolation with the use of the values at the first and second level above the surface.

As the initial disturbance a thermal bubble is used which has a maximal in center (+3 ℃) and decreases to zero in cosin form at the bubble boundaries. The thermal bubble is 1 km x 2 km or 1 km x 1 km and can move freely in the whole domain but 2 km above the ground.

2.4 Numerical Procedure

The computational scheme is the 'forward -upstream' scheme proposed by Ogura et al (1971) and the diffusion terms are used by centre second-order difference.

The stream field is calculated by using super- relax iteration to solve the Poisson's equation.

3. NUMERICAL EXPERIMENT

3.1 Natural Merger of Clouds

During dates of having weather system, such as the typhoon or the easterly wave weather,clouds often grow thickly and merge naturally and produce large rainfall.

Ex.1 On August 3,1984 the sounding shows that there is inversion layer (100- 500 m) above the ground, height of updraft condensation is about 450 m,height of free convection is 1500 m and height of convective condensation is 110 m. At 14: 00 in local time the ground temperature is 35 .6℃ and great the convective temperature 34 ℃.Radar observation finds echoes in many places and the height of the toppest echo reached 15 km. In finally, 45. 9 mm rainfall is observed on the ground. Seedble degree, which is calculated by one -dimensional constant model, is 3.6 km in this day.

The first simulation uses one thermal bubble.After initialization, top of cloud A is 5 km at 31 min. At 36 min, when the top of A reached 7.5 km a new cloud cell B occurs at the left of A. At 45 min, another new cell C grows at the right of A. After that ,the cloud A merges cloud B first in a low level and then A and B combine completely,but there are two cores yet (Fig .1). Rainfall appeares first below cloud A.

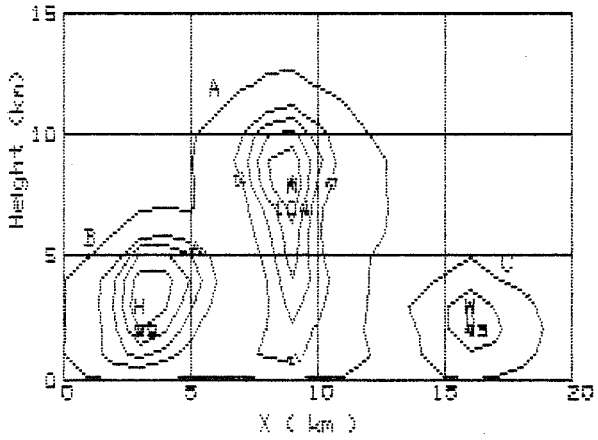

Fig. 1 Cloud content in g/kg. Gap of contour is 1.5 g/kg.

Cloud A continually develops and B appears wearing. By then cloud C combine into AB and rainfall intensity add up to 90 mm/h

reaches15 km in the end. The amount of rainfall in this simulation is 57.6 mm, which has a 11.7 mm more rainfall compare with the observation.

Now two thermal bubbles are used in the model.The place of the first bubble is as same as that in the first simulation, the second one is located away from the first one 8.5 km in the same horizontal level but the size is only half of the first one. Both grow individually in the begining 20 mins and then the second cloud disperses while the first cloud grows keeply. At 40 min, two small cells occur at the two sides of the first cloud. Since then the development is similar with the first simulation which has only one bubble. Rainfall is 57.0 mm on the ground in the second simulation.

This result shows that the weather is suitable for merging clouds and the cloud development is consistent with that of radar observation.

Now the third simulation is added a constant work condition to the second simulation and begin the third one. When the top of cloud reaches 9. 0 km in the second simulation, ice- forming nuclei temperature is changed from -18.0℃ to -6℃ to simulate the effect of seeding. After seeding, the top of cloud increase rapidly and cloud body thickly speedly. The merger is early compare with unseeding. Rainfall reaches 62 mm which has a increase of 7. 8% compare with unseeding.

Now we continue repeat the second simulation but the distance of the two bubbles changes to 3.5 km. In the first 30 mins, the first cell grows and the second one disperses. After that the result is similar with that of the second simulation. At last the rainfall is 77 mm.

From the results of the above four simulations,we can conclude that different number of thermal bubble, different distance of them, and seeding is used or not, have no effect essentially to the merger of clouds. And it has very large rainfall,so the seeding is not necessary.

3. 2 MakeMerger Occuring

On some dates of the seedble degree > 0 km cloud generates independently and almost don't interact each other with middle rainfall. However merger enhances the process of development and precipitation, if a cloud follows another nearly.

Ex.2 on July 29,1984 radar finds that the clouds occur individually and distance of them is so large that they hardly interact each other.The top of maximal one cloud is 14.3 km and it's rainfall is 23. 6 mm on the ground. In that day seedble degree of cumulus clouds is 2.5 km.

The model cloud is given one thermal bubble.There is only a isolated cloud after initialization 40 min. As showed in Fig. 2. At the end rainfall 25 mm is observated on the ground.

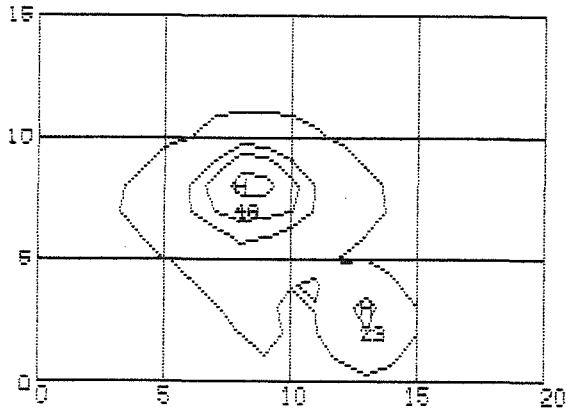

Fig. 3 Similar to Fig. 2, but two clouds have merged.

Now the model cloud is put two thermal bubbles with distance of 3.5 km in order to compared with above simulation that has one only thermal bubble.In the begining 20 mins both them develop individually and then the second cell is restrained.After 40 min, as in the Fig.3, they has merged. The total rainfall on the ground is 36 mm and is more 44% than that of above having one

According to the above results of simulation,it is appearance to us that there potention of weather modification is essential, and worth to continue this research direction in deep.

3. 3 The Seedble Degree = 0 km Without Mergering

On some dates of the seedble degree = 0 km growth of cumulus clouds is restrained and never merge and disperse one after another,even if there is very near distance between them.

Ex.3. on August 22, 1984 at 07:00 in the local time the sounding shows the water vapour is poor and there are two dry layers. At 14:00 in local time the ground temperature is 34. 8 ℃ below the convective temperature of 35.5 ℃. Top of radar echo is only 7.3 km and rainfall is 1.7 mm on the ground.

Results of simulations show that no matter how many are there thermal bubbles or near is distance,the top of cloud is only 7.5 km and rainfall of 1.9 mm on the ground. There is no any potention of weather modification.

ACKNOWLEDGEMENTS

This research was sponsored by foundation of cloud physics provided by Meteorology office of China. The authors wish to thank Dr. Shong Ming who read the manuscript and proposed many useful suggestions.

REFERENCES

Huang Meiyuan and Wang Angsheng, 1980: Introduce of Weather Modification for Prevent Hail, Science Pressing House, 145-147.

Simpson, J.,N.E.Westcott,R.J.Clerman, and R.A. Pielke, 1980: On Cumulus Mergers, *Arch. Meteor. Geophys. Bioklim*, A29, 1-40.

Orville,H.D.,Y.-H.Kuo,R.D.Farler, and C.S. Hwang, 1980: Numerical Simulation of Cloud Interactions, *J.Rech. Atmos*.,14, 499-516.

Huang Meiyuan Hong Yanchao Xu Huaying, and Zhou Heng, 1987: The Effects of The Existence of Stratiform Cloud on The Development of Cumulus Cloud and Its Precipitation, *Acta Meteorological Sinica*, 45,1,72-77.

Xu Huaying,Li Guishen,and Hao Jingpu, 1986: Papers on Cloud Physics And Weather Modification in Southern China , The Meteorological Pressing House, 110-120.

Xiong Huanan, Chen Lishu, Han Siying, Jia Zhanyun, and Wang Yingchai, 1990: Numerical Simulations of Cumulus Cloud of Weather Modification, Conference on Cloud Physics And Weather Modification in Souther China.

Ogura,Y., and Takahashi,T.,1971: Numerical Simulasion of The Life Cycle of A Thunderstorm Cell,*Mon.Wer.Rev*.,99,12,895 -911.

Shiino, J. , 1978: A Numerical Study of Precipitation Development in Cumulus, *Papers in Meteorology and Geophysics*, 29,4,157-194.

Han Siying and Xiong Huanan, 1993: Primary Study of Cnmulus Cloud Seedble Degree During Summer-Autamn in Hunan of China, *Meteorology*,19,3, 13-16.

THE CHARACTERISTICS OF THE ATMOSPHERIC WATER OVER TROPICAL WESTERN PACIFIC 'WARM POOL' DURING TOGA COARE IOP

WEI CHONG AND XUAN YUEJIAN

(Institute of Atmospheric Physics, CAS, Beijing 100029)

I. INTRODUCTION

A continuous measurements with high time resolution (5 minute) were obtained of the total atmospheric water (including precipitable water vapor, vertically path-integrated cloud liquid water content and rain intensity) over the tropical Western Pacific at a fixed point (2°S, 158°E) during TOGA COARE IOP (Nov., 1992 — Feb., 1993). This paper gives the statistical analyses of the measurements as well as the observation instruments and their accuracies. If necessary, some comparisons are indicated of these statistical results with those of the measurements obtained during previous meteorological and oceanic surveys, sponsored by the Chinese Academy of Sciences, in the tropical western Pacific Ocean.

II. OBSERVATION EQUIPMENT AND THEIR ACCURACIES

A ship-borne dual-wavelength (0.86 cm, 1.35 cm) microwave radiometer developed by ourselves was used to measure both precipitable water vapor and vertically path-integrated cloud liquid water content (Wei, C., 1989a). An automatic rain rate measurement system (ARRMS) of Integrated Sounding System (ISS) provided by the United States was used for monitoring rain intensity.

A comparison was made of the precipitable water vapor measured by radiometer with that by in-situ OMEGA Radiosonde System of ISS. The statistical comparison of a total of 261 cases for all weather (including clear, cloudy and rainy days) during whole period of TOGA COARE IOP shows that the relative deviation is within 13.3% . It can be considered that the accuracy of the ship-borne dual-wavelength microwave radiometer can be compared to that of radiosonde.

The accuracy of radiometric estimation of vertically path-integrated cloud liquid water content was discussed in details by the author in another paper (C. Wei, 1989b). The numerical simulation showed the relative error is within the limits of acceptable accuracy.

The measurements of rain intensity by the ARRMS were compared with those by a side-by-side shipborne rain gauge. The results show that the ARRMS has reasonable and believable accuracy.

III. MAIN RESULTS

1. The time series with a total of 23,000 set data (5-minute time resolution) for about 90 days are given in Fig.1 of the radiometric atmospheric precipitable water vapor and the vertically path-integrated cloud liquid water content as well as the ARRMS' 5-min average rain intensity over the 'warm pool' during TOGA COARE IOP. It is such total, persistent and high time resolution monitoring that is fundamental to quantitative study of the

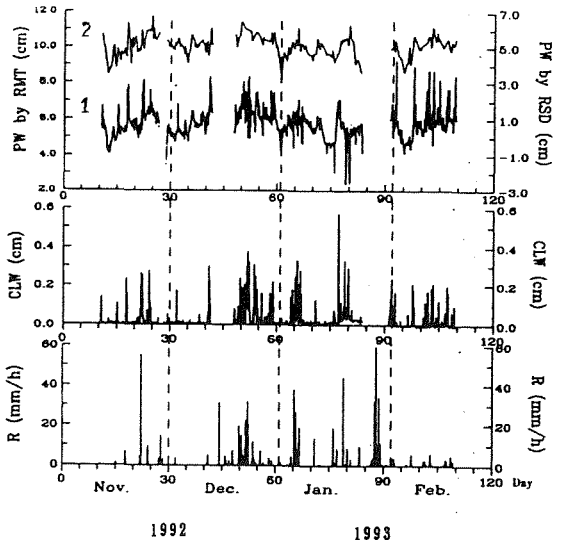

Fig.1 The time series of atmospheric water over the western pacific 'warm pool' during TOGA COARE IOP. Curve 1 (measured by radiometer) and curve 2 (by radiosonde) have different ordinates in order to be clear.

characteristics of the atmospheric water over the 'warm pool'.

2. The quantitative proportions of the two atmospheric water components (cloud water content and rain water) to the water vapor over the 'warm pool' is obtained. During TOGA COARE IOP, the overall average of whole period, including the cases of cloudless, of the vertically path-integrated cloud liquid water content is 0.036cm and the average precipitable water vapor is 5.63 cm, from which it is concluded that the atmospheric water in cloud liquid drop is around 0.6% of that in gaseous state (water vapor) over the 'warm pool' during TOGA COARE IOP; The accumulating precipitation are 976.4 mm (1385 mm) during the period of 85.7 days (100 days), namely, on the average, every day about 20% (24%) of the water vapor suspended in the atmosphere over the observation site comes back to the ocean in precipitation, from which we can learn the characteristics of the 'warm pool' in atmospheric water cycle.

3. The 'warm pool' is a large storage of water vapor: its average vertical column water vapor is about 5.6 g/cm^2, which is 1.0-1.5 g/cm^2 more than the zonal mean value along equator and 3.0-4.0 g/cm^2 more than that in the middle latitude continental air in the same season. The statistics of precipitable water vapor obeys normal distribution and the particular fitting curve during TOGA COARE IOP shows that the probability of precipitable water vapor value Q(cm), $P(Q)$, can be written as

$$P(Q)=\frac{1}{\sqrt{2\pi}\sigma}\exp\left(-\frac{(Q-\overline{Q})^2}{2\sigma^2}\right)$$

where $\overline{Q}$=5.63 cm is the mathematical expectation or the average value of Q, σ=0.732 cm is the variance. The average value and the variance vary annually and it might be considerable that the variances in the Elnino years are larger than those in the non-Elnino years (Wei, C., 1992).

4. Grouping the inspection cloud types, the occurrence frequencies of the clouds of relevant groups are: weak convection cloud (Cu hum, Ac, Sc, Fc) is 58%, strong convection cloud (Cu Cong, Cb) 21%, Cirrus (Ci, Cs) 19%, and sheet cloud (As, Ns, St) 2%. This shows that over these area convective transport is an important way of the transport of the atmospheric water and the effect of the cirrus on the

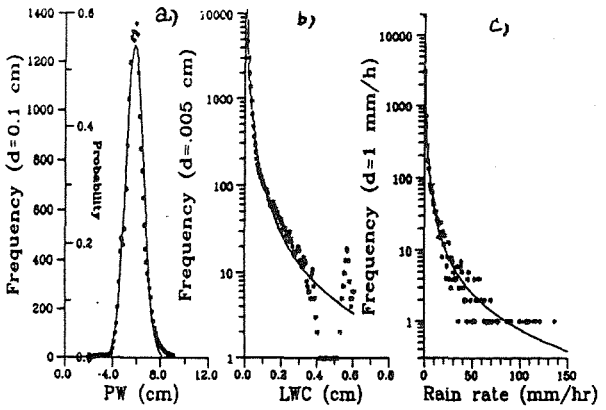

Fig.2 The statistical distribution of atmospheric water over western pacific 'warm pool' during TOGA COARE IOP.

radiation budget should not be neglected. The average values of vertically path-integrated cloud liquid water content (L) vary annually, ranging from 0.002 to 0.036cm. The frequency distribution of L have the same pattern (but different values of shape parameter) for different years, that is, the less the value of L is, the higher its occurrence frequency is, and the frequency decreases in a manner as $-\alpha$th power of L (α is constant and $\alpha>0$) when L increases. Shown in Fig.2b is the particular fitting curve during TOGA COARE IOP, that is, at the interval dL=0.005 cm, the occurrence frequency of L(cm), $N(L)$, can be written as

$$\frac{N(L)}{dL} = 1.259 \cdot L^{-1.939}$$

5. The relative rainfall frequency is about 8.8% at the observation point during TOGA COARE IOP. The showers with less than 1-hour rainfall duration occur frequently, recording 519 times, and their precipitation is about one fourth of the total precipitation during TOGA COARE IOP. Rainfalls with 1- to 2- hour duration occur 26 times and have the precipitation amount of about one third of the total; Those with duration between 2 and 5 hours amount to 16 times and one fourth of the total precipitation; so far as the rainfall with duration more than 5 hours, only 5 cases are found with one fifth of the total precipitation; so we can see here that about 80 percent of the precipitation over the 'warm pool' comes from meso- and micro-scale synoptic systems. The maximum 24-hour accumulating precipitation is 170.3 mm, and 70.2 mm for the one hour's, 13.8mm for the 5-minute's, respectively. The largest rainfall duration is 7.86 hours with 107.7 mm; the largest rainless interval is 4.5 days. The occurrence frequency distribution of 5-min-average rainfall intensity is in the similar manner as that of above-mentioned cloud liquid water L, that is, the less the R is, the higher the occurrence frequency $N(R)$ is, and $N(R)$ decreases in a manner as $-\beta$th power of R(β is constant and β >0). Fig.2C gives the particular fitting curves during TOGA COARE IOP: when dR= 1 mm/h,

$$\frac{N(R)}{dR} = 2267.3 \cdot R^{-1.735}.$$

6. The structure of the boundary layer over the 'warm pool' differs from that over the continents. Many years of observation show that the absolute humidity on the sea surface have little correlation with the total column water vapor over the 'warm pool', which shows a distinctive characteristics of the source of water vapor, see also reference (Wei,C., 1992) for detail. This fact should be paid attention to, when the air-sea boundary processes are studied.

ACKNOWLEDGMENTS

This study is supported by the National Natural Science Foundation of China and also belongs to the '8.5' program of Chinese Academy of Sciences.

REFERENCES

Wei Chong, Lin Hai, et al., 1989a, Microwave Remote Sensing of the Atmospheric Precipitable Water and Cloud Liquid Water over the Sea, *Chinese Journal of Atmospheric Sciences*, **13**(1), 101-107(in Chinese).

Chong Wei, H. G. Leighton and R. R. Rogers, 1989b, A Comparison of Several Radiometric Method of Deducing Path-integrated Cloud Liquid Water, *Journal of Atmospheric and Oceanic Technology*, AMS, **6**(6), 1001-1012.

Wei Chong, Xin Miaoxin,et al., 1992, Analysis of Precipitable Water and Cloud Liquid Water Content over the Equatorial Area of the Western Pacific on the Basis of Remote Sensing, *Chinese Journal of Atmospheric Sciences*, **16**(1), 118-128 (in English).

THE INFLUENCE OF SURFACE PARAMETERS ON RAINFALL DEVELOPMENT IN MESO-γ-SCALE MODELS; A SENSITIVITY STUDY

Jutta Thielen[1], Wolfram Wobrock[2], Patrice Mestayer[1], and J.-D. Creutin[3]

[1] ECN (LMF,DMEE), SUBMESO-GdR CNRS 1102, 44072 Nantes, France
[2] LAMP, Univ. Blaise Pascal, 68177 Clermont-Ferrand, France
[3] LTHE, 38041 Grenoble, France

1. INTRODUCTION

The urban environment modifies the local climate and processes in the boundary layer by the production of urban heat bias, turbulence through increased roughness, and strong injection of aerosol particles (Goldreich 1995). It also seems mostly to be accepted that urban areas have impact on meso-scale meteorological processes. Results of Changnon et al. (1977) and Huff and Vogel (1978), for example, suggest convective rainfall enhancement downwind of cities and industrial sites. However, these results have not always been confirmed. Lowry et al. (1978) showed in a statistical study using meteorological rainfall data before and after the development of a quickly growing Hungarian city, that no clear indication of rainfall enhancement could be found.

The objective of this study is to assess the sensitivity of meso-scale convective processes to surfaces parameters. For this purpose, a simple non-time dependent parameterisation scheme is proposed, consisting of 3 parameters describing surface roughness, and soil dependent sensible and latent heat fluxes. This parameterisation scheme was introduced into the Clark cloud physics model (Clark 1979). The impact of the individual surface parameters on meso-scale processes was assessed by analysing the rainfalls development. This allowed a comparison with the METROMEX experiment (Changnon et al. 1977).

2. THE CLARK MODEL

The Clark model (Clark 1979, Clark and Hall 1995) is a small-scale, dynamical model which represents a finite-difference approximation to the anelastic, non-hydrostatic equations of motion. It expands the system variables around profiles of an idealised atmosphere with constant stability. The microphysics in the model includes warm rain parameterisation based on the Kessler scheme (Kessler 1969), and ice parameterisation based on work of Koenig and Murray (1976). Improvement of the microphysics are described in Clark and Hall (1995). A complete presentation of the budget equations of energy and moisture is given in Bruintjes (1994). Reflection of waves at the artificial upper lid are damped by a newtonian sponge layer as described in Clark and Farley (1984).

2.1 SURFACE PARAMETERISATION:

A surface forcing has been introduced into the heat and moisture equations that

$$\bar{\varrho}\frac{d\Theta^*}{dt} = \frac{\bar{\varrho}L}{C_p\bar{T}}C_{d1,2} + \nabla\cdot(\bar{\varrho}K_H\nabla\Theta^*) + \frac{c}{c_p}\cdot e^{-\alpha z}\cdot S_S$$

$$\bar{\varrho}\frac{dq_v}{dt} = -\bar{\varrho}C_{d1,2} + \nabla\cdot(\bar{\varrho}K_H\nabla q_v) + \frac{c}{l_v}\cdot e^{-\alpha z}\cdot S_L$$

$$S_S = \mu(x,y)\cdot S_0\cdot f(Z,H,\varphi,\delta,h_x,h_y)$$

$$S_L = \frac{\mu(x,y)}{B(x,y)}\cdot S_0\cdot f(Z,H,\varphi,\delta,h_x,h_y)$$

Pot. temperature $\Theta^*=\Theta/\bar{\Theta}-1$, q_v is water vapour, ϱ is density, L is latent heat, $C_{d1,2}$ are rate of phase transitions of atmospheric water, K_H is the eddy mixing coefficient, C_p is the specific heat capacity at p=const, l_v.is the latent heat for changes of state ($2.5\ 10^6\ Jkg^{-1}$). The surface sensible and latent heat fluxes, S_S and S_l, depend on (i) $\mu(x,y)$, a factor describing the conversion from incoming solar radiation to sensible heat flux depending on the soil type, (ii) B, the Bowen ratio, (iii) f, a geometric function describing the reduction of the solar energy (S_0=1395 Wm^2) by variation of the angle of the sun to the surface (see Clark and Gall 1982, Oke 1987). The surface heat fluxes are distributed vertically depending on an attenuation length α, at which the surface values are reduced by a factor of 1/e. c is a conversion factor.

The relationship between the bulk drag coefficient C_D and the surface roughness is given by

$$C_D = \kappa^2\left(\ln\left(1+\frac{z_{surf}}{z_0(x,y)}\right)\right)^2$$

where z_{surf} is the height of terrain and κ the von Kármán constant. C_D is applied to the stress tensor components τ_{13} and τ_{23} at z=0. (Clark 1979)

μ, B, and z_0 have been estimated from available surface occupation data for the area of the "Ile de France". The range of μ was based of results of Clark and Gall (1982), while the estimations for B and z_0 were based on values quoted in standard literature such as Stull (1989) or Oke (1987). The range distribution of the values is shown in Tab.1.

Table 1: Estimates for the conversion rate of incoming solar radiation to sensible heat flux (μ), the Bowen ratio (B), and the roughness length (z_0)

Type of surface	*μ in %*	*B*	*z_0 in m*
city centres	30-40	2-4	3-4
urbanised areas	25-30	1-2	1-3
forest, grasland	20-30	0.2-1	0.2-1
lakes, rivers	10-20	0.1-0.2	0.2-0.001

3. SET-UP OF THE MODEL:

A 2D set-up was chosen, describing a 200 km West-East cross-section through the Paris area. The horizontal grid resolution was 500 m. The vertical coordinate was variable resolving the boundary layer with a resolution of up to 60 m, and the troposphere with an average spacing of 250 m. In order to exclude superimposition of soil forcing with differential terrain heating, topography was not considered. The model was initialised with a convectively unstable profile (CAPE=2140 J/kg), corresponding to the meteorological situation on June 27, 1990 in the Paris region (Thielen and Creutin 1995). The data were analysed after a total of 4 hr simulation.

Each of the surface parameters has 3 different states: a constant value (C), variations according to a "rural" environment including perturbations such as villages or small cities (R), and variations according to extended urban areas (U). As an example the xz-cross section of z_0 is given in Fig. 1 (Please note that the averaging of the data onto a 500x500 m^2 grid reduced peak values as shown in Tab. 1). The set-up of the different case studies is presented in Tab. 2.

4. RESULTS AND CONCLUSIONS

(a) In all runs cloud developed after about 60-70 minutes. In the reference simulation, CCC, where all surface parameters were kept constant, rainfall development started after 100 min and exhibited spatial and temporal periodicity: analyses of the individual time series showed that new formation of rain-bearing cells was likely to occur every 45-50 minutes; averaging of the total liquid water content over the whole simulation (Fig. 2) showed that increased rainwater totals occurred at regular distances of 70-80 km. The larger rainfall fields averaged a width of 10-15 km and lasted between 30-60 minutes; numerous cells of smaller extent and short duration occurred throughout the model domain.

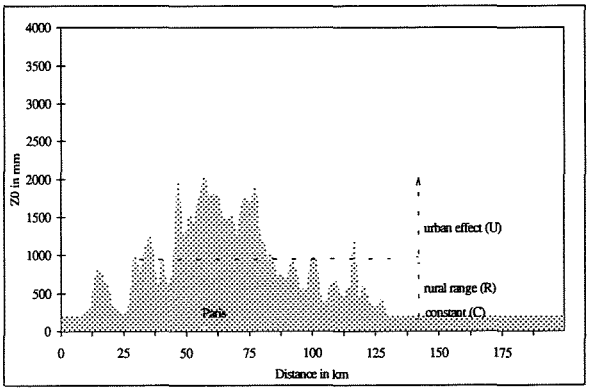

Fig. 1: xz-cross-section of the roughness length z_0 for the whole model domain and the z_0-thresholds for urban (U), rural (R) and constant runs (C).

Table 2: Description of the different simulations.

SET	*SIM*	*μ (%)*	*B*	*z_0(m)*
a	CCC	28	1	0.2
b	UUU	10-40	0.2-5	0.2-4
	RRR	10-40	0.2-5	0.2-1
c	UCC	10-40	1	0.2
	RCC	10-28	1	0.2
d	CUC	28	0.2-5	0.2
	CRC	28	0.2-1	0.2
e	CCU	28	1	0.2-4
	CCR	28	1	0.2-1

(b) Switching on of all surface parameters resulted for both urban and rural set-ups in rainfall enhancement and reorganisation of the rainfall fields. Rainfall developed 30 minutes earlier than in the reference run. It resulted in two peak rainfall totals, one located over the rural/urban area, and one circa 80 km downwind of the surface perturbation (Fig. 2). The rainfall cells were 30-50 % larger and longer-lasting. The number of small and short lasting cells was considerably reduced.

(c) Variation of μ only showed similar results as described in (b), indicating that the sensible heat flux was the dominant parameter in the simulations. The increased rainwater totals over the urban area (UCC) were accumulated by reoccurring rainfall throughout

the whole simulation, with strongest precipitation around 140 min (Fig. 3).

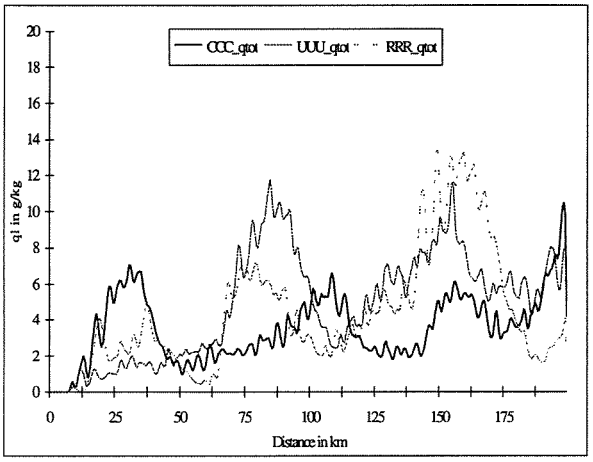

Fig 2: Total liquid water content q_l in g/kg averaged over 4 hours of simulation.

Most of the downwind precipitation was accumulated towards the end of the simulation (after 180 min). If only the rural range was considered (RCC), two principal cells developed and intensified (Fig. 3), one of which started over the rural variations, and one 80 km downwind of it. The highest liquid water content was accumulated in the downwind peak with $\overline{q}_{l\max} = 20$g/kg, while the peak over the rural area amounted only to 8 g/kg. The rural configuration resulted in locally higher rainfall totals than the urban configuration. This seems to confirm results of Thielen (1994) that strong surface heating 'smears' out the rainfall development in time and space, resulting in a higher number of cells with lower intensity and shorter duration than weak surface heating (Fig. 3).

(d) Variation of the Bowen ratio (CUC, CRC) had generally little effect and resulted only in a slight decrease of the liquid water content as compared to simulation CCC (Fig. 4). This indicates that local variations of the latent heat flux have little effect on rainfall processes with the considered time and length scales.

(e) Variable z_0 (CCU, CCR) initiated convection only 5-15 min. earlier than simulated in CCC. Its effect became most pronounced after 3 hours of simulation, and resulted in increased rainfall 80 km downwind of the perturbation.

Generally, effects were more pronounced when only one parameter was varied while the others were kept constant. This suggests that the different effects do not simply superimpose, but interact, which can results in damping of individual effects.

From the results of the 2D study it can be concluded that soil characteristics can modify convective rainfall development. On a relatively short

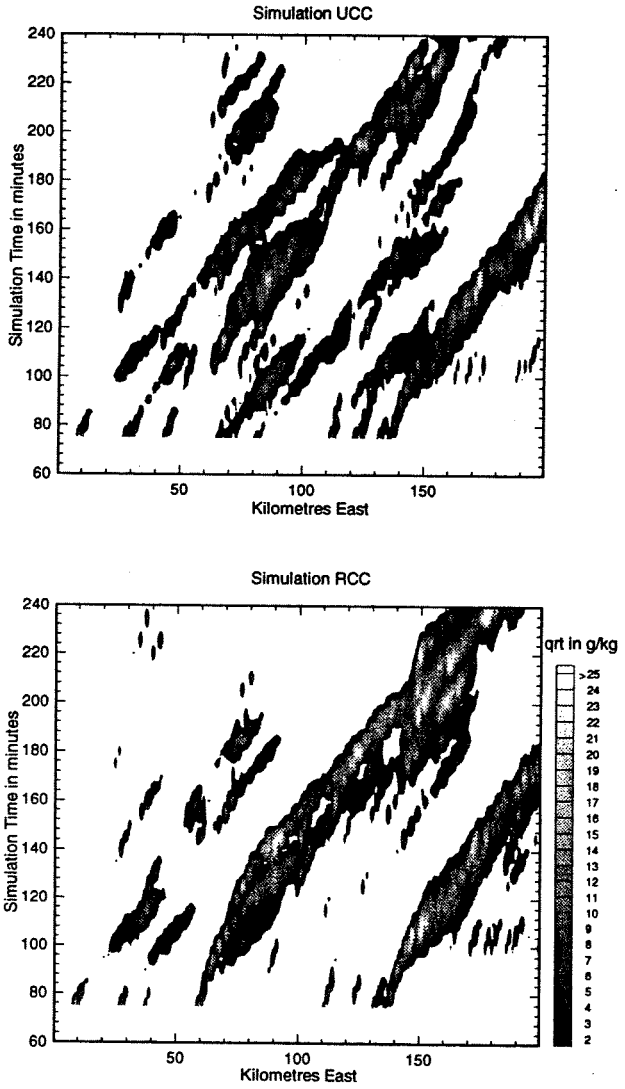

Fig. 3: Display of the total rainwater mixing ratio throughout the air column as a function of distance and time for the simulations UCC and RCC.

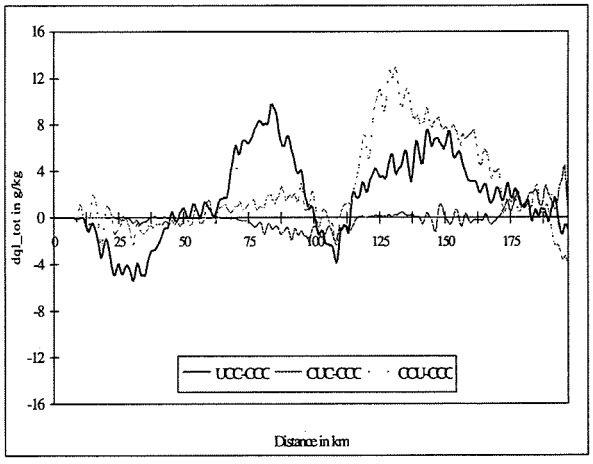

Fig. 4: Tendency of the liquid water content to in- or decrease when varying the conversion rate μ (UCC-CCC), the Bowen ratio B (CUC-CCC), and the roughness length z_0 (CCU-CCC).

time scale of 1-2 hours it is mostly variations in the sensible heat fluxes and subsequent variations in the buoyancy force that can cause increased rainfall downwind of a city and reoccurring rain development over the city itself. The strong influence of the sensible heat fluxes on the rainfall development suggests that a careful calibration of the parameter μ is necessary for realistic simulations.

The effect of increased turbulence supported the rainfall development particularly downwind of the perturbation zone. These results agree with findings of Changnon et al. (1977) during the METROMEX experiment.

Latent heat fluxes do not seem to play a role for processes with the considered time and length scales, but it cannot be excluded, that their influence becomes noticeable for longer term simulations.

The aim of this study was to assess the sensibility of different surface parameters on the development of rainfall. The results seem to confirm that precipitation can be enhanced by the presence of urban or rural agglomerations, particularly downwind of the perturbation, and thus are in agreement with the results of the METROMEX experiment (Changnon 1977). However, for a more realistic assessment of the effect of these parameters on rainfall development, the simulations should be in 3D, and also include time dependent surface parameters. A next step would therefore be to include a soil model calculating the heat fluxes at each time step. This is, however, only possible with a soil model that is able to cope with rural as well as urban soils and surfaces.

ACKNOWLEDGEMENTS

The authors would like to thank A. Gadian for fruitful discussions on the subject, and T. Clark for the permission to use his code. Financial support was given by the *Conseil Régional des Pays de la Loire* and the *Programme de Recherche en Hydrologie*' (N^0 Contract INSU_CNRS 94PRM19)

REFERENCES

Bruintjes, R.T., T.L. Clark and W.D. Hall (1994) Interactions between topographic airflow and cloud/precipitation development during the passage of a winter storm in Arizona. J. Atmos. Sci., 51, No. 1, 48-67.

Changnon S.A., Huff. F.A., Schickedanz, P.T., Vogel J.L. (1977) Summary of METROMEX, vol. I: Weather anomalies and impacts; Bull. 62, Ill.State Water Survey, Champaign, 260pp.

Clark T.L. (1979) Numerical simulations with a three-dimensional cloud model: lateral boundary condition experiments and multi-cellular severe storm calculations; J. Atmos. Sci., 34, pp 2191-2215

Clark T.L. and Farley D.,(1984) Severe downslope windstorm calculations in two and three spatial dimensions using anelastic interactive grid nesting: a possible mechanism for gustiness; J.Atm.Sci., 41: pp 329-350.

Clark T.L. and Gall R. (1982) Three-dimensional numerical simulations of airflow over mountainous terrain: a comparison with observations; Mon. Weath. Rev., Vol. 110, pp 766-791

Clark T.L. and Hall W.D., (1995) Documentation of the Clark anelastic model, Version G2tc38; NCAR, MMM, Boulder, 80307-3000 Colorado, USA

Goldreich Y. (1995) Urban climate studies in Israel; a review, Atm.Env., 29, No. 4, pp 467-478

Huff F.A. and Vogel (1978) Precipitation modification by major urban areas; Bull. Amer. Meteor. Soc., 54, pp 1220-1232

Kessler E. (1969) On the distribution and continuity of water substance in atmospheric circulations; Meteor. Monogr, 32, 84pp

Koenig L.R. and Murray F.W. (1976) Ice-bearing cumulus cloud evolution, Numerical simulation and general comparison against observation; J. Appl. Met., 15, pp 747-762

Lowry W.P. and Probald F. (1978) An attempt to detect the effects of a steel work on precipitation amounts in Central Hungary; J. Appl. Met., Vol. 17, pp 964-975

Oke, T.R., (1987). Boundary layer climates; Routledge, Chapman and Hall, Inc. , London

Stull, R.J., 1988. An introduction to boundary layer meteorology. Atmos. Sc. Library, Kluwer Academic, Dordrecht (NL): 666 pp.

Thielen J. (1994) The influence of the Pennines on severe convective storms; Ph.D. thesis at the Environmental Science Department, Lancaster Universiy, Lancaster, LA1 4YQ

Thielen J.and Creutin J.-D. (1995) Modélisation couplée atmosphère-hydrologie en milieu urbain; Atelier de Modélisation de l'Atmosphère, 28-30 novembre 1995, Vol. 1, pp 227-231

DRYING OUT OF ARAL SEA AND A REGIME OF CLOUD AND PRECIPITATION.
12th INTERNATIONAL CONFERENCE ON CLOUDS AND PRECIPITATION

Dr. B.A. Kamalov.,
Administration of Hydrometeorological Processes Modification,
85 Observatorskaya, 700052 Tashkent, Republik of Uzbekistan

In the second half of the XXth century the mankind has suffered from several ecological catastrophes.

The main cause of the Aral Sea crisis is considered to be the fact that agricultural changes have been carried out without taking into account the water resources possibilities and besides the water intake from the great rivers such as Amudarya and Syr Darya which formely had supplied the sea with the water for cotton and other cultures fields irrigation in the region had the catastrophic results for this unique water reservoir of the Central Asia.

The sea level had dropped from 53m in 1960 to 37m in 1990 The sea water volume in 1960 was 1064 km3, in 1990 it became 304km3, accordingly the sea area equalled 66,1 thous.km^2 and 34,8 thous km^2 And due to this process the sand and salt desert has appeared on the area of 30 thous.km^2.

For that period the salinity of the sea water has increased from 10,2% to 33,3%, i.e. 3 times as much.

All this has led to the radical changes in flora and fauna of the sea and adjoining territories.

This process has been accompanied by the deep social, ecological and sanitary and medical problems. Consequently sharp lessening of the sea area, the water surface transformation to the sand and salt desert on the area more than 30 thous. km^2, sharp increase of the sea salinity had prominent effect on meteorological regime of adjoining territory.

Nevertheless, many researches [1, 2, 3, 4] on the base of statistical analysis of meteorological data indicate that the changes of meteorological characteristics during the drying out of Aral Sea are caused mainly by the peculiarities of atmospheric circulation, and the impact of the Aral Sea drying out is manifested only in the coastal area of 100 km width. Is this really so?

For the revealing of the Aral Sea drying out effect on precipitation the decade rainfall data calculated by O.I.Subbotina which are presented in table 1 were used. As it is seen from this table 1, the annual total rainfall during the last decades since 1960 in the majority of observation sites are within the totals recorded during two preceding decades. Only the data registered in the narrow mountainous valleys and deep in the mountains showed some decrease of the rainfall during the last three decades comparing with the preceding ones (Talas, Pskem, Naryn, Suusamyr, Tien-Shan, the Gorbunov's), while the open mountainous passes showed the increase of precipitation (Anzob pass). The increase of precipitation is also registered almost by all observation sites located in the Aral Sea region.

During the last three decades such

Table 1. Mean annual precipitation total (mm) by decade

Station	1941--1950	1951--1960	1961--1970	1971--1980	1981--1990
Karakalpakia	115	143	118	134	173
Aral Sea	114	134	137	132	141
Muinak	88	97	109	120	155
Chimbai	77	83	126	113	131
Khiva	73	101	100	89	105
Repetek	98	127	109	124	125
Tamdy	95	122	117	123	131
Eloten	148	162	151	161	167
Termez	133	143	150	134	157
Sherabad	207	196	195	158	207
Tashkent	436	464	446	411	399
Fergana	183	186	183	161	196
Gushgy	244	305	278	307	304
Samarkand	333	401	388	344	338
Dushanbe	548	688	696	609	600
Dalverzin	303	364	342	307	305
Talas	297	341	351	298	270
Pskem	863	922	898	792	800
Issykkul	124	160	125	114	145
Cholponata	243	287	243	248	313
Khaidarkan	489	616	513	467	561
Naryn	308	353	316	269	314
Suusamyr	378	381	395	320	370
Khorog	249	312	283	285	276
Dekhauz	301	363	321	325	304
Sarytash	339	418	403	342	373
Ansob pass	269	430	486	477	494
Tien-Shan	304	346	342	296	291
the Corbunov's	1273	1474	1085	1137	1327

synoptical processes as south-Caspian Murgab and Upper-Amudarja cyclones, the north-western and northern intrusions, wave processes when there is substantial precipitation were observed more rarely than during the preceding decades. As for the western intrusions, the changes were not registered (table 2). As it seems true, the precipitation in the Aral Sea basin should decrease. But this wasn't registered. It is likely,that this lack in the moisture inflow into this region was compensated by the sea drying out in the course of the last three decades.

This is substantiated by the decrease of fair and dull days number and the increase of the number of semi-clear days, the increase of frequency of cumulus and cumulonimbus clouds during the spring-summer period, etc.

REFERENCES

1. Diagnostic study for the elaboration of Plan of actions aimed at the preservation of the Aral Sea. UNER. 105 p.

2. Zolotokrylin A.N., Tokarenko A.A. On the climate variation in the Aral Sea region for the last 40 years 1991,News of USSR Ac. of Sc. beogr.ser. N4, p. 75.

3. Climate variability of the Central Asia. 1995. Central Asia Research Hydrometeorological Institute. Tashkent, 216p.

4. Data on the climatic changes of the Aral Sea region. 1994. Central Asian Research Hydrometeorological Institute. Tashkent, 86p.

Table 2. Occurrence (%) of synoptic processes type over the Central Asia by decades

Decades	Types of synoptic processes								
	1,2,3	5,6	7	8	9 9a 9b	10	11	12	13
1935-1940	14	31	3	1	28	19	4	-	-
1941-1950	12	21	4	2	36	18	2	3	2
1951-1960	10	23	8	4	35	16	1	2	1
1961-1970	8	20	6	7	26	18	2	6	7
1971-1980	8	14	4	5	30	19	1	8	11
1981-1990	9	7	3	5	35	16	1	13	14
	10	17	5	4	33	16	2	6	7

Note: 1,2,3 - south-Caspian, Murgab, Upper-Amudarja cyclones; 5,6 - north-western and northern intrusions; 7-wave processes; 8-stationary cyclone; 9- south-western (eastern,southern) periphery of anticyclone; 10- western intrusions; 11- summer thermal depression; 12- small gradient field of high pressure; 13- small gradient field of lav pressure.

SYSTEMATIC VARIATIONS OF RAINDROP SIZE DISTRIBUTIONS MEASURED IN NORTHERN GERMANY DURING 7 YEARS

Igor G Doelling[1], Jürg Joss[2] and Johann Riedl[1]

[1]Deutscher Wetterdienst, Meteorologisches Observatorium, D-82383 Hohenpeissenberg, Germany
[2]Istituto Svizzero di Meteorologia, Osservatorio Ticinese, Via ai Monti 146, CH-6605 Locarno-Monti, Switzerland

1. INTRODUCTION

Raindrop size distributions were measured with a Joss- Waldvogel disdrometer at Hamburg during 1979-1988. The total recording time was 7 years 1 month. 2'498 rain events with 324'171 spectra (one minute per spectrum) were analyzed and classified into four precipitation type classes: warm air advection, cold air advection, weak gradient type, thunderstorm. Hamburg data, influenced by North Sea, are compared with disdrometer data from Berlin (north east, flat country, measurements since 1993) and from Rostock (Baltic Sea coast line, measurements since 1994). The number of analyzed spectra (each one cumulated to contain at least 100 drops and to have at least one minute duration) for each location and precipitation type are given in Tab. 1.

For different locations and different precipitation type classes we try to find Z-R-relations $Z=a*R^b$. The recorded one minute drop size distributions contain between 1 and 8'678 drops each. Distributions with few drops are poorly defined (*Smith et al. 1993*) and the Z-R-relations depend strongly on the sample area (volume) which is small for disdrometer and large for radar. The parameters of the Z-R-relations also depend on the type of regression used, e.g. dBR=f(dBZ) or dBZ=f(dBR).

For large (i.e. for radar) sample volumes the raindrop size distributions tend to be exponential (*Joss and Gori, 1978*). The Appendix shows that exponential raindrop size distributions under „natural" conditions lead to a „constant" exponent $1.4<b<1.6$. By setting $b=1.5$, the variation of the Z-R-relation are considered only by changing the factor „a" in $Z=a*R^{1.5}$.

Under this assumptions and considering the large number of recorded spectra, the next steps of analysis are:

1.To cumulate the spectra containing only a few drops to statistically better defined accumulated spectra.

2.To analyze these cumulated, „better" spectra and find the distribution of the factor „a" of the Z-R-relationship for different precipitation types and different locations.

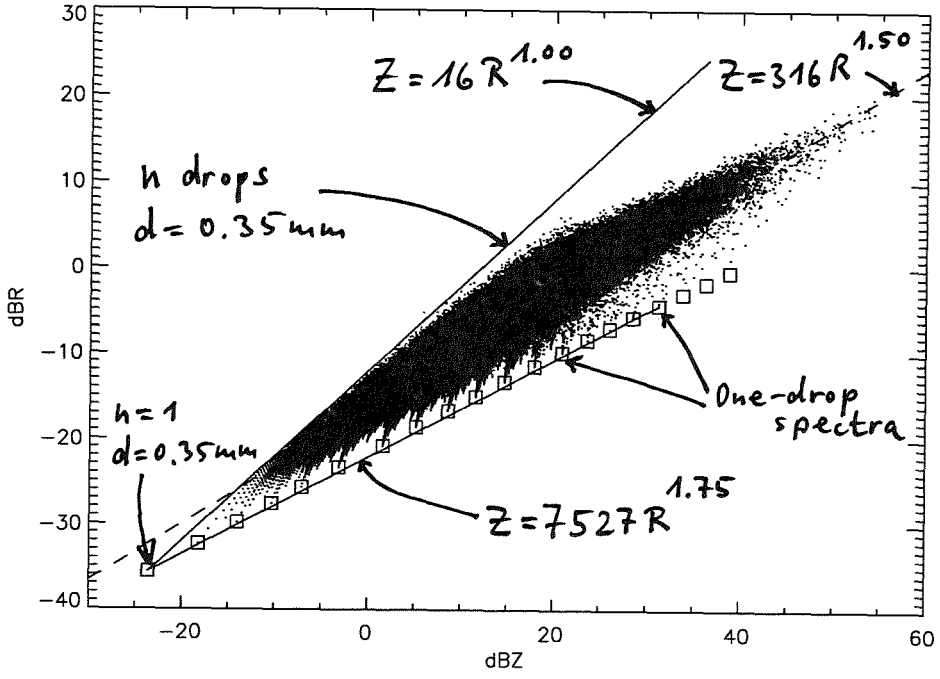

Fig. 1: dBZ- and dBR-values of all 186'040 one-minute spectra from Hamburg, recorded in cold air advections during 85 months. All points lie between $Z=16*R^{1.00}$ (n drops in the smallest class with d=0.35mm) and $Z=7527*R^{1.75}$ (one drop of variable size). Artifacts are caused by small sample sizes.

2. ANALYSES

2.1 dBZ-dBR-diagrams for one-minute-spectra

For all locations and all precipitation types we plotted dBR- versus dBZ-values (with dBR=10logR and dBZ=10logZ, where R is the rain intensity in mm/h and Z the radar reflectivity factor in mm^6m^{-3}). Each single spectrum of all cases recorded during 85 months of cold air advection at Hamburg is plotted in Fig. 1. From Fig. 1 we clearly see artifacts. All points are inclosed between the two relationships $Z=16*R^{1.00}$ and $Z=7527*R^{1.75}$.

The analysis of the number of (dBZ, dBR)-pairs occurring in an 1dBZx1dBR-box allows to guess the error caused by poorly defined spectra with small sample sizes if we use a simple linear regression. We found e.g. that ~2'100 spectra at -18.3dBR and -32.4dBZ contain each just one drop of 0.45mm diameter. Such spectra with small number of drops influence the parameters of the Z-R-regression considerably. Furthermore, using a simple cut-off criterion for the rain rate, we found the linear regression to depend also strongly on this cut-off criterion.

2.2 Cumulation of spectra

To find a well defined criterion for merging spectra with small sample sizes for obtaining statistically better defined spectra we plotted for each geographical location the number of spectra and the rain amount (Fig. 2). It shows that in Hamburg 50% of the spectra had less than 87 drops, but these 50% of the spectra contributed only 6% of the rain amount. For Berlin and Rostock the results are similar. From these results we decided to accumulated spectra with less than 100 drops to spectra with a minimum number of 100 drops. With that we strongly reduced the weights of spectra with only few drops, thus reducing artifacts. Furthermore, large samples correspond better to what the radar „sees" in its large volume.

2.3 Analyses of the factor „a" in $Z=a*R^{1.5}$

To ease finding differences between different locations and different precipitation types and assuming exponential distributions for the reasons explained

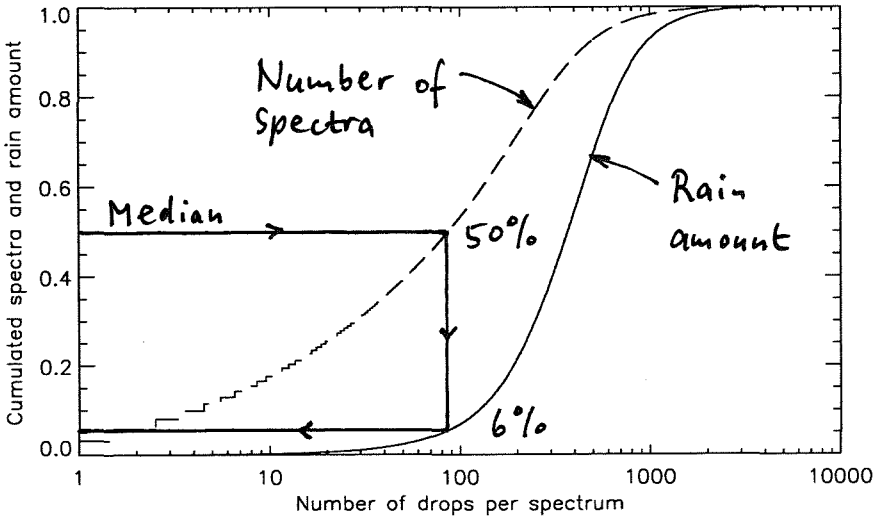

Fig. 2: Cumulated normalized number of all spectra in all weather conditions in Hamburg (dashed line, 321'682 spectra) and cumulated normalized rain amount (solid line, total of 4341mm). Note that 50% of the spectra contain less than 87 drops and contribute only 6% of the rain.

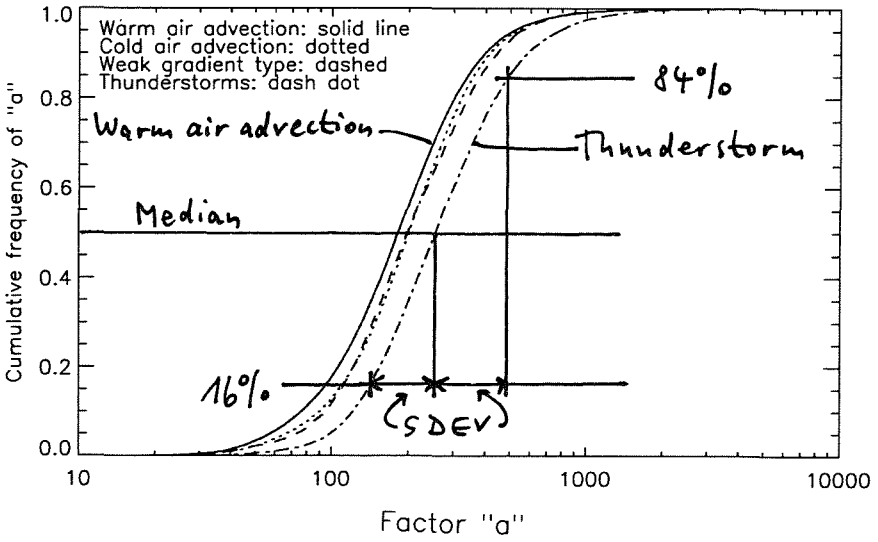

Fig. 3: Cumulated normalized frequency distribution of „a" in $Z=a*R^{1.5}$ of all spectra in Hamburg, cumulated to have at least 100 drops or one minute duration for 4 types of weather conditions (data from Hamburg in Tab. 1). Note that the standard deviation SDEV for single spectra within each weather type is wider than the change caused by different weather type, e.g. warm advection and thunderstorms.

Table 1: Number of spectra N, median value of „a" in $Z=a*R^{1.5}$ and standard deviation of „a" of single spectrum in dB. The N, „a" and SDEV are given for the cumulated spectra with at least 100 drops and one minute duration.

Location	Warm air advection			Cold air advection			Weak gradient type			Thunderstorms		
	N	a	SDEV	N	a	SDEV	N	a	SDEV	N	a	SDEV
Berlin	17'524	210	3.0 dB	16'703	202	5.0 dB	13'234	205	4.7 dB	1'385	286	5.0 dB
Hamburg	44'328	182	5.4 dB	111'504	200	5.0 dB	3'721	201	5.3 dB	13'620	253	5.4 dB
Rostock	11'113	194	4.3 dB	4'965	248	4.1 dB	4'062	203	5.9 dB	987	319	4.1 dB

above, we tentatively set the value of the exponent b=1.5, which is fairly correct for exponential spectra (see Appendix). The results for Hamburg are plotted in Fig. 3. Similar results were found for Berlin and Rostock. For all locations and all precipitation types the median of „a" and the standard deviation of „a" for single spectra (with at least 100 drops per spectrum) are given in Tab. 1.

3. RESULTS AND CONCLUSIONS

The analyses to find differences in Z-R-relations for different locations and different weather conditions needs two steps: 1. Find statistical well defined spectra, and 2. calculate regressions for data sorted according to physical (or meteorological) questions. We found that:

1.Our criterion (number of drops at least 100) leads to well defined spectra with statistically „good enough" drop sample sizes (we hope). Only after this first step we can reasonably try to find the meteorologically caused differences for weather types and locations.

2.The differences between median values of „a" for different locations and different weather conditions are small, only thunderstorms are significantly different with „a" about 300 as compared to „a" about 200 for the rest of the cases. The variation of „a" of single spectra within a weather type is larger than the difference between weather types. Note that SDEV of „a" in Tab. 1 belongs to a single spectrum.

3.If spectra are independent (not always the case!) the error of estimate of a population value such as the „mean" or the „median" decreases with the square root of the number of independent cases in the population. In this case all the „a"-values from all the locations and all weather situations are statistically significant different. E.g. for cold air advection at Hamburg the use of the square root of 111'504=334 leads to an error of estimate of the population value of 2*5.0/334=0.03dB or 0.7% or 1.4 „a"-units, which is statistically significant different from the other population „a"-values.

4.The question is open to what extent the assumption of exponential distributions in the radar volume is justified. Clearly, this assumption simplifies the analyzes a lot by not having to cope with variable exponents.

APPENDIX: LIMITS TO THE VARIABILITY OF Z-R-RELATIONSHIPS FROM EXPONENTIAL DROP SIZE DISTRIBUTIONS (J. Joss)

A.1 Introduction

Considering the vast amount of Z-R-relationships found in the literature, the question arises about possible reasons causing the observed variations. The usual answer is that drop size distributions are different in different countries and weather types and that Z and R are weighting the distribution with a different power law. A consistent relationship may only be obtained if some "stable law" between drops contributing mainly to Z and those contributing mainly to R exists. As an example, this condition is fulfilled for exponential distributions. According to *Joss and Gori (1978)* exponential distributions are found when enough individual samples are averaged over time and/or space. They also showed a tendency to find less exponential distributions for smaller sample sizes. But what parameters - i.e. what range of variation - do we have to assume? What are the consequences on the Z-R-relations? For what geographical region is a given sample representative? What sample size do we need? *Smith et al. (1993)* show that the already the variability caused by poor statistics of a single population (having **one R and one Z**) may cause Z-R-relations which look very similar to what we are used to from ground-based and airborne measurements. The small samples cause a "statistical" variability, as opposed to a "natural" variability originating from varying meteorological conditions. Often the small sample size is limited by instrumental attributes or simply by the large effort involved (especially on an airplane!) in obtaining a "reasonable" sample size, i.e. one where statistical fluctuations in drop concentration can be neglected. Here radar with its immense sample size offers an important advantage. The question, however, over what geographical area this sample remains "representative", is still open for discussion. It is a relevant issue for future work, if we want to use radar for hydrological applications. Applying the above cited results (*Joss and Gori, 1978*) to the large samples of operational radars, it seems save to expect exponential distributions in the pulse volume.

Table 2: "Natural, typical" variation of parameters and their percentage influence on relationships (100*Variation/AVE of the parameter, caused by the variation)

Parameter	Average	Log(R/[mm/h])	Log(N_0[m^3mm])	p/[hPa]	T/[°C]	H/[m]
Average value		Log(10 mm/h)	Log(8000/m^3mm)	850 hPa	5.7 °C	1436 m
Variation		0.5~Faktor 3.16	0.5~Faktor 3.16	8 hPa	6.0°C	1000 m
a/[mm^6/m^3]	206.12	-5.650%	-39.900%%	0.535%	-0.701%	-6.202%
b in $Z = a R^b$	1.4904	1.698%	-1.618%	0.027%	-0.134%	-0.213%
c/[mm^{-1}]	4.317	0.834%	21.770%	-0.076%	0.101%	0.919%
d in $\Lambda = cR^d$	-0.2129	1.698%	-1.618%	0.027%	-0.134%	-0.213%
e/[dB/km]*	.005347	-3.750%	6.198%	0.351%	-0.461%	-4.120%
f in $A = e R^f$	0.9794	1.698%	-1.618%	0.027%	-0.134%	-0.213%

*The relationship for two-way attenuation is given here for a wavelength of 5.6cm. Note that at 10cm wavelength the attenuation is ~3 times smaller, at 3.2cm ~5.5 times.

A.2 Summary of results

After assuming a given set of parameters for N_0, p and T, the slope Λ ($N=N_0 \exp(-\Lambda D)$ of the drop size distribution) is adjusted to yield the desired R and, by varying Λ slightly, power-laws between the desired parameter and the rain rate R are calculated (reflectivity-rainrate Z-R, slope-rainrate Λ-R and attenuation-rainrate A-R), always using for the fall velocity the "full" relationship by *Berry and Pranger (1974)*. This fall velocity depends of the drop diameter (drop shape!), the air pressure p and the temperature T. Tab. 2 gives in row 1 a list of the "natural" parameters, in row 2 their assumed average value, in row 3 their "natural" variation and in rows 4 to 9 their percentage-influence on the reflectivity Z, the slope Λ of the distribution, and the two-way attenuation A [dB/km]. Note that all percentage-influences on exponents (Z-R, Λ-R and A-R) have the same dependence from the "natural" variation (row 3) of parameters in Tab. 2 (R, N_0, p, T and H). If we vary all parameters within reasonable, natural conditions to produce an ***extremely high*** exponent, we find

$Z=462R^{1.599}$, $\Lambda=3.00R^{-0.228}$ and $A=0.00499R^{1.0505}$

for R=100mm/h, N_0=1400, p=1050hPa, T=0°C.

If we push all parameters within reasonable, natural conditions to produce an ***extremely low*** exponent, we find

$Z=105R^{1.391}$, $\Lambda=5.74R^{-0.199}$ and $A=0.00529R^{0.9141}$

for R=0.3mm/h, N_0=30,000, p=700hPa, T=0°C.

A.3 Conclusions

The exponent of power-laws (Z-R, Λ-R and A-R) remain constant within very narrow limits for the natural range of p and T and R. An important premises is that N_0 is not significantly changing in the population analyzed (e.g. the rain must be of the same type, produced by an exponential distribution such as proposed by *Marshall and Palmer (1948)*).

An important deviation of the exponent from 1.5 would have to be caused by a single one or a combination of the following three phenomena: 1) N_0 is systematically changing with rain rate, 2) the distributions deviate significantly from exponential ones or/and 3) the sample sizes used are too small.

REFERENCES

Berry E.X. and M. Pranger, 1974: Equations for calculating the terminal velocity of water drops. J. Appl. Meteorol., Vol. 32, No7, Feb.1974, pp 108-113.

Della Bruna G., J. Joss and R. Lee, 1995: Automatic calibration and verification of the accuracy of radar for precipitation estimates. 27th Int. Conf. Radar Meteorol., Amer. Meteor. Soc., 3 pages.

Joss J. and E.G. Gori, 1978: Shapes of raindrop size distributions. J. Appl. Meteorol., 17, pp 1054-1061.

Joss J. and A. Waldvogel, 1990: Precipitation measurements and Hydrology, a Review.'Radar in Meteorology' (David Atlas Editor), Amer. Meteorol. Soc., pp. 577-606.

Joss J., G. Galli, A. Pittini, G. Della Bruna and R. Lee, 1995: Seven years of (dis-)agreement between radar, rain gauges and river flow: possible improvements?. 27th Int. Conf. Radar Meteorol., Amer. Meteorol. Soc., 2 pages.

Joss J. and R. Lee, 1995: The Application of Radar/ Gauge Comparisons to Operational Precipitation Profile Corrections. J. Appl. Meteorol., Vol. 34, pp 2612-2630.

Lee R., G. Della Bruna and J. Joss, 1995: Intensity of ground clutter and of echoes of anomalous propagation and its elimination. 27th Int. Conf. Radar Meteorol., Amer. Meteor. Soc., 2 pages.

Smith P.L., Z. Liu and J. Joss, 1993: A study of sampling variability in raindrop size observations. J. Appl. Meteorol., Vol. 32, No7, July 1993, pp 1259-1269.

APPLICATION OF CLOUD AND PRECIPITATION IN FLOOD–WATERLOGGING DISASTER ASSESSMENT MODEL

Dong Jia–Rui Wang Ang–Sheng
(Institute of Atmospheric Physics, Chinese Academy of Sciences)

ABSTRACT

Natural disasters occur frequently and cause great damages every year in China[1]. The most serious one among them is flood–waterlogging disaster caused by heavy rain which is the direct reason to produce such disaster. It is important to assess flood–waterlogging disaster correctly for dicision making of natural disaster reduction. So, an assessmet model has been set up by coupling atmospheric motion equations of soil hydrology and heat conductivity. In this paper, a test has been made by using this model with the data of meteorology on July 12, 1994, and the results are satisfactory.

1. INTRODUCTION

Recent years, weather forcast has been rapidly developed, and atmospheric motion equations are perfect in forecasting rainfall. The parameterazition of cloud and precipitation has played important roles in improving forecast precision by successfully discribing the formation, development and convection of cloud and precipitation. In order to predict heavy rain and other strong rainfall more precisely, it is not enough use atmospheric motion equation only. In realistic calculation, forecasting values of precipitation are often underestimated. To face these problems, some scientists has set up couple models of atmosphere and ocean and have got better effects in climate numerical simulations. In this paper, we give an assessment model by coupling the atmospheric motion equations and the equations of soil hydrology and heat conductivity in limited forecasting area. The results are given in this paper at last.

2. BASIC EQUATIONS OF THIS MODEL

1) Atmospheric motion eqations

Here, atmospheric motion basic equations are used in spherical coordinates with an eta coordinate system[2] in the vertical direction.

$$\frac{\partial U}{\partial t} = \alpha(U) + \beta_U + \gamma(U) \tag{1}$$

$$\frac{\partial V}{\partial t} = \alpha(V) + \beta_V + \frac{PRL}{C_0 C_p} P^* + \gamma(V) \tag{2}$$

$$\frac{\partial \Pi}{\partial t} = \alpha(\Pi) + \beta_\Pi + \gamma(\Pi) \tag{3}$$

where $\alpha(F)$, β_F and $\gamma(F)$ are advection term, adaptation term and diffusion term of atmospheric motion respectively.

$$\alpha(F) = \pounds_1(F) + \pounds_2(F) + \pounds_3(F)$$

$$\beta(U) = -f^* V - \left(P\frac{\partial \varphi}{a\sin\theta\partial\lambda} + C_0 S\Pi\frac{\partial \ln P^2}{a\sin\theta\partial\lambda}\right)$$

$$\beta(V) = f^* U - \left(P\frac{\partial \varphi}{a\partial\theta} + C_0 S\Pi\frac{\partial \ln P^2}{a\partial\theta}\right)$$

$$\beta(\Pi) = S\left(C_0 + \frac{R\Pi}{C_p P}\right)\left(\frac{1}{P\eta}\Omega^{(1)} + \Omega^{(2)}\right)$$

$$\gamma(U) = K_u P^{-3}|\triangle' u|\triangle' u$$

$$\gamma(V) = K_v P^{-3}|\triangle' v|\triangle' v$$

$$\gamma(\Pi) = K_T P^{-3} R C_0^{-1}|\triangle' T|\triangle' T$$

The continuty equation:

$$\frac{\partial P^2}{\partial t} = -\frac{1}{\eta_s}\int_0^{\eta_s} D_{xy}\, d\eta \tag{4}$$

The geopotential equation:

$$\frac{\partial P}{\partial \eta} = -C_0 \frac{S\Pi}{P\eta} \qquad (5)$$

2) Moisture balance equation

$$\frac{\partial Q}{\partial t} = -\sum_{m=1}^{3} \pounds_m(Q) - PP^* + K_q P^{-3} |\triangle' q| \triangle' q \qquad (6)$$

where:

$$P = \sqrt{\frac{P_s - P_t}{H_s}}$$

$$\Pi = \frac{RPT}{C_0}$$

$$S = \frac{P - P_t}{P}$$

$U = Pu$, $V = Pv$, $Q = Pq$, η expresses eta coordinate, P_t is the pressure at the top of model, P_s is the surface pressure, Z_s is the topographic height of the model, $P_{rf}(Z)$ is a defined reference pressure.

Energy conversion terms at horizonal and vertical directions:

$$\Omega^{(1)} = -\int_0^{\eta} D_{xy} d\eta$$

$$\Omega^{(2)} = V\frac{\partial InP^2}{a\partial\theta} + U\frac{\partial lnP^2}{asin\theta\partial\lambda}$$

where: D_{xy} is mass convergence, K_u, K_v, K_T and K_q are diffusion coefficient of each component at horizonal and vertical directions, P^* is the rate of vapor condensation, L is the latent heating of condensation.

3) Soil heat and moisture flow equation

Heat and moisture flow in the soil is described by diffusion patial differential equations based primarily on the Phillip and de Vries [1957] equations:

$$\frac{\partial \theta}{\partial t} = -\frac{\partial q_\theta}{\partial Z} \qquad (7)$$

$$\frac{\partial T_s}{\partial t} = -\frac{1}{C}\frac{\partial q_h}{\partial Z} \qquad (8)$$

where θ is soil moisture, T_s is soil temperature, and C is the soil heat capacity.

The moisture flux q_θ and heat flux q_h are given by:

$$q_\theta = -D_\theta(\frac{\partial\theta}{\partial Z}) - D_T(\frac{\partial T_s}{\partial Z}) - K \qquad (9)$$

$$q_h = -\lambda(\frac{\partial T_s}{\partial Z}) - L_s D_{\theta vap}(\frac{\partial\theta}{\partial Z}) \qquad (10)$$

L_s is the latent heat of evaporation.

Both matric potential ψ and hydraulic conductivity K may be described as functions of moisture using the Clapp and Hornberger[1978] parameterization:

$$K(\theta) = K_s(\frac{\theta}{\theta_s})^{2b+3} \qquad (11)$$

$$\psi(\theta) = \psi_s(\frac{\theta}{\theta_s})^b \qquad (12)$$

Here θ_s is the soil moisture at aturation, K_s and ψ_s are soil conductivity and matric potential at saturation respectively, and b is determined by the soil texture.

D_T and D_θ are the diffusion coeffients of heat and moisture flux, which have both liquid and vapor contributions:

$$D_\theta = D_{\theta liq} + D_{\theta vap} \qquad (13)$$

$$D_T = D_{Tliq} + D_{Tvap} \qquad (14)$$

where:

$$D_{\theta liq} = K\frac{\partial\psi}{\partial\theta} \qquad (15)$$

$$D_{\theta vap} = \frac{D_{atm} f(\theta)\rho_0 gh\frac{\partial\psi}{\partial\theta}}{RT_s} \qquad (16)$$

$$D_{Tliq} = K\frac{\partial\psi}{\partial T_s} \qquad (17)$$

$$D_{Tvap} = D_{atm} f(\theta)h\frac{d\rho_0}{dT_s} \qquad (18)$$

D_{atm} is the diffusion coefficient for water vapor in the air, $f(\theta)$ is the tortuosity and porosity function, ρ_0 is the saturation density of water vapor, g is the acceleration of gravity, h is the relative humidity, R is the gas constant for water vapor.

The thermal conductivity coefficient λ can be given from McCumber, M. C. and R. A. Pielke[1981]:

$$\lambda = \begin{cases} e^{-(lg|\psi|+2.7)} & lg|\psi| \leqslant 5.1 \\ 0.00041 & lg|\psi| > 5.1 \end{cases} \qquad (19)$$

3. GENERAL DESCRIPTION OF THIS COUPLE MODEL

The couple model is integrated in the limited area from 95°E to 135°E and 20°N to 55°N. In the atmospheric motion model section, the vertical direction is divided into 7 layers, and in the soil section, the vertical direction is also divided into 7 layers.

Here, we only consider hydrology interactions between atmosphere and soil. The effect of heat conductivity will be involved in this couple model in the futh.r. The hydrology interactions between atmosphere and soil equations are realized through evaporation from soil to air, rainfall and condensation from air to the ground.

water evaporation equation of soil:

$$E_v = C_E(q_g^* - q_a) \qquad (20)$$

C_E is the heat transfer coefficient, q^* is the saturation specific humidity at the ground surface, q_a is the specific humidity of the air at height Z_a.

$$C_E = \rho_a C_D V_s \beta \qquad (21)$$

where C_D is the drag coefficient between the air and the ground surface, ρ_a is the air density at the ground, V_s is the ground wind velocity, β is the ratio of the realistic evaporation to potential evaporation.

When rainfall, we suppose that a thin soil layer at saturation state is formed, and then infiltrate into soil according to soil hydrology conductivity and diffusivity property.

The maximum infiltration rate[5] of water on the ground:

$$I_{max} = K(\theta_s) + D(\theta_s)\frac{(\theta_s - \theta_1)}{\frac{\triangle Z_1}{2}} \qquad (22)$$

Where θ_1 and $\triangle Z_1$ are the soil moisture and thickness of the first layer.

When no rainfall, the ground infiltration rate $I=0$, when precipitation rate(Pr) is less than the maximum infiltration rate, $I=Pr$, and when precipitation rate is more than the I_{max}, $I=I_{max}$.

The ground temperature T_g can be given by:

$$C_g\frac{\partial T_g}{\partial t} = I_g + R_g + S_g + L_g \qquad (23)$$

C_g is the heat capacity on the ground, I_g is the solar radiation absorbed by the ground, R_g is the ground long wave radiation, S_g is the sensible heat flux, and L_g is the latent heat flux.

4. THE RESULT AND DISCUSSION

This couple model is used to forecast 24 hours precipitation and compared to atmospheric motion model with the meteorological data on July 12, 1994. Fig.1 gives the result of 24 hours precipitation only using atmospheric motion equations, and Fig.2 gives the result of 24 hours precipitation using the couple model of soil and atmosphere. It is clear from Fig.1 and Fig.2 that the value of precipitation calculated by the couple model is bigger than that calculated by the atmospheric motion model only, which can be explained by Fig.3 and Fig.4. Such as, in the place of 40°N and 118°E, the maximum values of precipitation from atmospheric motion equation and couple model are 120mm and 160mm respectively. The actual total precipitation of that day is over 160mm.

Fig.3 and Fig.4 are the total 24 hours actual and potential evapoations in the forecasting area respectively. From the view of potential evaporation, the evaporation in rainfall area is small on account of lower temperature. But from the actual 24 hours evaporation figure, the actual maximum evaporation lies in the rainfall area. The reason is that enough water in rainfall soil can satisfy the need of evaporation. The evaporation is connected with not only atmospheric condition but also the soil moisture. In rainfall area, air humidity is increased by soil evaporation, which can have

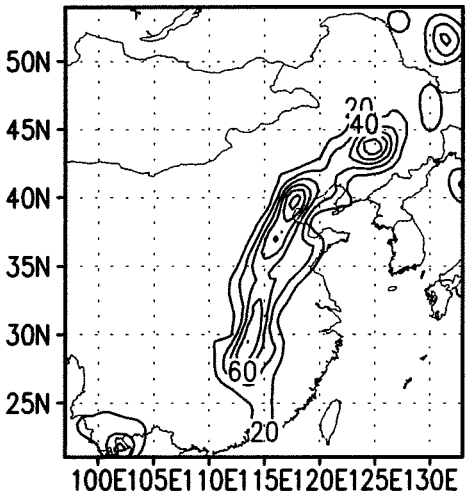

Fig.1 One day precipitation of Atmosphere Model from July 12 to July 13, 1994

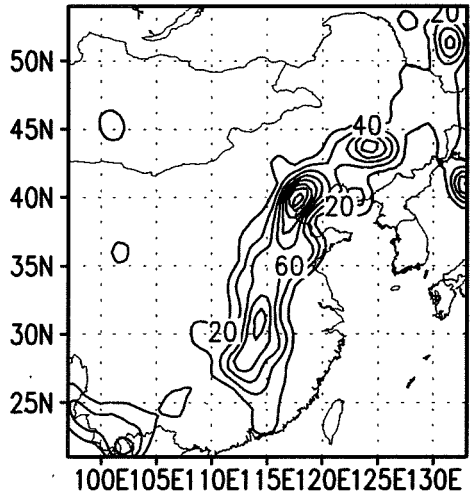

Fig.2 One day precipitation of Couple Model from July 12 to July 13, 1994

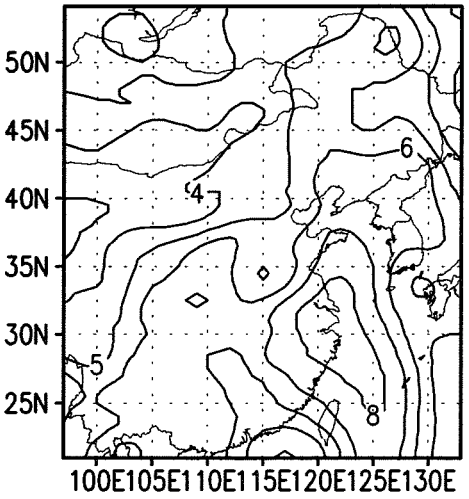

Fig.3 One day actual evaporation from July 12 to July 13, 1994

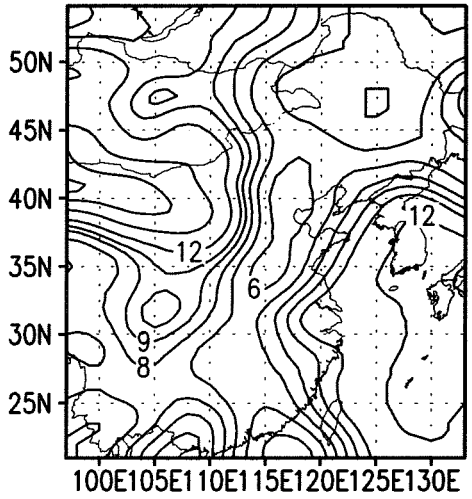

Fig.4 One day potential evaporation from July 12 to July 13, 1994

chance to make bigger rainfall and precipitation. The results can be seen from Fig.1 and Fig.2.

The interactions between atmosphere and soil exist many elements, besides evaporation, rainfall, condensation, solar radiation and ground long-wave radiation. So, more detial interactions between atmosphere and soil, such as the conductivity of temperature and so on, will be considered in the futher reseach work, which can improve the computation results more precisely.

REFERENCE

[1] Ang-Sheng Wang, 1991: A Brief Discussion on Strategy of Serious Natural Disaster Reduction,**NDR IN CHINA, 2**,12-15;

[2] Yu Rucong, 1989: Design of the Limited Area Numerical Weather Prediction Model With Steep Mountain, **Chinese Journal of Atmos. Sci., 13(2),** 145-158.

[3] J. R. Philip, 1957: Evaporation and Moisture and Heat Fields in The Soil, **Soil Sci., 14,** 354-366;

[4] MICHAEL C. McCumber et al., 1981: Simulation of the effects of Surface Fluxes of Heat and Moisture in a Mesoscale Numerical Model, **J. of Geo. Res., 86, C10,** 9929-9938;

[5] L. MAHRT and H.PAN, 1984: A Two-Layer Model of Soil Hydrology, **Boundary Layer Meteo., 29**,1-20;

AIRCRAFT ICING FROM SUPERCOOLED DRIZZLE

Stewart G. Cober, George A. Isaac, and J. Walter Strapp

Atmospheric Environment Service
Downsview, Ontario, Canada

1. INTRODUCTION

In-flight aircraft icing occurs when an aircraft encounters supercooled cloud droplets which freeze to the aircraft surface upon collision. Ice accumulation on a wing can cause a potentially dangerous loss of lift by disrupting the laminar flow over the wing surface. In order for an aircraft to be certified for flight in icing conditions, the manufacturer must demonstrate that the aircraft can be safely flown in "worst case" icing environments. In North America, such conditions are described by the Federal Aviation Regulation Part 25 Appendix C (FAR 25-C), where icing environments are characterized by cloud droplet median volume diameter (MDVD), supercooled liquid water content (LWC), temperature, and horizontal extent, with higher MDVD or higher LWC implying more severe icing. FAR 25-C provides 0.1% exceedance curves of MDVD versus LWC for specific temperature ranges (Fig. 1) and for a horizontal extent of 17.6 n mi (33 km). Any icing environment characterized by a MDVD-LWC point which is on or to the right of the curves is expected to be observed less than 0.1% of the time, and is considered a "worst case" environment. The curves were based on in-flight measurements with icing cylinders taken during the 1940s, and were not extended to MDVD values greater than 40 μm. Consequently, there has been some effort in recent years to validate and expand the curves (Sand et al. 1984; Jeck 1983; Isaac 1991). The 1994 crash of a modern commuter aircraft (ATR-72) in Roselawn Indiana was attributed to in-flight aircraft icing, and has demonstrated the importance of such research.

Two recent field projects conducted by the Canadian Atmospheric Environment Service have included in-flight measurements of the icing environments in winter storms on the Canadian east coast. Icing measurements made during thirty one research flights in the Second Canadian Atlantic Storms Program (CASP II) (Stewart 1991) were made to determine the validity of the FAR 25-C curves (Cober et al. 1995). They found that the icing environments were generally well below the FAR 25-C curves (Fig. 1), and attributed this to limited convective activity, relative cool cloud base temperatures and an efficient glaciation process within the synoptic clouds of the winter storms. Two exceptions occurred when the icing observed was associated with supercooled drizzle droplets up to 500 μm in diameter. One case (Cober et al. 1996) is shown in Fig. 1 (labelled 14 March 92), where it is clearly well in excess of the FAR 25-C envelopes. These observations led to the development of the Canadian Freezing Drizzle Experiment (CFDE) which was conducted in March 1995. Twelve research flights were made into regions where drizzle droplets were forming, with the aim of providing data to assist in expanding the FAR 25-C envelopes to larger MDVD values. Preliminary analysis of the icing environments associated with supercooled drizzle based on CFDE measurements is reported here.

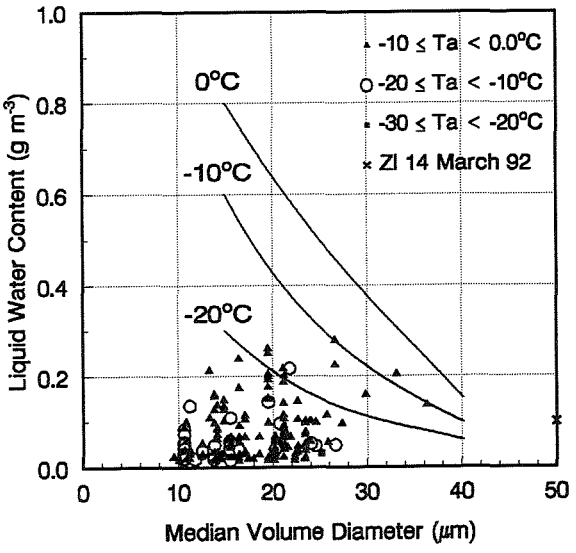

Fig. 1. FAR 25-C icing envelopes compared to measurements from CASP II. Each data point represents a 300 s average. Only the 14 March 92 case was associated with drizzle.

2. INSTRUMENTATION

In-flight microphysics measurements were made with a Convair-580 aircraft from the Canadian National Research Council. Instrumentation used for measuring the hydrometeor spectra reported in this analysis included the following: King probe liquid water probe

accurate to ± 0.02 g m^{-3}, Nevzorov liquid water and total water (ice plus liquid) probes which were accurate to ± 10%, PCASP-100x 0.13-3 μm aerosol probe, FSSP-100x 3-45 μm probe, FSSP-100x 5-95 μm probe, 2DC mono 25-800 μm probe, 2DP mono 200-6400 μm probe, 1DC 20-300 μm probe, and 1D260 10-640 μm probe. Calibrations of the King probes and FSSP instruments have been reported in Cober et al. (1995), while the accuracy of the Nevzorov probes are reported in Korolev et al. (1996). Measurements in the first four channels of the 2DC (< 125 μm) were discounted because of depth of field errors associated with its lower channels, and significant undersizing errors for droplets smaller than 100 μm (Korolev et al. 1991). Between 2 and 9 channels from the 2DP, 1D260, and 1DC probes were similarly discounted. The 2D data was processed using the centre-in technique following Heymsfield and Parrish (1978). The PCASP, two FSSPs, 2DC and 2DP instruments collectively covered the hydrometeor spectra from 0.13 μm to 6.4 mm in diameter with only the region between 95 and 125 μm not measured. The 1D data were not used in the numerical analysis, but were used to confirm the accuracy of the other measurements in regions of overlap.

3. ANALYSIS

For each of the 12 CFDE flights, cloud regions with drizzle were identified by visually examining the 2DC imagery. The data were then averaged over 300 s intervals, which corresponds approximately to horizontal distances of 30 km. This allows direct comparison with the FAR 25-C data which are based on a horizontal extent of 33 km. Regions with ice crystals were not included in the analysis because of the potential bias that crystals could have on the 2D, 1D and FSSP analysis. To date, 147 data points have been analyzed for cloud regions where droplets greater than 50 μm were measured, and where ice crystal concentrations were insignificant. For each data point, data from the two FSSPs, 2DC and 2DP instruments were used to calculate an integrated droplet spectra, from which characteristics of the droplet spectra such as MDVD could be calculated. Fig. 2 shows an example of the data from each probe and the integrated spectra curves for concentration and LWC. The 1DC data is also shown for comparison. Data from channels which were discounted for reasons discussed in Section 2 are not shown. FSSP channels with less than 10 particle counts, and 2D channels with less than 5 counts are not shown and were not used in the integration. Peaks in the cloud droplet and drizzle spectra are evident at approximately 10 μm and 200 μm respectively. The total droplet concentration was 85 cm^{-3}, with a liquid water content (LWC) of 0.14 g m^{-3} and a MDVD of 175 μm.

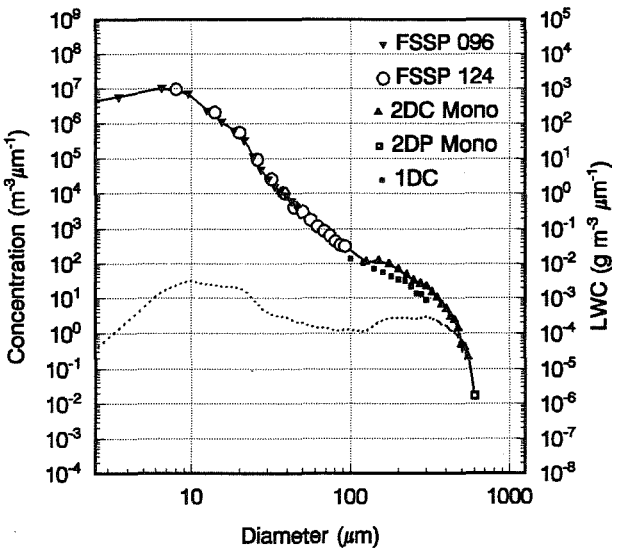

Fig. 2. Hydrometeor concentration (solid) and LWC (dotted) spectra for a 300 s average on 09 March 1995. The concentration measurements from five instruments are also shown. The integrated curve was based on the FSSP, 2DC and 2DP probes. The excellent agreement between the instruments was typical.

A comparison of the Nevzorov total water content (TWC) measurement versus the integrated LWC for each data point is shown in Fig. 3. The Nevzorov TWC measurement was used because this instrument, unlike the King and Nevzorov LWC probes, does not appear to suffer a reduced response to droplets larger than 50 μm (Korolev et al. 1996; Biter et al. 1987). Since cloud regions with ice crystals were not included in the analysis, the Nevzorov TWC measurement represents a more accurate LWC measurement than that of the King or Nevzorov LWC probes. While, uncertainties in the FSSP and 2DC concentrations cause the integrated LWC to be only accurate to within ± 50% (Baumgardner 1983), the agreement in Fig. 3 is much better, giving confidence in both the integrated spectra and the TWC measurements.

Fig. 4 shows a comparison of the data with the FAR 25-C envelopes for 0 and -10°C. During CFDE, measurements were mainly confined to cloud regions with temperatures warmer than -10°C, and consequently the minimum temperature for the data shown in Fig. 4 is -11°C. The drizzle formation mechanism for each measurement is also shown in Fig. 4. Drizzle formed through a condensation-collision-coalescence (CCC) mechanism accounted for 80% of the observations, while drizzle formed through a melting-resupercooling (MRS) mechanism accounted for the remainder (Isaac et al. 1996). Of the 147 data points, 33 had MDVDs exceeding 40 μm, and 12 points had MDVDs exceeding 500 μm. All observations of MDVDs greater than 250 μm occurred when the aircraft was flying below a

melting layer in a region of precipitation, with a maximum MDVD observed of 970 μm. The maximum MDVD observed for drizzle formed through a CCC process was 208 μm. Intuitively, larger MDVDs were expected through the MRS formation mechanism because the associated warm frontal clouds above the melting layer tended to be deeper with higher total water contents. The majority of the observations where the formation mechanism was CCC were made in low stratiform clouds which were less than 1 km thick. In general, the average LWCs were between 0.05 and 0.2 g m^{-3} when the MDVD exceeded 40 μm, and were relatively independent of the formation mechanism.

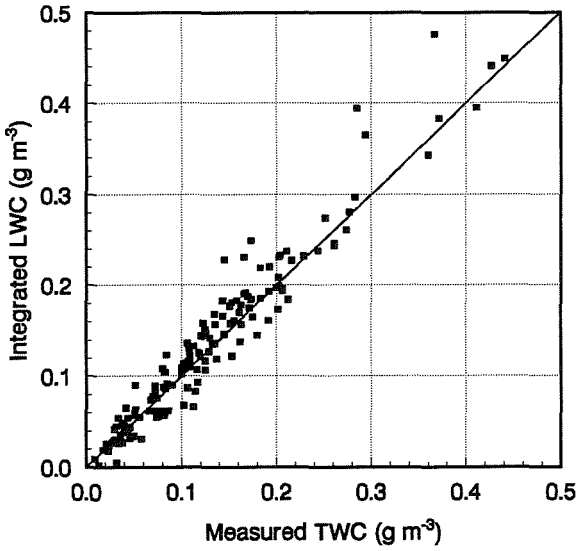

Fig. 3. Comparison of the measured total water content from the Nevzorov TWC probe, and the calculated liquid water content. The latter were determined from the integrated spectra of FSSP, 2DC and 2DP data. The solid line shows the 1:1 correlation.

4. DISCUSSION

The data shown in Fig. 4 has some biases, and by itself is not yet considered sufficient for extension of the FAR 25-C envelopes. With only 33 data points with MDVDs larger than 40 μm, it is difficult to extend the FAR 25-C curves which represent 0.1 percentiles. The geographical bias in the data must also be considered, since the data are limited to winter storms on the Canadian Atlantic coast. St. John's Newfoundland has the highest frequency of surface observed freezing precipitation in North America, with 150 hours per year (Isaac et al. 1996). While the CFDE data shown in Fig. 4 are likely representative of east coast freezing precipitation conditions, observations of large supercooled droplets over the continental U.S. (Rasmussen et al. 1995; Politovich 1989; Sand et al. 1984) are indicative that other meteorological conditions are capable of causing hazardous concentrations of supercooled drizzle drops.

Finally, there is the possibility of instrumentation bias in the analysis. 2DC probes are known to oversize droplets larger than 100 μm, possibly by up to 125 μm (Korolev et al. 1991) and no corrections have been made for this effect in the analysis presented here. However, this error will not change the integrated spectra MDVDs by more than 50 to 100 μm at worst. Consequently, conclusions about the worst case conditions will not change significantly when this error is corrected in future analysis.

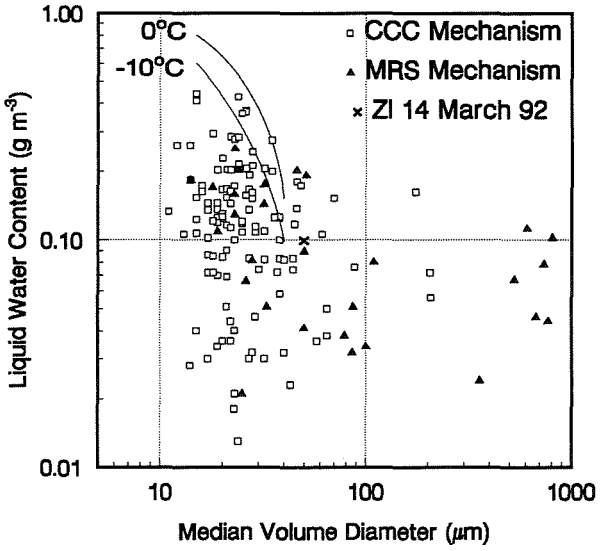

Fig. 4. Comparison of MDVD-LWC points measured in CFDE to the FAR 25-C envelopes. The 14 March 92 point is shown for comparison to the CASP II data shown in Fig. 1. Each point represents a 300 s average where the LWC exceeded 0.01 g m^{-3}.

Regardless of the limitations of the data discussed above, in terms of certification of aircraft, the extreme data presented in Fig. 4 certainly reflects the minimum "worst case" icing environments for which aircraft should be proven to operate safely. Since little data has been previously reported, this represents an improvement in attempts to define the "worst case" environments. The percentiles for LWCs incorporated in droplets between specific size ranges are listed in Table 1, and represents an alternative means of characterizing the data as suggested by Jeck (1996). Engineers certifying aircraft need only ensure that the maximum icing conditions for each interval are exceeded simultaneously. Table 1 shows that the LWC incorporated in droplets larger than 50 μm averaged 0.02 g m^{-3}, with the maximum being 0.11 g m^{-3}. While the LWC of droplets greater than 50 μm is small compared to the LWC for droplets smaller than 50 μm, the effects on the aircraft are believed to be out of proportion to the droplet size. Sand et al. (1984) and Politovich (1989) have reported that drizzle droplets can flow back over the wing surface prior to freezing, thereby causing a significant loss of lift. Similarly,

drizzle droplets which flow back may freeze behind ice protection mechanisms. Cloud droplets freeze to the front surface of a wing where ice protection is available, thereby having little effect on the lift, and presenting much less of a hazard.

Table 1: LWC average and percentiles for ranges of droplet diameters based on 147 CFDE data points.

Range μm	Average g m^{-3}	50% g m^{-3}	75% g m^{-3}	90% g m^{-3}	99% g m^{-3}
1-50	0.11	0.089	0.16	0.23	0.43
>50	0.022	0.010	0.032	0.057	0.108
50-100	0.0078	0.003	0.011	0.022	0.067
100-200	0.0039	0.0002	0.0049	0.015	0.027
200-300	0.0022	0	0.0017	0.006	0.028
300-400	0.0013	0	0.0007	0.004	0.023
400-500	0.0007	0	0.0006	0.003	0.007
500-1000	0.0018	0	0	0.008	0.020

5. CONCLUSIONS

Measurements of the aircraft icing environments associated with supercooled drizzle have been made in 12 flights in the Canadian Freezing Drizzle Experiment. Icing environments had median volume diameters up to 970 μm, and liquid water contents to 0.44 g m^{-3}. The contribution of LWC from droplets greater than 40 μm averaged 0.02 g m^{-3} with a maximum of 0.11 g m^{-3}. Comparisons to the icing envelopes used for aircraft certification have been made to assist regulatory agencies in setting guidelines for certifying aircraft in large droplet icing conditions.

6. ACKNOWLEDGEMENTS

This work was funded by the Canadian National Search and Rescue Secretariat, Transport Canada, the Atmospheric Environment Service and the Institute for Aerospace Research of the National Research Council.

7. REFERENCES

Baumgardner, D., 1983: An analysis and comparison of five water droplet measuring instruments. *J. Climate Appl. Meteor.*, **22**, 891-910.

Biter, C.J., J.E. Dye, D. Huffman, and W.D. King, 1987: The drop-size response of the CSIRO liquid water probe. *J. Atmos. Oceanic. Technol.*, **4**, 359-367.

Cober, S.G., G.A. Isaac, and J.W. Strapp, 1995: Aircraft icing measurements in east coast winter storms. *J. Appl. Meteor.*, **34**, 88-100.

Cober, S.G., J.W. Strapp, and G.A. Isaac, 1996: An example of supercooled drizzle droplets formed through a collision-coalescence process. Accepted by *J. Appl. Meteor.*

Heymsfield, A.J., and J.L. Parrish, 1978: A computational technique for increasing the effective sampling volume of the PMS two-dimensional particle size spectrometer. *J. Appl. Meteor.*, **17**, 1566-1572.

Isaac, G.A., A. Korolev, J.W. Strapp, S.G. Cober, A Tremblay, and R.A. Stuart, 1996: Freezing drizzle formation mechanisms. Proceedings of 12th Intl. Conf. Clouds and Precipitation.

Isaac, G.A., 1991: Microphysical characteristics of Canadian Atlantic storms. *Atmos. Res.*, **26**, 339-360.

Jeck, R.K., 1996: Representative values of icing-related variables aloft in freezing rain and freezing drizzle. 34th Aerospace Sci. Meeting, Reno Nevada, 15-18 Jan 1996.

Jeck, R.K., 1983: A new data base of supercooled cloud variables for altitudes up to 10,000 feet AGL and the implications for low altitude aircraft icing. U.S. Dept. of Transportation Report DOR/FAA/CT-83/21, 137 pp.

Korolev, A.V., J.W. Strapp, and A.N. Nevzorov, 1996: On the accuracy of Nevzorov airborne hot wire LWC/TWC probe. Proceedings of 12th Intl. Conf. Clouds and Precipitation.

Korolev, A.V., S.V. Kuznetsov, Y.E. Makarov, and V.S. Novikov, 1991: Evaluation of measurements of particle size and sample area from optical array probes. *J. Atmos. Oceanic. Technol.*, **8**, 514-522.

Politovich, M.K., 1989: Aircraft icing caused by large supercooled droplets. *J. Appl. Meteor.*, **28**, 856-868.

Rasmussen, R.M., B.C. Bernstein, M. Murakami, G. Stossmeister, and J. Reisner, 1995: The 1990 Valentine's Day Arctic outbreak. Part 1: Mesoscale and microscale structure and evolution of a Colorado front range shallow upslope cloud. *J. Appl. Meteor.*, **34**, 1481-1511.

Sand, W.R., W.A. Cooper, M.K. Politovich, and D.L. Veal, 1984: Icing conditions encountered by a research aircraft. *J. Climate Appl. Meteor.*, **23**, 1427-1440.

Stewart, R.E., 1991: Canadian Atlantic Storms Program: Progress and plans of the meteorological component. *Bull. Amer. Meteor. Soc.*, **72**, 364-371.

A SEMI-ANALYTICAL MODEL OF GLOBALLY AVERAGED ATMOSPHERIC RESPONSE TO ENHANCED GREENHOUSE WARMING WITH CLOUDS

Krzysztof Szilder, Edward P. Lozowski and Gerhard W. Reuter

Department of Earth and Atmospheric Sciences, University of Alberta
Edmonton, Alberta, T6G 2E3, Canada

1. INTRODUCTION

Clouds are very important to the sensitivity of the climate system, since they affect both short- and longwave radiation. While much has been learned in recent years about the relative significance of these effects for different cloud types, the magnitude and even the sign of global cloud feedback are uncertain (Arking, 1991). Cloud feedback therefore remains one of the major uncertainties in climate sensitivity studies. It is the purpose of this paper to shed some light on cloud and precipitation effects in the global climate system by using a box model with a simple hydrological cycle, which includes evaporation, condensation and precipitation.

Climate models range in complexity from simple energy balance models to coupled ocean-atmosphere models. Often simple climate models are used to develop hypotheses, while GCMs are used to verify them and work out the details. Szilder *et al.*, (1996) have shown that it is possible to develop some insight into cloud effects using a low-order climate model. In this paper, we describe an improved version of the model and examine the role of enhanced greenhouse forcing in changing the present climate and altering the global hydrological cycle.

2. THE MODEL DESCRIPTION

The model consists of two elements or boxes: the atmosphere and the underlying surface, Figure 1. We do not explicitly consider the vertical or lateral extent of these elements, so that the model may be thought of as zero-dimensional, representing global mean and vertically integrated conditions. The details of the model have been described by Szilder and Lozowski (1995).

The first law of thermodynamics for the atmosphere is:

$$C_A\frac{dT_A}{dt} = (1-\alpha_A)aS + (1-\alpha_A)(1-a)\alpha_S a S + H_S(T_S-T_A) + m_C L + \epsilon\sigma T_S^4 - 2\epsilon\sigma T_A^4 + \Delta F \quad (1)$$

Similarly, for the surface:

$$C_S\frac{dT_S}{dt} = (1-\alpha_A)(1-a)(1-\alpha_S)S - H_S(T_S-T_A) - m_E L - \sigma T_S^4 + \tfrac{4}{3}\epsilon\sigma T_A^4 \quad (2)$$

where: a is the atmospheric shortwave absorptivity, C is the heat capacity per unit area, H_S is the sensible heat transfer coefficient, L is the specific latent heat of vaporization, m_C is the cloud condensation flux, m_E is the global surface evaporation flux, S is the global and annual mean top of the atmosphere insolation, T is temperature, α is albedo, ΔF is the net longwave enhanced greenhouse forcing, and ϵ is the atmospheric longwave emissivity. The subscripts A and S refer to the atmosphere and surface, respectively.

The mass continuity equation for cloud liquid water is:

$$\frac{p_O}{g}\frac{dq_L}{dt} = m_C - m_P \quad (3)$$

where: p_O is the atmospheric pressure, g is the acceleration of gravity, q_L is the cloud liquid water mixing ratio, and m_P is the global precipitation flux.

To simulate cloud feedback, we specify the atmospheric albedo and atmospheric emissivity as functions of the departure of the cloud liquid water mixing ratio from its present mean value:

$$\alpha_A = \alpha_{AO} + \Delta\alpha_A \tanh\left[\frac{D_A}{\Delta\alpha_A}(q_L - q_{LO})\right]$$
$$\epsilon = \epsilon_O + \Delta\epsilon \tanh\left[\frac{D_L}{\Delta\epsilon}(q_L - q_{LO})\right] \quad (4)$$

where: D_A is the cloud albedo feedback sensitivity parameter (kg g^{-1}), D_L is the cloud emissivity feedback sensitivity parameter (kg g^{-1}), and $\Delta\alpha_A$ and $\Delta\epsilon$ are the ranges of atmospheric albedo and atmospheric emissivity due to cloud feedback, respectively. The subscripts O refers to the present global annual mean conditions. The snow-ice albedo and water vapor feedbacks are also simulated.

The values of the model parameters have been derived for global, annual mean present-day conditions using the global, annual mean energy fluxes given by Ramanathan et al. (1989) and estimates of the present hydrological cycle reservoirs and fluxes. The surface heat capacity corresponds to an ocean mixed layer of depth 70 m.

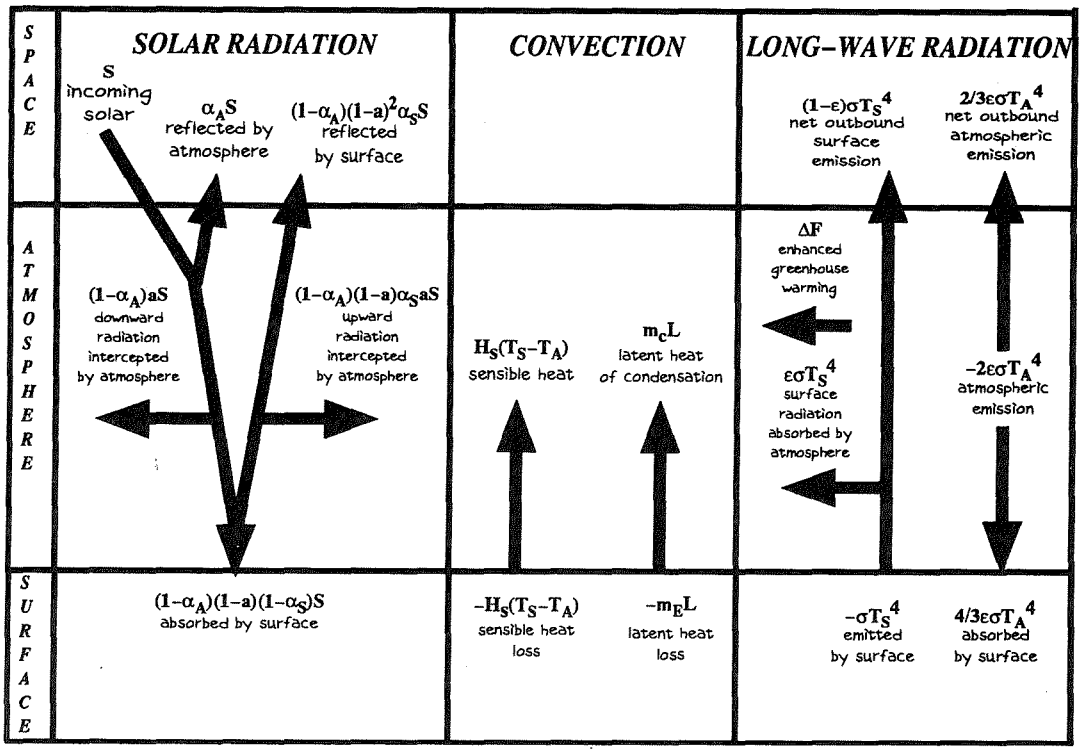

Fig. 1. Mathematical formulation of the global mean energy fluxes exchanged between space, atmosphere and surface by solar radiation, convection and longwave radiation.

3. MODEL RESULTS AND DISCUSSION

3.1 Present climate system

We begin by ignoring enhanced greenhouse forcing setting $\Delta F=0$. We then determine the climate equilibria predicted by the model and examine their stability. For the present equilibrium, the regions of stability and instability are functions of the cloud albedo feedback parameter, D_A, and the cloud emissivity feedback parameter, D_L. Over much of this stable domain, the cloud albedo feedback parameter equals or exceeds the cloud emissivity feedback parameter. We have found additional equilibria with temperatures either colder or warmer than in the present equilibrium. If the cloud albedo and cloud emissivity feedback parameters are sufficiently large five equilibria are possible: stable, unstable, present stable, unstable and stable, in order of increasing surface temperature. While the unstable equilibria are of little physical consequence, the possibility of three stable equilibria, resulting from cloud feedback, is intriguing.

3.2 Influence of enhanced greenhouse warming

Although the model predicts that the climate system has three stable equilibria if the cloud feedback is sufficiently strong, it is not obvious whether these states are attainable. Consequently, we examine whether enhanced greenhouse forcing might promote a transition between climate equilibria.

When the radiative properties of the atmosphere do not change with cloud liquid water content (i.e. $D_L = D_A = 0$ so there is no cloud feedback), an increase in ΔF leads to a gradual increase of the surface temperature and precipitation. However, with increasing cloud feedback strength, two additional equilibria arise, one stable and one unstable. These equilibria are characterized by higher temperatures, increased precipitation and increased cloud liquid water mixing ratio. More solar radiation is absorbed in and reflected by the atmosphere, more terrestrial radiation is trapped in the atmosphere-surface system, and there is enhanced cooling of the surface by latent and sensible heat transfers.

For a particular strength of the cloud feedback, there is a critical value of enhanced greenhouse forcing, ΔF_C, which controls the nature and number of equilibria. When $\Delta F < \Delta F_C$, only a single stable equilibrium exists. When $\Delta F > \Delta F_C$, there are three equilibria; one of them being unstable. A gradual increase in ΔF from zero, leads initially to a moderate increase of temperature and precipitation. This may be followed by an abrupt transition when $\Delta F = \Delta F_C$ to a significantly warmer and wetter equilibrium. Paradoxically, the model predicts that when the initial response to ΔF is small, the subsequent climate transition is more catastrophic. **Strong negative cloud feedback can diminish the thermal and hydrological consequences of enhanced longwave forcing, but only within a limited range.**

Figure 2 shows the influence of cloud feedback strength on the change in equilibrium precipitation in response to an enhanced longwave forcing of 4 Wm^{-2}. Only the region

where the present equilibrium is stable has been examined. Two domains can be distinguished: a modified present equilibrium where the precipitation increases by about 10% or less; and a new, warmer and wetter equilibrium where the precipitation increase exceeds about 40%. **The model suggests that the strengths of the two opposing cloud feedbacks do not have to be large but only similar in magnitude, for the transition to this warmer and wetter equilibrium to occur.**

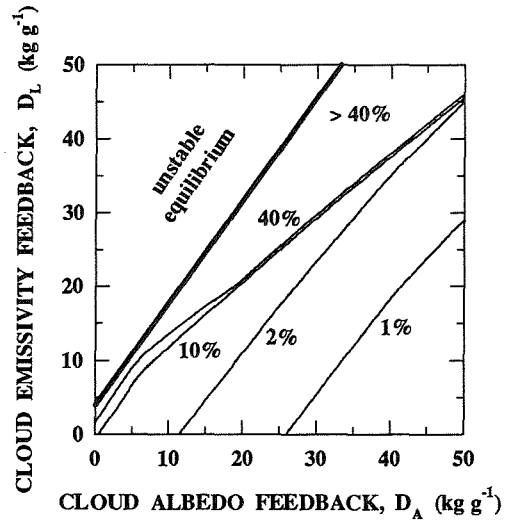

Fig. 2. Contours of the relative increase of precipitation as a function of the cloud albedo feedback and cloud emissivity feedback parameters for an enhanced longwave forcing, ΔF, of 4 Wm^{-2}.

4. CONCLUSIONS

We have examined cloud feedback in a zero-dimensional climate model which includes the atmospheric component of the hydrological cycle. The model indicates the possibility of a warmer stable climate with increased precipitation, and a colder stable climate with reduced precipitation, in addition to the present climate. The model also shows that a critical enhanced greenhouse longwave forcing may lead to an abrupt transition to a warmer and wetter climate with greater cloudiness. For such a transition to occur, the strengths of the cloud albedo and emissivity feedbacks do not need to be large, only similar in magnitude. Values of the cloud feedback parameters within the range of current estimates, can give rise to a catastrophic climate transition in the model, with a value of ΔF of only 4 Wm^{-2} (corresponding approximately to current estimates of a $2\times CO_2$ scenario). Further model development and comparison with GCM simulations will be required to confirm or reject this hypothesis.

ACKNOWLEDGMENTS

The authors would like to thank the Natural Sciences and Engineering Research Council and Environment Canada for financial support.

REFERENCES

Arking, A. 1991: The radiative effects of clouds and their impact on climate, *Bull. Amer. Meteor. Soc.* **72**, 795-813.

Ramanathan, V., Barkstrom, B. R. and Harrison, E. F. 1989: Climate and the earth's radiation budget, *Physics Today*, **42, 5**, 22-32.

Szilder, K. and Lozowski, E. P. 1995: Cloud feedback examined using a two-component time-dependent climate model, *Contributions to Atmospheric Physics*, **68**, 43-57.

Szilder, K., Sado, K. and Lozowski, E. P. 1996: Climate stability in a simple climate model with the hydrological cycle. *J Japan Soc Hydrology Water Resources*, **9**, 68-76.

Microphysical response of summer convective clouds in West Texas to AgI "dynamic" seeding

Daniel Rosenfeld(1) and William L. Woodley(2)

[1]Institute of Earth Sciences, The Hebrew University of Jerusalem, Jerusalem 91904, Israel
[2]Woodley Weather Consultants, 11 White Fir Court, Littlton Colorado 80127, USA

1. INTRODUCTION

Testing of dynamic cold-cloud seeding concepts for the enhancement of rainfall has been conducted in west Texas on an intermittent, as-funds-permitted basis since the summer of 1986.

The value of the Texas rainfall results lies not so much in the apparent large rainfall increases, but in the insights that they have provided, which are now manifested in the revised dynamic-seeding conceptual model that is discussed by Rosenfeld and Woodley (1993). These results have provided added understanding of the physical processes that are likely operative in west Texas clouds and they have underscored the importance of continuing this Texas Experiment in Augmenting Rainfall through Cloud-Seeding (TEXARC).

The focus of the TEXARC 1994 and 1995 research was on the first few steps in the revised dynamic seeding conceptual model that involve seeding-induced glaciation followed by the formation and rapid growth of graupel particles which are sustained aloft by the invigorated seeded updraft (Rosenfeld and Woodley, 1993). Initial findings and impressions are presented here.

Aircraft and radar were used in the effort. The cloud physics aircraft were the T-28 of the South Dakota School of Mines and Technology in 1994 and the Piper Cheyenne of Weather Modification, Inc. in 1995. Temperature (Reverse-Flow and/or Rosemount), dew point, updraft (Ball variometer), cloud water (King hot wire), GPS position, and particle sizes (PMS FSSP and 2D-C) were measured. Seeding was accomplished from a Cessna 340 in 1994 and from the Cheyenne in 1995.

The research plan was to document the physical processes in vigorous supercooled cloud towers before and after randomized treatment. In 1994, the T-28 cloud physics aircraft made a pass through the subject tower immediately prior to its treatment from the Cessna 340 and made repetitive passes through the tower afterwards. In 1995, the Cheyenne made measurements during the treatment run and thereafter.

Presented are three pairs of experimental units of seeded and unseeded clouds, in the corresponding types of convective clouds. The cases are selected to best illustrate our impressions from the two years study.

2. MODERATE COLD BASE CLOUDS

Seeding cold based clouds (i.e., clouds without supercooled rain) caused very slow glaciation, which appeared as many small equidimensional graupel that grew slowly, with little impact on cloud water within the first 5 minutes. The graupel diameter did not exceed 2 mm before the collapse of the cloud top. Most seeded clouds without supercooled rain started to collapse BEFORE significant glaciation occured. In many clouds glaciation progressed during their collapse, and was associated with accelerated dissipation, leaving holes in the cloud field. In the rare cases that the cloud did not collapse by 6 to 10 minutes (time for significant glaciation) no large graupel formed, probably due to the competition among hydrometeors or fallout from cloud top.

This was the case on August 22, 1996. Cloud base temperature was 12°C, and cloud tops were capped at temperature warmer than -10°C (See Fig. 1). Cloud 22.2 received 14 AgI flares in the first three passes, at a temperature of -7°C. The cloud developed slowly many small graupel which did not deplete efficiently the cloud water even by 15 minutes after initial seeding. After 18 minutes the cloud collapsed and left a crater in the cloud field. This "cratering was typical to the behavior of other seeded clouds that developed slowly large concentrations of small ice, but did not grow after seeding.

The cloud that had the strongest updraft for the day, cloud 22.6, had an updraft of 15 ms^{-1} and KSLWC (King Supercooled Liquid Water Contents) of 2.1 gm^{-3} at the first penetration (see Fig. 2). It received 7 simulated flares, but collapsed quickly after that, with the cloud top descending to below the seeding level 6 minutes after initial penetration. The cloud never produced any ice or rain drops at the -7°C level.

3. VIGOROUS COLD BASE CLOUDS

In clouds with no supercooled rain, but with very vigorous updrafts which grew to 1 km or more above the seeding level (-10°C isotherm), larger graupel did grow among the kind of graupel described earlier. Such clouds occured on August 25, 1995, when cloud base temperature was 11°C.

Cloud 25.2 (see Fig. 3) was vigorous during first aircraft penetration when 7 flares were ejected. Cloud 25.2 showed one of the better apparent temporary

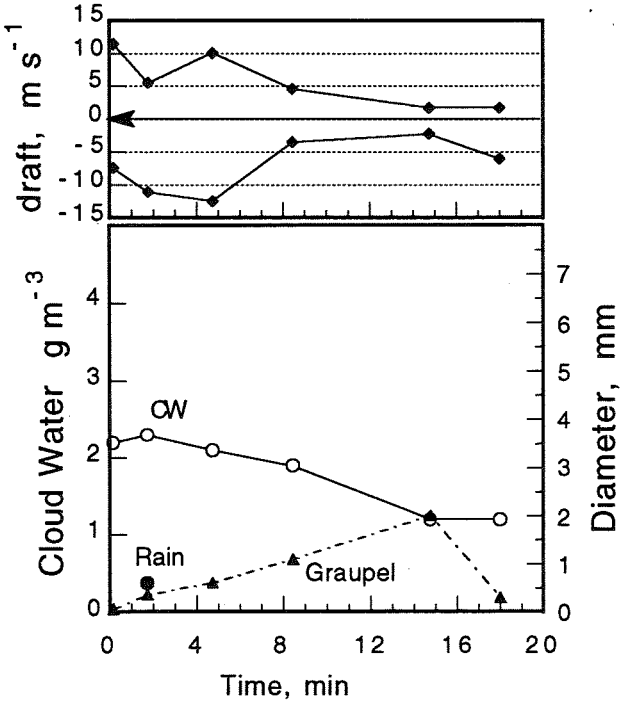

Fig. 1: The evolution of cloud properties at the seeding level, for the seeded cloud 22.2.
Plotted are the peak minimum and maximum vertical drafts, supercooled cloud water contents (CW), and peak diameters of the precipitation particles.

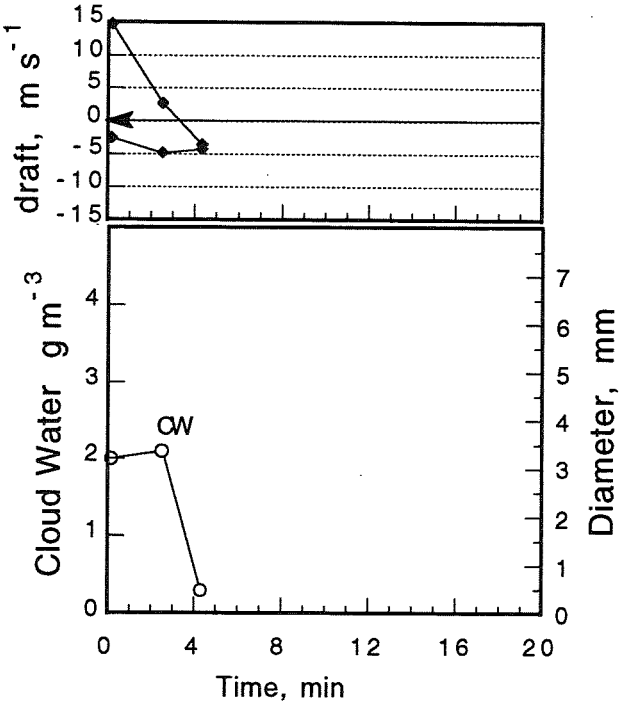

Fig. 2: The evolution of cloud properties at the seeding level, for unseeded cloud 22.6.

responses to seeding in TEXARC 1995. Five minutes after seeding, the cloud was growing hard with pileus draped on it. This coincided with the rapid development of ice particles and the depletion of the cloud water. With some graupel growing steadily to a maximum diameter of 4 mm by 11 minutes, most of

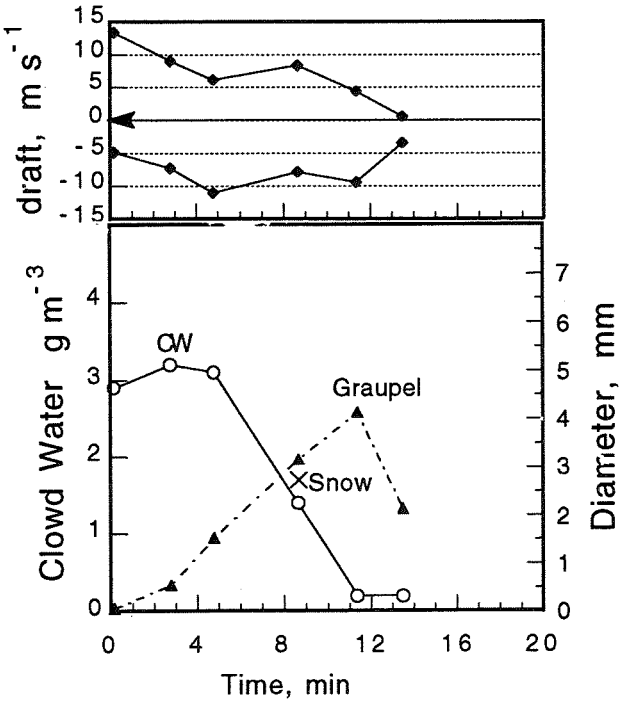

Fig. 3: The evolution of cloud properties at the seeding level, for the seeded cloud 25.2.

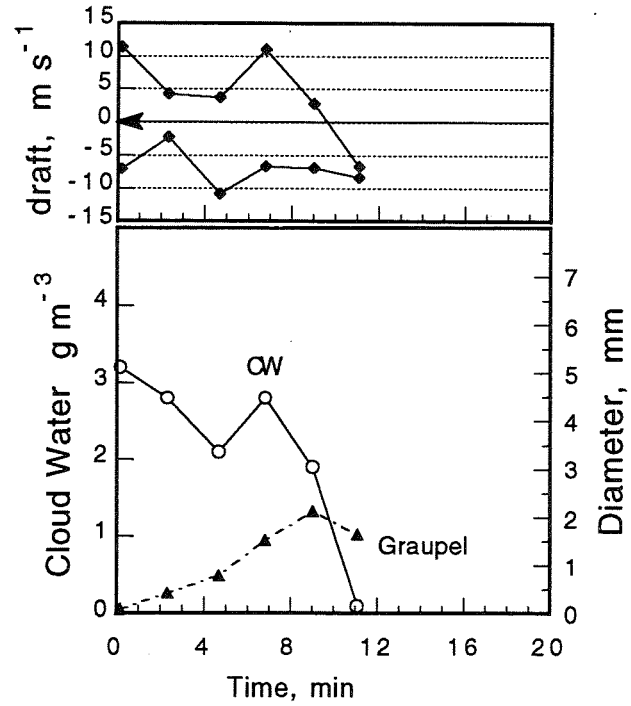

Fig. 4: The evolution of cloud properties at the seeding level, for unseeded cloud 25.1.

the ice was in particles < 1 mm. This sequence of events differed from its non-seeded predecessor. The entire cloud mass was looking glaciated and it had turned totally to ice by 11 minutes after initial treatment.

Cloud 25.1 (see Fig. 4) was larger initially, less isolated and more vigorous than cloud 25.2 had been. It received 10 simulated flares on initial penetration, in a strong updraft and high KSLWC. It grew

somewhat during the 10 minutes that it was monitored, but it had all but disappeared by the 6th and last pass. It had ample KSLWC right up to the time of its dissipation. Small graupel grew slowly mainly in the downdraft, and reached a maximal size of only 2 mm by 9 minutes.

4. WARM BASE CLOUDS

Clouds with bases warmer than about 15°C often produced supercooled rain at the

\-10°C level. Many of the natural clouds with supercooled rain collapsed with freezing of the supercooled rain drops only in the downdraft (see Cloud 31.17), or without ever freezing at all. In contrast, seeding such clouds (see Cloud 31.9) froze the rain drops still in the updraft within two to three minutes. According the 2DC probe, by 5 to 6 minutes after seeding most of the frozen rain drops were heavily rimed into very large graupel that kept growing very rapidly (to 5-8 mm), while rapidly depleting the cloud water. This was associated with invigoration of the updraft, that by this time would normally turn into downdraft in unseeded clouds. The cloud shortly thereafter totally glaciated with a mixture of small and large ice. The updraft continued with virtually no water at the -8 to -10°C level.

Cloud base temperature on August 31, 1996, was 16°C. Some of the clouds that formed in that day developed large supercooled rain drops at the -10°C level, and provided the best microphysical evidence obsrved yet for the seeding effects in such clouds.

Cloud 31.9 (see Fig. 5) was seeded near its top with 14 AgI flares. The cloud consisted of supercooled cloud water and large rain drops in the updraft. After its seeding, it was monitored on 7 passes. The cloud developed a fairly strong persistent updraft and eventually developed into a small glaciated Cb. The growth of the cloud was substantial to about 10 km, but it did not seem to be commensurate with the updraft. It is possible that much of the updraft was being used to support the large precipitation mass that formed in the cloud, especially large graupel.

The first pass into cloud 9 showed high KSLWC of 4.1 gm^{-3}, supercooled rain drops of up to 5 mm diameter, and a relatively weak updraft. There were no signs of glaciation except upon exit where some graupel was noted in a downdraft of about 8 ms^{-1}.

By the second pass, 2.5 minutes after seeding, there were signs of a seeding signature in the form of many small ice crystals. The small crystals existed with large graupels and frozen drops, presumably the result of the seeding. The updraft had increased considerably in the seeded region. The peak KSLWC had decreased to 3.4 gm^{-3}. Pockets of cloud unaffected by seeding still existed in the cloud. Most of the large drops had been frozen, however, and were starting to rime.

The third pass, 6 minutes after seeding, showed large concentrations of equi- dimensional graupels < 1 mm diameter (probably due to growth from initial small ice crystals), along with much larger (up to 8 mm) graupel particles (probably with cores of large frozen rain drops). The peak updraft was about 10 ms^{-1}. The peak KSLWC was reduced to 1.7 gm^{-3}.

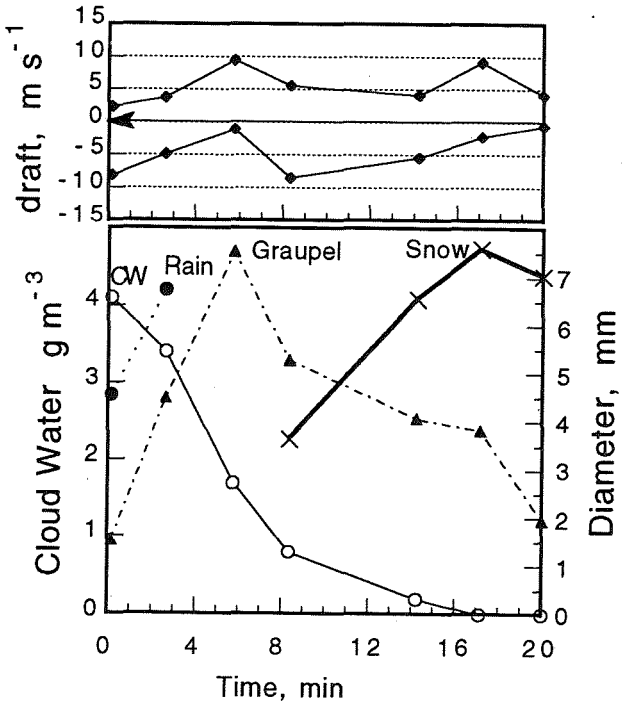

Fig. 5: The evolution of cloud properties at the seeding level, for the seeded cloud 31.9.

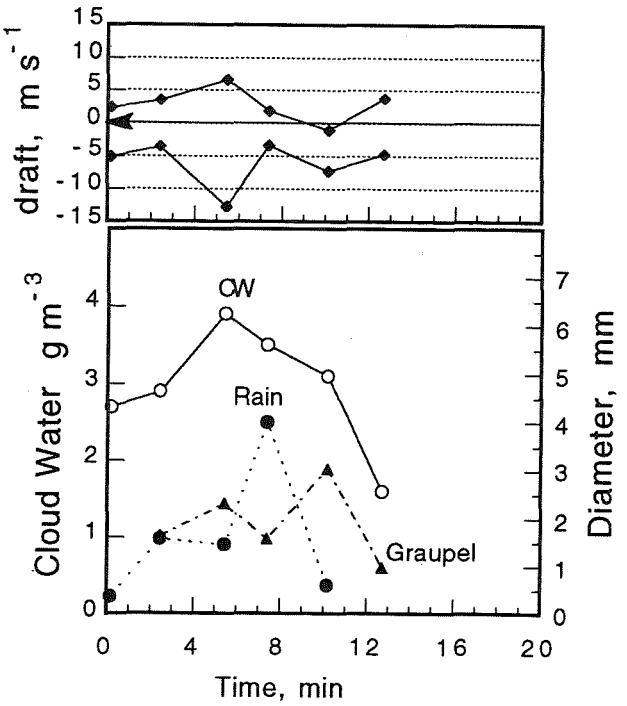

Fig. 6: The evolution of cloud properties at the seeding level, for unseeded cloud 31.17.

The fourth pass was at 9 minutes after seeding. It showed diminished KSLWC, an a wide region of updraft > 5 m s^{-1}, some rimmed particles, some aggregates and much small ice. Most of the ice particles existed in updraft. Very little cloud water was available for further rimming of the graupel particles. The updraft continued to be wide and strong in a totally glaciated cloud through the 7th pass (20 minutes after seeding). The graupel size decreased gradually, with some unrimed frozen drops evident. Snow flakes (up to 8 mm) were observed, mainly in downdraft portions of the cloud

Cloud 31.17 (see Fig. 6) had high KSLWC for nearly 10 minutes after the initial simulated seeding pass in which the ejection of 4 flares were simulated. Supercooled rain drops grew up to the size of 4 mm by 7 minutes after simulated seeding, and these drops had begun to freeze gradually in the downdrafts, but not experiencing much further growth because of their association with the downdraft.

By 10 minutes the cloud consisted of mostly small graupel in downdrafts and a few water drops. The cloud was dominated by downdraft as it collapsed while the larger hydrometeors were freezing. The peak KSLWC still had a value of about 3.0 gm^{-3}, which was remarkable considering the age of the cloud. The cloud top sank below the simulated seeding level by 13 minutes, when it still had 1.6 gm^{-3}, along with numerous small ice particles (max size of 1 mm).

5. SUMMARY

Nothing in the observations contradicted the revised dynamic seeding conceptual model of Rosenfeld and Woodley (1993). Furthermore, it was observed that:

1. Seeding of clouds without supercooled rain leads to:

a. Slow growth of graupel, at a rate that is too slow to convert cloud water into precipitatable size particles (several mm) during the lifetime of the updraft, except for the most vigorous and vertically developed clouds.
b. Slow glaciation and a lack of significant positive dynamic response.
c. Glaciation during the collapse of the cloud, which accelerated its dissipation, leaving holes in the cloud field.

It is suggested that these clouds glaciate too slowly to induce dynamic effects. The ice that develops in the downdraft does not reach large sizes, but accumulates in sufficient quantities to produce negative dynamic effects at the melting level.

2. Seeding of clouds with supercooled rain leads to:

a. Very fast freezing of the supercooled rain, and its continued growth as graupel.
b. Enhanced growth rate of the graupel as compared to supercooled rain drops, in accordance with the theoretical calculations of Sednev et al. (1996).
c. Fast seeding-induced glaciation within the active updraft, which increases cloud buoyancy and further invigorates the updraft, while the cloud is still in a position to use this to support the growth of large precipitation particles.

The preliminary conclusions suggest that freezing of supercooled rain drops before the rest of the cloud water leads to the formation of large graupel, whose growth is the fastest way to freeze cloud water. The respective fast release of latent heat occurs in the updraft, thus available for its further invigoration and for supporting the added precipitation loading. At the same time, it is also the microphysically most efficient process for conversion of cloud water into precipitation.

These results suggest also the importance of when and where the various microphysical processes take place within the cloud and when and where the seeding takes place that is intended to alter these processes. Both the Rosenfeld/Woodley conceptual model and these results suggest that, when seeding for rain enhancement, it is crucial to produce glaciation artificially within the vigorous supercooled updraft region of the cloud. It is in this region that large artificially-nucleated precipitation-sized particles can be grown most efficiently. Accomplishing this through seeding requires great care in the placement of the nucleant either in the updraft directly near cloud top or in the strong inflow region at cloud base in well-developed convective systems. Those engaged in such seeding would do well to keep this in mind when conducting their seeding operations.

ACKNOWLEDGEMENTS

This research was supported by the National Oceanic and Atmospheric Administration (NOAA) and the Texas Natural Resource Conservation Commission (TNRCC) through a cooperative agreement with the TNRCC, a participant in NOAA's Atmospheric Modification Program (Grant No. NA46RA0320).

REFERENCES

Rosenfeld D. and W. L. Woodley, 1993: Effects of cloud seeding in West Texas: additional results and new insights. Journal of Applied Meteorology. 32, 1848-1866.

Sednev I. L., M. B. Pinsky, A. P. Khain and D. Rosenfeld, 1996: The role of ice generation in precipitation formation as seen from the results obtained using a mixed-phase cloud model with spectral microphysics. Proceedings, 12th International Conference on Clouds and Precipitation, Zurich.

HIGH EFFICIENCY AEROSOL GENERATORS FOR CLOUD PHYSICS RESEARCHES

Anatoly V. Savchenko,[1] Vladimir V. Smirnov,[1] Michail B. Anipko,[1]
Valentin S. Kayro,[1] Sergey M. Kontush,[2] Leonid M. Makalsky[3]

[1]Institute of Experimental Meteorology, 82 Lenin st., Obninsk, Russia.
[2]Odessa State University, The Peter Great st., Odessa, Ukraine.
[3]Moscow Energy Institute, 7 Krasnokazarmennaya st., Moscow, Russia.

Compact but enough effective generators of different modelling aerosol ensembles, atmospheric aerosols and condensation nuclei, smoke, mists and fogs, sandy and droplet clouds, drizzle and precipitation particles are needing for cloud experiments in large chambers. Existing at the market similar laboratory equipment is not sufficiently productive, and equipment designed for industrial purposes often appeared to be ineffective.

This report discusses the peculiarities and examples of different aerosols generators using in cloud chambers with 100 and 3200 cub. m. volume in Institute of Experimental Meteorology.

1. The liquid drops, fogs, mists and smoke generators.

1.1. Small droplet aerosol generator. It generates quasi monodisperse water solutions droplets with mean mass diameter 1-2 mcm and relative dispersion 0.2-0.3. The action principle is two stages pneumatic dispergation of liquid. The first step consist of from 1 to 10 Collison type dispergators in united corps, the second step is system with contrary orifice (Fig. 1).

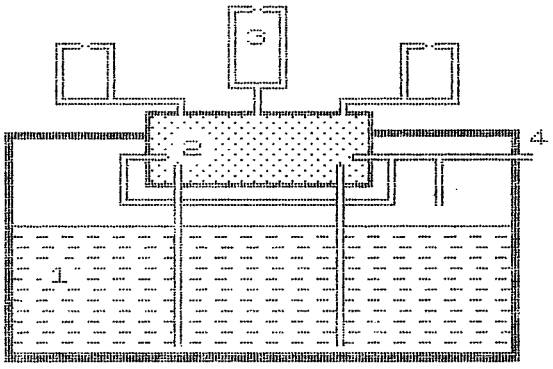

Fig. 1. Small droplet aerosol generator.
1. Reservoir with liquid.
2. First step sprayer.
3. Second step sprayer.
4. Compressed air magistral.

At compressed air superfluous pressure in range from 1 to 5 atm water droplet mass flow may vary from 0.1 to 0.5 kg/min., and compressed air volume flow varies in range 0.45...0.55 cub. m/min. The small droplet mist formation time is about 30 min in 3200 cub. meter volume chamber at initial relative humidity 40%. The generator described was used for industrial mists modelling, and for testing of evaporation cooling and humidifying system.

1.2. The charge large droplet aerosol

generator. It consists crucial pneumatic orifice 6mm diameter with coronazing needle type charger (Basiev 1982). Mean Zauter droplet diameter varies in range D=5...12 mcm, dispersion is 0.5-1 when air pressure varies from 2.2 to 0.5 atm.

Mean droplet mass flow is about 0.1 - 0.2 Kg/min, charge current in 3200 cub. m. chamber is 10 mcA. The generator above mentioned was used for heap clouds electrization and charged droplets jets modelling and also for fog dissipation stimulation.

1.3. The charged small droplets aerosol generator. It is designed for generating of unipolarly charged or neutral droplets condensed out of water, diesel or transformator oils. It is a high pressure (5-10 atm) electric power boiler with droplets outlet about 0.1 Kg/ min. Outlet supersound (1.7 mm in diameter) orifice is provided by aeroion generator (needle - cylinder) (Fig. 2). Charge current approached 80 mcA when needle potential was 9 KV and pressure 7.5 atm. The generator was used for preparing a stable high - charged aerosol jets and atmosphere electrodeless discharges modelling (Smirnov 1992).

1.4. The charged oil aerosol thermocondensation generator. It was used for preparing of charged monodisperse drops from high boiling oil products (diesel fuel, transformator oil, etc.). The oilproduct was sprayed and entirely evaporated in air jet, heated to 380-580K by means of Kerosene combustion. The vapor condensation to 0.1-0.2 mcm diameter small droplets occurred at 0.1 sq. cm. cross section orifice outlet. Flow velocity was 250-300 m/sec, air mass flow 0.24 Kg/sec or 0.2 cub. m/sec, diesel fuel mass flow 0.15 Kg/sec. Unipolar corona system of 7 needles at 18 KV negative potential located in condensation zone and consumed electric current about 200 mcA and charged aerosol outlet current achived 20 mcA.

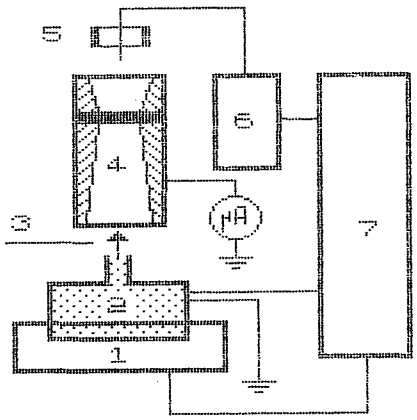

Fig. 2. The charge small droplet aerosol generator.

1. Electric heater.
2. Steam bowl.
3. Steam.
4. Orifice.
5. Corona charger "needle--cylinder" type.
6. High voltage supply.
7. Control unit.

2. The condensation nuclei generators.

Generator construction is analogues to the small droplets aerosol generator (1.1). Generator sprays quasi monodisperse small 1-2 mcm diameter droplets of hygroscopic ionogenic and non-ionogenic substances in water and other solutions. After droplet evaporation condensation nuclei mean diameter varies in range 0.01-1 mcm relative to the solution concentration. Generator productivity achieves 100-1000 g/hr of dried condensation nuclei.

3. Drizzle and precipitation particles generators.

This vibration type generator produces large droplets 20-400mcm diameter (Fig. 3). Its output for described above droplets size varies from 1 to 10 l/hr.

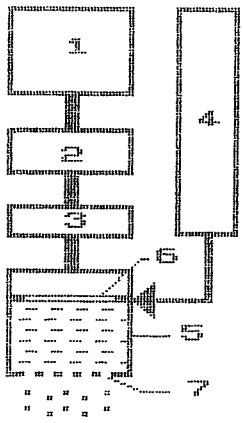

Fig. 3. Drizzle and precipitation particle generator.
1. Reservoir with liquid.
2. Coarse-cleaning filter.
3. Fine-cleaning filter.
4. Exitating generator.
5. Sprayer.
6. Vibrating membrane.
7. Multi orifise diafragm.

The operation principle of this multi-jet generator is based on breaking liquid through calibrated hole membrane under air superfluous pressure 50-120 Pa (Kontush 1990). Simultaneously iquid is disturbed by resonance frequencies 30-60 kHz. Forming droplets have dimensions d =2d , where d is the diameter of membrane calibrated hole (d = 10-100 mcm).

The generator may be used for:
- drizzle and precipitation simulation;
- liquid precipitation optical detectors calibrating.

4. The hollow spheres (bubbles) generator.

It generates bubbles from water solution of surface-active substances at compressed air superfluous pressure 1 atm. Bubbles size reach 0.1-5 cm in diameter. This device consists from foam generator and dispergator. For different types of dispergators the hollow spheres generator productivity may vary from 1-10 to 100 g/sec of foam and about 1000 bubbles per sec. Device may be used for studies of interactions with droplets in warm clouds.

5. Dust and salt aerosol generators.

This generator was designed for dust and salt transfer modelling during dusty storms in desert regions. Generator produces dust and salt mixture aerosol 0.01-10 mcm diameter in 100 cub. m. volume. The output of this generator, based on boilyng layer method, reaches about 1 Kg/min, dispergated particles diameter about 10 mcm, mass concentration of dust and salt air suspension reaches about 1 g/cub.m.

6. Warm clouds and fogs generators.

For modelling warm fogs and clouds was used steam generating set on base of 2 stationary steam bowls. Maximum steam pressure in steam generating set is 8 Kg/sq. cm, output - 2 tn/hr at steam temperature 150 C.

This set permits to model or modify chemical composition of cloud condensation nuclei by adding chemical solutions from separate vessel 2 cub. m. volume.

Dense steam fog (visibility 2-3 m) forms in 3200 cub. m. experimental chamber during 2-3 min after genera-

tor starting. Fog existence time in chamber depends on amount of steam feeding and initial air humidity. Maximum fog existence time achieves 1.5-2 hours. Water content of steam fogs may achieve 10 g/cub. m. The mean droplet diameter in fogs with such water content achieves 25-30 mcm.

REFERENCES

Kontush, S.M., and V.V. Smirnov, 1990: Methods and devices for monodisperse aerosol generation. Proceedings Institute of Experimental Meteorology 11(132), 3-19(In Russian).

Basiev, T.S., Vereshagin I.P., Makalskyi L.M., et.al.; 1982: Charged aerosol generators. Izv. AN SSSR. Energetics and transport, 5, 118-127 (In Russian).

Smirnov, V.V., 1992: Ionization in troposphere. St.-Peterbourg. Hydrometeoizdat, 312pp. (In Russian).

INVESTIGATION OF INTERACTION BETWEEN DROPLET AND DUST-SALT CLOUDS

D.A. Gillette[1], G.S. Golitsyn[2], I.G. Granberg[2], A.A. Pronin[3], A.B. Savchenko[3] and V.V. Smirnov[3]

[1] ARS/ARL, NOAA, Research Triangle Park, NC 27711; USA
[2] Institute Atmospheric Physics, 3 Pyzhevsky str, Moscow, 109017, Russia.
[3] Institute Experimental Meteorology, 82 Lenin str, Obninsk, 249020, Russia.

1. INTRODUCTION

Results of field experiments, provided by the authors in Tadjikistan salina (September 1989), Kara-Kalpak playa (summer 1991), Kalmyk salina (summer 1995) and at the drying bottom of large pools, such as Aral Sea (May 1992) and Owens Lake at East California (March 1993) show, that during wind erosion of similar soils are formed specific dust-salt clouds (Golitsyn et al., 1993; Cahill et al., 1994; Smirnov et al., 1994; Gill et al., 1995). By USA and Russian satellite data it is observed the dust clouds having many thousands km^2 in surface on removals 2-3 thousand km from a dust source (see, for example, Gillette et al.,1992; Smirnov et al., 1994).

Specific of these clouds lays, in-first, in very high dust dispersity, secondly, in certain toxicity because of the high content of alkali and some metals (arsenic and other), in- third, in high hygroscopic and condensation activity of dust particles, in-fourth, in higher ability to absorb solar radiation, in- fifth, in comparatively low value of wind speed, at which a sole erosion and wind rising of a dust are occurred. And, at last, the certain influence to the dust cloud stability renders an electrical charges on sand and salt particles (Smirnov 1995).

These features are explained by structure of soil after drying of pools and peculiar conditions of wind rising. In given work the accent is made on natural and laboratory study of main factors of interaction of sand and salt dust and water droplet clouds.

2. ELEMENTAL AND MINERAL COMPOSITION

For the majority of dust generating regions a elemental structure of soil is similar. About 40 % of mass are silicon in a kind the alpha-quartz, calcium in a form calcite and aluminum in a form metallosilicates. For a dust sample from dried mountain pools, for example, the lakes Owens Lake and Mono are characterize the high contents strontium, arsenic, magnum and other (Cahill et al.,1994) as well as elements, which are present in next mountain files.

Mineral composition of soil determine a particular dust in considerably more detail and more reliable than elemental structure (Smirnov 1993). For first judgments about the ecological and geophysical importance of a particular dust it is enough to consider a parity of main mineral groups (see Table)

TABLE. Comparative contents (in % from common weight of sample) main minerals in dust clouds from sand desert and from two drying large pools. The samples were analyzed by x-ray diffractometer.

SITE	THE MAIN MINERALS			
	SILICATES	QUARTZ	CALCITE	CHLORATES
Aral Sea soil	25	35	23	2
Owens Lake dust	35	34	18	1
Owens Lake crust	28	15	45	2
Global desert dust	27	55	12	1,5

Chlorates: $NaCl + NaClO_3 + MgCl_2$;
Calcite - $CaCO_3$; ; Quartz - α - SiO_3;
Silicates: anortite $CaAl_2Si_2O_8$, microcline $KAlSi_3O_8$, akermanite $Ca_2MgSi_2O_7$, enstatite $MgSiO_3$

At the analysis of the Table pays attention the surprising low contents the chlorate salts and that in dust aerosols, emitted from the Owens Lake dry bed, about 50% makes calcite. It and other alkali determine high condensation activity of salt dust. In comparison high concentration

clay-forming metallosilicates (25-35 %), permit to predict good disperse and hygroscopic ability, as well as ability to absorb light radiation, at least better, than sand dust.

3. SIZE DISTRIBUTION OF DUST

Fig. 1 illustrates characteristic accumulated functions of aerosol size distribution in sand storm at the drying bottom Aral Sea (5) and in dust-salt storm on the Owens Lake dry bed at strong (4) and moderate (3) surface wind. For comparisons are indicate also average cumulative spectra of atmospheric aerosols in polar (Western Arctic, Franz-Joseph Archipelago, March 1994) and continental (Obninsk, May 1994) boundary layer of atmosphere. For measurements was used portable electrostatic analyzer DAES-2, described Savchenko et al., 1994 (size interval is D= 0.005μm up to 1.0μm on 12- size gradation, volumetric speed of aerosols is 250 cm^3/s, linear speed is 10m/s, weight 8 kgs). In a interval D=0.5-10μm was used photoelectric counter Royco Inc., model 218.

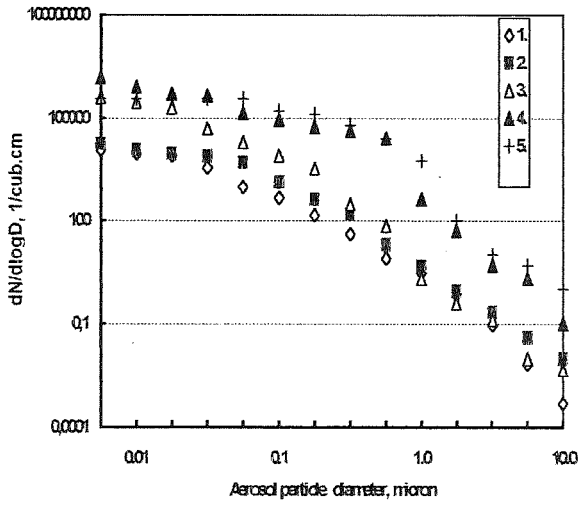

Fig. 1. Averaged cumulative size spectra of the atmospheric aerosols for a boundary layers of various regions.
1-Arctic, Franz -Joseph Archipelago, spring 1994;
2- Russia, Obninsk, May 1994;
3-California, Owens valley, 5 km from dust source, wind speed 5-7 m/ s, noon, March 1993;
4- the same, but wind speed 10-12 m/s, dust storm, 22 March 1993;
5- Aral Sea dry bed, 40 km from a new shore, wind speed 10-11 m/s, noon, dust storm, 30 May 1992;

As can see from Fig. 1, appropriate dust clouds were characterized by a increasing of concentration all dust particles, but especially submicron particles (D = 0.1-1μm). The concentration of all particle sizes (D > 0.005 μm) reached the order 10^6 $1/cm^3$. More than 98 % of all particles had the sizes less than 0.1μm.

Prevailing electrical charges at small particles are negative. Coarse particles (D=1-20 μm) transported predominantly a positive charges.

4. FOG AND CLOUD INITIATION

Wind rising and vertical diffusion involve dust particles in main cloud processes - condensation and coagulation. The conversion of dust particle to cloud droplet occurs in two stages: wetting and condensation growth in a field of supersaturation. The wetting stage watering can, as will be shown below, to be finished by formation rather dense mist.

Idea of experiences in the chamber volume 3200 m^3 are consisted in dispersion the natural or model sand and/or salt particles. Initial diameter of particles at H=40% was within the limits of D = 0.05 - 0.15 μm, the concentration in 3-4 times exceeded background. Further adiabatic cooling of dusty air gradually increase relative humidity H.

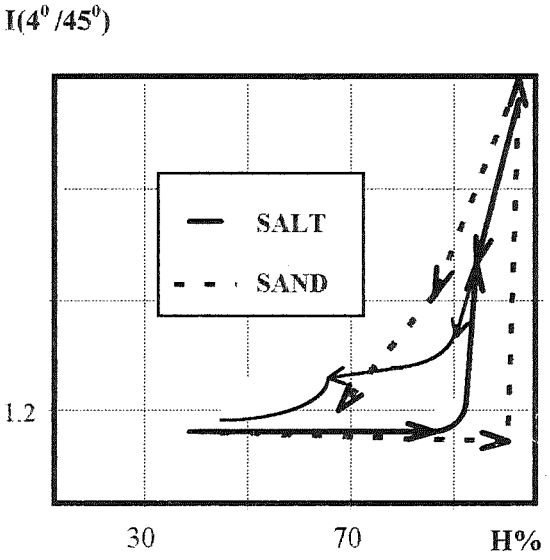

Fig. 2. Intensity of light-scattering of salt and sand condensation nuclei $I(4^0/45^0)$ vs. air relative humidity H%. The arrows show on a direction of process: condensation or evaporation. Initial size spectra see Fig. 3, run t=0.

As it is visible from Fig. 2, where are indicated by dynamics of aerosol light scattering in a right direction ($\theta = 4 \pm 1^0$, normalized on a signal for $\theta = 4 \pm 1^0$, the increase of humidity above 70 % stimulate the appreciable growth of the salt particles. So, at H=90 % the increasing has made 300%.

The stationary size distribution for wetted particles is shown on Fig. 3. We shall notice, that practically the adequate modeling of salt dust condensation processes is reached by using sodium chloride and/or carbamide nuclei.

Sand particles begin to wet only after achievement of humidity H=85 %, but the light scattering H >90% have appeared closest to salt particles curve. We shall remind, that in a sand dust always enter as impurity metallosilicates. Please attention also, that the hysteresis of light scattering I (4^0/ 45^0) is inherent not only salt, but also to sand nucleuses. The upper fact justifies the forecast stated higher about a capillarity of dust particles and their ability to adsorb the water vapor.

5. CLOUD STABILIZATION

As well as in the previous experience, a salt particles were entered into a chamber 3200 m^3 after dispersing of salt-water solution (Fig. 2).

The accounting concentration could vary in limits from 50 up to 5000 $1/cm^3$. The initial relative humidity was at level of 90-95 %, therefore in the chamber are formed the steady chemical mist.

The visibility has decreased with 1000-2000 m to 300-500 m. On Fig. 3 a example of record for time t=0 the size spectrum after the introduction of carbamide particles $(NH_2)_2 CO$ is indicated. The average diameter of dry nucleuses was within the limits of 0.2 - 0.5 μm.

Fog was formed by adiabatic expansion of air with initial pressure 1.3 ata, temperature 293 K, equivalent speed of air rising u_z =10-20 cm/s. As it is visible, in lognormal spectrum in the size area D = 6-8μm is well allocated mode. The disposition this mode did not practically depend on the initial size of nucleuses and their concentration Z, if $Z < 10^3$ $1/cm^3$.

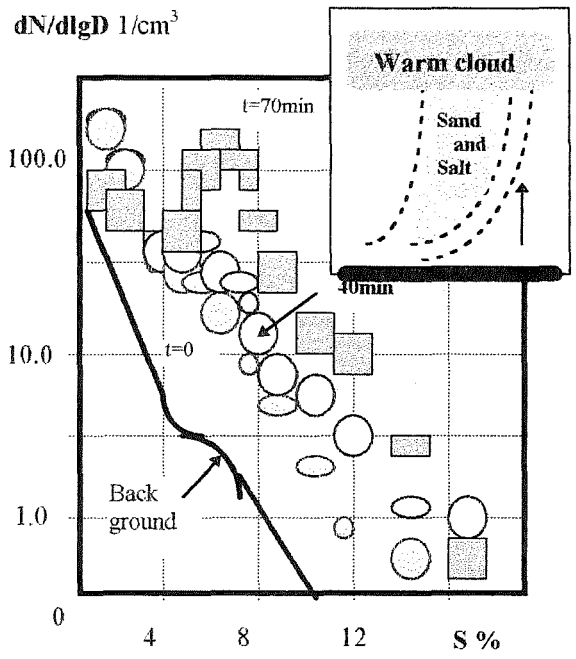

Fig. 3. Size droplet spectra evolution of adiabatic growing cloud after salt nuclei ejection.
The initial air temperature 23 ± 3° C, relative humidity 93 ± 3%, equivalent velocity of air elevation u_z = 40 ± 5 cm/s. For a salt and dust generation equipment see Savchenko et al.,1996.

It is important, that at a further increasing of nuclei concentration up to Z <1500 $1/cm^3$ known effect of the underseeding by hygroscopic nucleuses was observed. Then the size spectrum are transformed in the mist-similar and rather extended.

For planning of the future experiments one moment is interesting yet. I has appeared, that the introduction in adiabatic fog the small-sized dust particles or dust-salt mixes did not change the previous conclusion only in two cases:

- if within the cloud chamber there were natural condensation nucleuses. The kind of a background size spectrum is given on Fig. 3.
- if the equivalent speed adiabatic expansion of normal air exceeded u_z >20 cm/s.

Reason of observed weak dependence of concentration of large cloud droplet (D > 12-15 μm) from initial concentration giant salt nucleuses (D > 1-2 μm) requires also added consideration.

Thus, on the basis of submitted experimental data it is possible to judge that dust and especially salt products of a soil erosion can, being involved in cloud or fog environment, actively to modify them disperse and chemical structure.

REFERENCES

Cahill T.A., T.E. Gill., D.A. Gillette, E.A. Gearhart, J.S. Reid., and Mee-Ling Yau,1994: Generation, Characterization and Transport of Owens (Dry) Lake Dusts. *Report to CARB by Crocker Nuclear Laboratory. Univ. of California at Davis,* 166p

Gill T.E., V.V. Smirnov, T.A. Cavil, and A.V. Savchenko. 1995: Dust aerosols from the Aral Sea and Owens (Dry) Lake: Comparable geo physical aspects of desertification. *Abstract of AGU 1995 Fall Meeting, Trans. American Geophysical Union, Suppl. to EOS,* Nov.7, A12-8, F76.

Gillette D.A., G.S. Golitsyn, D. MacKinnon, and V. Smirnov. 1992: Satellite observation of interaction between droplet and dust clouds in Central Asia. *Proceed. 11-Th. Intern. Conf. on Clouds and Precipitation. Montreal, 17-21 Aug. 1992.* Elsevier Sci. Publ., 1156-1158,

Golitsyn G.S. (editor), 1993: *Soviet-American experiment on arid aerosols.* St.- Petersburg, Hydrometeoizdat, 220p.

Savchenko A.V., V.V. Smirnov, A.A. Pronin., and M.B. Anipko, 1994: A Portable Station for Monitoring Atmospheric Aerosols. Pro ceed. Intern. Conf. on Aerosols and Atmos pheric Optics: Radiation Balance and Visual Air Quality. 26-30 Sept. 1994, Snowbird, Utah, USA,. Air & Waste Management As soc., Pittsburgh, vol. A, 897- 904.

Savchenko, A. V. , V. V. Smirnov, M. B. Anipko, V. S. Kayro, S. M. Kontush, L. M. Makalsky, 1996: High efficiency aerosol generator for cloud physics research. See given book.

Smirnov, V.V. ,1993: Morphological, structural and chemical peculiarities of dust storm aerosol in Tadjikistan. *Joint Soviet - American Experiment on Arid Aerosol: Tadjikistan, USSR, Sept.1989 (edit. by G. S. Golitsyn),* Hydrometeoizdat, St. Peters burg, 127-134

Smirnov V.V., D.A. Gillette, and L. Gomes, 1994: Atmospheric aerosol in the surrounding of large dried pools. *Proceed. of the 1994 Euro pean Aerosol Conference. May 30 - June2,* Blois, France, p.23,

Smirnov, V.V., D.A. Gillette, G.S. Golitsyn, and D.J. MacKinnon, 1994: The origin and evolu tion of dust clouds in the Central Asia. *Atmos pheric Research,* vol. 34, 169-176.

Smirnov, V. , 1995: Electric field variation in space in the vicinity of dust clouds produced by erosion of Owens Dry Lake, Ca. *abstract of AGU 1995 Fall Meeting, Trans. American Geoph. Union, Suppl. to Eos,* Nov.7, A12-9, F76.

INVESTIGATION OF THE RELATIVE ROLE OF DIFFERENT ICE CRYSTAL FORMATION MECHANISMS IN CONVECTIVE CLOUDS USING A MODEL WITH DETAILED MICROPHYSICS

Zev Levin, Tamir Reisin and Shalva Tzivion
Raymond and Beverly Sackler, Faculty of Exact Sciences
Department of Geophysics and Planetary Sciences
Tel Aviv University, Ramat Aviv 69978, Israel.

1. INTRODUCTION

In their recent paper, Reisin et al. (1996) showed that the contribution of ice crystal formation to the total amount of rain from convective clouds is relatively low. The only clouds in which ice played a more dominant role were those with extremely high drop concentrations (~1000 cm^{-3}).

The reason for this result is that the ice concentrations are so low compared to that of the cloud drops, that their effect on the growth of the precipitation is small. Precipitation development is therefore, mostly affected by the growth due to collision-coalescence of drops. Fig. 1, taken from Reisin et al (1996b), shows that changing the ice crystal concentrations by more than three orders of magnitude hardly changes the total rainfall from a deep convective cloud with cloud base at 4^0C and tops at -20^0C.

The purpose of this paper is to evaluate the role of the three different ice forming mechanisms used in the model in order to better understand the reasons for the lack of dependence of total rainfall on ice crystal concentrations. In doing this, we also tested the effects of the clouds' vertical dimensions and temperature profiles on the development of ice and its effects on precipitation.

2. THE CLOUD MODEL

The cloud model of Reisin et al (1996a) was used for this purpose. The model is axisymmetric non-hydrostatic with detailed description of the microphysical processes. The model uses the multi-moment method (Tzivion et al., 1987) for calculating all the microphysical processes and it contains full size spectra of drops (36 bins), ice crystals, graupel particles and snow.

In the model, ice is created by a number of mechanisms. Crystals can be formed by nucleation through deposition and condensation freezing. Both of these depend on temperature and supersaturation and are formulated based on Meyers et al. (1992):

$$N_{id} = \exp(-0.639 + 0.1296\, S_i)$$

where N_{id} is the number of ice crystals per liter that can be nucleated at supersaturation S_i with respect to ice (in %).

Ice crystals can also be formed by contact between aerosols and supercooled drops due to thermophoretic and diffusiophoretic effects as well as due to brownian motion. We used a formulation based on Cotton et al. (1986) and Meyers et al. (1992):

$$N_{ic} = \exp[-2.8 + 0.262\,(T_0 - T)]$$

where N_{ic} is the number of crystals that are formed by contact nucleation at temperature T. T_0 is set at 0^0C.

The last process that enhances ice crystal concentrations is the Hallett-Mossop ice multiplication mechanism. This mechanism is not fully understood but it was shown that drops larger than 24.8 μm need to be present before collisions between them and graupel particles can produce splinters. It was also demonstrated that this mechanisms is effective within the temperature range of -4^0C to -8^0C. In our model the dependence on size was taken from Mossop (1978) and the dependence on temperature was taken from Cotton et al. (1986).

3. RESULTS

Three different types of clouds were tested:

1) Deep convective clouds with cloud base at 4^0C and cloud top at -20^0C. Using the same dynamics as that used by Reisin et al (1996) we modified the cloud microstructure by testing three different initial CCN spectra: a) maritime, M, (100 CCN cm^{-3} active at 1% supersaturation), b) continental (600 CCN cm^{-3}), CM, and c) extreme continental (1000 CCN cm^{-3}), CE.

2) A deep convective cloud (named CMB) having warmer cloud base and hence having a larger fraction of the cloud in the liquid phase. Cloud base was set at 15^0C and cloud top at -15^0C.

3) A shallower convective cloud (named CMS) with cloud base at 4^0C and cloud top at -12^0C.

Table 1 presents the results from the different runs. We see that the total amount of rain decreases sharply as one goes from maritime, M (10.2 x 10^4 m^3) to moderate continental, CM (3.0 x 10^4 m^3) to extreme continental, CE (1.5 x 10^4 m^3). The time to initiate rain is relatively rapid in M (30 min) and is delayed in the CE (49 min). The reason for this is clearly the slow growth of the precipitation particles in the CE cloud.

Note that the maximum concentration of ice crystals in these clouds is achieved after the initiation of the rain, namely after the drops reach large enough sizes.

This can also be seen in Figs. 2,3 and 4 in which the cumulative maximum concentrations of ice crystals produced by each of the three mechanisms at the specific time is shown for M, CM and CE clouds, respectively. We see that the rate of ice formation by deposition and condensation freezing is the first to operate and the total number produced is slowly increasing until about 26, 40 and 30 min in M, CM and CE, respectively. This result seem reasonable since the deposition and condensation freezing is temperature and supersaturation dependent processes. As the cloud develops, it reaches lower temperatures and so that more ice is nucleated.

Case	M	CM	CE	CMS	CMB
Max. updraft [m s^{-1}]	14.9	14.6	14.2	9.1	20.3
Time [min]	28	32	32	44	20
Location (r,z) [km]	0, 3	0, 3	0, 3	0, 2.7	0, 4.2
Max. LWC [g kg^{-1}]	3.8	3.9	3.8	3.0	5.9
Time [min]	24	32	32	44	24
Location (r, z) [km]	0, 3.9	0, 4.2	0, 4.2	0, 3.3	0, 5.7
Max. Ice Cont. [g kg^{-1}]	0.5	0.8	1.0	0.7	0.9
Time [min]	EOS	EOS	72	EOS	EOS
Location (r, z) [km]	0, 3.3	0, 3.3	0, 3.3	0, 2.7	0, 4.2
Max. Garupel Cont. [g kg^{-1}]	5.0	1.9	1.2	0.5	4.9
Time [min]	36	48	52	60	32
Location (r, z) [km]	.75,2.4	.45,2.4	0.6, 2.7	0, 2.4	1.05, 3.6
Max. Ice Conc. [L^{-1}]	27	43	26.3	63.9	45.6
Time [min]	40	48	52	64	36
Location (r, z) [km]	0, 3.6	0, 2.4	0, 2.4	0, 2.4	0.75, 3.9
Ice Conc. [L^{-1}] at -10C at time of max. updraft	4.7	4.3	4.4	4.5	2.8
Max. Graupel Conc. [L^{-1}]	0.7	1.2	1	0.8	0.7
Time [min]	32	48	56	72	44
Location (r,z) [km]	1.65, 3	.6, 1.8	.45, 1.5	0, 1.8	0.9, 3.6
Max. rate of production of ice crys. by Depos. & Conden. Freez. [L^{-1} s^{-1}]	0.2	0.11	0.1	0.04	0.25
Time [min]	40	32	32	44	24
Location (r,z) [km]	.15,3.3	.15,3.9	.15, 3.6	.15,2.7	0.16, 6.6
Max. rate of production of Ice cryst. by Contact [L^{-1} s^{-1}]	0.03	0.05	0.06	0.01	1.0
Time [min]	36	20	20	28	20
Location (r,z) [km]	.75, 3	.3, 2.7	.45, 2.1	.15,2.1	0.45, 4.5
Max. Production rate of ice cryst. by Ice multip. [L^{-1} s^{-1}]	0.3	0.4	0.15	0.23	0.5
Time [min]	32	44	48	60	32
Location (r,z) [km]	.9, 2.4	.6, 2.4	0.6, 2.4	.3, 2.4	0.9, 3.6
Rain Initiation [min]	30	40	49	53	30.5
Rain Duration [min]	31	26.5	21.5	20	26.5
Total Rain [10^4 m^3]	10.2	3	1.5	0.4	9.8

Table 1. Results of all simulated clouds. EOS stands for End of Simulation.

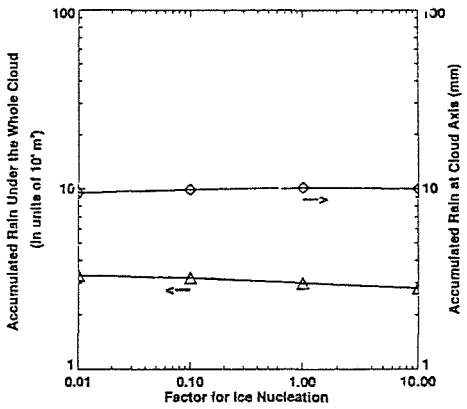

Fig. 1: Accumulated rain under the whole cloud (triangles, left axis) and accumulated rain at cloud (diamonds, right axis) as a function of the factor that multiplies normal ice crystal concentrations calculated in the model for a CM cloud (taken from Reisin et al, 1996).

Production of ice by contact becomes effective a little later but in most cases remains below the production by deposition and condensation-freezing. Since contact is most effective near the edges of the clouds (evaporation) and when the drops are larger, it is clear why this mechanism starts later.

Ice multiplication starts much later but at a rapid rate. It reaches significant numbers, however, only after rain has already formed. It should be noted that the figures represent the accumulated number of crystals produced and do not include the losses of crystals to the formation of snow flakes or to graupel production. This is the reason the numbers in the figures are larger than those shown in Table 1.

The results from the two other clouds (CMB and CMS) are also presented in Table 1. We see that the smaller cloud, CMS, produces considerably less rain than all the other clouds tested. On the other hand, the total amount of rain from the deep cloud, CMB, resembles the maritime cloud. This is in spite of the fact that many of the other features are quite different. For example, the CCN is 600 in CMB as compared to 100 in M. The updraft is about 30% larger in CMB and it is reached about 8 min earlier. LWC is higher due to the larger fraction of the cloud at the warmer region, leading to more moisture and subsequently more cloud water.

Generally similar results of ice crystal production as a function of time are obtained when CMB and CMS

are used. In both cases the maximum number of ice crystals produced reach values of a few per liter after rain is initiated. In the deep cloud, CMB, ice multiplication becomes significant after about 26 min, since large drops formed in the deeper warm sector of the cloud. Once they reach the -5°C region, large drops in relatively high concentrations are already present. After about 30 min the production of ice crystals by ice multiplication surpasses the production by the other mechanisms. In the smaller cloud, CMS, ice multiplication is delayed until about 50 min and surpasses the other mechanisms only after 60 min, well beyond the time of rain formation.

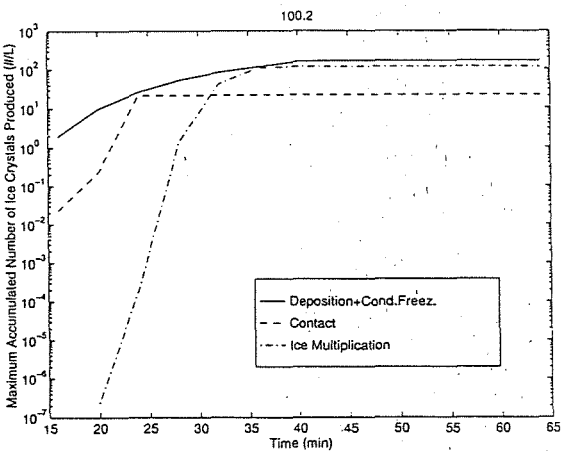

Fig. 2: Maximum accumulated ice crystals produced by the three production processes in the maritime cloud, M.

Production of ice in the different clouds depends on the temperature, supersaturation and on the size of the drops in them. Clouds that produce large drops rapidly, will form more ice by contact. If the large drops appear at the right temperatures for ice multiplication to occur, the rate of ice production will increase. We find that in all the clouds tested, the maximum ice production by ice multiplication varied between about 0.15 to 0.5 crystals per second. The lowest values appear in the CE, because of the slow drop growth in it. The maximum production of ice appears in the deep cloud with the warmest cloud base. In it, the growth of the drops is rapid, but more importantly, they reach the right size at the -5°C level so that ice multiplication becomes effective while the cloud is still growing. In all the clouds tested, except the CMB, ice production by ice multiplication occurs very late in the lifetime of the precipitation development.

By comparison to the other mechanisms, ice production by contact nucleation is small (between 0.01 and 0.06 for all clouds) except in the deep cloud CMB in which the value reaches about 1.0 L^{-1} s^{-1}.

Since in all our tests ice appears in high concentrations after rain is initiated, it is no wonder that the contribution of ice to the total rain amount is relatively small.

The transfer of some of the liquid mass to the ice crystals, however, does change the distribution of rainfall on the ground. Under sheared environment, the presence and growth of ice crystals strongly affects the horizontal spread of the anvil, but it may have only secondary effect on the total rainfall amount.

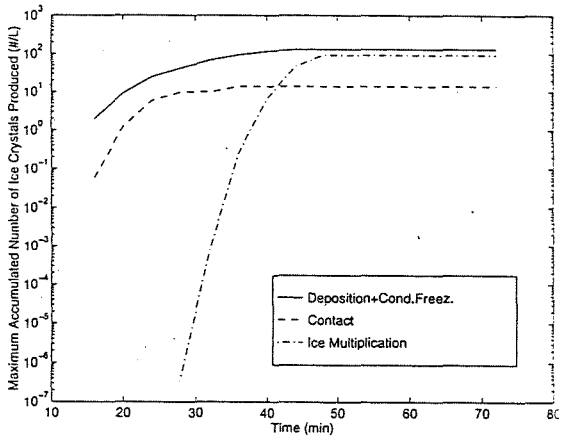

Fig. 3: Like Fig. 2 except for the continental cloud, CM.

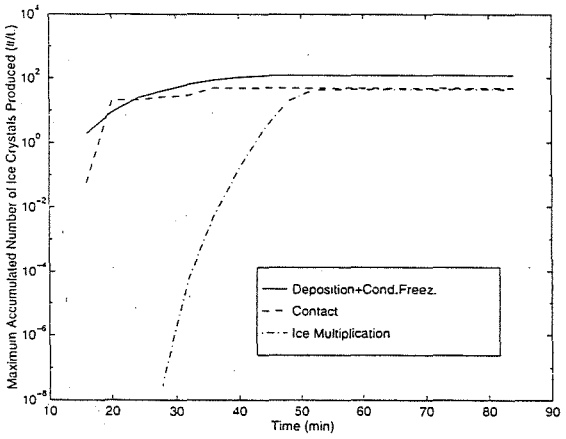

Fig. 4: Like Fig. 2 except for the extreme continental cloud, CE.

4. REFERENCES

Reisin, T., Z. Levin and S. Tzivion, 1996: Rain production in convective clouds as simulated in an axisymmetric model with detailed microphysics. Part II: Effects of varying drops and ice initiation. *J. Atmos. Sci.*, In Press.

Reisin, T., Z. Levin and S. Tzivion, 1996: Rain production in convective clouds as simulated in an axisymmetric model with detailed microphysics. Part I: Description of the model. *J. Atmos. Sci.*, In press.

Tzivion, S., G. Feingold and Z. Levin, 1987: An efficient numerical solution to the stochastic collection equation. *J. Atmos. Sci.*, **44**, 3139-3149.

Meyers, M. P., P. J. DeMott and W. R. Cotton, 1992: New primary ice-nucleation parameterizations in an explicit cloud model. *J. Appl. Meteor.*, **31**, 708-721.

Mossop, S. C., 1978: The influence of drop size distribution on the production of secondary ice particles during graupel growth. *Quart. J. Roy. Meteor. Soc.*, **118**, 105-126.

Cotton, W. R., G. J. Tripoli, R. M. Rauber and E. A. Mulvihill, 1986: Numerical simulation of the effects of varying ice crystal nucleation rates and aggregation processes on orographic snowfall. *J. Climate and Appl. Meteor.*, **25**, 1658-1680.

ESTIMATION OF CIRRUS MICROPHYSICAL PARAMETERS FROM MULTISPECTRAL MEASUREMENTS IN THE NEAR INFRARED

Stephan Bakan[1] and Claudio Costanzo[2]

[1] Max Planck-Institut für Meteorologie
[2] Department of Meteorology, Universität Hamburg
Bundesstraße 55, D–20146 Hamburg
Tel. +49 40 41173213, Fax +49 40 41173391
Email costanzo@dkrz.de

1. INTRODUCTION

The impact of cirrus clouds on climate is one of the major unresolved problems in climate research. The magnitude and the signature of the cirrus cloud feedback to climate are dependent upon the mean optical thickness and the microphysical properties of the cloud (Stephens, 1990). Existing remote sensing techniques do not provide accurate enough estimates of these parameters. However, a number of studies have indicated the potential to derive cloud parameters as optical thickness, particle size, phase, and possibly the particle habit, from spectral measurements of the cloud reflection in the near infrared (Hansen, 1970).

In the last years intensive field campaigns have been conducted to investigate cirrus physical properties (FIRE, ICE, EUCREX). During the European Cloud Radiation Experiment EUCREX'94 near Brest/France several missions have been flown above cirrus with the multispectral analyzer OVID (Bartsch, 1996) aboard the DLR-Falcon. These measurements in the solar and near infrared region between 0.6 and 1.6 μm shall be investigated in regard to the potential of estimating cirrus cloud parameters.

Section 2 discusses the data sources used in this investigation. Section 3 outlines the theoretical ideas to determine microphysical parameters, as well as the radiative transfer model used. Section 4 compares measured and simulated estimations of the cloud parameters optical depth and particle size. Section 5 summarizes the results and gives a short outlook.

2. MULTISPECTRAL MEASUREMENTS

Representative of the four cirrus flights during the EUCREX campaign we focus this study on 17 April. In the morning mission 204, two aircraft were flying on a straight line between two points at a distance of nearly 180 km, oriented perpendicular to the mean wind direction. The cloud was found between 8 and 10 km height. The german Falcon flew one leg above the cloud at an altitude of 11.5 km to measure the upward pointing radiances and subsequently three legs in the upper, middle and lower parts of the cloud field between 8 and 9.5 km to allow the PMS probes to document the microphysical properties. At the same time the french ARAT flew several legs below the cloud at an altitude of 4.5 km to measure the downwelling solar and infrared fluxes.

Figure 1 shows a satellite image of the investigated cloud field and the two points A and B limiting the chosen flight legs. From consecutive METEOSAT images cloud displacement vectors were derived to shift the cloud structures in the satellite image into the instant of aircraft overflight. In figure 1 this is represented by the two points C and D in the north east of the flight leg.

The Falcon was equipped with the Optical Visible and near Infrared Detector OVID, a "high" resolution multichannel spectral analyzer for remote sensing. In addition, the Falcon carried the multispectral imaging polarimeter POLDER (Brogniez, 1995) and the PMS cloud particle probes.

The OVID system consists of two separate, but almost identical detector units, covering the spectral ranges of 0.6 to 1.05 μm (VIS) and 1.0 to 1.65 μm (NIR). Figure 2 shows the schematic structure of one detection system of OVID together with a summary of the technical data.

A mirror telescope is focusing the incoming radiation to a bundle of fibre cables, which is connected to the spectrograph located at the front of the thermoelectrically cooled detector. In the near infrared a linear InGaAs detector array is used to measure simultaneously at 256 wavelengths at a spectral resolution of about 5.9 nm. The CCD array for the VIS part allows for 1024 spectral points measurements at a resolution of 1.7 nm. Typical exposure times of around 100 to 3000 ms were chosen, resulting in sample rates between 0.35 and 10 Hz. The spatial resolution 2000 m above the cloud is 12 m (9 m in VIS) perpendicular to the flight direction and 25 m (12 m in VIS) in parallel direction. The detector is operated by a controller, which is connected to a PC. Both telescopes are fixed on a mounting plate with parallel orientation looking downward through one of the aircraft bottom windows. Between the two telescopes a video camera was installed to observe the measuring conditions below the aircraft.

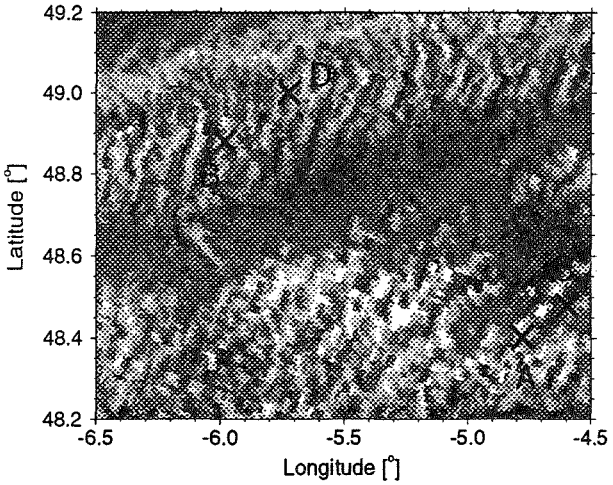

Fig. 1: Difference image of the two AVHRR IR-channels 4 and 5 at 08:46 UTC. The bright pixels correspond to ice clouds. The two points A and B bound the flight leg investigated in this analysis. Additionally plotted are the two points C and D of the real "cloud line" affecting the spectral measurements, estimated from cloud displacement vectors of consecutive METEOSAT IR-images.

The wavelength calibration is done with the aid of an argon spectral lamp. The intensity calibration is carried out by a uniform source sphere which is intercalibrated absolutely within ±5%. The calibration procedure includes a careful evaluation of all error sources.

3. RADIATION MODELLING

The single scattering behavior of an ensemble of particles is a function of the complex index of refraction, the distribution of particle sizes and the form of the particles (Hansen, 1970). In Figure 3 the spectral variation of the complex index of refraction is exhibited for liquid water and ice, respectively. The imaginary part, which is related to the absorption coefficient, increases between 1.0 and 1.6 μm by about 3 orders of magnitude. The maxima of ice and water are displaced by about 60 nm and the maximum of ice is obviously higher than that of liquid water. This different spectral gradient from ice and liquid water near 1.5 μm may be used to distinguish between the two phases.

The single scattering albedo of ice at 1.55 μm generally decreases monotonically with increasing particle size. This is understandable because the absorption increases with the path length

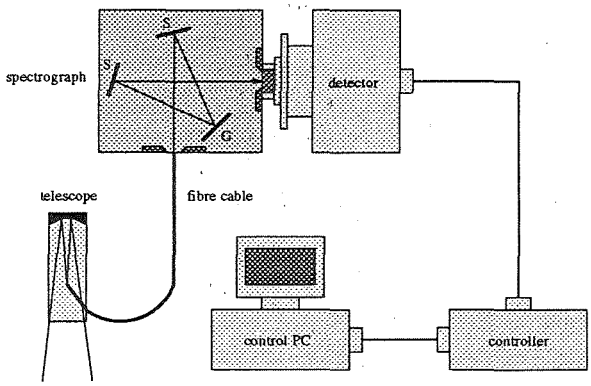

	VIS	nIR
used gratings	300 l/mm	120 l/mm
detector type	Si	InGaAs
number of pixels	1024 × 256	256 × 1
spectral range	0.60 - 1.05 μm	1.0 - 1.65 μm
spectral resolution	1.7 nm	5.9 nm
sample rate	2 - 25 Hz	0.35 - 10 Hz
telescope aperture	0.27°	0.34°

Fig. 2: Schematic structure of one detection system and summary of the technical data during the EUCREX campaign.

through the particle and consequently with the particle size. On the other side the shape of the particles determines the number of internal reflections and thus the single scattering albedo, too. The reflectivity at 1.55 μm of a cloud depends directly on the single scattering albedo and thus on a mixed parameter containing information about the particle size and shape.

In the atmospheric window at 1.05 μm the reflectance values are influenced only very weakly by Rayleigh scattering and ice or liquid water absorption in the cloud particles. Therefore this wavelength can be used to derive the optical thickness of the cloud.

Thus, radiative transfer simulations at the described wavelengths provide a theoretical data set for the comparison with OVID measurements to estimate cloud optical depths, particle shapes and sizes. The radiative transfer is calculated using the Matrix Operator Method in a version described by Fell (1994). The optical properties of cloud particles are obtained from ray tracing calculations with a code provided by Macke (1994). These calculations were performed for distorted and undistorted hexagonal columns and plates, hollow columns and random fractals for a set of 40 different particle sizes between 5 and 2000 μm. The aspect ratios of the particles have been selected from a parameterization by Heymsfield (1972).

Figure 4 shows the particle size spectra used. The spectra have been achieved in terms of simple relations between particle size and ambient temperature (Heymsfield, 1984). For the simulations discussed in the following section these spectra are represented by an effective particle radius, defined as the ratio of mean particle volume to mean particle cross-section.

4. RESULTS

In this preliminary study no further stress is laid upon the investigation of the particle habit. Therefore the optical properties of 25% distorted hexagonal columns have been chosen arbitrary for the calculations of the cloud radiative transfer.

Figure 5 shows the relation between the two radiances at 1.046 μm and 1.55 μm for all measuring points along the highest flight leg between 09:06 and 09:16 UTC. In addition, the figure shows the simulated radiances for different optical thicknesses and effective particle sizes. The figured radii correspond to particle size spectra of ambient temperatures between -37°C and -45°C shown in figure 4. The real temperatures found between 8 and 10 km height are of the order of -40°C to -53°C.

The measured radiances can be described by effective particle radii between 25 and 38 μm. As could be better seen in the results of another mission there seems to be a tendency to increasing particle size with increasing optical depth. This can be explained by aggregation of small

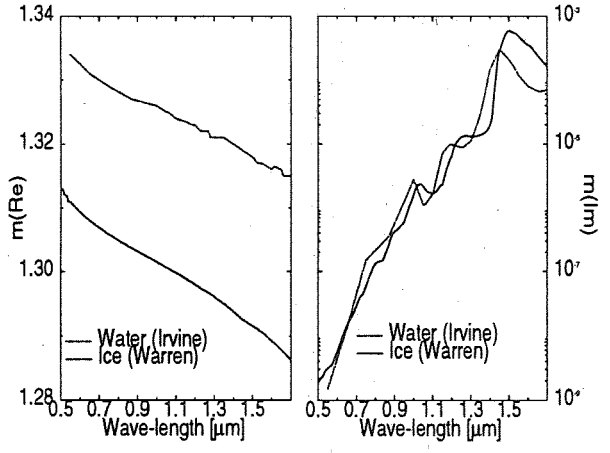

Fig. 3: Complex index of refraction for water and ice in the near infrared region of the OVID detector (Betancor 1996). The left side shows the real part and the right side the imaginary part.

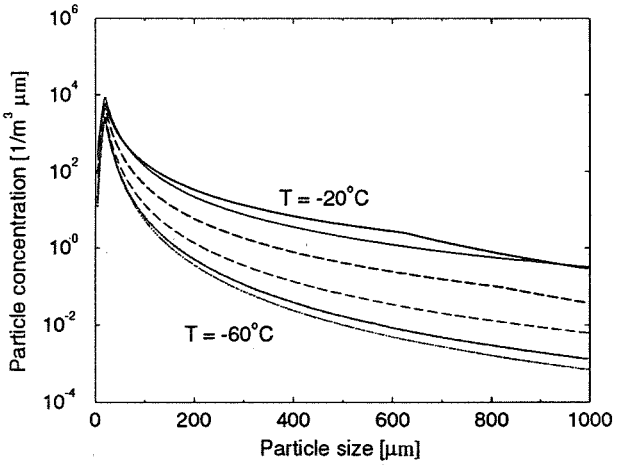

Fig. 4: Particle size distributions used in dependence on the ambient temperature from measurements by (Heymsfield 1984). The distributions are modified for small particles.

particles as well as a larger supply of water vapor in optically thick clouds.

5. CONCLUSIONS

The EUCREX 17 April 1994 data provide a good opportunity to compare measured and theoretical cloud properties for cirrus clouds. A first analysis of the spectral radiances in the near infrared region yields realistic results for the estimation of the particle size. Preliminary comparisons with the particle size distributions, derived from FSSP and PMS-2D in-situ measurements, agrees well with the parameterized distributions in figure 4, represented by an estimated effective radius between 25 and 38 μm.

On the other side there is a time shift of 10 to 20 minutes between OVID and in-situ measurements. This is equivalent to a cloud movement of 10 to 20 km. It has to analyzed carefully, in how far these time shifted measurements correspond to comparable cloud structures. AVHRR satellite images shall help to investigate the influence of this cloud movement.

Future simulations for other particle shapes will contribute to the interesting question in how far different particle habits may change the estimated particle sizes. Is it possible to define a characteristic shape composition in dependence on the ambient conditions to minimize the error in the size estimation?

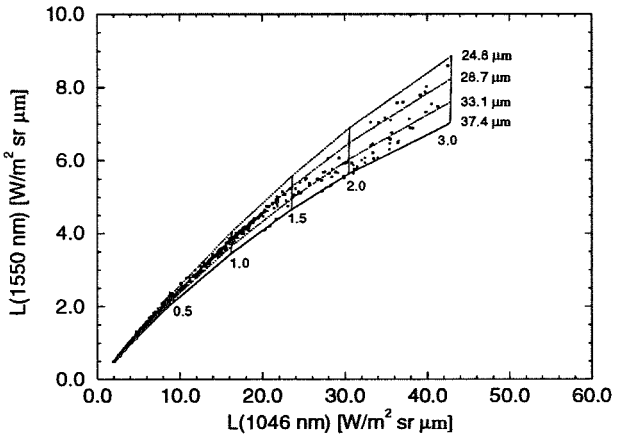

Fig. 5: Spectral radiances at 1046nm and 1550nm for the flight leg between 09:06 and 09:16. The points show the OVID measured radiances. The lines represent the simulated radiances for different effective particle sizes and optical depths.

The afternoon flight on the 17 April 1994 offers a good data source for the investigation of the thermodynamical phase. There are different areas along the flight leg with pure cirrus clouds, pure altocumulus clouds and mixed structures. However, the approach to use the spectral measurements between 1.43 and 1.5 μm to derive the phase is handicapped by the water vapor absorption in this spectral region.

Acknowledgments. We would like to thank Frank Albers for the preparation of the in-situ measurements of the EUCREX mission 204.

6. REFERENCES

Bartsch,B., 1996: Fernerkundung des Wasserdampfgehalts der Atmosphäre über Land aus rückgestreuter Sonnenstrahlung. *Ph.D. thesis, Universität Hamburg*, 111 pp.

Betancor, M., 1996: Fernerkundung von optisch dünnen Eiswolken im nahen Infraroten. *Ph.D. thesis, Universität Hamburg*, 111 pp.

Brogniez, G., H. Chepfer, Y. Fouquart, J.-F. Gayet, P. Flament, R. Valentin, J. Pelon, V. Trouillet, C. Flamant and F. Albers, 1995: Radiative properties of cirrus clouds observed during the EUropean Cloud Radiation EXperiment 94 in Brittany by active and passive remote sensing observations. *Conf. on Passive infrared remote sensing of clouds and the atmosphere III.*, Paris.

Hansen, J.E., and J.B. Pollack, 1970: Near-Infrared Light Scattering by Terrestrial Clouds. *J. Atmos. Sci.*, **27**, 265 – 281.

Fell, F., 1994: MOMO - The FU-Berlin Radiative Transfer Model based on the Matrix-Operator-Method. Model Description and User Manual. *MAST-II, Technical Progress Report of the European Comission*, MAS2-CT92-0020.

Heymsfield, A.J., 1972: Ice crystal terminal velocities. *J. Atmos. Sci.*, **29**, 1348 – 1357.

Heymsfield, A.J., and C.M.R. Platt, 1984: A Parameterization of the Particle Size Spectrum of Ice Clouds in Terms of the Ambient Temperature and the IWC. *J. Atmos. Sci.*, **41**, 846 – 855.

Macke, A., 1994: Modellierung der optischen Eigenschaften von Cirruswolken. *Ph.D. thesis, Universität Hamburg*, 98 pp.

Stephens, G.L., S. Tsay, P.W. Stackhouse, J. and P.J. Flateau, 1990: The relevance of the microphysical and radiative properties of cirrus clouds to climate and climatic feedback. *J. Atmos. Sci.*, **47**, 1742 – 1753.

Formation and Influence Of Precipitation-Sized Drops In Cumulus Clouds

John Latham
National Center for Atmospheric Research*
Boulder, CO 80301, USA
Alan M. Blyth, Paul R. Krehbiel and Rasmus E. Benestad†
New Mexico Tech, Socorro, NM 87801, USA

1 Introduction

Supercooled raindrops have been observed in New Mexico cumulus clouds during the summers of 1987 and 1993, and in Florida cumuli during the Small Cumulus Microphysics Study (SCMS) in 1995.

2 New Mexico Cumuli

Measurements were made of New Mexican summertime cumulus clouds with the NCAR King Air in 1987 (Blyth and Latham 1993). Most of the precipitation particles in New Mexico summertime cumulus clouds develop through the ice phase. However, supercooled raindrops were observed in a few clouds when the temperature of cloud base was 7°C or warmer and the cloud depth was greater than about 2.5 km.

Figure 1 shows the variation with time of the altitude of cloud top for the 10 August 1987 cloud. Cloud top height was determined using video observations from a forward-looking camera onboard the aircraft and is accurate to about 200 m. Cloud base height was slightly below 3 km MSL, corresponding to a temperature $T_{base} \approx 10°C$. The height of cloud top gradually ascended to about 5.5 km MSL ($T \approx$ -6°C) by 18:18. It then decreased to less than 4.0 km and increased to 5.5 km again at 19:10. Thereafter, cloud top continued to rise and was near 6.5 km ($T \approx$ -12°C) when the aircraft had to leave at 19:35. The times when supercooled raindrops were measured by the 1D and 2DC probes are indicated in the figure. The penetration levels were about 500 m below cloud top. Raindrops were measured in a single penetration at 18:18 by the 1D probe and later by the 2DC in several penetrations from 19:10 to 19:20. The depth of the cloud was about 2.5 km or greater when the raindrops were observed. The first 2D images of ice were not measured until 19:25. It is therefore likely that the drops formed by collision and coalescence.

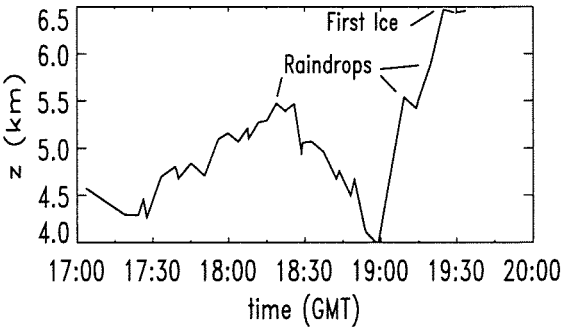

Figure 1. Altitude of cloud top on 10 August 1987. Values of cloud top height are uncertain between 18:50 and 19:05. The observation of raindrops at 18:18 was made with the 1D probe and between 19:10 and 19:20 with the 2DC. The time of first ice is also shown.

The temperature of cloud base was 7°C or warmer in the five New Mexican clouds studied in 1987 where there were either 2D images of supercooled raindrops or particles that we believe

*NCAR is supported by the National Science Foundation

†Current address, Dept. of Atmospheric, Oceanic and Planetary Physics, University of Oxford, England

to be supercooled raindrops detected by the 1D probe. Also drops were not detected until the cloud depth was about 2.5 km or greater in the three clouds where there was a good measure of cloud depth. In particular, raindrops were observed on separate occasions in the 10 August cloud when the cloud depth reached about 2.5 km.

Measurements were made on 24 August 1993 with the New Mexico Tech dual polarization radar (Krehbiel *et al.* 1996). The radar operates at a frequency of 9810 MHz (3.0 cm wavelength) with about 10 kW peak transmitted power. Alternate horizontal and vertical linear polarizations were transmitted for these observations. The presence of large liquid drops can be inferred from measurements of the differential reflectivity, defined as $Z_{DR} = 10\log(Z_H/Z_V)$, where Z_H and Z_V are the reflectivity factors measured with horizontally and vertically polarized radiation, respectively. The horizontal dimension of large, falling raindrops is greater than the vertical dimension and this results in positive values of Z_{DR}.

Figures 2 and 3 show a sequence of vertical scans through the center of a small cloud that developed about 12 km distant from the radar. Figure 2 shows the reflectivity values versus time and Figure 3 shows the differential reflectivity. The reflectivity scans show that two precipitation events occurred in the cloud. The first, less intense event began in the core of the cloud at 20:11 with the development of 15 dBZ reflectivity between 3 and 4.5 km altitude above ground level (4.5–6 km MSL; $T \approx 0 \rightarrow$ -10°C) (Figure 2b). The second precipitation event began at 20:14 at 5 km altitude AGL (6.5 km MSL, $T \approx$ -13 °C) on the upper right side of the storm (Figure 2e). Its echo intensified and spread more quickly than that of the initial precipitation event, increasing in intensity to 35 dBZ by 20:20 and becoming the dominant echo in the cloud.

The differential reflectivity results of Figure 3 show positive values for the first precipitation event but not for the second. For the first event Z_{DR} values were between 1 and 2 dB with the top of the enhanced Z_{DR} region extending up to 4.5 km AGL (6.0 km MSL, $T \approx$ -10°C) in the two scans shown in Figures 3b and 3c. By 20:13 (Figure 3d) the top of the enhanced Z_{DR} region had descended to about 3 km altitude AGL (4.5 km MSL), corresponding to the 0 °C level, where it stayed for the remainder of the observations.

In sharp contrast, the second more intense precipitation event did not produce positive Z_{DR} values. Rather, Z_{DR} tended to be zero or even slightly negative, which is typical of graupel or hail. The difference between the two events leaves little doubt that the initial precipitation, with its column of positive Z_{DR} values above the 0°C level, contained large supercooled raindrops. The fact that the echo grew in place (Figures 2b-d) suggests that the precipitation also grew in place, as a result of collision and coalescence with supercooled cloud drops.

3 Florida Cumuli

SCMS took place near Cocoa Beach, Florida from 17 July - 13 August, 1995. The majority of the observations were made in small cumuli with three aircraft and the CP2 radar of NCAR to try to understand the production of raindrops. However, we report here on observations made with CP2 of a larger cloud. Figures 4a and b show reflectivity and Z_{DR} at 18:14:32 and 18:17:07 GMT, 25 July, 1995. The 0°C level was between 4.5 and 5 km MSL. The dark regions in Figure 4a, between 22 and 26 km range near 6 km altitude represent values of Z_{DR} between about 2 and 4 dB. This indicates the presence of supercooled raindrops. The top of the region is lower in altitude at the later time (Figure 4b), especially at a range of about 26 km. Notice that this is a region of high reflectivity. It is likely therefore that some of the supercooled drops have frozen in the time between the scans.

4 Discussion

The results from the aircraft observations suggest the raindrops in New Mexico cumuli form when cloud bases are warmer than about 7°C and when the depth of the cloud increases to about 2.5 km. The results from the NM radar measurements are consistent with this latter finding.

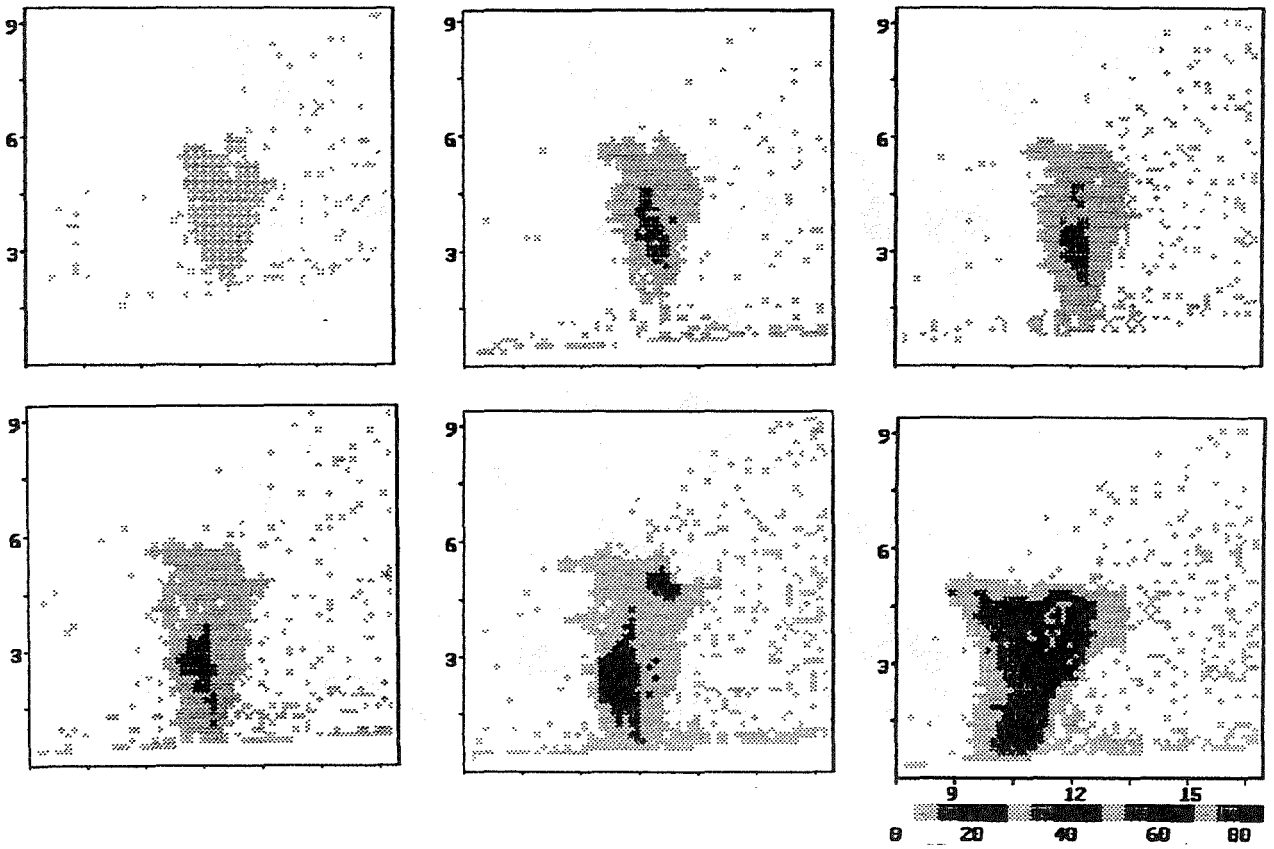

Figure 2. Reflectivity in dBZ measured with the New Mexico Tech radar on 24 August, 1993. The times (GMT) for each display are: a) 20:10:13; b) 20:11:24; c) 20:12:08; d) 20:13:04; e) 20:14:17; f) 20:20:04

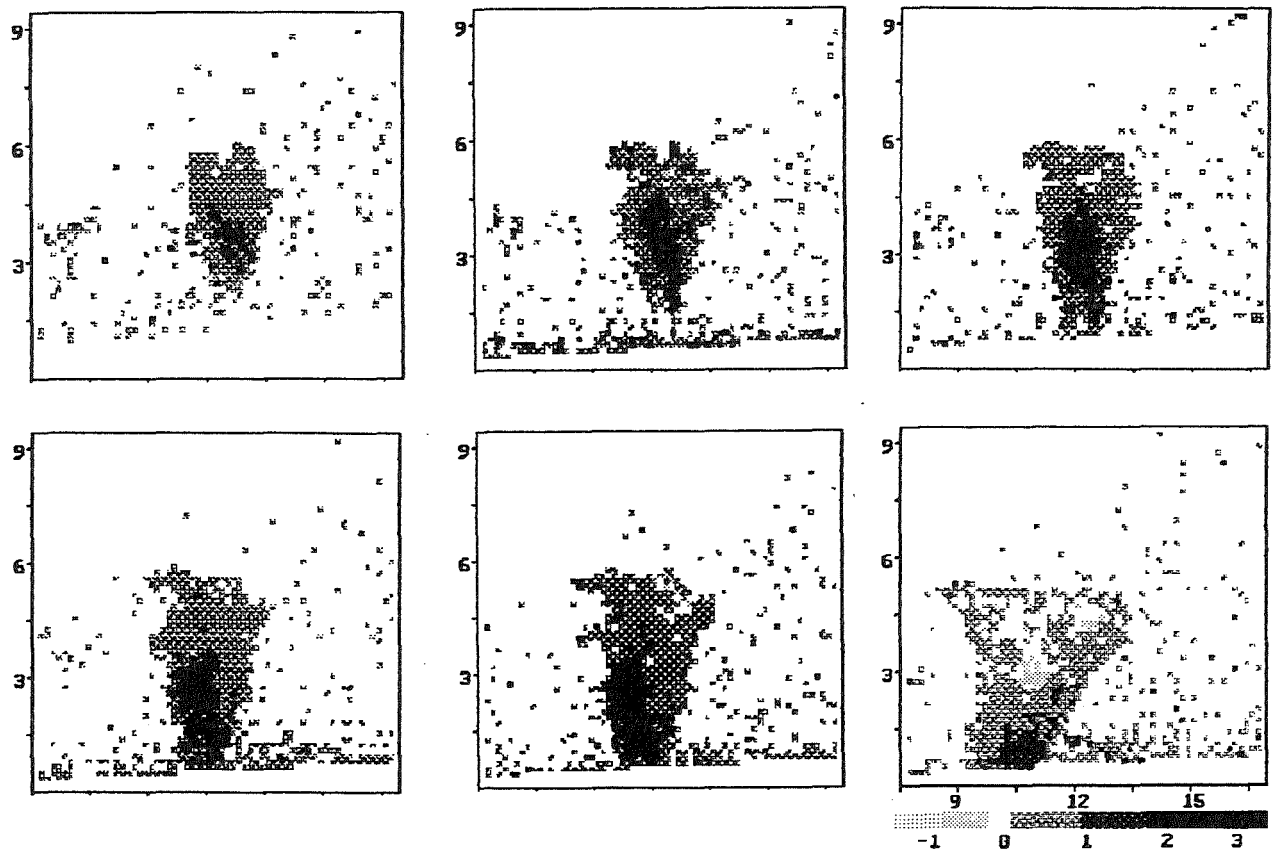

Figure 3. Z_{DR} measured in dB for times (GMT): a) 20:10:13; b) 20:11:24; c) 20:12:08; d) 20:13:04; e) 20:14:17; f) 20:20:04

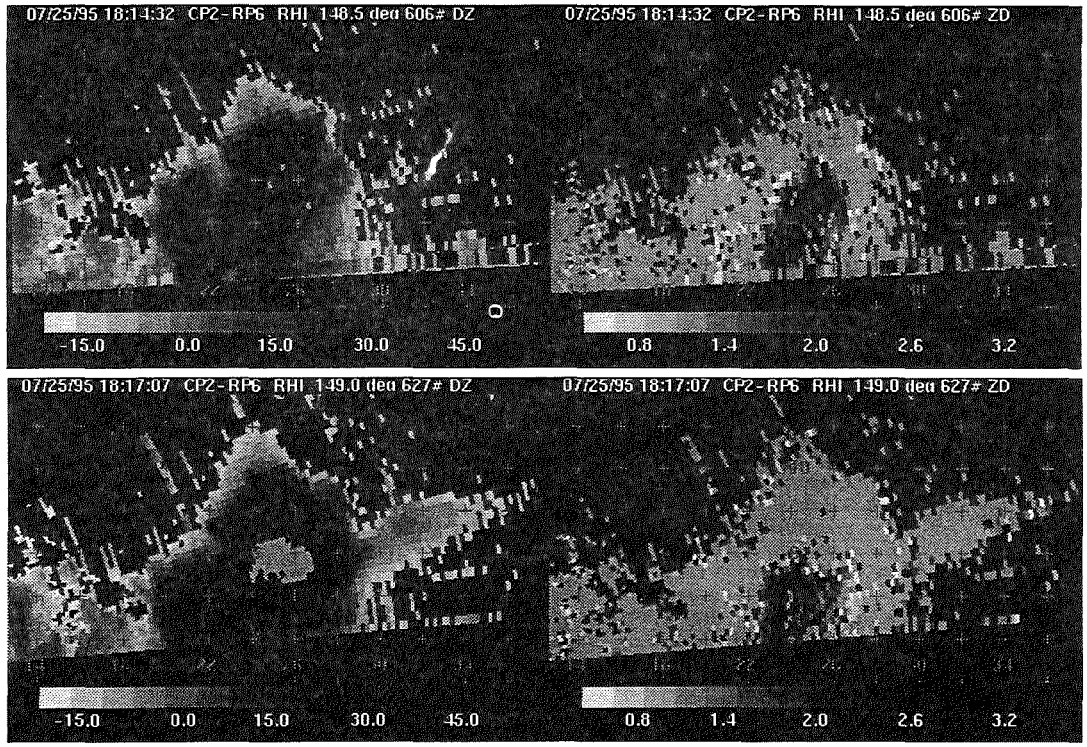

Figure 4. Vertical radar scans made with CP2, 25 July 1995. (a) Reflectivity (left) and Z_{DR} (right) at 18:14:32 GMT. The enhanced values of Z_{DR} from 4.5 - 6km indicate the presence of supercooled raindrops. (b) Reflectivity and Z_{DR} less than three minutes later at 18:17:07. Z_{DR} observations show that some of the raindrops had frozen since the earlier scan.

We note that raindrops continued to be observed in the two aircraft penetrations made after 19:10 on 10 August, 1987. In fact, raindrops were observed in a strong updraft at 19:20 at $T \approx$ -5°C. The presence of supercooled raindrops can be important for the development of ice, because of splinters that may be produced when the drops freeze (Chisnell and Latham 1976). In the radar data gathered in New Mexico (Figures 2 and 3) the graupel echo developed above and to the side of the supercooled raindrop echo subsequent to the inferred freezing of the raindrops. Observations made in the Florida cumuli show a similar effect. The graupel echos may have been produced by frozen raindrops and ice splinters ejected when the raindrops froze.

Acknowledgements. We are grateful for the help of Dr. Charles Knight in gathering the CP2 radar data and organising the project. This work was supported by the National Science Foundation under grants ATM-8914116 and ATM-9115694, and by the U.S. Air Force under grant AFOSR-89-0450. One of us (JL) is grateful for support from the UK Meteorological Office (Hadley Centre).

5 References

Blyth, A. M., and J. Latham, 1993: Development of ice and precipitation in New Mexican summertime cumulus clouds. *Quart. J. Roy. Meteorol. Soc.*, **119**, 91 - 120.

Chisnell, R. F., and J. Latham, 1976: Ice particle multiplication in cumulus clouds. *Quart. J. Roy. Meteorol. Soc.*, **102**, 133-156.

Krehbiel, P. R., T. Chen, S. McCrary, W. Rison, G. Gray, and M. Brook, 1996: The use of dual-channel circular-polarization radar observations for remotely sensing storm electrification. *Meteorol. and Atmos. Physics*. In press.